an Open Access Journal Published by MDPI

Impact Factor 1.3
CiteScore 2.3

International Journal of Turbomachinery, Propulsion and Power

mdpi.com/journal/ijtpp

EUROTURBO
european turbomachinery society

Message from the Editor-in-Chief

The *International Journal of Turbomachinery, Propulsion and Power* (*IJTPP*, ISSN 2504-186X) is owned by Euroturbo (www.euroturbo.eu), a not-for-profit international scientific organization legally established in February 2012. Euroturbo was founded by a group of committed scientists and engineers who have actively contributed to the success of several scientific events in the field of turbomachinery over the past twenty-five years. The Journal was conceived as an interdisciplinary dissemination tool and, although the core of the Journal focusses on the design, the Journal also engages the analysis, the modeling and testing of turbomachinery and turbomachinery-based propulsion and energy conversion systems. Technological innovation at system and component level, the development and application of new flow concepts, and advanced experimental and numerical techniques all fit naturally within the scope. The Journal welcomes manuscripts of high scientific quality addressing fundamental and applied issues of turbomachinery flows.

Editor-in-Chief
Prof. Marcello Manna

Associate Editors
Prof. Dr. Tony Arts
Prof. Dr. Gerard Bois
Prof. Dr. Cengiz Camci
Dr. Ruud Eggels
Prof. Dr. Peter Ireland
Prof. Dr. Reinhard Niehuis
Prof. Dr. Kenichiro Takeishi

Aims

International Journal of Turbomachinery, Propulsion and Power focuses on the current and future science and technology development of turbomachinery in the related fields of turbomachinery-based propulsion and power systems. Of primary interest are the thermodynamics, the fluid mechanics, the heat transfer and the applied combustion of aerospace, marine and industrial energy devices and systems, both from a component and system perspective. Likewise, fundamental and applied studies of energy conversion systems based on single or multi-phase fluid flows, single or multi-species, involving one or more turbomachines are solicited. The *IJTPP* is intended to offer a high quality research and development dissemination tool to colleagues with a primary interest in turbomachinery from academia, research institutes and industry.

Scope

- Turbomachinery
- Aerospace propulsion
- Marine propulsion
- Turbochargers
- Power generation
- Thermodynamics
- Fluid mechanics
- Heat Transfer
- Vibrations
- Aero-acoustics
- Applied combustion (aeronautic, aerospace, stationary power systems)
- Wind energy
- Marine energy

Author Benefits

Open Access

Unlimited and free access for readers

No Copyright Constraints

Retain copyright of your work and free use of your article

Thorough Peer-Review

Discounts on Article Processing Charges (APC)

If you belong to an institute that participates with the MDPI Institutional Open Access Program

No Space Constraints, No Extra Space or Color Charges

No restriction on the maximum length of the papers, number of figures or colors

Rapid Publication

A first decision is provided to authors approximately 63.9 days after submission; acceptance to publication is undertaken in 27.6 days (median values for papers published in this journal in the first half of 2024)

MDPI is a member of

Partner Society:
European Turbomachinery Society (Euroturbo)

Editorial Office
ijtpp@mdpi.com

MDPI
Grosspeteranlage 5
4052 Basel, Switzerland
Tel: +41 61 683 77 34
mdpi.com

July 2024

International Journal of
Turbomachinery
Propulsion and Power

MDPI

Article

Characterization of Unsteady Leakage Flow in an Axial Fan †

Matteo Dellacasagrande *, Edward Canepa ‡, Andrea Cattanei ‡ and Mehrdad Moradi ‡

Department of Mechanical, Energy, Management and Transportation Engineering (DIME), University of Genova, 16145 Genova, Italy; edward.canepa@unige.it (E.C.); andrea.cattanei@unige.it (A.C.); mehrdad.moradi@edu.unige.it (M.M.)

* Correspondence: matteo.dellacasagrande@edu.unige.it

† This paper is an extended version of our meeting paper ETC15-187 published in the 15th European Turbomachinery Conference, Budapest, Hungary, 24–28 April 2023.

‡ These authors contributed equally to this work.

Abstract: The present work reports an experimental study of the leakage flow in a low-speed fan ring. Existing 2D Particle Image Velocimetry (PIV) measurements taken in a meridional plane in front of the rotor gap have been further processed and analyzed by means of the Proper Orthogonal Decomposition (POD). Three values of the dimensionless pressure rise across the rotor have been investigated. Namely, attention has been focused on the intermediate case—the one for which a strong radial oscillation in the leakage flow has been observed: POD results have shown that, in this condition, the leakage flow exhibits periodic radial oscillations that are not correlated to the periodic blade passing. Moreover, such coherent motions have been found to promote turbulence transport at different radial positions, whereas rotor-related oscillations have a negligible effect in this sense. The present POD procedure can be generally applied to turbomachinery flows to characterize their unsteady behavior beside the classical phase-averaging methods based on rotor-related quantities. The present approach is novel for the study of leakage flow dynamics in axial fans.

Keywords: axial-flow fan; rotating shroud; leakage flow; PIV; POD

check for updates

Citation: Dellacasagrande, M.; Canepa, E.; Cattanei, A.; Moradi, M. Characterization of Unsteady Leakage Flow in an Axial Fan. *Int. J. Turbomach. Propuls. Power* **2023**, *8*, 34. https://doi.org/10.3390/ijtpp8030034

Academic Editor: Antoine Dazin

Received: 10 July 2023
Revised: 4 September 2023
Accepted: 7 September 2023
Published: 13 September 2023

Copyright: © 2023 by the authors. Licensee MDPI, Basel, Switzerland. This article is an open access article distributed under the terms and conditions of the Creative Commons Attribution (CC BY-NC-ND) license (https://creativecommons.org/licenses/by-nc-nd/4.0/).

1. Introduction

Axial fans employed in automotive cooling systems are commonly provided with a rotating shroud—a ring connecting the blade tips that improves the volumetric efficiency and also strengthens the whole assembly. Unfortunately, it causes a strong increase in the radiated noise due to the presence of coherent flow structures (Longhouse [1]) that are contained in the leakage flow released from the gap between the ring and the stationary enclosure and are eventually re-ingested by the rotor. Such a noise is often predominant in the low- to medium-frequency range and may also constitute the major contribution to the radiated power, e.g., see Canepa et al. [2,3]. The qualitative features of the leakage flow are known, e.g., see Fukano et al. [4], Fukano and Jang [5], Piellard et al. [6], Magne et al. [7], Moreau and Sanjose [8], Zenger et al. [9], Na et al. [10], Canepa et al. [11–13], and Zhu et al. [14]. However, coherent flow structures generally constitute a rather complicated fluid dynamic problem and, in the present case, their properties are not completely known: the fact that noise humps at sub-harmonics of the blade passing frequency appear indicates that they are co-rotating, but the relation with gap geometry and operating point is not completely clear. In order to find effective solutions for noise reduction and also to provide reliable test cases for numerical simulations, a deeper insight into these aspects is necessary.

The present paper continues the aerodynamic investigation reported in Canepa et al. [13], which was based on 2D PIV measurements taken in the meridional plane. In that study, a detailed analysis of the effect of the operating point on the leakage flow pattern was reported. Namely, it was showed that, about the design operating point, a sudden modification in the flow pattern takes place that strongly affects the radiated noise. This modification consists

of a switch between a recirculating flow attached to the ring lip and directly re-ingested by the rotor and a radial flow that mixes with the main rotor inflow after having left the measuring domain radially. By means of conditional averages, it was also shown that, when the modification takes place, both flow patterns are present together with all of the intermediate ones. However, it was not possible to deepen the features of the transition and also to determine whether such patterns follow a regular time sequence or they alternate randomly. In the present work, which is an extended version of the authors' conference paper Dellacasagrande et al. [15], the coherent flow structures embedded in the flow are studied by means of a POD-based procedure that employs the phase averaging technique previously presented in Lengani et al. [16]. This approach has allowed the identification of the periodic dynamics of the leakage flow that are not necessarily correlated to the rotor position.

2. Experimental Setup and Measuring Techniques

Data presented here are a part of the experimental database collected in the previous authors' work Canepa et al. [13]. The measurement campaign has been carried out in the DIME Aeroacoustics laboratory with the fan mounted on a test rig designed based on ISO 5801 norms; see Figure 1a. The tested rotor is a nine-blade aluminum prototype obtained by means of a numerically controlled milling machine (Figure 1b). The rotor stiffness prevents the geometry from being altered by aerodynamic load and centrifugal force, avoiding cross-effects on the modification of the leakage flow, e.g., see Canepa et al. [11]. The rotor has a tip radius r_{tip} of 222 mm, a hub-to-tip radius ratio r_{hub}/r_{tip} of 0.374, and a chord that varies between 43 mm and 50 mm from hub to tip. At the design point, the flow coefficient is $\Phi_{des} = Q_{des}/(u_{tip}\pi r_{tip}^2) = 0.0869$, and the pressure rise coefficient is $\Psi_{des} = \Delta p_{des}/(0.5\rho_0 u_{tip}^2) = 0.0993$, with Q the volume flow rate and Δp the fan pressure rise (outlet static pressure minus inlet total one). The measurements have been carried out at a constant rotational speed Ω of 2400 rev/min; depending on the operating point, the chord-based Reynolds number approximately ranges between 31,000 and 41,000 at the hub and between 186,000 and 188,000 at the tip. During the tests, Δp and Ω have been continuously measured. The rotational speed has been controlled by means of an optical tachometer and a stripe of reflecting tape stuck on one rotor blade, thus generating a one-per-revolution TTL signal. The gap between the rotating ring and the stationary casing is constituted by 5-mm-width axial and radial parts; see Figure 1c. In order to investigate the effect of pressure rise on the leakage flow dynamics, three Ψ values have been considered out of the 12 previously investigated in Canepa et al. [13], i.e., ψ = 0.0788, 0.0899, 0.103. At these operating points, the most interesting behavior of the leakage flow has been observed.

The flow field has been investigated in the meridional plane close to the tip gap by means of a 2D-PIV system, namely in a rectangular area located at $x = 3$ mm from the ring with an extension of $L_x = 123$ mm and $L_r = 171$ mm, i.e., $r/r_{tip} = 0.698 - 1.468$ and $x/r_{tip} = 0.014 - 0.581$; see Figure 1c. Measurements have been carried out using two cameras with a maximum frame rate of 6 Hz. The axial (u) and radial (v) velocity components have been obtained using a spatial cross-correlation function yielding instantaneous vector fields constituted by 83×116 points on a square grid of steps $\Delta x = \Delta r = 1.5$ mm. In the present measurement campaign, 2000 instantaneous vector fields have been collected, and the TTL signal generated by the optical tachometer has been employed as reference signal for the rotor-based ensemble average technique. Since the adopted PIV system does not allow the TTL signal to be used to trigger the PIV acquisition, the PIV snapshots have been ordered a posteriori for the computation of the rotor-based phase averaged field. The instantaneous vector fields have been sorted into 90 phase bins per revolution. In order to increase the statistical reliability, the data have been ensemble averaged over a blade pitch, yielding 10 meridional distributions based on about 198 samples. Other details on the experimental setup and measuring technique may be found in Canepa et al. [13].

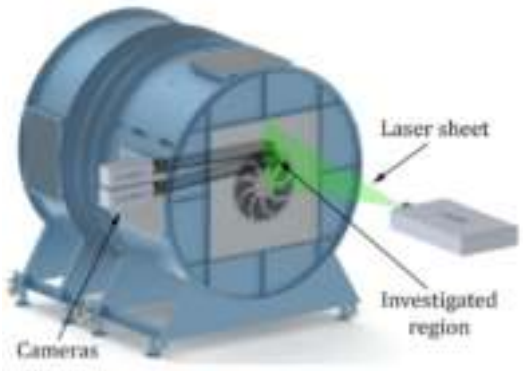

(**a**) ISO 5801 norm test rig.

(**b**) 9-blade aluminum fan.

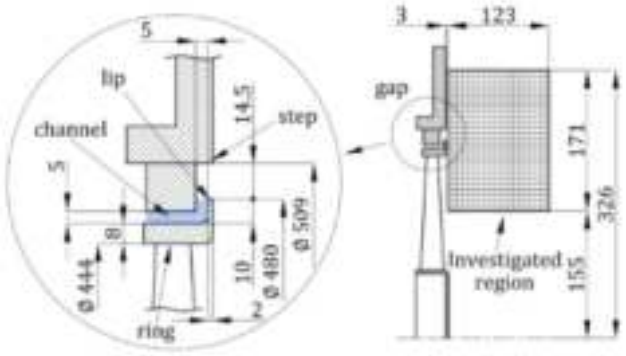

(**c**) Geometry of the gap region and PIV field of view.

Figure 1. (**a**) Experimental facility; (**b**) tested aluminum fan prototype; (**c**) geometry of the rotor gap region and measuring field of view.

3. Time Averaged Flow Field

Figure 2 provides the time-mean velocity fields with the contour plot of the overall turbulent kinetic energy (TKE) superimposed. For the case $\Psi = 0.0788$, the leakage flow is directly re-ingested by the rotor. This, together with the region of elevated TKE observed at about $1 < r/r_{tip} < 1.15$, makes this operating condition the most critical one in terms of noise production (see Canepa et al. [3]). A completely different scenario characterizes the flow case at $\Psi = 0.103$: the flow leaving the gap moves radially outwards and exits the measuring plane before entering the rotor. Therefore, the leakage flow does not directly interact with the rotor blades since it first mixes with the incoming flow at larger radii. Additionally, lower values of TKE are observed, with the maximum ones occurring for $r/r_{tip} > 1.1$.

The most interesting condition is the case $\Psi = 0.0899$. Here, the time-mean radial velocity ($\overline{v}$) is positive for $r/r_{tip} > 1$, thus leading to a larger recirculating region compared to the case $\Psi = 0.0788$. However, the leakage flow enters the rotor before leaving the measuring plane, in contrast to the case $\Psi = 0.103$. As shown in the following, a marked radial oscillation of the leakage flow is responsible for the enlarged region of high TKE values for $\Psi = 0.0899$ (see also Canepa et al. [13]). Otherwise, the conditions $\Psi = 0.0788$ and 0.103 have been found to be significantly more stable in terms of the leakage flow dynamics. Based on the above-reported observations, the present work focuses on the analysis of the case $\Psi = 0.0899$ and the associated unsteady behavior of the leakage flow. The aim is to inspect all the possible sources of periodic unsteadiness affecting the leakage flow dynamics, and that could not be necessarily linked to the rotor angular position. To this end, a POD-based phase averaging technique is employed for the detailed investigation of the coherent motions affecting the leakage flow for this specific flow case.

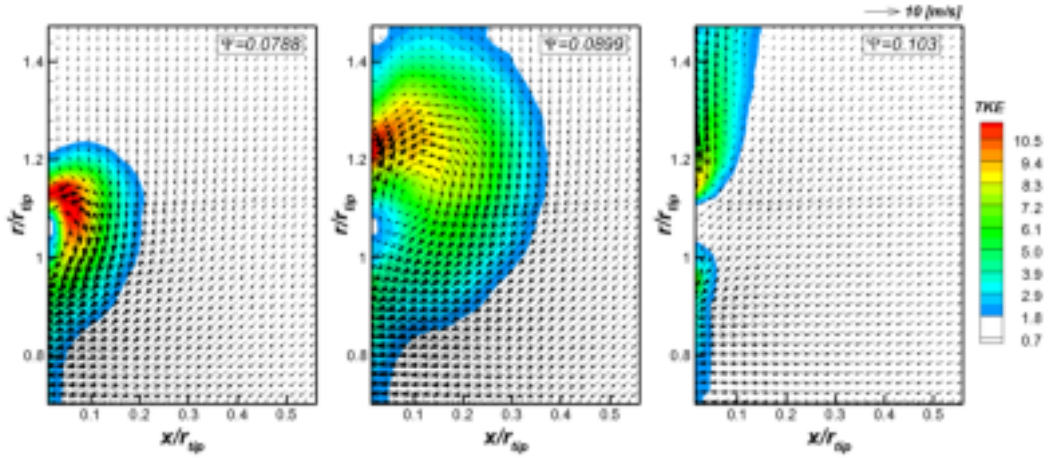

Figure 2. Vectorial representation of time-mean flow field with the contour plot of the overall TKE $[m^2/s^2]$ superimposed. The cases $\Psi = 0.0788$, 0.0899, and 0.103 are presented.

4. Proper Orthogonal Decomposition of Unsteady Leakage Flow

4.1. POD Mathematical Framework

The proper orthogonal decomposition was proposed first by Lumley [17] for the analysis of turbulent flows. Given a certain velocity field (i.e., $u(\boldsymbol{x}, t)$), the POD procedure provides spatial modes $\zeta(\boldsymbol{x})$ (resembling the flow structures) and temporal coefficients $\chi(t)$ (retaining the mode dynamics). According to the original formulation of Lumley [17], POD modes are computed as the eigenvectors of the spatial cross-correlation tensor of flow samples. In the present work, the successive formulation of Sirovich [18] has been adopted, in which the POD coefficients are directly obtained as the eigenvectors of the temporal cross-correlation matrix C:

$$CX = \Lambda X \tag{1}$$

where $C = U^T U$, U is the snapshot matrix containing the instantaneous realizations of the field, X is the matrix containing the eigenvectors of C, and Λ is a diagonal matrix with the sorted eigenvalues. Once the POD temporal coefficients are computed from Equation (1), the corresponding spatial modes are obtained by projection as

$$Z = UX\Lambda^{-\frac{1}{2}} \tag{2}$$

where Z is the matrix containing the POD modes $\zeta(\boldsymbol{x})$ normalized with their corresponding eigenvalues. POD can be also used to construct reduced order models providing a filtered snapshot matrix U_K that retains the contribution of the first K modes only. This is done by inverting Equation (2):

$$U_K = Z\Lambda^{\frac{1}{2}}X^T \tag{3}$$

where the last $N_t - K$ columns of Z are set to zero.

Once the POD modes have been computed, a POD-based phase averaging technique has been applied, where the reference signal is directly extracted from the leading modes (see Lengani et al. [16]). Particularly, if periodic convective structures occur within the flow, coupled modes are typically observed, i.e., modes with similar energy content and spatial distribution (see Legrand et al. [19]). Therefore, the corresponding low-order models can be used to sort the instantaneous snapshots based on the main period highlighted by the modes. According to Equation (3), the contribution of the kth POD mode to the ith PIV snapshot can be written as

$$u^{(k)}(x, r, t_i) = \zeta^{(k)}(x, r)\lambda^{(k)\frac{1}{2}}\chi^{(k)}(i) \tag{4}$$

where $\chi^{(k)}(i)$ is the ith element of the kth POD coefficient. Then, if the kth and the $(k+1)$th modes are coupled and representative of the same convective structures, the phase angle θ_i of the ith record is defined as

$$\theta_i = \frac{\zeta^{(k)}(x_1, r_1)\lambda^{(k)\frac{1}{2}}\chi^{(k)}(i)}{\zeta^{(k+1)}(x_2, r_2)\lambda^{(k+1)\frac{1}{2}}\chi^{(k+1)}(i)} \tag{5}$$

where (x_1, r_1) and (x_2, r_2) are control points used for the computation of each snapshot phase. According to the above-mentioned method, all snapshots may be sorted based on their corresponding phase angle, and a POD-based phase averaged velocity field can be computed. Since this work aims at the characterization of the radial motions involving the leakage flow, the POD modes of the radial velocity component are taken as reference for the present POD analysis. This latter has been carried out considering the quota of the fluctuating velocity field, which is not affected by the rotor position. Namely, the periodic components obtained from the rotor-based phase averaging procedure have been removed from the original snapshots before applying the POD procedure. This has been done because the rotor-based phase-averaged field, not shown here for brevity, did not show any radial oscillations of the flow leaving the gap; see Canepa et al. [13].

4.2. POD Analysis of Rotor-Unrelated Fluctuations

The dominant coherent motions that are not related to the rotor position are studied in this section by means of the Proper Orthogonal Decomposition. Figure 3 depicts the percentage energy of the first 20 POD modes obtained from the POD total kernel (i.e., filling the matrix U with both u and v, $uv-$modes) and from the radial velocity only ($v-$modes). For the cases $\Psi = 0.0788$ and 0.0899, the first mode of the total kernel captures more than 16% of the overall energy of fluctuations, while for $\Psi = 0.103$, the leading mode energy is significantly smaller. This indicates that for the cases $\Psi = 0.0788$ and 0.0899, the rotor-unrelated fluctuations are dominated by few large coherent patterns, which capture a higher quota of the turbulent kinetic energy compared to the case $\Psi = 0.103$. Similar considerations still hold for the POD modes of the radial velocity component. Interestingly, modes 3 and 4 of v show a similar energy content for the case $\Psi = 0.0899$ (Figure 3b), contrary to the other cases. As discussed in the following, these modes are representative of the same coherent structures, and they are referred to for the analysis of the unsteady behavior characterizing the leakage flow for this operating condition.

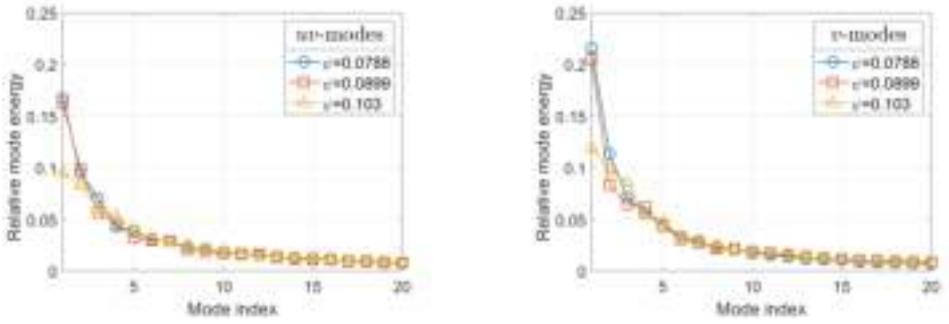

(**a**) (**b**)

Figure 3. Energy of (**a**) uv-modes and (**b**) v-modes for $\psi = 0.0788$, 0.0889, and 0.103. POD results are obtained considering the quota of velocity fluctuations that are unrelated to the rotor position.

Figure 4 shows exemplary modes of the total kernel for the three values of Ψ here considered. These modes have been chosen among the first 10 to highlight the main coherent patterns within the rotor-unrelated fluctuating velocity field. Modes among the first 10 showing similar patterns to those depicted in Figure 4 are not reported here for the sake of brevity. Additionally, the mode index strictly depends on the analysed flow case.

Beside the dominant POD modes, the probability density function (pdf) of the occurrence of vortical structures is shown for each case in the form of gray surfaces (bottom plots). Such pdf distributions have been obtained by means of a wavelet-based vortex identification technique (see Simoni et al. [20]) applied to the overall fluctuating velocity field, i.e., retaining also the rotor-related unsteadiness, in contrast to what has been done for the computation of the modes. Therefore, the comparison between the pdf and the POD mode distributions provides information about the spatial location of vortical structures that are or are not related to the rotor position. Particularly, one may clearly see that a dominant pdf peak occurs for all cases at the spatial positions where large-scale coherent structures are highlighted by the modes. Most of the vortical events observed in the present measuring plane are therefore not necessarily linked to the rotor position.

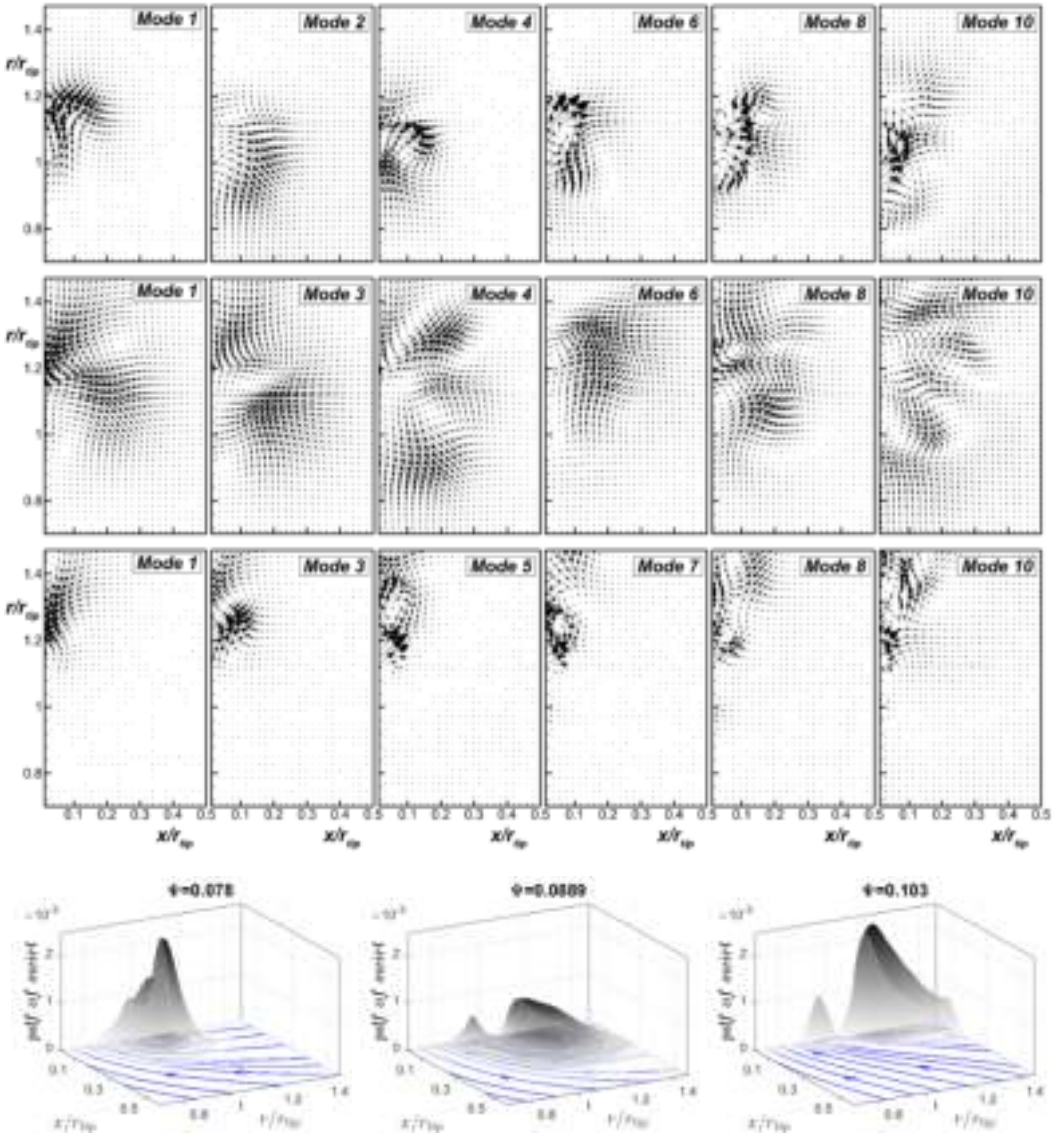

Figure 4. (**Top plots**): vectorial POD modes of rotor-unrelated fluctuations (from top to bottom $\Psi = 0.0788$, 0.0899, and 0.103). (**Bottom plots**): pdf of vortical events superimposed to the time-mean flow streamlines; probability density functions are computed considering the overall fluctuating velocity field.

For the case $\Psi = 0.0788$, the dominant POD modes resemble vortical structures near the rotor gap and the blade tip. They are representative of the coherent fluctuations of the leakage flow that, for the present case, stay attached to the rotor ring. In contrast, the

POD modes for the case ψ = 0.103 show regions of high vorticity for $r/r_{tip} > 1$, while the energy of the modes is almost null in front of the rotor blades. This clearly indicates that for $\Psi = 0.103$, the minor pdf peak observed in the blade region (i.e., $r/r_{tip} < 1$) is substantially linked to rotor related unsteadiness.

The modes computed for the case ψ = 0.0899 depict coherent fluctuations covering a wider spatial region than for the other cases; vorticity cores are indeed observed in the blade region as well as above the rotor gap, thus showing similarities with the cases at the lowest and the highest Ψ values. This is consistent with the increment of the pdf variance (i.e., the base area). Note that since the POD modes depicted in Figure 4 are obtained from the rotor-unrelated unsteadiness, the captured flow patterns are not linked to the rotor position. The flow features highlighted by the modes in front of the rotor blade are therefore expected to be linked to a different source of unsteadiness causing the radial motion of the flow leaving the gap. As a consequence, the pdf peak observed in the blade region for ψ = 0.0899 is due to the superposition of both rotor-related and -unrelated coherent vortical structures. It is mentioned here that based on the inherent three-dimensionality of the instigated flow field, the cores of vorticity observed in the present measuring plane may be the trace of vorticity tubes extending in the circumferential direction, as described in the previous authors' work Canepa et al. [3]. Nevertheless, the radial motions involving the leakage flow for the intermediate value of the pressure rise coefficient are shown to be well captured by the present set of measurements. Further measurements are being carried out to investigate the evolution of leakage flow fluctuations in the tangential direction.

The POD modes presented in Figure 4 highlighted existing similarities between the tested conditions. More precisely, the modes computed for the mid-pressure coefficient have been shown to partially resemble the coherent patterns highlighted by the leading modes obtained for the lowest and the highest pressure rises. This suggests that, for the intermediate pressure coefficient, the leakage flow oscillates between an attached-like (as for $\Psi = 0.0788$) and a radial-like (similar to the case $\Psi = 0.103$) configuration. In order to provide a quantitative view of the existing similarities between the dominant flow features occurring for the case ψ = 0.0899 and for the other two operating conditions, we computed the cross-correlation matrix of the spatial POD modes obtained independently for each value of the pressure coefficient. To this end, the POD modes have been normalized so that their scalar product provides a direct measurement of mode similarity. Figure 5a depicts the absolute value of the correlation matrix between the first 15 modes obtained for the cases ψ = 0.0899 and 0.0788, where modes 3 and 2, respectively, show the highest degree of correlation. On the other hand, modes 6 and 3 show the highest similarity when computing the POD correlation matrix for the cases ψ = 0.0899 and 0.103 (Figure 5b). The inspection of the spatial distributions of the correlating modes highlighted here (see Figure 4) provides evidence of the similarities between the flow cases. Mode 3 for the case ψ = 0.0899 depicts coherent fluctuations near the rotor gap, as in mode 2 for the case ψ = 0.0788. Otherwise, mode 6 is representative of vorticity nuclei that occur for $r/r_{tip} > 1$, similarly to mode 3 for the case ψ = 0.103. The fourth mode computed for the intermediate pressure coefficient shows instead coherent motions affecting the entire measuring plane, thus being representative of the leakage flow oscillation.

According to Equation (4), the POD temporal coefficients retain the contribution of the corresponding modes to each of the PIV snapshots. The inspection of the coefficients 3 and 6 for the case ψ = 0.0899 therefore provides the statistical distribution of the acquired velocity fields between the two flow states highlighted by the corresponding modes, which were shown to resemble the most *attached* and the most *radial*-like conditions. In this sense, all the PIV snapshots collected for the intermediate pressure rise can be reported in a 2D plane defined by the POD coefficients $\chi^{(6)} - \chi^{(3)}$, where the ith flow record is expressed in terms of the set of coordinates $\left(\chi^{(6)}(i), \chi^{(3)}(i)\right)$. This is shown in Figure 6a, where each symbol represents a different PIV snapshot in the coordinate system defined by the chosen temporal coefficients. These latter are computed by the projection of the snapshot matrix on the normalized modes; thus, their norms retain the energy of fluctuations. It is

worth noticing that the snapshots acquired for the case ψ = 0.0899 exhibit a quasi-Gaussian distribution on both coefficients (see Figure 6b,c). Therefore, the projection of the acquired snapshots onto the POD subspace defined by the coefficients 3 and 6 does not highlight any bi-modal distributions that may indicate the occurrence of well-defined clusters within the data associated to an intermittent flow pattern. The leakage flow is therefore expected to oscillate continuously between different states that rarely reach a pure radial and attached-like configuration. In the following section, the POD procedure presented in Section 4.1 is used to shed light on the coherent motions driving the radial fluctuations of the flow leaving the gap.

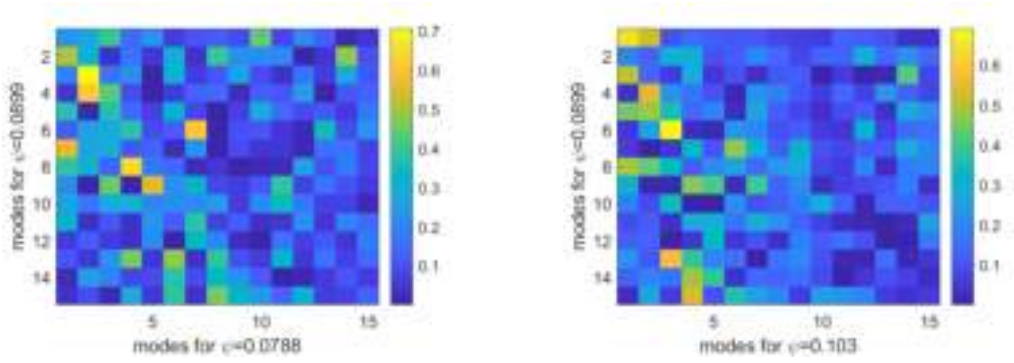

(**a**) (**b**)

Figure 5. Cross-correlation matrix of POD modes for the cases (**a**) ψ = 0.0788–0.0899 and (**b**) ψ = 0.103–0.0899.

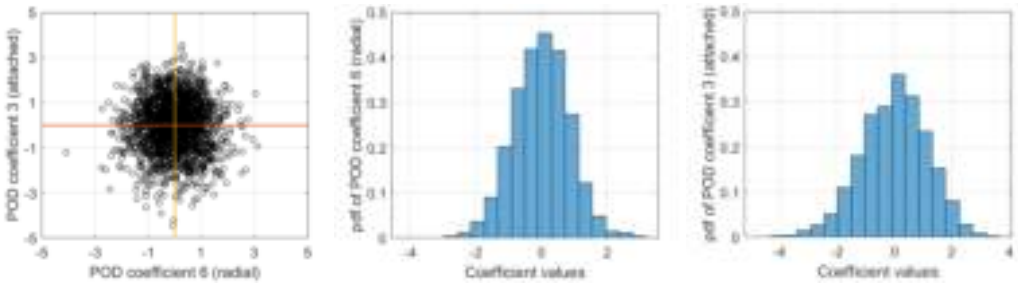

(**a**) (**b**) (**c**)

Figure 6. (**a**) Scatter plot of the POD coefficients 6 and 3 for the case ψ = 0.0899; each symbol refers to a different PIV snapshot, which in the present coordinate system is defined by the the corresponding coefficient values. (**b**) Probability density function of coefficient 6 for all snapshots; (**c**) probability density function of coefficient 3 for all snapshots.

4.3. Characterization of the Leakage Flow Dynamics for the Case Ψ *= 0.0899*

In order to investigate the oscillating behavior of the leakage flow for the case $\Psi = 0.0899$, the modes of v are further processed in this section. Particularly, modes 3 and 4 have been shown to be coupled in terms of their energy content (see the right plot of Figure 3, squared symbols) and their spatial distributions, which are reported in Figure 7a, are similar but shifted in the mean flow direction. According to Legrand et al. [19], these modes are therefore representative of the same periodic convective structures and can be used for the computation of a POD-based phase averaged velocity field. This may highlight the existing link between the periodic patterns captured by the modes and the oscillating behavior characterizing the leakage flow for $\Psi = 0.0899$. According to Equation (5), the phase related to each snapshot has been computed based on modes 3 and 4. To do that, two control points have been chosen in regions with the opposite sign of the modes (see the white crosses in Figure 7a). Once the correct phase angle is assigned to each flow record, the PIV snapshots can be re-ordered, and then the corresponding phase averaged field can be computed. Figure 7b reports the rotor-unrelated fluctuations in the radial direction

probed at the control point 1. Notice that the PIV snapshots have been acquired with a sampling rate that is significantly smaller than the characteristic frequencies of the flow field; thus, the flow records are randomly positioned within the main period highlighted by the modes. Instead, Figure 7c reports the sorted velocity values plotted versus the phase angle assigned to the corresponding snapshots. Additionally, the phase-averaged values obtained by means of a fifth-order polynomial fit to the phase-sorted velocity data are reported with a solid red line, showing a well defined periodic pattern. The present method has been applied to all measuring points to compute a POD-based phase averaged field retaining the periodic coherent motions that are not related to the rotor angular position.

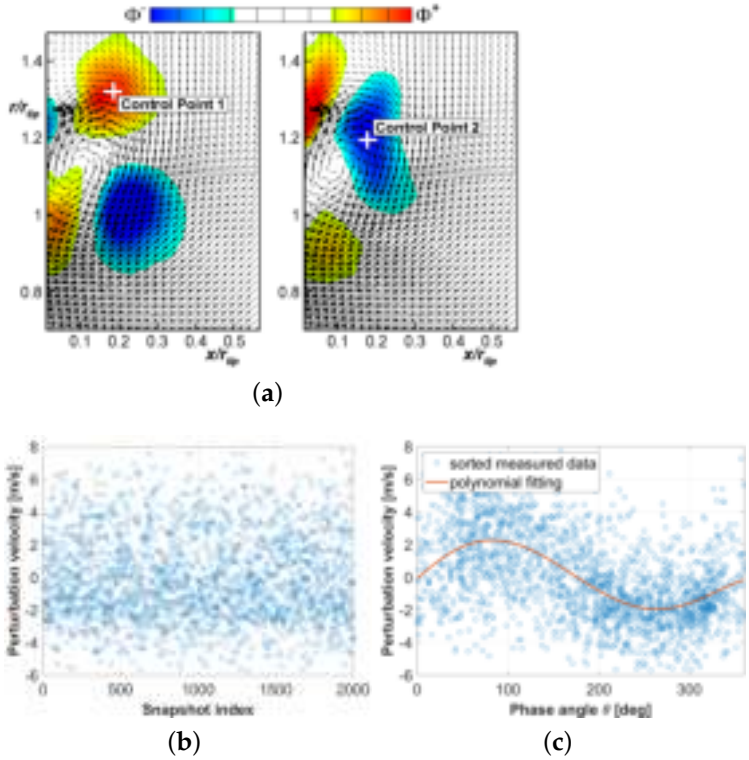

(**a**) (**b**) (**c**)

Figure 7. (**a**) Contour plots of normalized modes 3 and 4 of the radial velocity component superimposed to the vectorial representation of the time-mean velocity field; (**b**) non-sorted perturbation velocity values probed at control point 1; (**c**) sorted perturbation velocity values probed at control point 1 plotted as a function of the phase angle θ.

The top plot of Figure 8 reports the POD-based phase averaged fluctuating velocity field $(\hat{u}, \hat{v})$ at different phase angles, while in the bottom plot, the contribution of the time-mean velocity is also included, i.e., $(\hat{u} + \overline{u}, \hat{v} + \overline{v})$. The contour plot of $\hat{v}$ is also superimposed to the corresponding vector fields. It is mentioned here that even if the phase angle of each snapshot is computed with reference to modes 3 and 4 of the radial velocity only, the phase averaged field is computed considering all the dominant modes. The snapshots reported in the top plots of Figure 8 depict counter rotating vortices that form near the blade tip (see the red and blue circles in the plots). These are the signatures of vorticity tubes that evolve in the tangential direction as described by Canepa et al. [3]. Once formed, they rotate and then move towards the rotor inlet section (see the plots at $\theta = 120°$ and $300°$). For $300° < \theta < 360°$, a new vortex-like structure is expected to occur outside of the measuring plane ($r/r_{tip} > 1.3$). Such a structure moves at lower radii leading to the flow pattern observed in the first plot ($\theta = 0°$). It is worth noting that the periodic fluctuations highlighted by the present procedure are characterized by the inversion of the radial velocity component from the largest positive values observed for $\theta = 60°$ to the most negative ones occurring for $\theta = 240°$. This is further highlighted in Figure 9, showing the velocity data probed above the blade tip at $x/r_{tip} = 0.05$ and $r/r_{tip} = 1.3$. The same trend

was not observed instead in the rotor-based phase-averaged field (see Canepa et al. [3]). Interestingly, when the periodic fluctuations depicted in the top plots of Figure 8 are added to the time-mean velocity field (bottom plots), this latter exhibits a marked vertical motion in the surrounding area of the rotor gap. The large scale vortical structure centered at about r/r_{tip} = 1.1 for $\theta = 0°$ stretches in the vertical direction, and v again switches from negative to positive values for r/r_{tip} >1.22. The present results clearly indicate that the oscillating behavior and the mean flow deformation observed for ψ = 0.0889 are linked to the periodic motion of the coherent structures related to modes 3 and 4 of v, which is independent of the rotor position. The computation of its own frequency would therefore be of great relevance. Nevertheless, it may not be directly provided from the present set of measurements due to the low sampling rate adopted. Further investigations will be carried out in a dedicated work for the detailed inspection of the frequency content of the flow patterns depicted in Figure 8.

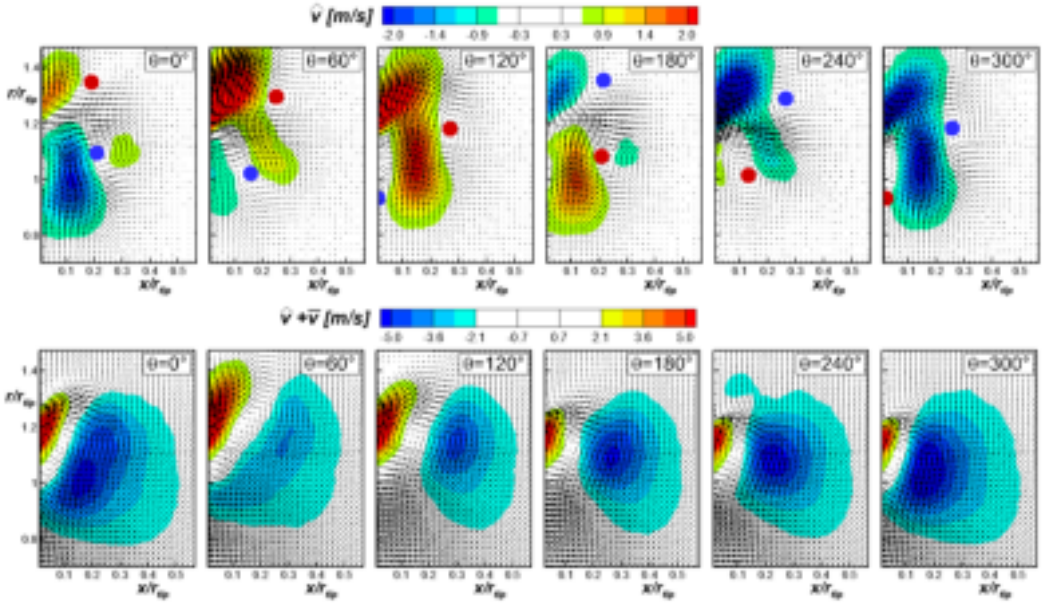

Figure 8. (**Top**): POD-based phase-averaged field of the rotor-unrelated unsteadiness at fixed phase angles. (**Bottom**): POD-based phase-averaged field of the rotor-unrelated unsteadiness summed up to the time-mean velocity field.

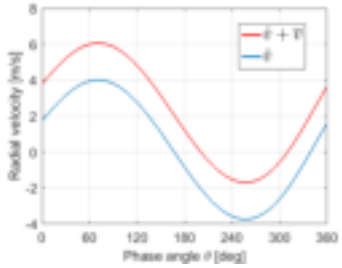

Figure 9. Radial component of POD averaged unresolved velocity $\hat{v}$ with (red) and without (blue) the contribution of the time averaged field. Data are probed at $x/r_{tip} = 0.05$ and $r/r_{tip} = 1.3$.

With the aim of inspecting the regions of the measuring plane that are mostly affected by the coherent motions embedded in the flow, the energy of the periodic fluctuations provided by the rotor-based and POD-based phase averaging procedures has been computed. The so-derived energy distributions are compared in Figures 10 snd 11 with the energy of the overall axial and radial fluctuating velocities. The highest energy of the rotor phased field (subscript *rotor*) are found in the blade and the gap regions for both the velocity components. In contrast, the energy of the periodic motions highlighted in Figure 8 is maximum above the rotor gap. This further highlights the role of the rotor-unrelated

fluctuations in promoting the vertical motion of the leakage flow above the gap region. Moreover, the energy of the POD phased radial fluctuations are significantly larger than those phased with the rotor period. When comparing the contributions due to the periodic sources of unsteadiness with the overall energy of fluctuations, one can see that this latter is much larger compared to the others. This indicates that the unresolved unsteadiness plays a key role in the definition of the overall energy of fluctuations, especially for what concerns the radial velocity component. In the next section, the POD- and the rotor-based phase averaged fields are referred to for the computation of the phase averaged distributions of the quasi turbulent kinetic energy and its production, thus showing the effects of the different periodic source of unsteadiness on turbulence generation and transport.

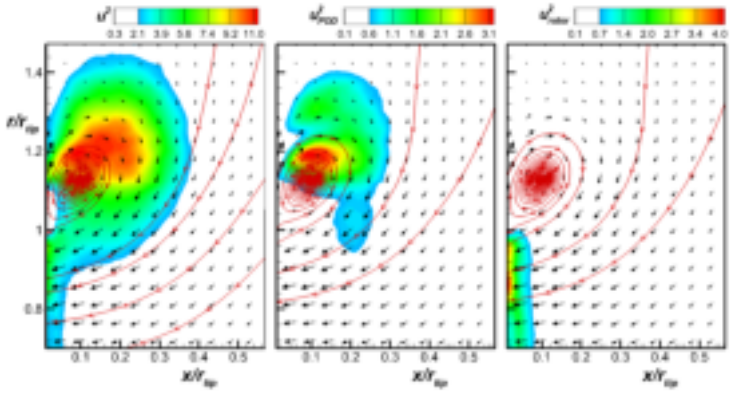

Figure 10. Contour plots of the energy of axial velocity fluctuations computed from the overall velocity field (left, u^2), from the POD phase averaged field (center, u^2_{POD}), and from the rotor-related fluctuations (right, u^2_{rotor}). The time-mean vector field is reported. Time-mean streamlines are depicted with red color.

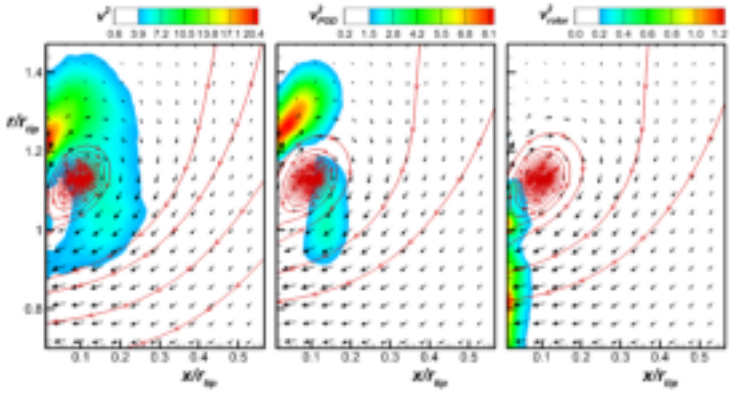

Figure 11. Contour plots of the energy of radial velocity fluctuations computed from the overall velocity field (left, v^2), from the POD phase averaged field (center, v^2_{POD}), and from the rotor related fluctuations (right, v^2_{rotor}). The time-mean vector field is reported. Time-mean streamlines are depicted with red color.

4.4. Phase Averaged Distributions of Quasi Turbulent Kinetic Energy and Its Production.

This section reports the phase-averaged TKE distributions based on the blade period and the periodic motion extracted by the modes. Additionally, the TKE production has been computed based on phase averaged quantities (see e.g., Michelassi and Wissink [21]):

$$\langle P_{TKE} \rangle = \left\langle \overline{u'^2} \right\rangle \frac{\partial \langle \hat{u} \rangle}{\partial x} + \left\langle \overline{v'^2} \right\rangle \frac{\partial \langle \hat{v} \rangle}{\partial r} + \left\langle \overline{u'v'} \right\rangle \left(\frac{\partial \langle \hat{u} \rangle}{\partial r} + \frac{\partial \langle \hat{v} \rangle}{\partial x} \right) \tag{6}$$

where $\langle \cdot \rangle$ denotes phase dependent quantities, (u', v') is the turbulent velocity field, and $(\hat{u}, \hat{v})$ is the phase averaged one. The stress terms appearing in Equation (6) have been

computed from the non-periodic unsteadiness, which has been obtained by subtracting the rotor- and POD-based phase averaged fields from the overall fluctuating velocity. Then, the measured data have been sorted based on the corresponding phase index of the two periodic patterns and then combined with the strain tensor accounting for the deformation of the mean and phase dependent fields.

Figure 12 shows the contour plots of the rotor-based phase-averaged turbulent kinetic energy ($\langle TKE \rangle_{ROT}$) and its related production ($\langle P_{TKE} \rangle_{ROT}$). Plots are shown at the phase angles $\theta = 0°, 72°, 144°, 216°$ and $288°$. Additionally, the gradient vectors of $\hat{u}$ and $\hat{v}$ are depicted with black and red color, respectively, to highlight the regions of high strain. Interestingly, both $\langle TKE \rangle_{ROT}$ and $\langle P_{TKE} \rangle_{ROT}$ show negligible variations with the phase angle; thus, the turbulent kinetic energy and its production do not depend on the rotor phase. Moreover, the maximum of both quantities is observed in the gap region where the largest gradients of the phase-averaged field occur. Turbulence production is therefore given by the combination of high levels of phase dependent strain with turbulent stresses. It is worth noting that both positive and negative values of $\langle P_{TKE} \rangle_{ROT}$ are observed for all phase angles. The occurrence of negative $\langle P_{TKE} \rangle_{ROT}$ indicates energy back transfer from the unresolved unsteady field to the corresponding phase-averaged one. However, the integral value of $\langle P_{TKE} \rangle_{ROT}$ is positive, thus leading to the increment of the overall turbulence level within the flow field.

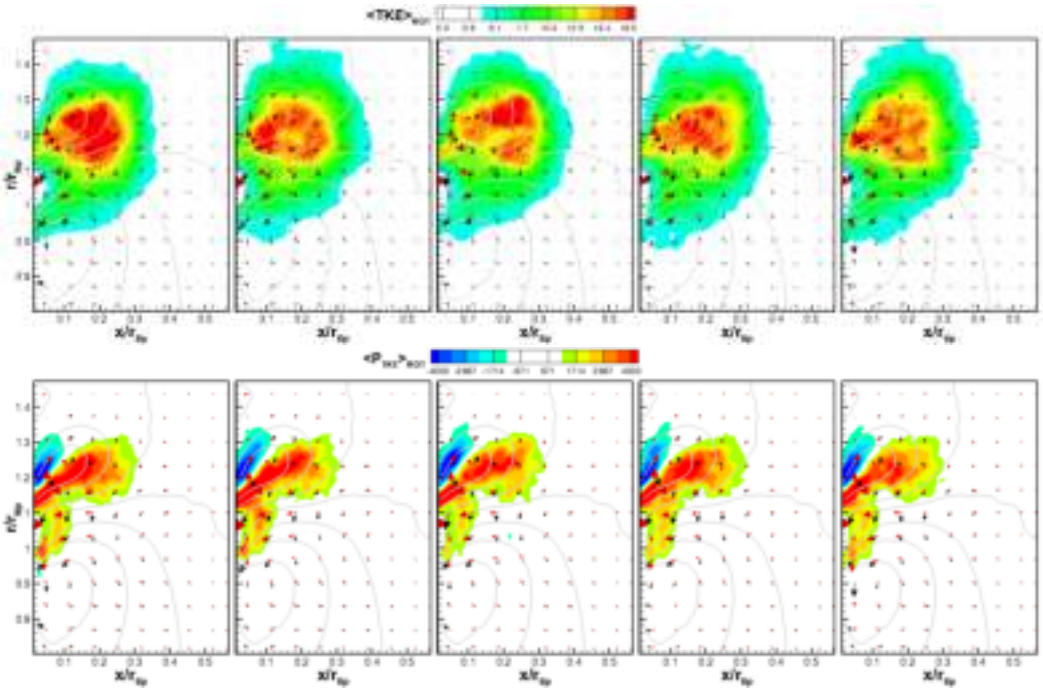

Figure 12. (**Top**): Contour plot of rotor-based phase-averaged turbulent kinetic energy based on blade period $\langle TKE \rangle_{ROT} [m^2/s^2]$. (**Bottom**): Contour plot of phase-averaged turbulent kinetic energy production based on blade period $\langle P_{TKE} \rangle_{ROT} [m^2/s^3]$. Plots are shown at the phase angles $\theta = 0°, 72°, 144°, 216°$ and $288°$. Black and red vectors represent the axial and radial velocity gradients, respectively, of the phase averaged field. Contour lines of time-mean axial velocity are shown with grey color.

A completely different scenario characterizes the POD-based phase averaged TKE ($\langle TKE \rangle_{POD}$) and related production ($\langle P_{TKE} \rangle_{POD}$), see Figure 13. The $\langle TKE \rangle_{POD}$ distribution shows high dependence on the phase angle in terms of its maximum values and their spatial positions. The highest values of $\langle TKE \rangle_{POD}$ always occur for $r/r_{tip} > 1$, while lower ones are observed in front of the blade. Additionally, the region of maximum TKE moves at different radii within the reference period. This behavior well resembles the one observed in the phase-averaged field reported in Figure 8. This indicates that the periodic pattern

highlighted by the POD analysis may cause turbulence transport at different radial locations. Since the interaction between the flow unsteadiness generated by the leakage flow and the rotor may produce different noise levels depending on the region where interaction occurs, the capability of the currently adopted procedure in highlighting turbulence transport due to coherent motions within the flow might be useful for the acoustic optimization of the aerodynamic component tested here. Interestingly, negative values of $\langle P_{TKE} \rangle_{POD}$ dominate; thus, the periodic motion captured by the POD modes is mostly responsible for energy back transfer from the unresolved to the POD-based phased-averaged velocity field. This behavior is different from what has been found based on the rotor-based phase averaging procedure.

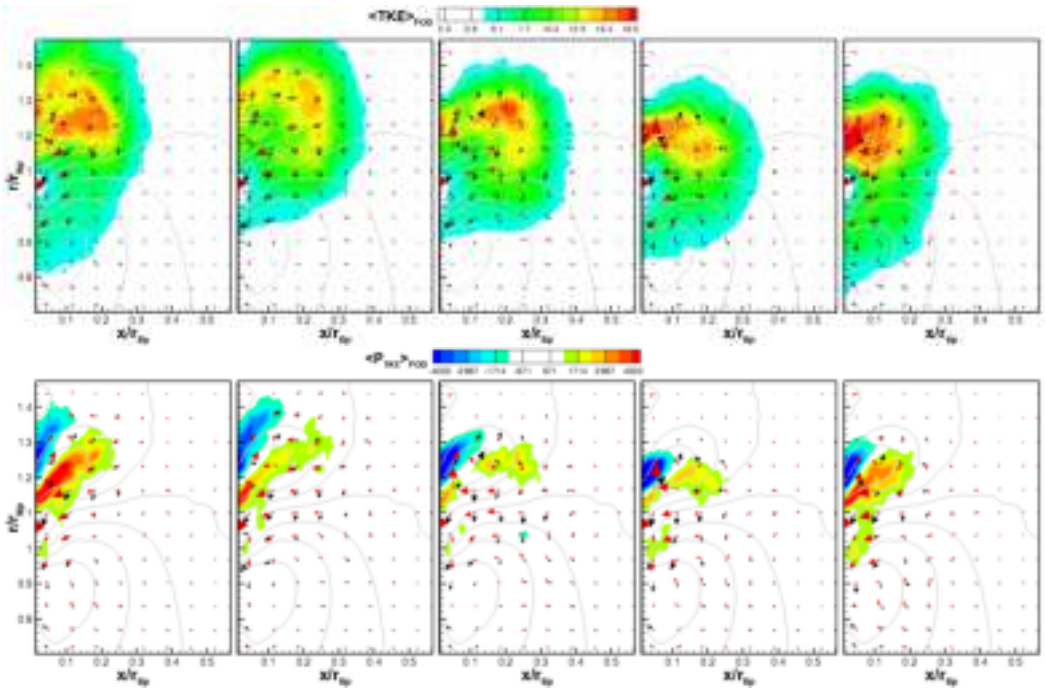

Figure 13. (**Top**): Contour plot of POD-based phase-averaged turbulent kinetic energy $\langle TKE \rangle_{POD} [m^2/s^2]$. (**Bottom**): Contour plot of POD-based phase-averaged turbulent kinetic energy production $\langle P_{TKE} \rangle_{POD} [m^2/s^3]$. Plots are shown at the phase angles $\theta = 0°, 72°, 144°, 216°$ and $288°$. Black and red vectors represent the axial and radial velocity gradients, respectively, of the phase averaged field. Contour lines of time-mean axial velocity are shown with grey color.

5. Conclusions

The present work presented a POD-based analysis of the unsteady leakage flow of an axial fan equipped with rotating shroud. Three values of the loading coefficients have been examined, among which the intermediate loading one has showed a strongly unsteady behavior of the flow leaving the gap. For this operating condition, the leakage flow has been found to move at different radial positions, while it is significantly more stable for the other cases. The POD-based technique adopted here has clearly shown that this behavior is governed by the occurrence of coherent vortical structures characterized by a marked periodicity that is different from the blade passing period. Indeed, the rotor-based phased-averaged field did not show any coherent motions affecting the leakage. Herein, POD-based phase-averaged TKE and P_{TKE} distributions have been computed and then compared to those obtained based on the rotor reference. Rotor-unrelated fluctuations have been shown to provoke high turbulence transport at different radial positions, thus possibly affecting the noise generation of the rotor. The phase averaging procedure here adopted is therefore thought to be functional to the acoustic optimization of a wide range of aerodynamic components, other than that tested here.

Author Contributions: Conceptualization, E.C. and A.C.; methodology, E.C. and M.M.; software, M.D.; validation, M.D. and E.C.; writing—original draft preparation, M.D. and A.C.; writing—review and editing, M.D. All authors have read and agreed to the published version of the manuscript.

Funding: This research received no external funding.

Institutional Review Board Statement: Not applicable.

Informed Consent Statement: Not applicable.

Data Availability Statement: Data are available upon reasonable request to the authors.

Conflicts of Interest: The authors declare no conflict of interest.

Abbreviations

The following abbreviations are used in this manuscript:

PIV	Particle Image Velocimetry
POD	Proper Orthogonal Decomposition
LDV	Laser Doppler Velocimetry
TKE	Turbulent Kinetic Energy
P_{TKE}	Production of Turbulent Kinetic Energy
ROT	Rotor

References

1. Longhouse, R. Control of tip-vortex noise of axial flow fans by rotating shrouds. *J. Sound Vib.* **1978**, *58*, 201–214. [CrossRef]
2. Canepa, E.; Cattanei, A.; Zecchin, F.M.; Milanese, G.; Parodi, D. An experimental investigation on the tip leakage noise in axial-flow fans with rotating shroud. *J. Sound Vib.* **2016**, *375*, 115–131. [CrossRef]
3. Canepa, E.; Cattanei, A.; Mazzocut Zecchin, F. Leakage noise and related flow pattern in a low-speed axial fan with rotating shroud. *Int. J. Turbomach. Propuls. Power* **2019**, *4*, 17. [CrossRef]
4. Fukano, T.; Takamatsu, Y.; Kodama, Y. The effects of tip clearance on the noise of low pressure axial and mixed flow fans. *J. Sound Vib.* **1986**, *105*, 291–308. [CrossRef]
5. Fukano, T.; Jang, C.M. Tip clearance noise of axial flow fans operating at design and off-design condition. *J. Sound Vib.* **2004**, *275*, 1027–1050. [CrossRef]
6. Piellard, M.; Coutty, B.B.; Le Goff, V.; Vidal, V.; Perot, F. Direct aeroacoustics simulation of automotive engine cooling fan system: effect of upstream geometry on broadband noise. In Proceedings of the 20th AIAA/CEAS Aeroacoustics Conference, Atlanta, GA, USA, 16–20 June 2014; p. 2455.
7. Magne, S.; Moreau, S.; Berry, A. Subharmonic tonal noise from backflow vortices radiated by a low-speed ring fan in uniform inlet flow. *J. Acoust. Soc. Am.* **2015**, *137*, 228–237. [CrossRef]
8. Moreau, S.; Sanjose, M. Sub-harmonic broadband humps and tip noise in low-speed ring fans. *J. Acoust. Soc. Am.* **2016**, *139*, 118–127. [CrossRef]
9. Zenger, F.J.; Renz, A.; Becher, M.; Becker, S. Experimental investigation of the noise emission of axial fans under distorted inflow conditions. *J. Sound Vib.* **2016**, *383*, 124–145. [CrossRef]
10. Na, G.D.; Kameier, F.; Springer, N.; Mauß, M.; Paschereit, C. URANS simulations and experimental investigations on unsteady aerodynamic effects in the blade tip region of a shrouded fan configuration. *Turbo Expo Power Land Sea Air. Am. Soc. Mech. Eng.* **2017**, *50770*, V001T09A003.
11. Canepa, E.; Cattanei, A.; Jafelice, F.; Zecchin, F.M.; Parodi, D. Effect of rotor deformation and blade loading on the leakage noise in low-speed axial fans. *J. Sound Vib.* **2018**, *433*, 99–123. [CrossRef]
12. Canepa, E.; Cattanei, A.; Zecchin, F.M.; Parodi, D. Large-scale unsteady flow structures in the leakage flow of a low-speed axial fan with rotating shroud. *Exp. Therm. Fluid Sci.* **2019**, *102*, 1–19. [CrossRef]
13. Canepa, E.; Cattanei, A.; Moradi, M.; Nilberto, A. Experimental Study of the Leakage Flow in an Axial-Flow Fan at Variable Loading. *Int. J. Turbomach. Propuls. Power* **2021**, *6*, 40. [CrossRef]
14. Zhu, T.; Lallier-Daniels, D.; Sanjosé, M.; Moreau, S.; Carolus, T. Rotating coherent flow structures as a source for narrowband tip clearance noise from axial fans. *J. Sound Vib.* **2018**, *417*, 198–215. [CrossRef]
15. Dellacasagrande, M.; Canepa, E.; Cattanei, A.; Moradi, M. Characterization of the unsteady leackage flow in an axial fan. In Proceedings of the 15th European Turbomachinery Confeerence, Paper n. ETC2023-187, Budapest, Hungary, 24–28 April 2023. Available online: https://www.euroturbo.eu/publications/conference-proceedings-repository/ (accessed on 3 September 2023).
16. Lengani, D.; Simoni, D.; Ubaldi, M.; Zunino, P. POD analysis of the unsteady behavior of a laminar separation bubble. *Exp. Therm. Fluid Sci.* **2014**, *58*, 70–79. [CrossRef]
17. Lumley, J.L. Stochastic Tools in Turbulence. *Appl. Math. Mech.* **1970**, *12*, 1–194.
18. Sirovich, L. Turbulence and the dynamics of coherent structures. Part I–III. *Q. Appl. Math.* **1987**, *45*, 561–590. [CrossRef]

19. Legrand, M.; Nogueira, J.; Lecuona, A. Flow temporal reconstruction from non-time-resolved data part I: Mathematic fundamentals. *Exp. Fluids* **2011**, *51*, 1047–1055. [CrossRef]
20. Simoni, D.; Lengani, D.; Guida, R. A wavelet-based intermittency detection technique from PIV investigations in transitional boundary layers. *Exp. Fluids* **2016**, *57*, 145. [CrossRef]
21. Michelassi, V.; Wissink, J.G. Turbulent kinetic energy production in the vane of a low-pressure linear turbine cascade with incoming wakes. *Int. J. Rotat. Mach.* **2015**, *2015*, 650783. [CrossRef]

Disclaimer/Publisher's Note: The statements, opinions and data contained in all publications are solely those of the individual author(s) and contributor(s) and not of MDPI and/or the editor(s). MDPI and/or the editor(s) disclaim responsibility for any injury to people or property resulting from any ideas, methods, instructions or products referred to in the content.

International Journal of
Turbomachinery Propulsion and Power

MDPI

Article

Acoustic Boundary Conditions for Can-Annular Combustors †

James Brind

Whittle Laboratory, University of Cambridge, Cambridge CB3 0DY, UK; jb753@cam.ac.uk

† This paper is an extended version of our ETC15-140 paper published in the Proceedings of the 15th European Turbomachinery Conference, Budapest, Hungary, 24–28 April 2023.

Abstract: This paper derives and validates an analytical model for acoustic boundary conditions on a can-annular gas turbine combustion system composed of discrete cans connected to an open annulus upstream of a turbine. The analytical model takes one empirical parameter: a connection impedance between adjacent cans. This impedance is extracted from time-marching computations of two-can sectors of representative combustors. The computations show that reactance follows the Rayleigh conductivity, while resistance takes a value of order 0.1 as a weak function of geometry. With a calibrated value of acoustic resistance, the analytical model reproduces can-to-can transfer functions predicted by full-annulus computations to within 0.03 magnitude at compact frequencies. Varying the combustor–turbine gap length, both model and computations exhibit a minimum in reflected energy, which drops by 63% compared to the datum gap. A parametric study yields a design guideline for gap length at the minimum reflected energy, allowing the designer to maximise transmission from the combustion system and reduce damping requirements.

Keywords: can-annular; combustor; turbine; acoustic impedance; aeroacoustics

1. Introduction

In gas turbine combustors, thermoacoustic instability is a self-excited oscillation caused by feedback between unsteady heat release and acoustic waves. The resulting large pressure fluctuations are undesirable for noise and structural design considerations. In-phase pressure and heat release perturbations act as a source of acoustic energy, which a designer balances against acoustic losses by transmission through the turbine and damping devices. Therefore, predicting thermoacoustic instability requires a combustor model with accurate boundary conditions to characterise waves reflected from the turbine interface.

Industrial gas turbines use can-annular combustion systems, where transition ducts connect discrete burners to an axial gap upstream of the turbine nozzle guide vane. Due to rotational symmetry, historical design practice has assumed a single can to be a good model of the entire combustion system. This simplification is convenient, as experimental or computational costs scale with the number of cans under test, but neglects coupling between adjacent cans by azimuthal waves.

Kaufmann et al. [1] measured a peak in the pressure fluctuation spectra of an annular rig which was not present in a single-can test. Quarter-annulus thermoacoustic computations were sufficient to capture the extra peak, and revealed that it corresponds to a 'push-pull' mode where adjacent cans oscillate in antiphase. Venkatesan et al. [2] showed experimentally that blocking the connection area in the combustor–turbine gap suppressed a 'push–pull' mode in their two-can test apparatus.

Ghirardo et al. [3] performed Helmholtz simulations of a can-annular combustor and provided experimental evidence of their predicted azimuthal mode shapes. The simulations yielded boundary conditions suitable for thermoacoustic modelling: acoustic wave transfer functions between all possible can pairs. They emphasise that stability is a system property and can only be determined by a system thermoacoustic model including a ring of reacting burners linked by a complete set of can-to-can transfer functions.

check for updates

Citation: Brind, J. Acoustic Boundary Conditions for Can-Annular Combustors. *Int. J. Turbomach. Propuls. Power* **2023**, *8*, 32. https://doi.org/10.3390/ijtpp8030032

Academic Editor: Antoine Dazin

Received: 8 June 2023
Revised: 11 July 2023
Accepted: 4 September 2023
Published: 8 September 2023

Copyright: © 2023 by the author. Licensee MDPI, Basel, Switzerland. This article is an open access article distributed under the terms and conditions of the Creative Commons Attribution (CC BY-NC-ND) license (https://creativecommons.org/licenses/by-nc-nd/4.0/).

In an iterative design process, a low-order model is useful to complement more time-consuming experimental testing or numerical computations. von Saldern et al. [4] used mass conservation over a compact gap and a Rayleigh conductivity for the connection impedance between adjacent cans to develop analytical expressions for can transfer functions at low reduced frequencies. Their predictions are qualitatively similar to the can transfer functions from the simulations of Ghirardo et al. [3]. Fournier et al. [5] showed that augmenting the Rayleigh conductivity with a characteristic length, a function of azimuthal mode empirically fitted from two-dimensional Helmholtz simulations, matches acoustic impedance phase results to within 2%.

Overall, the literature shows that a single-can combustor model, lacking communication between cans, is not representative of a can-annular combustor. The connection impedance model of von Saldern et al. [4] is promising; instability frequencies in large industrial gas turbines are typically low and in the compact regime. However, the empirical connection impedance parameter has not been characterised in fully representative configurations.

The present work first determines the sensitivity of connection impedance to geometry by extracting values from non-linear time marching computations of two-can combustor sectors. Then, analytical and numerical full-annulus predictions of can transfer functions are compared. Finally, the analytical model is used to explore the can-annular combustor design space.

This paper, an extended version of a previous conference submission [6], makes the following contributions:

- Validation of the von Saldern et al. [4] connection impedance model in an industrially representative can-annular combustor;
- Clarification of the importance of intra-can acoustic resistance in predicting can-to-can transfer functions;
- A new design guideline for selection of combustor–turbine gap to minimise reflected energy, hence easing stability issues by reducing the required damping.

2. Connection Impedance Analytical Model

The current analytical model follows the method proposed by von Saldern et al. [4] and later extended by Orchini [7]. This section gives a derivation that includes the effect of a general downstream impedance without other complications. In outline: the model conserves mass over the combustor–turbine gap, an empirical connection impedance relates intra-can velocities with pressure fluctuations in adjacent cans, and a Fourier series relates the pressure in adjacent cans by a phase shift.

The model makes four assumptions: (i) acoustic wavelength is much larger than can or gap cross-sections, so that the gap is compact; (ii) the combustor comprises N identical cans each with symmetry about a constant-θ plane; (iii) there is no mean flow in the gap; (iv) the combustor connects to a turbine with known (non-dimensional) acoustic impedance to plane pressure waves, $\mathcal{Z}_{\text{plane}} = p'/\rho a v_{\text{d}}$.

Although further analytical models are available for $\mathcal{Z}_{\text{plane}}$, in this paper, the downstream turbine impedance is prescribed using CFD results for plane wave forcing in an open annulus after Brind and Pullan [8], isolating errors in the combustor model from possible errors in a turbine analytical model.

Figure 1 shows notation required for the derivation. The real three-dimensional combustor and turbine geometry in Figure 1a, is modelled as the network shown in Figure 1b. Each of the combustor cans has a control volume, CVn, defined over its sector of the combustor–turbine gap. The analytical model provides an acoustic impedance at the leading edge of CVn to be used as a boundary condition in a separate thermoacoustic calculation of the combustor cans.

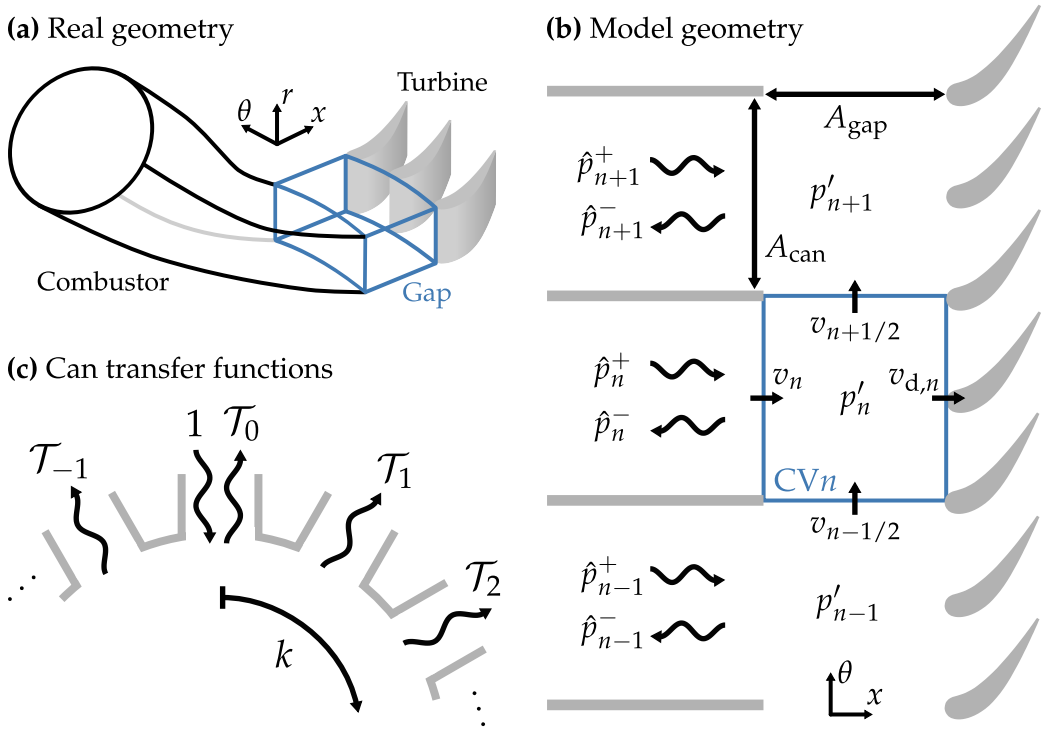

Figure 1. Notation for connection impedance analytical model: (**a**) real combustor and turbine geometry, with control volume; (**b**) model geometry with quantities required for the derivation; (**c**) definition of can transfer functions $\mathcal{T}_k$. Note that cans may be oriented axially or radially.

In the compact regime, the acoustic pressure perturbation p' is uniform over each control volume, and the velocity perturbations v are uniform over each of the four bounding control surfaces. Within the assumptions of the model, can transfer functions are independent of the detailed shape of the combustor, and two areas A_{can} and A_{gap} are sufficient to characterise the geometry. This means that the cans may be oriented axially or radially.

With quantities defined in Figure 1b, conservation of mass in control volume CVn requires

$$A_{\text{can}}\left(v_n - v_{\text{d},n}\right) + A_{\text{gap}}\left(v_{n-1/2} - v_{n+1/2}\right) = 0\,. \tag{1}$$

To evaluate intra-can velocities, define a non-dimensional impedance of the connections between cans,

$$\zeta = \frac{1}{\rho a}\frac{p'_n - p'_{n+1}}{v_{n+1/2}}\,, \tag{2}$$

and substitute into Equation (1),

$$A_{\text{can}}\left(v_n - v_{\text{d},n}\right) + \frac{1}{\zeta}\frac{A_{\text{gap}}}{\rho a}\left(p'_{n-1} - 2p'_n + p'_{n+1}\right) = 0\,. \tag{3}$$

Invoking linearity, a general circumferential distribution of pressure fluctuations can be expressed as a Fourier series,

$$p'(\theta) = \sum_m \tilde{p}'_m \exp(\mathrm{i}m\theta)\,, \tag{4}$$

where a tilde denotes amplitudes of the azimuthal harmonics. At fixed azimuthal mode m, pressures in two adjacent cans spaced an angle $\Delta\theta = 2\pi/N$ apart are related by a phase

shift $p'_{n+1} = p'_n \exp(\mathrm{i}m\Delta\theta)$. Substituting the phase shift into Equation (3) and simplifying using trigonometric identities,

$$\rho a \left(\frac{v_n}{p'_n} - \frac{v_{\mathrm{d},n}}{p'_n} \right) - \frac{4}{\zeta} \frac{A_{\mathrm{gap}}}{A_{\mathrm{can}}} \sin^2 \frac{m\pi}{N} = 0 \,. \tag{5}$$

Then, rearranging for the overall impedance at a given azimuthal mode,

$$\mathcal{Z}_m = \frac{1}{\rho a} \frac{p'_n}{v'_n} = \left[\frac{1}{\mathcal{Z}_{\mathrm{plane}}} + \frac{1}{\mathcal{Z}_{\mathrm{can},m}} \right]^{-1} \text{ with } \mathcal{Z}_{\mathrm{can},m} = \frac{A_{\mathrm{can}}}{A_{\mathrm{gap}}} \frac{\zeta}{4 \sin^2 \frac{m\pi}{N}} \,. \tag{6}$$

When building a thermoacoustic model, it is more convenient to work with can transfer functions $\mathcal{T}_k$, as shown in Figure 1c, instead of modal impedances $\mathcal{Z}_m$. The kth transfer function is defined to reflected waves in an arbitrary can, from incident waves in another can offset k positions away,

$$\mathcal{T}_k = \frac{\hat{p}^-_n}{\hat{p}^+_{n-k}} \,, \tag{7}$$

where a hat denotes characteristic wave amplitudes,

$$\hat{p}^\pm = \frac{1}{2} \left(\frac{p'}{p} \pm \gamma \frac{u'}{a} \right) . \tag{8}$$

Following Ghirardo et al. [3], the can transfer functions are given by the inverse discrete Fourier transform of modal reflection coefficients $\mathcal{R}_m$,

$$\mathcal{T}_k = \frac{1}{N} \sum_m \mathcal{R}_m \exp(-\mathrm{i}km\Delta\theta) \quad \text{where} \quad \mathcal{R}_m = \frac{\tilde{p}^-_m}{\tilde{p}^+_m} = \frac{\mathcal{Z}_m - 1}{\mathcal{Z}_m + 1} \,. \tag{9}$$

Equation (9) is justified as follows. Forcing a single can is equivalent to an impulse in the can domain and so excites all azimuthal modes equally. The acoustic response in the modal domain is weighted by the reflection coefficients at each harmonic. Taking the inverse Fourier transform returns to the can domain and yields the reflected waves in each can resulting from the original impulse.

3. Time-Marching Computational Approach

This section describes the computational fluid dynamics approach of the present work, following methods developed by Brind and Pullan [8]. Applying forcing to non-linear time-marching computations and analysing the resulting acoustic response allows can transfer functions to be calculated.

3.1. Domain and Boundary Conditions

The datum combustor and turbine under consideration are representative of a large industrial gas turbine. The combustor comprises $N = 20$ cylindrical cans, each identical and symmetric about a constant-θ plane, connecting via transition ducts to an open annulus upstream of the turbine. The analytical model does not describe acoustic behaviour upstream of the can trailing edge, so a simplified can geometry omitting fuel injectors and cooling flows is sufficient for these validation calculations. An axial gap of length $L_{\mathrm{gap}}/c_x = 0.9$ separates combustor and turbine. Figure 2 illustrates schematically the computational domain and boundary conditions.

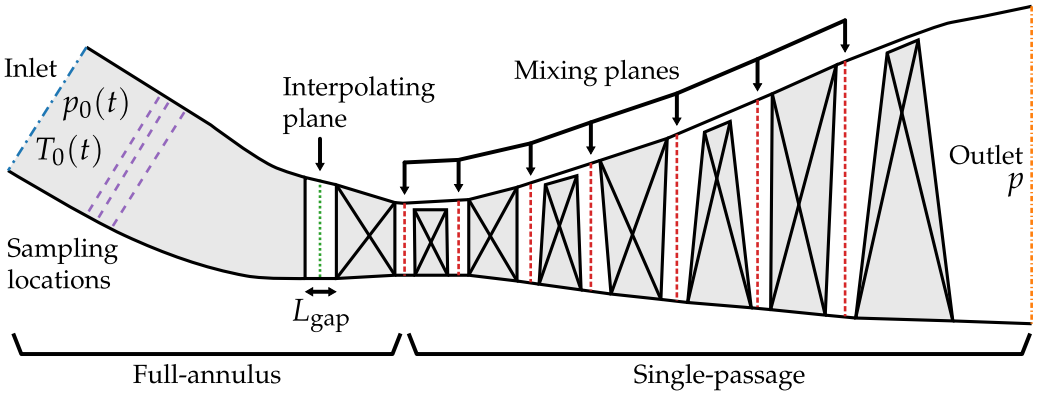

Figure 2. Domain and boundary conditions for coupled combustor and turbine CFD simulations.

The turbine design is a realistic four-stage geometry with coolant flows, leakage flows, and three-dimensional blading. Surface patches, imposing additional fluxes of mass, momentum, and energy, inject a total coolant flow of order 25% the turbine inlet mass flow. Flow is subsonic, with a Mach number of $Ma \approx 0.1$ in the combustor and a vane exit Mach number of $Ma \approx 0.7$. The Reynolds number, based on nozzle guide vane axial chord and exit velocity, is of order $Re \approx 4 \times 10^6$.

To capture all possible azimuthal modes, the computational model couples combustor and nozzle guide vane in a full-annulus configuration, joined to single-passage representations of downstream blade rows using mixing planes. Alternatively, with even N, two-can computational models provide data sufficient to extract a value for connection impedance at reduced computational cost (ζ is independent of m).

The domain is circumferentially periodic. Inlet boundary conditions are prescribed uniform values of stagnation pressure and temperature; the outlet boundary condition is a prescribed static pressure, with spanwise variations assuming radial equilibrium (Figure 2). Although spatially uniform, the inlet boundary conditions are functions of time. Because the multi-stage turbine allows negligible upstream transmission, reflections from the outlet boundary have no influence on the solution in the combustor. Reflections from the inlet boundaries are accounted for and corrected in post-processing.

A circumferential interpolating plane joins the combustor and nozzle guide vane grids at an interface within the combustor–turbine gap (Figure 2). Interpolation uncouples the pitchwise grid densities of combustor and turbine. Mixing planes connect subsequent rows of the turbine; this model yields a reduction in computational cost of one order of magnitude with negligible loss of accuracy compared to an entirely full-annulus turbine. To confirm this fact, computations with the first three turbine rows full-annulus yielded can transfer functions within 2% of the nozzle guide vane only model.

3.2. Computational Details

Simulations were performed using TURBOSTREAM 3, a multi-block structured, compressible, unsteady Reynolds-averaged Navier–Stokes solver developed by Brandvik and Pullan [9]. The code uses a finite-volume formulation that is second-order accurate in space and implicit dual time stepping with a second-order accurate backward difference scheme. The simulations employ an algebraic mixing-length turbulence model: a computationally inexpensive choice that gives accurate results when calibrated against measurements. Nevertheless, the focus of the simulations is inviscid wave propagation, because acoustic viscous effects are confined to a thin boundary layer with thickness of order $\sqrt{\nu/\pi f}/c_x = 1.6 \times 10^{-3}$. The turbulence model only needs to set up a representative mean flow, and quantitative predictions of turbine performance are not essential. A fully-turbulent wall function yields shear stress on solid boundaries, at a distance $\Delta y^+ \approx 30$ in wall units. Resolution studies confirmed discretisation independence with at least 100 grid points per acoustic wavelength and 72 time steps per acoustic period. This requires of order

10^6 nodes in each combustor can and blade passage. Duplicating combustor and nozzle to form a full-annulus sector yields a mesh with 58×10^6 nodes.

In forced computations, inlet boundary conditions take the form

$$\frac{p_0(t)}{\overline{p_0}} = 1 + F(t) \quad \text{and} \quad \frac{T_0(t)}{\overline{T_0}} = \left(\frac{p_0(t)}{\overline{p_0}}\right)^{\frac{\gamma-1}{\gamma}}, \quad \text{with} \quad F(t) = \sum_{j=2}^{J} \delta \sin(2\pi j f_0 t)\,. \tag{10}$$

In Equation (10), $\delta = 0.1\%$ is a small amplitude parameter, and values of f_0 and J are selected to span a reduced frequency range range $0.02 \leq \kappa \leq 0.1$, where $\kappa = f c_x / a$. This frequency range is typical of combustion instability in large industrial machines.

In full-annulus computations, to excite all azimuthal modes, an arbitrary set of can indices $n = \{1, 7, 8, 14, 16\}$ are forced, while $\delta = 0$ in the other cans. Preliminary simulations showed that calculated transfer functions were independent of the forcing pattern, confirming that the problem is linear. In two-can computations, both cans are forced in antiphase, exciting the $m = N/2$ mode only.

Unsteady computations are started from a converged steady solution and run for eight forcing periods, then flow field data are sampled for a further eight forcing periods. One case requires two days of wall-clock time on four Nvidia A100 graphical processing units.

3.3. Post-Processing for Can Transfer Functions

This section describes calculation of can transfer functions $\mathcal{T}_k$ from the CFD results to compare with the analytical model. The solver outputs unsteady flow field data at three cross-section sampling planes, shown in Figure 2, for each of the N combustor cans. At each instant in time, the pressure fluctuations are area averaged over the sampling planes to give scalar but unsteady quantities.

The least-squares multi-microphone wave separation technique of Poinsot et al. [10] yields upstream- and downstream-running characteristic wave amplitudes in all N cans, $\hat{p}_n^-$ and $\hat{p}_n^+$, from pressure fluctuations on the three sampling planes in each can, given spacings between the planes and the acoustic speed. Phase shifting waves to the centre of the combustor–turbine gap ensures consistency with the analytical model. The segmentation approach of Miles [11,12] accounts for area variation along the transition duct.

Forcing the $(n-k)$th can alone, from Equation (9) the reflected wave in the nth can is $\hat{p}_n^- = \hat{p}_{n-k}^+ \mathcal{T}_k$. In general, the total reflected wave is a linear superposition of contributions from all cans. Summing over k,

$$\hat{p}_n^- = \sum_k \mathcal{T}_k \, \hat{p}_{n-k}^+ \quad \text{or} \quad \hat{\boldsymbol{p}}^- = \boldsymbol{\mathcal{T}} * \hat{\boldsymbol{p}}^+ \,. \tag{11}$$

Equation (11) is by definition a discrete convolution, of a periodic vector of N transfer functions $\boldsymbol{\mathcal{T}}$ with a periodic vector of N incident waves $\hat{\boldsymbol{p}}^+$ to make a periodic vector of N reflected waves $\hat{\boldsymbol{p}}^-$. By the convolution theorem, the solution of Equation (11) is $\boldsymbol{\mathcal{T}} = \mathcal{F}^{-1}\left(\mathcal{F}(\hat{\boldsymbol{p}}^-)/\mathcal{F}(\hat{\boldsymbol{p}}^+)\right)$, where $\mathcal{F}$ denotes the discrete Fourier transform operator. The formulation of Equation (11) does not require an assumption of non-reflecting inlet boundaries.

3.4. Extracting Connection Impedance

There are two ways to post-process connection impedance, ζ, from a CFD solution. The direct method is to evaluate Equation (2) using area-averaged Fourier-transformed quantities: static pressure on a plane at the can trailing edge and azimuthal acoustic velocity on a plane spanning the gap. The indirect method employs 'push–pull' forcing at fixed azimuthal mode $m = N/2$. Wave separation on sampling planes away from the can trailing edge, where the acoustics are one-dimensional, yields characteristic wave amplitudes

and a reflection coefficient $\mathcal{R}_{N/2} = \tilde{p}^- / \tilde{p}^+|_{m=N/2}$ for this mode. Converting $\mathcal{R}_{N/2}$ to an impedance $\mathcal{Z}_{N/2}$ as in Equation (9), setting $m = N/2$, and rearranging Equation (6),

$$\zeta = \frac{4A_{\text{gap}}}{A_{\text{can}}} \left[\frac{1}{\mathcal{Z}_{N/2}} - \frac{1}{\mathcal{Z}_{\text{plane}}} \right]^{-1}. \tag{12}$$

The direct method involves an arbitrary averaging procedure that is not strictly consistent with the assumption of one-dimensional acoustics but applies at all frequencies. The indirect method has no area-averaging but assumes validity of the analytical model and hence only applies at compact frequencies. This paper quotes reactances calculated using the direct method to capture frequency trends and resistances using the indirect method for most consistency with the analytical model.

4. Quantifying Connection Acoustic Impedances

The analytical model takes one empirical parameter: a connection impedance ζ between adjacent cans, defined in Equation (2). This section uses time-marching simulations of two-can computational models to extract values for resistive (lossy) and reactive (inertial) parts of $\zeta = \xi + \mathrm{i}\eta$ and determine its sensitivity to geometry. Figure 3 shows four geometries used for this study. The 'Datum' case is fully representative. The 'Clocked' geometry is the datum rotated by half a vane pitch to align combustor can walls with nozzle mid-passage. The 'Slip' and 'Thick' geometries have square combustor cans of constant cross section, with a zero-thickness inviscid wall and a wall of width 0.36 c_x.

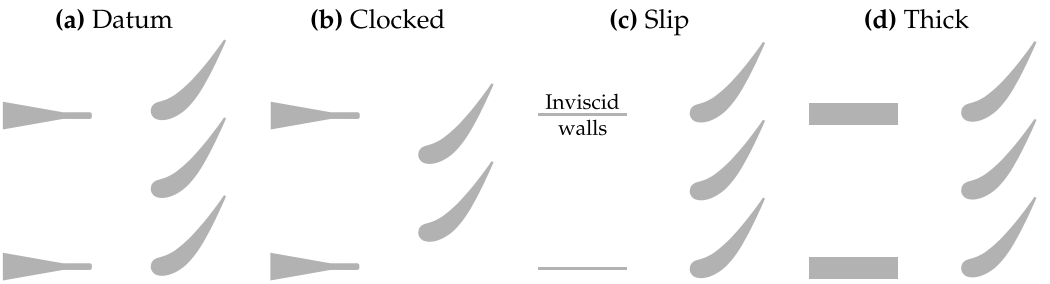

Figure 3. Four geometries of combustor can: (**a**) datum can and transition duct, (**b**) datum clocked by half a vane pitch, (**c**) square with thin inviscid walls, (**d**) square with thick trailing edge. Not to scale.

4.1. Acoustic Reactance

Figure 4a shows acoustic reactances, η, for the four combustor geometries as a function of reduced frequency $\kappa = fc_x/a$. For Datum and Slip cases, η is proportional to frequency, as expected for an inertial effect, and within 6% of the classical Rayleigh conductivity $\eta_{\text{Ray}} = 2\pi f\sqrt{A_{\text{gap}}}/a$. The Clocked reactance has a slope of twice the Rayleigh conductivity. When the combustor wall is not circumferentially aligned with vane leading edges, the volume of fluid in motion and hence inertia is greater than an ideal thin-walled aperture for which the Rayleigh conductivity is derived.

The Thick combustor has similar reactance to the Datum and Slip cases for $\kappa \leq 0.06$. At high reduced frequencies, the Thick reactance departs from a linear trend as the trailing-edge vortex shedding locks in to the forcing frequency. The vortex shedding amplifies acoustic motion and acts to reduce effective inertia. In real combustors, with representative thin trailing edges $w/c_x < 0.1$, the vortex shedding effect is negligible at typical combustion instability frequencies $\kappa \leq 0.1$.

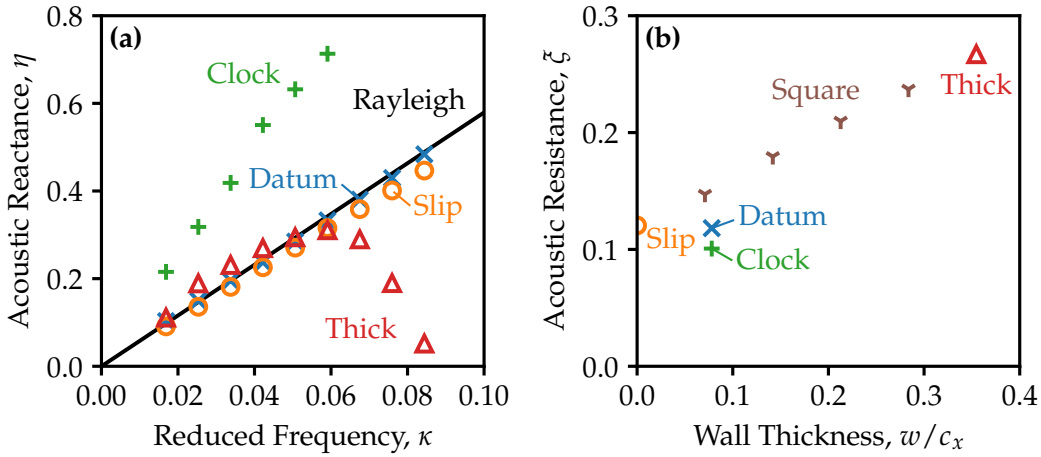

Figure 4. Connection impedance for different combustor geometries: (**a**) real part, acoustic reactance; (**b**) imaginary part, acoustic resistance at $\kappa = 0.017$. For representative cases, reactance is within 6% of the classical Rayleigh conductivity. Resistance increases linearly with combustor wall thickness.

4.2. Acoustic Resistance

Figure 4b shows acoustic resistances for the four cases in Figure 3, plus additional square combustors with varying wall thickness. The resistances are calculated using the indirect method at a reduced frequency of $\kappa = 0.017$ and plotted as a function of wall thickness.

All resistances with wall thicknesses $w/c_x \leq 0.1$ fall in the range $0.1 \leq \xi \leq 0.15$, a variation of $\pm 20\%$ about the mean. The non-zero resistance of the Slip case shows acoustic loss does not require a viscous wake behind the combustor wall, suggesting an inviscid effect is responsible. For the family of Square combustor geometries ranging from $0 \leq w/c_x \leq 0.36$, resistance increases linearly from $\xi = 0.121$ to $\xi = 0.267$. A linear increase in resistance is consistent with an effect that scales with connection volume. For the same wall thickness, the Datum and Clocked geometries have smaller values of acoustic resistance compared to the Square combustors, showing that the effect of combustor trailing edge shape, and clocking with the turbine, cannot be neglected.

4.3. Effect of Combustor–Turbine Gap Length

The length of the combustor–turbine gap is a degree of freedom available to the designer, selected by compromise between overall machine size and non-uniformity of the turbine inlet flow field. If the connection impedance were a strong function of gap length, the analytical model would require multiple calibrations to investigate the influence of gap length on can transfer functions.

Translating the Datum combustor in the axial direction, and extracting acoustic resistances for each length from two-can computations, yields the points shown in Figure 5. Over the range $0.15 \leq L_{\text{gap}}/c_x \leq 2.35$ acoustic resistance varies by $\pm 15\%$ with respect to the representative value $L_{\text{gap}}/c_x = 0.92$. The insensitivity of acoustic resistance over this wide range suggests that the present model can achieve good accuracy with calibration at only a single gap length.

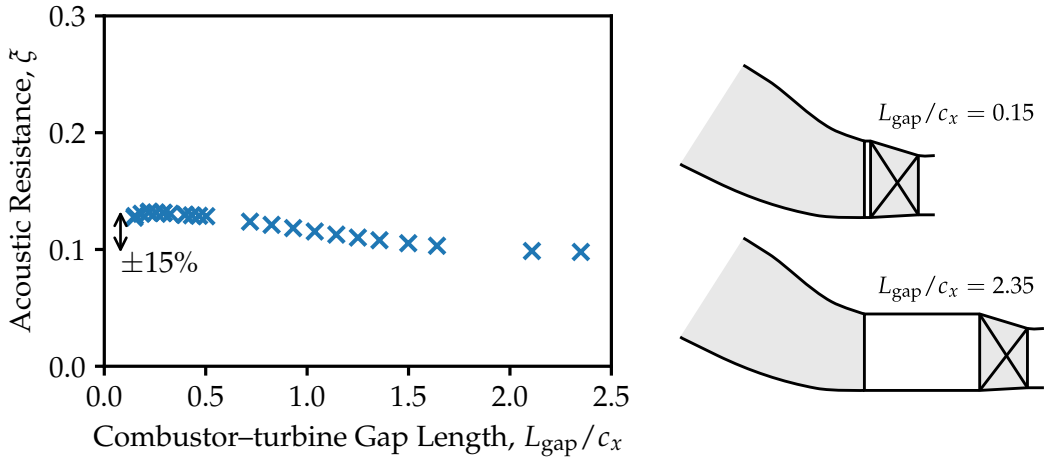

Figure 5. Acoustic resistance of the Datum combustor with varied axial combustor–turbine gap. Resistance is insensitive to gap length, varying by ±15% over the entire simulated range.

4.4. Physical Mechanism

To identify the physical mechanism for acoustic resistance requires tracking acoustic energy on a local level. Morfey [13] defined a generalised acoustic energy flux,

$$N_i^* = (p'v_i) + \frac{V_i}{\rho a^2}(p')^2 + \sum_j \frac{V_i V_j}{a^2}(p'v_j) + \rho V_j (v_i v_j)\,, \tag{13}$$

where p' and v_i are static pressure and velocity component fluctuations, while ρ, V_i, and a are the mean density, velocity components, and acoustic speed. The first term in Equation (13) is the classical acoustic energy flux after Kirchoff, which is only conserved in a stationary uniform medium; the remaining terms account for a moving medium. Time averaging Equation (13) gives the generalised acoustic intensity, $I_i^* = \overline{N_i^*}$, and the local acoustic energy production is $\nabla \cdot \boldsymbol{I}^*$. As Morfey [13] showed, $\nabla \cdot \boldsymbol{I}^* = 0$ to second order in an irrotational, inviscid, uniform-entropy flow.

Figure 6 shows acoustic energy production, $\nabla \cdot \boldsymbol{I}^*$, over the midspan plane of the Datum combustor. Apart from a region downstream of the combustor wall, acoustic energy loss is negligible. In the region of negative $\nabla \cdot \boldsymbol{I}^*$, interaction between streamwise mean flow and azimuthal acoustic fluctuations leads to an acoustic energy sink into vorticity fluctuations (like grazing flow over an orifice).

Acoustic loss by streamwise mean flow interaction is a distinct mechanism from interactions with combustor trailing edge vortex shedding. If trailing edge vortex shedding were dominant, the region of negative acoustic energy production would be located on the upstream side of the gap—loss by shedding is inconsistent with the contours in Figure 6. The shedding frequency is a factor of five higher than the acoustic frequency, so there is no interaction in this Datum geometry with a thin trailing edge.

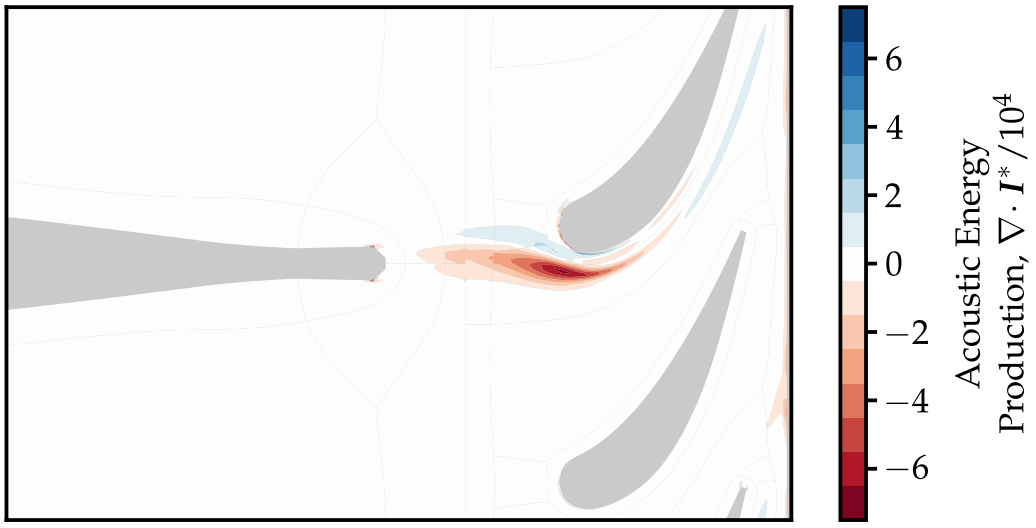

Figure 6. Acoustic energy production in the combustor–turbine gap at mid-span of the Datum geometry, at reduced frequency $\kappa = 0.017$. Loss is concentrated downstream of the combustor wall.

5. Can Transfer Function Predictions

The previous section showed that, for representative can-annular combustors, the acoustic reactance between cans is close to the Rayleigh conductivity, and the acoustic resistance is approximately $\xi = 0.12$ with a weak sensitivity to geometry, varying by up to 20% over a wide variety of cases. This section compares full-annulus CFD results for can transfer functions of the Datum geometry against predictions from the analytical model. To calibrate the connection impedance, reactance is set to the Rayleigh value and resistance is set to the value extracted from a two-can computation.

Figure 7 illustrates the importance of both modelling can-to-can communication and allowing for acoustic resistance. Naïvely applying the plane-wave reflection coefficient $\mathcal{R}_{\text{plane}}$ at the trailing edge of the combustor can, discounting transmission to other cans, is in error by a factor of two compared to the can reflection coefficient $\mathcal{T}_0$. Setting $\xi = 0$ for a pure Rayleigh conductivity model after von Saldern et al. [4] ignores acoustic resistance and over-predicts $|\mathcal{T}_0|$ by up to 68%.

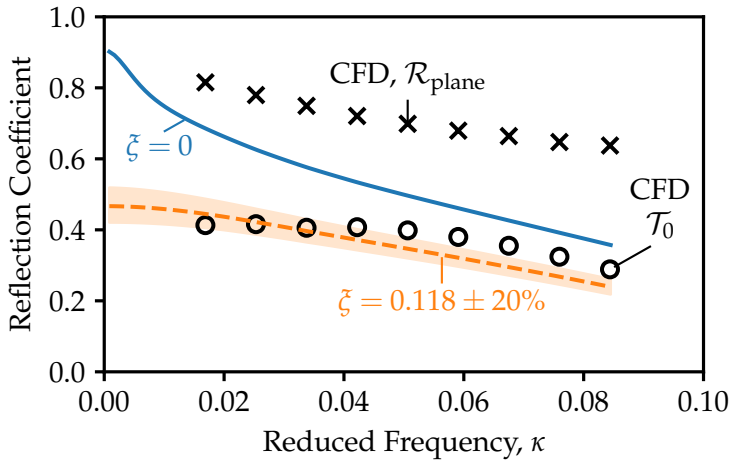

Figure 7. Plane and can reflection coefficient magnitudes for Datum combustor, model (lines) and CFD (symbols). The Rayleigh conductivity model with $\xi = 0$ over-predicts $\mathcal{T}_0$ by up to 68%; using acoustic resistance $\xi = 0.118$ extracted from a two-can simulation matches CFD to within 23%.

Using the resistance value $\xi = 0.118$ extracted from a two-can computation of this geometry matches CFD to within 23% and is accurate to 8% at the compact reduced

frequency $\kappa = 0.017$. The shaded band in Figure 7 shows the sensitivity of $\mathcal{T}_0$ predictions to the range of variation in ξ observed across representative geometries with $w/c_x \leq 0.1$ in Figure 4b. A 20% perturbation in ξ leads to a 12% variation in $\mathcal{T}_0$—predicted can transfer function magnitudes are robust to inaccuracies in acoustic resistance.

Thermoacoustic stability of a can-annular ring of combustors depends on all can transfer functions $\mathcal{T}_k$. With the calibrated value of acoustic resistance $\xi = 0.118$, Figure 8 shows can transfer functions for $k = 0, 1, 2, 3$ as a function of reduced frequency. As k increases, transfer to more distant cans reduces, justifying a focus on small k (by symmetry $\mathcal{T}_{-k} = \mathcal{T}_k$).

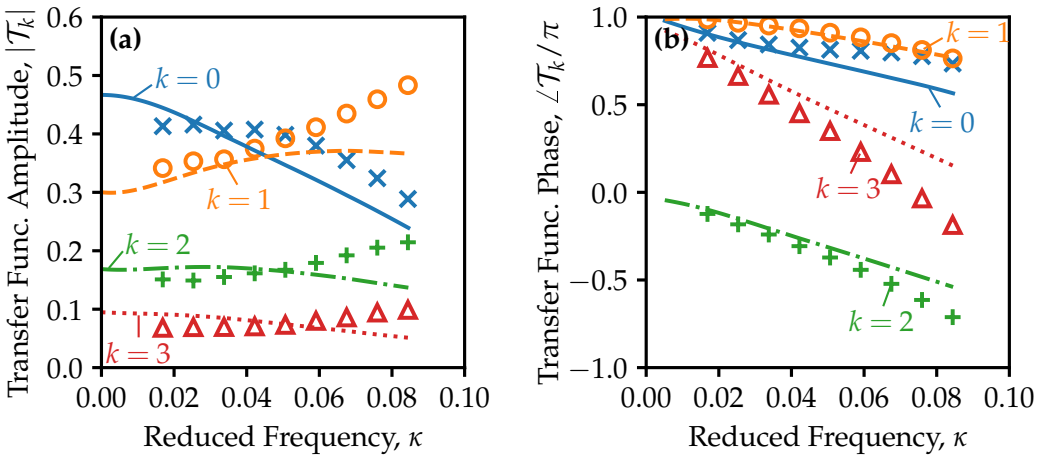

Figure 8. Can transfer functions for Datum combustor: (**a**) magnitude, (**b**) phase. Comparison of analytical model (lines) to CFD simulations (symbols). With calibrated acoustic resistance $\xi = 0.118$, the analytical model agrees to within 0.03 magnitude at $\kappa = 0.017$.

CFD computations and analytical model agree to within 0.03 magnitude at a low reduced frequency $\kappa = 0.017$; see Figure 8a. The gap is assumed compact in the analytical model, however, which results in first-order magnitude errors at high reduced frequencies $\kappa \geq 0.05$. Compactness is the most fundamental and strongest assumption of the model. Accounting for non-compact effects would require a higher-fidelity two-dimensional solution of the acoustic field in the combustor–turbine gap. Phase predictions in Figure 8b agree to within 0.15 rad at $\kappa = 0.017$ and qualitatively match the trend.

Figure 9 shows the effect of combustor–turbine gap length on can transfer functions. The assumption of compactness restricts the analysis to a low reduced frequency $\kappa = 0.017$. The model quantitatively captures variations in the transfer functions, including a minimum $|\mathcal{T}_0|$ near $L_{\text{gap}}/c_x = 0.2$; see Figure 9a. A constant acoustic resistance $\xi = 0.118$ at the representative gap is sufficient to give good agreement across the range of gaps (the full results in Figure 5 are not used). If full-annulus computations at one gap length are available, fitting resistance a posteriori based on $|\mathcal{T}_0|$ yields closer agreement, and the $|\mathcal{T}_0|$ minima coincide between CFD and analytical model (results not shown).

Returning to Equation (6), the total impedance is given by turbine and combustor contributions in parallel. At a fixed frequency and azimuthal mode, there exists a value of $\zeta A_{\text{can}}/A_{\text{gap}}$ where these two contributions align in destructive interference, giving a low total impedance. Although the can transfer functions are a combination of modal reflections (Equation (9)), the sharp phase shift of $\angle\mathcal{T}_0$ in Figure 9b near the inflection point supports this explanation for the existence of the minimum.

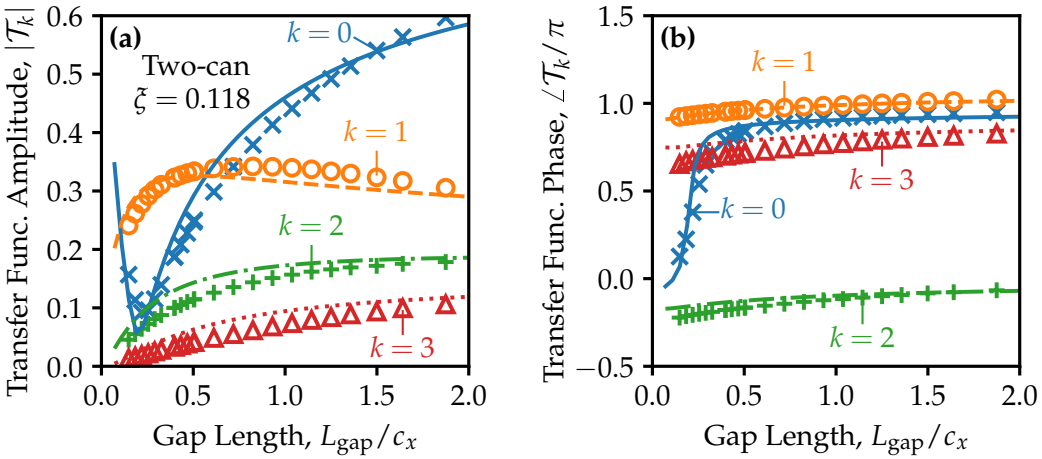

Figure 9. Effect of combustor–turbine gap length on can transfer functions for Datum combustor at $\kappa = 0.017$, model (lines) and CFD (symbols): (**a**) magnitude, (**b**) phase. Using one value of acoustic resistance $\xi = 0.118$ calibrated at the datum gap, the model quantitatively captures the trends. A minimum $\mathcal{T}_0$ occurs near $L_{gap}/c_x \approx 0.2$.

6. Design Space Study—Minimising Reflected Energy

Both the CFD simulations and analytical model identify in Figure 9 a minimum can reflection coefficient occurring at non-zero gap length. This section uses the analytical model to determine the parameters affecting this minimum and the implications for coupled combustor and turbine design.

Greatest thermoacoustic stability benefit corresponds to minimum reflected acoustic energy, calculated as $\mathcal{E} = \sum_k |\mathcal{T}_k|^2$. With less reflected energy, the combustor requires less acoustic damping to maintain stability. Summing over all cans accounts for the fact that a minimum in just $\mathcal{T}_0$ may correspond to redistribution of transmission to other cans, rather than increasing transmission through the turbine.

For the case presented in Figure 9, at the representative gap length $L_{gap}/c_x = 0.9$ the reflected energy takes a value $\mathcal{E} = 0.43$. Reducing the gap length until a minimum is reached at $L^*_{gap}/c_x = 0.15$, the reflected energy reduces to a low of $\mathcal{E}^* = 0.16$, a 63% drop with respect to the representative gap.

The analytical model in Equation (6) contains four independent parameters:

$$\mathcal{E} = \text{function}\Big(A_{can}/A_{gap}\,,\ \zeta\,,\ \mathcal{R}_{plane}\,,\ \kappa \Big)\,. \tag{14}$$

Fixing the annulus mean radius and hub-to-tip radius ratio, and varying the number of cans, is one way to change A_{can}/A_{gap}. The choice of hub-to-tip ratio is arbitrary because both A_{can} and A_{gap} are proportional to annulus height. In common with the predictions presented so far, acoustic reactance is set to the Rayleigh value, while the acoustic resistance is a free parameter. This design study assumes a constant reduced frequency, $\kappa = 0.02$, in the compact regime where the analytical model is most accurate. The design study also assumes a real downstream reflection coefficient $\mathcal{R}_{plane}$ with no phase shift, a valid simplification in the compact regime.

Figure 10a illustrates the variation in gap length at minimum reflected energy, L^*_{gap}, when the remaining three non-dimensional parameters are perturbed away from a baseline condition representative of large industrial gas turbines. L^*_{gap} is inversely proportional to the number of cans. Because $A_{can} \sim 1/N$ and $A_{gap} \sim L_{gap}$, this corresponds to the minima occurring at a constant value of $A_{can}/A_{gap} \sim 1/(NL_{gap})$, when other parameters are fixed. Figure 10a also shows that L^*_{gap} is directly proportional to acoustic resistance and downstream turbine reflection coefficient.

Figure 10b plots the minimum reflected energy, $\mathcal{E}^*$, as a function of the parameters in Equation (14). The number of cans has a weak effect, with $\mathcal{E}^*$ increasing by 21% as N drops

from the datum 20 to 7. As acoustic resistance drops towards zero, $\mathcal{E}^*$ rises rapidly—the existence of a minimum requires non-zero resistance and would not be captured by a pure Rayleigh conductivity model. Minimum reflected energy increases as the downstream turbine becomes more reflective, consistent with the parallel form of Equation (6).

The relationships in Figure 10a imply the optimum gap length corresponds to

$$\xi \mathcal{R}_{\text{plane}} A_{\text{can}} / A_{\text{gap}} = \text{constant} = 1.91 \pm 12\% \,, \tag{15}$$

where analytical modelling over the entire design space of Figure 10 has been used to calculate the constant, at a compact reduced frequency $\kappa = 0.02$. Raising reduced frequency to $\kappa = 0.05$ increases the constant by 13%. Equation (15) is a design guideline that informs selection of the combustor–turbine gap for minimum reflection and maximum acoustic loss from the combustion system.

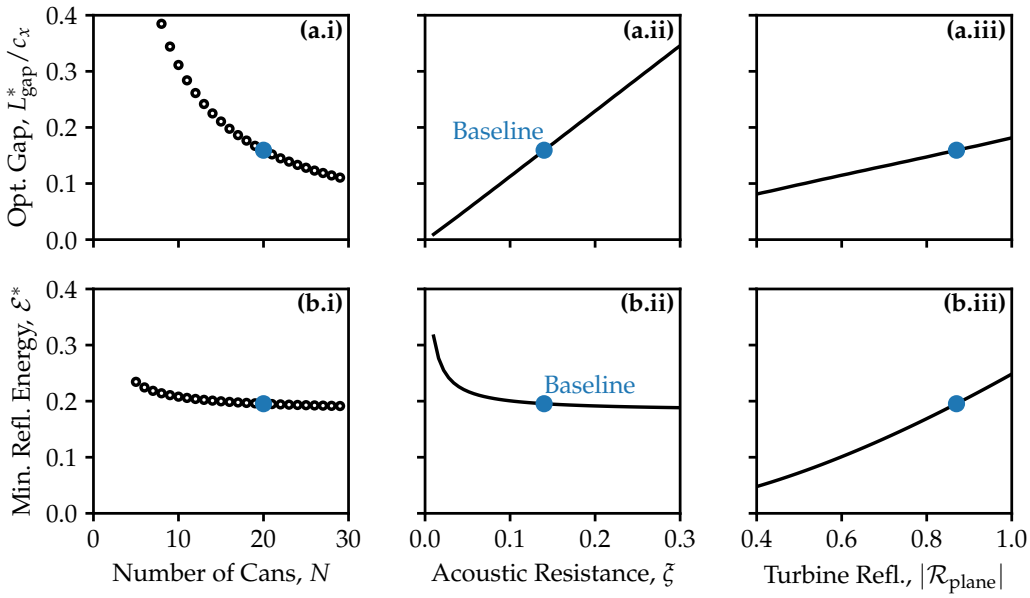

Figure 10. Effect of design parameters (**i**) number of cans, N; (**ii**) acoustic resistance, ξ; and (**iii**) turbine reflection coefficient, $|\mathcal{R}_{\text{plane}}|$ on (**a**) optimum combustor–turbine gap length, (**b**) minimum reflected energy. Optimum gap length L^*_{gap} is inversely proportional to N and proportional to ξ and $|\mathcal{R}_{\text{plane}}|$.

To use the guideline in practice, an engineer has several options for assigning an acoustic resistance. With no computations available, a first guess from past experience could be $\xi \approx 0.1$. A two-can computation of a novel geometry provides a more accurate resistance, and if necessary, reactance. Fitting to a full-annulus computation gives the most precise value for ζ. Then, rearranging Equation (15) for A_{gap} and dividing by annulus height gives the optimum gap length.

7. Conclusions

This paper applied time-marching CFD and an analytical model to predict transfer functions between incident and reflected waves in a can-annular combustor. These transfer functions are necessary boundary conditions for a thermoacoustic model to determine stability of the combustion system. The results show:

1. The connection impedance analytical model of von Saldern et al. [4] requires acoustic resistance of order $\xi \sim 0.1$ for can transfer functions to match CFD simulations of a representative gas turbine combustor. The resistance arises due to streamwise mean flow and for representative combustor wall thicknesses is a weak function of combustor can geometry.

2. With a calibrated acoustic resistance, the analytical model reproduces full-annulus CFD can transfer functions to within 0.03 amplitude and 0.15 rad phase in the compact regime, indicating validity of the modelling assumptions. Prediction errors increase rapidly for $\kappa \geq 0.05$ due to non-compact effects.
3. As combustor–turbine gap length is varied, for a given compact frequency, there is a minimum reflected energy at a non-zero gap length. In the datum case, reflected energy drops by 63% at $L_{\mathrm{gap}}/c_x = 0.15$ compared to the datum $L_{\mathrm{gap}}/c_x = 0.9$. The minimum, where contributions from downstream turbine and other cans align in antiphase, is captured by both CFD simulations and the analytical model.
4. Analytical exploration of the coupled can-annular combustor–turbine design space yields a guideline for minimum reflected energy: at optimum gap length,

$$\zeta \mathcal{R}_{\mathrm{plane}} A_{\mathrm{can}} / A_{\mathrm{gap}} \approx 1.91 \,.$$

The present analytical model is shown to be a useful tool for estimating acoustic boundary conditions in a rapid, iterative combustor design process, subject to two limitations. First, the value of acoustic resistance must be calibrated; the transfer functions, however, are not strongly sensitive to this parameter. Second, the model assumes low reduced frequencies, which are typical of instability in large industrial machines but cannot be assumed in general. The mechanism of separate can and turbine impedance contributions resulting in an optimum gap length will remain at higher frequencies.

Funding: This research was funded by Mitsubishi Heavy Industries, grant number G106034.

Data Availability Statement: The author does not have permission to share data.

Acknowledgments: The author thanks Mitsubishi Heavy Industries for funding this project, in particular S. Uchida, K. Saitoh, and T. Koda for their interest and support. The author is grateful to G. Pullan for his comments on a draft of this manuscript.

Conflicts of Interest: The author declares no conflict of interest.

Nomenclature

Roman

a	[m s^{-1}]	Acoustic wave speed
A	[m^2]	Area
c_x	[m]	Vane axial chord
f	[Hz]	Frequency
i	[–]	Imaginary unit
k	[–]	Can offset index
L_{gap}	[m]	Combustor–turbine gap
m	[–]	Azimuthal mode index
n	[–]	Can index
N	[–]	Number of cans
p	[Pa]	Pressure
$\mathcal{R}$	[–]	Reflection coefficient
T	[K]	Temperature
$\mathcal{T}$	[–]	Transmission coefficient
V	[m s^{-1}]	Velocity
w	[m]	Combustor wall thickness
$\mathcal{Z}$	[–]	Non-dim'l. impedance

Greek

γ	[–]	Specific heat ratio
$\mathcal{E}$	[–]	Reflected acoustic energy
ζ	[–]	Connection impedance
η	[–]	Acoustic reactance
θ	[rad]	Angular coordinate
κ	[–]	Reduced frequency
ν	[m^2 s^{-1}]	Kinematic viscosity
ξ	[–]	Acoustic resistance
ρ	[kg m^{-3}]	Density

Subscripts and accents

0	Stagnation conditions
$\hat{\square}$	Characteristic wave
$\square'$	Perturbation relative to mean
$\square^{\pm}$	Upstream- or downstream-running
$\tilde{\square}$	Azimuthal mode
$\overline{\square}$	Time average
$\square^*$	Minimum reflected acoustic energy

References

1. Kaufmann, P.; Krebs, W.; Valdes, R.; Wever, U. 3D Thermoacoustic Properties of Single Can and Multi Can Combustor Configurations. In *Proceedings of the ASME Turbo Expo*; ASME: New York, NY, USA, 2008. [CrossRef]
2. Venkatesan, K.; Cross, A.; Yoon, C.; Han, F.; Bethke, S. Heavy Duty Gas Turbine Combustion Dynamics Study Using a Two-Can Combustion System. In *Proceedings of the ASME Turbo Expo*; ASME: New York, NY, USA, 2019. [CrossRef]
3. Ghirardo, G.; Di Giovine, C.; Moeck, J.P.; Bothien, M.R. Thermoacoustics of Can-Annular Combustors. *J. Eng. Gas Turbines Power* **2019**, *141*, 011007. [CrossRef]
4. von Saldern, J.G.R.; Orchini, A.; Moeck, J.P. Analysis of Thermoacoustic Modes in Can-Annular Combustors Using Effective Bloch-Type Boundary Conditions. *J. Eng. Gas Turbines Power* **2021**, *143*, 071019. [CrossRef]
5. Fournier, G.J.J.; Meindl, M.; Silva, C.F.; Ghirardo, G.; Bothien, M.R.; Polifke, W. Low-Order Modeling of Can-Annular Combustors. *J. Eng. Gas Turbines Power* **2021**, *143*, 121004. [CrossRef]
6. Brind, J. Acoustic Boundary Conditions for Can-Annular Combustors. In Proceedings of the 15th European Turbomachinery Conference, paper No. ETC2023-140, Budapest, Hungary, 24–28 April 2023.
7. Orchini, A. An effective impedance for modelling the aeroacoustic coupling of ducts connected via apertures. *J. Sound Vib.* **2022**, *520*, 116622. [CrossRef]
8. Brind, J.; Pullan, G. Modelling Turbine Acoustic Impedance. *Int. J. Turbomach. Propuls. Power* **2021**, *6*, 18. [CrossRef]
9. Brandvik, T.; Pullan, G. An Accelerated 3D Navier–Stokes Solver for Flows in Turbomachines. *J. Turbomach.* **2011**, *133*, 021025. [CrossRef]
10. Poinsot, T.; Le Chatelier, C.; Candel, S.; Esposito, E. Experimental determination of the reflection coefficient of a premixed flame in a duct. *J. Sound Vib.* **1986**, *107*, 265–278. [CrossRef]
11. Miles, J.H. Acoustic transmission matrix of a variable area duct or nozzle carrying a compressible subsonic flow. *J. Acoust. Soc. Am.* **1981**, *69*, 1577–1586. [CrossRef]
12. Miles, J.H. Author's reply. *J. Sound Vib.* **1995**, *182*, 328–335. [CrossRef]
13. Morfey, C. Acoustic energy in non-uniform flows. *J. Sound Vib.* **1971**, *14*, 159–170. [CrossRef]

Disclaimer/Publisher's Note: The statements, opinions and data contained in all publications are solely those of the individual author(s) and contributor(s) and not of MDPI and/or the editor(s). MDPI and/or the editor(s) disclaim responsibility for any injury to people or property resulting from any ideas, methods, instructions or products referred to in the content.

International Journal of
Turbomachinery
Propulsion and Power

MDPI

Article

Potential of Static Pressure Recovery of Rotor-Only Low-Pressure Axial Fans †

Hauke Witte *, Christoph Bode and Jens Friedrichs

Institute of Jet Propulsion and Turbomachinery, Technische Universität Braunschweig, Hermann-Blenk-Str. 37, 38108 Braunschweig, Germany; chr.bode@ifas.tu-braunschweig.de (C.B.); j.friedrichs@ifas.tu-braunschweig.de (J.F.)

* Correspondence: h.witte@ifas.tu-braunschweig.de; Tel.: +49-531-391-94229

† This manuscript is an extended version of the ETC2023-157 meeting paper published in the Proceedings of the 15th European Turbomachinery Conference, Budapest, Hungary, 24–28 April 2023.

Abstract: Typically installed in a rotor-only configuration, low-pressure axial fans discharge directly into a free atmosphere and the discharge shows a strong swirl component. Since such designs, without guide vanes, cannot convert the dynamic pressure in the swirl component back into static pressure, the dynamic pressure is usually considered a loss. However, the radial equilibrium shows that a significant part of the kinetic energy contained in this swirl component is recovered as static pressure in the free atmosphere. This additional pressure increase has been sparsely researched. A comparison between two configurations with and without outlet guide vanes allows for the formulation of an evaluation criterion of the rotor-only configuration. Utilizing this evaluation criterion, the investigation of velocity profiles corresponding to generic rotor designs shows promise in terms of pressure recovery for new designs.

Keywords: low-pressure axial fans; pressure recovery; free discharge

check for updates

Citation: Witte, H.; Bode, C.; Friedrichs, J. Potential of Static Pressure Recovery of Rotor-Only Low-Pressure Axial Fans. *Int. J. Turbomach. Propuls. Power* **2023**, *8*, 33. https://doi.org/10.3390/ijtpp8030033

Academic Editor: Colin Scrivener

Received: 22 May 2023
Revised: 21 August 2023
Accepted: 4 September 2023
Published: 8 September 2023

Copyright: © 2023 by the authors. Licensee MDPI, Basel, Switzerland. This article is an open access article distributed under the terms and conditions of the Creative Commons Attribution (CC BY-NC-ND) license (https://creativecommons.org/licenses/by-nc-nd/4.0/).

1. Introduction

In a broad range of applications, low-pressure axial fans are designed to achieve large volumetric flow rates while maintaining small pressure ratios. Typically, due to cost and space constraints, these fans are installed in a rotor-only configuration, discharging a swirling jet flow into a free atmosphere. Such a design, without outlet guide vanes, cannot convert the dynamic pressure of the swirl component back into static pressure. This reduces the static pressure at the outlet of the machines. However, simple considerations show that in this free discharge, a static pressure recovery takes place. Indeed, a significant portion of the total-to-static pressure increase from low-pressure axial fans can take place in the discharge; thus, a thorough evaluation of this pressure recovery with regards to fan design is necessary.

Available experimental investigations on the achievable static pressure recovery downstream of rotor-only axial fans are first found in [1]. Here, a free vortex design with a hub-to-tip ratio of $\nu = 0.5$ is used. For this machine, the measured static pressure recovery in the free discharge corresponds to an increase in efficiency of 4–7%. It is quite interesting that the potential of efficiency increase via downstream guide vanes for such machines is given in [2] as 4–12%, which is within similar orders of magnitude.

In [3], a study on maximizing the efficiency of axial fans was performed. The authors used a CFD method trained by neural networks from [4], which was coupled with an evolutionary optimization algorithm. The main result of their numerical study was a maximum total-to-static efficiency of 68%, taking into account certain geometrical design criteria such as fixed sweep angle or axial design space. In contrast, the typical achievable total-to-static efficiencies of industrial machines tend to be 50–55%.

In the remaining relevant literature, no focus was set on the integral quantity of pressure recovery. Instead the flow field of the discharge itself has been investigated in great detail.

Experimental studies of the flow field downstream of rotor-only axial fans are performed in [5]. Here, optical measurements of a fan discharging into a pipe show that a strongly heterogeneous and non-uniform turbulent outflow is formed, which is characterized by high turbulence intensities, especially in the forming vortex core, revealing the complexity of fan discharge flows.

In [6], numerical investigations of the near downstream flow of a rotor-only axial fan at low flow rates were performed. The studies show that the downstream flow in the near-field, which has a direct influence on the pressure recovery, depends significantly on the flow rate. The latter, in turn, has a direct influence on the flow phenomena within the blade passage, which varies depending on the design method.

Considering the available studies, the behavior of the static pressure recovery remains an open question. In particular, two questions are investigated in this work, which corresponds to our paper published in the 15th European Turbomachinery Conference [7]:

1. What is the maximum effect that can be achieved via optimum static pressure recovery and how can it be evaluated?
2. To what extent can the static pressure recovery be influenced by the geometric features of the machine and the vortex design?

2. Static Pressure Recovery of Rotor-Only Low-Pressure Axial Fans

2.1. Assumptions and General Mechanism

Figure 1 shows a rotor-only axial fan configuration discharging into a free atmosphere with the qualitative radial profiles of the circumferential velocity v_θ (blue) and the static pressure p (red). As explained in Section 1, the flow field generally is strongly heterogeneous and non-uniform. Consequently, several assumptions are necessary for the derivations in this paper:

1. At location 0, immediately downstream of the trailing edge, the flow is axisymmetric, inviscid, and has no radial velocity components and no meridional curvature of the exit streamlines;
2. The ambient pressure p_{amb} is imprinted on the shear layer between the fan discharge and the free atmosphere (i.e., at r_{shear});
3. Location 1 is positioned sufficiently far downstream of location 0, such that the circumferential velocity component of the discharge has entirely vanished via momentum exchange (i.e., mixing) with the environment;
4. The free atmosphere is sufficiently large, such that walls and other obstructions are not influencing the free exhaust;
5. The flow is assumed to be steady and incompressible.

Under assumptions 1 and 2, the radial distributions of the static pressure p and the circumferential velocity component v_θ are coupled through the radial equilibrium:

$$p(r) = \int_r^{r_{shear}} \rho \frac{v_\theta(r)^2}{r} dr + p_{amb}. \tag{1}$$

Considering location 0 of Figure 1, the discharge shows a non-zero radial distribution of the circumferential velocity. Evaluating Equation (1) with such a distribution yields a monotonically increasing static pressure distribution with p_{amb} as the maximum value at the shear layer. Consequently, the average static pressure at location 0 is below ambient pressure.

Further downstream at location 1, the circumferential velocity has vanished under assumption 3. Considering Equation (1) again, this results in the static pressure being constant over the radius, and, subsequently, the average pressure at location 1 is equal to the ambient pressure. Following this argumentation, the average static pressure must have

increased from location 0 to location 1. In fact, from location 0 to location 1, a considerable amount of the kinetic energy contained in the fan discharge is converted into potential energy in form of a static pressure increase. Therefore, the free atmosphere acts as an outlet guide vane.

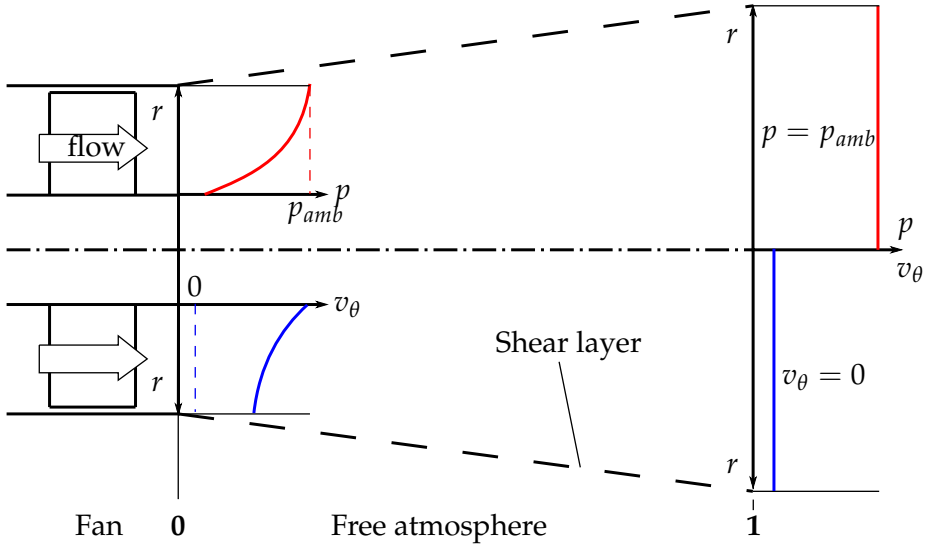

Figure 1. Schematic radial distributions of static pressure (red) and circumferential velocity (blue) at two locations in the fan discharge.

2.2. Evaluation Criterion of the Static Pressure Recovery

To investigate the potential of static pressure recovery in the free atmosphere, it has to be properly evaluated. A reasonable evaluation criterion should be able to compare different fan designs regardless of their vortex design, operating point, and geometric features.

To derive such an evaluation criterion, the rotor-only configuration of Figure 1 is compared to a configuration with outlet guide vanes, schematically visualized in Figure 2. The axial progressions of the average total and static pressure from the inlet to location 1 are shown in red and green, respectively. These curves are highly idealized in the sense that losses in the ducts up- and downstream of the rotor and stator are neglected.

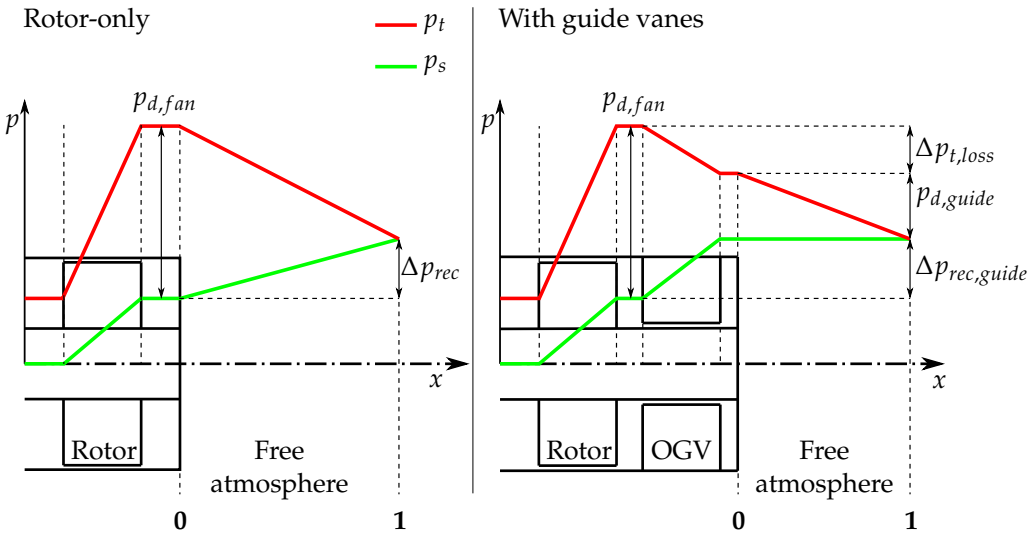

Figure 2. Comparison of two fan configurations—a rotor-only configuration (**left**) and a configuration with downstream guide vanes (**right**)—and their corresponding total (red) and static (green) pressure progressions from the inlet to location 1.

In the rotor-only configuration (left side of Figure 2), the fan increases the average static and total pressure from inflow conditions resulting in the dynamic pressure in the fan discharge $p_{d,fan}$. In the free atmosphere downstream of the fan, the static pressure increases by Δp_{rec} and the total pressure decreases until, eventually, the dynamic pressure is equal to zero.

The right side of Figure 2 shows a configuration with outlet guide vanes downstream of the fan. In this configuration, the fan is assumed to be equivalent to the rotor-only case, achieving the same pressure increase and, consequently, the same dynamic pressure $p_{d,fan}$. In contrast to the rotor-only case, the circumferential velocity component of the discharge is decelerated in the outlet guide vanes and, accordingly, the static pressure is increased by $\Delta p_{rec,guide}$. The discharge of the guides vanes has an average dynamic pressure of $p_{d,guide}$. Furthermore, the outlet guide vanes introduce a total pressure loss $\Delta p_{t,loss}$ to the flow. The discharge of the guide vanes into the free atmosphere does not lead to a static pressure recovery, since it has, by its idealized definition, no circumferential velocity component and, consequently, the mechanism of static pressure increase described earlier does not apply. Analogous to the rotor-only case, the residue dynamic pressure in the free atmosphere will eventually tend to zero at location 1 by dissipation.

From the right side of Figure 2, it is apparent that in the case of the installed outlet guide vanes, the dynamic pressure of the fan $p_{d,fan}$ is split exactly into the total pressure loss of the guide vanes $\Delta p_{t,loss}$, the dynamic pressure downstream of the outlet guide vanes $p_{d,guide}$, and the static pressure increase the guide vanes $\Delta p_{rec,guide}$, as in

$$p_{d,fan} = \Delta p_{t,loss} + p_{d,guide} + \Delta p_{rec,guide}. \tag{2}$$

An evaluation criterion can be derived from this, when requiring the pressure increase of the guide vanes $\Delta p_{rec,guide}$ to be equal to the static pressure recovery of the rotor-only configuration:

$$\Delta p_{rec,guide} = \Delta p_{rec}. \tag{3}$$

Adapting this into Equation (2) and isolating the total pressure loss of the guide vanes $\Delta p_{t,loss}$ yields

$$\Delta p_{t,loss} = p_{d,fan} - \Delta p_{rec} - p_{d,guide}. \tag{4}$$

More precisely, outlet guide vanes that induce a total pressure loss of $\Delta p_{t,loss}$, as computed by Equation (4) to the system, achieve exactly the same amount of static pressure increase as a corresponding rotor-only configuration does in the free atmosphere. To increase comparability between different designs, this total pressure loss can be formulated into a total pressure loss coefficient leading to the desired evaluation criterion of the static pressure recovery by

$$\zeta_{guide} = \frac{\Delta p_{t,loss}}{p_{d,fan} - p_{d,guide}}. \tag{5}$$

Replacing the total pressure loss of the guide vanes by Equation (4) eventually yields

$$\zeta_{guide} = 1 - \frac{\Delta p_{rec}}{p_{d,fan} - p_{d,guide}}. \tag{6}$$

When comparing different fans in a rotor-only configuration and computing ζ_{guide} for each design, fan designs with low values of ζ_{guide} achieve a better static pressure recovery than design with high values of ζ_{guide}. From a different perspective, fan designs in a rotor-only configuration, for which a certain value of ζ_{guide} is determined, achieve the same total-to-static pressure increase as configurations with guide vanes, where the guide vanes have an total pressure loss coefficient of exactly ζ_{guide}.

2.3. Modeling of Static Pressure Recovery

To utilize ξ_{guide} as an evaluation criterion from a design point of view, it is necessary to be able to assess it from fan design parameters directly. Central parameters of fan design are the radial profiles of the axial ($v_x(r)$) and circumferential ($v_\theta(r)$) velocity downstream of the fan, which are defined by the vortex design. With knowledge of the velocity profiles, all pressures entering ξ_{guide} can be computed as described in the following.

The local dynamic pressure in the discharge of the fan $p_{d,fan}(r)$ is a function of local velocity magnitude $v(r)$ and thus a function of $v_x(r)$ and $v_\theta(r)$ only. Mass flow weighted averaging of the dynamic pressure eventually yields

$$p_{d,fan} = \frac{2\pi}{\rho\dot{V}} \int_{r_{hub}}^{r_{tip}} r\rho v_x(r) \frac{\rho}{2} \left(v_x(r)^2 + v_\theta(r)^2 \right) dr. \tag{7}$$

To compute $p_{d,guide}$, the discharge of the configuration with guide vanes is assumed to be constant over radius and purely axial. Consequently, the dynamic pressure downstream of the outlet guide vanes $p_{d,guide}$ can be simplified to a function of the volume flow and the geometry:

$$p_{d,guide} = \frac{\rho}{2} \left(\frac{\dot{V}}{A_{fan}} \right)^2. \tag{8}$$

To compute the total pressure loss coefficient ξ_{guide} through Equation (6), the pressure recovery in the free atmosphere of the rotor-only configuration Δp_{rec} is still unknown and has to be estimated. Generally, this pressure recovery is defined as the difference between the average pressure at location 1 and location 0:

$$\Delta p_{rec} = \overline{p_1} - \overline{p_0}. \tag{9}$$

As described in Section 2.1, the average pressure at location 1 is equal to the ambient pressure. To estimate the average static pressure at location 0, Equation (1) is recapped, linking the static pressure to the circumferential velocity. Since p_0 is a static pressure, the average pressure $\overline{p_0}$ is derived as an area weighted average. Setting the area weighted average of $p_0(r)$ computed by Equation (1) into Equation (9), the static pressure recovery in the free atmosphere is

$$\Delta p_{rec} = -\frac{1}{A_{fan}} \int_{r_{hub}}^{r_{tip}} 2\pi r \left(\int_r^{r_{tip}} \rho \frac{v_\theta(r)^2}{r} dr \right) dr. \tag{10}$$

Eventually, with all corresponding pressures set into Equation (6), ξ_{guide} is given as a function of v_x and v_θ by

$$\xi_{guide} = 1 - \frac{-\frac{1}{A_{fan}} \int_{r_{hub}}^{r_{tip}} 2\pi r \left(\int_r^{r_{tip}} \rho \frac{v_\theta(r)^2}{r} dr \right) dr}{\frac{2\pi}{\rho\dot{V}} \int_{r_{hub}}^{r_{tip}} r\rho v_x(r) \frac{\rho}{2} \left(v_x(r)^2 + v_\theta(r)^2 \right) dr - \frac{\rho}{2} \left(\frac{\dot{V}}{A_{fan}} \right)^2}. \tag{11}$$

3. Methodology

3.1. Idealized Reference Design

To explore a design space defined later in this work towards the potential of ξ_{guide}, an idealized reference design is generated as a starting point. To compute ξ_{guide}, only the downstream velocity profiles and the hub and tip radius are needed. Consequently, no real fan designs themselves but rather only the resulting downstream velocity profiles are considered in this work, implying the corresponding airfoil design. To keep these downstream velocity profiles as simple as possible, the flow is highly idealized in the sense that boundary layers and secondary flows are neglected. The idealized reference

design is then assumed to be a free vortex design, which is characterized by a downstream circumferential velocity proportional to $1/r$. Considering the radial equilibrium, this yields a constant axial velocity over the radius:

$$v_{\theta,ref}(r) = \frac{c_\theta}{r} \qquad \text{and} \qquad v_{x,ref}(r) = c_x. \tag{12}$$

The overall level of the profiles (or the value of the constants c_θ and c_x, respectively) is adjusted to match the operating point. The operating point of the reference design is defined in terms of flow coefficient φ and total-to-total work coefficient ψ by

$$\varphi = \frac{\dot{V}}{A_{fan} \cdot u_{tip}} \qquad \text{and} \qquad \psi_t = \frac{2 \cdot \overline{\Delta p_t}}{\rho \cdot u_{tip}^2}. \tag{13}$$

The total-to-total pressure increase $\overline{\Delta p_t}$ is derived from the mass averaged Euler-work and is thus a function of the velocity profiles. The inflow circumferential velocity is assumed to be zero. The blade tip speed u_{tip} is given by the tip radius r_{tip} and the rotational speed. Additionally, a hub-to-tip ratio ν is given to assess the hub radius. Table 1 summarizes the operating point and the geometric parameters, which are set to the values of conventional low-pressure axial fans. The investigated hub-to-tip ratios of 0.3 and 0.5 respresent the lower and upper limits of usual designs.

Table 1. Operating point and geometric parameters.

Parameter	φ	ψ_t	r_{tip}	RPM	ν
Value	0.215	0.300	0.250 m	1350 min^{-1}	0.3, 0.5

3.2. Two-Dimensional Design Space

With the downstream velocity profiles of the idealized reference design, a two-dimensional design space can be spanned open by individually varying the axial and circumferential velocity profiles, although, as discussed later, this leads to non-physical design. This variation of the velocity profiles is achieved by adding the linear shifting functions $s_x(r)$ and $s_\theta(r)$.

Since the shifting functions $s_x(r)$ and $s_\theta(r)$ are linear, they are fully defined by their radial gradients ds_x/dr and ds_θ/dr and constants $c_{x,op}$ and $c_{\theta,op}$. Positive values of ds_x/dr and ds_θ/dr generate velocity profiles shifted to the casing, and negative values generate velocity profiles shifted to the hub, respectively. During the shifting process of the velocity profiles, their overall level is adjusted by $c_{x,op}$ and $c_{\theta,op}$, respectively, to ensure that the operating point in terms of φ and ψ is constant for all generated profiles. Adding the linear shifting functions to the velocity profiles of the reference design in Equation (12), the shifted downstream velocity profiles are given by

$$v_{\theta,shifted}(r) = \frac{c_\theta}{r} + \frac{ds_\theta}{dr} \cdot r + c_{\theta,op}, \tag{14}$$

$$v_{x,shifted}(r) = c_x + \frac{ds_x}{dr} \cdot r + c_{x,op}. \tag{15}$$

Consequently, ds_x/dr and ds_θ/dr are the parameters spanning a two-dimensional design space for the variation of the velocity profiles, whereas c_θ and c_x are kept constant to the values of the reference-free vortex design. These two parameters are varied independently. Obviously for axial fans, such an independent variation is impossible to achieve. In fact, Equation (14) is analogue to a more general vortex design, where the term c_θ/r represents a free vortex and the term $ds_\theta/dr \cdot r$ denotes the solid vortex. When varying the solid vortex part by varying ds_θ/dr, each resulting circumferential velocity profile is coupled to a specific axial velocity profile through the isentropic simple radial equilibrium. The resulting axial velocity profile, in turn, can be approximated by a linear profile and

subsequently linked to a certain value of ds_x/dr. This yields a single line of theoretically realizable velocity profiles of axial fans in the two-dimensional design space of ds_θ/dr and ds_x/dr, which will be discussed later in this work. Theoretically, deviations from this line might be possible when opening the design space to diagonal or radial machines which induce a considerable streamline curvature, but this will not be considered in this work.

The upper and lower limits of the gradient of the axial shifting function ds_x/dr are set such that the axial velocity reaches zero at the casing or hub, respectively, at the boundaries of the design space. The minimal and maximal values of ds_θ/dr are set equal to the extremes of ds_x/dr. Finally, ds_x/dr and ds_θ/dr are normalized by their extremes such that the vectors of the two-dimensional design space $ds_{x,norm}/dr$ and $ds_{\theta,norm}/dr$ are defined on $[-1, 1]$.

Figure 3 shows samples of the velocity profiles in the design space. The abscissa shows $ds_{x,norm}/dr$. For velocity profiles on the left side in Figure 3, where $ds_{x,norm}/dr$ is negative, the mass flow is concentrated at the hub, and subsequently, for the profiles on the right side, $ds_{x,norm}/dr$ it is positive and the mass flow is concentrated at the casing. The ordinate shows $ds_{\theta,norm}/dr$, resembling the solid vortex part of Equation (14). For velocity profiles on the bottom side in Figure 3, where $ds_{\theta,norm}/dr$ is negative, the Euler work is increased at the hub, and subsequently, for the profiles on the top side, $ds_{\theta,norm}/dr$ it is positive and the Euler work is increased towards the casing. The velocity profiles at coordinates (0, 0) in Figure 3 correspond to the reference-free vortex design of Equation (12).

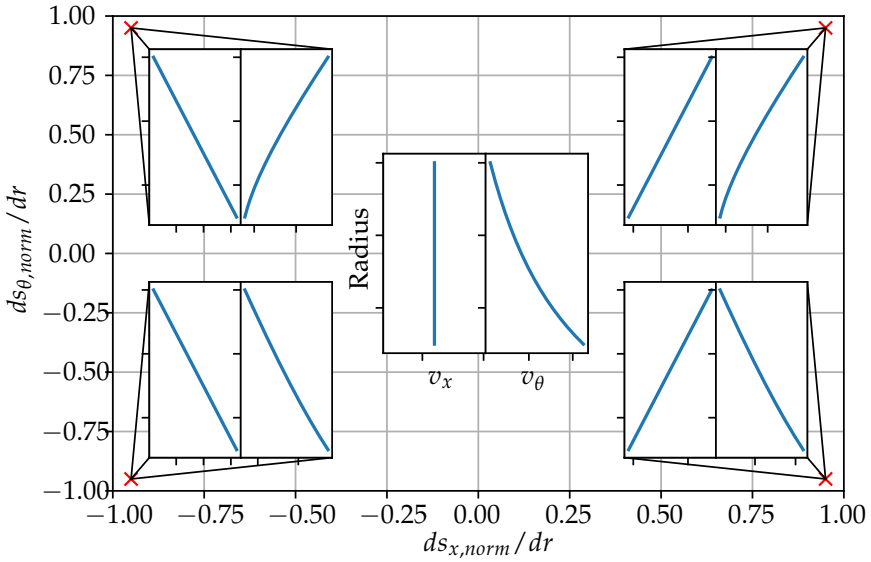

Figure 3. Velocity profile samples of the design space formed by the normalized gradients of the linear shifting functions. The profiles at (0, 0) correspond to a free vortex design. The resulting velocity profiles at the corners of the designs space (red crosses) are shown for comparison.

4. Results of the Design Space Exploration

Since every point of the two-dimensional design space represents a set of velocity profiles implying a fan design, ζ_{guide} can be evaluated for each point, regardless of the fact, that some profiles are non-physical. This yields a contour plot of ζ_{guide} over $ds_{x,norm}/dr$ and $ds_{\theta,norm}/dr$, as shown in Figure 4 for two values of the hub-to-tip ratio ν of 0.3 (left) and 0.5 (right). In these contours, the black lines represent the points at which the velocity profiles obey the isentropic simple radial equilibrium and which are thus theoretically realizable in axial fan designs. The red crosses mark the optimal, i.e., minimal, value of ζ_{guide} on these lines.

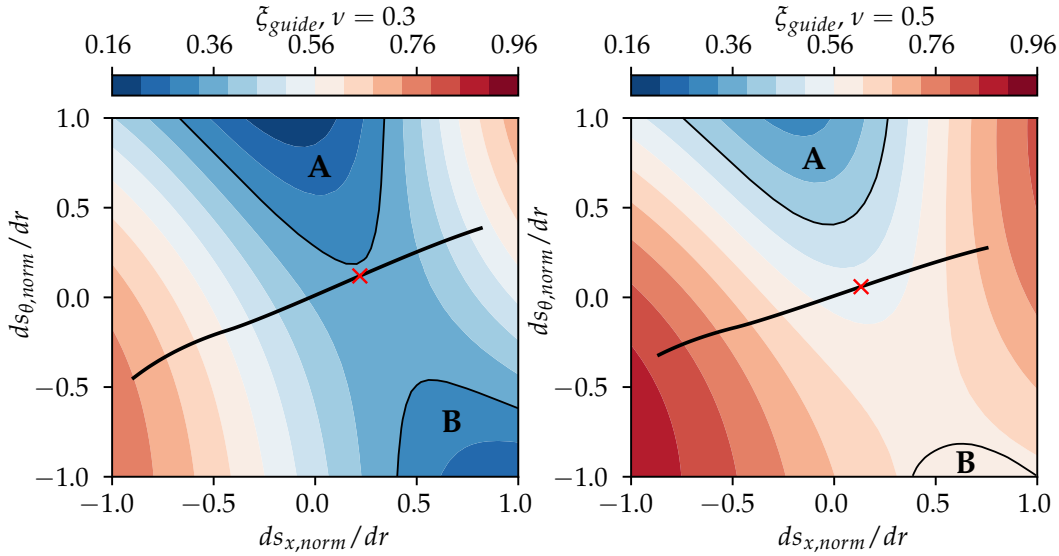

Figure 4. Contours of ξ_{guide} on the design space for a hub-to-tip ratio ν of 0.3 (**left**) and 0.5 (**right**). Velocity profiles obeying the isentropic simple radial equilibrium are shown in black, while the red cross marks the optimal point on this line.

Considering, first, the whole contour for both hub-to-tip ratios, it is apparent that, generally, the lower value of $\nu = 0.3$ (left) yields lower (i.e., better) values of ξ_{guide}. In fact, the global minimal value of ξ_{guide} is approximately 0.18 for $\nu = 0.3$, whereas for $\nu = 0.5$, it is 0.31. The best values of ξ_{guide} for the realizable fan designs (black lines) are 0.35 and 0.53 for $\nu = 0.3$ and $\nu = 0.5$, respectively.

Besides quantitative differences, qualitative observations can be made equally for both hub-to-tip ratios. Generally favorable fan designs in terms of ξ_{guide} are found in two separate regions, **A** and **B**, of the contour plots. Region **A** at the top center with

$$\frac{ds_{x,norm,A}}{dr} \approx 0 \quad \text{and} \quad \frac{ds_{\theta,norm,A}}{dr} > 0 \tag{16}$$

corresponds to fan designs with a constant downstream axial velocity and a circumferential velocity shifted towards to the casing. Region **B** towards the bottom right with

$$\frac{ds_{x,norm,B}}{dr} > 0 \quad \text{and} \quad \frac{ds_{\theta,norm,B}}{dr} < 0 \tag{17}$$

corresponds to fan designs with a downstream axial velocity shifted to the casing and a circumferential velocity shifted towards the hub.

Focusing on the set of downstream velocity profiles that obey the isentropic simple radial equilibrium (black lines in Figure 4), strong variations of ξ_{guide} can be observed. For the designs with a hub-to-tip ratio of $\nu = 0.3$, the optimal value of ξ_{guide} is 0.35, while adverse designs only reach values around 0.76. In the case of $\nu = 0.5$, the optimal value of the realizable designs is 0.53, while other designs fall off to values of 0.84. These harsh differences indeed indicate that it is important to consider the static pressure recovery in the free atmosphere already in the vortex design of the fan. The optimal vortex design in terms of ξ_{guide} (red crosses in Figure 4) seems to be slightly shifted from a pure free vortex design (coordinates (0, 0)) towards a design with a mix of free vortex and solid vortex.

5. Discussion

The physical interpretation for smaller hub-to-tip ratios yielding favourable values of ξ_{guide} is a larger annular channel which contains more rotating mass. Consequently, more rotating mass results in higher inertial (i.e., centrifugal) forces, which are initially causing

the sub-atmospheric pressure in the fan discharge. Thus, the difference to the ambient pressure in the fan discharge is stronger.

The reason for regions A and B of the design space being favorable become evident when considering Figure 5, which depicts contour plots of the static pressure recovery Δp_{rec} and the downstream dynamic pressure of the fan $p_{d,fan}$. To reiterate Equation (6), both these pressures are the central quantities defining ζ_{guide}, whereas $p_{d,guide}$ is constant for a fixed operating point under the assumptions made. Equation (6) shows that high values of Δp_{rec} and low values of $p_{d,fan}$ result in good (i.e., low) values of ζ_{guide}.

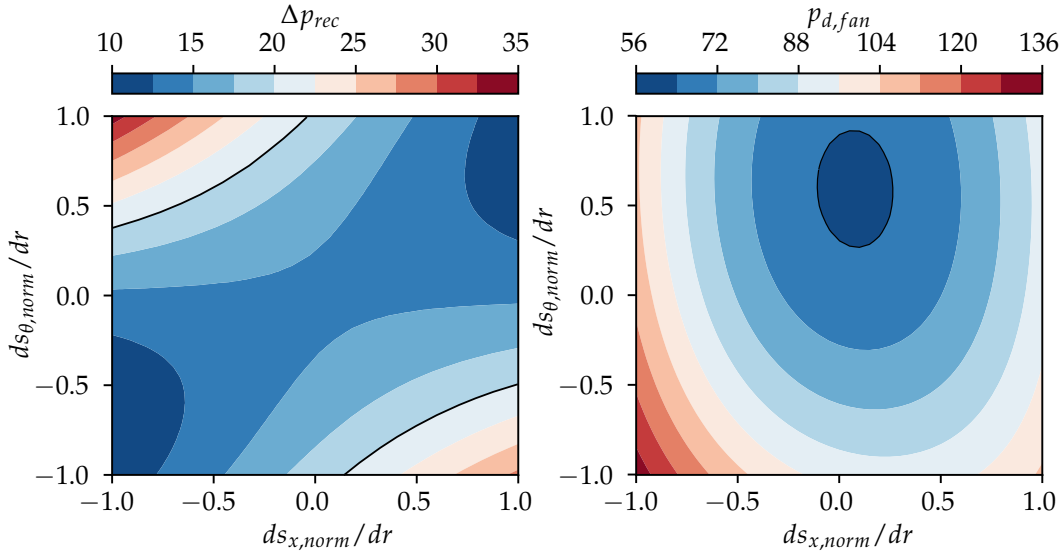

Figure 5. Contour of the static pressure recovery (**left**) and the dynamic pressure in the fan discharge (**right**) for $\nu = 0.5$. Black lines encircle favorable regions of the design space.

When considering, first, the contour of Δp_{rec} on the left side of Figure 5, favorable regions are at the top left and the bottom right of the design space. In the top left region of the design space, the circumferential velocity is shifted towards the casing. This results in lower pressures at the outer radii and, simultaneously, in higher pressures at the inner radii when compared to the reference design. When area averaging the static pressure over the radius to compute Δp_{rec}, the lower pressures at the casing outweigh the higher pressures at the hub since they are acting on a larger area. Additionally, in this region, the mass flow is concentrated in regions with the lowest circumferential velocity, i.e., the lowest Euler-work. When requiring the mass-averaged Euler-work to be equal for all velocity profiles, this necessitates a global increase in the circumferential velocity. Eventually, both effects result in higher values of Δp_{rec}. On the bottom right region of the design space, the circumferential velocity is shifted towards the hub. Here, the effect is opposite to the region on the top left. Although there are higher pressures at the outer radii acting on larger areas, the minimal values of the pressures which arise at the hub compensate for this. Furthermore, in this region, the same global increase in v_θ is necessary due to analog reasons, as in the top left region of the design space. Thus, in total, higher values of Δp_{rec} are achieved in this region. In fact, the free vortex reference design at coordinates (0, 0) achieves quite low values of static pressure recovery when considering the whole design space. In contrast to the contour of Δp_{rec}, the contour of $p_{d,fan}$ only shows a singular favorable region of minimal values at the top center of the design space. This is due to both the axial and the circumferential velocities being approximately constant over the radius in this region. Constant velocity profiles result in minimal average dynamic pressure because of the quadratic influence of the velocity on the dynamic pressure. This quadratic influence leads to the fact that non-constant profiles, with their corresponding higher maximum values, result in higher average dynamic pressures. The combination of these different

favorable regions of Δp_{rec} and $p_{d,fan}$ in the design space eventually result in the favorable regions **A** and **B** in the contour of ξ_{guide}.

6. Conclusions

The general mechanism of the pressure recovery described in Section 2.1 follows directly from a strong circumferential velocity component present in the discharge of the fan, yielding a sub-atmospheric pressure which is vanishing downstream in the free atmosphere. Considering this mechanism, the two questions presented in the introduction are answered in this paper:

The total pressure loss coefficient ξ_{guide} derived in this work provides a metric by which to evaluate the static pressure recovery in the free atmosphere. The minimal values of ξ_{guide} are 0.35 and 0.53 for hub-to-tip ratios of $\nu = 0.3$ and $\nu = 0.5$, respectively, when considering the velocity profiles obeying the simple isentropic radial equilibrium. Both values of these total pressure loss coefficients are quite high, especially considering the fact that these are optimal values. Consequently, these results indicate that it is generally possible to design outlet guide vanes for low-pressure axial fans that improve the total-to-static pressure increase when compared to the rotor-only configuration.

The hub-to-tip ratio ν and the vortex design of the machine significantly impact the static pressure increase. From the two hub-to-tip ratios investigated, the smaller value of ν generally results in better static pressure recoveries. In fact, for a fixed $\nu = 0.5$, the values of ξ_{guide} vary between 0.53 and 0.84 as a function of the vortex design. For $\nu = 0.3$, these ξ_{guide} reach values between 0.35 and 0.76. So, while generally, outlet guide vanes, which are properly designed in terms of total pressure loss, are beneficial to the total-to-static pressure increase, these results indicate that it is indeed important to consider the static pressure recovery already in the vortex design of the fan when OGVs are not an option due to external constraints. In both cases, the optimal vortex design in terms of static pressure recovery is close to a pure free vortex with the slight addition of a solid vortex part where the exact blending factor depends on the hub-to-tip ratio. With an outlook for real fan design, it is important to point out that for low hub-to-tip ratios, it is increasingly challenging to realize such vortex designs due to the large required flow deflection towards the hub.

Author Contributions: Conceptualization, H.W. and C.B.; methodology, H.W. and C.B.; software, H.W.; validation, H.W.; formal analysis, H.W.; investigation, H.W.; resources, C.B.; data curation, H.W.; writing—original draft preparation, H.W.; writing—review and editing, C.B. and J.F.; visualization, H.W.; supervision, C.B. and J.F.; project administration, J.F.; funding acquisition, J.F. All authors have read and agreed to the published version of the manuscript.

Funding: This research was funded by the Forschungsvereinigung für Luft- und Trocknungstechnik (FLT) (IGF-Nr. 59 EWN). The FLT is part of the German Federation of Industrial Research Associations (AiF), and the projects are financed by the German Federal Ministry for Economic Affairs and Climate Action (BMWK).

Data Availability Statement: The data presented in this study are available on request from the corresponding author.

Conflicts of Interest: The authors declare no conflict of interest.

References

1. Marcinowski, H. Optimalprobleme bei Axialventilatoren. Ph.D. Thesis, Technische Hochschule Karlsruhe, Karlsruhe, Germany, 1957.
2. Marcinowski, H. Druck- und Geschwindigkeitsverteilung hinter dem Laufrad eines Axialventilators. *Voith Forsch. Und Konstr.* **1957**, *2*, 5:1–5:17
3. Bamberger, K.; Carolus, T. Achievable Total-to-Static Efficiencies of Low-Pressure Axial Fans. In Proceedings of the International Conference on Fan Noise, Fan Technology and Numerical Methods, Lyon, France, 15–17 April 2015.
4. Bamberger, K.; Carolus, T. Performance Prediction of Axial Fans by CFD-Trained Meta-Models. In Proceedings of the ASME Turbo Expo 2014: Turbine Technical Conference and Exposition, Düsseldorf, Germany, 16–20 June 2014.

5. Čantrak, Đ.S.; Janković N. Laser Insight Into the Turbulent Swirl Flow Behind the Axial Flow Fan. In Proceedings of the ASME Turbo Expo 2014: Turbine Technical Conference and Exposition, Düsseldorf, Germany, 16–20 June 2014.
6. Louw, F.G.; von Backström, T.W.; van der Spuy, S.J. Investigation of the Flow Field in the Vicinity of an Axial Flow Fan during Low Flow Rates. In Proceedings of the ASME Turbo Expo 2014: Turbine Technical Conference and Exposition, Düsseldorf, Germany, 16–20 June 2014.
7. Witte, H.; Bode, C.; Friedrichs, J. Potential of Static Pressure Recovery of Rotor-Only Low Pressure Axial Fans. In Proceedings of the 15th European Turbomachinery Conference, paper n. ETC2023-157, Budapest, Hungary, 24–28 April 2023. Available online: https://www.euroturbo.eu/publications/conference-proceedings-repository/ (accessed on 6 September 2023).

Disclaimer/Publisher's Note: The statements, opinions and data contained in all publications are solely those of the individual author(s) and contributor(s) and not of MDPI and/or the editor(s). MDPI and/or the editor(s) disclaim responsibility for any injury to people or property resulting from any ideas, methods, instructions or products referred to in the content.

International Journal of
Turbomachinery
Propulsion and Power

MDPI

Article

Experimental Validation of a Numerical Coupling Environment Applying FEM and CFD †

Christopher Hartmann [1,*], Julia Schweikert [1], François Cottier [2], Ute Israel [2], Jochen Gier [2] and Jens von Wolfersdorf [1]

[1] Institute of Aerospace Thermodynamics (ITLR), University of Stuttgart, Pfaffenwaldring 31, 70569 Stuttgart, Germany; julia.schweikert@itlr.uni-stuttgart.de (J.S.); jens.vonwolfersdorf@itlr.uni-stuttgart.de (J.v.W.)
[2] MTU Aero Engines AG, Dachauer Strasse 665, 80995 München, Germany; francois.cottier@mtu.de (F.C.); ute.israel@mtu.de (U.I.); jochen.gier@mtu.de (J.G.)
* Correspondence: christopher.hartmann@itlr.uni-stuttgart.de
† This paper is an extended version of our meeting paper published in the 15th European Turbomachinery Conference, Budapest, Hungary, 24–28 April 2023.

Abstract: Experimental results for the transient heat transfer characteristics over a flat plate and over a plate with V-shaped ribs were compared to numerical results from a coupling environment applying FEM and CFD. In order to simulate transient effects in the cooling process of engine components during typical flight missions, the temperature and the velocity at the inlet of the channel were varied over time. The transient temperature distribution at the plate was measured using infrared thermography. Five different plate materials (perspex, PEEK, quartz, aluminum, and steel) were considered to investigate the influence of thermal conduction on the heat transfer between solid and fluid depending on the Biot number. The experimental results represent a reference database for a Python-based coupling environment applying CalculiX (FEM) and ANSYS CFX (CFD). The results were additionally compared to numerical results simulating the complete transient conjugated heat transfer with CFD. A good agreement between the numerical and the experimental results was achieved using different coupling sizes at different Biot numbers for the flat plate and the plate with V-shaped ribs.

Keywords: transient; conjugate; heat-transfer; IRT; coupling; CHT

check for updates

Citation: Hartmann, C.; Schweikert, J.; Cottier, F.; Israel, U.; Gier, J.; von Wolfersdorf, J. Experimental Validation of a Numerical Coupling Environment Applying FEM and CFD. *Int. J. Turbomach. Propuls. Power* **2023**, *8*, 31. https://doi.org/10.3390/ijtpp8030031

Academic Editor: Michel Dumas

Received: 20 June 2023
Revised: 25 June 2023
Accepted: 29 August 2023
Published: 4 September 2023

Copyright: © 2023 by the authors. Licensee MDPI, Basel, Switzerland. This article is an open access article distributed under the terms and conditions of the Creative Commons Attribution (CC BY-NC-ND) license (https://creativecommons.org/licenses/by-nc-nd/4.0/).

1. Introduction

An essential task in the development process of modern aero engines is designated to the cooling mechanisms of the thermally high-stressed engine components. The component life—and, consequently, that of the entire engine—depends strongly on the material temperatures and requires, therefore, reliable prediction of the material temperatures for typical flight missions. Conjugate heat transfer (CHT), first formulated by Perelman [1], considers the interaction between solid and fluid. The flow conditions strongly influence the material temperatures and thermal interactions. Thus, secondary flows occur in cavities in compressors and turbines. For optimum design, transient processes and solid–fluid interaction, as well as the thermal time disparity for the solid and fluid, have to be considered. Transient analyses of temperature and stress distributions in turbine components usually use the finite element method. The occurring thermal loads are described by simplified boundary condition models from empirical correlations using advective one-dimensional models, as presented by Fiedler et al. [2]. Heselhaus and Vogel [3] have shown that, through transient, conjugate-flow, and heat-transfer simulations that take three-dimensional effects into account, a significant improvement in accuracy can be achieved without relying on empirical correlations. Thus, the prediction of component temperatures can be significantly improved, as Felippa et al. [4] have shown. Inappropriate modeling of the transient effects

during flight changes can lead, in contrast, to critical clearances or thermal stress, like Sun et al. [5] and Amirante et al. [6] have reported. Thermal time disparities make conjugated heat transfer simulations of a complete mission considering all time scales extremely expensive because convective heat transfer in the fluid is up to 10^4 times faster than the solid heat conduction, which was reported by He and Oldfield [7].

In order to reduce the computational effort, Errera and Baqué [8] and Sun et al. [5] introduced coupled aerothermomechanical methods, where optimized programs are used to independently simulate the heat transfer in the fluid and solid. This so-called weak coupling makes it possible to calculate the thermal behavior of the solid using an FEM code, whereas the adjacent flow is calculated by means of CFD. In order to ensure a physical, accurate, and stable solution for the conjugate system, the FEM and CFD codes need to exchange information at their common interface. For this different strategies exist in the literature. Errera and Duchaine [9] investigated different coupling coefficients and the continuity of exchange variables for aerothermal simulations. They showed that, if a criterion based on the ratio of thermal resistances at the interface is met, the Dirichlet–Robin transmission procedure leads to stable and fast convergence. Gimenez et al. [10], Khoury et al. [11], and Moretti et al. [12]) presented approaches updating boundary conditions between coupling points. They showed that a quasi-dynamic coupling method with transient calculations for the solids and steady fluid calculations is the most promising in terms of accuracy and efficiency. Further, Gimenez et al. [10] demonstrated that a relaxation parameter value close to the heat transfer coefficient is beneficial. For conjugate heat transfer problems, the Biot number is a key parameter for the stability of the coupling scheme, as Verstraete and Scholl [13] identified.

Sun et al. [14] evaluated the applicability of such an approach for operating point changes in a low-pressure turbine cavity, Verdicchio et al. [15] for turbine discs, Dixon et al. [16] for main annulus gas path interactions, and Ganine et al. [17] for an internal air system with multiple cavities. Errera and Baqué [8] used this approach to investigate transient heat conduction in a flat plate subjected to a time-varying flow. For this particular case, computational time saving of up to 90% compared to strong coupling was documented with good accuracy.

In this context, an external Python-based coupling interface has been developed at the Institute of Aerospace Thermodynamics (ITLR) by Schindler et al. [18]. The interface couples the open-source FEM code CalculiX introduced by Dhondt [19] in transient mode with a steady-state CFD simulation for the fluid. For the present study, the commercial CFD software ANSYS CFX was used. In order to qualify the coupling interface, a reference database was generated using transient measurements. The experimental setup involved a channel flow over a flat plate, as well as an arrangement of five periodic V-ribs. Whereas most test facilities allow the regulation of just one boundary condition, the present setup allowed the independent setting of time-variable temperature and velocity inlet conditions. With simultaneous spatial and temporal high-resolution IRT, the wall temperature can be measured and the wall heat flux at the solid–fluid interface can be calculated with the semi-analytical approach described by Estorf [20]. Thereby, a reference dataset with which the coupling environment can be stressed in terms of different parameters can be generated where changes in the boundary conditions as they may occur in real applications are considered. Israel et al. [21] showed the applicability of the presented coupling environment for industry-related uses.

The aim of this study was to generate and demonstrate the capabilities of the experimental facility as validation for both CHT simulations and a coupling environment with different Biot numbers, different geometries, and different time-dependent inlet boundary conditions as an extended version of Hartmann et al [22].

2. Experimental Setup

An experimental test facility for local time-resolved transient heat transfer measurements has been designed by Liu et al. [23]. Brack et al. [24] modified the basic setup

to investigate unsteady convective heat transfer under controlled airflow velocity and temperature variation.

For the present work, the test rig was adapted to measure time-resolved transient heat transfer phenomena for different materials and turbulator geometries under generic and industry-related operating conditions. The experimental setup is shown in Figure 1. A vacuum pump was used to suck air from the ambient environment through a dust filter. The air is heated by a mesh heater and enters a test section with a constant cross-section of 0.12 m × 0.15 m. The time-variable temperature and velocity at the inlet of the channel can be set independently using a LabVIEW routine, which adjusts the power of the electrical mesh heaters and the positioning of the rotating vanes at the end of the channel (see Brack et al. [24]). With two hot-wire anemometers from SVMtec, the inlet boundary conditions were monitored, with one working in constant current mode to measure the inlet temperature (CCT) and the other in constant temperature mode to measure the inlet velocity (CTA). Both were located 0.205 m upstream of the flat plate. The plate with the dimensions 0.92 m × 0.12 m × 0.03 m was positioned in the center of the channel, dividing the test section into two subchannels. A trip wire at the beginning of the flat plate ensures a turbulent flow. On the top of the test section, a 5 mm thick CaF_2 window was installed to offer optical access for the IRT camera, an FLIR SC7600, which measured the surface radiation in a spectral range from 1.5 µm to 5.1 µm at 25 Hz. To ensure constant and equal emittance, the test plate was sprayed with a black paint (type SPB100 from Hallcrest). For in situ calibration of the IRT data, two surface thermocouples were inserted into the plate to measure the surface temperature.

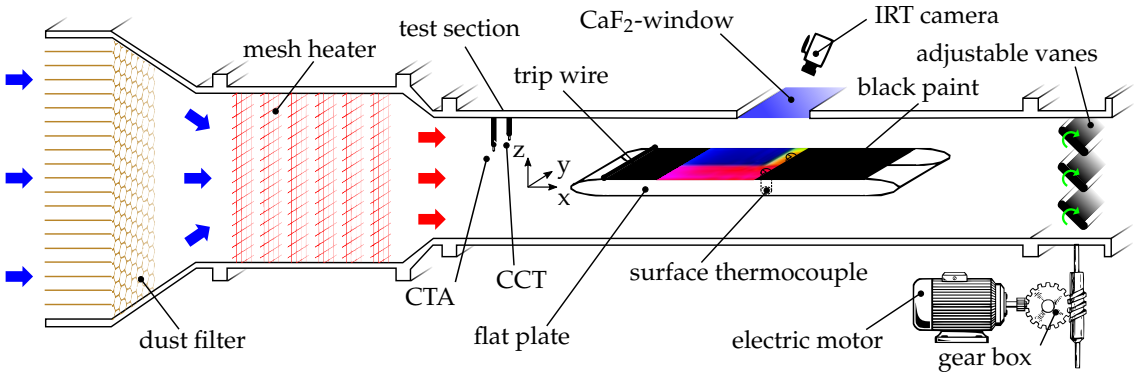

Figure 1. Experimental setup.

For the baseline configuration, the flat plate was made from perspex. In order to investigate the influence of heat conduction to convection between the solid and fluid, the material of the plate was varied in one section with the dimensions 0.25 m × 0.06 m × 0.015 m. As visualized in Figure 2a, the material was changed using two inlays, with one always being made from perspex to ensure repeatability. The field of view (FOV) of the IRT camera started from 110 mm behind the beginning of the inlays and included the thermocouples for in situ calibration. Besides the flat plate, a plate with five V-shaped ribs was further investigated, which can be seen in Figure 2b. The 90° squared ribs with dimensions $e = 10$ mm were glued on the test plate with a pitch of $p = 0.1$ m, resulting in two visible ribs for the IRT camera. Both geometries were investigated in five different test cases, which are shown in Figure 3. First, generic test cases were investigated, including a temperature jump (jump), a temperature ramp (ramp A) with constant velocity, and a velocity ramp (ramp B) with constant temperature. Afterwards, two transient cycles were investigated. One was typical for a flight mission, with opposite changes in temperature and velocity (cycle A), and one used an inversion in the heat flux to amplify the conjugate situation (cycle B).

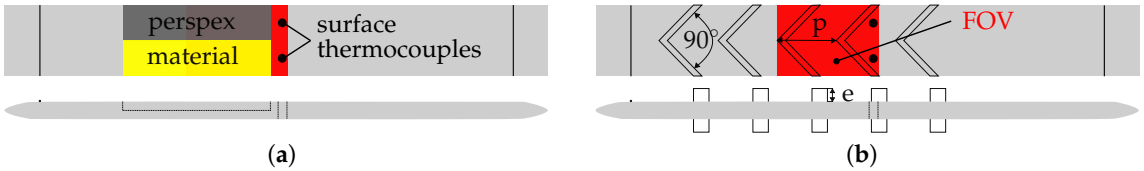

Figure 2. Test geometries: (**a**) flat plate, (**b**) plate with V-shaped ribs.

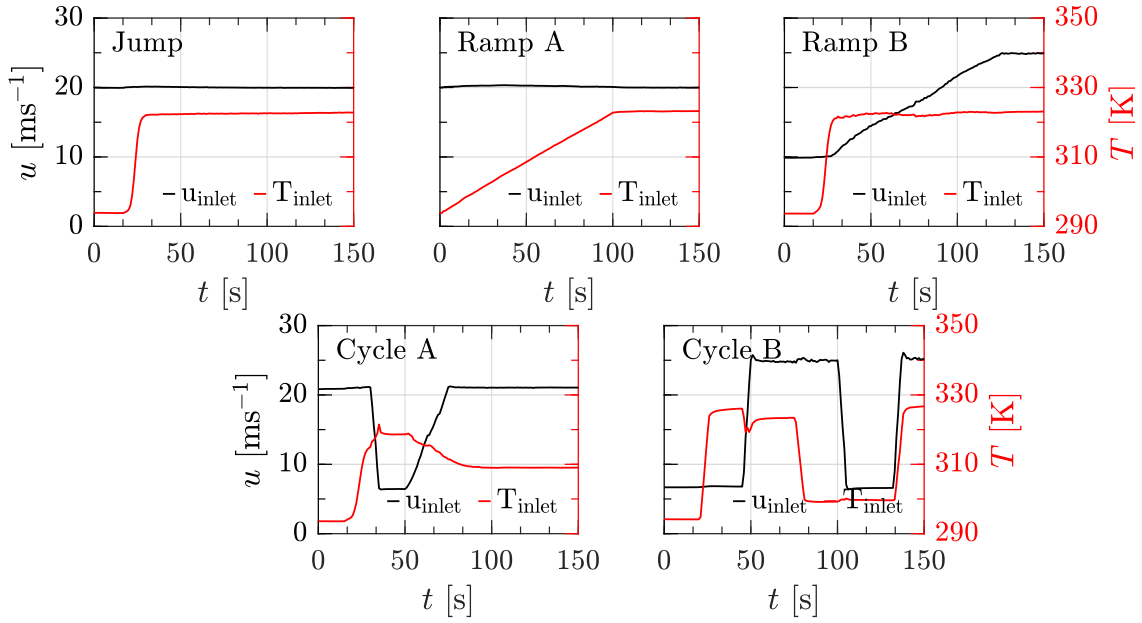

Figure 3. Boundary conditions.

3. Numerical Setup

The numerical setup consisted of one part of the channel, including the complete test plate, as is shown in Figure 4a. The inlet to the fluid domain was located 0.25 m upstream of the plate. The outlet was positioned 0.25 m downstream of the plate. Only one half of the channel height was simulated, using a symmetry condition at $z = 0$. The flat plate divided the channel height (0.15 m) into two sub-channels, each 0.06 m high. This resulted in an aspect ratio of 2:1 for each sub-channel. Due to the absence of lateral flow effects in the case of the flat plate, sidewalls and the lateral effects were negligible, and a 2D setup was simulated. To further validate this, a 3D setup for the flat plate case was investigated in a pre-test, showing negligible differences in the results. For the case with five V-ribs, a 3D setup was used. The fluid domain was discretized with a block-structured C- or H-grid in ANSYS ICEM 20.2. The dimensionless distance of the first node near the wall lay within $y_1^+ < 1$. For the ribbed geometry, the region directly behind and in front of the ribs was finely meshed with a C-shaped grid to guarantee the required near-wall resolution and to consider boundary layer effects. For the CHT simulations in the fully implicit, coupled multigrid solver ANSYS CFX, the solid domain was discretized with a block-structured grid in ANSYS ICEM, resulting in an 1:1 mesh connection at the interface. For the coupling with CalculiX, the solid domain consisted of four-node tetrahedral elements, as shown in Figure 4b, while the fluid mesh was identical. The data transfer between the two meshes used for the coupling environment was undertaken by transforming the respective grid into a universal format. There, each data point was assigned to a Cartesian point. The mapping between the two grids was then undertaken using the griddata function and a nearest-neighbor interpolation algorithm.

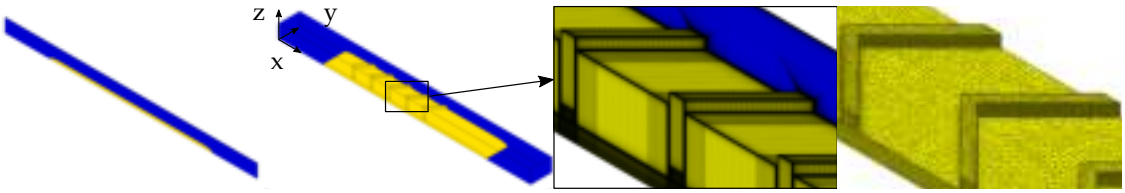

Figure 4. Numerical setup: (**a**) flat plate (**left**) and V-shaped ribs (**right**). (**b**) CFX (**left**) and CCX (**right**) mesh.

To solve the unsteady Reynolds-averaged Navier–Stokes equations, the SST turbulence model developed by Menter [25] was used, which provides a good compromise between high accuracy and acceptable computation time. For the rib geometry, reattachment modification and curvature correction were enabled, as the standard SST model tends to overpredict the separation region of a detached flow (see Menter et al. [26]). The advection terms were discretized with the default quasi-second-order discretization scheme in CFX, which is called High Resolution. The transient terms were discretized with a second-order backward Euler scheme, while the convergence criteria were of a root-mean-square type for the conservation equations targeted to be 10^{-7}. The modified setup has shown good results in comparable complex cooling channels (see Göhring et al. [27]). At the inlet, the transient boundary conditions of the temperature and velocity were taken according to the hot-wire measurements. At the outlet, a constant pressure was imposed as an averaged value from the experiment. For the CHT simulations, a time-step size of $t_{\mathrm{CHT}} = 1\,\mathrm{s}$ was used to simulate the whole experimental duration of $t_{\mathrm{total}} = 150\,\mathrm{s}$. Even though the time-step size was relatively large, a stable solution was achieved, and the results from the monolithic approach were intended to function as a reference for the coupling. The channel walls were set as adiabatic and the fluid was modeled as an ideal gas. Dynamic viscosity η and thermal conductivity k, were modeled as temperature-dependent using the formula presented by Sutherland [28] with the coefficients presented by White [29]. The material quantities for the respective solid domain, which were taken from the manufacturers, are summarized in Table 1.

Table 1. Material quantities.

	Perspex	PEEK	Quartz	Steel	Aluminum
$\rho\left[\mathrm{kg\,m^{-3}}\right]$	1190	1310	2200	7900	2700
$c_p\left[\mathrm{J\,kg^{-1}\,K^{-1}}\right]$	1470	1340	670	500	888
$k\left[\mathrm{W\,m^{-1}\,K^{-1}}\right]$	0.19	0.25	1.4	15	237

4. Coupling Environment

The coupling environment, developed by Schindler et al. [18], controls the communication between the thermal FEM solver CalculiX for the solid domain and a user-defined FVM solver for the fluid domain. For the present study, the commercial solver ANSYS CFX V21.1 was used, which is a common tool for industrial applications (Cottier et al. [30]).

With the Python-based coupling environment, the transient effects inside the solid were simulated using CalculiX. This yielded the spatially and temporally resolved temperature evolution in the structure. By means of steady-state CFD simulations at selected times, thermal feedback, flow, and an interface update were enabled. The procedure of the coupling algorithm is demonstrated in Figure 5. After initialization of both codes (1), CalculiX ran in transient mode with a time interval of $\Delta t_{\mathrm{ccx}} = 0.2\,\mathrm{s}$ (2) until the coupling time interval t_{cpl} was reached. In the course of this, a Robin condition $\left(\dot{q}^{\nu}_{\mathrm{solid}}(t) = h^{\nu}(t)\left(T^{\nu}_{\mathrm{solid}}(t) - T^{\nu}_{\mathrm{ref}}(t)\right)\right)$ was imposed on the solid-side interface. For the first subiteration $\nu = 1$, a constant T^{ν}_{ref} and h^{ν} based on t_{i-1} was used. At each coupling point,

the FEA results were than imposed as a Dirichlet condition on the fluid side for the steady CFD ($T^{\nu}_{\text{fluid}}(t_i) = T^{\nu}_{\text{solid}}(t_i)$). Thus, a combination of Dirichlet and Robin conditions to exchange T_{ref} or h (via $\dot{q}$), respectively, at the interface between adjacent fluid and solid domains was used (3). Using a root-mean-square evaluation of $T^{\nu}_{\text{fluid}} - T^{\nu-1}_{\text{fluid}}$ at the interface for all points at the interface, convergence was checked (4). If no convergence was reached, T_{ref} and h were updated with a linear interpolation from the converged values of the old coupling step at t_{i-1} (5). Then, CalculiX was run with the updated transient Robin condition. This was repeated until $\epsilon < \epsilon_{\max}$ or the maximum number of subiterations ν was reached (6). Thereby, the coupling interval depended on the variation of the boundary conditions. To additionally accelerate convergence, a relaxation method proposed by Aitken [31] was implemented.

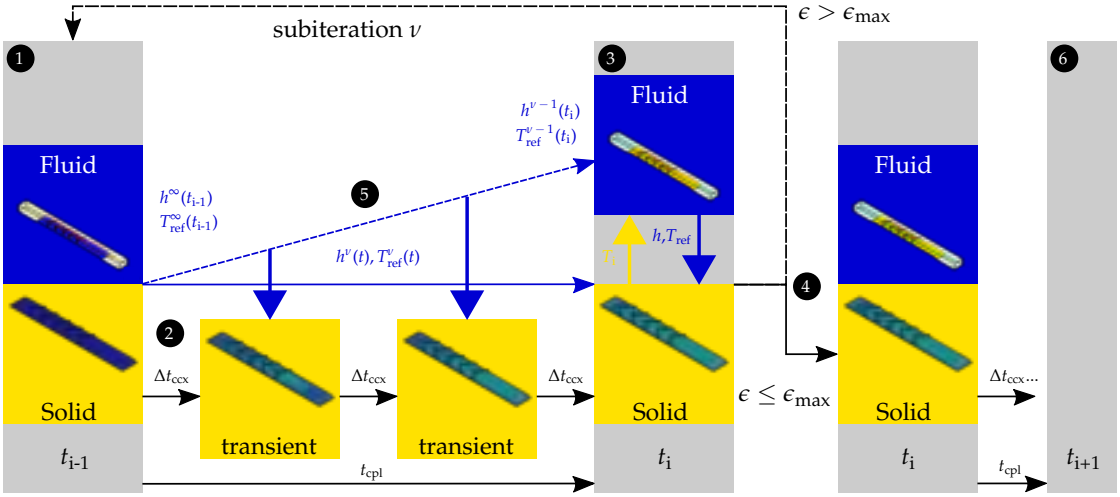

Figure 5. Coupling scheme.

An overview of the studied geometries, numerical approaches, test cases, and investigated materials is given in Table 2.

Table 2. Overview of the studied geometries, approaches, cases and materials.

Geometry	Approach			Test Case					Material				
					Ramp		Cycle						
	Exp	CHT	Cpl	Jump	A	B	A	B	Perspex	PEEK	Quartz	Aluminium	Steel
Flat plate	X	X	X	X	X	X	X	X	X	X	X	X	X
V-ribs	X	X	X	X	X	X	X	X	X				

5. Data Reduction and Evaluation

Using the two hot-wire anemometers at the channel inlet, the boundary conditions T_{inlet} and u_{inlet} were measured with a frequency of 4000 Hz. The wall temperature T_{w} was temporally and spatially resolved with a frequency of 25 Hz and a spatial resolution of 0.4 mm/pixel for $t_{\text{exp}} = 150$ s. The data were filtered by means of a 3D Gaussian filter and, for better handling, the frequency for all measurements was afterwards reduced to 5 Hz. Even with a frequency of 5 Hz, it was ensured that the step changes in the boundary conditions (see Figure 3), which always occur within 5 s, could be sufficiently resolved and did not affect the results. To evaluate the temporally and spatially resolved wall heat flux $\dot{q}_{\text{w}}$, a method developed by Estorf [20] was used. The method ensures the equality of the heat flux into the solid and of the fluid. It is based on the analytical solution of the transient heat transfer equation within the wall for constant material properties and considers 3D

lateral heat conduction effects by taking into account the transient surface temperature of an area surrounding each evaluation point within the infrared image. For the validity of the method, isothermal initial conditions for the whole experimental setup have to be ensured. So, the plate was at ambient temperature at the beginning of each experiment and was subsequently heated up by a time-dependent hot flow. Second, the wall has to be semi-infinite, limiting the experiment duration to

$$t_\infty = \frac{\rho c_\mathrm{p}}{k}\frac{L^2}{4} \tag{1}$$

as indicated by Vogel and Weigand [32]. This criterion ensures a deviation from the analytical solution for an adiabatic backside of less than 2% (cf. Wagner et al. [33]). For the investigated materials given in Table 1, this resulted in valid evaluation times for the wall heat flux from less than 1 s for aluminum to over 500 s for perspex (see Table 3). With T_w, $\dot{q}_\mathrm{w}$, and the inlet temperature as the reference temperature of the fluid ($T_\mathrm{ref} = T_\mathrm{inlet}$), the wall heat transfer coefficient h_w can be calculated using Newton's law of cooling:

$$h_\mathrm{w} = \frac{\dot{q}_\mathrm{w}}{T_\mathrm{w} - T_\mathrm{ref}}. \tag{2}$$

To investigate the influence of thermal conduction on the heat transfer between solid and fluid, the Biot number,

$$Bi = \frac{hL}{k}, \tag{3}$$

was varied. With a typical heat transfer coefficient for a flat plate at the given flow velocities of 60 $\mathrm{W\,m^{-2}\,K^{-1}}$ (cf. Kays et al. [34]) and a characteristic length of $L = 0.015$ m, a wide range of Biot numbers could be investigated with the chosen materials (see Table 3).

Table 3. Time for semi-infinite evaluation and Biot numbers for investigated materials.

	Perspex	PEEK	Quartz	Steel	Aluminum
t_∞ (s)	517.9	395.0	59.2	14.8	0.6
Bi ($h_\mathrm{w} = 60\ \mathrm{W\,m^{-2}\,K^{-1}}$)	4.7	3.6	0.64	0.06	0.0038

The measured quantities T_inlet, u_inlet, and T_w, as well as the evaluated ones, $\dot{q}_\mathrm{w}$ and h_w, were subject to uncertainties. The hot-wire probes were calibrated directly by the manufacturer to 0.1 $\mathrm{m\,s^{-1}}$ (CTA) or in situ to 0.1 K (CCT). The surface thermocouples were calibrated with a dry block calibrator (AMETEK RTC-159B) to an uncertainty of 0.1 K. Based on the method described by Moffat [35], the relative uncertainties for $\delta\dot{q}_\mathrm{w}/\dot{q}$ and $\delta h_\mathrm{w}/h_\mathrm{w}$ vary between 10 % and 15 % depending on the mission, evaluation position, and time (see Brack et al. [24] for details). Figure 6 shows the field of view of the IRT camera, including the positions for the final evaluation for the flat plate and the ribbed geometry.

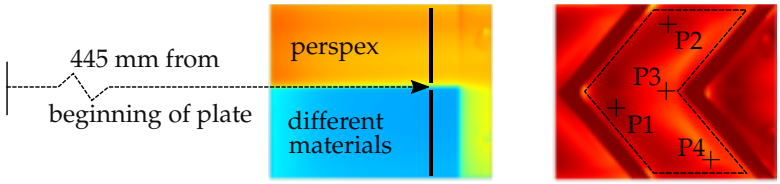

Figure 6. Positions for final evaluation.

The method used by Estorf [20] to calculate heat flux was derived for rectangular adiabatic edges. In order to minimize the uncertainties of the method near the edges, for the flat plate, the results were averaged in the lateral direction at $x = 445$ mm, neglecting the near wall region and the region near the interface between the different material inlays.

For the ribbed geometry, the surface between the two visible ribs was considered. Within this context, the evaluations were performed with four selected pixels.

6. Results

In the first step, a comparison of the experimental and numerical results for the flat plate with different materials was undertaken. In terms of validation, the coupling step was set constant with $t_{\mathrm{cpl}} = 1\,\mathrm{s}$. The coupling step was afterwards varied over time, depending on the inlet boundary conditions for the perspex plate. Subsequently, the findings were transferred to the ribbed geometry, where the flow and heat transfer characteristics were more complex.

6.1. Flat Plate

For the validation of the coupling environment, the results from the FEM and CFD were coupled every $t_{\mathrm{cpl}} = 1\,\mathrm{s}$. The physical time-step size in the CHT simulations was set to $t_{\mathrm{CHT}} = 1\,\mathrm{s}$ to accordingly model the transient effects in the coupling. A further reduction of t_{CHT} showed no effect on the transient behavior. In Figure 7, the resulting local wall temperature distributions for the investigated inlet conditions shown in Figure 3 are plotted. The solid line with the star symbols shows the experimental results. The dashed line describes the CHT solution and the dashed and dotted line the coupling environment. The different materials are shown in different colors. Since the tests were carried out on different days, the ambient temperature at the beginning of the tests was not exactly identical, but this was taken into account in the numerical simulations. The numerical results for T_{w} were in good accordance with the experimental data for all investigated inlet conditions and materials. This shows that, with the chosen time-step size, the transient heat transfer characteristics at the interface could be captured. Between the numerical simulations (CHT and coupling), no differences were visible for either of the cases. Even for materials with low Biot numbers, like steel and aluminum, the numerical values fit the experimental ones accurately.

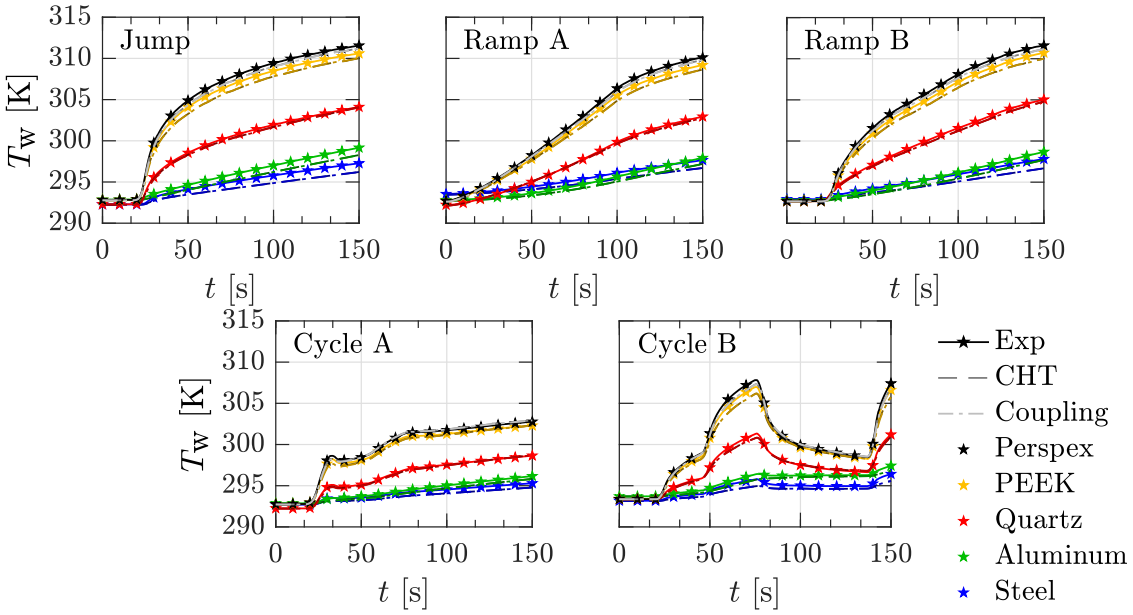

Figure 7. Transient wall temperature at $x = 455\,\mathrm{mm}$ for the flat plate with different materials.

The corresponding $\dot{q}_{\mathrm{w}}$ is given in Figure 8. The overall agreement between the experiment and the numerical simulations was good and the numerical data were identical. For the experimental evaluation of the wall heat flux, the method described by Estorf [20] showed good agreement for all investigated materials, as long as its assumptions were valid. As the semi-infinite wall assumption was not valid for steel and aluminum (see Table 3),

no experimental results are shown. According to Vogel and Weigand [32], the limit for quartz is reached 60 s after a heat flux is imposed. For the generic cases, this resulted in diverging heat fluxes shown by experimental and numerical values 60 s after the initial temperature jump, which corresponded to 85 s from the start. As the driving temperature difference for cycle A was lower, the deviations were less pronounced. For cycle B, it was visible that, even for a negative heat flux, the semi-infinite wall assumption time was not extended and the agreement between the experiment and numerical simulations remained. As the Biot number is a typical definition used to characterize conjugate thermal systems, it can be summarized that the coupling environment stability was proven with a wide range of Biot numbers and validated by experimental data with a generic character, as well as for transient cycles.

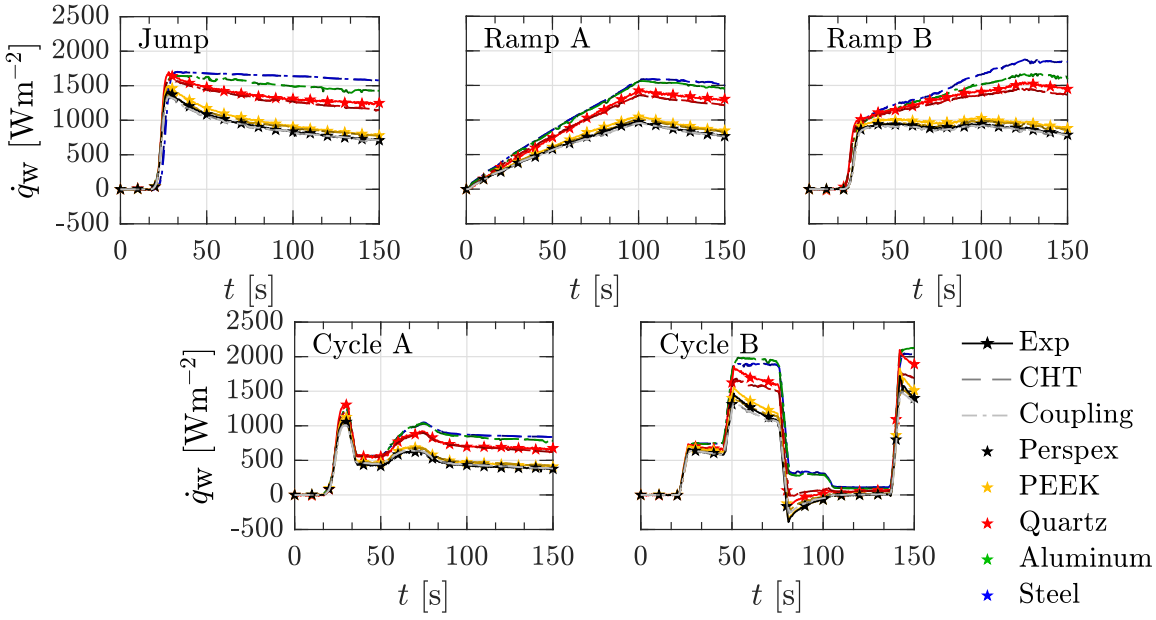

Figure 8. Transient wall heat flux at $x = 455$ mm for the flat plate with different materials.

In order to reduce the computational time, the coupling environment provides the opportunity to couple the FEM and CFD only at specific coupling points. In this respect, a coupling point was set at every step change in the inlet boundary conditions. To evaluate the quality of the coupling scheme, only the results for perspex are discussed. In Figure 9, the experimental values of T_w and $\dot{q}_w$, as well as the numerical ones, from the coupling with variable coupling sizes are shown. The coupling points are marked with the dots.

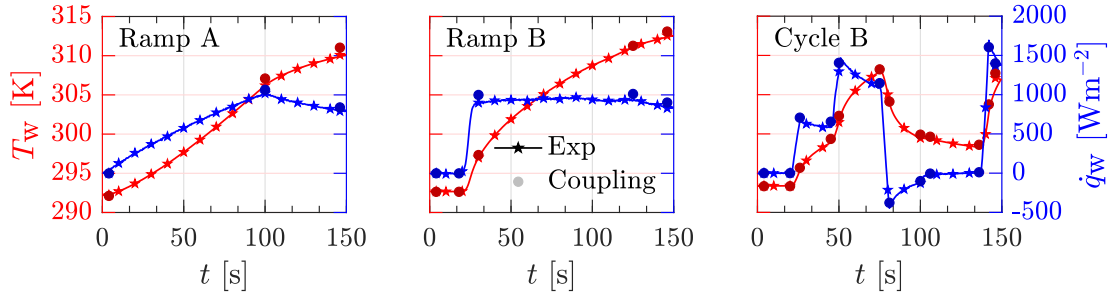

Figure 9. Transient wall temperature and transient wall heat flux at $x = 455$ mm for the flat plate with variable coupling sizes for different test cases.

For all test cases, the numerical simulation showed good agreement with the experimental results. In comparison to a constant coupling time step of $t_{cpl} = 1$ s, the simulation time was reduced to 10% or less. In summary, the coupling environment with its inner

subiterations and linear changing of the boundary conditions was validated for different materials with variable coupling sizes for linear changing inlet boundary conditions at the flat plate.

6.2. Plate with V-Shaped Ribs

In order to obtain a deeper understanding of the heat transfer phenomena, the local wall temperatures for two ribs from the CHT and experiment are plotted in Figure 10a at $t = 50\,\mathrm{s}$. The overall agreement was good, but in the numerical results, the region with the highest temperatures in the reattachment zone was slightly shifted towards the upstream rib. The increase in heat transfer in the near-wall region was also overestimated compared to the experimental results. A comparison of the transient behavior of T_w and $\dot{q}_\mathrm{w}$ at four selected points is given in Figure 10b for cycle A. The overall agreement was fair. Compared to the experiment, larger deviation in the temperature and heat flux for P4 occurred, whereas the differences between the numerical data were negligible.

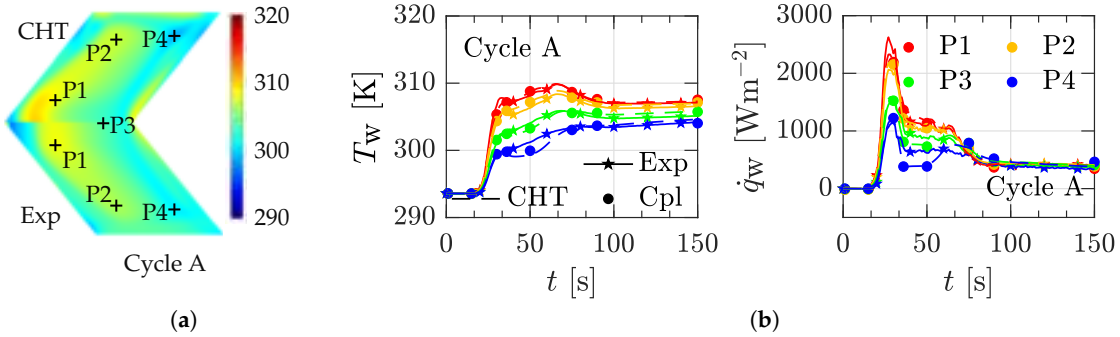

(**a**) (**b**)

Figure 10. Comparison of experimental and numerical results for the V-shaped ribs: (**a**) surface plot at $t = 50\,\mathrm{s}$; (**b**) wall heat temperature (**left**) and wall heat flux (**right**).

To investigate this further, the heat transfer coefficient for the experiment and CHT is shown in Figure 11a. At the beginning of the experiment, T_w equaled T_ref, so the heat transfer coefficient was not defined. It varied with the change in velocity at the inlet, and the deviation between the experiment and CHT was more pronounced in the low-velocity region (see Figure 3). Figure 11b shows the ratio of the heat transfer coefficients of the experiment and CHT for cycle A and the jump. While it remained constant around unity for the jump, h_w at low velocities was partly overestimated by the numerical data. A reason for this could have been an incorrect prediction for the entropy generation in the turbulence model. Due to the complex flow situation, different probe locations can be differently influenced by viscous effects, so dissipation depending on the local flow structures can be influenced by vortices. Probe P4, in particular, was in an area with unsteady and unstable vortices combined with flow separation before the next rib, whereas for P3, where the flow structures were relatively stable, the SST turbulence models showed good results compared to the experiment. According to Esfahani and Jafarian [36], for low velocities, the thermal component of entropy generation dominates over the frictional component in the boundary layer and has a large contribution, especially at the wall. This also introduces changes in local dissipation, which are not well accounted for in the numerical model, regardless of the CHT or coupled simulations, and leads to difficulties in predicting the correct flow and heat transfer characteristics with the used SST model (see Herwig [37]). After $t = 75\,\mathrm{s}$, h_w was less reliable due to the small differences in T_w and T_ref for cycle A, which explains the deviations in Figure 11b.

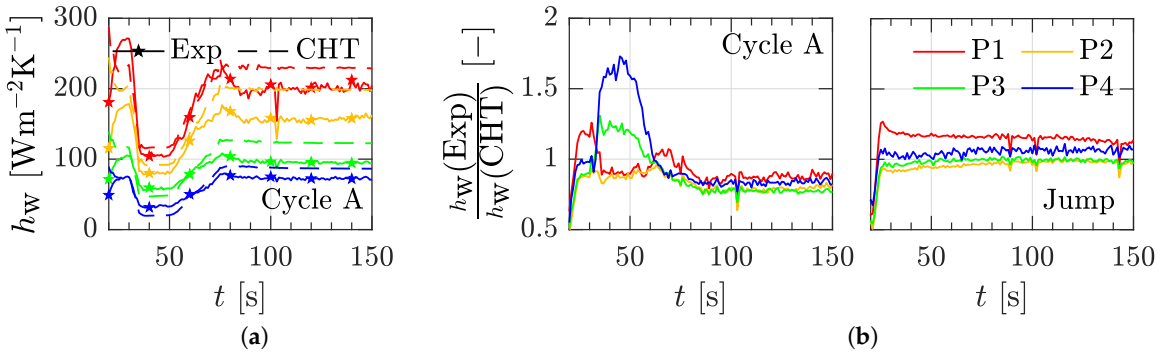

Figure 11. Transient wall heat transfer coefficient for different test cases: (**a**) transient h_w for cycle A; (**b**) ratio of experimental and numerical heat transfer coefficients for cycle A (left) and the jump (right).

However, the idea of linear ramping of boundary conditions between coupling points worked for all evaluation points with moderate changes in inlet boundary conditions, as shown in Figure 12 for different test cases using coupling points. The coupling points were again set at each step change in the inlet boundary conditions. The overall agreement for all evaluation points and test cases was fair, even for long coupling times of $t_{\mathrm{cpl}} = 120\,\mathrm{s}$ (jump), linear velocity changes (ramp B), and opposite changes in boundary conditions (cycle B).

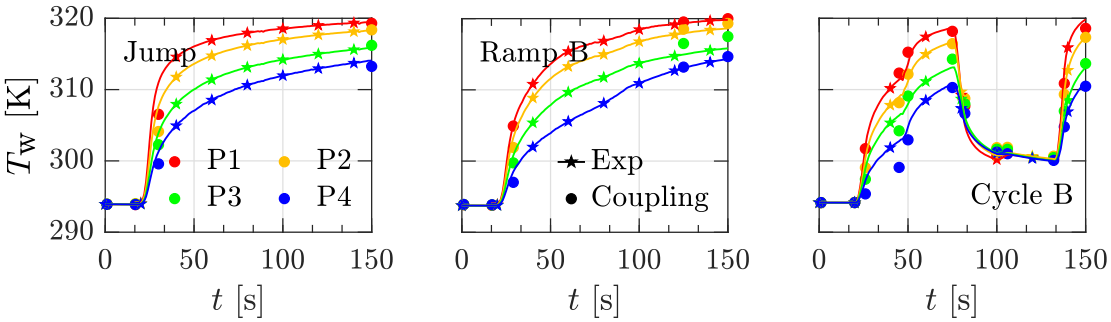

Figure 12. Transient wall temperature for different test cases using coupling points.

7. Conclusions

An experimental test rig for transient conjugate heat transfer measurements using IRT was presented in order to validate numerical simulations with a coupling environment for different Biot numbers. A channel flow over a flat plate and a plate with V-shaped ribs was investigated. The linear approach to efficiently couple the transient FEM code and steady-state FVM solver was successfully demonstrated. It was shown that the stability of the coupling process was guaranteed over a wide range of Biot numbers. For the comparison of experimental and numerical results, no significant differences were found for the flat plate. In the case of the V-shaped ribs, the numerical setup showed difficulties in the simulation of parts of the anisotropic turbulent effects. The overall agreement with the experimental results was still satisfying. With the coupling environment and its possibility of coupling the FEM and FVM only at defined points, the computational time can be extremely reduced while maintaining good temperature prediction. In the future, the described procedure can be extended to include multiple more complex independent boundary conditions through the introduction of transition curves. For modern aero engines, by using the transient temperature data of the FEM solver, structural analysis and stress calculation can be improved and the operational lifetime of thermally high-stressed engine components can be increased. Moreover, the results underline the capabilities of the experimental facility as validation for transient conjugated heat transfer phenomena.

Author Contributions: Conceptualization, C.H. and J.v.W.; methodology, C.H., J.S. and F.C.; software, C.H. and U.I.; validation, C.H. and F.C.; formal analysis, C.H.; investigation, C.H.; resources, J.v.W.; data curation, C.H. and F.C.; writing—original draft preparation, C.H.; writing—review and editing, J.S., F.C. and J.v.W.; visualization, C.H.; supervision, J.G. and J.v.W.; project administration, J.G. and J.v.W.; funding acquisition, J.v.W. All authors have read and agreed to the published version of the manuscript.

Funding: The investigations were conducted as part of the joint research program KuepLe in the frame of AG Turbo. The work was supported by the Federal Ministry for Economic Affairs and Climate Action (BMWK) as per the resolution of the German Federal Parliament under grant number 0324358I.

Institutional Review Board Statement: Not applicable.

Informed Consent Statement: Not applicable.

Data Availability Statement: Not applicable.

Acknowledgments: Not applicable.

Conflicts of Interest: Not applicable.

Nomenclature and Abbreviations

The following nomenclature is used in this manuscript:

Roman characters

c_p	specific heat capacity in $\mathrm{J\,kg^{-1}\,K^{-1}}$
e	characteristic rib height in m
h	heat transfer coefficient in $\mathrm{W\,m^{-2}\,K^{-1}}$
i	index
k	thermal conductivity in $\mathrm{W\,m^{-1}\,K^{-1}}$
L	length in m
p	pitch of ribs in m
p	pressure in $\mathrm{kg\,m^{-1}\,s^{-2}}$
$\dot{q}$	heat flux in $\mathrm{W\,m^{-2}}$
t	time in s
T	temperature in K
u	velocity in $\mathrm{m\,s^{-1}}$
x, y, z	coordinates in m
y^+	dimensionless wall distance

Greek characters

ϵ	norm
η	dynamic viscosity in $\mathrm{kg\,m^{-1}\,s^{-1}}$
ν	subiteration number
ρ	density in $\mathrm{kg\,m^{-3}}$

Subscripts

ccx	CalculiX
cpl	coupling
ref	reference
w	wall

The following abbreviations are used in this manuscript:

CCT	constant current thermometry
CFD	computational fluid dynamics
CHT	conjugate heat transfer
CTA	constant temperature anemometry
Exp	experiment
FEM	finite element method
FOV	field of view
FVM	finite volume method
IRT	infrared thermography
SST	shear stress transport

References

1. Perelman, T. On conjugated problems of heat transfer. *Int. J. Heat Mass Transf.* **1961**, *3*, 293–303. [CrossRef]
2. Fiedler, B.; Muller, Y.; Voigt, M.; Mailach, R. Comparison of Two Methods for the Sensitivity Analysis of a One-Dimensional Cooling Flow Network of a High-Pressure-Turbine Blade. In *Volume 2D: Turbomachinery*; American Society of Mechanical Engineers: New York, NY, USA, 2020. [CrossRef]
3. Heselhaus, A.; Vogel, D. Numerical simulation of turbine blade cooling with respect to blade heat conduction and inlet temperature profiles. In Proceedings of the 31st Joint Propulsion Conference and Exhibit, San Diego, CA, USA, 10–12 July 1995. [CrossRef]
4. Felippa, C.A.; Park, K.; Farhat, C. Partitioned analysis of coupled mechanical systems. *Comput. Methods Appl. Mech. Eng.* **2001**, *190*, 3247–3270. [CrossRef]
5. Sun, Z.; Chew, J.W.; Hills, N.J.; Lewis, L.; Mabilat, C. Coupled Aerothermomechanical Simulation for a Turbine Disk Through a Full Transient Cycle. *J. Turbomach.* **2011**, *134*, 011014. [CrossRef]
6. Amirante, D.; Hills, N.J.; Barnes, C.J. Thermo-Mechanical Finite Element Analysis/Computational Fluid Dynamics Coupling of an Interstage Seal Cavity Using Torsional Spring Analogy. *J. Turbomach.* **2012**, *134*, 051015. [CrossRef]
7. He, L.; Oldfield, M.L.G. Unsteady Conjugate Heat Transfer Modeling. *J. Turbomach.* **2010**, *133*, 031022. [CrossRef]
8. Errera, M.P.; Baqué, B. A quasi-dynamic procedure for coupled thermal simulations. *Int. J. Numer. Methods Fluids* **2013**, *72*, 1183–1206. [CrossRef]
9. Errera, M.P.; Duchaine, F. Comparative study of coupling coefficients in Dirichlet–Robin procedure for fluid–structure aerothermal simulations. *J. Comput. Phys.* **2016**, *312*, 218–234. [CrossRef]
10. Gimenez, G.; Errera, M.P.; Baillis, D.; Smith, Y.; Pardo, F. A coupling numerical methodology for weakly transient conjugate heat transfer problems. *Int. J. Heat Mass Transf.* **2016**, *97*, 975–989. [CrossRef]
11. Khoury, R.R.E.; Errera, M.P.; Khoury, K.E.; Nemer, M. Efficiency of coupling schemes for the treatment of steady state fluid-structure thermal interactions. *Int. J. Therm. Sci.* **2017**, *115*, 225–235. [CrossRef]
12. Moretti, R.; Errera, M.P.; Feyel, F. Temporal Interpolation Methods for Transient CHT. In Proceedings of the AIAA Scitech 2019 Forum, San Diego, CA, USA, 7–11 January 2019; American Institute of Aeronautics and Astronautics: Reston, VI, USA, 2019. [CrossRef]
13. Verstraete, T.; Scholl, S. Stability analysis of partitioned methods for predicting conjugate heat transfer. *Int. J. Heat Mass Transf.* **2016**, *101*, 852–869. [CrossRef]
14. Sun, Z.; Chew, J.; Hills, N.; Volkov, K.; Barnes, C. Efficient Finite Element Analysis/Computational Fluid Dynamics Thermal Coupling for Engineering Applications. *J. Turbomach.* **2010**, *132*, 031016. [CrossRef]
15. Verdicchio, J.A.; Chew, J.W.; Hills, N.J. Coupled Fluid/Solid Heat Transfer Computation for Turbine Discs. In *Volume 3: Heat Transfer; Electric Power; Industrial and Cogeneration*; American Society of Mechanical Engineers: New York, NY, USA, 2001. [CrossRef]
16. Dixon, J.A.; Valencia, A.G.; Coren, D.; Eastwood, D.; Long, C. Main Annulus Gas Path Interactions—Turbine Stator Well Heat Transfer. *J. Turbomach.* **2013**, *136*, 021010. [CrossRef]
17. Ganine, V.; Javiya, U.; Hills, N.; Chew, J. Coupled Fluid-Structure Transient Thermal Analysis of a Gas Turbine Internal Air System With Multiple Cavities. *J. Eng. Gas Turbines Power* **2012**, *134*, 102508. [CrossRef]
18. Schindler, A.P.; Brack, S.; von Wolfersdorf, J. Coupled FE-CFD analysis of transient conjugate heat transfer. In Proceedings of the 13th European Conference on Turbomachinery Fluid Dynamics and Thermodynamics, Lausanne, Switzerland, 8–12 April 2019. [CrossRef]
19. Dhondt, G. *The Finite Element Method for Three-Dimensional Thermomechanical Applications*; Wiley: Hoboken, NJ, USA, 2004.
20. Estorf, M. Image based heating rate calculation from thermographic data considering lateral heat conduction. *Int. J. Heat Mass Transf.* **2006**, *49*, 2545–2556. . [CrossRef]
21. Israel, U.; Cottier, F.; Hartmann, C.; von Wolfersdorf, J. Method for transient and steady state partitioned fluid-structure interaction analysis in conjugate heat transfer for aero engines applications. In Proceedings of the 15th European Conference on Turbomachinery Fluid Dynamics and Thermodynamics, Budapest, Hungary, 24–28 April 2023. [CrossRef]
22. Hartmann, C.; Schweikert, J.; Cottier, F.; Israel, U.; Gier, J.; von Wolfersdorf, J. Experimental Validation of a Numerical Coupling Environment between FEM and CFD. In Proceedings of the 15th European Conference on Turbomachinery Fluid Dynamics and Thermodynamics, Budapest, Hungary, 24–28 April 2023. [CrossRef]
23. Liu, C.; von Wolfersdorf, J.; Zhai, Y. Time-resolved heat transfer characteristics for steady turbulent flow with step changing and periodically pulsating flow temperatures. *Int. J. Heat Mass Transf.* **2014**, *76*, 184–198. [CrossRef]
24. Brack, S.; Poser, R.; von Wolfersdorf, J. Experimental investigation of unsteady convective heat transfer under airflow velocity and temperature variations. *Meas. Sci. Technol.* **2021**, *33*, 015106. [CrossRef]
25. Menter, F.R. Two-equation eddy-viscosity turbulence models for engineering applications. *AIAA J.* **1994**, *32*, 1598–1605. [CrossRef]
26. Menter, F.R.; Kuntz, M.; Langtry, R. Ten years of industrial experience with the SST turbulence model. *Heat Mass Transf.* **2003**, *4*, 625–632.

27. Göhring, M.; Krille, T.; Feile, J.; von Wolfersdorf, J. Heat Transfer Predictions in Smooth and Ribbed Two-Pass Cooling Channels under Stationary and Rotating Conditions. In Proceedings of the 16th International Symposium on Transport Phenomena and Dynamics of Rotating Machinery, Honolulu, HI, USA, 10–15 April 2016. Available online: https://hal.archives-ouvertes.fr/hal-01884254 (accessed on 13 April 2021).
28. Sutherland, W. LII. The viscosity of gases and molecular force. *Lond. Edinb. Dublin Philos. Mag. J. Sci.* **1893**, *36*, 507–531. [CrossRef]
29. White, F. *Viscous Fluid Flow*; McGraw-Hill Higher Education: New York, NY, USA, 2006.
30. Cottier, F.; Pinchaud, P.; Dumas, G. Aerothermal predictions of combustor/turbine interactions using advanced turbulence modeling. In Proceedings of the 13th European Conference on Turbomachinery Fluid Dynamics and Thermodynamics, Lausanne, Switzerland, 8–12 April 2019. [CrossRef]
31. Aitken, A.C. On Bernoulli's Numerical Solution of Algebraic Equations. *Proc. R. Soc. Edinb.* **1927**, *46*, 289–305. [CrossRef]
32. Vogel, G.; Weigand, B. A new evaluation method for transient liquid crystal experiments. In Proceedings of the 2001 National Heat Transfer Conference, ASME, Anaheim, CA, USA, 10–12 June 2001.
33. Wagner, G.; Kotulla, M.; Ott, P.; Weigand, B.; von Wolfersdorf, J. The Transient Liquid Crystal Technique: Influence of Surface Curvature and Finite Wall Thickness. *J. Turbomach.* **2005**, *127*, 175–182. [CrossRef]
34. Kays, W.; Crawford, M.; Weigand, B. *Convective Heat and Mass Transfer*; McGraw-Hill Series in Mechanical Engineering: New York, NY, USA, 2005; Volume 30.
35. Moffat, R.J. Contributions to the Theory of Single-Sample Uncertainty Analysis. *J. Fluids Eng.* **1982**, *104*, 250–258. [CrossRef]
36. Esfahani, J.A.; Jafarian, M.M. Entropy Generation Analysis of a Flat Plate Boundary Layer with Various Solution Methods. *Sci. Iran.* **2005**, *12*, 233–240.
37. Herwig, H. The Role of Entropy Generation in Momentum and Heat Transfer. *J. Heat Transf.* **2012**, *134*, 031003. [CrossRef]

Disclaimer/Publisher's Note: The statements, opinions and data contained in all publications are solely those of the individual author(s) and contributor(s) and not of MDPI and/or the editor(s). MDPI and/or the editor(s) disclaim responsibility for any injury to people or property resulting from any ideas, methods, instructions or products referred to in the content.

International Journal of
Turbomachinery Propulsion and Power

MDPI

Article

Effect of Tip Gap Size on the Performance of an Axial Compressor Stage with and without Active Flow Control †

Clémence Rannou [1,2,*], Julien Marty [1], Geoffrey Tanguy [2] and Antoine Dazin [2]

[1] Département Aérodynamique, Aéroélasticité, Acoustique, Office National d'Études et de Recherches Aérospatiales (ONERA), Université Paris Saclay, F-92190 Meudon, France; julien.marty@onera.fr
[2] Université Lille, Centre National de la Recherche Scientifique (CNRS), ONERA, Arts et Metiers Institute of Technology, Centrale Lille Institut, LMFL, Laboratoire de Mécanique des Fluides de Lille—Kampé de Fériet, F-59000 Lille, France; geoffrey.tanguy@onera.fr (G.T.); antoine.dazin@ensam.eu (A.D.)
* Correspondence: clemence.rannou@onera.fr
† This manuscript is an extended version of the ETC2023-207 meeting paper published in the Proceedings of the 15th European Turbomachinery Conference, Budapest, Hungary, 24–28 April 2023.

Abstract: The tip gap region of an axial compressor rotor is a source of complex flows, inducing losses and stability issues. Recent works have proven the ability of blowing high-speed jets in the tip region to improve the surge margin of an axial compressor stage with a narrow tip gap configuration. However, the tip gap size can evolve during the compressor lifetime, possibly affecting its performance and operability. The objective is to evaluate the performance of an active flow control system on a compressor with different tip gap sizes. The present work is based on the single-stage compressor CME2 located at the Laboratory of Fluid Mechanics of Lille and equipped with actuators blowing at the rotor tip leading edge. Configurations with two different values of the tip gap to chord ratio (0.6% and 2.4%) are experimentally tested. RANS simulations are also performed. The effect of tip gap sizes and tip blowing on the flow topology and compressor performance is evaluated (surge margin improvement of the order of 200% for the larger tip gap size).

Keywords: axial compressor; active flow control; surge margin

check for updates

Citation: Rannou, C.; Marty, J.; Tanguy, G.; Dazin, A. Effect of Tip Gap Size on the Performance of an Axial Compressor Stage with and without Active Flow Control. *Int. J. Turbomach. Propuls. Power* **2023**, *8*, 30. https://doi.org/10.3390/ijtpp8030030

Academic Editor: Francesco Martelli

Received: 12 June 2023
Revised: 25 June 2023
Accepted: 7 August 2023
Published: 1 September 2023

Copyright: © 2023 by the authors. Licensee MDPI, Basel, Switzerland. This article is an open access article distributed under the terms and conditions of the Creative Commons Attribution (CC BY-NC-ND) license (https://creativecommons.org/licenses/by-nc-nd/4.0/).

1. Introduction

The Air Transport Action Group has set a target of achieving net-zero carbon emissions by 2050 [1]. Among other solutions, this means improving the performance of aero-engines. Improving the pressure ratio of axial compressor stages is a significant challenge due to operating range limitations caused by flow instabilities like rotating stall and surge. Rotating stall typically occurs in the clearance region between the blades and casing when the tip leakage flow interacts with the main flow. To overcome these limitations, control systems that manipulate the flow near the casing have proven to be effective in increasing the safety margin against stall and, thus, in expanding the compressor's operational range. These control systems can be passive (modifying the geometry without external energy) or active (requiring an external energy source). Recent research has demonstrated that active control, specifically injecting air upstream of the leading edge of the rotor tip, can delay the onset of stall. Indeed, active control provides a more versatile option in comparison to passive control, as it can be adapted to the machine operating point and can accommodate engine cycling and wear issues. Previous works have experimentally investigated the influence of the main geometric and fluidic parameters that have an influence on the injection performance [2,3]. CFD calculations have also been used to evaluate the ability of such systems to reduce losses and increase the compressor surge margin. Marty et al. [4] analyzed the benefit of blowing and the effect of blade tip suction. Neuhaus et al. [5] focused on continuous blowing to reduce the tip clearance noise with various configurations.

Nevertheless, all the above-cited works focused on a fixed compressor geometry, whereas the tip clearance of a compressor evolves with the machine age and depends on the rotor location and speed variations, and whereas it is well established that a modification of the tip gap size has a strong impact on compressor performance [6,7].

As an example, isentropic efficiency is significantly reduced as the ratio, R ($= \frac{\tau}{c}$), defined by the tip gap size, τ, over the axial chord, c, is increased from 0.9% to 3.4% [6]. The operating zone is also minimized due to a reduction of almost 10% in the stall safety margin [6]. According to the work of [7], the tip gap size is inversely proportional to the peak pressure rise of a blade: for every percent of increase in the tip gap size, 4% additional pressure losses are observed.

The main goal of the present paper is to evaluate the performance of an active flow control system on a compressor with different tip gap sizes and to investigate the fluid behavior at the blade tip with continuous air injection. The CME2, a single-stage compressor located at the Lille Fluid Mechanics Laboratory (LMFL), is used for this study. Previous works have experimentally and numerically investigated the tip gap size ratio, R, at R = 0.6% [8,9] for the CME2. This paper presents the effect of control on a larger tip clearance defined as R = 2.4%. The paper is organized as follows: first, the test bench and the CFD methodology are described. Then, a reference case is presented. Finally, the impact of the active flow control parameters is discussed. This manuscript corresponds to our paper published in the Proceedings of the 15th European Turbomachinery Conference [10].

2. Materials and Methods

2.1. Experimental Facility and Active Flow Control System

The experimental set-up under consideration is the CME2, a single-stage axial compressor operated at the Lille Fluid Mechanics Laboratory [11]. All the tests presented were performed at the rotational velocity Ω = 3200 rpm. The CME2 is $2\pi/10$ periodic with 30 blades for the rotor and 40 blades for the stator. The stagnation pressure ratio is 1.03 at Ω, and the nominal mass flow rate is equal to 5.3 kg/s. The rotor tip velocity is 94 m/s. The design axial velocity at the leading edge is 43 m/s.

More details about the geometrical configuration are given in [11]. As shown in Figure 1, the CME2 blowing system includes 20 pairs of actuators, located around the CME2 circumference. The center of the injector is upstream of the leading edge of the rotor, at −10 mm. The injectors were designed to benefit from the Coandă effect, and the jet is attached to the wall casing to interact efficiently with the rotor blade tip flow. The active control characteristics are summarized in Figure 1.

The injectors are fed with an external compression system that allows for adjusting the mass flow injected by the control system. The absolute injection angle is also adjustable and is defined as follows: the angle is positive when the jet tangential velocity component is in the same direction as the speed of rotation (Figure 2).

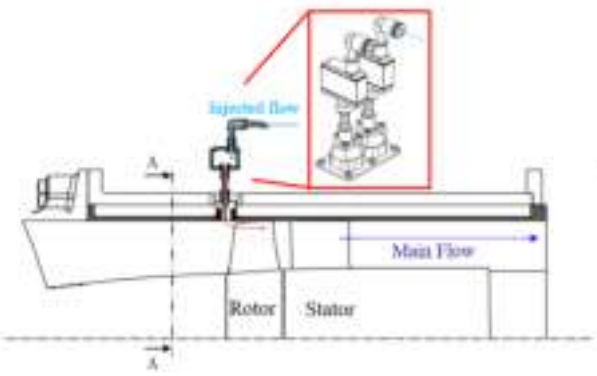

CME2 Injection System

Number of injectors	40
Axial position	−10 mm
Injection angle (pitch)	0°
Outlet section	5 mm²

Figure 1. CME2 air injection system.

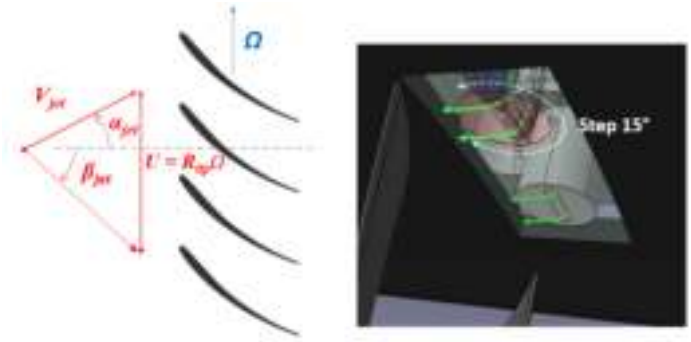

Figure 2. Definition of the absolute angle of injection and CAD view of adjustable yaw blowing angle of the injectors.

2.2. Numerical Set-Up

2.2.1. Presentation of the $2\pi/10$ Configurations

A preliminary computational domain was designed to obtain a $2\pi/10$ configuration using the natural periodicity of the machine (Figure 3). This consists of a single-blade channel composed of one rotor blade and one stator blade with one pair of fluidic actuators. The all mesh is composed of 7×10^6 nodes. The y^+ values at the blade wall are lower than 1 in the entire domain. When the tip gap size is changed, the number of points is adjusted to maintain the cells aspect ratio. It is presented in [12] that for the smaller tip gap (R = 0.6%), the single-blade channel (SBC) and $2\pi/10$ configurations give very similar results from nominal to stall conditions, which are very close to the experimental data. However, for the larger tip gap (R = 2.4%), the SBC simulations fail to predict the critical mass flow rate at stall conditions. Hence, in the present paper, the results from the RANS $2\pi/10$ configuration are presented.

Concerning the injectors, the elements of prisms, pyramids, and tetrahedra comprise the mesh for the interface between the injector and the channel (upstream, rotor and stator parts). The channel is meshed with structured blocks using an 'O-nH' topology. Finally, the software Pointwise® allowed the conversion of the hexahedra mesh of the injectors into unstructured blocks.

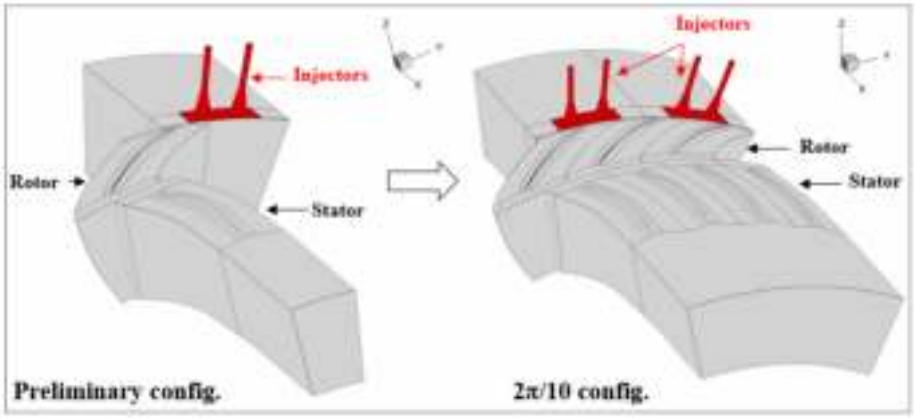

Figure 3. Preliminary and $2\pi/10$ configurations.

2.2.2. General Parameters

The RANS $2\pi/10$ calculations are performed with the elsA solver, developed at ONERA and co-owned by ONERA and SAFRAN [13]. This code relies on a cell-centered finite-volume discretization on structured and unstructured multi block meshes. A convergence study based on two types of mesh for a single-blade channel configuration without injectors, one at 10^6 and the other at 3×10^6 nodes was performed in [14]. The last mesh was selected as it presented a good compromise between numerical cost and reliability.

Laws of ideal gas, of Sutherland (for fluid viscosity), and of Fourier (for heat fluxes) are used together with Reynolds-averaged Navier–Stokes (RANS) equations to simulate the compressible flow within the CME2 compressor. RANS equations are solved by using the second-order upwind scheme of Roe for convective fluxes, for both the transport equations of turbulence models and the Navier–Stokes equations, and a classical second-order-centered scheme for the diffusive fluxes. The Spalart–Allmaras model [15] is applied for turbulence modeling. A backward Euler scheme is used for time integration with local time stepping in order to improve the convergence rate in the steady flow state. For the implicit phase, this is associated with a lower–upper symmetric successive over-relaxation scheme (LU-SSOR).

Table 1 presents all the boundary conditions for the simulations. A mixing plane is used in order to solve the rotor–stator interface and connect these blade rows in RANS calculations. Additionally, a subsonic outlet condition is used downstream of the domain: a static pressure is imposed with a radial equilibrium law defined by a valve law ($P_s = P_{ref} + \alpha_{relax}(\dot{m}/\dot{m}_{ref})^2$) based on a valve coefficient, α_{relax}, allowing us to set new operating conditions with a specific mass flow rate (P_{ref} = 101,325 Pa, $\dot{m}_{ref}$ = 10.0 kg/s).

Different meshes are undertaken in order to evaluate the influence of the absolute injection angle of the jets (0°; −30°) on performance at the defined rotation speed of 3200 rpm. The considered hybrid meshes are characterized in Figure 4, illustrating the injector mesh for each injection angle, α_{inj}: 0°, −30°.

Table 1. Boundary Conditions.

Upstream	- Subsonic inlet condition with prescribed total pressure - Axial flow direction, P_t = 101,325 Pa, T_t = 288.15 K
Blades, casing, hub	- Adiabatic wall condition - Fixed wall condition for casing and a part of the hub - Mobile wall condition for hub and blades
Downstream	- Subsonic outlet condition with radial equilibrium using a valve law on static pressure
Inlet of the injector	- Subsonic inlet condition with prescribed mass flow rate, Q_{inj} - Flow direction normal to boundary, T_t = 288 K
Injector walls	- Adiabatic wall conditions

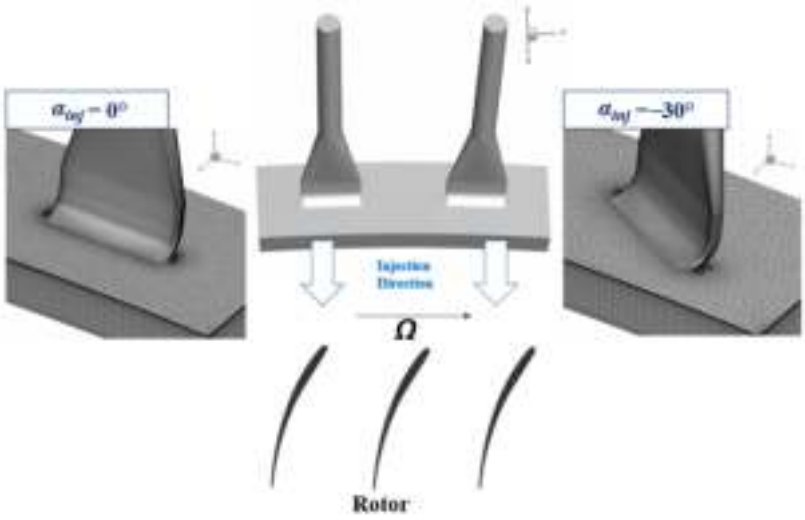

Figure 4. Different mesh configurations at α_{inj} = 0°, −30°.

3. Results and Discussion

3.1. Reference without Control: Baseline Performance Assessment

First, to assess agreement between the experimental data and numerical results, simulations were performed without control with $2\pi/10$ configurations for a narrow tip gap

size at R = 0.6% and a larger one at R = 2.4%. The test campaign was conducted on both tip gap sizes without control on the CME2. A valve was throttled progressively from nominal to stall conditions. For R = 0.6%, the experimental data are provided by [9]. As a reference case, the simulations were compared at the same configuration of the experimental data, with the injectors oriented at $\alpha_{inj} = 0^\circ$ without blowing (Figure 5).

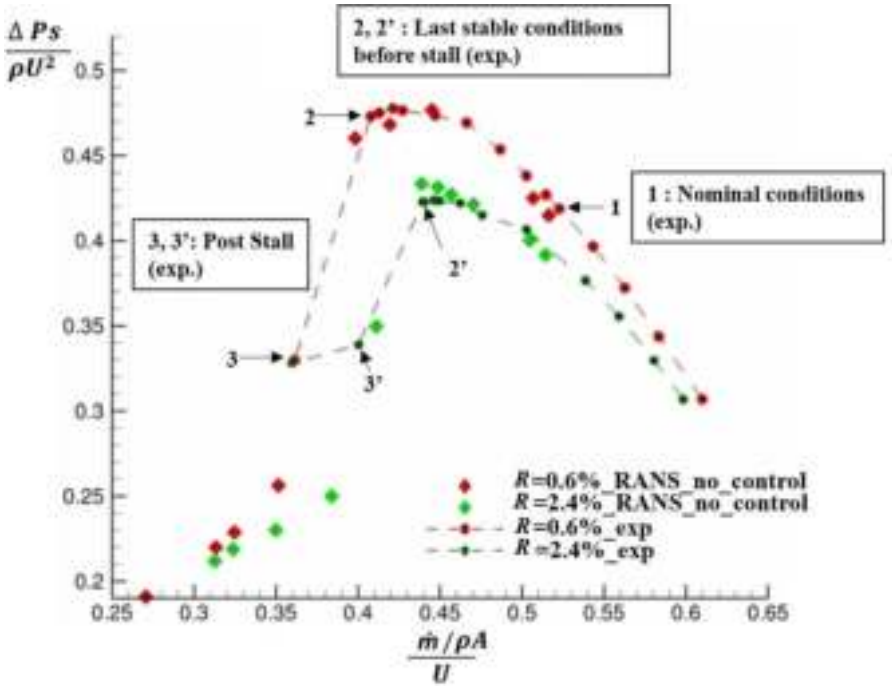

Figure 5. CME2 performance map at two tip gap sizes (R = 2.4% and R = 0.6%) for configuration with injectors at $\alpha_{inj} = 0^\circ$ without blowing for experimental tests and numerical results.

3.1.1. Specific Operating Conditions for Ratio R = 0.6% and R = 2.4%

The design compressor flow coefficient is 0.53. The critical flow rate for which the compressor encounters stall is 0.41 and 0.44 at R = 0.6% and R = 2.4%, respectively (Figure 5). A range of mass flow coefficients from 0.25 to 0.53 is investigated. Among the conditions considered, several operating points are identified as follows: (i) nominal conditions ($\phi_1 = 0.53$); (ii) last stable conditions before stall: the last experimental point (S) before a clear break in the slope of the performance curve (at ϕ_{S2} and $\phi_{S2'}$); and (iii) post-stall conditions at a mass flow rate lower than ϕ_S.

3.1.2. Results from Nominal to Last Stable Conditions at Ratio R = 0.6% and R = 2.4%

The performance chart is provided with the RANS numerical results for the two tip gap sizes (R = 0.6% and R = 2.4%) and with the experimental data (Figure 5). The $2\pi/10$ simulations provide excellent results when they are compared with the experimental data at R = 0.6%. In particular, it gives discrepancies less than 1% to the last stable conditions for R = 0.6%, even if the numerical results slightly underestimate $\Psi = \frac{\Delta P_S}{\rho U^2}$ from ϕ = 0.53 to ϕ = 0.45. Similarly, for R = 2.4%, the numerical results give acceptable performance data at this larger tip clearance. Indeed, from ϕ = 0.53 to ϕ = 0.45, RANS $2\pi/10$ simulations produce discrepancies less than 1%. The largest deviation from the experimental data is related to the conditions close to stall. For R = 0.6%, the experimental critical mass flow rate is ϕ_{S2} = 0.41, whereas the numerical simulations predict the slope discontinuity characteristics at ϕ_S = 0.39. Moreover, the numerical results slightly underestimate Ψ compared to the experimental data at the top of the curve, but it captures well the same trend of performance just before stall. In the same way, for R = 2.4%, the RANS results seem to define a last stable point at a lower mass flow rate but close to $\phi_{S2'} = 0.44$. The compressor pressure rise just before stall is slightly over-evaluated.

3.2. Performance of Flow Control at Different Tip Gap Sizes

The impact of the active flow control is investigated in continuous blowing at 3200 RPM with 40 injectors activated at R = 0.6% and 2.4%, with the injection angle set to $\alpha_{inj} = -30°$. The absolute injection angle was chosen as a reference for R = 0.6%, as this corresponds to the optimal performance of the compressor in terms of stall margin improvement according to [9].

The experimental and numerical compressor performance maps are presented in Figure 6. The blowing flow rate is set in the simulation to Q_{inj} = 2.0% to correspond with the experimental results. The injected mass flow rate, Q_{inj}, is defined as the percentage of the compressor mass flow rate at the last operating point without control for the nominal geometry, R = 0.6%. If the last operating point without control for R = 2.4% is chosen, a slight discrepancy of 0.025% is observed, which is why, to compare each case, R = 0.6% is taken as the reference. Moreover, according to [16], the injected mass flow rate in each pair of injector valves was observed as constant with a slight variation of 1%, regardless of the pair considered.

As already experimentally observed in [9,16], for R = 0.6%, the control system proves its capacity to push the stability limit to lower flow rates (ϕ_S is decreased from 0.41 to 0.32) and improves the static pressure rise in the compressor. At the largest gap size, R = 2.4%, the effect of blowing is even more efficient as the stall limit, with control being $\phi_S = 0.335$, which is very close to the one observed for the narrow gap size. Moreover, compared with the baseline characteristic curves, the controlled cases present an increase in the static pressure ratio, with the slope of the curves becoming positive, especially for R = 2.4%.

Concerning the CFD predictions, the static pressure drop is also delayed due to the lower mass flow rates compared to cases with no control for both tip clearances. The $2\pi/10$ simulations provide a similar controlled performance trend, but they underestimate the pressure coefficient, Ψ, when the experimental data curves flatten toward the top from $\phi = 0.4$ to $\phi_S = 0.335$ for R = 2.4% and from $\phi = 0.41$ to $\phi_S = 0.32$ for R = 0.6%. This means that the $2\pi/10$ simulations are sufficient to predict the change in slope when stall occurs with blowing control but lack accuracy for the sudden static pressure drop captured in the experiments. The unsteady simulations of the compressor with a 360° configuration should capture the effect of blowing with further accuracy when the mass flow rate is close to stall.

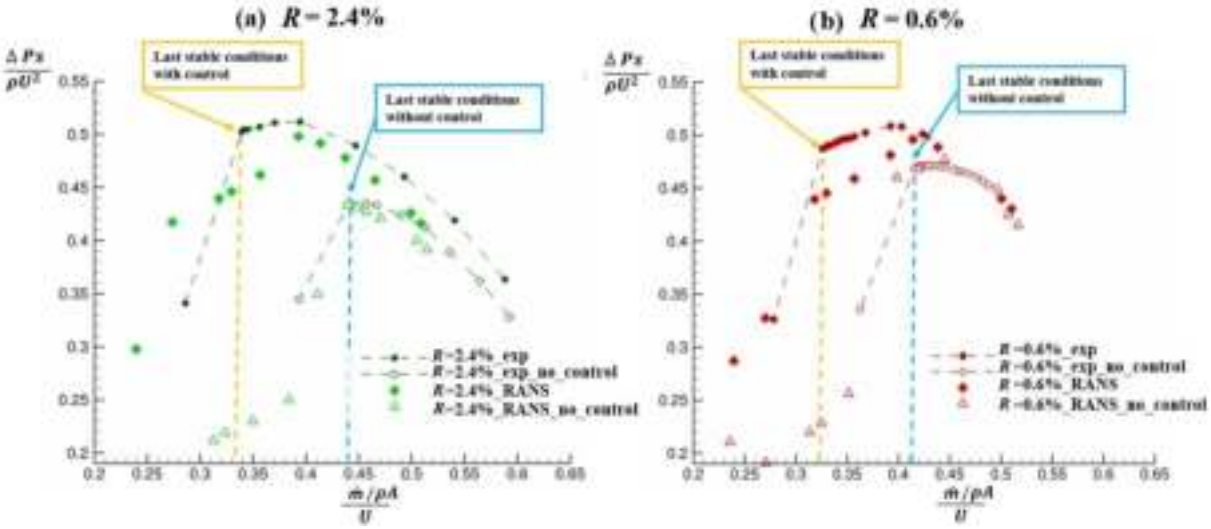

Figure 6. CME2 performance map at (**a**) R = 2.4%, (**b**) R = 0.6%, with $\alpha_{inj} = -30°$ ($Q_{inj} = 2.0\%$).

To illustrate the effect of blowing on the flow near the casing, the slices of static pressure at 96% of the rotor blade height for the specific operating conditions are plotted (Figure 7). Some variation in the intensity of static pressure between the two configurations with and without control can be observed. For the configuration without control, a characteristic low relative pressure region at the leading edge can be observed (Figure 7a). This specific

static pressure drop region is associated with tip leakage vortical flow. At the last stable point without control, Figure 7b highlights the modification of incidence of the tip leakage vortex with the nominal case as it moves toward the leading edge. At stall conditions (Figure 7c), there is a drop in static pressure variation shown in the performance map, and the tip leakage vortex is no longer visible longer as the flow is detached. When blowing is activated, at each operating condition (Figure 7a–c), this lower static pressure region seems to be confined along the suction side of the rotor, preventing compressor stall at $\phi = 0.44$. This suggests that CFD is able to capture the main effect of blowing on leakage flow and its effect on stall delay.

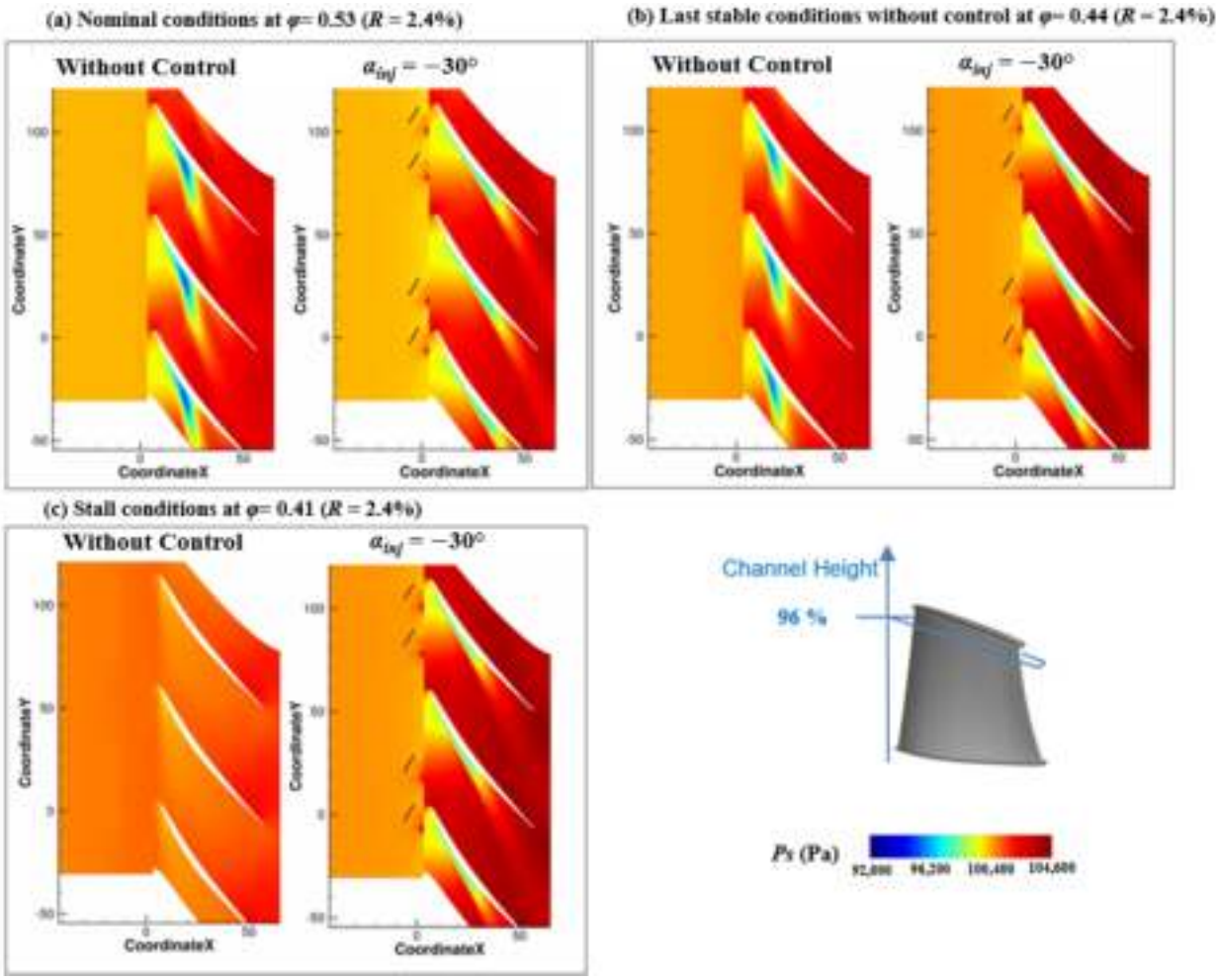

Figure 7. Static pressure field for $R = 2.4\%$ at nominal, last stable, and stall conditions for configurations: without and with control ($\alpha_{inj} = -30°$ and $Q_{inj} = 2.0\%$).

To characterize the effect of the control system on the compressor performance, two parameters are introduced: the power balance (Equation (1)) [9] and *SMI* (Equation (4)) presented by [17]. The mass averaged power balance is defined as the additional total power provided to the flow by the compressor due to the control. The total pressure at the inlet includes the jet's dynamic pressure. This can be simply defined by the net benefit (energy gain in terms of pressure rise in the compressor stage - energy cost due to the blowing system) of the control system.

$$\overline{PB} = \frac{\left((Q_{S,B} + Q_{inj})\frac{\Delta p_{tt,C,int}}{\rho_C}\right) - \left((Q_{S,B})\frac{\Delta p_{tt,B}}{\rho_B}\right)}{P} \times 100 \quad (1)$$

where P, Q, and Δp_{tt} are the compressor nominal power ($P = 23{,}000$ W), the mass flow rate, and the total-to-total pressure rise, respectively. Within Equation (1), the subscripts

refer to *B* for the baseline case without control, *C* for the controlled case, *S* for the last stable operating point with the lowest flow rate before stall, inj is the injection for the global injected mass flow rate, and int is the interpolation for the controlled total-to-total pressure.

With similar nomenclature, *SMI* is determined by the ratio of the surge margin with control, SM_C, and without control, SM_B (Figure 8a):

$$SM_B = ((\frac{\Delta p_{tt,B}}{Q_{S,B}})(\frac{Q_{nom}}{p_{nom}}) - 1) \times 100 \quad (2)$$

$$SM_C = ((\frac{\Delta p_{tt,C}}{Q_{S,C}})(\frac{Q_{nom}}{p_{nom}}) - 1) \times 100 \quad (3)$$

$$SMI = \frac{SM_C - SM_B}{SM_B} \times 100 \quad (4)$$

Contrary to [9], the inlet total pressure, in the controlled case, contains the energy added by the jets. Figure 8b shows an *SMI* vs. power balance comparison between the two tip clearances at $\alpha_{inj} = -30°$ for configurations with the control at 20 injectors and 40 injectors. Different Q_{inj} are tested with a range from Q_{inj} = 0.5% to Q_{inj} = 2.5%. The interesting configurations are the ones that achieve significant *SMI* and positive power balance. Therefore, the points at the top and/or the right of the map are targeted. It appears that the configurations with 40 injectors offer the best results for each tip clearance size compared to 20 injectors. Consequently, it allows an acceptable angular coverage around the circumference of the compressor. The cases at Q_{inj} = 1% and 1.5% offer interesting applicative configurations, as they can obtain a satisfied *SMI* and a positive power balance, reaching 5.8% of the compressor nominal power. The cases at Q_{inj} = 2.5% correspond to the maximum energetic cost, as this represents the maximum number of injectors with the maximum flow rate per injector. Additionally, at *R* = 2.4%, the *SMI* provides excellent results compared with *R* = 0.6%: the *SMI* and power balance are up to nearly 200% and 6%, respectively. Nevertheless, it has to be kept in mind that the *SMI* is calculated by taking the last stable point from the baseline case without control, as shown in Figure 6: the baseline at *R* = 2.4% is lower than the one at *R* = 0.6%, which is due to the higher losses that happen between the carter and the rotor blade with a lower height.

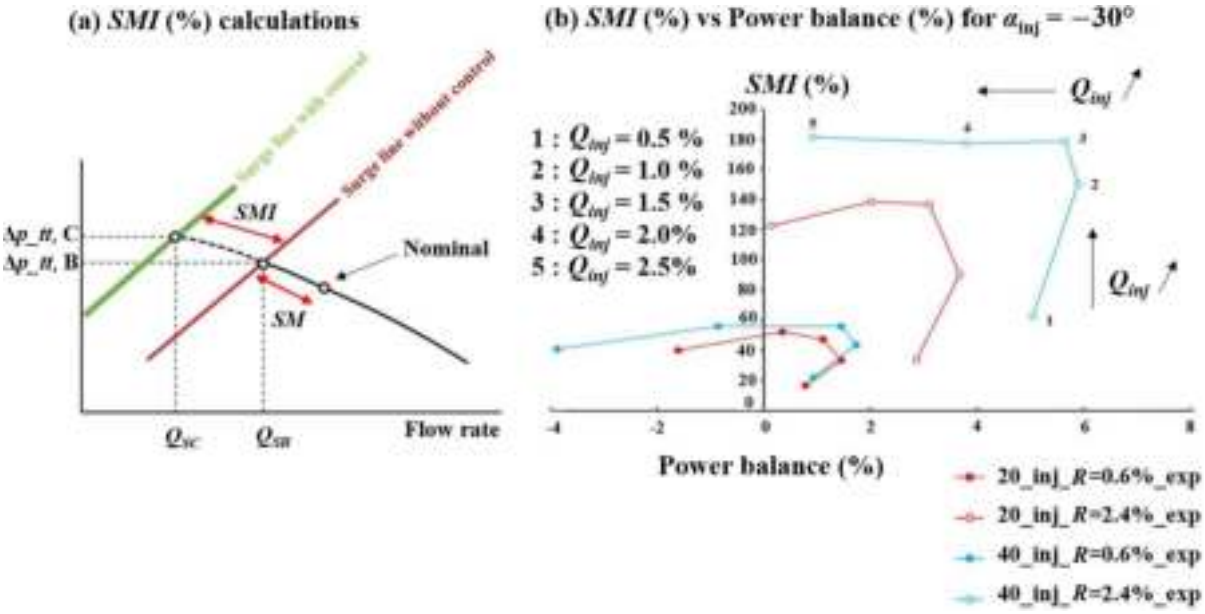

Figure 8. (**a**) *SMI* calculations. (**b**) *SMI* (%) and power balance (%) of the control system with experimental data at *R* = 0.6% and 2.4% for $\alpha_{inj} = -30°$ with 20 and 40 injectors.

Finally, it is shown that the active control with α_{inj}= −30° seems to be efficient as it postpones the stall limit with a stall mass flow rate decrease and a pressure ratio increase. This improves the *SMI*, offering a possible strategy to stabilize the tip gap region.

3.3. Impact of the Injection Control Parameters

Further configurations are explored experimentally with different control parameters. In this section, the active flow control for continuous blowing at 3200 RPM is tested with 40 and 20 injectors activated and various absolute flow angles: the performance curves are presented with α_{inj} = 0°, −30°, −45°, −60° at Q_{inj} = 1.5% (Figure 9). For the configurations with 40 injectors, the best results are obtained at α_{inj} = −45°, and with 20 injectors, the best results are obtained at α_{inj} = −30°. Indeed, the effect of blowing control generates higher static pressure rise at these angles. In addition, the stall onset is delayed, especially for the 40-injector configuration.

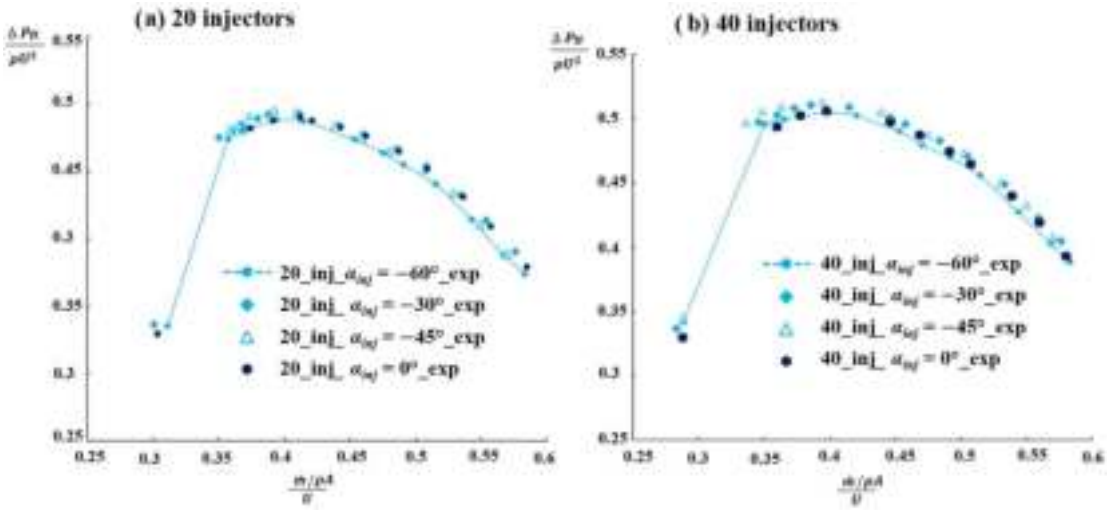

Figure 9. Experimental CME2 performance map for R = 2.4% at 0°, −30°, −45°, −60°: with (**a**) 20 injectors, (**b**) 40 injectors.

The global performance of the other fluidic parameters is then analyzed, focusing on the configurations with 40 injectors, as this configuration produces the best results in terms of performance. In Figure 10a, the power balance vs. *SMI* is investigated for continuous blowing at specific angles of injection. As expected, blowing control configurations allow for providing the best *SMI* with a high positive power balance with α_{inj} = −45°, especially for the injected mass flow rates at Q_{inj} = 1% and 1.5%. Consequently, it seems that for a larger tip gap size, the best configuration for active control is obtained with 40 injectors at α_{inj} = −45°. In Figure 10b, the *SMI* is reported as a function of the relative blowing angle, β. The results are extracted for different values of V^*_{jet} defined by the jet velocity scaled by the rotor tip blade velocity (U). The *SMI* clearly presents maxima for a relative blowing angle around 60° (Figure 10b). In a previous study [9], at R = 0.6%, this value for the relative blowing angle allowed for obtaining the best *SMI*. Moreover, this value approximately matched with the inlet blade angle at the tip for the CME2 compressor.

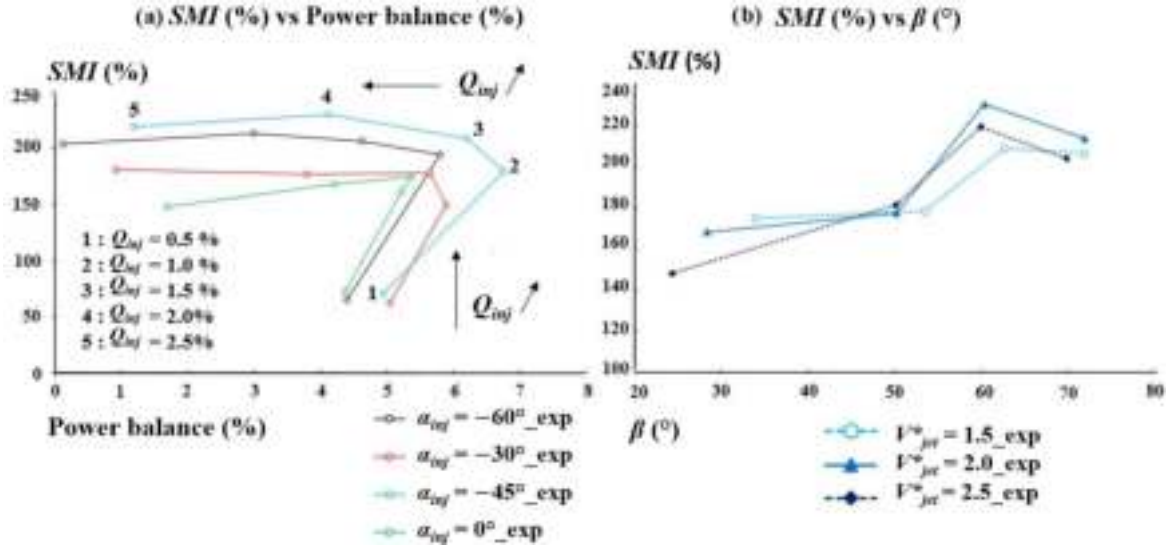

Figure 10. (**a**) *SMI* and power balance. (**b**) *SMI* (%) and β (°) at R = 2.4% for α_{inj} = 0°, −30°, −45°, −60° with 40 injectors.

4. Conclusions

The present study reported the effect of active flow control on narrow and large tip gap sizes. The experimental campaign was conducted on a single-stage axial compressor test bench equipped with fluidic actuators around the circumference. The measurements were performed from design conditions to operating points close to stall for configurations with and without control.

Compared with previous studies carried out for a narrow tip gap size on the CME2 test bench (R = 0.6%), the present work highlighted the benefit of active flow control on a large tip gap size (R = 2.4%). The impact of blowing allowed a longer delay in stall onset (*SMI* of the order of 200% and power balance up to nearly 6%), as well as a pressure increase that allowed a net positive power balance of the system. This study also demonstrated that the optimal configurations for blowing were based on the specific injection angle (α_{inj} = 45°) and full injector activation (40 injectors) around the compressor circumference. For the larger tip gap size (R = 2.4%), it seems that the air injection limits better the losses induced by the tip gap flow, generating a higher *SMI* than for narrow tip clearance (R = 0.6%). Further experimental tests should enhance the analysis of the development of stall with active control, thanks to the unsteady measurements, and attest the efficiency of tip blowing leading to the stabilization of the tip gap flow.

In parallel, RANS $2\pi/10$ simulations were achieved for the same configurations. The RANS $2\pi/10$ simulations rather accurately predicted the performance map without control (discrepancies less than 1% from nominal to last stable conditions) and were able to qualitatively catch the performance improvement induced by the control system. The analysis of the static pressure maps close to the casing showed that blowing confined the tip leakage vortex near the blade wall. Hence, this contributes to stall delay.

Author Contributions: Conceptualization, C.R., A.D., and J.M.; methodology, C.R., A.D. and J.M.; software, C.R. and J.M.; validation, C.R., A.D., J.M. and G.T.; formal analysis, C.R.; investigation, C.R.; resources, A.D., J.M. and G.T.; data curation, C.R., A.D., J.M. and G.T.; writing—original draft preparation, C.R.; writing—review and editing, C.R., J.M., A.D. and G.T.; visualization, C.R.; supervision, J.M., A.D. and G.T.; project administration, J.M., A.D. and G.T.; funding acquisition, J.M., A.D. and G.T. All authors have read and agreed to the published version of this manuscript.

Funding: This research was funded by the French Defence Innovation Agency (AID) and the Clean Sky 2 Joint Undertaking under the European Union's Horizon 2020 research and innovation program (grant number: 886352).

Institutional Review Board Statement: Not applicable.

Informed Consent Statement: Not applicable.

Data Availability Statement: Not applicable.

Acknowledgments: This work was supported by the CIRT (Consortium Industrie-Recherche en Turbomachines). The authors wish to thank the members of the ACONIT project for providing the numerical database. The authors would like to thank the French Defence Innovation Agency (AID) for co-funding this Ph.D. All simulations were performed in the framework of the elsA agreement between SAFRAN and ONERA, who are co-owners of this software.

Conflicts of Interest: The authors declare no conflicts of interest.

Abbreviations

The following abbreviations are used in this manuscript:

A	Annulus area at the rotor inlet ($A = 0.1029$ m^2)
α_{inj}	Injection angle (°)
β	Relative blowing angle (°)
ρ	Density ($\rho = 1.225$ kg/m^3)
ΔP_s	Static pressure variation (Pa)
ϕ	Flow coefficient: $\frac{\dot{m}/\rho A}{U}$ (-)
$\dot{m}$	Mass flow rate (kg/s)
Ω	Rotational velocity (rpm)
Ψ	Pressure coefficient: $\frac{\Delta P_S}{\rho U^2}$ (-)
P	Nominal compressor power (W)
$P_{s,t}$	Static, total pressure (Pa)
PB	Power balance (%)
Q_{inj}	Global injected mass flow rate (kg/s)
RANS	Reynolds-averaged Navier–Stokes
R	Ratio (tip gap size over the axial chord) (%)
SBC	Single-blade channel
SMI	Stall margin improvement (%)
SM	Stall margin (%)
T_t	Total temperature (K)
U	Rotor tip velocity (m/s)
V^*_{jet}	Jet velocity scaled (-)

References

1. Air Transport Action Group. Waypoint 2050. 2021. Available online: https://www.atag.org/ (accessed on 11 June 2023).
2. Suder, K.L.; Hathaway, M.D.; Thorp, S.A.; Strazisar, A.J.; Bright, M.B. Compressor Stability Enhancement Using Discrete Tip Injection. *J. Turbomach* **2001**, *123*, 14. [CrossRef]
3. Li, J.; Du, J.; Geng, S.; Li, F.; Zhang, H. Tip air injection to extend stall margin of multi-stage axial flow compressor with inlet radial distortion. *Aerosp. Sci. Technol. Elsevier Masson SAS* **2020**, *96*, 105554. [CrossRef]
4. Marty, J.; Castillon, L.; Boniface, J.C.; Burguburu, S.; Godard, A. Numerical and Experimental Investigations of Flow Control in Axial Compressors. *Aerospacelab J.* **2013**, *6*, 1–13. [CrossRef]
5. Neuhaus, L.; Neise, W. Active Control to Improve the Aerodynamic Performance and Reduce the Tip Clearance Noise of Axial Turbomachines. In Proceedings of the AIAA Aeroacoustics Conference, Monterey, CA, USA, 23–25 May 2005.
6. Cumpsty, N.A. Compressor aerodynamics. *Longman Sci. Tech.* **1989** . [CrossRef]
7. Smith, H. The effect of tip clearance on the peak pressure rise of axial flow fans and compressors. In *ASME Symposium on Stall*; American Society of Mechanical Engineers: New York, NY, USA, 1958; Volume 149, pp. 149–152.
8. Marty, J.; Castillon, L.; Joseph, P. Numerical Investigations on the Rotating Stall in an Axial Compressor and its Control by Flow Injection at Casing. *ASME. J. Turbomach.* **2023**, *145*, 051009. [CrossRef]
9. Moubogha, J.; Margalida, G.; Joseph, P.; Roussette, O.; Dazin, A. Surge Margin Improvement by Continuous and Pulsed Tip injection. *Int. J. Turbomach. Propuls. Power* **2022**, *7*, 10. [CrossRef]
10. Rannou, C.; Marty, G.; Dazin, A. Effect of Tip Gap Size on the Performance of an Axial Compressor Stage With and Without Active Flow Control. In Proceedings of the 15th European Turbomachinery Conference, Budapest, Hungary, 24–28 April 2023; Paper n. ETC2023-207. Available online: https://www.euroturbo.eu/publications/conference-proceedings-repository/ (accessed on 7 June 2023)

11. Veglio, M. Etude Expérimentale et Numérique des Écoulements dans un étage de Compresseur Axial à Basse Vitesse en Régime de Fonctionnement Instable. Ph.D. Thesis, ENSAM, Paris, France, 2016.
12. Rannou, C.; Dazin, A.; Marty, J.; Tanguy, G.; Castillon, L.; Moughoba, J. Effect of the Axial Compressor Tip Clearance Size: Performance and Transition to Rotating Stall. In Proceedings of ASME Turbo Expo 2022, Turbomachinery Technical Conference and Exposition (GT2022-80914), Rotterdam, The Netherlands, 13–17 June 2022. [CrossRef]
13. Cambier, L.; Heib, S.; Plot, S. The Onera *elsA* CFD software: Input from research and feedback from industry. *Mech. Ind.* **2013**, *14*, 159–174. [CrossRef]
14. Baretter, A.; Godard, B.; Joseph, P.; Roussette, O.; Romano, F.; Barrier, R.; Dazin, A. Experimental and Numerical Analysis of a Compressor Stage under Flow Distortion. *Int. J. Turbomach. Propuls. Power* **2021**, *6*, 621–656. [CrossRef]
15. Spalart, P.; Allmaras, S. A one-equation turbulence model for aerodynamic flow. In Proceedings of the 30th Aerospace Science Meeting & Exhibit, Reno, NV, USA, 6–9 January 1992 ; Volume 439, pp. 92–0439.
16. Margalida, G.; Joseph, P.; Roussette, O.; Dazin, A. Active flow control in an axial compressor for stability improvement: on the effect of flow control on stall inception. *Exp. Fluids* **2021**, *62*. [CrossRef]
17. Weigl, H.J.; Paduano, J.D.; Fréchette, L.G.; Epstein, A.H.; Greitzer, E.M.; Bright, M.M.; Strazisar, A.J. Active Stabilization of Rotating Stall and Surge in a Transonic Single Stage Axial Compressor. In Proceedings of the ASME 1997 International Gas Turbine and Aeroengine Congress and Exhibition, Orlando, FL, USA, 2–5 June 1997; Volume 4. [CrossRef]

Disclaimer/Publisher's Note: The statements, opinions and data contained in all publications are solely those of the individual author(s) and contributor(s) and not of MDPI and/or the editor(s). MDPI and/or the editor(s) disclaim responsibility for any injury to people or property resulting from any ideas, methods, instructions or products referred to in the content.

International Journal of
Turbomachinery
Propulsion and Power

MDPI

Article

Suitability of a Profile with Tubercles for Axial Pumps—Investigation Using Flow Simulation

Mareen Derda *, Ferdinand Neumann and Paul Uwe Thamsen

Chair of Fluid System Dynamic, Institute of Fluid Dynamics and Technical Acoustics, Technische Universität Berlin, Straße des 17. Juni 135, 10623 Berlin, Germany
* Correspondence: mareen.derda@tu-berlin.de; Tel.: +49-3031473206

Abstract: Even if wind tunnel tests and simulations have confirmed that tubercles can influence the behaviour of a profile, research in the field of axial pumps has so far been lacking. However, previous studies cannot be transferred to the application of axial pumps, since the requirements for the profile geometry as well as the Reynolds number range differ. The present study aims to address this research gap by performing a CFD simulation with a profile common for axial pumps, the Goe11K, testing four different tubercle configurations. At the same time, this simulation is a preliminary study for experimental tests. The results show that certain tubercle configurations improve the behaviour of the profile in the post-stall area, i.e., increase the lift of the profile at large angles of attack (α). In general, the curve of the profiles with tubercles runs more evenly, without the drastic drop in lift. This improved property comes at the expense of lower maximum lift and increased drag at lower α. With regard to the use of axial pumps, it can be concluded that there are advantages, particularly in the partial load range. These could ultimately enlarge the operation range of an axial pump.

Keywords: axial pumps; CFD; tubercles

check for updates

Citation: Derda, M.; Neumann, F.; Thamsen, P.U. Suitability of a Profile with Tubercles for Axial Pumps—Investigation Using Flow Simulation. *Int. J. Turbomach. Propuls. Power* **2023**, *8*, 29. https://doi.org/10.3390/ijtpp8030029

Academic Editors: János Gábor Vad, Csaba Horváth and Tamás Benedek

Received: 11 February 2023
Revised: 19 July 2023
Accepted: 9 August 2023
Published: 1 September 2023

Copyright: © 2023 by the authors. Licensee MDPI, Basel, Switzerland. This article is an open access article distributed under the terms and conditions of the Creative Commons Attribution (CC BY-NC-ND) license (https://creativecommons.org/licenses/by-nc-nd/4.0/).

1. Introduction

Previous research by Fish et al. [1] and many others have already shown that sinusoidal wing leading edges, modelled on the leading edge of humpback whale fins and called tubercles, can strongly influence flow behaviour. The aforementioned study showed that the tubercles change the stall and post-stall behaviour of a wing, resulting in a smoother flow separation and an increased post-stall lift [1].

However, known research on the application of tubercles in pumps is either limited or non-existent for axial pumps. Due to the different profile selections, results from existing studies cannot be relied on when designing axial pump blades with tubercles. Therefore, this study aims to address this research gap by using CFD methods on an infinite vane using a Goe11K, a profile commonly used in axial pumps, within a Reynolds number (Re) range of $Re = 1.5 \times 10^6$ and an angle of attack (α–[°]) range from 0° to 24°. Since axial pumps represent a wide area of application and therefore an important area of research, this is a first step towards the investigation of the suitability of tubercled profiles for axial pumps. Based on this, experimental investigations are to be carried out.

2. State of Research

2.1. Basic Mechanism of Tubercles

In the previous research literature, four mechanisms of action of tubercles are mainly distinguished. The first effect was mentioned by van Nierop et al. [2]. It was claimed that the pressure distribution on the wing in the flow direction, which is different behind tubercle tips and valleys, influences separation behaviour. Due to a higher pressure gradient behind the tubercle valleys (compare Figure 1), the flow separates there first while still remaining attached behind the tips. This contributes to the smoother separation characteristics of a tubercled wing.

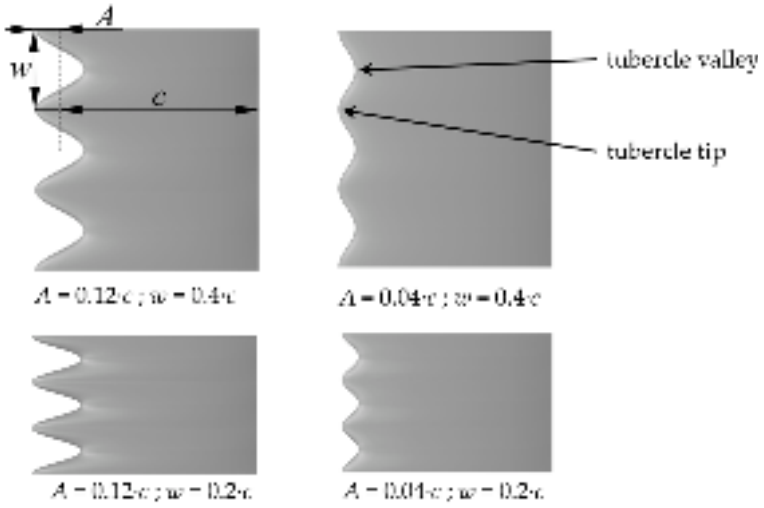

Figure 1. Selected tubercle configurations.

The second effect has been mentioned by Miklosovic et al. [3]. The resulting vortices behind the tubercle valleys are thought to increase the momentum exchange between the boundary layer and the free stream near the trailing edge of the wing, resulting in the flow staying attached in these regions at higher α. This working mechanism is comparable to that of "vortex generators".

A third working mechanism has been mentioned by Pedro et al. [4]. The vortices that appear behind tubercle valleys act as a barrier to the spanwise flow on wing-like wing fences. Therefore, on finite wings tubercles reduce the expansion of separation zones along the wing span, resulting in an increased lift at high α, where parts of a finite wing are already stalled. It is important to note that this effect is only seen in experiments and simulations with finite wings with changing profile contours along the span. As a result, those phenomena will not occur in the presented simulation approach, where the wing profile is an infinite wing that does not change along the span. Therefore, no spanwise pressure gradient and no changeable separation behaviour along the span can be expected, which tubercles could potentially help reduce.

The fourth effect has been described by Custodio [5]. The author argues that the vortices accelerate the flow on the wing, resulting in lower pressure and lift, often called "vortex lift" [5].

2.2. Influence of Tubercles on the Behaviour of a Profile

The aforementioned study by Miklosovic et al. [3] showed how tubercles can improve the flow around a wing. In their research, a finite wing with a NACA 0012 profile, with a maximum thickness of 12% at 30% chord length (c–[m]), was tested in a wind tunnel at a Reynolds number range from $Re = 1.35 \times 10^5$ up to $Re = 5 \times 10^5$. The wing with tubercles showed an increased maximum lift by 6% and a decreased drag by up to 32% at high α. In addition, the stall characteristics of the wing were smoother on the wing with tubercles than those on the wing without tubercles. At low α, the tubercles showed no change in lift and drag compared to the unmodified wing.

A study by Cai et al. [6] investigated the influence of tubercles on an infinite wing with a NACA 634-021 profile at Reynolds number $Re = 2 \times 10^5$ using CFD methods. The results of this research show a different influence of the tubercles on wing performance. At high α, where the flow on the unmodified wing is still attached, the tubercled wing has an increased drag and reduced lift. The tubercled wing only showed improved flow behaviour in the separated flow region, where drag corresponds to that of the unmodified wing and lift is increased.

These two studies highlight that the influence of tubercles on the wing characteristics is not the same for all applications but rather depends on parameters such as the selected airfoil, Reynolds number, and test setup.

The influence of tubercles on flow characteristics also depends on the geometry of the tubercles, which is defined by the tubercle amplitude (A–[m]) and the tubercle wavelength (w–[m]). Both parameters are shown in Figure 1 for better understanding.

Studies by Johari [7] and Hansen et al. [8] demonstrate that, at higher amplitudes, the flow around the wing is more influenced by the tubercles; therefore, the lift and drag are changed more compared to a wing without tubercles. This can be seen in the study by Johari [7], where a small amplitude of $A = 0.025 \cdot c$ only slightly reduces the maximum lift and improves the post-stall lift by a small amount, while versions with a high amplitude of $A = 0.12 \cdot c$ have a greater reduction in the maximum lift, but also a higher lift in the post-stall regime.

The influence of the tubercle wavelength does not seem to be as decisive as that of the amplitude. Also, no general rule for the influence of the wavelength can be found in the studies presented here. However, at high wavelengths, such as $w = 0.86 \cdot c$, tested by Hansen et al. [8], the flow behaviour on the wing tends to be very similar to that on the unmodified wing.

2.3. Hypotheses

Even if research findings to date cannot be directly transferred to the application in axial pumps, due to the completely different profile requirements, hypotheses related to the subject of the study can still be derived. These are:

1. The profiles with tubercles do not reach the maximum lift coefficient (c_L) of the profile without tubercles but show better lift behaviour in the post-stall area;
2. The drag coefficient (c_D) of the profiles with tubercles will be slightly higher at angles without flow separation compared to the reference wing;
3. The lift behaviour of the profile with tubercles depends on the configuration used;
    a. Smaller amplitudes result in higher maximum lift, but only minor improvements in the post-stall area;
    b. Larger amplitudes result in lower maximum lift, but better post-stall behaviour;
4. A smoother stall characteristic can be expected on the tubercled wings than on the baseline wing.

These hypotheses are to be examined in the present study using a CFD simulation.

3. Method

As already mentioned, previous research findings cannot be transferred, partly due to the different profile requirements for axial pumps. Therefore, the profile selection and the selection of the tubercle configurations to be simulated will be discussed here first before the setup of the CFD simulation is described.

3.1. Profile Selection and Selected Configurations

The main profile requirements for axial flow pumps include slimness combined with a high thickness reserve, reducing the suction peak at the leading edge and therefore making the pump vanes less prone to cavitation. Furthermore, a high maximum glide ratio in the design point is desired for the high efficiency of the pump [9]. The selected Goe11K is shown in Figure 2.

This profile meets these requirements [10] and has already been used in axial pumps at the Department of Fluid System Dynamics at the Technical University of Berlin; therefore, previous test results can be compared.

Four configurations of tubercled wings and the baseline version were simulated to investigate a variety of different designs while keeping the computational effort at a reasonable level. A preselection of amplitudes and wavelengths was made, considering

the analysis performed by Hansen et al. [8]. From these studies, the configurations were selected to stay within a presumably promising range. Four configurations were created by combining two amplitude values with two wavelength values. The selected amplitudes are $A = 0.04 \cdot c$ and $A = 0.12 \cdot c$, and the wavelengths are $w = 0.2 \cdot c$ and $w = 0.4 \cdot c$. The leading edge of the baseline wing was taken as the axis around which the defined sinusoid oscillated. This was done to ensure that the projected wing area on the modified wings was the same as on the reference. The four resulting configurations are shown in Figure 1. With these wings, an amplitude–wavelength ratio A/w of 0.1 for the smoothest to 0.6 for the sharpest tubercles is covered. Each of the four configurations and the reference profile without tubercles was simulated in the α range from 0° to 24°, with 3° steps, with a Reynolds number of $Re = 1.5 \times 10^6$.

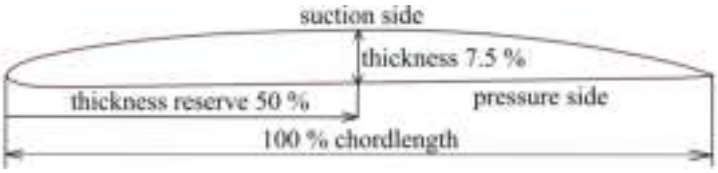

Figure 2. Selected profile Goe11K.

3.2. CFD Setup

The CFD model was set up with the use of OpenFOAM according to general information and guidelines on CFD setup, e.g., from Schwarze [11]. The presented CFD model reflects a transient and incompressible flow state and uses the RANS approach. Turbulence in the domain is modelled using the k–ω SST model (as described in [11]), a two-equation model that well reflects the turbulence in the free stream and the boundary layer. By adding only two new variables, the turbulent kinetic energy (k–[J/kg]) and the specific dissipation rate (ω–[1/s]), computation time is kept at a reasonable level while still achieving a good representation of the turbulence in the domain. Because of those properties, it is an industry standard and is used in this paper.

The computational domain (cf. Figure 3) was designed to represent an infinite vane. Therefore, both sidewalls were set to a symmetry condition.

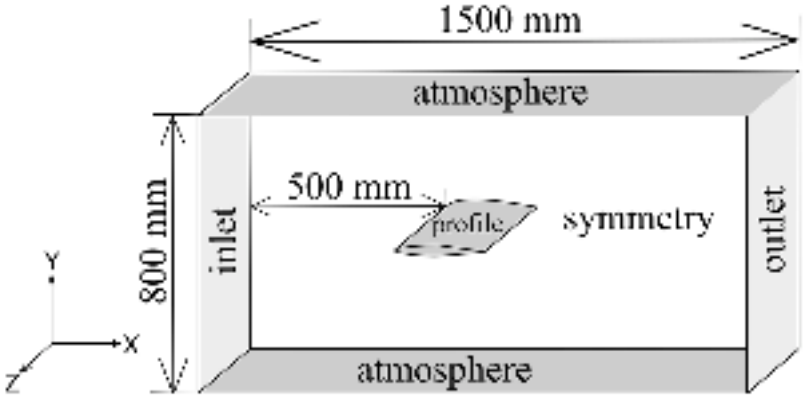

Figure 3. Computational domain.

The mesh, created with the open-source software SALOME, is an unstructured mesh (compare Figure 4) consisting of roughly two million cells. The free stream cells are tetraeders while the boundary layers around the wing are resolved using prism layers. Since no wall function was used, the resolution of the boundary layers was needed to ensure accurate drag and lift predictions. The maximum aspect ratio of all generated meshes was around 90, and the maximum non-orthogonality of all meshes was around 65°. The mesh quality is therefore sufficient for the intended use.

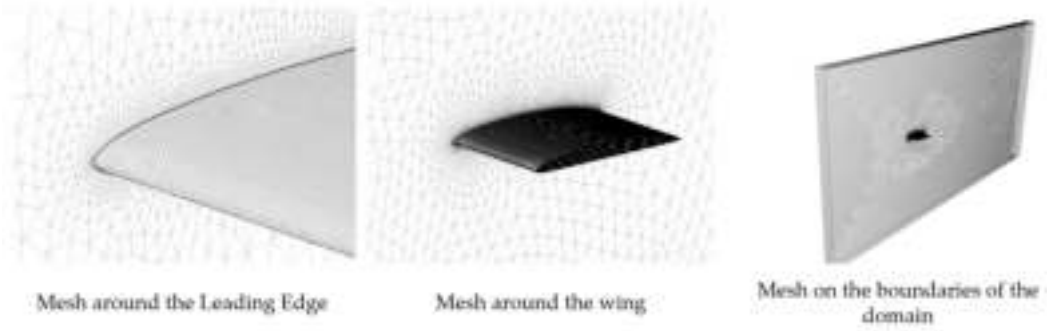

Figure 4. Mesh structure.

Solving was performed using the pisoFoam solver, which uses the PISO algorithm. Linear upwind, a second-order scheme [12], was selected for the discretisation of the divergence terms. For Laplacian terms, linear interpolation was chosen for the diffusion coefficient, and explicit non-orthogonal correction with the correction coefficient set to 1 was chosen for normal surface gradients. To further address non-orthogonality, two inner non-orthogonal corrector loops of the pressure equation were used. The linear interpolation scheme was also used for the gradient terms. An implicit scheme, the Crank–Nicolson scheme, with a mixing factor of 0.7, was used for the temporal discretisation. The time step was addressed with an adjustable time step and a fixed maximum CFL number of 7 for all simulations. The simulated physical time was 0.3 s. At the end of the simulated time, a quasi-steady state or periodic condition was reached for all simulations.

3.3. Mesh Study

A mesh study was carried out to ensure that the results were independent of the mesh. To investigate the influence of the mesh resolution on the results, four different resolutions were tested with the baseline wing at $\alpha = 6^\circ$ using the transient setup described above. To change the resolution of the mesh, multiple parameters like the growth rate of the cells and the first layer thickness of the prism layers, and, thereby, the dimensionless wall distance ($y+$), were adapted. For good results, the requirement $y+ < 5$ should be reached in all cells at the wall to keep the cells within the viscous sublayer [11].

Table 1 shows the time-averaged force coefficients, the relative error of both coefficients compared to the finest mesh, and the maximum $y+$ value for the mesh study. It can be seen that poor mesh resolution has a considerable influence on the calculated drag. Between the two highest resolutions, the drag value does not vary by more than two percent, which makes the error that occurs tolerable. The maximum $y+$ for this resolution is above five. To save computation time, a resolution of about two million cells was chosen for this study, because only about 0.5% of the cells on the wing surface had a $y+$ value greater than five.

Table 1. Overview of the mesh study.

Cell Count in Million	Max $y+$	c_D [-]	c_L [-]	Error in c_D [%]	Error in c_L [%]
0.52	8.809	0.0281	0.998	47	0.5
1.42	7.942	0.0235	1.005	23	1.2
2.195	6.01	0.0194	1.007	1.6	1.4
4.210	3.74	0.0191	0.993	-	-

The constructed simulation model was validated by comparing the simulated lift and drag behaviour of the Goe11K baseline profile with profile data from Riegels [10]. The results, seen in Figure 5, show good agreement for lift and reasonable agreement for drag, with the highest prediction error being 34% at $\alpha = 0^\circ$.

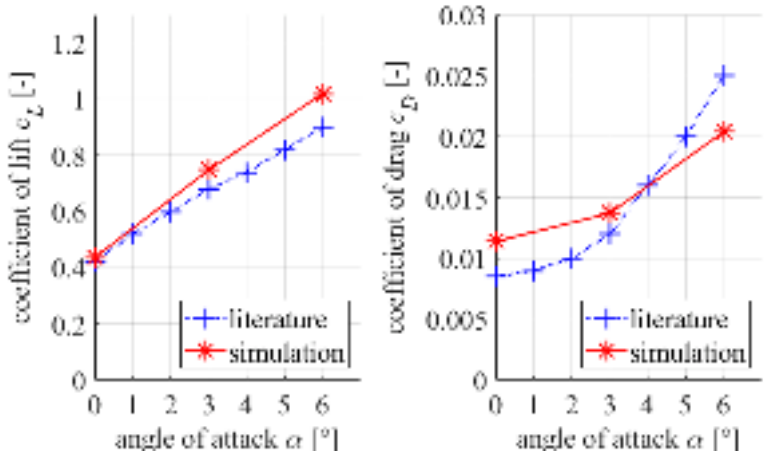

Figure 5. Comparison between simulation results and profile data from Riegels [10].

4. Results

First, the results of the simulation are presented using the calculated coefficients and then a qualitative evaluation is carried out using the simulated pressure distribution.

4.1. Quantitative Evaluation

Figure 6 shows the results for the lift coefficients c_L of all the tubercle versions and the base wing from the simulation over the simulated α range from 0° to 24°. As can be seen, the lift of the baseline wing increases with α up to 18°, where the maximum lift of c_L = 1.6 is reached. A further increase in α leads to flow separation at the leading edge of the wing. The maximum lift achievable by the tubercle configurations is only c_L = 1.2. Depending on the tubercle configuration, this corresponds to a maximum loss of lift of about 35%. Furthermore, it was found that all tubercle configurations show a smoother separation behaviour than the baseline.

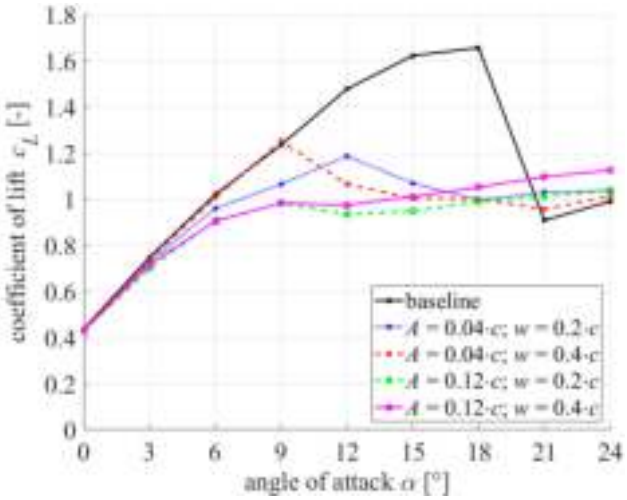

Figure 6. Calculated coefficient of lift c_L for tubercled configurations and baseline.

Apart from that, all tubercle configurations have a higher lift coefficient c_L in the post-stall area than the reference wing. The improvement in post-stall lift is greatest at α = 21°, where the tubercles improve lift by up to 20%.

Figure 7 shows the coefficient of drag c_D, which was calculated in the simulations for all versions with a modified leading edge. The reference wing was plotted over the α range. It can be seen that the drag of all configurations between 9° and 18° is higher than on the unmodified wing. In the post-stall region of the base wing, three of the four tubercle configurations tested achieve lower drag than the unmodified wing.

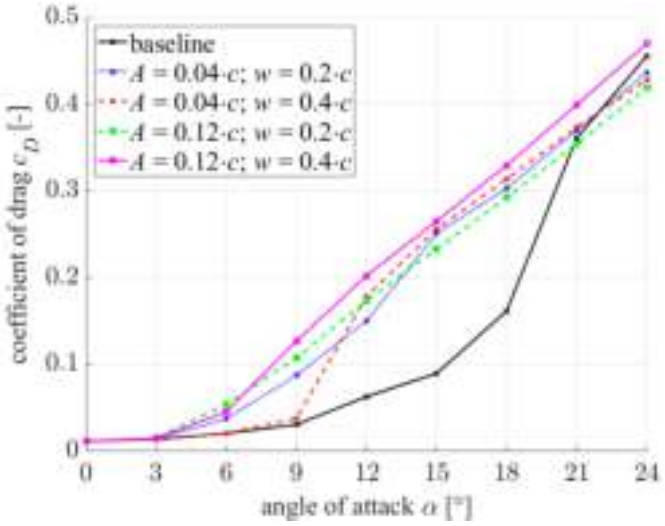

Figure 7. Calculated coefficient of drag c_D for tubercled configurations and baseline.

The quantitative evaluation has shown that the aerodynamic coefficients are heavily influenced by the application of tubercles. The next section investigates the reasons for this change in flow behaviour.

4.2. Qualitative Evaluation

In this section, the flow around the tubercled wing is analysed using pictures created after post-processing the simulation data. The investigation starts at a low α and describes the changes in the flow field as α is increased up to and beyond the separation angle of the reference wing.

Figure 8 compares the pressure distribution on the suction side of the base wing (the upper wing in Figure 7) with that of one selected configuration for $\alpha = 3°$. For this comparison, the surface is coloured according to the local pressure, where blue symbolises low pressures and orange high pressures. The reference wing has a uniform pressure distribution along the whole width, while the tubercled wing has a higher negative pressure in the tubercle valleys than at the tips. The observed negative pressure also exceeds the suction peak of the reference wing.

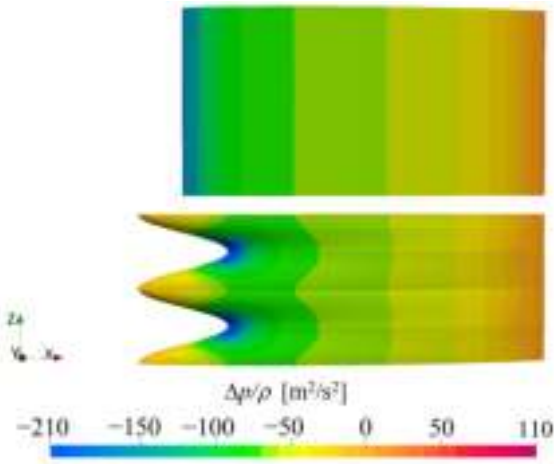

Figure 8. Pressure distribution on the base wing and the tubercle configuration with $A = 0.12 \cdot c$ and $w = 0.2 \cdot c$ at $\alpha = 3°$.

When looking at the simulation results, it was found that, on the simulated wings with an amplitude of $A = 0.12 \cdot c$, a pair of vortices, which can be seen in Figure 9, starts to develop only behind the tubercle valleys on the suction side at $\alpha = 6°$ and above. Figure 9

shows the surface of the selected tubercle configuration, which is coloured according to the local pressure. In addition, streamlines are shown in grey to highlight the flow above the wing and to show the vortex behind the tubercle valley. These vortices, although they create some negative pressure and hence vortex lift at the surface, are the reason for the reduction in lift, since the vortex lift is less than the lift present on the wings with a fully attached flow; they are also the reason for the increase in drag observed in Figures 6 and 7 for these configurations. These vortices grow as α increases.

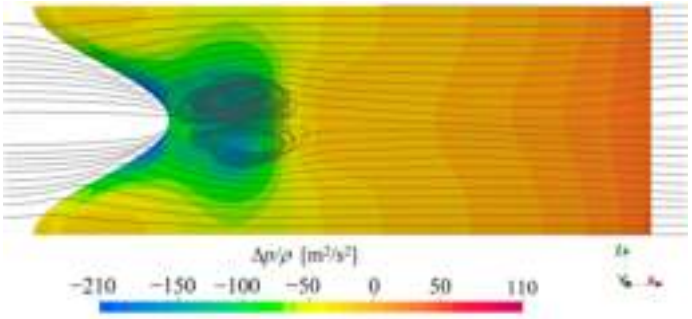

Figure 9. Pair of vortices on the configuration with $A = 0.12 \cdot c$ and $w = 0.2 \cdot c$ at $\alpha = 6°$ visualized by streamlines with constant colour.

Regarding the separation behaviour, it was found that some configurations already lose c_L compared to the baseline wing at $\alpha = 6°$ resulting from the mentioned vortices. However, the flow on the configuration with the lowest amplitude-to-wavelength ratio of $A/w = 0.1$, which is the version with the smoothest tubercles, stays completely attached until $\alpha = 9°$. At $\alpha = 12°$, the flow is separated over a large part of this wing, as shown in Figure 10, but high negative pressure is still present at the tubercle tips.

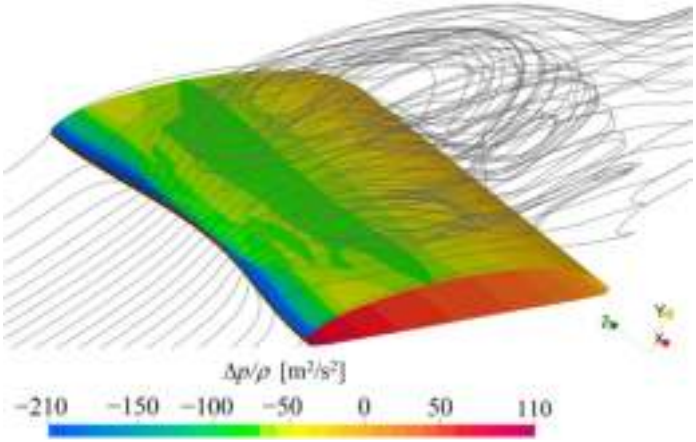

Figure 10. Flow on the configuration with $A = 0.04 \cdot c$ and $w = 0.4 \cdot c$ at $\alpha = 12°$ visualized by streamlines with constant colour.

The flow on the reference wing remains attached up to an $\alpha = 18°$. As α increases, the suction pressure on the leading edge increases to very high values. Regarding these high simulated negative pressures, it should be mentioned that cavitation could appear at those points when used in water, which strongly influences the behaviour of a pump.

Above $\alpha = 18°$, the wing without tubercles stalls and the lift achieved is rapidly reduced. In comparison, at these high α values, the flow on the tubercled wing is still attached to small parts of the wing behind the tubercle tips (cf. Figure 11).

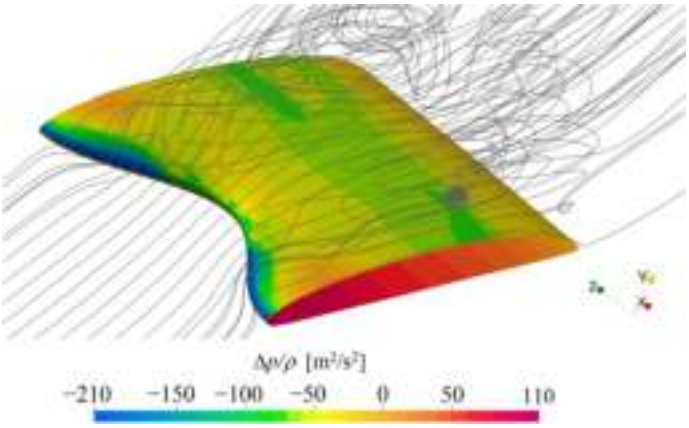

Figure 11. Partially attached flow on the tubercled wing with $A = 0.12 \cdot c$ and $w = 0.2 \cdot c$ at $\alpha = 21°$ visualized by streamlines with constant colour.

5. Discussion

The simulation results show that, for the selected profile, the setup and Reynolds number improvements in the post-stall lift can be found, while there is a loss at lower α. Therefore, the first hypothesis is confirmed. However, the magnitude of this trend has been underestimated and appears large compared to the literature, e.g., [6]. The loss in lift in the pre-stall region is large at around 35%, while the improvement in the post-stall region is smaller at around 10% to 20%. The best-tested configuration is the one with an amplitude of $A/c = 0.12$ and a wavelength of $w/c = 0.4$. While the loss of this version at low angles is comparable to that of the version with the same tubercle amplitude, the lift is the highest for all tubercle configurations from $\alpha = 18°$ upwards.

Regarding the second hypothesis, because the drag values in the area of the adjacent flow should be slightly higher for the tubercled versions, it can be argued that, again, the overall trend follows this hypothesis, but the extent of the increase in drag is greater than expected, with an increase of about 50% compared to the baseline, which is greater than expected. Therefore, the hypothesis cannot be verified, as only a small increase in drag was expected, but the results showed a rather significant increase.

The differing results, when compared to the literature, can be attributed to multiple factors. Firstly, the chosen Goe11K profile, with a chord thickness of 7.5%, is slimmer than the profiles described in the literature. It is designed to achieve a high glide ratio at low α. This leads to a significant increase in drag when vortices start to appear behind the tubercle valleys at $\alpha = 6°$, where the drag of two tubercle configurations is more than doubled (cf. Figure 6). Secondly, the infinite wing approach does not show the benefit of tubercles created using spanwise flow suppression, which can be seen when comparing the results of Miklosovic et al. [3] and Cai et al. [6]. When using the infinite wing model, the third working mechanism of tubercles (see Section 2) does not improve the flow around the wing because there is no spanwise flow due to the lack of a spanwise pressure gradient or spanwise forces to suppress. However, the spanwise effects that are expected in an axial flow pump differ fundamentally from the ones observed on a typical finite wing, e.g., because of the casing, which suppresses the formation of tip vortices. Therefore, improvements seen on a finite wing model cannot be expected to be transferred to this application. Thirdly, a study by Dropkin et al. [13] has shown that the maximum lift of a tubercled wing does not increase in the same way as the maximum lift of an unmodified wing at higher Reynolds numbers. Therefore, the selected Reynolds number of $Re = 1.5 \times 10^6$, which is high compared to most studies on tubercle application, results in a greater difference in maximum lift between the base wing and tubercle configurations. Lastly, it must be noted that the lift on the base wing at high α from 12° to 18° can be partly attributed to the simulated high negative pressures. When using tubercles in an axial pump with water as the pumping medium, those high negative pressures could lead to cavitation at the leading edge and therefore the lift would

be reduced. As a result, the difference in lift between the tubercle configurations and the baseline wing at those α values might be smaller in reality.

The third hypothesis, which claimed that lift behaviour depends on the selected tubercle configuration, is confirmed by the simulation results. The lower amplitude versions follow the lift slope of the unmodified wing up to $\alpha = 9°$ and achieve a higher maximum lift in the pre-stall area of the baseline than the higher amplitude versions. Furthermore, these configurations show a sudden decrease in lift at $\alpha = 9°$ or $\alpha = 12°$. This is due to the fact that, at those α values, the wing stalls have a large area, decreasing the lift. This effect cannot be observed with the higher amplitude tubercle configurations. The lift does not increase as much at low α as for the other versions but also does not drop noticeably at any α. This is due to the smoother separation behaviour of these wings. In the post-stall region, only the wavelength version with $w/c = 0.4$ has a better lift value than the lower amplitude configurations. This might be due to the fact that the amplitude-to-wavelength ratio is too high for the configuration with $A/c = 0.12$ and $w/c = 0.2$.

The fourth hypothesis, regarding the stall characteristics, can also be accepted. The separation behaviour of the tubercled versions is indeed smoother than that of the baseline wing. While no tubercled version shows a rapid lift decrease like the baseline, the low amplitude versions with $A/c = 0.04{\cdot}c$ show a slight lift decrease at $\alpha = 9°$ and $\alpha = 12°$, respectively. In contrast, the lift curve for the higher amplitude wings shows no lift decrease at any α.

6. Conclusions

From the simulation results and the studies presented in Section 2, it can be concluded that the benefit of tubercles is at operating points where a flow separation on unmodified wings/blades is likely. For axial flow pumps, this is the case at operating points well below the design point. The simulation showed that an optimised tubercle configuration can improve lift by 20% at those points while maintaining similar drag values. This is because tubercles not only delay flow separation by energising the boundary layer at the trailing edge but also locally confine the separation zones that do occur. As a result, the flow should stay attached to larger parts of the blades for longer.

In addition, the application of tubercles would also most likely reduce or completely erase the phenomenon of "rotation stall" described in [9], where a stalled region rotates in the opposite direction to the blades. This is because of the smoother separation characteristics of the tubercled blades compared to the version with a conventional leading edge.

Concerning the Reynolds number, it can be concluded that the selected Reynolds number of $Re = 1.5 \times 10^6$, which was chosen based on an existing pump with an outer pump diameter (d_A–[mm]) of $d_A = 149$ mm, an average chord length of about $c = 100$ mm, and a rotational speed (n–[rpm]) of $n = 2865$ rpm at the design point, reduces the positive effect of the tubercles. The use of tubercles in axial flow pumps with a lower Reynolds number, due to the smaller chord length of the blades or the lower rotational speed, could be more advantageous.

At the design point, which would be at around $\alpha = 3°$, where the highest glide ratio is achieved on the reference wing, the lift and drag of the tubercle configurations do not change much, and the maximum glide ratio is reduced from 54 to around 50 depending on the selected configuration. However, when α is increased, the efficiency and lift of the unmodified wing cannot be achieved with tubercles. Compared to studies shown in Section 2, the difference between unmodified and tubercled wings is greater in the presented simulation. Reasons for this included profile selection, Reynolds number, and the infinite wing approach. Regarding profile selection, tubercles seem to be less effective on profiles needed for axial flow pumps than on thicker profiles used for other applications. In terms of the infinite wing model chosen, it is true that axial pump blades do not have a free tip like on, e.g., aeroplane wings, where spanwise flow is to be expected because of the casing around the blades. However, some crossflow can still be expected because of centrifugal forces or partial flow separation at the blades.

Another important influence on axial flow pumps is cavitation. It was already briefly mentioned in the discussion that the appearance of cavitation might change results. However, the simulation was not set up to cover this phenomenon, and, therefore, the influence of cavitation could not be investigated. Research by Johari [7] suggests that tubercles influence cavitation behaviour depending on the selected configuration. In this study [7], a wing with a NACA 634-021 was tested with different tubercle configurations at $Re = 7.2 \times 10^5$ and using a range of α from 12° to 24°. For low amplitude and higher wavelength versions, the cavitation characteristics are similar to that of the baseline wing. Sheet cavitation occurs along the entire leading edge of the wing and increases in size with higher α. For configurations with higher amplitudes and smaller wavelengths, cavitation occurs earlier than on the baseline wing but is confined to the regions behind the tubercle valleys for all α. Sheet cavitation did not appear on those wings. Because only the area behind the tubercle valleys is affected by cavitation on these wings, the lift can still be created at the tubercle tips. Since the simulation has shown that a major part of the lift is created in the affected region, it remains unclear whether the total lift created by these configurations under cavitation conditions is really higher than on an unmodified wing.

Nonetheless, it is likely that more uniform lift behaviour, due to the smoother separation of the wings with tubercles, enlarges a pump's operating range, benefiting the application.

Overall, tubercles on axial flow pumps are expected to bring general improvement if a wide operation range, good efficiency, and suction head are required, especially at low speeds that are well below the operation point.

7. Summary and Outlook

Due to missing research on the application of tubercles in axial pumps, the aim of this study was to determine the possible influences of tubercles when used on axial pump vanes. The Goe11K profile was selected for the simulation because it is a slim profile with a high thickness reserve and is, consequently, well suited for use in axial pumps.

The Reynolds number was chosen to be $Re = 1.5 \times 10^6$ based on an existing axial pump tested previously. Four tubercled wings were selected based on the results of earlier studies [7,8], covering a good range of amplitudes and wavelengths. The simulation was set up as a transient and incompressible CFD simulation in OpenFOAM. The infinite wing approach was used. This setup was selected to keep the computational effort at a reasonable level, allowing the investigation of four tubercle configurations at a large α range. A mesh independence study was carried out to make sure the results were not reliant on the discretisation of the domain. The simulation results show only small improvements in the post-stall region due to the leading edge tubercles, while a significant reduction in the maximum lift was observed in the pre-stall region. This was attributed to the selected Reynolds number, the profile selection, and the infinite wing model. In the discussion, an aspect outside the simulation model was also considered, namely the "rotation stall", leading to the conclusion that the benefit of tubercles at lower Reynolds numbers might be higher than in the simulation. Furthermore, the simulation results showed that the tubercled wings have a smoother separation behaviour. This gain, leading to a wider operation range, still comes at the cost of lower lift and higher drag at the design point.

Despite that, it was argued that tubercles could improve axial pumps used at lower Reynolds numbers when a suitable tubercle configuration is selected and a good suction head is needed at low speeds that are well below the design point.

Further studies should investigate whether these results can be transferred to applications in axial pumps as expected, or whether other effects not yet considered, such as centrifugal forces, dominate the flow. For this purpose, a test bench according to ISO 9906 is currently being set up at the Department of Fluid System Dynamics at the Technische Universität Berlin. This will be used to investigate the extent to which tubercles on the leading edge of the blades of a three-bladed axial pump impeller with the Goe11K profile used in the simulation change the efficiency, the head, the power consumption, and the cavitation behaviour.

Author Contributions: Conceptualization, M.D.; methodology, M.D. and F.N.; software, F.N.; validation, M.D., F.N. and P.U.T.; formal analysis, F.N.; investigation, M.D. and F.N.; resources, M.D. and P.U.T.; data curation, F.N. and M.D.; writing—original draft preparation, M.D. and F.N.; writing—review and editing, M.D. and P.U.T.; visualization, M.D. and F.N.; supervision, P.U.T.; project administration, M.D. All authors have read and agreed to the published version of the manuscript.

Funding: This research received no external funding.

Institutional Review Board Statement: Not applicable.

Informed Consent Statement: Not applicable.

Data Availability Statement: Data are contained within the article. Additional data and information from this study are available upon request from the corresponding author.

Conflicts of Interest: The authors declare no conflict of interest.

References

1. Fish, F.E.; Battle, J.M. Hydrodynamic Design of the Humpback Whale Flipper. *J. Morphol.* **1995**, *225*, 51–60. [CrossRef] [PubMed]
2. Van Nierop, E.A.; Alben, S.; Brenner, M.P. How Bumps on Whale Flippers Delay Stall: An Aerodynamic Model. *Phys. Rev. Lett.* **2008**, *100*, 54502. [CrossRef] [PubMed]
3. Miklosovic, D.S.; Murray, M.M.; Howle, L.E.; Fish, F.E. Leading-Edge Tubercles Delay Stall on Humpback Whale (*Megaptera novaeangliae*) Flippers. *Phys. Fluids* **2004**, *16*, L39–L42. [CrossRef]
4. Pedro, C.; Kobayashi, M. Numerical Study of Stall Delay on Humpback Whale Flippers. In Proceedings of the 46th AIAA Aerospace Sciences Meeting and Exhibit, Reno, NV, USA, 7–10 January 2008.
5. Custodio, D. The Effect of Humpback Whale-like Protuberances on Hydrofoil Performance. Master's Thesis, Worcester Polytechnic Institute, Worcester, MA, USA, 2007.
6. Cai, C.; Zuo, Z.G.; Liu, S.H.; Wu, Y.L.; Wang, F.B. Numerical Evaluations of the Effect of Leading-Edge Protuberances on the Static and Dynamic Stall Characteristics of an Airfoil. *IOP Conf. Ser. Mater. Sci. Eng.* **2013**, *52*, 52006. [CrossRef]
7. Johari, H. Effects of Leading-Edge Protuberances on Airfoil Performance. *AIAA J.* **2007**, *45*, 2634–2642. [CrossRef]
8. Hansen, K.L.; Kelso, R.M.; Dally, B.B. Performance Variations of Leading-Edge Tubercles for Distinct Airfoil Profiles. *AIAA J.* **2011**, *49*, 185–194. [CrossRef]
9. Pfleiderer, C.; Petermann, H. *Strömungsmaschinen*, 7th ed.; Springer: Berlin/Heidelberg, Germany, 2005.
10. Riegels, F.W. *Aerofoil Selections. Results From Wind-Tunnel Investigations*; Butterworth & Co: London, UK, 1961.
11. Schwarze, R. *CFD-Modellierung*; Springer: Berlin/Heidelberg, Germany, 2013.
12. OpenCFD Ltd. Numerical Schemes, OpenFOAM Documentation. 2023. Available online: https://www.openfoam.com/documentation/user-guide/6-solving/6.2-numerical-schemes#x23-890115 (accessed on 8 June 2023).
13. Dropkin, A.; Custodio, D.; Henoch, C.W.; Johari, H. Computation of Flow Field Around an Airfoil with Leading-Edge Protuberances. *J. Aircr.* **2012**, *49*, 1345–1355. [CrossRef]

Disclaimer/Publisher's Note: The statements, opinions and data contained in all publications are solely those of the individual author(s) and contributor(s) and not of MDPI and/or the editor(s). MDPI and/or the editor(s) disclaim responsibility for any injury to people or property resulting from any ideas, methods, instructions or products referred to in the content.

International Journal of
Turbomachinery
Propulsion and Power

MDPI

Article

Three-Dimensional Flow Simulation by a Hybrid Two-Phase Solver for the Assessment of Liquid/Gas Transport in a Volute-Type Centrifugal Pump with Twisted Blades †

Markus Hundshagen [1,*], Kevin Rave [1], Michael Mansour [2,3], Dominique Thévenin [3] and Romuald Skoda [1]

[1] Chair of Hydraulic Fluid Machinery, Ruhr University Bochum, Universitätsstr. 150, 44801 Bochum, Germany
[2] Department of Mechanical Power Engineering, Faculty of Engineering—Mattaria, Helwan University, Cairo 11718, Egypt
[3] Laboratory of Fluid Dynamics & Technical Flows, University of Magdeburg "Otto Von Guericke", 39106 Magdeburg, Germany
* Correspondence: markus.hundshagen@ruhr-uni-bochum.de
† This paper has also been published in the Proceedings of 15th European Turbomachinery Conference, Budapest, Hungary, 24–28 April 2023.

Abstract: A hybrid two-phase flow solver is proposed, based on an Euler–Euler two-fluid model with continuous blending of a Volume-of-Fluid method when phase interfaces of coherent gas pockets are to be resolved. In a preceding study on a two-dimensional bladed research pump with reduced rotational speed, the transition from bubbly flow to coherent steady gas pockets observed in optical experiments with liquid/gas flow could be well captured by the hybrid solver. In the present study, the experiments and solver validation are extended to an industrial-scale centrifugal pump with twisted three-dimensional blades and elevated design rotational speed. The solver is combined with a population balance model, and a scale-adaptive turbulence model is employed. Compared to the two-dimensional bladed pump, the transition from agglomerated bubbles flow to attached gas pockets is shifted to larger gas loading, which is well captured by the simulation. The pump head drop with increasing gas load is also reproduced, showing the hybrid solver's validity for realistic pump operation conditions.

Keywords: liquid/gas transport; radial centrifugal pumps; computational fluid dynamics; hybrid two-phase solver; population balance modeling; scale-adaptive simulation

check for updates

Citation: Hundshagen, M.; Rave, K.; Mansour, M.; Thévenin, D.; Skoda, R. Three-Dimensional Flow Simulation by a Hybrid Two-Phase Solver for the Assessment of Liquid/Gas Transport in a Volute-Type Centrifugal Pump with Twisted Blades. *Int. J. Turbomach. Propuls. Power* **2023**, *8*, 28. https://doi.org/10.3390/ijtpp8030028

Academic Editor: Gerard Bois

Received: 12 June 2023
Revised: 16 June 2023
Accepted: 1 August 2023
Published: 30 August 2023

Copyright: © 2023 by the authors. Licensee MDPI, Basel, Switzerland. This article is an open access article distributed under the terms and conditions of the Creative Commons Attribution (CC BY-NC-ND) license (https://creativecommons.org/licenses/by-nc-nd/4.0/).

1. Introduction

Radial volute-type centrifugal pumps are frequently required in industrial processes to transport multi-phase flows consisting of liquid and non-condensable gas. However, they are usually designed to convey pure liquids and, hence, even a small load of gas, i.e., an inlet gas volume fraction $\varepsilon \approx 3\%$ [1], may cause a considerable disturbance in conveying. In the worst case, even a full breakdown of the pump head may occur [2], and flow instabilities may destroy the pump's components.

The resolution of experimental measurements is inherently limited [3,4]. As pointed out by, for example, Yin et al. [5] and De Santis et al. [6], computational fluid dynamics (CFD) simulation of liquid/gas flow provides a high amount of local flow information and may complement experimental results. In a preceding study [7], we presented a hybrid two-phase (H2P) solver for the 3D simulation of a water/air pump flow. A transparent research pump with a 2D cylindrical blade design facilitated detailed optical accessibility and a unique validation database. However, the impeller speed was reduced to $n = 650$ min^{-1} to protect the damageable transparent impeller material. It was shown that the transition of flow morphology from dispersed bubbly to segregated pocket flow was captured by the H2P solver. In the current study, the experiments and H2P solver validation are extended

to an industrial-scale volute-type centrifugal pump with twisted 3D blades and a design rotational speed $n = 1450$ min^{-1}, which is considerably higher than the corresponding design speed of the 2D bladed pump used by Hundshagen et al. [7].

Experimental validation data is essential for assessing CFD models, and optical data of the two-phase flow field offer a sound validation basis. For example, Stel et al. [8,9], He et al. [10], Zhang et al. [11], Parikh et al. [12] and, also, the present authors [7] used optical measurement data to access the prediction of gas distribution within 2D bladed impellers in CFD studies. Recent high-speed imaging experiments [1,13–18] confirmed the existence of gas pockets inside the pump impeller channels, which block a part of the blade channel, making the flow guidance inefficient and causing the head drop. Based on optical measurements, together with the head drop characteristics, several authors [1,8,13–15,19–24] provided performance maps of the conveyance of a mixture. Subject to the volumetric flow rate and the inlet gas volume fraction, some of the present authors [1,13–15] observed a transition from bubbly flow to steady gas accumulation in the blade channel and introduced a categorization in terms of flow regime maps. Experimental studies by Mansour et al. [1,13–15], and the corresponding simulations with the H2P solver by Hundshagen et al. [7], were, however, confined to a 2D bladed impeller at reduced speed, as mentioned above. In studies where 3D twisted blades were used, the assessment of CFD models was restricted to integral pump characteristics, such as those of the pump head, or inner efficiency [25,26]. In this study, optical measurements of a 3D bladed impeller, having an elevated design speed, were performed and used for the validation of the H2P solver, which is a major novelty of this study.

The optical experimental results provided by Mansour et al. [15] and Parikh et al. [12] also pointed out that there is a significant size variation of gas bubbles within the pump. Chen et al. [27] even concluded that coalescence is one of the primary mechanisms for the formation of gas pockets. Inspired by the observations made in experiments, the H2P solver is extended by a population balance model (PBM) to take into account bubble polydispersity, which is a further novelty of this study. The class method of Lo [28] is adopted, together with coalescence and breakup models.

A high unsteadiness of particular void regions was observed in experiments by Mansour et al. [15] and Liao et al. [29], which is also confirmed by an inspection of video sequences in this study. Alternating unsteady pockets are present in the transition zone between bubbly and pocket flow regime. Even inherently steady adherent void regions in the pocket flow regime show an unsteady wake [7]. Statistical turbulence models may be inappropriate to resolve the highly unsteady flow regions observed in experiments, so that a turbulence-scale resolving approach is preferred. The scale-adaptive simulation (SAS) approach of Egorov & Menter [30], together with the hybrid H2P solver, has already been applied in our preceding study [7]. The SAS treatment of turbulence is also adopted in this study. The liquid/gas flow is investigated in terms of a water/air system in the following. This manuscript corresponds to our paper published in the proceedings of the 15th European Turbomachinery Conference [31].

2. Experiments

2.1. Experimental Set-Up and Pump Characteristics

A 3D view of the pump and a photograph of the test rig are provided in Figure 1. The pump casing and the impeller are made of transparent acrylic glass and transparent polycarbonate, respectively, to allow flow visualization. The two-phase flow patterns are captured using two high-speed cameras with a 2016 × 2016 pixel resolution. The cameras are located in axial (camera 1) and isometric (camera 2) views, as depicted in Figure 1b.

Acrylic glass, polycarbonate and water have different optical refractive indices. In this study, only images obtained by camera 1 are used for direct comparison with simulation results, while images from camera 2 serve as a means for additional visual inspection of air accumulation zones. The arrangement of camera 1 is orthogonal to the casing wall. Therefore, it is assumed that the effect of refraction is minor. For a more quantitative

comparison, the actual location and size of bubbles may be calibrated and double-checked, based on the geometrical pump dimensions, such as impeller diameter and blade thickness. However, this is out of scope of this study. Six LED lamps are distributed around the pump casing to illuminate the flow, as shown in Figure 1a, making the water/air interfaces visible. A dashed rectangle in Figure 1a indicates the window where the two-phase flow patterns are observed. A rotational speed of $n = 1450$ min^{-1} is applied, resulting in a specific speed of about $n_q = 24$ min^{-1}, according to the definition of Gülich [32], and corresponding to a non-dimensional specific speed of $N_s = 0.44$. A semi-open impeller is applied, and its meridional view is sketched in Figure 2. Two tip clearance gap sizes s are investigated in the experiments: $s/b_2 = 2.5\%$ and $s/b_2 = 4.5\%$, where b_2 is the outlet width of the impeller blades.

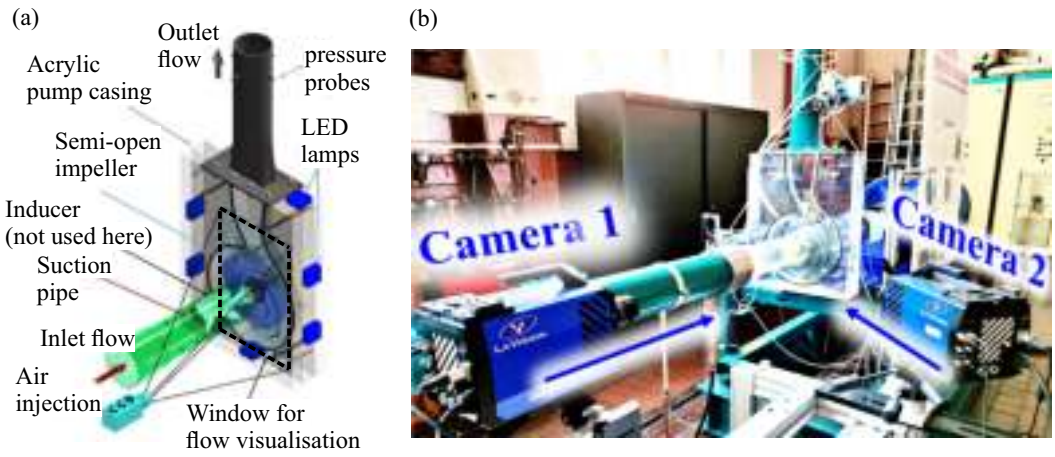

Figure 1. Test-rig (**a**) and photograph of the test-rig (**b**).

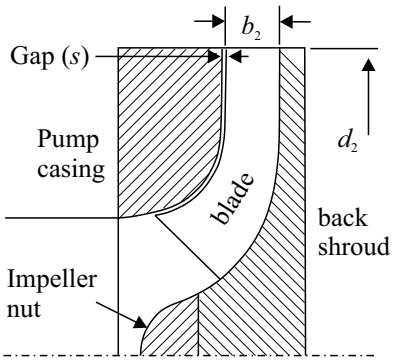

Figure 2. Sketch of the meridional view of the semi-open impeller.

It is found that the void patterns are not significantly affected by tip clearance size. Therefore, this study focuses on the smaller clearance gap. The volumetric flow rates of air and water, Q_a and Q_w, are separately measured to calculate the inlet air volume fraction ε. The static pressure difference across the pump is recorded to calculate the pump head. No bubble size spectra are measured. Therefore, we confine our investigations to a qualitative comparison between experimental and simulation results. Details of the experimental set-up, measurement techniques, and data evaluation are provided elsewhere [1,7,15,33].

2.2. Flow Regimes

The flow regime map observed in the experiments, in terms of pump head H versus total flow rate Q_t is depicted in Figure 3. The bubbly flow, agglomerated bubbles flow, alternating pocket flow, and pocket flow regime are discernible. The basic structure of the regimes essentially corresponds to the one of the 2D bladed pump from our previous study [7]. However, there are distinctive shifts in individual regimes.

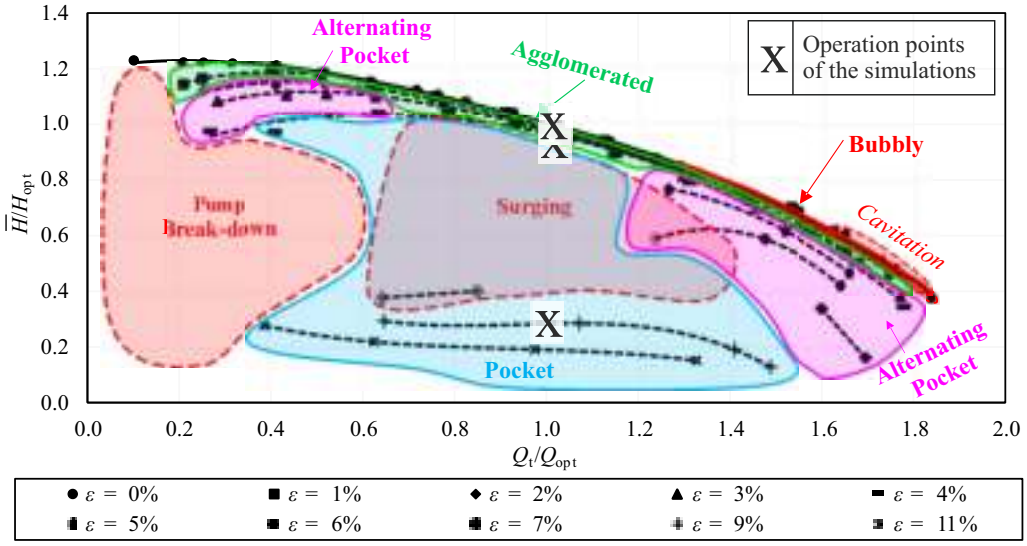

Figure 3. Pump head performance map and flow regimes observed in the experiments. The operation points investigated in the simulations are marked with an "X".

A detailed analysis of the effect of blade geometry and impeller design speed on the flow regimes is out of scope of this study. We confine our discussion to the effects which are immediately helpful for solver validation. For example, the bubbly flow regime is shifted to overload conditions, while the agglomerated bubbles flow regime is near the nominal flow rate, presumably because a rise in speed enhances Coriolis forces, so that the pressure gradient in the cross-flow direction and the tendency of bubble agglomeration are also enhanced. Furthermore, the pocket flow regime is present at rather large values of the inlet air volume fraction, $\varepsilon \geq 9\%$. A wide surging range between $3\% < \varepsilon < 9\%$ is discernible, which means that the pump jumps back and forth between two operation points. Alternating pockets occur only at part-load and overload, and at moderate air loading $3\% < \varepsilon < 7\%$. Ref. [15] showed that, by increasing the rotational speed, the water/air mixing and, therefore, the two-phase pump performance is improved. Hence, it is assumed that the shift of pocket flow to higher levels of ε can be traced back to a rise in design speed. It is interesting to note that the Reynolds number evaluated by the impeller diameter and circumferential impeller outlet velocity is the same for the present pump and the 2D bladed pump of our previous investigations [7], so that the shift of flow regime maps to higher values of ε was not a Reynolds number effect. A more in-depth analysis of experimental data for assessing flow regime maps is left to further studies. In this study, the validation of the H2P method for a 3D bladed pump with elevated design speed is the focus. Therefore, three operation points are considered with $\varepsilon = 1\%$, 3%, and 9%, additionally marked in Figure 3. $\varepsilon = 1\%$ and 3% correspond to the agglomerated bubbles flow regime, while $\varepsilon = 9\%$ corresponds to the pocket flow regime.

3. Simulation Method

3.1. Flow Solver

The H2P solver from our preceding studies [7,34] is adopted, and its main features are summarised here. It is an extension of the Euler–Euler two-fluid (EE2F) model with the ability to continuously activate Volume-of-Fluid (VOF) features for a proper interface resolution of coherent void structures. According to Wardle & Weller [35], the balance equations for mass and momentum for each isothermal phase φ (water and air) read:

$$\frac{\partial \alpha_\varphi}{\partial t} + \nabla \cdot (\alpha_\varphi \boldsymbol{c}_\varphi) + \underbrace{C_\alpha \nabla \cdot (\boldsymbol{c}_c \alpha_\varphi (1 - \alpha_\varphi))}_{\text{interface compression}} = 0 \tag{1}$$

$$\frac{\partial\, \alpha_\varphi \rho_\varphi \boldsymbol{c}_\varphi}{\partial t} + \nabla \cdot \left(\alpha_\varphi \rho_\varphi \boldsymbol{c}_\varphi \boldsymbol{c}_\varphi^T\right) + \nabla \cdot \left(\alpha_\varphi \rho_\varphi \boldsymbol{R}_\varphi^{\text{eff}}\right) = -\alpha_\varphi \nabla p + C_\beta M_{\text{D},\varphi} + M_{\text{vm},\varphi} + M_{\text{s},\varphi} \quad . \quad (2)$$

The volume fraction, density, and velocity of phase φ are symbolized by α_φ, ρ_φ, and $\boldsymbol{c}_\varphi$, respectively, and $\boldsymbol{R}_\varphi^{\text{eff}}$ represents the stress tensor combining Reynolds (turbulent) and viscous stresses. Note that the marking of Reynolds-averaged quantities is omitted for convenience. Both phases share the same static pressure field p. Water and air are treated as incompressible fluids, which enhances solver stability [36]. The interfacial momentum exchange terms, i.e., drag and virtual mass force, are symbolized by $M_{\text{D},\varphi}$ and $M_{\text{vm},\varphi}$. For the former, the drag model of Schiller & Naumann [37], and, for the latter, a constant virtual mass coefficient of 0.5 [38], are applied, respectively. The force $M_{\text{s},\varphi}$ is the surface tension force, estimated as a continuum force, according to Brackbill et al. [39].

The hybrid multi-scale character of the solver is facilitated by two blending functions for the interface compression term in Equation (1) and the drag force $M_{\text{D},\varphi}$, respectively. By following Hänsch et al. [40], the blending function for the interface compression C_α reads:

$$C_\alpha = [\,0.5 \tanh(\mathrm{a_B}(\alpha_\mathrm{a} - \mathrm{a_{min}})) + 0.5\,][\,0.5 \tanh(\mathrm{a_B}\,(\mathrm{a_{max}} - \alpha_\mathrm{a})) + 0.5\,]. \quad (3)$$

We set the constants $\mathrm{a_B}$, $\mathrm{a_{min}}$, and $\mathrm{a_{max}}$ to 35, 0.1, and 0.9, respectively. If C_α is set to 0, the original EE2F formulation is retained, while with $C_\alpha = 1$, a VOF-like interface resolution is achieved, which counteracts the numerical diffusion at the phase interface by including the compression velocity $\boldsymbol{c_c}$ in Equation (1). Details of the $\boldsymbol{c_c}$ evaluation can be found in Wardle & Weller [35]. A second blending function C_β blends the drag force between the formulation of [37] for spherical bubbles and a treatment of large coherent air structures where the drag is set to a low finite value of 10^{-4}. The C_β function is presented in [7] and is not repeated here. Note that applying two different blending functions for the interface compression and the drag force is attributed to the complexity of the pump flow, since it would be more consistent to use the same blending function for both sub-models. However, using Equation (3) for the drag force as well has produced stability issues [7].

The limitations of a monodisperse approach have been pointed out by Hundshagen et al. [7]. Therefore, a polydisperse bubble size distribution is considered here. An additional transport equation for the specific number density $n_\mathrm{B}(d_\mathrm{B})$ of bubbles is solved in each computational cell and timestep. Beyond the transport of $n_\mathrm{B}(d_\mathrm{B})$, birth and death rates, due to coalescence and breakup, are treated by source and sink terms. Thereby, a variable bubble diameter d_B is facilitated, e.g., in the drag force $M_{\text{D},\varphi}$. By adopting the approach of Kumar & Ramkrishna [41], the population balance equation is discretized in size groups, leading to the class method of Lo [28]. Twelve size classes, with a duplication of the bubble volume between consecutive classes, are adopted, resulting in a spectrum of bubble diameters for each size class, ranging from roughly $0.16\,\mathrm{mm} < d_\mathrm{B} < 2.00\,\mathrm{mm}$. This bubble diameter range corresponds to the one observed by Barrios & Prado [20] in electrical submersible pump flow for speed variation. Each bubble size class comprises the same velocity, and coalescence and breakup kernels are evaluated for each class. The coalescence kernel of Prince & Blanch [42], and the breakup kernel of Luo & Svendsen [43] are chosen. The coalescence kernel is used with an extension for maximum bubble packing, as proposed by [44], resulting in a formulation similar to the one suggested by Stel et al. [9] for a centrifugal rotor flow. Although the breakup and coalescence kernels are simply adopted from entirely different applications, e.g., bubble columns or mixer vessels, they have also been adopted in other two-phase pump studies, such as those by He et al. [10] and Yan et al. [25]. Hence, this is also done in this study. From the resulting bubble size distribution, the Sauter mean diameter d_{32} is evaluated, corresponding to a time and space distribution of d_B.

The SAS approach by Egorov & Menter [30] is adopted, which is based on the k-ω shear stress transport turbulence model of Menter [45]. A separate turbulence field, in

terms of turbulence kinetic energy k_φ and specific dissipation rate ω_φ, is calculated for air and water. The wall functions of Kalitzin et al. [46] are employed for both phases. Hence, c_φ, k_φ, and ω_φ are directly integrated to the wall or calculated by the logarithmic wall law depending on the value of the non-dimensional wall distance $y^+_{w,\varphi}$.

The *multiphaseEulerFoam* solver of OpenFOAM-9 (https://github.com/OpenFOAM/OpenFOAM-9 accessed on 1 May 2022) was used, customized by means of several model extensions, as described above. The PIMPLE solution algorithm with pressure relaxation was chosen, which is a combination of the pressure-implicit with splitting of operators (PISO) [47] method and the semi-implicit method for pressure-linked equation (SIMPLE) [48] algorithms. The timestep is set in such a way that the Courant–Friedrich–Levy number does not exceed 0.75 at the maximum, to achieve numerical stability. Three outer PIMPLE iteration loops turned out to yield a drop of non-linear residuals below $5 \cdot 10^{-4}$ in each time step. Additionally, a drop of residuals of linear solvers below 10^{-8} is applied. Different discretization schemes for the respective balance equations are used, which are summarized in Table 1.

Table 1. Discretization schemes of the simulations.

Term	Scheme
Time discretization	*First-order implicit Euler*
Discretization of convective terms (momentum eqns.)	*Second-order hybrid scheme* [49]: *LUST* scheme of Weller [50] (Scale-resolving region) or *Second-Order upwind* of Warming & Beam [51] (URANS region)
Discretization of convective terms (phase fraction eqns.)	*Second-order TVD* with limiter of Sweby [52] (phase interface) or *first-order upwind* (disperse flow region)
Discretzsation of convective terms (size fraction eqns.)	*Second-order TVD* with limiter of Sweby [52]
Discretization of convective terms (k and ω eqns.)	*First-order upwind*

3.2. Simulation Set-Up

The simulation set-up consists of the suction and discharge pipe, volute casing, side chamber, and 360° impeller to reflect the entire pump geometry. An explosion view of the computational domain is shown in Figure 4. Constant Dirichlet inlet boundary conditions are chosen for c_φ, α_φ, d_B, k_φ, and ω_φ. The phase velocity is set according to the measured flow rate and water and air have the same inlet velocity. A constant bubble diameter of 0.5 mm is set at the inlet, following the estimation by Barrios & Prado [20]. At the suction side cross-section, i.e., the inlet boundary of the computational domain, a constant value of α_φ is prescribed. A Neumann boundary condition with zero gradient is set for pressure at the inlet, while a constant static pressure is defined at the outlet. At the outlet, Neumann zero gradient boundary conditions are set for c_φ, α_φ, d_B, k_φ, and ω_φ.

Numeca AutoGrid® is used for the impeller and side chamber grid generation. For the suction and discharge pipes and the volute casing, Numeca HexPress® is employed, and local grid refinement by hanging nodes is utilized. The grids are optimized in terms of non-orthogonality, following the *OpenFOAM* nomenclature of Jasak [47]. In this way, grids with reasonably high quality are generated, taking into account the complexity of the 3D-twisted blade design. A grid study, by means of refining grid level G1 to G2, is performed, and some grid parameters are summarized in Table 2.

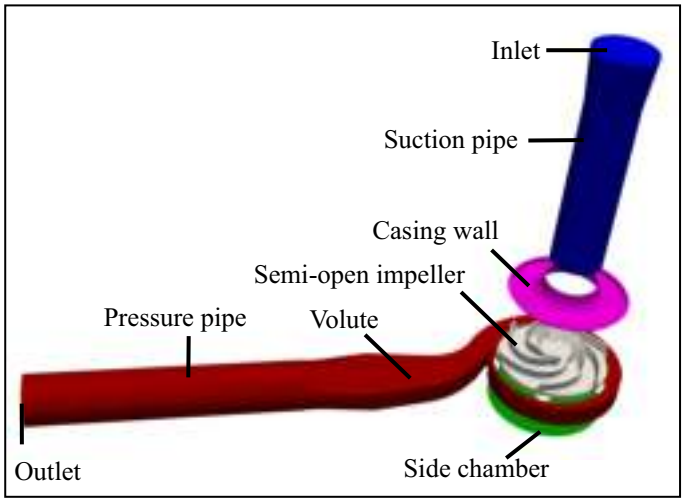

Figure 4. Explosion view of the computational domain.

Table 2. Computational grid data.

Name	# of Cells (10^6)	# of Tip Gap Cells	$y^+_{w,Blade}$	$y^+_{w,Volute}$	Non-Orthogonality
G1	3.5	7	27	6	<70
G2	32.2	14	9	3	<70

The single-phase simulation results, regarding the pump head and the inner efficiency for the same impeller geometry, but with a different volute casing, were investigated elsewhere [53,54]. Therefore, the single-phase results are not again discussed here in detail. Preliminary simulation results showed that the change in single-phase pump head between G1 and G2 simulations approaches at maximum 1.5% in over-load conditions and less than 0.5% in nominal and part-load conditions. Regarding the two-phase flow, by means of a grid refinement, successively finer void structures are resolved by the H2P solver, which transitions from EE2F mode towards a VOF-like scheme with phase–interface resolving capabilities. Thus, an inherent grid dependence of the results cannot be avoided. The same holds for the SAS, since a successively larger portion of the turbulence spectrum is directly resolved by the computational grid. Details of a two-phase grid study are omitted here for brevity, but were presented elsewhere [7], and it is ensured that the conclusions drawn from the simulation results in the following are not affected by grid dependence. The G1 results are described below.

4. Results and Discussion

In the 2D bladed pump of our prior study [7], air accumulations extended over the entire blade height, which enabled a direct comparison between experimental results in the front view and contour plots of air volume fraction in the midspan of the impeller. This assumption does not hold any more for 3D-twisted blades. Figure 5 presents plots over lines located near the hub, midspan, and shroud in the middle of a blade-to-blade surface in an example blade channel. The aligned coordinate along the line is denoted by l, and l_{max} is the line length. It can be seen that significantly less air is located near the shroud region than near the midspan or hub regions. Therefore, the α_a distribution changes over the blade height, and a direct comparison of the air distribution from simulation results with experiments is facilitated by virtual Schlieren imaging. This visualization technique of the simulation results is based on spatial gradients of α_a, and described elsewhere by Nguyen et al. [34]. Virtual Schlieren images are shown in Figure 6, together with the grey-scale images obtained by the experimental scattered-light technique. White areas in the virtual Schlieren images and the experimental results represent regions with high dispersed air loading. Dark regions indicate continuous phase regions of either water or

air. Example snapshots of the flow field are shown, and coloured arrows are depicted to highlight similarities between simulation and measurement results derived from an intensive inspection of video sequences.

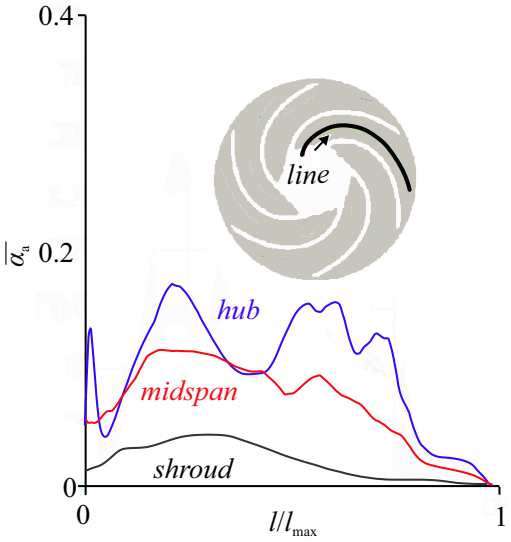

Figure 5. Plots of time-averaged air volume fraction $\bar{\alpha}_a$ along arbitrarily chosen lines in the middle of a blade-to-blade surface near the hub, midspan, and shroud for the $\varepsilon = 3\%$ operation point.

For $\varepsilon = 1\%$ (Figure 6a), a maximum of dispersed air loading is visible near the suction side of the blade (red arrow), while a minimum is discernible on the pressure side (blue arrow). For $\varepsilon = 3\%$ (Figure 6b), regions of dispersed air loading increase in size. Thus, the tendency of water and air to separate increases with a rising value of ε. For $\varepsilon = 9\%$ (Figure 6c), a vast region with continuous air phase is discernible with maxima of dispersed loading downstream of this continuous region. Hence, the local air distribution obtained by the virtual Schlieren results from the simulations agrees well with the experimental results for the investigated operation range from $\varepsilon = 1\%$ to $\varepsilon = 9\%$.

Contour plots of the time-averaged air volume fraction $\bar{\alpha}_a$ and its temporal standard deviation $\alpha_{a,RMS}$ are shown in the impeller midspan in Figure 7a and b, respectively. Even for $\varepsilon = 1\%$, a slightly elevated level of $\bar{\alpha}_a$ is discernible near the suction side of each blade, which means that a slight tendency for phase separation is present. This tendency has already been observed in Figure 6, and is confirmed here. The highest values of $\alpha_{a,RMS}$ correlate with the highest values of $\bar{\alpha}_a$. These temporal and spatial characteristics of the air distribution indicate the presence of the agglomerated bubbles flow regime, according to Figure 3. For $\varepsilon = 3\%$, the peaks of both $\bar{\alpha}_a$ and $\alpha_{a,RMS}$ increase significantly and span over a greater region within each blade channel. For $\varepsilon = 9\%$, the $\alpha_{a,RMS}$ field shows minima in the region of the highest values of $\bar{\alpha}_a$, which means that the correlation between $\bar{\alpha}_a$ and $\alpha_{a,RMS}$ observed for low levels of ε completely reverses. Downstream of these stationary regions, highly unsteady wakes develop. Hence, a steady air pocket with an unsteady wake is observable. These characteristics can be assigned to the pocket flow regime, according to Figure 3. The analysis of transition between flow regimes has been extensively discussed by Hundshagen et al. [7] for a 2D bladed pump with reduced speed. From our brief discussion here, it is clear that, essentially, the same transition processes are present for the 3D bladed pump with elevated design speed, albeit on higher levels of ε. This transition is well captured by the H2P simulation approach.

The instantaneous distribution of the Sauter mean diameter d_{32} at impeller midspan is presented in Figure 8. d_{32} rises with rising ε, which indicates enhanced coalescence activity, according to the findings of Chen et al. [27]. A cross-check to Figure 7a reveals that this is most pronounced for $\varepsilon = 9\%$. The location of large bubble diameter correlate with the air accumulation zones, i.e., preferably, large bubbles accumulate, which is in agreement

with similar findings by Zhang et al. [11]. Small bubbles are present downstream of the accumulation, indicating that the breakup mostly occurs in the wake of the accumulation zone. Due to these spatial characteristics, the d_{32} distribution appears to be reasonable.

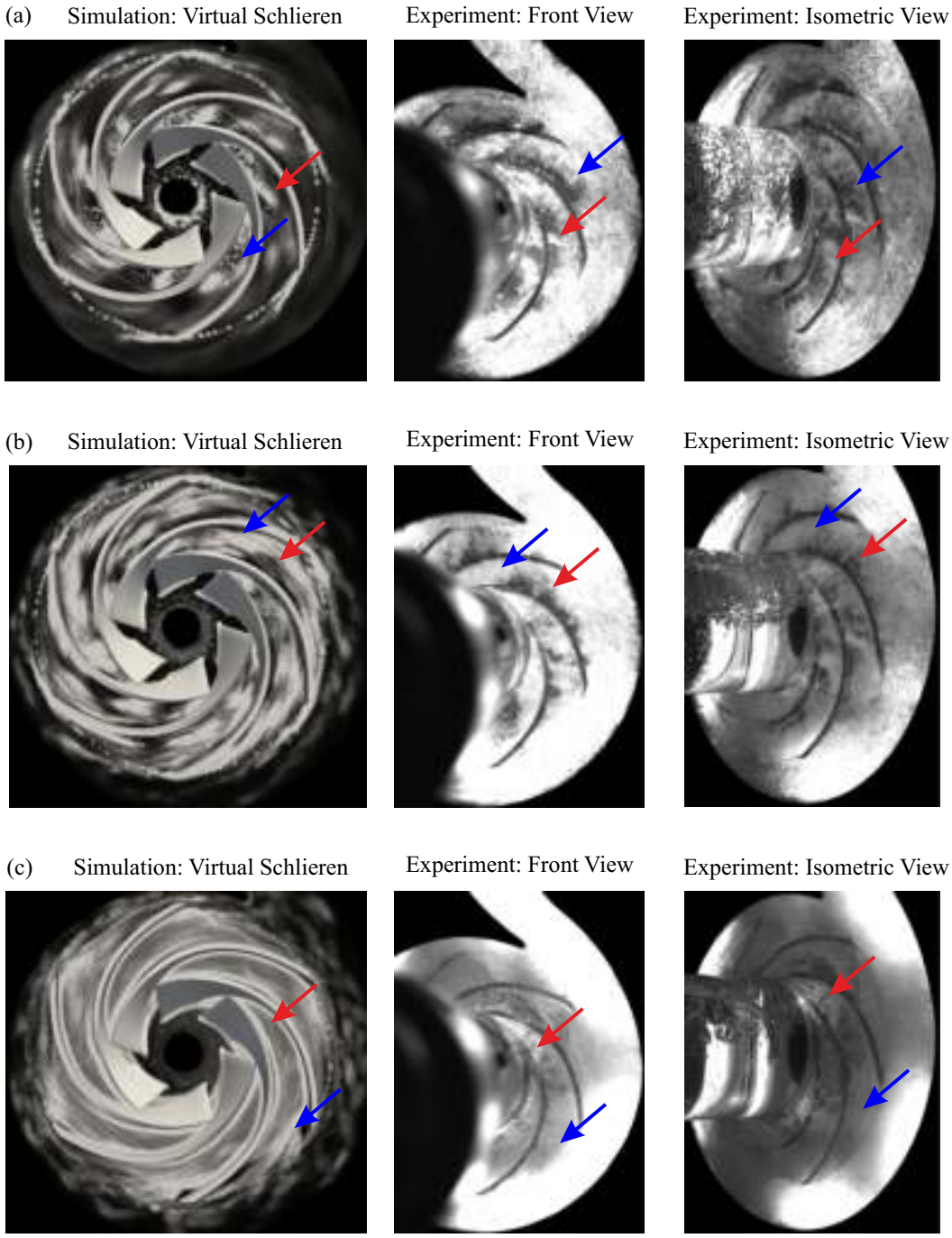

Figure 6. Comparison between virtually-derived Schlieren images (left) and experimental results of a grey-scale analysis from the front view (middle) and isometric view (right) for $\varepsilon = 1\%$ (**a**), $\varepsilon = 3\%$ (**b**), and $\varepsilon = 9\%$ (**c**). Similarities between simulation results and measurement data are marked by red and blue arrows.

The time-averaged pump head versus inlet air volume fraction is shown in Figure 9. The experimental trend of decreasing head with increasing ε and the head drop between $\varepsilon = 3\%$ and $\varepsilon = 9\%$ are well reproduced. The transition of flow regimes, which is captured by the new H2P approach, is also reflected in a good reproduction of the measured pump head characteristics.

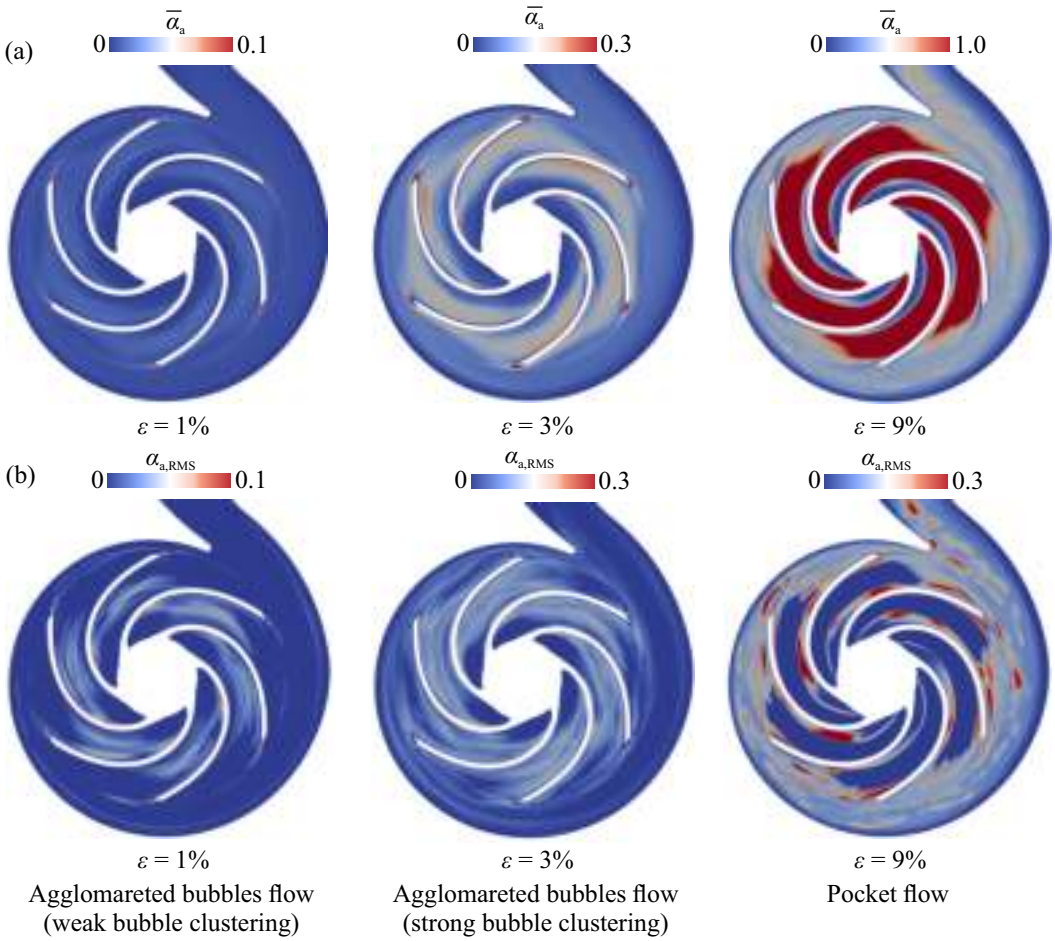

Figure 7. Contour plots at impeller's midspan for time-averaged air volume fraction $\overline{\alpha}_a$ (**a**) and its temporal standard deviation $\alpha_{a,RMS}$ (**b**) for $\varepsilon = 1\%$, $\varepsilon = 3\%$, and $\varepsilon = 9\%$ simulation results.

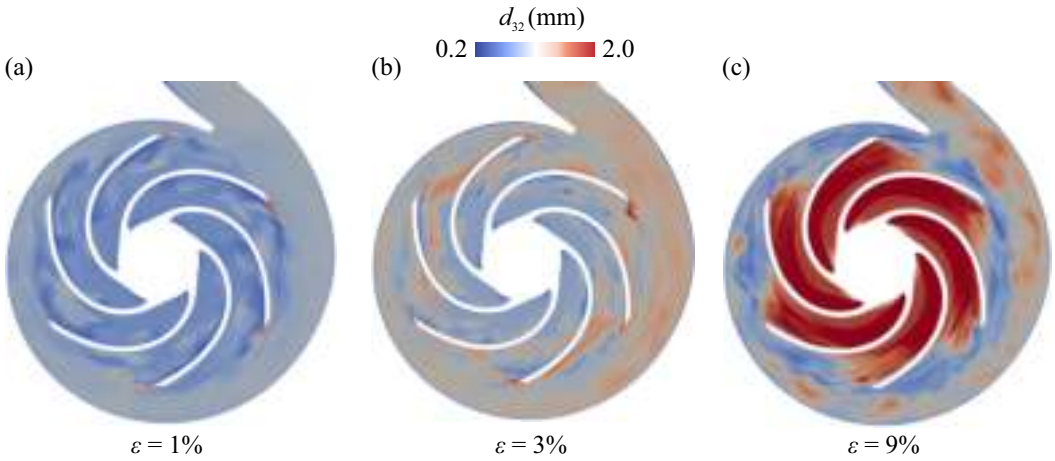

Figure 8. Contour plots of Sauter mean diameter at impeller's midspan for $\varepsilon = 1\%$ (**a**), $\varepsilon = 3\%$ (**b**), and $\varepsilon = 9\%$ (**c**) simulation results.

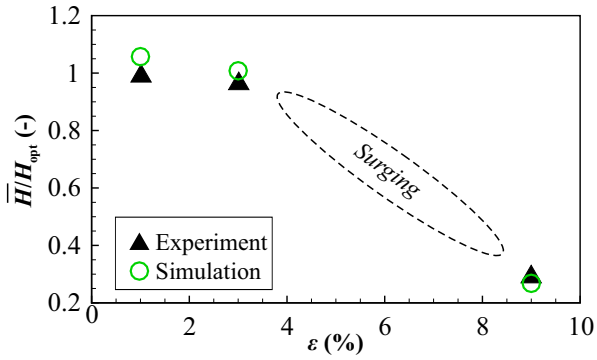

Figure 9. Time-averaged two-phase pump head $\bar{H}$ versus inlet air volume fraction ε.

5. Conclusions

A hybrid two-phase (H2P) solver for the simulation of liquid/gas transport has been presented and assessed by experimental validation data of an industrial-scale centrifugal pump flow with 3D-twisted blades and increased impeller design speed. As a continuation of our previous study [7], it is the elevated speed that raises the pump resistance against air loading [15], probably due to its more substantial mixing effect, which shifts the pocket flow regime to higher values of inlet air volume fraction ε. It could be shown that the transition from bubbly flow to adherent pockets is also reproduced by the H2P method for a more industry-oriented pump design, i.e., twisted 3D blading and elevated design speed, which is a major novelty of this study.

A further novelty of the simulation method is the inclusion of a PBM to capture a variation of bubble sizes. It is interesting to note that the transition between flow regimes can also be captured by a monodisperse approach (not shown here), i.e., constant diameter, which, however, has to be prescribed and is, thus, not a result of the simulation. By the polydisperse approach employed here, a reasonable bubble size distribution is obtained. The hybrid approach, in combination with a scale-adaptive turbulence treatment and a PBM, enables the description of fluid dynamical processes of gas accumulation on a sound physical basis. This is a basic requirement for more predictive CFD tools and a knowledge-based design and optimization of centrifugal pumps for gas-laden liquid transport. Coalescence and breakup kernels have been, so far, adopted from entirely different applications, such as bubble columns or mixer vessels. For a sound validation of bubble spectra and the development of enhanced kernels, more in-depth experiments are indispensable and should be the focus of future studies.

Author Contributions: Conceptualization, M.H. and R.S.; methodology, M.H., K.R. and R.S.; software, M.H. and K.R.; investigation, M.H., M.M., D.T. and R.S.; writing—original draft preparation, M.H. and R.S.; writing—review and editing, M.H. and R.S.; supervision, D.T. and R.S.; funding acquisition, D.T. and R.S. All authors have read and agreed to the published version of the manuscript.

Funding: The research project was carried out in the framework of the industrial collective research program (IGF no. 20638 BG). It was supported by the Federal Ministry for Economic Affairs and Climate Action (BMWK) through the AiF (German Federation of Industrial Research Associations eV), based on a decision taken by the German Bundestag. Simulations were performed with computing resources granted by RWTH Aachen University under project bund0013.

Acknowledgments: The authors also thank our project partners Christian Hasse and Bich-Diep Nguyen (TU Darmstadt), for their valuable contribution to the OpenFOAM-9 implementations of the solver and for providing the post-processing tool for the virtual Schlieren images.

Conflicts of Interest: The authors declare no conflict of interest.

Abbreviations

The following *nomenclature* is used in this manuscript:

$a_{(min,max,B)}$	Model constants for C_α	(-)
b	Blade width	(m)
$\boldsymbol{c}$	Velocity vector	($m\,s^{-1}$)
C_α & C_β	Switching functions	(-)
c_c	Compression velocity	($m\,s^{-1}$)
d	Diameter	(m)
d_{32}	Sauter mean diameter	(m)
H	Pump head	(m)
k	Turbulence kinetic energy	($m^2\,s^{-2}$)
l	Line length	(m)
M	Momentum transfer terms	($kg\,m\,s^{-2}$)
M_s	Surface tension force	($kg\,m\,s^{-2}$)
n	Rotational speed	(s^{-1})
n_q	Specific speed	s^{-1})
n_B	Number density function	(-)
N_s	Nondimensional specific speed	(-)
p	Pressure	(Pa)
Q	Volume flow rate	($m^3\,s^{-1}$)
$\boldsymbol{R}^{eff}$	Effective stress tensor	($kg\,m\,s^{-2}$)
s	Tip gap height	(m)
y_w^+	Nondimensional wall distance	(-)
α	Volume fraction	(-)
ε	Inlet air volume fraction	(-)
ω	Specific dissipation	(s^{-1})
ρ	Density	($kg\,m^{-3}$)
∇	Divergence operator	(-)

Subscripts

2	Discharge area
a	air
B	Bubble
max	Maximum
opt	Best efficiency operating point
t	Total
w	Water
φ	Phase

The following *abbreviations* are used in this manuscript:

2D	two-dimensional
3D	three-dimensional
CFD	Computational fluid dynamics
EE2F	Euler-Euler two-fluid
Exp	Experimental result
G1 & G2	Computational grids
H2P	Hybrid two-phase
PBM	Population balance modeling
SAS	Scale-adaptive simulation
URANS	Unsteady Reynolds-averaged Navier-Stokes
VOF	Volume-of-Fluid

References

1. Mansour, M.; Wunderlich, B.; Thévenin, D. Effect of tip clearance gap and inducer on the transport of two-phase air-water flows by centrifugal pumps. *Exp. Therm. Fluid Sci.* **2018**, *99*, 487–509. [CrossRef]
2. Murakami, M.; Minemura, K. Effects of Entrained Air on the Performance of a Centrifugal Pump: 1st Report, Performance and Flow Conditions. *Bull. JSME* **1974**, *17*, 1047–1055. [CrossRef]
3. Poelma, C. Measurement in opaque flows: A review of measurement techniques for dispersed multiphase flows. *Acta Mech.* **2020**, *231*, 2089–2111. [CrossRef] [PubMed]
4. Perissinotto, R.M.; Monte Verde, W.; Biazussi, J.L.; Bulgarelli, N.A.V.; Fonseca, W.D.P.; de Castro, M.S.; de Moraes Franklin, E.; Bannwart, A.C. Flow visualization in centrifugal pumps: A review of methods and experimental studies. *J. Pet. Sci. Eng.* **2021**, *203*, 108582. [CrossRef]
5. Yin, J.; Zhang, T.; Krull, B.; Meller, R.; Schlegel, F.; Lucas, D.; Wang, D.; Liao, Y. A CFD approach for the flow regime transition in a vane-type gas-liquid separator. *Int. J. Multiph. Flow* **2023**, *159*, 104320. [CrossRef]
6. de Santis, A.; Hanson, B.C.; Fairweather, M. Hydrodynamics of annular centrifugal contactors: A CFD analysis using a novel multiphase flow modelling approach. *Chem. Eng. Sci.* **2021**, *242*, 116729. [CrossRef]
7. Hundshagen, M.; Rave, K.; Nguyen, B.D.; Popp, S.; Hasse, C.; Mansour, M.; Thévenin, D.; Skoda, R. Two-Phase Flow Simulations of Liquid/Gas Transport in Radial Centrifugal Pumps with Special Emphasis on the Transition From Bubbles to Adherent Gas Accumulations. *ASME J. Fluids Eng.* **2022**, *144*, 101202. [CrossRef]
8. Stel, H.; Ofuchi, E.M.; Alves, R.F.; Chiva, S.; Morales, R.E.M. Experimental Analysis of Gas–Liquid Flows in a Centrifugal Rotor. *ASME J. Fluids Eng.* **2020**, *142*, 031101 . [CrossRef]
9. Stel, H.; Ofuchi, E.M.; Chiva, S.; Morales, R.E. Numerical simulation of gas-liquid flows in a centrifugal rotor. *Chem. Eng. Sci.* **2020**, *221*, 115692. [CrossRef]
10. He, D.; Ge, Z.; Bai, B.; Guo, P.; Luo, X. Gas–Liquid Two-Phase Performance of Centrifugal Pump Under Bubble Inflow Based on Computational Fluid Dynamics–Population Balance Model Coupling Model. *ASME J. Fluids Eng.* **2020**, *142*, 081402. [CrossRef]
11. Zhang, F.; Zhu, L.; Chen, K.; Yan, W.; Appiah, D.; Hu, B. Numerical Simulation of Gas–Liquid Two-Phase Flow Characteristics of Centrifugal Pump Based on the CFD–PBM. *Mathematics* **2020**, *8*, 769. [CrossRef]
12. Parikh, T.; Mansour, M.; Thévenin, D. Investigations on the effect of tip clearance gap and inducer on the transport of air-water two-phase flow by centrifugal pumps. *Chem. Eng. Sci.* **2020**, *218*, 115554. [CrossRef]
13. Mansour, M.; Wunderlich, B.; Thévenin, D. Experimental Study of Two-Phase Air/Water Flow in a Centrifugal Pump Working with a Closed or a Semi-Open Impeller. In Proceedings of the ASME Turbo Expo 2018: Turbine Technical Conference and Exposition, Oslo, Norway, 11–15 June 2018. [CrossRef]
14. Mansour, M.; Parikh, T.; Thévenin, D. Influence of the shape of the impeller blade trailing edge on single and two-phase air water flows in a centrifugal pump. In Proceedings of the Turbomachinery & Pump Symposia, Housten, TX, USA, 13–16 December 2020.
15. Mansour, M.; Kopparthy, S.; Thévenin, D. Investigations on the effect of rotational speed on the transport of air-water two-phase flows by centrifugal pumps. *Int. J. Heat Fluid Flow* **2022**, *94*, 108939. [CrossRef]
16. Schäfer, T.; Bieberle, A.; Neumann, M.; Hampel, U. Application of gamma-ray computed tomography for the analysis of gas holdup distributions in centrifugal pumps. *Flow Meas. Instrum.* **2015**, *46*, 262–267. [CrossRef]
17. Schäfer, T.; Neumann-Kipping, M.; Bieberle, A.; Bieberle, M.; Hampel, U. Ultrafast X-Ray Computed Tomography Imaging for Hydrodynamic Investigations of Gas–Liquid Two-Phase Flow in Centrifugal Pumps. *ASME J. Fluids Eng.* **2020**, *142*, 041502. [CrossRef]
18. Neumann, M.; Schäfer, T.; Bieberle, A.; Hampel, U. An Experimental Study on the Gas Entrainment in Horizontally and Vertically Installed Centrifugal Pumps. *ASME J. Fluids Eng.* **2016**, *138*, 12–19. [CrossRef]
19. Gambao, J.; Prado, M.G. Visualization study of performance breakdown in two-phase performance of an electrical submersible pump. In *Twenty-Sixth International Pump User Symposium, Texas, USA*; Springer: Berlin/Heidelberg, Germany, 2010. [CrossRef]
20. Barrios, L.; Prado, M.G. Experimental Visualization of Two-Phase Flow Inside an Electrical Submersible Pump Stage. *J. Energy Resour. Technol.* **2011**, *133*, 042901. [CrossRef]
21. Trevisan, F.E.; Prado, M. Experimental Investigation of the Viscous Effect on Two-Phase-Flow Patterns and Hydraulic Performance of Electrical Submersible Pumps. *J. Can. Pet. Technol.* **2011**, *50*, 45–52. [CrossRef]
22. Monte Verde, W.; Biazussi, J.L.; Sassim, N.A.; Bannwart, A.C. Experimental study of gas-liquid two-phase flow patterns within centrifugal pumps impellers. *Exp. Therm. Fluid Sci.* **2017**, *85*, 37–51. [CrossRef]
23. Shao, C.; Li, C.; Zhou, J. Experimental investigation of flow patterns and external performance of a centrifugal pump that transports gas-liquid two-phase mixtures. *Int. J. Heat Fluid Flow* **2018**, *71*, 460–469. [CrossRef]
24. Zhao, L.; Chang, Z.; Zhang, Z.; Huang, R.; He, D. Visualization of gas-liquid flow pattern in a centrifugal pump impeller and its influence on the pump performance. *Meas. Sens.* **2021**, *13*, 100033. [CrossRef]
25. Yan, S.; Sun, S.; Luo, X.; Chen, S.; Li, C.; Feng, J. Numerical Investigation on Bubble Distribution of a Multistage Centrifugal Pump Based on a Population Balance Model. *Energies* **2020**, *13*, 908. [CrossRef]
26. Si, Q.; Asad, A.; Wang, B.; Wang, P.; Bois, G.; Jianping, Y.; Kubar, A.A. Numerical Study on Gas-Liquid Two Phase Flow Characteristic of Multistage Electrical Submersible Pump by Using a Novel Multiple-Size Group (MUSIG) Model. *Phys. Fluids* **2022**, *34*, 063311. [CrossRef]

27. Chen, Y.; Patil, A.; Chen, Y.; Bai, C.; Wang, Y.; Morrison, G. Numerical Study on the First Stage Head Degradation in an Electrical Submersible Pump With Population Balance Model. *J. Energy Resour. Technol.* **2019**, *141*, 022003. [CrossRef]
28. Simon, L. Application of the MUSIG model to bubbly flows. *AEAT-1096 AEA Technol.* **1996**, *230*, 826.
29. Liao, M.; Si, Q.; Fan, M.; Wang, P.; Liu, Z.; Yuan, S.; Cui, Q.; Bois, G. Experimental Study on Flow Behavior of Unshrouded Impeller Centrifugal Pumps under Inlet Air Entrainment Condition. *Int. J. Turbomach. Propuls. Power* **2021**, *6*, 31. [CrossRef]
30. Egorov, Y.; Menter, F. Development and Application of SST-SAS Turbulence Model in the DESIDER Project. In *Advances in Hybrid RANS-LES Modelling*; Peng, S.H., Haase, W., Eds.; Notes on Numerical Fluid Mechanics and Multidisciplinary Design; Springer: Berlin/Heidelberg, Germany, 2008; Volume 97, pp. 261–270. [CrossRef]
31. Hundshagen, M.; Rave, K.; Mansour, M.; Thévenin, D.; Skoda, R. 3D flow simulation by a hybrid two-phase solver for the assessment of liquid/gas transport in a volute-type centrifugal pump with twisted blades. In Proceedings of the 15th European Conference on Turbomachinery Fluid Dynamics & Thermodynamics, Paper n. ETC2023-326, Budapest, Hungary, 24–28 April 2023. Available online: https://www.euroturbo.eu/publications/conference-proceedings-repository/ (accessed on 1 June 2023).
32. Gülich, J.F. *Centrifugal Pumps*; Springer: Berlin/Heidelberg, Germany, 2010. [CrossRef]
33. Mansour, M.; Parikh, T.; Thévenin, D. Influence of Blade Pitch and Number of Blades of a Pump Inducer on Single and Two-Phase Flow Performance. In Proceedings of the ASME Turbo Expo 2020, New York, NY, USA, 21–25 September 2020; Volume 9. [CrossRef]
34. Nguyen, B.D.; Popp, S.; Hundshagen, M.; Skoda, R.; Mansour, M.; Thévenin, D.; Hasse, C. Large Eddy Simulations of Turbulent Gas-Liquid Flows in a Diverging Horizontal Channel Using a Hybrid Multiphase Approach. *ASME J. Fluids Eng.* **2023**, *145*, 031501. [CrossRef]
35. Wardle, K.E.; Weller, H.G. Hybrid Multiphase CFD Solver for Coupled Dispersed/Segregated Flows in Liquid-Liquid Extraction. *Int. J. Chem. Eng.* **2013**, *2013*, 128936. [CrossRef]
36. Müller, T.; Limbach, P.; Skoda, R. Numerical 3D RANS Simulation of Gas-Liquid Flow in a Centrifugal Pump with an Euler-Euler Two-Phase Model and a Dispersed Phase Distribution. In Proceedings of the 11th European Conference on Turbomachinery Fluid Dynamics & Thermodynamics, Madrid, Spain, 23–27 March 2015.
37. Schiller, L.; Naumann, A. Über die grundlegenden Berechnungen bei Schwerkraftaufbereitung. *Z. Vereines Dtsch. Ingenieure* **1933**, *77*, 318–321
38. Rzehak, R.; Krepper, E.; Liao, Y.; Ziegenhein, T.; Kriebitzsch, S.; Lucas, D. Baseline Model for the Simulation of Bubbly Flows. *Chem. Eng. Technol.* **2015**, *38*, 1972–1978. [CrossRef]
39. Brackbill, J.; Kothe, D.; Zemach, C. A continuum method for modeling surface tension. *J. Comput. Phys.* **1992**, *100*, 335–354. [CrossRef]
40. Hänsch, S.; Lucas, D.; Krepper, E.; Höhne, T. A multi-field two-fluid concept for transitions between different scales of interfacial structures. *Int. J. Multiph. Flow* **2012**, *47*, 171–182. [CrossRef]
41. Kumar, S.; Ramkrishna, D. On the solution of population balance equations by discretization—I. A fixed pivot technique. *Chem. Eng. Sci.* **1996**, *51*, 1311–1332. [CrossRef]
42. Prince, M.J.; Blanch, H.W. Bubble coalescence and break-up in air-sparged bubble columns. *AIChE J.* **1990**, *36*, 1485–1499. [CrossRef]
43. Luo, H.; Svendsen, H.F. Theoretical model for drop and bubble breakup in turbulent dispersions. *AIChE J.* **1996**, *42*, 1225–1233. [CrossRef]
44. Liao, Y.; Rzehak, R.; Lucas, D.; Krepper, E. Baseline closure model for dispersed bubbly flow: Bubble coalescence and breakup. *Chem. Eng. Sci.* **2015**, *122*, 336–349. [CrossRef]
45. Menter, F. Two-equation eddy-viscosity turbulence models for engineering applications. *AIAA J.* **1994**, *32*, 1598–1605. [CrossRef]
46. Kalitzin, G.; Medic, G.; Iaccarino, G.; Durbin, P. Near-wall behavior of RANS turbulence models and implications for wall functions. *J. Comput. Phys.* **2005**, *204*, 265–291. [CrossRef]
47. Jasak, H. Error Analysis and Estimation for the Finite Volume Method with Applications to Fluid Flows. Ph.D. Thesis, Imperial College of Science, Technology and Medicine, London, UK, 1996.
48. Patankar, S.; Spalding, D. A calculation procedure for heat, mass and momentum transfer in three-dimensional parabolic flows. *Int. J. Heat Mass Transfer* **1972**, *15*, 1787–1806. [CrossRef]
49. Travin, A.; Shur, M.; Strelets, M.; Spalart, P.R. Physical and Numerical Upgrades in the Detached-Eddy Simulation of Complex Turbulent Flows. In *Advances in LES of Complex Flows*; Moreau, R., Friedrich, R., Rodi, W., Eds.; Fluid Mechanics and Its Applications; Springer: Dordrecht, The Netherlands, 2002; Volume 65, pp. 239–254. [CrossRef]
50. Weller, H. Controlling the Computational Modes of the Arbitrarily Structured C Grid. *Mon. Weather. Rev.* **2012**, *140*, 3220–3234. [CrossRef]
51. Warming, R.F.; Beam, R.M. Upwind Second-Order Difference Schemes and Applications in Aerodynamic Flows. *AIAA J.* **1976**, *14*, 1241–1249. [CrossRef]
52. Sweby, P.K. High Resolution Schemes Using Flux Limiters for Hyperbolic Conservation Laws. *SIAM J. Numer. Anal.* **1984**, *21*, 995–1011. [CrossRef]

53. Casimir, N.; Zhu, X.; Hundshagen, M.; Ludwig, G.; Skoda, R. Numerical Study of Rotor–Stator Interaction of a Centrifugal Pump at Part Load With Special Emphasis on Unsteady Blade Load. *ASME J. Fluids Eng.* **2020**, *142*, 081203. [CrossRef]
54. Hundshagen, M.; Casimir, N.; Pesch, A.; Falsafi, S.; Skoda, R. Assessment of scale-adaptive turbulence models for volute-type centrifugal pumps at part load operation. *Int. J. Heat Fluid Flow* **2020**, *85*, 108621. [CrossRef]

Disclaimer/Publisher's Note: The statements, opinions and data contained in all publications are solely those of the individual author(s) and contributor(s) and not of MDPI and/or the editor(s). MDPI and/or the editor(s) disclaim responsibility for any injury to people or property resulting from any ideas, methods, instructions or products referred to in the content.

International Journal of
Turbomachinery
Propulsion and Power

MDPI

Article

Effect of the von Karman Shedding Frequency on the Hydrodynamics of a Francis Turbine Operating at Nominal Load †

Giacomo Zanetti [1,2,*], Giovanna Cavazzini [1] and Alberto Santolin [2]

[1] Department of Industrial Engineering, University of Padova, Via Venezia 1, 35131 Padova, Italy; giovanna.cavazzini@unipd.it
[2] 45 Engineering S.r.l., Corte delle Filande 16, 36075 Montecchio Maggiore, Italy; alberto.santolin@45-eng.com
* Correspondence: giacomo.zanetti.4@phd.unipd.it; Tel.: +39-349-344-2920
† This manuscript is an extended version of our paper published in the Proceedings of the 15th European Turbomachinery Conference, Budapest, Hungary, 24–28 April 2023; paper No. ETC2023-137.

Abstract: This paper presents a numerical analysis of the influence of the von Karman vortex shedding at the blade trailing edge on the hydrodynamics of a recently installed small hydro Francis turbine manifesting very loud and high-frequency acoustic pulsations when operating close to the nominal load. A reduced single-passage numerical model is developed to reduce the computational effort of the simulation while ensuring high accuracy in the assessment of fluid flow. The accuracy of the proposed numerical approach is investigated by comparing the frequency spectrum of the experimentally acquired acoustic frequency and the numerical pressure signals, confirming the nature of the machine's vibrations. The validated numerical model represents a useful tool for an in-depth analysis of the machine's hydrodynamics in the preliminary design phases. The proposed approach represents a valid alternative to the traditional correlation-based approach for the evaluation of the von Karman shedding frequency with less computational effort compared with a transient simulation of the entire machine.

Keywords: Francis turbines; interblade vortices; von Karman vortices; mechanical resonance

check for updates

Citation: Zanetti, G.; Cavazzini, G.; Santolin, A. Effect of the von Karman Shedding Frequency on the Hydrodynamics of a Francis Turbine Operating at Nominal Load. *Int. J. Turbomach. Propuls. Power* **2023**, *8*, 27. https://doi.org/10.3390/ijtpp8030027

Academic Editor: Antoine Dazin

Received: 30 June 2023
Revised: 5 July 2023
Accepted: 3 August 2023
Published: 7 August 2023

Copyright: © 2023 by the authors. Licensee MDPI, Basel, Switzerland. This article is an open access article distributed under the terms and conditions of the Creative Commons Attribution (CC BY-NC-ND) license (https://creativecommons.org/licenses/by-nc-nd/4.0/).

1. Introduction

Vibration control represents a key issue in the field of hydraulic turbines. Although many types of vibration can occur, the most common vibrational phenomenon is represented by the vibrations induced by the shedding of the von Karman vortexes from the blade trailing edge [1]. If the vortex shedding frequency also synchronizes with the cross-flow structural frequency [2], resulting in the so-called "lock-in" condition, the vibrations become even more severe and are accompanied by hissing sounds. The occurrence of lock-in entails an increase in the dynamic load on the blade trailing edge with the potential occurrence of structural damages due to fatigue phenomena.

Although vibration phenomena can occur in all machine components, the lock-in condition occurs most frequently on the stay vanes because the flow at the trailing edges is relatively uniform and structural damping is low [3]. An example of cracks in stay vanes induced by wake vortices is reported in [4], while in [5], the excitation frequency of the von Karman shedding frequency is found to be close to the natural frequency of a runner manifesting severe damages due to fatigue effects.

In the traditional approach, the shedding frequency of the vortexes is estimated by assuming a reference value for the Strouhal number, which is defined as follows:

$$S = \frac{fd}{v} \tag{1}$$

where

f = vortex shedding frequency [Hz];

ν = reference fluid speed (e.g., free stream velocity at the point of boundary-layer separation) [m/s];

d = reference thickness (e.g., thickness of the wake at the point of boundary-layer separation) [m].

The so-defined Strouhal number should be independent of the geometry and the Reynolds number [6].

Once a reasonable value for the Strouhal number is assigned, the shedding vortex frequency is estimated and then compared with the natural frequencies of the component: the machine is considered safe from vortex-induced vibrations if the natural frequency is at least 30% higher than the shedding frequency [7]. However, a proper estimation of the Strouhal number for hydraulic turbine components is rather difficult, and the values suggested in the literature (in the range between 0.16 and 0.24) [8] are based on experimental studies carried out on bluff bodies, for which it is possible to easily assess the boundary layer and the separation point, such as cylinders and cones.

This simplified approach has been used successfully in the past because the geometries were simpler, and the chamfering adopted in the past was more like that of a bluff body than an airfoil. However, the new design strategies of hydraulic machines have increased the complexity of the geometry and have made this simplified approach less effective, highlighting the need for a more in-depth investigation, like the one carried out by Zobeiri et al. [9], on the influence of the trailing edge geometry on the wake vortex development.

In a scenario in which the correct prediction of the vortex shedding frequency represents a key issue in the design strategy of a hydraulic turbine, the computational fluid dynamics undoubtedly represents a powerful tool for supporting the design procedure. Nevertheless, numerical simulations may require great effort, both in terms of resources and time consumption, slowing the development phase and increasing the costs.

The aim of this paper is to propose a simple numerical model capable of evaluating the unsteady behavior of the fluid flow in a Francis turbine with a very low computational cost.

For this purpose, a reduced numerical model of a Francis turbine with a mean drop height and a specific speed, exhibiting resonance phenomena that are presumably due to the vortex shedding frequency at the trailing edge of the impeller blades, was created in order to limit the computational effort and still ensure a detailed representation of the fluid flow in the turbine.

This paper is organized as follows: Section 2 presents the numerical model of the hydraulic machine under study; Section 3 reports the results of the validation procedure performed by comparing the numerical estimated hydraulic efficiency with the experimental data; finally, in Section 5, the potential of the model is demonstrated by analyzing the capability of reproducing the small- and large-dimensional flow turbulent structures occurring when the machine is working at the design point. Moreover, the von Karman shedding frequencies are analyzed in depth, comparing the numerical shedding frequency with the available experimental data.

2. The Case Study

The case study of this analysis consists of a run-on-river small hydropower plant built in 2020, located on a river in the north of the Veneto region (northern Italy). The power plant consists of two twin units, with a total rated power of 0.8 MW. Regarding the hydraulic machines, the two Francis turbines provide a rated power of 400 kW each at the nominal discharge of 1.05 m^3/s. The gross head is equal to 39 m, while the nominal rotational speed is 750 rpm.

From the very beginning, since the unit's commissioning, loud and high-frequency whistling noises were recorded in the powerhouse when the machines operated near the nominal discharge (1.05 m^3/s). As a result, the operators of the power plant decided to

limit the operating ranges of the machines to a power range below 300 kW per machine in order to avoid the development and propagation of fatigue cracks until corrective measures were carried out on the turbine parts.

To characterize the noise emission, the acoustic signals were acquired on-field during maintenance activity at a sampling frequency of 44.1 kHz, and an FFT analysis was carried out. The FFT at nominal discharge of one machine was dominated by two frequency peaks around 188 Hz and 2000 Hz (Figure 1a), whereas at partial load, the high-frequency disappeared and the FFT showed just one frequency peak around 188 Hz likely due to the runner's rotor–stator interaction. Indeed, the product of the runner blade number, equal to 15, and the rotational speed highlights a rotor–stator interaction equal to 187.5 Hz.

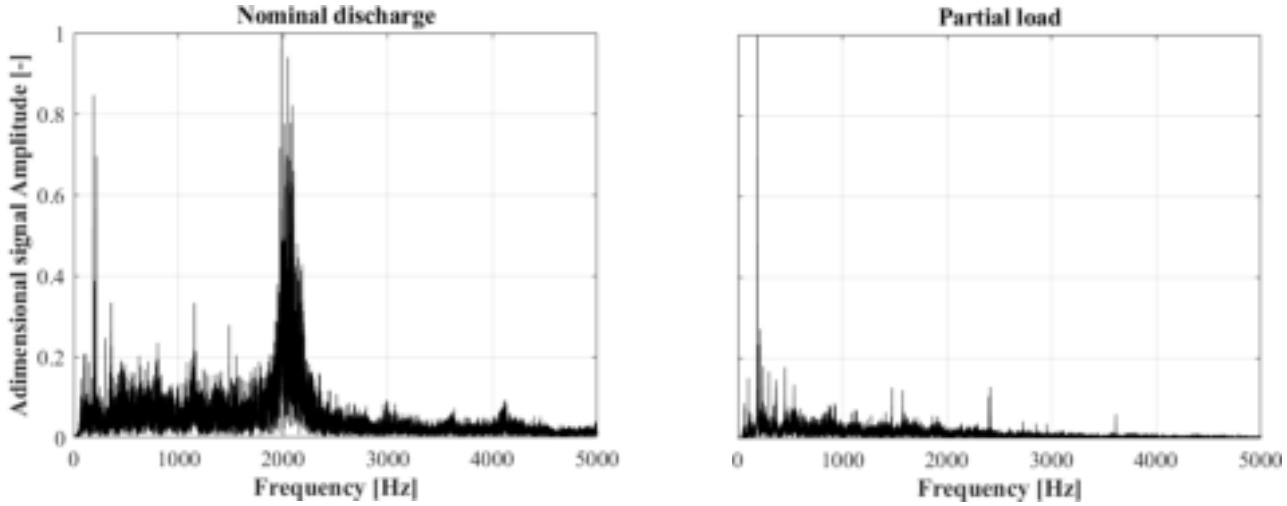

Figure 1. Frequency spectrum of the machine acoustic emission: (**a**) nominal discharge, (**b**) partial load.

The source of the noise emission at nominal discharge was most likely a vibration phenomenon occurring in the runner, caused by the resonance between the system frequency and the von Karman vortex shedding frequency at the runner blade trailing edge. In cases like this, the only option available for plant owners is to disassemble the runner and to rework the blade trailing edge, so as to vary the geometry and the separation point and hence to affect the vortex shedding frequency. However, this approach is extremely expensive due to the costs of the extraordinary maintenance activities and the profit loss caused by the production stop. It would have been preferable to know the existence of the resonance condition during the design phase. However, in this case, the standard approach estimating the vortex shedding frequency starting from the Strouhal number failed because of the above-mentioned limits, and detailed CFD analyses of the machine cannot represent a standard design tool due to the unacceptably long computational time. Therefore, to provide an investigation strategy that is more effective in the design phase, an innovative reduced numerical model was proposed and validated with reference to this case study. The model is presented below.

3. The Numerical Model

The hydraulic machine under investigation consists of a medium specific speed Francis turbine (n_s = 157 rpm $m^{3/4}s^{-1/2}$) characterized by a radial shrouded runner with 15 blades. The distributor comprises 16 stay vanes and 16 guide vanes while the draft-tube is a straight cone type.

Since the aim of the approach is to reduce the computational effort, a single blade channel was modeled, including hence only 1/15 of the runner domain and 1/16 of the

stay and guide vanes. As regards the other stationary components, the entire draft tube was included, while the spiral case was not considered (Figure 2).

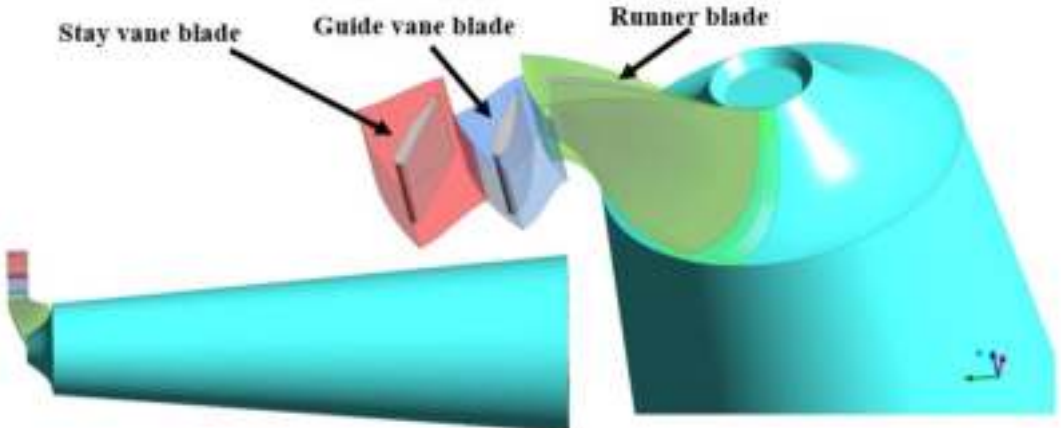

Figure 2. Computational fluid domain.

Since the von Karman vortex shedding phenomenon is significantly affected by the boundary-layer thickness near the blade trailing edge, an accurate prediction of the vortex shedding requires a high boundary-layer resolution. Special attention was, hence, paid to the boundary mesh refinement of the stay vanes, guide vanes, and runner, adopting a structured mesh with an O-grid topology. A structured mesh was also built for the draft tube with the commercial software ICEM CFD 2022, while the Ansys Turbogrid 2022 software was adopted for the discretization of the remaining domains.

The mesh independency was studied in a preliminary analysis by considering four different grid resolutions, named coarser, coarse, medium, and fine mesh (Table 1). Then, the mesh independency was evaluated by comparing the head H values and the runner torque T, adopting the simulation settings reported in the next section. As seen in Figure 3, computational meshes with greater than 4 million nodes show negligible differences, and hence, the medium size mesh was selected.

Table 1. Summary of spatial discretization per domain component.

Component	Number of Nodes, Coarser Mesh	Number of Nodes, Coarse Mesh	Number of Nodes, Medium Mesh	Number of Nodes, Fine Mesh
Stay vane	1.25×10^5	3×10^5	3×10^5	3×10^5
Guide vane	1.25×10^5	3×10^5	3×10^5	3×10^5
Runner	4.5×10^5	1.2×10^6	2.2×10^6	3.5×10^6
Draft tube	1.2×10^6	1.2×10^6	1.2×10^6	1.2×10^6
Total	1.9×10^6	3×10^6	4×10^6	5.3×10^6

The y+ value distribution for each domain component is reported in Table 2.

Table 2. Summary of y+ distribution per domain component.

Component	Y+ Coarser Mesh			Y+ Coarse Mesh			Y+ Medium Mesh			Y+ Fine Mesh		
	Min	Ave	Max	Min	Ave	Max	Min	Ave	Max	Min	Ave	Max
Stay vane	13	37	87	1	9.2	20	1	9.2	20	1	9.2	20
Guide vane	8	48	67	1.8	20	29	1.8	20	29	1.8	20	29
Runner	0.7	12	400	0.2	11	360	0.07	7	238	0.02	4.6	180
Draft tube	21	102	240	21	102	240	7	44	200	7	44	200

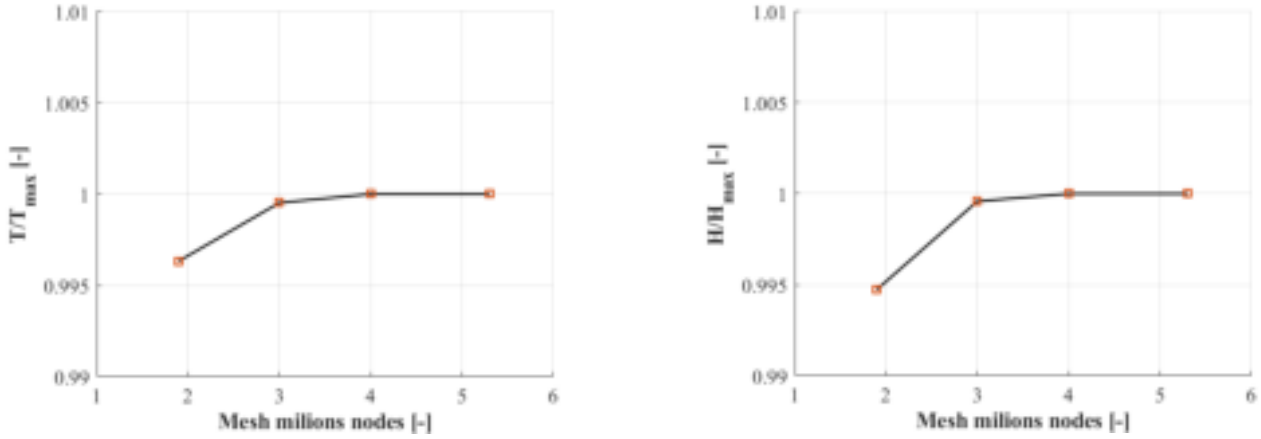

Figure 3. Grid convergence study based on the water head and runner torque: (**a**) runner torque, (**b**) water head.

Regarding the turbulent model, wall functions are not suitable in such applications, and a very fine mesh resolution near the solid wall is required to properly resolve the flow behavior in the boundary-layer region. In this case, a proper turbulence model is the k-ω, since it allows a direct integration to the wall without having to subdivide the flow domain into low- and high-Reynolds-number regions as required by the k-ε turbulence model [10].

Although the SST (Shear Stress Transport) formulation of the k-ω turbulence models has also proved to be valid in the evaluation of the von Karman shedding phenomena [11], a hybrid URANS-scale resolved approach with SAS-SST (Scale Adaptive Simulation–Shear Stress Transport) was preferred for this study. In fact, as reported by Neumann et al. [4], the SAS turbulent model has been proven to give good accuracy in frequency prediction, and it results in more realistic force amplitudes compared with other two-equation turbulence models such as the SST. Moreover, such an approach has been successfully adopted for the evaluation of the tridimensional behavior of the fluid flow in hydraulic turbines [12]. Indeed, the SAS model allows the turbulent model to be adapted to the local-turbulence length scale by switching from the LES model in the unsteady flow regions to the RANS, in this case, the SST model, in the steady ones. Compared to the RANS-SST model, smaller turbulence structures can be generated with a resolution down to the grid size [13].

Simulation Settings

The commercial software ANSYS CFX 20.0 was used to perform an unsteady incompressible turbulent flow numerical simulation of the reduced machine model.

As regards the boundary conditions, the mass flow rate was applied at the stay vane inlet section while the relative static pressure was applied at the draft tube outlet sections. A stochastic fluctuation of the velocities with a 5% free-stream turbulent intensity was set for the inlet mass flow. In order to reproduce the effect induced on the fluid trajectories by the spiral case geometry, the fluid velocity at the domain inlet section was tilted, in referment to the radial direction, for an angle equal to 32° representing the design angle adopted in the design procedure of the stay vane blades. At the draft tube outlet section, an opening condition was adopted.

The walls were defined as no-slip smooth walls, while the runner blade, hub, and shroud were set as rotating walls. Rotational periodic interfaces were adopted between the domains' periodic faces. A general connection interface was set between the stay vane and the guide vane domains, while a mixing plane interface was set between the runner and guide vane. The stage (mixing plane) interface was adopted to reduce the effect on the domain coupling introduced by the relative position between the runner and guide vanes. Indeed, in order to realize the data transfer between regions, the mixing plane

method constructs the inlet and outlet boundary conditions at the interface, and the data are transmitted to the downstream region in a circumferential or radial average [14].

The high-resolution advection scheme of the CFX software, based on the second-order backward Euler method for time integration, was used with a residual target set at 1×10^{-5} for the root mean square (RMS) values (u momentum, v momentum, w momentum, turbulence kinetic energy).

Since the time step was expected to play a significant role in the simulation accuracy, a sensitivity analysis was also carried out to evaluate the influence of the time-step value on the shedding frequency. As shown in Figure 4a, the analysis indicated a neglected variation in the shedding frequency after a time step of 75 cycle per period (2000 Hz) equivalent to 0.03° of runner revolution per time step. For this reason, this value was fixed in the numerical simulations.

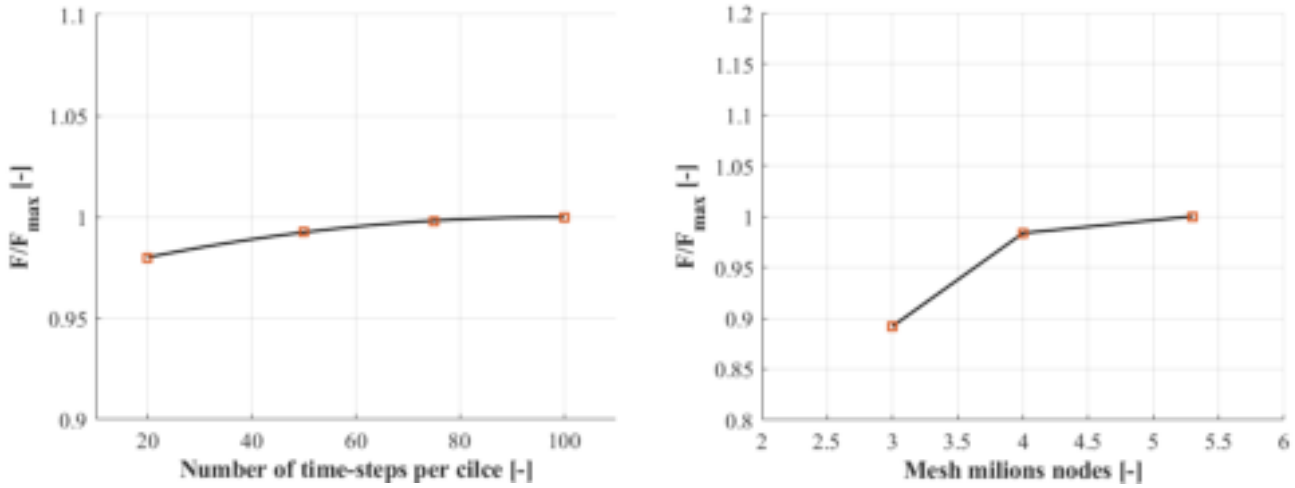

Figure 4. Influence of time-step size and grid density on shedding frequency: (**a**) time-step, (**b**) grid density.

Finally, the influence of the grid resolution was evaluated by comparing the vortex shedding frequency at the runner blade trailing edge in correspondence of the midspan section (Figure 4b). As result, the coarser mesh was proven to be unsuitable for the analysis since it was not able to capture the vortex shedding. Meanwhile, a difference of 1.5% was evaluated between the medium and fine mesh shedding frequency, testifying to the high sensitivity of the phenomena to the runner grid resolution.

With these settings, the average Courant number of the simulation was found to be below 0.2.

Thanks to this approach, the numerical model is able to evaluate the von Karman shedding frequency within a reduced computational time of approximately 200 CPU h.

4. Validation of the Numerical Model

To validate the numerical model, a series of steady-state simulations with different guide vane openings were carried out to replicate the experimental efficiency curve of the machine. Specifically, seven configurations with a progressive guide vane opening from 12° to 30° with a 3° step were tested.

A variable discharge value at the inlet section of the machine was set as a boundary condition. A calculation routine was implemented in the software to determine the correct discharge value for each vane opening, corresponding to the nominal head. This approach circumvented the disadvantages of the pressure boundary condition in terms of stability of the numerical solution by adopting the mass flow condition, which at the same time guarantees the correct value for the head.

As shown in Figure 5, the numerical model reproduces, with sufficient accuracy, the machine hydraulic efficiency curve pattern, with a foreseeable efficiency overestimation that increases as the operating point moves away from the nominal operating condition. The efficiency overestimation is due to the simplifications introduced in the numerical model, since the absence of the spiral case and the labyrinth seal fluid domains involve an underestimation in the head losses as well as an overestimation in the runner torque. Although the head losses occurring in the spiral case can be considered minor, the friction losses occurring in the labyrinth seal can significantly affect the overall machine efficiency with a greater influence in the case of lower machine specific speeds [15].

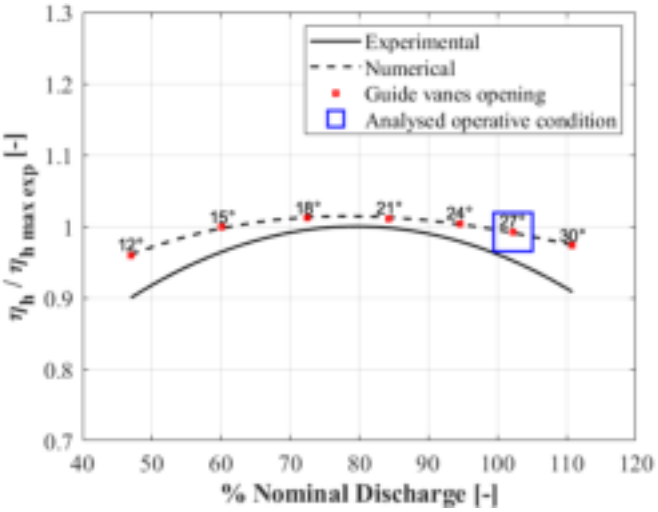

Figure 5. Comparison between experimental and numerical efficiency.

5. Results and Discussion

As mentioned above, the intense and high-frequency noises recorded in the power-house are most likely the result of resonance phenomena between the vibration modes of one or more machine parts and the von Karman vortex shedding frequency. To confirm or refute this hypothesis, the proposed simplified numerical approach, based on a transient numerical simulation of the reduced machine model, was tested.

5.1. Fluid-Dynamic Analysis

First, in order to propose a complete characterization of the machine hydrodynamics at the nominal discharge operative condition, the tridimensional topology of the main turbulent structures occurring in the flow was carefully analyzed.

Two different visualization strategies were adopted, and both of them confirmed the capability of the simplified numerical approach to capture—at least qualitatively—the phenomena causing the high-frequency resonance phenomena.

On one side, to visualize the development of the vortex street at the runner trailing edge, the representation of the velocity curl evaluated with reference to the runner rotational axis (z-axis) was also adopted (Figure 6).

On the other side, to better capture the 3D evolution of the vortexes developing in the runner, the Q-criterion method, identifying the areas where the vorticity magnitude is greater than the magnitude of the rate of strain, was applied. This method allowed the capture of both the propagation of the von Karman vortex street in the runner (Figure 7a) and the presence of a large-dimension interblade vortex located on the blade pressure side (Figure 7b).

This vortex structure develops as a consequence of a negative angle of attack in the inlet region of the runner. The mismatch between the blade angles and flow trajectories varies in the spanwise direction with an increasing trend in proximity to the runner hub surface. As result, the inception of the interblade vortex is confined in a restricted portion of

the blade leading edge in correspondence with the blade pressure side. The flow separation then propagates in the runner interblade channel due to the advection of the main flow.

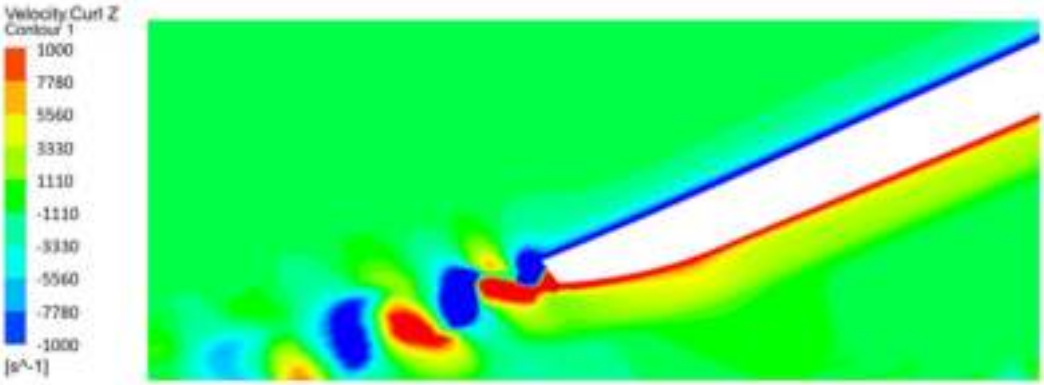

Figure 6. Von Karman vortex street at the runner midspan outlet section.

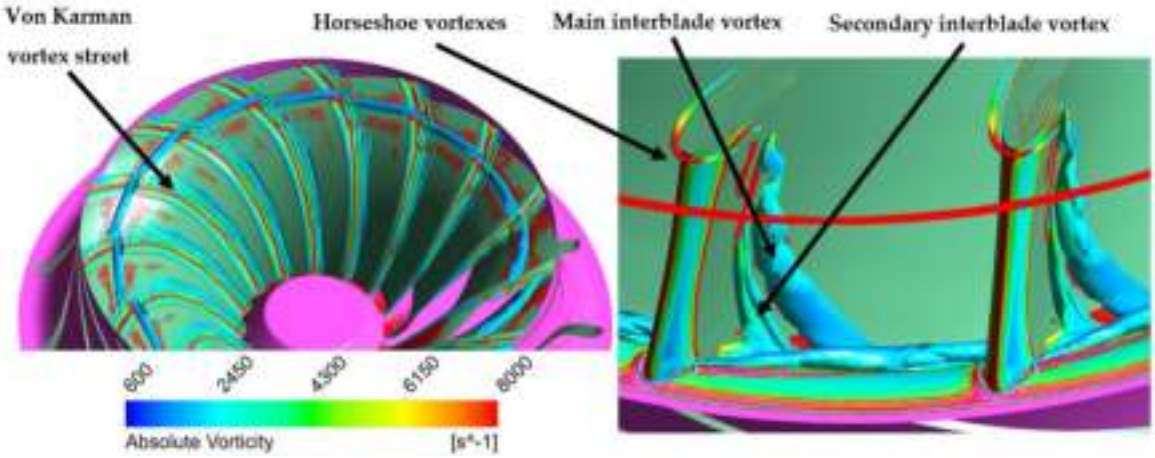

Figure 7. Iso Q-criterion surface in the runner colored according to the absolute vorticity: (**a**) outlet section, (**b**) inlet section.

Although this interblade vortex topology has been studied previously in the literature, this analysis allowed a second vortex structure to be identified, developing at the junction between the blade leading edge and the shroud surface (Figure 7b). A similar vortex structure was identified by Zhou et al. [16], and its origin was thought to be related to the propagation of the shroud horseshoe vortex downstream in the interblade channel. However, this paper suggests a different nature of this vortex, which seems to be the result of a more complex interaction between different vortex structures.

In more detail, as seen in Figure 8 reporting the streamlines of the different vortex structures, the main interblade vortex is composed of two different counter-rotating structures: the first, marked in blue, develops near the hub surface for the above-mentioned reasons and then propagates from the hub to the shroud, also moving downstream in the runner channel due to the advection of the main flow; the second one, marked in purple, develops in the same region and then propagates just crossways to the shroud surface. The incidence between the second structure with the shroud creates a secondary interblade vortex independent from the shroud horseshoe vortex.

Moreover, the secondary vortex increases in volume as a result of mixing with the main flow, marked in red in Figure 8, and with the horseshoe vortex, marked in green, thus propagating in the whole channel.

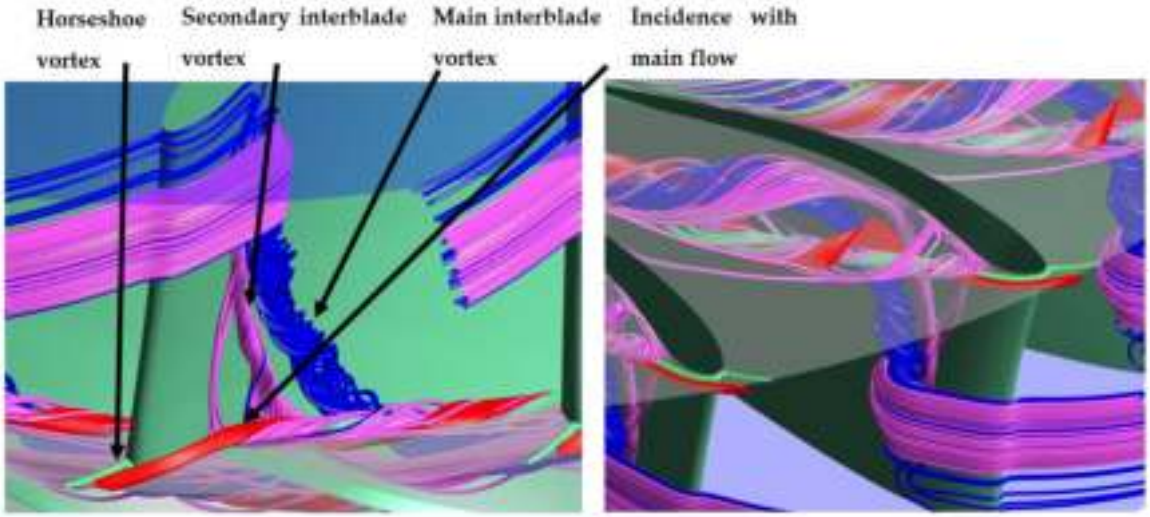

Figure 8. Pressure-side interblade vortexes: main vortex (blue line); secondary vortex (purple line); horseshoe vortex (green line); main flow (red line).

Therefore, regarding the origin of two separate interblade vortex regions in proximity to the blade leading edge, close to the hub, the secondary one appears to be consequent to the development of the main interblade vortex. Indeed, the interaction between the main interblade vortex and the boundary layer generates a low-energy-density region, which is then driven toward the shroud surface by the centrifugal force, evolving into a counter-rotating vortex structure.

The counter-rotating nature of these two turbulent structures is highlighted in Figure 9 showing the z-velocity contour at the runner midspan section.

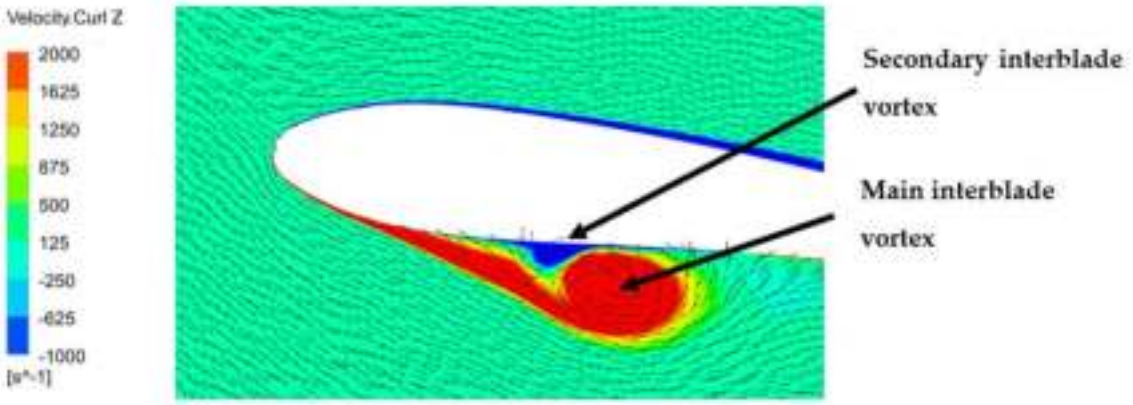

Figure 9. Main and secondary interblade vortex at the runner midspan section.

The development of the interblade vortex structure also drastically influences the blade pressure distribution due to the occurrence of a low-pressure area in correspondence of the blade pressure side (Figure 10).

Despite a restricted low-pressure area developing at the leading edge due to the flow incidence on the blade suction side, the presence of the pressure-side interblade vortex is clearly visible starting from the 25% span load distribution, with a low-pressure area located at 12% of the streamwise coordinate. This area then progressively moves downstream from 15% to 28% of the streamwise coordinate passing from 50% to 75% in the hub-to-shroud direction.

The influence of the interblade vortex on the runner blade pressure distribution is due to the position of the turbulent structures, which firstly appear to be adherent to the pressure side. Secondarily, after the incidence with the runner shroud surface, the turbulent

structure moves progressively in the runner channel then adhering to the following blade's suction side.

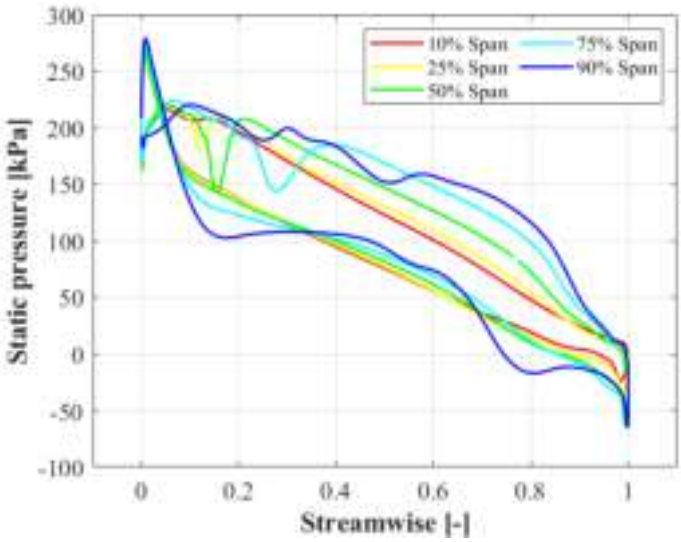

Figure 10. Runner blade static pressure distribution for different spanwise locations.

Because of this, the presence of the interblade vortex also affects the pressure distribution on the blade suction side with the occurrence of a low-pressure area located in proximity to the trailing edge, close to the shroud surface. As results, the pressure distribution at 90% span manifests a local depression located at around 80% of the spanwise coordinate.

The influence of the interblade vortex on the blade pressure distribution is also visible in Figure 11, which shows the static pressure distribution on the runner blade pressure and suction side. In this scenario, it is possible to assert that the development of the interblade vortex negatively influences the cavitation behavior of the hydraulic machine by creating a local depression band in proximity to the runner trailing edge (Figure 11a).

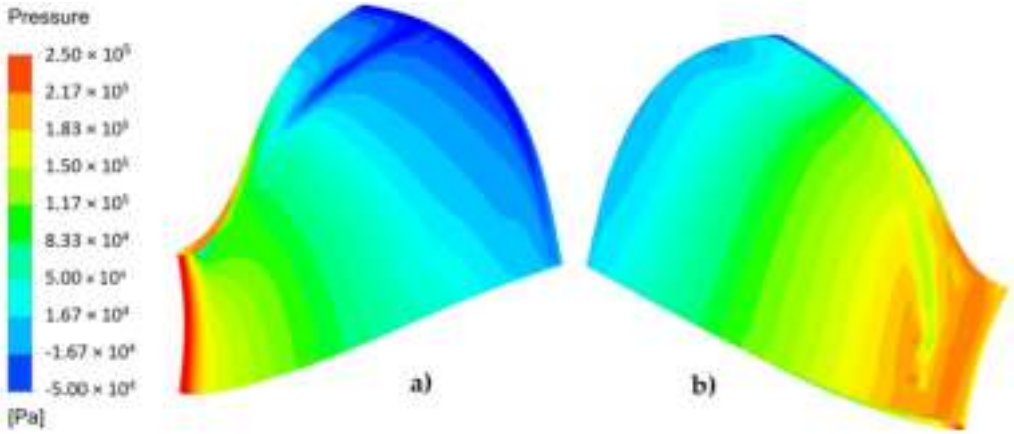

Figure 11. Runner blade static pressure distribution: (**a**) suction side, (**b**) pressure side.

Nevertheless, the von Karman's vortex street does not seem to be disturbed by the development of these large-scale interblade turbulent structures, whose development exhibits an almost steady behavior.

5.2. The Spectral Analysis

Once we verified the effectiveness of the model in qualitatively capturing the von Karman vortex shedding, the simplified numerical approach was also tested from a quantitative point of view, investigating its effectiveness in identifying the shedding frequency.

Therefore, to investigate the spectral content of the machine and the correlation with the fluid-dynamic behavior, three control points were set on the runner blade trailing edge (Figure 12a) in five different sections in the spanwise direction (Figure 12b).

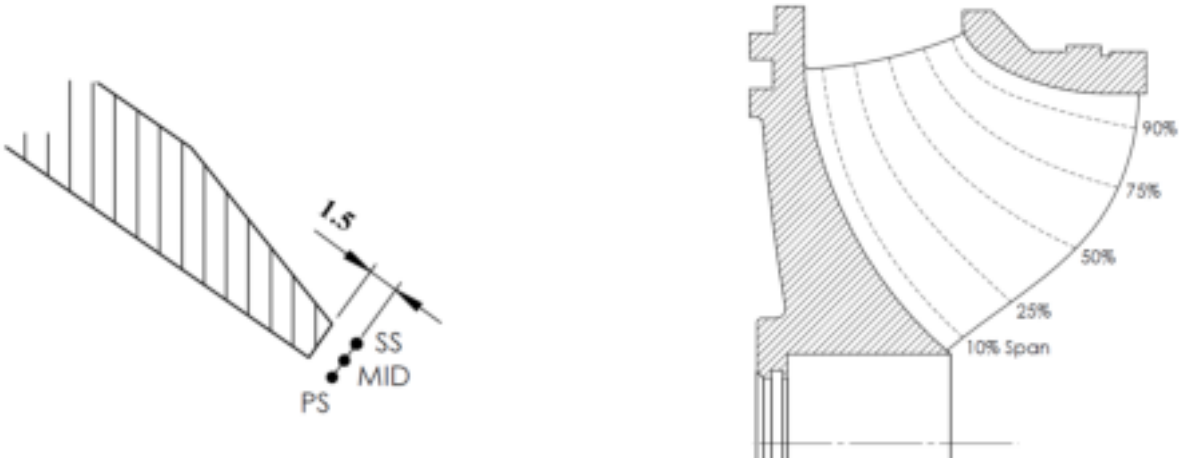

(**a**) (**b**)

Figure 12. Pressure-control points: (**a**) location on the blade trailing edge; (**b**) blade sections in the spanwise direction.

As clearly visible in Figure 13, the FFT analysis performed on the pressure signals acquired at the control points confirmed a dominant peak in the spectra around 2000 Hz, in agreement with the experimental results (Figure 1) and, therefore, demonstrated the capability of the simplified numerical approach to capture the resonance excitation source. In particular, the pressure-side pressure distribution appears to be more sensitive to the shedding of the vortex street.

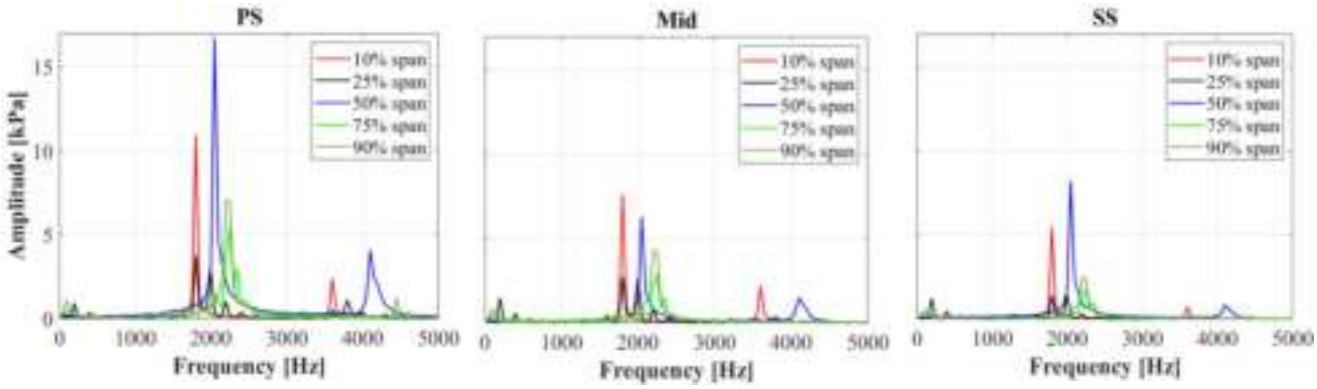

Figure 13. Frequency spectrum of the pressure signals acquired at the runner blade trailing edge.

Moreover, the same peak can also be seen in the frequency spectrum of the torque acting on the runner blade signal (Figure 14). Indeed, the pressure perturbation induced by the shedding of the von Karman vortex street influences the blade pressure distribution, hence, resulting in the fluctuation of the blade torque.

In order to better describe the influence of the pressure perturbation on the runner torque, Figure 15b reports the blade pressure distribution in correspondence to the runner midspan trailing edge section at two different time instants, respectively, related to a peak and a valley of the midspan pressure signal (Figure 15a).

The frequency spectra also show the existence of a low-amplitude, low-frequency phenomenon that lies in a frequency range between 110 Hz and 180 Hz and appears in the 25% span signals in almost good agreement with the measured signal at 190 Hz (Figure 1a,b). Since this perturbation remains unchanged under different flow conditions,

it can be assumed that the phenomenon is independent of von Karman's vortex shedding, which indeed strictly depends on the flow rate. In particular, this low-frequency band is very close to the blade passage frequency in the rotating frame (187.5 Hz), a hypothesis confirmed by the wakes of the guide vanes disturbing the runner inlet.

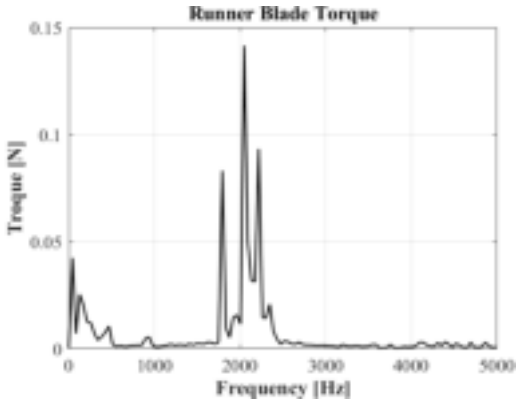

Figure 14. Frequency spectrum of the runner blade torque.

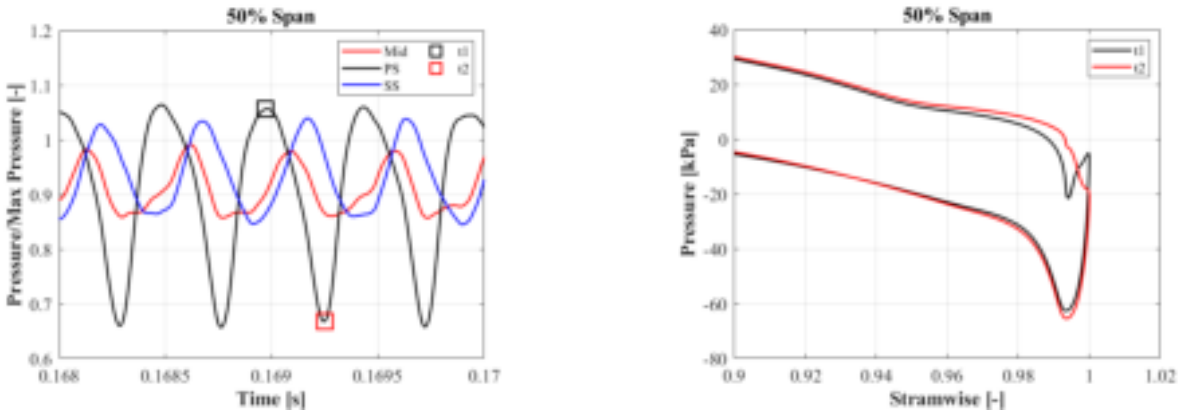

(**a**) (**b**)

Figure 15. Effect of the shedding frequency on the pressure distribution at the runner trailing edge: (**a**) static pressure trend at 50% span control points; (**b**) detail of the pressure distribution at the runner blade trailing edge at two different time instants.

The reason for the approximation in the frequency determination is the average influence of the stage interface on the total pressure field. Nevertheless, this perturbation does not appear in the torque signals of the runner blades, thus pointing out a minor effect compared to the von Karman vortex street shedding.

Finally, in order to evaluate the possible contribution of the stay vanes' trailing edge on the resonance occurrence, the spectral content of a pressure-control point located in the midspan section of the stay vane trailing edge was analyzed, showing a shedding frequency equal to 500 Hz (Figure 16). However, this peak is not present in the runner signals and, hence, does not seem to provide any significant contribution to the resonance phenomena. This is also in agreement with the experimental measurements.

Summing up the frequency analysis, the runner Strouhal number resulting from the numerical simulation was determined. In particular, considering the numerically evaluated shedding frequency (2070 Hz), the blade trailing edge width, and the relative flow speed at the runner midspan section, the runner Strouhal number result was 0.186, which falls within the suggested range for Francis turbines (0.16–0.24), thus supporting the goodness of this numerical approach.

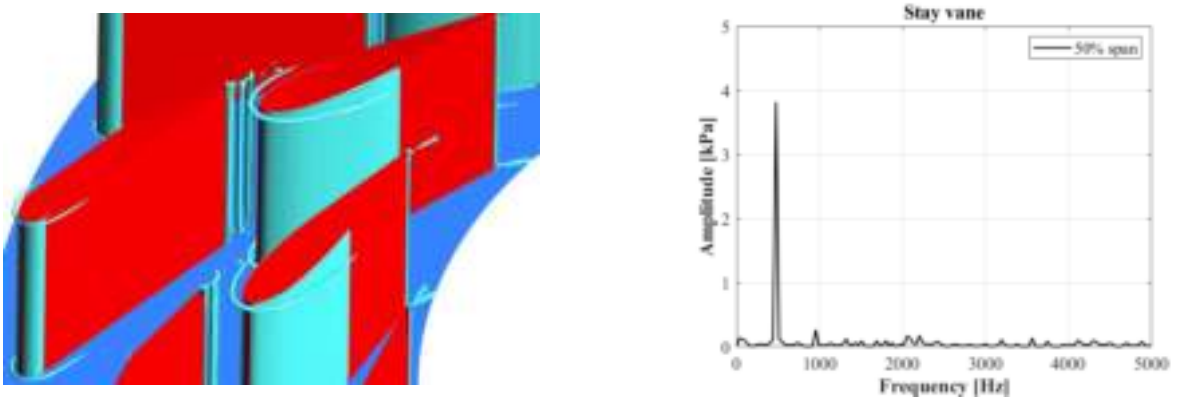

(**a**) (**b**)

Figure 16. Vortex street at stay vane trailing edge: (**a**) Q-criterion iso-surface; (**b**) frequency spectrum.

6. Conclusions

This work represents the extended version of the paper presented by the authors at the 15th European Turbomachinery Conference (ETC15) in Budapest, Hungary [17].

A simplified single-passage numerical model has been developed to evaluate the effect induced by the von Karman shedding frequency at the trailing edge of the blades on the hydrodynamic behavior of a Francis turbine, requiring reduced computational effort.

The case under study involves a medium specific speed Francis turbine manifesting structural resonance phenomena during operation at the rated power.

The proposed approach demonstrated its effectiveness in capturing the vortex shedding phenomena from both the fluid-dynamical and spectral points of view. In particular, the spectral content of the signals, numerically acquired in the runner, showed good agreement with the experimental acoustic ones, identifying with good accuracy the vortex shedding frequency in a reduced computational time of approximately 200 CPU h in comparison with a transient simulation of the entire machine.

Moreover, the machine's hydrodynamic behavior was investigated in depth, giving a detailed description of the main turbulent structures characterizing the fluid flow when operating close to the nominal discharge. In particular, it allowed us to determine the existence of two interblade vortexes and the causes of the 3D development of the secondary vortex.

Although a more simplified numerical model could be built by reconducting the 3D machine geometry into a 2D model, the proposed numerical approach represents a compromise between the computational effort and the result accuracy. Hence, it represents a useful tool to be adopted in the preliminary design phase. Indeed, thanks to this approach, von Karman vortex shedding could be also captured at off-design conditions characterized by a more pronounced 3D flow, which cannot be captured by a 2D approach.

Author Contributions: Conceptualization, G.Z. and G.C.; Data analysis, G.Z.; Methodology, G.Z. and G.C.; Writing—original draft preparation, G.Z.; Writing—review and editing, G.C. and A.S.; Supervision, G.C. All authors have read and agreed to the published version of the manuscript.

Funding: This research received no external funding.

Data Availability Statement: Restrictions apply to the availability of the data presented in this study. Data are available on request from the authors with prior permission of 45 Engineering S.r.l.

Conflicts of Interest: The authors declare no conflict of interest.

References

1. Donaldson, R.M. Hydraulic-Turbine Runner Vibration. *Trans. Am. Soc. Mech. Eng.* **1956**, *78*, 1141–1144. [CrossRef]
2. Bourguet, R.; Karniadakis, G.E.; Triantafyllou, M.S. Lock-in of the vortex-inducedvibrations of a long tensioned beam in shear flow. *J. Fluids Struct.* **2011**, *27*, 838–847. [CrossRef]

3. Nennemann, B.; Monette, C. Prediction of vibration amplitudes on hydraulic profiles under Von Karman vortex excitation. *IOP Conf. Ser. Earth Environ. Sci.* **2019**, *240*, 062004. [CrossRef]
4. Alexandre, A.N.; Gissoni, H.; Gonçalves, M.; Cardoso, R.; Jung, A.; Meneghini, J. Engineering diagnostics for vortex-induced stay vanes cracks in a Francis turbine. *IOP Conf. Ser. Earth Environ. Sci.* **2016**, *49*, 072017.
5. Luna-Ramírez, A.; Campos-Amezcua, A.; Dorantes-Gómez, O.; Mazur-Czerwiec, Z.; Muñoz-Quezada, R. Failure analysis of runner blades in a Francis hydraulic turbine—Case study. *Eng. Fail. Anal.* **2016**, *59*, 314–325. [CrossRef]
6. Etter, S.; Otto, A.; Gummer, A.N. Benefits of chamfering the trailing edges of Francis turbine blades. *Hydropower Dams* **2007**, *14*, 68–72.
7. Neidhardt, T.; Jung, A.; Hyneck, S.; Gummer, J. An alternative approach to the Von Karman vortex problem in modern hydraulic turbines. *Hydropower Dams* **2018**, *3*, 58–62.
8. Hans, G.P.; Zanutto, J.C.; Ferreira, W.P. Hydraulic power plant machine dynamic diagnosis. *Shock Vib.* **2006**, *13*, 409–427.
9. Zobeiri, A. Effect of Hydrofoil Trailing Edge Geometry on the Wake Dynamics. Ph.D. Thesis, École Polytechnique Fédérale de Lausanne, Lausanne, Switzerland, 2012.
10. Vu, T.; Nennemann, B.; Ausoni, P.; Farhat, M.; Avellan, F. Unsteady CFD prediction of von Kármán vortex shedding in hydraulic turbine stay vanes. In Proceedings of the Hydro 2007, Granada, Spain, 15–17 October 2007.
11. Amalia, E.; Moelyadi, M.A.; Ihsan, M. Effects of Turbulence Model and Numerical Time Steps on Von Karman Flow Behavior and Drag Accuracy of Circular Cylinder. *IOP Conf. Ser. J. Phys. Conf. Ser.* **2018**, *1005*, 012012. [CrossRef]
12. Zanetti, G.; Cavazzini, G.; Santolin, A. Three-dimensional evolution of the flow unsteadiness in the S-shape of pump-turbines and its correlation with the runner geometry. *J. Energy Storage* **2023**, *57*, 106176. [CrossRef]
13. Krappel, T.; Ruprecht, A.; Riedelbauch, S.; Jester-Zuerker, R.; Jung, A. Investigation of Francis Turbine Part Load Instabilities using Flow Simulations with a Hybrid RANS-LES Turbulence Model. *IOP Conf. Ser. Earth Environ. Sci.* **2014**, *22*, 032001. [CrossRef]
14. Wang, S.; Tan, J.; Yu, Z. Study on the influence of dynamic/static interface processing methods on CFD simulation results of the axial-flow blood pump. *Adv. Mech. Eng.* **2020**, *12*, 1–12. [CrossRef]
15. Osterwalder, J.; Hippe, L. Guidelines for efficiency scaling process of hydraulic turbomachines with different technical roughnesses of flow passages. *J. Hydraul. Res.* **1984**, *22*, 77–102. [CrossRef]
16. Zhou, L.; Liu, M.; Wang, Z.; Liu, D.Y.; Zhao, Y. Numerical simulation of the blade channel vortices in a Francis turbine runner. *Eng. Comput.* **2016**, *34*, 364–376. [CrossRef]
17. Zanetti, G.; Cavazzini, G.; Santolin, A. Von Karman vortex induced vibration in a Francis turbine: A reduced numerical model for estimating the shedding frequency. In Proceedings of the 15th European Conference on Turbomachinery Fluid Dynamics and Thermodynamics 2023, Budapest, Hungary, 24–28 April 2023; paper n. ETC2023-137. Available online: https://www.euroturbo.eu/publications/conference-proceedings-repository (accessed on 29 June 2023).

Disclaimer/Publisher's Note: The statements, opinions and data contained in all publications are solely those of the individual author(s) and contributor(s) and not of MDPI and/or the editor(s). MDPI and/or the editor(s) disclaim responsibility for any injury to people or property resulting from any ideas, methods, instructions or products referred to in the content.

International Journal of
Turbomachinery
Propulsion and Power

MDPI

Article

Scale-Resolving Hybrid RANS-LES Simulation of a Model Kaplan Turbine on a 400-Million-Element Mesh †

Simon Joßberger * and Stefan Riedelbauch

Institute of Fluid Mechanics and Hydraulic Machinery, University of Stuttgart, Pfaffenwaldring 10, 70569 Stuttgart, Germany; stefan.riedelbauch@ihs.uni-stuttgart.de

* Correspondence: simon.jossberger@ihs.uni-stuttgart.de

† This manuscript is an extended version of the ETC2023-343 meeting paper published in the Proceedings of the 15th European Turbomachinery Conference, Budapest, Hungary, 24–28 April 2023.

Abstract: Double-regulated Kaplan turbines with adjustable guide vanes and runner blades offer a high degree of flexibility and good efficiency for a wide range of operating points. However, this also leads to a complex geometry and flow guidance with, for example, vortices of different sizes and strengths. The flow in a draft tube is especially challenging to simulate mainly due to flow phenomena, like swirl, separation and strong adverse pressure gradients, and a strong dependency on the upstream flow conditions. Standard simulation approaches with RANS turbulence models, a coarse mesh and large time step size often fail to correctly predict performance and can even lead to wrong tendencies in the overall behavior. To reveal occurring flow phenomena and physical effects, a scale-resolving hybrid RANS-LES simulation on a block structured mesh of about 400 million hexahedral elements of a double-regulated five-blade model Kaplan turbine is carried out. In this paper, first, the results of the ongoing simulation are presented. The major part of the simulation domain is running in LES mode and seems to be properly resolved. The validation of the simulation results with the experimental data shows mean deviations of less than 0.8% in the global results, i.e., total head and power, and a good visual agreement with the three-dimensional PIV measurements of the velocity in the cone and both diffuser channels of the draft tube. In particular, the trend of total head and the results for the draft tube differ significantly between the scale-resolving simulation and a standard RANS simulation. The standard RANS simulation exhibits a highly unsteady behavior of flow, which is not observed in the experiments or scale-resolving simulation.

Keywords: Kaplan turbine; hydropower; computational fluid dynamics; scale-resolving simulation; hybrid RANS-LES turbulence modeling

check for updates

Citation: Joßberger, S.; Riedelbauch, S. Scale-Resolving Hybrid RANS-LES Simulation of a Model Kaplan Turbine on a 400-Million-Element Mesh. *Int. J. Turbomach. Propuls. Power* **2023**, *8*, 26. https://doi.org/10.3390/ijtpp8030026

Academic Editor: Antoine Dazin

Received: 18 June 2023
Revised: 17 July 2023
Accepted: 20 July 2023
Published: 2 August 2023

Copyright: © 2023 by the authors. Licensee MDPI, Basel, Switzerland. This article is an open access article distributed under the terms and conditions of the Creative Commons Attribution (CC BY-NC-ND) license (https://creativecommons.org/licenses/by-nc-nd/4.0/).

1. Introduction

The increasing use of volatile renewable energies, like wind and solar power, has led to higher fluctuations of available power in the electricity grid. Hydropower, as a predictable and reliable source of electricity, can be used to compensate the fluctuating power output and stabilize the energy grid. Double-regulated Kaplan turbines with adjustable guide vanes and runner blades offer high efficiency over a wide range of operating points. This wide operational flexibility requires a substantial change in the runner blade opening. The gaps on both the tip and hub of the runner blades create flow vortices interacting with the decelerated flow of the draft tube. The flow in a draft tube is especially challenging to simulate due to flow phenomena, like swirl, separation and strong adverse pressure gradients (cf. [1]), and a strong dependency on the flow conditions at the inlet defined by the quality and fidelity of the simulation upstream (cf. [2]). Typical Kaplan turbines are applied for small to medium heads. Therefore, even small errors in flow-dependent losses can lead to wrong predictions of performance and overall operating range.

The overall goal of this ongoing investigation is to detect and understand occurring flow phenomena and identify their importance to accurately simulate Kaplan turbines.

To achieve this, a highly resolved simulation with a hybrid RANS-LES turbulence model on a very fine mesh with about 400 million hexahedral elements is carried out. Advanced turbulence models have demonstrated an improvement in the results and level of detail (cf. [3–7]), but their numerical requirements, e.g., time step size and mesh resolution, have been generally much higher than standard RANS simulation approaches and typically too costly for industrial development processes. A comparison of the high-resolution simulation with different less complex simulations allows for the identification of important flow phenomena and how standard simulation approaches and development processes can be improved. To validate the simulation results, time-averaged experimental values for the total head and power of the runner are available, as well as phase-resolved three-dimensional PIV measurements in a plane just downstream of the runner and in a plane in each of the two diffuser channels of the draft tube. The details of the experimental investigation were published in [8].

In this part of the study, an estimation of the achieved numerical resolution and first results of the high-resolution simulation are described. Furthermore, a comparison of the experimental data and a standard RANS simulation on a mesh with 20 million hexahedral elements is presented. This manuscript is an extended version of the ETC2023-343 meeting paper published in the Proceedings of the 15th European Turbomachinery Conference, Budapest, Hungary, 24–28 April 2023 [9].

2. Numerical Setup and Model Turbine

The investigated turbine is a Kaplan turbine in model scale. The whole simulation domain consists of five subdomains (cf. Figure 1) and begins with the rectangular semi spiral intake, which includes two piers. The following subdomain consists of 23 stay vanes and 24 adjustable guide vanes. The runner consists of a hub and five adjustable blades. No geometric simplifications are used for the runner blades. Both the tip and hub clearance and the fillets between the runner blades and the hub are modeled. The currently investigated operating point is an on-cam point, where the pitch angles of guide vanes and runner blades are matched. An elbow-type draft tube with one pier leads to the tailwater tank. The geometry of the tailwater tank matches the model test arrangement at the hydraulic laboratory. The outlet of the simulation domain is defined at the end of the pipe downstream of the tailwater tank. This minimizes the impact of the boundary conditions on the flow in the draft tube and allows an accurate evaluation of results even at the end of the draft tube. Due to the fact that the flow in the tailwater tank is of no particular interest, the tailwater tank will be neglected in the following Section 3.

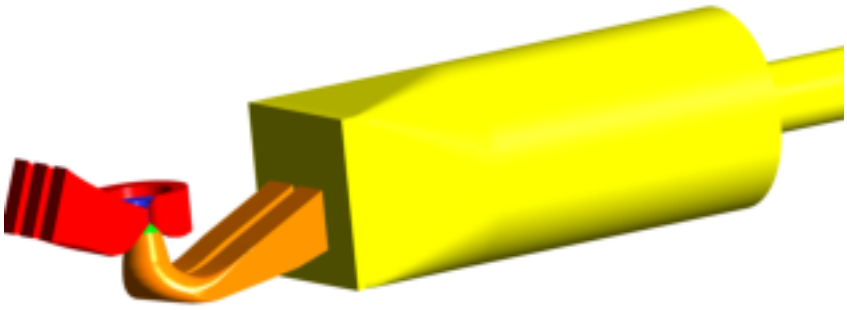

Figure 1. Simulation domain. Red: inlet area and semi spiral casing (SC). Blue: stay and guide vanes (SVGVs). Green: runner (RU). Orange: draft tube (DT). Yellow: tailwater tank (TW).

ICEM CFD is utilized to generate the block-structured hexahedral mesh with about 20 and 400 million elements for the standard RANS approach and the high-resolution simulation, respectively. The main differences between the 20 million element (20 M) and 400 million element (400 M) meshes are in the resolution of the boundary layer and overall element size while preserving the distribution of elements as much as possible. To properly resolve the boundary layer without the use of wall functions, a fine mesh at the wall, and a

small growth rate normal for the wall is required (cf. Figure 2). With an unchanged overall element size, this leads to a mesh with about 50 million elements. For the 400 M mesh, the element size is additionally approximately halved in all directions while maintaining the general block structure as much as possible. The number of cells in the five subdomains intake with semi spiral casing (SC), stay and guide vanes (SVGVs), runner (RU), draft tube (DT) and tailwater tank (TW) for both meshes is listed in Table 1.

Figure 2. Characteristic mesh distribution at the wall coloured by time-averaged velocity. (**Left**) A 20 M simulation with boundary layer wall function. (**Right**) A 400 M simulation with direct calculation of boundary layer.

Table 1. Number of cells of the subdomains in million elements.

Sim	Total	SC	SVGV	RU	DT	TW
20 M	19.8	2.1	7.0	4.7	4.9	1.1
400 M	399.5	29.8	78.6	63.3	218.2	9.6

The simulations are conducted with ANSYS CFX, version 19.5. Automatic wall treatment is activated for the boundary layer (cf. [10]). Depending on the local dimensionless wall distance, y^+, either wall functions or the direct calculation of the boundary layer is applied (cf. Figure 2). The average and maximum values and the 95th percentile of the time-averaged y^+ values of the subdomains neglecting the tailwater tank are listed in Table 2. In the 20 M simulation the average y^+-value ranges between 57 and 82 depending on the subdomain. This leads to the use of wall functions. As indicated by the 95th percentile and the average, most of the elements of the 400 M simulation have a y^+-value smaller than 2. This should lead to direct calculation of the boundary layer in most parts of the domain. In both simulations, the same time-averaged three-dimensional distributions of velocity and turbulence properties from a preceding unsteady simulation of the flow in the head water tank are specified as inlet boundary conditions (cf. [8,11]). An average static pressure is set as the outlet boundary condition. General grid interfaces (GGIs) are employed between stationary subdomains. Full 360° transient rotor–stator interfaces connect the rotating runner subdomain with the stationary stay vane and draft tube subdomain.

Table 2. Average, maximum and 95th percentile of time-averaged y^+ value in the subdomains.

	SC			SVGV			RU			DT		
Sim	**Ave**	**Max**	**p95**	**Ave**	**Max**	**p95**	**Ave**	**Max**	**p95**	**Ave**	**Max**	**p95**
20 M	62.1	145.1	99.9	81.7	267.1	132.9	57.0	135.1	88.5	60.5	221.3	105.5
400 M	0.54	1.86	0.89	0.59	69.7	1.07	0.96	6.63	3.84	0.42	2.02	0.93

Turbulence is modeled by the RANS k $-$ ω shear-stress transport (SST) model for the 20 M simulation and by the hybrid RANS-LES stress-blended eddy simulation (SBES) model

for the 400 M simulation. The SST model combines the advantages of the k − ω model in wall-bounded flows with the advantages of the k − ϵ model in free shear flows (cf. [12]). It is a standard RANS model and is commonly applied in simulating hydraulic turbomachinery. The SBES model uses an unpublished shielding function, f_S, to blend between the stress tensor, τ_{ij}, modeled by the RANS and LES model (cf. [13]):

$$\tau_{ij}^{SBES} = f_S \tau_{ij}^{RANS} + (1 - f_S)\tau_{ij}^{LES} \quad (1)$$

In this study, the SST model and the wall-adapted local eddy viscosity model (WALE) are used for the RANS and LES parts, respectively. Compared to other hybrid RANS-LES approaches, the SBES model has the advantage of a quick transition from RANS to LES mode and a clear distinction between both regions by the shielding function, f_S (cf. [14]).

For spatial discretization, the high-resolution scheme is applied for the SST simulation, and a bounded central differencing scheme is used for the SBES simulation (cf. [10]). A second-order backward Euler scheme is employed for temporal discretization in all simulations (cf. [14]). A fixed number of five inner loops per time step is used. With the final time step size, this leads to maximum root mean square values of the residuals of about 8.0×10^{-6} and 1.5×10^{-4} in the 20 M and 400 M simulations, respectively. A time step size of $\Delta t = 2 \times 10^{-4}$ s, which is equivalent to a 1.8° runner revolution, is used for the 20 M simulation. This is a typical order of magnitude for unsteady RANS simulations of hydropower turbines. The unsteady simulation is initialized with a steady-state SST simulation on the same mesh. Due to numerical instabilities, the 400 M simulation can not be initialized with a steady-state simulation, and the results of a preceding unsteady simulation have to be used. In theory, the build-up time necessary to obtain statistically valid results can be reduced by a higher quality of initial conditions. Therefore, an unsteady simulation with the SBES turbulence model on the 20-million-element mesh and a time step size of $\Delta t = 1 \times 10^{-4}$ s, equivalent to a 0.9° runner revolution, is used as the initial conditions. After 10 revolutions, the time step size is ramped down to $\Delta t = 5 \times 10^{-5}$ s over the course of about 100 iterations. After an additional five revolutions, the time step size is ramped down to a final value of $\Delta t = 2.5 \times 10^{-5}$ s, equivalent to 0.225° of runner revolution.

For both simulations, the averaging of data and the evaluation of results are started after a build-up time of 20 revolutions. This is equivalent to 4000 and 15,920 time steps in the 20 M and 400 M simulations, respectively, and corresponds to about two convective flows from the inlet of the semi spiral casing to the outlet of the draft tube. The number of build-up iterations is chosen by experience with similar simulations of hydropower turbines and by the trend of integral values of interest in the subdomains. Due to the unsteady behaviour of the flow in the draft tube in the 20 M simulation, this subdomain is less suited for the consideration of build-up time.

3. Results

In the following sections, the 20 build-up revolutions are neglected and only results of the subsequent revolutions are presented.

3.1. Estimation of Achieved Resolution in the 400 M Simulation

To derive the RANS equations of the Navier–Stokes equations, the flow variables are decomposed into a mean or time-averaged component and a fluctuating turbulent component. Since the latter component and the resulting turbulence energy cascade is almost completely modeled by the turbulence model, the time step size of an unsteady RANS simulation is, in theory, sufficiently small when it is able to capture the unsteady fluctuations of the mean values excited by external influences, such as interactions between the guide vanes and runner blades. In contrast to this, in an LES simulation, all but the smallest turbulent scales are directly simulated. To avoid excessive damping of turbulence in the LES region, [14] recommends a Courant number of $CFL \approx 1$ or smaller.

In Table 3, the average and maximum values and the 95th percentile of the time-averaged Courant number are presented. The values for the 400 M simulation are divided into the LES region and the RANS region. In the LES region of all subdomains, the average Courant number is smaller than 1, and most of the elements have a Courant number smaller than 2, as indicated by the 95th percentile. The left part of Figure 3 shows the root mean square of about 30 revolutions of the Courant number on a cut through the turbine for the 400 M simulation. The areas exceeding the recommendation of $CFL \leq 1$ are mostly in regions with a fine mesh resolution, like leading and trailing edges and the gaps of the runner blades. The time step size would have to be approximately halved to achieve a Courant number smaller than 1 for almost all elements. This would, in turn, approximately double the computing time for one revolution. With the used time step size, one revolution requires about 240,000 core hours or about 2.5 days wall-clock time on 4096 cores at the High Performance Computing Center Stuttgart. Hence, the selected final time step size of the 400 M simulation is a compromise between accuracy and feasibility.

Table 3. Average, maximum and 95th percentile of time-averaged Courant number in the subdomains.

	SC			**SVGV**			**RU**			**DT**		
Sim	**Ave**	**Max**	**p95**	**Ave**	**Max**	**p95**	**Ave**	**Max**	**p95**	**Ave**	**Max**	**p95**
20 M	0.07	2.78	0.17	1.21	19.1	3.30	4.20	358	9.23	0.39	12.8	1.58
400 M RANS region	0.02	1.01	0.04	1.29	146	4.05	3.04	423	9.59	0.08	5.25	0.33
400 M LES region	0.03	0.60	0.08	0.81	123	1.89	0.87	220	1.77	0.11	3.36	0.26

The shielding function, f_S, of the SBES turbulence model is used to visualize whether the RANS or LES model is used. The black lines in the right picture of Figure 3 represent a value of $f_S = 0.99$, and the magenta lines represent a value of $f_S = 0.01$. The regions outside the black lines are basically completely in RANS mode, while the regions inside the magenta lines are in LES mode. The small regions in-between the lines are the transition zones between the two models. The transition from RANS to LES primarily occurs in the semi spiral casing and stay and guide vanes. Downstream of the guide vanes, almost all of the simulation domain is in LES mode. In the runner and draft tube, only the boundary layer is in RANS mode, while all other areas are in LES mode. This is the intended state for a hybrid RANS-LES simulation. In the LES region, the amount of modeled turbulence, depicted by the eddy viscosity ratio, ν_t/ν, built with the turbulent viscosity, ν_t, and the dynamic viscosity, ν, is quite small. In the RANS region, the viscosity ratio is about two orders of magnitude higher. This can also be seen in Figure 4, where the resolved turbulent structures in the draft tube are visualized. The turbulent structures are depicted by an isosurface of the second invariant of the velocity gradient tensor, $Q = 0.5(||\Omega||^2 - ||S||^2) = 50$, built with the vorticity tensor, $\Omega = 0.5(\partial u_i/\partial u_j - \partial u_j/\partial u_i)$, and the strain rate tensor, $S = 0.5(\partial u_i/\partial u_j + \partial u_j/\partial u_i)$, and colored by the viscosity ratio. Compared to the 20 M simulation, the 400 M simulation resolves much finer structures and calculates the energy transfer due to turbulence on a much finer scale.

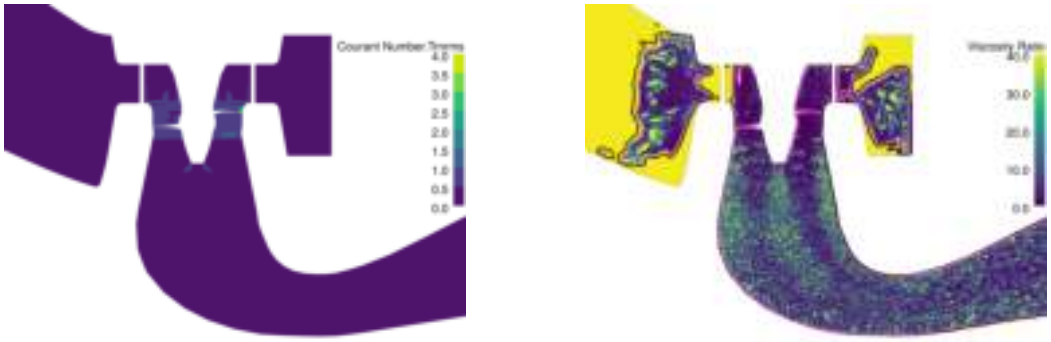

Figure 3. Cut through the turbine for 400 M simulation. (**Left**) Root mean square of Courant number. (**Right**) Viscosity ratio, ν_t/ν, and shielding function, f_S, of the SBES turbulence model (black line: $f_S = 0.99$; magenta line: $f_S = 0.01$).

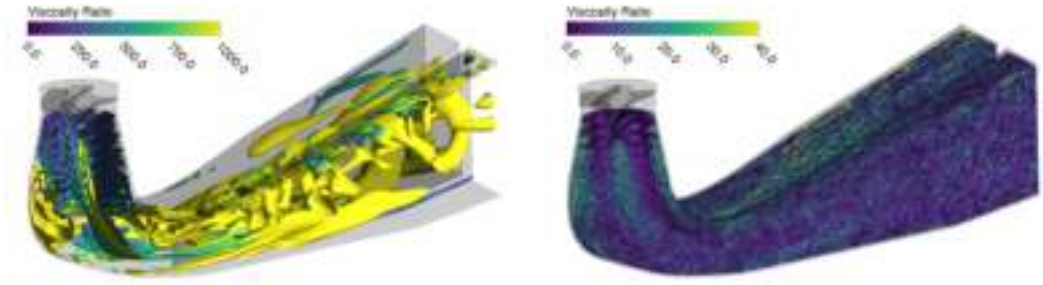

Figure 4. Instantaneous isosurface of velocity invariant $Q = 0.5\left(||\Omega||^2 - ||S||^2\right) = 50$ to depict resolved turbulent structures colored by viscosity ratio, ν_t/ν. Different scales are used for the viscosity ratio. (**Left**) 20 M simulation. (**Right**) 400 M simulation.

3.2. Comparison of Simulations and Measurement

The left part of Figure 5 shows the power and the right part the total head of the 20 M and 400 M simulation relative to the measurement. Both simulations match the measured power very well, with a little advantage for the 20 M simulation. The power trend of the 20 M simulation exhibits only minor oscillations without high random deflections. In comparison, the power trend of the 400 M simulation shows slightly higher oscillations and an overall noisier behavior. This is probably an effect of the higher temporal and spatial resolutions and the ability of the SBES model to resolve much smaller turbulent structures. Nonetheless, the power trend of both simulations reached a quasi steady state. The trend of the total head exhibits a different behavior. The result for the 400 M simulation is in good agreement with the measurement and reached a quasi steady state, which was also observed in the experiment. The trend of the 20 M simulation is highly unsteady and overestimates the head by more than 6 % at the maximum. During the course of 50 additionally calculated but not shown revolutions, the trend does not settle and, therefore, seems to be not a singular event but normal behavior for this simulation approach.

Figure 6 shows an instantaneous circumferential velocity field on the measurement plane in the cone of the draft tube just downstream of the runner blades. Basic flow features, e.g., the wake of the runner blades, are visible in both simulations and the measurement. However, the 20 M simulation shows a very smooth flow field. The level of detail is much higher for the 400 M simulation and the measurement, where small flow features are resolved. The granularity and magnitude of the resolved flow features are quite comparable between the 400 M simulation and the measurement.

Figure 7 shows the time-averaged velocity and corresponding standard deviation on the measurement plane in the left diffuser channel of the draft tube. The underlying data used to build the time-averaged flow field are quite different between simulations and the measurement. In the simulations, all time steps of about 30 revolutions are used, leading to 30 $\times$ 200 = 6000 and 30 $\times$ 1600 = 48,000 individual data sets in the 20 M and 400 M

simulations, respectively. The measurement consists of 1000 revolutions, but only nine data sets per revolution are taken with a time lag equivalent to an 8° runner revolution between subsequent data sets. This leads to a total of 9000 data sets. Despite the different data basis, the results of the 400 M simulation and the measurement are in good agreement. Both velocity and standard deviation show a similar distribution and pattern, as well as comparable magnitudes. The velocity distribution of the 20 M simulation differs and exhibits a much more unsteady behavior, as can be seen by the higher standard deviation. The data of the measurement plane in the right diffuser channel exhibit comparable results and are, therefore, not presented.

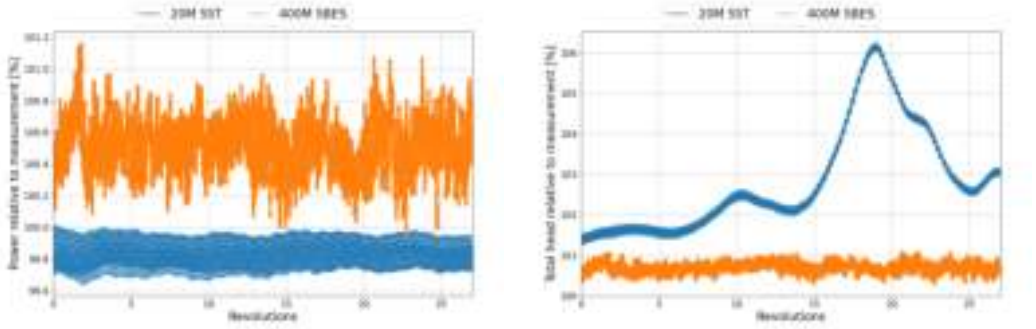

Figure 5. Power (**left**) and total head (**right**) relative to measurements.

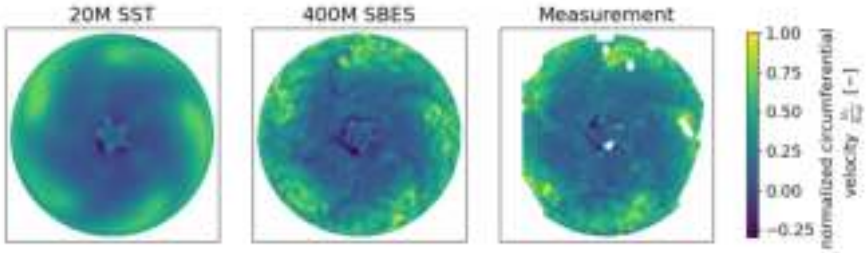

Figure 6. Instantaneous circumferential velocity on the measurement plane in the draft tube cone. Values normalized with the maximum value of the 400 M simulation. (**Left**) 20 M simulation. (**Middle**) 400 M simulation. (**Right**) measurement.

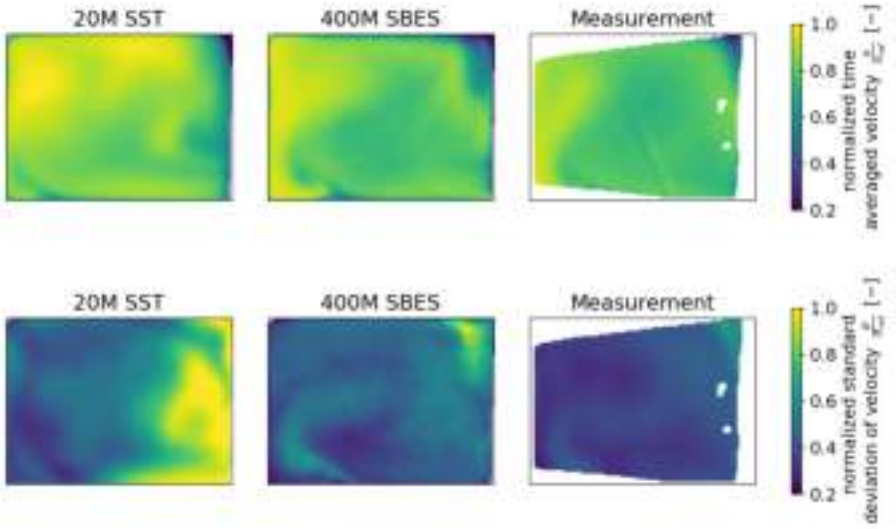

Figure 7. Time -veraged velocity (**top row**) and standard deviation (**bottom row**) on the measurement plane in the left diffuser channel. Values normalized with the maximum value of the 400 M simulation. (**Left**) 20 M simulation. (**Middle**) 400 M simulation. (**Right**) measurement.

3.3. Comparison of Time-Resolved Results for 20 M and 400 M Simulations

To identify the origin of the unsteady trend of the total head (cf. Figure 5), the head losses of the individual subdomains normalized with the corresponding mean of the 400 M simulation are shown in Figure 8. It is evident that the unsteady behavior of the total head in the 20 M simulation is mostly determined by the losses in the draft tube. The other subdomains exhibit a more or less constant course similar to the power and reach quasi steady states. In comparison to the 400 M simulation, the losses in the 20 M simulation are higher in all subdomains but show smaller oscillations.

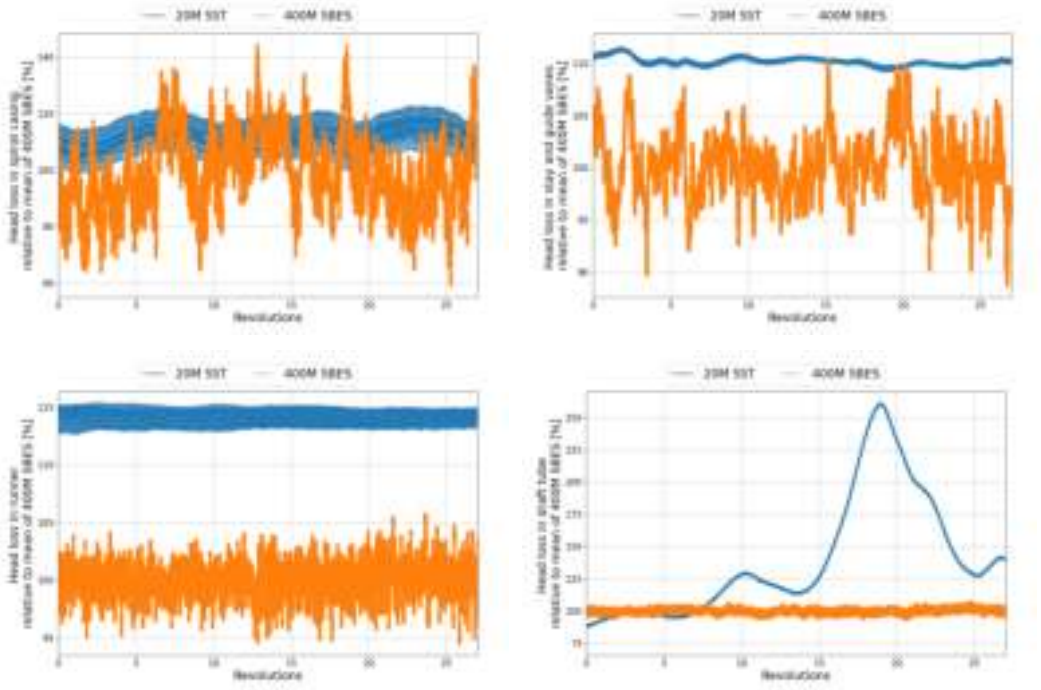

Figure 8. Head loss in individual subdomains relative to corresponding mean of the 400 M simulation. (**Top left**) spiral casing. (**Top right**) stay and guide vanes. (**Bottom left**) runner. (**Bottom right**) draft tube.

The origin of the unsteady losses in the draft tube are further isolated with the help of monitor planes. Specific variables, like velocity and pressure, are saved for every iteration on different monitor planes in the turbine. The monitor planes used in the following analysis are shown in Figure 9 and are located in downstream direction as follows: Runner Out is a monitor plane just downstream of the runner blades at the beginning of the draft tube cone. Cone Out is at the end of the cone and at the transition to the elbow. DT Left In and DT Right In are near the inlet to the left and right diffuser channels of the draft tube. DT Left Out and DT Right Out are at the outlet of the left and right diffuser channels.

Figure 10 shows the mass-flow-averaged kinetic energy and pressure on the monitor planes. The trend of kinetic energy on the monitor plane Cone Out of the 20 M simulation correlates very well with the trend of head loss in the draft tube in Figure 8. An increase in kinetic energy leads to an increase in head loss. The change in kinetic energy is transported downstream to the diffuser channels with a time delay. No upstream influence on the runner is observed. At the outlet of the draft tube, the disturbance has mostly subsided. The trend of pressure shows a similar behavior with two major differences. The first difference is that the two diffuser channels exhibit an opposing trend. An increase in pressure in the cone leads to a time-delayed increase in the left channel and a time-delayed decrease in the right channel. The second difference is that a change in pressure in the cone leads to a time-delayed opposing change in pressure in the upstream direction. The shown

results lead to the conclusion that the unsteady behavior of the draft tube originates in the cone of the draft tube.

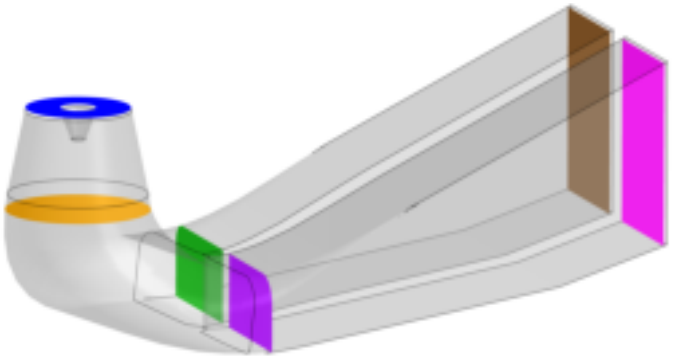

Figure 9. Monitor planes in the draft tube.

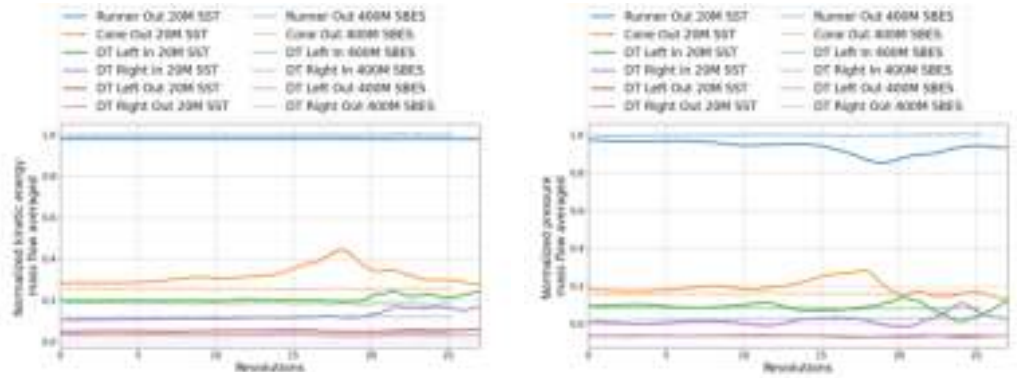

Figure 10. Mass-flow-averaged kinetic energy (**left**) and pressure (**right**) on different monitor planes in the draft tube (cf. Figure 9). The values are normalized with the respective value of Runner Out 400 M SBES.

This conclusion is further confirmed by Figure 11, where instantaneous velocity fields are shown on multiple monitor planes in the draft tube for different revolutions. For revolution five, the head loss in the draft tube (cf. Figure 8) has a similar value for both the 20 M and 400 M simulations. The flow field in the draft tube is largely comparable. Extensive flow features, e.g., higher velocities at the top than the bottom of the elbow, are present in both simulations. In detail, there are differences. These are particularly visible on the plane at the end of the cone. The 20 M simulation shows a region of low velocity near the wall, which is not present in the 400 M simulation. Furthermore, the overall granularity is much finer in the 400 M simulations. The following shown revolutions from 15 to 25 comprise the major peak in the trend of the total head and head loss in the draft tube of the 20 M simulation. The 400 M simulation does not change drastically with time. Major flow features remain preserved, and only spatial limited fluctuations occur. The flow of the 20 M simulation exhibits a substantially different behavior. Starting with revolution 15, the region with low velocities at the end of the cone becomes unstable and detaches from the wall in the following revolutions. In the last two shown pictures, the flow in the cone stabilizes again. The detachment is transported downstream and leads to major vortices downstream of the cone, which is especially visible on the monitor plane in the elbow. With increasing distance in the downstream direction, the impact of the detachment on the flow field weakens. At the outlet of the draft tube, only minor changes in the flow field are visible. The flow upstream at the inlet to the cone is only slightly influenced. The shown instability explains the differences in velocity and standard deviation on the measurement planes in the diffuser channels between the 20 M simulation, 400 M simulation and measurement shown in Figure 7.

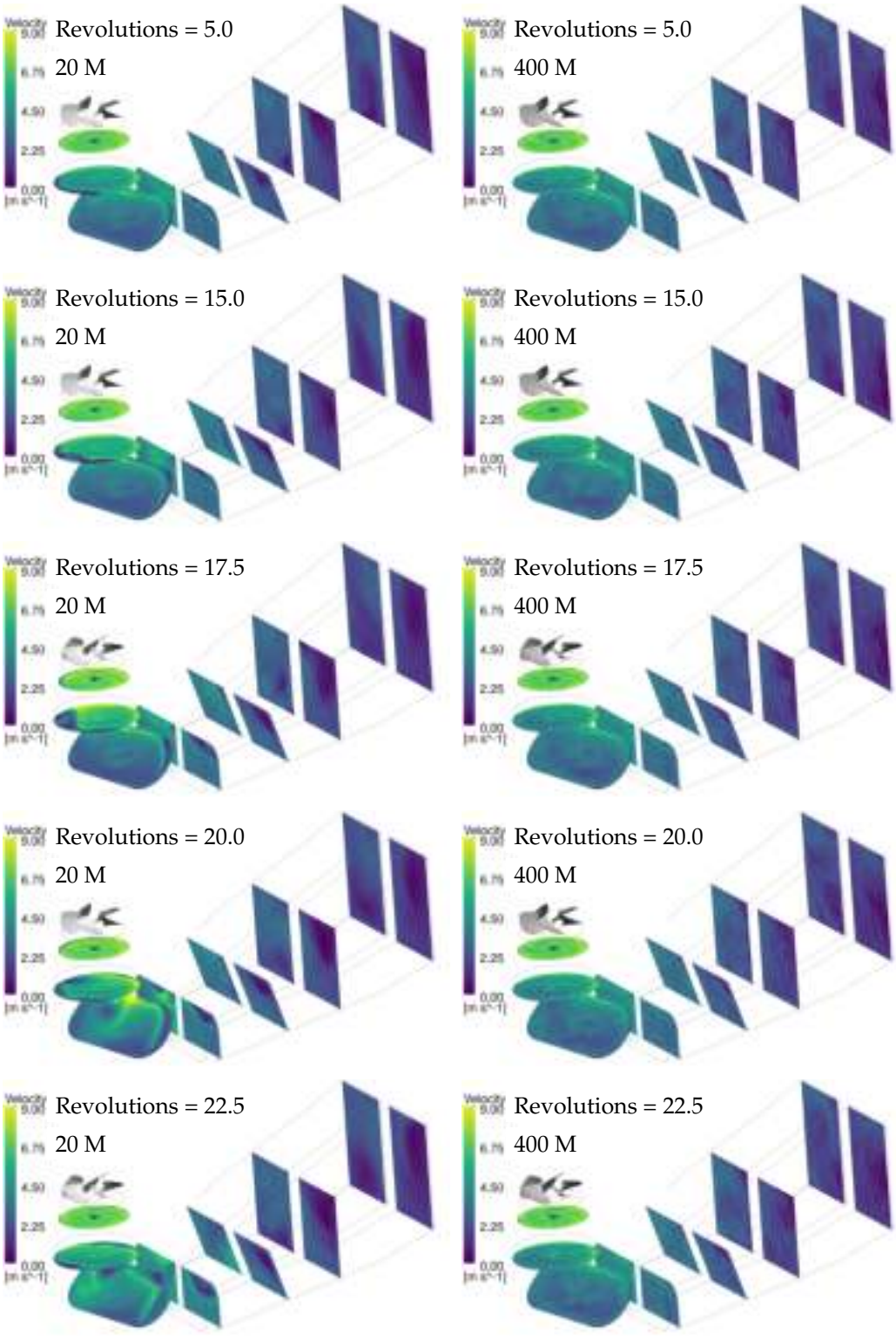

Figure 11. *Cont.*

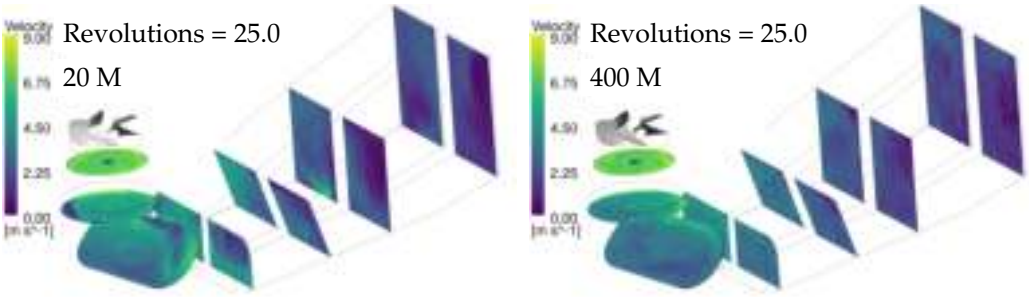

Figure 11. Instantaneous velocity fields on monitor planes in the draft tube at different revolutions. Left rows: 20 M simulation. Right rows: 400 M simulation.

4. Conclusions and Outlook

The first results of a hybrid RANS-LES simulation on a mesh with 400 million hexahedral elements and of a standard RANS simulation with 20 million hexahedral elements were presented and compared to each other as well as measurements. The results of the 400 M simulation indicate that most of the simulation domain ran in LES mode and that the regions in LES mode were properly resolved. Furthermore, the results are in good agreement with the measurement, and the simulation seems to accurately predict the flow in the turbine. A time-resolved analysis of the 400 M simulation shows that this simulation reached a quasi steady state in the integral values and flow field, which was also observed in the experiment. The 20 M simulation exhibited a highly unsteady behavior in the draft tube, leading to an unsteady trend of the total head. This instability arose in the cone of the draft tube and was transported primarily in downstream direction.

Currently, the most crucial flow features and primary influencing factors for precise simulations of Kaplan turbines, such as the turbulence model and time step size, remain unclear. In order to determine these factors, a comprehensive analysis is required, which involves comparing current simulations and experiments and conducting additional simulations with varied settings.

Author Contributions: Conceptualization, S.J. and S.R.; methodology, S.J. and S.R.; software, S.J.; validation, S.J. and S.R.; formal analysis, S.J.; investigation, S.J.; resources, S.J. and S.R.; data curation, S.J.; writing—original draft preparation, S.J.; writing—review and editing, S.J. and S.R.; visualization, S.J.; supervision, S.R.; project administration, S.J. and S.R.; funding acquisition, S.R. All authors have read and agreed to the published version of the manuscript.

Funding: This research received no external funding.

Data Availability Statement: Restrictions apply to the availability of the data presented in this study. Data are available on request from the authors with prior permission of Voith Hydro Holding GmbH.

Acknowledgments: The research leading to the results presented in this paper was part of a common research project of the University of Stuttgart and Voith Hydro Holding GmbH. The authors thank the High Performance Computing Center Stuttgart for the support and supply of computation time. The authors thank Euroturbo for covering the Journal publication costs.

Conflicts of Interest: The authors declare no conflicts of interest.

Nomenclature and Abbreviations

y^+	Dimensionless wall distance
Δt	Time step size
ν_t	Turbulent viscosity
ν	Dynamic viscosity

f_S	Shielding function of SBES turbulence model
Q	Q-criterion—second invariant of the velocity gradient tensor
S	Strain rate tensor
Ω	Vorticity tensor
20 M	Simulation on a 20-million-element mesh
400 M	Simulation on a 400-million-element mesh
RANS	Reynolds-averaged Navier–Stokes (equation)
LES	Large eddy simulation
SBES	Stress-blended eddy simulation
PIV	Particle image velocimetry
SC	Spiral casing
SVGV	Stay vane and guide vane
RU	Runner
DT	Draft tube
TW	Tailwater

References

1. Cervantes, M.; Engstrom, T.; Gustavsson, L. Turbine-99 III. In Proceedings of the Third IAHR/ERCOFTAC Workshop on Draft Tube Flows, Porjus, Sweden, 8–9 December 2005.
2. Nilsson, H.; Cervantes, M. Effects of the inlet boundary conditions, on the computed flow in the Turbine-99 draft tube, using OpenFOAM and CFX. *IOP Conf. Ser. Earth Environ. Sci.* **2012**, *15*, 032002. [CrossRef]
3. Jošt, D.; Škerlavaj, A.; Lipej, A. Improvement of Efficiency Prediction for a Kaplan Turbine with advanced Turbulence Models. *Stroj. Vestn./J. Mech. Eng.* **2014**, *60*, 124–134. [CrossRef]
4. Krappel, T.; Riedelbauch, S. Scale Resolving Flow Simulations of a Francis Turbine Using Highly Parallel CFD Simulations. *High Perform. Comput. Sci. Eng.* **2016**, *16*, 499–510.
5. Krappel, T.; Riedelbauch, S.; Jester-Zuerker, R.; Jung, A.; Flurl, B.; Unger, F.; Galpin, P. Turbulence Resolving Flow Simulations of a Francis Turbine in Part Load using Highly Parallel CFD Simulations. *High Perform. Comput. Sci. Eng.* **2016**, *49*, 421–433. [CrossRef]
6. Javadi, A.; Nilsson, H. Detailed numerical investigation of a Kaplan turbine with rotor-stator interaction using turbulence-resolving simulations. *Int. J. Heat Fluid Flow* **2017**, *63*, 1–13. [CrossRef]
7. Minakov, A.; Platonov, D.; Litvinov, I.; Shtork, S.; Hanjalić, K. Vortex ropes in draft tube of a laboratory Kaplan hydroturbine at low load: An experimental and LES scrutiny of RANS and DES computational models. *J. Hydraul. Res.* **2017**, *55*, 668–685. [CrossRef]
8. Beck, J.; Joßberger, S.; Jester-Zürker, R.; Riedelbauch, S. PIV measurements on a Kaplan turbine and comparison with scale-adaptive numerical analysis. *IOP Conf. Ser. Earth Environ. Sci.* **2019**, *405*, 012024. [CrossRef]
9. Joßberger, S.; Riedelbauch, S. Scale resolving hybrid RANS-LES simulation of a model Kaplan turbine on a 400 million element mesh. In Proceedings of the 15th European Turbomachinery Conference, Paper N. ETC2023-343, Budapest, Hungary, 24–28 April 2023. Available online: https://www.euroturbo.eu/publications/conference-proceedings-repository (accessed on 17 June 2023).
10. ANSYS Inc. *ANSYS CFX-Solver Modeling Guide Release 19.5*; Technical Report; ANSYS Inc.: Canonsburg, PA, USA, 2019.
11. Joßberger, S.; Riedelbauch, S. Influence of the Inlet Boundary Conditions on Numerical Flow Simulations of a Model Kaplan Turbine. In Proceedings of the 13th European Conference on Turbomachinery, Fluid Dynamics and Thermodynamics, Lausanne, Switzerland, 8–12 April 2019.
12. ANSYS Inc. *ANSYS CFX-Solver Theory Guide Release 19.5*; Technical Report; ANSYS Inc.: Canonsburg, PA, USA, 2019.
13. Menter, F. Stress-Blended Eddy Simulation (SBES)—A new Paradigm in hybrid RANS-LES Modeling. *Notes Numer. Fluid Mech. Multidiscip. Des.* **2016**, *137*, 27–37.
14. Menter, F. *Best Practice: Scale-Resolving Simulations in ANSYS CFD—Version 2.0*; Technical Report; ANSYS Germany GmbH: Darmstadt, Germany, 2015.

Disclaimer/Publisher's Note: The statements, opinions and data contained in all publications are solely those of the individual author(s) and contributor(s) and not of MDPI and/or the editor(s). MDPI and/or the editor(s) disclaim responsibility for any injury to people or property resulting from any ideas, methods, instructions or products referred to in the content.

International Journal of
Turbomachinery Propulsion and Power

MDPI

Article

Numerical Investigation of Rotating Instability Development in a Wide Tip Gap Centrifugal Compressor †

Xavier Flete [1,2,*], Nicolas Binder [2], Yannick Bousquet [2] and Sandrine Cros [1]

[1] Liebherr-Aerospace Toulouse SAS, 408 Avenue des Etats Unis, 31016 Toulouse, France
[2] ISAE-SUPAERO, 10 Av. Edouard Belin, 31400 Toulouse, France; nicolas.binder@isae-supaero.fr (N.B.); yannick.bousquet@isae-supaero.fr (Y.B.)
* Correspondence: xavier.flete@isae-supaero.fr
† This manuscript is an extended version of our paper published in the proceedings of the 15th European Turbomachinery Conference, Budapest, Hungary, 24–28 April 2023.

Abstract: In the current study, full-stage unsteady simulations were performed to investigate rotating instability inception mechanisms in a particularly large tip clearance centrifugal compressor with a vaneless diffuser and a volute. Four operating points along a speed line were analysed to understand the influence of the mass flow reduction on flow structures. Close to the peak efficiency, an unsteady interaction between the tip clearance vortices and splitter blades was observed. Considering other studies, the influence of the tip gap size was analysed. Then, a large-scale vortex shedding from the leading edges of the main blades was detected when the stage operated near the maximum pressure ratio. It was demonstrated that shed vortices were caused by the combination of the radial gradient of the tangential velocity under the tip vortex and the reverse backflow near the casing. Previous studies on axial compressors refer to these vortical structures as backflow vortices. These vortices cause a significant increase in the incidence angle in the tip region.

Keywords: backflow vortices; centrifugal compressor; rotating instability; tip leakage flow; wide tip clearance

check for updates

Citation: Flete, X.; Binder, N.; Bousquet, Y.; Cros, S. Numerical Investigation of Rotating Instability Development in a Wide Tip Gap Centrifugal Compressor. *Int. J. Turbomach. Propuls. Power* **2023**, *8*, 25. https://doi.org/10.3390/ijtpp8030025

Academic Editor: Antoine Dazin

Received: 8 June 2023
Revised: 20 June 2023
Accepted: 13 July 2023
Published: 1 August 2023

Copyright: © 2023 by the authors. Licensee MDPI, Basel, Switzerland. This article is an open access article distributed under the terms and conditions of the Creative Commons Attribution (CC BY-NC-ND) license (https://creativecommons.org/licenses/by-nc-nd/4.0/).

1. Introduction

The automotive industry is still keen on the design of centrifugal compressors with an ever-increasing operating range and compactness. However, the tip clearance size remains constant due to the technology choice, while the impeller size decreases. As a result, new automotive compressors have relatively large tip gaps compared to the blade span. But, as shown in the literature, tip leakage flows have a predominant role in the emergence of flow instabilities.

Inoue and Kuroumaru [1] demonstrated that in an axial compressor, the interaction between the tip leakage flow and the main flow leads to the formation of tip leakage vortices. As the clearance increases, a reverse flow due to the vortex grows near the casing wall. Further works of Inoue et al. [2–4] showed that when the tip gaps were large, the flow at the leading edge became unsteady and degenerated into a leading edge separation. They proposed a theory based on a tornado-like vortex extending radially inward, from the shroud to the blade's suction side, which leads to the onset of short length-scale stall cells. Other tip clearance vortices were observed by März et al. [5] in pre-stall conditions. These vortical structures, confined to the tip region of a rotor, moved from the suction side to the pressure side of the neighbouring blade. According to Mailach et al. [6] and the works cited above, these unsteady disturbances are identified as 'rotating instabilities' whereby the compressor operates in 'mild stall' conditions. In 2008, Vo et al. [7] suggested that such a tip flow could be linked to the onset of short length-scale rotating stalls. This assumption was confirmed by numerical investigations from Pullan et al. [8], which demonstrated that the short length-scale stall is caused by a separation at the leading edge due to a high

incidence causing the emergence of tornado vortices. They also described the propagation of these structures according to the mechanisms observed by März by adding the idea of a self-sustaining mechanism.

Bousquet et al. [9] observed similar vortex shedding at the leading edge of a centrifugal compressor with a vaned diffuser without a volute in near-stall conditions. The interaction between the leading edge separation and the incoming flow resulted in a Kelvin–Helmholtz instability inducing the tornado vortex shedding. However, in this configuration, the vortices' trajectory was such that no short length-scale rotating disturbances were observed. More recently, a similar Kelvin–Helmholtz mechanism was mentioned by Cao et al. [10] to explain the onset of massive vortex shedding from a tip leakage flow breakdown process close to the leading edges. This numerical and experimental investigation of a centrifugal compressor with a vaneless diffuser and a volute outlines the emergence of vortex tubes that propagate circumferentially and that strongly interact with the next blade's leading edge. The main difference between Bousquet et al.'s observations and those of Cao et al. is the direction of the vortical structures. Those mentioned by Cao are tubes oriented in the blade-to-blade direction and depend on the downstream pressure field imposed by the volute's tongue. Such phenomena are reminiscent of the residuals of the broken main tip leakage vortex described by Iwakiri et al. [11] as a result of single-impeller simulations. Like the previous authors, Tomita et al. [12] linked these tip leakage flow instabilities to the degradation of the compressor performances. However, they also demonstrated that the tip leakage vortex breakdown can stabilise the flow field and increase the operating range at a low mass flow by accelerating the incoming flow near the hub, unaffected by the vortical structures.

As an extended version of the study introduced by Flete et al. [13] at the 15th European Turbomachinery Conference, the present work complements the recent studies on flow instabilities in centrifugal compressors belonging to the turbocharger family in the following ways:

- It highlights the interaction between tip leakage vortices and splitter blades (related to a wide tip clearance), which degrades performances near the peak efficiency.
- It proposes an inception mechanism for vortex tube shedding described by Cao et al. [10] according to the investigation carried out by Chen et al. [14].

First, the studied compressor and numerical method are introduced. The next part presents a detailed analysis of the flow topology's gradual evolution caused by the mass flow reduction. Full-stage simulations are used to highlight the tip clearance vortex behaviour and the emergence of rotating instabilities in near-stall conditions. In particular, the propagation of massive vortices oriented perpendicular to the streamwise direction highly similar to those observed by Cao et al. [10] is described. Considering the velocity distribution, these vortical structures are identified as backflow vortices according to previous studies on axial machines. However, the inception mechanisms proposed by Cao et al. for centrifugal configurations and Chen et al. for axial configurations are different, and questions remain about the origin of such structures. Hence, the last part of the present study aims to clarify the development process of this vortex tube shedding.

2. Methodology

2.1. Test Case Geometry

The studied centrifugal compressor was designed by Liebherr-Aerospace Toulouse to supply air into an automotive fuel cell. Two of the most important requirements are a wide operating range and a small diameter. To meet these specifications, an impeller with splitter blades followed by a short vaneless diffuser and a volute was designed. Considering the flow field in choke conditions, the leading edges of the splitter blades are located at a relative meridional position of $M_x = 0.31$. This metric was defined based on the leading edges of the main blades ($M_x = 0$) until the trailing edges ($M_x = 1$). Numerical simulations were performed on the full-stage configuration shown in Figure 1. Table 1 describes the main compressor operating parameters. The impeller's particularity is the

wide tip clearance changing from the leading edge (6% of the blade span) to the trailing edge (18%).

Figure 1. Computational domain.

Table 1. Main compressor features.

Parameter	Value
Blade number	7 + 7
Design rotation rate	100 krpm
Design mass flow rate	0.1 kg/s
Design pressure ratio	2
Diffuser radius ratio	1.4
Diffuser width ratio	0.07

2.2. Flow Solver

Simulations were carried out by Siemens, STAR-CCM+ using a finite volume solver, and thus, the three-dimensional unsteady compressible Reynolds-averaged Navier–Stokes equations were solved on unstructured meshes. The eddy viscosity was computed with the two-equation turbulence model $k-\omega$ SST from Menter [15]. This improved version of the original $k-\omega$ combined the good near-wall performances for boundary layers under adverse pressure gradients with the $k-\epsilon$ accuracy in free stream. A coupled flow solver was used to solve the conservation equations for mass and momentum simultaneously using a pseudo-time-marching approach. The convective and diffusive fluxes were computed with an implicit second-order upwind scheme. The time-marching was performed with an implicit second-order discretisation scheme, and governing equations were solved in the absolute reference frame to avoid artificial dissipation leading to a nonphysical rotational flow in the far field region. Each impeller revolution was described by 860 physical time steps, corresponding to 122 time steps per the main blade's passage, and 30 inner iterations were carried out at each time step.

2.3. Mesh

The full-annulus computational domain was discretised with a polyhedral unstructured mesh using near-wall prism layer meshing. The size of the first cell was set to 1.5 µm, ensuring a normalised wall distance y^+ below 1.3 and mostly between 0 and 0.6. After several mesh convergence studies, the best compromise between computational time and solution accuracy was found for 48×10^6 cells in the impeller with an average of 33 cells in the tip gap's height. The vaneless diffuser and the volute were discretised into 14×10^6 cells. The information transfer between the impeller and the diffuser was handled

by a sliding-mesh interface, which was considered the most accurate method for simulating rotor-stator interactions.

2.4. Boundary Conditions

Stagnation conditions are uniformly applied to the inlet section. This method imposes the total pressure, temperature and flow direction and calculates other quantities using the isentropic relations. A study from Kulak et al. [16] demonstrated that a mass flow boundary condition tends to over-stabilise the flow and, thus, stifles initiations of instabilities. Furthermore, a uniform static pressure outlet condition prevents one from reaching a lower mass flow than the highest of the zero slope section. Hence, all the simulations in this study used a throttle law as an outlet condition.

This condition updates the outlet static pressure P_{Sout} at each time step according to the following relation:

$$P_{Sout}(t + \Delta t) = P_{S0} + \lambda \cdot \dot{m}(t)^2 \quad (1)$$

where P_{S0} is the reference static pressure, λ the throttle parameter and $\dot{m}$ the mass flow rate through the exit section. Such a boundary condition allows regulation of the outlet pressure according to the mass flow rate and gives enough freedom to move along the flat part of the characteristic curve.

2.5. Validation

A global performance validation was conducted at Liebherr Aerospace. The stage outlet static pressure was measured downstream of the volute. Hence, the comparison between measurements and numerical data is based on a total-to-static pressure ratio normalised by the local maximum value and plotted as a function of the corrected mass flow rate. Figure 2 shows good agreement between the experiment and numerical simulations for a rotation speed set to 97% of the one investigated in the present paper. Moreover, the stability limit is reached at a similar mass flow rate. This last finding demonstrates the reliability of the numerical method used to describe the stage destabilisation mechanisms.

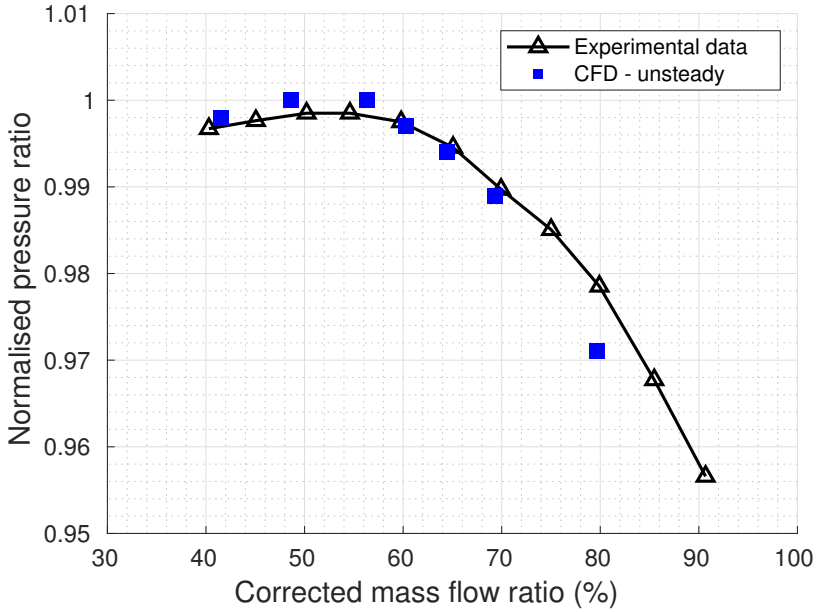

Figure 2. Comparison of experimental data and CFD results.

3. Unsteady Phenomenon near the Peak Efficiency

Four operating points (OP1, OP2, OP3 and OP4) along a speed line describe the development of instabilities in the impeller. The first operating point, OP1, illustrates the flow field in the impeller of the present compressor at design conditions. The second one, OP2, corresponds to the mass flow rate at which the tip leakage vortices hit the splitter blades' leading edges, causing unexpected unsteady behaviour near the peak efficiency. By reducing the mass flow, the compressor operates at OP3, where vortex tubes similar to those observed by Cao et al. emerge under the tip leakage vortices. Finally, the last described operation point OP4 shows the flow field topology in stall conditions. Each one is located in Figure 3, representing the stage total-to-total pressure ratio and the isentropic efficiency as a function of mass flow rate. These quantities are normalised by their respective mean values at the peak efficiency.

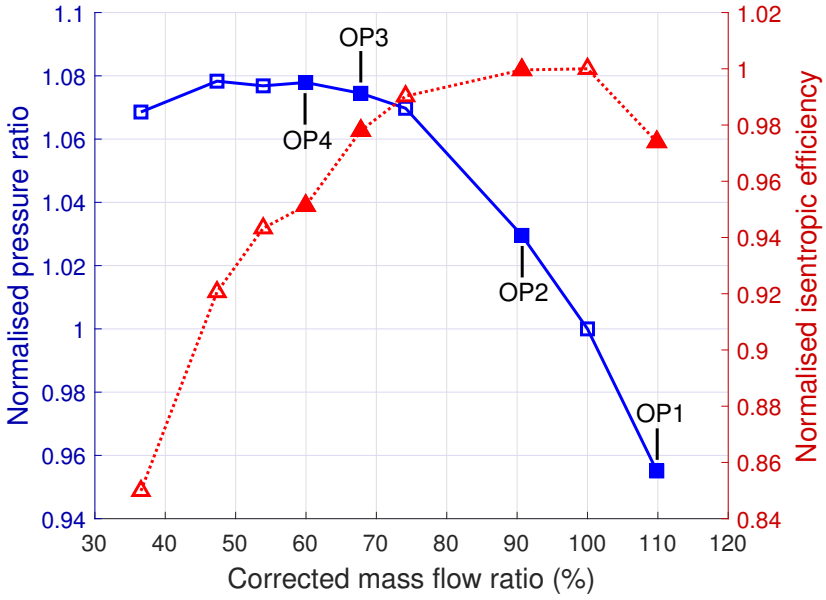

Figure 3. Studied operating points' locations on the compressor characteristic.

3.1. Flow Structures near Choke Conditions

At the highest mass flow rate OP1, the strong tip leakage flow is confined to the lower part of the half-passage near the trailing edges ($M_x > 0.65$). The recirculation from the leakage flow in the passage leads to an accumulation of low-momentum fluid near the casing wall, which, associated with the adverse pressure gradient from the vaneless diffuser, causes a near-shroud backflow in the impeller outlet tip region. However, this tip reverse flow weakens in the meridional direction before reaching the splitter blade's leading edges. Except for the trailing edge vicinity, the flow field is mostly steady. By using λ_2 criterion, it is possible to visualise the vortical structures in the impeller. λ_2 is the second eigenvalue of the sum of strain-rate tensors squared and the spin tensor squared when sorted from minimum to maximum. According to Jeong and Hussain [17], its negative values can be interpreted as vortex regions, while values equal to or greater than zero have no physical significance. Instantaneous iso-surfaces of λ_2 are shown in Figure 4. They highlight fully developed tip leakage vortices (TLV) that roll up midway between the main and the splitter blades' leading edges and extend until the downstream half-passage. In these half-passages, another tip leakage vortex emerges from the splitter blade's tip gap. At this operating point, the two wide structures are steady and do not appear to interact.

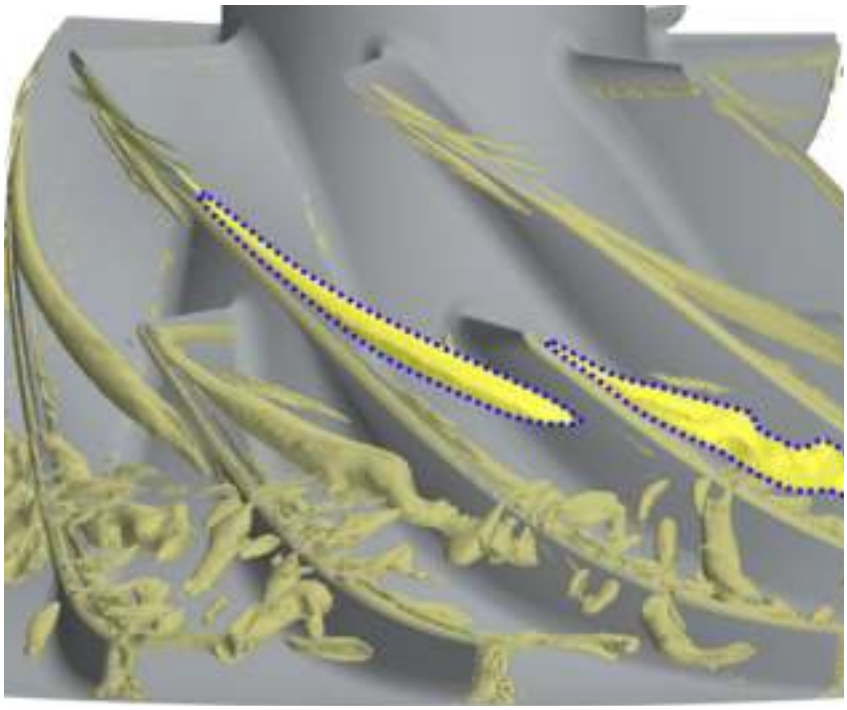

Figure 4. Iso-surfaces of λ_2 criterion at OP1.

At OP2, the strong leakage flow region overtakes the splitter blades' leading edges due to the adverse pressure gradient increase. Thus, the interface between the tip clearance and the underlying incoming flow is located diagonally between $M_x = 0.1$ and $M_x = 0.25$. Figure 5 shows that in this configuration, the initial rolling-up positions of the tip leakage vortex have migrated, and the trajectories have straightened upstream in such a way that the vortices from the main blades hit the splitter blade's leading edges, thus breaking the second TLV. Even if the upper part of the passage ($M_x < 0.3$) is mainly stationary, the interaction between the main blade TLV's tail and the splitter blade's leading edge leads to the emergence of a horseshoe vortex that collapses further downstream. These shed vortices penetrate the tip gap of the next blade under the influence of the strong tip leakage flow. In this way, they disturb the neighbouring horseshoe vortex before being transported by the main flow toward the diffuser. This local unsteady vortex shedding phenomenon is observed almost identically in every blade passage but does not significantly affect the stage performances. These disturbances can be observed on the static pressure spectrum, as illustrated in Figure 6. The plotted spectra are from a probe located close to the casing wall at $M_x = 0.42$. At OP2, the phenomenon described earlier causes an increase in pressure oscillations within the frequency range between the passing frequencies of the splitter blades and the main blades. During further throttling, the main TLV moves away from the splitter blade, driving the compressor to a stable operating point, while remaining in the negative slope section of the characteristic curve. Hence, the spectrum related to the OP3 signal reveals a stabilised flow field in which pressure fluctuations remain lower than those observed at OP2. Consequently, even if the disturbance observed near the peak efficiency seems to have rotating instability features, it must not be interpreted as a stall precursor signature.

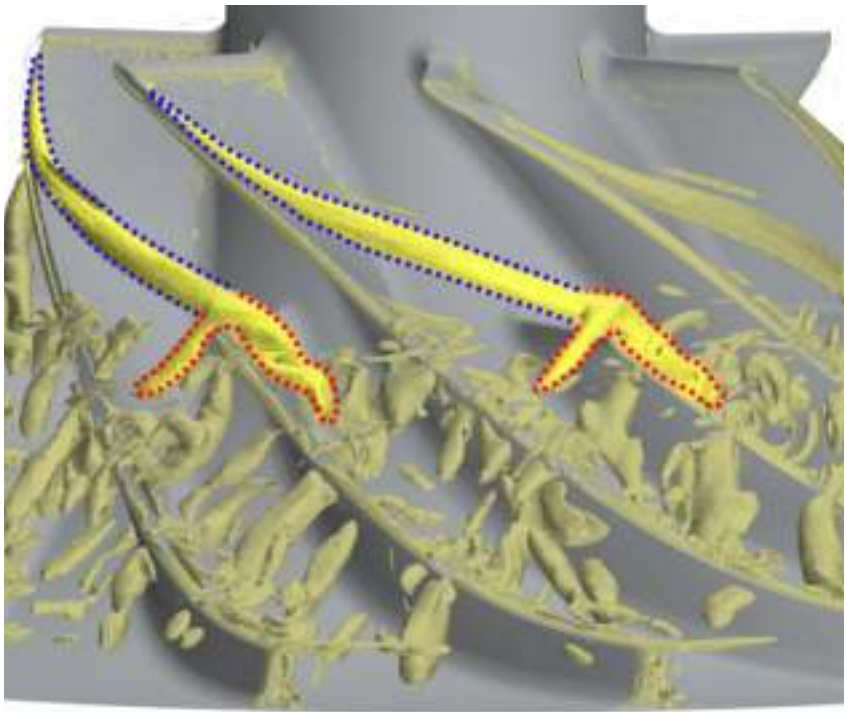

Figure 5. Iso-surfaces of λ_2 criterion at OP2.

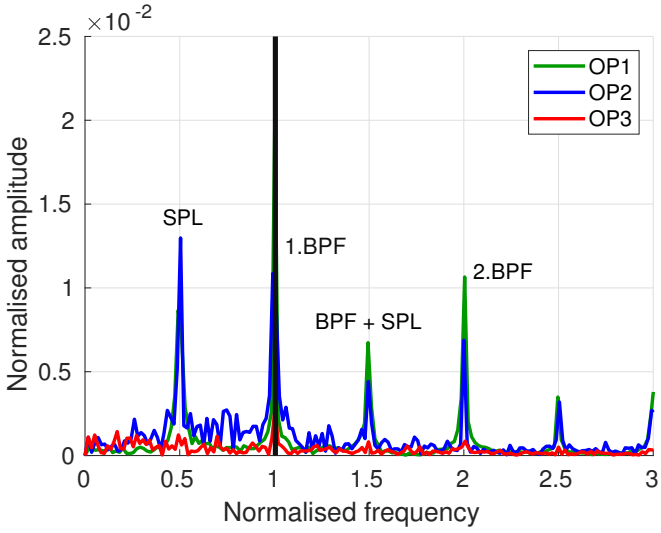

Figure 6. Static pressure spectra from the region of the splitter blade's leading edge ($M_x = 0.42$).

3.2. Flow Structures at Design Conditions

This interaction was observed in the simulations of Iwakiri et al. [11] in an impeller of a transonic compressor in near-stall conditions. Nonetheless, this previous study identified this phenomenon as one of the causes of the compressor performance reduction close to the zero slope part of the characteristic curve. In the present case, these vortical structures occurred earlier on the compressor's characteristic curve than the ones mentioned by Mitsubishi researchers. This could be explained by the geometry differences between the two configurations. Indeed, the present compressor has a wider tip gap than the impeller analysed by Iwakiri. Compared to the blade height, the present geometry has a tip clearance that is more than five times larger at the impeller inlet and around twice as large at the outlet. Through large eddy simulations, You et al. [18] demonstrated that increasing the tip gap size increases the angle between the blade and the tip leakage vortex. This could explain why the current compressor presented this unsteady interaction earlier on the

characteristic curve than the one studied by Iwakiri. Furthermore, the present splitter blades are shorter than those used in the configuration described by Iwakiri. As a result, the loss mechanisms at OP2 are confined to the region under the splitter blades' leading edges ($M_x > 0.31$), while the ones observed in Mitsubishi's compressor occurred on most of the passage's length. This also explains why the present compressor operating at OP2 provides enough work to keep the characteristic slope unchanged, whereas the one studied by Iwakiri shows performance reductions. However, considering the proximity of the best efficiency operating point, it can be assumed that OP2 would be the peak efficiency point without this phenomenon. Therefore, the angle between the tip leakage vortex and the blade's suction side must be considered when designing splitter blades, especially for impellers with wide tip clearances.

4. Backflow Vortices Emergence

4.1. Flow Structures in Near-Stall Conditions

With the decrease in the mass flow rate, the present compressor reaches the operating point, OP3, in which the TLV rolls up earlier near the main blade's leading edge and becomes shorter than those observed at OP2. According to Tan et al. [19], the angle defining the tip leakage vortex's trajectory from the main blade suction side increases with the blade loading. Furthermore, as reported by Zhang et al. [20], the reverse tip clearance flow at the impeller's outlet extends further upstream until it reaches a meridional position of $M_x = 0.1$. Figure 7 shows that at this operating point, some notable vortices emerge in front of the TLV tail before propagating in the passage. The upstream extremities of the released vortices are slightly oriented upstream, while the lower extremities remain attached to the blade's suction side. In this way, these large structures, oriented perpendicular to the streamwise direction, propagate downstream until they hit the splitter blades' leading edges. Moreover, this phenomenon proves to be periodic, and for the present mass flow rate, those vortices strike the splitter blade's leading edge approximately once per revolution. During the oncoming flow, these vortex tubes occurring at $M_x = 0.2$ occupy around the 15% of the span. Such vortices are highly similar to flow structures arising from the tip leakage flow breakdown described by Cao et al. [10]. However, the present case shows the coexistence of these wide vortices with an established tip leakage vortex.

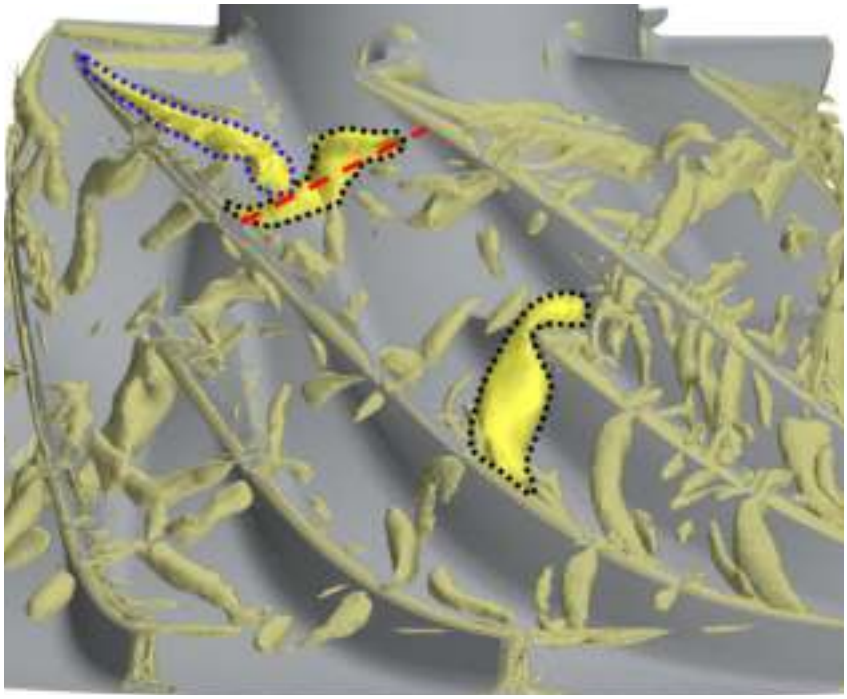

Figure 7. Iso-surfaces of λ_2 criterion at OP3.

4.2. Flow Structures in Stall Conditions

With further throttling, the compressor reaches the operating point OP4, where the interface between the tip clearance and incoming flows is parallel to the leading edges. For this mass flow, the TLV still rolls up at the main blade's leading edge, but it is shorter and tends to align with the leading edges' plane. Furthermore, the reverse tip clearance flow moves further upstream until it reaches the main blades' leading edges. In these conditions, the tip leakage vortex is sheared by the underlying axial flow and the tip gap backflow. As a result, the tip leakage vortices break down in some passages, causing the massive vortex shedding shown in Figure 8. The flow topology at this operating point closely resembles the field structures described by Cao et al. The shed vortices are similar to those observed at OP3, but they roll up nearer to the impeller inlet ($M_x = 0.08$), are oriented more diagonally upstream and are larger by around 33% span for the biggest ones. Besides, the emergence frequency of large-scale vortices has increased so that the shed vortices hit the splitter blades' leading edges between two and three times per revolution. Moreover, the upstream end is now associated with a high tangential velocity zone and propagates circumferentially. Thus, this part reaches the pressure side of the adjacent blade before passing through the tip gap and disturbing the flow structures in the next passage. This new mechanism disturbing the flow field in the neighbouring passage is illustrated in Figure 9. At (t_0), a vortex tube (black) emerges from under the tip leakage vortex (blue). At ($t_0 + 40\Delta t$), its upper part has moved circumferentially, while the downstream extremity is advected by the main flow. At ($t_0 + 80\Delta t$), the upstream part passes through the next tip gap. At ($t_0 + 120\Delta t$), the part remaining in the first passage is advected downstream toward the splitter blade's leading edge, whereas the other interacts with the neighbouring TLV. Thus, this interaction breaks the following tip leakage vortex and contributes to the creation of a new large vortex oriented perpendicular to the blade in the next passage. At the same time, the advected downstream parts of the vortices hit the splitter blades' leading edges, causing substantial pressure fluctuations.

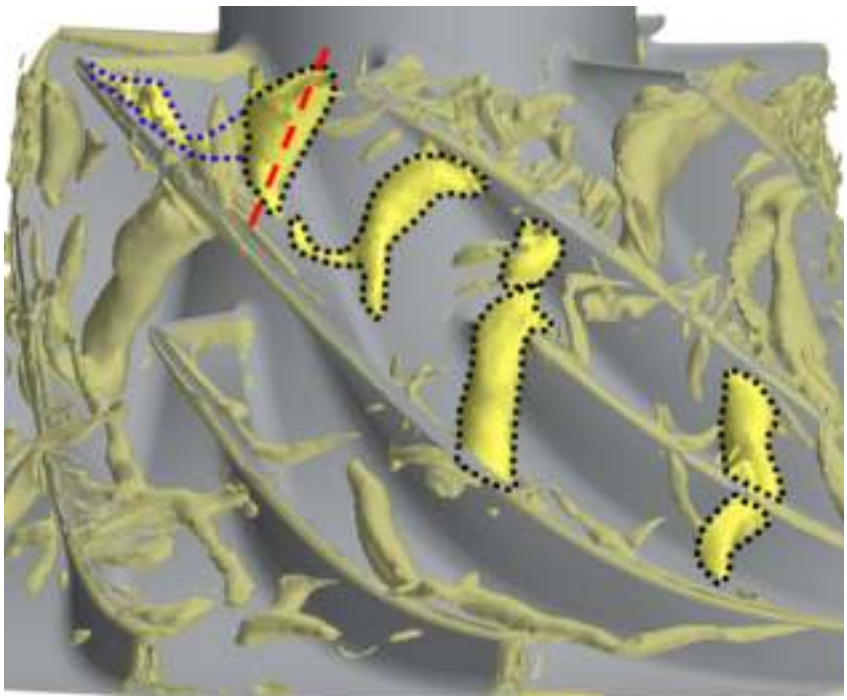

Figure 8. Iso-surfaces of λ_2 criterion at OP4.

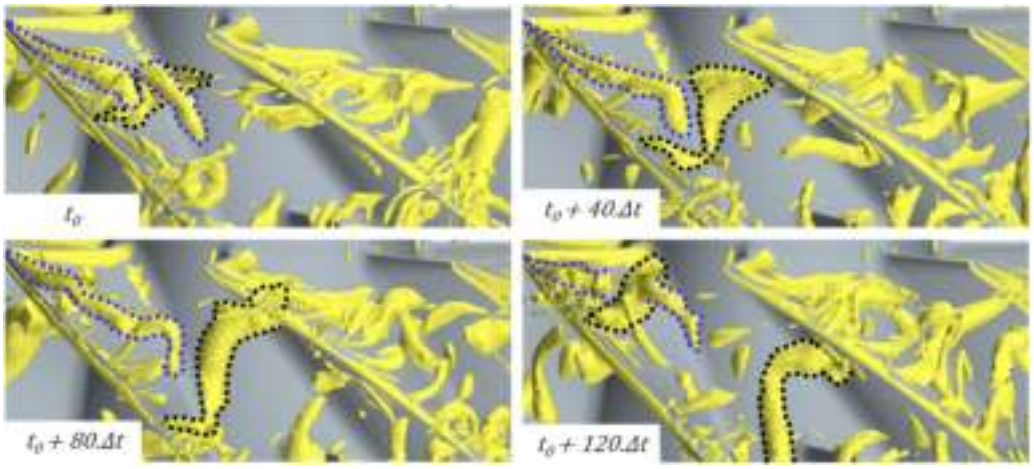

Figure 9. Large-scale vortices disturbing the neighbouring passage (OP4).

Previous works [2,4–6,21] on axial configurations have referred to these kinds of pre-stall disturbances as rotating instability. These instabilities are mainly encountered in compressors with wide tip clearances operating in near-stall conditions. As reported by Day [22], they are defined by their small size (about one pitch), low-pressure spots moving from the suction of a blade to the pressure side of the next one, and by a characteristic hump (about one-third of the blade's passing frequency) on frequency spectra. A Fourier transform has been performed on the pressure signal recorded by a fixed probe located at $M_x = 0.09$ to identify the present instabilities. Figure 10 shows the related frequency spectrum in which abscissa has been normalised by the main blade's passing frequency (BPF). A distinctive hump is observed around one-third of the BPF, strengthening the rotating instability assumption. The discrete peak located just under one-third of the BPF is related to the passage of the vortex tubes that propagate circumferentially close to the leading edges.

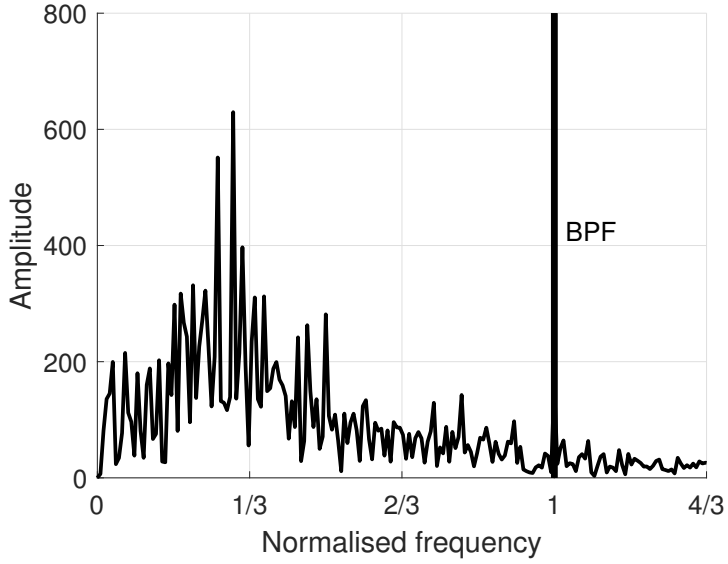

Figure 10. Static pressure spectrum from the tip region of the main blade's passage at OP4 ($M_x = 0.09$).

Some passages are ahead of the instabilities development. Indeed, passages coexist simultaneously with collapsed tip leakage vortices and ones with stable TLV in the impeller. The passages with broken TLV were noted to be associated with large vortical structures aligned with the leading edges' plane. In contrast, the passages linked to unbroken TLV

contain thin structures that roll up further downstream. This last flow topology is similar to the flow field observed at a higher mass flow rate when the compressor operates at OP3. This phenomenon is due to the non-uniformity of the pressure distribution induced by the volute in the vaneless diffuser. The asymmetry of the volute leads to a high-pressure region in front of the volute's tongue, followed by a low-pressure zone. Figure 11 outlines the non-uniformity of the flow field in the vaneless diffuser by plotting the time-averaged static pressure variations, $\widetilde{P_S}$, around the impeller, where $P_S(\theta, t_k)$ is the static pressure in the vaneless diffuser at t_k and $\overline{P_S(t_k)}$ is the circumferential average of $P_S(\theta, t_k)$.

This downstream distortion that ramps up with the mass flow reduction causes a periodic disturbance that drives the development of the instabilities in the impeller passages. In agreement with Zhang et al. [20], the potential effect propagates upstream through the subsonic flow until it reaches the plane of the main blades' leading edges. This mechanism explains the instant disparity of tip leakage vortices' behaviours in the different rotor passages.

$$\widetilde{P_S}(\theta) = \sum_{k=i}^{N} \frac{1}{(N-i+1)} \frac{P_S(\theta, t_k) - \overline{P_S(t_k)}}{\overline{P_S(t_k)}}$$

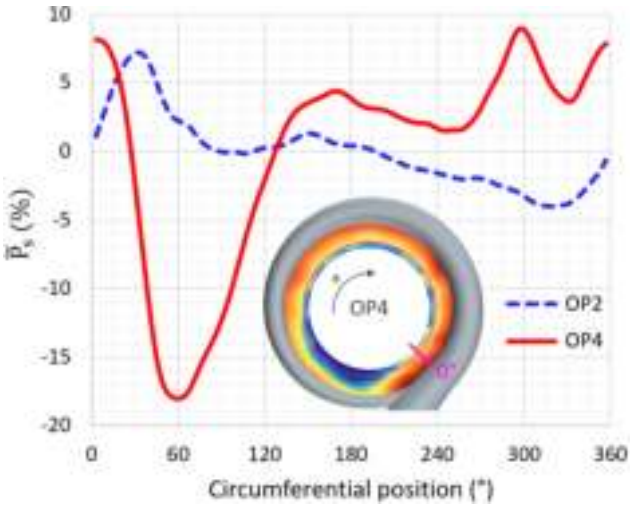

Figure 11. Volute influence on pressure distribution in the diffuser near impeller trailing edges.

4.3. Backflow Vortices Inception Mechanisms

Cao et al. [10] assumed that these large vortices are induced by a Kelvin–Helmholtz instability of the shear layer formed between the main-stream flow and the tip leakage flow. However, this theory does not explain the vortex tube orientation. The first vortex rolling up caused by a Kelvin–Helmholtz instability of a shear layer in a centrifugal compressor was described by Bousquet et al. [9]. In this work, the shed vortices extended radially from the blade's suction side to the casing wall without growing diagonally upstream or being aligned perpendicular to the blade. Furthermore, the tip leakage flow breakdown process described by Cao is incompatible with the coexistence of a stable TLV and a vortex tube shedding, as observed at OP3. This fact encouraged further study of the mechanisms behind the present flow structures. A similar flow pattern was experimentally observed within an axial compressor by Chen et al. [14]. They refer to this vortical structure as the backflow vortex (BFV) and describe it as a filament that emerges from the bottom of the TLV near the blade's leading edge. The explanation set out in this study is that a shear layer exists under the tip leakage vortex whose primary vorticity direction is such as if this layer has to roll up, then it will roll up perpendicularly to the blade. They also suggest that the shear layer rolling up is triggered by the interaction between the main incoming flow under it and the reverse flow close to the shroud, hence the name, backflow vortex.

To compare the present flow field (at OP3) with the one analysed by the Baltimore research team, the relative velocity components around the tip leakage vortex are shown in Figure 12. The displayed components are expressed in the rotating frame (e_r, e_θ, e_x) and are normalised by a reference blade speed defined as $U_{ref} = \omega \cdot r_{tip}$. In accordance with

the analysis conducted by Chen et al. [14] on the axial configuration, Figure 12 reveals the coexistence of two distinct regions A and B around the tip leakage vortex. The first one, located near the TLV centre, is characterised by a high relative tangential velocity W_θ and a negative axial velocity W_x. The second one is observed under the TLV and, contrary to the region A, has a low tangential component associated with a high axial component related to the blockage effect induced by the tip leakage vortex. Both have similar radial velocities, but there are significant radial gradients in W_θ and W_x between the two zones. Figure 12 also outlines that the resulting relative velocity (between B and A) W_{B-A} is parallel to the blade's suction side. As the vorticity is defined by the curl of the velocity field, the resultant of the vorticity components around the shear layer is aligned perpendicular to the blade. Furthermore, W_x distribution demonstrates that, in our case, the shear layer rolling up is probably caused by the influence of the upper reverse flow from the tip clearance and the forward main flow under it. This flow pattern, which is highly similar to the one highlighted by Chen, agrees with the vortical structures observed in the present centrifugal compressor. Therefore, from now on, the massive vortex tubes observed at OP3 and OP4 aligned perpendicular to the blade will be named "backflow vortices".

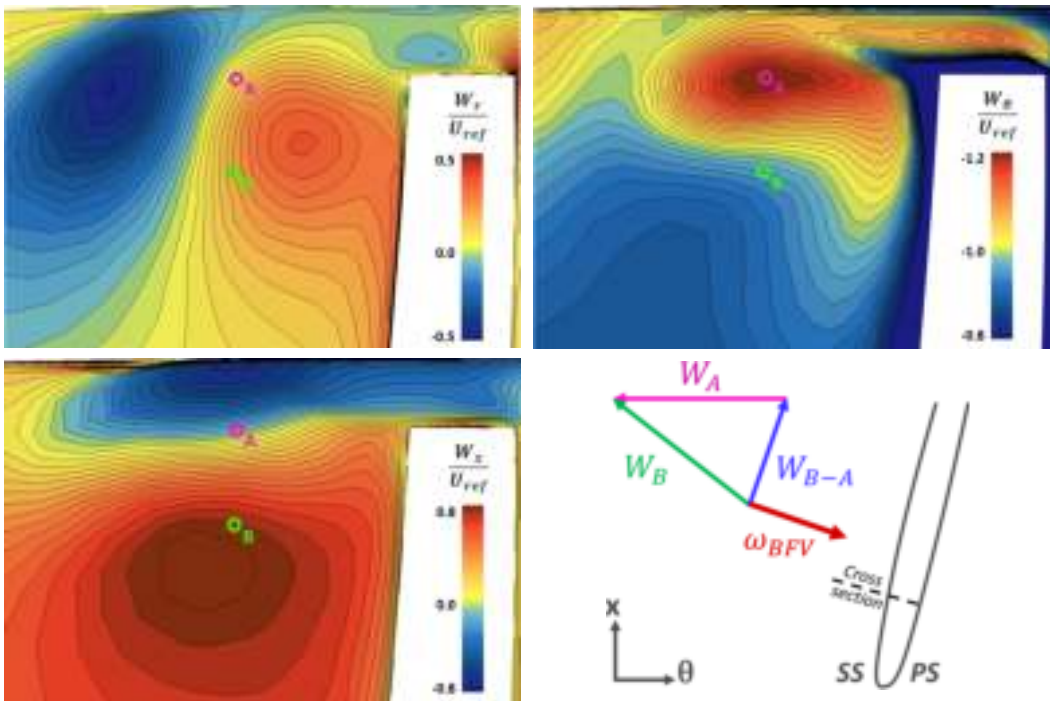

Figure 12. Relative velocity components plotted on a cross-section in the tip region (OP3 $-$ $M_x = 0.08$).

5. Conclusions

Based on the flow mechanisms reported here, unsteady three-dimensional calculations of the full compressor stage are required to simulate the rotating instability onset. The first operating points analysis has shown that even during design conditions, this kind of geometry with wide tip clearances leads to unsteady loss mechanisms due to the interaction between the main blade's tip vortex and the splitter blade. Hence, this phenomenon must be considered during the design of the splitter blades. Then, at lower mass flow rates, the highlight of the relative tangential velocity radial gradient under the TLV complements the previous study of the large-scale vortex shedding carried out at the Whittle Laboratory. Furthermore, it has been brought to light that the volute's shape significantly impacts the axisymmetric balance that drives the development of instabilities in the impeller passages. The vortices reported here lead to a significant increase in the incidence angle in the tip region. It is thus interesting to study the role of these structures in the stall inception.

Author Contributions: Conceptualization, X.F., N.B., Y.B. and S.C.; methodology, X.F., N.B., Y.B. and S.C.; validation, X.F., N.B., Y.B. and S.C.; formal analysis, X.F.; investigation, X.F.; data curation, X.F.; writing—original draft preparation, X.F.; writing—review and editing, X.F., N.B., Y.B. and S.C.; visualization, X.F.; supervision, N.B., Y.B. and S.C.; project administration, N.B., Y.B. and S.C.; funding acquisition, N.B., Y.B. and S.C. All authors have read and agreed to the published version of the manuscript.

Funding: This work was funded by Liebherr-Aerospace Toulouse S.A.S.

Data Availability Statement: The data presented in this study are available upon request from the corresponding author.

Acknowledgments: The authors would like to thank Liebherr Aerospace Toulouse S.A.S for supporting the present research program. The researchers was granted access to the HPC resources of CINES under the allocation 2023-A0132A06879 made by GENCI and to the HPC resources of CALMIP supercomputing centre under the allocation 2023-P18021.

Conflicts of Interest: The authors declare no conflict of interest.

Abbreviations

The following abbreviations are used in this manuscript:

BFV	Backflow Vortex.
BPF	Blade Passing Frequency.
SPL	Splitter blade.
TLV	Tip Leakage Vortex.
V_i	Absolute velocity component on direction 'i'.
W_i	Relative velocity component on direction 'i'.
M_x	Relative meridional position.
ω_{BFV}	Backflow vortex primary vorticity.

References

1. Inoue, M.; Kuroumaru, M. Structure of Tip Clearance Flow in an Isolated Axial Compressor Rotor. *J. Turbomach.* **1989**, *111*, 250–256. [CrossRef]
2. Inoue, M.; Kuroumaru, M.; Iwamoto, T.; Ando, Y. Detection of a Rotating Stall Precursor in Isolated Axial Flow Compressor Rotors. *J. Turbomach.* **1991**, *113*, 281–287. [CrossRef]
3. Inoue, M.; Kuroumaru, M.; Tanino, T.; Furukawa, M. Propagation of Multiple Short-Length-Scale Stall Cells in an Axial Compressor Rotor. *J. Turbomach.* **1999**, *122*, 45–54. [CrossRef]
4. Inoue, M.; Kuroumaru, M.; Tanino, T.; Yoshida, S.; Furukawa, M. Comparative Studies on Short and Long Length-Scale Stall Cell Propagating in an Axial Compressor Rotor. *J. Turbomach.* **2000**, *123*, 24–30. [CrossRef]
5. März, J.; Hah, C.; Neise, W. An Experimental and Numerical Investigation into the Mechanisms of Rotating Instability. *J. Turbomach.* **2002**, *124*, 367–374. [CrossRef]
6. Mailach, R.; Lehmann, I.; Vogeler, K. Rotating Instabilities in an Axial Compressor Originating From the Fluctuating Blade Tip Vortex. *J. Turbomach.* **2000**, *123*, 453–460. [CrossRef]
7. Vo, H.D.; Tan, C.S.; Greitzer, E.M. Criteria for spike initiated rotating stall. *J. Turbomach.* **2008**, *130*, 011023. [CrossRef]
8. Pullan, G.; Young, A.M.; Day, I.J.; Greitzer, E.M.; Spakovszky, Z.S. Origins and Structure of Spike-Type Rotating Stall. *J. Turbomach.* **2015**, *137*, 051007. [CrossRef]
9. Bousquet, Y.; Binder, N.; Dufour, G.; Carbonneau, X.; Roumeas, M.; Trébinjac, I. Numerical simulation of stall inception mechanisms in a centrifugal compressor with vaned diffuser. *J. Turbomach.* **2016**, *138*, 121005. [CrossRef]
10. Cao, T.; Kanzaka, T.; Xu, L.; Brandvik, T. Tip Leakage Flow Instability in a Centrifugal Compressor. *J. Eng. Gas Turbines Power* **2021**, *143*, 041012. [CrossRef]
11. Iwakiri, K.; Furukawa, M.; Ibaraki, S.; Tomita, I. Unsteady and three-dimensional flow phenomena in a transonic centrifugal compressor impeller at rotating stall. In Proceedings of the ASME Turbo Expo 2009: Power for Land, Sea, and Air, Orlando, FL, USA, 8–12 June 2009; Volume 48883, pp. 1611–1622. [CrossRef]
12. Tomita, I.; Ibaraki, S.; Furukawa, M.; Yamada, K. The Effect of Tip Leakage Vortex for Operating Range Enhancement of Centrifugal Compressor. *J. Turbomach.* **2013**, *135*, 051020. [CrossRef]
13. Flete, X.; Binder, N.; Bousquet, Y.; Cros, S. Numerical investigation of rotating instabilities development in a wide tip gap centrifugal compressor. In Proceedings of the 15th European Turbomachinery Conference, Budapest, Hungary, 24–28 April 2023; Paper n. ETC2023-119. Available online: https://www.euroturbo.eu/publications/conference-proceedings-repository/ (accessed on 7 June 2023)

14. Chen, H.; Li, Y.; Tan, D.; Katz, J. Visualizations of Flow Structures in the Rotor Passage of an Axial Compressor at the Onset of Stall. In Proceedings of the ASME Turbo Expo 2016: Turbomachinery Technical Conference and Exposition, Seoul, Republic of Korea, 13–17 June 2016. [CrossRef]
15. Menter, F.R. Two-equation eddy-viscosity turbulence models for engineering applications. *AIAA J.* **1994**, *32*, 1598–1605.
16. Kulak, M.; Grapow, F.; Liśkiewicz, G. Numerical analysis of centrifugal compressor operating in near-surge conditions. *J. Phys. Conf. Ser.* **2018**, *1101*, 012017. [CrossRef]
17. Jeong, J.; Hussain, F. On the identification of a vortex. *J. Fluid Mech.* **1995**, *285*, 69–94. [CrossRef]
18. You, D.; Wang, M.; Moin, P.; Mittal, R. Effects of tip-gap size on the tip-leakage flow in a turbomachinery cascade. *Phys. Fluids* **2006**, *18*, 105102. [CrossRef]
19. Tan, D.; Li, Y.; Chen, H.; Wilkes, I.; Katz, J. The Three Dimensional Flow Structure and Turbulence in the Tip Region of an Axial Flow Compressor. In Proceedings of the ASME Turbo Expo 2015: Turbine Technical Conference and Exposition, Montreal, QC, Canada, 15–19 June 2015. [CrossRef]
20. Zhang, H.; Yang, C.; Shi, X.; Yang, C.; Chen, J. Two stall stages in a centrifugal compressor with a vaneless diffuser. *Aerosp. Sci. Technol.* **2021**, *110*, 106496. [CrossRef]
21. Young, A.; Day, I.; Pullan, G. Stall Warning by Blade Pressure Signature Analysis. *J. Turbomach.* **2012**, *135*, 011033. [CrossRef]
22. Day, I. Stall, surge, and 75 years of research. *J. Turbomach.* **2016**, *138*, 011001. [CrossRef]

Disclaimer/Publisher's Note: The statements, opinions and data contained in all publications are solely those of the individual author(s) and contributor(s) and not of MDPI and/or the editor(s). MDPI and/or the editor(s) disclaim responsibility for any injury to people or property resulting from any ideas, methods, instructions or products referred to in the content.

International Journal of
Turbomachinery
Propulsion and Power

MDPI

Article

Heat Transfer Analysis of Damaged Shrouded High-Pressure Turbine Rotor Blades †

Mario Carta [1,*], Tiziano Ghisu [1] and Shahrokh Shahpar [2]

[1] Department of Mechanical, Chemical and Materials Engineering, University of Cagliari, 09123 Cagliari, Italy; t.ghisu@unica.it
[2] Rolls-Royce plc, Innovation Hub—Future Methods, Derby DE24 8BJ, UK; shahrokh.shahpar@rolls-royce.com
* Correspondence: mario.carta@unica.it
† This manuscript is an extended version of the ETC2023-321 meeting paper published in the Proceeding of the 15th European Turbomachinery Conference, Budapest, Hungary, 24–28 April 2023.

Abstract: Due to the increasingly high turbine inlet temperatures, heat transfer analysis is now, more than ever, a vital part of the design and optimization of high-pressure turbine rotor blades of a modern jet engine. The present study aimed to find out how shape deviation and in-service deterioration affect heat exchange patterns on the rotor blade. The rotor geometries used for this analysis are represented by a set of high-resolution 3D structured light scans of blades with the same number of in-service hours. An automatic meshing technique was employed to generate high-resolution meshes directly on the scanned rotor geometries, which captured all the surface features with high fidelity. Steady-state 3D RANS flow simulations with a *k-ω SST* turbulence model were conducted on a one-and-a-half stage computational domain of the scanned geometries. First, the distribution of the heat transfer coefficient was calculated for each blade; then, a correlation was sought between the heat transfer coefficient and parametrized shape deviation, to assess the impact of each parameter on HTC levels.

Keywords: high-pressure turbine; heat transfer; shrouded blade; level set meshing; multi-fidelity simulation

check for updates

Citation: Carta, M.; Ghisu, T.; Shahpar, S. Heat Transfer Analysis of Damaged Shrouded High-Pressure Turbine Rotor Blades. *Int. J. Turbomach. Propuls. Power* **2023**, *8*, 24. https://doi.org/10.3390/ijtpp8030024

Received: 8 June 2023
Revised: 17 July 2023
Accepted: 21 July 2023
Published: 1 August 2023

Copyright: © 2022 by the authors. Licensee MDPI, Basel, Switzerland. This article is an open access article distributed under the terms and conditions of the Creative Commons Attribution (CC BY-NC-ND) license (https://creativecommons.org/licenses/by-nc-nd/4.0/).

1. Introduction

To achieve high cycle efficiencies and to maximize power outputs, modern gas turbine engines employ increasingly high turbine inlet temperatures, exceeding 2000 K [1]. These temperatures are significantly higher than the metal's melting point, which is around 1400 K [2]. A prolonged overheating of the blade surface, even by a relatively low value in the order of the tens of Kelvins, can lead to a dramatic acceleration of thermal barrier coating (TBC) erosion and melting of the metal alloy. High-pressure turbine (HPT) rotors are known to experience the most arduous thermal conditions, particularly towards the tip region [3]. Higher-than-nominal temperatures may accelerate the creep process locally [4], and have been shown to degrade the metal alloy on a microstructural level [5]. For these reasons, the temperature of the HP components must be managed carefully through the use of sophisticated internal and external cooling mechanisms. The amount of coolant that is injected must be kept to a minimum, to limit mixing losses and overall cycle losses due to the compressor bleed. Therefore, the heat transfer systems need to be highly efficient and finely optimized to fulfil their purpose.

These systems are conceived around the nominal "running" geometries, and a set of operating conditions (usually takeoff and cruise), where they operate at peak performance. There are, however, a number of factors that may lead to deviations from the nominal. These include geometric modifications due to manufacturing variations [6,7], defects and handling damage, fouling near the film-cooling holes, as well as variations in operating conditions such as outboard traverse bias [8], or engine over-throttling due to an overall

performance deficit. The 'aim'of the present analysis was to study the correlation between the geometric deviation from the design intent and the distribution of surface heat transfer coefficient, for a large set of in-service shrouded HP turbine rotor blades of a modern jet engine resulting from high-resolution 3D-structured light optical scans. Thermal results were obtained through the use of a CFD methodology published by Maffulli and He (Maffulli and He, 2013, 2014), which calculates the heat transfer coefficient (HTC) by fitting a quadratic relation between the local wall temperature and heat flux. This technique is described in further detail in the Methodology section of this paper. This three-point non-linear fitting process requires three CFD simulations of the flow around the same blade geometry, with prescribed wall temperatures. Previous work [9] has focused on studying the correlation between aerodynamic efficiency loss and parametrized geometric deviation, and understanding the main loss mechanisms that characterize the flow field around in-service HP turbine blades. The objective of this analysis was to determine whether in-service deterioration, by virtue of inducing a modification in the geometry of the blades and the flow conditions, can cause an increase in the heat transfer coefficient in critical areas such as the blade shroud, leading the blades to experience a consequential acceleration of their degradation process.

2. Methodology

2.1. Geometries

The rotor geometries considered for this analysis had a shrouded tip design. Compared with its unshrouded counterpart, the shrouded design (see Figure 1A) has its main advantage in the higher aerodynamic stage efficiency due to reduced tip leakages. However, this comes at a price: increased difficulty in cooling the shroud region [10]. A set of HP in-service shrouded rotor geometries are analyzed in the present study. The blades belonged to a single "test" engine that operated in an experimental rig beyond its normal life timeframe, with the intent of determining the modes and rate of deterioration.

(**A**) (**B**)

Figure 1. HP turbine rotor blades: nominal (**A**) and a blue-light scan (**B**) (pictures distorted).

This section presents a description of geometries and methods that have been used to quantify the amount of damage. The rotor domain of each individual case constituted a single circumferential repetition of the same geometry, to enable single-passage CFD analysis with periodic boundaries. All the blade-to-blade measurements described in this section were taken between two identical blades with an angular shift equal to the periodicity angle.

These geometries (see Figure 1B) were obtained through high-resolution blue-light scanning, carried out using GOM Metrology (GOM scans). The blades exhibited different degrees of in-service deterioration, commonly including elongation, twist, erosion, and local loss of the thermal barrier coating. On this set of blades, the most damage could be seen in the shroud region, with an increase in all the clearances (tip gaps and inter-platform

gaps). Measurements taken in the shroud region of each blade were used to quantify the deformation of the shroud region. The measurements included the two tip clearances, T_1, T_2, and the three inter-platform shroud gaps, S_1, S_2, and S_{3max}, as depicted in Figure 2. On this set of scans, a V-shaped opening could be observed in the rear half of the platform region. To quantify the extent of this opening on each blade, the inter-platform gap distance was measured throughout all the rear half portion of the shroud (between the dashed lines in Figure 2B), and the maximum distance value is exported as S_{3max}. Conversely, S_1 and S_2 shroud gap measurements were taken for all blades at two fixed axial positions. T_1 and T_2 were measured as the radial distances between the tip of the respective fin and the design intent casing at the top center position. The relative orientation of the shroud fins in Figure 2B also indicates that the typical scan displays a twist of the platform with respect to the design intent geometry. This counter-clockwise twist was, in part, responsible for the increase in shroud gap, as discussed in a previous study [9]. To quantify this, a parameter called the "shroud angle" was measured on all the blades as the angle formed by the shroud gap mean line with the axial direction. To quantify elongation, the blade radius at three points, R_1, R_2, and R_3, on the upper face of the shroud platform was measured, as shown in Figure 2B.

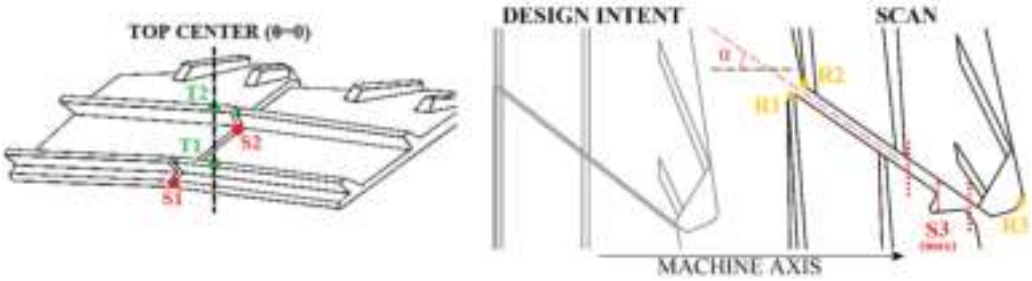

(**A**) (**B**)

Figure 2. Representation of two neighboring shrouds from the front (**A**) and from the top (**B**). Measurement points of the shroud gaps. S_1, S_2, and S_3, between the neighboring blades, tip clearances T_1 and T_2, the shroud angle, α, and the shroud platform radii R_1, R_2, and R_3.

Finally, the volume of the rear half of the inter-platform shroud gap was measured directly on the computational grids by calculating the volume of the mesh in between the two neighboring shroud platforms. In order to do so, three points, R_1, R_2, and R_3, and the shroud angle on each blade, were used as a reference to place a cuboid in the gap region. The cuboid includes the gap space and the side platform metal from two neighboring blades. The volume occupied by the fluid mesh within the cuboid was then calculated in the Paraview-based proprietary Rolls-Royce software SS02. This measurement is proportional to the volume of metal that was lost to erosion in the rear shroud gap region (between dashed lines in Figure 2B). Table 1 reports all the parameters used to quantify geometric deviation in the present analysis.

Table 1. Damage parametrization.

Parameter	Description
S_1	Front inter-platform shroud gap
S_2	Middle inter-platform shroud gap
S_{3max}	Rear inter-platform maximum shroud gap
T_1	Front fin tip-to-casing clearance
T_2	Rear fin tip-to-casing clearance
α	Shroud angle with respect to the machine axis
R_1	Radius of the shroud platform in the front suction side corner
R_2	Radius of the shroud platform in the front pressure side corner
R_3	Radius of the shroud platform above the blade's trailing edge
V	Volume lost due to erosion

2.2. CFD Modelling Technique

The computational domain used in the present study was a one-and-a-half stage comprising an HP stator, HP rotor, and IP stator, as shown in Figure 3A. CFD simulations were conducted on various combinations of this computational domain where, for each case, the rotor blade (HPR in Figure 3A) was represented by a different in-service geometry. The case with the design intent rotor geometry was also simulated to serve as a reference. The stator geometries (HPS, IPS) were, in every case, the design intents. Prior to meshing, a cold-to-hot transformation was applied to the geometries, in order to scale them to running/operational conditions. This transformation included an axial translation and 3D scaling by three different (x, y, and z) factors. The HP stator (HPS) and HP rotor (HPR) were fitted with source terms called "strip models" to surrogate the presence of multiple rows of cooling holes ejecting coolant from the internal cooling circuit. Both stator domains presented cooling flow slots at the trailing edges. The rotor domain also included the front and rear hub cavities, with their respective leakage inflows (USH and DSH). Casing upstream (CSF) and downstream (CSD) leakages were also included in the model. The three rows were connected using mixing-plane interfaces.

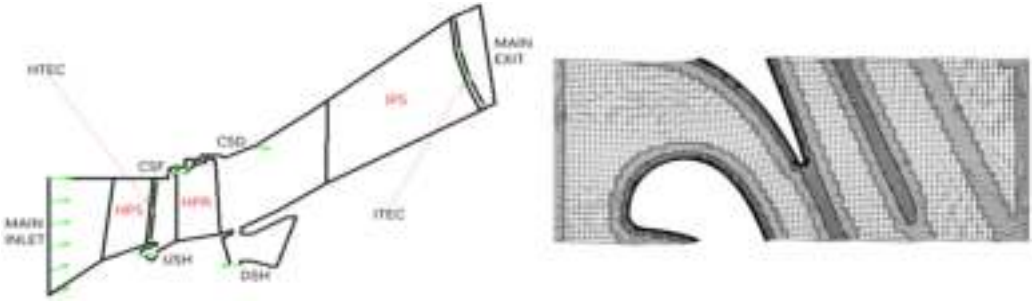

(**A**) (**B**)

Figure 3. Schematic representation of the 1 $\frac{1}{2}$ stage computational domain with arrows indicating the flow inlets (**A**) acronyms are defined in the nomenclature section; a spanwise section view of the BOXER rotor mesh (**B**) (pictures distorted and not to scale).

Standard practice for the CFD meshing of turbine domains in Rolls-Royce is to use the in-house tool PADRAM (Parametric Design and Rapid Meshing) [11], a tool that enables the rapid generation of high-quality meshes using templates, as well as the deformation of existing geometries using a rich set of parameters. The two stator domains are meshed in PADRAM with an H-O-H multi-block structured approach, with a process requiring only a few seconds to complete. Conversely, BOXER [12] is adopted for meshing the rotor domains in all cases, with an octree-based unstructured approach. This enables

the degraded surfaces to be meshed directly, thus capturing all the small-scale surface features that characterize the scanned geometries. Twenty structured prismatic layers are generated on the wall surfaces. Different mesh refinement settings are used in BOXER to locally increase mesh density in critical areas such as the shroud, TE, cavities, and wake regions. A solution from a preliminary CFD run was used to identify the approximate physical location (within the rotor domain volume) of the main flow features such as the wake, cavity flows, leakage flows, and main vortical structures. Once these features were located, the domain was re-meshed with "refinement shells" positioned at each location, to locally refine the mesh for better resolution of the flow features. On average, the BOXER rotor meshes have 35 million elements. The meshing process is executed automatically on all the blades through a script. Figure 3B shows a section of the BOXER mesh on the design intent rotor geometry. The complete multi-row CFD domain mesh has an average of approximately 40 million elements. A verification study for this modelling technique was carried out previously [9], and as such is omitted here.

Three-dimensional steady-state RANS simulations of the compressible flow were carried out using Rolls-Royce's proprietary finite volume solver HYDRA [13], with *k-ω SST* turbulence modelling and an implicit time-marching scheme. Convergence of the CFD simulations was monitored both in terms of residuals of the momentum equations (converged for $R \leq 10^{-12}$ and a drop 4 orders of magnitude relative to the initial values) and the stabilization of the quantities of interest. Boundary conditions used for the present analysis are representative of the engine's "cruise" operating point. One-dimensional total pressure and total temperature radial distributions are specified at the HP stator inlet. The secondary inlets shown in Figure 3A (USH, DSH, CSF, CSD, HTEC, and ITEC), with green arrows fitted with prescribed mass inflow boundary conditions. A non-reflective outflow boundary condition was assigned to the IP stator exit, where a one-dimensional radial distribution of static pressure was specified. In order to collect information on the isentropic stage efficiency, monitors were placed on the flow inlets and exits, as shown in Figure 3A, and at the exit boundary of the HP rotor domain. Each monitor was used to obtain the converged values of mass flow and total enthalpy, the latter being calculated by mass-averaging the total pressure and temperature values. The formula used to compute stage efficiency is detailed in Equation (1), where the ideal total enthalpy exit term at the denominator is calculated as that resulting after the isentropic expansion of every gas stream to the total mass-averaged pressure of the main rotor exit. The gas model used was selected within HYDRA's BS29 library [14] to be the kerosene–air exhaust gas mix. For this gas model, both the ratio of specific heats and the heat capacities of the gas varied non-linearly with temperature.

$$\eta = \frac{\sum_{i=inlets} \left(\dot{m}H_0\right)_i - \left(\dot{m}H_0\right)_{out}}{\sum_{i=inlets} \left(\dot{m}H_0\right)_i - \left(\dot{m}H_{0_ideal}\right)_{out}} \tag{1}$$

2.3. Heat Transfer Coefficient Calculation Technique

The expression that defines the heat transfer coefficient was derived from Newton's Law of cooling, as given in Equation (2): the heat flux on the left-hand side is defined as the product of heat transfer coefficient "h" and the difference between wall temperature T_w and recovery temperature (or adiabatic wall temperature) T_{rec}.

$$\dot{q} = h(T_w - T_{rec}) \tag{2}$$

Equation (2) can be used to estimate the heat transfer coefficient on a turbine blade, by conducting two CFD runs. The first one is the simulation of the flow, assuming adiabatic wall surfaces, which enables calculation of the recovery temperature distribution on the blade. The second one is a prescribed-wall-temperature run, where the blade's surface temperature is specified as a boundary condition. This prescribed temperature distribution can be obtained by offsetting the recovery temperature distribution derived from the

adiabatic run by a few tens of Kelvins. However, this method is based on the hypothesis that the heat transfer coefficient is independent from the wall temperature, which is often not very realistic [15,16]. A new three-point non-linear method was published by Maffulli and He [17] to account for the HTC's dependency on the wall temperature by introducing a linear relation between the heat transfer and the temperature difference.

$$\dot{q} = (h_0 + j_1 T_w)(T_w - T_{rec}) \tag{3}$$

$$\begin{cases} \dot{q_{w1}} = (h_0 + j_1 T_{w1})(T_{w1} - T_{rec}) \\ \dot{q_{w2}} = (h_0 + j_1 T_{w2})(T_{w2} - T_{rec}) \end{cases} \tag{4}$$

This new formulation is reported in Equation (3), where the locally corrected HTC (with the "j" linear correction terms) value is represented by the first term on the right-hand side. To solve Equation (3) for the HTC, three CFD runs are necessary. The first one is still represented by the adiabatic case for initial calculations of the recovery temperature, and the remaining two consist of two separate prescribed-wall-temperature runs. The HTC distribution on the blade surfaces is then calculated by solving the system in Equation (4) where the flow solutions provide the values for the q and T terms, enabling calculation of the unknowns (h_0 and j_1). In the present study, the specified wall temperature boundary conditions for the two cases listed in Equation (4) are created by offsetting the recovery surface temperature calculated during the adiabatic run, by +50 K and −50 K, respectively. This quantity is chosen as a trade-off between the fitting accuracy (ideally requiring the smallest possible offset) and the stability of the fitting process, which, in turn, becomes less robust the closer together the two prescribed temperature values are.

3. Results

The scanned blades displayed notable differences from the nominal, both in terms of geometry and heat transfer, particularly in the shroud region. Figure 4 shows a comparison of the heat transfer patterns on the design intent rotor and on a typical in-service scans from the present set. By visual inspection of the HTC results from flow simulations carried out on the scans, it can be seen that higher-than-nominal heat transfer zones formed due to the deterioration and modification of the flow conditions. It can be seen in Figure 4A that the many sharp corners on the design intent geometry are marked as high-HTC areas, which is expected since heat transfer is usually higher in stagnation and sharp-turning points. The same corners appear to have been rounded off by erosion in the in-service component. In the baseline design, the inter-platform shroud gap is near zero, and there is no significant amount of flow passing through it.

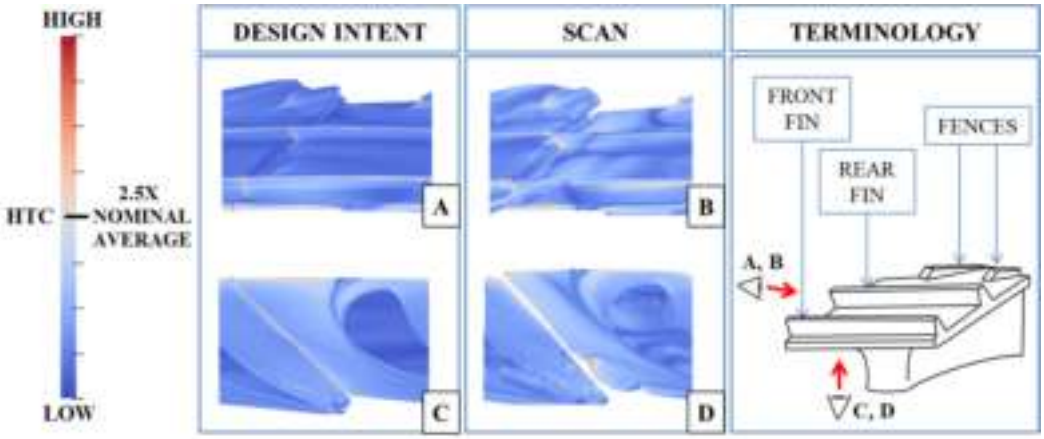

Figure 4. Comparison of the HTC contours on the design intent case (left) against the same contours on one of the scans (right), displaying the outer (**A**,**B**) and inner (**C**,**D**) surfaces of the shroud, where the blade has been sectioned off, to attain a full view of the shroud (pictures distorted).

The figures show that there was a notable overall increase in shroud HTC due to damage. It was found that the overall shroud HTC (calculated as the average HTC on the whole shroud region) on the scanned blades was approximately 11% higher than the corresponding nominal value. The damaged geometry shown in Figure 4B,D also displays a high-HTC patch in the rear part of the shroud gap, where erosion has carved the aforementioned V-shaped opening in the suction-side platform. This patch is clearly visible when looking at the shroud from below (Figure 4D). The contours of Figure 5 show the near-wall gas static temperatures for the same blades used in Figure 4. In the scanned rotor case (Figure 5B,D), the gas that comes in contact with the upper face of the shroud platform is 25 K to 50 K hotter with respect to the nominal case.

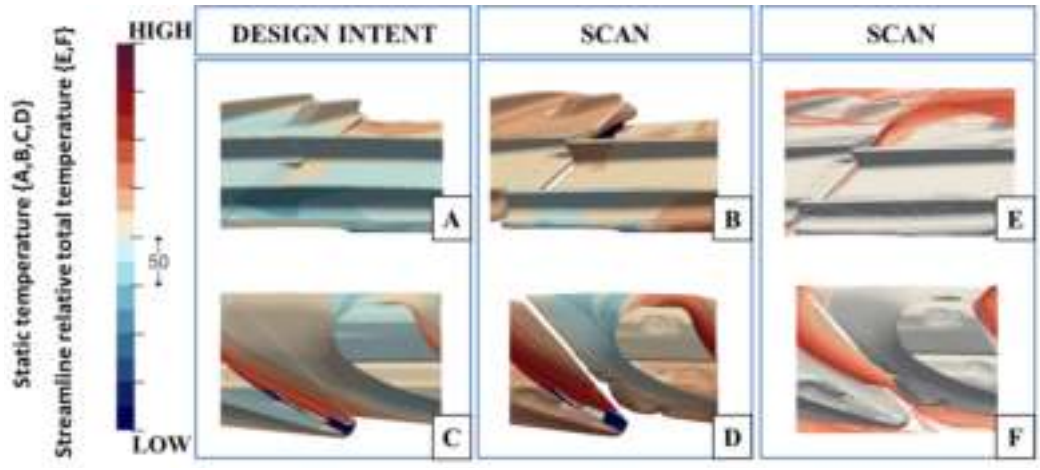

Figure 5. Comparison in terms of near-wall gas static temperatures on the design intent (**A**,**C**) and the same scan shown in (**B**,**D**)—trajectories of the flow particles crossing the shroud gap in the rear portion of the platform are also shown (**E**,**F**) (pictures distorted).

By looking at the contours on the lower face (Figure 5A,C), it can be seen that a stream of high-temperature gas from the main passage reaches and crosses the aft portion of the inter-platform shroud gap, where most of the erosion is taking place. This is confirmed by the streamline visualization of Figure 5E,F, showing the trajectories of the stream particles passing through the rear shroud gap opening. This particular region of the shroud sees a combination of high HTC and high near-wall gas temperatures, which can accelerate the erosion process.

The progressive erosion and formation of the opening can be seen from the views of the bottom face of the shroud displayed in Figure 6, where HTC contours are shown for three in-service blades named "A", "B", and "C", representing the low, medium, and high HTC levels of the set, respectively. HTC levels increasingly worsen with damage, as the amount of hot passage flow that is able to cross the opening in the gap increases. This, for the current set of blades and flow conditions, indicates a degenerative process.

A linear correlation analysis was conducted to determine the effect of the parameters listed in Table 1 on shroud heat transfer. The metric used to quantify the level of HTC on the shroud platforms of the in-service blades is the fraction of surface area with an HTC value exceeding 2.5 times the average value on the nominal shroud. A linear correlation between this metric and the parameters in Table 1 was sought through multiple runs of a random-search algorithm. A linear combination variable was formulated with the set of coefficients achieving the best R^2. The resulting best-fit linear combination called "SDV_{HTC}" (shroud damage variable for HTC correlation) achieved good correlation (R^2 = 0.8706) and is reported in Equation (5), where the terms that ended up having a near-zero (<0.01) coefficient are removed.

$$SDV_{HTC} = 0.2 \cdot S_1 + 0.39 \cdot S_{3max} + 0.04 \cdot T_2 + 0.13 \cdot R_1 + 0.24 \cdot V \quad (5)$$

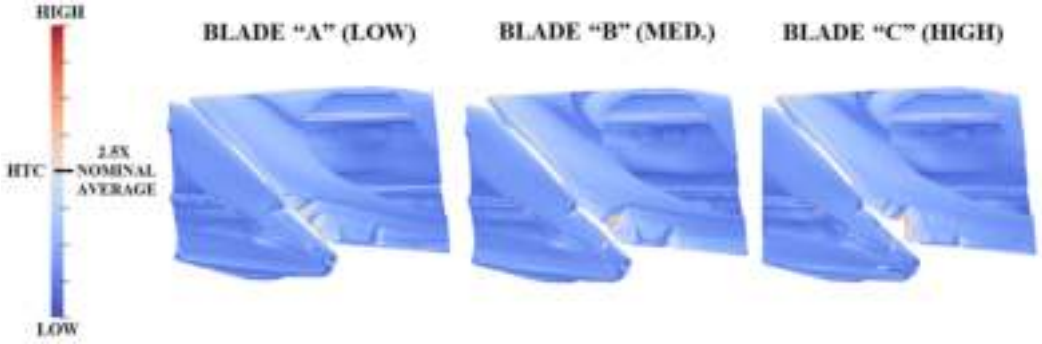

Figure 6. Views of the shroud platform from below in three cases of low (**A**), medium (**B**), and high (**C**) HTC. The surface is colored by HTC value (pictures distorted).

The results shown in Figure 7 indicate that there is significant linear correlation between the combination variable SDV_{HTC} and the shroud surface area with high HTC. The values of the coefficients also indicate which parameters are more associated with the formation of high-HTC regions on the shroud surface. The maximum shroud gap amplitude in the rear half of the platform ($S_{3\max}$) and the volume loss (V) are the most important parameters with coefficients equal to 0.33 and 0.2, respectively. This is in agreement with what can be seen from the contours of Figure 6, where the highest HTC levels are associated with large amounts of erosion in the rear portion of the inter-platform shroud gap, both in terms of depth of the V-shaped opening and metal volume loss.

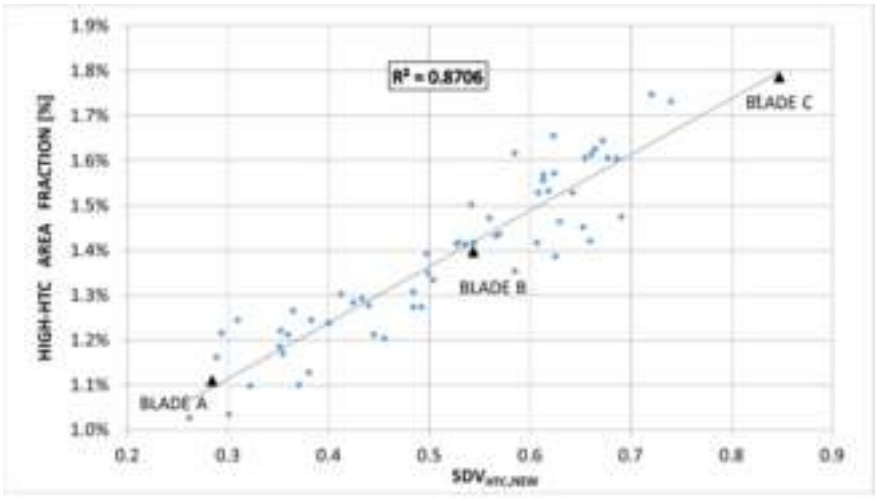

Figure 7. Distribution of the SDV combination variable against the fraction of the high-HTC shroud surface area of the scanned rotors. The trend-line and linearity score are also displayed in the chart. The three blades, A, B, and C, used in Figure 6 are highlighted.

The scanned geometries used in the present analysis also suffered from different degrees of aerodynamic performance loss. Isentropic stage efficiency (Equation (1)) for the present set of blades was correlated against the shroud damage, employing the same parametrization used in the previous section for the HTC analysis. Likewise, a linear combination variable was constructed through a combination of the damage parameters with a set of best-fit coefficients, as reported in Equation (6).

$$SDV_{ETA} = 0.04 \cdot S_1 + 0.27 \cdot S_2 + 0.03 \cdot S_{3max} + 0.03 \cdot T_1 + 0.2 \cdot T_2 + 0.01 \cdot \alpha + 0.08 \cdot R_1 + 0.06 \cdot R_2 + 0.24 \cdot R_3 + 0.04 \cdot V \quad (6)$$

Figure 8 presents the distribution of isentropic stage efficiency for the scanned geometries as a function of the "SDV_{ETA}" variable. Similarly to what was observed with the HTC

correlation study, there was significant correlation between the variable SDV_{ETA} and the isentropic stage efficiency loss with respect to the nominal, with an R^2 of 0.754. In this case, however, the most relevant parameter to aerodynamic performance is the mid-chord shroud gap "*S2*". This finding is in line with that observed in previous work conducted by the authors: a large pressure differential can be found at that particular position between the passage and top cavity flows. This creates a large amount of leakage through the inter-platform shroud gap, which is severely detrimental to aerodynamic performance. A more detailed description of this loss mechanism can be found in [9].

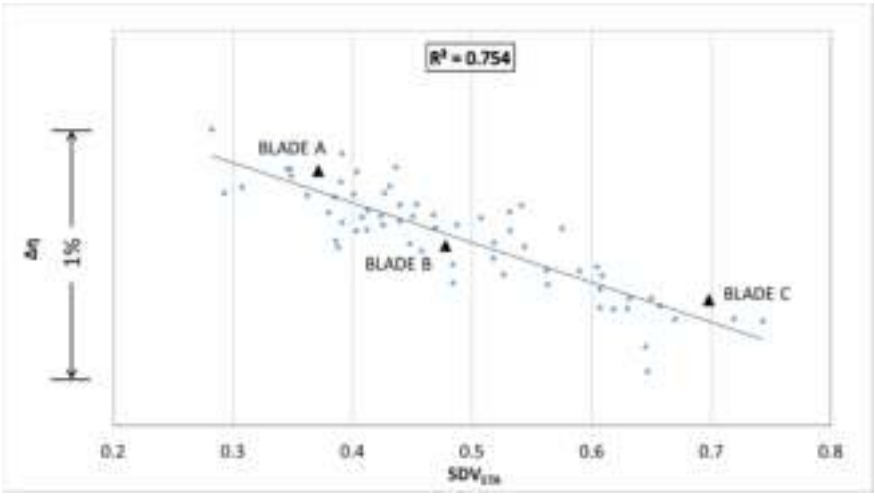

Figure 8. Distribution of the SDV_{ETA} combination variable against the isentropic stage efficiency values of the scanned rotors. The trend-line and linearity score are also displayed in the chart. The three blades, A, B, and C, used in Figure 6 are highlighted.

The trailing edge elongation, R_3, and rear fin tip gap are also associated with a relatively high impact on efficiency for this set of blades. In contrast with what was presented in the previous section for heat transfer, it appears that the depth of the V-shaped opening (S_{3max} parameter) has a low impact when looking at aerodynamic performance. In Figure 8, the points pertaining to the three blades, "A", "B", and "C", shown in Figure 6 are also highlighted. It is interesting to note that the SDV combination variables (Figures 7 and 8) rank these blades in the same order in terms of parametric damage vs. performance, indicating that a low aerodynamic performance is also associated with high heat transfer. It is hypothesized that the twisting of the blades is what causes the initial rotation of the shrouds, which, in turn, results in a wider inter-platform shroud gap. At that point, the blades that display the highest values of the heat transfer coefficient (HTC) are those where flow leaking through the gap was able to carve an opening in the sides of the platforms, through progressive erosion of the metal. The impact of blade twist, and its effect on the component's aerodynamics, was assessed in a previous study [9]. A parameter expressing the amount of twist measured on the blades was included in the present work under the name of "shroud angle". This represents the angle formed by the shroud platform with the machine axis, and this parameter is directly affected by the rotation (twisting) of the blade sections below the shroud. In the present study, it was found that the twist itself has a negligible impact on the HTC on the blade shroud, as demonstrated by the fact that the corresponding correlation coefficient was near-zero and was thus omitted in Equation (5).

4. Conclusions

This work represents the extended version of the paper presented by the authors at the 15th European Turbomachinery Conference (ETC15) in Budapest, Hungary [18].

A series of CFD simulations was conducted on a set of blue-light optical scans of in-service HP turbine rotor geometries from a modern jet engine, with the objective of

identifying the damage modes that are associated with increased heat transfer in the shroud region. All the blades belonging to this set display overall higher (+11%) HTC values on the shroud when compared with the average value measured on the nominal shroud region. All the sharp corners originally present in the nominal design appear to have been rounded off in the in-service blades, as a result of erosion. Furthermore, significant HTC increases were observed locally, particularly in the shroud gap region. Shroud damage levels on the present set of blades have been measured in terms of a set of parameters including shroud gaps, tip gaps, elongation, and volumetric loss. A correlation analysis was then conducted to assess the impact of each parameter on HTC levels, intended as the fraction of shroud surface area with an HTC 2.5 times greater than the average value on the nominal shroud surface. A linear correlation between this measure and the set of parameters was sought, obtaining an R^2 of 0.871, with the largest coefficients being those pertaining to the amplitude of the shroud gap in the rear platform part, and the metal volume loss due to erosion in the same region. A notable isentropic stage efficiency loss was observed with a 1% variability within the set. A linear correlation study was conducted between efficiency and the set of parameters, achieving an R^2 of 0.754, with the highest-ranking coefficient being the S_2 inter-platform shroud gap at the mid-chord. This finding is in line with the results of previous work conducted by the authors on a similar set of scanned geometries.

It is interesting to note that the thermal and aerodynamic aspects are markedly sensitive to damage in different areas of the shroud: the mid-chord gap for the aerodynamic performance and maximum rear platform gap for the thermal exchange performance. It is hypothesized that, due to an initial twist of the shroud platforms due to blade turning, the blades experience an increase in inter-platform shroud gap. Consequently, a stream of hot passage gas is able to cross the shroud gap, reaching the top cavity. Over time, the leakage flow through the rear portion of the shroud gap carves a V-shaped opening in the suction side of the shroud platform, exposing a larger surface of the internal alloy to the erosion process. Analysis of the CFD results revealed that an increase in the size of the opening causes higher local HTC values, which further increases heat exchange and can lead to degenerative acceleration of the erosion process. This study focused on a specific industrial case; however, it describes a process that can be found in modern jet engine turbines in general, by virtue of the extremely high turbine entry temperatures that characterize these engines, and the tendency of modern blades to experience a steep loss in performance during real-world operation.

Due to multi-disciplinary interactions between teams within Rolls-Royce plc, the authors have discovered that many HPT blades from different engines were experiencing what can be defined as a "vicious circle", where deterioration of the HPT blades (deformation and erosion) translates into even faster deterioration rates during the upcoming operation cycles of the engine. For instance, initial geometric deviations from the nominal of the components can cause aerodynamic performance loss (and thus, a thrust deficit), which is compensated by over-throttling the engine to achieve the desired thrust, but this causes higher temperatures on the hot end, which accelerates deterioration rates by causing further damage and geometric deviation. The trigger of this aero-thermal deterioration mechanism was identified to be the initial blade twist below the shroud platform; therefore, it is recommended to periodically monitor this parameter during service. This could be achieved with less-invasive techniques (e.g., borescope analysis). The temperature distribution provided by the combustor also plays a key role in this phenomenon. By shifting the distribution peak towards the inner radii, the temperature of the flow streams that end up crossing the shroud gap may be reduced. This will be the subject of further optimization studies.

Author Contributions: Conceptualization, M.C., S.S. and T.G.; methodology, M.C., S.S. and T.G.; software, S.S.; validation, M.C., S.S. and T.G.; formal analysis, M.C., S.S. and T.G.; investigation, M.C.; resources, S.S. and T.G.; data curation, M.C.; writing—original draft preparation, M.C.; writing—review and editing, M.C., S.S. and T.G.; visualization, M.C.; supervision, S.S. and T.G.; project

administration, S.S. and T.G.; funding acquisition, S.S. and T.G. All authors have read and agreed to the published version of the manuscript.

Funding: This work was conducted within the framework of the NEXTAIR project. The NEXTAIR project has received funding from the European Union's Horizon Europe research and innovation programme under grant agreement No 101056732. Views and opinions expressed are however those of the author(s) only and do not necessarily reflect those of the European Union. Neither the European Union nor the granting authority can be held responsible for them.

Data Availability Statement: The data is protected because of the industrial relevance. For inquiries about the data presented in this paper, please contact the corresponding author.

Acknowledgments: The authors would like to thank Rolls-Royce plc for their support and permission to publish this work.

Conflicts of Interest: The authors declare no conflict of interest.

Nomenclature

CSD	Casing cooling downstream to rotor blade
CSF	Casing cooling upstream to rotor blade
DSH	Hub cavity inflow downstream to rotor blade
HPR	High-pressure rotor
HPS	High-pressure stator
HTEC	HPS trailing edge cooling slot
IPS	Intermediate-pressure stator
ITEC	IPS trailing edge cooling slot
LE, TE	Leading edge, trailing edge
PS, SS	Pressure side, suction side
RANS	Reynolds-averaged Navier–Stokes
TBC	Thermal barrier coating
USH	Hub cavity inflow upstream to the rotor blade

References

1. Bunker, R.S. Integration of New Aero-Thermal and Combustion Technologies with Long-Term Design Philosophies for Gas Turbine Engines. In Proceedings of the US-Ukrainian Workshop on Innovative Combustion and Aerothermal Technologies in Energy and Power Systems, Kiev, Ukraine, 21–26 May 2001.
2. Harvey, N.W. Aerothermal Implications of shroudless and shrouded blades. In *VKI LS 2004-02, Turbine Blade Tip Design and Tip Clearance Treatment*; von Karman Institute for Fluid Dynamics: Rhode-St-Genese, Belgium, 2004; ISBN 2-930389-51-6.
3. Colón, S.; Ricklick, M.; Nagy, D.; Lafleur, A. Geometric Effects of Thermal Barrier Coating Damage on Turbine Blade Temperatures. In Proceedings of the ASME Turbo Expo: Turbomachinery Technical Conference and Exposition, Phoenix, AZ, USA, 17–21 June 2019.
4. Jarrett, A.; Erukulla, V.V.; Koul, A.K. Untwist Creep Analysis of Gas Turbine First Stage Blade. In Proceedings of the ASME Turbo Expo: Turbomachinery Technical Conference and Exposition, Phoenix, AZ, USA, 17–21 June 2019.
5. Guo, X.; Zheng, W.; Xiao, C.; Li, L.; Antonov, S.; Zheng, Y.; Feng, Q.C. Evaluation of microstructural degradation in a failed gas turbine blade due to overheating. *Eng. Fail. Anal.* **2019**, *103*, 308–318. [CrossRef]
6. Kamenik, J.; Shahpar, S.; Keane, A.J.; Hogner, L.; Meyer, M.; Toal, D.J.J. Modelling and Impact of High-pressure Turbine Blade Trailing Edge Film Cooling Hole Variations. In Proceedings of the AIAA Scitech 2020 Forum, Orlando, FL, USA, 6-10 January 2020.
7. Sidwell, V. On the Impact of Variability and Assembly on Turbine Blade Cooling Flow and Oxidation Life. Ph.D. Thesis, Massachusetts Institute of Technology, Cambridge, MA, USA, 2004.
8. Jean-Roch, J.; Nor, N.A.M. A Methodology and Case Study of Outboard Traverse Flame Detection on Aeroderivative Gas Turbines. In Proceedings of the ASME Turbo Expo: Turbomachinery Technical Conference and Exposition, Phoenix, AZ, USA, 17–21 June 2019.
9. Carta, M.; Ghisu, T.; Shahpar, S. High-Fidelity CFD Analysis of In-Serviced Shrouded High-Pressure Turbine Rotor Blades. *J. Turbomach.* **2022**, *144*, 121001. [CrossRef]
10. Glezer, B.; Arts, T. Thermal-mechanical design factors affecting turbine blade tip clearance. In *VKI LS 2004-02, Turbine Blade Tip Design and Tip Clearance Treatment*; von Karman Institute for Fluid Dynamics: Rhode-St-Genese, Belgium, 2004; pp. 1–23. ISBN 2-930389-51-6.
11. Shahpar, S.; Lapworth, L. PADRAM: Parametric Design and Rapid Meshing System for Turbomachinery Optimisation, GT2003-38698. In Proceedings of the ASME Turbo Expo and International Joint Power Generation Conference, Atlanta, GA, USA, 16–19 June 2003; pp. 579–590.

12. Demargne, A.J.; Evans, R.O.; Tiller, P.J.; Dawes, W.N. Practical and Reliable Mesh Generation for Complex, Real World Geometries. In Proceedings of the AIAA 52nd Aerospace Sciences Meeting, National Harbor, MD, USA, 13–17 January 2014.
13. Lapworth, L. Hydra CFD: A Framework for Collaborative CFD Development. In Proceedings of the International Conference on Scientific and Engineering Computation (IC-SEC), Singapore, 30 June–2 July 2004.
14. Cobell, P.A. *Computer Programmers Guide for The BS09/BS29—RRAP Compatible Thermodynamic Subroutines—Issue 7*; CUG BS09; Rolls-Royce plc Internal Report; Rolls-Royce plc.: Derby, UK, 1996.
15. Fitt, A.; Forth, C.; Robertson, B.; Jones, T. Temperature Ratio Effects in Compressible Turbulent Boundary Layers. *Int. J. Heat Mass Transf.* **1986**, *29*, 159–164. [CrossRef]
16. Kays, W.; Crawford, M. *Convective Heat and Mass Transfer*, 2nd ed.; Tata Mc Graw Hill Publishing Co., Ltd.: New York City, NY, USA, 1983.
17. Maffulli, R.; He, L. Dependence of External Heat Transfer Coefficient and Aerodynamics on Wall Temperature For 3D Turbine Blade Passage—GT2014-26763. In Proceedings of the Asme Turbo Expo, Dusseldorf, Germany, 16–20 June 2014.
18. Carta, M.; Ghisu, T.; Shahpar, S. Heat Transfer Analysis of Damaged Shrouded High-Pressure Turbine Rotor Blades. In Proceedings of the 15th European Conference on Turbomachinery Fluid Dynamics and Thermodynamics 2023, Budapest, Hungary, 24–28 April 2023; paper n. ETC2023-321. Available online: https://www.euroturbo.eu/publications/conference-proceedings-repository/ (accessed on 7 June 2023).

Disclaimer/Publisher's Note: The statements, opinions and data contained in all publications are solely those of the individual author(s) and contributor(s) and not of MDPI and/or the editor(s). MDPI and/or the editor(s) disclaim responsibility for any injury to people or property resulting from any ideas, methods, instructions or products referred to in the content.

International Journal of
Turbomachinery
Propulsion and Power

MDPI

Article

Rotor Cascade Assessment at Off-Design Condition: An Aerodynamic Investigation on Platform Cooling †

Hamed Abdeh, Giovanna Barigozzi * and Nicoletta Franchina

Department of Engineering and Applied Sciences, Università degli Studi di Bergamo, 24044 Dalmine, Italy; hamed.abdeh@unibg.it (H.A.); nicoletta.franchina@unibg.it (N.F.)

* Correspondence: giovanna.barigozzi@unibg.it; Tel.: +39-035-2052317

† This manuscript is an extended version of the ETC2023-131 meeting paper published in the Proceeding of the 15th European Turbomachinery Conference, Budapest, Hungary, 24–28 April 2023.

Abstract: Off-design condition of a rotor blade cascade with and without platform cooling was experimentally investigated. The ability of the gas turbine to operate down to 50% to 20% of its nominal intake air flow rate has an important consequence in the change in the inlet incidence angle, which varied from nominal to -20°. Platform cooling through an upstream slot simulating the stator-to-rotor interface gap was considered. The impact of rotation on purge flow injection was simulated by installing fins inside the slot to give the coolant flow a tangential direction. Aerodynamic measurements to quantify the cascade aerodynamic loss and secondary flow structures were performed at Ma_{2is} = 0.55, varying the coolant to main flow mass flow ratio (*MFR*%) and the incidence angle. The results show that losses strongly increase with *MFR*. A negative incidence allows a reduction in the overall loss even when coolant is injected with a high *MFR*. The more negative the incidence, the greater the loss reduction.

Keywords: gas turbine; platform; secondary flows; incidence angle

check for updates

Citation: Abdeh, H.; Barigozzi, G.; Franchina, N. Rotor Cascade Assessment at Off-Design Condition: An Aerodynamic Investigation on Platform Cooling. *Int. J. Turbomach. Propuls. Power* **2023**, *8*, 23. https://doi.org/10.3390/ijtpp8030023

Academic Editor: Sergio Lavagnoli

Received: 5 June 2023
Revised: 10 July 2023
Accepted: 21 July 2023
Published: 22 July 2023

Copyright: © 2023 by the authors. Licensee MDPI, Basel, Switzerland. This article is an open access article distributed under the terms and conditions of the Creative Commons Attribution (CC BY-NC-ND) license (https://creativecommons.org/licenses/by-nc-nd/4.0/).

1. Introduction

Recent trends in power generation aim to reduce the environmental impact of anthropic activities since concerns about the irreversible consequences of global warming have grown over the past few years. The reduction in energy-related CO_2 emissions to limit climate change is at the heart of the energy transition scenario [1]. The competitiveness of renewable energies vs. fossil fuels has been increasing, especially concerning electricity generation. Renewable primary energy (excluding hydro) increased by around 5.1 EJ in 2021 over the world, corresponding to an annual growth rate of 15%, stronger than the previous year's 9% [2]. The contribution of renewable energies is expected to increase further in the upcoming decade. In the short term, gas turbine engines will be the partner of renewable energies and will play a key role in the global energy sector's transformation from fossil-fuel-based to carbon-neutral energy sources. Gas turbines can be used to balance the energy fluctuations of renewables in the grid, as well as provide immediate emission reductions using carbon-neutral fuels like ammonia, hydrogen, or bio-jet fuel.

In order to remain competitive in the market, new-generation turbines must be designed to increase and decrease power rapidly, start up and shut down promptly, and tolerate output reductions while complying with emission regulations. Fast start-up and shutdown, with frequent load adjustments down to reduced minimum load, lead engines to operate under more critical thermo-mechanical conditions with metal distortions, which may heavily impact the fluid dynamics of the secondary air system (SAS) and, consequently, the whole engine.

A better understanding of aero-thermo-mechanical interactions and more accurate predictions of aerodynamics, heat transfer, and cooling flows in variable load operating

conditions are decisive to modern engine designs. Although transient regimes might represent a significant portion of the working time of industrial gas turbines in the next coming energy production scenario, the knowledge of the behavior in reduced minimum load conditions of typical SAS components is currently limited. This is all the more true for their interactions with the main flow path in view of the deformations of stator/rotor parts. Purge air, bled from the latter stages of the compressor, is introduced into the turbine wheel space at a low radius before exiting through the rim seal at the periphery of the discs, immediately upstream of the blade endwall. Labyrinth seals are used as contactless solutions to limit as much as possible the leakage between the stationary and rotating components and to control the cooling air supply to the elements lying in the hot gas path [3]. Many studies document the performance of labyrinth seals, mostly reporting the discharge coefficient as a function of pressure ratio data [4,5], from which simple 1D design correlations can be argued. The flow through labyrinth seals has been shown to be highly sensitive to geometric variations due to changes in rotational speed, and the discharge coefficient varies significantly when the seal clearance is changed by only 2% [6,7]. Off-design flow conditions due to large variations in the clearance must be considered for further improvement of the SAS system and, consequently, of the whole engine performance.

The sealing flow emerging from the stator to the rotor interface gap interacts with the main flow, influencing both the aerodynamic and thermal performance of the rotor cascade. An exhaustive review of the available literature on this topic can be found in [8]. Loss for the blade row increases with the purge flow rate (see, for example, [9]) due to the strengthening of the horseshoe vortex-pressure side leg, which entraps most of the purge air. The increased thermal load on the first rotor has prompted designers to utilize this purge flow not only for sealing purposes but also for cooling. Typically, a ratio of purge mass flow to main flow in the range of 0.7–1.0% is sufficient to effectively seal the disk cavity from the ingress of hot gases, but larger mass fractions may be required for cooling. Indeed, raising the coolant-to-mainstream mass flow rate (*MFR*) has a positive effect on platform cooling (see, for example, [10]). To fully capture all flow and heat transfer phenomena related to purge to main flow interaction across the rotor, investigations on rotating rigs ([11] among others) and stationary blade cascades (e.g., [12]) have been performed over the years. Only a few researchers investigated the impact of variable rotational speed [13] and of slot dimension and shape variation (e.g., [14–19]). To the author's knowledge, the impact of mainstream incidence variation has never been investigated before.

Turbine operating conditions can change due to a different load requirements but also due to different ambient conditions. Whatever the motivation, a reduced mass flow at fixed rotational speed translates into a negative incidence to the first rotor blade cascade for a subsonic flow condition, resulting in a reduction in secondary flows and related losses [20]. But, incidence along the blade span can significantly vary, due to the complex flow coming from the stator, resulting from the interaction between swirling combustion gases, coolant flow emerging from the combustor to stator interface gap, and stator secondary flows [21–23]. All these make the flow pattern interacting with the sealing flow emerging from the stator to rotor interface gap highly complicated, impacting its sealing and cooling capabilities. Lastly, reducing the operability of the turbine to the minimum load could result in a mismatch between what the compressor can deliver to the SAS and what the turbine requires for sealing, potentially compromising the safe operation of the whole engine.

This study experimentally investigates the aerodynamic behavior of a rotor blade cascade with platform cooling through an upstream slot under different incidence angles from nominal to -20°, representing possible off-design flow conditions down to the minimum load. For discrete values of this parameter, the coolant to mainstream mass flow rate *MFR* was varied at fixed density ratio $DR = 1.0$, inlet turbulence intensity level $Tu_1 = 7.5\%$, and downstream Mach number $Ma_{2is} = 0.55$. The decision to keep the main flow rate at a fixed level was motivated by the desire to isolate the effect of incidence. Indeed, varying the

main flow rate would have resulted in a combined change in Reynolds number Re_{2is} and Mach number, making it difficult to identify the different contributions. On the other hand, the presented results constitute a starting point of a wider investigation whose aim is to assess the impact of off-design conditions on both aerodynamic and heat transfer behavior of a rotor blade cascade, also considering gap geometrical modifications. This manuscript is an extended version of the ETC2023-131 meeting paper, published in the Proceedings of the 15th European Turbomachinery Conference, Budapest, Hungary, 24–28 April 2023 [24].

2. Experimental Setup

The experimental campaign was carried out at the continuous running, suction-type wind tunnel for rotor blade cascades shown in Figure 1. This facility and the cascade model (Figure 2) were described in-depth in [25], even if some upgrades were implemented, mostly on the fan section, allowing for a much higher exit Mach number to be reached. The wind tunnel test section hosts a 7-blade cascade typical of first-stage high-pressure turbines: the cascade is characterized by a pitch-to-chord ratio s/C of 0.637 and an aspect ratio H/C of 1.24 (Table 1). The profile of the cylindrical airfoil (Figure 2) replicates the hub section of an industrial first rotor airfoil. Similarly, the blade-to-hub junction is made through a 3D fillet, replicating the real engine design.

Figure 1. Wind tunnel.

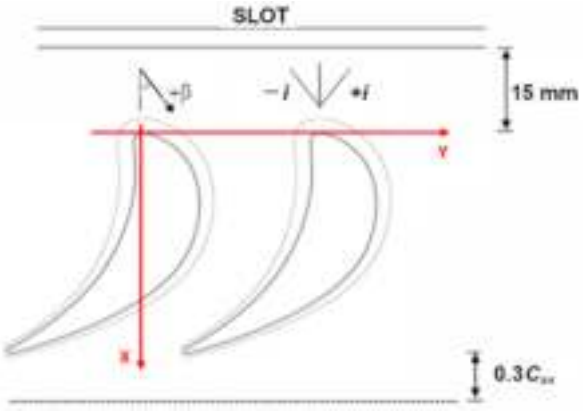

Figure 2. Rotor blade cascade.

Table 1. Cascade geometry and nominal operating conditions.

Cascade Geometry	Operating Conditions
$s/C = 0.637$	$Ma_{2is} = 0.55$
$H/C = 1.24$	$Tu_1 = 7.5\%$
$\beta_1 = -30.87°$	$Re_{2is} = 1.51 \times 10^6$

Tests were carried out at a fixed inlet Mach number $Ma_1 = 0.24$, roughly corresponding to a downstream isentropic Mach number $Ma_{2is} = 0.55$, varying the inlet flow angle from 0° incidence down to −20° incidence, with a regular step of 10°. In order to obtain these discrete incidence variations (−20°, −10°, 0°), the wind tunnel inlet section was re-designed. Figure 3 shows the picture of the lowest tested incidence setup ($i = -20°$).

Figure 3. Setup for $i = -20°$.

The wind tunnel was operated in steady state conditions, artificially increasing the free stream turbulence intensity. This was achieved by installing a grid made of cylindrical rods in the entrance section. The turbulence decay was similar to those shown in [25], providing a $Tu_1 = 7.5\%$ at the leading edge plane, as verified by a two-component Laser Doppler Velocimeter.

Inlet flow condition was monitored 1.0 C_{ax} upstream of the leading edge plane using a 3-hole aerodynamic probe, while exit conditions were monitored by a set of 31 pressure taps distributed over four passages in the tangential direction at a distance of 0.5 C_{ax} from the trailing edge plane. The inlet flow velocity profile and turbulence content were measured by means of a flattened pitot probe ($\delta Ma = \pm 0.01$) and a single wire hot wire probe. Figure 4 shows the resulting inlet boundary layer profile, from which integral parameters were computed, like the boundary layer thickness δ, the displacement thickness δ^*, and the shape factor H_{12}, defined as the ratio between δ^* and the momentum thickness θ. The turbulence intensity and the integral length scale Λ_x are also reported, the latter computed numerically integrating the autocorrelation function of the acquired hot wire signal.

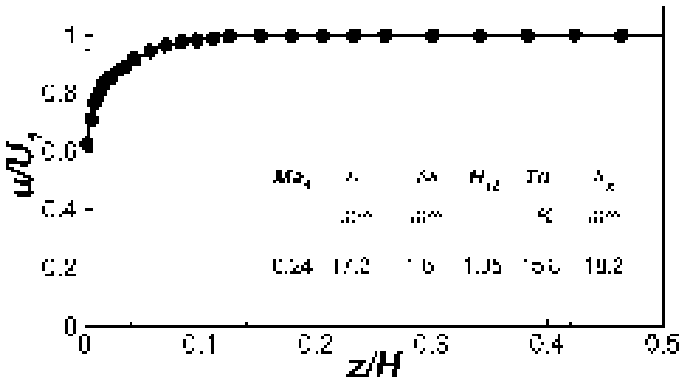

Figure 4. Inlet boundary layer ($X/C_{ax} = -1$).

Rotor platform cooling is accomplished by a slot simulating the stator-to-rotor interface gap (Figure 5). The slot width is 0.042 C, and it is located 0.158 C_{ax} upstream of the leading

edge plane (see Figure 2), covering three and a half blade passages. In order to give the purge flow the proper injection angle, 8 fins were installed inside the slot. The same cooling scheme was previously tested by the authors in a different rotor blade cascade at a lower Ma_{2is} of 0.3 and Tu_1 of 0.6% [26]. The fin's inclination angle has to be selected to simulate as close as possible the combined influence of rotation and injection condition. Generally, doubling the *MFR* would roughly result in also doubling the tangential injection angle at a fixed rotational speed. The nominal value of $-10°$ here considered (see Figure 5-right) roughly represents the design engine operating condition with a 1.0% *MFR*.

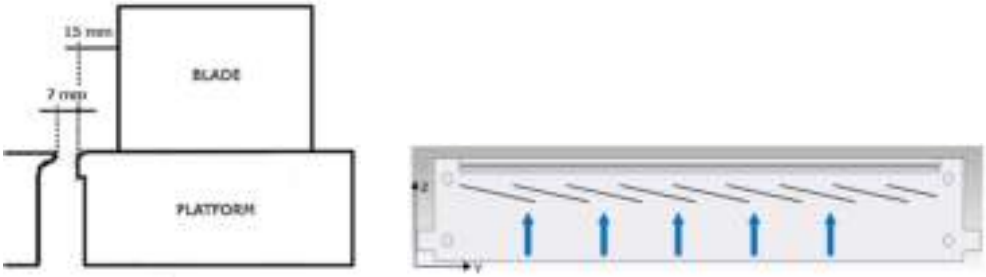

Figure 5. Platform cooling scheme.

Testing conditions included variations in *MFR* up to 2.0% and injecting air at room temperature as coolant. The investigated *MFR* range is large enough to cover any possible engine operating conditions. Coolant mass flow (orifice device $-\delta m_c < \pm 2.1\%$), coolant total pressure ($\delta p_c = \pm 10$ Pa), and temperature ($\delta T_c = \pm 0.5$ °C) inside the plenum were monitored to control the injection conditions. A confidence interval of 95% was always considered for all uncertainty evaluations.

3. Measurement Techniques

Each wind tunnel setup was first tested to assess the actual inlet flow angle and, thus, the incidence of the cascade. Moreover, the purge flow emerging from the slot was also characterized in the design cascade condition when *MFR* = 1%. This is to verify its injection angle and even distribution between adjacent passages. The inlet flow to the mid-span blade-to-blade plane and the flow exiting the slot were characterized by a two-component Laser Doppler Velocimeter (LDV). The LDV system is based on a 300 mW Ar + laser, with sawdust smoke used as seeding particles. Twenty-thousand burst signals were acquired at each location, assuring statistically accurate averages: uncertainties of ±0.14% and ±1.0% for mean and RMS values, respectively, were obtained for a turbulence intensity level of 10% and a 95% confidence level.

The combined impact of mainstream incidence and platform cooling on the aerodynamics of the cascade flow was assessed by traversing a miniaturized 5-hole aerodynamic pressure probe at 30% of the axial chord downstream of the trailing edge plane. The probe was internally designed. The probe head was made by sintering: it has a 2 mm diameter conical nose, advanced 50 mm from the stem. It was in-house calibrated for variable yaw and pitch angles in the range ±25°, varying the Mach number in the 0.05–0.7 interval. Traverses extend over two pitches, covering half of the blade span. Distributions of kinetic energy loss coefficient ($\delta\zeta = \pm 0.3\%$), deviation angle $\beta - \beta_{ms}$ ($\delta\beta = \pm 1°$), and streamwise vorticity Ω_s were derived from local data. The latter was normalized using the inlet flow velocity and the true chord.

4. Results

The experimental results highlighted the aerodynamic behavior of the considered rotor platform cooling scheme at variable *MFR*, in the range between 0.5% and 2.0%, and variable inlet flow incidence from nominal down to $-20°$. For guidance, the inlet flow and the slot exit flow characterizations are first described to estimate the actual incidence of the

cascade. The influence of incidence on secondary flow losses is then discussed, taking the uncooled case as a reference.

4.1. Cascade Inlet Flow Characterization

Figure 6 shows the Mach number and flow angle distributions measured at $X/C_{ax} = -0.5$ along the tangential direction for the three tested incidence values. This upstream location was selected since it is far enough from the blade leading edge to be not influenced by the stagnation effect. Inlet flow angle β is defined with respect to the axial direction: according to [27] incidence definition, a negative incidence corresponds to an inlet flow angle larger or less negative than in the design case. The pitch-wise flow distributions show good stability. Moreover, the averaged inlet Mach number Ma_1 was always close to 0.24, with a maximum variation in the order of ±1.5% over two pitches, showing a good consistency between the three tested incidence cases. Pitch-wise distributions were averaged to obtain the actual incidence angles reported in Table 2. The flow angle measured at the theoretical 0° incidence case is considered as a reference. The slightly negative incidence measured at the theoretical 0° case is probably due to the turbulence generator, which induces a flow deviation upstream of the cascade, similar to [21,28].

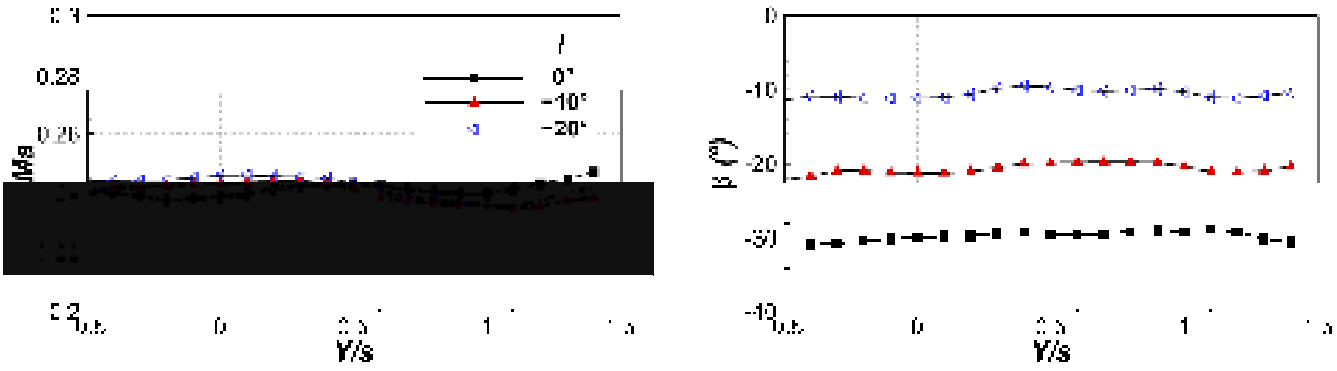

(**a**) (**b**)

Figure 6. Approaching flow characterization ($X/C_{ax} = -0.5$): (**a**) Ma_1; (**b**) β.

Table 2. Inlet incidence angle for variable testing conditions.

i Theoretical (°)	β (°)	*i* Actual (°)
0	−29.8	−1.1
−10	−20.8	−10.1
−20	−10.6	−20.3

4.2. Purge Flow Characterization

In order to check the quality of purge flow ejection from the slot, coolant flow velocity was measured by the LDV system at the slot exit mid-section. Tests were carried out for a coolant to mainstream mass flow rate ratio $MFR = 1.0\%$ at design incidence. Figure 7 shows that the purge flow discharged by the slot is sufficiently periodic in a pitch-wise direction. Pitch-to-pitch variation in the three velocity components was always below ±5.5%. The stagnation effect in front of the blades is evident at $Y/s = 0$ and 1. The mean purge flow angle in the (Y,Z) plane was 12°, computed by averaging the measured velocity components along the pitch-wise direction.

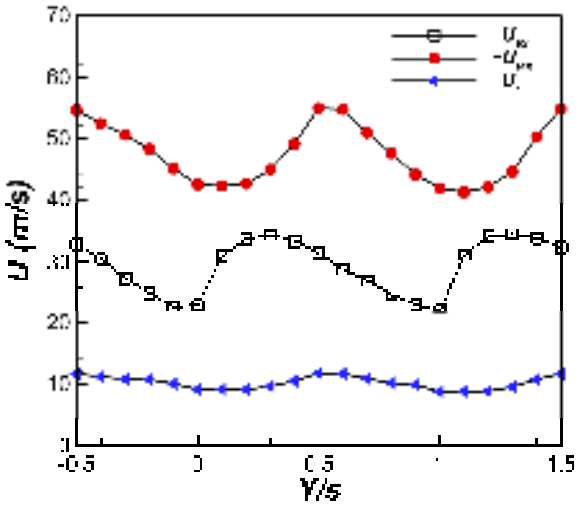

Figure 7. Purge flow characterization at slot exit ($i = 0°$).

4.3. Local Flow Behavior—Uncooled Cascade

Figures 8 and 9 show the kinetic energy loss coefficient (ζ) distributions and the normalized vorticity (Ω) with superimposed the secondary velocity vectors measured downstream of the trailing edge plane for the design ($i = 0°$) and the minimum tested incidence angle of $-20°$ with a continuous platform (i.e., without slot). The $-10°$ incidence case is not reported since it is close to the design case. These data are considered as a reference for the following cooled platform investigation.

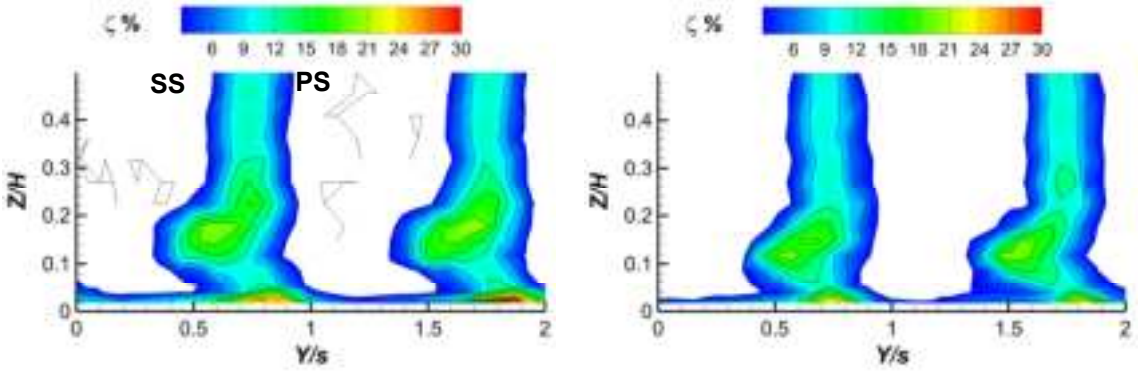

(**a**) (**b**)

Figure 8. Kinetic energy loss coefficient distributions—uncooled case: (**a**) 0°; (**b**) −20° incidence.

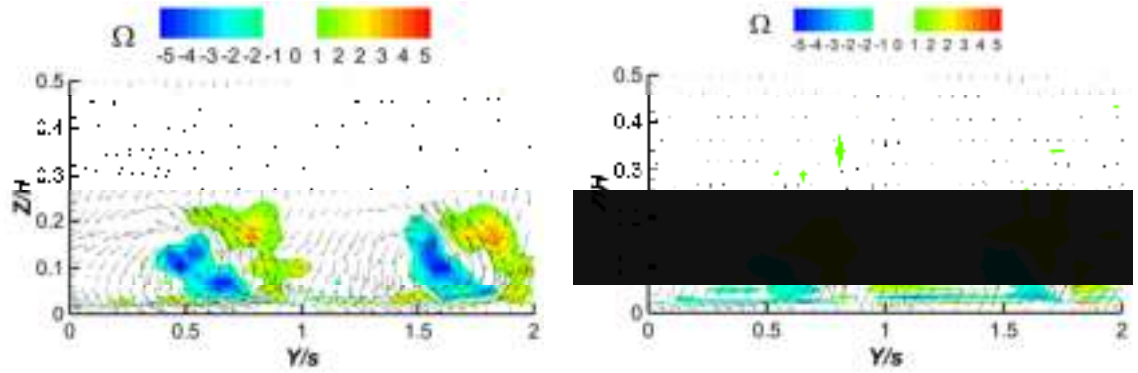

(**a**) (**b**)

Figure 9. Vorticity and secondary velocity vectors—uncooled case: (**a**) 0°; (**b**) −20° incidence.

Two passages are reported to appreciate the flow periodicity at both incidence values tested. Maximum pitch-to-pitch variation in the order of $\Delta\zeta/\zeta = \pm 4\%$ does exist. At design incidence, the flow downstream of the cascade is characterized by a well-defined passage vortex structure that can be easily identified both from the loss concentration on the suction side of the wakes between $Z = 0.1\ H$ and $0.2\ H$ (Figure 8a) and the negative vorticity region in Figure 9a. The counter-clockwise rotating vortical structure with the corresponding positive vorticity related to the trailing shed vortex can also be identified in Figures 8a and 9a. An indication of the presence of a corner vortex can also be seen, corresponding to a second region of high loss close to the wall. A significant passage vortex-related cross flow can also be identified at the wall proximity.

As expected, according to the literature (see, for example, [19]), a decrease in the incidence of negative values gives rise to a reduction in secondary flows. The passage vortex-related loss peaks keep the same intensity but move towards the wall, while the corner vortex intensity reduces (Figure 8b). Vorticity also attenuates together with the endwall cross flow (Figure 9b).

4.4. Local Flow Behavior—Cooled Cascade

Figure 10 shows the impact of incidence variation (from 0° down to −20°) at fixed cascade operating conditions ($Ma_1 = 0.24$ and $Tu_1 = 7.5\%$) for the tested coolant to mainstream mass flow ratio *MFR* values (from 0.5% to 2.0%). Only one pitch is shown, thanks to the good flow periodicity. Figure 11 reports the corresponding vorticity distributions with superimposed secondary velocity vectors. For safe space, only vorticity data belonging to the design (0°) and −20° incidence are reported, as they allow for discussing the general trend even for the −10° case.

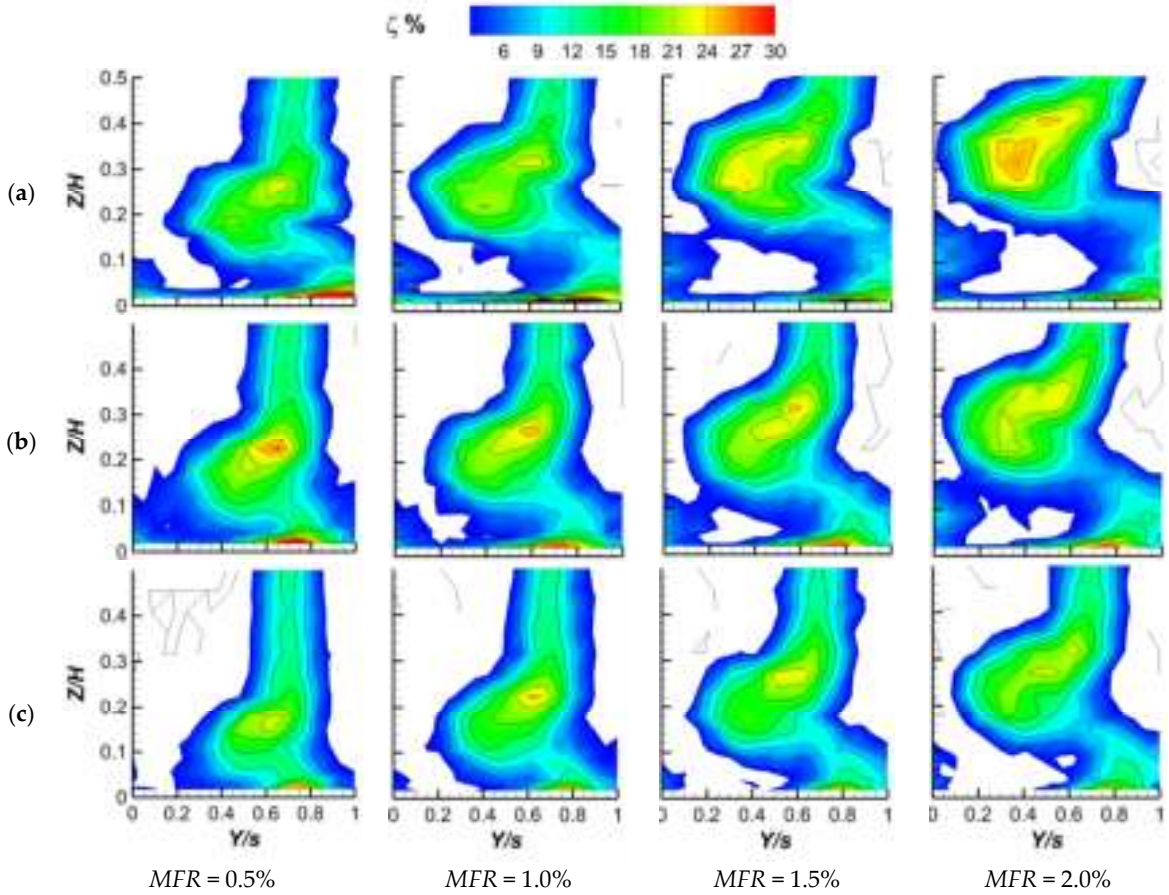

Figure 10. Kinetic energy loss coefficient distributions for variable *MFR*: (**a**) 0°; (**b**) −10°; (**c**) −20° incidence.

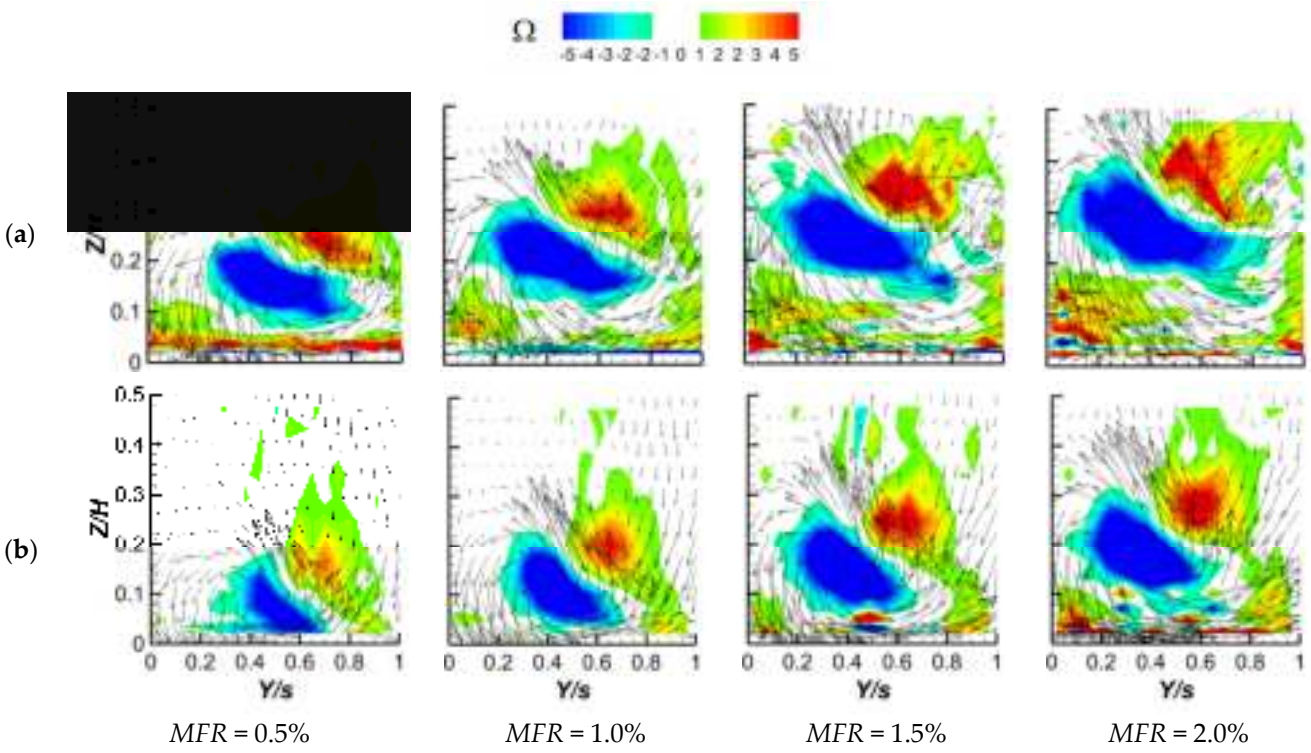

Figure 11. Ω distributions for variable *MFR*: (**a**) 0°; (**b**) −20° incidence.

As expected [12,18,26], at design incidence (Figure 10a), coolant injection always increases the kinetic energy losses; the greater the injected mass flow, the more it increases. Coolant injection with a negative tangential velocity component (i.e., in the same direction of the passage vortex-related endwall cross flow) enforces the passage vortex that lifts from the wall, resulting in a highly three-dimensional flow structure leaving the cascade. This behavior is consistent with the vorticity distributions shown in Figure 11a for the same testing conditions. The measurement plane is dominated by the passage vortex motion providing the subsequent stator a highly skewed approaching flow. The negative vorticity core corresponding to the trailing shed vortex slightly widens, increasing injection, and moves towards midspan, following the passage vortex displacement.

Reducing the incidence angle to −10° and −20° results in similar behavior when injecting the purge flow at rising *MFR* (Figures 10b,c and 11b). But, even if the trend is similar for the two tested negative incidence values, the impact on the loss behavior is different. Thanks to the beneficial effect of negative incidence, the passage vortex-related loss core moves back to the wall and reduces in intensity and size, reducing *i*, as also shown by the vorticity contour maps of Figure 11b. For example, at an *MFR* of 2.0%, the loss peak decreases from about 25% at 0° to 23% at −10° down to about 15% at −20°. Moreover, at the same *MFR* of 2.0% and *i* of −20°, a 2D wake is established at the mid-span section, even if with a limited radial extension. Moreover, the corner vortex trace tangentially moves when incidence reduces from 0° to −10° as a consequence of the reduced endwall cross flow. A further incidence reduction seems to have a marginal impact on the corner vortex.

4.5. Span-Averaged Loss and Deviation Angle

To calculate the span averaged distributions of kinetic energy loss coefficient and deviation angle, local data coming from Figures 10 and 11 (Figures 8 and 9 for the solid case) were mass averaged over the pitch. The results are shown in Figures 12 and 13. Reference data related to the uncooled case (no gap–solid endwall) are also reported (dashed lines). At 0° incidence, a rise in the *MFR* resulted in the increase in the passage vortex loss peak from 6% at *MFR* = 0.5% to 8.5% at *MFR* = 2.0%, and in the migration of the same towards mid span. Both underturning and overturning values increase up to

−/+6°, with angle variations all over the investigated half span. At −10° incidence, similar behavior is observed, even if with some differences: at low injection rates, the increase in deviation angle is reduced when compared to the design case. The loss increase is similar to the 0° case, but the passage vortex-related loss peak is closer to the wall. At high injection rates, a similar overturning and underturning is observed, but its spanwise extension is reduced. Something similar also happens at the −20° incidence case, with a further loss reduction (the loss peak at *MFR* = 2.0% is now about 7.5% against 8.5% of the 0° case) and shifts towards the endwall, which also characterizes overturning and underturning.

Finally, Figures 12d and 13d compare the pitch averaged deviation angle and loss coefficient variations along the span at a fixed *MFR* = 1.0% and variable incidence. These pictures clearly show that injecting the purge flow at 0° incidence results in a significant increase in aerodynamic loss and a huge change in the mean flow angle distribution in the spanwise direction at the exit of the cascade, which could be detrimental to the following stator. Reducing the incidence seems to be advantageous as it reduces losses and helps to confine the change in deviation angle to the endwall region.

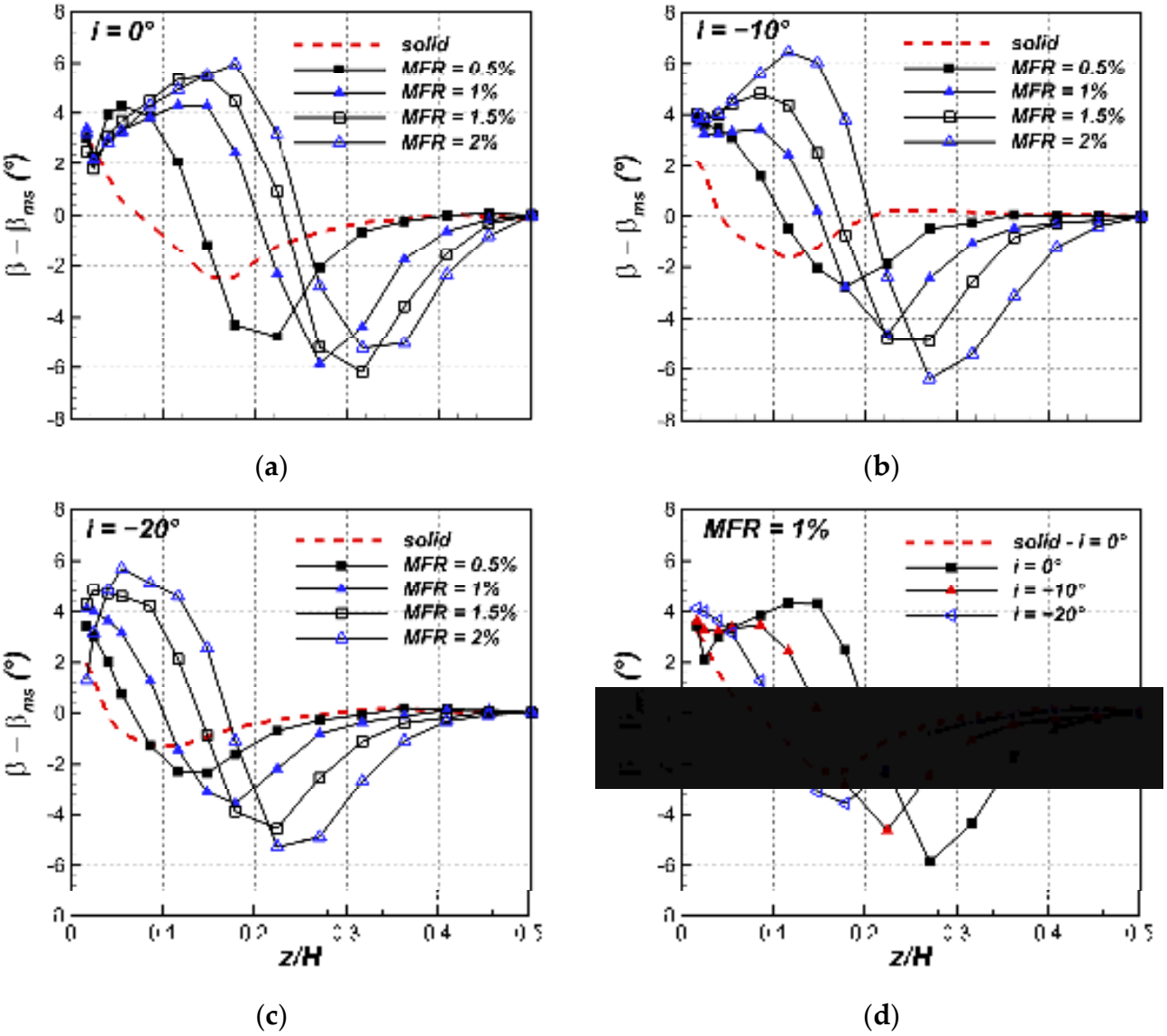

Figure 12. $\beta - \beta_{ms}$ for variable *MFR*: (**a**) 0°; (**b**) −10°; (**c**) −20°; (**d**) at fixed *MFR* = 1.0% and variable *i*.

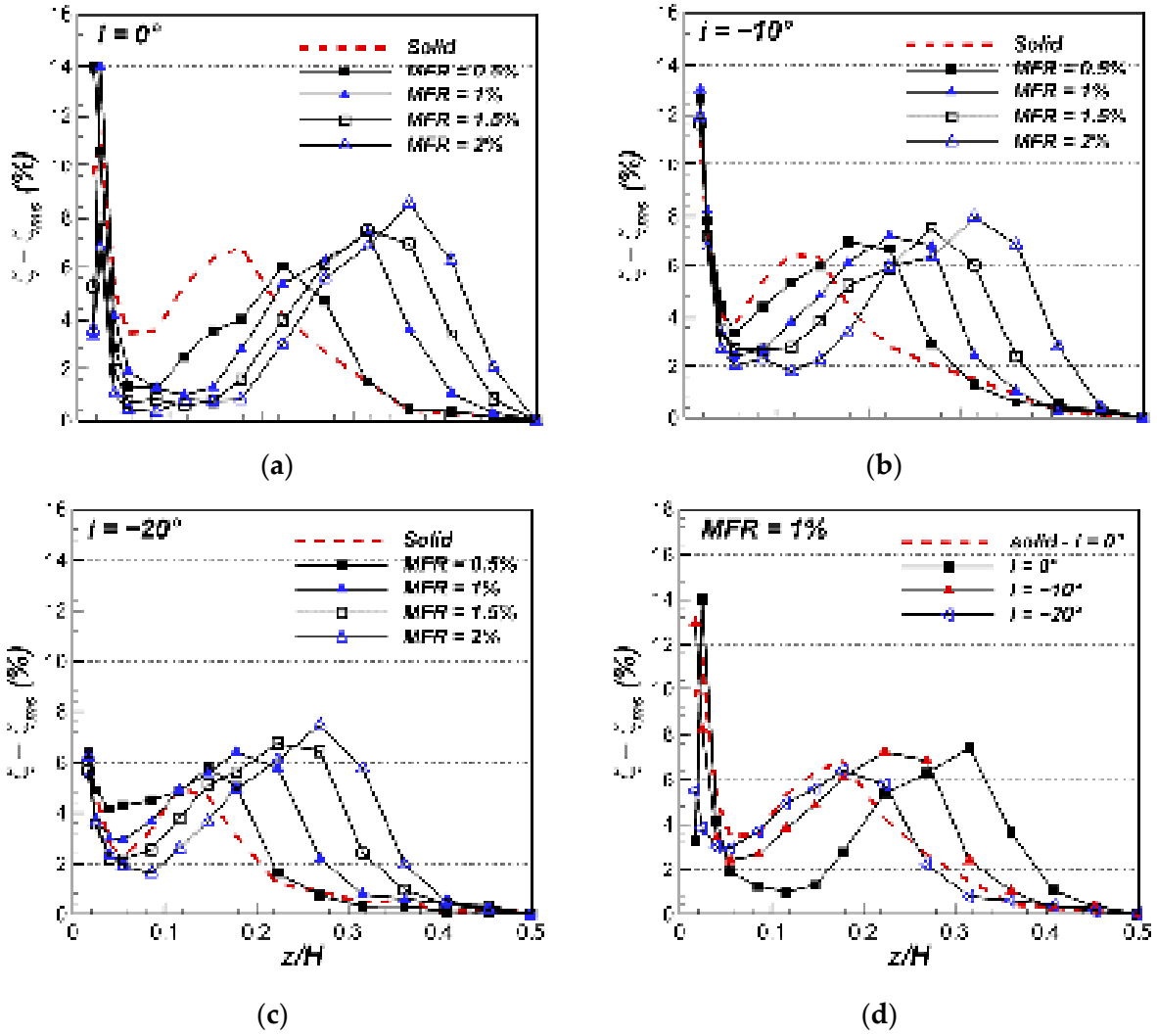

Figure 13. ζ for variable *MFR*: (**a**) 0°; (**b**) −10°; (**c**) −20°; (**d**) at fixed *MFR* = 1.0% and variable *i*.

4.6. Overall Loss

In order to allow more quantitative comparison between the tested operating conditions, overall mass-averaged energy loss coefficients were computed from flow field data. The so-called primary loss coefficient was computed as follows:

$$\bar{\bar{\zeta}} = \frac{\bar{\bar{U}}^{2}_{2is} - \bar{\bar{U}}^{2}_{2}}{\overline{U}^{2}_{2is,ms}} \tag{1}$$

This definition was adopted because the calculated values almost coincide with the thermodynamic loss formulation, which also includes coolant internal losses. A maximum difference of 0.44% was observed at *MFR* = 2.0%. Figure 14 shows the overall mass-averaged kinetic energy loss coefficient for variable *MFR* at constant incidence. The overall loss coefficient continuously increases, raising the *MFR*, similar to [12]. Changing the incidence toward negative values does not modify this general behavior but lowers the loss level, especially at −20°. The impact of a −10° incidence is limited, reducing the overall loss coefficient of about −0.5%, whatever the *MFR*. The loss reduction at −20° is much higher and not constant, reaching −1.6% at *MFR* = 2.0%.

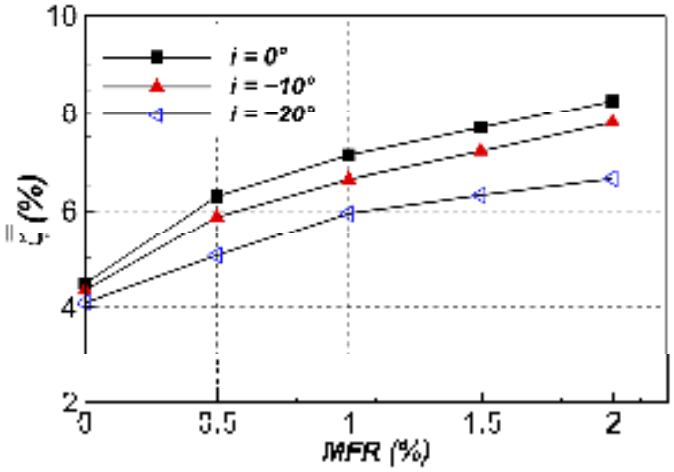

Figure 14. Overall ζ for variable *MFR* and *i*.

5. Conclusions

Aerodynamic measurements were carried out in a rotor cascade under realistic engine conditions (Tu_1 = 7.5%, Ma_{2is} = 0.55) to evaluate the performance of a platform cooling scheme simulating the stator-to-rotor interface gap at various *MFR* values between 0.5% and 2.0% with main flow incidence angles of 0°, −10°, and −20°. The objective was to evaluate the aerodynamic performance of this cooled blade cascade by simulating some effects of low-load operating conditions. The key highlights of the present study are the following:

- As expected, negative incidence reduces secondary flows generation and development across the cascade, reduces the endwall cross flow and overall losses;
- In the investigated *MFR* range, increasing the coolant flow rate is detrimental to the cascade performance; the larger the injected mass flow, the higher the loss. This is whatever the incidence of the cascade. In the worst case, i.e., at design incidence, doubling the *MFR* from 1% to 2% resulted in a loss increase of $\Delta\zeta$ = +1.1%;
- The combination of negative incidence and coolant injection only marginally reduces the loss production at a moderate incidence of −10° ($\Delta\zeta$ = −0.5% as an average);
- A stronger decrease in *i* down to −20° results in a significant reduction in overall losses, particularly significant at high *MFR*. When *MFR* = 2.0%, the loss reduction becomes $\Delta\zeta$ = −1.6%;
- In the presence of a moderate negative incidence, high *MFR* values could not only be responsible for a huge loss generation but also for the deterioration of flow quality approaching the following stator due to huge variations in the spanwise distribution of $\beta - \beta_{ms}$.

Author Contributions: Conceptualization, G.B. and H.A.; methodology, G.B., H.A. and N.F.; investigation, H.A.; data curation, G.B.; writing—original draft preparation, G.B. and N.F.; writing—review and editing, G.B. and N.F.; visualization, H.A.; supervision, G.B. All authors have read and agreed to the published version of the manuscript.

Funding: This research received no external funding.

Data Availability Statement: The data presented in this study are available on request from the corresponding author.

Conflicts of Interest: The authors declare no conflict of interest.

References

1. Ray, A.; De, S. Renewable Electricity Generation—Effect on GHG Emission. In *Encyclopedia of Renewable and Sustainable Materials*; Hashmi, S., Choudhury, I.A., Eds.; Elsevier: Amsterdam, The Netherlands, 2020; pp. 728–735.
2. BP Statistical Review of World Energy 2022, 71st Edition. Available online: https://www.bp.com/content/dam/bp/business-sites/en/global/corporate/pdfs/energy-economics/statistical-review/bp-stats-review-2022-full-report.pdf (accessed on 1 February 2023).
3. Owen, J.M. Air-cooled gas–turbine discs: A review of recent research. *Int. J. Heat Fluid Flow* **1988**, *9*, 354. [CrossRef]
4. Bozzi, L.; D'Angelo, E.; Facchini, B.; Micio, M.; Da Soghe, R. Experimental Investigation on Leakage Losses and Heat Transfer in a Non- Conventional Labyrinth Seal. In Proceedings of the ASME Turbo Expo 2011: Turbine Technical Conference and Exposition, Vancouver, BC, Canada, 6–10 June 2011; Paper No GT2011-46362.
5. Szyma'ński, A.; Wróblewski, W.; Bochon, K.; Majkut, M.; Strozik, M.; Marugi, K. Experimental validation of optimised straight-through labyrinth seals with various land structures. *Int. J. Heat Mass Transf.* **2020**, *158*, 119930. [CrossRef]
6. Nayak, K.C. Effect of Rotation on Leakage and Windage Heating in Labyrinth Seals with Honeycomb Lands. *J. Eng. Gas Turbines Power* **2020**, *142*, 4047180. [CrossRef]
7. Fraczek, D.; Bochon, K.; Wroblewski, W. Influence of Honeycomb Land Geometry on Seal Performance. In Proceedings of the ASME Turbo Expo 2016: Turbomachinery Technical Conference and Exposition, Seoul, Republic of Korea, 13–17 June 2016; Paper No GT2016-57569.
8. Barigozzi, G.; Abdeh, H.; Rouina, S.; Franchina, N. The Aero-Thermal Performance of Purge Flow and Discrete Holes Film Cooling of Rotor Blade Platform in Modern High Pressure Gas Turbines: A Review. *Int. J. Turbomach. Propuls. Power* **2022**, *7*, 22. [CrossRef]
9. Regina, K.; Kalfas, A.I. Experimental investigation of purge flow effects on a high pressure turbine stage. *J. Turbomach.* **2015**, *135*, 041006. [CrossRef]
10. Narzary, D.P.; Liu, K.C.; Rallabandi, A.P.; Han, J.C. Influence of coolant density on turbine blade film-cooling using pressure sensitive paint technique. *J. Turbomach.* **2012**, *134*, 031006. [CrossRef]
11. Schuepbach, R.S.; Abhari, M.G.; Rose, T.; Germain, I.; Raab, J.G. Effects of Suction and Injection Purge-Flow on the Secondary Flow Structures of a High-Work Turbine. In Proceedings of the ASME Turbo Expo 2008: Power for Land, Sea, and Air, Berlin, Germany, 9–13 June 2008; Paper No GT2008-50471.
12. Popovíc, I.; Hodson, H.P. Aerothermal impact of the interaction between hub leakage and mainstream flows in highly-loaded high pressure turbine blades. *J. Turbomach.* **2013**, *135*, 061014. [CrossRef]
13. Suryanarayanan, A.; Mhetras, S.P.; Schobeiri, M.T.; Han, J.C. Film-Cooling Effectiveness on a Rotating Turbine Platform using Pressure Sensitive Paint Technique. *J. Turbomach.* **2010**, *132*, 041001. [CrossRef]
14. Schlienger, J.; Pfau, A.; Kalfas, A.I.; Abhari, R.S. Effects of labyrinth seal variation on multistage axial turbine flow. In Proceedings of the ASME Turbo Expo 2003, Atlanta, GA, USA, 16–19 June 2003; Paper No GT2003-38270.
15. Lynch, S.P.; Thole, K.A. Heat Transfer and film cooling on a contoured blade endwall with platform gap leakage. *J. Turbomach.* **2017**, *139*, 051002. [CrossRef]
16. Barigozzi, G.; Franchini, G.; Perdichizzi, A.; Maritano, M.; Abram, R. Purge flow and interface gap geometry influence on the aero-thermal performance of a rotor blade cascade. *Int. J. Heat Fluid Flow* **2013**, *44*, 563–575. [CrossRef]
17. MacIsaac, G.D.; Sjolander, S.A.; Praisner, T.J.; Grover, E.A.; Jurek, R. Effects of Simplified Platform Overlap and Cavity Geometry on the Endwall Flow: Measurements and Computations in a Low-Speed Linear Turbine Cascade. In Proceedings of the ASME Turbo Expo 2013: Power for Land, Sea, and Air, San Antonio, TX, USA, 3–7 June 2013; Paper No. GT2013-95670.
18. Popović, I.; Hodson, H.P. The effects of a parametric variation of the rim seal geometry on the interaction between hub leakage and mainstream flows in HP turbines. In Proceedings of the ASME Turbo Expo 2012: Power for Land, Sea, and Air, Copenhagen, Denmark, 11–15 June 2012; Paper No. GT2012-68025.
19. Zhang, Z.; Zhang, Y.; Dong, X.; Qu, X.; Lu, X.; Zhang, Y. Flow mechanism between purge flow and mainstream in different turbine rim seal configurations. *Chin. J. Aeronaut.* **2020**, *33*, 2162. [CrossRef]
20. Perdichizzi, A. Mach Number Effects on Secondary Flow Development Downstream of a Turbine Cascade. In Proceedings of the ASME 1989 International Gas Turbine and Aeroengine Congress and Exposition, Toronto, ON, Canada, 4–8 June 1989.
21. Abdeh, H.; Barigozzi, G.; Perdichizzi, A.; Henze, M.; Krueckels, J. Incidence Effect on the Aero-Thermal Performance of a Film Cooled Nozzle Vane Cascade. *J. Turbomach.* **2019**, *141*, 4041923. [CrossRef]
22. Chen, A.F.; Shiau, C.C.; Han, J.C. Turbine blade platform film cooling with simulated swirl purge flow and slashface leakage conditions. *J. Turbomach.* **2017**, *139*, 031012. [CrossRef]
23. Schreiner, B.D.; Wilson, M.; Li, Y.S.; Sangan, C.M. Effect of Purge on the Secondary Flow-Field of a Gas Turbine Blade-Row. *J. Turbomach.* **2020**, *142*, 4047185. [CrossRef]
24. Abdeh, H.; Barigozzi, G.; Franchina, N. Rotor Cascade Assessment at Off-Design Condition: An Aerodynamic Investigation on Platform Cooling. In Proceedings of the 15th European Turbomachinery Conference, Paper N. ETC2023-131, Budapest, Hungary, 24–28 April 2023. Available online: https://www.euroturbo.eu/publications/conference-proceedings-repository (accessed on 4 June 2023).

25. Barigozzi, G.; Perdichizzi, A.; Pestelli, L.; Abram, R. Combined Experimental and Numerical Investigation of the Aero-Thermal Performance of a Rotor Blade Cascade with Platform Cooling. In Proceedings of the ASME Turbo Expo 2019: Turbomachinery Technical Conference and Exposition, Phoenix, AZ, USA, 17–21 June 2019; Paper No. GT2019-91601.
26. Barigozzi, G.; Franchini, G.; Perdichizzi, A.; Maritano, M.; Abram, R. Influence of purge flow injection angle on the aerothermal performance of a rotor blade cascade. *J. Turbomach.* **2014**, *136*, 041012. [CrossRef]
27. Craig, H.R.M.; Cox, H.J.A. Performance Estimation of Axial Flow Turbines. *Proc. Inst. Mech. Eng.* **1971**, *187*, 32–71. [CrossRef]
28. Chavez, K.F.; Packard, G.R.; Slavens, T.N.; Bogard, D.G. Experimentally Determined External Heat Transfer Coefficient of a New Turbine Airfoil Design at Varying Incidence Angles. In Proceedings of the 16th International Symposium on Transport Phenomena and Dynamics of Rotating Machinery ISROMAC 2016, Honolulu, HI, USA, 10–15 April 2016.

Disclaimer/Publisher's Note: The statements, opinions and data contained in all publications are solely those of the individual author(s) and contributor(s) and not of MDPI and/or the editor(s). MDPI and/or the editor(s) disclaim responsibility for any injury to people or property resulting from any ideas, methods, instructions or products referred to in the content.

International Journal of
Turbomachinery
Propulsion and Power

MDPI

Article

Performance Evaluation in a Fully Purged High-Pressure Turbine Stage Using Seed Gas Concentration Measurements †

Filippo Merli, Nicolas Krajnc, Asim Hafizovic and Emil Göttlich *

Institute of Thermal Turbomachinery and Machine Dynamics, Graz University of Technology, Inffeldgasse 25A, 8010 Graz, Austria

* Correspondence: emil.goettlich@tugraz.at

† This manuscript is an extended version of the ETC2023-268 meeting paper in the Proceedings of the 15th European Turbomachinery Conference, Budapest, Hungary, 24–28 April 2023.

Abstract: The efficiency assessment of a high-pressure turbine (HPT) stage is complicated by the presence of upstream and downstream purge flows. In fact, the efficiency calculation is often based on mass flow-averaged values of total temperature at the stage inlet and outlet planes. Moreover, the purge flow distribution in the annulus is usually unknown and therefore assumed to be uniform. This paper presents and applies an alternative method to calculate the efficiency of a fully purged HPT stage. Such a definition relies on seed gas concentration measurements at the HPT stage outlet plane to determine the outlet purge flow distribution. After comparing the alternative method to the standard definition (based on the assumption of uniform purge) for the nominal purge case, the efficiency variation between the case with nominal purge and the case without purge is investigated.

Keywords: high-pressure; turbine; cavity; purge; rim seal; performance; efficiency; concentration effectiveness; seed gas

check for updates

Citation: Merli, F.; Krajnc, N.; Hafizovic, A.; Göttlich, E. Performance Evaluation in a Fully Purged High-Pressure Turbine Stage Using Seed Gas Concentration Measurements. *Int. J. Turbomach. Propuls. Power* **2023**, *8*, 22. https://doi.org/10.3390/ijtpp8030022

Academic Editor: Antoine Dazin

Received: 12 June 2023
Revised: 16 June 2023
Accepted: 10 July 2023
Published: 17 July 2023

Copyright: © 2023 by the authors. Licensee MDPI, Basel, Switzerland. This article is an open access article distributed under the terms and conditions of the Creative Commons Attribution (CC BY-NC-ND) license (https://creativecommons.org/licenses/by-nc-nd/4.0/).

1. Introduction

Efficiency is one of the most important parameters characterizing the performance of a turbine stage, given its direct relation to the amount of extractable power from the flow. When the performance investigation concerns High-Pressure Turbine (HPT) stages, the systematic injection of cooling flows (both from the airfoil surfaces and the stator-rotor cavities) complicates the definition of the stage efficiency, generating ambiguities in the actual and ideal power calculations. Numerous efficiency formulations are available in the open literature. Hartsel [1] proposed a first adaptation of the blade row efficiency definition to account for the presence of cooling flows. Young and Horlock [2] developed around Hartsel's definition, suggesting new versions of the ideal power to better represent the maximum achievable output. Berdanier [3] used a formulation that takes into account the cooling flow distribution at the turbine outlet, thanks to coolant effectiveness data. No matter which definition is adopted, studies about efficiency with stator-rotor cavities mainly focus on the (rotor-) upstream hub purge effect in a 1–1.5 HPT stage. Ong et al. [4] and Jenny et al. [5] described an intensification of the hub rotor passage vortex with increased purge mass flow, combined with a radial migration of this feature towards midspan. Such a phenomenon is generally associated with an efficiency drop; Regina et al. [6] quantified it as −0.8% on the total-to-total isentropic stage efficiency per percent of injected cavity mass flow. Additionally, Dahlqvist and Fridh [7] suggested an analytical expression for the entropy generation due to purge and mainstream flow mixing. There are very few works available involving more or different cavities than the upstream hub one; for instance, Zlatinov et al. [8] numerically studied the effect of the upstream shroud purge injection, concluding that it was partially recovering the associated losses by inhibiting the tip leakage flow. Also, Merli et al. [9] experimentally investigated the total pressure loss across intermediate turbine ducts, varying the injection rates in a fully purged HPT stage. A

thorough review of the open literature yielded no publications regarding the performance of a fully purged HPT stage. This paper aims to fill the gap by analyzing a state-of-the-art HPT stage; integrated into a two-stage, dual-spool test setup. Furthermore, the authors would like to provide the engine designers with an appropriate performance parameter and useful insights into the local effects of stator-rotor cavity cooling. At the beginning of the paper, the experimental setup and the measurement techniques are described. Then, an efficiency definition is introduced, which takes into account the purge distribution after it reaches the annulus. After that, the outcome of the mentioned definition is examined and compared to the standard total-to-total efficiency. Finally, the performance discrepancy between the nominal purge case and the no purge case is assessed. This manuscript is an extended version of the ETC2023-268 meeting paper, published in the Proceedings of the 15th European Turbomachinery Conference, Budapest, Hungary, 24–28 April 2023 [10].

2. Experimental Setup

2.1. Transonic Test Turbine Facility (TTTF)

The experimental data were all obtained in the Transonic Test Turbine Facility (TTTF) at the Institute of Thermal Turbomachinery and Machine Dynamics (ITTM, Graz University of Technology). A scheme of the facility is shown in Figure 1. The test section consists of two independent rotor shafts (HPT and LPT), and it is primarily supplied by a 3 MW compressor station (CS1) in an open circuit configuration. Both shafts are overhanging to facilitate maintenance operations. Furthermore, the entire LPT frame can move axially, allowing for flexibility in the turbine design and simplified access to the rotors during the assembly and disassembly phases. The HPT shaft drives a three-stage radial brake compressor (BC), which provides additional mass flow to the test rig up to a maximum of 22 kg/s and 4 bar, while the power extracted at the LPT shaft is dissipated in a 700 kW water brake (WB). The 560 kW suction blower (SB) at the LPT outlet extends the achievable overall pressure ratio and decouples the turbine exit pressure from ambient pressure oscillations. More details about the TTTF can be found in Neumayer et al. [11] and Hubinka et al. [12].

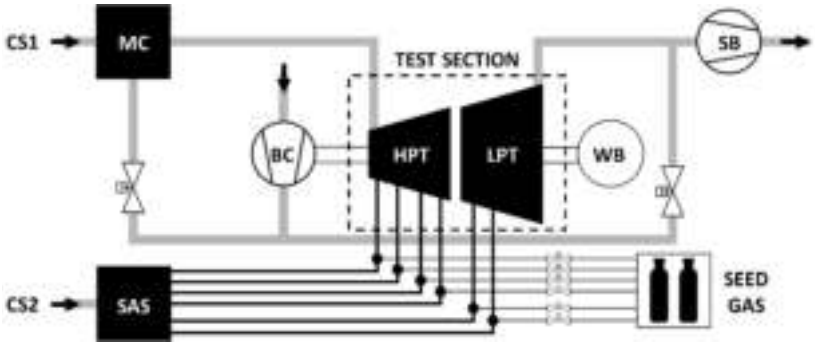

Figure 1. TTTF Layout.

To achieve engine-representative conditions in terms of rotor-stator cavity purge flows, a secondary air system (SAS) was introduced in 2015 (see Steiner et al. [13]). The SAS is supplied by a 1.1 MW electric compressor station (CS2). The secondary air, up to 2.5 kg/s and 12 bar, is split into a cooled and an uncooled strand, feeding two separate reservoirs. A set of servo control valves allows the operator to independently draw the desired ratio of hot and cold air into each cavity line, thus fixing the required purge temperatures and mass flows. As introduced by Patinios et al. [14], the SAS was upgraded in 2019 to enable the injection of tracing gases in the purge lines for concentration measurements. Two pressurized vessels, containing CO_2 and N_2O, respectively, are connected to the purge lines via remotely actuated control valves so that each line can be seeded with the desired concentration of one of those gases.

2.2. Test Vehicle and Operating Conditions

The test setup considered for this study is a two-stage turbine, with the cross-section and meridional view reported in Figure 2. It is constituted by an HPT stage, an intermediate turbine duct with turning vanes and splitter, called the Turbine Vane Frame (TVF), and an LPT counter-rotating blade row. The arrangement is representative of the last HPT stage and first LPT stage in a state-of-the-art turbofan engine, and it includes six purged stator-rotor cavities: four in the HPT stage and two in the LPT stage. The HPT and LPT hub cavities are engine-relevant radial-clearance rim seals, while the shroud cavities are circumferentially continuous axial slots. Out of the whole assembly depicted in Figure 2, this investigation focuses its attention on the HPT side, in particular on the blue, dash-contoured control volume. The control volume is bounded radially by the position of the HPT cavity instrumentation and axially by two $r - \vartheta$ measurement planes: the HPT inlet plane (Plane A) and the HPT outlet plane (Plane B). The detailed description of the measurement apparatus in the control volume is postponed to the Section 3.

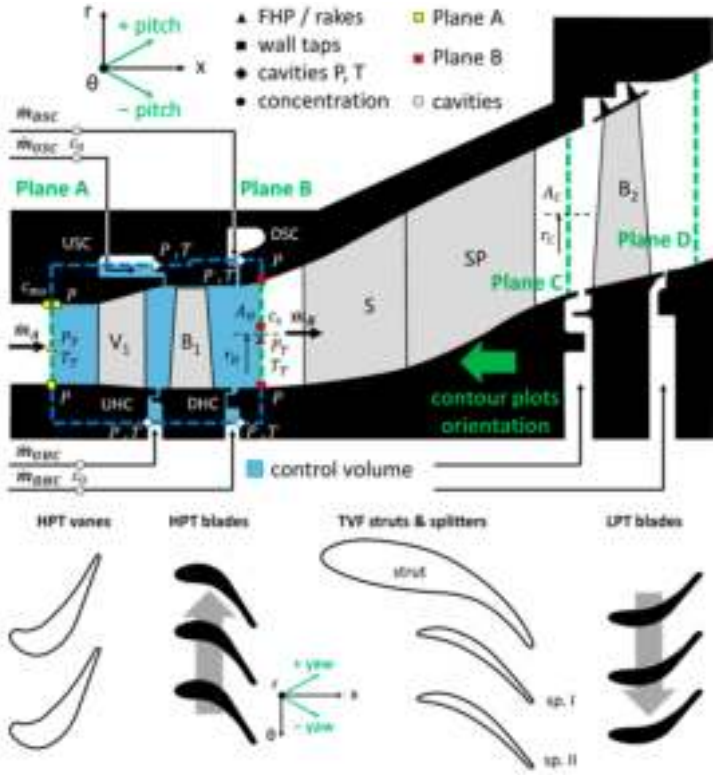

Figure 2. Test vehicle cross-section and meridional view.

The nominal operating conditions, namely the HPT total pressure ratio, the HPT exit Mach number, the TVF Reynolds number, and the HPT purge mass flows, are illustrated in Table 1 (some are given as broad intervals due to confidentiality reasons). Concerning the purge mass flows, they are expressed as fractions of the UHC supply, which is in the range $(0.5\% - 1\%)\dot{m}_A$. In addition to the nominal case, an off-design case was tested, which is obtained by switching off the HPT purge supply while keeping the other parameters in Table 1 unchanged. Throughout the rest of the paper, the nominal case will be referred to as PFR 100% and the case without HPT purge as PFR 0%, where the Purge Flow Ratio is defined as $PFR = \dot{m}_{purge}/\dot{m}_{purge,nominal}$. Finally, it should be mentioned that the LPT cavities are also fed with purge air, and their supply is kept the same during PFR 0% and PFR 100% measurements.

Table 1. Test vehicle nominal operating conditions (PFR 100%) for annulus and cavity flows.

Annulus Flow	Value	Purge Flow	$\dot{m}_{purge}/\dot{m}_{UHC}$ [%]
$P_{T,A}/P_{T,B}$ [−]	2 − 2.5	Upstream Hub (UHC)	100
M_B [−]	0.5	Upstream Shroud (USC)	77
α_B [°]	0 − 5	Downstream Hub (DHC)	102
$Re_B = (\rho v/\mu)_B L_{B-C}$ [−]	1.7×10^6	Downstream Shroud (DSC)	113

3. Measurement Techniques

3.1. Aerodynamic Measurements

The aerodynamic measurements are performed to retrieve pressure, temperature and mass flow values at the HPT stage inlet (Plane A), at the HPT stage outlet (Plane B), and inside the HPT cavities.

In Plane A, the total pressure and the total temperature are acquired by two Kiel-head rakes. The rakes were designed at the ITTM, and they have six equispaced heads each, with an angle of 90° from the radial stem and 0° from the axial direction. The total pressure heads are connected to a NetScanner 9116 Pressure Scanner, while the type K thermocouples in the temperature heads are connected to a NI 9214 Temperature Input Module. For each pressure and temperature head, 30 values are acquired at a sampling frequency of 5 Hz and then averaged, with a final combined uncertainty of ±5 mbar and ±1 K, respectively. Both rakes are traversable across the full 360° extent; however, the circumferential uniformity of the inlet flow, evaluated in a different test campaign, allowed to measure the radial profiles at a fixed location, with a deviation from the circumferentially averaged profiles within the uncertainty of the instruments. In order to capture the steep gradients in the near-endwall flow, the P_T rake profile is integrated with data from boundary layer rakes (hub and shroud, six heads each), as well as wall taps (hub and shroud, seven taps each). On the other hand, the endwall temperature is assumed to be equal to the mixing chamber temperature (MC in Figure 1), due to the thermal conduction between the casings. The resulting radial profiles $P_{T,A}(r)$ and $T_{T,A}(r)$ are represented in Figure 3a for the PFR 100% case.

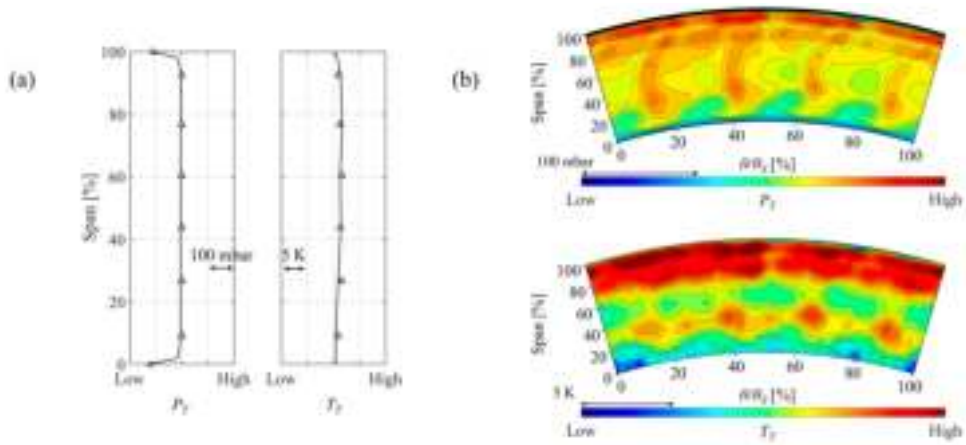

Figure 3. Aerodynamic measurements: (**a**) P_T and T_T radial profiles in Plane A. The triangles and squares indicate the position of rake heads and wall pressure taps, respectively; (**b**) P_T and T_T contour plots in Plane B.

Plane B total pressure and total temperature are acquired with a Five-Hole Probe (FHP). The FHP was manufactured and calibrated at the Institute of Jet Propulsion and Turbomachinery (RWTH Aachen University). The head is inclined 90° from the stem axis and is integrated with a shielded, calibrated type K thermocouple. The 30 values at 5 Hz for each measurement point are acquired with a NetScanner 9116 Pressure Scanner (pressure lines) and a NI 9214 Temperature Input Module (thermocouple), for a combined uncertainty of ±3 mbar and ±0.8 K, respectively. During the experimental tests, the probe

is traversed across a 20 × 60 measurement grid (radial × tangential), which covers a 1 TVF pitch and approximately 90% of the channel height in Plane B. The P_T data from the FHP is complemented by boundary layer rakes readings (hub and shroud rakes, six heads each) and wall taps (hub and shroud walls, seven taps each), while the T_T boundary layer profile is obtained from a RANS simulation of the HPT stage using experimental boundary conditions. The resulting $P_{T,B}(r,\theta)$ and $T_{T,B}(r,\theta)$ contour plots are depicted in Figure 3b.

The pressure and temperature values inside the HPT cavities are acquired with a set of three wall taps and three type K thermocouples, uniformly spaced across the circumference at the radial positions displayed in Figure 2. The acquisition procedure (number of values, sampling rate and acquisition modules) is the same as the one described for the other planes. The estimated uncertainty is ±5 mbar for pressure measurements and ±1 K for temperature measurements.

Finally, the main mass flow and the purge mass flow are measured upstream of the test section: the former is the sum of the readings from two Venturi flow meters (±2%), placed at the exit of the compressor station and brake compressor (see Figure 1); the latter are measured with McCrometer V-Cone Flow Meters (±0.5%), one on every purge supply line. It is also worth mentioning that all the aerodynamic measurements described in this section are taken within a single test run to avoid the application of day-to-day corrections to the dataset.

3.2. Concentration Measurements

Seed gas concentration measurements are performed to characterize the HPT purge flow distribution at the outlet of the HPT stage. The technique consists of the following steps: A certain mass of tracing gas is fed to one of the purge supply lines to reach the desired concentration in the stator-rotor cavity ($c_0 \approx 5\%_{vol.}$ in this study) The preexisting concentration of tracing gas in the unseeded mainstream flow c_{ms} is acquired, as well as the concentration c_s in the location of interest (i.e., Plane B). Finally, the purge flow effectiveness is calculated with:

$$\varepsilon(r,\theta) = \frac{c_s(r,\theta) - c_{ms}}{c_0 - c_{ms}}, \tag{1}$$

where (r,θ) indicates each point of the 2D measurement grid in Plane B. With reference to Equation (1), $\varepsilon = 0$ indicates that no trace of purge flow is present in the analyzed sample; $\varepsilon = 1$ indicates that the sample is completely constituted by purge gas; and $0 < \varepsilon < 1$ indicates that the sample is a mixture of mainstream and purge gas. During the test campaign, c_{ms} was sampled through one of the heads of the Plane A shroud boundary layer rake, while $c_s(r,\theta)$ is obtained by traversing a pitot probe across the same Plane B annulus sector covered by the FHP. The concentration values are measured with a Siemens Ultramat 6E gas analyzer. Such devices are dual-gas (CO_2, N_2O), meaning that two cavities can be seeded in the same test run and the two corresponding $\varepsilon(r,\theta)$ fields can be retrieved from the same set of samples. The estimated uncertainty for the resulting effectiveness values is ±0.003.

After applying the described procedure to all the cavities, the combined effectiveness is calculated as follows: $\varepsilon_c = \varepsilon_{UHC} + \varepsilon_{USC} + \varepsilon_{DHC} + \varepsilon_{DSC}$ and its contour plot is shown in Figure 4. A thorough interpretation of the rotor upstream and downstream purge distribution in Plane B is available in Merli et al. [15]; for the sake of this work, it is important to underline that the downstream purge is responsible for the high-effectiveness bands at Span > 90% and Span < 10% ($\varepsilon_{c,max} \approx 0.2$), while the upstream purge is entrained in the rotor secondary structures, therefore it is far more diluted with mainstream flow ($\varepsilon_{UHC+USC} \ll \varepsilon_{DHC+DSC}$) and it spreads across a larger portion of the annulus (Span > 60% and Span < 40%).

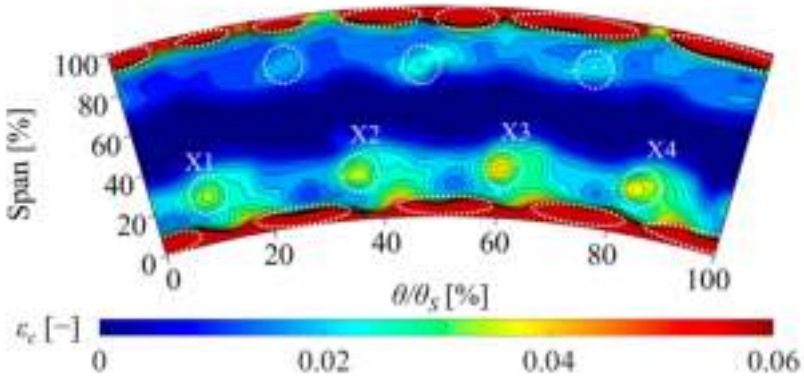

Figure 4. Plane B combined effectiveness ε_c contour plot.

4. Methodology

The Section 4 first presents the definitions of efficiency utilized in this study. The terminology adopted in such definitions refers to Figure 2. After that, the strategy for the efficiency uncertainty calculation is explained.

4.1. Efficiency Calculation

The turbine efficiency is usually intended as the ratio between actual power output and a hypothetical ideal power extracted from the working gas:

$$\eta = \frac{P_{real}}{P_{ideal}}, \quad P_{real} = P_{real,ad} + P_{heat} = P_{shaft} + P_{mech} + P_{windage} + P_{heat}, \tag{2}$$

where P_{heat} is the power dissipated through heat transfer in a nonadiabatic stage; P_{shaft} is the net power delivered at the shaft; P_{mech} is the power loss in the mechanical elements (e.g., bearings); and $P_{windage}$ is the power loss due to friction inside the rotor-stator cavities. For an adiabatic, uncooled stage inside a multistage turbine arrangement, the total-to-total adiabatic efficiency is normally adopted.

$$\eta_{TT} = \frac{P_{real,ad}}{P_{ideal}} = \frac{h_{T,inlet} - h_{T,outlet}}{h_{T,inlet} - h_{T,is,\ outlet}}. \tag{3}$$

Now, it should be clarified that the tested turbine is not adiabatic; however, the present work aims to compare different efficiency definitions and operating conditions rather than providing absolute efficiency values. Additionally, the mentioned conditions only differ in terms of PFR, i.e., in terms of a relatively small amount of mass flow. On such grounds, P_{mech}, $P_{windage}$ and P_{heat} are assumed to be unaltered among the analyzed cases and thus not considered in the efficiency calculation.

4.1.1. Turbine Efficiency–Based on Uniform Purge Assumption (UP)

Applying the same approach behind Hartsel's cooled blade-row efficiency (see Hartsel [1]) to Equation (3), the well-known total-to-total efficiency for cooled stages is obtained:

$$\eta_{\mathrm{UP}}(r,\theta) = \frac{\dot{m}_A\left[\overline{h_{T,A}} - h_{T,B}(r,\theta)\right] + \sum_{k=UHC,\ldots,DSC} \dot{m}_k\left[\overline{h_k} - h_{T,B}(r,\theta)\right]}{\dot{m}_A\left[\overline{h_{T,A}} - h_{T,is,B}(r,\theta)\right] + \sum_{k=UHC,\ldots,DSC} \dot{m}_k\left[\overline{h_k} - h_{k,is,B}(r,\theta)\right]}, \tag{4}$$

where $h_{k,is,B}$ derives from the isentropic, unmixed expansion of the purge flows from their initial supply conditions (inside cavities UHC, USC, DHC and DSC) to the Plane B total pressure. It should be noted that, while Plane B is represented by 2D enthalpy fields, it is not possible to have the same characterization for the main flow and purge flow inlet terms, at least without first performing particle tracking through the HPT stage. For this reason, $\overline{h_{T,A}}$ and $\overline{h_k}$ are averaged scalar values. To avoid the perfect gas approximation

$\Delta h_{T,A-B} = \bar{c}_{P,A-B}\Delta T_{T,A-B}$, which leads to important errors on c_P for the large temperature drops in the tested turbine, enthalpies are calculated using the dry air properties from the CoolProp free digital library (Bell et al. [16]). Given two thermodynamic values, the software can return the other properties of the desired gas, for example, $h_{T,B} = f(P_{T,B}, T_{T,B})$ and $h_{T,is,B} = f(P_{T,B}, s_A)$.

The fundamental limitation of the uniform purge assumption (UP) is that the overall mass flows $\dot{m}_A$ and $\dot{m}_k$ are associated with the enthalpy drop at each (r, θ) point. In other words, the main mass flow and the purge mass flow are assumed to be fully mixed across the measured sector. Such an approximation, which is far from true in real engine HPT stages, is necessary where no information about the purge flow distribution in the annulus is available.

4.1.2. Turbine Efficiency–Based on Measured Purge Distribution (PD)

When the 2D purge flow distribution at the HPT outlet is experimentally or numerically assessed, the mass flow associated with each measured point of Plane B can be separated into multiple contributors: the fraction coming from Plane A main flow, which undergoes the enthalpy drop $\left(\overline{h_{T,A}} - h_{T,B}\right)$; the k fractions coming from the HPT cavities, which experience the drop $\left(\overline{h_k} - h_{T,B}\right)$. This leads to the efficiency definition of Equation (5), based on the measured purge distribution (PD):

$$\eta_{\mathrm{PD}}(r,\theta) = \frac{\dot{m}_A(r,\theta)\left[\overline{h_{T,A}} - h_{T,B}(r,\theta)\right] + \sum_k \dot{m}_k(r,\theta)\left[\overline{h_k} - h_{T,B}(r,\theta)\right]}{\dot{m}_A(r,\theta)\left[\overline{h_{T,A}} - h_{T,is,B}(r,\theta)\right] + \sum_k \dot{m}_k(r,\theta)\left[\overline{h_k} - h_{k,is,B}(r,\theta)\right]}, \tag{5}$$

where $\dot{m}_A(r,\theta)$ and $\dot{m}_k(r,\theta)$ have to fulfill the mass balance for each measurement point and, in turn, the overall mass balance:

$$\dot{m}_B(r,\theta) = \dot{m}_A(r,\theta) + \Sigma_k \dot{m}_k(r,\theta) \quad \overset{\Sigma_i \Sigma_j}{\rightarrow} \quad \dot{m}_B = \dot{m}_A + \Sigma_k \dot{m}_k. \tag{6}$$

In this case, $\dot{m}_B(r,\theta) = (\rho v \Delta A)(r,\theta)$ is determined using the FHP results, while for $\dot{m}_k(r,\theta)$ it is assumed that $\varepsilon_{c,k}(r,\theta) \approx x_k(r,\theta) = \dot{m}_k(r,\theta)/\dot{m}_B(r,\theta)$, i.e., that the purge effectiveness is analogous to the purge mass fraction in the annulus (the density effect is considered negligible). $\dot{m}_A(r,\theta)$ can be then calculated as $\dot{m}_B(r,\theta) - \Sigma_k \dot{m}_k(r,\theta)$.

A similar approach to the efficiency calculation has been proposed by Berdanier [3]. In that work, 1D total pressure and total temperature rake data are utilized both at the HPT stage inlet and outlet. Moreover, the effectiveness profiles are borrowed from a different turbine stage. To the best of the authors' knowledge, this is the first publication involving a full 2D FHP dataset at the HPT stage outlet, also combined with a full 2D effectiveness distribution measured in the same plane.

Finally, in the scenario without purge (PFR 0%), both η_{UP} and η_{PD} collapse into the same equation, analogous to Equation (3):

$$\eta_{\mathrm{PFR\ 0\%}}(r,\theta) = \frac{\dot{m}_A\left[\overline{h_{T,A}} - h_{T,B}(r,\theta)\right]}{\dot{m}_A\left[\overline{h_{T,A}} - h_{k,is,B}(r,\theta)\right]}. \tag{7}$$

4.2. Efficiency Calculation

It is common practice in engineering applications to assess the uncertainty $U_Y = \pm\sigma_Y$ of a derived variable $Y = f(X_1, \ldots, X_n)$ by means of (see for example Holman [17])

$$\sigma_Y = \sqrt{\sum_{m=1}^{n}\left(\frac{\partial f}{\partial X_m}\sigma_{X_m}\right)^2}. \tag{8}$$

In the case of the analyzed HPT stage, $\eta = f(P_{T,A}, T_{T,A}, P_{T,B}, T_{T,B}, P_k, T_k, \dot{m}_B, \dot{m}_k)$. The large number of variables involved and their non-linear dependencies make the evaluation of the partial derivatives rather cumbersome. The uncertainty is therefore calculated numerically through a result perturbation approach: $\Delta Y_m = f(X_1, \ldots, X_m, \ldots, X_n) - f(X_1, \ldots, X_m + \sigma_{X_m}, \ldots, X_n)$ is calculated for each X_m variable and, assuming that $\partial f / \partial X_m \approx \Delta Y_m / \sigma_{X_m}$, the standard deviation becomes

$$\sigma_Y \approx \sqrt{\sum_{m=1}^{n} \Delta Y_m{}^2}. \tag{9}$$

An analogous application of the result perturbation process to the evaluation of an HPT stage efficiency uncertainty can be found in Dénos et al. [18]. The resulting efficiency uncertainty is $U_\eta = \pm 1.28\%$ for the PFR 100% case with the PD definition. A sensitivity analysis revealed that $T_{T,B}$ and $T_{T,A}$ have the highest effect on the uncertainty, followed by $P_{T,B}$ and $P_{T,A}$, while the impact of the purge-related quantities is negligible.

5. Results and Discussion

The Section 5 is divided into three sub-sections: in the first one, the 2D map of the PD efficiency is investigated; in the second one, the outcome of the PD and UP efficiency definitions is compared; and in the third one, the effect of the purge mass flow variation on the HPT stage efficiency is described. The charts and contour plots presented below are built by interpolating the experimental values, reported in the charts as white triangles (FHP), on a finer grid to improve rendering and pattern recognition. The interpolated grid has 0.1° circumferential and 0.1 mm radial steps, while the interpolation algorithm is MATLAB's Modified Akima cubic scheme.

5.1. HPT Stage Efficiency 2D Map

Figure 5 represents the contour plot of PD efficiency, calculated through Equation (5) for the PFR 100% case. The superposed black dashed lines, reported by Merli et al. [15], isolate regions of strongly positive and strongly negative streamwise vorticity in order to understand the impact of the HPT secondary structures on the efficiency map. A high-efficiency circumferential band is located around midspan, between 40% and 70% of the Span; in this core region, the flow is affected the least by the HPT secondary vortices, thus the extracted work is higher. On the other hand, the adjacent bands (20–40% Span and 70–80% Span) appear as regions of low efficiency, with a max-to-min efficiency drop of up to 10 pts between core flow and adjacent bands. In fact, such regions are affected by the HPT rotor's Lower Passage Vortex (LPV_{B1}) and Upper Passage Vortex (UPV_{B1}), which are known to be detrimental to the turbine's performance. For Span > 80%, the efficiency remains low with respect to the core flow; this is ascribed to the hot (see Figure 3b), undeflected Tip Leakage Flow (TLF) between 80% and 90% Span and to the associated Scraping Vortex (SV) at Span > 90%. It is interesting to notice how the LPV_{B1}, UPV_{B1} and TLF bands are not circumferentially uniform, as one would expect from rotating structures investigated with steady-state techniques, but they show a lobed pattern. The reason behind it is the downstream influence of the HPT vanes, which modulate the rotor-related features in a circumferential direction. A clear example of the stator effect is visible below the 20% Span, where the white dotted circles indicate the location of the vanes of the Lower Passage Vortices (LPV_{V1}) at $\theta/\theta_S \approx 25\%$, 50%, 75% and 90%. Finally, the combined analysis of Figures 4 and 5 shows that the purge-rich flow is generally delivering lower efficiency values compared to the undiluted mainstream flow; the white dotted circles are located at the same positions in both plots, revealing that local effectiveness maxima are in fact coupled with local efficiency minima. As discussed in the Section 1, this connection has been observed before in partially purged turbines (UHC purge only), and it is hereby validated for a fully purge turbine as well.

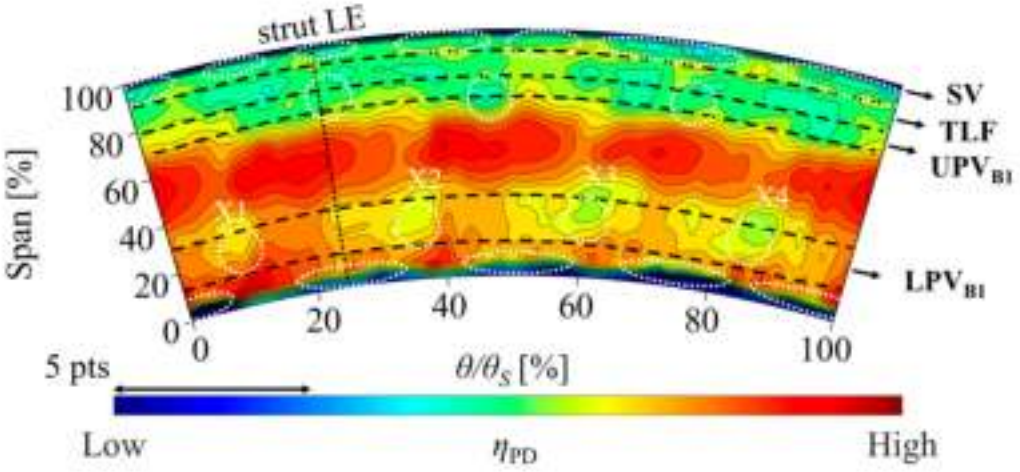

Figure 5. PD efficiency η_{PD} contour plot for the PFR 100% case.

5.2. Efficiency Definition Effect

Further insight into the relationship among purge distribution, secondary flows and efficiency can be retrieved from the discussion of Figure 6. Figure 6a represents the mass-averaged radial profiles of η_{PD} (black solid line) and η_{UP} (black dashed line) for the PFR 100% case, as per Equations (4) and (5), respectively. Additionally, the area-averaged radial profile of ε_c (grey solid line) and the radial position of the secondary flows are depicted. The local differences between η_{PD} and η_{UP} are substantial, with peaks above 1 pt. The highest deviations are located in the core flow region, where $\varepsilon_c \approx 0$, as well as for Span > 90% and Span < 10%, where ε_c is high due to the significant presence of downstream purge. This behavior, also discussed by Berdanier [3], is associated with the different interpretations of the Plane A–Plane B enthalpy drop depending on the local purge flow content. In order to better explain such a concept, the fully mixed effectiveness $\varepsilon_{c,fm} = \varepsilon_{UHC,fm} + \varepsilon_{USC,fm} + \varepsilon_{DHC,fm} + \varepsilon_{DSC,fm}$ is plotted (grey dotted line), where for each cavity k:

$$\varepsilon_{k,fm} = \frac{c_{k,fm} - c_{ms}}{c_0 - c_{ms}}, \quad c_{k,fm} = \frac{\dot{m}_A c_{ms} + \dot{m}_k c_{k,0} + \Sigma_{l=1}^{\text{all cavities}-k} \dot{m}_l c_{ms}}{\dot{m}_A + \Sigma_k \dot{m}_k}. \tag{10}$$

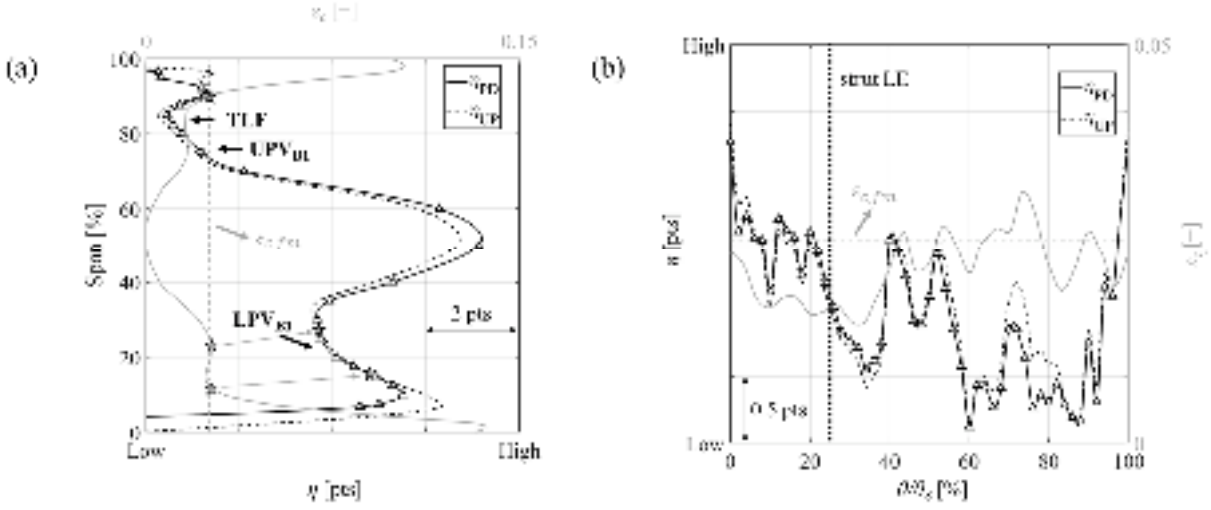

Figure 6. Efficiency definition effect: (**a**) η_{PD}, η_{UP} and ε_c radial profiles; (**b**) η_{PD}, η_{UP} and ε_c circumferential profiles. The triangles represent the FHP measurement grid in Plane B.

The fully mixed effectiveness represents the theoretical condition in which purge flows and annulus flows are perfectly amalgamated, i.e., the purge distribution is uniform across Plane B. By definition, if $\varepsilon_c = \varepsilon_{c,fm}$, then $\eta_{PD} = \eta_{UP}$. The experimental data in Figure 6a show good agreement with this statement: the intercepts between η_{PD} and η_{UP} and between ε_c and $\varepsilon_{c,fm}$ are indicated by grey stars. The slight radial mismatch is ascribed to small purge mass flow variations when the seed gas is injected. In the regions where $\varepsilon_c > \varepsilon_{c,fm}$, η_{PD} takes into account that a higher fraction of the local enthalpy goes into the purge–mainstream flow mixing instead of being converted into power output, thus $\eta_{PD} < \eta_{UP}$ (η_{UP} assumes $\varepsilon_c(r,\theta) = \varepsilon_{c,fm}\ \forall\ r,\theta$). Vice versa, $\eta_{PD} > \eta_{UP}$ where $\varepsilon_c < \varepsilon_{c,fm}$, due to opposite considerations.

Figure 6b shows the mass-averaged circumferential profiles of the same quantities in Figure 6a, preserving colors and line styles. Once again, the highest deviation between η_{PD} and η_{UP} are found when $\varepsilon_c \neq \varepsilon_{c,fm}$, in particular $\eta_{PD} < \eta_{UP}$ if $\varepsilon_c > \varepsilon_{c,fm}$ and $\eta_{PD} > \eta_{UP}$ if $\varepsilon_c < \varepsilon_{c,fm}$, for the same reasons discussed above. It is also noticeable that the segment $10\% < \theta/\theta_S < 40\%$ has lower effectiveness values compared to the symmetric segment $60\% < \theta/\theta_S < 90\%$. The cause is the TVF strut LE potential effect, which produces higher hub pressure at $\theta/\theta_S \approx 25\%$ (black dotted line), reducing the amount of egress flow accumulating there and, in turn, increasing the local efficiency. The same considerations can be qualitatively drawn by looking at Figures 4 and 5, where the lobes X1–X2 have lower effectiveness and higher efficiency than X3–X4. Finally, it should be mentioned that, although the local differences between η_{PD} and η_{UP} are significant, they are only marginally affecting the overall mass-averaged scalar efficiency since $\Delta\eta_{PD-UP} = -0.06\ pts$.

5.3. Purge Flow Variation Effect

Figure 7 displays the efficiency contour plot for the PFR 0% case. The black dashed lines and the white dotted circles indicate the position of the secondary flow structures and of the high-effectiveness spots in the PFR 100% case to help visualize the changes of such features between the two operating conditions. The midspan, high-efficiency core flow region appears to be wider in the case without purge (from 30% Span to 75% Span). The low-efficiency adjacent bands, corresponding to LPV_{B1}-LPV_{V1} and UPV_{B1}-TLF-SV, are instead confined to narrower corridors, closer to the endwalls (Span < 30% and Span > 75%, respectively). Moreover, in the PFR 0% case, the low-efficiency lobes X1–X4 all appear circumferentially shifted against the direction of rotation of the HPT blades due to a yaw angle decrease of about 5° in the region of such flow features, calculated using the FHP data. This is a direct consequence of the HPT purge absence, already observed by Sterzinger et al. [19], at the outlet of a similar stage.

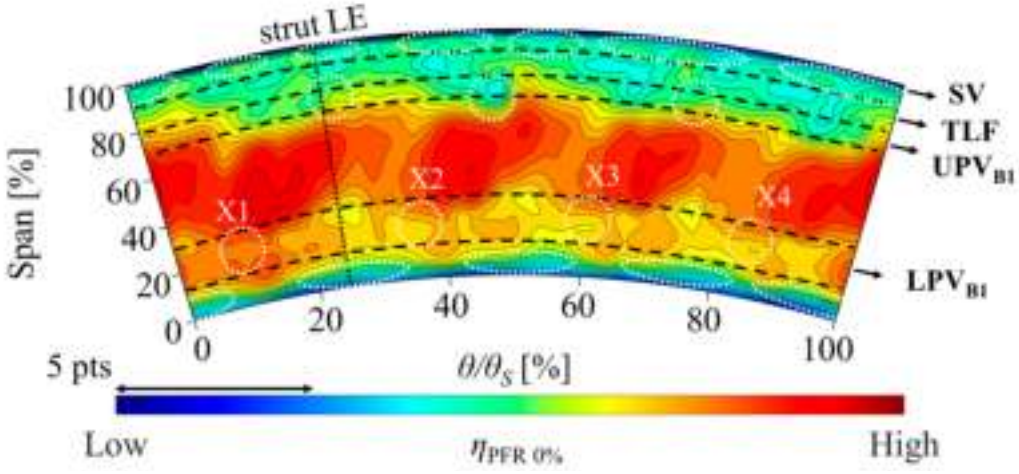

Figure 7. Efficiency contour plot for the PFR 0% case.

For a more quantitative analysis, the mass-averaged radial profiles of $\eta_{PFR\ 100\%}$ and $\eta_{PFR\ 0\%}$ are reported in Figure 8a (black solid lines and black dashed lines, respectively),

together with the radial distribution of $\dot{m}_A/\dot{m}_B$ (grey line). The PD efficiency definition is utilized for $\eta_{\text{PFR 100\%}}$, while η_{PD} and η_{UP} converge into Equation (7) for $\eta_{\text{PFR 0\%}}$. Interestingly, Figure 8a shows that peak core flow efficiency is basically the same for $\eta_{\text{PFR 100\%}}$ and $\eta_{\text{PFR 0\%}}$: the difference lies in the radial extension of the core flow band, unperturbed by LPV_{B1} and UPV_{B1}. In agreement with the existing literature (Regina et al. [6] and Zerobin et al. [20], among others), the upstream hub purge is entrained in LPV_{B1} and UPV_{B1}, intensifying and pushing them toward midspan. In Figure 8a, the LPV_{B1} magnitude and position change between the cases leads to local efficiency deviations up to 2 pts in favor of $\eta_{\text{PFR 0\%}}$, and to a radial offset of about 10% Span. This trend is still recognizable but less pronounced for UPV_{B1}, possibly due to the presence of the TLF, which increases the dilution of the purge air in the annulus gas, smearing out its effect. At the same time, the upstream shroud purge seems to partially suppress the TLF-related losses, producing experimental evidence for the numerical findings of Zlatinov et al. [8]. Finally, it is quite surprising to see that $\Delta\eta_{\text{PFR 100\%}-\text{PFR 0\%}} \approx 1.5\ pts \gg 0$ at approximately 90% Span and 10% Span. This is explained by the action of the downstream purge, which in Plane B is concentrated in the near-endwall regions of the channel (Span > 90% and Span < 10%). In fact, the downstream purge, in combination with the rotor passage vortices radial migration, forces a redistribution of the annulus flow (see the peaks in the $\dot{m}_A/\dot{m}_B$ curve at 15% Span and 85% Span). The outcome is that venae of mainstream, high-performance fluid are enclosed between the rotor passage vortices and the endwalls. Such a phenomenon, clearly recognizable also in Figure 5 at 15% Span, disappears in the absence of purge. The explanation above would also justify why, to the authors' knowledge, such $\Delta\eta > 0$ spots have never been described in the open literature, which mostly focuses on partially purged HPT stages, especially with upstream hub purge only.

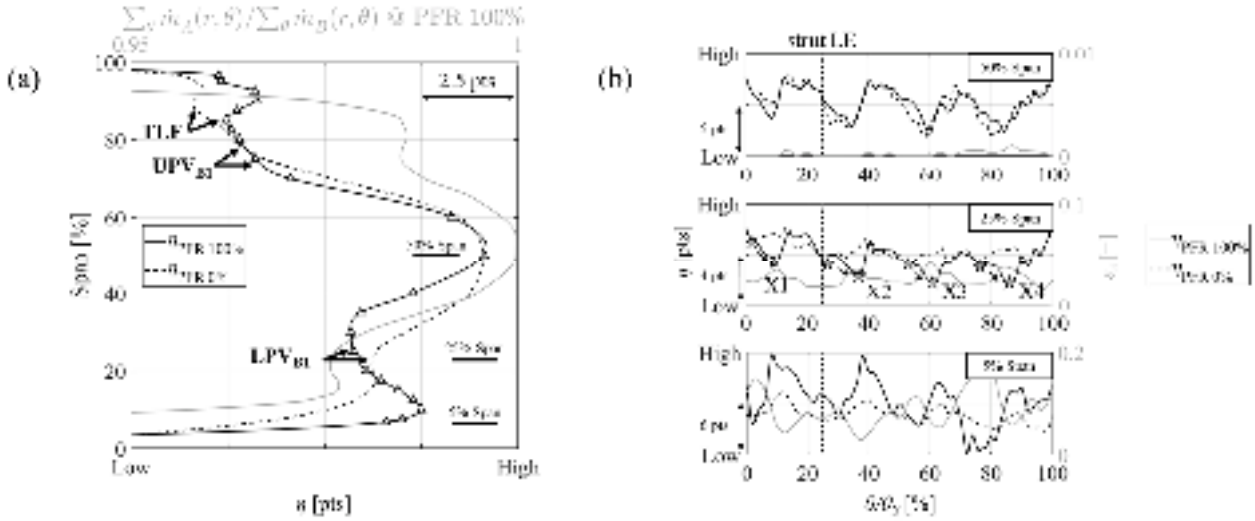

Figure 8. Purge flow variation effect: (**a**) $\eta_{\text{PFR 100\%}}$, $\eta_{\text{PFR 0\%}}$ and $\dot{m}_A/\dot{m}_B$ at PFR 100% radial profiles; (**b**) $\eta_{\text{PFR 100\%}}$, $\eta_{\text{PFR 0\%}}$ and ε_c circumferential profiles at 5%, 25% and 50% Span. The triangles represent the FHP measurement grid in Plane B.

Figure 8b reports the circumferential efficiency profiles for both purge cases at three interesting radial locations: 5% Span, where there is a high concentration of downstream purge; 25% Span, where the upstream purge is transported inside LPV_{B1}; and 50% Span, where almost no cooling air is detected. The grey line in each plot represents the ε_c profile at the corresponding radial position. At 5% Span, $\eta_{\text{PFR 100\%}}$ follows a sinusoidal behavior, in phase opposition with the effectiveness profile and with larger spatial oscillations compared to the $\eta_{\text{PFR 0\%}}$ case. The trend is produced by the HPT vanes since their hub pressure distribution circumferentially clocks the upstream purge egress, thus affecting the efficiency. However, a second contribution is visible in the form of a higher $\eta_{\text{PFR 100\%}}$ mean value in the segment $0\% < \theta/\theta_S < 50\%$, which is caused by the already described potential field of

the TVF strut LE (black dotted line), which locally reduces the downstream purge egress. At 25% Span, the sinusoidal trend of $\eta_{\text{PFR 100\%}}$ persists, but the fluctuations have lower intensity and more circumferential uniformity. In fact, the location is mostly influenced by the upstream hub coolant flow, whose egress and distribution are less affected by the TVF strut. In addition, the local $\eta_{\text{PFR 100\%}}$ and $\eta_{\text{PFR 0\%}}$ minima indicated with grey stars show the circumferential shift of the peaks X1–X4, also noticed in Figure 7. To conclude, at 50% Span, the effectiveness values are low; therefore, the PFR 100% and PFR 0% lines are practically superposed, showing a very good match.

6. Conclusions

The paper investigates the performance of a fully purged HPT stage operating in a dual-spool, engine-representative configuration. An alternative definition (PD) of the total-to-total adiabatic stage efficiency is proposed, which takes into account the HPT purge distribution at the stage outlet, calculated using dual tracing gas concentration measurements. Such a definition is compared to the standard Hartsel-based formulation (UP). The UP efficiency is found to underestimate the stage performance in the core flow, where the purge effectiveness values are below the fully mixed threshold, compared to the PD version. At the same time, the UP definition overestimates the performance of the purge-rich flows because it underpredicts the amount of energy lost in the mixing process. Finally, the PFR 100% case efficiency is compared to one of the PFR 0% cases. The upstream purge is entrained in the rotor passage vortices, magnifying their losses (local differences up to 2 pts in the radial profiles) and shifting them towards midspan (10% Span offset for LPV_{B1}). However, the additional losses of the shroud purge are mitigated by the partial suppression of the TLF. On the other hand, the downstream purge, collected in thin layers next to the endwalls, is responsible for a mass flow redistribution that traps streaks of high-efficiency annulus flow between the rotor passage vortices and the walls. The circumferential distribution in the lower half of the HPT stage outlet plane shows that, in the near-endwall region, rich in downstream purge air, the potential effect of the strut leading edge is beneficial for the efficiency, locally reducing the coolant egress; already at 25% Span, the effect of the strut is negligible, while the HPT vanes downstream propagation are determining the effectiveness maxima (i.e., the efficiency minima).

The authors argue that the PD efficiency better represents the flow physics inside the turbine stage, with deviations between mass-averaged radial profiles of the PD and UP efficiencies up to 1 pts. If the local deviations are remarkable, it should be noted that the overall scalar efficiency values do not appear significantly different. The main drawback of the proposed method is that additional seed gas measurements are necessary. The problem could be sidestepped by using the results from a CFD simulation to calculate the purge mass flow distribution in the annulus (e.g., with particle tracking). Nevertheless, the numerical approach would introduce a different set of uncertainty, modeling and cost issues, which should be carefully evaluated to understand whether computing the purge distribution is more or less convenient than the uniform purge assumption. Another issue is that the calculated uncertainty is relatively high compared to the typical needs of engine manufacturers ($\pm$0.5–1%). This aspect could be improved by optimizing the temperature measurement chain and providing a reliable estimation for the mechanical, windage and heat transfer losses.

Author Contributions: Conceptualization, F.M. and E.G.; methodology, F.M.; software, F.M. and N.K.; validation, F.M., N.K. and A.H.; formal analysis, F.M. and E.G.; investigation, F.M., N.K. and A.H.; resources, N.K. and A.H.; data curation, F.M.; writing—original draft preparation, F.M.; writing—review and editing, E.G.; visualization, F.M.; supervision, E.G.; project administration, E.G.; funding acquisition, E.G. All authors have read and agreed to the published version of the manuscript.

Funding: The project leading to this application has received funding from the Clean Sky 2 Joint Undertaking under the European Union's Horizon 2020 research and innovation program (grant agreement No. 785313).

Institutional Review Board Statement: Not applicable.

Informed Consent Statement: Not applicable.

Data Availability Statement: Restrictions apply to the availability of the data presented in this study. The data are available on request from the corresponding author with prior authorization from GE Aviation.

Acknowledgments: The authors would like to thank M. Daneri and F. Mangini for their contributions to operating the test facility and GE Aviation for their permission to publish this paper.

Conflicts of Interest: The authors declare no conflict of interest. The funders had no role in the design of this study; in the collection, analyses, or interpretation of data; in the writing of the manuscript; or in the decision to publish the results.

Nomenclature

Abbreviations	
HPT, LPT	high-pressure, low-pressure turbine
TVF	turbine vane frame
PFR	purge flow ratio
FHP	five-hole probe
LE	leading edge
LPV, UPV	lower, upper passage vortex
TLF	tip leakage flow
SV	scraping vortex
PD	purge distribution
UP	uniform purge
UHC, USC	upstream hub/shroud cavity
Symbols	
r, θ	radial, tangential coordinate
A, B, C, D	Plane A, B, C, D
P_T, T_T, h_T	total pressure, temperature, enthalpy
L	axial length
c_P	specific heat capacity at constant pressure
η	efficiency
c	concentration
$\dot{m}$	mass flow
ε	effectiveness
Re	Reynolds number
v, M	absolute velocity, Mach number
ρ, μ	density, dynamic viscosity
s	entropy
Subscripts and Superscripts	
1, 2	HPT stage, LPT stage
k, l	cavity indices
0, ms, s	cavity, mainstream, sample
c, fm	combined, fully mixed
$\bar{}$	average
is, ad	isentropic, adiabatic
vol	volumetric

References

1. Hartsel, J. Prediction of effects of mass-transfer cooling on the blade-row efficiency of turbine airfoils. In Proceedings of the 10th Aerospace Sciences Meeting, San Diego, CA, USA, 17–19 January 1972. [CrossRef]
2. Young, J.B.; Horlock, J.H. Defining the Efficiency of a Cooled Turbine. *J. Turbomach.* **2006**, *128*, 658–667. [CrossRef]

3. Berdanier, R.A. Calculating Cooled Turbine Efficiency with Weighted Cooling Flow Distributions. *J. Turbomach.* **2023**, *145*, 061007. [CrossRef]
4. Ong, J.; Miller, R.J.; Uchida, S. The Effect of Coolant Injection on the Endwall Flow of a High Pressure Turbine. *J. Turbomach.* **2012**, *134*, 051003. [CrossRef]
5. Jenny, P.; Abhari, R.S.; Rose, M.G.; Brettschneider, M.; Engel, K.; Gier, J. Unsteady Rotor Hub Passage Vortex Behavior in the Presence of Purge Flow in an Axial Low Pressure Turbine. *J. Turbomach.* **2013**, *135*, 051022. [CrossRef]
6. Regina, K.; Kalfas, A.I.; Abhari, R.S. Experimental Investigation of Purge Flow Effects on a High Pressure Turbine Stage. *J. Turbomach.* **2014**, *137*, 041006. [CrossRef]
7. Dahlqvist, J.E.; Fridh, J. Experimental flow and performance investigations of cavity purge flows in a high pressure tur-bine stage. In Proceedings of the 11th European Conference on Turbomachinery Fluid Dynamics and Thermodynamics, ETC 2015, Madrid, Spain, 23 March 2015.
8. Zlatinov, M.B.; Tan, C.S.; Montgomery, M.; Islam, T.; Harris, M. Turbine Hub and Shroud Sealing Flow Loss Mechanisms. *J. Turbomach.* **2012**, *134*, 061027. [CrossRef]
9. Merli, F.; Hafizovic, A.; Krajnc, N.; Schien, M.; Peters, A.; Heitmeir, F.; Göttlich, E. Aerodynamic Assessment of Turbine Center Frames and Turbine Vane Frames Under the Influence of Purge Flows. In Proceedings of the ASME Turbo Expo 2022: Turbomachinery Technical Conference and Exposition, Rotterdam, The Netherlands, 13–17 June 2022. [CrossRef]
10. Merli, F.; Krajnc, N.; Hafizovic, A.; Göttlich, E. Performance Evaluation in a Fully Purged High-Pressure Turbine Stage Using Seed Gas Concentration Measurements. In Proceedings of the 15th European Turbomachinery Conference, Paper N. ETC2023-268, Budapest, Hungary, 24–28 April 2023; Available online: https://www.euroturbo.eu/publications/conference-proceedings-repository (accessed on 11 June 2023).
11. Neumayer, F.; Kulhanek, G.; Pirker, H.-P.; Jericha, H.; Seyr, A.; Sanz, W. Operational Behavior of a Complex Transonic Test Turbine Facility. In Proceedings of the ASME Turbo Expo 2001: Power for Land, Sea, and Air, New Orleans, LA, USA, 4–7 June 2001. ASME Paper No. GT2000-489. [CrossRef]
12. Hubinka, J.; Santner, C.; Paradiso, B.; Malzacher, F.; Göttlich, E.; Heitmeir, F. Design and construction of a two shaft test turbine for investigation of mid turbine frame flows. In Proceedings of the ISABE, Montreal, QC, Canada, 7–11 September 2009; pp. 7–11.
13. Steiner, M.; Zerobin, S.; Bauinger, S.; Heitmeir, F.; Göttlich, E. Development and Commissioning of A Purge Flow System in A Two Spool Test Facility. In Proceedings of the 12th European Conference on Turbomachinery Fluid dynamics & Thermodynamics, Stockholm, Sweden, 3–7 April 2017. ETC Paper No. ETC2017-115. [CrossRef]
14. Patinios, M.; Merli, F.; Hafizovic, A.; Göttlich, E. The Interaction of Purge Flows with Secondary Flow Features in Turbine Center Frames. In Proceedings of the ASME Turbo Expo 2021: Turbomachinery Technical Conference and Exposition, Online, 7–11 June 2021. [CrossRef]
15. Merli, F.; Hafizovic, A.; Krajnc, N.; Schien, M.; Peters, A.; Heitmeir, F.; Göttlich, E. The Interaction of Main Stream Flow and Cavity Flows in Turbine Center Frames and Turbine Vane Frames. *J. Eng. Gas Turbines Power* **2022**, *145*, 021027. [CrossRef]
16. Bell, I.H.; Wronski, J.; Quoilin, S.; Lemort, V. Pure and Pseudo-pure Fluid Thermophysical Property Evaluation and the Open-Source Thermophysical Property Library CoolProp. *Ind. Eng. Chem. Res.* **2014**, *53*, 2498–2508. [CrossRef] [PubMed]
17. Holman, J.P. *Experimental Methods for Engineers*, 7th ed.; International ed.; McGraw-Hill: New York, NY, USA, 2001.
18. De´nos, R.; Paniagua, G.; Yasa, T.; Fortugno, E. Determination of the Efficiency of a Cooled HP Turbine in a Compression Tube Facility. In Proceedings of the ASME Turbo Expo 2006: Power for Land, Sea, and Air, Barcelona, Spain, 8–11 May 2006; pp. 607–618. [CrossRef]
19. Sterzinger, P.Z.; Zerobin, S.; Merli, F.; Wiesinger, L.; Peters, A.; Maini, G.; Dellacasagrande, M.; Heitmeir, F.; Göttlich, E. Impact of Varying High- and Low-Pressure Turbine Purge Flows on a Turbine Center Frame and Low-Pressure Turbine System. *J. Turbomach.* **2020**, *142*, 101011. [CrossRef]
20. Zerobin, S.; Peters, A.; Bauinger, S.; Ramesh, A.B.; Steiner, M.; Heitmeir, F.; Goettlich, E. Aerodynamic Performance of Turbine Center Frames With Purge Flows—Part I: The Influence of Turbine Purge Flow Rates. *J. Turbomach.* **2018**, *140*, 061009. [CrossRef]

Disclaimer/Publisher's Note: The statements, opinions and data contained in all publications are solely those of the individual author(s) and contributor(s) and not of MDPI and/or the editor(s). MDPI and/or the editor(s) disclaim responsibility for any injury to people or property resulting from any ideas, methods, instructions or products referred to in the content.

International Journal of
Turbomachinery
Propulsion and Power

MDPI

Article

Experimental Analysis of the Three Dimensional Flow in a Wells Turbine Rotor †

Fabio Licheri *, Tiziano Ghisu, Francesco Cambuli and Pierpaolo Puddu

Department of Mechanical, Chemical and Materials Engineering, University of Cagliari, Via Marengo 2, 09123 Cagliari, Italy; t.ghisu@unica.it (T.G.); francesco.cambuli@unica.it (F.C.); puddu@unica.it (P.P.)

* Correspondence: fabio.licheri@unica.it

† This manuscript is an extended version of the ETC2023-148 meeting paper in the Proceedings of the 15th European Turbomachinery Conference, Budapest, Hungary, 24–28 April 2023.

Abstract: An experimental investigation of the local flow field in a Wells turbine has been conducted, in order to produce a detailed analysis of the aerodynamic characteristics of the rotor and support the search for optimized solutions. The measurements were conducted with a hot-wire anemometer (HWA) probe, reconstructing the local three-dimensional flow field both upstream and downstream of a small-scale Wells turbine. The multi-rotation technique has been applied to measure the three velocity components of the flow field for a fixed operating condition. The results of the investigation show the local flow structures along a blade pitch, highlighting the location and radial extension of the vortices which interact with the clean flow, thus degrading the turbine's overall performance. Some peculiarities of this turbine have also been shown, and need to be considered in order to propose modified solutions to improve its performance.

Keywords: Wells turbine; experimental investigation; flow field reconstruction; hot-wire anemometer (HWA); local performance

check for updates

Citation: Licheri, F.; Ghisu, T.; Cambuli, F.; Puddu, P. Experimental Analysis of the Three Dimensional Flow in a Wells Turbine Rotor. *Int. J. Turbomach. Propuls. Power* **2023**, *8*, 21. https://doi.org/10.3390/ijtpp8030021

Academic Editor: Antoine Dazin

Received: 22 May 2023
Revised: 25 May 2023
Accepted: 10 July 2023
Published: 16 July 2023

Copyright: © 2023 by the authors. Licensee MDPI, Basel, Switzerland. This article is an open access article distributed under the terms and conditions of the Creative Commons Attribution (CC BY-NC-ND) license (https://creativecommons.org/licenses/by-nc-nd/4.0/).

1. Introduction

The interest in renewable energy sources has grown even stronger in recent years, due to their relevance to emission reduction. Among all renewable sources, wave energy is one of the most interesting, due to its large availability and relatively high predictability [1]. Thus, in recent decades a number of technological solutions [2], based on different physical principles have been proposed to conveniently harvest and convert this energy source.

The Oscillating Water Column (OWC) principle is probably one of the most applied in Wave Energy Converters (WECs), as highlighted by Ref. [3]. A typical OWC consists of a chamber, partially submerged under the sea free surface and opened at its bottom, which generates an alternating flow in a duct connected to the upper side of the chamber, owing to water-column movement inside the chamber. The vast majority of proposed devices use a turbine to convert the pressure energy of this alternating airflow into mechanical energy, from which electrical energy is produced by means of a generator.

The bi-directional nature of this airflow, and its intrinsic unsteady behavior, represent peculiar issues for the turbine operation. The Wells turbine, proposed by Dr. A. A. Wells [4], provides simplicity of construction and reliability. It is characterized by a symmetrical blade profile staggered at 90 degrees with respect to the axis of rotation, that provides a self-rectifying behavior to the rotor: the direction of the output torque, hence the direction of rotation, is independent of the airflow direction. A number of researchers, such as Refs. [5–8], have investigated the Wells turbine performance in order to understand the limitations and suggest improvements. Nevertheless, the flow field in a Wells rotor has not yet been completely explained, and only few detailed experimental analyses have been presented. More recently, Licheri et al. [9] presented a local reconstruction of the flow field in a Wells turbine by means of an aerodynamic pressure probe, assuming the flow

is two-dimensional, i.e., neglecting the radial velocity component. With a similar probe, Alves et al. [10] conducted an analogous investigation for a biplane Wells turbine.

The present work, which is an extension of our meeting paper [11], aims to reduce the existing gap in the literature with an accurate reconstruction of the flow field in a Wells rotor. An experimental investigation is conducted on a small-size Wells turbine coupled to an OWC simulator housed at the Department of Mechanical, Chemical and Materials Engineering (DIMCM) in the University of Cagliari. The flow field is characterized within a blade pitch both upstream and downstream of the rotor, using a miniaturized hot-wire-anemometer (HWA) probe capable of capturing the three-dimensional flow field, at a fixed operating point, corresponding to a relatively large value of flow coefficient, before stall.

The remainder of the paper is structured as follows. The experimental facility housed at the DIMCM is first presented, followed by a description of the probe and of the measurement technique adopted. Subsequently, the flow reconstruction results and mean radial distribution of velocity components are presented and analyzed. In the final section, the findings are summarized and concluding remarks are provided.

2. Experimental Facility

Experimental tests were conducted in an OWC simulator housed at the DIMCM in Cagliari. The facility is schematized in Figure 1. A piston, driven by a hydraulic system, is moved inside a cylindrical steel chamber, simulating the motion of the water surface as it happens inside an OWC system. At the top of the chamber, a Wells turbine is placed, whose main geometric characteristics are listed in Table 1.

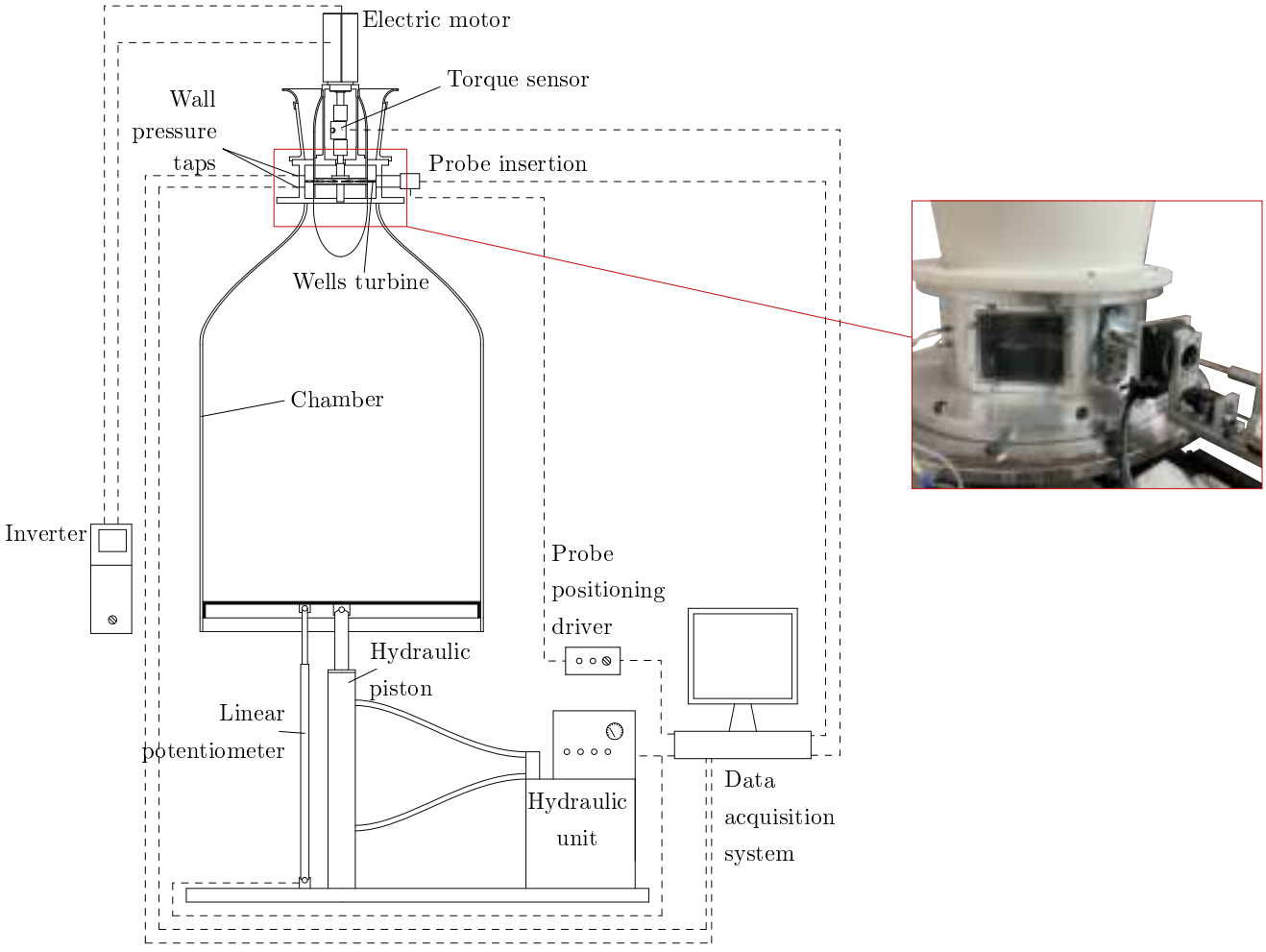

Figure 1. Experimental setup scheme and test section.

Table 1. Geometric parameters of the Wells turbine.

rotor tip dia, D_{tip}	250 mm
rotor hub dia, D_{hub}	190 mm
tip clearance	1 mm
chord length, c	36 mm
number of blades, z	12
airfoil profile	NACA 0015
solidity	0.625
sweep ratio	0.5 (18/36)
hub-to-tip ratio, ν	0.76

The experimental facility is fully instrumented: a wire potentiometer is used to record the piston displacement and to feedback-control the hydraulic unit driving the piston movement; wall pressure taps are placed upstream and downstream of the rotor; a torque sensor with a built-in encoder is placed between the turbine and motor shafts in order to measure the turbine output torque and its rotational speed; a slot has been made in the test section, in order to simplify probe insertion near the rotor. The maximum uncertainties of these measured variables have been estimated as follows:

- 0.3% of transducer's full-scale (1 kPa) for the wall pressure measurement at the ambient side;
- 0.2% of transducer's full-scale (7 kPa) for the wall pressure measurement at the piston side;
- 0.1% of sensor's full-scale ($\pm$2 Nm) for the output torque;
- $\pm$0.1% of sensor full scale (1000 mm) for the piston position.

The facility configuration is suitable for reproducing different shapes of piston motion by regulating the hydraulic unit's parameters. A sinusoidal piston motion is typically set to simulate a regular wave, as done in Refs. [9,12], while a triangular motion is set in this study to obtain a constant flow speed for a finite time interval. Both the amplitude and the period of the piston motion can be adjusted through the settings of the hydraulic unit.

3. Measuring Technique

The local flow field near the rotor, both upstream and downstream, was reconstructed by means of a slanted hot-wire-anemometer (HWA) probe, a DANTEC type 55P12. The sensor was placed at an axial distance of 5.5 mm from the blade chord, both upstream and downstream of the rotor.

The rotating slanted HW technique [13–15] was adopted for the reconstruction of the flow field. Using the relations proposed by Jøorgensen [16], the method allows the measurement, in a given steady or periodic flow field, of the three velocity components of the mean flow and the six components of the Reynolds stress tensor. As this measuring technique uses probes with only one sensor, the flow distortion due to the probe size is reduced [17]. Independent measurements are obtained using different orientations of the sensor, by rotating the probe around its stem at different angles. More than three different measurements are generally used, in order to reduce the error associated with data reduction, thus requiring an overdetermined system of equations to be solved. Measurements were performed only during the outflow phase, by scanning the blade span at 20 radial positions not equally spaced in order to properly reconstruct the flow field in the boundary layer region near the walls. At each radial position, seven different angular positions of the probe were considered. A motorized system has been used to move the probe radially and to orient the probe around its axis.

The instantaneous cooling velocities have been obtained from the instantaneous voltage signals, using a calibration curve approximated with a fourth degree polynomial equation, thus obtaining a better approximation and reducing uncertainties with respect to the inversion of the law proposed by King [18], as demonstrated by Erriu et al. [19]. The modified Jørgensen's law of Ref. [20] has been used to relate the velocity components, in

the sensor's reference frame system, with the effective cooling velocity. The values of the directional sensitivity coefficients have been evaluated experimentally by performing the angular calibration of the probe in an open wind tunnel. Angular calibration curves have thus been used to calculate the angular sensitivity coefficient of the Jøorgensen's law, as a function of yaw and pitch angles. The directional sensitivity coefficients are considered dependent on pitch and yaw angles, while in Ref. [16] they were proposed constants. More details on relations used to represent the angular calibration curves can be found in Ref. [20].

Uncertainties in hot-wire measurements have been estimated following Ref. [19], by considering: (a) errors introduced in the calibration process and related to the measurement of the flow speed and the angles of rotation; (b) uncertainties in the polynomial expression used to approximate the calibration curve; (c) uncertainties in the calculation of the velocity components in the sensor's reference system. The results of the uncertainty estimations include the following:

- mean velocity $\pm 2.5\%$ of the actual value,
- flow angle ± 2 deg,
- radial position ± 0.1 mm.

In order to correctly use the multi-rotation technique, a fixed flow condition has been reproduced within the OWC simulator, by setting a periodic triangular piston motion which main parameters are summarized in Table 2, together with the other settings used for the present experiments.

Table 2. Settings of experimental tests.

piston stroke amplitude	≈850 mm
piston period, T_w	7 s
turbine rotational frequency, f	65 Hz
flow coefficient of the mean flow at rotor tip radius, $\phi = C_z/(\pi\, f\, D_{tip})$	≈0.195
Reynolds' number based on blade chord and on the mean outlet relative velocity	$\approx 1.3 \times 10^5$

The linear variation in piston position ensures a constant piston velocity, hence a constant flow rate through the rotor. Figure 2 shows the piston displacement during a test and its velocity as a function of the non-dimensional piston period.

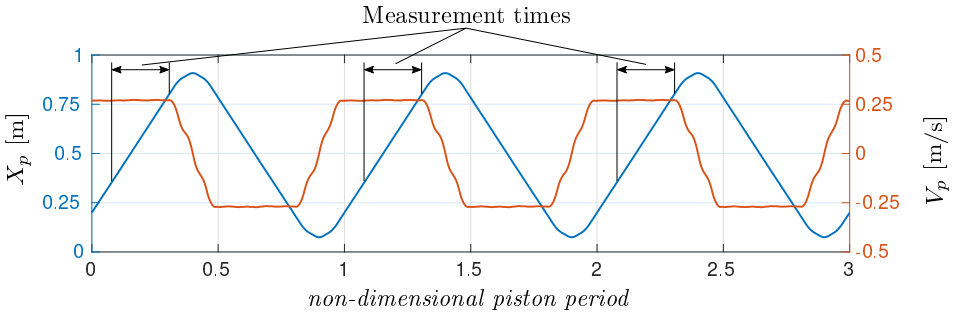

Figure 2. Piston motion characteristics during a test.

Signals were acquired only during the piston ramps that correspond to outflow phases and the corresponding measurement times are also indicated in Figure 2. They have been selected in order to: (a) exclude measurements near the inversion of piston motion and (b) acquire at least 100 rotor revolutions for each piston period (thus, by acquiring 3 piston ramps, 300 revolutions have been used for the phase averaging). The flow rate is calculated based on the piston displacement. A sampling rate of 100 kHz has been set, allowing at least 150 measurement points to be taken along a blade pitch. The signal anemometer was amplified and filtered at 50 kHz before acquisition and submitted to a phase-locked

ensemble averaging technique synchronized with the rotor passage to obtain a periodic mean distribution of flow velocity in a blade passage.

The turbine performance is reported in Figure 3a,b. It should be observed that the operating condition selected for the present investigation (the red cross) falls in the stable region, before the stall point, with a safe distance from the latter in order to avoid incipient stall conditions on the blade that are associated with local flow separations which are not investigated in this work. The selected operating condition, i.e., with $\phi \approx 0.195$, is characterized by a turbine global efficiency of 48.1%, which is near its maximum, as it can be evinced from Licheri et al. [21].

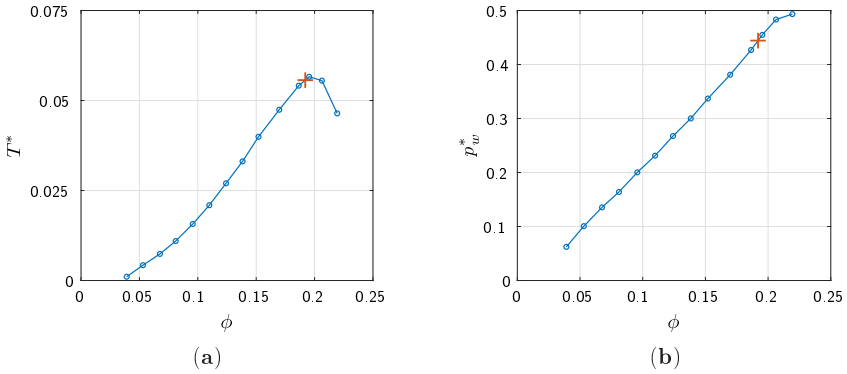

Figure 3. Non-dimensional turbine's performance under stationary flow. (**a**) Torque coefficient. (**b**) Pressure coefficient.

4. Results

The flow characteristics are presented here in terms of the velocity components non-dimensionalized with respect to the blade tip velocity U_{tip}. All the present results refer to a single operating condition, as indicated in Table 2, before stall and representative of the maximum efficiency point of the tested turbine [22].

4.1. Inlet Flow

A preliminary investigation has been conducted in order to characterize the flow at the turbine's inlet. The inlet flow has been reconstructed in a plane located at an axial distance of 5.5 mm from the rotor. The velocity components have been mass-weighted averaged in the circumferential direction and the resultant velocity distributions have been reported in Figure 4a. The mass-weighted radial distribution of the turbulence intensity Tu has also been reported in Figure 4b. Note that the radial position, r^*, has been non-dimensionalized with respect to the blade height.

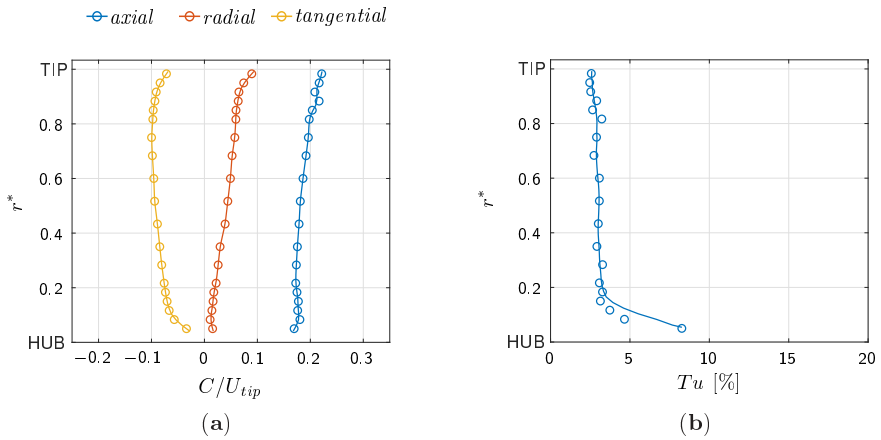

Figure 4. Mass-averaged flow characteristics upstream the rotor. (**a**) Absolute velocity components. (**b**) Turbulence intensity.

Results show an almost constant axial velocity along the blade span, with slightly larger values at high radii where the blade pitch is larger and the mass-flow encounters a lower resistance through the rotor. This effect results in a greater positive radial velocity in the tip region. The tangential velocity presents small negative values due to the presence of a swirling flow generated by the previous inflow phase, as well described by Puddu et al. [12].

Measures of the turbulence intensity *Tu* suggest that an almost constant value of 3% can be assumed at the turbine's inlet when the flow is coming from the chamber, i.e., during the outflow phase. Higher values have been detected near walls, in particular near the hub where the rotor has the highest solidity. This result can be useful to correctly set-up numerical simulations on similar case studies.

4.2. Flow Structures at the Turbine's Outlet

A complete visualization of the relative flow field downstream of the rotor is shown in Figure 5, in the form of contour plots of the relative velocity components. Velocity maps were built based on pitchwise distributions with the superposition of blades outline to aid the interpretation.

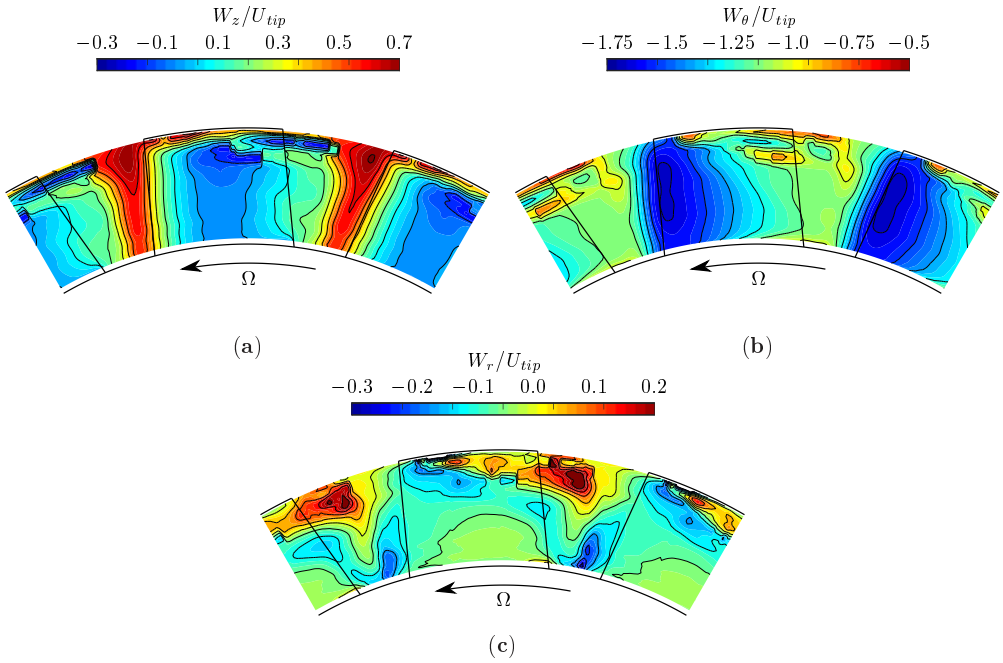

Figure 5. Contour plots of the relative velocity components downstream the rotor in two adjacent blade passages. (**a**) Axial velocity. (**b**) Tangential velocity. (**c**) Radial velocity.

The maps give an overall representation of the flow field in a blade vane that is strongly related to the uncommon 90-degree stagger of the Wells turbine's blade. In fact, the maps in Figure 5 represent the flow that develops on the blades suction side and the typical wake region downstream the trailing edge (TE) cannot be identified. Moreover, the interaction between the wake detached from a TE and the flow on the leading edge (LE) of the adjacent blade complicates the flow structure interpretation.

It can be observed how the leakage flow interacts with the clean flow in proximity of the blade trailing edge at higher radii, thus resulting in a distortion of the flow field with respect to all the velocity components. Another peculiar feature of the flow is the near zero axial velocity components in the region close to the suction side of the blade, which is present at this high flow coefficient, even if a complete stall has not yet been reached. As a consequence, the flow is forced through a narrow circumferential area, recognizable by the higher values of W_z. The presence of a vortical structure at higher radii is more easily identifiable referring to the radial velocity component in Figure 5c, which shows negative

values in the proximity of the leading edge, probably due to the blockage effect of the blade. Moving towards the trailing edge, the tip vortex forms and detaches from the blade, as can be seen from the positive radial velocity values in a zone near the tip. In the proximity of the trailing edge, the vortex is strengthened and affects a wider area, around 30% of the blade height.

Near the hub, the passage vortex formed in the pressure side is forced to pass in the reduced circumferential zone with higher axial velocity. This can be deduced by the rapid changes in radial velocity from strongly positive to strongly negative values that can be observed in this region. This vortex also influences the flow field near the suction side of the blade, as the effects of the counter vortex are not clearly visible.

In a more quantitative representation, Figure 6 shows the relative velocity components, i.e., in the axial (W_z), radial (W_r) and tangential direction (W_θ), at different circumferential positions, non-dimensionalized with respect to the blade pitch t, and for three different radial positions. The TE and leading edge LE locations have also been reported in order to facilitate reading of the graphs, as well as the direction of rotation.

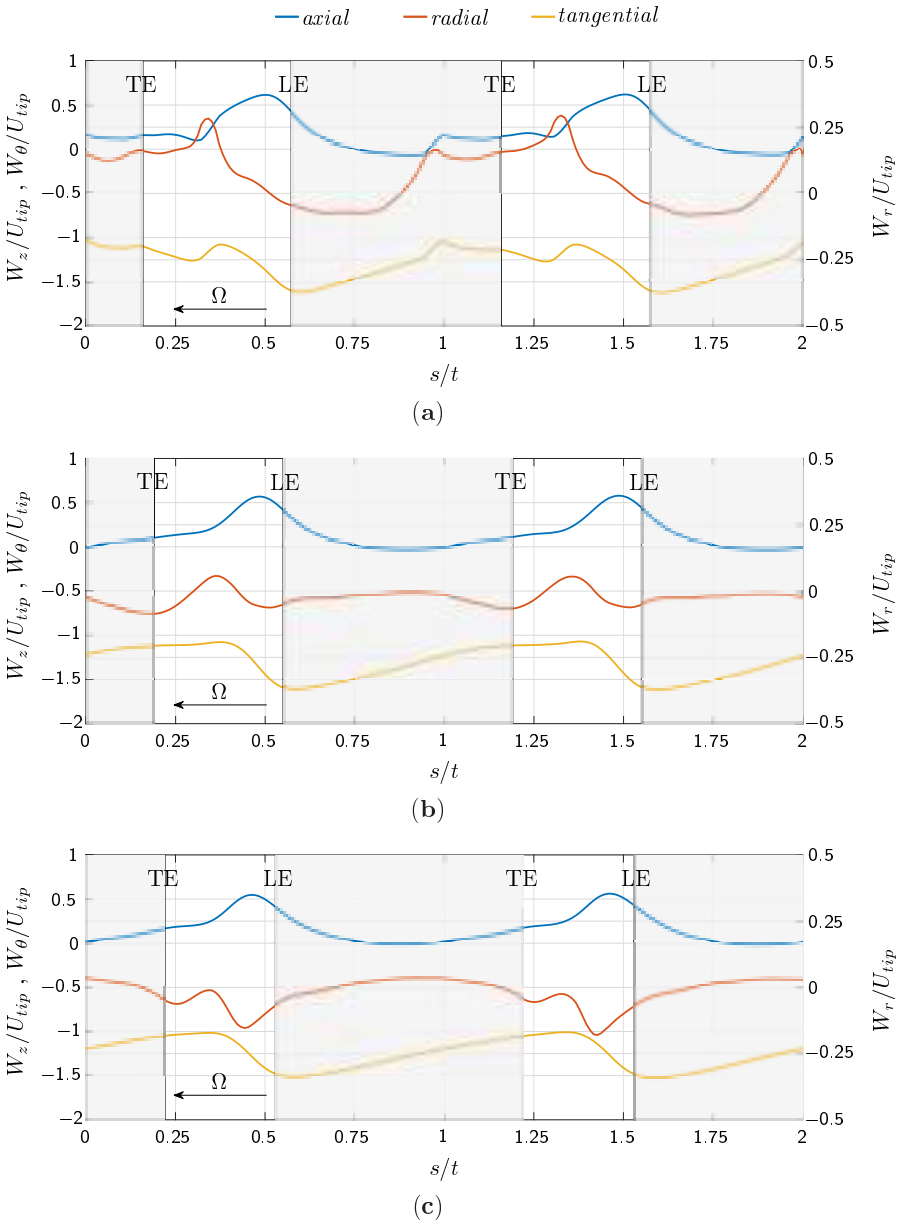

Figure 6. Circumferential distribution of the relative velocity components downstream of the rotor at (**a**) 80% of span, (**b**) 50% of span and (**c**) 20% of span.

The axial velocity presents higher values in the region between two adjacent blades, with a peak in the proximity of the LE, along the whole blade span as also highlighted in Figure 6a. This trend, which is not common for typical axial turbine configurations, is due to the 90-degree stagger of the blades: the mass flow is forced to pass through the space between two adjacent blades, thus producing a jet close to the LE, which energizes the wake detached from the TE of the previous blade. Moving from the hub to the tip region, i.e., from Figures 6a–c, higher values of W_z are detected in the jet region while the latter tends to occupy a larger portion of the free space between two blades. This is due to the reduced solidity of the rotor, that allows much more mass flow to pass. Most of the pitchwise axial velocity distribution is affected by the flow along the blade suction side where low values, close to zero, can be observed. Near the tip region, values of negative axial velocity are observed due to the presence of the leakage vortex, which takes up a wide portion of the blade vane.

The radial velocity component, W_r, shows lower values and limited gradients in the hub and midspan regions, with negative values in the region between two blades, in particular at low radii as shown in Figure 6c. Both gradients and absolute values of W_r are larger in the tip region where the presence of the leakage flow strongly affects the three-dimensional behavior of the flow field with a significative radial component.

The tangential velocity component, W_θ, is always negative, as expected, and its module smoothly decreases from the leading edge to the trailing edge, with higher gradients close to the leading edge.

4.3. Radial Distribution of Tangentially Averaged Flow

A mass-weighted averaging of the relative velocity components was performed in the circumferential direction along a blade pitch, in order to compute their mean radial distributions, as shown in Figure 7.

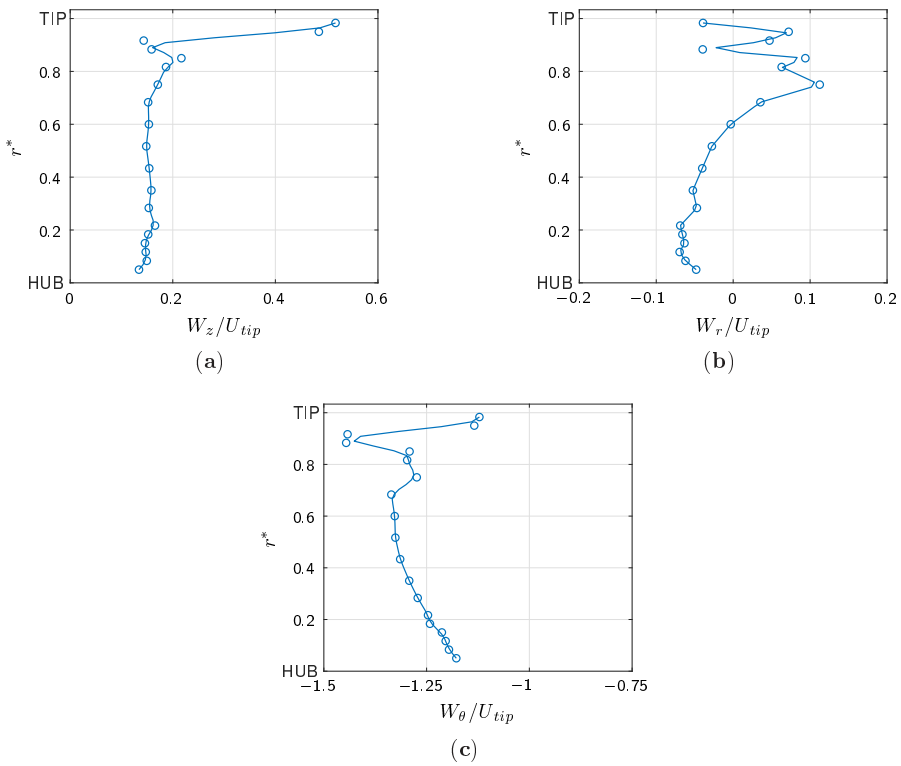

Figure 7. Relative velocity components at the turbine's outlet averaged on a blade pitch. (**a**) Axial component. (**b**) Radial component. (**c**) Tangential component.

The radial distribution of the relative axial velocity W_z is characterized by an almost constant value for r^* = 10–75%. The tip region shows larger (positive) values of W_z due

to the leakage flow that affects at least 20% of the blade span. Lower wall effects can be observed near the hub region. These effects can be better appreciated from the radial component W_r that is affected by larger gradients in the tip region than near the hub. A negative value of W_r is observed from the hub to the midspan where the flow is moving from higher to lower radii, driven by the higher losses in the hub region. This trend is overturned in the upper part of the blade height, in proximity of 60% of the blade span. This positive trend of the radial component can be justified considering the leakage flow at the tip, which considerably reduces the height of the blade channel where the clean flow can pass through, thus introducing a highly three-dimensional behavior of the flow field.

Based on averaged velocities distributions of Figures 4 and 7, inlet and exit velocity triangles can be drawn as shown in Figure 8 at three spanwise locations.

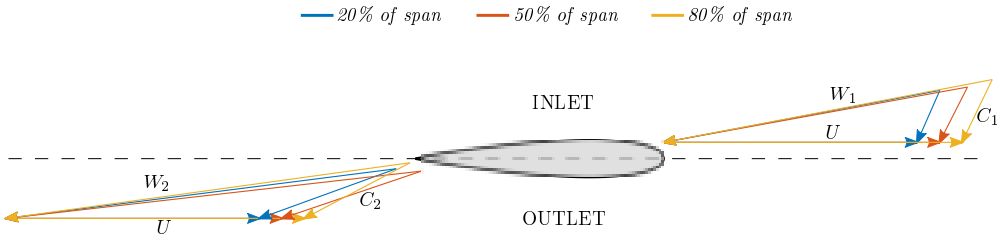

Figure 8. Velocity triangles at the rotor inlet and outlet sections.

This representation helps to highlight a few interesting characteristics: (a) The presence of the inlet swirl, (b) non-uniform distribution of mass flow and (c) radial variation of the Euler work (associated with difference in tangential velocity components between the rotor inlet and outlet).

4.4. Rotor Performance

Local performance has been evaluated based on the reconstructed flow field at the turbine's outlet, in terms of the non-dimensional work coefficient Λ which is evaluated as the ratio between the Euler work and the square of the blade tip velocity:

$$\Lambda = \frac{l}{U_{tip}^2} \tag{1}$$

The work coefficient is reported in Figure 9 in the form of a contour map in two adjacent blade vanes.

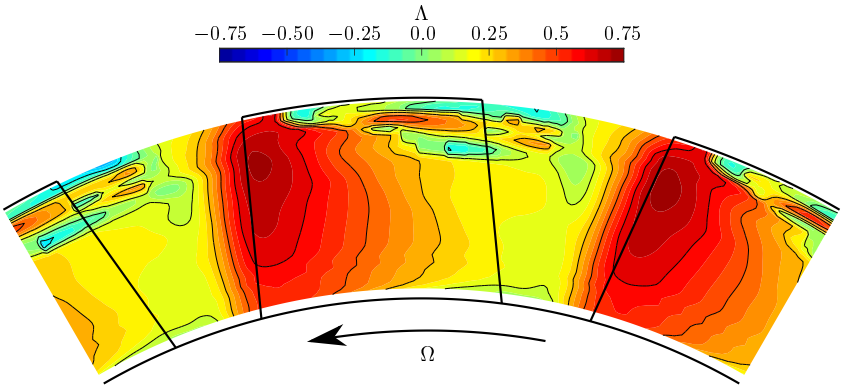

Figure 9. Contour plots of the work coefficient in two adjacent blade passages.

The contour plot demonstrates that the region with the highest exchanged work is located near the leading edge and around 40–80% of the blade span. This value tends to reduce to very low values, but still positive, moving from the leading edge to the trailing edge. Then, in the regions characterized by the presence of the tip leakage flow, i.e., at high radii and near the trailing edge, the work coefficient assumes very low, close to zero, values,

thus emphasizing the presence of high losses. The resulting output work from the turbine is reduced by the presence of this wide region of losses; therefore, this local characterization can aid in finding geometry modifications of the rotor in order to improve its efficiency. In order to better quantify the effect of the tip leakage vortex on the output work, Figure 10 shows the work coefficient averaged on a blade pitch along the blade span.

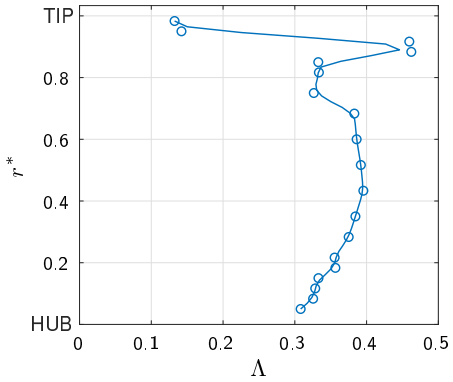

Figure 10. Work coefficient averaged on a blade pitch.

This representation makes it more evident that the detrimental effect of the leakage vortex in reducing performance takes up a relevant portion of the blade height. It also appears clear that the work coefficient distribution follows the same trend as the tangential velocity of Figure 7c.

5. Conclusions

A detailed experimental investigation of the local flow field inside a Wells rotor is presented herein. The high-frequency response and low intrusiveness of the HWA probe has allowed the flow reconstruction in a blade pitch and along its span as never done before for a Wells turbine. The main results of this investigation can be summarized as follows:

- The tip leakage flow has been shown to play a significant role in modifying the clean flow distribution downstream of the rotor; its interaction with the flow at the suction side produces a vortex in the tip region that encompasses a relevant portion of the blade channel, due to the relatively high hub-to-tip ratio of the tested rotor.
- The variable rotor solidity along the blade span contributes to distortion of the flow field at higher radii, as the flow moves to higher radii where the space in between the blades is larger;
- The regions affected by the presence of the leakage vortex result in negative values of the exchanged work, thus the overall output work from the rotor is sensibly reduced.

The present experimental results could help define the rotor geometry modifications that can improve the performance of a Wells turbine. Moreover, these findings may provide highly useful data for the validation of numerical simulations.

Author Contributions: Conceptualization, P.P.; methodology, F.L. and P.P.; software, F.L. and P.P.; formal analysis, F.L. and P.P.; investigation, F.L. and P.P.; data curation, F.L. and P.P.; writing—original draft preparation, F.L.; writing—review and editing, F.L., T.G., F.C. and P.P.; visualization, F.L., T.G., F.C. and P.P.; supervision, P.P.; project administration, P.P. All authors have read and agreed to the published version of the manuscript.

Funding: This study was carried out within the "e.INS - Ecosystem of Innovation for Next Generation Sardinia" funded by the Italian Ministry of University and Research under the Next-Generation EU Programme (National Recovery and Resilience Plan—PNRR, M4C2, INVESTMENT 1.5—DD 1056 of 23/06/202, ECS00000038). This manuscript reflects only the authors' views and opinions, neither the European Union nor the European Commission can be considered responsible for them.

Institutional Review Board Statement: Not applicable.

Informed Consent Statement: Not applicable.

Data Availability Statement: The data presented in this study are available on request from the corresponding author.

Conflicts of Interest: The authors declare no conflict of interest.

Nomenclature

Acronyms

HWA	hot-wire anemometer
OWC	Oscillating Water Column
WEC	Wave Energy Converter

Dimensional properties

C	absolute flow velocity
c	blade chord
D	rotor diameter
f	turbine rotational frequency
l	$= U(C_{\theta,1} - C_{\theta,2})$ Euler work
Ω	angular velocity
s	circumferential position
t	blade pitch
T_w	piston period
U	peripheral rotor speed
V_p	piston velocity
W	relative flow velocity
X_p	piston position
z	number of blades

Non-dimensional properties

Λ	work coefficient
ν	hub-to-tip ratio
ϕ	flow coefficient
p_w^*	pressure drop coefficient
Re	Reynolds' number
r^*	$= (r - r_{hub})/(r_{tip} - r_{hub})$ non-dimensional turbine radius
T^*	torque coefficient
Tu	turbulence intensity

Subscripts and superscripts

1	turbine's inlet
2	turbine's outlet
hub	turbine hub
LE	leading edge
r	radial direction
ref	reference value
TE	trailing edge
θ	tangential direction
tip	turbine tip
z	axial direction

References

1. Pelc, R.; Fujita, R. Renewable energy from the ocean. *Mar. Policy* **2002**, *26*, 471–479. [CrossRef]
2. Aderinto, T.; Li, H. Ocean Wave Energy Converters: Status and challenges. *Energies* **2018**, *11*, 1250. [CrossRef]
3. Falcão, A.F.O. Wave energy utilization: A review of the technologies. *Renew. Sustain. Energy Rev.* **2010**, *14*, 899–918. [CrossRef]
4. Wells, A.A. Fluid Driven Rotary Transducer. BR Patent 1595700, 13 November 1976.
5. Raghunathan, S.; Tan, C.P.; Ombaka, O.O. Performance of the Wells self-rectifying air turbine. *Aeronaut. J.* **1985**, *89*, 369–379. [CrossRef]
6. Curran, R.; Gato, L.M.C. The energy conversion performance of several types of Wells turbine designs. *Proc. Inst. Mech. Eng. Part A J. Power Energy* **1997**, *211*, 133–145. [CrossRef]
7. Paderi, M.; Puddu, P. Experimental investigation in a Wells turbine under bi-directional flow. *Renew. Energy* **2013**, *57*, 570–576. [CrossRef]

8. Torresi, M.; Stefanizzi, M.; Gurnari, L.; Filianoti, P.; Camporeale, S. Experimental Characterization of the Unsteady Performance Behavior of a Wells Turbine Operating at High Flow Rate Coefficients. In Proceedings of the 75th Italian National Congress ATI, Rome, Italy, 15–16 September 2020; Volume 197, p. 08009. [CrossRef]
9. Licheri, F.; Ghisu, T.; Cambuli, F.; Puddu, P. Detailed investigation of the local flow-field in a Wells turbine coupled to an OWC simulator. *Renew. Energy* **2022**, *197*, 583–593. [CrossRef]
10. Alves, J.S.; Gato, L.M.C.; Falcão, A.F.O.; Henriques, J.C.C. Experimental investigation on performance improvement by mid-plane guide-vanes in a biplane rotor Wells turbine for wave energy conversion. *Renew. Sustain. Energy Rev.* **2021**, *150*, 111497. [CrossRef]
11. Licheri, F.; Ghisu, T.; Cambuli, F.; Puddu, P. Experimental Analysis of the Three Dimensional Flow in a Wells Turbine Rotor. In Proceedings of the 15th European Turbomachinery Conference, Paper n. ETC2023-148, Budapest, Hungary, 24–28 April 2023. Available online: https://www.euroturbo.eu/publications/conference-proceedings-repository/ (accessed on 21 May 2023).
12. Puddu, P.; Paderi, M.; Manca, C. Aerodynamic characterization of a Wells turbine under bi-directional airflow. In Proceedings of the 68th Italian National Congress ATI, Bologna, Italy, 11–13 September 2013; Volume 45, pp. 278–287. [CrossRef]
13. Fujita, H.; Kovasznay, L.S.G. Measurement of Reynolds Stress by a Single Rotated Hot Wire Anemometer. *Rev. Sci. Instruments* **1968**, *39*, 1351–1355. [CrossRef]
14. He, X. *Measurement with a Rotating Slant-Sensor Probe*; Dantec Information; Tonsbakken 16–18 DK-2740 Skovlunde Denmark; DANTEC Elektronik: Copenhagen, Denmark, 1988; pp. 9–12.
15. Puddu, P. Tip leakage flow characteristics downstream of an axial flow fan. In Proceedings of the ASME 1996 International Gas Turbine and Aeroengine Congress and Exhibition, Birmingham, UK, 10–13 June 1996; Volume 1. Turbomachinery. [CrossRef]
16. Jørgensen, F.E. *Directional Sensitivity of Wire and Fiber Film Probes*; Tech. Rep. DISA Information, N. 11; DISA Elektronik A/S, DK-2740 Skovlunde Denmark; DANTEC Elektronik: Copenhagen, Denmark, 1971; pp. 11–31.
17. Lòpez Penã, F.; Arts, T. The rotating slanted hot wire anemometer in practical use. In Proceedings of the 2nd International Conference on Experimental Fluid Mechanics (ICEFM '94), Torino, Italy, 4–8 July 1994; pp. 388–399.
18. King, L.V.; Barnes, H.T. XII. On the convection of heat from small cylinders in a stream of fluid: Determination of the convection constants of small platinum wires with applications to hot-wire anemometry. *Philos. Trans. R. Soc. Lond. Ser. A Contain. Pap. Math. Phys. Character* **1914**, *214*, 373–432. [CrossRef]
19. Erriu, N.; Mandas, N.; Puddu, P. Alcune considerazioni sulla valutazione dell'incertezza nelle misure con anemometro a filo caldo. In Proceedings of the VII MIS-MAC Conference, Quartu S. Elena, Italy, 21 April 2001.
20. Nurzia, F.; Puddu, P. Experimental investigation of secondary flows in a low hub-tip ratio fan. In Proceedings of the ASME 1994 International Gas Turbine and Aeroengine Congress and Exposition, The Hague, The Netherlands, 13–16 June, 1994; Volume 1. Turbomachinery. [CrossRef]
21. Licheri, F.; Puddu, P.; Cambuli, F.; Ghisu, T. Experimental Investigation on a Speed Controlled Wells Turbine for Wave Energy Conversion. In Proceedings of the ASME 2022 41st International Conference on Ocean, Offshore and Arctic Engineering, Hamburg, Germany, 5–10 June 2022; Volume 8. Ocean Renewable Energy. [CrossRef]
22. Licheri, F.; Cambuli, F.; Puddu, P.; Ghisu, T. A comparison of different approaches to estimate the efficiency of Wells turbines. *J. Fluids Eng.* **2021**, *143*, 051205. [CrossRef]

Disclaimer/Publisher's Note: The statements, opinions and data contained in all publications are solely those of the individual author(s) and contributor(s) and not of MDPI and/or the editor(s). MDPI and/or the editor(s) disclaim responsibility for any injury to people or property resulting from any ideas, methods, instructions or products referred to in the content.

International Journal of
Turbomachinery
Propulsion and Power

MDPI

Article

Aerodynamics and Sealing Performance of the Downstream Hub Rim Seal in a High-Pressure Turbine Stage

Filippo Merli [1], Nicolas Krajnc [1], Asim Hafizovic [1], Marios Patinios [2] and Emil Göttlich [1,*]

[1] Institute of Thermal Turbomachinery and Machine Dynamics, Graz University of Technology, Inffeldgasse 25A, 8010 Graz, Austria
[2] GE Aviation, Freisinger Landstrasse 50, 85748 Garching bei München, Germany
* Correspondence: emil.goettlich@tugraz.at

Abstract: The purpose of the paper is to characterize the aerodynamic behavior of a rotor-downstream hub cavity rim seal in a high-pressure turbine (HPT) stage. The experimental data are acquired in the Transonic Test Turbine Facility at the Graz University of Technology: the test setup includes two engine-representative turbine stages (the last HPT stage and first LPT stage), with the intermediate turbine duct in between. All stator-rotor cavities are supplied with purge flows by a secondary air system, which simulates the bleeding air from the compressor stages of the real engine. The HPT downstream hub cavity is provided with wall taps and pitot tubes at different radial and circumferential locations, which allows the performance of steady pressure and seed gas concentration measurements for different purge mass flows and HPT vanes clocking positions. Moreover, miniaturized pressure transducers are adopted to evaluate the unsteady pressure distribution, and an oil flow visualization is performed to retrieve additional information on the wheel space structures. The annulus pressure asymmetry depends on the HPT vane clocking, but this is shown to have negligible impact on the minimum purge mass flow required to seal the cavity. However, the hub pressure profile drives the distribution of the cavity egress in the turbine channel. The unsteady pressure field is dominated by blade-synchronous oscillations. No non-synchronous components with comparable intensity are detected.

Keywords: cavity; wheel space; purge; rim seal; turbine; aerodynamics; concentration effectiveness; oil flow visualization

check for updates

Citation: Merli, F.; Krajnc, N.; Hafizovic, A.; Patinios, M.; Göttlich, E. Aerodynamics and Sealing Performance of the Downstream Hub Rim Seal in a High-Pressure Turbine Stage. *Int. J. Turbomach. Propuls. Power* **2023**, *8*, 20. https://doi.org/10.3390/ijtpp8030020

Academic Editors: Tony Arts and Rodolfo Bontempo

Received: 9 May 2023
Revised: 11 June 2023
Accepted: 23 June 2023
Published: 10 July 2023

Copyright: © 2023 by the authors. Licensee MDPI, Basel, Switzerland. This article is an open access article distributed under the terms and conditions of the Creative Commons Attribution (CC BY-NC-ND) license (https://creativecommons.org/licenses/by-nc-nd/4.0/).

1. Introduction

In the continuous effort to achieve higher thermal efficiencies, modern turbofan engines underwent a significant increase in turbine inlet temperatures over the last decades. The trend strengthens the importance of cooling flows in both high-pressure (HPT) and low-pressure (LPT) turbines. In state-of-the-art turbofans, an internal secondary air system redirects fluid from the main stream of different compressor stages to the turbine stator-rotor cavities. A fraction of the secondary air, often referred to as sealing or purge flow, is used to prevent hot main gas ingestion through the rim seals, normally placed between the rotor disks and the stator platforms. It helps maintain the internal metal temperatures within a limit that safeguards the integrity and life of the components. The interaction between sealing and main stream flow is known to produce a drop in turbine efficiency. Consequently, it is of interest for engine designers to use the minimum purge mass flow rate to seal the cavities. At the same time, it is crucial to investigate the aerothermal behavior inside the stator-rotor cavities, to understand the ingress and egress mechanism and further reduce the efficiency loss. This study aims to address the mentioned designer needs by:

- evaluating the sealing performance of the rim seal in the rotor-downstream hub cavity (DHC) of a high-pressure turbine stage;
- characterizing the aerodynamics inside the same HPT cavity.

The HPT stage is integrated into an engine-representative two-stage turbine, including an intermediate turbine duct with turning struts, to guarantee realistic conditions, especially in terms of annulus Mach number. Wall taps are distributed inside the DHC and on the corresponding stator hub platform to retrieve pressure and concentration effectiveness data. Furthermore, unsteady pressure sensors and oil flow visualization are utilized to get a deeper insight into the cavity flow field. Several purge flow rates are analyzed, as well as multiple HPT vane and strut clocking settings. To the extent of the authors' knowledge, the combination of the described measurement techniques with the wide range of operating conditions applied within such a relevant test vehicle is a *unicum* in the open turbomachinery literature and is expected to provide original information to the engine manufacturers.

2. Brief Literature Review

According to Owen [1], the ingress of main air into the wheel space can be of three types:

- Externally induced, when it is caused by annulus (external) flow asymmetries, e.g., the ones caused by the presence of a vane row in a turbine stage;
- Rotationally induced, when the rotating fluid in the cavity generates a pressure gradient, such that a radial outflow arises near the rotor (disk pumping) and ingress happens close to the stator wall;
- Combined ingress, when externally and rotationally induced ingress, is of the same order of magnitude.

The externally driven ingress is generally the dominant type in conventional turbines, especially with single-rim seals (double-rim seals may show rotationally induced ingress for the inner one).

Given the detrimental effect of the sealing flow on the turbine efficiency (Regina et al. [2] estimated a 0.8% drop for each injection rate percent), many researchers focused on the prediction of the minimum sealing flow rate necessary to prevent externally induced ingress. Phadke and Owen [3] found that, for non-axisymmetric external flow, the minimum non-dimensional sealing flow, $C_{0,min} = \dot{m}_{0,min}/\mu b$, is independent of the rotational Reynolds number, Re_Ω, and increasing with the annulus bulk Reynolds number, Re_W. They also obtained a correlation between $C_{0,min}$, Re_W and the maximum non-dimensional pressure asymmetry $\Delta C_{P,max}$:

$$C_{0,min} = 2\pi K G_c Re_W (0.5\Delta C_{P,max})^{0.5}, \quad (1)$$

where the parameter $K = 0.6$ produced a good fitting for different seal geometries in a vaneless and bladeless case. Bohn and Wolff [4] adopted the same correlation inside a turbine setup with vanes and blades. They found a higher dependence of K on the tested seal configurations. Hamabe and Ishiba [5] provided one of the first examples of ingress and egress modeling through separate orifices, where the associated discharge coefficients were determined empirically. Many research groups then developed and tuned orifice models to evaluate the seal performance ([1,6] among others).

More recently, Scobie et al. [7] investigated the egress-main flow interaction in the downstream hub cavity of a turbine stage. They measured an asymmetric egress distribution in the annulus at the edge of the seal clearance, driven by the annulus pressure profile. Scobie et al. [8] quantified the re-ingestion of the upstream hub cavity purge into the downstream one, using seed gas concentration measurements. They concluded that the upstream injection partially mixes with the annulus air stream close to the downstream seal, reducing the adverse effects of ingress. In any case, many of the experimental works on the subject are performed in facilities operating at low speed, with annulus Mach number ranging approximately from $M = 0.2$ to 0.4 upstream of the rotor blade [9,10] and $M < 0.2$ downstream [7,11].

In terms of the cavity's unsteady flow field, many experimental and numerical studies [12–15] identified unsteady rim seal rotating structures whose frequency is unrelated to the blade passing or disk frequency. Despite the exact nature of these structures still

being debated, they are often attributed to Kelvin–Helmholtz instabilities [16] or inertial waves [17] at the rim seal region. In his review paper, Chew [18] observed that simple, high-clearance axial seals normally show lower non-synchronous frequencies, while the opposite holds for more complex and tight seals. However, not all the available literature was found to fit the trend.

3. Experimental Setup

3.1. Facility and Test Vehicle

The measurement campaign is carried out in its entirety in the Transonic Test Turbine Facility (TTTF) of the Graz University of Technology (Institute of Thermal Turbomachinery and Machine Dynamics, ITTM). The TTTF is a dual-spool, continuous, open-circuit test bench historically devoted to the aerothermal investigation of intermediate turbine frames [19–21]. The main flow is supplied to the turbine by a 3 MW compression station, while a 560 kW suction blower, placed downstream of the test section, allows to decrease and stabilize the backpressure against ambient condition variations. In the two-stage arrangement, the TTTF's high-pressure shaft speed is controlled by a radial brake compressor, whose outflow is mixed with the compressor station flow in a settling chamber and then fed to the test section. The resulting maximum pressure and mass flow rate at the inlet of the turbine are 4 bar and 22 kg/s, respectively. On the other side, the low-pressure turbine speed is regulated with a 700 kW water brake.

A secondary air system, supplied by a 1.1 kW electric compressor, provides up to 2.5 kg/s of purge air to six different lines, with the independent mass flow and temperature control. Each purge line is connected via independent regulation valves to two pressurized reservoirs containing CO_2 and N_2O, respectively. They are used to seed the cavity flows and perform concentration measurements, as described in the Measurement Techniques section. Further details about the TTTF are available in Hubinka et al. [22] and Steiner et al. [23].

The test section, in which the measurements are taken, is sketched in Figure 1. It consists of a fully purged, two-stage turbine, aerodynamically representative of the last high-pressure turbine (HPT) stage, the intermediate turbine duct, and the first low-pressure turbine (LPT) stage in a state-of-the-art turbofan engine. In particular, the HPT stage vane and blade counts are indicated as V and B_1, respectively, while B_2 is the LPT stage blade count. The intermediate turbine duct is populated by S strut fairings, which integrate the turning function of the LPT stage vane row. Such a setup is commonly known as turbine vane frame (TVF) or turning mid-turbine frame. The TVF struts are interspersed with splitters (SP), two for each strut passage, to reduce the strut loading without introducing excessive blockage at the duct inlet. The HPT stage features four stator-rotor cavities: the upstream and downstream hub cavities (UHC and DHC in the figure) are radial-clearance rim seals, while the upstream and downstream shroud cavities (USC and DSC) are continuous 360° axial slots. All of them can be fed with independent purge streams, as well as the LPT hub cavities. For the purpose of this study, the attention is focused on the flow field of the DHC, which is highlighted by the red rectangle in Figure 1.

3.2. Cavity Geometry and Instrumentation

The detailed DHC geometry is illustrated in Figure 2a, which also includes the cavity instrumentation radial-axial layout. The table on the right side of the figure contains a list of geometric parameters made non-dimensional using the rotor lip inner radius, b. An inner axial seal, with $G_{c,in} > G_{c,z}$, homogenizes the coolant before entering the outer part of the cavity. Finally, Figure 2b reports the circumferential occurrence of the instrumentation presented below.

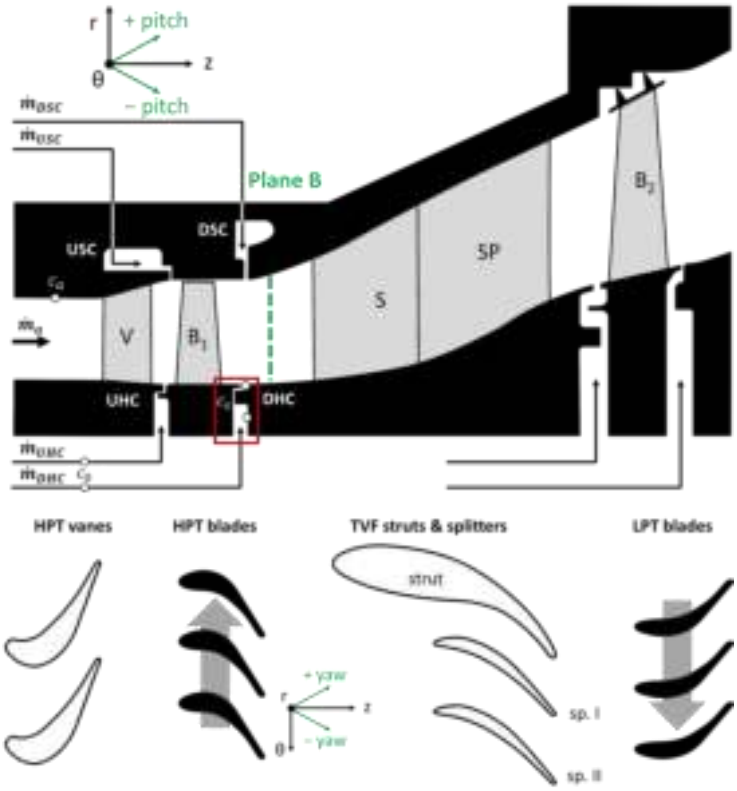

Figure 1. Test section scheme.

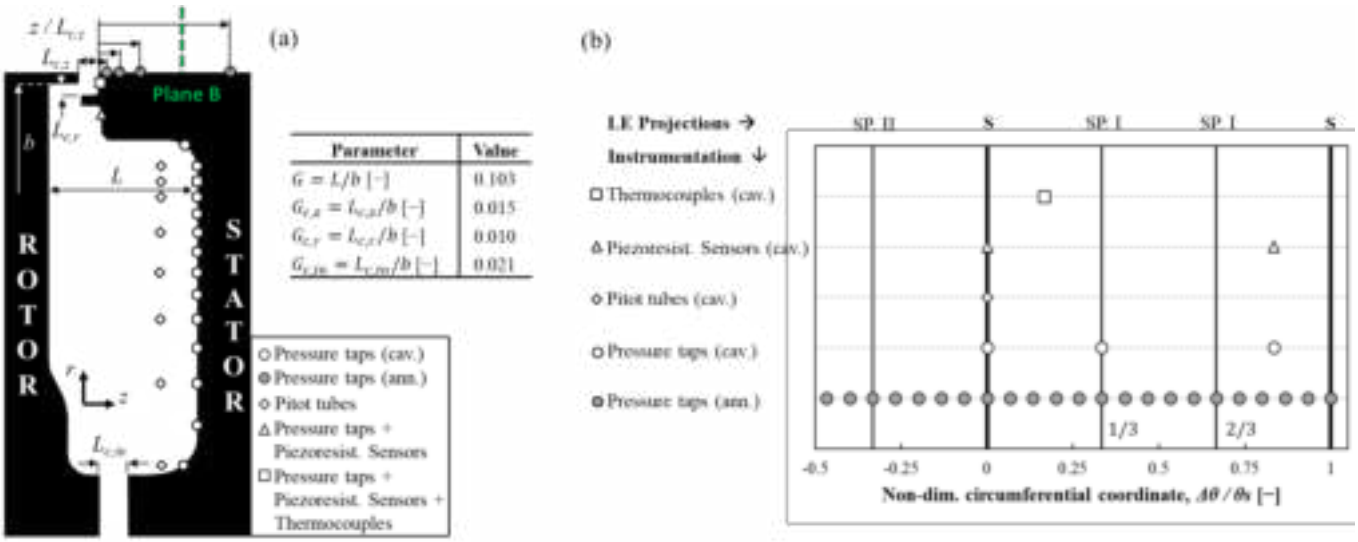

Figure 2. HPT downstream hub cavity instrumentation layout: (**a**) radial distribution (**left**), with a list of relevant geometric parameters (**top-right**); (**b**) circumferential distribution.

3.2.1. Time-Averaged Pressure Measurements

Static pressure values inside the DHC are obtained using wall taps located on the TVF stator platform. Three radial arrays of taps, circumferentially positioned in correspondence with the strut leading edge (LE), the splitter I LE, and the splitter II-strut mid-passage, are available. In terms of non-dimensional circumferential coordinates, they are at $\Delta\theta_S/\theta_S = (\theta - \theta_{LE,S})/\theta_S = 0,\ 1/3,\ 5/6$ respectively, where $\theta_S = 2\pi/S$ is the strut pitch and $\theta_{LE,S}$ is the position of the strut LE. Each tap array is constituted by 16 elements (white circles), distributed between $x = 0.74$ and $x = 1$, where $x = r/b$ is the non-dimensional radial coordinate. At $\Delta\theta_S/\theta_S = 0$, a radial array of pitot tubes is placed in correspon-

dence with some of the wall pressure taps, sampling the flow 10 mm away from the stator wall, as indicated by the white diamonds in Figure 2a. On the TVF hub platform, four circumferential arrays, with 23 wall pressure taps each (grey circles), cover $1.5 \cdot \theta_S$, at the non-dimensional axial coordinates $z/L_{c,z} = 0.28,\ 0.71,\ 2.12,\ 6.36$. The time-averaged pressures are acquired with NetScanner 9116 Pressure Scanners (FS 30 psi, uncertainty $\pm 0.05\%$ FS). For every operating point and measurement location, 30 values are sampled at 5 Hz and then averaged to get the desired pressure readings.

3.2.2. Concentration Measurements

Concentration measurements are performed to calculate the concentration effectiveness ε. After seeding the DHC purge flow, the wall pressure taps (white and grey circles in Figure 2a) can be connected to a gas analyzer to retrieve concentration values. In this experimental campaign, a Siemens Ultramat 6E gas analyzer is employed. Its dual channel configuration allows for the simultaneous concentration measurement of two seed gases (CO_2 and N_2O) from the same air sample. The channels are calibrated using N_2 as zero gas, and the analyzer is kept in an air-conditioned cabinet to remove the effect of ambient temperature variations. The concentration at each measurement point is the average of 5 values, acquired at 1 Hz. The propagated uncertainty on the effectiveness can be assumed: roughly equal to 0.003 for $\varepsilon < 0.1$, linearly varying from 0.003 to 0.013 for $0.1 \leq \varepsilon \leq 1$. More details about the measurement technique are provided by Patinios et al. [24].

3.2.3. Time-Resolved Pressure Measurements

The unsteady pressure field in the DHC is evaluated through two radial sets of Kulite XCQ-062-25D miniaturized piezoresistive transducers (FS 25 psi). A set is placed in front of the strut LE ($\Delta\theta_S/\theta_S = 0$), while the other is at $\Delta\theta_S/\theta_S = 1/3$, in front of splitter I leading edge. Each array includes three sensors, at $x = 0.92,\ 0.98,\ 1$, represented by the white triangles in Figure 2a. The unsteady signals are amplified with an Endevco Model 136 and then acquired with a NI PCI-6123 I/O Device, together with the shaft encoders. The sampling frequency and duration are 500 kHz and 2 s. Finally, the extended uncertainty associated with the time-resolved pressure measurements is estimated as $\pm 0.2\%$ FS.

3.2.4. Oil Flow Visualization

To illustrate the surface flow on the cavity walls and on the TVF hub platform, an oil flow visualization is carried out after the aerodynamic and concentration tests. Once the desired operating condition is set, a viscous mixture of motor oil and titanium dioxide (TiO_2) is simultaneously injected into the DHC through 10 of the wall taps displayed in Figure 2a. The mixture has to be liquid enough to be transported by the surface flow across the stator wall, delineating the shear stress trajectories. At the same time, the mixture should be viscous enough not to be immediately blown away by the flow as soon as it enters the test section. After about 20 min, when the oil has dried up and the pigment is fixed, the rig is shut down, disassembled, and documented with pictures.

3.3. Operating Conditions

A broad range of operating conditions is considered to fully characterize the DHC nominal and off-design behavior. More specifically, the annulus flow coefficient and the rotational Reynolds number

$$C_F = \frac{Re_W}{Re_\Omega} = \frac{W}{\Omega b} \text{ and } Re_\Omega = \frac{\rho \Omega b^2}{\mu} \tag{2}$$

are kept constant, while 15 different sealing flow rates are investigated, extending from $PFR = 0$ to $PFR = 2$, where

$$PFR = \frac{\dot{m}_0}{\dot{m}_{0,nominal}} \tag{3}$$

and the subscript 0 refers to the purge mass flow rate injected in the considered cavity. The annulus inlet mass flow is measured with two Venturi flow meters (uncertainty ±2%), quantifying the main compressor station and HPT brake compressor flows to the turbine intake. The cavity injection rates are determined with McCrometer's V-Cone flow meters (±0.5%), one for each purge supply line. In terms of non-dimensional sealing parameters and turbulent flow parameters,

$$\Phi_0 = \frac{C_0}{2\pi G_c Re_\Omega} = \frac{\dot{m}_0/(\mu b)}{2\pi G_c Re_\Omega} \text{ and } \lambda_T = C_0 Re_\Omega^{-0.8} \quad (4)$$

the abovementioned PFR interval corresponds to $\Phi_0 = 0$ to 0.135 and $\lambda_T = 0$ to 0.249.

Table 1 summarizes the operating conditions for five of the considered operating points ($PFR = 0,\ 0.5,\ 1,\ 1.5,\ 2$). The nominal ($PFR = 1$) Φ_0 and λ_T values are in line with the $C_{0,min}$ prediction from the simple relation

$$C_{0,min} = 0.61 G_{c,r} Re_\Omega, \quad (5)$$

originally developed by Bayley and Owen [25] for axial clearance rim seals and no annulus flow. According to Daily and Nece [26], the tested gap ratio G and rotational Reynolds number Re_Ω guarantee turbulent flow in the wheel space, with separated boundary layers. The cavity-to-annulus temperature ratio is confined between 0.9 and 1.1, depending on the PFR. Moreover, it is noteworthy that, while the DHC parameters are varied, Φ_0 and λ_T are maintained at the nominal point for the other purged HPT and LPT cavities throughout all the considered test cases. The inlet total temperature, the inlet-to-outlet total pressure ratio, and the rotational speeds of the two rotors are also kept constant for all the tests, with an uncertainty of ±0.3 °C, ±0.5%, and ±0.1%, respectively. In terms of main stream quantities, the annulus Mach number is approximately $M \approx 0.5$, much higher than the values reported in [7,11].

Table 1. Investigated flow operating conditions.

Case	***PFR* = 0**	***PFR* = 0.5**	***PFR* = 1**	***PFR* = 1.5**	***PFR* = 2**
C_F [−]			0.653		
Re_Ω [−]			3.22×10^6		
Φ_0 [−]	0	0.034	0.068	0.100	0.135
λ_T [−]	0	0.062	0.125	0.185	0.249

In addition to the PFR variation, four different HPT vanes clocking positions are investigated. The HPT vanes are, in fact, mounted on a rotatable casing, which allows the operators to modify the strut-vane relative displacement and study its effect on the cavity flow field. The analyzed clocking cases, sketched in Figure 3, are $\Delta\theta_V/\theta_V = (\theta - \theta_{des,V})/\theta_V = 0,\ 0.2,\ 0.45,\ 0.7$, where $\theta_V = 2\pi/V$ is the HPT vane pitch and $\theta_{des,V}$ is the design reference position. At the same time, strut clocking investigations are performed by comparing the results of different radial arrays in the DHC (with fixed PFR and HPT vane clocking position).

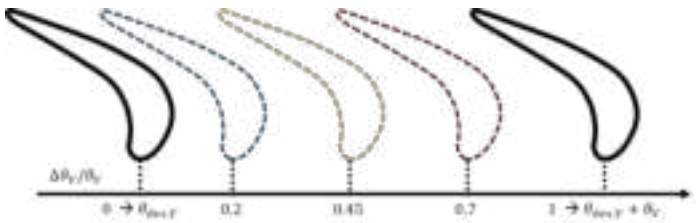

Figure 3. Scheme of the investigated HPT vane clocking positions.

4. Methodology

The static pressure values obtained from the taps listed in the previous section are expressed in terms of the pressure coefficient:

$$C_P = \frac{P - P_{ref}}{0.5\rho\Omega^2 b^2}, \tag{6}$$

where P_{ref} is a reference pressure value arbitrarily chosen by the authors and kept constant throughout all the operating conditions. However, the selected P_{ref} is different between the measurements inside ("cav." in Figure 2b) and outside ("ann.") of the DHC. The tangential speed inside the inviscid core flow in the cavity is calculated with

$$V_\theta = \sqrt{\frac{2(P_T - P)}{\rho}}, \tag{7}$$

using the readings from the pitot tubes and the corresponding wall pressure taps. The swirl ratio is then calculated as follows:

$$\beta = \frac{V_\theta}{\Omega r} \tag{8}$$

According to the ISRE (Isentropic Simple Radial Equilibrium) theory [27], the radial momentum equation for the rotating core returns

$$\frac{1}{\rho}\frac{dP}{dr} = \frac{V_\theta^2}{r}, \tag{9}$$

which can be integrated across the probed radial extent ($x = 0.74 - 1$), to obtain another expression for the swirl ratio, in this case, based only on the wall static pressure distribution:

$$C_{P,x=1} - C_{P,x=0.74} = 2\int_{x=0.74}^{x=1} x\beta^2 dx \tag{10}$$

The circumferential pressure variations, measured with the wall tap sets on the TVF platform, are associated with a combination of two sources:

- the downstream propagation of the HPT vanes pressure distribution;
- the potential upstream effect of the TVF strut.

Merli et al. [28] show that the upstream effect of the splitters is negligible in Plane B, close to the locations probed in this paper. To discern the impact of the HPT vanes from one of the struts onto the TVF hub platform pressure distribution, an analytical model is introduced. The model (analogous to the one shown in [28]) interprets the circumferential pressure profile as the superposition of two sinusoidal contributions, HPT vanes, and TVF struts, with different amplitude k, phase shift φ, and periodicity:

$$C_P(\theta) = \overline{C}_P + k_V \cos[V(\theta + \varphi_V)] + k_S \cos[S(\theta + \varphi_S)] \tag{11}$$

The model is fit to the experimental data in MATLAB [29], using a nonlinear least-squares procedure, to estimate the values of k_V, k_S, φ_V and φ_S. It should be mentioned that the geometric vane-strut clocking is known, therefore φ_V and φ_S are constrained to $\pm\theta_V/2$ and $\pm\theta_S/2$ around the respective geometric value: this solves the uncertainty related to the periodic nature of the sinusoidal function while keeping a certain flexibility on φ_V and φ_S, to account for non-axial propagation of vanes and struts pressure fields. It is also worth mentioning that, in the charts showing circumferential variations of quantities, the positive direction of θ is against the rotor revolution, as specified in Figure 1.

The concentration effectiveness profiles, reported in the Results and Discussion section, are obtained from

$$\varepsilon = \frac{c_s - c_a}{c_0 - c_a}, \tag{12}$$

where c_s is the seed gas concentration retrieved from the sampled air in the test section, c_0 is the seed gas concentration in the purge supply line (upstream of the cavity) and c_a is the seed gas concentration in the annulus flow (not artificially seeded). The measurement locations of c_0 and c_a are specified in Figure 1. $\varepsilon = 1$ means that $c_s = c_0$, i.e., the sample contains undiluted sealing flow, while $\varepsilon = 0$ ($c_s = c_a$) signifies absence of the seeded cavity supply. Values in the range $0 < \varepsilon < 1$ indicated the presence of purge flow in the sampled air, diluted with the mainstream flow.

Finally, the unsteady pressure readings of the piezoresistive sensors are reported as non-dimensional pressure fluctuations:

$$C'_P(t) = \frac{P(t) - \overline{P}}{P_{ref}} \tag{13}$$

and they are illustrated in the frequency domain after the application of a discrete Fourier transform (DFT).

5. Results and Discussion

The Results and Discussion section is divided into three subsections: the first one describes the time-averaged field inside the DHC; the second one the time-averaged measurements on the stator platform downstream of the DHC; the third one the unsteady pressure field characterizing the DHC.

5.1. Time-Averaged Flow Inside the DHC

5.1.1. Effect of the Sealing Flow Rate

Figure 4a describes the impact of the PFR onto the pressure coefficient radial profile at $\Delta\theta_S/\theta_S = 0$. The average pressure level in the cavity increases with higher purge mass flow rates, while the slope of the profiles decreases with higher coolant injection. Both effects reduce the ingress of annulus flow inside the wheel space, improving the sealing performance. Focusing on the taps at $x = 0.98$ and $x = 1$, respectively inside and outside of the seal lip, a large pressure difference $C_{P,x=1} - C_{P,x=0.98} > 0$ is visible for $PFR = 0$, signifying an important ingestion of main stream flow. The pressure gradient progressively decreases moving towards $PFR = 2$, where the difference becomes negative, suggesting that ingress is locally suppressed. Between the two extremes, it should be possible to find the minimum purge flow rate that maximizes the sealing effectiveness.

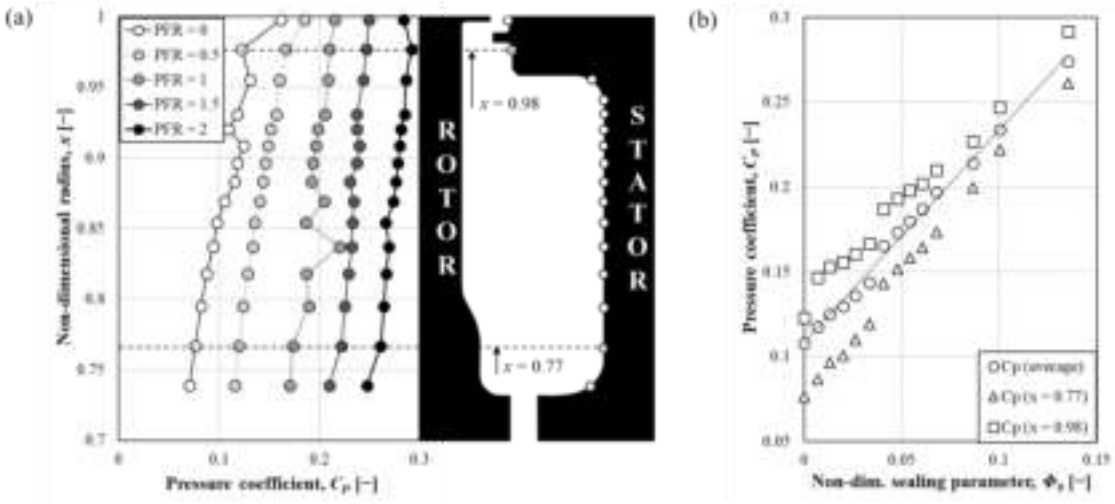

Figure 4. Pressure coefficient inside the DHC: (**a**) radial profiles with varying PFR. Data are acquired at $\Delta\theta_S/\theta_S = 0$ and $\Delta\theta_V/\theta_V = 0$; (**b**) pressure coefficient as a function of the sealing flow rate parameter (radial average and local values at $x = 0.77,\ 0.92$).

Figure 4b shows the variation of the radially averaged pressure coefficient with the non-dimensional sealing parameter (white circles). In agreement with Beard et al. [15], the data are well represented by a straight line (the linear regression's coefficient of determination is $R^2 = 0.9931$). Such a line is a good estimator of the trend across the full radial extent, especially at high injection rates. In fact, the markers of $C_{P,x=0.77}$ (white triangles) and $C_{P,x=0.98}$ (white squares) are enclosed in relatively narrow intervals around the average values.

The radial development of the DHC swirl ratio β is depicted in Figure 5a. The maximum values are reached for $PFR = 0$ (white circles), with an overall decrease of the swirl ratio across x at higher PFRs. This trend has been reported, among others, by Sangan et al. [30] and Patinios et al. [31] for several seal configurations. For the case without injection, the average β between $x = 0.79$ and $x = 0.89$ is 0.41, approaching the theoretical (0.44) and experimental (0.43) values found by Daily and Nece [26] in an enclosed rotating disk with similar G and Re_Ω. At $x = 0.74$ and $x = 0.93$, the profile diverges from the theoretical threshold because of the proximity to the inner and outer seals, respectively. The swirl ratio data in Figure 5a are pitot-based, meaning that they are obtained from both static and total pressure measurements, according to Equations (7) and (8).

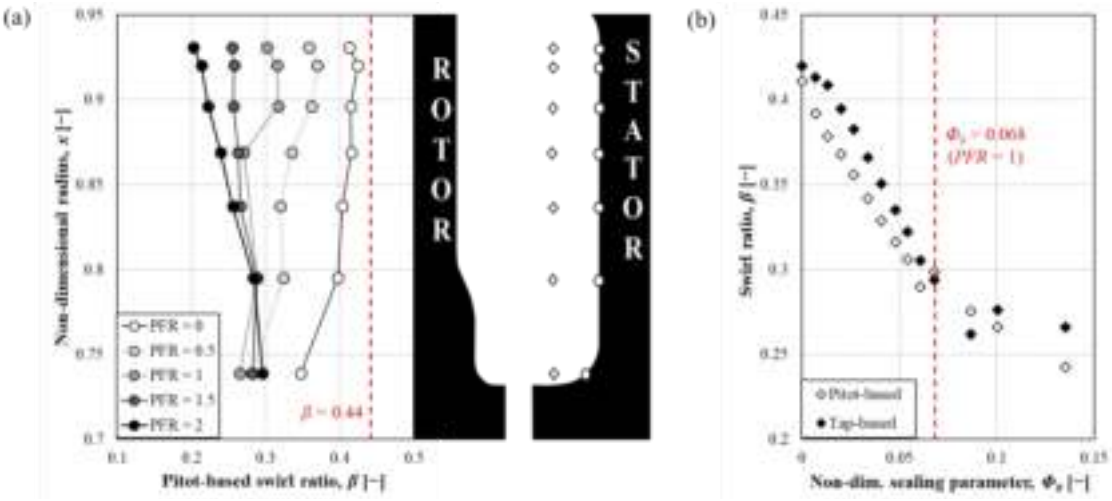

Figure 5. Swirl ratio inside the DHC: (**a**) radial profiles with varying PFR. Data are acquired at $\Delta\theta_S/\theta_S = 0$ and $\Delta\theta_V/\theta_V = 0$; (**b**) radially averaged swirl ratio as a function of the sealing flow rate parameter (pitot-based and tap-based calculation).

Figure 5b displays the comparison between the pitot-based swirl ratio (white diamonds, radially averaged) and the swirl ratio estimated as per Equation (9), i.e., purely based on the wall taps readings (black diamonds). The pitot-based and tap-based results are in good agreement, showing the same response to the PFR variation. When the sealing flow increases, the swirl ratio undergoes a steep drop up to $\Phi_0 \approx 0.068$ ($PFR = 1$), where both curves flatten.

5.1.2. Effect of Vane and Strut Clocking

Figure 6a includes the pressure coefficient profiles inside the DHC for the tested HPT vane clocking arrangements at $PFR = 0$ and $PFR = 1$. The data are acquired at $\Delta\theta_S/\theta_S = 0$, i.e., with the taps aligned to the strut LE. The vane clocking effect can penetrate the DHC up to $x \approx 0.96$ without injection, while for $x < 0.96$ all the clocking cases collapse onto the same profile. At $PFR = 1$, the penetration is lower (up to $x \approx 0.98$) and the maximum C_P variation generated by the clocking is smaller. Although the impact of the individual clocking positions remains unclear, the case $\Delta\theta_V/\theta_V = 0.7$ (squared markers) features the highest pressure at $x = 1$, for both purge conditions.

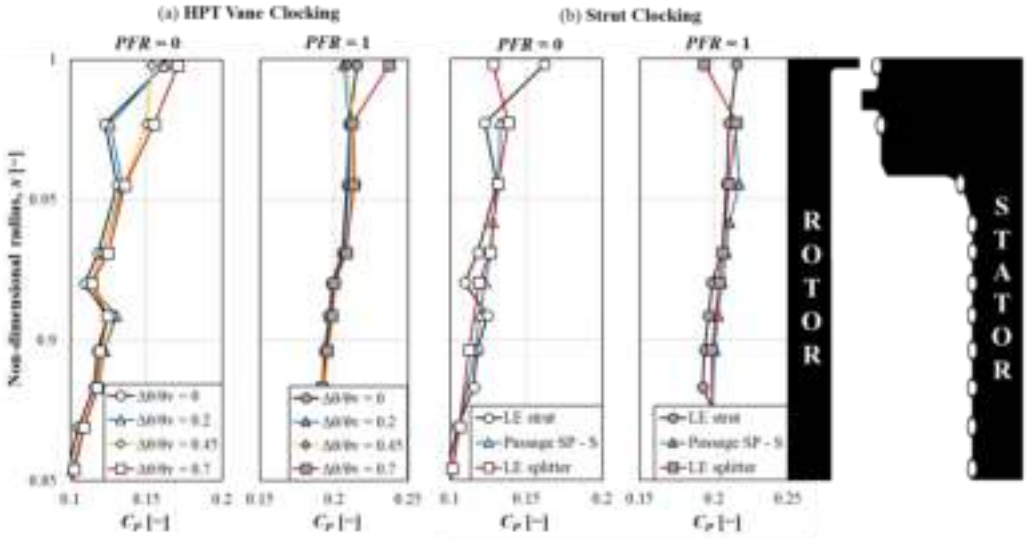

Figure 6. Radial pressure coefficient profiles inside the DHC: (**a**) with varying HPT vane clocking ($\Delta\theta_V/\theta_V$); (**b**) with varying strut clocking ($\Delta\theta_S/\theta_S$). Data at $PFR = 0$ (**left**) and $PFR = 1$ (**right**) are shown for both cases.

The strut clocking effect is evaluated in Figure 6b, at $PFR = 0$ and $PFR = 1$. In this case, the HPT vane position is kept nominal ($\Delta\theta_V/\theta_V = 0$). The penetration appears higher for the strut clocking than for the vane clocking, with perturbations detected up to $x \approx 0.91$ at $PFR = 0$. Once again, the sealing air tends to suppress the influence of clocking in the cavity, reducing the maximum C_P variation and its penetration in the cavity, as evidenced by the $PFR = 1$ radial lines. The pressure measured in front of the strut LE (squared markers) always tops the one at the splitter II-strut mid-passage (circular markers) for $x = 1$, due to the strut potential effect (the splitter LE tap is not available for this comparison). Although not shown in the paper, data at $PFR = 2$ are also acquired and analyzed, confirming the qualitative trends observed between the no-purge and the nominal conditions, both in terms of HPT vane and strut clocking.

5.1.3. Sealing Performance

The sealing effectiveness, calculated sampling DHC fluid from the stator taps at $x = 1$ (white markers) and $x = 0.93$ (black markers), is plotted in Figure 7a as a function of the sealing flow parameter for all the tested purge mass flows. As expected, the effectiveness generally increases with Φ_0, and the values obtained outside of the rim seal are generally lower than the ones inside the cavity, taken at the same PFR. All the represented datasets, corresponding to different HPT vane clocking configurations, show a plateau for $\Phi_0 > 0.068$ ($PFR = 1$). This value can thus be associated with the minimum sealing flow rate to prevent ingress ($\Phi_0 = \Phi_{0,min} \approx 0.068$). The maximum effectiveness at $x = 1$ is $\varepsilon \approx 0.90 < 1$, demonstrating that, outside of the stator lip, the annulus flow penetrates the rotor-stator gap even with high purge mass flows. On the other hand, the maximum effectiveness at $x = 0.93$ is $\varepsilon = 0.99 \approx 1$ (within the uncertainty of the analyzer). Therefore the rim seal is capable, with a suitable purge air supply, of guaranteeing fully sealed operation in the wheel space. The fact that $\Phi_{0,min}$ is in the proximity of the nominal case means that the DHC is properly designed to suppress hot annulus flow ingestion in normal operating conditions without injecting excessive coolant, which would diminish the turbine efficiency. $\Phi_{0,min}$ obtained in this work is much higher than the value obtained by Scobie et al. [7] for a similar DHC ($\Phi_{0,min} \approx 0.033$): the difference in annulus Mach number ($M < 0.2$ for [7]) is identified as the main cause of the discrepancy, leading higher Re_W and $C_{0,min}$. As a counterproof, the minimum sealing flow rate is closer to the outcome of [10] ($\Phi_{0,min} \approx 0.09$), obtained for an upstream radial-clearance seal, but with $M \approx 0.4$.

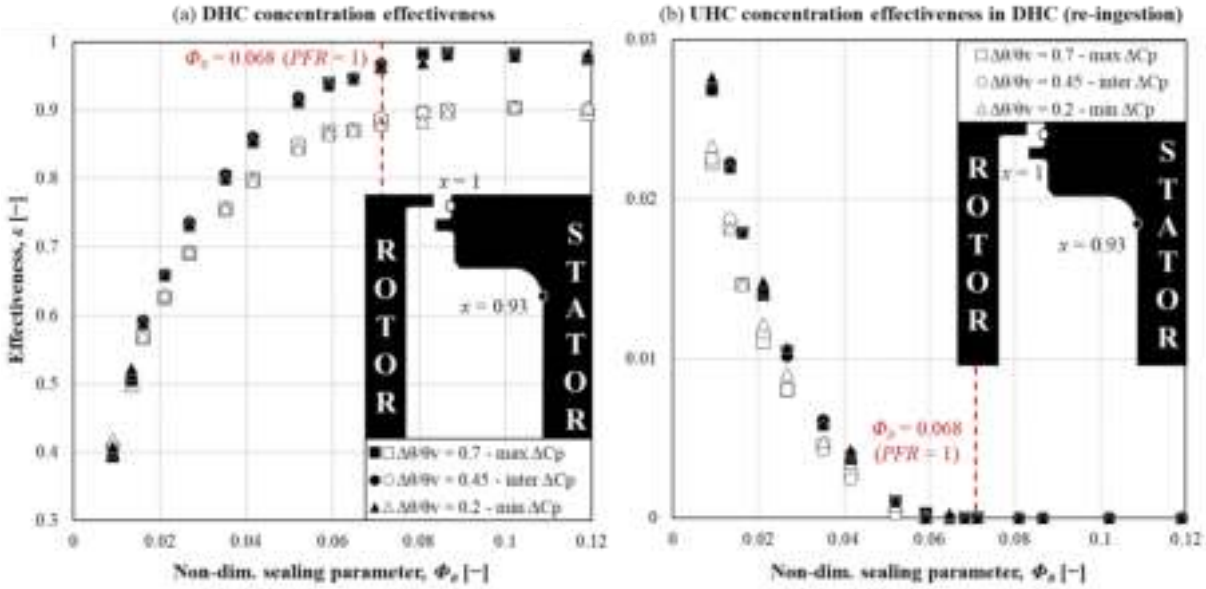

Figure 7. Concentration effectiveness as a function of the DHC sealing flow parameter: (**a**) in the DHC; (**b**) in the UHC. Data are acquired in the DHC at $x = 0.93,\ 1$ for both cases.

The marker shapes in Figure 7a symbolize different vane clocking positions, which practically collapse all on the same curves, one for each measurement location. As indicated in the legend of the plot, the clocking positions correspond to different $\Delta C_{P,max} = \max[C_P(\theta)] - \min[C_P(\theta)]$, where $C_P(\theta)$ are the pressure coefficients retrieved from the first array of wall taps on the TVF hub wall ($z/L_{c,z} = 0.28$). In the following section, it will be shown that at $PFR = 1$, $\Delta\theta_V/\theta_V = 0.2$ returns the minimum $\Delta C_{P,max}$, $\Delta\theta_V/\theta_V = 0.7$ the maximum $\Delta C_{P,max}$, and $\Delta\theta_V/\theta_V = 0.45$ an intermediate $\Delta C_{P,max}$. Contrary to what is expected from the traditional models/correlations (see the Introduction section), in which the predicted $\Phi_{0,min}$ is proportional to $\Delta C_{P,max}^{0.5}$, the results reveal the insensitivity of the sealing performance to the vane clocking arrangement, thus to $\Delta C_{P,max}$. Such an outcome is in line with the findings of Hualca et al. [9], who varied $\Delta C_{P,max}$ by axially displacing the upstream vane row. This suggests that the mentioned models may not provide the most appropriate description of the ingress phenomenon for the setup under examination, where the presence of upstream and downstream airfoils generates a complex hub flow field, and the annulus Reynolds and Mach are relatively high. In this sense, Graikos et al. [11] recently proposed a novel interpretation of ingress, correlated to the swirl ratio difference between annulus and rim seal clearance rather than to $\Delta C_{P,max}$. Unfortunately, the test vehicle is not equipped for annulus swirl ratio measurements at the axial location of the DHC gap, which could back up their interpretation.

The dual-channel configuration of the gas analyzer is exploited by seeding the HPT upstream hub cavity (UHC) with a different gas in order to evaluate the UHC purge re-ingestion in the DHC. The results are illustrated in Figure 7b, with varying DHC purge mass flow. For all the measured data, the UHC PFR is maintained at 1 (nominal mass flow). The UHC effectiveness is maximum with small Φ_0 in the DHC, indicating relatively high re-ingestion levels when little to no DHC sealing flow is injected. Interestingly, ε at $x = 0.93$ appears higher than at $x = 1$: this is ascribed to the presence of small leaks between the UHC and the DHC through the rotor blade roots at $x > 0.96$, where the silicone sealant locally deteriorated. Even for the case $\Phi_0 = 0.009$, where the leakage shows the highest impact in the effectiveness chart, its mass flow is estimated to be marginal ($< 1\%$ of the DHC injection), hence aerodynamically negligible. Finally, the HPT vane clocking does not produce relevant changes in the amount of re-ingestion, as also found for the DHC purge effectiveness.

5.1.4. Oil Flow Visualization

The pseudo-streamlines obtained with the oil flow visualization are presented in Figure 8. The rotor and stator pictures are limited to $x < 0.6$ and $0.7 < x < 1$, respectively,

hiding confidential mechanical details. Figure 8a reports a scheme of the flow structures expected in a rotor-stator cavity with sealing flow injection to be compared with the experimental results. The fact that the sealing configuration in the scheme is different from the tested rim seal is irrelevant to the current discussion. A Batchelor-like flow structure is thought to form in the cavity [30]: the fluid moves radially inwards on the stator boundary layer and outwards on the rotor one, while the inviscid core rotates at a fraction of the rotor speed and transports fluid from the stator boundary layer to the rotor one. According to the Taylor-Proudman theorem, no axial and tangential velocity gradients are present in the core, and the radial velocity is zero.

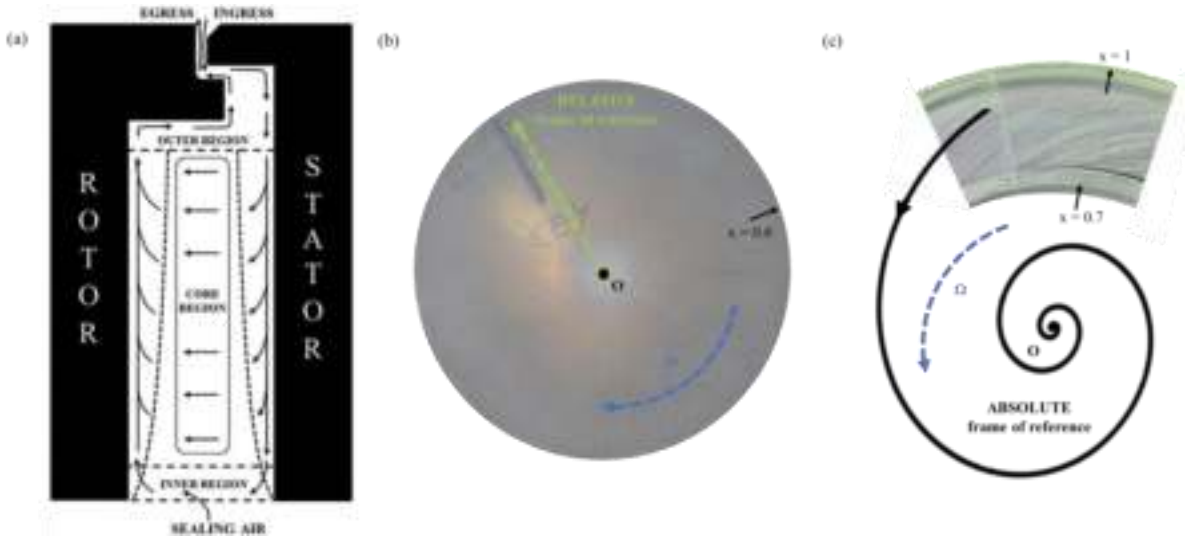

Figure 8. Flow structures in the DHC: (**a**) theoretical scheme, adapted from Patinios et al. [31]; (**b**) oil flow visualization results (rotor side); (**c**) oil flow visualization results (stator side). Oil flow visualization is performed at $PFR = 1$ and $\Delta\theta_V/\theta_V$, $\Delta\theta_S/\theta_S = 0$.

The wall shear stress trajectories on the rotor wall (Figure 8b) appear as straight lines (green arrow) departing from the center of the rotor and spreading radially outwards due to the disk pumping effect on the boundary layer flow. As explained in Section 3.2.4, the rotor disk was not initially painted with oil, meaning that the pattern is produced by the stator boundary layer air, feeding the rotor boundary layer. Being on the rotor disk, the straight lines represent the flow motion in the relative frame of reference: after including the contribution of the rotor speed (blue arrow), the stress trajectories in the absolute frame of reference would appear as spirals. The pigment pattern on the stator wall (Figure 8c) also assumes the shape of spirals, produced by the combination of the flow absolute tangential velocity in the same direction of the rotor speed, and the absolute radial velocity, directed inwards to satisfy the continuity in the DHC. The pseudo-streamlines are in agreement with the theoretical model, and, to the authors' knowledge, they constitute the first open-literature example of oil flow visualization inside an engine-representative cavity.

5.2. Time-Averaged Flow on the Stator Platform

5.2.1. Pressure Measurements—Effect of the Sealing Flow Rate

The circumferential pressure coefficient profiles, acquired at $z/L_{c,z} = 0.28$, are displayed in Figure 9a, for $PFR = 0$, 0.5, 1, 1.5, 2. Although the stage total pressure ratio is kept constant during the tests, the secondary air injection causes local boundary layer energization on the TVF hub platform, resulting in a static pressure decrease when the PFR rises. The analytical model, described by Equation (11), has been fitted to all the investigated cases but is here reported only for the extremes $PFR = 0$ (dotted line) and $PFR = 2$ (dashed line). The agreement with experimental data is very good, and the adjusted coefficient of determination, averaged across the tested PFRs, is $R^2_{adj} \approx 0.9$. The

model is capable of capturing the low-spatial-frequency oscillations related to the TVF struts, as well as the high-spatial-frequency peaks derived from the HPT vanes. By plotting the amplitude ratio k_V/k_S against Φ_0, as in Figure 9b, the relative contribution of the vane and the strut pressure fields on the hub circumferential distribution is assessed. The amplitude of the vane-related pressure oscillations (propagating downstream) is consistently about 30% of the strut-related oscillations (propagating upstream) for $\Phi_0 < 0.054$ ($PFR = 0.8$). The k_V/k_S ratio then experiences a sudden drop, with the minimum found at $\Phi_0 = 0.068 \approx \Phi_{0,min}$ ($PFR = 1$), where the vane-related amplitude is only 20% of the strut-related amplitude. Finally, the amplitude ratio undergoes a steep increase for $\Phi_0 > \Phi_{0,min}$, reaching approximately 45% at $\Phi_0 = 0.135$ ($PFR = 2$).

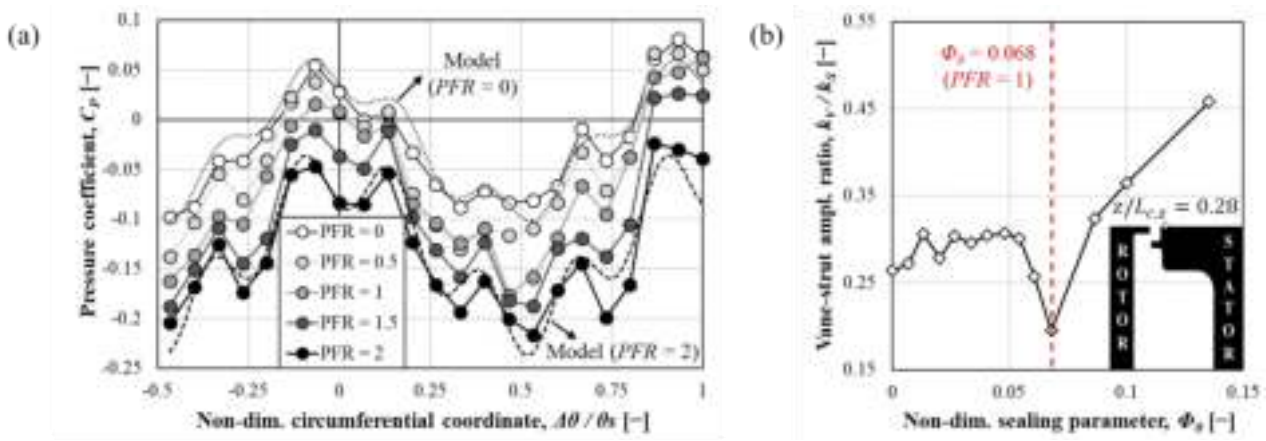

Figure 9. Pressure coefficient on the TVF hub platform: (**a**) circumferential profiles with varying PFR; (**b**) vane-strut amplitude ratio, estimated from the analytical model in Equation (11), as a function of the sealing flow parameter. Experimental and model results are for $z/L_{c,z} = 0.28$ and $\Delta\theta_V/\theta_V = 0$.

A non-monotonic behavior is also observed for the variation of $\Delta C_{P,max}$ over Φ_0, depicted by the white diamonds in Figure 10a. The peak-to-through pressure coefficient variation reaches a maximum at $\Phi_0 = 0.068 \approx \Phi_{0,min}$ ($PFR = 1$). In other words, the minimum sealing flow rate to prevent ingress is the one that faces the largest $\Delta C_{P,max}$. This indicates a tight connection between $\Phi_{0,min}$ and $\Delta C_{P,max}$ exists, although Figure 7 seems to refute $\Delta C_{P,max}$ as the main driver for ingress. The average C_P (black diamonds) has instead a monotonic decreasing trend, already evidenced in Figure 9a and associated to the stator platform boundary layer energization. More specifically, for low purge injection rates, the interaction between ingress and egress flows is thought to form a recirculation zone [32] in the outer region, leading to increased blockage ahead of the stator hub surface and thus, higher static pressure. At high PFRs, the recirculation disappear, the purge flow travels radially up to the rotor seal lip and then is deflected onto the stator platform, lifting up the annulus fluid and locally increasing the velocity in the boundary layer, with a corresponding pressure drop.

The trend of $\Delta C_{P,max}$ and average C_P, moving axially downstream of the cavity on the stator platform, is represented in Figure 10b, for five PFRs. The peak-to-through difference (squared marker) is maximum in the proximity of the cavity, reaches a minimum between $z/L_{c,z} = 0.71$ and $z/L_{c,z} = 2.12$, then increases again at higher $z/L_{c,z}$. This development is related to the vane-strut contribution on the hub circumferential pressure profile: the decay of the vane-related amplitudes is predominant immediately downstream of the DHC, causing the local minimum; approaching the strut LEs, the strut-related oscillations intensify and overcompensate the previously described effect, leading to higher $\Delta C_{P,max}$. The PFR influence loses strength moving further from the stator-rotor gap, becoming negligible at $z/L_{c,z} = 6.36$. The average C_P (diamond markers) rapidly rises on the TVF hub platform, consistently with the annulus geometry: in fact, the first bent of the S-shaped duct is known to produce a hub (+)-to-shroud (−) pressure gradient [33]. Interestingly, the average pressure decrease with purge, observed in Figure 10a, is completely reversed in

the interval $z/L_{c,z} = 0.71 - 2.12$, after which C_P grows with higher PFRs. The behavior is attributed to the purge injection impact on the average tangential velocity in the near-end wall region, which affects the radial equilibrium in the annulus.

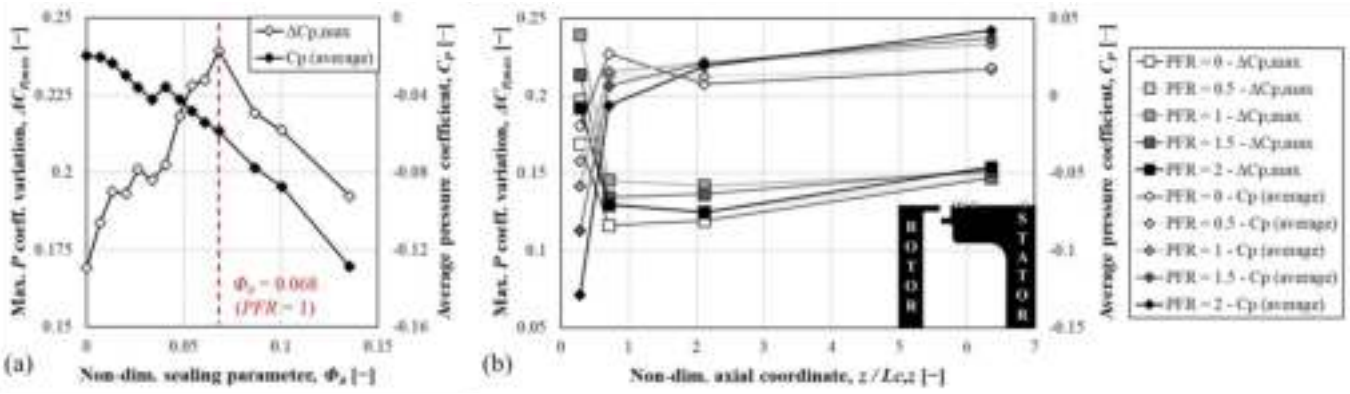

Figure 10. Annulus pressure coefficient, peak-to-trough variation and average value: (**a**) at $z/L_{c,z} = 0.28$, as a function of the sealing flow parameter; (**b**) as a function of the axial distance from the cavity, for a selection of PFRs. Data are acquired at $\Delta\theta_V/\theta_V = 0$.

5.2.2. Pressure and Effectiveness Measurements—Effect of Vane Clocking

Figure 11 includes a side-by-side comparison of the pressure coefficient, measured on the TVF hub platform at $z/L_{c,z} = 0.28$, and the corresponding DHC concentration effectiveness, calculated from the same wall taps. The plots allow us to evaluate both the effect of the sealing flow rate ($PFR = 0,\ 1,\ 2$) and the effect of the HPT vane clocking ($\Delta\theta_V/\theta_V = 0,\ 0.2,\ 0.7$). Since it is not possible to perform concentration measurements without seed gas, thus without purge, the $PFR = 0.2$ is plotted in Figure 11d instead of $PFR = 0$. As anticipated in Section 5.1.3, Figure 11b indicates that at $PFR = 1$, $\Delta C_{P,max}$ for $\Delta\theta_V/\theta_V = 0.7$ is about 10% larger than the same value for $\Delta\theta_V/\theta_V = 0$ and 25% larger than the value for $\Delta\theta_V/\theta_V = 0.2$ (the $\Delta\theta_V/\theta_V = 0.45$ case, not reported here, is analogous to the $\Delta\theta_V/\theta_V = 0$ case in terms of $\Delta C_{P,max}$). The point-to-point pressure difference is high at some locations (e.g., around $\Delta\theta/\theta_S = 0.5$ in Figure 11a). In fact, the measurement resolution is limited by the size of the stator platform and of the taps' lead-out paths, which have to fit inside the hollow struts. Nonetheless, the curves are in good agreement with the analytical model in Equation (11), with proper values of the fitting parameters. The purge increase is responsible for the reduction of average C_P in Figure 11a–c (from left to right), already described in Section 5.2.1. At the same time, the average ε level increases (Figure 11d–f, from left to right). Interestingly, the case of overall maximum $\Delta C_{P,max}$, which is $PFR = 1$ and $\Delta\theta_V/\theta_V = 0.7$ (red line in Figure 11b), coincide with the one of maximum $\Delta\varepsilon_{max}$ (red line in Figure 11e), where $\Delta\varepsilon_{max} = \max[\varepsilon(\theta)] - \min[\varepsilon(\theta)]$. Moreover, the k_V/k_S ratio was found to be maximum for $PFR = 2$ (see Section 5.2.1): this explains why, in the profiles of Figure 11c, the vane-related periodicity is more pronounced than the strut-related one. The k_V/k_S trend also influences the effectiveness curves in Figure 11f, where the θ_S-periodic oscillation is barely recognizable.

When looking at the tangential C_P and ε asymmetries, the observed overall trend is that low pressure corresponds to high effectiveness and vice versa. Such a trend can be better appreciated in Figure 12, where the C_P (squared markers) and ε (circular markers) data for $PFR = 1$ and $\Delta\theta_V/\theta_V = 0$ are singled out. The two profiles are almost in opposition to phase, with only a slight circumferential shift. All the considerations above point to the conclusion that, although the pressure hub profile appears not to affect $\Phi_{0,min}$, it remains the main driver for the distribution of the cavity egress inside the annulus. The same conclusion is reached by Scobie et al. [7], although, in their experiments, the high-effectiveness peaks are aligned with the high-pressure peaks.

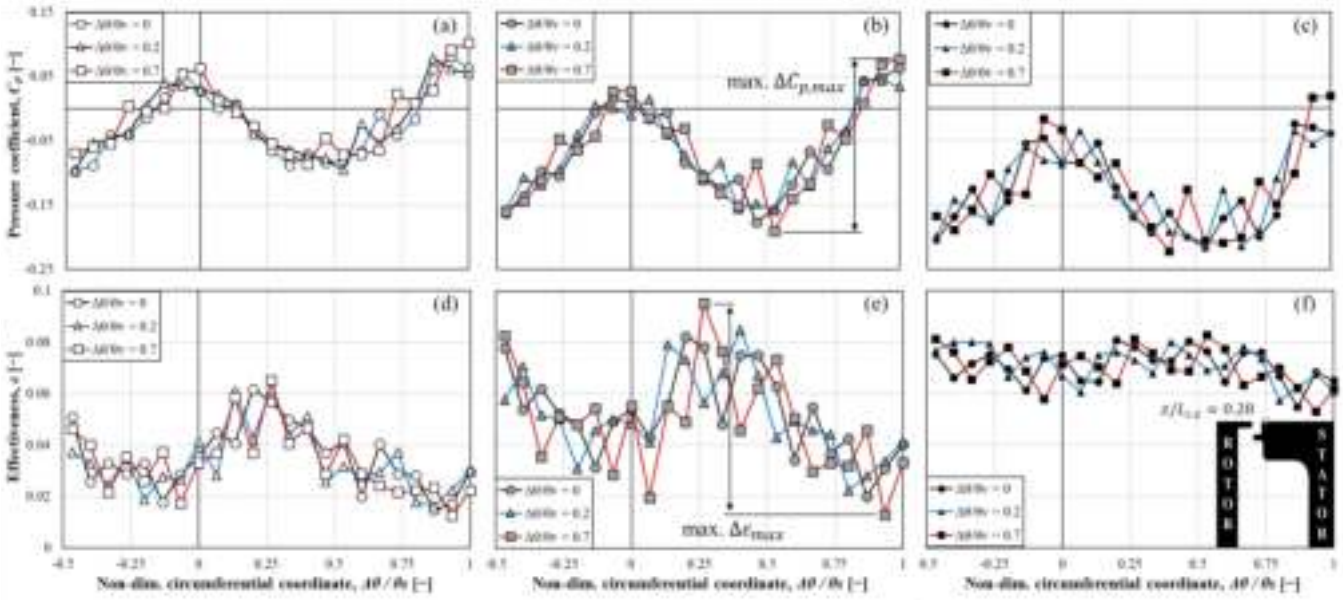

Figure 11. Annulus pressure coefficient circumferential profiles for: $PFR = 0$ (**a**), $PFR = 1$ (**b**), and $PFR = 2$ (**c**). Annulus effectiveness circumferential profiles for $PFR = 0.2$ (**d**), $PFR = 1$ (**e**), and $PFR = 2$ (**f**). Data are acquired at $z/L_{c,z} = 0.28$ and $\Delta\theta_V/\theta_V = 0,\ 0.2,\ 0.7$.

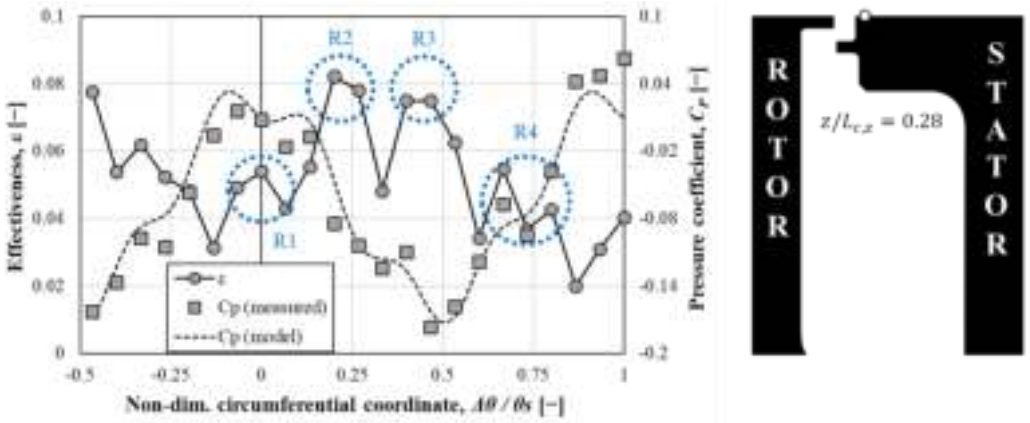

Figure 12. Annulus pressure coefficient and circumferential effectiveness profiles for $PFR = 1$. Data are acquired at $z/L_{c,z} = 0.28$ and $\Delta\theta_V/\theta_V = 0$. Both measured (grey squares) and modeled (dashed line) pressure coefficients are plotted. High-effectiveness peaks are indicated by the labels R1–R4.

5.2.3. Oil Flow Visualization

A picture of the oil flow traces on the TVF hub wall is reported in Figure 13. Since the oil-pigment mixture is injected through the DHC stator wall taps (see the Experimental Setup section), the colored pattern represents the sealing flow distribution on the downstream hub surface across a full TVF strut pitch ($\Delta\theta_S/\theta_S = 0 - 1$, as indicated by the red text and dashed lines). Such distribution can be therefore compared to the concentration effectiveness circumferential profile in Figure 12. The figures show good agreement in terms of correspondence between pigment streaks and effectiveness peaks. More specifically, four regions with heavy residues of pigment, interspersed by as many uncolored areas, are highlighted in Figure 13 by the blue dotted circles and labeled as $R1 - R4$. The circumferential position of $R1 - R4$ matches the position of the local ε maxima in Figure 12, suggesting that the adopted visualization technique is suitable to qualitatively study the egress phenomenon.

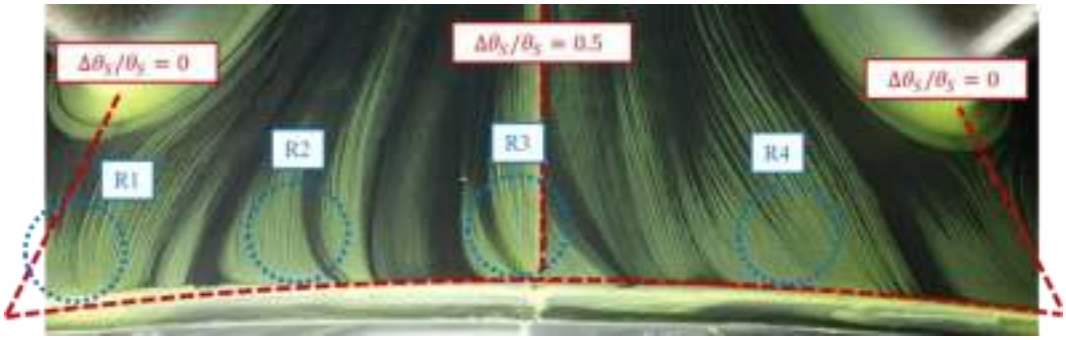

Figure 13. Oil flow visualization in the annulus (stator hub platform) for $PFR = 1$ and $\Delta\theta_V/\theta_V = 0$. Regions with high pigment accumulation are indicated by the labels R1–R4.

5.3. Time-Resolved Pressure Measurements Inside the DHC

The unsteady pressure fluctuations, measured at $PFR = 1$ and $\Delta\theta_S/\theta_S = 0$, are depicted in Figure 14 for three radial positions ($x = 0.92,\ 0.98,\ 1$). All the spectra are dominated by the HPT blade passing frequency component ($f = 1 \cdot BPF$), which reaches up to $2 - 2.6\%$ of the reference pressure, depending on the radial sensor location. Additionally, secondary peaks are visible at the BPF harmonics ($f = 2 \cdot BPF,\ 3 \cdot BPF,\ 4 \cdot BPF$). While the investigated radial positions show comparable amplitudes at the BPF, the outermost sensor ($x = 1$, outside of the stator seal lip) always measures the highest magnitude at the BPF multiples. A minor peak is spotted at $f \approx 0.63 \cdot BPF$, which corresponds to a linear combination of the HPT and LPT blade passing frequencies: Merli et al. [34] also found pressure fluctuations with the mentioned periodicity in the annulus, upstream of the TVF struts. No non-synchronous components, which could be associated with rotating flow modes [18], are detected with the current measurement setup, at least not in the same order of magnitude as the BPF-related components.

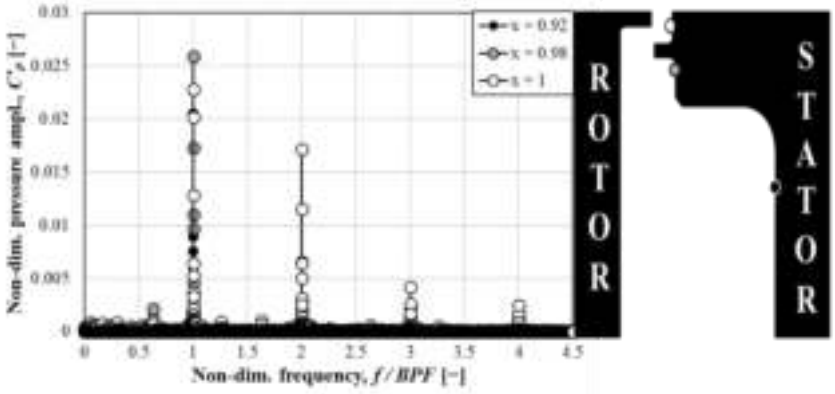

Figure 14. Non-dimensional pressure spectra at different radial positions in the DHC. Data are acquired at $PFR = 1$, $x = 0.92,\ 0.98,\ 1$ and $\Delta\theta_V/\theta_V,\ \Delta\theta_S/\theta_S = 0$.

The effects of sealing flow rate and strut clocking on the non-dimensional BPF pressure component ($C'_{P,BPF}$) are evaluated in Figure 15. In particular, the figure compares $C'_{P,BPF}$ at $\Delta\theta_S/\theta_S = 0$ (strut LE, black line) and $\Delta\theta_S/\theta_S = 1/3$ (splitter LE, red line) across the investigated Φ_0 range. Figure 15a shows the results for $x = 0.92$: two local maxima are found, at approximately $\Phi_0 = 0.02$ and $\Phi_0 = 0.068$. The strut clocking effect seems not to penetrate the analyzed location inside the DHC, as the two curves are almost overlapping. Figure 15b illustrates the results for $x = 1$: the fluctuations at $f = BPF$ are generally higher compared to the previous case and, in terms of strut clocking, the fluctuations at $\Delta\theta_S/\theta_S = 1/3$ (red line) are more intense. The trend with PFR is diametrically opposite to what is reported in Figure 15a: low $C'_{P,BPF}$ values are measured for $\Phi_0 \leq 0.02$, then the oscillations rise up to a maximum before $\Phi_0 = 0.068$, where a sudden drop is noticed.

Interestingly, such behavior is analogous to the k_V/k_S curve in Figure 9b, suggesting that the periodic unsteadiness is driven by the interaction of the vane-strut steady pressure field with the time-dependent blade contribution.

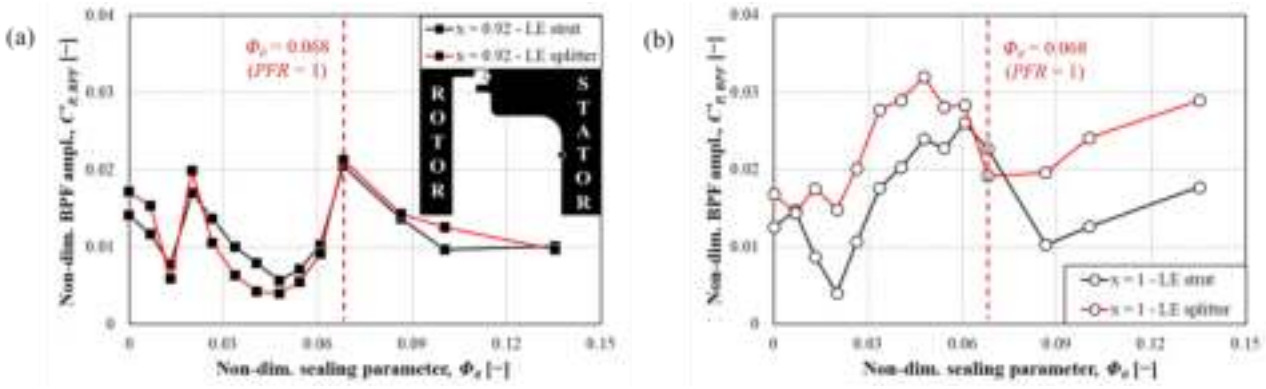

Figure 15. Non-dimensional pressure amplitude at $f = 1 \cdot BPF$ as a function of the sealing flow parameter for two strut clocking positions ($\Delta\theta_S/\theta_S = 0,\ 2/3$). (**a**) Results at $x = 0.92$. (**b**) Results at $x = 1$. Data are acquired at $\Delta\theta_V/\theta_V = 0$ for both cases.

Finally, the C'_P spectra with different HPT vane clocking arrangements ($\Delta\theta_V/\theta_V = 0.2$, $0.45, 0.7$) are plotted in Figure 16. As expected from the analysis of the pneumatic measurements, no significative change is noticeable at $x = 0.92$ (Figure 16a), where the vane clocking effect appears not to penetrate. Conversely, at $x = 1$ (Figure 16b), the configuration $\Delta\theta_V/\theta_V = 0.45$, indicated with the diamond markers and corresponding to an intermediate $\Delta C_{P,max}$, shows a $1 \cdot BPF$ component about 75% larger than both the other cases.

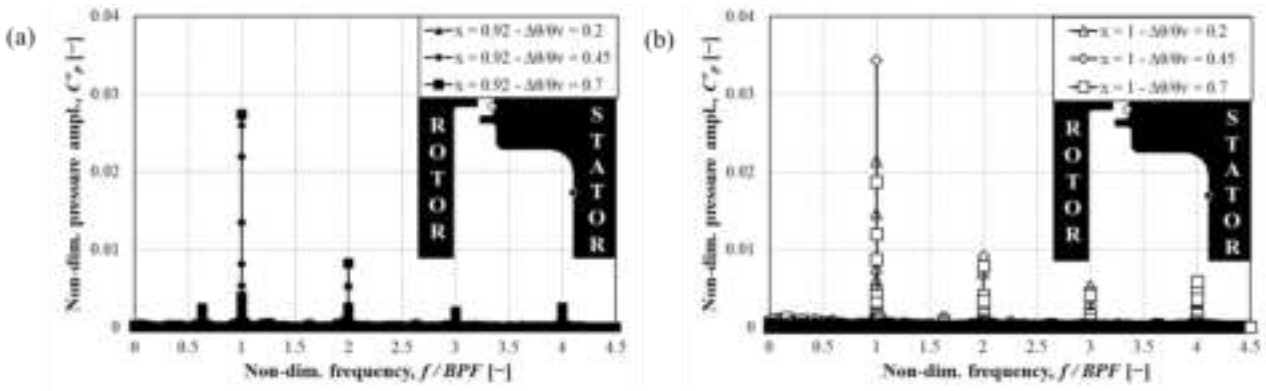

Figure 16. Non-dimensional pressure spectra at different HPT vane clocking positions ($\Delta\theta_V/\theta_V = 0.2$, $0.45, 0.7$). (**a**) Results at $x = 0.92$. (**b**) Results at $x = 1$. Data are acquired at $PFR = 1$ and $\Delta\theta_S/\theta_S = 0$.

6. Conclusions

The paper presents the outcome of steady and unsteady measurements inside the downstream hub cavity of an HPT stage integrated into a two-stage turbine setup. The engine-relevant test vehicle and the realistic annulus flow conditions adopted in the study constitute an important novelty with respect to the available literature on the topic. The steady measurements consist of both aerodynamic (pressure) measurements inside the wheel space and on the stator platform and concentration effectiveness measurements. Additionally, unsteady pressure measurements and oil flow visualization are carried out to further characterize the cavity flow features. A large number of sealing flow rates is investigated, extending from $PFR = 0$ to $PFR = 2$. The effects of the HPT vane and TVF strut clocking are also assessed.

The static pressure on the DHC stator wall linearly increases with PFR, thus with Φ_0. The swirl ratio in the cavity is maximum at $PFR = 0$ and steeply decreases with the sealing flow rate up to $\Phi_0 \approx 0.068$ ($PFR = 1$), where its sensitivity to the injection drops.

For the case without purge, the pressure variation due to vane and strut clocking is found to penetrate up to $x = 0.95$ and $x = 0.9$ inside the DHC, respectively. The purge injection reduces both the radial penetration and the strength of the pressure variation.

The concentration effectiveness data reveal that for $\Phi_0 \geq 0.068 = \Phi_{0,min}$ ($PFR \geq 1$), ingress is mainly confined to the rim seal region ($x > 0.93$), which, in real engine applications, can be protected with heat-resistant alloys. Moreover, re-ingestion of the upstream hub cavity sealing flow is detected for low DHC injection rates.

The pressure on the TVF hub platform is fitted to an analytical model, which allows isolating the vane and strut contributions on the measured circumferential profile. The average pressure in the annulus decreases with higher PFRs, while the peak-to-trough variation is maximized at $\Phi_{0,min}$. Additionally, $\Delta C_{P,max}$ varies with the HPT vane clocking, but this is demonstrated to have negligible impact on the value of $\Phi_{0,min}$. This appears in contrast with the traditional ingress models, developed in less engine-representative test environments. Further analyses would be required to consolidate the limits of the mentioned models in testbeds of similar complexity. Nevertheless, the hub pressure profile predominantly drives the distribution of the DHC egress inside the annulus, as confirmed by the effectiveness of circumferential profiles and the oil flow visualization.

Finally, the unsteady pressure spectra are dominated by the BPF ccomponent and its harmonics for each tested purge and clocking condition. No non-synchronous oscillations with the same order of magnitude are identified. Higher harmonics of the BPF are particularly strong at $x = 1$, and they are partially suppressed inside the cavity. At the same time, the $1 \cdot BPF$ component shows minor strut and vane clocking effects at $x = 0.92$, coherently with the pneumatic measurements. Such effects are instead considerable at $x = 1$, where the sensor at $\Delta\theta_S/\theta_S = 2/3$ and the vane clocking position $\Delta\theta_V/\theta_V = 0.45$ have the highest BPF-periodic fluctuations.

Author Contributions: Conceptualization, M.P. and E.G.; methodology, F.M. and M.P.; software, F.M. and M.P.; validation, F.M., N.K. and A.H.; formal analysis, F.M. and M.P.; investigation, F.M., N.K., A.H. and M.P.; resources, N.K. and A.H.; data curation, F.M.; writing—original draft preparation, F.M.; writing—review and editing, M.P. and E.G.; visualization, F.M.; supervision, E.G.; project administration, E.G.; funding acquisition, E.G. All authors have read and agreed to the published version of the manuscript.

Funding: The project leading to this application has received funding from the Clean Sky 2 Joint Undertaking under the European Union's Horizon 2020 research and innovation program (grant agreement No 785313).

Institutional Review Board Statement: Not applicable.

Informed Consent Statement: Not applicable.

Data Availability Statement: Restrictions apply to the availability of the data presented in this study. The data are available on request from the corresponding author, prior authorization of GE Aviation.

Acknowledgments: The authors would like to thank F. Mangini for his contribution in operating the test facility and GE Aviation for the permission to publish this paper.

Conflicts of Interest: The authors declare no conflict of interest. The funders had no role in the design of the study; in the collection, analyses, or interpretation of data; in the writing of the manuscript; or in the decision to publish the results.

Nomenclature

Abbreviations

BPF	blade passing frequency
DFT	discrete Fourier transform
HPT, LPT	high-pressure, low-pressure turbine
ITD	intermediate turbine duct
LE	leading edge

PFR	purge flow ratio
TVF	turbine vane frame
UHC, USC	upstream hub/shroud cavity
DHC, DSC	downstream hub/shroud cavity
Symbols	
z, r, θ	axial, radial, tangential coordinate
V, S, SP	HPT vane, TVF strut, TVF splitter
b	rotor lip inner radius
c	concentration
C	non-dimensional coefficient
f, t	frequency, time
G	gap ratio
k, φ	pressure model amplitude, phase
L	length
$\dot{m}$	mass flow
P	pressure
Re	Reynolds number
V	core absolute velocity
W, M	annulus absolute velocity
x	non-dimensional radius
β	swirl ratio
ε	concentration effectiveness
λ_T	turbulent flow parameter
ρ, μ	density, dynamic viscosity
Φ	non-dimensional sealing parameter
Ω	disk rotational speed
Subscripts and Superscripts	
$0, a, s$	cavity, annulus, sample
c	clearance
des	design vane position
F	flow
in	inner seal
min	minimum sealing flow
max	peak-to-trough difference
P	pressure
T	total
W	annulus
Ω	rotational
$\bar{}$	average component
$'$	time-dependent component

References

1. Owen, J.M. Prediction of Ingestion Through Turbine Rim Seals—Part II: Externally Induced and Combined Ingress. *J. Turbomach.* **2010**, *133*, 11. [CrossRef]
2. Regina, K.; Kalfas, A.I.; Abhari, R.S. Experimental Investigation of Purge Flow Effects on a High Pressure Turbine Stage. *J. Turbomach.* **2014**, *137*, 41006. [CrossRef]
3. Phadke, U.P.; Owen, J.M. Aerodynamic aspects of the sealing of gas-turbine rotor-stator systems: Part 3: The effect of nonaxisymmetric external flow on seal performance. *Int. J. Heat Fluid Flow* **1988**, *9*, 113–117. [CrossRef]
4. Bohn, D.; Wolff, M. Improved Formulation to Determine Minimum Sealing Flow—Cw, min—for Different Sealing Configurations. In Proceedings of the ASME Turbo Expo 2003, Collocated with the 2003 International Joint Power Generation Conference, Atlanta, GA, USA, 16–19 June 2003; Volume 5.
5. Hamabe, K.; Ishida, K. Rim Seal Experiments and Analysis of a Rotor-Stator System With Nonaxisymmetric Main Flow. In Proceedings of the ASME 1992 International Gas Turbine and Aeroengine Congress and Exposition, Cologne, Germany, 1–4 June 1992; Volume 1: Turbomachinery.

6. Chew, J.W.; Green, T.; Turner, A.B. Rim Sealing of Rotor-Stator Wheelspaces in the Presence of External Flow. In Proceedings of the ASME 1994 International Gas Turbine and Aeroengine Congress and Exposition, The Hague, The Netherlands, 13–16 June 1994; Volume 1: Turbomachinery.
7. Scobie, J.A.; Hualca, F.P.; Sangan, C.M.; Lock, G.D. Egress Interaction Through Turbine Rim Seals. *J. Eng. Gas Turbines Power* **2018**, *140*, 4. [CrossRef]
8. Scobie, J.A.; Hualca, F.P.; Patinios, M.; Sangan, C.M.; Owen, J.M.; Lock, G.D. Re-Ingestion of Upstream Egress in a 1.5–Stage Gas Turbine Rig. *J. Eng. Gas Turbines Power* **2018**, *140*, 4. [CrossRef]
9. Hualca, F.P.; Horwood, J.T.M.; Sangan, C.M.; Lock, G.D.; Scobie, J.A. The Effect of Vanes and Blades on Ingress in Gas Turbines. *J. Eng. Gas Turbines Power* **2020**, *142*, 1. [CrossRef]
10. Sangan, C.M.; Pountney, O.J.; Zhou, K.; Wilson, M.; Owen, J.M.; Lock, G.D. Experimental Measurements of Ingestion Through Turbine Rim Seals—Part I: Externally Induced Ingress. *J. Turbomach.* **2012**, *135*, 11.
11. Graikos, D.; Tang, H.; Sangan, C.M.; Lock, G.D.; Scobie, J.A. A New Interpretation of Hot Gas Ingress Through Turbine Rim Seals Influenced by Mainstream Annulus Swirl. *J. Eng. Gas Turbines Power* **2022**, *144*, 9. [CrossRef]
12. Cao, C.; Chew, J.W.; Millington, P.R.; Hogg, S.I. Interaction of Rim Seal and Annulus Flows in an Axial Flow Turbine. *J. Eng. Gas Turbines Power* **2004**, *126*, 786–793. [CrossRef]
13. Jakoby, R.; Zierer, T.; Lindblad, K.; Larsson, J.; Bohn, L.D.E.; Funcke, J.; Decker, A. Numerical Simulation of the Unsteady Flow Field in an Axial Gas Turbine Rim Seal Configuration. In Proceedings of the ASME Turbo Expo 2004: Power for Land, Sea, and Air, Vienna, Austria, 14–17 June 2004; Volume 4: Turbo Expo 2004.
14. Roy, R.P.; Feng, J.; Narzary, D.; Paolillo, R.E. Experiment on Gas Ingestion Through Axial-Flow Turbine Rim Seals. *J. Eng. Gas Turbines Power* **2005**, *127*, 573–582. [CrossRef]
15. Beard, P.F.; Gao, F.; Chana, K.S.; Chew, J. Unsteady Flow Phenomena in Turbine Rim Seals. *J. Eng. Gas Turbines Power* **2016**, *139*, 9.
16. Savov, S.S.; Atkins, N.R.; Uchida, S. A Comparison of Single and Double Lip Rim Seal Geometries. *J. Eng. Gas Turbines Power* **2017**, *139*, 7. [CrossRef]
17. Gao, F.; Chew, J.W.; Marxen, O. Inertial waves in turbine rim seal flows. *Phys. Rev. Fluids* **2020**, *5*, 2. [CrossRef]
18. Chew, J.W.; Gao, F.; Palermo, D.M. Flow mechanisms in axial turbine rim sealing. *Proc. Inst. Mech. Eng. Part C J. Mech. Eng. Sci.* **2018**, *233*, 7637–7657. [CrossRef]
19. Marn, A.; Göttlich, E.; Cadrecha, D.; Pirker, H.P. Shorten the Intermediate Turbine Duct Length by Applying an Integrated Concept. *J. Turbomach.* **2009**, *131*, 7. [CrossRef]
20. Zerobin, S.; Aldrian, C.; Peters, A.; Heitmeir, F.; Göttlich, E. Impact of Individual High-Pressure Turbine Rotor Purge Flows on Turbine Center Frame Aerodynamics. In Proceedings of the ASME Turbo Expo 2017: Turbomachinery Technical Conference and Exposition, Charlotte, NC, USA, 26–30 June 2017.
21. Sterzinger, P.Z.; Merli, F.; Peters, A.; Behre, S.; Heitmeir, F.; Göttlich, E. Impact of Turbine–Strut Clocking on the Performance of a Turbine Center Frame. *J. Turbomach.* **2021**, *143*, 51011. [CrossRef]
22. Hubinka, J.; Santner, C.; Paradiso, B.; Malzacher, F.; Göttlich, E.; Heitmeir, F. Design and construction of a two shaft test turbine for investigation of mid turbine frame flows. In Proceedings of the ISABE, Montreal, QC, Canada, 7–11 September 2009; pp. 7–11.
23. Steiner, M.; Zerobin, S.; Bauinger, S.; Heitmeir, F.; Göttlich, E. Development and Commissioning of a Purge Flow System in a Two Spool Test Facility. In Proceedings of the 2th European Conference on Turbomachinery Fluid dynamics & Thermodynamics, Stockholm, Sweden, 3–7 April 2017.
24. Patinios, M.; Merli, F.; Hafizovic, A.; Göttlich, E. The Interaction of Purge Flows With Secondary Flow Features in Turbine Center Frames. In Proceedings of the ASME Turbo Expo 2021: Turbomachinery Technical Conference and Exposition, Virtual, 7–11 June 2021; Volume 2C: Turbomachinery—Design Methods and CFD Modeling for Turbomachinery; Ducts, Noise, and Component Interactions.
25. Bayley, F.J.; Owen, J.M. The Fluid Dynamics of a Shrouded Disk System with a Radial Outflow of Coolant. *J. Eng. Power* **1970**, *92*, 335–341. [CrossRef]
26. Daily, J.W.; Nece, R.E. Chamber Dimension Effects on Induced Flow and Frictional Resistance of Enclosed Rotating Disks. *J. Basic Eng.* **1960**, *82*, 217–230. [CrossRef]
27. Childs, P. *Rotating Flow*; Elsevier Science: Amsterdam, The Netherlands, 2010.
28. Merli, F.; Hafizovic, A.; Krajnc, N.; Schien, M.; Peters, A.; Heitmeir, F.; Göttlich, E. The Interaction of Main Stream Flow and Cavity Flows in Turbine Center Frames and Turbine Vane Frames. *J. Eng. Gas Turbines Power* **2022**, *145*, 12.
29. *MATLAB*, version 9.7.0 (R2019b); The MathWorks Inc.: Natick, MA, USA, 2019.
30. Sangan, C.M.; Lalwani, Y.; Owen, J.M.; Lock, G.D. Experimental Measurements of Ingestion Through Turbine Rim Seals: Part 5—Fluid Dynamics of Wheel-Space. In Proceedings of the ASME Turbo Expo 2013: Turbine Technical Conference and Exposition, San Antonio, TX, USA, 3–7 June 2013; Volume 3A: Heat Transfer.
31. Patinios, M.; Scobie, J.A.; Sangan, C.M.; Owen, J.M.; Lock, G.D. Measurements and Modeling of Ingress in a New 1.5-Stage Turbine Research Facility. *J. Eng. Gas Turbines Power* **2016**, *139*, 8. [CrossRef]
32. Savov, S.S.; Atkins, N.R. A Rim Seal Ingress Model Based on Turbulent Transport. In Proceedings of the ASME Turbo Expo 2017: Turbomachinery Technical Conference and Exposition, Charlotte, NC, USA, 26–30 June 2017; Volume 5B: Heat Transfer.

33. Göttlich, E. Research on the aerodynamics of intermediate turbine diffusers. *Prog. Aerosp. Sci.* **2011**, *47*, 249–279. [CrossRef]
34. Merli, F.; Krajnc, N.; Hafizovic, A.; Patinios, M.; Göttlich, E. Unsteady Investigation of Intermediate Turbine Ducts under the Influence of Purge Flows. In Proceedings of the ASME Turbo Expo 2023, Boston, MA, USA, 26–30 June 2023.

Disclaimer/Publisher's Note: The statements, opinions and data contained in all publications are solely those of the individual author(s) and contributor(s) and not of MDPI and/or the editor(s). MDPI and/or the editor(s) disclaim responsibility for any injury to people or property resulting from any ideas, methods, instructions or products referred to in the content.

International Journal of
Turbomachinery
Propulsion and Power

MDPI

Article

Development of Sewage Pumps with Numerical and Experimental Support

David Beck * and Paul Uwe Thamsen

Chair of Fluid System Dynamics, Faculty of Mechanical Engineering and Transport Systems, Technische Universität Berlin, 10623 Berlin, Germany
* Correspondence: david.beck@tu-berlin.de; Tel.: +49-30-314-70941

Abstract: Especially in the field of sewage pumps, the design of radial impellers focuses not only on maximum efficiency but also on functionality in terms of susceptibility to clogging by fibrous media. In general, the efficiency of sewage impellers is significantly lower than that of clear water impellers. These sewage impellers are designed with a low number of blades to ensure that fibrous media can be pumped. This paper describes the methodology of an optimisation for a sewage impeller. The optimisation is carried out on a semi-open two-channel impeller as an example. Therefore, a new impeller is designed for a given volute casing. Based on a basic design for given boundary conditions, the impeller is verified by means of numerical simulation. The manufactured impeller is then tested on the test rig to verify the simulation. With regard to the optical investigations, the clogging behaviour of the impeller is specifically improved over three different modifications in order to finally present an impeller with good efficiency and a low clogging tendency.

Keywords: sewage impeller; CFD; optical measurement

check for updates

Citation: Beck, D.; Thamsen, P.U. Development of Sewage Pumps with Numerical and Experimental Support. *Int. J. Turbomach. Propuls. Power* **2023**, *8*, 18. https://doi.org/10.3390/ijtpp8020018

Academic Editors: János Gábor Vad, Csaba Horváth and Tamás Benedek

Received: 13 February 2023
Revised: 3 May 2023
Accepted: 21 May 2023
Published: 2 June 2023

Copyright: © 2023 by the authors. Licensee MDPI, Basel, Switzerland. This article is an open access article distributed under the terms and conditions of the Creative Commons Attribution (CC BY-NC-ND) license (https://creativecommons.org/licenses/by-nc-nd/4.0/).

1. Introduction

Sewage pumps face increased operational problems due to clogging, for example, clogging within the impeller or the volute casing, according to increased contamination of solids in sewage. This represents the main reason for downtime, wear and manual labour in wastewater plants [1,2]. These solids, which are mainly responsible for pump clogging, are often tear-resistant fibrous materials, for example wet wipes. Figure 1 shows the components of a pump blockage, where tear-resistant fibrous materials are the main component for the pump blockage, which were found in [3].

Figure 1. Constituents of pump blockage [3].

In contrast to freshwater pumps, impellers with a low number of blades or special impeller shapes are deliberately used in sewage pumps to handle solids in sewage as efficiently as possible. Typical impellers for sewage conveyance are closed and semi-open

multi-channel impellers, closed and semi-open single-channel impellers, as well as special forms such as the vortex impeller [4].

Up to now, pumps have been evaluated according to DIN EN ISO 9906 only with regard to their clear water values. There is no general criterion about the susceptibility to clogging for pumping sewage containing solids [5].

Compared to the described classical approach, the functional performance test has already been introduced in [6], which tests both the efficiency η and the clogging susceptibility of pumps.

In this paper, the methodology of an optimization for a sewage impeller is described. As an example, a semi-open two-channel impeller is designed. By means of simulation and functional performance tests on the test rig, a hydraulic system is to be developed, which, in addition to good efficiency, should have a low susceptibility to clogging. A classification of the susceptibility to clogging for the semi-open two-channel impeller is carried out using the evaluation criteria of the long-time functional performance test.

2. Materials and Methods

2.1. Basic Design

The new impeller is designed as a semi-open two-channel impeller. In contrast to closed impellers, which have both a hub and a shroud, semi-open impellers do not have a rotating shroud. For this impeller, the shroud is installed stationary in the housing, which creates a small gap between the impeller and the volute casing. This gap shall assist the discharge of added fibrous materials.

The impeller should be designed as a radial impeller and be within a range for the specific speed of $n_q = 30 \ldots 50$, which is typical for radial sewage impellers [7]. The specific speed n_q is calculated according to [8] as follows, using the speed n (1/min), the flow Q (m^3/s) and the head H (m):

$$n_q = n \frac{\sqrt{Q}}{H^{3/4}} \tag{1}$$

The design point for this impeller is given in normalised form, as the main focus in this paper is on the methodology of optimisation. The design point is continuously given for the flow with $Q_{design} = 1.0$; analogously, the head results in $H_{design} = 1.0$.

One requirement of the impeller is the maximum variability for changing the leading-edge geometry of the blades. Previous investigations have shown that impellers with classic leading edges often tend to increase clogging in two-channel impellers. The aim for this impeller is to be able to incorporate a 3D-printed geometry to connect the leading edges of the impeller, so-called connected leading edges (CLE), with maximum variability for the basic impeller. The classic impeller with two leading edges and a possible design of CLE are shown schematically in Figure 2.

The upper part of Figure 2 shows a classic approach for a semi-open two-channel impeller. The lower part of the figure shows two variants of a possible meridional contour for CLE: (A) shows a convex shape, which is intended to follow the course of the blade widths of the original blades. (B) shows a meridional contour for CLE that is flat and parallel to the suction side of the pump.

For the basic design of the impeller, the shape of two leading edges is chosen according to the upper part of Figure 2. The impeller is designed for the maximum specific speed according to the said range with a specific speed of $n_{q,design} = 50$, since a shift of the best efficiency point (BEP) due to the CLE in the direction of smaller flows is expected. This shift of the best efficiency point towards smaller flows is caused, among other things, by the fact that the effective area of the impeller suction side due to a decreasing inlet diameter as well as the blade inlet angle β_1 are reduced. Accordingly, a steeper characteristic curve is to be expected for the impeller with CLE compared to the impeller with two leading edges [4].

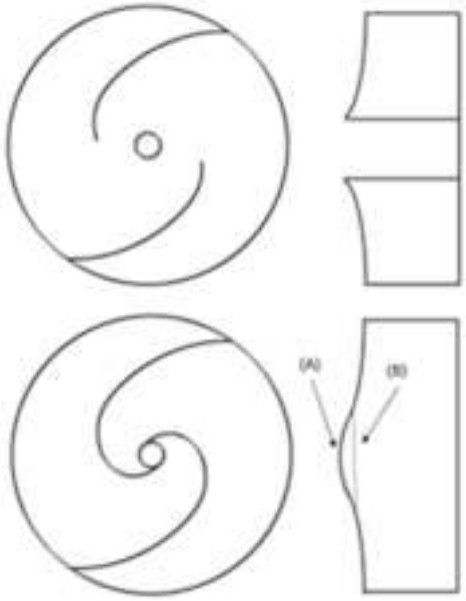

Figure 2. Meridional section and plan view for the semi-open two-channel impeller with two leading edges (**top**) and for the CLE (**bottom**), with a convex shape (A) as well as a flat shape (B).

The impeller is designed for a given sewage volute. Previous investigations of this volute casing have shown that it is particularly resistant to clogging. This is necessary in order to evaluate the impeller in terms of susceptibility to clogging. Clogging in the volute casing has a negative influence on the general susceptibility of the hydraulic and thus on the measurement result, because it is only possible to measure the total amount of wet wipes within the pump after the end of the test.

The spiral contour of the volute casing is circular. The built-in stationary shroud is used for all measurements.

The theoretical throttle curve is calculated for the impeller according to [8]. However, this is only a reference and is verified by the subsequent simulation and the measurement results of the tests.

2.2. Numerical Support

The impeller with two leading edges is simulated before manufacturing to evaluate the design.

For the numerical simulation, the software ANSYS CFX is used. For the impeller, a structured mesh is used. The volute is meshed as an unstructured mesh. The setup including the mesh is shown in Figure 3. Details on the mesh qualities are shown in Table 1.

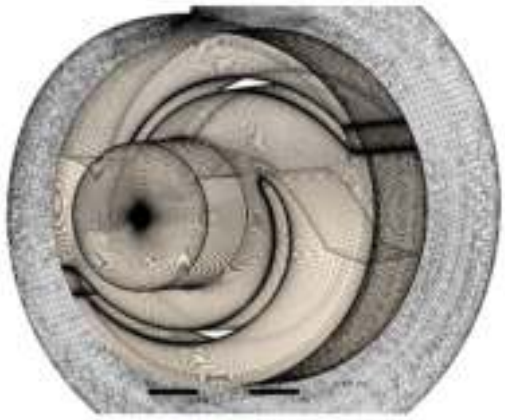

Figure 3. Mesh used for simulation.

Table 1. Mesh statistics.

Part	Elements
Impeller	827,772
Volute	864,356

The simulation is calculated in a stationary manner in order to shorten the calculation time. The shear stress transport model (SST) is chosen as the turbulence model in order to generate good resolution and convergence both in near-wall areas and free streams [9].

Some simplifications are applied for the simulation: The impeller, which is designed as a semi-open two-channel impeller, is simulated without the sidewall gap, as primarily the simulation is used for estimating the general design. The same applies to the gap between the impeller and the stationary shroud, as the size of the gap has an influence on the discharge of the wet wipes, which must be determined experimentally. Likewise, disk friction losses are not represented in their entirety by the setup.

Accordingly, the focus of the simulation is on verifying the basic geometry of the impeller. It can be assumed that the simulated results are better than the manufactured impeller due to the neglected losses. This applies in particular to the efficiencies at higher volume flows, as the hydraulic losses for higher volume flows have greater influence.

Ten operating points are simulated. Of these, the design point as well as three operating points to smaller flows compared to the design point and six points to higher flows compared to the design point are simulated.

Since the impeller is a semi-open two-channel impeller simulated without a gap, the shroud is assumed to be a counter-rotating wall. In addition, the shaft-hub connection of the hub is assumed to be a free-slip wall, as this does not exist in the prototype, so that the described CLE can be installed.

2.3. Impeller Prototyping

The basic impeller with two leading edges is made of cast iron, the only design change compared to the simulation is the shaft–hub connection. The impeller is manufactured in such a way that a 3D-printed attachment can be placed on the central shaft screw to connect the leading edges.

The impeller manufactured from cast iron is shown in Figure 4.

Figure 4. Modification 0—manufactured impeller.

The attachments are made from plastic polylactic acid (PLA) using a 3D printer, as this manufacturing is relatively inexpensive and fast concerning design changes. In addition, previous tests have shown that PLA exhibits sufficient strength when used with artificial sewage.

2.4. Test Procedure

The test rig for functional performance of the Chair of Fluid System Dynamics at the Technische Universität Berlin has two tanks, the wastewater tank (WWT) and the freshwater tank (FWT), each with a volume of 4 m^3.

Two different clogging tests can be carried out on the test rig using tear-resistant wet wipes—the functional performance test and the long-time functional performance test. The test rig has pinch valves, which make it possible to switch between the different tests and shut off the pump. In addition, a filter is installed in the FWT, which is decoupled from the system and removes all residual fibres in the test rig. The results of this paper are generated with the long-time functional performance test. Tear-resistant wet wipes according to the contamination classes in Table 2 are used for the tests.

Table 2. Contamination classes.

Contamination Class	Wipes/m^3
Clear water (CW)	0
Low contamination (L25)	25
Medium contamination (L50)	50
High contamination (L100)	100

Figure 5 shows the wet wipes used for the experiment. These have the dimensions of 22 × 30 cm and a surface weight of 60 g/m^2.

Figure 5. Wet wipes used for tests.

Generally, for both tests, the pumps are tested at their BEP, as well as at 80% of the BEP in partial load and at 120% of the BEP in overload. A total of nine measurements per impeller are thus carried out on the test bench.

Long-time functional performance test:

The long-time functional performance test describes the 60 min pumping of the artificial wastewater in a loop from the WWT to the WWT, shown in Figure 6. In the process, the measured values of the head, the flow and the electrical power are recorded every second. The efficiency η is determined using these data. After the test, the pump is shut off and opened, and the remaining wet wipes are documented and removed. From this, the degree of long-time functional performance (D_{LTF}) is determined according to Equation (2):

$$D_{LTF} = \frac{1}{2}\frac{\eta_{test,0\text{–}60min}[-]}{\eta_{CW,OP}[-]} + \frac{1}{2}\frac{m_{W,total}[g] - m_{W,pump}[g]}{m_{W,total}[g]} \quad (2)$$

Here, the first part of the D_{LTF} represents the ratio of the averaged efficiency over the 60-min measurement period ($\eta_{test,0\text{–}60min}$) to the clear water efficiency at the corresponding operating point ($\eta_{CW,OP}$). The second term of the D_{LTF} represents the ratio of the difference

between the total amount of wipes supplied ($m_{W,total}$) and the wipes remaining in the pump ($m_{W,pump}$) to the total amount of wipes supplied.

A D_{LTF} of 0 indicates that the impeller is completely clogged, and conveying is no longer possible, while a value of 1 describes clog-free operation. Based on the tests already carried out, a D_{LTF} of at least 0.7 is required for the prototype, as it has been shown that impellers above a value of 0.7 exhibit good clogging behaviour and can handle the added fibrous material well.

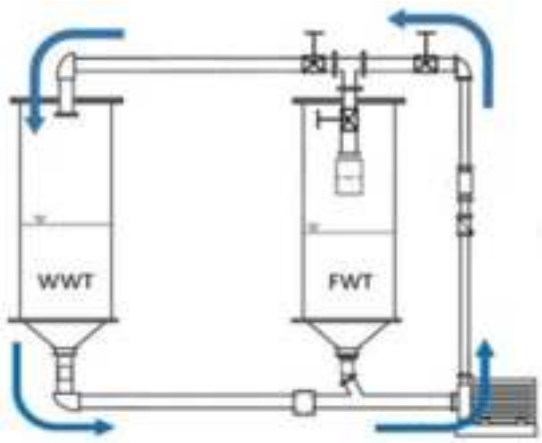

Figure 6. Long-time functional test cycle.

2.5. Optical Access

The test rig has an optical access on the suction side, which is similar to the optical access presented in [10]. By means of an endoscope, an LED light ring and a high-speed camera, it is possible to obtain closer insights at the impeller inlet during operation. Figure 7 shows the installed access.

Figure 7. Test setup for optical access.

As an additional measurement method, this approach provides an opportunity to describe the interaction between the flow and the wet wipes during operation and to make targeted changes in the geometry from the results. For these tests, the camera records at 1000 frames per second (fps) over a period of 20 seconds with a resolution of 768 × 768 pixels. The test cycle is analogous to the long-time functional performance test, but the contamination class is different. For these tests, ten wet wipes per m^3 of water are used, as it has been shown that with this quantity, initial clogging behaviour can be easily seen, while there are not too many wipes to impair the optimal measurement.

The endoscope has a diameter of 10 mm and a viewing direction of 45°. Due to the resulting installation position, this angle ensures that the wipes do not clog on the endoscope and thus a uniform supply of the wipes into the inlet of the pump is possible. The field of view is 88°. The LED light ring consists of eight individual LEDs, which provide a luminous flux of 5595 lumen each.

3. Results and Discussion

3.1. Results—Simulation

The simulation results in relation to the theoretical design curve are shown in Figure 8. For the simulation results, only the throttle curves are compared with each other, as an efficiency estimate was not carried out.

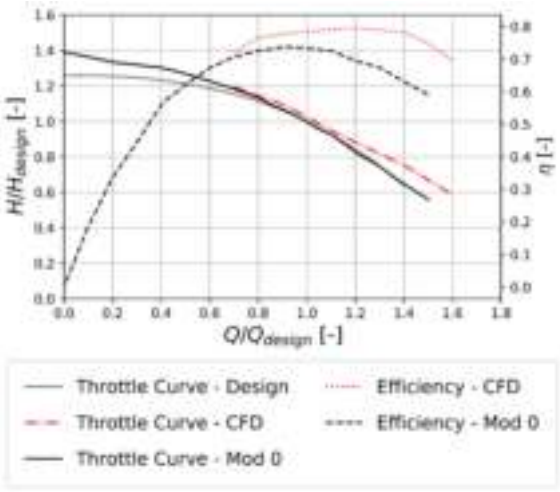

Figure 8. Modification 0—characteristic curves.

The results of the simulation show the same trend of the design characteristic. The simulated throttle curve shows a slightly higher level and is superior to all calculated operating points of the design throttle curve. This is due, among other things, to the simplifications of the simulation described above. This can also be said about the efficiency, for which a value of $\eta_{BEP,CFD}$ = 79.5% is achieved in the simulation. However, it can be seen that the BEP of the hydraulic with $Q_{BEP,CFD}$ = 1.2 is slightly larger than the design point.

Overall, this comparison shows that the design is well represented by the simulation with regard to its design characteristic. Due to the simplified assumptions, the efficiency reaches a higher value in the simulation than is to be expected in the measurement. Especially not all hydraulic losses are taken into account by the simplifications. Since these increase with higher flows, a shift of the optimal efficiency is to be expected with smaller flows. Likewise, a reduced efficiency at the BEP of the manufactured impeller can be assumed.

3.2. Results—Modification 0

Figure 8 additionally shows the measurement of the characteristic curves of the impeller with two leading edges on the test bench in relation to the simulation results as well as the design throttle curve.

The measured characteristic curves show the same trend of the simulation around the design point. Especially in the direction of smaller flows of the design point, the simulated and the measured throttle curves show an almost identical trend.

For strong partial load and overload, the measured throttle curve deviates from the design throttle curve. However, the design throttle curve only represents a trend and is mainly to be assumed for the range of best efficiency.

The maximum efficiency of the measured impeller is around 5% lower than the best efficiency value of the simulation. The BEP of the impeller is thus at a flow of $Q_{BEP,0}$ = 0.9

with an efficiency value of $\eta_{BEP,0}$ = 73.9%. This deviation is again due to the simplified assumptions of the simulation. This BEP results in a specific speed of $n_{q,0}$ = 48, which, taking into account the boundary conditions for the specific speed, provides a good starting point for the further process of inserting a printed part for CLE.

To obtain an impression of the susceptibility to clogging of the basic impeller, the long-time functional performance test with medium contamination (L50) is carried out for the impeller in Modification 0.

The impeller clogs with a result of $D_{LTF,0}$ = 0.32. The amount of wet wipes removed from the impeller at the end of the test corresponds to 72% of the amount of wet wipes supplied. The clogging has accumulated at the leading edges during the test and has grown from there. The clogging inside the impeller after the end of the long-time functional performance test can be seen in Figure 9.

Figure 9. Modification 0—clogging after long-time functional test (BEP, L50).

This impeller geometry is not able to discharge the wet wipes. Due to the high susceptibility to clogging, no further tests of the impeller are carried out.

3.3. Results—Optimization

Modification 1: For the first modification, a printed part for the CLE with a strongly convex shape in the meridional section as shown in Figure 2, example (A), is used, which follows the width progression of the two blades. The characteristic curves of modification 1 compared to modification 0 are shown in Figure 10.

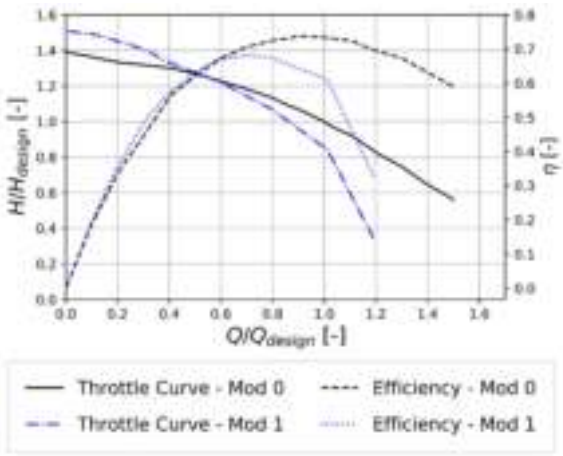

Figure 10. Modification 1—characteristic curves.

The characteristic curves of Modification 1 show that the BEP shifts towards smaller flows due to the CLE. The optimum efficiency of $\eta_{BEP,1}$ = 68.1% is achieved for a flow of $Q_{BEP,1}$ = 0.7. The resulting specific speed is $n_{q,1}$ = 37 and is therefore within the specified limits.

The long-time functional performance test with low contamination (L25) at the BEP shows a poor clogging result with a $D_{LTF,1}$ = 0.19, which is insufficient. Overall, 91% of 310 g of supplied wet wipes are absorbed. A conveying of the wipes does not seem possible due to this result of the long-time functional performance test.

The result of the long-time functional test suggests that conveying of the wet wipes cannot take place with high numbers of wet wipes arriving in the impeller at the same time, which clogs the impeller. In addition, the convex shape of the CLE extends very far forward into the inlet that the wipes cannot be discharged via the gap between the impeller and the volute casing as soon as the clogging has reached a certain degree.

In Figure 11 on the left-hand side, it is shown that the accumulation of the wet wipes extends into the suction pipe. As soon as the wipes are lying on the CLE and are not conveyed, the clogging grows in the direction of the suction pipe. In this case, self-cleansing of the impeller can no longer be expected.

Figure 11. Modification 1—clogging after long-time functional test (BEP, L25) (**left**) and optical investigations (**right**).

The optical measurement shows the extent to which the wet wipes interact with the impeller. The investigation has shown that single wet wipes lay loose on the printed part for the CLE but are conveyed within a few revolutions. A screenshot from the optical investigation is shown in Figure 11 on the right-hand side.

The impeller has suitable free-flushing characteristics for the arrival of single wet wipes, as the investigation has shown. Nevertheless, it can be said that the impeller is no longer able to flush off the wet wipes for higher incoming concentrations of wet wipes.

Modification 2: The second modification has a printed part for the CLE that is plane and parallel to the inlet of the pump, according to shape (B) in Figure 2. This is intended to prevent the flow from decreasing due to throttling on the suction side in the inlet pipe because of wet wipes, as can be seen for Modification 1.

While looking at the characteristic curves in Figure 12, the maximum efficiency of $\eta_{BEP,2}$ = 69.1% is reached at a flow of $Q_{BEP,2}$ = 0.7. As a result, the impeller achieves a specific speed of $n_{q,2}$ = 35. The throttle curve of Modification 2 shows a similar behaviour to Modification 1.

The long-time functional performance test for Modification 2 results in a $D_{LTF,2}$ = 0.43 for the BEP with low contamination (L25). In total, 64% of 309 g of supplied wet wipes are absorbed, which shows a significant improvement in clogging compared to Modification 1.

The clogging inside the impeller after the end of the long-time functional performance test can be seen in Figure 13 on the left-hand side.

Contrary to Modification 1, the wipes do not grow into the suction pipe and do not throttle the incoming flow. The impeller appears to have a degree of saturation, which, once reached, cannot accommodate any further wipes. This is particularly evident from the fact that a significantly lower proportion of wet wipes are absorbed compared with Modification 1.

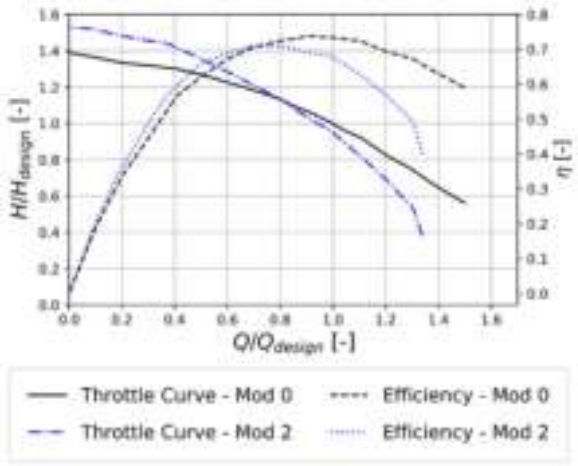

Figure 12. Modification 2—characteristic curves.

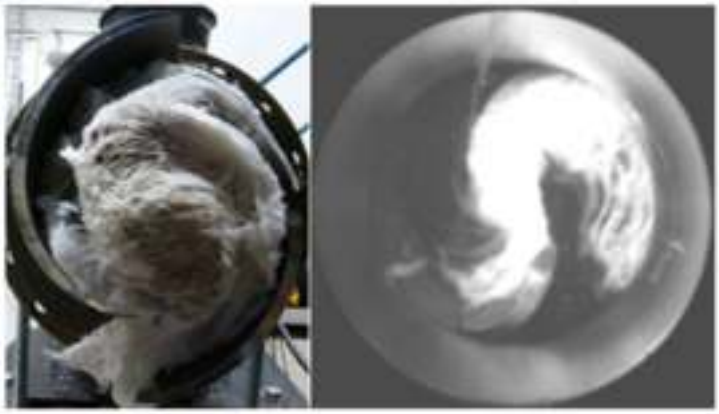

Figure 13. Modification 2—clogging after long-time functional test (BEP, L25) (**left**) and optical investigations (**right**).

By means of optical observations, it can be seen in Figure 13 on the right-hand side, that the wet wipes, which are sucked in centrally, also hit the centre of the CLE analogously to Modification 1, where they accumulate. In addition, the clogging on the CLE increases between the beginning of the test and the end of the test, which could be detected through the optical investigations. The geometry of the impeller is not able to discharge the wet wipes. Likewise, the wet wipes cannot be loosened by the impact of further incoming wet wipes. Accordingly, this flat contour is also not optimal for conveying wet wipes and tends to clog, even if the clogging result is improved compared to Modification 1.

Altogether, the modification is not able to convey wet wipes even in small concentrations, even if this modification shows a minor saturation of wet wipes and therefore has a higher D_{LTF}.

Modification 3: Another printed part is manufactured for the third modification, which combines the good conveying characteristics of Modification 1 with the advantages of the axial length of Modification 2 concerning the maximum amount of wet wipes absorbed.

The third modification shows a significantly smaller convex shape compared to Modification 1 to reduce the axial length and maintain the conveyance characteristics. Analogous to the first two modifications, Figure 14 shows the characteristic curves of Modification 3.

Modification 3 has its BEP as well as the other two modifications at $Q_{BEP,3}$ = 0.7. The best efficiency for this modification is $\eta_{BEP,3}$ = 64.5%. This modification results in a specific speed of $n_{q,3}$ = 37.

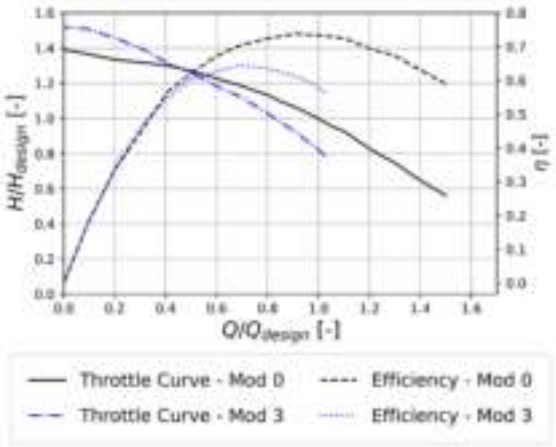

Figure 14. Modification 3—characteristic curves.

A long-time functional performance test with low contamination (L25) is also carried out for this modification. The impeller achieved a $D_{LTF,3}$ = 0.98. At the end of the measurement, the impeller had not absorbed any wet wipes from the 299 g supplied. The missing 2% of the D_{LTF} also can be attributed concerning Equation (2) to slight hydraulic dips during the test, which occur due to brief blockages within the test caused by the wet wipes. However, the impeller manages to continuously discharge the wet wipes.

The impeller manages to convey the wet wipes into the channels continuously over the measurement period for this type of CLE.

Table 3 shows the results for the long-time functional performance tests for all nine measurement setups:

Table 3. Measurement results: D_{LTF} for Modification 3 for three operating points.

Q/Q_{BEP}	L25	L50	L100
0.8	0.97	0.99	0.94
1.0	0.98	0.91	0.94
1.2	0.74	0.90	0.74

No further modification is necessary, as the impeller exceeds the required degree of long-time functional performance of 0.7 for all measurement points and thereby has the best clogging behaviour of all modifications.

3.4. Comparison of Results

Overall, the optimisation shows a considerable improvement in the D_{LTF} and thus the susceptibility to clogging, as can be seen in Figure 15.

Modification 0 shows a poor clogging result for the medium contamination with two leading edges. By using the CLE, the first modification also achieves an insufficient result in the long-time functional performance test. This is improved by targeted changes in the geometry through the detection of the weak points by means of optical tests as well as the long-time functional test.

The second modification still shows a high susceptibility to clogging with wet wipes, even though the D_{LTF} is improved a lot.

Through renewed optimization based on the findings of the optical tests and the test results of both previous modifications, a modification is tested that delivers a clog-free result for the low contamination. Likewise, the required D_{LTF} of over 0.7 will be achieved for all contaminations, in the BEP, in partial load and in overload.

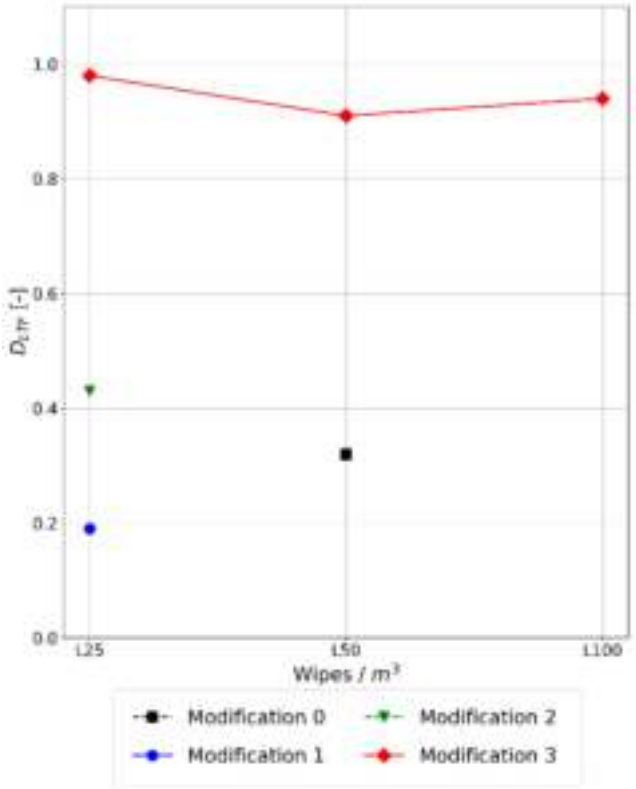

Figure 15. Overview over D_{LTF} for tested modifications for Q/Q_{BEP} = 1.0.

4. Conclusions

The use of simulations for a calculated sewage impeller in combination with a test rig to test the susceptibility to clogging has shown that impellers for sewage pumps can be designed and optimised according to specific criteria. The use of optical access is particularly noteworthy to specifically address the interaction between the wet wipes and the impeller and for making specific design changes.

Author Contributions: Conceptualization, D.B. and P.U.T.; methodology, D.B. and P.U.T.; software, D.B.; validation, D.B. and P.U.T.; formal analysis, D.B.; investigation, D.B.; resources, D.B. and P.U.T.; data curation, D.B.; writing—original draft preparation, D.B.; writing—review and editing, P.U.T.; visualization, D.B.; supervision, P.U.T.; project administration, P.U.T. All authors have read and agreed to the published version of the manuscript.

Funding: This research received no external funding.

Data Availability Statement: The data presented in this study are available on request from the corresponding author. The data are not publicly available due to the fact that it is standardized data that only supports the methodology of optimizing sewage impellers at the test bench in general.

Conflicts of Interest: The authors declare no conflict of interest.

References

1. Von Sperling, M. *Wastewater Characteristics, Treatment and Disposal*; IWA Publishing: London, UK, 2007; Volume 1.
2. Gerlach, S.; Thamsen, P.U. Cleaning sequence counters clogging—A quantitative Assessment under real operation conditions of a wastewater pump. In Proceedings of the ASME 2017 Fluids Engineering Division Summer Meeting, Waikoloa, HI, USA, 31 July–3 August 2017.
3. Mitchell, R.-L. *Causes, Effects and Solutions of Operational Problems in Wastewater Systems Due to Nonwoven Wet Wipes*; Mensch und Buch Verlag: Berlin, Germany, 2019.
4. Gülich, J. *Centrifugal Pumps*, 3rd ed.; Springer: Berlin, Germany, 2008.
5. *DIN EN ISO 9906: 2013-03*; Kreiselpumpen–Hydraulische Abnahmeprüfungen–Klassen 1, 2 und 3. Beuth Verlag: Berlin, Germany, 2013.

6. Pöhler, M. *Experimentelle Entwicklung Eines Standardisierten Abnahmeverfahrens für Abwasserpumpen*; Mensch und Buch Verlag: Berlin, Germany, 2020.
7. Surek, D. *Pumpen für Abwasser-und Kläranlagen: Auslegung und Praxisbeispiele*; Springer: Berlin/Heidelberg, Germany, 2014.
8. Pfleiderer, C.; Petermann, H. *Strömungsmaschinen*, 7th ed.; Springer: Berlin/Heidelberg, Germany, 2006.
9. Versteeg, H.K.; Malalasekera, W. *An Introduction to Computational Fluid Dynamics*, 2nd ed.; Pearson Education Limited: Essex, UK, 2007.
10. Steffen, M.; Thamsen, P.U. Visualization of interactions between impeller and textile in a wastewater pump. In Proceedings of the ASME 2021 Fluids Engineering Division Summer Meeting, Virtual, 10–12 August 2021.

Disclaimer/Publisher's Note: The statements, opinions and data contained in all publications are solely those of the individual author(s) and contributor(s) and not of MDPI and/or the editor(s). MDPI and/or the editor(s) disclaim responsibility for any injury to people or property resulting from any ideas, methods, instructions or products referred to in the content.

International Journal of
Turbomachinery
Propulsion and Power

MDPI

Article

Effects of Tip Leakage Vortex Cavitation on Flow Field under Cavitation Instability

Youngkuk Yoon and Seung Jin Song *

Department of Mechanical Engineering, Seoul National University, Seoul 08826, Republic of Korea; truesky1218@snu.ac.kr
* Correspondence: sjsong@snu.ac.kr

Abstract: Cavitation instabilities can induce axial and circumferential vibrations, as well as noise in turbopump inducers. Therefore, the purpose of the present study is to investigate the mechanism of cavitation instability. The flow field near the two-bladed inducer leading edge under alternate blade cavitation was experimentally investigated using particle image velocimetry (PIV). It was found that the tip leakage vortex cavitation draws the flow toward its region of collapse and induces a negative change in the incidence to the adjacent blade. Moreover, this blade-to-blade interaction was identified as the main cause of alternate blade cavitation. Furthermore, it was demonstrated that this blade-to-blade interaction is strongest when the cavity collapse occurs in the inducer throat area, where the leading edge of the following blade is located.

Keywords: turbopump inducer; cavitation instability; particle image velocimetry (PIV)

1. Introduction

Inducer cavitation instabilities can cause serious noise and vibration, which may result in the failure of the propulsion system. Therefore, their types and identification have received significant attention. For instance, Tsujimoto et al. [1] observed various cavitation instabilities that occurred in a three-bladed inducer and categorized them into local instabilities such as super-synchronous rotating cavitation and global instabilities such as cavitation surge. Similarly, Cervone et al. [2] experimentally observed a cavitation instability called alternate blade cavitation in a two-bladed inducer. These various cavitation instabilities have different frequency and spatial mode characteristics, which can be identified using Fourier transformation and circumferential unsteady pressure measurements.

Various analytical models have been suggested to predict cavitation instability and analyze its mechanism. Tsujimoto et al. [3] used an actuator disk method to predict rotating cavitation, where quasi-steady lumped parameters, such as mass flow gain factor and cavitation compliance, were introduced. The study showed that the mass flow gain factor plays a key role in the cavitation instability. Similarly, Watanabe et al. [4] and Horiguchi et al. [5] performed stability analysis using the singularity method, predicting various cavitation instabilities, including forward and backward propagating rotating cavitation. However, these methods cannot adequately reflect the 3-D nature of the inducer cavitation, which is primarily composed of tip leakage vortex cavitation (TLVC). Previous studies showed TLVC has a highly complex 3-D structure including severe turbulence, rather than having a quasi-steady feature with glossy surfaces which can be observed in 2-D sheet-type cavities. Cheng et al. [6] suggested the development of the TLVC would significantly alter the vorticity and turbulence kinetic energy distribution of the flow field, and due to the complex flow features, there is still no simple way to control the TLVC. Also, Cheng et al. [7] performed a Large Eddy Simulation (LES) and showed that the large amount of turbulent kinetic energy is produced around the TLVC region due to the interaction between three different vortex structures (tip leakage vortex, tip separation vortex, and induced vortex).

check for updates

Citation: Yoon, Y.; Song, S.J. Effects of Tip Leakage Vortex Cavitation on Flow Field under Cavitation Instability. *Int. J. Turbomach. Propuls. Power* **2023**, *8*, 17. https://doi.org/10.3390/ijtpp8020017

Academic Editors: János Gábor Vad, Csaba Horváth and Tamás Benedek

Received: 13 February 2023
Revised: 18 April 2023
Accepted: 4 May 2023
Published: 1 June 2023

Copyright: © 2023 by the authors. Licensee MDPI, Basel, Switzerland. This article is an open access article distributed under the terms and conditions of the Creative Commons Attribution (CC BY-NC-ND) license (https://creativecommons.org/licenses/by-nc-nd/4.0/).

Hence, 3-D numerical approaches and experiments have been conducted to investigate the cavitation instability mechanism. For instance, Kang et al. [8] conducted 3-D numerical simulations, showing that cavitation instabilities begin to occur when the cavity on a blade interacts with the adjacent blade leading edge. Additionally, Kim and Song [9] performed an experimental investigation on rotating cavitation, demonstrating that cavitation reduces the incidence of the following blade using particle image velocimetry (PIV) and high-speed visualization. Nevertheless, although these studies proposed the mechanism of blade-to-blade interaction for cavitation instability, only a few selected cases have been examined in the research.

Therefore, the present research investigates the interaction between the cavity and the flow field under various operating conditions for a two-bladed inducer, using PIV to quantify the change in the velocity field around the blade leading edge. Furthermore, the study aims to analyze the blade-to-blade interaction under alternate blade cavitation.

2. Experimental Setup

Experiments were conducted in the Seoul National University Water Tunnel (SNU-WT), as schematically shown in Figure 1. The SNU-WT comprises a water tank, electric heater, flow meter, booster pump, control valve, and an inducer test section, which enables the independent control of flow coefficient and cavitation number. Moreover, to prevent particles larger than 1 micron from entering the test facility, a filtration chamber was incorporated. For a detailed description of the facility, refer to Kim and Song [9].

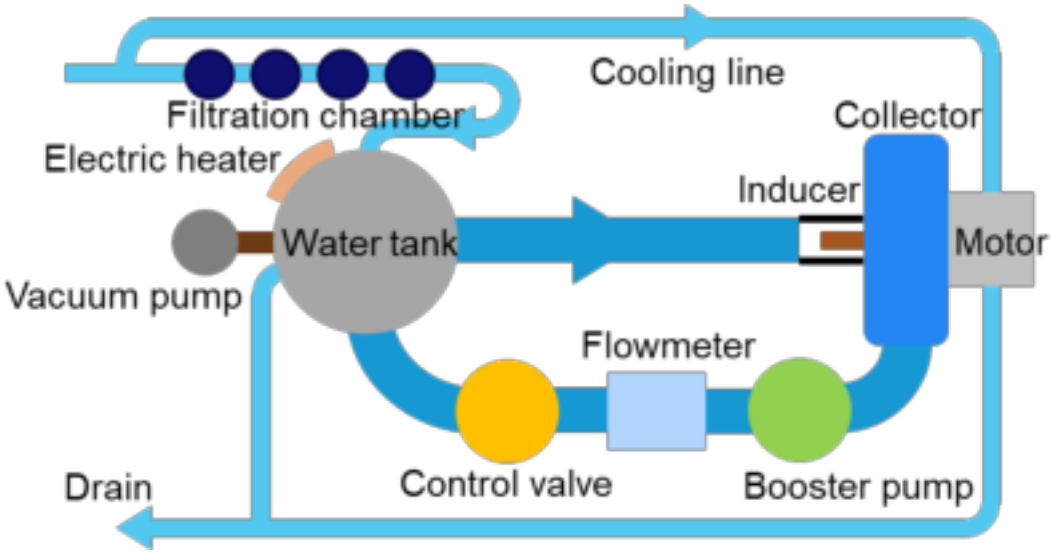

Figure 1. Schematic diagram of Seoul National University Water Tunnel.

To determine the cavitation number and identify cavitation instability, both steady and unsteady pressure measurements were performed. Four pneumatic pressure sensors (Druck PMP 5073) were mounted at the inlet and outlet of the inducer, while five unsteady pressure transducers (Kulite HKM-375) were flush-mounted at the inducer inlet casing. In addition, for the PIV measurement, the inducer casing was constructed using transparent acrylic. The flow field was measured using a Litron L 200-15 PIV laser and a Phantom v2640 camera.

In the present study, a two-bladed inducer (Figure 2) was examined. Details about the inducer can be found in [10]. All experiments were conducted under the design flow coefficient, and the cavitation number was gradually reduced from the non-cavitating condition to a near super-cavitating condition, which induced severe alternate blade cavitation.

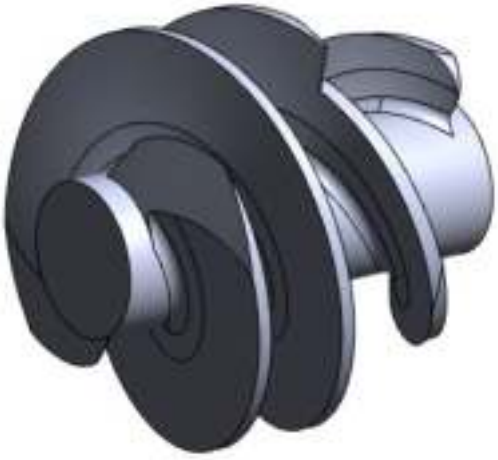

Figure 2. Geometry of the test inducer.

3. Experiment Results and Discussion

To quantify the blade-to-blade interaction, the flow field near the blade leading edge was obtained under non-cavitating conditions and averaged over a region of interest, as shown in Figure 3.

The background image in Figure 3 is a raw image captured under continuous lighting using a high-speed camera. Overlapped particle images were obtained under pulsed laser lighting, and the resulting velocity vectors are shown in green. The red dotted box indicates the area over which the velocity vectors were averaged to determine the mean velocity vector near the blade leading edge.

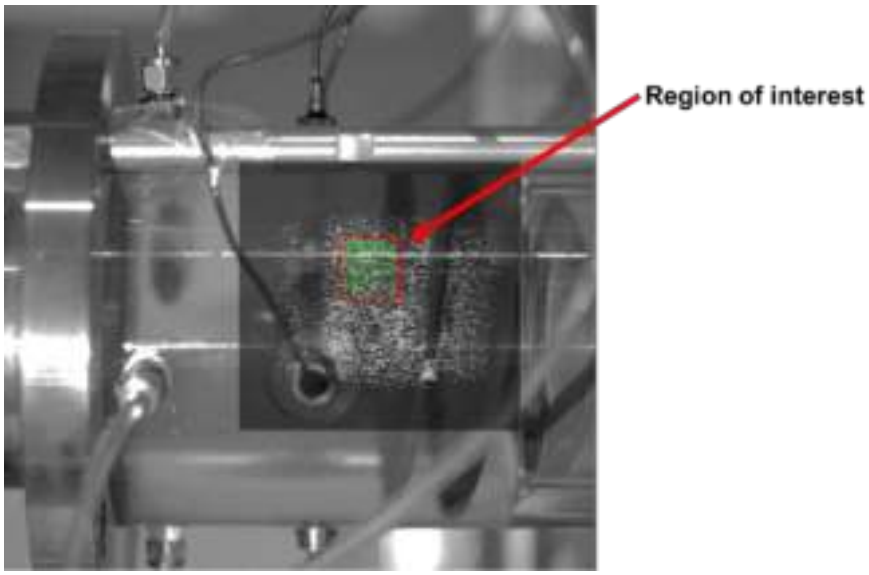

Figure 3. PIV region of interest.

At the cavitating condition, the same calculation was performed, and the difference between the mean velocity vectors was obtained. Under alternate blade cavitation, the leading edges of the two blades were treated separately due to the asymmetry of the cavity. Finally, these velocity differences were converted to changes in the incidence in the rotating frame, $\Delta\alpha$. In the present study, $\Delta\alpha$ was used to represent the blade-to-blade interaction. (In this study, incidence ($\alpha_1 - \alpha_1{}'$), which is defined as the difference between the flow angle (α_1) and the blade angle ($\alpha_1{}'$), was used instead of angle of attack. Although the numerical difference between the two values is small due to the small camber angle of the inducer blade, incidence is more suitable for the turbomachinery analysis conducted in this paper).

In this study, the occurrence of alternate blade cavitation was examined using unsteady pressure measurements at the inducer casing inlet. At a distance of 0.15 D upstream of the inducer tip leading edge (where D is the inducer casing diameter), an unsteady pressure transducer was flush-mounted, and the data was sampled at 2000 samples per second. As the cavitation number was decreased during the experiment, the unsteady pressure signal, with its DC component filtered out, was Fourier-transformed to examine the alternate blade cavitation. The results of the Fourier transformation are shown in Figures 4 and 5 for equal length cavitation and alternate blade cavitation, respectively. In both cases, a peak was observed at a normalized frequency of 2 due to the blade passing frequency of the two-bladed inducer. However, if the system was under alternate blade cavitation, as shown in Figure 5, a peak at a normalized frequency of 1 (which equals the shaft rotating frequency) was excited due to the asymmetry of the alternate blade cavitation. Figure 6 visually demonstrates the asymmetry of cavity development under alternate blade cavitation, where both long and short cavities are developed on different blades, forming an asymmetric pattern that remains stationary in the rotating frame. Therefore, the peak at a normalized frequency of 1 was used to judge whether the alternate blade cavitation occurred, and its magnitude represented the strength of the instability. In the experiment, both the magnitude of the Fourier coefficient and the difference between the two cavity lengths showed the same trend, and thus both were used to represent the magnitude of the alternate blade cavitation.

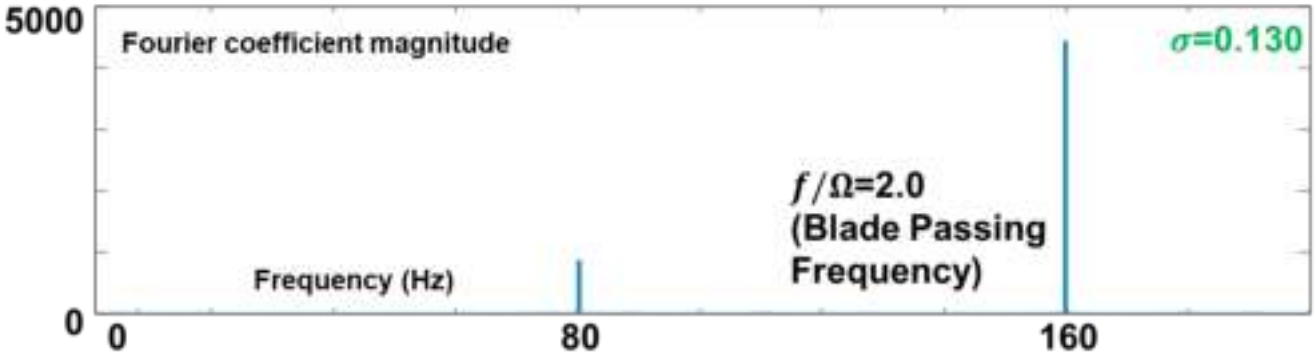

Figure 4. Typical frequency traces under equal length cavitation.

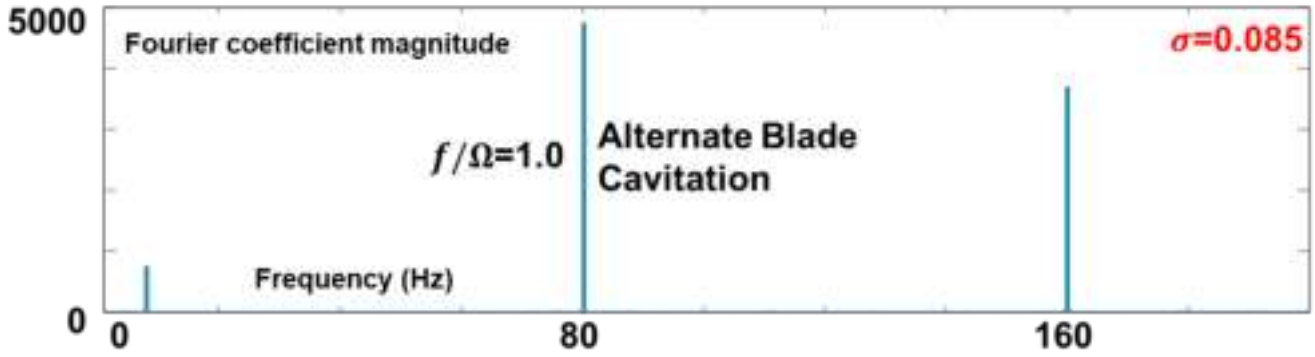

Figure 5. Typical frequency traces under two-bladed inducer alternate blade cavitation.

Figure 6 also shows the 3-D nature of the cavity on the current inducer. Due to the back-swept leading edge of the inducer, 2-D sheet-type cavity at the hub region is suppressed, and most of the cavity is developed at the tip region. At the tip region, pressure difference between the pressure side and suction side of the blade drives the fluid to go through the tip clearance. This tip clearance flow creates a shear layer with the main flow and, consequently, vortex is generated (tip clearance vortex). While low pressure region is created at the vortex core, cavitation occurs inside the vortex (TLVC). Additionally, TLVC shows highly intermittent behavior because of the large turbulent kinetic energy at the

vortex region [5,6]. Thus, rather than glossy surface, bubbly surface is observed as a bright region from the high-speed visualization. Cavitation at the tip separation vortex region shown in the right side of Figure 6 further indicate the tip clearance flow is the main source of cavitation for the test inducer.

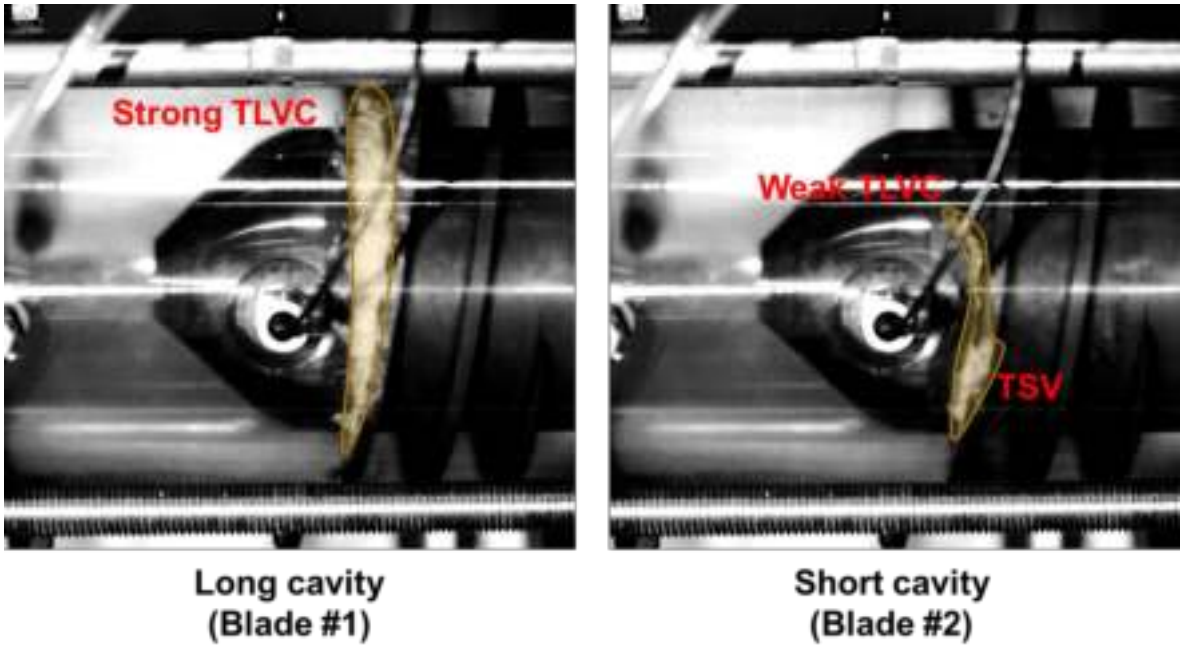

Figure 6. Visualization of alternate blade cavitation.

Due to the strong axial flow induced by the collapsing cavity, $\Delta\alpha$ has a negative sign in most situations. Figures 7–9 show the flow field vector plots at the PIV region of interest under non-cavitating conditions and alternate blade cavitation. The x-axis and the y-axis of the vector plots are normalized with the width and height of the region of interest (shown in Figure 3). Thus, the square defined by the coordinate (0,0) and (1,1) corresponds to the entire region of interest. In Figures 8 and 9, both blades 1 and 2 are shown to compare the effect of the larger and smaller cavities. In Figure 7, it can be seen that backflow is developed near the blade leading edge due to the adverse pressure gradient of the inducer. In Figure 8, a similar flow structure is developed near the blade 1 leading edge (blades are numbered as 1 and 2, corresponding to the blade with larger cavity and smaller cavity under alternate blade cavitation, respectively). Therefore, the smaller cavity induced at blade 2 is not developed enough to interact with the leading edge of the following blade.

However, as shown in Figure 9, a strong axial flow is developed at the leading edge of blade 2. This is a result of the cavity collapse occurring near the leading edge of blade 2. The cavity developed at blade 1 is large enough to interact with the following blade's leading edge. Therefore, it collapses due to high pressure at the throat area and drags the surrounding fluid to create a strong axial flow. This axial flow reduces the incidence of the following blade and inhibits the cavity development.

The existence of a critical cavity length that enables the cavity to interact with the following blade leading edge can also be confirmed during the early stages of cavity development. At the cavitation number of 0.130 and 0.115, the normalized cavity length is less than 0.5, and the cavity develops in the form of equal length cavitation (the same cavity develops at both blades). Figures 10 and 11 visualize the cavity in both cavitation numbers. It can be seen that the cavities are not large enough to reach the following blade's leading edge, and no impact is exerted on the incidence. With respect to the following blade, those cavities are the same as the non-cavitating condition.

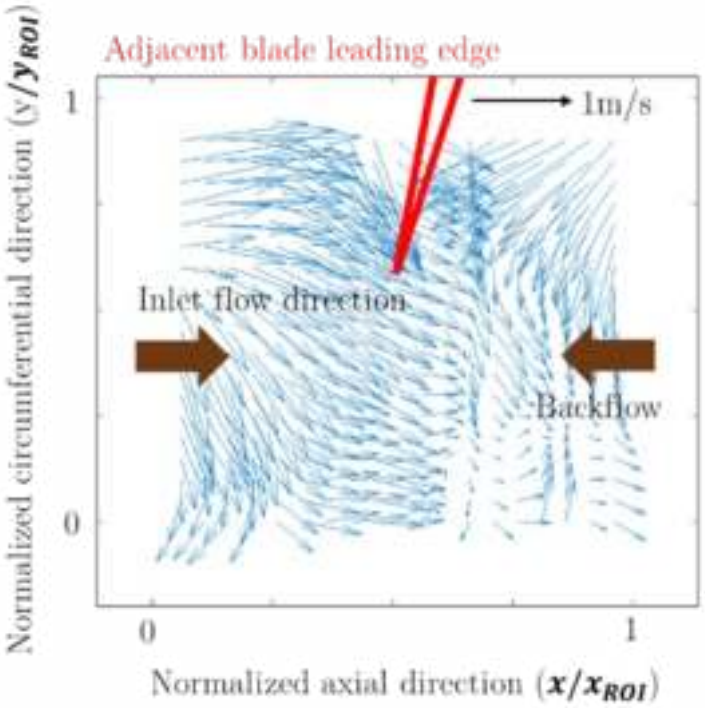

Figure 7. Flow field near blade leading edge at non-cavitating condition.

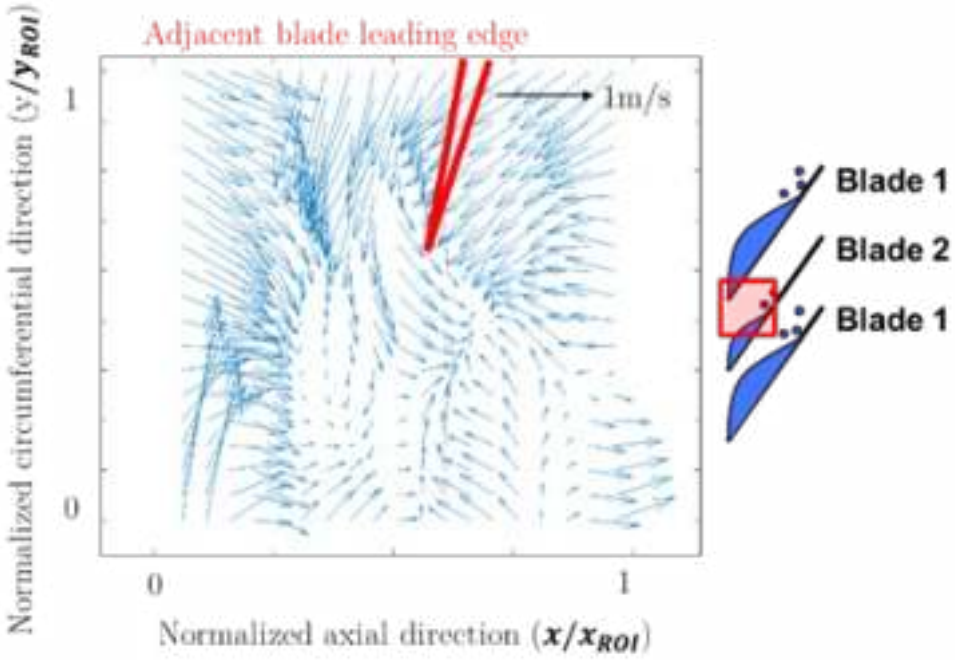

Figure 8. Flow field near blade 1 leading edge during alternate blade cavitation.

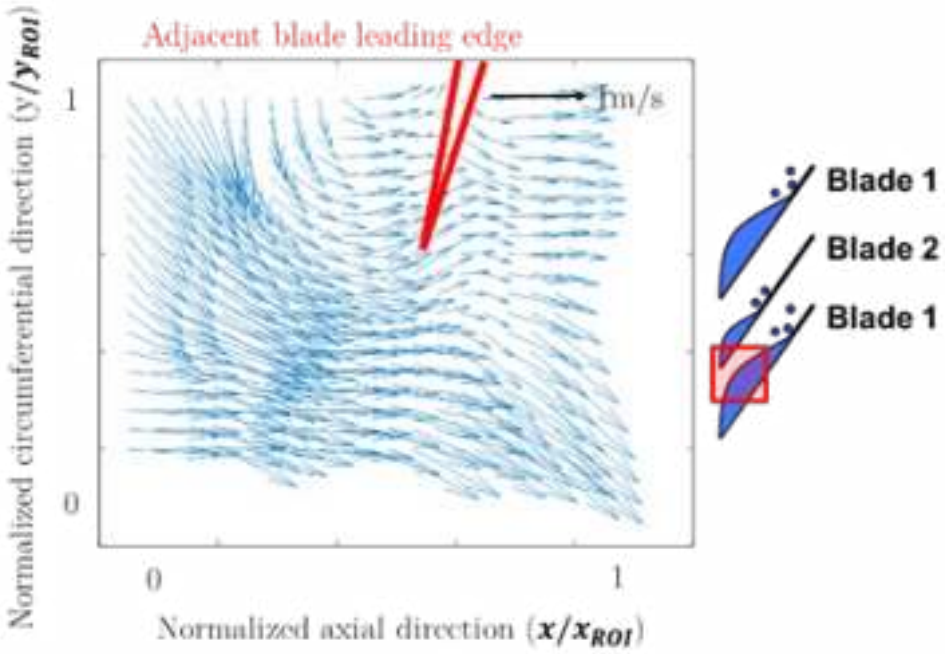

Figure 9. Flow field near blade 2 leading edge during alternate blade cavitation.

Figure 12 summarizes the experiment results under various cavitation numbers, which is defined as follows:

$$\sigma = \frac{p_{\text{inlet}} - p_v}{\frac{1}{2}\rho U_{tip}^2}. \tag{1}$$

The ordinate of Figure 12 is the normalized cavity length, which is the length of the cavity divided by the inducer throat chord length, as illustrated in the right inset of Figure 12. As the cavitation number drops below 0.110, the cavity length graph bifurcates, and the maximum difference occurs at approximately $\sigma = 0.085$. The red line represents the longer cavity length, while the blue line represents the shorter one. Figure 12 demonstrates that, after the onset of alternate blade cavitation, the magnitude (or difference between the two cavity lengths) increases until it reaches a certain cavitation number, after which it starts to decrease again.

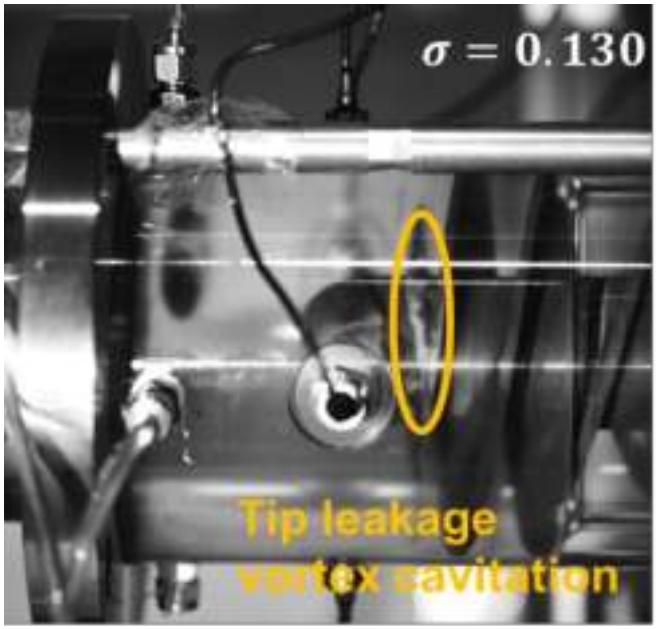

Figure 10. High-speed visualization of the cavity at $\sigma = 0.130$.

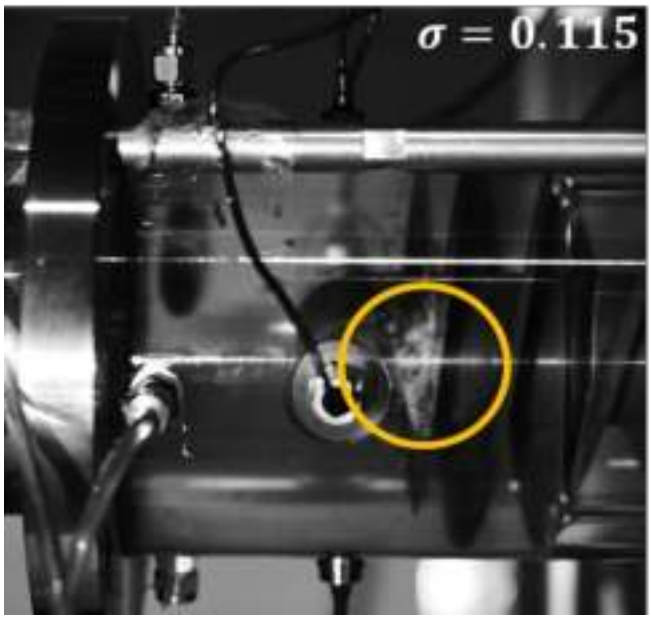

Figure 11. High-speed visualization of the cavity at $\sigma = 0.115$.

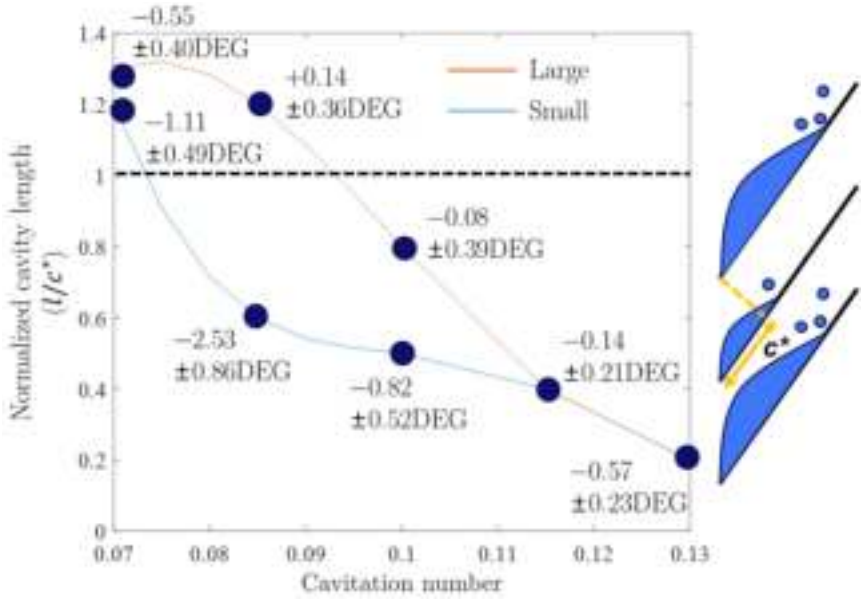

Figure 12. Cavity length and change in incidence under various cavitation number.

The dark blue dots and captions in Figure 12 represent $\Delta\alpha$s at the given cavitation number and blade. The alternate blade cavitation is caused by uneven incidence for each blade, as shown in Figures 8 and 9. The cavity on the red branch is large enough to interact with the leading edge of the following blade, and it induces strong axial flow, leading to a decrease in the incidence of the following blade. As a result, the blade loading of the following blade (blue branch) decreases, and the tip leakage vortex cavitation (TLVC) extent also decreases. The measured $\Delta\alpha$s at various cavitation numbers can explain the changing magnitude of the alternate blade cavitation, as also observed by Huang et al. [11]. The alternate blade cavitation reaches its maximum magnitude when the normalized length of the larger cavity is around 1. The decrease in incidence due to the larger cavity becomes smaller before and after that point. Therefore, it can be concluded that the magnitude of $\Delta\alpha$ is at its highest when the normalized cavity length is close to 1 ($l \approx c^*$, where c^* is the chord length between the leading edge of the blade and the throat). As the cavitation number decreases, the cavity length increases, resulting in an increase in the magnitude

of $\Delta\alpha$ and the alternate blade cavitation until the cavity length reaches c^*. Once the cavity length reaches c^*, $\Delta\alpha$ and the alternate blade cavitation start to decrease.

Physically, the maximized $\Delta\alpha$ at $l \approx c^*$ can be explained by the position of cavity collapse. When the cavity bubble at the TLVC trailing edge collapses, it induces a large axial flow and decreases the incidence of the following blade. According to Kang et al. [8], the position of the TLVC trailing edge plays a key role. Therefore, if the position of the cavity collapse coincides with the leading edge of the following blade, $\Delta\alpha$ is maximized, and the alternate blade cavitation becomes the strongest. This can be seen more clearly in Figures 13 and 14. Figure 13 shows a larger cavity at $\sigma = 0.085$, and Figure 14 shows a larger cavity at $\sigma = 0.070$. At $\sigma = 0.085$, most of the cavities collapse near the leading edge of the following blade. However, at $\sigma = 0.070$, the TLVC extends further until $l/c^* = 1.3$, and much fewer cavities collapse near the leading edge of the following blade. This reduces the induced axial flow and, accordingly, decreases the incidence of the following blade less.

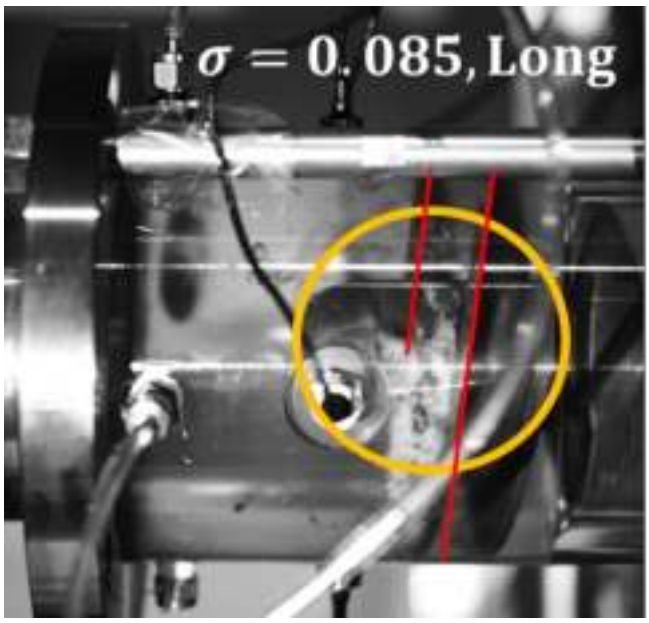

Figure 13. Visualization of the cavity at $\sigma = 0.085$.

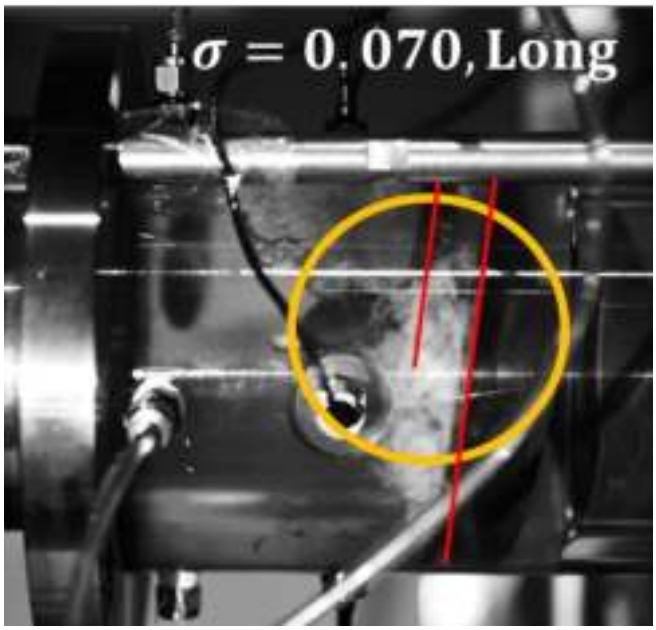

Figure 14. Visualization of the cavity at $\sigma = 0.070$.

4. Summary and Conclusions

In summary, this study explores the relationship between cavity and its interaction with the following blade in a two-bladed inducer. The study employs experimental techniques such as PIV and high-speed visualization of the cavity to quantify the interaction and its effects on the TLVC extent of the following blade. The results show that the cavity collapse decreases the incidence of the following blade, resulting in alternate blade cavitation. The study further explains that the maximum magnitude of alternate blade cavitation occurs when the normalized cavity length is around 1 and the cavity collapses near the following blade leading edge.

Author Contributions: Conceptualization, Y.Y. and S.J.S.; Methodology, Y.Y.; Software, Y.Y.; Validation, Y.Y.; Formal Analysis, Y.Y.; Investigation, Y.Y.; Resources, S.J.S.; Data Curation, Y.Y.; Writing—Original Draft Preparation, Y.Y.; Writing—Review & Editing, Y.Y. and S.J.S.; Visualization, Y.Y.; Supervision, S.J.S.; Project Administration, S.J.S.; Funding Acquisition, S.J.S. All authors have read and agreed to the published version of the manuscript.

Funding: This research received no external funding.

Institutional Review Board Statement: Not applicable.

Informed Consent Statement: Not applicable.

Data Availability Statement: Not applicable.

Acknowledgments: This work was supported by BK21+ Program and Seoul National University Institute of Advanced Machines and Design (SNU-IAMD).

Conflicts of Interest: The authors declare no conflict of interest.

References

1. Tsujimoto, Y.; Yoshida, Y.; Maekawa, Y.; Watanabe, S.; Hashimoto, T. Observation of Oscillating Cavitation of an Inducer. *J. Fluids Eng. Trans. ASME* **1997**, *119*, 775–781. [CrossRef]
2. Cervone, A.; Bramanti, C.; Rapposelli, E.; Torre, L.; d'Agostino, L. Experimental Characterization of Cavitation Instabilities in a Two-Bladed Axial Inducer. *J. Propuls. Power* **2006**, *22*, 1389–1395. [CrossRef]
3. Tsujimoto, Y.; Kamijo, K.; Yoshida, Y. A Theoretical Analysis of Rotating Cavitation in Inducers. *J. Fluids Eng. Trans. ASME* **1993**, *115*, 135–141. [CrossRef]
4. Watanabe, S.; Sato, K.; Tsujimoto, Y.; Kamijo, K. Analysis of Rotating Cavitation in a Finite Pitch Cascade Using a Closed Cavity Model and a Singularity Method. *J. Fluids Eng. Trans. ASME* **1999**, *121*, 834–840. [CrossRef]
5. Horiguchi, H.; Watanabe, S.; Tsujimoto, Y. A Linear Stability Analysis of Cavitation in a Finite Blade Count Impeller. *J. Fluids Eng. Trans. ASME* **2000**, *122*, 798–805. [CrossRef]
6. Cheng, H.; Ji, B.; Long, X.; Huai, W.; Farhat, M. A Review of Cavitation in Tip-Leakage Flow and its Control. *J. Hydrodyn.* **2021**, *33*, 226–242. [CrossRef]
7. Cheng, H.; Bai, X.; Long, X.; Ji, B.; Peng, X. Large Eddy Simulation of the Tip-Leakage Cavitating Flow with an Insight on how Cavitation Influences Vorticity and Turbulence. *Appl. Math. Model.* **2020**, *77*, 788–809. [CrossRef]
8. Kang, D.; Yonezawa, K.; Horiguchi, H.; Kawata, Y.; Tsujimoto, Y. Cause of Cavitation Instabilities in Three-Dimensional Inducer. *Int. J. Fluid Mach. Syst.* **2009**, *2*, 206–214. [CrossRef]
9. Kim, J.; Song, S.J. Visualization of Rotating Cavitation Oscillation Mechanism in a Turbopump Inducer. *J. Fluids Eng. Trans. ASME* **2019**, *141*, 091103. [CrossRef]
10. Yoon, Y.; Kim, J.; Song, S.J. Identification of Inducer Cavitation Instabilities Using High-Speed Visualization. *Exp. Therm. Fluid Sci.* **2022**, *132*, 110548. [CrossRef]
11. Huang, J.-D.; Aoki, M.; Zhang, J.-T. Alternate Blade Cavitation on Inducer. *JSME Int. J. Ser. B Fluids Therm. Eng.* **1998**, *41*, 1–6. [CrossRef]

Disclaimer/Publisher's Note: The statements, opinions and data contained in all publications are solely those of the individual author(s) and contributor(s) and not of MDPI and/or the editor(s). MDPI and/or the editor(s) disclaim responsibility for any injury to people or property resulting from any ideas, methods, instructions or products referred to in the content.

International Journal of
Turbomachinery
Propulsion and Power

MDPI

Review

Advanced Gas Turbine Cooling for the Carbon-Neutral Era

Kenichiro Takeishi [1,*] and Robert Krewinkel [2]

[1] Department of Mechanical Science and Engineering, Graduate School of Engineering Science, Osaka University, Toyonaka 560-8531, Japan
[2] Faculty of Mechanical Engineering and Economic Sciences, Graz University of Technology, Inffeldgasse 25, 8010 Graz, Austria; robert.krewinkel@tugraz.at
* Correspondence: takeishi@mech.eng.osaka-u.ac.jp

Abstract: In the coming carbon-neutral era, industrial gas turbines (GT) will continue to play an important role as energy conversion equipment with high thermal efficiency and as stabilizers of the electric power grid. Because of the transition to a clean fuel, such as hydrogen or ammonia, the main modifications will lie with the combustor. It can be expected that small and medium-sized gas turbines will burn fewer inferior fuels, and the scope of cogeneration activities they are used for will be expanded. Industrial gas turbine cycles including CCGT appropriate for the carbon-neutral era are surveyed from the viewpoint of thermodynamics. The use of clean fuels and carbon capture and storage (CCS) will inevitably increase the unit cost of power generation. Therefore, the first objective is to present thermodynamic cycles that fulfil these requirements, as well as their verification tests. One conclusion is that it is necessary to realize the oxy-fuel cycle as a method to utilize carbon-heavy fuels and biomass and not generate NO_x from hydrogen combustion at high temperatures. The second objective of the authors is to show the required morphology of the cooling structures in airfoils, which enable industrial gas turbines with a higher efficiency. In order to achieve this, a survey of the historical development of the existing cooling methods is presented first. CastCool® and wafer and diffusion bonding blades are discussed as turbine cooling technologies applicable to future GTs. Based on these, new designs already under development are shown. Most of the impetus comes from the development of aviation airfoils, which can be more readily applied to industrial gas turbines because the operation will become more similar. Double-wall cooling (DWC) blades can be considered for these future industrial gas turbines. It will be possible in the near future to fabricate the DWC structures desired by turbine cooling designers using additive manufacturing (AM). Another conclusion is that additively manufactured DWC is the best cooling technique for these future gas turbines. However, at present, research in this field and the data generated are scattered, and it is not yet possible for heat transfer designers to fabricate cooling structures with the desired accuracy.

Keywords: carbon neutrality; industrial gas turbine; turbine cooling; double-wall cooling; additive manufacturing; hydrogen; ammonia; CCGT; IGCC; Oxy-fuel combustion; HAT cycle

check for updates

Citation: Takeishi, K.; Krewinkel, R. Advanced Gas Turbine Cooling for the Carbon-Neutral Era. *Int. J. Turbomach. Propuls. Power* **2023**, *8*, 19. https://doi.org/10.3390/ijtpp8030019

Academic Editors: Tony Arts and Rodolfo Bontempo

Received: 29 January 2023
Revised: 2 May 2023
Accepted: 12 June 2023
Published: 24 June 2023

Copyright: © 2023 by the authors. Licensee MDPI, Basel, Switzerland. This article is an open access article distributed under the terms and conditions of the Creative Commons Attribution (CC BY-NC-ND) license (https://creativecommons.org/licenses/by-nc-nd/4.0/).

1. Introduction

The Paris Agreement, an international framework on climate change, was adopted at the Conference of the Parties to the United Nations Framework Convention on Climate Change (COP21) in 2015 and has entered into force in 2016. The first paragraph (a) of article 2 of the Paris Agreement states that the signees will be "holding the increase in the global average temperature to well below 2 °C above pre-industrial levels and pursuing efforts to limit the temperature increase to 1.5 °C above pre-industrial levels, recognizing that this would significantly reduce the risks and impacts of climate change" [1].

In response to the Paris Agreement, all parties to the agreement are required to prepare and submit nationally determined contribution (NDC) targets for greenhouse gas emission reductions every five years, based on their own national circumstances. Based on this agreement, the parties prepared a Long-term Strategies portal [2]. This section describes the long-term

strategies of Japan and Germany, to which the authors belong. Japan aims to reduce greenhouse gas emissions (GHG) by 46% in 2030 (compared to 2013) and to achieve net zero emissions in 2050. Germany, on the other hand, aims to achieve a GHG emission reduction of 65% in 2030 (compared to 1990), net zero in 2045 and negative emissions after 2050.

In Japan, the Cabinet approved the "Long-Term Strategy as a Growth Strategy Based on the Paris Agreement" in October 2021. The energy section of this strategy calls for Japan to use 50–60% renewable energy, 30–40% nuclear power and thermal power with carbon capture, utilization and storage (CCUS), and 10% hydrogen or ammonia as energy in 2050 [3]. In Germany, efforts are aligned with and need to be seen within the context of the goals and measures of the European Union. This is, in particular, the European Green Deal [4], which was put in a legal framework by the European Climate Law [5]. The Green Deal defines both natural gas and nuclear power as green (transition) technologies. The EU supports the erection of CHP plants as long as they adhere to the Emissions Performance Standard of 250 g CO_2/kWh, even if fossil fuels are used [6]. In future, these plants will be converted to burn hydrogen or other carbon-neutral fuels or, alternatively, retrofitted with CCS. Although general directives are defined by the EU, the realization of the goals defined therein is the task of the different countries. Germany plans to generate all of its electricity from renewables in 2050. The electricity will be predominantly generated by a mix of photovoltaics, wind and some geothermal energy; nuclear energy will not be a part of the energy mix, but a number of other countries in the EU are planning new nuclear capacity. Fluctuations will be compensated by combined cycles and combined heat and power plants burning hydrogen or biogas.

The long-term strategies of the two countries indicate that renewable energy sources will continue to grow significantly in order to achieve carbon neutrality. However, as the proportion of renewables—which are subject to load fluctuations—increases, thermal and nuclear power, which have inertia, will be required to stabilize a certain proportion of the power supply. Since nuclear power is a power generation system that is not suitable for adjusting to short-term load fluctuations, thermal power must exclusively play this role, which now accounts for about half of renewable energy.

Currently, the most advanced combined cycle gas turbine (CCGT), which is the most efficient large-scale power generation system, has a thermal efficiency of 64% (LHV), which is about 40% more efficient than coal-fired power generation, and can reduce CO_2 emissions to about one-third of those from coal-fired plants [7,8]. However, even CCGTs will need to undergo further changes and developments in order to be a major source of power generation and achieve carbon neutrality in 2050.

The purpose of this paper is to describe the trend of heat transfer to airfoils and cooling technologies for industrial gas turbines in a carbon-neutral environment. In order to achieve this, it is first necessary to clearly describe the differences in characteristics between industrial gas turbines and aviation jet engines. The first feature of industrial gas turbines is the diversity of fuel types. In particular, small industrial gas turbines are used for cogeneration, which is relatively inexpensive and allows the use of inferior fuels. The second feature is that in industrial gas turbines, there is no weight limit, and any coolant can be used. This feature allows the cooling air extracted from the compressor outlet to cool the turbine blades using a heat exchanger. Additionally, a coolant different from the working fluid, such as water, which has an excellent cooling performance, can be used as well. The third difference is that the industrial gas turbine can be configured with a variety of cycles, some of which are aligned with the second feature. One of these thermal cycles, the CCGT, is already in practical use. Understanding these three major characteristics of industrial gas turbines is necessary to consider future trends in turbine stationary vanes and rotor blades.

In addition to the above features, a carbon-neutral CCGT must have the ability to adjust its electricity output according to load fluctuations, as mentioned above. Considering the increase in cost of new CCUS for conventional natural-gas-fired CCGTs and the increase in production cost of new fuels, such as hydrogen or ammonia, compared to natural gas, it is necessary to further improve the thermal efficiency of the current CCGTs. This

will require increasing the turbine inlet temperature from the current 1600 °C class large industrial gas turbines to the 1900 °C–2000 °C level. This load flexibility is exactly the same as that possessed by aviation jet engines. The major difference is that the airfoils of a large industrial gas turbine are about four times larger than those of an aviation jet engine and have a very large heat capacity—more than four to the third power—so it is necessary to develop new cooling designs.

In this review paper, as a preliminary step to discuss the trend of heat transfer and cooling technologies for industrial gas turbines, we first review cooled airfoils applied to industrial gas turbines. In each stage of development, optimal power generation systems and CHP have been developed for industrial gas turbines taking advantage of the above three characteristics. In addition, there are many thermodynamic cycles that have been realized in demonstration plants but are not yet in practical use. Knowing these legacies, we believe this is a legitimate approach to discussing industrial gas turbines in the carbon-neutral era and the turbine cooling blades, which will be used for them.

Based on the above ideas, the turbine cooling blades researched and developed to date were examined, and the results show that CastCool® and wafer and diffusion bonding airfoils are suitable for future industrial gas turbines. In the light of these studies, double-wall cooling developed from the CastCool® blade structure is very promising. It is also clear that the ability to fabricate complex turbine cooling structures, such as double-wall cooling (DWC), using additive manufacturing (AM) methods is essential. However, no DWC blades for future ultra-high temperature gas turbines have been shown in the open literature to date, and the fabrication of vanes and blades with simple cooling structures using AM has just begun. Moreover, the standard thickness of AM layers is about 0.6 mm, making it impossible to fabricate elaborate film cooling holes and impingement nozzle holes. Accordingly, this paper reviews the current status of research on DWC blades and the AM method. The fabrication status of double-wall cooling blades is also reviewed, as are heat transfer studies on the cooling methods that comprise this cooling structure, such as internal impingement cooling, full coverage film cooling and effusion cooling. Finally, the trends in carbon-neutral cooling structures for turbine vanes and rotor blades of industrial gas turbines are summarized.

The paper also reviews the results of feasibility and R&D studies of various gas-turbine-based thermal cycles to address fuel diversification and performance improvement. It is also concluded that an oxy-fuel cycle is suitable as a cycle with gas turbines as the main heat source.

Note that wherever stationary vanes and rotor blades are discussed, it is assumed that a "vane" is stationary, and a "blade" rotates. When a statement is applicable to both, the term "airfoils" will be used.

2. Historical Development of Industrial Gas Turbines

2.1. Development of Large Industrial Gas Turbines to Date

Under the leadership of Aurel Stodola, the world's first industrial gas turbine was put into commercial operation for power generation in Neuchâtel, Switzerland, in 1939 [9,10]. The gas turbine was manufactured by Brown, Boveri & Company (BBC) with a speed of 3000 rpm, a turbine inlet temperature of 550 °C, a thermal efficiency of 17.4% and an output of 4000 kW. This period coincided with the successful development of the world's first jet engine for aviation by Whittle and Hans Von Ohain [11,12]. Aero jet engines had made great strides since then. However, improvements in the thermal efficiency of industrial gas turbines could not compete with the speed with which the thermal efficiency of steam turbines improved in the 1950s and 1960s. In the 1960s, steam turbines began to use steam at supercritical pressure and became heat engines with thermal efficiencies exceeding 40% (LHV). On the other hand, large industrial gas turbines were developed with turbine inlet temperatures in the 900 °C class, and the stand-alone thermal efficiency of gas turbines reached the upper half of the 20% range (LHV). Because their thermal efficiency was inferior to that of steam turbines, they were almost exclusively used for peak shaving.

In the 1970s, three aero engine manufacturers began the development of a 1250 °C class aero engine to be installed in the Boeing 747. Aero engines further evolved to 1350 °C. Following this technological trend, four OEMs of large industrial gas turbines (General Electric Corporation (GE), Westinghouse Electric Corporation (WH), Siemens, Brown, Boveri & Company (BBC, later ABB/Alstom)) succeeded in developing a large 1100 °C class industrial gas turbine in the late 1970s.

Various power generation systems and cogeneration thermal cycles using industrial gas turbines as the main engine have been studied [13]. Among these thermal cycles, the combined cycle gas turbine (CCGT), which combines a Brayton cycle gas turbine and a Rankine cycle steam turbine, was found to have a simple equipment configuration and to generate electricity with high thermal efficiency [14,15]. The CCGT was established as a response to the two oil crises that occurred in the 1970s.

One of the early examples of the development of large CCGTs is the combined cycle power plant of Tohoku Electric Power Co. The gas turbine used in this CCGT was a 701 D gas turbine with a frequency of 50 Hz designed and manufactured by Mitsubishi Heavy Industries Ltd. (MHI), Takasago, Japan. The gas turbine was developed by MHI based on the 60 Hz 501D5 gas turbine developed by WH, the turbine inlet temperature of which was 1154 °C [16]. The thermal efficiency of the CCGT using this gas turbine was over 48% (LHV), which was more than 10% higher than the thermal efficiency of the most advanced coal-fired thermal power generation systems of the time. The use of liquid natural gas (LNG) as fuel reduced the carbon dioxide emissions by approximately 20% compared to coal-fired power generation [17]. The development issues included turbine cooling technology to ensure the reliability of the airfoils—even for the long periods between major overhauls—and the combustion technology for a low NOx combustor that complied with Japanese environmental regulations. The world's first premixing combustor was therefore developed for the 701D.

In response to the strong global demand for CCGTs, gas turbine manufacturers focused on developing larger industrial gas turbines with higher temperatures and pressures. This led to the development of the 1300 °C class F-type gas turbine and the 1500 °C class G- and H-type gas turbines. The thermal efficiency (LHV) of CCGTs using these gas turbines is shown in Figure 1 [18]. Figure 2 also shows the thermal efficiency transition for the case where the gas turbine is used in a simple cycle operation [18]. The symbols A, B, and C in Figure 2 are the same as those in Figure 1, and the symbol D is taken from the cited Reference 20.

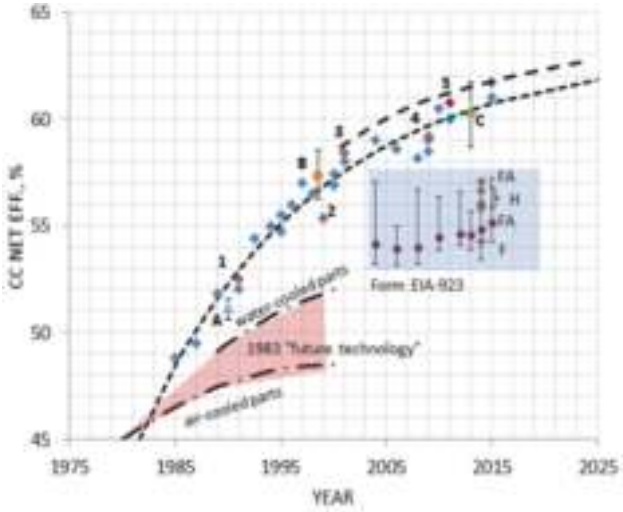

Figure 1. Evolution of CCGT efficiency in 1985–2015. CCGT evolution, 1985–2015 [18].

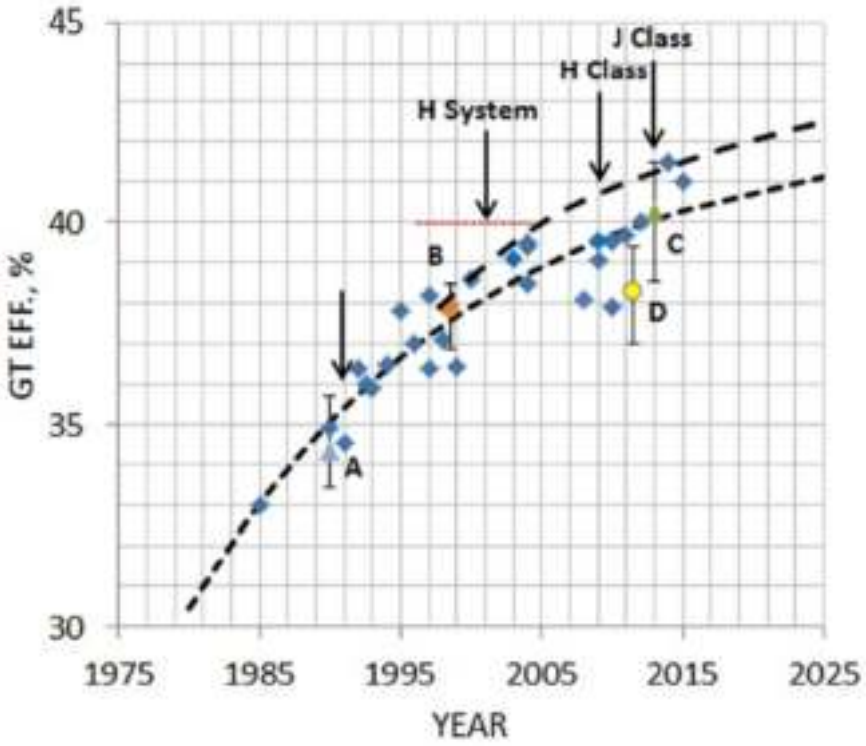

Figure 2. Evolution of large industrial gas turbine efficiencies in 1985–2015 [18].

Table 1 shows the status of development of F-type gas turbines with a turbine inlet temperature of 1300 °C by four OEMs [19,20]. First, GE developed the Frame 7F gas turbine, followed by WH. Both gas turbines had the same turbine inlet temperature, but the cooling design of the first-stage turbine blades was different: GE manufactured large directionally solidified (DS) first-stage rotor blades and used internal cooling with serpentine flow paths and no film cooling. WH and MHI collaborated on the development of the F-type gas turbine. MHI was in charge of the cooling design and the development of the low NO_x combustor. In this design, the first-stage rotor blades were manufactured by CC and used the world's first film cooling for an industrial gas turbine in the serpentine cooling flow path.

Table 1. Westinghouse, Siemens and ABB react to GE's "Frame 7F" [19].

Company	Turbine Model	Capacities		Efficiencies (%)		Key Dates	Capacities
		GT	CCGT	GT	CCGT	Announced	First Order
GE	Frame 7F	150 MW	230 MW	34.2	53	1987	1987
Westinghouse	501F	150MW	230 MW	35.4	54	1989	1989
Siemens	V94.3	200 MW	300 MW	35.7	54	1990	1992
ABB	GT13E2	164 MW	250 MW	35.7	54.7	1992	1992
	GT24	165 MW	250 MW	37.5	57.5	1993	1993

As can be seen in Table 1, the thermal efficiency of ABB's CCGT using their GT24/26 frames is remarkably high, even though the turbine inlet temperature is only 1300 °C. The company succeeded in achieving such high efficiency by adopting a reheat cycle. The use of the reheat cycle in gas turbines was proposed by Rice [21–23]. The pressure ratio of the GT24 gas turbine was set as high as 30, so that the gas temperature entering the re-combustor between the high and medium pressure turbines would be low. The design of the secondary combustor required a very sophisticated cooling technology.

Natural-gas-fired CCGTs using F-type gas turbines were highly efficient in power generation and contributed to the reduction in CO_2 emissions, leading to a worldwide

rush to construct such plants. Gas turbine manufacturers all planned to develop high-performance gas turbines, which would achieve next-generation CCGT thermal efficiency of 60% (LHV) [24], and the U.S. DOE's ATS project (1992–2001) was implemented to achieve this. In this project, GE focused on a cooling system with closed-loop steam cooling of the first- and second-stage vanes and blades. The advanced GT with closed-loop steam cooling of the turbine blades at the turbine inlet temperature (TIT) of 1500 °C was called the H class.

The power output and thermal efficiency of a gas turbine are determined by the inlet temperature at the first-stage blades. Therefore, the ratio of air used for combustion to air used for cooling the first-stage vanes is independent of performance and power output, as long as the gas temperature of the first-stage blades is the same. However, as the amount of air used to cool the first-stage vanes increases, the gas temperature in the combustor rises, which increases NO_x emissions. Therefore, the system of using steam extracted from the bottoming cycle to cool the vanes and blades, combustor walls and transition piece walls was a revolutionary method from the standpoint of establishing a low NO_x combustor. In addition, from the perspective of the steam turbine in the bottoming cycle, cooling the high-temperature components of the gas turbine with steam superheats the steam, thereby improving the thermal efficiency of the CC. While the closed steam-cooled GT cycle has the advantage of increasing the thermal output and thermal efficiency of the CCGT, it also poses a difficult problem to solve in terms of the reliability and service life of the steam-cooled components. In addition, any loss of steam to the gas turbine cycle for cooling purposes needs to be compensated for with make-up water. This can become a financial issue because the water in the steam cycle has to be demineralized.

Steam has superior cooling performance compared to air, so the cooling structure of the turbine cooling blade does not need to be complicated to achieve a high cooling performance. GE solved this problem by using large single-crystal castings for the airfoils. Another problem is that the condensation heat transfer coefficient of water vapor is extremely high at about 10^5 kW/m^{2}K. When the metal temperature of the rotor is lower than the temperature at which water vapor condenses, water flows over the surface of the rotating hot parts, which in some cases may cause thermal deformation of the rotor, resulting in vibration problems. To prevent this, it was necessary to heat the massive rotor of a large industrial GT to a temperature higher than the steam condensation temperature and to start the flow of steam only after the rotating body was warm enough. The need to heat the rotating parts meant that, while the CCGT gained the advantages of high power and high performance, it lost the advantage of being capable of a rapid start-up. However, GE developed the Frame 7H/9H GT [25], which achieved 60% (LHV) thermal efficiency for CCGTs, as shown in Table 2 [19].

Table 2. The GT24 heralds another new generation of gas turbines [19].

Company	Turbine Model	Capacities		Efficiencies (%)		Key Dates	
		GT	CCGT	GT	CCGT	Announced	First Order
ABB	GT24	165 MW	250 MW	37.5	57.5	1993	1993
Westinghouse	501G	230MW	345MW	38.5	58	1994	1997
Siemens	V84.3A	170 MW	245 MW	38	58	1995	1995
GE	Frame 7G	240 MW	350 MW	39.5	58	1995	none
	Frame 7H	n/a	400 MW	n/a	60	1995	2004
	Frame 9H	n/a	480 MW	n/a	60	1995	1998

WH also studied a gas turbine with a closed-loop steam-cooling system in the ATS project. However, they did not finalize the development. Instead, WH opted for a 1500 °C class G-type gas turbine in collaboration with MHI. WH was responsible for the design of the turbine section, and the cooling was developed in cooperation with Rolls-Royce [19]. Figures 3 and 4 show the cooling structure of the first-stage airfoils of this turbine [26].

Siemens acquired the power generation division of WH in 2001. This allowed Siemens to take over the 501F/G design to enhance the GT's high-temperature technology and also made available the steam-cooling technology developed for the U.S. government's ATS program [19].

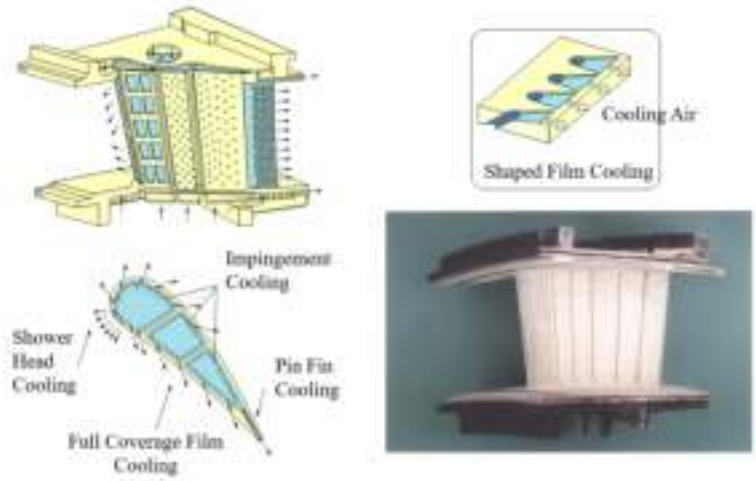

Figure 3. First vane of 1500 °C class G-type gas turbine [26].

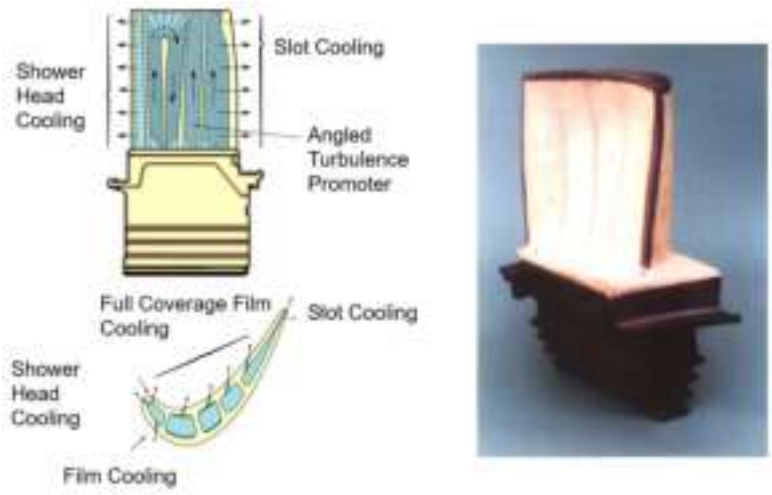

Figure 4. First blade of 1500 °C class G-type gas turbine [26].

In the new millennium, MHI independently developed a J-type gas turbine with a TIT of 1600 °C. This reflected the results of a Japanese national project started in 2004 to develop the technologies needed for a gas turbine with a TIT of 1700 °C. When the TIT of gas turbines was increased, the required parallel increase in coolant consumption counteracted the theoretical improvement in thermal efficiency [27]. In a Japanese national project, a revolutionary film-cooling hole geometry was developed, which significantly reduced the amount of coolant required [28]. The J-type gas turbine used steam to cool the combustor walls and the transition piece. The steam-cooling system was discontinued, and a JAC-type (J-class air-cooled) gas turbine with a TIT of 1650 °C was subsequently developed and employed in a combined cycle plant [8]. GE introduced the HA gas turbine, a fully modified version of the H-system, which had an open-air cooling system [29]. The HA gas turbine uses a system in which all hot components are cooled by air from the compressor discharge. Using the same definition of turbine inlet temperature (i.e., the average total temperature at the inlet of the first-stage vanes) as MHI, the temperature of GE's HA gas turbine is estimated to be 1670 °C [30]. The thermal efficiency of CCGTs

consisting of GE's HA-type gas turbine and MHI's JAC-type gas turbine achieved 64% (LHV). Because of the use of natural gas as fuel and such high thermal efficiency, these CCGTs have succeeded in reducing CO_2 emissions to about one-third of those emitted by state-of-the-art coal-fired power plants.

The history of the development of cooling structures for turbine airfoils used in large industrial gas turbines, described in this section, is described in detail in Ref. [31].

2.2. Development of Small and Medium Industrial Gas Turbines to Date

In this paper, gas turbines with an output of 50 MW or less will be defined as small and medium gas turbines. It is not economical to use small gas turbines of this size in a combined cycle. The amortization time of the investment costs of the steam turbine and steam generator is too long. This does not mean that small turbines are normally used in a simple cycle. Rather, they are used in some form of combined heat and power (CHP) application.

The basis for most small and medium-sized gas turbines was aero engine technology but modified for robustness and simplicity [32]. A multitude of companies have manufactured small and medium-sized gas turbines over the years (see Ref. [33]). Most of these are micro gas turbines with a power output well below 1 MW. These shall not be discussed any further, as they typically do not feature cooled blades and vanes.

In the 1970s, small gas turbines first became popular as a power source for emergency power generation facilities because of their compact size, because they did not require cooling water and because of their short start-up times. Up to the early 1970s, the airfoils could be made of uncooled super heat-resistant alloys, making them cost-competitive with gas engines, which was a factor in their widespread use. In the 1980s, the development of small and medium-sized gas turbines used for CHP applications was started. The gas turbines are thus used to produce electricity in various combinations with hot water, steam, both hot water and steam, or chilled water via absorption chillers. The most distinctive feature of small and medium-sized gas turbines is that they enable the optimal supply of electricity and heat in accordance with the needs of the plant side of the cogeneration system [34].

The development of small and medium-sized gas turbines has depended on competition with gas engines in terms of cost and thermal efficiency. If the power-to-heat ratio (PHR) (total power demand divided by total heat demand) of the application is less than approx. 0.8, the process is called heat-driven, and a gas turbine is usually used. If this ratio is exceeded, the process is considered power-driven, and an internal combustion engine (simple cycle efficiency >45%) is used [35]. Even when the PHR is greater than 0.8, a small gas turbine may be used when high-temperature steam is required. Plants using IC engines cannot generate high-temperature steam due to the inherently low exhaust gas temperature of the engine.

If there is excess steam produced by the exhaust gas boiler, it can be fed into the combustor chamber of the gas turbine, allowing the use of the steam-injected gas turbine (STIG) cycle or Cheng cycle, which enables a variable ratio of electricity to heat [36]. The Cheng cycle is shown in Figure 5.

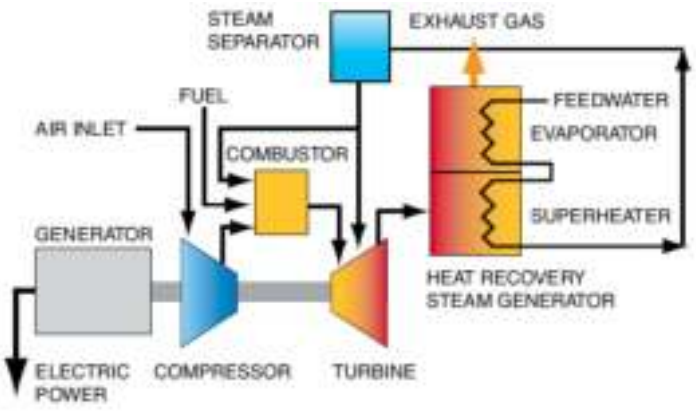

Figure 5. Steam-injected gas turbine cycle (STIG, Cheng cycle) [36].

Because most of the applications for small gas turbines are heat-driven, much emphasis is placed upon both the mass and the temperature of the exhaust gas. Therefore, the simple cycle efficiency of the gas turbine is of less relevance, and turbines with a large and hot exhaust gas flow may provide a solution that is superior to that provided by turbines with a higher simple cycle efficiency [37].

Due to cost constraints and the size of small and medium gas turbines, the level of high-temperature technology, expressed primarily in terms of turbine inlet temperature, is at a lower level than that of a similarly sized aircraft jet engine or large industrial gas turbines. However, the turbine inlet temperature of these gas turbines has increased over the years from the 800 °C to 900 °C level, at which uncooled turbine blades are used, up to a TIT of 1300 °C currently in operation [38]. Cleaner fuel is of great importance for these gas turbines; therefore, the development of combustors that can use fuels such as hydrogen and ammonia is the key to success.

Some small and medium gas turbines are still used in simple cycles. This encompasses those used as an emergency back-up, as well as the twin-shaft turbines used in the oil and gas industry as mechanical drives. Neither of these groups shall be discussed here any further because the first fill a niche where, in general, reliability outweighs efficiency, and the second are broadly covered by the discussion of their counterparts used in power generation. This being said, it may well be that small SCGT will become more common again as their importance for load balancing grows: these turbines can start up quicker because no steam cycle is included.

2.3. Integrated Gasification Combined Cycle (IGCC) Technologies

Coal is a very abundant energy source, with reserves that are about four times greater than those of oil and natural gas combined. In 2020, about 85% of the world's energy consumption came from fossil fuels, of which about 28% came from coal. In the same year, fossil fuels accounted for about 60% of global electricity generation, of which about 35% was coal fueled. As shown in Figure 6, the IAE estimates that the share of fossil fuels in electricity generation in 2030 and 2050 will be 40% and 20%, respectively, and that the share of coal will decrease to about 20% and 8% [39].

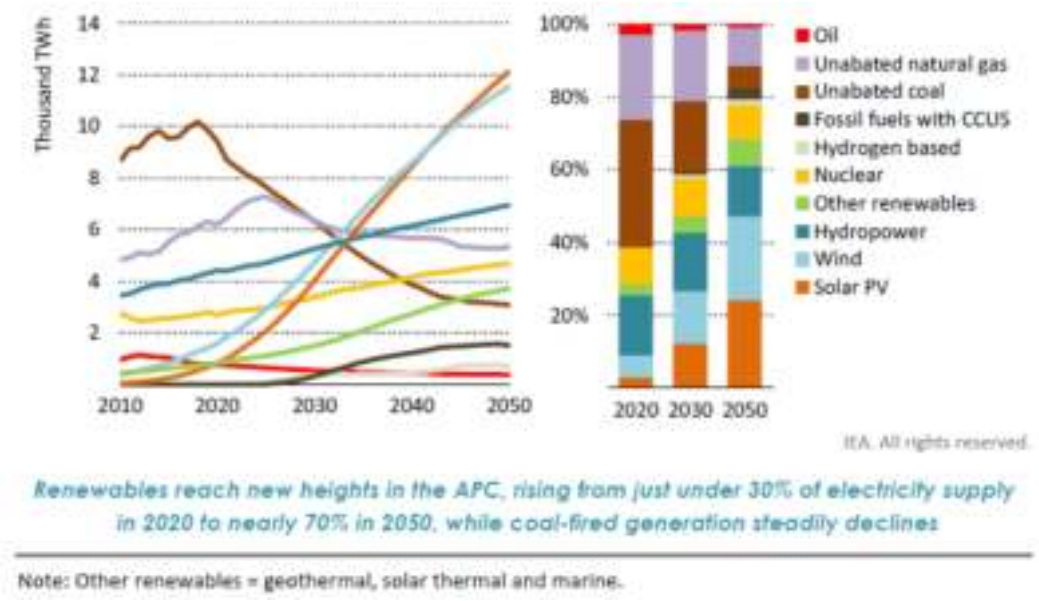

Figure 6. Global electricity generation by source in the APC [39].

Research on a system to generate electricity from coal in a clean and efficient manner with a gas turbine began in the mid-1960s by GE. In the late 1970s, a coal-fired combined cycle plant was studied with funding from EPRI. In addition, GE studied water-cooled closed-circuit gas turbines under the DOE's HTTT project. GE considered water cooling

for coal gasification gas turbines because the temperature of the blades should be kept below 538 °C to prevent adhesion of ash to the airfoils and to prevent corrosion of the super heat-resistant alloy. The HTTT project also had a development plan to gradually increase the TIT to 1100 °C, 1400 °C and 1600 °C [40]. In the late 1970s, the development of industrial gas turbines consisting of open-air-cooled circuits with TITs of 1100 °C had begun. However, the amount of air required to cool turbine blades for 1400 °C and 1600 °C class gas turbines using the cooling technology of the time would have been much too high. Furthermore, it was impossible to achieve a metal temperature of 538 °C using air-cooling technology.

GE knew that airfoils made of super heat-resistant alloys with internal water cooling could not meet the design life due to thermal fatigue caused by large temperature gradients in the thickness direction of the walls. Therefore, the company developed airfoils made of a copper alloy. The blades were developed with a system in which cooling water is blown out from the blade tips and collected at the shroud. The details of these problems are elucidated in Ref. [41]. Because of the difficulties encountered in solving problems such as water erosion in the cooling channels and vibration problems caused by boiling of the cooling water, the coal gasification water-cooled gas turbine was never put to practical use. The closed-circuit steam-cooling technology for hot parts used in the project as a back-up for water cooling was later developed by GE and commercialized as the H-system. This was already described in the CCGT section.

In the 1980s, R&D on IGCC using commercial gas turbines was pursued in the United States. The first of these projects was the Coolwater Project [42]. An 1100 °C class gas turbine modified from GE's 7001 E-type was used. Since then, many R&D projects have been conducted in Europe and the United States [43].

In Japan, the IGCC project in Nakoso, using a 701DA gas turbine with a TIT of 1200 °C, was used for power generation. The Nakoso IGCC cycle is shown in Figure 7 and its specifications in Table 3 [44]. The plant achieved a thermal efficiency of 42% (net LHV) or higher after successfully completing 2000 h of continuous operation and 5000 h of endurance testing at an output of 250 MW [45]. Currently, the development of an IGCC plant at Negishi using a 701F gas turbine with a TIT of 1400 °C is underway [43]. As shown in Figure 8, it is considered possible for IGCC to generate electricity with a thermal efficiency of more than 50% (net LHV) using ultra-high-temperature industrial gas turbines with a turbine inlet temperature from 1600° to 1700 °C in the future if clean coal gasified fuel is available [46].

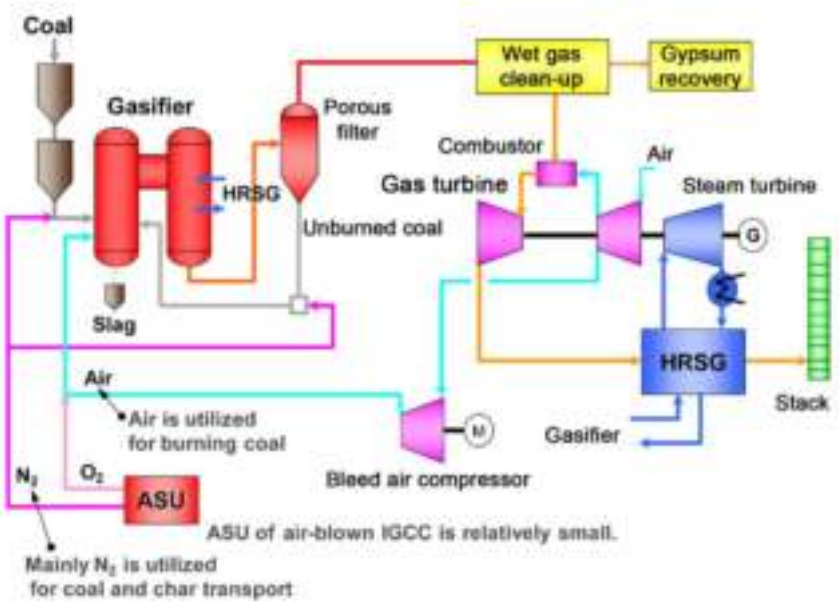

Figure 7. Schematic diagram of an air-blown IGCC demonstration plant [44].

Table 3. Specification of Nakoso IGCC demonstration plant [44].

Capacity	**250 MWe Gross**		
Coal consumption	approximately 1700 metric tons/day		
System	Gasifier	Air-blown and dry feed	
	Gas treatment	Wet (MDEA) + gypsum recovery	
	Gas turbine	1200°C class (50 Hz)	
Efficiency (Target values)	Gross	48% (LHV)	46% (HHV)
	Net	42% (LHV)	40.5% (HHV)
Flue gas properties (target values)	SOx	8 ppm	(16% 02 basis)
	NOx	5 ppm	
	Particulate	4 mg/m3N	
EPC	Mitsubishi Heavy Industries (MHI)		

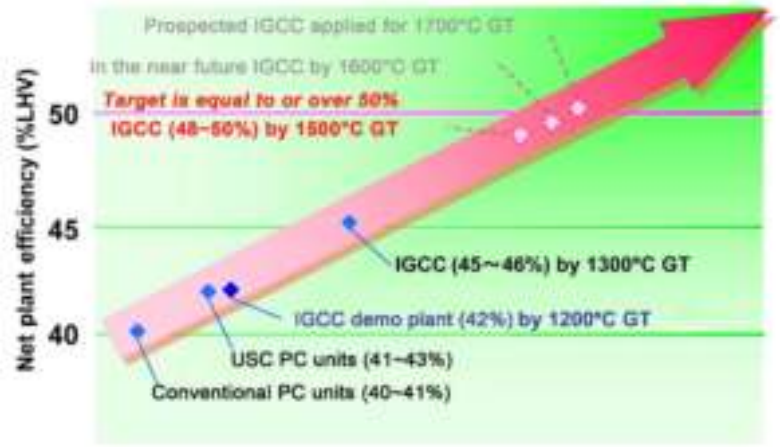

Figure 8. Thermal efficiency improvement of an air-blown IGCC [46].

An IGCC can be established by adding a gasifier, gas clean-up equipment upstream of the currently well-proven combined cycle and, if necessary, air separation. These modifications to the CCGT are considered important in the carbon-neutral era as power generation facilities, which expand the possibilities to burn dirty fuels, such as refinery residues, biomass, edible oil residues and plastic waste.

Coal contains components such as sulphur, chlorine, different alkalis and vanadium, which can cause high-temperature corrosion of hot parts. In an IGCC, the fuel gas for the gas turbine is produced by a gasifier, which converts coal to syngas, and clean-up equipment, which removes corrosive components and ash. The viability of an IGCC as a power generation facility depends on the performance of the gasifier and clean-up equipment. Furthermore, the question is whether the thermal efficiency of IGCC and the total cost of IGCC and associated CCS can compete with other power generation facilities. The gasifier technology, clean-up technology and CCS technology are advancing rapidly. The costs of the fuel cannot be forecast at the moment, but a number of countries will be using fossil fuels for the foreseeable future, and these technologies would still enable a carbon-neutral power generation. However, the cost of IGCC is currently higher than that of other power generation facilities, and research, development and demonstration tests are being conducted only with financial support from governments and other organizations.

2.4. Future Development of CCGTs, or What Is a CCGT in Line with the Carbon-Neutral Era?

In the coming carbon-neutral era, gas-turbine-based power generation facilities will continue to play an important role due to their high energy conversion efficiency and ability to use a variety of fuels.

Let us first consider the specifications an industrial gas turbine used in a carbon-neutral manner should have. When a gas turbine is operated using fossil fuels, the addition of a CCUS facility is mandatory. On the other hand, if hydrogen or ammonia are used as fuels, CO_2 emissions can be reduced to zero, but the unit cost of electricity generation will be considerably higher than that of natural gas. The only way to address these issues is to further improve the thermal efficiency of CCGTs with large industrial gas turbines. We would like to target a thermal efficiency of 70% (LHV), which is approximately 10% higher than the thermal efficiency of current state-of-the-art CCGTs. This implies a TIT from 1900 °C to 2000 °C and a pressure ratio of about 30.

In addition to improving the performance of gas turbines, it is also necessary to consider the functions that industrial gas turbines should have for the environment in which they are used. As mentioned in the Introduction, about half of the electricity generated in a carbon-neutral world will come from renewables. These power sources are susceptible to weather conditions and load fluctuations. In order to provide a stable power supply, thermal or nuclear power generation facilities with inertia is indispensable. The problem of power supply stability has already begun: it is already a challenge for grid operators in countries and power networks where renewable energy dispatch has priority. Figure 9 illustrates the increasing variability of electricity generation in California [47]. The authors of Ref. [47] examine the options for providing flexible distributed generation plants with outputs ranging from 25 MW to 300 MW. The measures proposed assume that large CCGTs are to operate at rated load. In a large CCGT, it is difficult to rapidly change the load on the steam turbine, so it is necessary to develop a CCGT, which can change the load only with the gas turbine while the steam turbine is at or near to rated load. This may mean an extended operation with partial admission or the use of twin-shaft gas turbines.

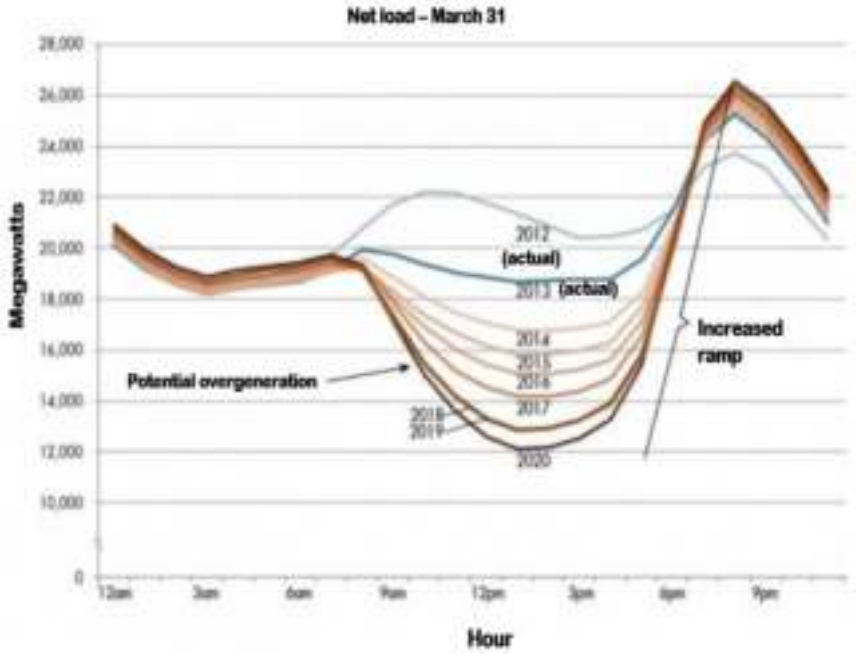

Figure 9. The California ISO "duck curve" illustrating the impact of intermittent renewable power generation [47].

The large industrial gas turbine used in such a CCGT should have the functionality of a jet engine, which can handle rapid load changes. Therefore, the structure of the turbine, from the airfoils to the discs, must be designed to reduce thermal stresses during transient

changes. The current industrial gas turbines used in CCGTs are designed to achieve the highest efficiency at rated load. However, large industrial gas turbines in carbon-neutral applications must maintain high efficiency even at partial load [18].

However, not all large industrial gas turbines need to be capable of following load fluctuations, since there are regional differences in the amount of electricity generated by renewables. In addition, gas turbines used for IGCC must operate at rated load.

For gas-turbine-based power generation facilities, various thermal cycle systems have been studied with the goal of achieving the highest thermal efficiency [48,49]. The results of these studies indicate that complex cycles are required. In particular, the operation of a closed-circuit cooling system is highly efficient, but it is not suitable for the carbon-neutral era because of the time required for the components of the combined plant to achieve thermal equilibrium. Based on a review of the R&D status of gas-turbine-based thermal systems developed to date and the estimation of future specifications, we conclude that a combined cycle consisting of a simple large gas turbine and a steam turbine with cooling of hot parts by the current compressor discharge air is the most suitable for carbon neutrality.

On the other hand, for small and medium-sized industrial gas turbines, the change of fuel to CO_2-free fuels, such as hydrogen or ammonia, means that the current restrictions on the (cooling) design imposed by the possible use of inferior fuels will be removed. This implies that a cooling structure similar to that of airfoils for aero engines with the same geometrical dimensions will be possible. Small to medium-sized gas turbines used as a stand-alone gas turbine—because of its fast start-up and load fluctuation capability—can function as a stabilizer for the power grid. This will enable the TIT of these gas turbines to be increased if the cooled airfoils can be manufactured at a lower cost, leading to a dramatic improvement in thermal efficiency. Since these gas turbines are not used in combined cycle applications, they can be designed for high thermal efficiency with a large pressure ratio and sufficiently low exhaust gas temperature. Simultaneously, small and medium-sized gas turbines are expected to continue to be used as cogeneration systems.

3. Industrial Gas Turbines of the Future

In order to achieve carbon neutrality, one has to either capture any emissions of CO_2 or burn a fuel that does not contain any (additional) carbon. The latter currently means burning either green hydrogen, ammonia based on green hydrogen or bio-fuels. Although the availability [50] and economic feasibility [51] of a green-hydrogen-based society have been called into question, these challenges will probably be overcome, and one has to prepare the technology needed for the carbon-neutral era now and not only when remedies to all objections have been found.

First, we consider the use of industrial gas turbines fueled by CO_2-free hydrogen or ammonia.

Among the various gas turbine cycles, this section discusses those that have been considered for use in the future carbon-neutral era, or advanced gas turbine cycles for which specific plants have been constructed to demonstrate their performance.

3.1. Hydrogen and Ammonia as Gas Turbine Fuels

It is technically possible to produce CH_4 from H_2 and CO_2 (the Sabatier reaction), but this is not economically viable at the moment. Therefore, CO_2-free fuel currently means burning either green hydrogen, ammonia based on green hydrogen or bio-fuels.

Bio-fuels in their pure form may contain contaminants, such as sulphur, but these can be eliminated comparatively easily [52]. This means that the use of these fuels should have little impact on the combustion system and cooling design. The use of hydrogen or ammonia as fuel for gas turbines has long been considered [53,54], and these fuels are expected to be used for gas turbines, boilers, internal combustion engines, industrial furnaces and other existing power and heat sources [55–62]. The main components of a gas turbine can remain largely the same, except for the combustor, which differs from the natural-gas-fired industrial gas turbines currently in operation [63–66]. Apart from

the modifications to the combustion system to take account of the higher flame speed of hydrogen and the long reaction times of ammonia compared to those of methane, the TIT will change as well.

Hydrogen has a calorific value of only 3.0 MJ/m^3, but this is equivalent to 120 MJ/kg. Natural gas ("L-gas"), on the other hand, has a calorific value of 31 MJ/m^3, which is equivalent to only 32 MJ/kg. This means that the overall mass flow through the turbine, i.e., air and fuel, will decrease when burning H_2. The constituents of the fuel gas also change: there will be no more CO_2, but additional H_2O. The average specific heat capacity of CO_2 is approx. 1.2 kJ/kgK and that of water vapor is approx. 2.4 kJ/kgK. The absolute changes in the mass fraction of the constituents combined with the differences in specific heat cancel each other out, meaning that the heat capacity of the exhaust flow changes only marginally. On the heat transfer side, it has to be taken into account that both CO_2 and water vapor radiate. Again, the changes largely cancel each other out. Nonetheless, the differences in calorific value and overall mass flow lead to changes in the TIT:

- If both the power output and the exhaust gas temperature have to remain constant while burning 100% hydrogen, the TIT increases by several dozens of degrees with the subsequent impact on the average component temperature.
- If both the TIT and the exhaust gas temperature remain constant, the power output of the gas turbine will decrease by more than 10%, but the efficiency will increase slightly and the exhaust gas mass flow substantially.
- If the power output and the TIT remain constant, the exhaust gas temperature will decrease by nearly 20 K, but again, both the gas turbine efficiency will increase slightly and the exhaust gas mass flow substantially.

It is possible to find a thermodynamically optimal solution within the boundaries mentioned above by varying all three parameters. Still, some adjustments to the cooling design will be necessary, especially in combination with the altered design of the combustor, which will lead to a different TIT profile, turbulent length scales and turbulence.

It should be noted that the above discussion is focused solely on the thermodynamic aspects of burning hydrogen. It may be necessary to consider the impact of increased water vapor on the oxidation behavior of alloys and ceramics. Combustion dynamics, NO_x emissions and flashback should also be taken into account. Therefore, a de-rating of the gas turbine may be necessary for other reasons.

The thermo-physical properties and combustion characteristics of hydrogen and ammonia are shown in Table 4 [67]. Hydrogen has a low liquefaction temperature of 20 K, making it difficult to transport and store. In addition, it is necessary to develop a combustor, which will not produce too much thermal NO_x and handle the high turbulent flame speed that can cause flashback. Ammonia, on the other hand, liquefies at about 10 atmospheres at common ambient temperatures, making it easier to handle for transportation and storage than LNG. However, it has a very low turbulent flame speed, and the presence of nitrogen in the fuel may cause fuel NO_x.

Table 4. Thermal properties and fundamental combustion characteristics of ammonia and hydrocarbon fuels [67].

Fuel	NH_3	H_2	CH_4	C_3H_8
Boiling temperature at 1 atm (°C)	−33.4	−253	−161	−42.1
Condensation pressure at 25 °C (atm)	9.90	N/A	N/A	9.40
Lower heating value, LHV (MJ/kg)	18.6	120	50.0	46.4
Flammability limit (Equivalence ratio)	0.63–1.40	0.10–7.1	0.50–1.7	0.5–2.5
Adiabatic flame temperature (°C)	1800	2110	1950	2000
Maximum laminar burning velocity (m/s)	0.07	2.91	0.37	0.43
Minimum auto ignition temperature (°C)	650	520	630	450

Since the production and supply chain for hydrogen and ammonia is still in the early stages of development, the operation of gas turbines using these fuels is still experimental. MHI has operated a CCGT demonstration facility using a 1600 °C J-type gas turbine with 30%$_{Vol}$ of hydrogen mixed with natural gas to demonstrate CCGT power generation [68]. KHI has successfully operated a 2 MW M1A-17 gas turbine with 100% hydrogen fuel at almost full load [69], and IHI has successfully operated a 2 MW IM270 gas turbine with 100% ammonia at full load [70]. In Europe and the United States, 100% hydrogen-fired power plants are currently under construction for CCGTs using large industrial gas turbines, and these power plants are expected to come on line as the infrastructure for hydrogen production and supply is developed.

3.2. Oxy-Fuel and Hydrogen-Oxy Cycle Combustion Turbine

The problem with burning H_2, however, is that hydrogen-fueled combustors, which tend to have higher flame temperatures, are anticipated to emit more NOx than natural-gas-fired combustors [71] if they use air. Steam cooling can be used to increase the amount of available combustion air and lower the combustion temperature to achieve low NO_x emissions. Carbon-neutral CCGTs will see an additional 200 °C to 300 °C increase in the combustor exit temperature to achieve their efficiency targets. The authors believe that the current combustion system using air as the oxidizer is reaching its limit for low NO_x combustion. A combustion method that does not generate NO_x at all is the oxy-fuel cycle (OFC), which separates oxygen from the air. This cycle was originally proposed for the capture of CO_2 from the combustion of coal in thermal power generation [72,73]. The oxy-fuel cycle can be used for a wide range of fuels, including natural gas, coal gasification gas, biomass, etc. Therefore, it is possible to develop the OFC thermodynamically without difficulty, although it is necessary to redesign the compressor, combustor and turbine based on existing CCGT technology to make them suitable for the cycle. This section describes only the application of the OFC to the CCGT [74].

There is a disadvantage in terms of thermal efficiency, in that additional energy is required for the process of separating oxygen from air. However, by adopting the OFC, the TIT can be increased to 1900 °C–2000 °C, and the gas turbine can be operated without producing any NO_x despite this high combustion temperature. In the future, when hydrogen and oxygen are produced by electrolysis using renewable energy, hydrogen will be used as fuel, and the excess oxygen can be effectively utilized in this cycle.

The cycle diagram of the OFC is shown in Figure 10 [75]. The components of the exhaust gas are CO_2 and water vapor. Capturing CO_2 can be achieved very easily at atmospheric pressure because when water vapor is converted to water in the condenser, gaseous CO_2 remains. When the gaseous CO_2 obtained in this way is recirculated, it becomes a Brayton cycle, whereas when the condensed water is circulated, it becomes a Rankine cycle [76]. In the following section, we will discuss the OFC when the Brayton cycle is employed as a gas turbine.

Different recirculation ratios of H_2O and CO_2 were studied for oxy-fuel CCGTs to find the optimal compressor, combustor and turbine specifications [77]. In the case of a CCGT with CO_2 recirculation, the compressor pressure ratio must be approximately doubled in order to achieve the same exhaust gas temperature in the HRSG as in a natural-gas-fired CCGT. The CCGT power output and thermal efficiency were also studied by calculating an oxy-fuel CCGT with the amount of coolant for the airfoils as a parameter [78,79]. The application of the oxy-fuel's CO_2 circulation system in a natural-gas-fired CCGT with a GE Model 9H gas turbine was studied [80]. According to the results of this study, the thermal efficiency of the OFC was 51.3% (net LHV), which is 8.1% lower than that of a natural-gas-fired CCGT. This lower efficiency compares favorably with the lower efficiency of CO_2 capture using the amine recovery process. However, because it is a CO_2 circulation system, the current 9H gas turbine cannot be used in its present form, and a new design is required for all components. The main flow is a mixed stream of CO_2 and superheated steam, which provides strong radiative heat transfer to the hot parts. The structural integrity of the

cooled airfoils should be evaluated considering the radiative heat transfer. The cooling performance of hot parts in the oxy-fuel CO_2 circulation system is superior to that of air cooling, since carbon dioxide from the compressor discharge is used.

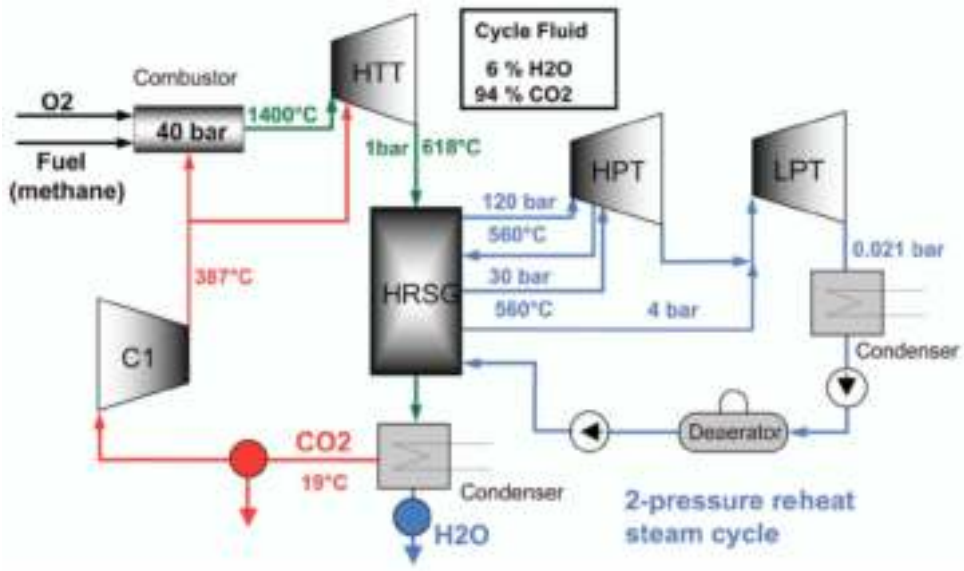

Figure 10. Principle of theflow scheme of the oxy-fuel cycle [75].

Jericha and others at the Graz University of Technology in Austria have proposed a highly efficient combined cycle using hydrogen–oxygen combustion. This cycle was named the "Graz Cycle" by Japanese researchers involved in the WE-NET project [81]. The basic configuration of the Graz cycle is shown in Figure 11 [82], in which natural gas is burned with pure oxygen [83]. This results in a working fluid, which consists exclusively of steam and CO_2, the latter of which can be easily separated from the steam. The exhaust gas is used to generate steam in a regenerative heat exchanger, and the low-pressure steam is used to drive the Rankine cycle and as the compressor inlet steam in the Brayton cycle. Since its inception, a steady stream of publications have refined the concept [75,82,84,85]. Cycle analysis has shown that the thermal efficiency of the Graz Cycle is more than 10% higher than that of a natural-gas-fired CCGT with the same TIT. The Graz Cycle is highly efficient because the exergy losses of combustion are reduced by increasing the combustion pressure and the temperature [85].

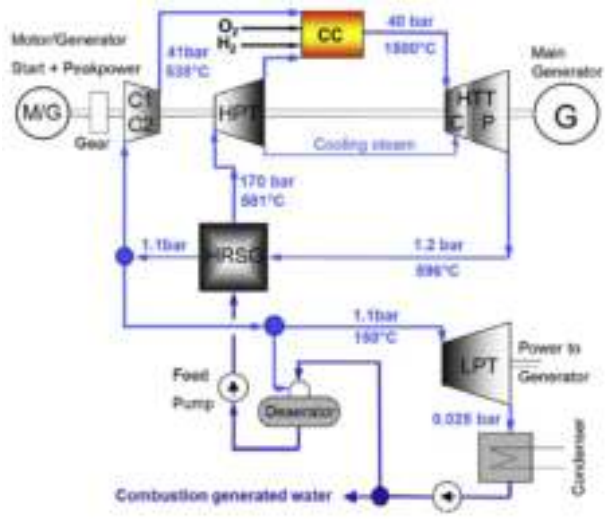

Figure 11. Principle of the flow scheme of the oxy-fuel cycle [82].

A good review of a number of other closed cycles can be found in Ref. [86].

3.3. The HAT Cycle

In the CCGT, the working fluids of the topping gas turbine cycle and the bottoming steam turbine cycle are physically separated. There are, however, many options for converting liquid water to steam and combining it with the working fluid of the gas turbine. The Cheng Cycle for small plants, in which the exhaust heat from the gas turbine is used to generate superheated steam in a heat recovery steam generator (HRSG), was already described.

Recuperated cycles enjoyed a certain popularity some decades ago when the overall pressure ratio of gas turbines was still rather low. The exhaust gas was used to pre-heat the compressor discharge air before it entered the combustion chamber. The heat below the compressor discharge air temperature cannot be recovered from the turbine exhaust gas within the gas turbine cycle. When the TIT is increased to achieve higher performance, it is necessary to increase the pressure ratio accordingly. Therefore, the amount of heat recovered using the recuperator decreases, and the exhaust gas is released into the atmosphere at a higher temperature, resulting in heat loss.

On the other hand, the specific heat of water vapor is about twice as large as that of air, and it has a large heat recovery capacity. Using this property of steam, a relatively low-temperature, high-humidity air can be used for heat recovery in a regenerator. In this case, a cycle can be constructed to recover heat from the exhaust gas down to nearly 100 °C, where the steam condenses at atmospheric pressure [87,88]. A typical example of this high-humidity regenerative gas turbine cycle is the humid air turbine (HAT) cycle shown in Figure 12 [89]. This cycle was developed by Nakamura in 1981 as an application of medium- to low-temperature heat recovery technologies in gas turbines [90]. It was recognized that this cycle can be expected to improve thermal efficiency by approx. 3 to 4 % (absolute value) compared to a normal combined cycle [91]. To achieve its performance, it was necessary to develop a new type of gas turbine with separate compressors and an intermediate cooler. In contrast to the HAT cycle, Hatamiya devised the AHAT cycle; its sequence is shown in Figure 13 [92]. This power generation system aims to achieve high efficiency without the need for the high pressure ratios and high combustion temperatures, which are currently the mainstream of highly efficient combined cycle systems. In the AHAT cycle, intake air is cooled by installing an intake air duct (called an aftercooler), which sprays fine water droplets into the compressor intake air. This lowers the intake air temperature by evaporation before the air reaches the first compressor stages. The remaining water droplets evaporate during the compression process, suppressing the increase in temperature of the air. The compressor discharge air flows into the humidification tower (called a saturator), where it comes into direct contact with hot water and becomes highly humid air. The humidification ratio is about 15 to 20%$_{wt}$ of the intake air flow.

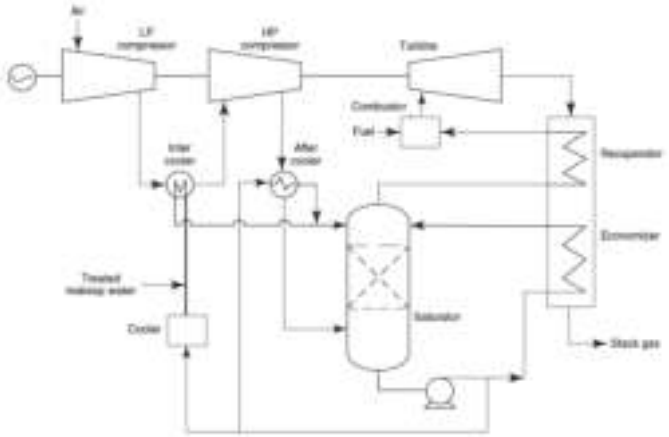

Figure 12. HAT cycle [89].

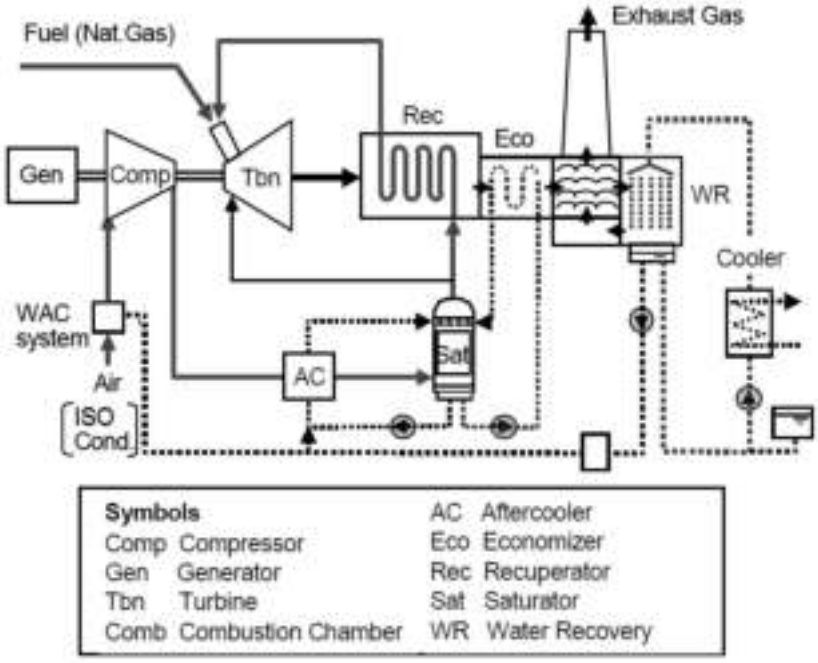

Figure 13. AHAT cycle [92].

Hitachi built an experimental plant to verify whether the cycle concept of the AHAT system and the target performance could be achieved using a 3 MW class gas turbine and conducted demonstration tests [93]. An output of 4.0 MW and a thermal efficiency of 40% LHV were achieved. These results show that if the AHAT cycle is designed under optimal conditions, the power generation efficiency will exceed that of a combined cycle. The difference in efficiency is particularly large for small and medium-sized gas turbines. Figure 14 shows an example of efficiency estimation of an AHAT cycle compared to existing gas turbine power generation systems [92].

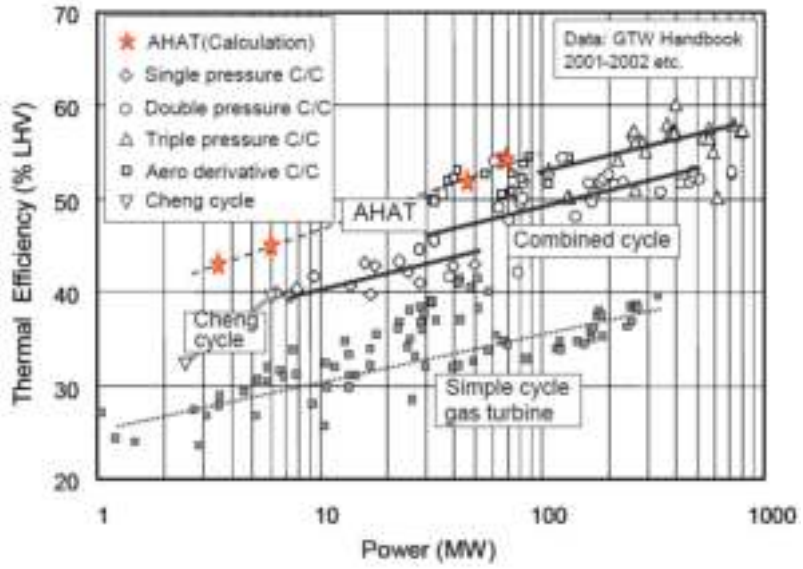

Figure 14. Comparison of thermal efficiencies of gas turbine cycles [92].

The AHAT cycle can be considered one of the best systems for small and medium-sized gas turbines in the carbon-neutral era. Furthermore, it is desirable to consider an AHAT cycle using renewable fuels, such as hydrogen and ammonia, instead of natural gas.

4. Cooling Structure for Gas Turbine Airfoils of Future Importance

Section 2 described the current status of industrial gas turbines in operation. In Section 3, several possible cycles and the preferred or ideal industrial gas turbine cycle for the carbon-neutral era were discussed. This section describes the cooling structures, which should be adopted. First, the current cooling methods for the latest 1650 °C level cooled airfoils are described. Next, the cooling strategies for vanes and blades that have been researched and developed so far are discussed. Then, the cooling structures and production methods that can be applied to airfoils in the carbon-neutral era are described based on those structures and production methods. It should be noted that the quantitative need for cooling will, to some extent, depend on the thermodynamic cycle. Although the temperature will be the same, the exhaust gas compositions will differ, leading to different thermal loads and different cooling requirements.

The first-stage turbine vanes and blades of a 1500 °C class G-type gas turbine are shown in Figures 4 and 5, respectively. The cooling structure of both turbine vanes and blades does not differ significantly from that of a high-pressure turbine of a jet engine with the same TIT. It should be noted, however, that the airfoils of a large industrial gas turbine are approximately four times larger than those of a jet engine. Although not shown in this paper, the cooling air used to cool the turbine rotor blades in the WH-MHI gas turbine does not reflect the fact that the compressor discharge air is taken out of the system and cooled with water from the bottoming cycle. In other words, the air used to cool the blades is cooled to approximately 150 °C. According to Figure 4, this cold cooling air is discharged directly to the outer surface of the blade as film cooling through a short internal cooling channel. In the F-type turbine first-stage blades designed by MHI, the cooling air is used internally as much as possible, and once the temperature has been increased as much as possible, it is discharged from the blade surface as film cooling—a concept unique to industrial gas turbines [31]. All of the blades of the 1500 °C class G-type gas turbine designed by WH were modified by MHI to achieve the optimal cooling geometry for an industrial gas turbine based on the above concept.

Impingement cooling, which is used in vanes, is a method of effectively cooling the vane inner surface at the leading edge and the center section of the airfoil (along the chord). With a serpentine flow passage, which is used in blades, the temperature distribution along the blade height is almost uncontrollable, whereas it can be easily controlled by adopting impingement cooling and adjusting the number of impingement cooling holes.

In the cooling structure of the vane shown in Figure 3, impingement cooling is provided from the inner surface by putting an insert into several cavities in a thin-walled structure. The number of cavities tends to increase as the TIT increases; in the 1150 °C class D-type gas turbine designed by Westinghouse for cooling, the number of cavities in the first-stage vanes was two. However, the number of cavities in the first stage of a 1200 °C class DA-type gas turbine modified by MHI was increased to three. The number of cavities in the first-stage vanes of the 1350 °C class F-type and 1500 °C class G-type turbines is also three, but the number of impingement cavities in the 1600 °C class J-type turbine is five [31]. The increase in the number of cavities is founded in the need to optimize the cooling air supply pressure and the film-cooling outflow velocity on the surface of the vane. The static pressure distribution on the surface varies both along the chord and span, and the cooling is adapted correspondingly. It is possible to form cavities by means of a sealing structure between the insert and the inner surface of the vane, rather than partitions inside the vane, to generate the number of cavities. A tight seal across the span of vanes guarantees a high cooling performance and high reliability. However, as the TIT increases, three-dimensional vane shapes are required to improve aerodynamic performance, making it extremely difficult to design a sealing structure with precise contact between the surfaces. In the combined impingement- and film-cooling section, attention should be paid to the ventral side of the turbine vane. Film cooling on a surface with a small radius of curvature promotes mixing of the film-cooled air with the mainstream due to the Görtler vortices on a concave surface. To avoid this mixing, the pressure surface is composed of sections

with a large radius of curvature. The leading edge of the first-stage vane, on the other hand, has the largest possible leading edge radius to reduce the heat transfer coefficient of the mainstream. Pin-fin cooling is used for the trailing edges of the turbine blades where impingement cooling is not possible due to the difficulty of incorporating inserts.

The cooling structure of the turbine blades shown in Figure 4, which employs film cooling in the tabulated serpentine flow path, is the same as that of a jet engine. The showerhead cooling of the leading edge is designed to distribute the coolant on both sides around the stagnation point. On the other hand, pin-fin cooling is used on the trailing edge of the blades.

The aspect ratio of the serpentine channel of the turbine rotor blade shown in Figure 4, which was designed based on an aircraft engine, is close to unity, which is an excellent cooling design when considered only from the perspective of heat transfer. When WH-MHI designed large industrial gas turbines of the D, F, and G classes, they adopted the same four-stage turbine layout. This implies that the load on the rotor blades increases with the increase in TIT because the load is distributed over the same number of stages. This, in turn, means that the shape of the blade is changing from a reaction type to an impulse type. This tends to increase the aspect ratio of the serpentine channel: the blade becomes thicker, meaning that the surface of the internal divider walls becomes larger than that of the actual inner walls on the pressure and suction sides of the airfoil. Since the ribs of a serpentine channel are generally installed on what is now the short side of the rectangular cross section, a serpentine channel shape with a large aspect ratio is inefficient in terms of cooling.

The improvement of the thermal efficiency of the cycle is roughly in proportion to the amount of coolant reduction, given that the reduction lowers the pumping loss and reduces the temperature of the mainstream less. For this reason, the cooling design of the blades needs to progress to more advanced cooling, which enables a more uniform temperature distribution in spanwise direction and one that is attuned to the creep rupture strength requirements along the blade height. Because the blade rotates by definition, the gas temperature around it can be considered to be the circumferentially averaged value of the mainstream gas temperature. The creep strength of a blade is determined by the centrifugal force acting on it in combination with the average metal temperature of its cross section. For the maximum creep strength to be attained, the gas temperature distribution should be designed in such way that the highest temperature is at about 50 to 60% of the span. Since the blade root has the cross section with the highest centrifugal stress, it must be sufficiently cooled to meet the strength requirements, even though the gas temperature is lower than at the mid-span. The cooling design from the mid-span to the tip of the blade could attain a gradual reduction in the amount of coolant to achieve an average metal temperature, which aligns the creep strength with the decay of centrifugal force. Turbine blade cooling by serpentine channels cannot control the average metal temperature in the blade height direction. However, if a cooling method that combines impingement and film cooling is used for turbine rotor blades, it is possible to achieve this.

Impingement cooling by introducing an insert into the blade is an excellent cooling method in terms of controlling the local metal temperature. However, two problems exist. First, since the inlet angle of a blade changes in the radial direction, the airfoil is twisted. When the blade rotates, the centrifugal force causes it to untwist to some degree. Therefore, the insert must be installed in a location where the relative position of the inner wall and the insert is unlikely to change. Next, the ribbed surface that holds the insert in place and the insert itself must be in contact with each other at a constant pressure. However, even if the sealing surfaces are manufactured very precisely, damage can occur due to fretting wear because of the relative motion caused by the rotational motion and thermal elongation differences. In the high-pressure turbine first-stage blade of the Pratt & Whitney 1250 °C class JT9D-7A jet engine, impingement cooling with a single insert integrated in a single cavity was used. However, PW abandoned the use of impingement cooling for the blade because of the fretting wear mentioned above. For the JT9D-59A, which increased the

turbine inlet temperature of the JT9D engine to 1360 °C, a cooling structure that combines serpentine channels and film cooling was adopted. Impingement cooling of the mid-chord region was no longer used. Currently, impingement cooling remains in use for the leading edge, where impingement nozzles can be produced by precision casting.

The cooling design of the airfoils has its roots in precision casting. From the viewpoint of seeking a cooling structure, which is more reliable, has a higher cooling efficiency and allows local control of the metal temperature, new manufacturing methods that break with this concept need to be conceived. One of the techniques developed for aero engines in the past is cast cooling; another is the wafer and diffusion bonded blade. The airfoils of large industrial gas turbines are thus much larger than those for which these technologies were originally planned, and therefore, one cannot simply apply them. As indicated before, the heat capacity of the airfoils of large gas turbines is much larger, necessitating a modified design that takes the altered thermal stress into account. Because the sizes of the airfoils of small and medium-sized industrial gas turbines and those of aero engines are approximately the same, it is possible to also apply the technology in these industrial gas turbines. Because industrial turbines will be operated more similarly to aero engines in future, the design rules and criteria should converge as well, making these technologies an interesting option. For these smaller gas turbines, the main challenge will be to keep the manufacturing costs down as much as possible.

First, we will discuss cast-cooled airfoils. In combustors for jet engines, the combustor dimensions are reduced to reduce the weight, and diffusion combustion using liquid fuel is the norm. For this reason, designs that can effectively cool the combustor wall with low pressure loss and a small amount of coolant were the focal point of R&D efforts. One combustor wall structure with such a function is Lamilloy®, which has a double-wall cooling structure [94–96]. It consists of an outer wall, an inner wall (combustion side) and a structure with fins, which promote heat transfer between them. The inner wall and fin structure are fabricated by photo-etching, and the outer wall is diffusion bonded to the inner structure. As the name suggests, CastCool® is a high-pressure first-stage blade manufactured by precision casting the cooling structure of Lamilloy®. The CastCool® first-stage blade is shown in Figure 15 [97,98]; this also gives a good overview of the general features and design of CastCool® airfoils. In the CastCool® blade, the impingement-cooling and its relative position to the film-cooling holes can be fabricated according to the design intent. This cooling structure allows the impingement-cooling heat transfer coefficient and the film-cooling blow-off rate to be controlled even with fluctuating turbine loads. Furthermore, the combination of the two cooling methods ensures that there is back pressure for the film cooling with no backflow and uniform metal temperatures across the leading edge can be achieved with minimal coolant mass flow. Figure 16 shows an example of the application of the above cooling method, which prevents reverse flow in partial load operation into the cavity of the leading edge [99].

Wafer and diffusion bonding blades are discussed next. The structures of the first-stage blades developed by ERDA, a project spawned by the DOE's HTTT program, are shown in Figures 17 and 18, respectively [100]. Again, these figures were chosen to give an overview of the design of such airfoils in general as well. The first-stage vane was manufactured by forming a fine cooling structure on a thin plate made of a super heat-resistant alloy by photo-etching, then overlapping the wafers in radial direction and integrating them by diffusion bonding. The blade was manufactured in the same way as that of the vane. However, the surfaces are diffusion bonded in the direction where the centrifugal force does not act, i.e., in the axial direction. In the same HTTT project, EPRI developed turbine blades called Shell/Spar. Figure 19 shows the structure of the first-stage Shell/Spar blade [101].

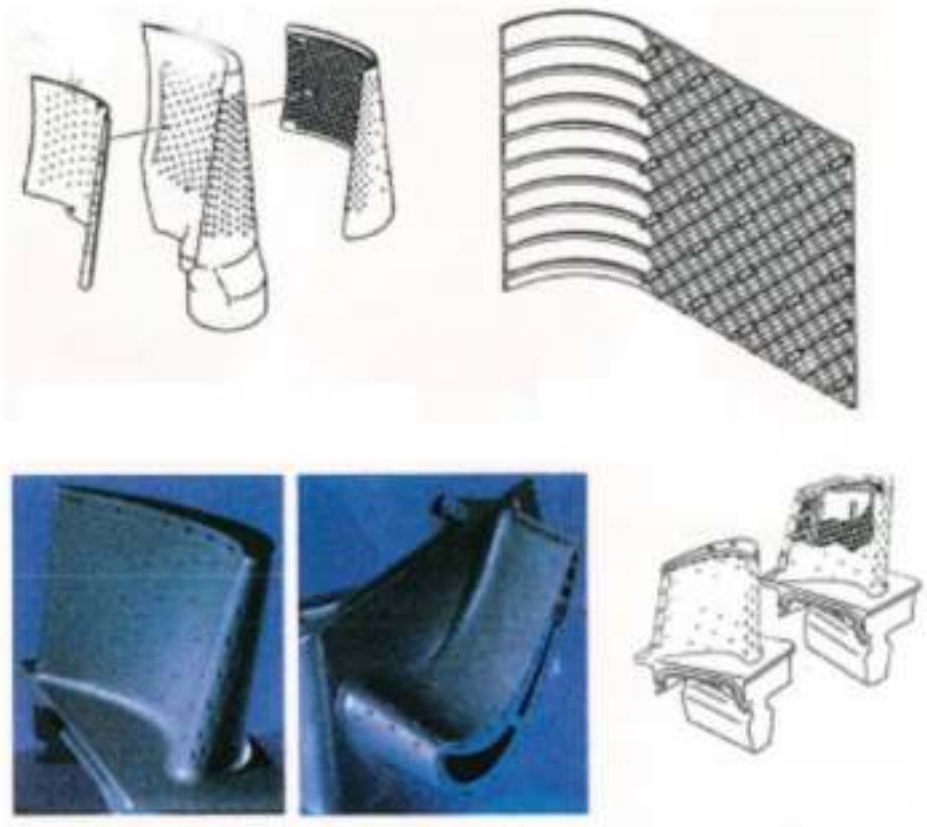

Figure 15. A CastCool® turbine blade [97].

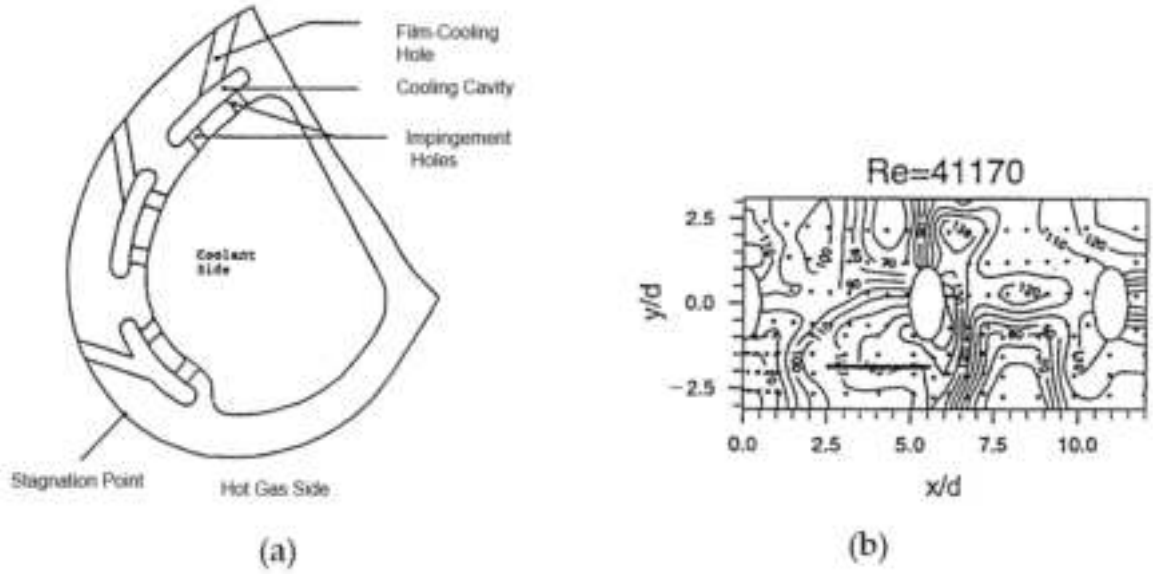

Figure 16. An impingement-cooled leading edge of a CastCool®: (**a**) Turbine blade with the integrally cast passage; (**b**) Nusselt number distribution on the target surface [99].

Figure 17. Wafer vane cooling configuration by ERDA—advanced industrial engines [100].

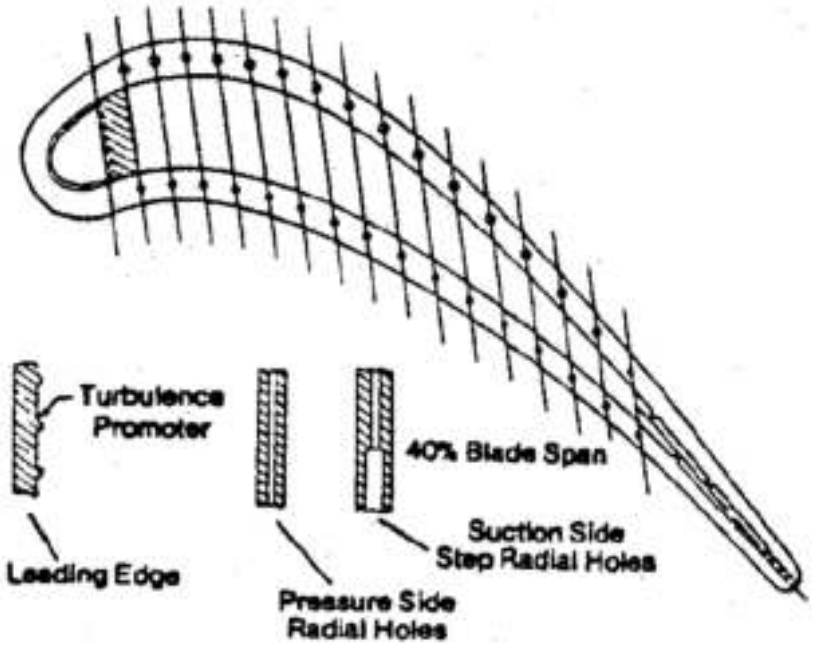

Figure 18. Wafer blade cooling configuration for ERDA advanced industrial engines [100].

The Lamilloy® cooling structure described above is currently used for the combustor walls of jet engines. CastCool® airfoils have not yet been put into operation. Photo-etching and diffusion bonding offer a superior cooling method, which can improve on the shortcomings of modern cooled airfoils, but they have yet to be commercialized due to their high cost. The only commercialized high-pressure turbine blade produced by wafer and diffusion bonding is operated in the F100 fighter jet engine [102].

Based on this, the cooling structure of the blades used in industrial gas turbines in the carbon-neutral era is considered next. Internal cooling alone will not suffice, even if its efficiency can be increased considerably. A dense effusion-cooling array will be needed to protect the material from the hot gas temperature. As mentioned above, industrial gas turbines are required to function as a regulator to stabilize the power supply. To satisfy this function, they must be able to maintain the thermal fatigue life of the blades and discs even under sudden load fluctuations. In order to improve the reliability of the turbine blades in part-load operation, it is necessary to adopt a cooling structure, which does not allow the mainstream to enter the cooling cavity even if the static pressure distribution around the turbine blades changes. This is contrary to the concept of designing at the point

of maximum film-cooling effectiveness (e.g., film-cooling efficiency reaches its maximum around M = 0.5 in the case of circular hole film cooling) by reducing the amount of cooling air. Currently, a design with a certain margin in the back pressure is used to prevent the occurrence of backflow.

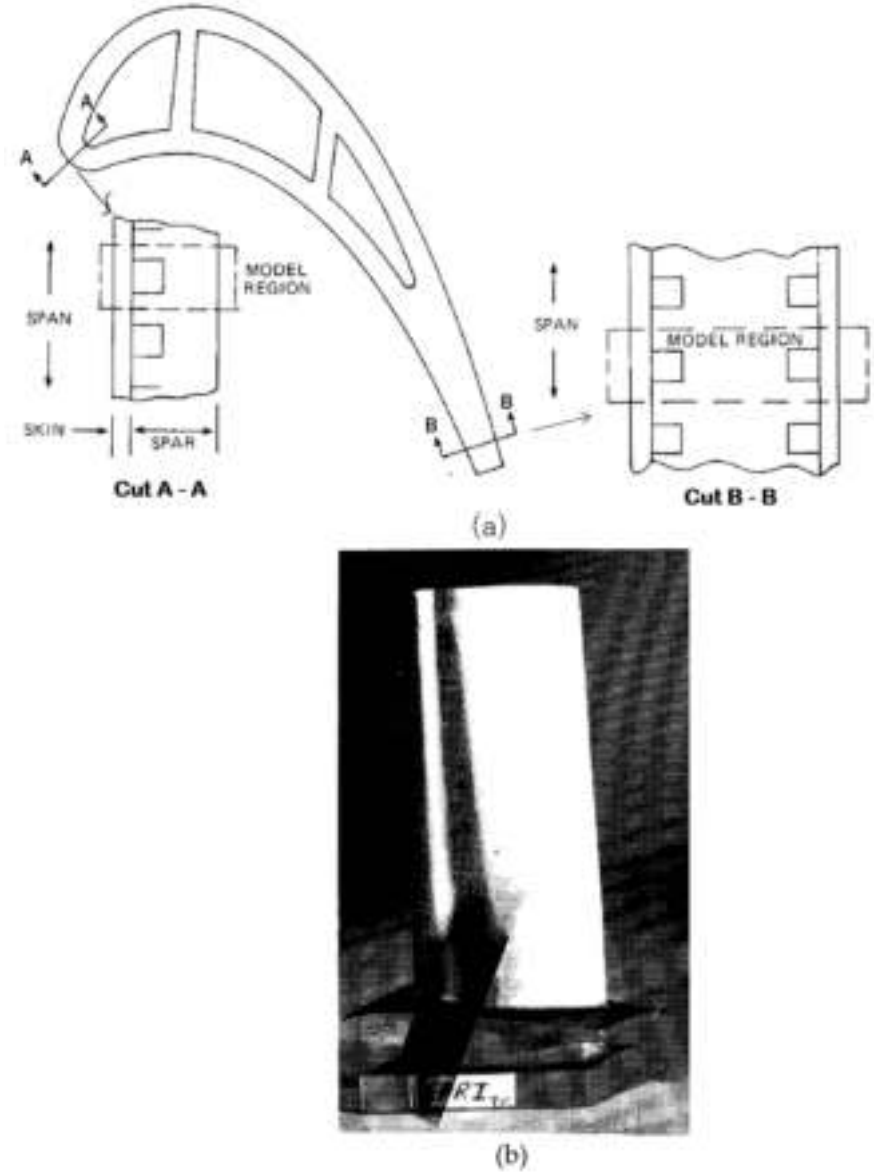

Figure 19. Shell/Spar cooling configuration: (**a**) Cooling configuration; (**b**) Fabrication demonstration blade [101].

Cooled blades have evolved in response to increasing turbine inlet temperatures. The authors have proposed a turbine inlet temperature of 1900~2000 °C and a pressure ratio of 30 for large and a TIT of 1500–1600 °C for small and medium-sized gas turbines. Research and development of airfoils suitable for these gas turbines should be pursued intensively. Ron Bunker has proposed "micro" cooling [103,104] and double-wall cooling [105], shown in Figure 20, as the cooling structures for future airfoils for aviation applications. These structures are an evolution of the Shell/Spar and Lamilloy® airfoils described above.

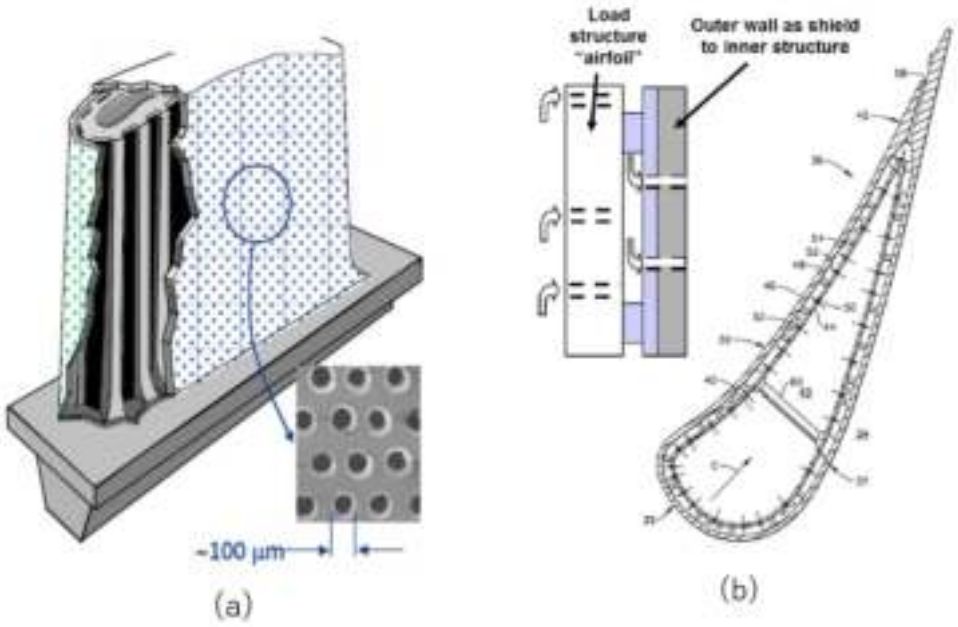

Figure 20. Future of turbine cooling: (**a**) "Micro" cooling [103,104]; (**b**) One example of double wall cooling [105].

The technology to fabricate such complex cooling structures out of metal by additive manufacturing (AM) is under development and is already being used to produce high-temperature components for jet engines. The structures manufactured before using all of the different technologies mentioned above can now be made relatively easily and cost effectively. The airfoils of a large industrial gas turbine are approximately four times larger than those of a jet engine. A solid blade would therefore have 4^3 times the heat capacity. Even for such large airfoils, the temperature difference across the airfoil can be reduced, and the transient response time can be modified to keep the metal temperature along the chord constant during rapid load changes. For this, a structure with low heat capacity but high strength needs to be adopted. The response can be delayed by increasing the thickness in the leading edge, where the heat transfer coefficient on the mainstream side is high. The thickness of the pin-fin section at the trailing edge cannot be increased, and therefore, a tight-lattice (or matrix) cooling structure is considered effective. Matrix cooling was originally developed in the former Soviet Union, and it has been used in some modern industrial gas turbines, e.g., in some of Siemens' Finspong engines and ABB's GT24/26. Some work has been performed on this in other countries as well (e.g., Refs. [106–108]), but difficulties in manufacturing and relatively high pressure losses have led to a limited number of applications, which might change when these structures can be additively manufactured. An added benefit of this cooling technique is its large heat capacity compared to, for example, pin-fin cooling. This means that, when applied to the trailing edge, the thermal inertia of the leading and trailing edges become more alike. Therefore, internal cooling enables the optimum temperature in the extreme points of the airfoil using complex cooling designs, whereas film cooling keeps the overall level of the structure at an acceptable level.

The manufacturing of turbine vanes and blades with a simple cooling structure using the AM method has already begun. Many studies have been conducted to evaluate the heat transfer characteristics of AM cooling geometries. The current cooling structures that can be produced by AM cannot meet the desired dimensional accuracy or surface roughness. However, as more and more components are produced in this way, the method will be improved to a satisfactory level. With "double-wall cooling", the insert and blade wall are integrated into a single geometry.

A first additively manufactured DWC (for a sketch of the principle, see Figure 21a) vane was tested in a large frame gas turbine by Ref. [109]. The design itself and the comparison with the traditionally cast vane and the normal cooling design are shown in Figure 21. The AM vane shows a much more homogeneous surface temperature. This can be mainly attributed to the double-wall cooling design adopted in the AM vane, with the higher number of impingement cavities in addition to the overall extension of film cooling over the entire surface. Each row of film-cooling holes is linked to a dedicated internal cavity, allowing for a better distribution of the feed pressure and overall lower blowing ratios. As a result, a very low thermal stress and a thin wall structure, which is highly resistant to transients, is achieved. This being said, it is important to point out that the gas turbine in question belonged to the F class and therefore had a TIT that probably did not exceed 1400 °C, which is a long way from the envisaged 1900 °C. Nonetheless, the feasibility of the concept can be considered proven in principle.

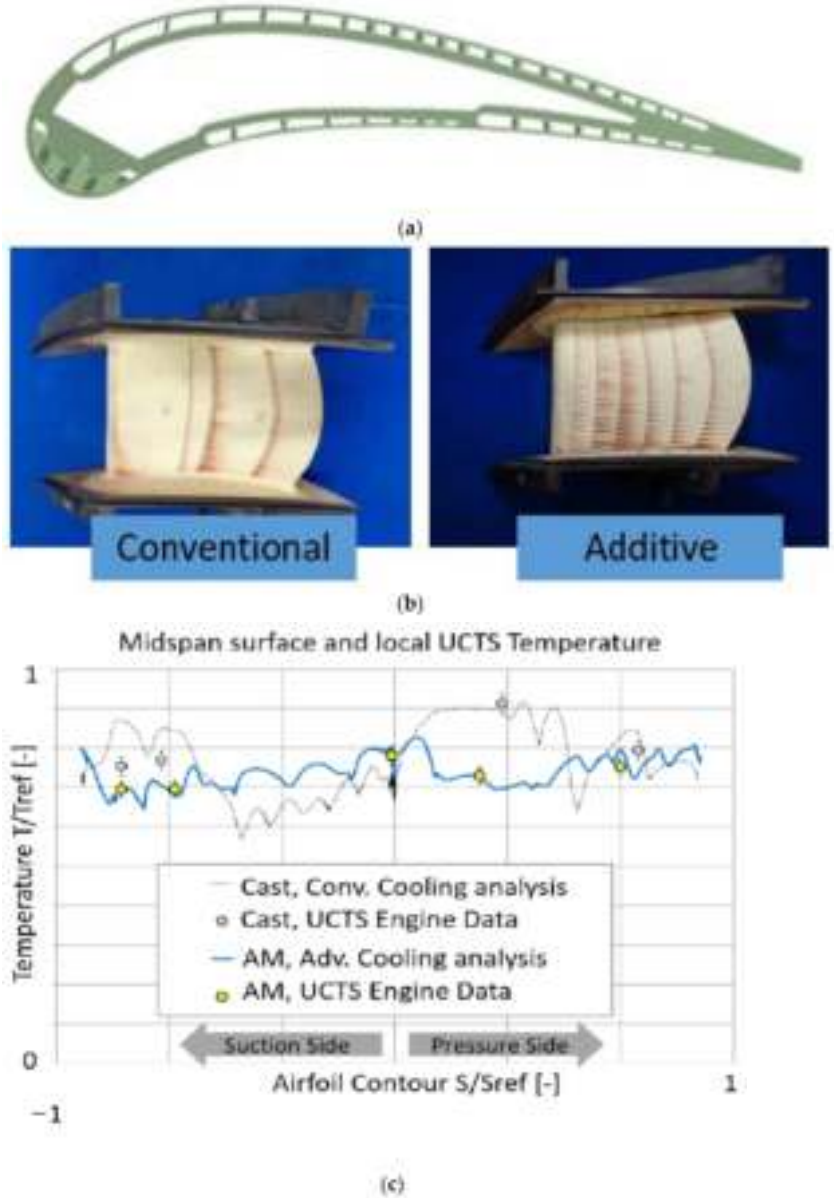

Figure 21. Comparison of cooling effectiveness of F-type gas turbine nozzles [109]: (**a**) F-type 1st nozzle cooling design concept of 3D printed internal cooling design; (**b**) Nozzles manufactured by conventional casting and additive manufacturing; (**c**) Cooling effectiveness distribution results of conventional and additive cooling design.

In the following two sections, research results on the heat transfer characteristics of AM cooling geometries and those of double-wall cooling (not necessarily AM-fabricated specimens) are described.

5. Additive Manufacturing

Additive manufacturing (AM) has been hailed as a game changer in the design of cooling geometries [105] because it will shift the paradigm from design for manufacturing to design for function. The reality is that there are severe restrictions on the geometries, which can be printed; the height of the layers printed is currently typically 0.6 mm (although 0.3 mm is possible). This is being continually reduced, and finer designs will become available in future. A multitude of challenges in the fields of materials' science and manufacturing have precluded the widespread use of the technology in high-temperature applications so far. As the material database is expanded and first long-duration engine trials are conducted, engineers will gain confidence and will expand the array of applications. One significant drawback is that the designers are still caught in old design rules based on design for manufacturing, and humans cannot easily process the complexity a truly innovative design for function would entail. One example of the latter would be a cooling design, which takes account of the stress distribution in a blade. AI/machine learning is not hampered by these restrictions but needs data that offer the required detail, a broader database and, above all, data that are attuned to the possibilities AM has to offer. All of this can be developed on the foundation of the current knowledge of what a good cooling design would be. This may not be the optimal solution at first but can constitute the basis for further development over the next decades. Furthermore, the tools necessary to fully utilize the potential of AM—for example, design tools for hollow, cellular structures instead of solid structures—are still under development. Since the demand from the industry at large, i.e., not only turbomachinery manufacturers, is significant, substantial advances can be expected here as well. Above all, currently, the costs of AM high-temperature components are in the same order of magnitude as those of their cast equivalents when the necessary heat treatment and machining are taken into account. The costs (especially of the printing hardware) will come down gradually but continuously over the next years, making AM components more cost competitive. This, in combination with the superior cooling characteristics it enables, will certainly lead to the breakthrough of this technology in the foreseeable future.

In the following sections, a brief overview of the state of the art of additive manufacturing will be given. This will show the current areas of research, which are concerned with the technology per se and its application in some cooling techniques; it excludes all topics pertaining to machine learning, since this would be a completely different and extensive field altogether.

As mentioned before, the size of the components in small and, to some extent, medium-sized gas turbines also limits the possibilities for a cost-effective and simultaneously innovative cooling design using today's commercial manufacturing techniques. Currently, the TIT of large frame turbines may exceed 1600 °C [110], but it rarely exceeds 1300 °C for the smaller industrial gas turbines. As the limit for the large frames is pushed toward 1900 °C, that of the smaller engines will increase to 1600 °C. The short-term development of completely new cooling schemes for these engines is questionable from an economic point of view. Rather, it may be more viable to optimize existing geometries to reduce costs and incrementally increase their cooling effectiveness. This approach entails the manufacturing by AM of components and geometries, which would normally be investment cast or are very close to such a shape. In the mid-term, i.e., in >10 years' time, the designs of aero engines and large frame turbines will be adapted to small and medium-sized ones.

5.1. Materials' Science

The airfoils designed for AM should, of course, have material properties, which will enable the desired lifetime. These properties are a function of the material temperature,

so a better cooling allows worse material properties, but for now, one would err on the side of caution and define that those of AM materials need to be at least equivalent to cast materials. When discussing the materials' science (or even cooling designs), it should be borne in mind that AM is essentially a form of welding, with all the implications this entails for the material selection and structure. Thus, an additively manufactured airfoil is characterized by the fine granular structure of the metal. In other words, it is the diametrical opposite of the directionally solidified or single-crystal airfoils, which were developed to improve the material characteristics some decades ago: SC materials were developed to give the blades and vanes a higher strength in the direction of the highest load. If AM wants to compete with these materials, it has to be considerably more cost effective and give a cooling effectiveness, which is vastly superior to a cast airfoil to compensate for the decrease in strength via the lower temperature. One cautionary note is in place here: one should consider that the material tests, which are being currently conducted, are on solid materials. However, finite-element analyses based on theories of solid mechanics and material strength do not apply to hollow materials, or such materials, which have inherent gradients. Exactly these tests are envisaged for future airfoils.

Currently, additive manufacturing is being used in a series design of low-temperature components [111], and its suitability for high-temperature components is being evaluated [109,112]. The remaining uncertainties for high-temperature components in particular lie with the printing of materials that contain γ'-phases [113], which are traditionally considered non-weldable. In addition, their susceptibility to cracking is well known and highly dependent on the geometry and the processing parameters [114]. In recent years, attention has turned to what one might call the side effects of additive manufacturing: a more or less distinct influence of the AM process on material properties. This is, first of all, the impact of the printing direction. For nickel-based materials, the properties are best when the samples are printed "in plane", i.e., lying on the plate, whereas this cannot be conclusively said for cobalt-based materials. Second, the effects of roughness also influence the material properties of AM components. As was shown by Ref. [115] and can be seen in Figure 22, when the surface remained "as printed", multiple cracks were initiated because of the cyclic load, and these developed along the grain boundaries, resulting in much faster crack growth and shorter LCF life than for polished samples. For the latter, the crack initialization was limited, and the cracks developed at first within the grains, resulting in a much improved LCF life. The implications for AM components with internal cooling features should be clear.

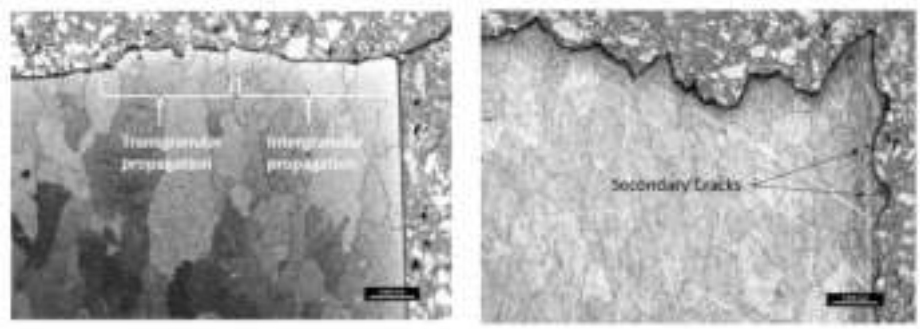

Figure 22. Crack propagation through as-printed and polished AM specimens [115].

A number of materials have been investigated for AM. In general, there is a tendency to move away from cobalt-based alloys (cobalt is an essential component of lithium-ion batteries). Therefore, the majority of the materials have been nickel based. Nonetheless, the vanes used in Ref. [116] were manufactured from MAR M-509 because they were used in direct comparison with cast NGVs, which were also made from this material. Others have investigated IN939 [109], which showed that the material parameters of the AM parts differed dramatically from cast ones or those made of IN738. This last material has received some attention, but its use is still at an experimental stage [117,118]. The main focus has been

firmly on IN718 [113,114,119–122], even though this material does not have the best material properties of the available nickel alloys (but does exhibit a very slow precipitation hardening).

All of these studies used alloy powders, which were either identical in their composition to the alloys used in casting or slightly modified. Recently, completely new alloys have been developed exclusively for AM, e.g., ABD900® [123,124]. In Ref. [124], a creep analysis of ABD900® was performed, and the results were compared with cast IN939 and IN738. As can be seen in Figure 23, in general, ABD900® showed superior values, but an effect of print direction on the results was seen. In addition, the material has a high ductility of approx. 10%, and the creep deformation is about two orders of magnitude higher for transverse than for longitudinal samples. These kinds of materials are the future of AM for high-temperature applications, since they allow for much better weldability, resulting in fewer material defects and better material properties.

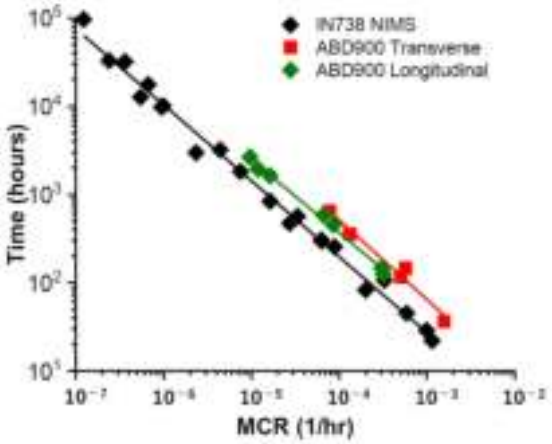

Figure 23. Comparison of creep resistance of different materials including ABD900 with different printing directions [124].

5.2. Impingement Cooling

Additive manufacturing enables the intensification of existing cooling techniques. A major part of the attention is focused on double-wall cooling, as discussed in the next section. However, as mentioned previously, "simple" impingement cooling in an AM blade can also substantially increase the cooling effectiveness and control the temperature profile over the blade height and chord. If the impingement cavity is divided into segments, film cooling can be adjusted to the mainstream pressure profile. This would lead to less structural stress and strain (see also the next section) than DWC with pin fins.

One promising development is the combination of impingement cooling with turbulators. As stated by Ref. [125], roughening or shaping the target wall does not, in general, alter the pressure loss over the impingement system. When using AM, the nozzle and turbulators can be positioned much better and more consistently relative to one another than when combining a cast part and an insert. Two strands of research can be distinguished: one in which the impingement cooling holes are of approximately the same size as the turbulators and one in which the target wall has a "micro-structure", i.e., the turbulators are significantly smaller than the impingement cooling holes. The combination of impingement with turbulators has been investigated in some detail, e.g., Refs. [126–129]. The value given in Ref. [126] for the increase in area-averaged Nusselt number by rib-like features is 15–20%. A good overview of the potential offered by these innovations, especially considering additive manufacturing, is given in Ref. [130]. The authors cover orifice shape, turbulators and crossflow.

The small cubic turbulators in Ref. [128] fall in the micro-structure category. It is shown that even though the heat transfer of the impinging jet decreases (Nu: −6%), the resulting heat flux will be more than compensated by the increase in target area (+48%). The authors of Ref. [131] showed that increasing the height of the cubic micro-structures can increase

the Nusselt number, but the majority of the improvement comes from the introduction of the structures per se (especially for the higher Reynolds numbers). Some publications from Virginia Tech also looked at this kind of turbulators [132,133]. Three different micro-shapes were investigated: cylindrical, cubic and concentric (see Figure 24). These last ones had a superior heat transfer enhancement for all target plate distances tested (the distance of z/d with the highest enhancement). In Ref. [133], some correlations are given.

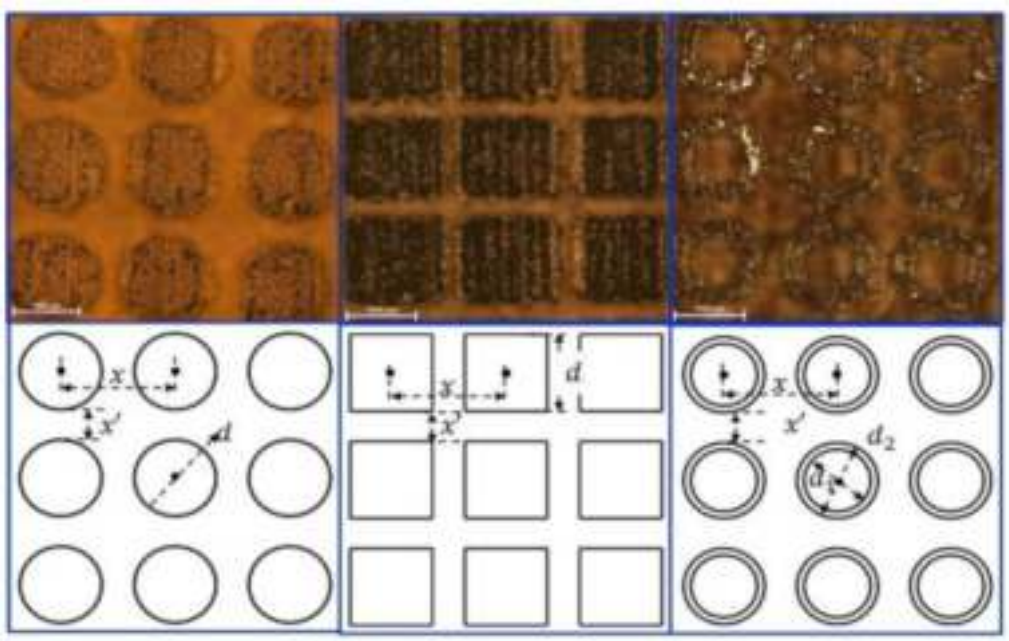

Figure 24. Different micro-roughness shapes on the target plate for impingement cooling, according to Ref. [133].

Takeishi et al. [134] discuss the experimental investigations of several geometrical variations of both circular turbulators and vortex generators (see Figure 25). The turbulators have the highest heat transfer enhancement when they are relatively close to the stagnation point of the impingement cooling. The effectiveness of the vortex generators increases with increasing height, but the investigation was limited to those within or slightly higher than the boundary layer thickness. These showed a very good performance, in line with the results of Ref. [135]. Higher fins extend into the recirculating flow, and this area is thus almost completely ineffective. Radially positioned turbulators were used by Ref. [136] as well. In Ref. [137], the shape of the impingement jets is modified. The holes that had a "V"-shape had the highest heat transfer augmentation but also rather high pressure losses for the coolant. Annerfeldt et al. [127] suggest that shielding the jet from the oncoming crossflow with geometrical features on the target plate may also be beneficial. In Ref. [138], a different approach is chosen, and an AM impingement plate with nozzles is presented. The suggestions from Refs. [136,138] were investigated by Ref. [139]. The combination of dimples with impingement cooling has been suggested, among others, by Ref. [140], but it is not the focal point of current research.

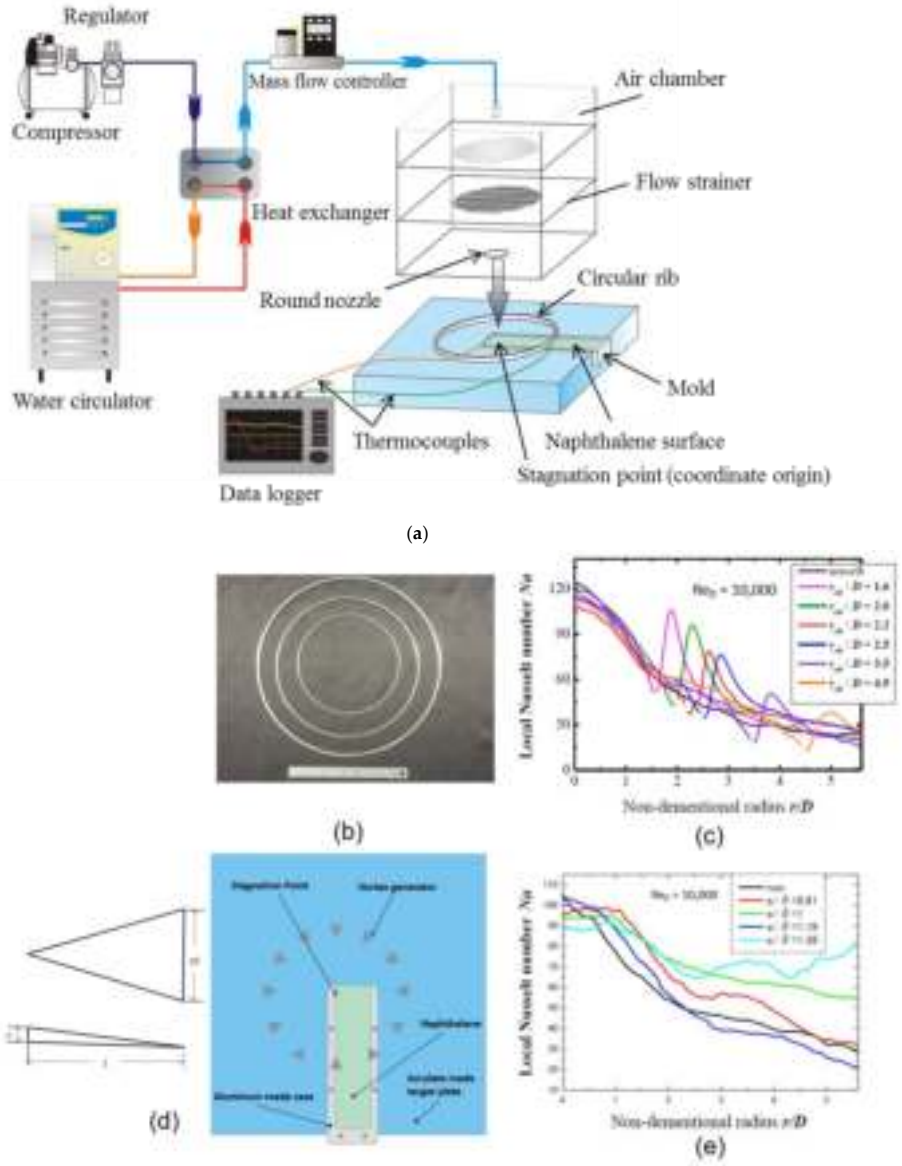

Figure 25. Heat transfer enhancement of impingement cooling using circular ribs and vortex generators [134]: (**a**) Experimental apparatus, (**b**) Circular ribs, (**c**) Nu distribution of circular ribs, (**d**) Vortex generator and layout of VGs on the target plate, (**e**) Nu distribution of VGs.

5.3. Internal Cooling

Internal cooling channels have received a considerable amount of attention because they form an essential part of future blade designs. This does not necessarily imply that serpentine channels will remain as dominant as they are today because (as discussed previously) a combined impingement/film-cooled blade would have a superior temperature profile in the spanwise direction. On the one hand, they will remain relevant in the short to medium term for small gas turbines until the newer designs based on aero engine airfoils are applied in industrial turbines. On the other hand, they may be integrated in more sophisticated designs. In fact, one may argue that they are an essential part of advanced impingement/film-cooling configurations.

As pointed out by Ref. [141], a large potential for optimization exists not only for cooled hot gas path components but also for heat exchangers in general. The authors of Ref. [142] considered the heat exchanger designs of various complexities and concluded that more complex designs do not necessarily lead to a better heat transfer performance, i.e., heat transfer per unit pressure loss. This was, to some extent, corroborated by Ref. [143]

whose authors investigated a void filled with a "lattice structure". Although the intent was to simulate a double-wall cooling geometry, one could imagine integrating such a structure in an internal cooling path as well. The results showed that the more complex structure did increase heat transfer, but it did so at the cost of vastly increased pressure losses. Therefore, the more complex structure had a lower heat transfer performance than the simpler or even traditional geometries. In Refs. [144,145], a traditional serpentine cooling channel was optimized for AM using methods for the prediction of sediment disposal. In the first publication, a turbulated cooling channel was optimized for pressure loss and heat transfer, and Ref. [145] focused on the U-bend. More intricate, V-shaped ribs suitable for AM were investigated in [146].

Moving away from the theoretical considerations into more practical ones, a brief overview of the application of internally cooled AM components in gas turbines is offered. Although the blades would profit most from AM designs (the vanes are already cooled well with impingement cooling), given the concerns about the material properties of AM parts, most work has been done on stationary components [109,116,147–150]. In Ref. [116], additively manufactured NGVs were tested. There were considerable difficulties in printing the very thin insert for the impingement cooling, which points to the limitations with respect to the manufacturability of double-wall cooling designs, which need to be overcome. The test results showed no appreciable difference between the two in terms of surface temperature. In Ref. [147], the showerhead cooling at the leading edge was optimized, taking the possibilities of AM into account. The NGV conceived in Ref. [148] focuses on even more innovative designs, for example, a sweeping-jet cooling. This puts this design more in the realm of large frame gas turbines. In addition, this type of cooling has not been tested in real operation with all the associated vibrations, etc. Therefore, this promising technique will likely only be implemented in the medium to long term. The authors of Refs. [149,150] focused on the casing segment opposite the first-stage blade. They evaluated this from a structural dynamic point of view and showed the impact of including wavy micro-channels in the design. This reduced the average material temperature relative to the baseline design by more than 11%. This points to the practical applicability of the technology.

The authors of Ref. [151] performed a CFD and FE analysis of a design for a non-cooled shrouded AM blade and showed the feasibility of its application. In Refs. [152,153], designs for cooled blades were investigated as well. The former publication investigated a double-wall configuration, matrix cooling and fin cooling for a small gas turbine and gave a first impression on their feasibility. For the latter publication, a number of cooling configurations were conceived as well: impingement, serpentine and double-wall cooling. These were tested under non-rotating conditions, and the double-wall cooling proved to be only slightly better than the conventional ones. The deviations between the prediction and test for the double-wall cooling were non-negligible. This shows that, first, DWC designs are not better by definition and need optimization. Second, this optimization can, for now, not be based on standard CFD because this is validated for and calibrated to conventional cases.

Comparatively little work has been conducted on the additive manufacturing of pin fins. This may be due to the consideration that the size of pin fins is, at least for small gas turbines, in a range where their shape cannot be controlled anymore: their diameter is 1–1.5 mm, while the layer thickness of the AM is approx. 0.6 mm. One investigation [154] showed that the friction losses of AM pin fins far exceeded those of their cast equivalents. This increase is a strong function of the density of the pin-fin array. The heat transfer of AM pin fins increased as well, but not to such an extent that the thermal effectiveness (heat transfer per unit pressure loss) came close to that of cast ones. Other authors [116] did not see any appreciable difference in the temperature within the region with pin fins in additively manufactured and cast NGVs. This may also be attributed to the relative sparsity of the pin-fin array used. One may still envisage more advanced geometries, which have a

higher heat transfer with lower pressure loss, for example, a wavy end wall with inclined pin fins [155,156] (see Figure 26), which cannot be cast but can be additively manufactured.

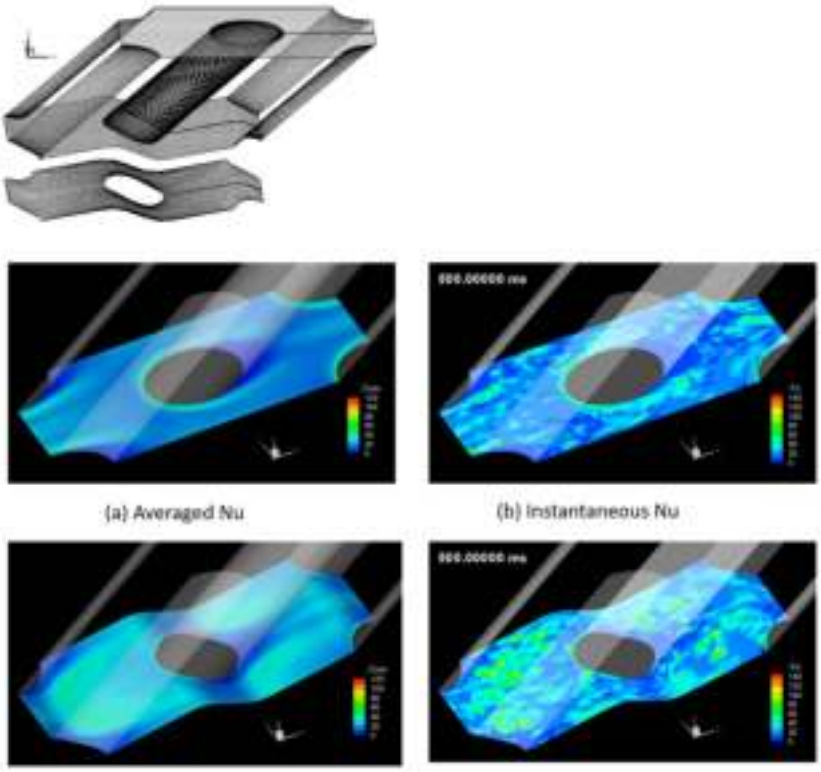

Figure 26. Computational grid and Nusselt number distribution for a pin-fin array with a wavy end wall [155].

In Ref. [157], the hypothesis from Townsend, i.e., that roughness information is not passed on beyond the boundary layer, and therefore, the flow in a channel with walls of different roughness can be simulated using current modeling strategies, is tested. The authors found evidence to support this hypothesis.

5.4. Film Cooling

As the thermal load on turbine airfoils increased, the film-cooling methods applied have been improved, and more efficient film-cooling structures have been developed with less cooling air. Bunker summarizes the historical development of film cooling in Figure 27 (Refs. [104,105]), and the current goal for film-cooling technology applied in DWC is to achieve an overall cooling efficiency of 0.75–0.8.

There is a case to be made that film cooling will become even more important than it is today because of the higher TITs. Therefore, future airfoils will have extensive film or effusion cooling, and it would result in a tremendous cost reduction if the holes could be printed rather than machined.

Effusion cooling can be, somewhat simplified, defined as consisting of a very dense array of small film-cooling holes from which the coolant is ejected at a very low blowing ratio, i.e., M = 0.5 or less. It has been employed primarily in combustion chambers, but its use for airfoils has been contemplated for nearly as long as film cooling itself exists. The growing importance and the low blowing ratios require an accurate modeling strategy.

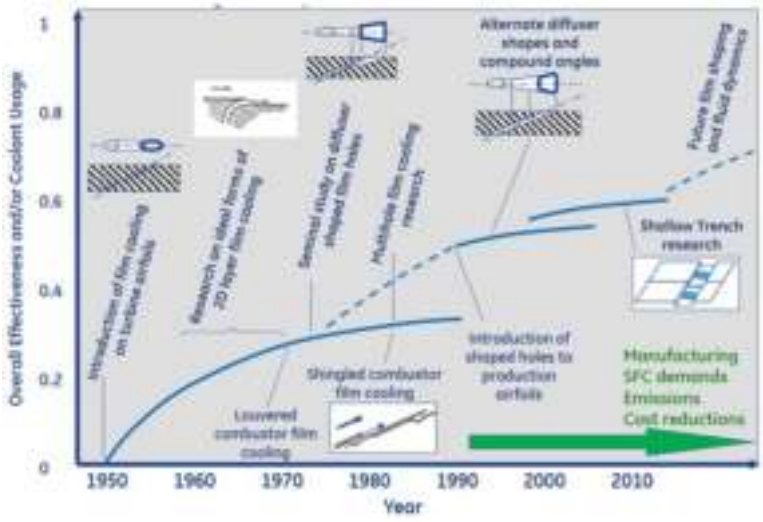

Figure 27. Historical development of film cooling in gas turbines [104,105].

It is not unusual to use Sellers' superposition principle to model film- and effusion-cooling arrays. This method has its deficits, but it works reasonably well on flat plates with a low blowing ratio. Its use for airfoils is disputed, as the flow here shows three-dimensional effects that a simple approach cannot depict. A number of correlations have been developed, but they are typically only valid for the geometry they were developed on. Although CFD is rarely an exact match with experiments, it does a much better job of calculating the heat load on a "random" surface than the two approaches mentioned previously.

Because of the difficulty in meshing large cooling arrays and the computational time this requires, many strategies for modeling effusion cooling as a source term have been developed. Normally, the source terms for mass, momentum, energy and turbulence are required. These can be applied either directly to the wall or as volumetric source terms in the cells of the boundary layer. One overview [158] reported a better prediction of both heat transfer coefficient and film-cooling effectiveness for the volumetric model. The authors of Ref. [159] proposed a source term model in which the in- and outflow were modeled separately and showed good results for low velocity ratios (i.e., attached jets) and low crossflow velocities. The distribution of the sources is often uniform, but Refs. [160,161] presented a set of semi-empirical correlations for the distribution of the source terms over the volume with very good results. Some other approaches have been followed, e.g., Ref. [162] discussed a spectral decomposition of the problem, where the number of simulated holes is reduced, akin to an FFT. Their results were very good, and the approach is especially suitable for very large numbers of holes.

Conjugate simulations are necessary to capture the combined effect of film and internal cooling. In this context, unsteady conjugate simulations, for which pioneering work has been performed by the Osney Laboratory in Oxford [163,164] need to be emphasized. The former proved the possibility of performing unsteady conjugate calculations based on an FFT decomposition of the fluctuating temperature component. Their theoretical considerations show that the mesh near the fluid/solid interface has to be much denser on the solid side than for steady calculations. Their practical calculations showed that not considering the fluctuating component of the flow leads to an over-estimation of the solid temperature, i.e., it is conservative. The authors of Ref. [165] picked up on the issue that the heat flux is not strictly linearly dependent on the difference between the fluid and wall temperatures and suggested a non-linear (basically quadratic) approximation.

The increased use of conjugate methods also triggered some limited interest in designing experiments for validation data, focusing on the Biot number, the ratio of internal to external HTC and bore cooling [165,166].

The rough walls of the cooling holes when using AM were already pointed out, but the inlet to the film-cooling holes is important as well. The latter may not be well defined

when using AM. The inflow into the cooling holes and the flow within the holes themselves need to be modeled properly based on CFD-grade experiments. By the very nature of it, the flow in a hole is difficult to visualize experimentally. The little experimental and ample numerical evidence shows that a separation bubble is formed, which determines the discharge coefficient. Some measurements were recorded, for example by Refs. [167,168] using MRI, and by Ref. [169] using PIV measurement of in-hole flow. The results of Ref. [169] were correlated directly with very high-fidelity LES with very satisfying results.

A good overview of the state of the art of cooling hole manufacturing, which considers the most important commercially available techniques, is given in Ref. [170]. All of these have their drawbacks. Furthermore, one has to bear in mind that manufacturing film-cooling holes in a DWC airfoil will be challenging because, regardless of the manufacturing method (EDM, laser drilling, ...), it will be difficult to avoid contact between the drilling tool and the backwall. This is understood as the impingement wall, pin fins and divider walls. Therefore, additively manufacturing film-cooling holes seems an attractive alternative. However, it should be borne in mind that the diameter of film-cooling holes is in the same order of magnitude as the layer thickness in AM, especially for small and medium-sized gas turbines. This presents its own challenges when it comes to geometrical accuracy and roughness. The holes will tend to approximate a certain geometry (e.g., round), and, if one takes the layer effect into account, the surface roughness will be in the order of magnitude of the hole diameter.

One strand of research investigates the impact of AM on traditional film-cooling holes [171,172]. The former publication looked at holes with a nominal diameter between 1.26 and 2.45 mm. The cooling holes manufactured using EDM had a significantly lower roughness than the AM holes, and small additively manufactured holes, which were positioned at an angle to the build direction, were almost completely blocked. For the holes that were not blocked, the added roughness in the cooling hole contributed significantly to the overall cooling effectiveness because the heat transfer within the cooling hole increased. The study was extended to a variety of different hole shapes [172] where the susceptibility to deviations between design intent and the achieved geometry was confirmed, as was the influence of roughness on the overall results.

Another strand looks into the possible blockage of smaller holes [173–175]. In the first publication, the impact of hole blockage of small (0.4 mm) cooling holes was investigated based on statistics. In Ref. [174] a number of different cooling hole configurations were tested. Exceptionally, the authors not only tested the thermal performance, but they investigated the tensile strength of the perforated structures as well. Perhaps unsurprisingly, the structures with the largest pitch between the holes showed the highest strength. The thermal investigation was expanded to a number of geometries and investigated experimentally in Ref. [176]. As for the large holes, the internal surface area contributed significantly to the overall cooling effectiveness. AM designs, which completely abandoned classical hole design and resembled packed spheres, a wire mesh or one inspired by blood vessels, were particularly good. Therefore, whereas much of the previous studies pointed toward the limitations that need to be overcome and the impact on existing cooling designs, this last study points the way to truly new ways of thinking.

Double-wall cooling implies the use of film cooling, and conventional film cooling may be applied. One possible improvement on this is swirling film cooling [176]. A swirl can be induced using an inclined impingement nozzle, a vortex generator, etc.; if the double-wall structure has one cavity per film-cooling hole, having the "correct" swirl becomes easier. With this swirl, the film-cooling effectiveness has maximum value at low M. With this combination, the blowing ratio can be reduced from M = 1.0 ... 2.0 to as little as M = 0.5.

5.5. Deviations, Tolerances and Roughness

It should be clear from the previous discussions that one of the most important challenges that need to be overcome from a cooling perspective are the deviations from the nominal dimensions of cooling features. In a research environment, more often than

not, scaled-up, ideal geometries are investigated. In real engine manufacturing, tolerances come into play, and these should be taken account of.heat transfer and wall temperature is given in Ref. [177]. These tolerances arise from the manufacturing process (precision casting) on the one hand and the subsequent machining on the other hand. Both the core itself and its positioning relative to the cast have some variability. In addition, the raw parts have to be fixated for machining, which also causes deviations. This is exacerbated by the sometimes opaque relationship between different parameters that determine the deviations and the fact that these may follow a non-Gaussian distribution. Therefore, these need to be quantified [178,179]. Most of this can be eliminated when AM is used because there are much fewer steps involved. From a cooling perspective, the layer thickness of AM needs to be reduced to allow finer features and reduce the roughness in general. However, the roughness is different on different surfaces, depending on their angle of inclination toward the build direction. This should be reduced as well because this angle cannot always be controlled, and it is difficult to account for it in the design process. As we have seen, it also influences the strength of the component.

Some authors [180] have investigated the factors relevant for AM, such as the different models manufactured on different machines, at different positions on the build plate, with different layer thicknesses and at different angles toward the plate. All of these parameters do have an effect, as does the wall thickness (if it is less than 0.6 mm, an effect can be seen; see also Ref. [116]). In summary, the build location has an appreciable impact on roughness; layer thickness, on the other hand, only has an impact on surfaces where a distinct "stair-stepping" effect occurs. Luckily, the machines do not have a large impact.

The issues with internal surface roughness have led to a large number of both experimental and numerical publications on this issue. The former are the center of attention of the researchers at Penn State University, although others are increasingly making contributions [181–188]. Stimpson et al. [187] emphasize the increased surface roughness in AM parts. In Ref. [188], it is shown that any overhanging features, such as turbulators, are bound to deviate from the nominal geometry due to constraints inherent to AM.

The classification and numerical modeling of roughness is an extremely complicated issue with a long tradition [189]. This research forms the basis for investigations in combination with AM. Much has been achieved by Refs. [181,190] who applied the Aupoix model of roughness to both pressure losses [191] and heat transfer [192], as shown in Figure 28, and validated their results with a substantial amount of data from the Penn State group. Others have, for example, applied the distributed element roughness model to these geometries [193], with reasonable results. This will, in the foreseeable future, lead to numerical models, which are attuned to the peculiarities of AM surfaces. This will then also be the basis for detailed CHT models, which take the heightened heat transfer on AM surfaces into account.

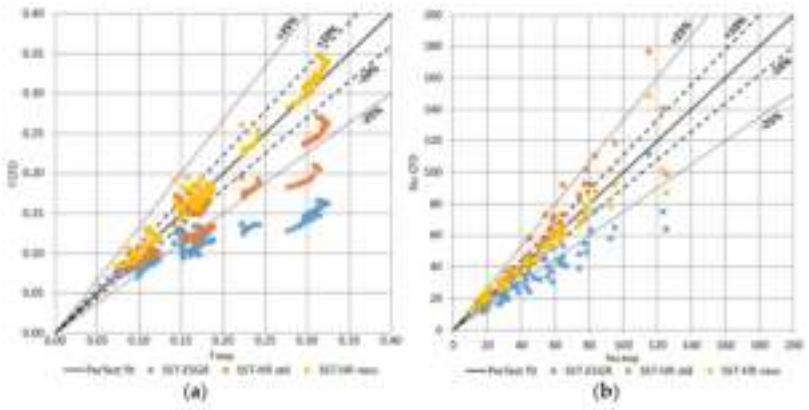

Figure 28. Benchmark on predicted friction factor and Nusselt number [181]: (**a**) Correlation of calculated versus measured friction factors; (**b**) Nusselt numbers of experiments and CFD.

6. Double-Wall Cooling

Innovative cycles, as well as cycles with a higher TIT, need airfoils, which are adapted to the changed boundary conditions. The current state of the art of cooled blades is succinctly summarized in Ref. [194]. It consists of serpentine cooling in the leading edge and mid-chord regions and a pin-fin bank in the trailing edge. This is combined throughout with film cooling.

The number of papers in the public domain dedicated to innovative cooling technologies enabled by additive manufacturing is increasing continuously. The majority of these are concerned with double-wall cooling. This concept is not new as such; it creates a void between an inner and an outer (hot gas path) wall, which means that a combination of impingement, pin fin and film cooling can be applied. Similar concepts were pursued in the 1970s, for example, with Lamilloy® [94]. One of the first sets of papers, which discussed potential new designs adapted to the new hot gas path boundary conditions, were Refs. [195,196], where the authors already discussed the advantages of double-wall cooling relative to the classic serpentine cooling; the wall temperature decreased by up to 100 K.

One group who investigated the precursors of double-wall cooling early on was based at Leeds University. The experimental investigation described in Ref. [197] focused on the optimum number of impingement-cooling holes for a given number of effusion-cooling holes. This was found when the number of holes for both cooling techniques was the same, and there was exactly half-a-pitch distance in both streamwise and lateral direction between the impingement- and effusion-cooling holes. In another excellent experimental investigation, Ref. [198], the same group varied the number and size of the effusion-cooling holes. As long as the effusion-cooling jets were attached to the surface ($M < 0.5$), the number of holes had a limited effect. Once the lift-off occurred, the importance of the impingement cooling increased considerably. The concept was also investigated at Yonsei University. The pattern of impingement- and effusion-cooling holes was optimized both experimentally and numerically in Ref. [199], and the effect of crossflow was quantified in Ref. [200]. The authors noted that the effect of the impingement was severely curtailed when the crossflow ratio rose above 0.5, but this is common for normal impingement cooling as well and should not normally occur in combined impingement/film-cooling (DWC) configurations. The same group suggested introducing fins into the space between the impingement- and effusion-cooling plates to increase the heat transfer [201]. Furthermore, they looked at the effects of rotation on the flow in the gap between the two plates [202], which is, of course, highly relevant for the application of DWC to blades. Investigations of this kind gave rise to a number of patents [203–206] before the possibilities of AM were widely recognized.

The double-wall concept has gained more traction with the advent of AM because these geometries can now be much more easily manufactured. Currently, a significant amount of work is being conducted at the University of Oxford [207–211]. As shown in Ref. [209], modeling effusion cooling with Sellers' superposition methodology is challenging, although it does provide a quick (if not entirely accurate) solution. This becomes relevant when modeling double-wall cooling [210]. In this last paper, the authors investigated several geometries and proposed a varying set-up of double-wall cooling, which is adjusted to the local aerodynamic and thermal boundary conditions in the main flow. It should be emphasized here that the experiments were performed at engine-relevant Reynolds numbers, but the test specimens were scaled by a factor 10. When optimizing the interaction of effusion-cooling jets, the stream- and spanwise distances should be varied independently from one another to achieve the best solution [208]. Modeling these complex geometries with CFD or even CHT is still too computationally expensive. Therefore, the group also provided (experimentally validated) simplified models of double-wall cooling geometries [207,211].

For those industrial gas turbines that employ a system, which cools the cooling air using the water of the bottoming cycle, it may be difficult to raise the temperature of the cooling air sufficiently to achieve the optimum thermodynamic and cooling effectiveness with this combination of impingement cooling and film cooling. In such cases, a cooling

mechanism is necessary to increase the temperature to an appropriate level by using the coolant to reduce the temperature of the inner surface of the blade before impingement cooling. Such a cooling structure, which also serves as a supply passage for the impingement air, can be called triple-wall cooling. In addition, it is necessary to design an optimal structure, which satisfies fatigue life, by means of conjugate analysis of the blade surface, cavity including the impingement nozzle, and the internal cooling and rib structure through steady-state and transient thermal analyses.

The efforts of the group at Yonsei University mentioned before continued with emphasis on additively manufactured geometries [212,213]. Tests and simulations were performed on scaled-up sections, in which the impingement-cooling hole simultaneously functions as a pin fin in a multi-layer system. Because the system consists of three plates and two voids, the distance between these plates is a parameter, which can be varied. The highest heat transfer performance was observed in a system where the "cold-side" void was small, and the "hot-side" void was large [212] (see Figure 29).

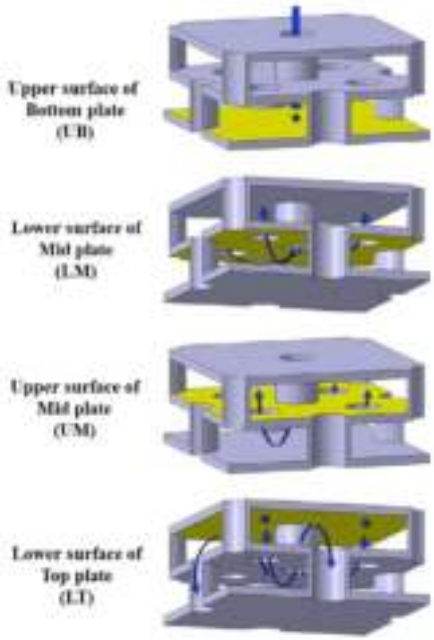

Figure 29. The double-wall cooling configuration conceived by Ref. [213].

An early example of an FE analysis of the effusion wall is Ref. [214]. The creep characteristics of a simulated double-wall specimen were investigated by Ref. [215]. They concluded that the impingement hole and pin-fin distribution were more important for the creep characteristics than the effusion-cooling holes. Elmukashfi et al. [216], on the other hand, investigated the entire system using unit cells (an approach also used for effusion cooling, cf. Ref. [217]) and showed that the area of maximum load changes depending on the relative strength of the various components of the entire system, i.e., impingement, pin fin and effusion cooling. A number of other publications (Refs. [218–222]) also focused on the entire double-wall system applied to a blade. It was shown in Ref. [218] that a significant temperature gradient exists in the double-wall system, which drives thermal stress. The low cycle fatigue of a blade with double-wall cooling is driven by thermal and centrifugal stresses around the cooling holes due to the stress concentration factor, which works here. The same authors discussed the optimization of the resulting stresses in Ref. [219] and recommended spacing the pin fins rather tightly. If the thicknesses of the outer wall increase, the stress here decreases, but it increases in the inner wall. In Ref. [220], the impact of the angle of the cooling hole was evaluated (as a less sharp angle to the outer surface is beneficial). In the last papers of the series (Refs. [221,222]), the authors looked at the convex and concave curvature (see Figure 30) and introduced temperature-dependent

thermo-elastic properties. They point out that the compressive stresses on the pin fins at the hot wall can become exceedingly large, and therefore, a minimum pin-fin diameter is required. In conclusion, the authors suggest a variable ratio of inner and outer wall thicknesses along the chord of the blade.

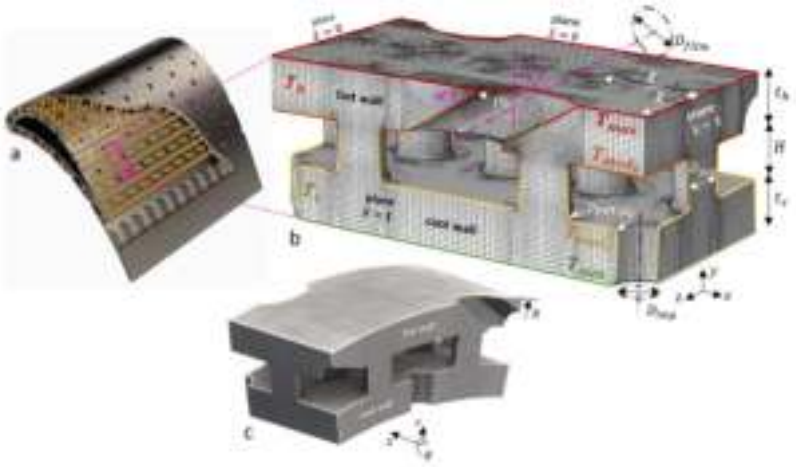

Figure 30. The area considered for the FE analysis in Ref. [221]: (**a**) A typical double wall transpiration cooling (DWTC) system for a gas turbine blade; (**b**) Repeating unit cell for a flat DWTC system; (**c**) Back view of a curved version of the unit cell in (**b**).

For both FEA and the precise calculation of the temperatures of the coolant and cooling effectiveness of the DWC, conjugate analyses on life-sized components with the correct surface structuring will be required.

Other work is concerned with the impingement in narrow channels [223]. Here, it is shown that the optimum configuration depends on, for example, jet diameter and spacing, with smaller diameters having a smaller optimum ratio of D/H. Additionally, as seen before, numerical optimization does not always predict the best configuration in practice, even for these relatively simple geometries. Additively manufacturing such micro-channels enables the generation of an angled connection between the individual channels—something, which is investigated in Ref. [224] and shown in Figure 31. The authors show that this enhances heat transfer considerably.

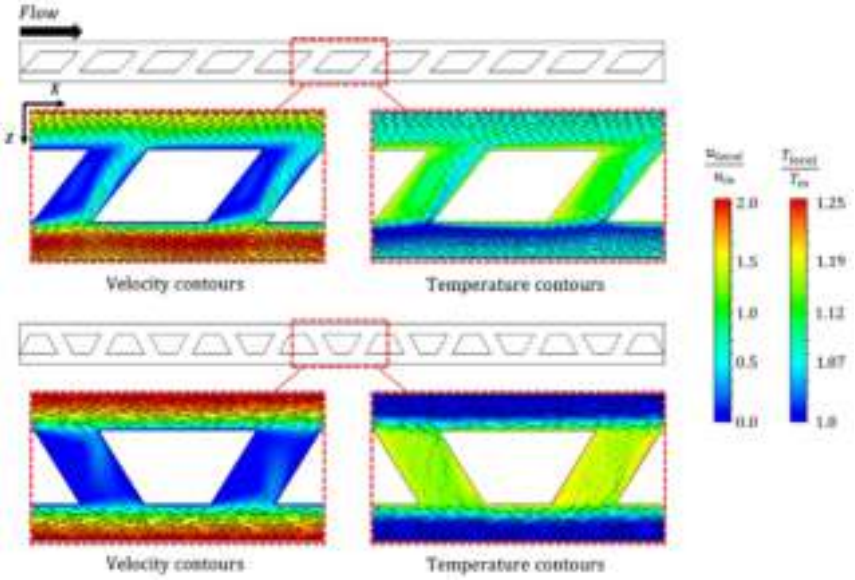

Figure 31. Numerically derived velocity and temperature contours plots along the channel mid-section height in the angled connection between micro-channels [224].

Due to the strong curvature of the walls, the leading edge deserves a separate discussion [131]. The authors of Ref. [225] noted that the pin fins had little influence on the heat transfer on the strongly curved target wall itself, but the heat transfer to the pins depended on their position and size. They suggest that the Lamilloy® structure needs to be optimized for the case at hand. The coolant injection into a 90° section of a cylinder representative of a leading edge was investigated in Ref. [226]. The injection angle had a noticeable impact on the heat transfer.

7. Conclusions

The paper discusses the configurations of airfoils for industrial gas turbines used in the carbon-neutral era. First, the evolution of cooling methods for industrial gas turbines, which have come to play a major role in the society as energy conversion equipment, is surveyed. The research status of cooled airfoils, cast-cooled blades, and wafer and diffusion bonded blades, which have not been commercialized but offer high performance and reliability, was also investigated. Research on new gas-turbine-based cycles, such as the use of carbon-free fuels (hydrogen or ammonia), the clean use of fossil fuels (including coal) in the gas turbine cycle, a method that does not generate NO_x when combustion occurs at high temperatures, and a new gas turbine cycle with easy CCS, was discussed. The research and demonstration tests of new cycles using gas turbines were surveyed. As a result, industrial gas turbines and airfoil cooling configurations suitable for the carbon-neutral era were identified.

Industrial gas turbines will become increasingly important as a source of power generation to stabilize fluctuations. For this reason, gas turbines must be able to handle rapid start-up and load fluctuations and maintain a high performance even under partial load. The need to use carbon-free fuel or CCS will increase the unit cost of power generation. To address this issue, it will be necessary to develop high-performance gas turbines with a TIT from 1900 to 2000 °C and a pressure ratio of 30 for large industrial gas turbines and 1500 to 1600 °C for medium-sized gas turbines. The oxy-fuel cycle, which includes hydrogen as a fuel, could be useful as a countermeasure against the generation of NO_x with hydrogen combustion and as a carbon-free power generation system for fossil fuels, including coal.

When burning hydrogen or ammonia, small and medium-sized industrial gas turbines can be used for fast and flexible operation, both in CHP applications and (perhaps more than now) as SCGT. Introducing AM will reduce the manufacturing costs and simultaneously increase cooling effectiveness, enabling larger load gradients than are currently deemed acceptable.

The preferred cooling structure to be used in future industrial gas turbines described above is double-wall cooling. Various DWC cooling structures have been proposed, and their heat transfer characteristics have been investigated. Among them, the structure combining impingement cooling with film cooling or effusion cooling is considered the best. AM is considered the best solution for fabricating these DWC cooling structures. As was pointed out, three major issues need to be addressed: the availability of appropriate materials and the determination of their high-temperature properties, the control of the AM process as such (layer thickness, surface roughness) and the costs. In order to realize DWC blades fabricated by AM, research including conjugate analysis of the cooling structure and lifetime evaluation through steady-state and transient thermal structure analyses should be conducted.

Author Contributions: Conceptualization, K.T.; writing—original draft preparation, K.T. and R.K.; writing—review and editing, K.T. and R.K. All authors have read and agreed to the published version of the manuscript.

Funding: This research received no external funding.

Conflicts of Interest: The authors declare no conflict of interest.

Nomenclature and Acronyms

D	Impingement-cooling hole diameter
d	film-cooling hole diameter
M	film-cooling hole blowing ratio: $\rho_c u_c / \rho_\infty u_\infty$
Nu	Nusselt number
Re	Reynolds number
u	velocity
x	horizontal (in-plane) axis/direction of flat plate
y	horizontal (in-plane) axis/direction of flat plate
z	vertical (out-of-plane) axis/direction of flat plate
δ	boundary layer thickness
ρ	density
Subscripts	
c	coolant
f	film
∞	mail stream
Abbreviations	
ABB	Asea Brown Boveri
AHAT	humid air turbine
AM	additive manufacturing
APC	announced pledges case
ATS	advanced turbine systems
BBC	Brown, Boveri & Company
CC	conventional casting
CC	combined cycle
CCGT	combined cycle gas turbine
CFD	computational fluid dynamic
CHP	combined heat and power
CCS	carbon capture and storage
CCUS	carbon capture usage and storage
COP	Conference of the Parties
DOE	department of energy
DS	dictionary solidified
DWC	double-wall cooling
DWTC	double wall transpiration cooling
EDM	electric discharge machining
EPRI	Electric Power Research Institute
ERDA	Energy Research and Development Administration
FE	Finite element
FEA	finite element analysis
FFT	Fast Fourier Transform
GE	General Electric Corporation
GHG	greenhouse gas emissions
GT	gas turbine
GTW	gas turbine world
HAT	humid air turbine
HHV	high heating value
HRSG	heat recovery steam generator
HTTT	High Temperature Turbine Technology
IEA	International Energy Agency
IGCC	integrated gasification combined cycle
LCF	low cycle fatigue
LNG	liquid natural gas
LHV	low heating value
MHI	Mitsubishi Heavy Industries, Ltd.
MRI	magnetic resonance imaging

NDC	nationally determined contribution
NGV	nozzle guide vane
OEM	original equipment manufacturing
OFC	oxy-fuel cycle
PIV	particle image velocimetry
PHR	power-to-heat ratio
PW	Pratt and Whitney
SCGT	steam-cooling gas turbine
SLM	selective laser melting
STIG	steam-injected gas turbine
TBC	thermal barrier coating
TIT	turbine inlet temperature
UCTS	uniform crystal temperature sensors
VG	vortex generator
WH	Westinghouse Electric Company

References

1. United Nations Climate Actions. The Paris Agreement. Available online: https://www.un.org/en/climatechange/paris-agreement (accessed on 24 December 2022).
2. United Nations Climate Change. Long-Term Strategies Portal. Available online: https://unfccc.int/process/the-paris-agreement/long-term-strategies (accessed on 24 December 2022).
3. The Government of Japan. The Long-Term Strategy under the Paris Agreement. 2021. Available online: https://unfccc.int/sites/default/files/resource/Japan_LTS2021.pdf (accessed on 9 October 2022).
4. Regulation (EU) 2021/1119 of the European Parliament and of the Council of 30 June 2021 Establishing the Framework for Achieving Climate Neutrality and Amending Regulations (EC) No 401/2009 and (EU) 2018/1999 ('European Climate Law'). Available online: https://eur-lex.europa.eu/legal-content/EN/TXT/?uri=CELEX:32021R1119 (accessed on 24 December 2022).
5. A European Green Deal. Striving to Be the First Climate-Neutral Continent. 2019. Available online: https://commission.europa.eu/strategy-and-policy/priorities-2019-2024/european-green-deal_en (accessed on 24 December 2022).
6. EIB Group Climate Bank Roadmap 2021–2025. 2020. Available online: https://www.eib.org/en/publications/the-eib-group-climate-bank-roadmap (accessed on 24 December 2022).
7. GE's 7 HA and 9 HA Plants Rated at More than 61% CC Efficiency. Available online: https://www.mcilvainecompany.com (accessed on 24 December 2022).
8. Takamura, K.; Iijima, T.; Wakazono, S.; Hada, S.; Yuri, M.; Kataoka, M. Development of 1650 °C Class Next Generation JAC Gas Turbine based on J Experience. *Mitsubishi Heavy Ind. Tech. Rev.* **2019**, *56*, 1–9. Available online: https://www.mhi.co.jp/technology/review/pdf/e563/e563020.pdf (accessed on 11 October 2022).
9. ASME. The World's First Industrial Gas Turbine Set at Neuchâtel (1939), An International Historic Mechanical Engineering Landmark, 2 September 1988, Neuchâtel, Switzerland. Available online: https://www.asme.org/wwwasmeorg/media/resourcefiles/aboutasme/who%20we%20are/engineering%20history/landmarks/135-neuchatel-gas-turbine.pdf (accessed on 24 December 2022).
10. Wettstein, H.E. 80 years open GT development in Baden. In Proceedings of the ASME Turbo Expo 2019, Phoenix, AZ, USA, 17–21 June 2019; Paper No. GT2019-90177. [CrossRef]
11. Meher-Homji, C.B. The Development of the Whittle Turbojet. *ASME J. Eng. Gas Turbines Power* **1998**, *120*, 249–256. [CrossRef]
12. Meher-Homji, C.B.; Prisell, E. Pioneering turbojet developments of Dr. Hans Von Ohain—From the HeS 1 to the HeS 011. *J. Eng. Gas Turbines Power* **2000**, *122*, 191–201. [CrossRef]
13. Horlock, J. *Advanced Gas Turbine Cycles*; Elsevier Science Ltd.: Oxford, UK, 2003, ISBN 0-08-044273-0.
14. Horlock, J. *Combined Power Plants Including Combined Cycle Gas Turbine (CCGT) Plants*; Pergamon Press: Oxford, UK, 1992, ISBN 0-08-040502-9.
15. Horlock, J. Combined Power Plants—Past, Present, and Future. *J. Eng. Gas Turbines Power* **1995**, *117*, 608–616. [CrossRef]
16. Yamakawa, A.; Araki, R.; Saito, I. Design and Construction of Gas-Steam Combined Cycle Plant for Higashi Niigata Thermal Power Station No. 3. In Proceedings of the 1983 Tokyo International Gas Turbine Congress, Tokyo, Japan, 23–29 October 1983; Paper No. IGTC-107.
17. Sudo, Y.; Sato, M.; Kobayashi, Y. Construction and Operation of Gas-Steam Combined Cycle Plant for Higashi Niigata Thermal Power Station No. 3. In Proceedings of the ASME 1986 International Gas Turbine Conference and Exhibit, Dusseldorf, Germany, 8–12 June 1986; Paper No. 86-GT-236. [CrossRef]
18. Gülen, S.C. Étude on gas turbine combined cycle power plant—Next 20 years. *J. Eng. Gas Turbines Power* **2015**, *138*, 051701. [CrossRef]
19. Bergek, A.; Tell, F.; Berggren, C.; Watson, J. Technological capabilities and late shakeouts: Industrial dynamics in the advanced gas turbine industry, 1987–2002. *Ind. Corp. Chang.* **2008**, *17*, 335–392. [CrossRef]
20. Ol'khovskii, G.G.; Radin, Y.A.; Mel'nikov, V.A.; Tuz, N.E.; Mironenko, A.V. Thermal Tests of the 9FB Gas Turbine Unit Produced by General Electric. *Therm. Eng.* **2013**, *60*, 607–612. [CrossRef]

21. Rice, I. The Combined Reheat Gas Turbine/Steam Turbine Cycle: Part I-A Critical Analysis of the Combined Reheat Gas Turbine/Steam Turbine Cycle. *J. Eng. Gas Turbines Power* **1980**, *102*, 35–41. [CrossRef]
22. Rice, I. The Combined Reheat Gas Turbine/Steam Turbine Cycle: Part II-The LM 5000 Gas Generator Applied to the Combined Reheat Gas Turbine/Steam Turbine Cycle. *J. Eng. Gas Turbines Power* **1980**, *102*, 42–49. [CrossRef]
23. Rice, I. The Reheat Gas Turbine with Steam-Blade Cooling- A Means of Increasing Reheat Pressure, Output, and Combined Cycle Efficiency. *J. Eng. Gas Turbines Power* **1982**, *104*, 9–22. [CrossRef]
24. Briesch, M.; Bannister, R.; Diakunchak, I.; Huber, D. A Combined Cycle Designed to Achieve Greater Than 60 Percent Efficiency. *J. Eng. Gas Turbines Power* **1995**, *117*, 734–741. [CrossRef]
25. Pritchard, J. H System^{TM} Technology Update. In Proceedings of the ASME Turbo Expo, Atlanta, GA, USA, 16–19 June 2003; Paper No. GT2003-38711. [CrossRef]
26. Southall, L.; McQuiggan, G. New 200 MW Class 501G Combustion Turbine. *J. Eng. Gas Turbines Power* **1996**, *118*, 572–577. [CrossRef]
27. Horlock, J.; Watson, D.; Jones, T. Limitations on Gas Turbine Performance Imposed by Large Turbine Cooling Flows. *J. Eng. Gas Turbines Power* **2001**, *123*, 487–494. [CrossRef]
28. Takeishi, K.; Komiyama, M.; Oda, Y.; Mori, S.; Kitamura, T. Study on the Thermal and Flow Fields of Shaped Film-Cooling Holes. *Heat Transf. Res.* **2011**, *42*, 83–100. [CrossRef]
29. Vandervort, C. Advancements in H Class Gas Turbines and Combined Cycle Power Plants. In Proceedings of the ASME Turbo Expo, Oslo, Norway, 11–15 June 2018; Paper No: GT2018-76911. [CrossRef]
30. Gülen, S. *Gas Turbine Combined Cycle Power Plants*; CRC Press: Boca Raton, FL, USA, 2019, ISBN 9780429244360. [CrossRef]
31. Takeishi, K. Evolution of Turbine Cooled Vanes and Blades Applied for Large Industrial Gas Turbines and Its Trend Toward Carbon Neutrality. *Energies* **2022**, *15*, 8935. [CrossRef]
32. Otsuki, Y. Development and History and State of the Art of Kawasaki Gas Turbines. In *Selected Topics in Turbomachinery and Jet Propulsion*; Bohn, D., Ed.; RWTH Aachen University: Aachen, Germany, 2004. Available online: https://www.ikdg.rwth-aachen.de/cms/ikdg/Studium/Wintersemester/~olev/Ausgewaehlte-Kapitel-der-Turbomaschinen/?lidx=1 (accessed on 24 December 2022).
33. Hunt, R. *The Development and History of the Gas Turbine for Power Generation, Industrial and Marine Purposes*, 1st ed.; Power + Energy Associates Ltd.: Morpeth, UK, 2019, ISBN 13 9781527239401.
34. Saidi, K.; Orth, U.; Boje, S.; Frekers, C. A Comparative Study of Combined Heat and Power Systems for a Typical Food Industry Application. In Proceedings of the ASME Turbo Expo, Düsseldorf, Germany, 16–20 June 2014; Paper No. GT2014-26234. [CrossRef]
35. Hoops, H.; Saidi, K. A Comparative Study of a Gas Turbine and Gas Engine Regarding Efficiency and Flexibility for Typical Combined Heat and Power Processes. *Gwf Gas Energie* **2017**, *6*, 1–10. Available online: https://www.man-es.com/docs/default-source/energy-storage/orchestrate-heat-and-power/man-es_mgt_technical_paper_preview.pdf?sfvrsn=51cf6dd6_6 (accessed on 11 October 2022).
36. Brun, K.; Kurz, R. *Introduction to Gas Turbine Theory*, 3rd ed.; Solar Turbines Incorporated: San Diego, CA, USA, 2019, ISBN 978-0-578-48386-3.
37. Krewinkel, R. MAN ExpertTalk: Gas Turbine Basics & Applications, Oberhausen. 2021. Available online: https://www.man-es.com/digitalcenter/MAN-ExpertTalk-center/2021/06/23/webinar/gas-turbines{-}{-}basics-applications (accessed on 24 December 2022).
38. Tanaka, R.; Koji, T.; Ryu, M.; Matsuoka, A.; Okuto, A. Development of High Efficient 30MW Class Gas Turbine the Kawasaki L30A. In Proceedings of the ASME Turbo Expo, Copenhagen, Denmark, 11–15 June 2012; Paper No. GT2012-68668. [CrossRef]
39. IEA. Net Zero by 2050: A Roadmap for the Global Energy Sector—A Special Report by the International Energy Agency, International Energy Agency. 2021. Available online: https://iea.blob.core.windows.net/assets/deebef5d-0c34-4539-9d0c-10b13d840027/NetZeroby2050-ARoadmapfortheGlobalEnergySector_CORR.pdf (accessed on 24 December 2022).
40. Cohn, A. Water Cooled Gas Turbine Development Summary. In Proceedings of the Joint Power Generation Conference: GT Papers, Denver, CO, USA, 17–21 October 1982; Paper No. 82-JPGC-GT-5. [CrossRef]
41. Caruvana, A.; Day, W.; Cincotta, G.; Rose, R. System Status of the Water-Cooled Gas Turbine for the High Temperature Turbine Technology Program. In Proceedings of the International Gas Turbine Conference and Exhibit and Solar Energy Conference, San Diego, CA, USA, 12–15 March 1979; Paper No. 79-GT-39. [CrossRef]
42. Plumley, D. Cool Water Coal Gasification—A Progress Report. *J. Eng. Gas Turbines Power* **1985**, *107*, 856–860. [CrossRef]
43. Phillips, J.; Booras, G.; Marasigan, J. The History of Integrated Gasification Combined-Cycle Power Plants. In Proceedings of the ASME Turbo Expo, Charlotte, NC, USA, 26–30 June 2017; Paper No. GT2017-64507. [CrossRef]
44. Asano, A. Case Study: Nakoso IGCC Power Plant Japan. In *Integrated Gasification Combined Cycle (IGCC) Technologies*; Wang, T., Stiegel, G., Eds.; Woodhead Publishing: Kidlington, UK, 2017; pp. 799–816, ISBN 978-0-08-100185-1.
45. Shinada, O.; Yamada, A.; Koyama, Y. The Development of Advanced Energy Technologies in Japan: IGCC—A Key Technology for the 21st Century. *Energy Convers. Manag.* **2002**, *43*, 1221–1233. [CrossRef]
46. Wang, T.; Stiegel, G. *Integrated Gasification Combined Cycle (IGCC) Technologies*; Woodhead Publishing: Kidlington, UK, 2017, ISBN 978-0-08-100185-1.
47. Welch, M.; Pym, A. Improving the Flexibility and Efficiency of Gas Turbine-Based Distributed Power Plant. In Proceedings of the Future of Gas Turbine Technology, 8th International Gas Turbine Conference, Brussels, Belgium, 12–13 October 2016; Paper No.

08-IGTC16. Available online: https://etn.global/wp-content/uploads/2018/09/Improving-the-flexibility-and-efficiency-of-gas-turbine-based-distrivuted-power-plant.pdf (accessed on 10 July 2022).
48. Bhargava, R.; Campanari, S.; Montenegro, G.; Bianchi, M.; De Pascale, A.; Peretto, A. High Efficiency Gas Turbine Based Power Cycles—A Study of the Most Promosing Solutions: Part 1—A Review of the Technology. In Proceedings of the ASME Turbo Expo, Berlin, Germany, 9–13 June 2008; Paper No. GT2008-51275. [CrossRef]
49. Bhargava, R.; Campanari, S.; Montenegro, G.; Bianchi, M.; De Pascale, A.; Peretto, A. High Efficiency Gas Turbine Based Power Cycles—A Study of the Most Promosing Solutions: Part 2—A Parametric Performance Evaluation. In Proceedings of the ASME Turbo Expo, Berlin, Germany, 9–13 June 2008; Paper No. GT2008-51277. [CrossRef]
50. Gülen, S. Gas Turbines Fueled by Green Hydrogen: The Numbers Don't Add Up, Gas Turbine World. 2022. Available online: https://gasturbineworld.com/gas-turbines-burning-green-hydrogen/ (accessed on 24 December 2022).
51. Bossel, U.; Eliasson, B. Energy and the Hydrogen Economy. 2003. Available online: https://afdc.energy.gov/files/pdfs/hyd_economy_bossel_eliasson.pdf (accessed on 12 July 2022).
52. Becker, C.; Marder, M.; Junges, E.; Konrad, O. Technologies for Biogas Desulfurization—An Overview of Recent Studies. *Renew. Sustain. Energy Rev.* **2022**, *159*, 112205. [CrossRef]
53. Newhall, H.; Starkman, E. *Theoretical Performance of Ammonia as a Gas Turbine Fuel*; SAE Technical Papers; SAE International: Warrendale, PA, USA, 1966; Paper No. 660768. [CrossRef]
54. Verkamp, F.; Hardin, M.; Williams, J. Ammonia Combustion Properties and Performance in Gas-Turbine Burners. *Symp. Combust.* **1967**, *11*, 985–992. [CrossRef]
55. Gupta, R. (Ed.) *Hydrogen Fuel—Production, Transport and Storage*; CRC Press: Boca Raton, FL, USA, 2009, ISBN 978-1-4200-4575-8.
56. Chiesa, P.; Lozza, G.; Mazzocchi, L. Using Hydrogen as Gas Turbine Fuel. *J. Eng. Gas Turbines Power* **2005**, *127*, 73–80. [CrossRef]
57. Winkler-Goldstein, R.; Rastetter, A. Power to Gas: The Final Breakthrough for the Hydrogen Economy? *Green* **2013**, *3*, 69–78. [CrossRef]
58. Capurso, T.; Stefanizzi, M.; Torresi, M.; Camporeale, S. Perspective of the Role of Hydrogen in the 21st Century Energy Transition. *Energy Convers. Manag.* **2022**, *251*, 114898. [CrossRef]
59. Aziz, M.; TriWijayanta, A.; Nandiyanto, A. Ammonia as Effective Hydrogen Storage: A Review on Production, Storage and Utilization. *Energies* **2020**, *13*, 3062. [CrossRef]
60. Cesaro, Z.; Ives, M.; Nayak-Luke, R.; Mason, M.; Bañares-Alcántara, R. Ammonia to Power: Forecasting the Levelized Cost of Electricity from Green Ammonia in Large-Scale Power Plants. *Appl. Energy Part A* **2021**, *282*, 116009. [CrossRef]
61. Yapicioglu, A.; Dincer, I. A Review on Clean Ammonia as a Potential Fuel for Power Generators. *Renew. Sustain. Energy Rev.* **2019**, *103*, 96–108. [CrossRef]
62. Valera-Medina, A.; Xiao, H.; Owen-Jones, M.; David, W.; Bowen, P. Ammonia for Power. *Prog. Energy Combust. Sci.* **2018**, *69*, 63–102. [CrossRef]
63. Pilavachi, P.; Stephanidis, S.; Pappas, V.; Afgan, N. Multi-Criteria Evaluation of Hydrogen and Natural Gas Fuelled Power Plant Technologies. *Appl. Therm. Eng.* **2019**, *29*, 2228–2234. [CrossRef]
64. Nose, M.; Nakamura, S.; Kataoka, M.; Kawakami, T.; Kuroki, H.; Yuri, M. Development of Hydrogen/Ammonia Firing Gas Turbine for Decarbonized Society. *Mitsubishi Heavy Ind. Tech. Rev.* **2021**, *3*, 1–11. Available online: https://www.mhi.co.jp/technology/review/pdf/e583/e583030.pdf (accessed on 10 October 2022).
65. Ditaranto, M.; Li, H.; Løvås, T. Concept of Hydrogen Fired Gas Turbine Cycle with Exhaust Gas Recirculation: Assessment of Combustion and Emissions Performance. *Int. J. Greenh. Gas Control* **2015**, *37*, 377–383. [CrossRef]
66. Keller, M.; Koshi, M.; Otomo, H.; Iwasaki, H.; Mitsumori, T.; Yamada, K. Thermodynamic Evaluation of an Ammonia-Fueled Combined-Cycle Gas Turbine Process Operated Under Fuel-Rich Conditions. *Energy* **2020**, *194*, 116894. [CrossRef]
67. Kobayashi, H.; Hayakawa, A.; Somarathne, K.; Okafor, E. Science and Technology of Ammonia Combustion. *Proc. Combust. Inst.* **2019**, *37*, 109–133. [CrossRef]
68. Inoue, K.; Miyamoto, K.; Domen, S.; Tamura, I.; Kawakami, T.; Tanimura, S. Development of Hydrogen and Natural Gas Co-firing Gas Turbine. *Mitsubishi Heavy Ind. Tech. Rev.* **2018**, *53*, 1–6. Available online: https://power.mhi.com/randd/technical-review/pdf/index_66e.pdf (accessed on 4 July 2022).
69. Horikawa, A.; Yamaguchi, M.; Aoki, S.; Fukue, H.; Kusterer, K.; Wirsum, M. 100% Hydrogen Dry Low NO_x Combustor Developments for 2MW Class Gas Turbine and Engine Demonstration Test. *J. Gas Turbine Soc. Jpn.* **2021**, *49*, 1–10. Available online: https://www.gtsj.or.jp/technical/contents/vol49no4-02.pdf (accessed on 21 October 2022). (In Japanese)
70. Ito, S.; Uchida, M.; Suda, T.; Fujimori, T. Development of Ammonia Gas Turbine Co-Generation Technology. *IHI Eng. Rev.* **2020**, *53*, 1–6. Available online: https://www.ihi.co.jp/en/technology/review_library/review_en/2020/_cms_conf01/__icsFiles/afieldfile/2021/01/14/Vol53No1_H.pdf (accessed on 4 July 2022).
71. Ditaranto, M.; Heggset, T.; Berstad, D. Concept of hydrogen fired gas turbine cycle with exhaust gas recirculation: Assessment of process performance. *Energy* **2020**, *192*, 116646. [CrossRef]
72. Zheng, L. (Ed.) *Oxy-Fuel Combustion for Power Generation and Carbon Dioxide (CO_2) Capture*; Woodhead Publishing Limited: Cambridge, UK, 2011, ISBN 978-1-84569-671-9.
73. Stanger, R.; Wall, T.; Spörl, R.; Paneru, M.; Grathwohl, S.; Weidmann, M.; Scheffknecht, G.; McDonald, D.; Myöhänen, K.; Ritvanen, J.; et al. Oxyfuel Combustion for CO_2 Capture in Power Plants. *Int. J. Greenh. Gas Control* **2015**, *40*, 55–125. [CrossRef]

74. Kvamsdal, H.; Jordal, K.; Bolland, O. A Quantitative Comparison of Gas Turbine Cycles with CO_2 Capture. *Energy* **2007**, *32*, 10–24. [CrossRef]
75. Sanz, W.; Jericha, H.; Bauer, B.; Göttlich, E. Qualitative and Quantitative Comparison of Two Promising Oxy-Fuel Power Cycles for CO_2 Capture. *J. Eng. Gas Turbines Power* **2008**, *130*, 031702. [CrossRef]
76. Richards, G.; Casleton, K.; Chorpening, B. CO_2 and H_2O Diluted Oxy-Fuel Combustion for Zero-Emission Power. *Proc. Inst. Mech. Eng. Part A J. Power Energy* **2005**, *219*, 121–126. [CrossRef]
77. Sundkvist, S.; Dahlquist, A.; Janczewski, J.; Sjödin, M.; Bysveen, M.; Ditaranto, M.; Langørgen, O.; Seljeskog, M.; Siljan, M. Concept for a Combustion System in Oxyfuel Gas Turbine Combined Cycles. *J. Eng. Gas Turbines Power* **2014**, *136*, 101513. [CrossRef]
78. Fiaschi, D.; Manfrida, G.; Mathieu, P.; Tempesti, D. Performance of an Oxy-Fuel Combustion CO_2 Power Cycle Including Blade Cooling. *Energy* **2009**, *34*, 2240–2247. [CrossRef]
79. Corchero, G.; Timón, V.; Montañés, J. A Natural Gas Oxy-Fuel Semiclosed Combined Cycle for Zero CO_2 Emissions: A Thermodynamic Optimization. *Proc. Inst. Mech. Eng. Part A J. Power Energy* **2011**, *225*, 377–388. [CrossRef]
80. Amann, J.; Kanniche, M.; Bouallou, C. Natural Gas Combined Cycle Power Plant Modified into an O_2/CO_2 Cycle for CO_2 Capture. *Energy Convers. Manag.* **2009**, *50*, 510–521. [CrossRef]
81. Jericha, H.; Fesharaki, M. The Graz Cycle −1500 °C Max Temperature Potential H_2—O_2 Fired CO_2 Capture with CH_4—O_2 Firing. In Proceedings of the ASME Cogen-Turbo Power Conference, Vienna, Austria, 23–25 August 1995; Paper No. 95-GTP-75. Available online: http://www.graz-cycle.tugraz.at/pdfs/grazcycle_asme_1995.pdf (accessed on 7 October 2022).
82. Sanz, W.; Braun, M.; Jericha, H.; Platzer, M. Adapting the Zero-Emission Graz Cycle for Hydrogen Combustion and Investigation of its Part Load Behaviour. *Int. J. Hydrog. Energy* **2018**, *43*, 5737–5746. [CrossRef]
83. Heitmeir, F.; Sanz, W.; Jericha, H. Graz Cycle—A Zero Emission Power Plant of Highest Efficiency. In *The NETL Gas Turbine Handbook*; Institute for Thermal Turbomachinery and Machine Dynamics, Graz University of Technology: Graz, Austria, 2006; pp. 81–95. Available online: https://netl.doe.gov/sites/default/files/gas-turbine-handbook/1-3-1-1.pdf (accessed on 10 July 2022).
84. Mitterrutzner, B.; Sanz, W.; Nord, L. A Part-Load Analysis and Control Strategies for the Graz Cycle. *Int. J. Greenh. Gas Control* **2022**, *113*, 103521. [CrossRef]
85. Yamashita, S.; Yajima, A.; Yoshimura, K.; Nishimura, M. Exergy Analysis on Oxy-hydrogen Combustion Turbine. *J. Gas Turbine Soc. Jpn.* **2017**, *40*, 170–177. Available online: https://www.gtsj.or.jp/technical/contents/vol45no3-02.pdf (accessed on 7 October 2022). (In Japanese)
86. Rogalev, N.; Rogalev, A.; Kindra, V.; Zlyvko, O.; Bryzgunov, P. Review of Closed SCO_2 and Semi-Closed Oxy-Fuel Combustion Power Cycles for Multi-Scale Power Generation in Terms of Energy, Ecology anf Economic Efficiency. *Energies* **2022**, *15*, 9226. [CrossRef]
87. Macchi, E.; Consonni, S.; Lozza, G.; Chiesa, P. An Assessment of the Thermodynamic Performance of Mixed Gas-Steam Cycles: Part A—Intercooled and Steam-Injected Cycles. *J. Eng. Gas Turbines Power* **1995**, *117*, 489–498. [CrossRef]
88. Chiesa, P.; Lozza, G.; Macchi, E.; Consonni, S. An Assessment of the Thermodynamic Performance of Mixed Gas-Steam Cycles: Part B—Water-Injected and HAT Cycles. *J. Eng. Gas Turbines Power* **1995**, *117*, 499–508. [CrossRef]
89. Rao, A. Evaporative Gas Turbine (EvGT)/Humid Air Turbine (HAT) Cycles. In *Handbook of Clean Energy Systems*; Yan, J., Ed.; Wiley: Hoboken, NJ, USA, 2014. [CrossRef]
90. Mori, Y.; Nakamura, H.; Takahashi, T.; Yamamoto, K. A Highly Efficient Regenerative Gas Turbine System by New Method of Heat Recovery with Water Injection. In Proceedings of the International Gas Turbine Congress and Exhibition, Tokyo, Japan, 23–29 October 1983; Paper No. IGTC-38.
91. Rao, A.; Francuz, V.; Shen, J.; West, E. *A Comparison of Humid Air Turbine (HAT) and Combined-Cycle Power Plants*; IE-7300 Project 2999-7 Final Report; EPRI: Palo Alto, CA, USA, 1991.
92. Hatamiya, S.; Araki, H.; Higuchi, S. An Evaluation of Advanced Humid Air Turbine System with Water Recovery. In Proceedings of the ASME Turbo Expo, Vienna, Austria, 14–17 June 2004; Paper No. GT2004-54031. [CrossRef]
93. Araki, H.; Koganezawa, T.; Myouren, C.; Higuchi, S.; Takahashi, T.; Eta, T. Experimental and Analytical Study on the Operation Characteristics of the AHAT System. *J. Eng. Gas Turbines Power* **2012**, *134*, 051701. [CrossRef]
94. Nealy, D.; Reider, S. Evaluation of Laminated Porous Wall Materials for Combustor Liner Cooling. *J. Eng. Gas Turbines Power* **1980**, *102*, 268–276. [CrossRef]
95. Sweeney, P.; Rhodes, J. An Infrared Technique for Evaluating Turbine Airfoil Cooling Designs. *J. Turbomach.* **2000**, *122*, 170–177. [CrossRef]
96. Essman, D.; Vogel, R.; Tomlinson, J.; Novick, A. TF41/Lamilloy® Accelerated Mission Test. *J. Aircr.* **1983**, *20*, 70–75. [CrossRef]
97. Halsey, J.; Warns, R.; Weisbrod, W. Allison Advanced Turbine Systems (ATS) Engine Cycle. In Proceedings of the ASME Turbo Expo, Orlando, FL, USA, 2–5 June 1997; Paper No. 97-GT-195. [CrossRef]
98. Broomfield, R.; Ford, D.; Bhangu, I.; Thomas, M.; Frasier, D.; Burkholder, P.; Harris, K.; Erickson, G.; Wahl, J. Development and Turbine Engine Performance of Three Advanced Rhenium Containing Superalloys for Single Crystal and Directionally Solidified Blades and Vanes. *J. Eng. Gas Turbines Power* **1998**, *120*, 595–608. [CrossRef]
99. Gillespie, D.; Wang, Z.; Ireland, P.; Kohler, S. Full Surface Local Heat Transfer Coefficient Measurements in a Model of an Integrally Cast Impingement Cooling Geometry. *J. Turbomach.* **1998**, *120*, 92–99. [CrossRef]

100. Sellers, R.; Dahlberg, D.; Calvert, G. New Approaches to Turbine Airfoil Cooling and Manufacturing. In Proceedings of the AIAA/SAE 13th Propulsion Conference, Orlando, FL, USA, 11–13 July 1977; Paper No. 77-948. [CrossRef]
101. George, D.; Brown, B.; Cox, A. The Application of Rapid Solidification Rate Superalloys to Radial Wafer Turbine Blades. In Proceedings of the AIAA/SAE/ASME 15th Joint Propulsion Conference, Las Vegas, NV, USA, 18–20 June 1979; Paper No. 79-1226. [CrossRef]
102. Levari, G.; Sauer, J.; Cohn, A. The Design of an Advanced Cooled First Stage for a Full-Scale Utility Combustion Turbine. In Proceedings of the ASME Turbo Expo, London, UK, 18–22 March 1982; Paper No. 82-GT-207. [CrossRef]
103. Bunker, R. Gas Turbine Heat Transfer: 10 Remaining Hot Gas Path Challenges. In Proceedings of the ASME Turbo Expo, Barcelona, Spain, 8–11 May 2006; Paper No. GT2006-90002. [CrossRef]
104. Bunker, R. Turbine Heat Transfer and Cooling: An Overview. In Proceedings of the ASME Turbo Expo, San Antonio, TX, USA, 3–7 June 2013; Paper No. GT2013-94174.
105. Bunker, R. Evolution of Turbine Cooling. In Proceedings of the ASME Turbo Expo, Charlotte, NC, USA, 26–30 June 2017; Paper No. GT2017-63205. [CrossRef]
106. Oh, I.; Kim, K.; Lee, D.; Park, J.; Cho, H. Local Heat/Mass Transfer and Friction Loss Measurement in a Rotating Matrix Cooling Channel. In Proceedings of the ASME Turbo Expo, Orlando, FL, USA, 8–12 June 2009; Paper No. GT2009-59873. [CrossRef]
107. Tsuru, T.; Ishida, K.; Fujita, J.; Takeishi, K. Three-Dimensional Visualization of Flow Characteristics Using a Magnetic Resonance Imaging (MRI) in a Lattice Cooling Channel. *J. Turbomach.* **2019**, *141*, 061003. [CrossRef]
108. Tsuru, T.; Morozumi, R.; Takeishi, K. Study on Thermofluid Characteristics of a Lattice Cooling Channel. *Int. J. Gas Turbine Propuls. Power Syst.* **2020**, *11*, 1–8. [CrossRef]
109. Torkaman, A.; Vogel, G.; Houck, L. Design, Development and Validation of Additively Manufactured First Stage Turbine Vane for F Class Industrial Gas Turbine. In Proceedings of the ASME Turbo Expo, Virtual, 7–11 June 2021; Paper No. GT2021-60201. [CrossRef]
110. Hada, S.; Yuri, M.; Masada, J.; Ito, E.; Tsukagoshi, K. Evolution and Future Trend of Large Frame Gas Turbines a New 1600 Degree C, J Class Gas Turbine. In Proceedings of the ASME Turbo Expo, Copenhagen, Denmark, 11–15 June 2012; Paper No. GT2012-68574. [CrossRef]
111. Bayar, T. The-3D Printing Future Has Arrived. *Power Eng. Int.* **2016**, *24*, 2–7. Available online: https://www.powerengineeringint.com/coal-fired/equipment-coal-fired/the-3d-printing-future-has-arrived/ (accessed on 22 April 2022).
112. Adair, D.; Kirka, M.; Ryan, D. Additive Manufacturing of Prototype Turbine Blades for Hot-Fired Engine Performance Validation Trials. In Proceedings of the ASME Turbo Expo 2019, Phoenix, AZ, USA, 17–21 June 2019. [CrossRef]
113. Trosch, T.; Strößner, J.; Völkl, R.; Glatzel, U. Microstructure and Mechanical Properties of Selective Laser Melted Inconel 718 Compared to Forging and Casting. *Mater. Lett.* **2016**, *164*, 428–431. [CrossRef]
114. Babu, S.; Raghavan, N.; Raplee, J.; Foster, S.; Frederick, C.; Haines, M.; Dinwiddie, R.; Kirka, M.; Plotkowski, A.; Lee, Y.; et al. Additive Manufacturing of Nickel Superalloys: Opportunities for Innovation and Challenges Related to Qualification. *Metall. Mater. Trans. A* **2018**, *49*, 3764–3780. [CrossRef]
115. Torkaman, A.; Bhattu, R. Low Cycle Fatigue Characterization of Additive Manufactured Specimen with as Printed Surface Roughness Made from Multiple Nickel Based Super Alloy. In Proceedings of the ASME Turbo Expo, Rotterdam, The Netherlands, 13–17 June 2022; Paper No. GT2022-82484. [CrossRef]
116. Krewinkel, R.; Such, A.; Torre, A.; Wiedermann, A.; Castillo, D.; Rodriguez, S.; Schleifenbaum, J.; Blaswich, M. Design and Characterization of Additively Manufactured NGVs Operated in a Small Industrial Gas Turbine. *Int. J. Gas Turbine Propuls. Power Syst.* **2020**, *11*, 36–44. [CrossRef] [PubMed]
117. Risse, J. Additive Manufacturing of Nickel-Base Superalloy IN738LC by Laser Powder Bed Fusion. 2019. Available online: http://publications.rwth-aachen.de/record/764478/files/764478.pdf (accessed on 22 April 2022).
118. Menon, N.; Mahdi, T.; Basak, A. Microstructure of IN738LC Fabricated Using Laser Powder Bed Fusion Additive Manufacturing. *J. Turbomach.* **2022**, *144*, 031011. [CrossRef]
119. Stößner, J.; Terock, M.; Glatzel, U. Mechanical and Microstructural Investigation of Nickel-Based Superalloy IN718 Manufactured by Selective Laser Melting (SLM). *Adv. Eng. Mater.* **2015**, *17*, 1099–1105. [CrossRef]
120. Wang, X.; Keya, T.; Chou, K. Build Height Effect on the Inconel 718 Parts Fabricated by Selective Laser Melting. *Procedia Manuf.* **2016**, *5*, 1006–1017. [CrossRef]
121. Wang, Z.; Guan, K.; Gao, M.; Li, X.; Chen, X.; Zeng, X. The Microstructure and Mechanical Properties of Deposited-IN718 by Selective Laser Melting. *J. Alloys Compd.* **2012**, *513*, 518–523. [CrossRef]
122. Mostafa, A.; Rubio, I.; Brailovski, V.; Jahazi, M.; Medraj, M. Structure, Texture and Phases in 3D Printed IN718 Alloy Subjected to Homogenization and HIP Treatments. *Metals* **2017**, *7*, 196. [CrossRef]
123. Waugh, I.; Moore, E.; Greig, A.; Macfarlane, J.; Dick-Cleland, W. Additive Manufacture of Rocket Engine Combustion Chamber Using the ABD®-900AM Nickel Superalloy. In Proceedings of the 7th Edition of the Space Proplusion Conference, Virtual Conference, 17–19 March 2021. Available online: https://www.researchgate.net/profile/Iain-Waugh/publication/350278621_Additive_manufacture_of_rocket_engine_combustion_chambers_using_the_ABDR-900AM_nickel_superalloy/links/60588a1c299bf173675caf79/Additive-manufacture-of-rocket-engine-combustion-chambers-using-the-ABDR-900AM-nickel-superalloy.pdf (accessed on 22 April 2022).

124. Bridges, A.; Shingledecker, J.; Clark, J.; Crudden, D. Creep Analysis and Microstructural Evaluation of a Novel Additively Manufactured Nickel-Base Superalloy (ABD®-900AM). *J. Eng. Gas Turbines Power* **2023**, *145*, 061005. [CrossRef]
125. Bunker, R.; Dees, J.; Palafox, P. Impingement Cooling in Gas Turbines: Design, Applications, and Limitations. In *Impingement Jet Cooling in Gas Turbines*; Sunden, B., Amano, A., Eds.; WIT Press: Southampton, UK, 2014.
126. Schlünder, E.; Gnielinski, V. Wärme- und Stoffübertragung zwischen Gut und aufprallendem Düsenstrahl. *Chem. Ing. Tech.* **1967**, *39*, 578–584. [CrossRef]
127. Annerfeldt, M.; Persson, J.; Torisson, T. Experimental Investigation of Impingement Cooling with Turbulators or Surface Enlarging Elements. In Proceedings of the ASME Turbo Expo, New Orleans, LA, USA, 4–7 June 2001; Paper No. 2001-GT-0149. [CrossRef]
128. Brakmann, R.; Chen, L.; Weigand, B.; Crawford, M. Experimental and Numerical Heat Transfer Investigation of an Impinging Jet Array on a Target Plate Roughened by Cubic Micro Pin Fins. *J. Turbomach.* **2016**, *138*, 111010. [CrossRef]
129. Oda, Y.; Takeishi, K. Concurrent Large-Eddy Simulation of Wall-Jet Heat Transfer Enhanced by Systematically-Deformed Turbulence Promoter. In Proceedings of the 15th International Heat Transfer Conference IHTC15, Kyoto, Japan, 10–15 August 2014; Paper No. IHTC15-9516. [CrossRef]
130. Dutta, S.; Singh, P. Impingement Heat Transfer Innovations and Enhancements: A Discussion on Selected Geometrical Features. In Proceedings of the ASME Turbo Expo, Virtual, 7–11 June 2021; Paper No. GT2021-59394. [CrossRef]
131. Ren, Z.; Yang, X.; Lu, X.; Li, X.; Ren, J. Experimental Investigation of Micro Cooling Units on Impingement Jet Array Flow Pressure Loss and Heat Transfer Characteristics. *Energies* **2021**, *14*, 4757. [CrossRef]
132. Singh, P.; Zhang, M.; Ahmed, S.; Ekkad, S. Effect of Nozzle-to-Target Spacing on Fin Effectiveness and Convective Heat Transfer Coefficient for Array Jet Impingement onto Novel Micro-Roughness Structures. In Proceedings of the IMECE2018, Pittsburgh, PA, USA, 9–15 November 2018; Paper No. IMECE2018-86501. [CrossRef]
133. Singh, P.; Zhang, M.; Ahmed, S.; Ramakrishnan, K.; Ekkad, S. Effect of Micro-Roughness Shapes on Jet Impingement Heat Transfer and Fin-Effectiveness. *Int. J. Heat Mass Transf.* **2019**, *132*, 80–95. [CrossRef]
134. Takeishi, K.; Krewinkel, R.; Oda, Y.; Ichikawa, Y. Heat Transfer Enhancement of Impingement Cooling by Adopting Circular Ribs or Vortex Generators in the Wall Jet Region of a Round Impingement Jet. *Int. J. Turbomach. Propuls. Power* **2019**, *5*, 17. [CrossRef]
135. Sugimoto, S.; Takeishi, K.; Oda, Y.; Harada, T. A Study on Heat Transfer Enhancement of Jet Impingement Cooling by Turbulence Promotors. In Proceedings of the International Gas Turbine Congress 2007 Tokyo, Tokyo, Japan, 2–7 December 2007; Paper No. TS-116.
136. Domnick, C. Device for Cooling a Component of a Gas Turbine/Turbo Machine by Means of Impingement Cooling. U.S. Patent 11280216, 22 March 2022. Available online: https://patents.google.com/patent/US11280216B2/en (accessed on 24 December 2022).
137. Singh, P.; Ravi, B.; Ekkad, S. Experimental Investigation of Heat Transfer Augmentation by Different Jet Impingement Hole Shapes under Maximum Crossflow. In Proceedings of the ASME Turbo Expo, Seoul, Republic of Korea, 13–17 June 2016; Paper No. GT2016-57874. [CrossRef]
138. Krewinkel, R. Gas Turbine Engine Having a Flow-Conducting Assembly Formed of Nozzles to Direct Cooling Medium Onto a Surface. U.S. Patent 10787927, 29 September 2020. Available online: https://patents.justia.com/patent/10787927 (accessed on 24 December 2022).
139. Yalcikkaya, O.; Durmaz, U.; Tepe, A.; Uysal, U.; Özel, M. Effect of Slot-Shaped Pins on Heat Transfer Performance in the Extended Jet Impingement Cooling. *Int. J. Sci.* **2022**, *179*, 107698. [CrossRef]
140. Khalatov, A.; Nam, C. Aerothermal Vortex Technologies in Aerospace Engineering. *J. Korean Soc. Mar. Eng.* **2004**, *28*, 163–184. Available online: http://www.koreascience.or.kr/article/JAKO200411922191209.page (accessed on 24 December 2022).
141. Zhang, C.; Wang, S.; Li, J.; Zhu, Y.; Peng, T.; Yang, H. Additive Manufacturing of Products with Functional Fluid Channels: A Review. *Addit. Manuf.* **2020**, *36*, 101490. [CrossRef]
142. Alsulami, M.; Mortazavi, M.; Niknam, S.; Li, D. Design Complexity and Performance Analysis in Additively Manufactured Heat Exchangers. *Int. J. Adv. Manuf. Technol.* **2020**, *110*, 865–873. [CrossRef]
143. Parbat, S.; Min, Z.; Yang, L.; Chyu, M.-K. Experimental and Numerical Analysis of Additively Manufactured Inconel 718 Coupons with Lattice Structure. *J. Turbomach.* **2020**, *142*, 061004. [CrossRef]
144. Pietropaoli, M.; Ahlfeld, R.; Montomoli, F.; Ciani, A.; D'Ercole, M. Design for Additive Internal Channel Optimization. *J. Eng. Gas Turbines Power* **2017**, *139*, 102101. [CrossRef]
145. Pietropaoli, M.; Montomoli, F.; Gaymann, A. Three-Dimensional Fluid Topology Optimization for Heat Transfer. *Struct. Multidiscip. Optim.* **2018**, *59*, 801–812. [CrossRef]
146. Chen, I.-L.; Sahin, I.; Wright, L.; Han, J.-C.; Krewinkel, R. Heat Transfer in a Rotating, Two-Pass, Variable Aspect Ratio Cooling Channel with Profiled V-Shaped Ribs. *J. Turbomach.* **2021**, *143*, 081013. [CrossRef]
147. Smith, R.; Dutta, S. Conjugate Thermal Optimization with Unsupervised Machine Learning. *J. Heat Transf.* **2021**, *143*, 052901. [CrossRef]
148. Hossain, M.; Ameri, A.; Gregory, J.; Bons, J. Experimental Investigation of Innovative Cooling Schemes on an Additively Manufactured Engine Scale Turbine Nozzle Guide Vane. *J. Turbomach.* **2021**, *143*, 051004. [CrossRef]
149. Wimmer, T.; Rühmer, T.; Mich, Y.; Wanf, L.; Weigand, B. Experimental and Numerical Investigation on an Additively Manufactured Gas Turbine Ring Segment with an In-Wall Cooling Scheme. In Proceedings of the ASME Turbo Expo, Phoenix, AZ, USA, 17–21 June 2019; p. GT2019-90227. [CrossRef]

150. Rühmer, T.; Wimmer, T.; Gampe, U.; Fischer, K.; Haberland, C. Structural Integrity Assessment and Engine Test of an Additive Manufactured First Stage Ring Segment of a Siemens Large Gas Turbine. In Proceedings of the ASME Turbo Expo, Phoenix, AZ, USA, 17–21 June 2019; p. GT2019-90344. [CrossRef]
151. Pinelli, L.; Amedei, A.; Meli, E.; Vanti, F.; Romani, B.; Benvenuti, G.; Fabbrini, M.; Morganti, N.; Rindi, A.; Arnone, A. Innovative Design, Structural Optimization and Additive Manufacturing of New-Generation Turbine Blades. *J. Turbomach.* **2022**, *144*, 011006. [CrossRef]
152. Magarramova, L.; Kinzburskiy, V.; Vasilyev, B. Novel Designs of Turbine Blades for Additive Manufacturing. In Proceedings of the ASME Turbo Expo, Seoul, Republic of Korea, 13–17 June 2016; Paper No. GT2016-56084. [CrossRef]
153. Straub, D.; Ramesh, S.; Searly, M.; Robey, E.; Floyd, T.; Roy, A.; Ames, F. Frmance of Additively Manufactured Internally Cooled Airfoils for Small Industrial Gas Turbines. In Proceedings of the ASME Turbo Expo, Rotterdam, The Netherlands, 13–17 June 2022; Paper No. GT2022-83333. [CrossRef]
154. Kirsch, K.; Thole, K. Pressure Loss and Heat Transfer Performance for Additively and Conventionally Manufactured Pin Fin Arrays. *Int. J. Heat Mass Transf.* **2017**, *108 Pt B*, 2502–2513. [CrossRef]
155. Takeishi, K.; Oda, Y.; Miyaka, Y.; Motoda, Y. Convective heat Transfer and Pressure Loss in Rectangular Ducts with Inclined Pin-Fin on a Wavy Endwall. *J. Eng. Gas Turbines Power* **2013**, *135*, 061902. [CrossRef]
156. Saglam, S.; Fujitai, J.; Takeishi, K.; Oda, Y. Three-dimensional Velocity Field Measurements of a Rectangular Channel with an Inclined Pin-Fin Array on a Flat and Wavy Endwall Using Magnetic Resonance Velocimetry. In Proceedings of the Asian Congress on Gas Turbines 2018, Morioka, Japan, 22–24 August 2018; Paper No. ACGT2018-TS78.
157. McClain, S.; Hanson, D.; Cinnamon, E.; Snyder, J.; Kunz, R.; Thole, K. Flow in a Simulated Turbine Blade Cooling Channel with Spatially Varying Roughness Caused by Additive Manufacturing Orientation. *J. Turbomach.* **2021**, *143*, 071013. [CrossRef]
158. Mazzei, L.; Andereini, A.; Facchini, B. Assessment of Modelling Strategies for Film Cooling. *Int. J. Numer. Methods Heat Fluid Flow* **2017**, *27*, 1118–1127. [CrossRef]
159. Zhang, Z.; Chen, Z.; Su, X.; Yuan, X. Non-Uniform Source Term Model for Film-Cooling with the Internal Cross Flow. In Proceedings of the ASME Turbo Expo, Virtual, 22–26 June 2020; Paper No. GT2020-14404. [CrossRef]
160. Kamp, T.; Völker, S.; Zehe, F. A Model for Cylindrical Hole Film Cooling: Part I—A Correlation for Jet-Flow with Application to Film Cooling. *J. Turbomach.* **2012**, *134*, 061010. [CrossRef]
161. Kamp, T.; Völker, S. A Model for Cylindrical Hole Film Cooling: Part II—Model Formulation, Implementation and Results. *J. Turbomach.* **2012**, *134*, 061011. [CrossRef]
162. He, L. Block-Spectral Approach to Film-Cooling Modeling. *J. Turbomach.* **2012**, *134*, 021018. [CrossRef]
163. He, L.; Oldfield, M. Unsteady Conjugate Heat Transfer Modelling. *J. Turbomach.* **2011**, *133*, 031022. [CrossRef]
164. Maffulli, R.; He, L. Impact of Wall Temperature on Heat Transfer Coefficient and Aerodynamics for Three-Dimensional Turbine Blade Passage. *J. Therm. Sci. Eng. Appl.* **2017**, *9*, 041002. [CrossRef]
165. Dyson, T.; Winka, J.; Helmer, D. Conjugate Scaling in the Presence of Bore Cooling. In Proceedings of the ASME Turbo Expo, Montreal, Canada, 15–19 June 2015; Paper No. GT2015-43625. [CrossRef]
166. Stewart, W.; Dyson, T. Conjugate Heat Transfer Scaling for Inconel 718. In Proceedings of the ASME Turbo Expo, Charlotte, NC, USA, 26–30 June 2017; Paper No. GT2017-64873. [CrossRef]
167. Issakhanian, E.; Elkins, C.; Eaton, J. In-Hole and Mainflow Velocity Measurements of Low-Momentum Jets in Crossflow Emanating from Short Holes. *Exp. Fluids* **2012**, *53*, 1765–1778. [CrossRef]
168. Milani, P.; Gunady, I.; Ching, D.; Banko, A.; Elkins, C.; Eaton, J. Enriching MRI Mean Flow Data of Inclined Jets in Crossflow with Large Eddy Simulations. *Int. J. Heat Fluid Flow* **2019**, *80*, 108472. [CrossRef]
169. Peterson, S.; Plesniak, M. Short-Hole Jet-in-Crossflow Velocity Field and Its Relationship to Film-Cooling Performance. *Exp. Fluids* **2002**, *33*, 889–898. [CrossRef]
170. Li, Z.; Wei, T.; Guo, Y.; Sealy, M. State-Of-Art, Challenges, and Outlook on Manufacturing of Cooling Holes for Turbine Blades. *Mach. Sci. Technol.* **2015**, *19*, 361–399. [CrossRef]
171. Stimpson, C.; Snyder, J.; Thole, K.; Mongillo, D. Effectiveness Measurements of Additively Manufactured Film Cooling Holes. *J. Turbomach.* **2018**, *140*, 011009. [CrossRef]
172. Snyder, J.; Thole, K. Performance of Public Cooling Geometries Produced Through Additive Manufacturing. *J. Turbomach.* **2020**, *142*, 051009. [CrossRef]
173. Yang, L.; Min, Z.; Parbat, S.; Chyu, M.-K. Effect of Pore Blockage on Transpiration Cooling with Additive Manufacturable Perforate Holes. In Proceedings of the ASME Turbo Expo, Oslo, Norway, 11–15 June 2018; Paper No: GT2018-75310. [CrossRef]
174. Min, Z.; Parbat, S.; Yang, L.; Chyu, M.-K. Thermal-Fluid and Mechanical Investigations of Additively Manufactured Geometries for Transpiration Cooling. In Proceedings of the ASME Turbo Expo, Phoenix, AZ, USA, 17–21 June 2019. [CrossRef]
175. Min, Z.; Huang, G.; Parbat, S.; Yang, L.; Chyu, M.-K. Experimental Investigation on Additively Manufactured Transpiration and Film Cooling Structures. *J. Turbomach.* **2019**, *141*, 031009. [CrossRef]
176. Takeishi, K.; Komiyama, M.; Oda, Y.; Egawa, Y. Aerothermal Investigations on Mixing Flow Field of Film Cooling With Swirling Coolant Flow. *J. Turbomach.* **2014**, *136*, 051001. [CrossRef]
177. Bunker, R. The Effects of Manufacturing Tolerances on Gas Turbine Cooling. *J. Turbomach.* **2009**, *131*, 041018. [CrossRef]
178. Högner, L.; Voigt, M.; Mailach, R.; Meyer, M.; Gerstberger, U. Probabilistic Finite Element Analysis of Cooled High-Pressure Turbine Blades—Part A: Holistic Description of Manufacturing Variability. *J. Turbomach.* **2020**, *142*, 101008. [CrossRef]

179. Högner, L.; Voigt, M.; Mailach, R.; Meyer, M.; Gerstberger, U. Probabilistic Finite Element Analysis of Cooled High-Pressure Turbine Blades—Part B: Probabilistic Analysis. *J. Turbomach.* **2020**, *142*, 101009. [CrossRef]
180. Wildgoose, A.; Thole, K.; Subramanian, R.; Kersting, L.; Kulkarni, A. Impacts of the Additive Manufacturing Process on the Roughness of Engine Scale Vanes and Cooling Channels. *J. Turbomach.* **2023**, *145*, 041013. [CrossRef]
181. Mazzei, L.; Soghe, R.; Bianchini, C. Calibration of a Computational Fluid Dynamics Methodology for the Simulation of Roughness Effects on Friction and Heat Transfer in Additively Maunfactured Components. *J. Turbomach.* **2022**, *144*, 081002. [CrossRef]
182. Wildgoose, A.; Thole, K. Heat Transfer and Pressure Loss of Additively Manufactured Internal Cooling Channels with Various Shapes. *J. Turbomach.* **2023**, *145*, 071011. [CrossRef]
183. Snyder, J.; Stimpson, C.; Thole, K.; Mongillo, D. Build Direction Effects on Microchannel Tolerance and Surface Roughness. *J. Mech. Des.* **2015**, *137*, 111411. [CrossRef]
184. Stimpson, C.; Snyder, J.; Thole, K.; Mongillo, D. Roughness Effects on Flow and Heat Transfer for Additively Manufactured Channels. *J. Turbomach.* **2016**, *138*, 051008. [CrossRef]
185. Kirsch, K.; Thole, K. Heat Transfer and Pressure Loss Measurements in Additively Manufactured Wavy Microchannels. *J. Turbomach.* **2016**, *139*, 011007. [CrossRef]
186. Lüscher, P.; Deflorin, M.; Vogesser, M.; Stuber, M.; Galoul, V.; Ko, M. Internal Heat Transfer Measurement on Metal-Based Additively Manufactured Channels Using a Transient Technique. In Proceedings of the ASME Turbo Expo, Rotterdam, The Netherlands, 13–17 June 2022; Paper No. GT2022-79547. [CrossRef]
187. Stimpson, C.; Snyder, J.; Thole, K.; Mongillo, D. Scaling Roughness Effects on Pressure Loss and Heat Transfer of Additively Manufactured Channels. *J. Turbomach.* **2016**, *139*, 021003. [CrossRef]
188. Ferster, K.; Kirsch, K.; Thole, K. Effects of Geometry and Spacing in Additively Manufactured Microchannel Pin Fin Arrays. *J. Turbomach.* **2018**, *140*, 011007. [CrossRef]
189. Bons, J. A Review of Surface Roughness Effects in Gas Turbines. *J. Turbomach.* **2010**, *132*, 021004. [CrossRef]
190. Mazzei, L.; Soghe, R.; Bianchini, C. Calibration of a CFD Methodology for the Simulation of Additively Manufactured Components Accounting for the Effects of Diameter and Printing Direction on Friction and Heat Transfer. In Proceedings of the ASME Turbo Expo, Rotterdam, The Netherlands, 13–17 June 2022; Paper No. GT2022-82391. [CrossRef]
191. Aupoix, B. Improved Heat Transfer Predictions on Rough Surfaces. *Int. J. Heat Fluid Flow* **2015**, *56*, 160–171. [CrossRef]
192. Aupoix, B. Roughness Corrections for the k–ω Shear Stress Transport Model: Status and Proposals. *J. Fluids Eng.* **2014**, *137*, 021202. [CrossRef]
193. Altland, S.; Yang, X.; Thole, K.; Kunz, R.; McClain, S. Application of a Distributed Element Roughness Model to Additively Manufactured Internal Cooling Channels. In Proceedings of the ASME Turbo Expo, Rotterdam, The Netherlands, 13–17 June 2022; Paper No. GT2022-81218. [CrossRef]
194. Town, J.; Straub, D.; Black, J.; Thole, K.; Shih, T. State-of-the-Art Cooling Technology for a Turbine Rotor Blade. *J. Turbomach.* **2018**, *140*, 071007. [CrossRef]
195. Chyu, M.-K.; Siw, S.; Karainov, V.; Slaughter, W.; Alvin, M. Aerothermal Challenges in Syngas, Hydrogen-Fired, and Oxyfuel Turbines—Part II: Effects of Internal Heat Transfer. *J. Therm. Sci. Eng. Appl.* **2009**, *1*, 011003. [CrossRef]
196. Chyu, M.-K.; Alvin, M. Turbine Airfoil Aerothermal Characteristics in Future Coal–Gas-Based Power Generation Systems. *Heat Transf. Res.* **2010**, *41*, 737–752. [CrossRef]
197. Dabagh, A.; Andrews, G.; Husain, R.; Husain, C.; Nazari, A.; Wu, J. Impingement/Effusion Cooling: The Influence of the Number of Impingement Holes and Pressure Loss on the Heat Transfer Coefficient. *J. Turbomach.* **1990**, *112*, 467–476. [CrossRef]
198. Andrews, G.; Dabagh, A.; Asere, A.; Bazdidi-Therani, F.; Mkpadi, M.; Nazari, A. Impingement/effusion cooling, Heat Transfer and Cooling in Gas Turbines, AGARD-CP-527, 1993; p. 30.1–30.10. Available online: https://www.sto.nato.int/publications/AGARD/Forms/AllItems.aspx?RootFolder=%2Fpublications%2FAGARD%2FAGARD-CP-527&FolderCTID=0x0120D5200078F9E87043356C409A0D30823AFA16F60B00B8BCE98BB37EB24A8258823D6B11F157&View=%7B7E9C814C-056A-4D31-8392-7C6752B2AF2B%7D (accessed on 24 December 2022).
199. Cho, H.; Rhee, D.; Goldstein, R. Effects of Hole Arrangements on Local Heat/Mass Transfer for Impingement/Effusion Cooling with Small Hole Spacing. *J. Turbomach.* **2008**, *130*, 041003. [CrossRef]
200. Rhee, D.; Choi, J.; Cho, J. Flow and Heat (Mass) Transfer Characteristics in an Impingement/Effusion Cooling System with Crossflow. *J. Turbomach.* **2003**, *125*, 74–82. [CrossRef]
201. Hong, S.; Rhee, D.; Cho, H. Effects of Fin Shapes and Arrangements on Heat Transfer for Impingement/Effusion Cooling with Crossflow. *J. Heat Transf.* **2007**, *129*, 1697–1707. [CrossRef]
202. Hong, S.; Cho, H. Effect of Rotation on Heat/Mass Transfer for an Impingement/Effusion Cooling System. *J. Heat Transf.* **2010**, *132*, 114501. [CrossRef]
203. Dailey, G.; Evans, P.; McCall, R. Cooled Aerofoil for a Gas Turbine Engine. Europe Patent EP 1 022 432 B1, 23 March 2005.
204. Lutum, E.; Semmler, K.; Wolfersdorf, J. Cooled Blade for a Gas Turbine. US Patent 2001/0016162 A1, 23 August 2001.
205. Liang, G. Stator Vane with Near Wall Integrated Micro Cooling Channels. US Patent 8,414,263 B1, 9 April 2013.
206. Liang, G. Turbine Airfoil with Multiple Near Wall Compartment Cooling. US Patent 7,556,476 B1, 7 July 2009.
207. Ngetich, G.; Ireland, P.; Murray, A.; Romero, E. A Three-Dimensional Conjugate Approach for Analysing a Double-Walled Effusion-Cooled Turbine Blade. *J. Turbomach.* **2019**, *141*, 011002. [CrossRef]

208. Courtis, M.; Murray, A.; Coulton, B.; Ireland, P.; Mayo, I. Influence of Spanwise and Streamwise Film Hole Spacing on Adiabatic Film Effectiveness for Effusion-Cooled Gas Turbine Blades. *Int. J. Turbomach. Propuls. Power* **2021**, *6*, 37. [CrossRef]
209. Murray, A.; Ireland, P.; Wong, T.; Tang, S.; Rawlinson, A. High Resolution Experimental and Computational Methods for Modelling Multiple Row Effusion Cooling Performance. *Int. J. Turbomach. Propuls. Power* **2018**, *3*, 4. [CrossRef]
210. Murray, A.; Ireland, P.; Romero, E. Experimental and Computational Methods for the Evaluation of Double-Wall, Effusion Cooling Systems. *J. Turbomach.* **2020**, *142*, 111003. [CrossRef]
211. Murray, A.; Ireland, P.; Romero, E. An Experimentally Validated Low-Order Model of the Thermal Response of Double-Wall Effusion Cooling Systems for High-Pressure Turbine Blades. *J. Turbomach.* **2021**, *143*, 111015. [CrossRef]
212. Bang, M.; Kim, S.; Park, H.; Kim, T.; Rhee, D.; Cho, H. Impingement/Effusion Cooling with a Hollow Cylinder Structure for Additive Manufacturing: Effect of Channel Gap Height. *Int. J. Heat Mass Transf.* **2021**, *175*, 121420. [CrossRef]
213. Bang, M.; Kim, S.; Choi, S.; Sohn, H.; Cho, H. Impingement/Effusion Cooling with a Hollow Cylinder Structure for Additive Manufacturing. *Int. J. Heat Mass Transf.* **2020**, *155*, 119786. [CrossRef]
214. Hahn, W.; Urner, G. Verbundvorhaben Schadstoffe in der Luftfahrt: Untersuchungen zur Kühlung von Brennkammerelementen. Forschungsbericht BMFT-20 T 9104t, 1995.
215. Li, L.; Wan, H.; Gao, W.; Tong, F.; Sun, S. Investigation on Creep Characteristics of Nickel-Base Single Crystal Alloy Double Wall Cooling Specimen. In Proceedings of the ASME Turbo Expo, Oslo, Norway, 11–15 June 2018; Paper No: GT2018-76285. [CrossRef]
216. Elmukashfi, E.; Murray, A.; Ireland, P.; Cocks, A. Analysis of the Thermomechanical Stresses in Double-Wall Effusion Cooled Systems. *J. Turbomach.* **2020**, *142*, 051002. [CrossRef]
217. Laschet, G.; Krewinkel, R.; Hul, P.; Bohn, D. Conjugate analysis and Effective Thermal Conductivities of Effusion-Cooled Multilayer Blade Sections. *Int. J. Heat Mass Transf.* **2013**, *57*, 812–821. [CrossRef]
218. Skamniotis, C.; Courtis, M.; Cocks, A. Multiscale Analysis of Thermomechanical Stresses in Double Wall Transpiration Cooling Systems for Gas Turbine Blades. *Int. J. Mech. Sci.* **2021**, *207*, 106657. [CrossRef]
219. Skamniotis, C.; Cocks, A. Minimising Stresses in Double Wall Transpiration Cooled Components for High Temperature Applications. *Int. J. Mech. Sci.* **2021**, *189*, 105983. [CrossRef]
220. Skamniotis, C.; Cocks, A. Designing Against Severe Stresses at Compound Cooling Holes of Double Wall Transpiration Cooled Engine Components. *Aerosp. Sci. Technol.* **2021**, *116*, 106856. [CrossRef]
221. Skamniotis, C.; Cocks, A. Thermal and Centrifugal Stresses in Curved Double Wall Transpiration Cooled Components with Temperature Dependent Thermoelastic Properties. *Int. J. Solids Struct.* **2022**, *234–235*, 111273. [CrossRef]
222. Skamniotis, C.; Cocks, A. 2D and 3D Thermoelastic Phenomena in Double Wall Transpiration Cooling Systems for Gas Turbine Blades and Hypersonic Flight. *Aerosp. Sci. Technol.* **2021**, *113*, 106610. [CrossRef]
223. Stoakes, P.; Ekkad, S. Optimized Impingement Configurations for Double Wall Cooling Applications. In Proceedings of the ASME Turbo Expo, Vancouver, BC, Canada, 6–10 June 2011. [CrossRef]
224. Panse, S.; Ekkad, S. Forced Convection Cooling of Additively Manufactured Single and Double Layer Enhanced Microchannels. *Int. J. Heat Mass Transf.* **2021**, *168*, 120881. [CrossRef]
225. Luo, L.; Zhang, Y.; Wang, C.; Wang, S.; Sunden, B. On the Heat Transfer Characteristics of a Lamilloy Cooling Structure with Curvatures with Different Pin Fin Configurations. *Int. J. Num. Methods Heat Fluid Flow* **2021**, *31*, 1268–1394. [CrossRef]
226. Yu, Z.; Xu, T.; Li, J.; Ma, L.; Xu, T. Comparison of a Series of Double Chamber Model with Various Hole Angles for Enhancing Cooling Effectiveness. *Int. Commun. Heat Mass Transf.* **2013**, *44*, 38–44. [CrossRef]

Disclaimer/Publisher's Note: The statements, opinions and data contained in all publications are solely those of the individual author(s) and contributor(s) and not of MDPI and/or the editor(s). MDPI and/or the editor(s) disclaim responsibility for any injury to people or property resulting from any ideas, methods, instructions or products referred to in the content.

International Journal of
Turbomachinery
Propulsion and Power

MDPI

Review

State of the Art on Two-Phase Non-Miscible Liquid/Gas Flow Transport Analysis in Radial Centrifugal Pumps-Part A: General Considerations on Two-Phase Liquid/Gas Flows in Centrifugal Pumps

Gerard Bois

Arts et Metiers Institute of Technology, University Lille, CNRS, ONERA, Centrale Lille, UMR CNRS 9014-LMFL-Laboratoire de Mécanique des Fluides de Lille-Kampé de Fériet, 59000 Lille, France; gerard.bois@ensam.eu

Abstract: Gas–liquid mixtures are present in numerous industrial applications, such as in the process industry, oil production and transport with natural gas, deep-sea extraction, and irrigation. Any pump may have to carry multiphase flows. However, the present document is related to non-miscible liquid/gas flow transport analysis in centrifugal pumps because which topic can be a more challenging task compared with axial and mixed flow machines due to specific body force and buoyancy actions and large density differences between the phases. The present document first introduces the main usual gas–liquid two-phase definitions and simplifications. A dimensional analysis introduces the main flow variables and parameters that are used for pumps. Basic physical aspects of flow motion in an impeller channel are explained, and a rapid description of two-phase flow patterns in radial flow pumps is described. Finally, a review of simplified empirical and semi-empirical analytical models is proposed with their limitations.

Keywords: two-phase; pumps; dimensional analysis; analytical models

check for updates

Citation: Bois, G. State of the Art on Two-Phase Non-Miscible Liquid/Gas Flow Transport Analysis in Radial Centrifugal Pumps-Part A: General Considerations on Two-Phase Liquid/Gas Flows in Centrifugal Pumps. *Int. J. Turbomach. Propuls. Power* **2023**, *8*, 16. https://doi.org/10.3390/ijtpp8020016

Academic Editors: Tony Arts and Rodolfo Bontempo

Received: 15 December 2022
Revised: 12 April 2023
Accepted: 25 April 2023
Published: 10 May 2023

Copyright: © 2023 by the author. Licensee MDPI, Basel, Switzerland. This article is an open access article distributed under the terms and conditions of the Creative Commons Attribution (CC BY-NC-ND) license (https://creativecommons.org/licenses/by-nc-nd/4.0/).

1. Introduction

The capability of pumps to convey a two-phase mixture depends, in the first place, on whether gas and liquid form a homogenous mixture or to what extent the two phases separate. Fine gas bubbles dispersed in a liquid can be considered as a quasi-homogenous mixture. The bubbles are supposed to be entrained by the liquid flow, but there is some slip between the phases, which may cause additional losses.

However, in a straight channel, pressure gradients in the flow direction are usually moderate, and the pressure field in a rotating impeller strongly influences the phase distribution. A gas bubble always moves in a pressure field to the location of the lowest pressure. Transporting mixtures with high fractions of gas by pumps is a challenging task since gas and liquid tend to separate because of their large density differences. This can be very inefficient or even impossible when phase separation is re-enforced due to intense pressure gradients perpendicular to the main flow direction, such as in centrifugal machines compared with axial ones. Depending on the inlet shape impeller design (e.g., purely two radial blades or 3D blade shapes), different phase velocities occur close to the suction surface region at the impeller inducer part. Because a negative pressure gradient prevails, the bubbles move more quickly than the water. Thus, in the space just after this region, the distributions of the void fraction obtained are higher and uneven. The change in the pressure distribution owing to air admission is also particularly evident in the inlet region of the impeller. These changes bring about an alteration of the whole flow pattern in the impeller and cause a drop in pump performance. With larger gas volume fractions, bubbly flow is no longer possible since small bubbles tend to coalesce to form larger gas

accumulations (as in slug or plug flow in a pipe). When gas accumulates in the pump, the delivery can be disrupted, and the pump becomes "gas-locked".

Liquid droplets that are transported inside a mainstream gas can also be considered a homogeneous mixture but are not considered here.

2. Two-Phase Parameters for Pump Applications

The parameters that are usually used for pumps are listed below. These parameters are deduced from basic two-phase definitions but with several assumptions. All details are given in Appendix A.1.

1. Gas fraction x:

$$x = \dot{m}_G / \left(\dot{m}_G + \dot{m}_L\right), \text{ assuming steady state condition.} \tag{1}$$

2. Void fraction α:

$$\alpha = \frac{Q_G}{Q_G + Q_L}, \text{ assuming steady state condition.} \tag{2}$$

3. Slip ratio between phases S_V:

$$S_V = \frac{V_G}{V_L}$$

$$\text{or } S_V = \frac{W_G}{W_L} \text{ depending on the absolute or relative frame.} \tag{3}$$

4. Mass flux G:

$$G = \left(\dot{m}_G + \dot{m}_L\right) / A \text{ in} \left(\text{kg/s/m}^2\right) \tag{4}$$

5. Homogeneous two-phase density ρ_{tp}:

$$\rho_{tp} = \alpha_V \rho_G + (1 - \alpha_V)\rho_L \tag{5}$$

3. Dimensional Analysis Application in Pumps

When a two-phase gas–liquid mixture is present in any rotating machine, the increase of pressure in the pump Δp_{tp} can be written as a function of several variables listed below:

- A characteristic length of the pump, i.e., the impeller diameter d_{imp};
- The rotational speed n;
- The gas and liquid flow rates, respectively, Q_G and Q_L;
- The gas and liquid densities ρ_G and ρ_L;
- The gas and liquid kinematic viscosities v_G and v_L;
- The surface tension σ;
- The gravitation acceleration.

$$\Delta p_{tp} = F\left(d_{imp}, n, Q_L, Q_G, \rho_L, \rho_G, v_L, v_G, \sigma, g\right) \tag{6}$$

This suggests that inlet pressure and temperature are not considered here, not because they are not important parameters but because their influences are neglected in the present approach. Therefore, cavitation effects are excluded here, although they effectively belong to the two-phase flow category that also affects pump performances but are governed by different physics.

If one takes d_{imp}, n and ρ_L (*) as fundamental variables, it is possible to define eight non-dimensional groups and write:

$$\begin{array}{l}\Delta p_{tp}/\rho_L((nd_{imp})^2) = \\ F'Q_L/(nd_{imp}^3),\ Q_G/(nd_{imp}^3),\ \rho_G,/\rho_L,\ (nd_{imp}^2)/v_L,(nd_{imp}^2)/v_G, \\ n^2 d_{imp}/g, \rho_L n^2 d_{imp}^3/\sigma\end{array} \tag{7}$$

(*) Note that the liquid density appears here instead of the density mixture (that must also be defined). The liquid phase is consequently supposed to be the primary flow that governs the main resulting pressure field in the pump.

- nd_{imp}^2/v_{G^L} is related to the liquid phase Reynolds number. Typical values reach 2×10^6, which means that viscous effects are mostly concentrated inside boundary layers. Viscous effects can be neglected compared with inertia terms.
- nd_{imp}^2/v_G is related to the gas phase Reynolds number, and typical values are close to 1×10^5.
- $\rho_L n^2 d_{imp}^3/\sigma$ is related to the Weber number. Typical values are around 3×10^6. This means that the surface tension effects can be considered negligible compared with liquid inertia effects.
- $\frac{g}{n^2 d_{imp}}$ is related to the ratio between gravitation and centrifugal forces, often represented by the Froude number. The order of magnitude is about 5×10^{-2}. The centrifugal acceleration can be considered the most important one compared with the gravitational one inside the rotating parts of the pump.
- $\frac{\rho_G}{\rho_L}$ is close to 10^{-3}, if an air–water mixture is considered. This suggests that the most important effects on the pressure field are dominated by the liquid phase, as already mentioned. Note that, in some cases, this density ratio may be controlled and may not be neglected.

By taking all the above assumptions and simplifications, one can write:

$$\Delta p_{T,tp}/\rho_L((nd_{imp})^2) = \mathrm{F}''(Q_L/(nd_{imp}^3), \frac{\rho_G}{\rho_L}) \tag{8}$$

For all other terms depending on $\frac{Q_L}{Q_G}$, another variable $\beta = \frac{Q_G}{Q_L}$ is introduced so that:

$$\alpha_V = \frac{Q_G}{Q_G + Q_L} \tag{9}$$

$$\alpha_V\left(1 + \frac{1}{\beta}\right) = \frac{\beta}{1+\beta} \tag{10}$$

Therefore, $\beta = \frac{\alpha_V}{1-\alpha_V}$ and $(1-\alpha_V)(1+\beta) = 1$.
Relation (8) can be written as follow:

$$\Delta p_{T,tp}/\rho_L((nd_{imp})^2) = \mathrm{F}'''((1 + \frac{Q_G}{Q_L}) \times nd_{imp}^3, \alpha_V) \tag{11}$$

or:

$$\Delta p_{T,tp}/\rho_{tp}((nd_{imp})^2) = \mathrm{F}'''((1 + \frac{Q_G}{Q_L}) \times Q_L nd_{imp}^3, \alpha_V) \tag{12}$$

$$\text{with } \rho_{tp} = (1-\alpha)\rho_L + \alpha\rho_G \tag{13}$$

This means that the pressure increase in a pump under two-phase conditions mainly depends on the flow coefficient and the local void fraction.

Note that the local void fraction can change inside the pump, being dependent on the flow coefficient. The separation of the variables that is proposed in this dimensional

analysis is thus questionable. In Section 5.1, the method proposed by Mikielewicz for correlating performance characteristics for pumps under two-phase flows leads to the same identification of these two major parameters.

4. Pumps Two-Phase Performance Representation—Basic Physical Aspects

Investigation on two-phase flows in pumps is often compared with single-phase liquid conditions using the inlet pump void fraction ε instead of the local one α, which is generally not known and is a result of how the flow mixture evolves inside each pump fixed or rotating parts.

The total head coefficient ψ_T and flow coefficient φ are introduced as follows:

$\psi_T = \frac{gH_T}{U_2^2} = F^1(\varphi, \alpha)$, for incompressible flow and iso thermal condition.

or

$$\psi_T = \frac{gH_T}{U_2^2} = F^1(\varphi, \varepsilon) \tag{14}$$

The pump performance curves usually consider the pump as a «black box».

Figure 1 gives an example of such curves. (Data from Gamboa and Prado [1]). The pump head decreases for increasing inlet void fraction values ε. Pump surging corresponds to the beginning of the sharp head decrease, the location of which depends on the liquid flow rate. Gas lock areas are related to constant head values on the left-hand side.

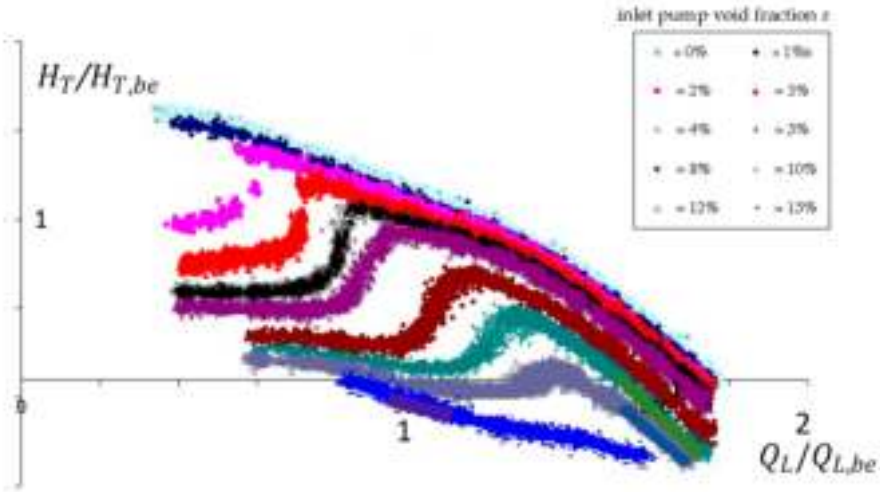

Figure 1. Experimental results of two-phase electric submersible pump (ESP) stage performances at best efficiency (be) point. Non-dimensional head versus liquid flow rate for several inlet void fraction values ε. (Data from Gamboa and Prado [1]).

Depending on the pump design and the operating point, the mean cross-section void fraction α inside the pump is always observed to be higher than the inlet value ε.

The way the liquid flow rate (that is finally delivered by the pump) is changing directly depends on the loss level inside the pump channels, which is also related to the increase in the inlet void fraction. Estevam et al. [2] and Barrios [3] propose the so-called "two-phase mapping" plot (Figure 2) to show how the liquid flow rate can be related to the gas flow rate in association with flow patterns that have been identified by several authors and described in the next section.

4.1. Two-Phase Flow Patterns Inside a Pump

The description and identification of local flow patterns inside a pump are considered using an analogy with what has been observed in horizontal or vertical pipes (Section 5.2), even if the physical phenomena that act on the main flow in pumps are different for pipes (no rotational effects).

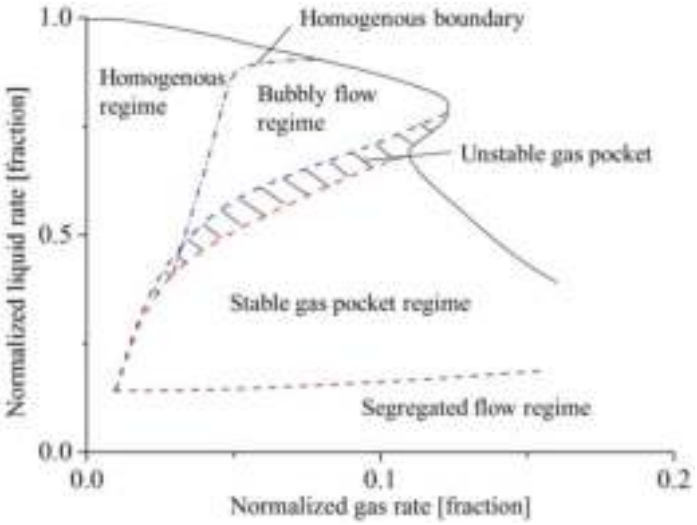

Figure 2. Example of two-phase mapping (Data from Estevam et al. [2] and Barrios [3] for ESP pumps.

Four different flow patterns are detected. Summarized by Verde et al. [4], the schematic representation of each flow pattern is shown in Figure 3 (increasing inlet void fraction from left to right). For small intake void fraction, the flow regime presents tiny and evenly dispersed bubbles inside impeller channels, as shown in Figure 3a. Under this regime, the bubbles are deemed to move together with the liquid phase also inside the impeller (the slippage between gas and liquid is small).

Figure 3. Flow two-phase regime patterns inside the impeller with increasing inlet void fraction (from left to right sides): (**a**) bubbly; (**b**) agglomerate bubbly; (**c**) gas pocket; (**d**) segregated. (Data from Verde et al. [4]).

As the intake void fraction increases, the tiny bubbles are prone to collide and aggregate to form bigger ones. In contrast to the bubbly flow regime, the phase slippage between gas and liquid, corresponding to a bubbly agglomerate regime (shown in Figure 3b), can no longer be neglected. Thus, depending on the intake void fraction, the local void fraction α, under bubbly flow, becomes higher than ε. A further increase in inlet void fraction induces more severe collision and aggregation of bubbles so that large gas pocket forms, including agglomerated bubble flow (Figure 3b), gas pocket flow (Figure 3c) and segregated flow (Figure 3d). The intensity of pump performance degradation is directly influenced by the flow pattern within the impeller. The occurrence of the gas pocket flow pattern is linked to the intensification of the deterioration of pump performance and the appearance of operation instabilities. Moreover, the segregated flow patterns correspond to the most severe performance degradation, which makes the pump incapable of generating pressure.

Each flow pattern can generally be associated with specific modifications of pump performance deterioration in relation to liquid flow rate change. More details can also be found in the review paper by Zhu and Zhang [5].

These deteriorations also depend on pump design, flow rate ratio, rotational speed, and inlet void fraction. Inlet bubble diameter is not considered here. A statistical analysis

based on two-phase experimental results performed on several conventional centrifugal pumps close to design conditions (Jiang et al. [6]) gives approximate estimations of the maximum admissible inlet void fraction for which homogenous assumption remains valid inside the impeller. This is illustrated in Figure 4, where three colored straight lines are shown for small, intermediate, and strong head slopes versus inlet void fraction. The first two slopes correspond to a quasi-homogeneous flow pattern inside the impeller channel. Keeping such a pattern up to an inlet void fraction of 7% is only possible for a few cases (3D twisted impeller inlet shapes and high rotational speeds).

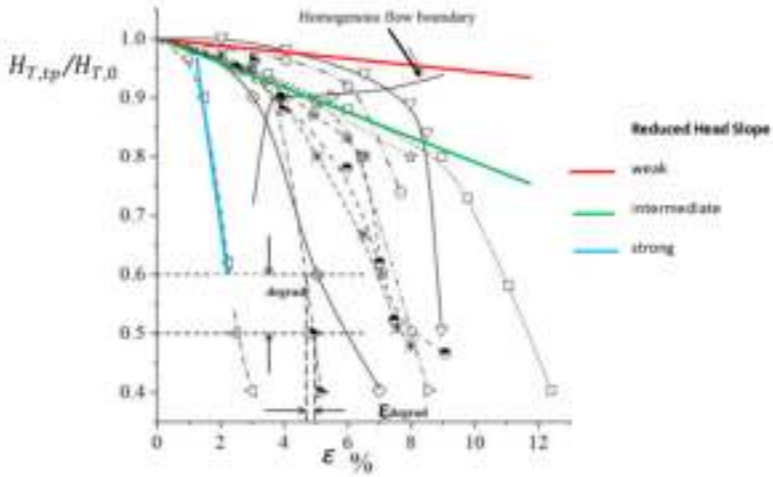

Figure 4. Pump head degradation ratio versus inlet void fraction. Each curve and symbol correspond to individual published results at pump design point from different authors that can be found in Jiang et al. [6].

A head ratio of 50% is reached for a maximum admissible inlet void fraction ε_{degrad} of 11–12% at design conditions, as shown in Figure 4. This can be observed for high rotational speeds (above 2500 rpm) or for large impeller outlet radius R (up to U_2 = 25 m/s). However, for low rotational speeds and 2D blade designs, stronger slope is observed (blue line) corresponding to rapid churn and slug flow patterns inside the impeller or even at the impeller inlet pipe. These cases are only able to pump flow mixtures up to 3 to 5% for the same head degradation level. This is summarized in Figure 5.

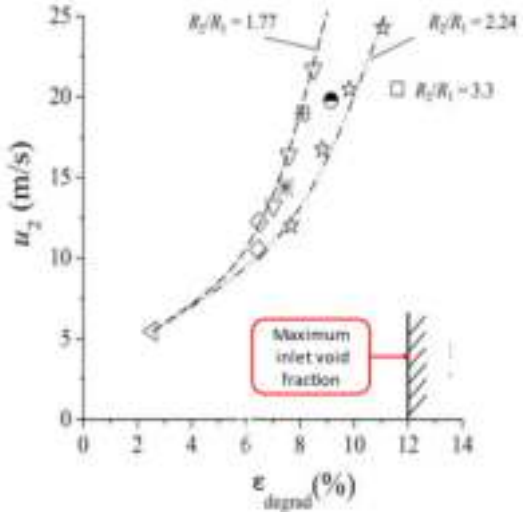

Figure 5. Effects of the impeller outlet rotational speed on the value of $\varepsilon_{\text{degrad.}}$ Each curve and symbol correspond to individual published results at pump design point from different authors that can be found in Jiang et al. [6].

4.2. Analogy with Flow Pattern inside a Tube

The flow pattern observed in Figure 3 is often compared with those found in vertical or horizontal tubes, such as in Figure 6, extracted from Baker [7]. This analogy is purely descriptive, as already pointed out in the previous section. However, such a flow pattern must be detected and well-known at the inlet pipe tube of any pump working under two-phase mixtures, especially when horizontal inlet pipes are used. Depending on the liquid flow rate, the inlet pump flow pattern may not always be a homogeneous bubbly flow regime as frequently supposed or set for inlet boundary conditions.

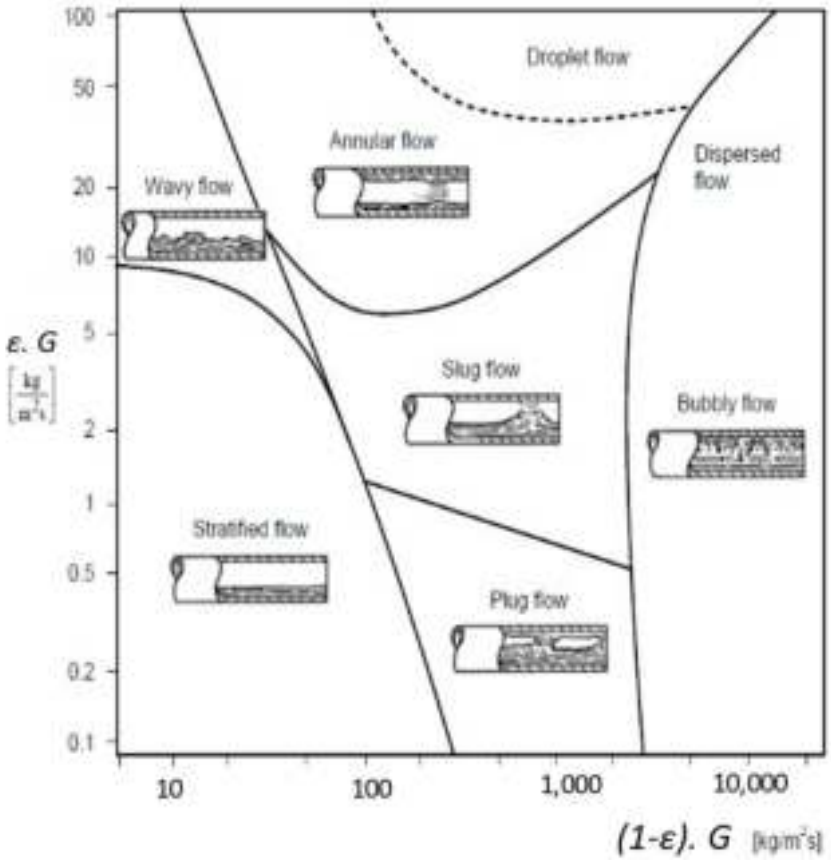

Figure 6. Two-phase flow patterns inside horizontal pipes (Data from Baker [7]).

For a given pump and a given inlet flow coefficient, the flow rate and the head depend on the rotational speed. If, for any purpose, the flow rate becomes lower than the rated one, inlet pipe two-phase flow conditions can jump from a homogeneous bubbly regime to plug or even stratified regimes. Thus, the rotational speed may also have an indirect effect on pump performances due to variable inlet two-phase patterns, as described above. In many experimental results, it is very difficult to distinguish whether the pump performance is affected by non-homogeneous inlet conditions or because of the internal void fraction variation. Shaoa et al. [8] presented an analysis related to this problem, but this is rarely investigated in the open literature.

4.3. Physical Mechanism—Single Phase Conditions

Let us consider the equilibrium of forces acting on a single-phase particle located at point M inside a centrifugal impeller passage. For steady-state conditions, when neglecting shear stresses and momentum exchange between streamlines, the pressure gradient equals the sum of the inertia and centrifugal forces that result from the flow turning plus the centrifugal forces due to both rotation and the Coriolis forces.

This can be expressed on the blade-to-blade plane (see Figure 7) using the streamline coordinates (s, n, b), where s is along the streamline, n is normal to the streamline in the blade-to-blade surface, and b is the binormal perpendicular to s and n:

$$\left(\frac{1}{\rho}\right) \underset{grad}{\rightarrow} p = - \underset{W}{\rightarrow} \left(\frac{\delta W}{\delta_S}\right) \cdot \underset{i_S}{\rightarrow} \pm \left(\frac{W^2}{R_b}\right) \cdot \underset{i_n}{\rightarrow} + \omega^2 \underset{R}{\rightarrow} - 2\omega \underset{W}{\rightarrow} \sin\varphi \cdot \underset{i_n}{\rightarrow} \tag{15}$$

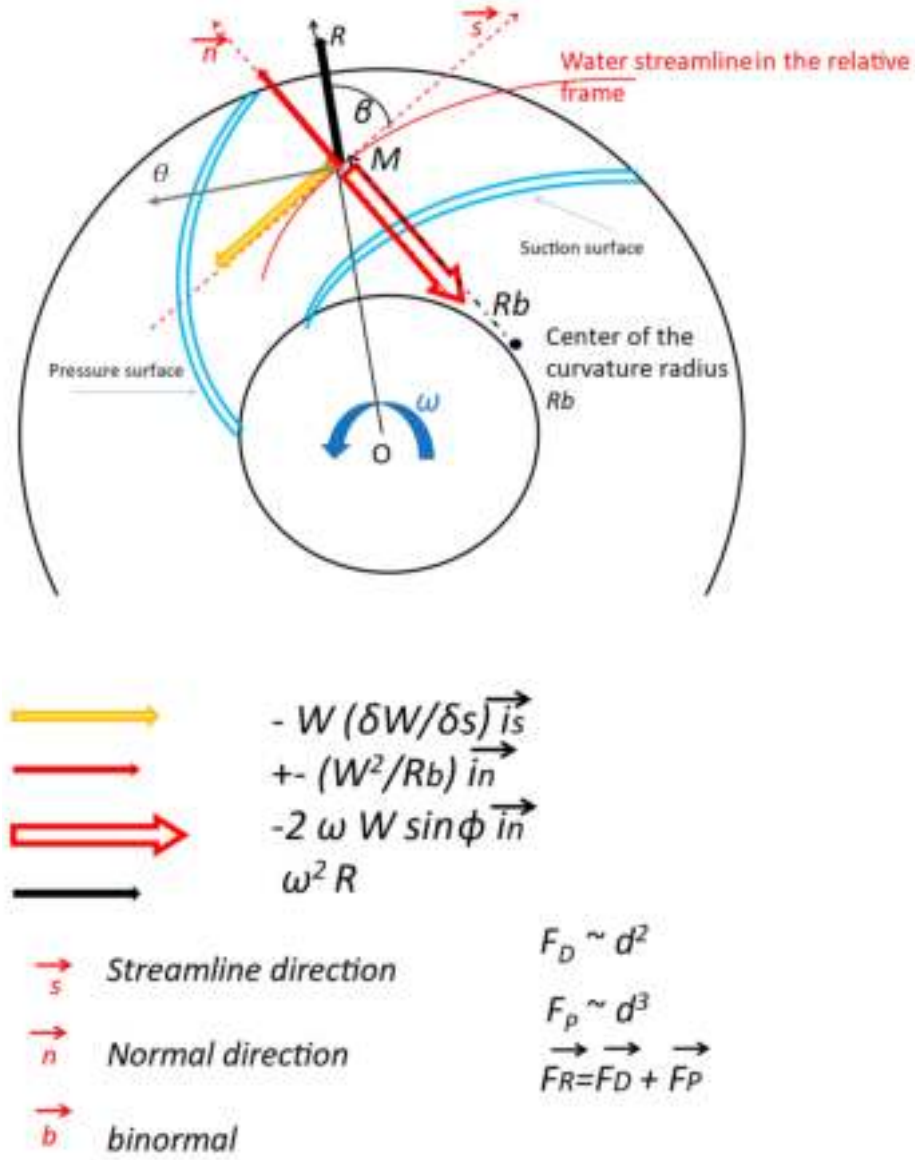

Figure 7. Blade to blade plane of a centrifugal impeller with backswept blades.

The right-hand side terms, respectively, correspond to the streamwise inertia force, the centrifugal force due to the curvature, the centrifugal force and the Coriolis force. The positive sign of the curvature term corresponds to a convex streamline, while the negative sign corresponds to a concave streamline.

Considering backswept blades designs, the radius of the curvature R_b is large, and the Coriolis term is bigger than the centrifugal term. A transverse pressure gradient is generated with the high pressure on the pressure side due to the Coriolis force term.

In the meridional plane shown in Figure 8, where the curvature $1/R_m$ is large at inlet regions of impellers, while the absolute tangential velocity is small (the tangential velocity component is normal to the meridional plane (Z, R)), a pressure gradient from shroud

to hub balances the centrifugal force due to the streamlined meridional curvature. The balance of forces along the normal direction n_m leads to:

$$\frac{\left(\frac{1}{\rho}\right)\Delta p}{\delta n_m} = (V_\theta^2/R)\cos\varphi - (V_m^2/R_m) \tag{16}$$

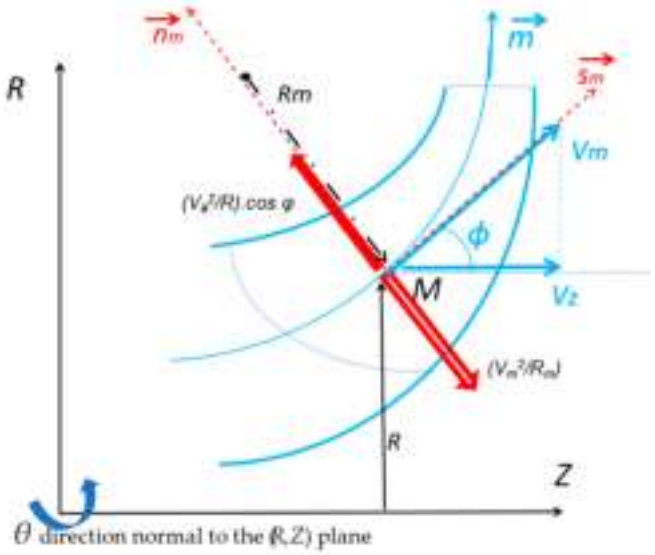

Figure 8. Meridional plane of a centrifugal impeller.

Hence, the inviscid balance of forces leads to a velocity increase from hub to shroud. The impeller flow is controlled by the inviscid forces in the inlet region, where viscous effects are not yet developed. In the radial parts of the impeller, both terms on the right-hand side of Equation (16) will become small and tend to zero.

4.4. Physical Mechanism—Forces Acting on a Single Bubble inside the Main Core Flow in an Axial and a Centrifugal Impeller

For an arbitrary pressure field, a gas bubble always tends to be pushed by the main surrounding liquid flow. This result is related to the fluid dynamic drag F_D, which the liquid exerts on the bubble, as shown in Figures 9 and 10.

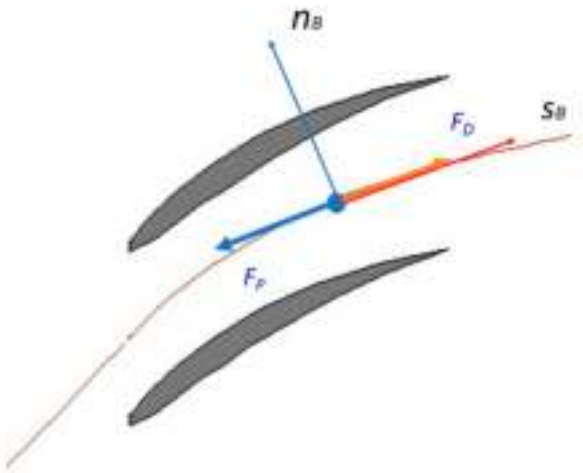

Figure 9. Blade-to-blade axial flow impeller passage.

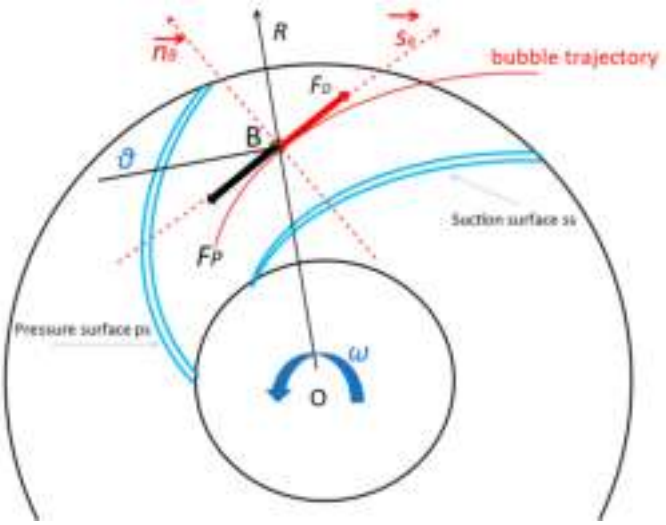

Figure 10. Blade-to-blade radial flow impeller passage.

Assuming that the bubble is mainly affected by the drag force and the pressure gradient force, along with its motion, the force balance on the bubble at a given instant is:

$$\frac{m_B \delta \underset{VB}{\rightarrow}}{\delta_t} = \underset{FP}{\rightarrow} + \underset{FD}{\rightarrow} \tag{17}$$

The left-hand term contains the bubble mass and can be neglected due to the difference between bubble and liquid densities.

Consequently, the velocity of a gas bubble relative to the liquid with a pressure field expressed by the gradient $\frac{\delta p}{\delta s_B}$ can be expressed by the following relation:

$$(V_L - V_G)^2 - \left(-\frac{\delta p}{\delta s_B}\right)\left(\frac{2d_B}{\rho_L}\right) C_D \tag{18}$$

where C_D is the drag coefficient, and d_B is the bubble diameter. Detailed development can be found in Part C.

In an axial flow impeller passage, the relative velocity deceleration induces less pressure gradient towards the outlet compared with radial machines. A stronger pressure gradient may have an influence when the bubble trajectory departs from its original one. Secondary flows also impact bubble trajectories and velocity change due to the combination of meridional and blade-to-blade curvatures (Gülich [9], chapter 5).

Gas bubble trajectory was experimentally and numerically investigated in a centrifugal impeller by Stel et al. [10] and, more recently, by Ofuchi et al. [11]. Stel et al. [10] found that the bubble trajectories inside the impeller passage are very sensitive to the bubble diameter. When the bubble diameter increases, its trajectory tends to move towards the blade pressure side when leaving the inter-blade second throat area.

Liquid and bubble streamlines also differ depending on the inter-blade location. Other factors, such as rotational speed, flow rate and impeller design parameters, influence bubble trajectories. Bubble deformation has also been observed with larger consequences on drag and trajectories.

However, in real situations, air–liquid mixture contains several bubbles that interact together and make their behavior more complicated. Depending on the flow rate ratio, strong deceleration can occur on the pressure side close to the blade inlet section at a high flow rate. At a low flow rate ratio, strong deceleration occurs on the impeller suction side, generally after the inlet impeller throat area. For both cases, bubbles tend to coalesce together, and a critical gas volume fraction can be reached, creating channel gas blockage and head degradation. Bubble coalescence creates an increase in bubble diameter and/or

bubble interactions. The physical analysis performed for a single bubble is no longer valid if phase separation occurs. Momentum exchange between each phase and slip ratio effects must be considered.

Finally, note that the drag force is proportional to the bubble surface, whereas the pressure force is proportional to the bubble volume. If the bubble diameter increases, the pressure force increases faster than the drag force. Each bubble trajectory tendency is thus reinforced.

5. Simplified Approaches for Pumps Two-Phase Performance Prediction

5.1. Semi-Empirical Correlation

Mikielewicz et al. [12] developed a method for correlating pump performance characteristics in two-phase flows producing a "Head- Loss Ratio" which corresponds to the apparent loss of head in a two-phase condition divided by the loss of head in a single-phase condition.

For each phase, Euler equations are developed so that head loss can be extracted from the theoretical head and real one for two-phase conditions.

The theoretical head coefficient obtained with two-phase flow conditions can be written as follows:

$$\psi_{t,th,tp} = 1 - f_{tp,2}\varphi \tan\beta_2 \text{ assuming no inlet tangential absolute velocity} \quad (19)$$

Introducing the two-phase function, a:

$$a = \left(\frac{\alpha}{1-\alpha}\right).\frac{\rho_G}{\rho_L} \quad (20)$$

f_{tp} is so defined as:

$$f_{tp} = \frac{(1+a)\left(1+as_v^2\right)}{1+as_v{}^2} \quad (21)$$

Note that $f_{tp} = 1$, when $s_v = 1$.

It is generally assumed that most of the head losses due to two-phase flow patterns mainly occur inside the impeller passage and in the volute but with less extent.

The total two-phase losses are defined as the sum of wall friction losses plus separation flow losses. The separation flow losses can be approximated as being proportional to the square of the actual flow rate Q_{tp} minus the best efficiency one Q_{be}.

This leads to the following:

$$\Delta p_{tp,sep}^{LOSS} = K_{sep}\left\{\left(\frac{Q_L}{Qtp}\right) - \left(\frac{Q_{be}}{Q_{tp}}\right)\right\}^2 Q_{tp}^2 \quad (22)$$

K_{sep} is a constant for separated loss correlation that can be obtained or predicted for single-phase conditions.

The expression for the total pressure loss for a given pump can be written as:

$$\Delta p_t^{LOSS} = \Delta p_{t,th,tp} - \Delta p_{t,tp} \quad (23)$$

which is expressed as the difference between the two-phase theoretical pressure increase in the pump $\Delta p_{t,th,tp}$ and the actual pressure increase $\Delta p_{t,tp}$.

$$\Delta p_t^{LOSS} = f_{sp}\left(\frac{R{\cdot}L}{A^2}\right)d_{hyd}\left(\frac{\rho_{tp}}{\rho_L}\right)^2 Q_{tp}^2\left(\frac{\rho_L}{2}\right) + K'\left\{\left(\frac{1-\alpha}{1-\alpha+\alpha s_V}\right) - \left(\frac{Q_{be}}{Q_{tp}}\right)\right\}^2 Q_{tp}^2 \quad (24)$$

In the above expression, the first term of the second member is directly related to the pressure losses due to wall friction and the second one to separation losses.

- f_{sp} corresponds to the usual single-phase friction factor that depends on the pump Reynolds number and the wall roughness factor, as can be found on the well-known Moody diagram.
- L is an approximated channel length (impeller or volute).
- A is a characteristic pump area.
- d_{hyd} is the hydraulic diameter (impeller or volute).
- $R = \left(\frac{1-x}{1-\alpha}\right)^2$
- $\frac{Q_L}{Q_{be}} = \frac{1-\alpha}{1-\alpha+\alpha s_V}$.

Note that for an air–liquid mixture and for $s_V = 1$, x is of the order of 10^{-4} when α< 30%. Therefore, R can be approximated by $R' \sim 1/(1-\alpha)^2$.

This means that the two-phase pressure losses due to friction can be modified by a factor $1/(1-\alpha)^2$

For a given pump operating point, let us consider that the two-phase pump head fits the system resistance curve so that:

$H_{tp} = K_{sp}\,(Q_G + Q_L)^2$, which suggests that the pump head is only proportional to the square of the total volume flow rate.

Then, it can be approximated by:

$H_{tp} = K_{sp}\,(1+\beta)^2\,Q_L{}^2 = K_{sp}.\ Q_L{}^2(1/(1-\alpha))^2 = K_{sp}Q_L{}^2R'$, which is equivalent to the previous relation except for high void fractions.

The final expression of the Head ratio H^*, as proposed by Michielewicz et al. [12], can be written as:

$$H^* = \frac{\Delta H_{t,tp}^{LOSS}}{\Delta H_{t,sp}^{LOSS}} = \frac{\Delta H_{t,tp,th} - \Delta H_{t,tp}}{\Delta H_{t,sp,th} - \Delta H_{t,sp}} = \left(\frac{1+a}{1+as}\right)^2 + K\left\{\left(\frac{1-\alpha}{1-\alpha+\alpha s_V}\right) - \left(\frac{Q^*}{Q_{tp}}\right)^2\right\} \Big/ \left\{(1-\alpha)(1+a)\left(1+K\left(1-\frac{Q_{be}}{Q_{tp}}\right)^2\right)\right\} \quad (25)$$

In this last relation, K is a combination of the geometrical constant of any one pump and a function of the flow regime, which directly depends on α.

Therefore, H^* is principally a function of void fraction and flow coefficient but also a function of rotational speed and slip ratio.

The main assumption about this one-dimensional approach is that each phase enters the rotor with the same absolute angle and leaves the impeller with the same relative angle. It is always possible to verify this assumption, but only when pumping external losses (disk friction and leakage losses) are correctly evaluated from experimental torque measurements (Gülich [9]).

The more homogeneous the flow regime, the more closely the relative losses approach the single-phase values. Therefore, the existence of flow regimes other than homogeneous is the principal determining factor for the prediction of the characteristics in two-phase flow. This includes the problem of loss prediction due to bubble diameter variation, bubble agglomeration and phase separation with associated slip ratio evaluation.

5.2. Analytical Approaches

Analytical approaches have been developed based on one-dimensional hypothesis considering the flow as:

(a) An average mixture of homogeneous bubbly flow.
(b) Considering separated phases called the two-phase modeling.

Both approaches lead to solving differential equations allowing for essentially determining the evolution of the local void fraction and slip velocity with flow rate; therefore, it gives more detailed flow features compared with the semi-empirical approach presented earlier.

All detailed development of these methods can be directly found in the related references that are given below. However, the main definitions, assumptions and closure relation that undergo each model are presented in Appendix A.

(a) *One-Dimensional Two-Phase Bubbly Flow Modeling*

An analytical method was proposed by Furuya et al. [13] with an inviscid flow assumption to investigate the head degradation due to two-phase pumping. The method is applied in a control volume bounded by two successive streamlines separated by a distance d_n, where the momentum equation is developed, then integrated from the impeller inlet to outlet sections assuming that the trajectory of liquid is identical to that of bubbles. A simple interfacial force is introduced using the momentum equation applied to a bubble. The final differential equation is written as follows (see Appendix B):

$$\begin{gathered}(\dot{m}_L{}^2/(\rho_L d_n^2))\left(\tfrac{1}{1-\alpha}\right)\left\{\left(\tfrac{1}{1-\alpha}\right)\tfrac{\delta\alpha}{\delta s}-(\tfrac{1}{d_n})(\tfrac{\delta d_n}{\delta s})\right\}+(\dot{m}_G{}^2/(\rho_G d_n^2))((1-\alpha)/\alpha^2)\left\{(1/\alpha)\tfrac{\delta\alpha}{\delta s}-(\tfrac{1}{d_n})(\tfrac{\delta d_n}{\delta s})\right\}+\\ 0.5\rho_L\left\{(\dot{m}_G/\rho_G d_n\alpha)^2\left[\left(\tfrac{1}{\alpha}\right)\tfrac{\delta\alpha}{\delta s}+(\tfrac{1}{d_n})(\tfrac{\delta d_n}{\delta s})\right]\right\}+(\dot{m}_L/(\rho_L d_n(1-\alpha)))^2\left[\left(\tfrac{1}{1-\alpha}\right)\tfrac{\delta\alpha}{\delta s}-(\tfrac{1}{d_n})(\tfrac{\delta d_n}{\delta s})\right]=\\ (\rho_L-\rho_G)(1-\alpha)r\omega^2\sin\beta\cos\varphi\\ -(3/8)(C_D/R_B)\rho_L\left[\dot{m}_L/(\rho_L d_n(1-\alpha))-(\dot{m}_G/\rho_G d_n\alpha)\right]\left|\dot{m}_L/(\rho_L d_n(1-\alpha))-(\dot{m}_G/\rho_G d_n\alpha)\right|\end{gathered} \tag{26}$$

With the following mass conservation equations:

$$\dot{m}_{tp}=(\dot{m}_G+\dot{m}_L)$$

$$\dot{m}_{tp}=d_n(1-\alpha)W_L\rho_{tp}$$

$$\dot{m}_L=d_n(1-\alpha)W_L\rho_L$$

$$\dot{m}_G=d_n\alpha W_G\rho_G$$

This differential equation contains only one variable α. All other quantities here are either constant or known as a function of s. Therefore, if the boundary conditions at the impeller inlet section are known, the ordinary differential Equation (26) can be solved for α along s. Once $\alpha(s)$ is obtained, all other parameters can be solved. Furthermore, each phase's relative velocity is determined from the mass conservation equations.

The comparison with experimental data proposed by Furuya et al. [13] shows that head degradation is mainly caused by a higher acceleration in the liquid phase and deceleration in the gas phase than in the case of single-phase flows. Because no relative outlet deviation angle model is proposed (neither slip factor), the results only appear valid when bubbles remain in the main core flow (or close to the suction side of the impeller), which corresponds to flow patterns observed in axial and mixed flow machines.

(b) *One-Dimensional Two-Fluid Modeling (Minemura et al. [14])*

This approach is like the one proposed by Furuya et al. [13] but introduces analytical functions for wall friction losses, shock losses, rapid expansion, mixing losses at the impeller outlet on one side, and slip coefficient on another side to determine the effective absolute tangential velocity used for theoretical head evaluation. It is so potentially more applicable to centrifugal pumps.

In addition, several models for interfacial friction coefficient and virtual mass coefficient are proposed and further adapted when applied in real cases.

The constitutive equations allow for calculating the effective performance change operating under two-phase flow conditions using the velocities and void fractions calculated under bubbly flow with slippage between the two phases. It is demonstrated that the head is scarcely affected by bubble diameter in the impeller and friction factor between the two phases for a reduced range of void fraction (α below 25%), whereas it was more affected by the outlet relative velocity differences using the Furuya's approach but for a wider range of α.

Minemura et al. [14] also presented the results of their model, looking at the evolution of the main parameters along the impeller passage of a centrifugal pump. The following Figures 11 and 12 give interesting comprehension of what should locally occur on the slip ratio, head coefficient and void fraction inside the impeller, such as in Figure 11 (for best efficiency point), and dimensionless loss variations versus inlet void fraction for two different flow coefficients, such as in Figure 12.

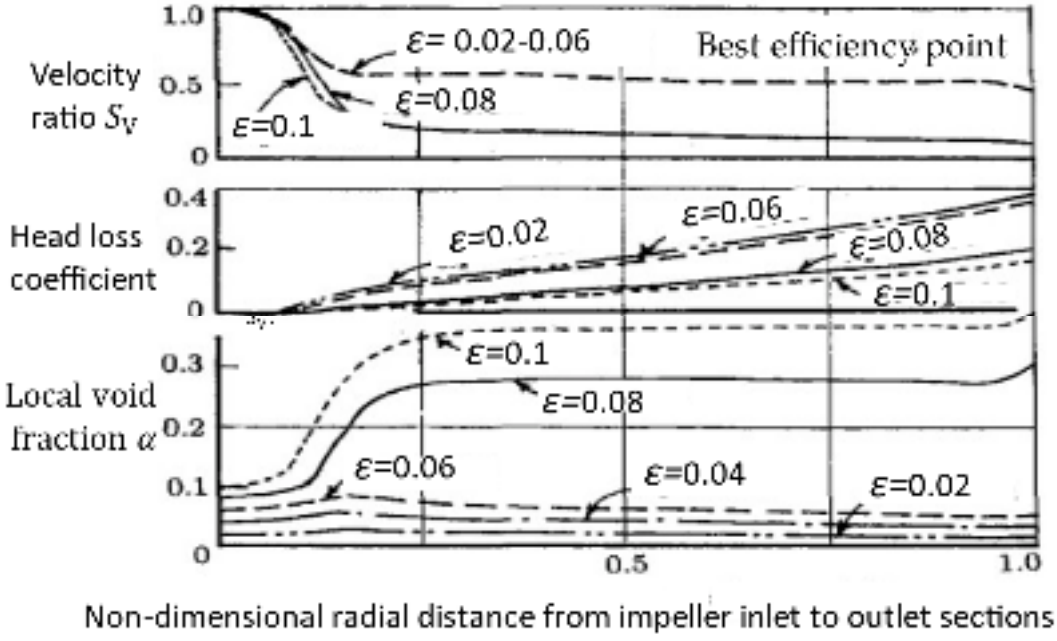

Figure 11. From top to bottom: example of radial evolutions of velocity ratio S_V, head loss coefficient and void fraction α inside an impeller channel at best efficiency point for different values of the inlet void fraction ε (Data from Minemura et al. [14]).

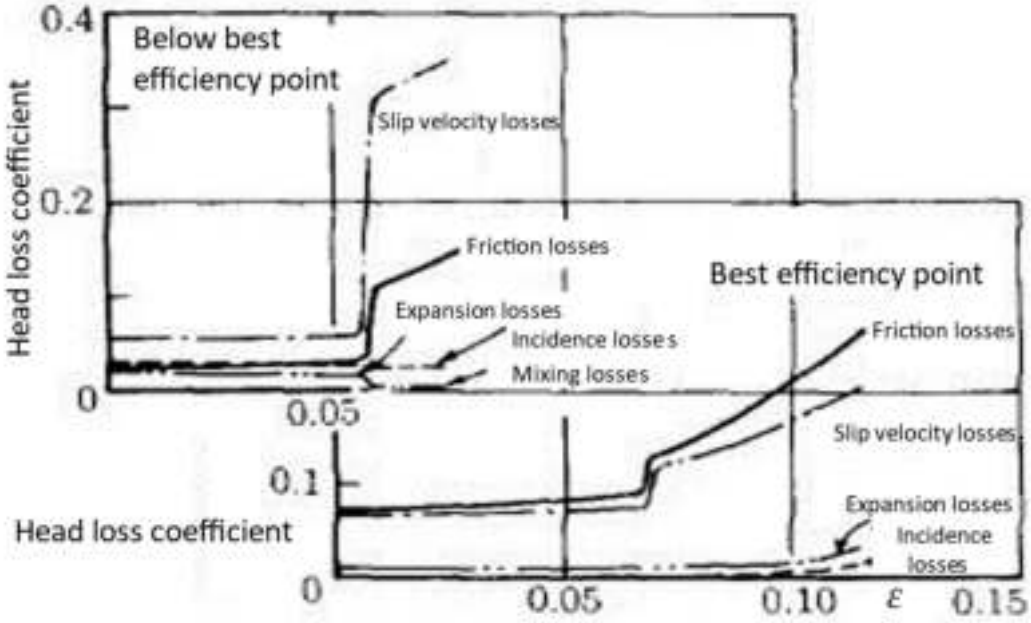

Figure 12. Evolutions of several head loss coefficients versus inlet void fraction for two different flow coefficients: top figure: below best efficiency point, bottom figure: best efficiency point. (Data from Minemura et al. [14]).

In Figure 11, the void fraction reaches maximum values after the impeller's first throat area and remains almost constant (about three times the inlet value). A significant increase

can be detected when the inlet void fraction ε is bigger than 0.06. A rapid decrease of the velocity ratio is also observed and corresponds to the increase of the head loss coefficient.

In Figure 12, one can observe that the head of friction loss is the maximum among all the losses and remarkably increases near the breakdown condition. The void fraction at the impeller exit region is so large that the liquid phase velocity is much greater than the gas phase velocity. All other losses are rather small for both flow rates. The sudden change in loss curve evolution corresponds to a given threshold value of ε that is chosen to match the experimental results. The first abrupt change corresponds to the bubble drag coefficient from homogeneous to slug flow pattern proposed by Hench and Johnston [15], and the second one, from slug to churn flow pattern, is proposed by Zuber and Hench [16].

5.3. Surging Criteria Detection

An interesting model to predict the operational conditions that cause two-phase pump surging is proposed by Barrios and Prado [17]. In this approach, surface tension and rotational speed are involved in determining the flow patterns and in predicting the occurrence of stagnant bubbles at the channel intake. These two variables were not present in the models presented in previous sections of the present paper. This model depends on two important variables, namely the stagnant bubble size and the bubble drag coefficient. A bubble size correlation is presented with a new correlation for the drag coefficient as a function of rotational speed and Reynolds number. Not many authors refer to such a work.

6. Conclusions

The present part A brings together the main two-phase flow definitions usually used for pumps and different approaches based on correlation and one-dimensional models that are proposed in the open literature.

Close to the best efficiency point, these models can predict pump performances under two-phase flow conditions accurately when homogeneous conditions are present. For off-design conditions and high inlet void fraction, the only way to predict the performances within an error of $\pm 20\%$ is to adapt interfacial loss and deviation outlet angle models.

For centrifugal pumps, because of strong 3D effects, the one-dimensional approach is limited to a small range of void fractions and is very dependent on bubble sizes that govern interfacial losses. Radial impeller flow channels display significant non-uniformity in void fraction distributions in the transverse as well as in meridional directions. This means that chum-turbulent flow and low-void fraction bubbly flow may co-exist at a given location.

This is the reason why an appropriate 3D CFD approach is necessary to obtain a better local flow understanding (see Part C) in association with the local experimental analysis presented in Part B.

Funding: This research received no external funding.

Data Availability Statement: Not applicable.

Conflicts of Interest: The author declares no conflict of interest.

Nomenclature

a	two-phase function, $a = \frac{\left(\frac{\alpha}{1-\alpha}\right)\rho_G}{\rho_L}$
A	cross area
b	outlet impeller width- binormal direction (intrinsic coordinate system)
C_D	Reynolds dependent drag coefficient
d	diameter
D	total derivative
F^x	function
G	mass flux

g	gravitational acceleration
H	head
H^*	head loss ratio
h	enthalpy
K	constant
$\dot{m}$	mass flow rate per unit time
m	mass
n	direction normal to s (intrinsic coordinate system)
n	rotational speed
p	pressure
Q	volume flow rate
R	radius
r	radial vector direction
s	direction of a streamline. (Intrinsic coordinate system)
S_V	phase slip ratio
t	blade pitch, time
U	rotating velocity
V	absolute velocity
$\mathcal{U}$	volume
W	relative velocity
x	gas fraction—gas quality
z	axial direction
α	local void fraction, absolute flow angle
β	gas to liquid ratio, relative flow angle
δ	derivative
Δ	increment, difference
ε	inlet void fraction
φ	flow coefficient, $\varphi = \frac{Q}{2\pi R_2 b_2 U_2} = \frac{Q}{2\pi\omega R_2^2 b_2}$
φ	meridional angle
μ	dynamic viscosity
v	kinematic viscosity = μ/ρ
ζ	loss coefficient
θ	tangential direction
ρ	density
ψ	head coefficient, $\Delta\psi = \frac{g\Delta H}{U_2^2}$
η	efficiency
ω	angular velocity
σ	surface tension
Indices	
be	best efficiency
B	bubble
cs	cross sectional
degrad	related to 50% head decrease.
D	drag
G	gas
H	homogenous
hyd	hydraulic
imp	impeller
L	liquid
LOSS	related to losses
m	meridional
opt	optimum
p	due to pressure gradient
ps	pressure side
R	resultant

rel	relative to the liquid phase
ss	suction side
sp	single phase
t	total
th	theoretical
tp	two-phase
v	volumetric
0	related to $\alpha = 0$
1	impeller inlet section
2	impeller outlet section

Appendix A

Appendix A.1. Two-Phase Basic Definitions

The following basic definitions are obtained in any channels in which gas and liquid phases exist, whether they are separated or not.

(a) Gas Fraction (or Gas Quality) x

$$x = m_G/(m_G + m_L) \tag{A1}$$

For steady state,

$$x = \dot{m}_G/(\dot{m}_G + \dot{m}_L). \tag{A2}$$

(b) Void Fraction

$$\alpha = \frac{U_G}{U_t} = U_G/(U_G + U_L) \tag{A3}$$

If steady state is assumed, then:

$$\alpha_V = Q_G/(Q_G + Q_L), \text{ is called thevolumetric void fraction} \tag{A4}$$

Q corresponds to the volume flow rate of each phase.
With 1D flow assumption, one can write:

$$\alpha_{cs} = A_G/(A_G + A_L) \tag{A5}$$

α_{cs} is thus called the cross-sectional void fraction. A_G is the area of the cross-section of a channel occupied by the gas phase, and A_L is that of the liquid phase. For simplicity, the cross-sectional void fraction is called α.

One can see that the volumetric void fraction introduces the notion of two consecutive cross-sections separated by a small-time difference Δt.

(c) Cross-Sectional Void Fraction

The most widely utilized void fraction definition is the cross-sectional average void fraction, which is based on the relative cross-sectional areas occupied by the respective phases. They are predicted using several types of approaches, such as the following:

- Homogeneous model, which assumes the two phases travel at the same velocity.
- One-dimensional models which account for differing velocities of the two phases.
- Two-dimensional models incorporating the normal distribution of the local void fraction and velocities.
- Models based on the physics of specific flow regimes.
- Empirical and semi-empirical methods.

Appendix A.2. Homogeneous Model and Velocity Ratio

(a) Homogeneous Void Fraction

From the definition of the cross-section void fraction of a channel of area A, the mean gas and liquid velocities V_G and V_L are given below by using the gas quality x and the volumetric flow rates of the gas and the liquid, respectively, Q_G and Q_L

$$V_G = \frac{Q_G}{A\varepsilon} = \left(\frac{\dot{m}}{\rho_G}\right)\left(\frac{x}{\varepsilon}\right) \tag{A6}$$

$$V_L = \frac{Q_L}{A(1-\varepsilon)} = \left(\frac{\dot{m}}{\rho_L}\right)\left(\frac{1-x}{1-\varepsilon}\right) \tag{A7}$$

The basis of the homogeneous model is that it assumes that both phases travel at the same velocities. Thus, equating the above equations for equal velocities $V_G = V_L$ leads to

$$\varepsilon_H = \left(\frac{x}{\rho_G}\right)/\left(\frac{(1-x)}{\rho_L} + \left(\frac{x}{\rho_G}\right)\right) \tag{A8}$$

or

$$\varepsilon_H = 1/\left(1 + \frac{1-x}{x}\right)(\rho_G/\rho_L) \tag{A9}$$

The homogeneous void fraction model is reasonably accurate for limited cases. The best agreements are found for bubbly and dispersed droplets or mist flows. Note that for bubbly flow, the continuous phase is liquid, and the gas is the entrained one. For the mist flow, the continuous phase is the gas, and the entrained phase is the water.

When approaching the critical pressure of a given mixture, the difference between each phase's densities disappears. The homogeneous void fraction model is also valid at very large mass velocities and high vapor qualities.

(b) Velocity Ratio: S_V.

The velocity ratio is a concept used in separated flow models, where it is assumed that the two phases travel at two different velocities V_G and V_L. It is also often referred to as the slip ratio. Moreover, a discontinuity cannot physically exist between the phase velocities since a boundary layer is formed at the interfaces of both phases. The slip ratio describes the relative mean velocities of the co-existing phases for simplicity.

$$S_V = V_G/V_L \tag{A10}$$

$$\text{Then } \varepsilon = 1/\left(1 + \left(\frac{1-x}{x}\right)S_V\left(\frac{\rho_G}{\rho_L}\right)\right)$$

$$\text{and } x = \frac{1}{1 + \frac{1-\varepsilon}{\varepsilon}\left(\frac{\rho_L}{\rho_G}\right)S_V}$$

$$S_V = \left(\frac{1-\varepsilon}{\varepsilon}\right)\left(\frac{x}{1-x}\right)(\rho_L/\rho_G)$$

For equal velocities, the expression of ε reverts to the same expression obtained for the homogeneous model expression.

The value of the velocity ratio depends on the mixture configuration. For upward and horizontal co-current flows, V_G is nearly always greater than V_L. For vertical down flows, V_G may be smaller than V_L due to gravity effects. Numerous analytical models and empirical correlations have been proposed for slip ratio determination in the open literature.

(c) Mass Flux G.

$$G = \dot{m}/A \tag{A11}$$

(d) Homogeneous Two-Phase Density ρ_{tp}

$$\rho_{tp} = \alpha_V \rho_G + (1-\alpha_V)\rho_L = \rho_L + \frac{1}{\rho_G - \rho_L} + 1/\left[(\frac{S_V \rho_G (1-x)}{\rho_L (\rho_G - \rho_L) x}) x \right] \tag{A12}$$

Appendix B.

An analytical method was proposed by Furuya [13] in 1985, with an inviscid flow assumption, to investigate the head degradation due to two-phase pumping. The method was applied in a control volume where momentum equation is developed, then integrated from impeller inlet to outlet sections assuming that the trajectory of liquid is identical to that of bubbles (here denotes by subscript *G*) so that the control volume is bounded by two successive streamlines separated by the distance d_n normal to s. One has:

$$(1-\alpha)\rho_L W_L \cdot \delta W_L/\delta s + \alpha \rho_G W_G \cdot \delta W_G/\delta s = (\rho_L(1-\alpha) + \alpha\rho_G) R\omega^2 - \delta p/\delta s \tag{A13}$$

Equation (13) can be written as:

$$\begin{array}{c} (\delta/\delta s)\left\{ \frac{(1-\alpha)\rho_L W_L^2}{2} + \frac{\rho_G \alpha W_G^2}{2} - (\alpha\rho_G + (1-\alpha)\rho_L)\cdot\left(\frac{(r\omega)^2}{2} + p \right) \right\} \\ + \left\{ \rho_L (W_L^2 - (r\omega)^2)/2 - \rho_G (W_G^2 - (r\omega)^2)/2 \right\} (\frac{\delta\alpha}{\delta s}) = 0. \end{array} \tag{A14}$$

This relationship explicitly shows the derivative of the void fraction α with s and that there is a difference between the two-phase velocities. This option makes it possible to have different outlet relative velocities between each phase. This mainly explains the two-phase head decrease due to the different absolute tangential velocities of each phase compared with single-phase conditions. The effects of condensation and compressibility are neglected for simplicity so that each phase density remains constant. The external force acting on the control volume is considered equal to the radial force and the pressure force, such as in Figure 9.

It can be integrated between the inlet (subscript *1*) and outlet (subscript *2*) impeller sections, assuming all quantities vary along a streamline. It is equivalent to Bernoulli's equation written in the relative reference frame. It leads to the following equation applied along a streamline for the steady state:

$$\begin{array}{c} \left\{ \frac{(1-\alpha_2)\rho_L (W_{2L}^2 - U_2^2)}{2} + \frac{\alpha_2 \rho_G (W_{2G}^2 - U_2^2)}{2} + p_2 \right\} - \left\{ \frac{(1-\alpha_1)\rho_L (W_{1L}^2 - U_1^2)}{2} + \frac{\alpha_1 \rho_G (W_{1G}^2 - U_1^2)}{2} + p_1 \right\} + \\ \int_1^2 \left\{ \frac{\rho_L (W_L^2 - U^2)}{2} - \frac{\rho_G (W_G^2 - U^2)}{2} \right\} \cdot \left(\frac{\delta\alpha}{\delta s} \right) \cdot ds = 0 \end{array} \tag{A15}$$

The difference $(p_2 - p_1)$ can be substituted using the two-phase total head defined as:

$$\Delta H_{t.tp} = \left(\frac{p_2 - p_1}{g\rho_{tp}^*} \right) + \frac{(V_{L2}^2 - V_{L1}^2)\cdot(1-x)}{2g} + \frac{(V_{G2}^2 - V_{G1}^2)\cdot x}{2g} \tag{A16}$$

With:

$\rho_{tp}^* = m_{tp}/(Q_L + Q_G)$,

$Q_L = d_n(1-\alpha)W_L$,

$Q_G = d_n \alpha W_G$

$x = (m_G/\dot{m}_{tp})$.

Note that:

$$\rho_{tp}^* = \rho_{tp} = (1-\alpha)\rho_L + \alpha\rho_G, \text{when } W_L = W_G$$

By introducing each phase total head increase $H_{t,G}$ and $H_{t,L}$ as:

$$\Delta H_{t,G} = \frac{p_2 - p_1}{g\rho_G} + (V_{G2}^2 - V_{G1}^2)/2g \tag{A17}$$

$$\Delta H_{t,L} = \frac{p_2 - p_1}{g\rho_L} + (V_{L2}^2 - V_{L1}^2)/2g \tag{A18}$$

The two-phase head increase between the inlet and outlet impeller section can be written as:

$$\Delta H_{t,tp} = (\Delta H_{t,L}\dot{m}_L + \Delta H_{t,G}\dot{m}_G)/\dot{m}_{tp} \tag{A19}$$

and leads to the final expression given below:

$$\Delta H_{t,tp} = \Delta H_{t,sp}^{W,L} - \Delta H_{W,2} - \Delta H_s - \Delta H_\alpha \tag{A20}$$

with:

$$\Delta H_{sp}^{W,L} = (1-x)\cdot\frac{V_{U,2L}^{sp} - V_{U,1L}^{sp}}{g} - \frac{x\left(V_{U2,G}^{sp} - V_{U,1G}^{sp}\right)}{g} \tag{A21}$$

$\Delta H_{sp}^{W,L}$ is different to ΔH_{sp}, defined in Section 5.1. It only reflects that the absolute tangential velocities at the impeller outlet are different for each phase, such as for jet and wake pattern for single phase conditions. This implicitly assumes that each phase is well separated, which is generally the condition obtained for high void fractions. Comparison with experimental data looks effectively better for void fractions bigger than 30% and for axial mixed flow pumps.

$\Delta H_{W,2}$ represents the phase relative speed modification at the pump exit caused by two-phase flow condition:

$$\Delta H_{W,2} = \frac{(1-x)U_2\Delta V_{U,2L}}{g} + \frac{xU_2\Delta V_{U,2G}}{g} \text{ with } \Delta V_{U,2} = V_{U,2}^{sp} - V_{U,2} \tag{A22}$$

ΔH_s is related to the slip velocity between the liquid and gas phases:

$$\begin{aligned}\Delta H_s = (1-x)&\left\{\left(\alpha_2\left(\frac{W_{2,G}}{W_{2,L}}\right)-1\right)\cdot\frac{W_{2,L}^2-U_2^2}{2g} - \left(\alpha_1\left(\frac{W_{1,G}}{W_{1,L}}\right)-1\right)\cdot\frac{W_{1,L}^2-U_1^2}{2g}\right\}+\\ x(1-\alpha_2)&\left\{\left(\left(\frac{W_{2,L}}{W_{2,G}}\right)-1\right)\cdot\frac{W_{2,G}^2-U_{2,G}^2}{2g}\right\} + (1-\alpha_1)\left\{\left(\left(\frac{W_{1,L}}{W_{1,G}}\right)-1\right)\cdot\frac{W_{1,G}^2-U_{1,G}^2}{2g}\right\}\end{aligned} \tag{A23}$$

ΔH_α is due to the variation in void fraction along the flow passage between the blades.

$$\Delta H_\alpha = (1/g\rho_{tp})\int_1^2\left(\frac{\rho_L(W_L^2 - U^2)}{2} - \frac{\rho_G(W_G^2 - U^2)}{2}\right)\left(\frac{\delta\alpha}{\delta s}\right)\cdot ds \tag{A24}$$

Finally, Equation (A19) can be written as follows, introducing the above set of equations

$$\Delta\frac{H_{t,tp}}{H_{t,sp}^{W,L}} = 1 - (\Delta H_{W,2} + \Delta H_S + \Delta H_\alpha)/\Delta H_{t,sp}^{W\cdot L} \tag{A25}$$

To calculate all quantities of the right terms of Equation (A24), it is necessary to know the evolution of the relative velocities for both liquid and gas phases, as well as the void fraction along the path of the impeller channel.

The addition of an analytical loss model for a bubble is proposed using the momentum equation, according to Hench and Johnston [13].

The momentum equation applied to a gas bubble is:

$$\rho_G W_G\left(\frac{DW_G}{Dt}\right) = \rho_G W_G\left(\frac{\delta W_G}{\delta t}\right) + W_G\left(\frac{\delta W_G}{\delta s}\right) = \sum Fs \tag{A26}$$

This leads to introducing all forces $\sum Fs$ acting on a bubble listed below:

Pressure force: $-V_G(\frac{\delta p}{\delta s})$;
Centrifugal force: $\rho_G V_G r\omega^2 \sin\beta\cos\varphi$;
Drag force: $C_D\rho_L(W_L - W_G)\cdot|W_L - W_G|\pi R_B^2$;
Virtual mass force: $0.5\rho_L V_G(\frac{\delta W_G}{\delta t} + W_G\left(\frac{\delta W_G}{\delta s}\right) - \frac{\delta W_L}{\delta t} - W_L\left(\frac{\delta W_L}{\delta s}\right))$.

Combining all previous relations, if the bubble's shape corresponds to a sphere, one can obtain the following equation that can be used to eliminate the term $\delta p/\delta s$ in Equation (A11).

$$\begin{aligned}\rho_G W_G\left(\tfrac{\delta W_G}{\delta s}\right) + 0.5\rho_L W_G\left(\tfrac{\delta W_G}{\delta s}\right) - W_L\left(\tfrac{\delta W_L}{\delta s}\right) = \left(\tfrac{\delta p}{\delta s}\right) + \\ \rho_G V_G r\omega^2 \sin\beta\cos\varphi + (\tfrac{3}{8})\rho_L(\tfrac{C_D}{R_B})(W_L - W_G)|W_L - W_G|\end{aligned} \tag{A27}$$

The value of C_D depends on the bubble Reynolds number.
The final differential equation is:

$$\begin{aligned}&(\dot{m}_L{}^2/(\rho_L d_n^2))\left(\tfrac{1}{1-\alpha}\right)\left\{\left(\tfrac{1}{1-\alpha}\right)\tfrac{\delta\alpha}{\delta s} - (\tfrac{1}{d_n})(\tfrac{\delta d_n}{\delta s})\right\} + (\dot{m}_G{}^2/(\rho_G d_n^2))((1-\alpha)/\alpha^2)\left\{(1/\alpha)\tfrac{\delta\alpha}{\delta s} - (\tfrac{1}{d_n})(\tfrac{\delta d_n}{\delta s})\right\} + \\ &0.5\rho_L\left\{(\dot{m}_G/\rho_G d_n\alpha)^2\left[\left(\tfrac{1}{\alpha}\right)\tfrac{\delta\alpha}{\delta s} + (\tfrac{1}{d_n})(\tfrac{\delta d_n}{\delta s})\right]\right\} + (\dot{m}_L/(\rho_L d_n(1-\alpha)))^2\left[\left(\tfrac{1}{1-\alpha}\right)\tfrac{\delta\alpha}{\delta s} - (\tfrac{1}{d_n})(\tfrac{\delta d_n}{\delta s})\right] = \\ &(\rho_L - \rho_G)(1-\alpha)r\omega^2\sin\beta\cos\varphi \\ &-(3/8)(C_D/R_B)\rho_L\left[\dot{m}_L/(\rho_L d_n(1-\alpha)) - (\dot{m}_G/\rho_G d_n\alpha)\right]\left|\dot{m}_L/(\rho_L d_n(1-\alpha)) - (\dot{m}_G/\rho_G d_n\alpha)\right|\end{aligned} \tag{A28}$$

With the following mass conservation equations:

$$\dot{m}_{tp} = (\dot{m}_G + \dot{m}_L)$$

$$\dot{m}_{tp} = d_n(1-\alpha)W_L\rho_{tp}$$

$$\dot{m}_L = d_n(1-\alpha)W_L\rho_L$$

$$\dot{m}_G = d_n\alpha W_G\rho_G$$

References

1. Gamboa, G.; Prado, M. Experimental Study of Two-Phase Performance of an Electric Submersible Pump Stage. *SPE Prod. Oper.* **2012**, *27*, 414–421. [CrossRef]
2. Estevam, V.; França, F.A.; Alhanati, F.J.S. Mapping the performance of centrifugal pumps under two-phase conditions. In Proceedings of the 17th Congress of Mechanical Engineering, COBEM 2003, Sao Paulo, Brasil, 10–14 November 2003.
3. Barrios, L. Visualization of Multiphase Performance inside an Electrical Submersible Pump. Ph.D. Thesis, The University of Tulsa, Tulsa, OK, USA, 2007.
4. Verde, W.M.; Biazussi, J.L.; Sassim, N.A.; Bannwart, A.C. Experimental study of gas-liquid two-phase flow patterns within centrifugal pumps impellers. *Exp. Therm. Fluid Sci.* **2017**, *85*, 37–51. [CrossRef]
5. Zhu, Z.J.; Zhang, H.Q. A Review of Experiments and Modeling of Gas-Liquid Flow in Electrical Submersible Pumps. *Energies* **2018**, *11*, 180. [CrossRef]
6. Jiang, Q.; Heng Liu, X.; Zhang, W.; Bois, G.; Si, Q. A Review of Design Considerations of Centrifugal Pump Capability for Handling Inlet Gas-Liquid Two-Phase Flows. *Energies* **2019**, *12*, 1078. [CrossRef]
7. Baker, O. Design of pipelines for simultaneous oil and gas flow. *Oil Gas J.* **1954**, 26.
8. Shaoa, C.; Lia, C.; Zhoua, J. Experimental investigation of flow patterns and external performance of a centrifugal pump that transports gas-liquid two-phase mixtures. *Int. J. Heat Fluid Flow* **2018**, *71*, 460–469. [CrossRef]
9. Gülich, J.F. *Centrifugal Pumps*; Springer: Berlin/Heidelberg, Germany, 2010; ISBN 978-3-642-12823-3. [CrossRef]
10. Stel, H.; Ofuchi, E.M.; Sabino, R.H.G.; Ancajima, F.C.; Bertoldi, D.; Neto AM, M.; Morales RE, M. Investigation of the Motion of Bubbles in a Centrifugal Pump Impeller. *ASME J. Fluids Eng.* **2018**, *141*, 031203. [CrossRef]
11. Ofuchi, E.M.; Silva, H.L.V.; Bertoldi, D.; Mancilla, E.; Stel, H.; Morales, R.E.M. Study of the bubble motion in a centrifugal rotor based on visualization in a rotating frame of reference. *Chem. Eng. Sci.* **2022**, *259*, 117829. [CrossRef]
12. Mikielewicz, J.; Gordon Wilson, D.; Chan, T.; Goldfinch, A. A Method for Correlating the Characteristics of Centrifugal Pumping Two-Phase flow. *J. Fluids Eng. Trans. ASME* **1978**, *100*, 395–409. [CrossRef]

13. Furuya, O. An Analytical Model for Prediction of Two-Phase (Non condensable) Flow Pump Performance. *J. Fluids Eng. Trans. ASME* **1985**, *107*, 139–147. [CrossRef]
14. Minemura, K. Prediction of Air-Water Two-Phase Flow Performance of a Centrifugal Pump based on one-dimensional Two- Fluid Model. *ASME J. Fluid Eng.* **1998**, *120*, 327–334. [CrossRef]
15. Hench, J.E.; Johnston, J.P. Two-Dimensional Diffuser Performance with Subsonic, Two-Phase, Air-Water Flow. *ASME J. Basic Eng.* **1972**, *94*, 105–121. [CrossRef]
16. Zuber, N.; Hench, J.E. *Steady State and Transient Void Fraction of Bubbling Systems and Their Operating Limits. (Part I, Steady State Operation)*; Technical Report No. 62GL100; General Electric Co.: Boston, MA, USA, 1962; 334p.
17. Barrios, L.; Prado, M.G. Experimental Visualization of Two-Phase Flow Inside an Electrical Submersible Pump Stage. *ASME J. Energy Resour. Technol.* **2011**, *133*, 042901. [CrossRef]

Disclaimer/Publisher's Note: The statements, opinions and data contained in all publications are solely those of the individual author(s) and contributor(s) and not of MDPI and/or the editor(s). MDPI and/or the editor(s) disclaim responsibility for any injury to people or property resulting from any ideas, methods, instructions or products referred to in the content.

International Journal of
Turbomachinery
Propulsion and Power

MDPI

Review

State of the Art on Two-Phase Non-Miscible Liquid/Gas Flow Transport Analysis in Radial Centrifugal Pumps Part C: CFD Approaches with Emphasis on Improved Models

Markus Hundshagen and Romuald Skoda *

Chair of Hydraulic Fluid Machinery, Ruhr University Bochum, Universitätsstr. 150, 44801 Bochum, Germany; markus.hundshagen@ruhr-uni-bochum.de
* Correspondence: romuald.skoda@ruhr-uni-bochum.de

Abstract: Predicting pump performance and ensuring operational reliability under two-phase conditions is a major goal of three-dimensional (3D) computational fluid dynamics (CFD) analysis of liquid/gas radial centrifugal pump flows. Hence, 3D CFD methods are increasingly applied to such flows in academia and industry. The CFD analysis of liquid/gas pump flows demands careful selection of sub-models from several fields in CFD, such as two-phase and turbulence modeling, as well as high-quality meshing of complex geometries. This paper presents an overview of current CFD simulation strategies, and recent progress in two-phase modeling is outlined. Particular focus is given to different approaches for dispersed bubbly flow and coherent gas accumulations. For dispersed bubbly flow regions, Euler–Euler Two-Fluid models are discussed, including population balance and bubble interaction models. For coherent gas pocket flow, essentially interface-capturing Volume-of-Fluid methods are applied. A hybrid model is suggested, i.e., a combination of an Euler–Euler Two-Fluid model with interface-capturing properties, predicting bubbly flow regimes as well as regimes with coherent gas pockets. The importance of considering scale-resolving turbulence models for highly-unsteady two-phase flow regions is emphasized.

Keywords: centrifugal pumps; liquid/gas transport; computational fluid dynamics; multi-phase modeling; scale-adaptive simulation; population balance modeling

check for updates

Citation: Hundshagen, M.; Skoda, R. State of the Art on Two-Phase Non-Miscible Liquid/Gas Flow Transport Analysis in Radial Centrifugal Pumps Part C: CFD Approaches with Emphasis on Improved Models. *Int. J. Turbomach. Propuls. Power* **2023**, *8*, 15. https://doi.org/10.3390/ijtpp8020015

Academic Editors: Tony Arts and Rodolfo Bontempo

Received: 15 December 2022
Revised: 11 April 2023
Accepted: 18 April 2023
Published: 4 May 2023

Copyright: © 2023 by the authors. Licensee MDPI, Basel, Switzerland. This article is an open access article distributed under the terms and conditions of the Creative Commons Attribution (CC BY-NC-ND) license (https://creativecommons.org/licenses/by-nc-nd/4.0/).

1. Introduction

In various industrial and engineering applications, a mixture of liquid and noncondensable gas, such as air, is encountered. Centrifugal pumps, which have been designed for single-phase liquid transport, are frequently required to convey two-phase mixtures. Two-phase pump applications can be found in nuclear [1] and geothermal [2] power stations, in the pulp and paper industry [3] or in the petroleum industry for artificial lifting [4]. Even a small load of gas may considerably disturb conveyance, and may even cause a break-down of the pump head [5]. As discussed in detail in Part A of this review paper series, a drop in the pump head is associated with a separation of air and water in the blade channels [3,6–8]. In pumps with high specific speeds, in terms of axial and mixed flow pumps, the action of the Coriolis force is directed from the shroud to the hub [9]. Thereby, secondary flow is promoted in the blade channels and this, to some extent, counteracts phase separation. In circumferential pumps, the Coriolis force acts in the direction of the blade pressure side. As a consequence, pressure gradients in the cross-flow direction develop. Since the densities of liquid and gas considerably deviate, pressure gradients lead to a slip between phases, and the gas tends to accumulate on the blade suction side, especially in part-load conditions, where the flow incidence at the blade trailing edge is high [10].

Although there is no difference in principle in the interaction of body forces in the liquid and the pressure gradients, which finally leads to phase segregation, the effect on segregation is considerably more pronounced for circumferential pumps, due to the

direction of the Coriolis forces. Thus, this review of CFD methods is essentially confined to this pump type, with a few exceptions. In Section 2, a review of CFD methods is provided. Unlike the review of, for example, Zhu and Zhang [11], who provided a rather broad overview of 3D simulation techniques of submersible pumps, we substantially focus on aspects of multiphase modeling. Section 2 starts with the physical reasoning of the model assumptions obtained from high-fidelity experiments. Based on experimental observations, two main branches of multiphase models can be identified in terms of the Euler–Euler Two-Fluid (EE2F) method, on the one hand, and the Volume-of-Fluid (VoF) method, on the other hand. State of the art and limitations of both approaches are presented in Sections 2.2 and 2.3, together with example results from the literature. It is important to note that cavitation, in terms of rapid phase change, is omitted here. Although cavitation and the mere transport of a gaseous phase in a liquid are closely related from a physical point of view [12–15], modeling approaches are still separated, so we confine our review to the latter. A discussion of cavitation in circumferential pumps is provided elsewhere, e.g., in Refs. [16–23].

2. Review of CFD Methods for Multiphase Flow in Pumps

2.1. Physical Reasoning

We start our review with important observations from experiments. Recent optical [24–27], Gamma [28–31] and X-Ray [32] experimental techniques provide detailed views of the multiphase flow fields in rotating systems. Based on the multiphase flow field, together with head drop characteristics, several authors [4,24–27,33–38] provide performance maps of the mixture conveying. Subject to the operation point and the air loading, Mansour et al. [24–27] observed a transition from bubbly flow to steady air accumulations in the blade channel, and introduced a categorization in terms of flow regime maps. Four different flow regimes are illustrated in the pump head performance map shown in Figure 1 for a semi-open impeller. It is noteworthy that, for a closed impeller, as investigated by Mansour et al. [24,25], a fifth regime, in terms of segregated flow regimes, was observed, where an air pocket is attached over the entire extent of the blade. This segregated flow regime is not present in a semi-open impeller due to the strong mixing effect, which flushes away parts of the attached air pockets. The flow regimes in semi-open impellers can be summarized as follows:

1. Bubbly flow: the air bubbles are dispersed everywhere in the impeller.
2. Agglomerated bubbles flow: air bubbles start to accumulate in small bubble clusters.
3. Alternating pocket flow: highly unsteady air pockets, with strongly variable sizes and locations, appear at the impeller blades but are not located at each blade.
4. Pocket flow: stable and steady air pockets are located at the suction side of each blade.

The different flow regimes make various demands on the simulation method. For example, the direct resolution of all phase interfaces in the bubbly flow regime (1), where a multitude of separated bubbles is dispersed in the liquid, is associated with tremendous computational effort. Therefore, a homogeneous mixture approach, with treatment of separate bubbles on the subgrid scale, is more efficient when small interfacial scales, in terms of bubbles, are present, and corresponding studies are summarized in Section 2.2. On the other hand, a large coherent air regime is present in the pocket flow regime (4), and the assumptions of a homogeneous mixture approach are violated. Instead, a sharp resolution of the phase interface by means of, for example, a VoF scheme, might be more appropriate. Corresponding studies are reviewed in Section 2.3. In between, in regimes (2) and (3), a transition of phase morphology within the impeller is present. What is more, even when a pocket flow regime (4) has developed in the blade passage, a bubbly flow may be present at the same time, for example, in the suction pipe. Due to these different flow regimes present in the pump, it can be concluded that the transition of phase morphology from bubbly flow to coherent air accumulations should be captured by the CFD method. This demands a hybrid approach, which is summarized in Section 2.4.

A further experimental observation corresponds to highly unsteady void regions, described, for example, in Refs. [24–27,39–44]. As discussed above, alternating unsteady

pockets are present in the transition zone between bubbly and pocket flow regimes. Even inherently steady adherent void regions in the pocket flow regime show unsteady wakes, which will be discussed in Section 4. This observation should be taken into account by reasonable turbulence models. For highly unsteady flow, the validity of Reynolds-averaging might be challenged, and turbulence-scale resolving models might be more accurate. Therefore, a brief review of turbulence-scale resolving simulations of pump flow is provided in Section 2.5.

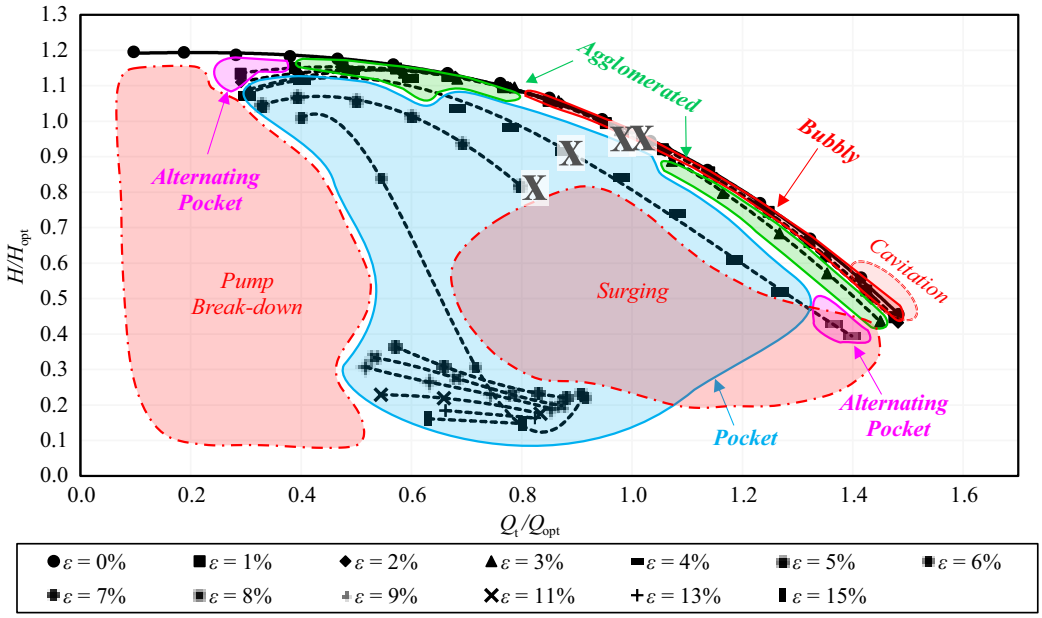

Figure 1. Performance map to characterize flow regimes observed in the experiments of Mansour et al. [27,39]. Some operational points are marked with an "X", and are slightly pulled apart for clarity due to their proximity. They are picked up in the flow simulations further below.

2.2. Euler–Euler Two-Fluid (EE2F) Approach

Most available studies on radial centrifugal pump flow have been performed using the EE2F model family. An Eulerian approach for the dispersed phase is preferred to the Lagrangian approach, since more moderate grid dependence and better statistical convergence of the Eulerian approach may be assumed [45]. Early simulations of two-phase flow in centrifugal pumps by Pak and Lee [46] and Minemura and Uchiyama [47] pointed out that bubbles move to the blade tip and accumulate on the blade's suction side and that the head drop is associated with phase separation and large air accumulation zones. Even with a simplified monodisperse approach and single-channel simulations, Müller et al. [48] obtained good agreement with the measured head drop at low air loading, while, with a rise in the inlet gas volume fraction, even a qualitative prediction could not be obtained, confirming the conclusion of several previous studies, e.g., [49–51]. A significant influence of the computational grid quality on the location and size of bubble accumulation was found by Müller et al. [52]. Si et al. [40–42] and Wang et al. [53] presented validated numerical results of a 3D-bladed centrifugal pump in two-phase air–water flow and compared different impeller designs. Zhou et al. [54] investigated transient, i.e., time-resolved, characteristics of the radial pump force, and Zhong et al. [55] analyzed the transient pump characteristics that start when air is injected in the suction pipe. The EE2F model was also adopted in our previous studies, comparing a closed and a semi-open impeller [56–58]. Several authors have utilized polydisperse bubble size distribution, together with population balance modeling (PBM) within the EE2F framework, enabling temporal and spatial variation of the bubble size. He et al. [59] highlighted the importance of considering the change of bubble diameter for volute-type centrifugal pumps and compared these results to

the results of a monodisperse EE2F simulation. An example result obtained by He et al. [59], in terms of the distribution of the air volume fraction α_a, is given in Figure 2. Stronger air aggregation was observed with the EE2F–PBM model than with the monodisperse approach, supposedly because the chosen monodisperse bubble diameter was too small. The benefit of using a PBM in combination with the EE2F approach is emphasized by having a better match to experimental data.

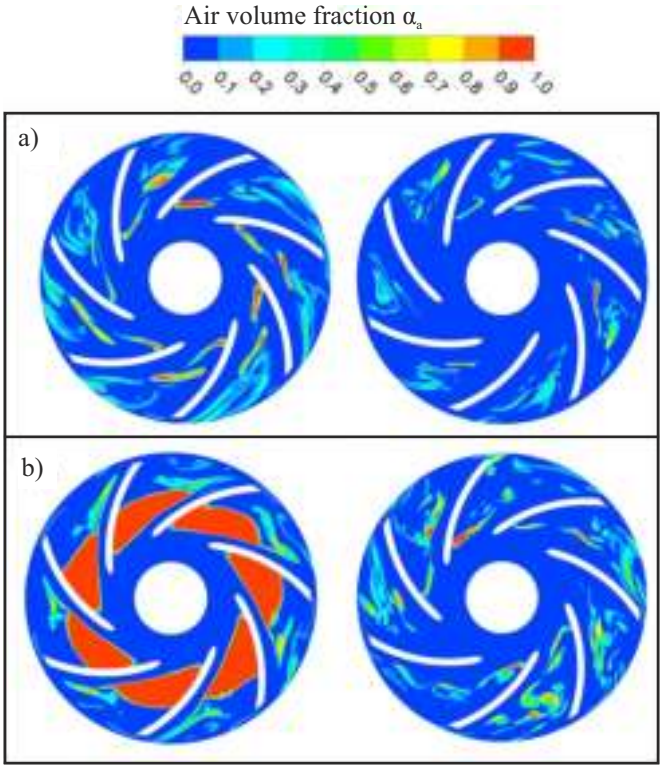

Figure 2. Development of air accumulations, calculated by the coupled EE2F–PBM model (left) and the monodisperse EE2F model (right) for $\varepsilon = 2.21\%$ (**a**) and $\varepsilon = 4.86\%$ (**b**) at $n = 1500$ 1/min and $Q = 7.7\,\mathrm{m}^3/\mathrm{h}$. The figure is adopted from He et al. [59].

Yan et al. [60] confirmed this conclusion. In Figure 3, the pump's pressure coefficient versus inlet gas volume fraction is given for the simulation results obtained by a coupled EE2F–PBM and by a monodosperse EE2F. For the latter, the bubble diameter d was varied. By an adjustment of d, the experimental data could be approached. Thus, d can be considered a kind of calibration parameter in the monodisperse EE2F variant, which is dispensable for the polydisperse EE2F–PBM. With this coupled EE2F–PBM model, Yan et al. [60] analyzed the bubble size distribution in a multistage centrifugal pump.

It is important to note that the term homogeneous (abbreviated "Hom." in Figure 3) used by the authors means that a common velocity field for water and air is assumed. This should not be confused with the homogeneous mixture approach, which means a treatment of bubbles on the subgrid scale and is inherent to any EE2F variant. The mismatch to data by using a common velocity field (result termed "Hom." in Figure 3) underlines the necessity of distinct velocity fields for water and air, to enable phase segregation.

In the simulations by Stel et al. [61,62], air accumulation zones within the impeller observed in the experiments of the same research group from Ref. [37] could be reproduced. Zhang et al. [63] observed large bubble sizes in regions of high air loading within the pump impeller. Chen et al. [64] analyzed the head drop of the first stage of an electrical submersible pump (ESP). Recently, Si et al. [65] reproduced the head drop observed in measurements of a five-stage ESP. They showed that the most significant portion of the head drop occurs in the first and the second stages under two-phase flow conditions, which

is underlined by Figure 4, in terms of the stage head coefficient Ψ. For single-phase, i.e., pure water flow, the first stage does most of the work, according to Figure 4a. For two-phase conditions and $\varepsilon > 2\%$, Ψ drops significantly for stages one and two, according to Figure 4b.

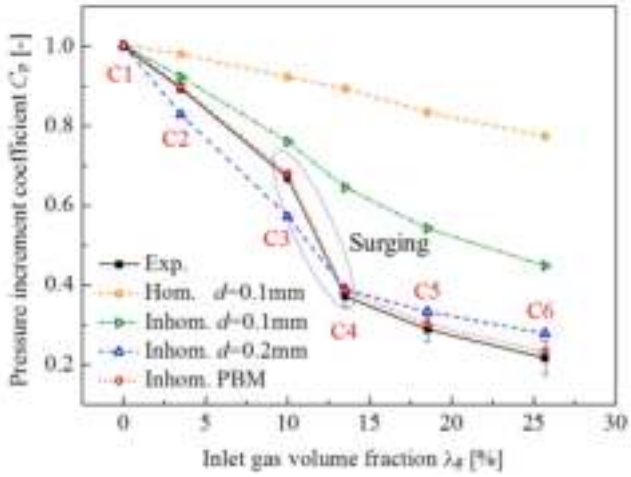

Figure 3. Pressure coefficient versus inlet gas volume fraction for different EE2F model variants and experimental data. The figure is adopted from Yan et al. [60].

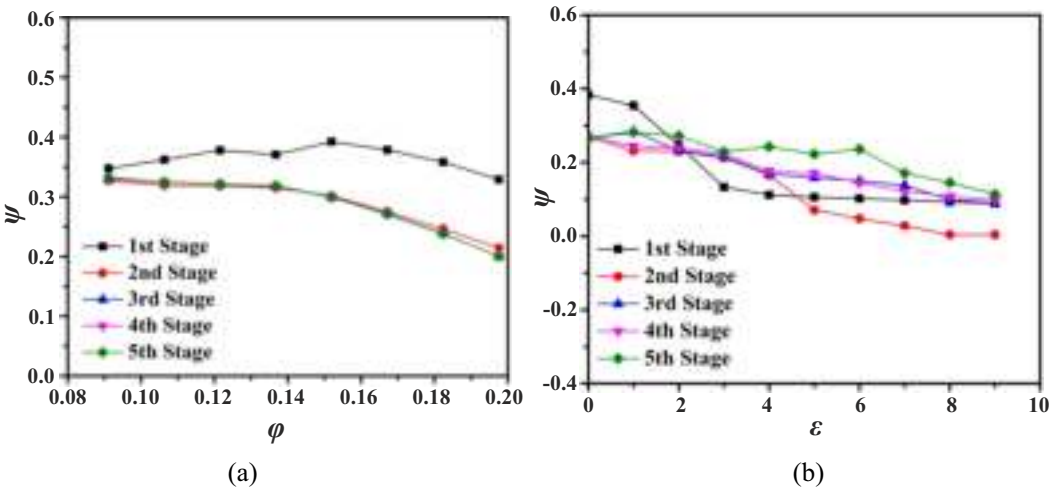

Figure 4. Simulation results of the stage performance in terms of head coefficient Ψ for (**a**) pure water versus the flow coefficient φ and for (**b**) two-phase flow conditions at $\varphi = 0.152$ versus the inlet gas volume fraction ε. The figure is adapted from Si et al. [65].

The EE2F model inherently presumes a dispersed bubbly flow [58], i.e., a homogeneous mixture of water and air within each computational cell. Thus, it can be assumed that in the EE2F approach, air accumulations are represented by clustering of densely dispersed bubbles. However, in the experimental investigations on a planar diffuser flow [66], a sharp interface between the water and the air accumulations was observed, which points out a coherent attached air structure, rather than a clustering of separated bubbles. It may be concluded that such large interface structures should be resolved by a VoF rather than an EE2F approach [67], which is outlined next.

2.3. Volume-of-Fluid (VoF) Approach

By utilizing a VoF approach, Parikh et al. [68] optimized an inducer design by employing a multi-objective optimization and assessed the influence of the inducer design on the pump flow. The same authors investigated the air distribution for different semi-open impellers [69], and compared these simulation results with the experimental results from the same research group [24,25,39]. For example, the air distribution is shown in Figure 5

for a variation of the inlet gas volume fraction. Parikh et al. [69] concluded that the instantaneous distribution of void regions observed in the experiments by a scattered-light technique could be reproduced well by the void fraction distribution in the simulation. However, steady air accumulations formed in the impeller channels for $\varepsilon \geq 3\%$, according to the experiments, which were not observed in the VoF simulation results.

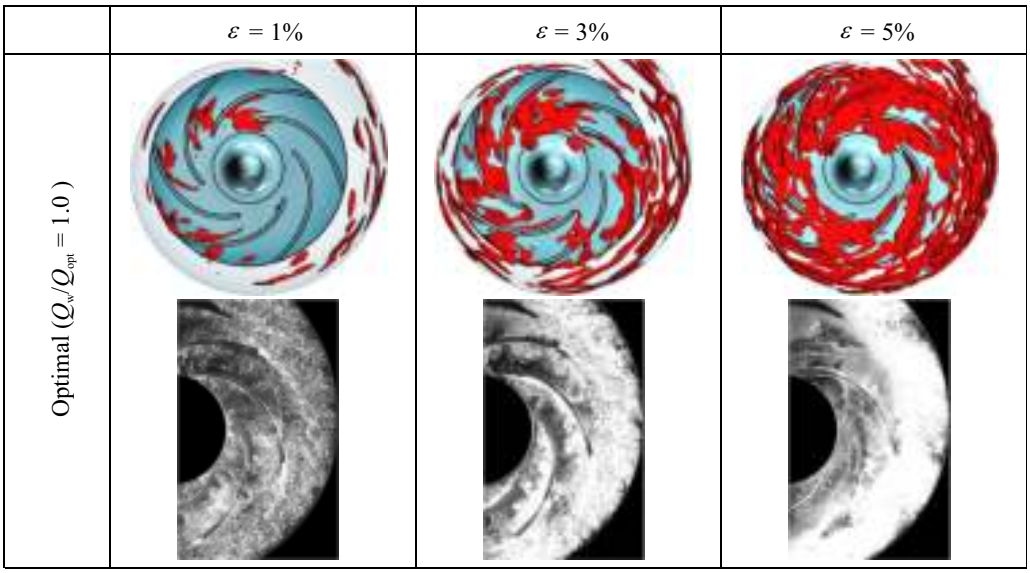

Figure 5. Instantaneous air distribution within a semi-open impeller for a variation of the inlet gas volume fraction ε: experimental images (bottom row) and numerical results of VoF simulations (top row). In the simulations, isosurfaces for $\alpha_a > 0.05$ are shown. The figure is adapted from Parikh et al. [69].

Pineda et al. [70] utilized the VoF method for flow simulations in ESPs and experienced up to 25% deviation from the results of the experimentally measured pump head. Zhu et al. [71] concluded that the VoF model is inferior to the EE2F model for the simulation of ESP flows. Mansour et al. [72] figured out the important physical mechanisms of attenuating pump performance and the beneficial effect of an inducer. However, it remains unclear if the spatial resolution limit allows an adequate resolution of void structures within the VoF simulations. According to De Santis et al. [73], VoF methods are only appropriate for capturing large interfacial structures, provided that a high spatial resolution is applied. Hundshagen et al. [74] showed that the grid resolution, which is feasible in centrifugal pumps, is by far too coarse to resolve all small scales encountered in bubbly, dispersed flow regimes. It is worth noting that, of course, like VoF methods, level set methods also provide an interface resolution. However, to the best knowledge of the authors, there are no centrifugal pump flow studies employing level set methods.

2.4. Hybrid Two-Phase (H2P) Approach

When using the EE2F and VOF approaches, two limiting morphological situations, encountered in radial centrifugal pumps, are addressed. Regarding the former, a homogeneous mixture is assumed, which means that a multitude of bubbles is dispersed within each computational cell and that the bubble diameter is much smaller than the cell size. This assumption is particularly valid in the bubbly flow region, while it is challenged for adherent air pockets. In particular, the validity of the EE2F model is challenged when the bubble size exceeds the grid scale, as discussed by, for example, Marschall [75]. Hundshagen et al. [56–58] showed that solver convergence issues may arise for the EE2F model, either in large coherent air regions or if the computational grid is very fine, i.e., if the bubble size locally exceeds the size of the computational cell. Regarding VoF schemes, the resolution of all small scales encountered in the bubbly flow region is not feasible with

available computational resources. In Ref. [76], it was shown that, by adopting a hybrid ansatz to pump flow simulations, a transition of bubbly flow to coherent air accumulations could be accounted for even without the tremendous spatial grid resolution required for interface capturing by pure VoF schemes. In the hybrid models by Hänsch et al. [77,78], Meller et al. [79], Yin et al. [80], and Frederix et al. [81], air is treated either as a continuous or a disperse phase. Since CFD simulations of centrifugal pumps comprise complex grids and are computationally expensive, a preferable simple approach of a hybrid model has been adopted for this first application, which means that air is treated as a single phase, irrespective of its morphology. Thus, a local blending of the EE2F and VoF method, in terms of the interface compression, as proposed by, for example, Wardle and Weller [82], Shonibare and Wardle [83] and Mathur et al. [84], seems to be an appropriate choice. This hybrid approach comprises only one single momentum and volume fraction equation set for the air phase, which means that the solution of additional momentum and volume fraction equations for the air phase is omitted. We adopted the hybrid two-phase model of Wardle and Weller [82], with in-house extensions (called the H2P model in the following), including the interface compression concept, for the simulation of two-phase centrifugal pump flows. The capability of the H2P model was demonstrated on a research pump where optical experimental data had been measured by Mansour et al. [26,27]. Based on this data, together with head measurements, the transition from dispersed bubbly flow to air accumulations, termed the bubbly and pocket flow regimes, respectively, was categorized [26,27], as described above in Section 2.1 and summarized in Figure 1. Thus, a unique validation database is available for the H2P approach, which is described in more detail in Section 3 below.

2.5. Turbulence-Scale Resolving Approach and Scale-Adaptive Simulations (SASs)

We assume that inherently unsteady void structures may only inaccurately be resolved by statistical, i.e., unsteady Reynolds-averaged Navier Stokes (URANS) turbulence models. Even for single-phase flow, there are several studies that show the limitations of statistical models and the benefits of scale-resolving models in terms of large-eddy simulations (LES). Examples are the prediction of an inhomogeneous flow distribution at part load [85], head instabilities [86], part load instabilities and flow separation [87–94], tip vortices [95], pressure and velocity fluctuations due to rotor–stator interaction [96–105], as well as entropy production [106]. According to Refs. [107,108], 80% of the spectral energy should be resolved, so an adequately resolved LES demands an extensively high number of computational cells. Therefore, highly-efficient numerical schemes are employed, e.g., in terms of immersed boundary methods, as proposed by Posa et al. [91,92], Kim and Choi [109] and Kye et al. [101], or small Reynolds numbers are investigated, e.g., [103,106]. Posa et al. [97–100] and Kye et al. [101] utilized cylindrical computational grids with up to 500 Mio cells. By a finite-element method, with body-fitted overset grids, Pacot et al. [102] performed simulations at a reduced Reynolds number and estimated a number of $600 \cdot 10^9$ computational cells required for adequate resolution at realistic Reynolds numbers. These examples illustrate the high demands of the simulation method and the spatial resolution required for an adequate LES.

One main issue concerning a wall-resolved LES is the poor prediction of the near wall behavior of resolved quantities by a subgrid scale model, which can be overcome by hybrid URANS-LES turbulence models. Several hybrid methods in terms of detached eddy simulation (DES) [110,111], delayed DES (DDES) [112], Very LES [113], partially-averaged Navier–Stokes (PANS) [114,115] or partially-integrated transport model (PITM) [116] have been proposed. Hybrid turbulence models and, in particular, DES and DDES are increasingly utilized for pump flow simulations as their computational requirements are lower than those of LES [117,118]. In hybrid approaches and in near-wall regions with attached boundary layers, an URANS model is utilized, while, far away from the wall, an LES approach is employed. The local grid density is utilized as a transition criterion between LES and URANS [119]. One drawback of DES may be mesh-induced separation zones [120]. Beyond DDES, this issue has been addressed, e.g., by shielding functions [121,122]. A differ-

ent approach for scale resolution is based on the exact length–scale equation by Rotta [123]. This scale-adaptive class of turbulence models can be understood as a class of enhanced statistical models [124], which may resolve the turbulent structures down to the grid limit. This is achieved by a local reduction of eddy–viscosity based on the von Kárman and integral length scale. According to Jakirlić et al. [125], the local grid resolution may be considered a further model parameter in the hybrid approaches listed above. Related to this assessment, it is interesting to note that, for the SAS, the filter which controls grid resolution is not immediately governed by the local grid resolution but rather by the local von Kármán length scale. A rather broadly used variant of this model is the *k*-*ω*-SST–SAS model [126], which can be understood as an extension of the URANS *k*-*ω*–SST model [120,127] towards scale resolution. A fall-back to an URANS solution in stationary flow regions or regions of low spatial and temporal resolution is an especially convenient way to avoid uncertainties in spectral energy resolution [128]. Several studies have shown the potential of scale-adaptive simulations (SAS) in highly transient pump flows compared to conventional statistical turbulence models, in terms of velocity distributions, pressure fluctuations, and integral characteristics [89,93,129–132]. The present authors have also demonstrated the benefit of scale-adaptive simulations in single-phase flow in a centrifugal pump [133] and a pump mixer [134]. It was concluded that the SAS yields a sound prediction of the local flow field at only moderately enhanced computational effort compared to URANS. This observation was confirmed for multiphase flow in a centrifugal pump [74,76] and an impeller channel [58].

3. Recent Enhancement of CFD Methods

3.1. Summary of State-of-the-Art Method Algorithms

As summarized in Section 2, the EE2F and VoF schemes are utilized for the simulation of multiphase flow transport in circumferential pumps. The present authors have also used EE2F [48,52,56–58,135] and VoF [74] approaches in their preceding studies, and these algorithms are briefly summarized here, before we proceed to recent enhancements, in terms of the H2P approach, in Section 3.2. Regarding the EE2F model, an Eulerian approach for the disperse phase is used. A dispersed bubbly air phase is assumed to be mixed within a continuous water phase, which means that each computational cell contains a homogeneous mixture of dispersed bubbles. Separate mass and momentum balance equations for water and air are solved, yielding a separate velocity field for each phase, according to Wardle and Weller [82]:

$$\frac{\partial \alpha_\varphi}{\partial t} + \nabla \cdot \left(\alpha_\varphi \boldsymbol{c}_\varphi\right) + \underbrace{\nabla \cdot \left(\boldsymbol{c}_c \alpha_\varphi \left(1-\alpha_\varphi\right)\right)}_{\text{interface compression term}} = 0 \tag{1}$$

$$\frac{\partial \alpha_\varphi \rho_\varphi \boldsymbol{c}_\varphi}{\partial t} + \nabla \cdot \left(\alpha_\varphi \rho_\varphi \boldsymbol{c}_\varphi \boldsymbol{c}_\varphi^T\right) + \nabla \cdot \left(\alpha_\varphi \rho_\varphi \boldsymbol{R}_\varphi^{\text{eff}}\right) = -\alpha_\varphi \nabla p + M_\varphi + M_{s,\varphi}. \tag{2}$$

Using separate velocity fields is often termed an *inhomogeneous approach* in the literature, e.g., by Yan et al. [60], and should not be confused with the assumption of a homogeneous mixture of two phases in each computational cell. Using separate velocity fields is indispensable to predict a phase separation and air accumulations, and its omission leads to an underestimation of head drop, as has been demonstrated by Yan et al. [60] and shown in Figure 3. Mass transfer between the phases is neglected in Equation (1). Note that the interface compression term in Equation (1) is also omitted in the pure EE2F model, but is noted here to facilitate the summary of the VoF algorithm further below. The diffusive mass transport is neglected, an assumption that is justified by a Peclet number higher than 100 for the investigated pump flow. The volume fraction, density, and velocity of phase φ are symbolized by α_φ, ρ_φ, and $\boldsymbol{c}_\varphi$, respectively, and $\boldsymbol{R}_\varphi^{\text{eff}}$ represents the stress tensor combining Reynolds (turbulent) and viscous stresses. Note that indicating Reynolds averaged quantities is omitted here for convenience. The sets of momentum equations are coupled by interfacial momentum transfer forces. The interfacial momentum

transfer terms, i.e., drag and virtual mass force, are represented by M_φ, while $M_{s,\varphi}$ is the surface tension force. Regarding M_φ, the drag force $M_{\mathrm{a,D}}$ and the virtual mass force $M_{\mathrm{a,vm}}$ dominate all other interfacial forces [37], so that only these forces are considered here. In the pure EE2F model, $M_{s,\varphi}$ is set to zero. The drag coefficient is evaluated according to Schiller and Naumann [136], and the virtual mass force coefficient is set constant to 0.5, according to Refs. [137,138]. A separate turbulence field is applied for both phases, i.e., balance equations for turbulence kinetic energy k_φ and turbulence specific dissipation ω_φ are solved for both phases. Both phases share the same pressure field, which means that a single mixture continuity equation, in terms of a pressure Poisson equation, is solved.

Thus, in the EE2F approach, and also in the H2P approach (the latter being presented further below), two sets of conservation equations are solved, which means one set for each phase φ. In the VoF approach, typically, one single set of conservation equations is solved, formally obtained by summing up the momentum equations of both phases (Equation (2)) and setting φ to mixture properties, assuming a common velocity and pressure field for both phases in the entire flow domain. A mass balance equation is solved for water, while the volume fraction of the air phase is calculated by $\alpha_\mathrm{a} = 1 - \alpha_\mathrm{w}$. The water/air interface is sharply resolved by an interface sharpening process [82] (interface compression term in Equation (1)) that counteracts the numerical diffusion and which is explicated in more detail in Section 3.2. For VoF, the surface tension force $M_{s,\varphi}$ is considered as a continuum force, according to Brackbill et al. [139], with a constant surface tension factor between water and air of 0.07275 (see also Equation (5) in Section 3.2), and M_φ is set to zero.

For both EE2F and VoF schemes, both phases are treated as incompressible fluids with a density of $\rho_\mathrm{w} = 998\ \mathrm{kg/m^3}$ and $\rho_\mathrm{a} = 1.185\ \mathrm{kg/m^3}$, which was justified, for example, by Hundshagen et al. [56–58,74,76]. The results hardly deviate when the air phase is treated compressible or incompressible, which was shown by Müller et al. [48] for the EE2F approach, and which is also assumed for the VoF and H2P approaches. The flow is assumed to be isothermal, so that a constant temperature of 25°C was chosen, omitting the energy conservation equation. Both EE2F and VoF schemes were implemented in *OpenFOAM* in different solvers, which were customized, where applicable, for example, for moving grid capabilities [74]. The EE2F and VoF implementations are based on *OpenFOAM* version 6 within the *reactingMultiphaseEulerFoam* and *interFoam* solver, respectively.

3.2. Hybrid Two-Phase (H2P) Approach

Recently, we presented an enhanced EE2F model with the capability of local phase interface resolution [76,140], so it locally works like a VoF scheme. The functionality of this hybrid scheme is best demonstrated by the interface compression term in Equation (1). To enable an interface resolution, according to Wardle and Weller [82], a correction flux at the phase interface is introduced in terms of interface compression. This correction flux is added in Equation (1) in the interface compression term by introducing the compression velocity $\boldsymbol{c}_\mathbf{c}$ and the volume fraction term $\alpha_\varphi(1-\alpha_\varphi)$. The compression velocity $\boldsymbol{c}_\mathbf{c}$ counteracts the numerical diffusion at the phase interface to prohibit interface smearing and to maintain a sharp interface. It is estimated by the blending function C_α, and the magnitude of the mixture velocity $|\boldsymbol{c}_\mathbf{m}|$ yielding:

$$\boldsymbol{c}_\mathrm{c} = C_\alpha\,|\boldsymbol{c}_\mathbf{m}|\,\frac{\nabla\alpha}{|\nabla\alpha|}. \tag{3}$$

The ratio $\nabla\alpha/|\nabla\alpha|$ affects that the interface compression term acts orthogonally to the phase interface, while $\alpha_\varphi(1-\alpha_\varphi)$ in Equation (1) ensures that the interface compression term essentially acts in proximity of the phase interface. The mixture velocity $\boldsymbol{c}_\mathbf{m}$ is calculated by a volume fraction-average of water and air velocity. For the evaluation of C_α in Equation (3), a blending function adopted from Hänsch et al. [77] is implemented:

$$C_\alpha = [\,0.5\tanh(\mathrm{a_B}(\alpha_\mathrm{a} - \mathrm{a_{min}})) + 0.5\,][\,0.5\tanh(\mathrm{a_B}\,(\mathrm{a_{max}} - \alpha_\mathrm{a})) + 0.5\,]. \tag{4}$$

In the limiting case $C_\alpha = 0$, the original EE2F formulation is retained, while with $C_\alpha = 1$, a VOF-like interface resolution is applied. At this point, it is important to mention that for pure VoF schemes, as described in Section 3.1, no blending for C_α is applied. Hence, a constant value of $C_\alpha = 1$ is set [141]. A second difference between pure VoF and H2P schemes is that, for VoF, only one set of mass and momentum equations is solved, while for H2P, one mass and momentum equation is solved for each phase.

The surface tension force $M_{s,\varphi}$ in Equation (2) is considered as a continuum force, according to Brackbill et al. [139], and reads:

$$M_{s,\varphi} = C_\alpha \sigma \kappa_\varphi \nabla \alpha_\varphi. \tag{5}$$

The surface tension factor for a water/air system and the interface curvature are $\sigma = 0.07275$ and $\kappa_\varphi = -\nabla\left(\frac{\nabla \alpha_\varphi}{|\nabla \alpha_\varphi|}\right)$ [82]. $M_{s,\varphi}$ is also blended with C_α according to Equation (5), so that the surface tension force is only active in regions where C_α differs from the value zero, which means that the phase interface resolving mode is activated.

In the dispersed phase (subscript $\varphi = \mathrm{a}$), dispersed air bubbles are mixed within a continuous water phase (subscript $\varphi = \mathrm{w}$). The momentum equations (Equation (2)) for each of the two phases φ are coupled by the forces M_φ. As already noted for the EE2F model in Section 3.1, the drag force $M_{\mathrm{a,D}}$ and the virtual mass force $M_{\mathrm{a,vm}}$ dominate all other interfacial forces [62], so only these forces were considered here. While the expression for $M_{\mathrm{a,vm}}$ is presented elsewhere [76], we note, for the drag force:

$$M_{\mathrm{a,D}} = \frac{3}{4} C_\beta \frac{\rho_\mathrm{w}}{d_\mathrm{B}} \alpha_\mathrm{a} C_\mathrm{D} |\boldsymbol{c}_\mathrm{w} - \boldsymbol{c}_\mathrm{a}| (\boldsymbol{c}_\mathrm{w} - \boldsymbol{c}_\mathrm{a}). \tag{6}$$

d_B is the bubble diameter and is explained further below in Section 3.3. In Equation (6), a second blending function C_β is used, adopted from Ref. [142] and customized for the H2P solver in Ref. [76]. C_β reads:

$$C_\beta = \min\left(\max\left(\frac{(1-\alpha_\mathrm{a})\mathrm{b_{max}}}{(1-\mathrm{b_{max}})\alpha_\mathrm{a}}, \frac{\mathrm{b_{min}}}{\alpha_\mathrm{a}}\right), 1\right). \tag{7}$$

This drag blending affects that the drag formulation is only active in the dispersed part of the flow and turned off within air accumulations, which is equivalent to the assumption that, inside air accumulations, only a continuous air phase is present while there is no dispersed water in the form of droplets. We set the constants to $\mathrm{b_{min}} = 10^{-4}$ and $\mathrm{b_{max}} = 0.8$. Thus, air accumulations were assumed to be present in a range of air volume fraction between 0.8 and 1.0.

In terms of Equations (4) and (7), different blending functions C_α and C_β were used for interface compression and drag. The particular functional and the constants of C_α and C_β were chosen and implemented to achieve stability for the complex centrifugal pump flow. Using the same blending function for interface compression and drag might be more consistent, as has been proposed, e.g., by De Santis et al. [73,143] and Mathur et al. [84]. To be more precise, we used two different blending functions in terms of C_α and C_β since we encountered stability issues when using C_α for drag as well. This is traced back to the complex grid and flow field of the centrifugal pump. Therefore, for the sake of simplicity, we limited the dispersed drag force to a low finite value by clipping C_β to 10^{-4} in regions of air accumulations, i.e., $\alpha_\mathrm{a} > 0.8$. A further optimization of C_α and C_β is left for future work.

The hybrid model described above was implemented in *OpenFOAM* versions 6 and 9 as an extension of the EE2F model within the *reactingMultiphaseEulerFoam* and *multiphaseEulerFoam* solver. It was the first time it was adopted for centrifugal pump flow and certainly leaves potential for further improvements. In the literature, more sophisticated hybrid multiphase approaches have been reported, such as the generalized multiphase modeling approach (GEMMA) of De Santis et al. and Colombo et al. [73,143,144] and the hybrid multi-scale model of Meller et al. [79]. The GEMMA model fundamentally deviates from the one described here by including an interfacial drag formulation for large-

scale interfaces, which was first proposed by Marschall [75] within the EE2F framework. Meller et al. [79] coupled two continuous phases by applying a drag model of Štrubelj and Tiselj [145]. The GEMMA model also introduced an interface resolution criterion, which was first described in Ref. [83] and is based on the ratio of local cell size V_c to the Sauter mean diameter of the dispersed phase d_{32}. The interphase compression term is activated when the criterion $d_{32}/V_c > \Gamma$ is fulfilled. The constant Γ is set to a value of ten [73,83,143], which may be case-dependent. Thus, the GEMMA model deviates from our approach also by including the droplet size in the blending function formulation. Both the GEMMA model and the ansatz of Meller et al. [79] should be tested for centrifugal pump flow in future studies.

3.3. Population Balance Model (PBM)

Optical measurement data by Mansour and Parikh et al. [24–27,69], and described in Part B of this review paper series, suggest a polydisperse bubble size distribution within the pump, which means that dispersed bubbles have a spectrum of properties. As summarized in Section 2.2, several authors [59–65] coupled an EE2F method with a population balance model (PBM) [146,147]. Thereby, an additional transport equation for the specific number density $n_B(d_B)$ of bubbles is solved. Beyond the transport of $n_B(d_B)$, birth and death rates due to coalescence and breakup of bubbles with diameter d_B are treated by source and sink terms. We adopted the *OpenFOAM* implementation of the PBM of Lehnigk et al. [148] and merge it into the dispersed part of the hybrid H2P solver. By adopting the approach of Kumar & Ramkrishna [149], the population balance equation is discretized in definite size groups, leading to the class method of Lo [146], also referred to as the multi-size group (MUSIG) model [147,150]. The coalescence kernel of Prince & Blanch [151] and the breakup kernel of Luo & Svendsen [152] were chosen. The coalescence model was extended by following Liao et al. [153], resulting in a formulation similar to the one suggested by Stel et al. [61] for the simulation of a liquid/gas centrifugal rotor flow. The kernels comprise empirical parameters, which were not adapted but retained at the original values suggested by Refs. [151,152]. From the resulting bubble size distribution, a statistical mean, in terms of d_{32}, is evaluated and enters the disperse part of the H2P, as, for example, in Equation (6).

3.4. Simulation Method

Preferably, customized versions of *OpenFOAM* were used as a software platform for our CFD simulations of multiphase flow in centrifugal pumps or pump mixers [74,76,154]. The implementation employed the Pressure Implicit with Splitting of Operators (PISO) algorithm of Jasak [155]. The PISO scheme works like a quasi-explicit solver and has turned out to be particularly efficient for small time steps, corresponding to a convective Courant–Friedrich–Lewy number not exceeding 0.5 [155]. For larger time steps, non-linear iteration loops and an under-relaxation were performed, resulting in the well-established PIMPLE algorithm, a combination of the PISO and Semi-Implicit Pressure Method for Pressure Linked Equations (SIMPLE) scheme, introduced by [156]. Discretization of convective terms was performed by second order Total Variation Diminshing (TVD) schemes. Particular care was taken when turbulence scale-resolving models, such as SAS, were used. Customized hybrid discretization schemes are used for adequate scale resolution, as described elsewhere [76,133].

4. Example Application of The Hybrid Two-Phase (H2P) Model

4.1. Test Case and Simulation Setup

A research pump with a semi-open impeller and 2D-blading, i.e., six cylindrical (non-twisted) blades, was investigated. The pump head $H = \Delta p/(\rho_w g) + \Delta z$ was evaluated by the static pressure and height difference Δp and Δz, respectively, between suction and pressure port. Beyond pump head and flow rate measurements, resulting in performance maps, according to Figure 1, high-speed visualization of the two-phase flow structures was performed by means of the scattered-light technique. Therefore, the im-

peller and the casing were manufactured from transparent acrylic glass to obtain optical access. Experiments were performed by Mansour et al. [26,27] at reduced rotational speed $n = 650\,1/\text{min}$ to avoid damage of acrylic components. Details of the experiments are provided elsewhere [24–27,39,56,58,76], as well as in the accompanying experimental Part B of this review paper series.

The simulation domain is depicted in Figure 6a. A preferably realistic image of the real geometry was aimed at, so that the domain includes the impeller, suction and pressure pipe, volute casing, and side chamber. To capture the rotor–stator interaction and to account for any unsteady effects, unsteady pump simulations in the absolute frame of reference and with moving impeller mesh were performed, and the arbitrary mesh interface of Farrell and Maddison [157] was used. The SAS turbulence model, as described in Section 2.5, was applied. Velocity and pressure were prescribed as Dirichlet boundary conditions at the inlet and outlet of the computational domain, respectively. Dispersed air bubbles were assumed at the inlet, which were prescribed in terms of a Dirichlet condition for α_φ and $d_\text{B} = 0.5\,\text{mm}$. The operation points considered in the simulation are indicated above in Figure 1. By having this range of operation conditions, all flow regimes from bubbly flow via agglomerated bubbles and alternating pocket flow to pure pocket flow were covered.

Particular care was taken for computational grid generation. By a grid refinement, first of all, the accuracy of the discretization scheme rose. At the same time, grid refinement also affected the turbulence and two-phase models. On the one hand, the turbulence scale-resolution capability of the SAS was enhanced, since turbulent fluctuations could be resolved down to the local grid resolution. On the other hand, successively finer void structures were resolved by the H2P solver, which transitioned towards a VoF-like scheme with phase–interface resolving capabilities. Thus, an inherent grid dependence of the results could not be avoided. What is more, the complex geometry of circumferential pumps required special care with regard to grid quality. For example, the meshing of round trailing edges or narrow gaps in semi-open impellers is particularly demanding [56–58]. Despite the considerable effort for grid generation, we prefer hexahedral cell grids wherever applicable due to their higher accuracy than, for example, triangular cells. Peculiarities of grid generation are provided in Refs. [56–58,76] and are not all repeated here. A grid study was performed, and the preferred computational grid, for which the results are presented further below, had about 16 Mio cells. A coarser version of the grid is shown in Figure 6b–d. Visually, smoothness and orthogonality appear to be poor. However, non-dimensional grid quality criteria, in terms of maximum non-orthogonality and minimum face volume ratio, were adopted from the *OpenFOAM* nomenclature [155] and indicated a fairly high quality, taking into account the complexity of the pump geometry. It was ensured that the conclusions drawn from the simulation results were not affected by grid dependence. Details of the simulation setup and the grid study are presented elsewhere [76].

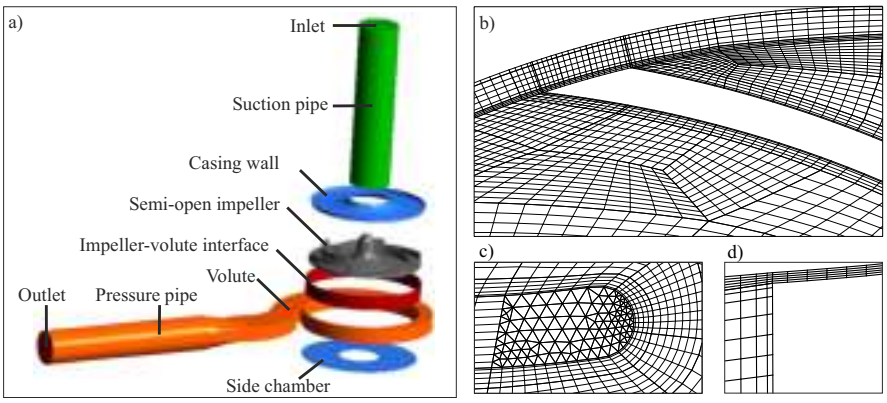

Figure 6. Explosion view of the computational domain (**a**). Detailed view of the impeller grid near the blade trailing edge at midspan (**b**), in the tip clearance gap at the leading edge from axial view direction (**c**), and in the tip clearance gap from radial view direction (**d**).

4.2. Selected Results

Selected results obtained by the H2P model in combination with the PBM are presented here. In Figure 7, the pump head drop by a rise of the inlet gas volume fraction ε is demonstrated. Albeit there were remaining differences to the experimental result, the trend was captured well at the first attempt. This is remarkable since, by means of a monodisperse ansatz, the predicted head level in the simulation can immediately be tuned to the experimental data by the prescribed bubble size d_B [56–58]. In fact, for the applied grid resolution, a value of $d_B = 2.0\,\text{mm}$ also yielded a reasonable head drop curve. Obviously, by using the PBM, a reasonable bubble size distribution was obtained without the need for tuning, which affected proper head drop characteristics. What is more, solver robustness was enhanced by the PBM, compared to the use of a constant value of d_B, which we trace back to the fact that, in flow regions with small cell size, shear and, thus, bubble breakup were enhanced, and bubbles larger than the computational cells occurred less often.

The air accumulation is visualized in Figure 8a by means of the ensemble-averaged experimental results of a gray-scale analysis. With rising ε, air successively accumulated at the blade suction side, which, in turn, caused a head drop. Air accumulation was observable for $\varepsilon = 1\%$ neither in the experimental nor in the simulation result. For $\varepsilon = 3\%$, the air started to agglomerate at the suction side of the blade. For $\varepsilon = 4\%$, the tendency of water and air to separate within the blade channel further increased. Air accumulations formed at the blade suction side near the leading edge. It is interesting that the accumulations were observable at every second blade in the simulation result. This behavior, in fact, reflects the alternating pocket flow regime, as discussed in detail by Hundshagen et al. [76]. For $\varepsilon = 5\%$, the air accumulations were attached at each blade and increased in size, which was, again, in good agreement with the experimentally observed trend. Summarizing, the size of air accumulations was captured well by the simulations, according to Figure 8b. Again, it should be pointed out that these accumulations developed without further tuning of the simulation parameters in terms of, for example, coalescence and breakup parameters.

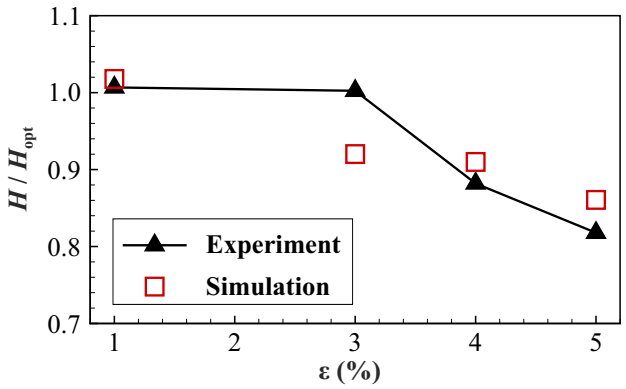

Figure 7. Normalized pump head H versus inlet gas volume fraction ε. Experimental values are taken from Mansour et al. [27,39].

Thus, from $\varepsilon = 1\%$ to $\varepsilon = 5\%$, a transition from the bubbly flow regime over the agglomerated bubbles flow regime to the pocket flow regime was observed. In Figure 8c, the standard deviation of the air volume fraction, in terms of $\alpha_{a,RMS}$, is depicted. In the agglomerated bubbles flow regime for $\varepsilon = 3\%$, the bubble clustering was highly unsteady since the highest values of $\alpha_{a,RMS}$ were observable in regions having the highest values of α_a. In the alternating pocket flow regime at $\varepsilon = 4\%$, the air pocket, attached only at every second blade, was steady according to the low $\alpha_{a,RMS}$ level within the attachment zone. At the other blades, local maxima of $\alpha_{a,RMS}$ were present at the same blade location (as in the agglomerated bubbles flow regime at every blade), which, in fact, reflected the unsteady behavior of the alternating pocket flow regime. With a rising value of ε from $\varepsilon = 3\%$ to $\varepsilon = 5\%$, the values of $\alpha_{a,RMS}$ successively decreased in the region of air accumulations,

which meant that the accumulations became more and more steady. The highest values of $\alpha_{a,RMS}$ were present in the wake of the accumulations, which corresponded to the experimental observations of an unsteady wake and underlined the benefit of using a scale-resolving turbulence model.

In Figure 9a, the Sauter mean diameter d_{32} of the bubbles is shown, and is, again, evaluated from the simulation results at mid-span. A cross-check to Figure 8b reveals that the location of large bubble diameter correlated with air accumulation zones, which meant that preferably large bubbles accumulated. A more detailed look at the coalescence kernel outcome (not shown here) showed high kernel activity in these regions, so that a self-energizing effect was present, leading to enforced growth of the accumulation. A look at the blending function C_β, according to Equation (7), which is illustrated in Figure 9b, by an isosurface $C_\beta = 0.8$ revealed that the H2P solver worked in a VoF-like mode in the accumulation regions. It is important to point out that by the transition of the solver towards VoF within the accumulation zones, the dispersed nature of the mixture had locally faded out, and the physical meaning of d_B and, thus, d_{32} degenerated. In fact, the diameter mutated into a purely numerical variable with a diminishing feedback to the local flow solution. It is interesting to note that no special means had to be applied to enhance solver stability in these flow situations. Thus, the air accumulations were treated in a reasonable way by a combination of an EE2F and VoF approach in terms of the H2P solver.

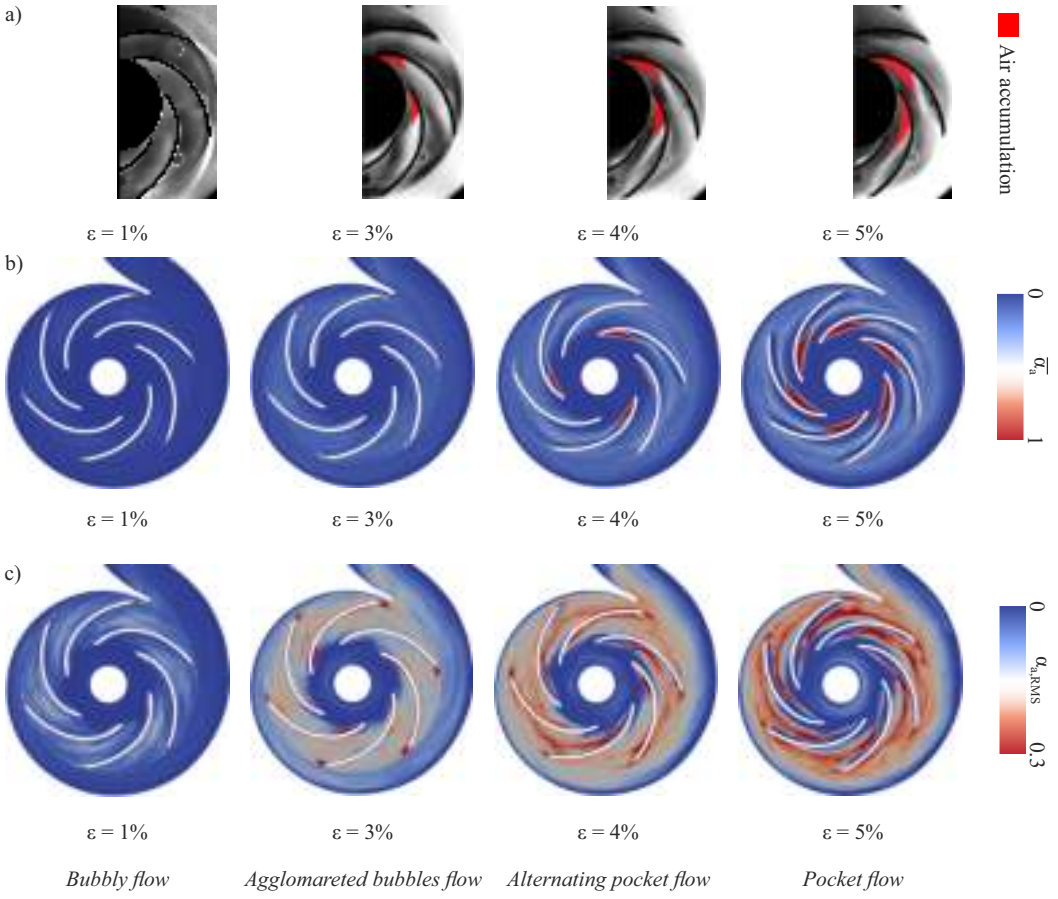

Figure 8. Air distribution in the impeller: ensemble-averaged experimental results of a gray-scale analysis (**a**). Time-averaged air volume fraction at impeller midspan (**b**) and its standard deviation (**c**), obtained from simulation results.

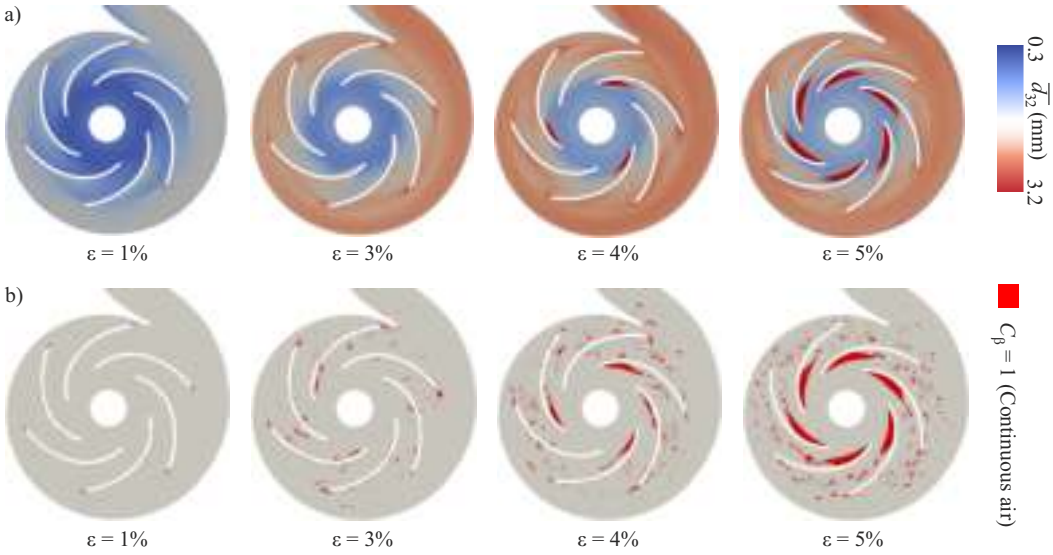

Figure 9. Contour plots at impeller midspan for the time-averaged Sauter mean diameter d_{32} (**a**) and isosurfaces of a blending function threshold value $C_\beta = 1.0$ (**b**).

5. Conclusions

We have pointed out the limitations of recent approaches for the 3D simulation of liquid/gas flow in centrifugal pumps. On the one hand, the resolution of all phase interfaces by Volume-of-Fluid (VoF) methods is not feasible, so that this kind of approach is confined to the resolution of large coherent air accumulations. On the other hand, Euler–Euler Two-Fluid (EE2F) models treat dispersed bubbles on a subgrid level. Inspired by CFD approaches resulting from chemical and process engineering research [73,77–79,82–84,143,144,158,159], a hybrid method (H2P) is suggested, which is based on an EE2F scheme in most regions of the flow field, and transitions to VoF-like resolution, when air accumulations are detected. The H2P is combined with a population balance model (PBM) to capture bubble size distribution in flow regions with dispersed bubbles, i.e., where the H2P works in the pure EE2F mode. It was shown that coalescence activities correlate with air accumulations, which means that, in accumulation zones, bubbles grow by coalescence, leading to large air pockets. By means of this approach, the transition of flow regimes from bubbly to pocket flow detected in the experiments could, for the first time, be reproduced in 3D flow simulations. The importance of a scale-resolving turbulence approach to capture unsteady wakes downstream of the air pockets was shown. In spite of this quite promising first application of the H2P scheme to centrifugal pumps [76], and rather generic diffusor flows [140], improvements, for example in regard to blending functions, are suggested for future work. The PBM, particularly the breakup and coalescence kernels, have, so far, simply been adopted from completely different applications, such as bubble columns, and should be tailored for centrifugal pump flow applications in the future. In future studies, it should also be assessed if the H2P method, in fact, converges to a VoF solution with excessive grid refinement.

Author Contributions: Conceptualization, M.H. and R.S.; methodology, M.H. and R.S.; software, M.H.; investigation, M.H. and R.S.; writing—original draft preparation, M.H. and R.S.; writing—review and editing, M.H. and R.S.; supervision, R.S.; funding acquisition, R.S. All authors have read and agreed to the published version of the manuscript.

Funding: The research project was carried out in the framework of the industrial collective research program (IGF no. 20638 BG). It was supported by the Federal Ministry for Economic Affairs and Climate Action (BMWK) through the AiF (German Federation of Industrial Research Associations eV), based on a decision taken by the German Bundestag. Simulations of Section 4 were performed with computing resources granted by RWTH Aachen University under project bund0013.

Acknowledgments: We gratefully thank Michael Mansour and Dominique Thévenin (University of Magdeburg "Otto-von-Güricke") for providing the measurement data of the research pump. We also

gratefully acknowledge Christian Hasse and Bich-Diep Nguyen (TU Darmstadt) for their valuable contribution to the hybrid solver development.

Conflicts of Interest: The authors declare no conflict of interest.

Nomenclature and Abbreviations

The following *nomenclature* is used in this manuscript:

Roman characters

$a_{(\mathrm{min,max,B})}$	Model constants for C_α	(-)
$b_{(\mathrm{min,max})}$	Model constants for C_β	(-)
$\boldsymbol{c}$	Velocity vector	(m/s)
C_α & C_β	Blending functions	(-)
C_D	Drag coefficient	(-)
C_p	Pressure increment coefficient	(-)
d	Diameter	(m)
d_{32}	Sauter mean diameter	(m)
H	Pump head	(m)
k	Turbulence kinetic energy	($\mathrm{m^2/s^2}$)
M	Momentum transfer terms	($\mathrm{kg\,m/s^2}$)
M_s	Surface tension force	($\mathrm{kg\,m/s^2}$)
n	Rotational speed	(1/s)
n_B	Bubble number density function	($\mathrm{1/m^3}$)
p	Pressure	(Pa)
Q	Volume flow rate	($\mathrm{m^3/s}$)
$\boldsymbol{R}^{eff}$	Effective stress tensor	($\mathrm{kg\,m/s^2}$)
V_c	Cell volume	($\mathrm{m^3}$)

Greek characters

α	Volume fraction	(-)
$\frac{\partial}{\partial t}$	Temporal derivative	(1/s)
Δ	Difference	(-)
ε	Inlet gas volume fraction	(-)
κ	Curvature	(1/m)
λ_g	Inlet gas volume fraction	(-)
∇	Divergence operator	(1/m)
ω	Specific dissipation	(1/s)
φ	Flow coefficient	(-)
ρ	Density	($\mathrm{kg/m^3}$)
σ	Surface tension factor	(-)
Ψ	Stage pressure coefficient	(-)
Γ	Constant	(-)

Subscripts

a	Air
B	Bubble
Exp	Experimental result
m	Mixture
opt	Optimal
RMS	Standard deviation
Sim	Simulation result
t	Total
w	Water
φ	Arbitrary phase

The following abbreviations are used in this manuscript:

3D	Three-dimensional
C1 to C6	Operation points in the study of Yan et al. [60]
CFD	Computational fluid dynamics
DES	Detached eddy simulation
DDES	Delayed DES
EE2F	Euler–Euler Two-Fluid
ESP	Electrical submersible pump
GEMMA	Generalized multiphase modeling approach
H2P	Hybrid Two-Phase
Hom.	Homogeneous
Inhom.	Inhomogeneous
LES	Large-eddy simulation
MUSIG	Multi-size group
PANS	Partially-averaged Navier–Stokes
PBM	Population balance modeling
PIMPLE	Combination of PISO and SIMPLE algorithm
PISO	Pressure Implicit with Splitting of Operators
PITM	Partially-integrated transport model
SIMPLE	Semi-Implicit Pressure Method for Pressure Linked Equations
SAS	Scale-adaptive simulation
SST	Shear Stress transport
TVD	Total variation diminishing
URANS	Unsteady Reynolds-averaged Navier Stokes
VoF	Volume-of-Fluid

References

1. Chan, A.; Kawaji, M.; Nakamura, H.; Kukita, Y. Experimental study of two-phase pump performance using a full size nuclear reactor pump. *Nucl. Eng. Des.* **1999**, *193*, 159–172. [CrossRef]
2. Amoresano, A.; Langella, G.; Niola, V.; Quaremba, G. Advanced Image Analysis of Two-Phase Flow inside a Centrifugal Pump. *Adv. Mech. Eng.* **2014**, *6*. [CrossRef]
3. Cappelino, C.A.; Roll, D.R.; Wilson, G. Design considerations and application guidelines for pumping liquids with entrained gas using open impeller centrifugal pump. In Proceedings of the 9th International Pump User Symposium, Houston, TX, USA, 24–27 September 2012; pp. 51–60. [CrossRef]
4. Monte Verde, W.; Biazussi, J.L.; Sassim, N.A.; Bannwart, A.C. Experimental study of gas-liquid two-phase flow patterns within centrifugal pumps impellers. *Exp. Therm. Fluid Sci.* **2017**, *85*, 37–51. [CrossRef]
5. Murakami, M.; Minemura, K. Effects of Entrained Air on the Performance of a Centrifugal Pump: 1st Report, Performance and Flow Conditions. *Bull. JSME* **1974**, *17*, 1047–1055. [CrossRef]
6. Murakami, M.; Minemura, K.; Suehiro, H. Effects of entrained air on the performance of centrifugal and axial flow pumps. *Mem. Fac. Eng. Kyushu Univ.* **1971**, 124–133.
7. Furukawa, A.; Togoe, T.; Sato, S.; Takamatsu, Y. Fundamental studies on a tandem bladed impeller of gas/liquid two-phase flow centrifugal pump. *Mem. Fac. Eng. Kyushu Univ.* **1988**, *48*, 231–240. [CrossRef]
8. Tillack, P. Förderverhalten von Kreiselpumpen bei viskosem, gasbeladenem Fördermedium. Ph.D. Thesis, Technical University Kaiserslautern, Kaiserslautern, Germany, 1998.
9. Gülich, J.F. *Centrifugal Pumps*; Springer: Berlin/Heidelberg, Germany, 2010. [CrossRef]
10. Sato, S.; Furukawa, A.; Takamatsu, Y. Air-water two-phase flow performance of centrifugal pump impellers with various blade angles. *JSME Int. J., Ser. B* **1996**, *39*, 223–229. [CrossRef]
11. Zhu, J.; Zhang, H.Q. A Review of Experiments and Modeling of Gas-Liquid Flow in Electrical Submersible Pumps. *Energies* **2018**, *11*. [CrossRef]
12. Iben, U.; Wolf, F.; Freudigmann, H.A.; Fröhlich, J.; Heller, W. Optical measurements of gas bubbles in oil behind a cavitating micro-orifice flow. *Exp. Fluids* **2015**, *56*, 114. [CrossRef]
13. Freudigmann, H.A.; Iben, U.; Pelz, P.F. Air release measurements of V-oil 1404 downstream of a micro orifice at choked flow conditions. *J. Phys. Conf. Ser.* **2015**, *656*, 12113. [CrossRef]
14. Freudigmann, H.A.; Dörr, A.; Iben, U.; Pelz, P.F. Modeling of Cavitation-Induced Air Release Phenomena in Micro-Orifice Flows. *ASME J. Fluids Eng.* **2017**, *139*, 111301 . [CrossRef]
15. Kowalski, K.; Pollak, S.; Skoda, R.; Hussong, J. Experimental Study on Cavitation-Induced Air Release in Orifice Flows. *ASME J. Fluids Eng.* **2018**, *140*, 61201. [CrossRef]

16. Frobenius, M.; Schilling, R.; Friedrichs, J.; Kosyna, G. Numerical and Experimental Investigations of the Cavitating Flow in a Centrifugal Pump Impeller. In Proceedings of the 2002 ASME Joint U.S.-European Fluids Engineering Conference, Montreal, QC, Canada, 14–18 July 2002; Rohatgi, U.S., Ed.; American Society of Mechanical Engineers: New York, NY, USA, 2002; pp. 361–368. [CrossRef]
17. Limbach, P.; Kimoto, M.; Deimel, C.; Skoda, R. Numerical 3D Simulation of the Cavitating Flow in a Centrifugal Pump With Low Specific Speed and Evaluation of the Suction Head. In Proceedings of the ASME Turbo Expo 2014: Turbine Technical Conference and Exposition, Düsseldorf, Germany, 16–20 June 2014. [CrossRef]
18. Limbach, P.; Müller, T.; Blume, M.; Skoda, R. Numerical and Experimental Investigation of the Cavitating Flow in a Low Specific Speed Centrifugal Pump and Assessment of the Influence of Surface Roughness on Head Prediction. In Proceedings of the International Symposium on Transport Phenomena and Dynamics (ISROMAC), Honululu, HI, USA, 10–15 April 2016.
19. Limbach, P.; Skoda, R. Numerical and Experimental Analysis of Cavitating Flow in a Low Specific Speed Centrifugal Pump With Different Surface Roughness. *ASME J. Fluids Eng.* **2017**, *139*, 101201. [CrossRef]
20. Liu, H.l.; Wang, J.; Wang, Y.; Zhang, H.; Huang, H. Influence of the empirical coefficients of cavitation model on predicting cavitating flow in the centrifugal pump. *Int. J. Nav. Archit. Ocean Eng.* **2014**, *6*, 119–131. [CrossRef]
21. Shi, W.; Wang, C.; Wang, W.; Pei, B. Numerical Calculation on Cavitation Pressure Pulsation in Centrifugal Pump. *Adv. Mech. Eng.* **2014**, *6*, 367631. [CrossRef]
22. Zhang, D.; Shi, W.; Pan, D.; Dubuisson, M. Numerical and Experimental Investigation of Tip Leakage Vortex Cavitation Patterns and Mechanisms in an Axial Flow Pump. *ASME J. Fluids Eng.* **2015**, *137*, 121103. [CrossRef]
23. Mousmoulis, G.; Karlsen-Davies, N.; Aggidis, G.; Anagnostopoulos, J.; Papantonis, D. Experimental analysis of the onset and development of cavitation in a centrifugal pump. *J. Phys. Conf. Ser.* **2017**, *813*, 12044. [CrossRef]
24. Mansour, M.; Wunderlich, B.; Thévenin, D. Effect of tip clearance gap and inducer on the transport of two-phase air-water flows by centrifugal pumps. *Exp. Therm. Fluid Sci.* **2018**, *99*, 487–509. [CrossRef]
25. Mansour, M.; Wunderlich, B.; Thévenin, D. Experimental Study of Two-Phase Air/Water Flow in a Centrifugal Pump Working With a Closed or a Semi-Open Impeller. In Proceedings of the ASME Turbo Expo 2018: Turbine Technical Conference and Exposition, Oslo, Norway, 11–15 June 2018; The American Society of Mechanical Engineers: New York, NY, USA, 2018. [CrossRef]
26. Mansour, M.; Parikh, T.; Thévenin, D. Influence of the shape of the impeller blade trailing edge on single and two-phase air water flows in a centrifugal pump. In Proceedings of the Turbomachinery & Pump Symposia, Houston, TX, USA, 13–16 December 2020.
27. Mansour, M.; Kopparthy, S.; Thévenin, D. Investigations on the effect of rotational speed on the transport of air-water two-phase flows by centrifugal pumps. *Int. J. Heat Fluid Flow* **2022**, *94*, 108939. [CrossRef]
28. Bieberle, A.; Schäfer, T.; Neumann, M.; Hampel, U. Validation of high-resolution gamma-ray computed tomography for quantitative gas holdup measurements in centrifugal pumps. *Meas. Sci. Technol.* **2015**, *26*, 95304. [CrossRef]
29. Schäfer, T.; Bieberle, A.; Neumann, M.; Hampel, U. Application of gamma-ray computed tomography for the analysis of gas holdup distributions in centrifugal pumps. *Flow Meas. Instrum.* **2015**, *46*, 262–267. [CrossRef]
30. Neumann, M.; Schäfer, T.; Bieberle, A.; Hampel, U. An Experimental Study on the Gas Entrainment in Horizontally and Vertically Installed Centrifugal Pumps. *ASME J. Fluids Eng.* **2016**, *138*, 12–19. [CrossRef]
31. Schäfer, T.; Neumann, M.; Bieberle, A.; Hampel, U. Experimental investigations on a common centrifugal pump operating under gas entrainment conditions. *Nucl. Eng. Des.* **2017**, *316*, 1–8. [CrossRef]
32. Schäfer, T.; Neumann-Kipping, M.; Bieberle, A.; Bieberle, M.; Hampel, U. Ultrafast X-Ray Computed Tomography Imaging for Hydrodynamic Investigations of Gas–Liquid Two-Phase Flow in Centrifugal Pumps. *ASME J. Fluids Eng.* **2020**, *142*, 41502. [CrossRef]
33. Gambao, J.; Prado, M.G. Visualization study of performance breakdown in two-phase performance of an electrical submersible pump. In Proceedings of the Twenty-Sixth International Pump User Symposium, Houston, TX, USA, 26–28 September 2010. [CrossRef]
34. Barrios, L.; Prado, M.G. Experimental Visualization of Two-Phase Flow Inside an Electrical Submersible Pump Stage. *J. Energy Resour. Technol.* **2011**, *133*, 42901. [CrossRef]
35. Trevisan, F.E.; Prado, M. Experimental Investigation of the Viscous Effect on Two-Phase-Flow Patterns and Hydraulic Performance of Electrical Submersible Pumps. *J. Can. Pet. Technol.* **2011**, *50*, 45–52. [CrossRef]
36. Shao, C.; Li, C.; Zhou, J. Experimental investigation of flow patterns and external performance of a centrifugal pump that transports gas-liquid two-phase mixtures. *Int. J. Heat Fluid Flow* **2018**, *71*, 460–469. [CrossRef]
37. Stel, H.; Ofuchi, E.M.; Alves, R.F.; Chiva, S.; Morales, R.E.M. Experimental Analysis of Gas–Liquid Flows in a Centrifugal Rotor. *ASME J. Fluids Eng.* **2020**, *142*, 31101. [CrossRef]
38. Zhao, L.; Chang, Z.; Zhang, Z.; Huang, R.; He, D. Visualization of gas-liquid flow pattern in a centrifugal pump impeller and its influence on the pump performance. *Meas. Sensors* **2021**, *13*, 100033. [CrossRef]
39. Mansour, M.; Parikh, T.; Thévenin, D. Influence of Blade Pitch and Number of Blades of a Pump Inducer on Single and Two-Phase Flow Performance. In Proceedings of the ASME Turbo Expo 2020; Volume 9: Oil and Gas Applications; Organic Rankine Cycle Power Systems; Steam Turbine; The American Society of Mechanical Engineers: New York, NY, USA, 2020. [CrossRef]
40. Si, Q.; Bois, G.; Zhang, K.; Yuan, J. Air-water two-phase flow experimental and numerical analysis in a low specific speed centrifugal pump. In Proceedings of the 12th European Turbomachinery Conference on Turbomachinery Fluid Dynamics & Thermodynamics, Stockholm, Sweden, 3–7 April 2017. [CrossRef]

41. Si, Q.; Bois, G.; Jiang, Q.; He, W.; Ali, A.; Yuan, S. Investigation on the Handling Ability of Centrifugal Pumps under Air–Water Two-Phase Inflow: Model and Experimental Validation. *Energies* **2018**, *11*, 48. [CrossRef]
42. Si, Q.; Bois, G.; Liao, M.; Zhang, H.; Cui, Q.; Yuan, S. A Comparative Study on Centrifugal Pump Designs and Two-Phase Flow Characteristic under Inlet Gas Entrainment Conditions. *Energies* **2020**, *13*, 65. [CrossRef]
43. Si, Q.; Liao, M.; Fan, M.; Yuan, S.; Cui, Q.; Bois, G. Experimental study on flow behavior of unshrouded impeller centrifugal pumps under inlet air entrainment condition. In Proceedings of the 14th European Turbomachinery Conference on Turbomachinery Fluid Dynamics & Thermodynamics, Gdansk, Poland, 12–16 April 2021.
44. Liao, M.; Si, Q.; Fan, M.; Wang, P.; Liu, Z.; Yuan, S.; Cui, Q.; Bois, G. Experimental Study on Flow Behavior of Unshrouded Impeller Centrifugal Pumps under Inlet Air Entrainment Condition. *Int. J. Turbomach. Propuls. Power* **2021**, *6*, 31. [CrossRef]
45. Wan, Y.; Peters, N. Scaling of Spray Penetration with Evaporation. *Atomiz. Spr.* **1999**, *9*, 111–132. [CrossRef]
46. Pak, E.T.; Lee, J.C. Performance and pressure distribution changes in a centrifugal pump under two-phase flow. *Proc. Inst. Mech. Eng. A: J. Power Energy* **1998**, *212*, 165–171. [CrossRef]
47. Minemura, K.; Uchiyama, T. Prediction of Pump Performance Under Air-Water Two-Phase Flow Based on a Bubbly Flow Model. *ASME J. Fluids Eng.* **1993**, *115*, 781–783. [CrossRef]
48. Müller, T.; Limbach, P.; Skoda, R. Numerical 3D RANS Simulation of Gas-Liquid Flow in a Centrifugal Pump with an Euler-Euler Two-Phase Model and a Dispersed Phase Distribution. In Proceedings of the 11th European Conference on Turbomachinery Fluid Dynamics & Thermodynamics, Madrid, Spain, 23–27 March 2015.
49. Minemura, K.; Uchiyama, T. Three-Dimensional Calculation of Air-Water Two-Phase Flow in Centrifugal Pump Impeller Based on a Bubbly Flow Model. *ASME J. Fluids Eng.* **1993**, *115*, 766–771. [CrossRef]
50. Caridad, J.; Asuaje, M.; Kenyery, F.; Tremante, A.; Aguillon, O. Characterization of a centrifugal pump impeller under two-phase flow conditions. *J. Pet. Sci. Eng.* **2008**, *63*, 18–22. [CrossRef]
51. Yu, Z.Y.; Zhang, Q.Z.; Huang, R.; Cao, S.L. Numerical analysis of gas-liquid mixed transport process in a multiphase rotodynamic pump. *IOP Conf. Ser. Earth Environ. Sci.* **2012**, *15*, 32062. [CrossRef]
52. Müller, T.; Limbach, P.; Skoda, R. Influence of Geometry Simplifications and Numerical Parameters in 3D URANS Liquid-Gas Flow Simulations of a Radial Pump with an Eulerian Mono-Dispersed Two-Phase Model. In Proceedings of the International Symposium on Transport Phenomena and Dynamics (ISROMAC), Honululu, HI, USA, 10–15 April 2016.
53. Wang, B.; Zhang, H.; Deng, F.; Wang, C.; Si, Q. Effect of Short Blade Circumferential Position Arrangement on Gas-Liquid Two-Phase Flow Performance of Centrifugal Pump. *Processes* **2020**, *8*, 1317. [CrossRef]
54. Zhou, L.; Han, Y.; Lv, W.; Yang, Y.; Zhu, Y.; Song, X. Numerical Calculation of Energy Performance and Transient Characteristics of Centrifugal Pump under Gas-Liquid Two-Phase Condition. *Micromachines* **2020**, *11*, 728. [CrossRef]
55. Zhong, G.; Shao, C.; Cheng, W.; Zhao, Z. Numerical simulation and experimental study on gas–liquid two-phase unsteady flow in a centrifugal pump during the transition process. *Proc. Inst. Mech. Eng. C: J. Mech. Eng. Sci.* **2022**, *236*, 2224–2241. [CrossRef]
56. Hundshagen, M.; Mansour, M.; Thévenin, D.; Skoda, R. Numerical investigation of two-phase air-water flow in a centrifugal pump with closed or semi-open impeller. In Proceedings of the 13th European Turbomachinery Conference on Turbomachinery Fluid Dynamics & Thermodynamics, Lausanne, Switzerland, 8–12 April 2019. [CrossRef]
57. Hundshagen, M.; Mansour, M.; Thévenin, D.; Skoda, R. Experimental investigation and 3D-CFD simulation of centrifugal pumps for gasladen liquids with closed and semi-open impellers. In Proceedings of the 4th International Rotating Equipment Conference, Wiesbaden, Germany, 24–25 September 2019.
58. Hundshagen, M.; Mansour, M.; Thévenin, D.; Skoda, R. 3D Simulation of Gas-Laden Liquid Flows in Centrifugal Pumps and the Assessment of Two-Fluid CFD Methods. *Exp. Comput. Multiph. Flow* **2021**, *3*, 186–207. [CrossRef]
59. He, D.; Ge, Z.; Bai, B.; Guo, P.; Luo, X. Gas–Liquid Two-Phase Performance of Centrifugal Pump Under Bubble Inflow Based on Computational Fluid Dynamics–Population Balance Model Coupling Model. *ASME J. Fluids Eng.* **2020**, *142*, 81402. [CrossRef]
60. Yan, S.; Sun, S.; Luo, X.; Chen, S.; Li, C.; Feng, J. Numerical Investigation on Bubble Distribution of a Multistage Centrifugal Pump Based on a Population Balance Model. *Energies* **2020**, *13*, 908. [CrossRef]
61. Stel, H.; Ofuchi, E.M.; Chiva, S.; Morales, R.E. Numerical simulation of gas-liquid flows in a centrifugal rotor. *Chem. Eng. Sci.* **2020**, *221*, 115692. [CrossRef]
62. Stel, H.; Ofuchi, E.M.; Chiva, S.; Morales, R.E.M. Numerical assessment of performance characteristics and two-phase flow dynamics of a centrifugal rotor operating under gas entrainment condition. *Exp. Comput. Multiph. Flow* **2021**, *17*, 221–240. [CrossRef]
63. Zhang, F.; Zhu, L.; Chen, K.; Yan, W.; Appiah, D.; Hu, B. Numerical Simulation of Gas–Liquid Two-Phase Flow Characteristics of Centrifugal Pump Based on the CFD–PBM. *Mathematics* **2020**, *8*, 769. [CrossRef]
64. Chen, Y.; Patil, A.; Chen, Y.; Bai, C.; Wang, Y.; Morrison, G. Numerical Study on the First Stage Head Degradation in an Electrical Submersible Pump With Population Balance Model. *J. Energy Resour. Technol.* **2019**, *141*. [CrossRef]
65. Si, Q.; Asad, A.; Wang, B.; Wang, P.; Bois, G.; Jianping, Y.; Kubar, A.A. Numerical Study on Gas-Liquid Two Phase Flow Characteristic of Multistage Electrical Submersible Pump by Using a Novel Multiple-Size Group (MUSIG) Model. *Phys. Fluids* **2022**, *34*, 063311. [CrossRef]
66. Mansour, M.; Kováts, P.; Wunderlich, B.; Thévenin, D. Experimental investigations of a two-phase gas/liquid flow in a diverging horizontal channel. *Exp. Therm. Fluid Sci.* **2018**, *93*, 210–217. [CrossRef]

67. Kopparthy, S.; Mansour, M.; Janiga, G.; Thévenin, D. Numerical investigations of turbulent single-phase and two-phase flows in a diffuser. *Int. J. Multiphase Flow* **2020**, *130*, 103333. [CrossRef]
68. Parikh, T.; Mansour, M.; Thévenin, D. Maximizing the performance of pump inducers using CFD-based multi-objective optimization. *Struct. Multidisc. Optim.* **2022**, *65*, 9. [CrossRef]
69. Parikh, T.; Mansour, M.; Thévenin, D. Investigations on the effect of tip clearance gap and inducer on the transport of air-water two-phase flow by centrifugal pumps. *Chem. Eng. Sci.* **2020**, *218*, 115554. [CrossRef]
70. Pineda, H.; Biazussi, J.; López, F.; Oliveira, B.; Carvalho, R.D.; Bannwart, A.C.; Ratkovich, N. Phase distribution analysis in an Electrical Submersible Pump (ESP) inlet handling water–air two-phase flow using Computational Fluid Dynamics (CFD). *J. Pet. Sci. Eng.* **2016**, *139*, 49–61. [CrossRef]
71. Zhu, J.; Zhu, H.; Zhang, J.; Zhang, H.Q. A numerical study on flow patterns inside an electrical submersible pump (ESP) and comparison with visualization experiments. *J. Pet. Sci. Eng.* **2019**, *173*, 339–350. [CrossRef]
72. Mansour, M.; Parikh, T.; Engel, S.; Thévenin, D. Numerical Investigations of Gas/Liquid Two-Phase Flow in a Pump Inducer. *ASME J. Fluids Eng.* **2020**, *142*, 21302. [CrossRef]
73. de Santis, A.; Colombo, M.; Hanson, B.C.; Fairweather, M. A generalized multiphase modelling approach for multiscale flows. *J. Comput. Phys.* **2021**, *436*, 110321. [CrossRef]
74. Hundshagen, M.; Rave, K.; Mansour, M.; Thévenin, D.; Skoda, R. Assessment of multi-phase CFD methods for gas-laden liquid flows in centrifugal pumps with particular emphasis on the change of flow morphology. In Proceedings of the 14th European Turbomachinery Conference on Turbomachinery Fluid Dynamics & Thermodynamics, Gdansk, Poland, 12–16 April 2021. [CrossRef]
75. Marschall, H. Towards the Numerical Simulation of Multi-Scale Two-Phase Flows. Ph.D. Thesis, Technische Universität München, München, Germany, 2011.
76. Hundshagen, M.; Rave, K.; Nguyen, B.D.; Popp, S.; Hasse, C.; Mansour, M.; Thévenin, D.; Skoda, R. Two-Phase Flow Simulations of Liquid/Gas Transport in Radial Centrifugal Pumps With Special Emphasis on the Transition From Bubbles to Adherent Gas Accumulations. *ASME J. Fluids Eng.* **2022**, *144*, 101202. [CrossRef]
77. Hänsch, S.; Lucas, D.; Krepper, E.; Höhne, T. A multi-field two-fluid concept for transitions between different scales of interfacial structures. *Int. J. Multiphase Flow* **2012**, *47*, 171–182. [CrossRef]
78. Hänsch, S.; Lucas, D.; Höhne, T.; Krepper, E. Application of a new concept for multi-scale interfacial structures to the dam-break case with an obstacle. *Nucl. Eng. Des.* **2014**, *279*, 171–181. [CrossRef]
79. Meller, R.; Schlegel, F.; Lucas, D. Basic verification of a numerical framework applied to a morphology adaptive multifield two–fluid model considering bubble motions. *Int. J. Numer. Meth. Fluids* **2021**, *93*, 748–773. [CrossRef]
80. Yin, J.; Zhang, T.; Krull, B.; Meller, R.; Schlegel, F.; Lucas, D.; Wang, D.; Liao, Y. A CFD approach for the flow regime transition in a vane-type gas-liquid separator. *Int. J. Multiphase Flow* **2023**, *159*, 104320. [CrossRef]
81. Frederix, E.; Dovizio, D.; Mathur, A.; Komen, E. All-regime two-phase flow modeling using a novel four-field large interface simulation approach. *Int. J. Multiphase Flow* **2021**, *145*. [CrossRef]
82. Wardle, K.E.; Weller, H.G. Hybrid Multiphase CFD Solver for Coupled Dispersed/Segregated Flows in Liquid-Liquid Extraction. *Int. J. Chem. Eng.* **2013**, *2013*, 128936. [CrossRef]
83. Shonibare, O.Y.; Wardle, K.E. Numerical Investigation of Vertical Plunging Jet Using a Hybrid Multifluid–VOF Multiphase CFD Solver. *Int. J. Chem. Eng.* **2015**, *2015*, 925639. [CrossRef]
84. Mathur, A.; Dovizio, D.; Frederix, E.; Komen, E. A Hybrid Dispersed-Large Interface Solver for multi-scale two-phase flow modelling. *Nucl. Eng. Des.* **2019**, *344*, 69–82. [CrossRef]
85. Byskov, R.K.; Jacobsen, C.B.; Pedersen, N. Flow in a Centrifugal Pump Impeller at Design and Off-Design Conditions—Part II: Large Eddy Simulations. *ASME J. Fluids Eng.* **2003**, *125*, 73–83. [CrossRef]
86. Kato, C.; Mukai, H.; Manabe, A. Large-Eddy Simulation of Unsteady Flow in a Mixed-Flow Pump. *Int. J. Rotating Mach.* **2003**, *9*, 345–351. [CrossRef]
87. Tang, X.; Wang, F.; Wu, Y. An improved large eddy simulation of two-phase flows in a pump impeller. *Acta Mech. Sin.* **2007**, *23*, 635–643. [CrossRef]
88. Tokyay, T.E.; Constantinescu, S.G. Validation of a Large-Eddy Simulation Model to Simulate Flow in Pump Intakes of Realistic Geometry. *J. Hydraul. Eng.* **2006**, *132*, 1303–1315. .:12(1303). [CrossRef]
89. Zhang, W.; Yu, Y.; Chen, H. Numerical Simulation of Unsteady Flow in Centrifugal Pump Impeller at Off-Design Condition by Hybrid RANS/LES Approaches. In *High Performance Computing and Applications*; Hutchison, D., Kanade, T., Kittler, J., Kleinberg, J.M., Mattern, F., Mitchell, J.C., Naor, M., Nierstrasz, O., Pandu Rangan, C., Steffen, B., et al., Eds.; Springer: Berlin/Heidelberg, Germany, 2010; Volume 5938, pp. 571–578. ._80. [CrossRef]
90. Wang, W.; Wang, Y. Analysis of inner flow in low specific speed centrifugal pump based on LES. *J. Mech. Sci. Technol.* **2013**, *27*, 1619–1626. [CrossRef]
91. Posa, A.; Lippolis, A.; Verzicco, R.; Balaras, E. Large-eddy simulations in mixed-flow pumps using an immersed-boundary method. *Comput. Fluids* **2011**, *47*, 33–43. [CrossRef]
92. Posa, A.; Lippolis, A.; Balaras, E. Large-Eddy Simulation of a Mixed-Flow Pump at Off-Design Conditions. *ASME J. Fluids Eng.* **2015**, *137*, 49. [CrossRef]

93. Si, Q.; Yuan, J.; Yuan, S.; Wang, W.; Zhu, L.; Bois, G. Numerical Investigation of Pressure Fluctuation in Centrifugal Pump Volute Based on SAS Model and Experimental Validation. *Adv. Mech. Eng.* **2014**, *6*, 972081. [CrossRef]
94. Cui, B.; Zhang, C.; Zhang, Y.; Zhu, Z. Influence of Cutting Angle of Blade Trailing Edge on Unsteady Flow in a Centrifugal Pump Under Off-Design Conditions. *Appl. Sci.* **2020**, *10*, 580. [CrossRef]
95. Shen, J.F.; Li, Y.J.; Liu, Z.Q.; Tang, X.L. Turbulent flow and pressure fluctuation prediction of the impeller in an axial-flow pump based on LES. *IOP Conf. Ser.: Mater. Sci. Eng.* **2013**, *52*, 032015. [CrossRef]
96. Posa, A.; Lippolis, A.; Balaras, E. Investigation of Separation Phenomena in a Radial Pump at Reduced Flow Rate by Large-Eddy Simulation. *ASME J. Fluids Eng.* **2016**, *138*, 121101. [CrossRef]
97. Posa, A.; Lippolis, A. A LES investigation of off-design performance of a centrifugal pump with variable-geometry diffuser. *Int. J. Heat Fluid Flow* **2018**, *70*, 299–314. [CrossRef]
98. Posa, A.; Lippolis, A. Effect of working conditions and diffuser setting angle on pressure fluctuations within a centrifugal pump. *Int. J. Heat Fluid Flow* **2019**, *75*, 44–60. [CrossRef]
99. Posa, A. LES investigation on the dependence of the flow through a centrifugal pump on the diffuser geometry. *Int. J. Heat Fluid Flow* **2021**, *87*, 108750. [CrossRef]
100. Posa, A. LES study on the influence of the diffuser inlet angle of a centrifugal pump on pressure fluctuations. *Int. J. Heat Fluid Flow* **2021**, *89*, 108804. [CrossRef]
101. Kye, B.; Park, K.; Choi, H.; Lee, M.; Kim, J.H. Flow characteristics in a volute-type centrifugal pump using large eddy simulation. *Int. J. Heat Fluid Flow* **2018**, *72*, 52–60. [CrossRef]
102. Pacot, O.; Kato, C.; Guo, Y.; Yamade, Y.; Avellan, F. Large Eddy Simulation of the Rotating Stall in a Pump-Turbine Operated in Pumping Mode at a Part-Load Condition. *ASME J. Fluids Eng.* **2016**, *138*. [CrossRef]
103. Zhang, N.; Liu, X.; Gao, B.; Wang, X.; Xia, B. Effects of modifying the blade trailing edge profile on unsteady pressure pulsations and flow structures in a centrifugal pump. *Int. J. Heat Fluid Flow* **2019**, *75*, 227–238. [CrossRef]
104. Zhang, T.; Wu, D.; Qiu, S.; Zhou, P.; Ren, Y.; Mou, J. LES Analysis of the Unsteady Flow Characteristics of a Centrifugal Pump Impeller. *Fluid Dyn. Mater. Process.* **2022**, *18*, 1349–1361. [CrossRef]
105. Zhou, P.; Dai, J.; Yan, C.; Zheng, S.; Ye, C.; Zhang, X. Effect of Stall Cells on Pressure Fluctuations Characteristics in a Centrifugal Pump. *Symmetry* **2019**, *11*, 1116. [CrossRef]
106. Sorguven, E.; Incir, S.; Highgate, J. Understanding loss generation mechanisms in a centrifugal pump using large eddy simulation. *Int. J. Heat Fluid Flow* **2022**, *96*, 108994. [CrossRef]
107. Pope, S.B. *Turbulent Flows*; Cambridge University Press: Cambridge, UK, 2000. [CrossRef]
108. Fröhlich, J.; Mellen, C.P.; Rodi, W.; Temmermann, L.; Leschziner, M.A. Highly resolved large-eddy simulation of separated flow in a channel with streamwise periodic constrictions. *J. Fluid Mech.* **2005**, *526*, 19–66. [CrossRef]
109. Kim, D.; Choi, H. Immersed boundary method for flow around an arbitrarily moving body. *J. Comp. Phys.* **2006**, *212*, 662–680. [CrossRef]
110. Spalart, P.R.; Jou, W.H.; Strelets, M. Comments on the Feasibility of LES for Wings and on a Hybrid RANS/LES Approach. In *Advances in DNS/LES*; Liu, C., Liu, Z., Sakell, L., Eds.; Greyden Press: Columbus, OH, USA, 1997.
111. Spalart, P.R. Detached-Eddy Simulation. *Annu. Rev. Fluid Mech.* **2009**, *41*, 181–202. . [CrossRef]
112. Spalart, P.R.; Deck, S.; Shur, M.L.; Squires, K.D.; Strelets, M.K.; Travin, A. A New Version of Detached-eddy Simulation, Resistant to Ambiguous Grid Densities. *Theoret. Comput. Fluid Dynamics* **2006**, *20*, 181–195. [CrossRef]
113. Speziale, C.G. Turbulence Modeling for Time-Dependent RANS and VLES: A Review. *AIAA J.* **1998**, *36*, 173–184. [CrossRef]
114. Basara, B.; Krajnovic, S.; Girimaji, S.; Pavlovic, Z. Near-Wall Formulation of the Partially Averaged Navier Stokes Turbulence Model. *AIAA J.* **2011**, *49*, 2627–2636. [CrossRef]
115. Girimaji, S.S. Partially-Averaged Navier-Stokes Model for Turbulence: A Reynolds-Averaged Navier-Stokes to Direct Numerical Simulation Bridging Method. *J. Appl. Mech.* **2006**, *73*, 413–421. [CrossRef]
116. Chaouat, B.; Schiestel, R. A new partially integrated transport model for subgrid-scale stresses and dissipation rate for turbulent developing flows. *Phys. Fluids* **2005**, *17*, 065106. [CrossRef]
117. Xin, T.; Zhili, L.; Meng, Z.; Haotian, Y.; Wei, J.; Yuchuan, W.; Diyi, C. Analysis of Unsteady Flow Characteristics of Centrifugal Pump under Part Load Based on DDES Turbulence Model. *Shock Vib.* **2021**, *2021*, 1–11. [CrossRef]
118. Zhang, N.; Liu, X.; Gao, B.; Xia, B. DDES analysis of the unsteady wake flow and its evolution of a centrifugal pump. *Renew. Energy* **2019**, *141*, 570–582. [CrossRef]
119. Strelets, M. Detached eddy simulation of massively separated flows. In Proceedings of the 39th Aerospace Sciences Meeting and Exhibit; American Institute of Aeronautics and Astronautics: Reston, VA, USA, 2001. [CrossRef]
120. Menter, F.; Carregal Ferreira, J.; Esch, T.; Konno, B. The SST Turbulence Model with Improved Wall Treatment for Heat Transfer Predictions in Gas Turbines. In Proceedings of the International Gas Turbine Congress, Tokyo, Japan, 2–7 November 2003.
121. Gritskevich, M.S.; Garbaruk, A.V.; Schütze, J.; Menter, F.R. Development of DDES and IDDES Formulations for the k-ω Shear Stress Transport Model. *Flow Turbul. Combust.* **2012**, *88*, 431–449. [CrossRef]
122. Menter, F.; Hüppe, A.; Matyushenko, A.; Kolmogorov, D. An Overview of Hybrid RANS–LES Models Developed for Industrial CFD. *Appl. Sci.* **2021**, *11*, 2459. [CrossRef]
123. Rotta, J.C. *Turbulente Strömungen: Eine Einführung in die Theorie und ihre Anwendung*; Vieweg+Teubner Verlag: Wiesbaden, Germany, 1972; Volume 15. [CrossRef]

124. Fröhlich, J.; von Terzi, D. Hybrid LES/RANS methods for the simulation of turbulent flows. *Prog. Aerosp. Sci.* **2008**, *44*, 349–377. [CrossRef]
125. Jakirlić, S.; Bopp, M.; Chang, C.Y.; Köhler, F.; Krumbein, B.; Kutej, L.; Kütemeier, D.; Maden, I.; Maduta, R.; Ullrich, M.; et al. RANS-based Sub-scale Modelling in Eddy-resolving Simulation Methods. *ERCOFTAC Bull.* **2019**, *121*, 5–16.
126. Egorov, Y.; Menter, F. Development and Application of SST-SAS Turbulence Model in the DESIDER Project. In *Advances in Hybrid RANS-LES Modelling*; Peng, S.H., Haase, W., Eds.; Springer: Berlin/Heidelberg, Germany, 2008; Volume 97, pp. 261–270. [CrossRef]
127. Menter, F. Two-equation eddy-viscosity turbulence models for engineering applications. *AIAA J.* **1994**, *32*, 1598–1605. [CrossRef]
128. Menter, F.; Egorov, Y. The Scale-Adaptive Simulation Method for Unsteady Turbulent Flow Predictions. Part 1: Theory and Model Description. *Flow Turbul. Combust.* **2010**, *85*, 113–138. [CrossRef]
129. Lucius, A.; Brenner, G. Unsteady CFD simulations of a pump in part load conditions using scale-adaptive simulation. *Int. J. Heat Fluid Flow* **2010**, *31*, 1113–1118. [CrossRef]
130. Schiffer-Rosenberger, J.; Bodner, C.; Jaberg, H. Performance analysis of a single-blade impeller pump based on unsteady 3D numerical simulation. In Proceedings of the 3rd International Rotating Equipment Conference, Düsseldorf, Germany, 14–15 September 2016; pp. 193–203.
131. Pavesi, G.; Dazin, A.; Cavazzini, G.; Caignaert, G.; Bois, G.; Ardizzon, G. Experimental and numerical investigation of unforced unsteadiness in a vaneless radial diffuser. In Proceedings of the 9th European Conference on Turbomachinery Fluid Dynamics & Thermodynamics, Istanbul, Turkey, 21–25 March 2011.
132. Zhao, X.; Luo, Y.; Wang, Z.; Xiao, Y.; Avellan, F. Unsteady Flow Numerical Simulations on Internal Energy Dissipation for a Low-Head Centrifugal Pump at Part-Load Operating Conditions. *Energies* **2019**, *12*, 13. [CrossRef]
133. Hundshagen, M.; Casimir, N.; Pesch, A.; Falsafi, S.; Skoda, R. Assessment of scale-adaptive turbulence models for volute-type centrifugal pumps at part load operation. *Int. J. Heat Fluid Flow* **2020**, *85*, 108621. [CrossRef]
134. Rave, K.; Lehmenkühler, M.; Wirz, D.; Bart, H.J.; Skoda, R. 3D flow simulation of a baffled stirred tank for an assessment of geometry simplifications and a scale-adaptive turbulence model. *Chem. Eng. Sci.* **2021**, *231*, 116262. [CrossRef]
135. Müller, T.; Limbach, P.; Skoda, R. 3D Liquid-Gas Flow Simulations of a Radial Pump with an Eulerian Mono-Dispersed Two-Phase Model. In Proceedings of the 3rd International Rotating Equipment Conference, Düsseldorf, Germany, 14–15 September 2016.
136. Schiller, L.; Naumann, A. Über die grundlegenden Berechnungen bei Schwerkraftaufbereitung. *Z. Des Vereines Dtsch. Ingenieure* **1933**, *77*, 318–320.
137. Auton, T.R.; Hunt, J.C.R.; Prud'Homme, M. The force exerted on a body in inviscid unsteady non-uniform rotational flow. *J. Fluid Mech.* **1988**, *197*, 241–257. [CrossRef]
138. Rzehak, R.; Krepper, E.; Liao, Y.; Ziegenhein, T.; Kriebitzsch, S.; Lucas, D. Baseline Model for the Simulation of Bubbly Flows. *Chem. Eng. Technol.* **2015**, *38*, 1972–1978. [CrossRef]
139. Brackbill, J.; Kothe, D.; Zemach, C. A continuum method for modeling surface tension. *J. Comput. Phys.* **1992**, *100*, 335–354. [CrossRef]
140. Nguyen, B.D.; Popp, S.; Hundshagen, M.; Skoda, R.; Mansour, M.; Thévenin, D.; Hasse, C. Large Eddy Simulations of Turbulent Gas-Liquid Flows in a Diverging Horizontal Channel Using a Hybrid Multiphase Approach. *ASME J. Fluids Eng.* **2023**, *145*, 31501. [CrossRef]
141. Blume, M.; Schwarz, P.; Rusche, H.; Weiß, L.; Wensing, M.; Skoda, R. 3D Simulation of Turbulent and Cavitating Flow for the Analysis of Primary Breakup Mechanisms in Realistic Diesel Injection Processes. *Atomiz. Spr.* **2019**, *29*, 861–893. [CrossRef]
142. Ansys Inc. ANSYS CFX-Solver Theory Guide, Release 18.0; ANSYS, Inc.: Canonsburg, PA, USA, 2017.
143. De Santis, A.; Hanson, B.C.; Fairweather, M. Hydrodynamics of annular centrifugal contactors: A CFD analysis using a novel multiphase flow modelling approach. *Chem. Eng. Sci.* **2021**, *242*, 116729. [CrossRef]
144. Colombo, M.; de Santis, A.; Hanson, B.C.; Fairweather, M. Prediction of Horizontal Gas–Liquid Segregated Flow Regimes with an All Flow Regime Multifluid Model. *Processes* **2022**, *10*, 920. [CrossRef]
145. Štrubelj, L.; Ťiselj, I. Two-fluid model with interface sharpening. *Int. J. Numer. Meth. Eng.* **2011**, *85*, 575–590. [CrossRef]
146. Lo, S. Application of the MUSIG model to bubbly flows. In Proceedings of the AEAT-1096, AEA Technology, Carlsbad, CA, USA, June 1996.
147. Krepper, E.; Frank, T.; Lucas, D.; Prasser, H.M.; Zwart, P. Inhomogeneous MUSIG model—A population balance approach for poly-dispersed bubbly flow. In Proceedings of the 6th International Conference on Multiphase Flow, Leipzig, Germany, 9–13 July 2007.
148. Lehnigk, R.; Bainbridge, W.; Liao, Y.; Lucas, D.; Niemi, T.; Peltola, J.; Schlegel, F. An open–source population balance modeling framework for the simulation of polydisperse multiphase flows. *AIChE J.* **2022**, *68*, e17539. [CrossRef]
149. Kumar, S.; Ramkrishna, D. On the solution of population balance equations by discretization—I. A fixed pivot technique. *Chem. Eng. Sci.* **1996**, *51*, 1311–1332. [CrossRef]
150. Krepper, E.; Lucas, D.; Frank, T.; Prasser, H.M.; Zwart, P.J. The inhomogeneous MUSIG model for the simulation of polydispersed flows. *Nucl. Eng. Des.* **2008**, *238*, 1690–1702. [CrossRef]
151. Prince, M.J.; Blanch, H.W. Bubble coalescence and break-up in air-sparged bubble columns. *AIChE J.* **1990**, *36*, 1485–1499. [CrossRef]

152. Luo, H.; Svendsen, H.F. Theoretical model for drop and bubble breakup in turbulent dispersions. *AIChE J.* **1996**, *42*, 1225–1233. [CrossRef]
153. Liao, Y.; Rzehak, R.; Lucas, D.; Krepper, E. Baseline closure model for dispersed bubbly flow: Bubble coalescence and breakup. *Chem. Eng. Sci.* **2015**, *122*, 336–349. [CrossRef]
154. Rave, K.; Hermes, M.; Wirz, D.; Hundshagen, M.; Friebel, A.; von Harbou, E.; Bart, H.J.; Skoda, R. Experiments and fully transient coupled CFD-PBM 3D flow simulations of disperse liquid-liquid flow in a baffled stirred tank. *Chem. Eng. Sci.* **2022**, *253*, 117518. [CrossRef]
155. Jasak, H. Error Analysis and Estimation for the Finite Volume Method with Applications to Fluid Flows. Ph.D. Thesis, Imperial College of Science, Technology and Medicine, London, UK, 1996.
156. Patankar, S.; Spalding, D. A calculation procedure for heat, mass and momentum transfer in three-dimensional parabolic flows. *Int. J. Heat Mass Transfer* **1972**, *15*, 1787–1806. [CrossRef]
157. Farrell, P.E.; Maddison, J.R. Conservative interpolation between volume meshes by local Galerkin projection. *Comput. Methods Appl. Mech. Eng.* **2011**, *200*, 89–100. [CrossRef]
158. Černe, G.; Petelin, S.; Ťiselj, I. Coupling of the Interface Tracking and the Two-Fluid Models for the Simulation of Incompressible Two-Phase Flow. *J. Comp. Phys.* **2001**, *171*, 776–804. [CrossRef]
159. Noroozi, M.M.; Maddahian, R.; Ramezani, M.H.; Ansari, M.R. An LES-Like Multiscale Multiphase Flow Model Based on Break-up and Coalescence Phenomena. *J. Appl. Fluid Mech.* **2022**, *15*, 1073–1085. [CrossRef]

Disclaimer/Publisher's Note: The statements, opinions and data contained in all publications are solely those of the individual author(s) and contributor(s) and not of MDPI and/or the editor(s). MDPI and/or the editor(s) disclaim responsibility for any injury to people or property resulting from any ideas, methods, instructions or products referred to in the content.

International Journal of
Turbomachinery
Propulsion and Power

MDPI

Article

Numerical Analysis of the Flow by Using a Free Runner Downstream the Francis Turbine †

Alin Ilie Bosioc [1,*], Raul-Alexandru Szakal [2], Adrian Stuparu [1,*] and Romeo Susan-Resiga [1]

[1] Department of Mechanical Machines, Equipment and Transportation, Politehnica University Timișoara, Bv. Mihai Viteazu, No.1, RO-300222 Timișoara, Romania
[2] Romanian Academy–Timisoara Branch, Bv. Mihai Viteazu, No. 24, RO-300223 Timișoara, Romania
* Correspondence: alin.bosioc@upt.ro (A.I.B.); adrian.stuparu@upt.ro (A.S.)
† This paper was published in the Proceedings of the 18th Conference on Modelling Fluid Flow (CMFF'22), Budapest, Hungary, 30 August–2 September 2022.

Abstract: The current requirements of industrialized countries require the use of as much renewable energy as possible. One significant problem with renewable energy is that the produced power fluctuates. Currently, the only method available for energy compensation in the shortest time is given by hydroelectric power plants. Instead, hydroelectric power plants (especially the plants equipped with hydraulic turbines with fixed blades) are designed to operate in the vicinity of the optimal operating point with a maximum ±10% deviation. The energy market requires that hydraulic turbines operate in an increasingly wide area between −35% to 20% from the optimum operating point. Operation of hydraulic turbines far from the optimum operating point involves the appearance downstream of the turbine of a decelerated swirling flow with hydraulic instabilities (known in the literature as the vortex rope). The main purpose of this paper is to investigate numerically a new concept by using a free runner downstream on the main hydraulic runner turbine more precisely in the draft tube cone. The free runner concept requires rotations at the runaway speed with vanishing mechanical torque. The main purpose is to redistribute the total pressure and the moment between the shaft and the periphery. In addition, the free runner does not modify the operating point of the main hydraulic turbine runner.

Keywords: free runner concept; hydraulic turbines; numerical simulation; Laser Doppler Velocity measurements; draft tube cone; validation; vortex rope; visualization; unsteady pressure

check for updates

Citation: Bosioc, A.I.; Szakal, R.-A.; Stuparu, A.; Susan-Resiga, R. Numerical Analysis of the Flow by Using a Free Runner Downstream the Francis Turbine. *Int. J. Turbomach. Propuls. Power* **2023**, *8*, 14. https://doi.org/10.3390/ijtpp8020014

Academic Editors: János Gábor Vad, Csaba Horváth and Tamás Benedek

Received: 2 February 2023
Revised: 5 April 2023
Accepted: 7 April 2023
Published: 4 May 2023

Copyright: © 2023 by the authors. Licensee MDPI, Basel, Switzerland. This article is an open access article distributed under the terms and conditions of the Creative Commons Attribution (CC BY-NC-ND) license (https://creativecommons.org/licenses/by-nc-nd/4.0/).

1. Introduction

The actual energy crisis increases the development of clean renewable energy (wind and solar), which makes introducing the electrical network a large fluctuating component. Therefore, many hydroelectric power plants are operated to flatten the fluctuation of wind and solar power. Although operating in an off-design condition for grid services (part load and high load), hydraulic turbines experience an abrupt decrease in terms of efficiency. An excess of residual swirl is ingested by the draft tube, downstream of the turbine runner [1–4]. When the hydraulic turbines operate in off-design conditions, the residual swirl from the discharge cone is the consequence of the mismatch between the flow generated by the wicked gates and the angular momentum extracted by the turbine runner [5]. In general, for all hydraulic turbines, the worst operating conditions are when the machine is operated at partial discharge. For the partial discharge regime, the residual swirl ingested by the conical diffuser of the draft tube leads to the development of the so-called vortex rope [6–10]. Usually, the vortex rope develops in all lengths of the discharge cone and is characterized by a well-defined fundamental frequency and pressure amplitude. According to Ciocan et al. [11] the fundamental frequency has values between 0.2 and 0.4 from the rotational frequency of the runner. The fundamental frequency is accompanied

by a pressure amplitude, and the fluctuating pressure is responsible for the high vibrations in the discharge cone and the closest components [12–14]. With the development of hydraulic turbines, different methods have been designed, tested, and implemented to mitigate the undesirable effect of the vortex rope. These methods can be divided into passive (not requiring auxiliary power) and active (requiring auxiliary power and control loop) [15]. One of the first passive techniques was proposed in the 1980s by Thicke [16]. Later, many other passive technologies such as J-grooves mounted on the cone wall [17], fins [18], runner cone extensions [19], diaphragm mounted downstream the conical diffuser [20], radial protrusion of solid bodies [21], the flow-feedback method [22] and stator mounted downstream the runner [23] were investigated. Active control techniques such as air or water injections through various zones of the hydraulic turbine [24–28] and the magneto-rheological control technique [29,30] were also investigated. All these techniques have incontestable advantages, especially in part-load or full-load operations, but in all operating regimes of a hydraulic machine, they have some drawbacks (Kougias et al. [1]). Together with these control technics, various measuring and observing systems were used to quantify the impact of control technics on hydrodynamic phenomena developed in the conical diffuser. The most common types of investigations on the hydrodynamic flow field generated at part-load conditions are the pressure measurements at the wall of the conical diffuser and the 2D Laser Doppler Velocimetry (LDV) measurements. In addition to these, high-speed camera observations and 2D or 3D particle image velocimetry (PIV) were used. The 2D LDV system is a non-invasive method that allows measuring the velocity profiles in the conical diffusers, offering a wider image of the entire flow fields. In contrast, the tools used to measure pressure are difficult to fit within the flow and, for this reason, are often used on the wall of the conical diffuser [22,31–33].

The experimental analysis combined with numerical simulation can provide a full image of the flow of the hydraulic machinery. Accordingly, this paper presents and analyzes the flow in the conical diffuser by combining experimental investigation and numerical simulation. The experimental investigations performed in this paper consist of measurements of velocity profiles with Laser Doppler Velocimetry (LDV) and pressure pulsations respectively. The numerical simulation performed in this paper is validated first from the numerical simulation and, second, the vortex rope is extracted for the investigated cases. From the experimental and numerical analysis, the new concept of the free runner mounted downstream of the main runner is analyzed. The concept was introduced by Susan Resiga et al. [5] and was further designed in the simplest way possible (three straight blades) and tested to prove the idea.

2. Experimental Setup

To analyze the decelerated swirling flow from the conical diffusers of the hydraulic turbines, model turbines or surrogate model turbines can be used. In our case, we have chosen a surrogate model, a swirl generator, capable of offering a decelerated swirling flow at the inlet in the conical diffuser similar to the flow outlet of a real hydraulic turbine [27,28].

The swirl apparatus is mounted on an experimental test rig developed in the laboratory, which serves by investigating different control methods by diminishing the flow instabilities associated with the vortex rope. Two main components are found in the swirl apparatus which is mounted on the main hydraulic circuit of the test rig: the swirl generator and the test section. The swirl generator has three components: the ogive, the stator and the main runner, which are mounted on a cylindrical Plexiglas section at an interior diameter of 0.150 m, as presented in Figure 1. The main runner and the stator generate at the inlet of the conical diffuser a rotating flow similar to the downstream flow of a Francis runner operated at a discharge of 70% from the nominal flow rate [11].

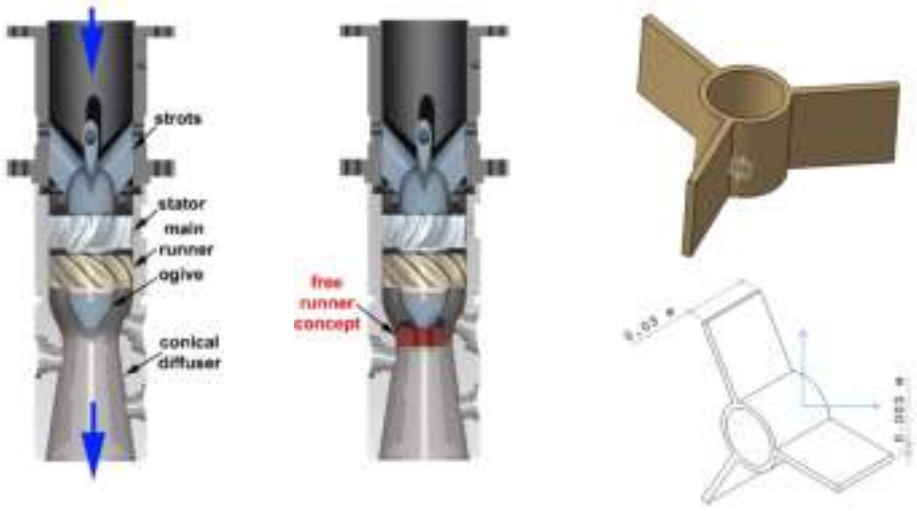

Figure 1. Swirl apparatus and test section from the experimental test rig. The original configuration (**left**), the configuration with the free runner concept implemented on the test rig (**middle**), and the shape of the free runner concept with three blades with main dimensions (**right**).

Downstream the main runner, on the experimental test rig the free runner concept was mounted, see Figure 1 (right). The free runner concept supposes that rotates at the runaway speed with vanishing mechanical torque. The main purpose is to redistribute the total pressure and the momentum between the shaft and the periphery so that the flux of the total pressure and the momentum are not altered. In addition, the free runner does not modify the operating point of the main hydraulic turbine runner. The benefits of the free runner approach downstream from the main-runner turbine are:

- Diminish the pressure pulsations from the draft tube cone, by reducing the volume of the vortex rope.
- Offer a better flow configuration at the inlet in the draft tube cone.

The free runner concept was introduced for the first time by Susan Resiga et al. [5], using the so-called Francis turbine with tandem runners. A similar approach can be found at Gokhman [22] using a stay apparatus downstream of the Francis runner. The free runner concept (see the sketch in Figure 1) downstream of the main turbine will add the required flexibility for the Francis turbine regulation and avoid deterioration of hydraulic turbine components.

The main dimensions of the components from the swirl apparatus, together with the dimensions of the free runner concept, are presented in the Table 1.

Table 1. Hydraulic parameters for the test rig and the main components.

Parameter	Value	Unit
Nominal discharge Qn	0.03	[m^3/s]
Nominal pressure on the main reservoir	30,000	[Pa]
Main runner-rotational speed n	940	[rpm]
Main runner-tip diameter Dt	0.150	[m]
Main runner-hub diameter Dh	0.06	[m]
Main runner-blade number z	10	[-]
Free runner-rotational speed nfr	850	[rpm]
Free runner-tip diameter Dt-fr	0.100	[m]
Free runner-hub diameter Dh-fr	0.03	[m]
Free runner-blade number zfr	3	[-]

According with Table 1, the nominal discharge in the main hydraulic circuit was 0.03 m^3/s for all measurements. The speed of the main runner was measured with the

existing acquisition system in the laboratory, while the speed of the free runner was established with the help of the stroboscope.

3. Numerical Setup

The numerical domain was represented in full 3D and consists of 5.8 million mixed cells. First, the numerical results were obtained without considering the presence of the free runner, and, after developing the vortex rope, the free runner with three blades was activated, according with the Figure 2.

Figure 2. Full 3D domain: without free runner (**left**) and with free runner (**right**).

A numerical simulation was performed with the help of ANSYS Fluent 2021R1. The unsteady solver was employed, together with the *Generalized* k-ω (GEKO) model for modeling the turbulence parameters. The velocity components, together with the turbulence parameters, from the exit section of the swirl generator, obtained from experimental measurements, were imposed on the inlet boundary of the domain. On the outlet boundary, the outflow condition was imposed. For all wall boundary conditions, the Fluent default setup was retained, with no slip shear condition and standard roughness model [34,35].

To compute the interaction between the rotating domain, containing the free runner with three blades, and the static domain, the sliding mesh technique was employed, and two mesh interfaces were defined with the matching option activated, upstream and downstream of the free runner. The rotational speed imposed on the rotating domain was 850 rpm, corresponding to the free movement of the runner, and it was experimentally determined.

To generate the vortex rope, first, the presence of the free runner was "hidden" by defining the boundary condition on the blades as interior, and the volume was set as water. After the vortex rope was generated, the free runner was activated by imposing the wall boundary condition on the blades and the volume was set as solid.

As a solution method, the SIMPLEC scheme was used to calculate the pressure-velocity coupling. The spatial discretization was set to Second-Order Upwind for pressure, momentum, and turbulence parameters and to Least Squares Cell Based for the gradient. The transient formulation was set to Bounded Second-Order Implicit.

The time step was set at 0.001 s, which corresponds to a movement of the free runner of approximately 5°, and 15 iterations were considered for each time step. The numerical simulation was carried out for a flow time of 4.458 s for the case without the free runner and for a flow time of 2.505 s for the case with the free runner.

4. Validation of the Results

The first step in the analysis of the new concept is the validation of the velocity profiles obtained from the 3D numerical simulation against the experimental results. Measurements

have been validated in the convergent part of the test section on the W0 survey axis. The comparison between the experimental analysis and the 3D numerical simulation shows that the numerical results agree very well with the experimental values. The comparison was centered on two velocity components: the meridional velocity and the circumferential velocity. Note that the experimental velocity components were used to validate the results of numerical simulations, not as boundary conditions. In Figure 3 (right), the length of the survey axis W0 (corresponding to the X axis in Figure 3) is presented in dimensionless form considering the reference radius R_{ref} from the throat (the inlet in the conical diffuser). The velocity is presented in dimensionless form (corresponding to the Y axis), considering the throat velocity at a flow discharge of 0.03 m^3/s.

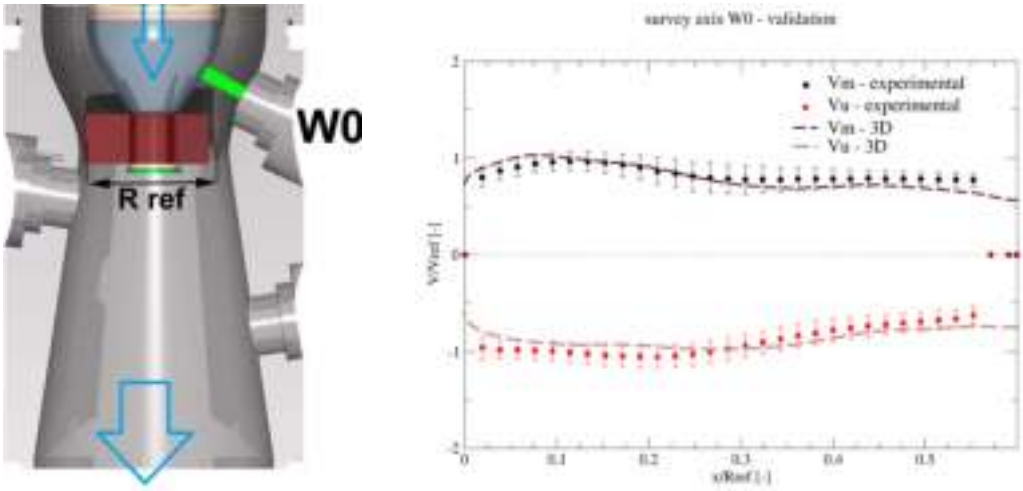

Figure 3. Validation of the velocities measured experimentally with the LDV on the survey axis W0 with the velocity profiles obtained from the 3D numerical simulation).

5. Results and Analysis

Considering the good validation of the numerical investigation, the next step is the analysis of the flow and of the pressure from the numerical simulation for the investigated cases, without and with the free runner. Figure 4 presents the flow evaluation in the conical diffuser for both cases, analyzing the vortex rope formation. To visualize the vortex rope, a constant pressure iso-surface was plotted, with green color, and the vortex cores of the flow field were calculated and plotted, the red-colored spheres. The pictures show that the vortex rope is present in the conical diffuser in the case without a free runner (left part of the images). It is forming close to the ogive and continues 2/3 from the length of the conical diffuser. When the free runner is inserted into the extension of the ogive, the vortex rope starts to decrease in length and thickness. It forms at the end of the shaft of the free runner and continues approximately 1/3 from the length of the conical diffuser.

Another analysis consists of evaluating the unsteady pressure registered 100 mm downstream of the inlet in the conical diffuser, as shown in Figure 5. The unsteady pressure is registered from the numerical simulation and after the FFT was performed. The analysis of the FFT shows the main frequency of the vortex rope (14.5 Hz). In the case without the free runner, the maximum amplitude reaches a value of 2000 Pa. When the free runner is introduced, the maximum amplitude reaches a value of 1500 Pa, which means a reduction of 25%. Nevertheless, it is pointed out that this case is testing a simple free runner with only three straight blades.

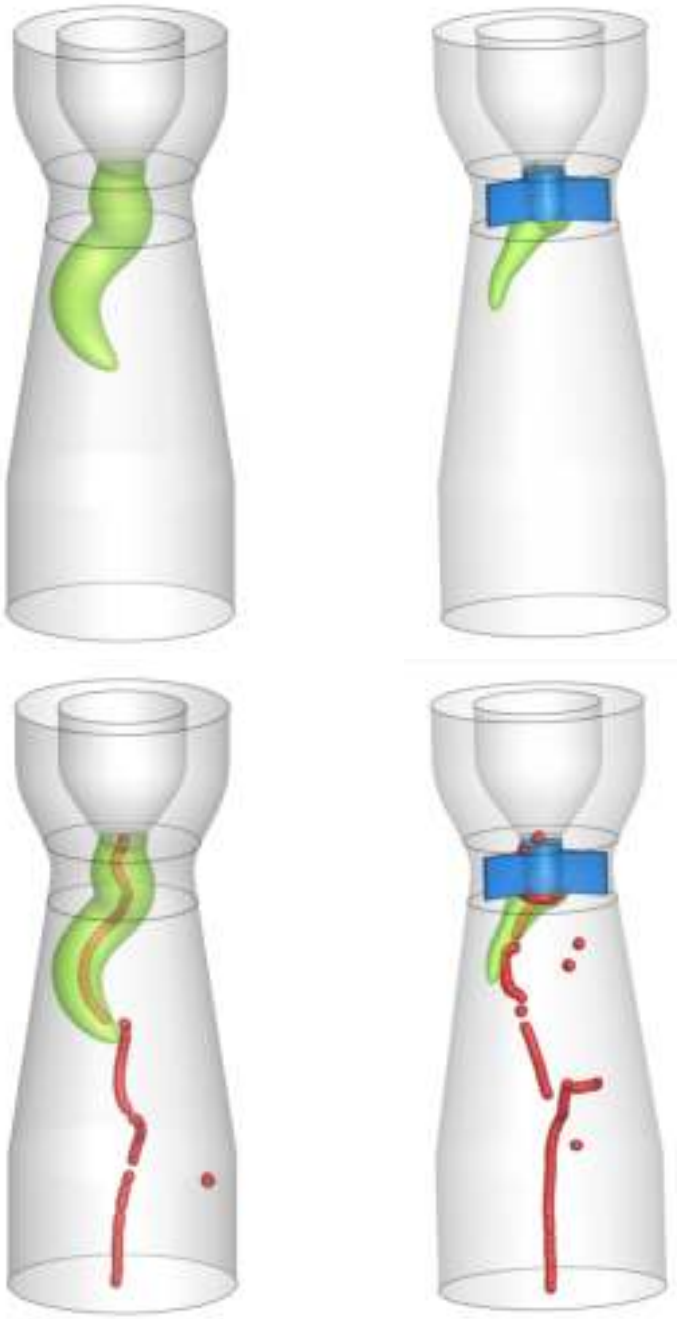

Figure 4. Visualization of the vortex rope for the case: without and with free runner.

Considering that the shape of the free runner blade is rectangular with a constant thickness of 3 mm, without a profiled leading edge and trailing edge, an evaluation of the total pressure was performed to determine the hydraulic losses. In the case without the free runner (with a developed vortex rope), the total pressure difference between the inlet and outlet in the numerical domain is 3695 Pa. When the free runner concept is implemented (with a diminished vortex rope), the total pressure difference is 4475 Pa. Therefore, in the case when the free runner is mounted at the inlet in the conical diffuser, the hydraulic losses increase by 21%. Further research with profiled blades on the free runner can better reduce hydraulic losses. Moreover, the minimum pressure moves from the ogive of the swirl generator (case without the free runner) to the shaft exit (case with the free runner), which means that neither the main runner nor the free runner works in cavitation.

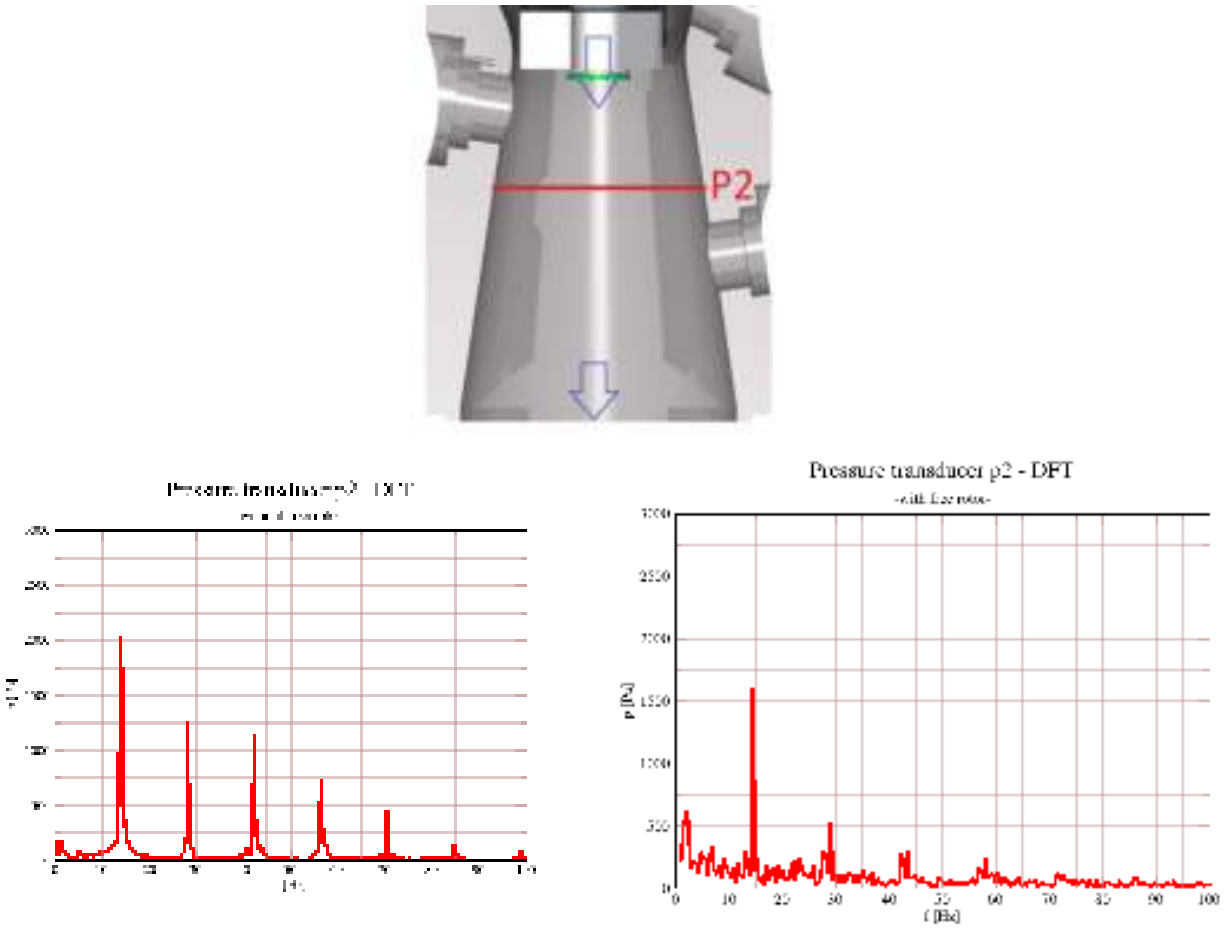

Figure 5. Evaluation of the Fourier transform on the point P2, 100 mm downstream of the inlet in the conical diffuser, for the cases without and with free runner from the numerical simulation.

6. Conclusions

In this paper, a new concept is proposed to diminish the hydrodynamic instabilities developed in the draft tube cone of hydraulic turbines. The concept is supposed to use a free runner (which rotates at the runaway speed) mounted downstream of the main hydraulic runner.

Considering that this is a new concept, the free runner was designed as simply as possible and was tested experimentally and numerically. The design of the free runner consists of using three rectangular sheets of metal with 3 mm thickness mounted on a shaft, between the main runner and the inlet in the conical diffuser. The ogive that closes the swirl generator was modified to sustain the free runner and allow it to rotate freely.

The experimental measurements and the numerical simulation have been performed without and with the free runner (at a speed of 850 rpm of the free runner). The vortex rope was evaluated from the 3D numerical simulation for both cases. It was clearly observed that when the free runner is installed, the vortex rope decreases in length and thickness. This conclusion can also be supported by the Fourier analysis of the unsteady pressure signals when the amplitude decreases by approximately 25% when the free runner is used. Nevertheless, the free runner concept investigated in this paper has used a simple runner with three straight blades only. Further investigations (a free runner with more blades and hydrodynamically designed) which are in progress, will confirm that the new concept could reduce the unsteadiness produced by the vortex rope.

Author Contributions: Conceptualization, A.I.B. and R.S.-R.; methodology, A.I.B. and R.S.-R.; software, A.S.; validation, A.I.B. and A.S.; investigation, A.I.B. and R.-A.S.; writing—original draft preparation A.I.B., R.-A.S. and A.S.; writing—review and editing, A.I.B., R.-A.S. and A.S. All authors have read and agreed to the published version of the manuscript.

Funding: This work was supported by a grant of the Romanian Ministry of Education and Research, CNCS-UEFISCDI, project number PN-III-P1-1.1-TE-2019-1594, within PNCDI III. The second author acknowledges the support of the Romanian Academy–Timișoara Branch thru the research programs of the Hydrodynamic, Cavitation, and Magnetic Liquid Division of the Center for Fundamental and Advanced Technical Research.

Institutional Review Board Statement: Not applicable.

Informed Consent Statement: Not applicable.

Data Availability Statement: Not applicable.

Conflicts of Interest: The authors declare no conflict of interest.

References

1. Kougias, I.; Aggidis, G.; Avellan, F.; Deniz, S.; Lundin, U.; Moro, A.; Muntean, S.; Novara, D.; Pérez-Díaz, J.I.; Quaranta, E.; et al. Analysis of emerging technologies in the hydropower sector. *Renew. Sustain. Energy Rev.* **2019**, *113*, 109257. [CrossRef]
2. Iliescu, M.S.; Ciocan, G.D.; Avellan, F. Analysis of the cavitating draft tube vortex in a Francis turbine using particle image velocimetry measurements in two-phase flow. *J. Fluid Eng.* **2008**, *130*, 146–157. [CrossRef]
3. Neidhardt, T.; Magnoli, M.; Gummer, J. High part-load fluctuations in Francis turbines and the applicability of model test data. *Hydro* **2017**, *2017*, 1–10.
4. Vu, T.C.; Retieb, S. Accuracy assessment of current CFD tools to predict hydraulic turbine efficiency hill chart. In Proceedings of the 21st IAHR Symposium on Hydraulic Machinery and Systems, Lausanne, Switzerland, 9–12 September 2002; pp. 93–198.
5. Susan-Resiga, R.; Stuparu, A.; Muntean, S. Francis turbine with tandem runners: A proof of concept. *IOP Conf. Ser. Earth Environ. Sci.* **2019**, *240*, 1–8. [CrossRef]
6. Kumar, S.; Cervantes, M.J.; Gandhi, B.K. Rotating vortex rope formation and mitigation in draft tube of hydro turbines—A review from experimental perspective. *Renew. Sustain. Energy Rev.* **2021**, *136*, 110354. [CrossRef]
7. Mohammadi, M.; Hajidavalloo, E.; Behbahani-Nejad, M.J. Investigation on combined air and water injection in Francis turbine draft tube to reduce vortex rope. *J. Fluid Eng.* **2019**, *141*, 051301. [CrossRef]
8. Pasche, S.; Avellan, F.; Gallaire, F. Part Load Vortex Rope as a Global Unstable Mode. *J. Fluid Eng.* **2017**, *139*, 1–12. [CrossRef]
9. Nicolet, C.; Zobeiri, A.; Maruzewski, P.; Avellan, F. On the upper part load vortex rope in Francis turbine: Experimental investigation. *IOP Conf. Ser. Earth Environ. Sci.* **2010**, *12*, 012053. [CrossRef]
10. Stuparu, A.; Resiga, R. The Complex Dynamics of the Precessing Vortex Rope in a Straight Diffuser. *IOP Conf. Ser. Earth Environ. Sci.* **2016**, *49*, 082013. [CrossRef]
11. Ciocan, G.D.; Iliescu, M.S.; Vu, T.C.; Nennemann, B.; Avellan, F. Experimental study and numerical simulation of the FLINDT draft tube rotating vortex. *J. Fluid Eng.* **2007**, *129*, 146–158. [CrossRef]
12. Cassidy, J.J.; Falvey, H.T. Observations of unsteady flow arising after vortex breakdown. *J. Fluid Mech.* **1970**, *41*, 727–736. [CrossRef]
13. Falvey, H.T.; Cassidy, J.J. Frequency and amplitude of pressure surges generated by swirling flows. In Proceedings of the International Association of Hydraulic Research Symposium on Hydraulic Machinery and System, Stockholm, Sweden, 29 June–2 July 1970.
14. Jacob, T.; Prenat, J.E. Francis turbine surge: Discussion and data base. In Proceedings of the Hydraulic Machinery and Cavitation: Proceedings of the XVIII IAHR Symposium on Hydraulic Machinery and Cavitation, Valencia, Spain, 16–19 September 1996; pp. 855–864.
15. Grein, H. Vibration phenomena in Francis turbines: Their causes and prevention. *Esccher Wyss News* **1981**, *54*, 37–42.
16. Thicke, R.H. Practical solutions for draft tube instability. *Water Power Dam Constr.* **1981**, *33*, 31–37.
17. Kurokawa, J.; Imamura, H.; Choi, Y.-D. Effect of J-groove on the suppression of swirl flow in a conical diffuser. *J. Fluid Eng.* **2010**, *132*, 071101. [CrossRef]
18. Nishi, M.; Wang, X.; Yoshida, K.; Takahashi, T.; Tsukamoto, T. An experimental study on fins, their role in control of the draft tube surging. In Proceedings of the Hydraulic Machinery and Cavitation: Proceedings of the XVIII IAHR Symposium on Hydraulic Machinery and Cavitation, Valencia, Spain, 16–19 September 1996; pp. 905–914.
19. Qian, Z.; Li, W.; Huai, W.-X.; Wu, Y. The effect of runner cone design on pressure oscillation characteristics in a Francis hydraulic turbine. *Proc. Inst. Mech. Eng. Part A J. Power Energy* **2012**, *226*, 137–150. [CrossRef]
20. Tănasă, C.; Bosioc, A.; Muntean, S.; Susan-Resiga, R. A Novel Passive Method to Control the Swirling Flow with Vortex Rope from the Conical Diffuser of Hydraulic Turbines with Fixed Blades. *Appl. Sci.* **2019**, *9*, 4910. [CrossRef]

21. Shiraghaee, S.; Sundström, J.; Raisee, M.; Cervantes, M.J. Mitigation of Draft Tube Pressure Pulsations by Radial Protrusion of Solid Bodies into the Flow Field: An Experimental Investigation. *IOP Conf. Ser. Earth Environ. Sci.* **2021**, *774*, 012004. [CrossRef]
22. Tanasa, C.; Susan-Resiga, R.; Muntea, S.; Bosioc, A.I. Flow-Feedback Method for Mitigating the Vortex Rope in Decelerated Swirling Flows. *J. Fluid Eng.* **2013**, *135*, 061304. [CrossRef]
23. Gokhman, A. Hydraulic Turbine and Exit Stay Apparatus Therefor. US Patent 6 918 744 B2, 19 July 2005.
24. Kjeldsen, M.; Olsen, K.; Nielsen, T.; Dahlhaug, O. Water injection for the mitigation of draft tube pressure pulsations. In Proceedings of the IAHR International Meeting of WG on Cavitation and Dynamic Problems in Hydraulic Machinery and Systems, Stuttgart, Germany, 9–11 October 2006.
25. Adolfsson, S. Expanding Operation Ranges Using Active Flow Control in Francis Turbines. Bachelor's Thesis, Umea University, Umea, Sweden, 2014.
26. Blommaert, G.; Prenat, J.; Avellan, F.; Boyer, A. Active control of Francis turbine operation stability. In Proceedings of the 3rd ASME/JSME Joint Fluids Engineering Conference, San Francisco, CA, USA, 18–23 July 1999; pp. 1–8.
27. Susan-Resiga, R.; Vu, T.C.; Muntean, S.; Ciocan, G.D.; Nennemann, B. Jet control of the draft tube vortex rope in Francis turbines at partial discharge. In Proceedings of the 23rd IAHR Symposium Conference, Yokohama, Japan, 17–21 October 2006; pp. 67–80.
28. Bosioc, A.I.; Susan-Resiga, R.; Muntean, S.; Tanasa, C. Unsteady Pressure Analysis of a Swirling Flow with Vortex Rope and Axial Water Injection in a Discharge Cone. *J. Fluid Eng.* **2012**, *134*, 081104. [CrossRef]
29. Bosioc, A.I.; Muntean, S.; Tanasa, C.; Susan-Resiga, R.; Vékás, L. Unsteady pressure measurements of decelerated swirling flow in a discharge cone at lower runner speeds. In Proceedings of the IOP Conference Series: Earth and Environmental Science, Montreal, QC, Canada, 22–26 September 2014; p. 22.
30. Szakal, R.A.; Doman, A.; Muntean, S. Influence of the reshaped elbow on the unsteady pressure field in a simplified geometry of the draft tube. *Energies* **2021**, *14*, 1393. [CrossRef]
31. Kirschner, O.; Ruprecht, A.; Göde, E.; Riedelbauch, S. Experimental investigation of pressure fluctuations caused by a vortex rope in a draft tube. In *IOP Conference Series: Earth and Environmental Science*; IOP Publishing: Bristol, UK, 2012; p. 15.
32. Bosioc, A.I.; Tanasa, C.; Muntean, S.; Susan-Resiga, R.F. Pressure Recovery Improvement in a Conical Diffuser with Swirling Flow Using Water Jet Injection. *Proc. Rom. Acad. Ser. A Math. Phys. Tech. Sci. Inf. Sci.* **2010**, *11*, 245–252.
33. Kirschner, O.; Ruprecht, A.; Göde, E. Experimental investigation of pressure pulsation in a simplified draft tube. In Proceedings of the 3rd IAHR International Meeting of the Workgroup on Cavitation and Dynamic Problems in Hydraulic Machinery and Systems, Brno, Czech Republic, 14–16 October 2009.
34. Anton, A.A. Reconstruction of a space-time window in a transient simulation of the breaking of a dam. In Proceedings of the 6th IEEE International Symposium on Applied Computational Intelligence and Informatics (SACI), Timisoara, Romania, 19–21 May 2011; pp. 335–340.
35. Anton, A.A. Numerical Investigation of Unsteady Flows using OpenFOAM. *Hidraulica* **2016**, *1*, 7–12.

Disclaimer/Publisher's Note: The statements, opinions and data contained in all publications are solely those of the individual author(s) and contributor(s) and not of MDPI and/or the editor(s). MDPI and/or the editor(s) disclaim responsibility for any injury to people or property resulting from any ideas, methods, instructions or products referred to in the content.

International Journal of
Turbomachinery
Propulsion and Power

MDPI

Article

Optimization, Control, and Design of Arbitrarily Shaped Fan Arrays

Daniel Conrad *, Jonathan Mayer and Erik Reichert

ebmpapst Mulfingen GmbH & Co. KG, 74673 Mulfingen, Germany
* Correspondence: daniel.conrad@de.ebmpapst.com

Abstract: In many air conditioning applications fan arrays offer an increasingly popular alternative to single large fans due to redundancy and ease of maintainability. Additionally, there is the possibility to dynamically resize the array by selectively turning off a number of fans. In this work, a new method for the optimal control of such fan arrays is derived with the goal to minimize the overall power consumption, i.e., maximizing the system efficiency. The approach is universal in the sense that a fan array can be composed of any number, size, and type of fans or mixtures thereof. We explore the achievable power savings for a real world example by applying the method. Moreover, we give an outline of the optimal design of fan arrays and future work.

Keywords: fan arrays; optimization; efficiency increase; power savings; sustainability

check for updates

Citation: Conrad, D.; Mayer, J.; Reichert, E. Optimization, Control, and Design of Arbitrarily Shaped Fan Arrays. *Int. J. Turbomach. Propuls. Power* **2023**, *8*, 12. https://doi.org/10.3390/ijtpp8020012

Academic Editor: Thomas Carolus

Received: 17 August 2022
Revised: 7 March 2023
Accepted: 20 March 2023
Published: 6 April 2023

Copyright: © 2023 by the authors. Licensee MDPI, Basel, Switzerland. This article is an open access article distributed under the terms and conditions of the Creative Commons Attribution (CC BY-NC-ND) license (https://creativecommons.org/licenses/by-nc-nd/4.0/).

1. Introduction

Although the aerodynamic efficiency of single fans still rises through further development, the research and development in the field of fan systems will get even more important in the future. Nowadays, medium to large-sized fans in traditional applications are increasingly replaced by fan arrays; that is, a number of usually smaller fans operating in parallel. This is due to a number of generally accepted advantages. One obvious benefit is the redundancy of fans. If there is a failure of a single fan in the fan array, the remaining fans can partially or completely compensate by managing their operating speed appropriately. Along with this goes the ease for replacement of smaller-sized fans as compared to one large device. On the other hand, there are also application-specific profits. In a heat exchanger application, for example, it can be shown that the use of fan arrays leads to a significantly lower pressure loss and higher convective heat transfer, because of the more even flow profile over the heat exchanger as compared to a more uneven profile generated by a large single fan [1]. In addition to the aforementioned advantages, fan arrays offer additional degrees of freedom [2]. In applications with varying operating points, large improvement in system efficiency and high energy savings can be archived [3]. This is achieved by selectively turning off some of the fans in an array while controlling the operation of the remaining active fans accordingly. For this purpose we propose a method for the optimal control of such fan arrays [4]. In our approach, the arrays can be composed of an arbitrary number of different-sized fans and/or fans with different fan curve characteristics.

The paper is organized as follows: In the first section, we will introduce the necessary physical quantities involved in the operation of a fan array and derive our method for optimal control of such arrays. In the second section, we will apply the proposed method to a real-world problem to demonstrate the achievable system performance improvements. Finally, we give an outline for the optimal design of fan arrays and conclude our findings.

2. Method Description

The A fan array of size k_{max} is defined as k_{max} (not necessarily identical) fans operating in parallel. That is, all fans in the array deliver the same static pressure rise. However,

depending on their individual speed, their individual contribution to the overall volume flow rate might be different. This is depicted schematically in Figure 1 with four ebm-papst R3G500 centrifugal fans in a 2 × 2 setup.

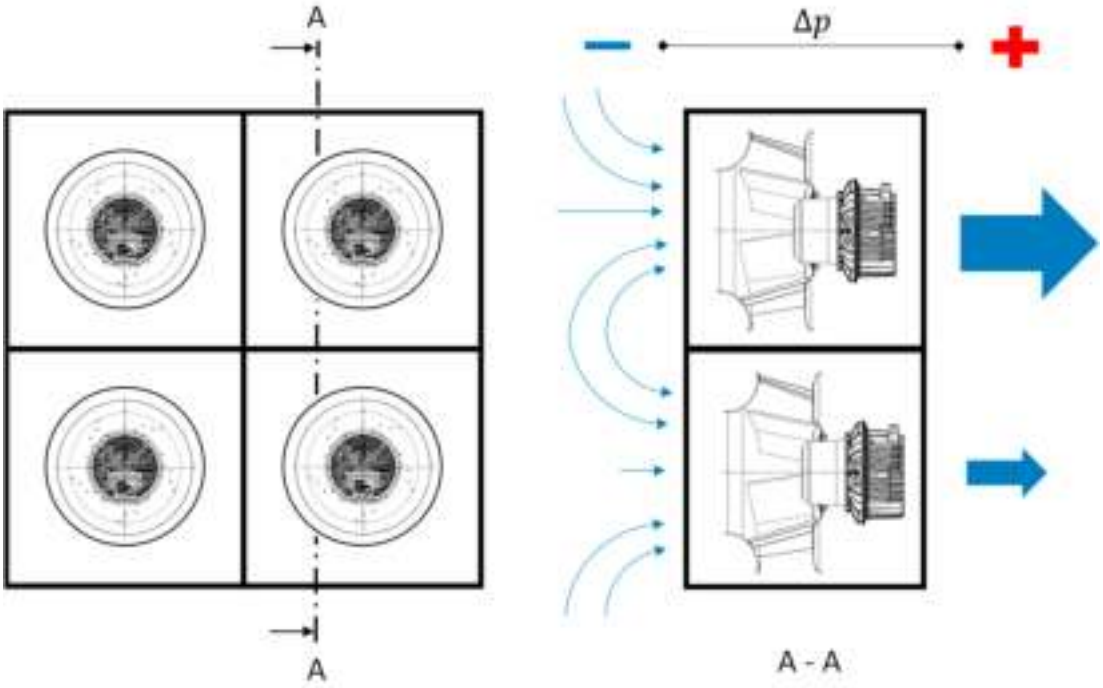

Figure 1. Four identical ebmpapst R3G500 centrifugal fans in a 2 × 2 array setup.

There are only two prerequisites present in the theoretical derivation of our method:

- It is assumed that the speed of each fan in the array of fans can be variably controlled up to its maximum rotational speed;
- It is assumed that no backflow occurs in situations where fans are turned off. In reality, this can be achieved using, i.e., some kind of shutters or backdraft dampers.

The non-dimensional fan power for each individual fan in the array, denoted by index i, is given by:

$$P_i^* = \frac{\psi_i \cdot \varphi_i}{\eta_i}, \tag{1}$$

with the well known pressure number ψ, flow number φ, and the efficiency η. The dimensional power is thus given by:

$$P_i = P_i^* \cdot \frac{\pi^4 \cdot D_i^5 \cdot n_i^3 \cdot \rho}{8}, \tag{2}$$

with diameter D and operating speed n of the i-th fan in the array and density ρ.

2.1. Fixed Array Size with identical Fans

Now, we consider the fan array with a fixed number k_{max} and fixed type of fans. That is, in the following, the D_i are set to a constant value and the operating speeds n_i become the sole free variables in the system. The goal of our method is to find the optimal speed for each individual fan.

The optimality condition for an array with size k and given operating point Δp and Q_{tot} is the minimization of the total power consumption of the array:

$$\text{min: } P_{tot} = \sum_{i=1}^{k} P_i(n_i), \text{Subject to: } Q_{tot} = \sum_{i=1}^{k} Q_i(n_i) \ ,$$

where $Q_i = \varphi_i \cdot \pi^2 \cdot D_i^3 \cdot n_i / 4$ is the volume flow rate for the i-th individual fan in the array. As this is a continuous non-linear programming problem (NLP) with a single equality constraint, we choose the method of Lagrange multipliers for its solution [5]. This formulation of the optimization problem leads to a non-linear system of equations with $k+1$ unknowns (k speeds plus one Lagrange multiplier λ for the volume flow rate constraint):

$$\frac{\partial P_1}{\partial n_1} = \lambda \cdot \frac{\partial Q_1}{\partial n_1} : \frac{\partial P_k}{\partial n_k} = \lambda \cdot \frac{\partial Q_k}{\partial n_k} Q_{tot} = \sum_{i=1}^{k} Q_i(n_i) \tag{3}$$

For the solution of this system of equations, the partial derivatives of the dimensional power with respect to the operating speed are required. In order to make the optimization problem accessible to a calculation, the power and the volume flow rate are transformed in such a way that they are pure functions of the speed. At this point, the dimensionless pressure and efficiency curves of the fans used in an array are introduced. In the following, we stick to the special case of an ebmpapst R3G500 centrifugal fan characteristic shown in Figure 2. However, this is for demonstration purposes and does not restrict the validity of our approach. The overall shape of the performance and efficiency characteristic curves will always be similar for all conventional fans due to well-known loss mechanisms [6,7].

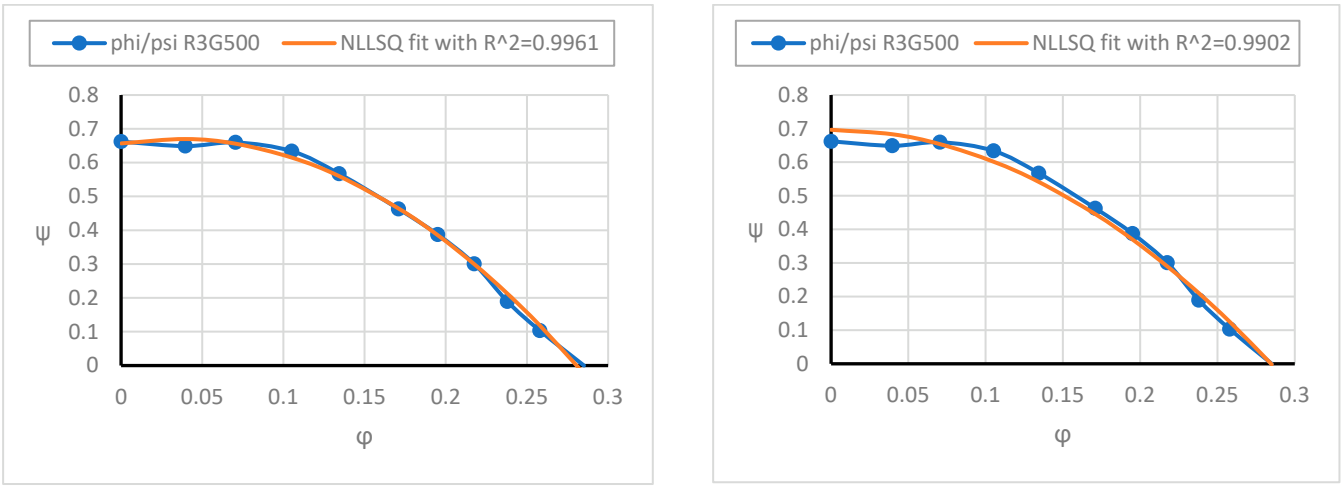

(**a**) (**b**)

Figure 2. Approximation of the non-dimensional fan pressure characteristics: (**a**) with a second-order polynomial; (**b**) with a quadratic ansatz.

From Equation (3) it is obvious that we need to approximate the fan characteristics using continuously differentiable functions. The respective dimensionless pressure characteristic of a fan is approximated with a second-order polynomial Equation (4). Preference is given here to the approximation with a quadratic approach Equation (5), since the approximation function is then strictly monotonic in the considered range $\varphi > 0$. This is an idealization because in reality, the fan stalls for low φ and the operation becomes unstable. One would have to define a minimum φ, but we opt for this approach to demonstrate the method.

$$\psi_i(\varphi_i) = a_{\psi,i} \cdot \varphi_i^2 + b_{\psi,i} \cdot \varphi_i + c_{\psi,i} \tag{4}$$

$$\psi_i(\varphi_i) = a_{\psi,i} \cdot \varphi_i^2 + c_{\psi,i} \tag{5}$$

With this description of the pressure number, the flow number can be expressed as a function of the constant coefficients of the polynomial approximation, diameter, density,

speed, and pressure increase. Resolving the quadratic Equation (4) for the flow number yields:

$$\varphi_i(n_i) = -\frac{b_{\psi,i}}{2a_{\psi,i}} + \sqrt{\left(\frac{b_{\psi,i}}{2a_{\psi,i}}\right)^2 - \frac{c_{\psi,i}}{a_{\psi,i}} + \frac{2\Delta p}{\rho \cdot \pi^2 \cdot D_i^2 \cdot n_i^2 \cdot a_{\psi,i}}}. \tag{6}$$

The derivative of the flow number with respect to the fan speed is given by:

$$\frac{\partial \varphi_i}{\partial n_i} = -\frac{\frac{2\Delta p}{\rho \cdot \pi^2 \cdot D_i^2 \cdot n_i^3 \cdot a_{\psi,i}}}{\sqrt{\left(\frac{b_{\psi,i}}{2a_{\psi,i}}\right)^2 - \frac{c_{\psi,i}}{a_{\psi,i}} + \frac{2\Delta p}{\rho \cdot \pi^2 \cdot D_i^2 \cdot n_i^2 \cdot a_{\psi,i}}}}. \tag{7}$$

Accordingly, the efficiency characteristics need to be approximated. Preference is given here to a fourth order polynomial:

$$\eta_i(\varphi_i) = a_{\eta,i} \cdot \varphi_i^4 + b_{\eta,i} \cdot \varphi_i^3 + c_{\eta,i} \cdot \varphi_i^2 + d_{\eta,i} \cdot \varphi_i + e_{\eta,i}. \tag{8}$$

Likewise, deriving Equation (7) yields:

$$\frac{\partial \eta_i}{\partial n_i} = \left(4a_{\eta,i} \cdot \varphi_i^3 + 3b_{\eta,i} \cdot \varphi_i^2 + 2c_{\eta,i} \cdot \varphi_i + d_{\eta,i}\right) \cdot \frac{\partial \varphi_i}{\partial n_i}. \tag{9}$$

Both Equations (7) and (9) are needed in the chain rule for the computation of the derivative of the non-dimensional power P^*:

$$\begin{aligned} \frac{\partial P_i^*}{\partial n_i} &= \frac{\partial\left(a_{\psi,i} \cdot \varphi_i^3 + b_{\psi,i} \cdot \varphi_i^2 + c_{\psi,i} \cdot \varphi_i\right)}{\partial \eta_i(\varphi_i)} \\ &= 3 \cdot a_{\psi,i} \varphi_i^2 \cdot \eta_i^{-1} \cdot \frac{\partial \varphi_i}{\partial n_i} - a_{\psi,i} \varphi_i^3 \cdot \eta_i^{-2} \cdot \frac{\partial \eta_i}{\partial n_i} \\ &+ 2 \cdot b_{\psi,i} \varphi_i \cdot \eta_i^{-1} \cdot \frac{\partial \varphi_i}{\partial n_i} - b_{\psi,i} \varphi_i^2 \cdot \eta_i^{-2} \cdot \frac{\partial \eta_i}{\partial n_i} \\ &+ c_{\psi,i} \cdot \eta_i^{-1} \cdot \frac{\partial \varphi_i}{\partial n_i} - c_{\psi,i} \varphi_i \cdot \eta_i^{-2} \cdot \frac{\partial \eta_i}{\partial n_i}. \end{aligned} \tag{10}$$

Finally, we are able to compute the derivative of the dimensional fan power with respect to the fan speed:

$$\frac{\partial P_i}{\partial n_i} = \frac{\pi^4 \cdot D_i^5 \cdot \rho}{8} \left(3n_i^2 \cdot P_i^* + n_i^3 \cdot \frac{\partial P_i^*}{\partial n_i}\right). \tag{11}$$

In a last step, we derive the dimensional volume flow rate with respect to the fan speed:

$$\frac{\partial Q_i}{\partial n_i} = \frac{\pi^2 \cdot D_i^3}{4} \cdot \left(\varphi_i + n_i \cdot \frac{\partial \varphi_i}{\partial n_i}\right). \tag{12}$$

At this point, we acquired all expressions needed in Equation (3). All approximations used are continuously differentiable by construction through polynomials. The solution of this system of equations yields the optimal operating speeds for each fan such that the array adheres to the operating point given by Δp and Q_{tot}.

By variation in the operating point specification and subsequent solving of the system of equations, we obtain a map of optimal operating speeds in the boundaries $\Delta p_{min} \leq \Delta p \leq \Delta p_{max}$ and $Q_{min} \leq Q \leq Q_{max}$ for the fan array.

In reality, the fan speed has an upper limit given by the motor and/or the material. There is also a lower fan speed limit, which is determined by the maximum pressure number for the considered operating point (i.e., the individual fan needs to be able to generate the operating pressure). Both limits are considered as a non-linear inequality constraint.

2.2. Variable Array Size with Identical Fans

So far, we assumed that all fans of an array with size k_{max} are actively in operation. Now, we investigate possible benefits of selectively turning off one or more fans in such an array. With this modification, the optimization problem becomes a mixed-integer nonlinear programming problem (MINLP).

We solve this by applying our method to different array sizes $k = 1, 2, \ldots, k_{max}$. That means, instead of solving the MINLP directly, we resort to solving a series of NLPs and choose the best configuration in a postprocessing step. In the case of $1 \leq k \leq k_{max}$, we turn off $k_{max} - k$ fans in the array. As stated above, we assume that there is no backflow for turned off fans.

This approach yields the optimal fan speeds along with the corresponding overall power consumption for each of the different arrays sizes. Picking the array size with minimum power consumption yields the optimal array size, i.e., the number of fans to turn off while operating the active fans using their optimal fan speeds.

2.3. Variable Array Size with Different Fan Sizes and/or Fan Types

The fans in a parallel setting do not need to be from the same type or size. A possible scenario for an array with different fans is shown in Figure 3:

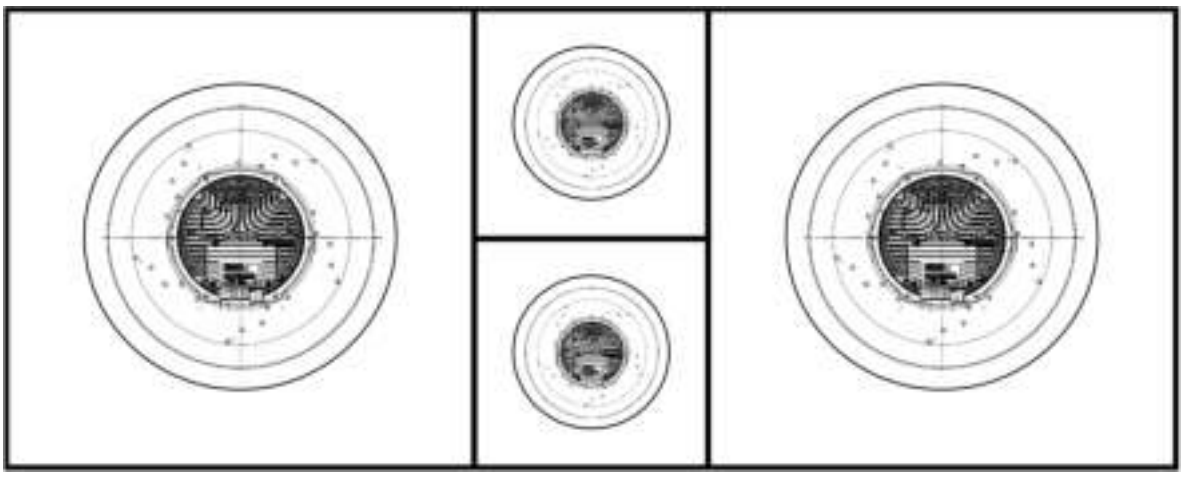

Figure 3. 2×2 fan array with two different sized centrifugal fans.

Our approach is able to account for arrangements where we mix, for example, different sizes of centrifugal fans with different sizes of axial fans. In order to describe this more formally, the fans can vary in their size (D_i) as well as their non-dimensional characteristics described with the coefficients $a_{\psi,i}$, $b_{\psi,i}$, $c_{\psi,i}$, $a_{\eta,i}$, $b_{\eta,i}$, $c_{\eta,i}$, $d_{\eta,i}$, and $e_{\eta,i}$ in Equations (4), (5), and (8).

In contrast to the approach used for varying array sizes with identical fans, we now have to distinguish between different settings of the array when one or more fans are turned off. This is a problem of unordered sampling without replacement. When shutting down $k_{max} - k$ fans, there are $\frac{k_{max}!}{k! \cdot (k_{max}-k)!}$ unique possible combinations for the operation of the fan array of size $k < k_{max}$.

For a given operating point, we need to vary the array size and additionally calculate all possible combinations of active fans. This approach yields $\sum_{k=1}^{k_{max}} \frac{k_{max}!}{k! \cdot (k_{max}-k)!}$ optimal fan speed combinations, power consumptions, and fan combinations, respectively. The minimum of these power consumptions determines the optimal array size k_{opt} and corresponding k_{opt} fan speeds, as well as the corresponding fan combinations. With this approach, we can assign every operating point in the map with $\Delta p_{min} \leq \Delta p \leq \Delta p_{max}$ and $Q_{min} \leq Q \leq Q_{max}$ a k_{opt}-tuple of optimal fan speeds and the corresponding optimal

combination of active fans, which maximizes the system efficiency, where $k_{max} - k_{opt}$ fans are turned off, respectively.

3. Real World Example

For the sake of illustration of our method and without loss of generality, we consider a 2×2 fan array consisting of four identical centrifugal fans as depicted in Figure 4:

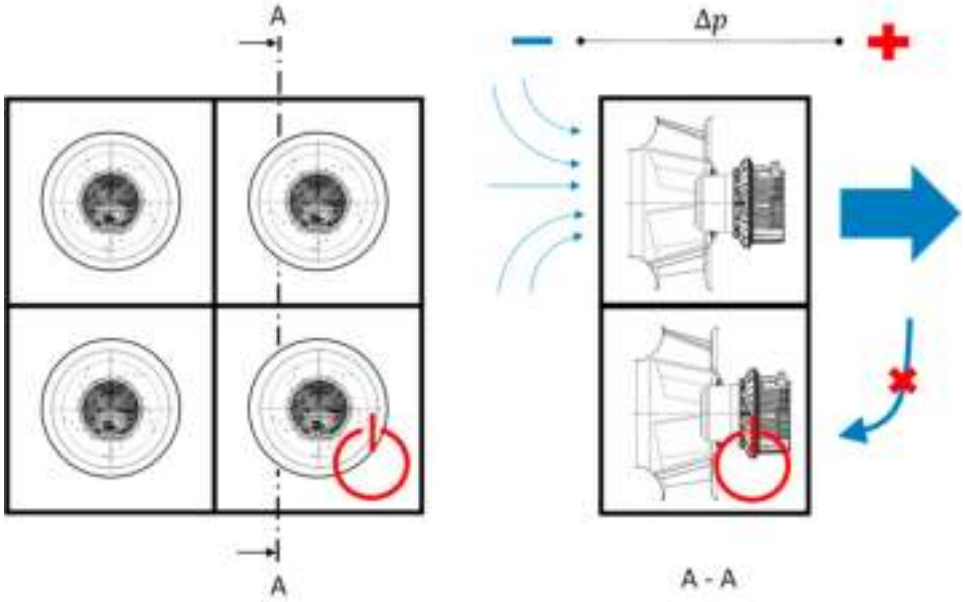

Figure 4. 2×2 fan array with four identical ebmpapst R3G500 centrifugal fans with exemplarily one fan turned off. There is no backflow through the turned off fan.

In order to make the findings more tangible, we omit a non-dimensional presentation and use dimensional values of ebmpapst's R3G500 centrifugal fan. Applying our method to this 2×2 array yields the result in Figure 5 for the operating map of the array where the color bar indicates the number of active fans in the array:

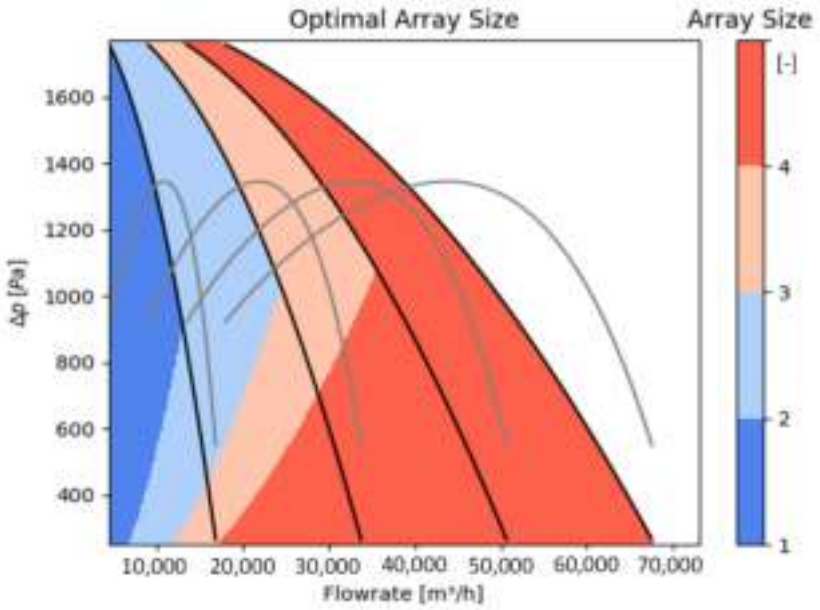

Figure 5. Fan map with optimal array size. Black solid lines are the pressure curves of a single fan, two fans, three fans, and the whole four-fan array at maximum fan speed, respectively. Grey lines are the corresponding efficiency curves.

3.1. Discussion of the Operating Map

At very low volume flow rates and pressure levels, it is most efficient to shut down three fans and operate the array with a single fan. With increasing volume flow rate, it becomes advantageous to operate with two fans instead. However, if there is also an increase in pressure demand, it might again be more beneficial to operate in single-fan mode with an adapted fan speed. However, this can only be realized up to the maximum performance of a single fan. Therefore, if the pressure demand further increases, it is mandatory to switch to two-fan mode because a single fan cannot deliver the prescribed volume flow rate anymore, since it already operates at its maximum fan speed. Depending on the operating point this pattern is generalized to higher numbers of active fans.

Additionally, as can be intuitively expected, there is no potential of shutting down any fans in the overload area of the fan array, i.e., in operating points where the full volume flow rate of the array is needed.

3.2. Comparison of an Optimally Controlled Array with on/off Operation to an Optimally Controlled Array without on/off:

The traditional way of improving the efficiency of such an array with identical fans is to synchronously manage the fan speed, as opposed to no control at all (i.e., operation with a fixed fan speed). The optimal way to do this is to apply our method to the full k_{max} sized array, where we compute the fan speeds that minimize the array power consumption across the whole fan map. This would correspond to a classical speed control.

The left plot in Figure 6 shows the solution for the optimally controlled fan array of size 4, where the total number of fans is always active. The color bar, along with some isolines, indicates the total power consumption.

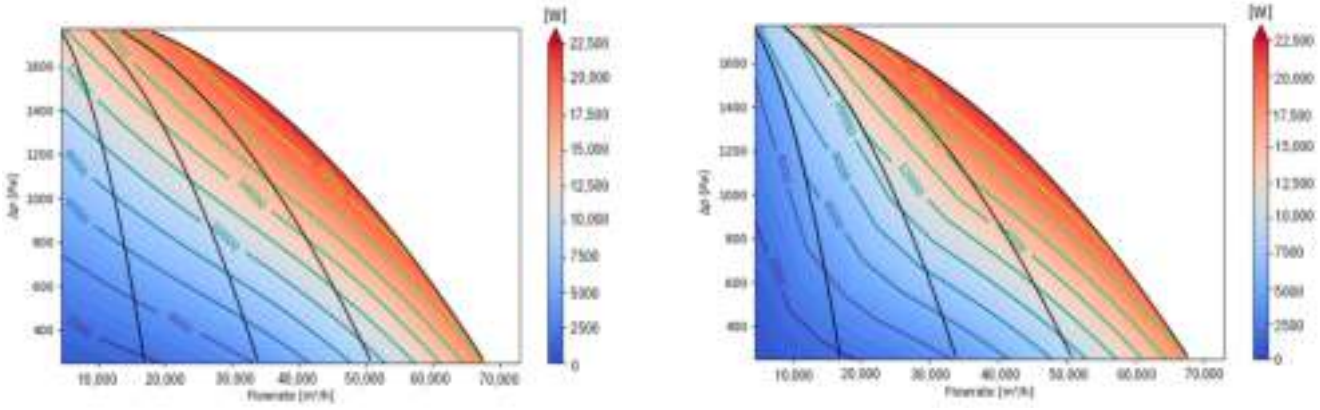

(**a**) (**b**)

Figure 6. Performance map of an array of size 4: (**a**) with optimal fan speeds; (**b**) with optimal array size and optimal fan speeds.

For comparison, there is the solution for the optimally controlled array with optimal array size (this means the number of active fans is variable) on the right-hand side of Figure 6.

In order to highlight the benefits of the new approach, we now have a look at the difference between the two methods of control. Thus, we subtract the values of power consumption of the classical speed control (all fans active) from the power consumption of the variable array approach. We do this for each operating point of the operating map.

Figure 7 shows that, in a moderate area of the operating map, it is already possible to save 1 kW of power consumption, as indicated by the yellow isoline when applying the described new method (with on/off).

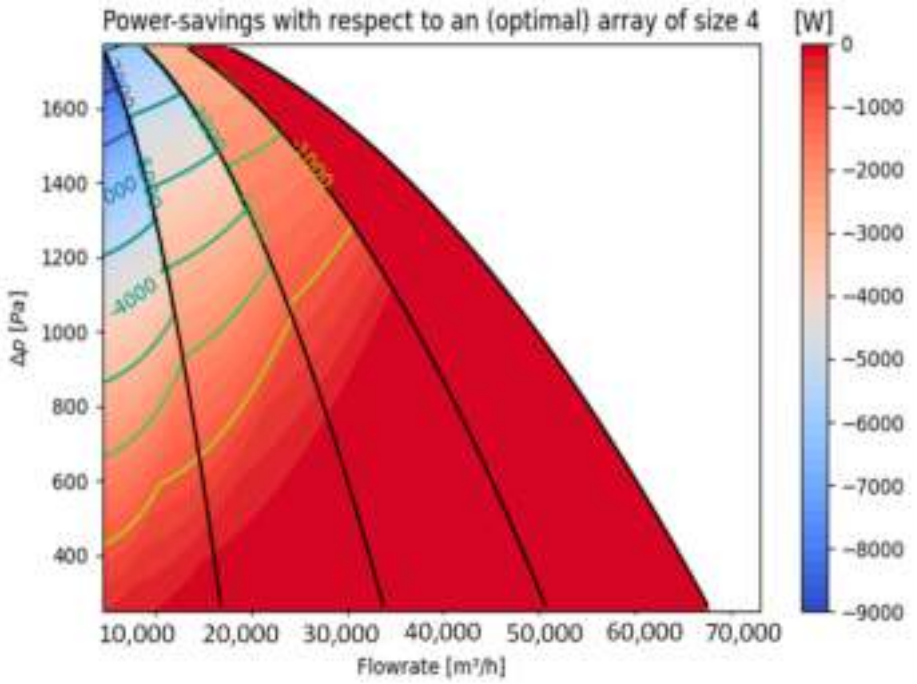

Figure 7. Difference between an optimally controlled array of size 4 and an optimally controlled array of optimal size.

Overall, it can be stated that the power consumption savings increase with decreasing volume flow rate and/or increasing pressure demand. The savings are highest in areas with high pressure and low volume flow rate.

This was expected since we can shut down fans in this area of the operating map. Again, there is no saving potential for the power consumption when the operating point can only be met with the full sized array. In this case, the solution of the optimally controlled size 4 array is reproduced.

Another way to investigate the benefits of our on/off approach is to have a look at varying volume flow rates at constant pressure levels. For this purpose, we select two different pressure levels, namely 800 Pa and 1200 Pa as depicted in Figure 8:

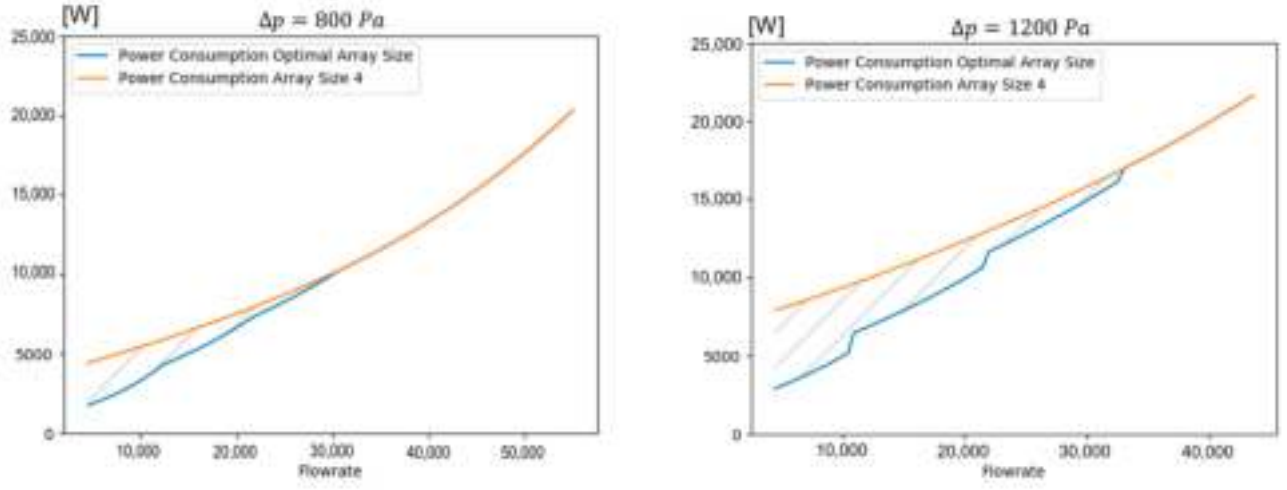

(**a**) (**b**)

Figure 8. Comparison of the power consumption with and without shutdown of fans: (**a**) for constant pressure of 800 Pa; (**b**) for constant pressure level of 1200 Pa.

Due to the reasons already mentioned, we cannot shutdown any fans in areas with a high volume flow rate. For Δp = 800 Pa, the saving potential kicks in at about 50% of the maximal volume flow rate for this pressure level and increases towards low volume flow rates while gradually reducing the active fan array size.

For the pressure level of 1200 Pa, the saving potential is even more prominent. The onset of the saving potential is already at about 75% of the possible volume flow rate for this pressure level with significantly higher savings for low volume flow rates.

3.3. Design of Fan Arrays

So far, only preexisting arrays were considered. Our method can also be used for the optimal design of new fan arrays.

To this end, we use the approach described above for variably sized arrays. For a given operating point, we consider the diameter of each fan as an additional free variable. Usually, we consider a discrete set of j diameters. By sweeping through the diameter set and subsequent application of our method, we can compute the parameter set, which yields the maximum system efficiency. In a more sophisticated approach, we can also consider the type of fans given by the coefficients $a_{\psi,i}$, $b_{\psi,i}$, $c_{\psi,i}$, $a_{\eta,i}$, $b_{\eta,i}$, $c_{\eta,i}$, $d_{\eta,i}$, and $e_{\eta,i}$ as additional free variables.

However, it should be noted that the problem size increases exponentially with the number of possible fans to test. This can pose a limit for the exhaustive search used above. A corresponding study will be conducted on how to solve this problem using a reformulation of the equation system (3).

4. Conclusions and Outlook

This work described an innovative method to control fan arrays with the goal of maximizing power savings using optimal fan speeds and the option to selectively shut down one or more fans in the array. This new approach is applicable to arbitrarily shaped fan arrays and a real world example of a 2 $\times$ 2 array of ebmpapst's R3G500 centrifugal fans was examined. It was shown that significant energy savings are possible in areas with moderate to low volume flow rate and/or high pressure level.

This method can also be used to determine an optimal design of fan arrays. Here, the diameter and coefficients that describe the fan characteristics are additional free variables. An in-depth study will be conducted for alternative approaches to the exhaustive search presented for sufficiently small number of possible fans. This is part of future work.

In this work, the target was the minimization of power consumption (optimality condition). We can also allow different target functionals by replacing the aerodynamic power in the system of equations Equation (3) with, e.g., acoustic power. This would enable an operator of fan arrays to control the fan array for minimal sound emission. Alternatively, a multiobjective tradeoff between two or more target functionals is also conceivable. This is also part of future work.

We hope our method is able to make a valuable contribution to the operation and design of fan arrays with the ultimate goal for saving precious energy resources.

Author Contributions: Conceptualization, D.C. and E.R.; methodology, D.C.; software, D.C.; validation, D.C. and J.M.; formal analysis, D.C.; investigation, D.C.; resources, D.C.; data curation, D.C.; writing—original draft preparation, D.C.; writing—review and editing, D.C. and J.M.; visualization, D.C.; supervision, E.R.; project administration, D.C.; funding acquisition not applicable. All authors have read and agreed to the published version of the manuscript.

Funding: This research received no external funding.

Institutional Review Board Statement: Not applicable.

Informed Consent Statement: Not applicable.

Data Availability Statement: Fan Data in general can be found at https://www.ebmpapst.com, accessed on 17 August 2022. Data for R3G500: https://www.ebmpapst.com/de/de/products/centrifugal-fans/p/R3G500PB2465.html, accessed on 17 August 2022.

Conflicts of Interest: The authors declare no conflict of interest.

References

1. Czwielong, F.; Soldat, J.; Becker, S. On the interactions of the induced flow field of heat exchangers with axial fans. *Exp. Therm. Fluid Sci.* **2022**, *139*, 110697. [CrossRef]
2. Groß, T.F.; Pöttgen, P.F.; Pelz, P.F. Analytical Approach for the Optimal Operation of Pumps in Booster Systems. *J. Water Resour. Plan. Manag.* **2017**, *143*, 04017029. [CrossRef]
3. Kallesøe, C.; Aarestrup, J.; Rokkjær, K. Energy optimization for booster sets. *World Pumps* **2011**, *2011*, 24–30. [CrossRef]
4. Dai, Y.; Jiang, Z.; Chen, P. Decentralized Optimal Control of Variable Speed Parallel-connected Pumps. In Proceedings of the BS2015, the 14th International Conference of the International Building Performance Simulation Association, Hyderabad, India, 7–9 December 2015; pp. 1103–1109.
5. Dodge, Y. Lagrange Multiplier. In *The Concise Encyclopedia of Statistics*; Springer: New York, NY, USA, 2008. [CrossRef]
6. Gülich, J.F. *Centrifugal Pumps*; Springer: New York, NY, USA, 2008.
7. Vieira, T.S.; Siqueira, J.R.; Bueno, A.D.; Morales, R.E.M.; Estevam, V. Analytical study of pressure losses and fluid viscosity effects on pump performance during monophase flow inside an ESP stage. *J. Pet. Sci. Eng.* **2015**, *127*, 245–258. [CrossRef]

Disclaimer/Publisher's Note: The statements, opinions and data contained in all publications are solely those of the individual author(s) and contributor(s) and not of MDPI and/or the editor(s). MDPI and/or the editor(s) disclaim responsibility for any injury to people or property resulting from any ideas, methods, instructions or products referred to in the content.

International Journal of Turbomachinery Propulsion and Power

MDPI

Editorial

Acknowledgment to the Reviewers of *IJTPP* in 2022

***IJTPP* Editorial Office**

MDPI AG, St. Alban-Anlage 66, 4052 Basel, Switzerland

High-quality academic publishing is built on rigorous peer review. *IJTPP* was able to uphold its high standards for published papers due to the outstanding efforts of our reviewers. Thanks to the efforts of our reviewers in 2022, a first decision is provided to authors approximately 48.5 days after submission, and acceptance to publication is undertaken in 6 days (median values for papers published in this journal in the second half of 2022). Regardless of whether the articles they examined were ultimately published, the editors would like to express their appreciation and thank the following reviewers for the time and dedication that they have shown *IJTPP*:

Aissa, Mohamed Hassanine
AL-Tubi, Moammer Ali Saud
Baert, Lieven
Baines, Nick
Bamberger, Konrad
Barigozzi, Giovanna
Benra, Friedrich Karl
Bianchini, Cosimo
Biedermann, Till M.
Binder, Nicolas
Böhle, Martin
Bontempo, Rodolfo
Brandstetter, Christoph
Brillert, Dieter
Brümmer, Andreas
Buchwald, Patrick
Camci, Cengiz
Carolus, Thomas
Casari, Nicola
Castegnaro, Stefano
Colmenero, Gerardo
Congiu, Franceso
Coull, John
Davidson, Lars
Demaison, Francois
Dolle, Bastian
Domercq, Olivier
Dufour, Guillaume
Dumas, Michel
Epple, Philipp
Eulitz, Frank
Feldmann, Carolin
Ferlauto, Michele
Flaszynski, Pawel
Frey, Yuri
Gebel, Gregor
Geoff Sheard, Anthony
Gicquel, Laurent Y.M.
Göttlich, Emil
Greco, Michele
Green, Jeffrey
Guedel, Alain
Haug, Jakob
Hillewaert, Koen
Iaccarino, Gianluca
Lampart, Piotr
Lavagnoli, Sergio
Lee, Jeong Ik
Lepot, Ingrid
Loftus, Peter
Lorenz, Ulf
Martelli, Francesco
Marty, Julien
Meyer, Marcus
Michelassi, Vittorio
Moreau, Stephane
Nau, Patrick
Pavesi, Giorgio
Peitsch, Dieter
Peng, Caetano
Picchi, Alessio
Pinelli, Michele
Pohl, Christian
Puente Rico, Ricardo
Reichert, Erik
Roger, Michel

Citation: *IJTPP* Editorial Office. Acknowledgment to the Reviewers of *IJTPP* in 2022. *IJTPP* **2023**, *8*, 2. https://doi.org/10.3390/ijtpp8010002

Published: 20 January 2023

Copyright: © 2023 by the author. Licensee MDPI, Basel, Switzerland. This article is an open access article distributed under the terms and conditions of the Creative Commons Attribution (CC BY) license (https://creativecommons.org/licenses/by/4.0/).

Sandberg, Mark
Sanjosé, Marlène
Sanz, Wolfgang
Schiffmann, Jürg Alexander
Schram, Christophe
Schuff, Matthias
Schuster, Sebastian
Schvallinger, Michaël
Semmler, Klaus
Seshadri, Pranay
Seume, Joerg R.
Simonassi, Loris
Sjolander, Steen
Skoda, Romuald
Stapelfeldt, Sina
Tiwari, Rajiv
Tunstall, Richard
Urbano, Annafederica
Verstraete, Tom
Wang, Jie
Witt, Henrik
Zangeneh, Mehrdad
Zhao, Fanzhou
Zhu, Tao

Disclaimer/Publisher's Note: The statements, opinions and data contained in all publications are solely those of the individual author(s) and contributor(s) and not of MDPI and/or the editor(s). MDPI and/or the editor(s) disclaim responsibility for any injury to people or property resulting from any ideas, methods, instructions or products referred to in the content.

International Journal of
Turbomachinery
Propulsion and Power

MDPI

Article

Axial Impeller-Only Fans with Optimal Hub-to-Tip Ratio and Blades Adapted for Minimum Exit Loss

Thomas Carolus [1,*] and Konrad Bamberger [2]

[1] Steinbeis-Transferzentrum FLOWTRANS, 57250 Netphen, Germany
[2] Independent Researcher, 57076 Siegen, Germany
* Correspondence: thomas.carolus@stw.de

Abstract: This study targets determining impellers of impeller-only axial fans with an optimal hub-to-tip ratio for the highest achievable total-to-static efficiency. Differently from other studies, a holistic approach is chosen. Firstly, the complete class of these fans is considered. Secondly, the radial distribution of blade sweep angle, stagger angle, chord length, and camber are varied to adapt the blades to the complex flow in the hub and tip regions. The tool being used is an optimization scheme with three key components: (i) a database created beforehand by Reynolds-averaged Navier–Stokes (RANS)-predicted performance characteristics of 14,000 designs, (ii) an artificial neural network as a metamodel for the fan performance as a function of 26 geometrical parameters, and (iii) an evolutionary algorithm for optimization, performed on the metamodel. Typically, the hub-to-tip ratios for the impellers proposed by the optimization scheme are smaller than those obtained by applying the classic design rules. A second outcome are the shapes of the blades, which are adapted for a minimum exit loss. These shapes deviate substantially from the classic and even the state-of-the-art "swept-only" or "swept with dihedral" designs. The chord length, stagger, and sweep angle are distributed from hub to tip in a complex manner. The inherent reason is that the scheme tries to minimize not only the dynamic exit loss but also frictional losses due to secondary flows in the hub and tip regions, which eventually results in the maximum achievable total-to-static efficiency. Upon request, the authors will provide the full geometry of the four impellers analysed in some detail in this study to any individual for experimental validation or further analysis of their performance.

Keywords: axial fan; impeller-only; hub-to-tip ratio; optimization

check for updates

Citation: Carolus, T.; Bamberger, K. Axial Impeller-Only Fans with Optimal Hub-to-Tip Ratio and Blades Adapted for Minimum Exit Loss. *Int. J. Turbomach. Propuls. Power* **2023**, *8*, 7. https://doi.org/10.3390/ijtpp8010007

Academic Editor: János Vad

Received: 28 August 2022
Revised: 4 January 2023
Accepted: 17 February 2023
Published: 1 March 2023

Copyright: © 2023 by the authors. Licensee MDPI, Basel, Switzerland. This article is an open access article distributed under the terms and conditions of the Creative Commons Attribution (CC BY-NC-ND) license (https://creativecommons.org/licenses/by-nc-nd/4.0/).

1. Introduction

For several applications, the impeller-only axial fan in a duct-type casing is the preferred choice. Examples are dry cooling towers in thermal power plants, installations for locomotive and automotive engine cooling, railway and automotive air conditioning systems, heat pumps, etc. The appropriate hub-to-tip ratio of the fan impellers (Figure 1) has been discussed for many years. Figure 2 illustrates a historic example; the data is taken from the classic textbook by ECK [1], 1972, where the recommended specific speed and diameter as well as the smallest hub-to-tip ratio of such fan impellers are given in the so-called Cordier diagram. Note that here and throughout this study, all values of non-dimensional coefficients refer to the optimal point of operation, i.e., the operating point of the performance characteristic, where the aerodynamic efficiency is maximal. The frequently used index "opt" is omitted for brevity.

Figure 1. Typical axial impellers with increasing hub-to-tip ratio from left to right (classic blade shape); duct-type casing is not shown.

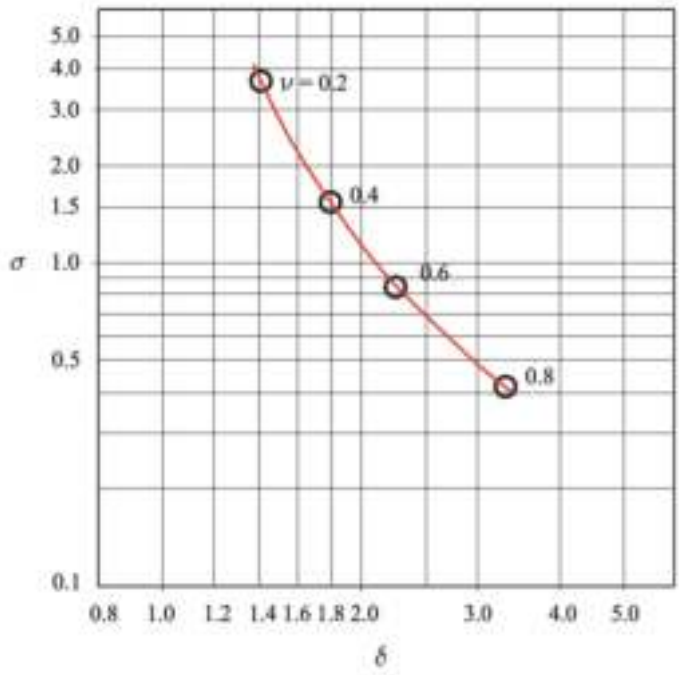

Figure 2. Axial fans and minimum hub-to-tip ratios ν for free-exhausting impeller-only fans, after ECK [1], 1972 (p. 271).

From fundamental aerodynamic findings, early hints for the minimum hub-to-tip ratio had been established by Strecheltzky (see Horlock [2], (p. 227), De Haller [3], and Schiller [4]). Nevertheless, designers frequently try to reduce the hub-to-tip ratio further. One driver is cost—a larger hub can be expensive. Another reason is reducing the blocked area of an impeller at stand-still. In automotive engine cooling units, for instance, the fan is mostly not running, as the outer airstream provides forced cooling at moderate and high speeds of the vehicle. A third argument is that too large a hub obstructs the throughflow through an up- or downstream installed heat exchanger matrix. This, however, is frequently incorrect. The near-hub sections of the blades on an inappropriate hub may experience or even generate a backflow which has the potential to increase the non-functional area of a heat exchanger.

Several authors worked on methods for designing impellers with a very low hub-to-tip ratio. For instance, Lindemann et al. [5] suggested a design method for a small hub-to-tip ratio with swept blades, based on an empirical axial and tangential velocity distribution in the spanwise direction from hub to blade. In a more recent paper, Wang and Kruyt [6] studied small hub-to-tip ratio fans. Among others, they analysed the influence of non-aerodynamically shaped parts of the blades and showed "that the presence of non-airfoil sections near the root has a minor influence on the pressure coefficient and hence on the total-to-static efficiency (of the fan), due the formation of a vortex upstream from the blades

near the hub. Overall, the 'main blade' part well represents the aerodynamic performance." The potential drawback in efficiency was not discussed in detail. Nevertheless, the idea in their subsequent paper [7] was to quantify the potential of the overall blade sweep, dihedral, and skew on the aerodynamic performance of such fans. They found only minor benefits.

This study aims at determining highly efficient impellers with the minimum hub-to-tip ratio. The efficiency considered is the total-to-static efficiency which is an adequate metric for the energetic quality of the fan when it is the last component in a plant and exhausts directly into the free atmosphere or a large room. The dynamic pressure of the discharge jet constitutes the exit loss that is taken into account by the definition of this efficiency. In this study the dynamic pressure is associated with the flow velocity immediately downstream of impeller in the annulus formed by hub and cylindrical casing, not with the area of the complete rotor. This avoids the problem of taking into account a potential pressure recovery, e.g. due to a downstream tail cone or Carnot diffuser.

Differently from other studies, a holistic approach is chosen. Possible design points cover the complete range common for this class of fans. The radial, i.e., spanwise, distributions of the blade sweep angle, stagger angle, and chord length are varied to adapt the blades to the complex flow in the hub and tip regions. The tool being used is an optimization scheme developed and validated by Bamberger [8]; see also Bamberger and Carolus [9].

2. Methodology

2.1. Non-Dimensional Coefficients Used

In this study, the common definitions of non-dimensional coefficients are used. Q (kg/m^3) is the volume flow rate, Δp (Pa) a pressure rise, n (1/s) is the rotational speed of the impeller, D_{tip} (m) is the rotor outer diameter (and approximately the clear diameter of the casing D), ρ (kg/m^3) is the (constant) density of the gas, and P (W) the shaft power. The volume flow and pressure rise coefficients as well as the efficiency are defined as

$$\phi \equiv \frac{Q}{\frac{\pi^2}{4} D_{tip}^3 n}, \tag{1}$$

$$\psi \equiv \frac{\Delta p}{\frac{\pi^2}{2} D_{tip}^2 n^2 \rho}, \tag{2}$$

$$\eta \equiv \frac{Q \Delta p}{P}. \tag{3}$$

The specific diameter and speed are:

$$\delta \equiv \frac{D_{tip}}{\left(\frac{8}{\pi^2}\right)^{\frac{1}{4}} \left(\frac{\Delta p}{\rho}\right)^{-\frac{1}{4}} Q^{\frac{1}{2}}}, \tag{4}$$

$$\sigma \equiv \frac{n}{(2\pi^2)^{-\frac{1}{4}} \left(\frac{\Delta p}{\rho}\right)^{\frac{3}{4}} Q^{-\frac{1}{2}}} \tag{5}$$

ϕ and ψ can be expressed in terms of δ and σ, and vice versa. Depending on the case of application, ψ and η can be defined using either the total-to-*total* (index „tt") or the total-to-*static* (index „ts") pressure rise. (In ISO 5801 [10] the total-to-*total* pressure rise is simply called the „fan pressure" with the symbol p_f; the total-to-*static* pressure rise is called „fan static pressure" p_{fs} which must not be mistaken for the true static pressure rise of the fan.) The total-to-*total* pressure rise Δp_{tt} is a measure of the total energy transferred from the shaft to the fluid and equals the difference between the total pressure downstream of the fan and the total pressure upstream of the fan. In applications where the dynamic pressure downstream of the fan dissipates in the free atmosphere or a large room, the total-to-*static*

pressure rise Δp_{ts} (i.e., Δp_{tt} diminished by the so-called exit loss) is more adequate to describe the design point, and ψ_{ts} and η_{ts} become the relevant dimensionless quantities. In contrast, σ and δ are always defined with Δp_{tt}, with most probably an exception in Figure 2, which will be discussed below.

The geometrical quantity which is most relevant in this paper is the hub-to-tip ratio (see Figure 3a)

$$\nu \equiv \frac{D_{hub}}{D_{tip}}. \tag{6}$$

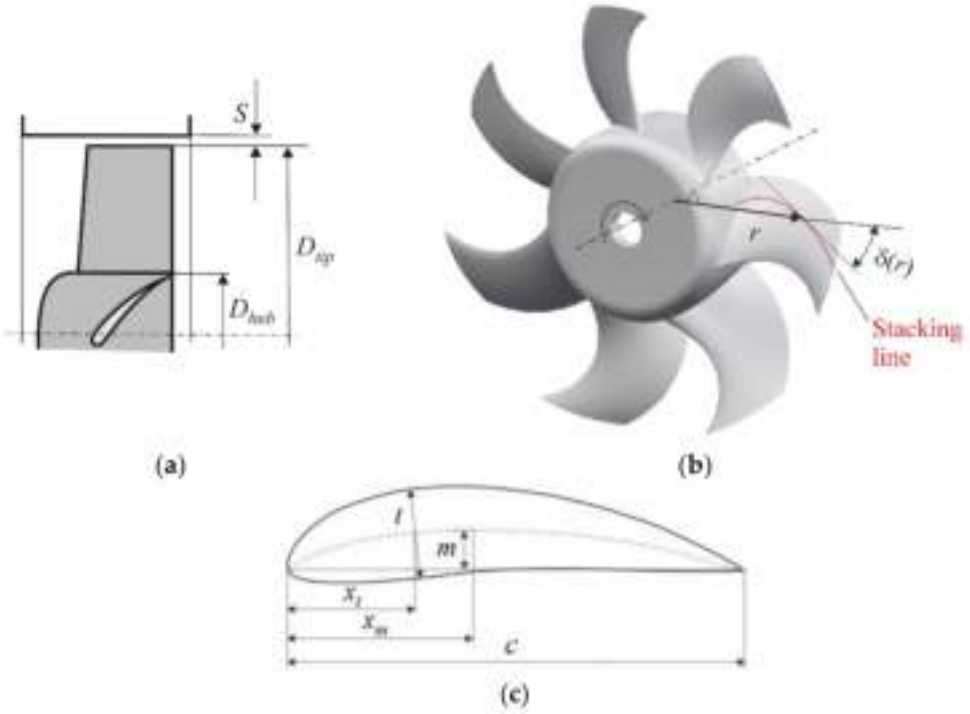

Figure 3. Illustration of geometrical parameters: (**a**) impeller with part of the duct-type casing; (**b**) definition of the sweep angle; (**c**) 4-digit NACA section.

2.2. Optimization Scheme

A short summary of the optimization scheme is given in this section. Details can be found in [8,9]. Three key components are essential: (i) a database of performance characteristics of 14,000 different axial fan impellers, (ii) a metamodel for the fan performance as function of the impeller parameters varied, and (iii) an evolutionary algorithm as an optimization method.

2.2.1. Database

The database consists of the performance characteristics of 14,000 individuals in the class of axial fan impellers. It was created beforehand by an automated Reynolds-averaged Navier–Stockes (RANS) prediction. Figure 3 shows the geometrical parameters varied. In Table 1 the geometrical parameters are compiled which are varied throughout the optimization. It is important to note that the range of permissible hub-to-tip ratios has been limited to values between 0.3 and 0.7. This means in particular that there are no impellers in the database with a hub-to-tip ratio <0.3. The blades are composed of 4-digit NACA airfoil sections with the parameters "maximum thickness", "maximum camber", and their respective "chordwise positions". The maximum blade thickness is fixed to 5% of the chord length, which may allow production in plastic injection molding.

Table 1. Geometrical parameters varied.

Parameter	Symbol	Range	Comment
Hub-to-tip ratio	ν	0.3–0.7	
Number of blades	z	5–11	Only integers
Chord-length ratio	c/D_{tip} [a]	0.13–0.33	
Maximum camber	m/c [a]	0–0.15	4-digit NACA sections
Position of max. camber	x_m/c [a]	0.1–0.7	
Position of max. thickness	x_t/c [a]	0.1–0.5	
Blade sweep angle	δ [a]	−60°–+60°	

[a] defined at three equidistant locations between hub and tip.

Empirically, the optimal points of operation of common high-efficiency single-flow and single-stage centrifugal, mixed-flow, and axial fans lie—in terms of specific diameter δ and speed σ—in a relatively narrow band called the Cordier band; see the hatched area in Figure 2. Guided by this Cordier band, Bamberger in [8] fixed the sensible range of aerodynamic design parameters of axial impeller-only fans according to Figure 4 and Table 2, here in terms of ϕ and ψ_{ts}. This design space is more or less adopted for the current study. Note that the range of aerodynamic design parameters is deliberately chosen to be broader than the conventional Cordier band suggests.

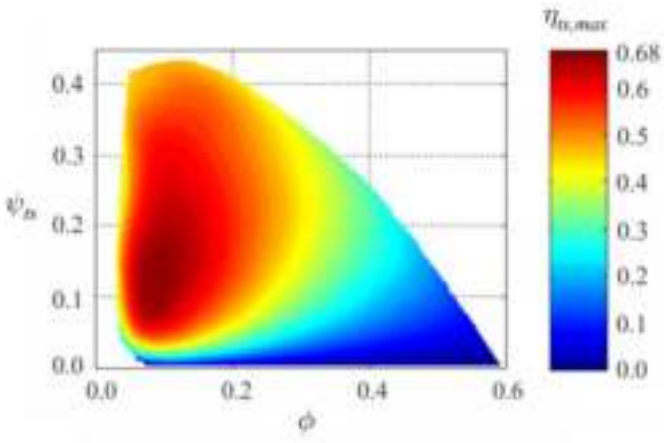

Figure 4. Design space (i.e., pairs of ϕ and ψ_{ts}) for the class of single-stage axial impeller-only fans; the colour indicates the peak efficiency achievable for each pair of ϕ and ψ_{ts}; after Bamberger [8].

Table 2. Aerodynamic design parameters varied in the present study.

Parameter	Symbol	Range
Pressure rise coefficient (at design point)	ψ_{ts}	0.1–0.4
Volume flow rate coefficient (at design point)	ϕ	0.1–0.45

A sketch of the computational domain for the CFD simulations is presented in Figure 5. The computational domain comprised one blade channel using periodic boundary conditions at the lateral surfaces. Further boundary conditions were: fixed mass flow at the inlet, ambient pressure at the outlet, and no slip at the walls. The turbulence was modelled using the *k*-ω SST model. The solver was Ansys CFX™. Numerical grid generation and evaluation of the RANS results were automated. Combinations of a total of 26 geometrical parameters were determined systematically with a method of design of experiment (DoE). The resulting pressures were evaluated in plane 1 and 2.

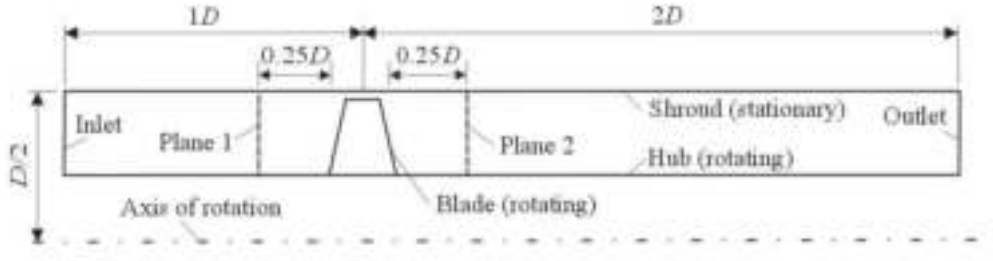

Figure 5. Sketch of the computational domain for creating the database with automated RANS predictions; $D \approx D_{tip}$, since the tip clearance is small (S/D = 0.001).

Three minor constraints associated with the database thus obtained are:

- The results of the complete optimization scheme may be not fully applicable to installations of the impellers that are substantially different from Figure 5; e.g., those without casings.
- The tip clearance was kept constant at 0.001 of $D \approx D_{tip}$. Substantially different tip clearances may require corrections, e.g., by empirical correlations.
- All RANS simulations were performed for a 0.3 m diameter impeller running at 3000 rpm. This leads to a typical chord-based Reynolds number of 200,000. If the results of the complete optimization scheme were to be applied for fans with substantially smaller or larger Reynolds numbers, at least the absolute value of the predicted efficiency could be scaled with Reynolds scale-up laws like the well-known Ackeret formula from 1948, see, e.g., Spurk [11], or more recent and complex methods as described by Pelz et al. [12].

2.2.2. Metamodel

The metamodel is based on an artificial neural network. It enables predicting the performance characteristics, including efficiency and the circumferentially averaged flow velocity in the impeller exit plane, of any impeller made of a reasonable combination of the 26 geometrical parameters. The neural network type selected is the multi-layer perceptron (MLP). MLPs consist of the input layer, an arbitrary number of hidden layers, and the output layer. The number of hidden layers and the number of neurons in each of them determines the model complexity. A too-simple model will lead to large errors because of insufficient flexibility. On the other hand, a too-complex model will suffer from overfitting effects, i.e., the error will be small on the training data but high on fresh data that was not used for the training. Therefore, the available data were split into training and test data, and the model complexity was optimized aiming at a minimal error on the test data.

2.2.3. Optimization Method

The actual optimization is performed on the metamodel. For optimization, an evolutionary algorithm is implemented. One essential advantage of evolutionary algorithms is their ability to find the global optimum, which is considered important for the present work. The main disadvantage compared to local optimization algorithms (e.g., gradient-based ones) is the high number of function evaluations that is required for convergence. Due to the extreme quickness of the metamodels, however, this disadvantage is less relevant for the present study. The main optimization target is always the maximization of η_{ts} with the constraint that the targeted design point must be fulfilled.

The complete scheme is implemented in Matlab™ and requires standard PC computer resources only.

3. Results and Discussion

A systematic design of impellers in the design space yields the hub-to-tip ratios plotted in the upper plot of Figure 6. For fans designed for large values of ϕ and low to moderate values of ψ_{ts} (such as B), a lower hub-to-tip ratio could be feasible. As mentioned before,

such a design has been excluded a priori because the initial training data for the metamodel were deliberately confined to the parameter range of ν = 0.3–0.7. The maximum achievable total-to-static efficiency for each design is depicted in the lower plot of Figure 6. Clearly, the fans with the highest efficiencies are those designed for ϕ / ψ_{ts} pairs in the region of the lower left corner with a hub-to-tip ratio $\nu \approx$ 0.3–0.4 accordingly.

Table 3. Results (selected fans).

#	ψ_{ts}	ϕ	ν	η_{ts}	Impeller
A	0.1	0.1	0.31	0.66	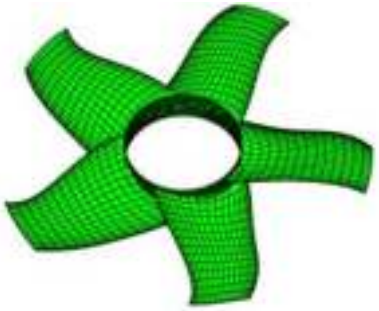
B	0.1	0.45	0.30	0.20	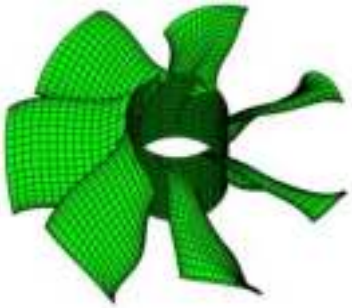
C	0.35	0.1	0.70	0.52	
D	0.35	0.25	0.50	0.45	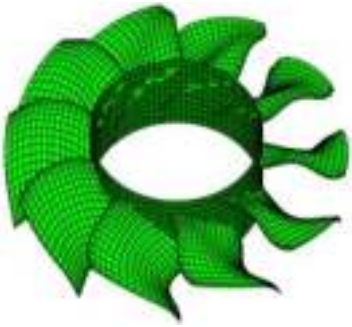

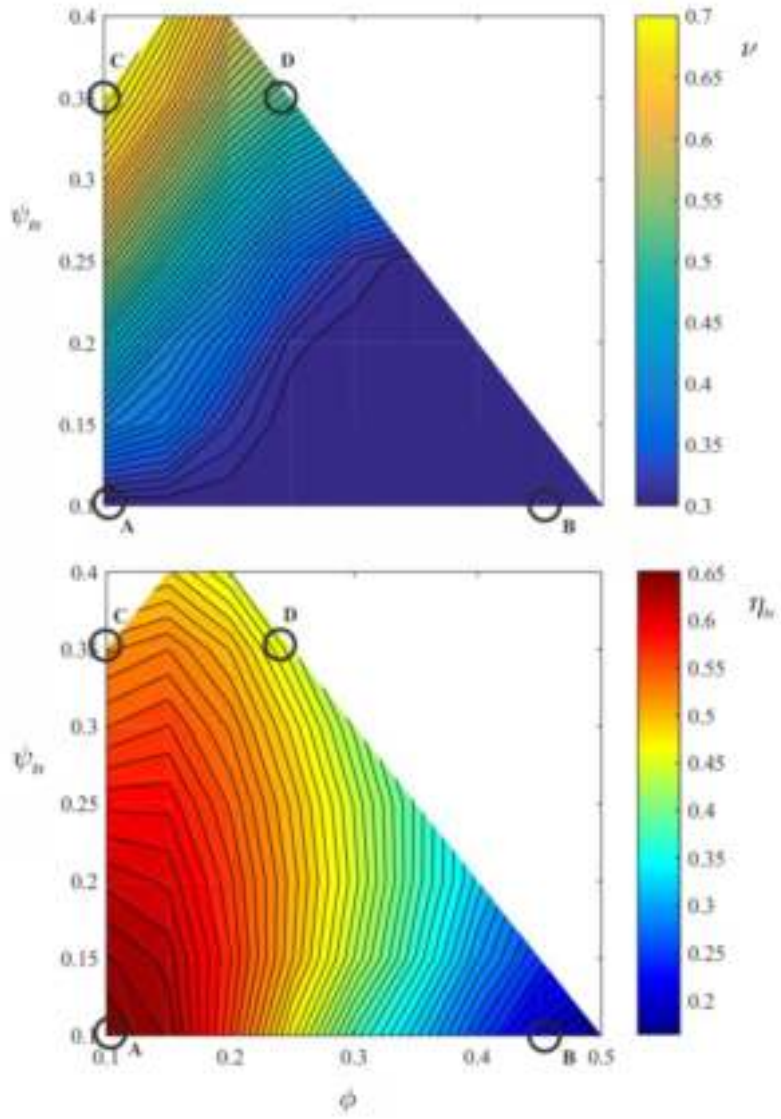

Figure 6. Upper: hub-to-tip ratios of optimal impellers; lower: total-to-static efficiencies of these impellers; the design points denoted with letters refer to Table 3.

Selected fans (i.e., pairs of ϕ and ψ_{ts}) in Table 3 illustrate the results. In contrast to conventional designs, the optimization suggests blade shapes with an unexpected spanwise distribution of chord length, stagger angle, and especially sweep angle.

The metamodel also yields the circumferentially averaged flow field at the impeller exit, as shown in Figure 7. Seemingly, the optimal blade shape causes a meridional velocity component at the fan exit c_{m2}, with a maximum in the middle or outer blade section. This means that the volume flow rate is not evenly distributed in the bladed annulus of the impeller. In the critical hub region the throughflow is reduced. The tangential velocity cu2, which is a measure of energy transfer to the fluid, is shown as well. In all graphs the velocities are normalized with the blade tip speed $\pi D_{tip} n$, indicated by a star as a superscript. Despite a small region of backflow, the most efficient impeller is A.

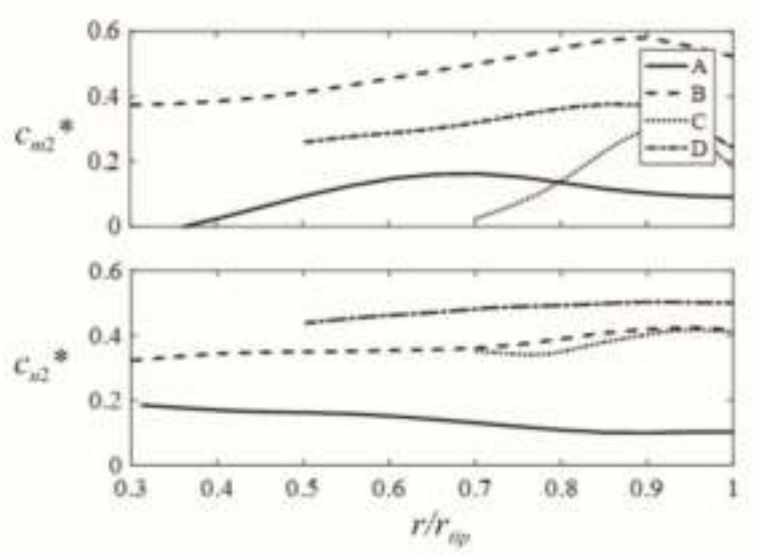

Figure 7. Distributions of the meridional (throughflow) and tangential flow velocities in the impeller exit plane; the velocities are normalized with the blade tip speed $\pi D_{tip} n$, indicated by the star as a superscript.

For comparison, for the same design point as A, an impeller was designed employing a standard textbook blade–element–momentum (BEM) method, cp. [13]. The hub-to-tip ratio was chosen as ν = 0.31 as well. As an empirical assumption, the frictional loss at each elemental blade section along the span was set to 10% (corresponding to a local hydraulic efficiency of 90%)—possible additional losses in the blade hub and tip regions were neglected. Furthermore, a volumetric loss in the tip gap region was neglected as well. A free vortex distribution was chosen which—in agreement with the requirement of radial equilibrium—results in r x c_{u2} = *const* and c_{m2} = *const* along the span. In Figure 8, these r x c_{u2}– and c_{m2}–distributions are compared to those from the optimal impeller A. Both velocity distributions show distinct differences. This is due to the fact that the optimization method, which is based on comprehensive CFD data, takes into account all local losses. No assumption for the local efficiency is necessary. The optimizer even predicts the overall achievable efficiency. Moreover, the optimizer identifies those spanwise c_{u2}– and c_{m2}–distributions which are associated with the minimum overall dynamic pressure at the impeller exit, i.e., the minimum exit loss. Note that the classic free vortex distribution is not optimal with respect to the exit loss; the axial exit flow velocity is constant, but the tangential varies substantially from hub to tip: c_{u2} (r) = $const/r$. Hence, it is understandable that the overall dynamic exit pressure, which is based on the integral of the squared exit velocities from hub to tip, can be minimized by choosing optimal $c_{u2}(r)$–and $c_{m2}(r)$–distributions. In general, those distributions will deviate from the classic free vortex design. Eventually, the blades which provide that optimal exit flow are characterized by complex distributions of chord length, as well as stagger, sweep, and dihedral angles.

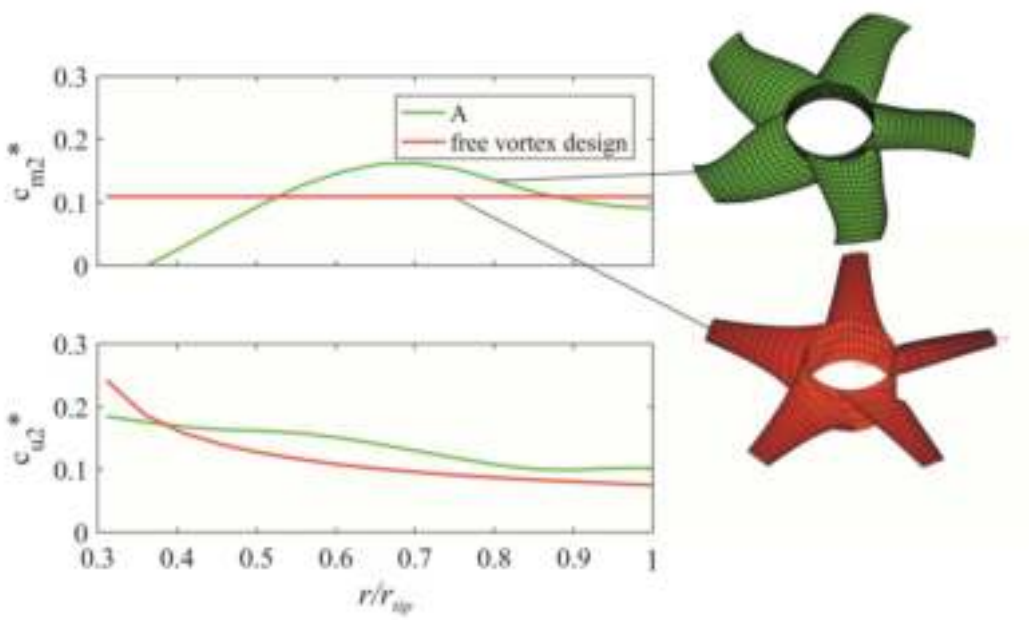

Figure 8. Comparison of optimal fan impeller A with a standard textbook design (i.e., free vortex, rc_{u2} = const and c_{m2} = const according to the requirement of radial equilibrium); the velocities are normalized with the blade tip speed $\pi D_{tip} n$, indicated by the star as a superscript.

It is important to note that the chosen hub-to-tip ratio for the textbook design was by far below the classic limits according to Strecheltzky, De Haller, and Schiller. This is a general observation: the hub-to-tip ratios suggested by the optimization scheme are always smaller than those obtained according to the classic rules. This even applies to ECK's recommendations, initially shown in Figure 2. (Some caution is necessary when interpreting Figure 2 qualitatively; most likely ECK obtained the Cordier-curve defining σ and δ with Δp_{ts} and not Δp_{tt}, as is customary today.)

4. Conclusions

The objective of this study was the design of impeller-only axial fans with optimal hub-to-tip ratios for highest achievable total-to-static efficiency. This in contrast to other studies, where a primary design target is a very small hub at the potential expense of the efficient aerodynamic function of the near-hub blade region.

Differently from other studies, a holistic approach was chosen. Firstly, the complete class of these fans is considered, not only one particular design case. Secondly, an optimization method is applied, which allows determining the optimal hub-to-tip ratio, the radial distribution of the blade sweep angle, the stagger angle, and the chord length. The classic hub-design rules by Strecheltzky, De Haller, and Schiller need not to be applied.

In general, the hub-to-tip ratios for the class of axial impeller-only fans proposed by the optimization scheme are smaller than those obtained applying the classic rules. It should be pointed out again, however, that the permissible hub-to-tip ratios have been limited to a range of 0.3 to 0.7. In particular, this means that impellers with hub-to-tip ratios <0.3 cannot to be expected with the scheme used here. In the case of impeller B, whose hub-to-tip ratio is exactly 0.3, the selected lower limit of the permissible hub-to-tip ratios may have acted as a non-physical limitation.

A second outcome are the shapes of blades, which are adapted for minimum exit loss. These shapes deviate substantially from the classic and even the state-of-the-art "swept-only" or "swept with dihedral" designs: the chord length, stagger, and sweep angle are distributed from hub to tip in a complex manner. The inherent reason is that the scheme tries to minimize not only the overall dynamic exit loss, but also frictional losses due to secondary flows in the hub and tip regions.

Essentially, the optimization method used is based on RANS simulations. In the past the underlying RANS method has been validated for several examples. Nevertheless, the authors do provide the full geometry of the four impellers A, B, C, and D to any individual for experimental validation or further analysis of their performance (see data availability statement below). This would also allow comparison with commercial fans with similar performance parameters, but whose hub-to-tip ratios are smaller than those proposed by the method used.

Author Contributions: Conceptualization, T.C. and K.B.; methodology, K.B.; software, K.B.; writing—original draft preparation, T.C.; writing—review and editing, K.B. and T.C. All authors have read and agreed to the published version of the manuscript.

Funding: This research received no external funding.

Data Availability Statement: Upon request the authors will provide a 3D CAD model free of charge of the four impellers A, B, C, and D to any individual. Inquiries should be addressed to Thomas Carolus at Steinbeis-Transferzentrum FLOWTRANS, 57250 Netphen, Germany; www.flowtrans-engineering.com (accessed on 28 August 2022); thomas.carolus@stw.de.

Conflicts of Interest: The authors declare no conflict of interest.

References

1. Eck, B. *Ventilatoren*, 5th ed.; Springer: Berlin/Heidelberg, Germany, 1972.
2. Horlock, J.H. *Axialkompressoren*; Verlag G. Braun: Karlsruhe, Germany, 1967.
3. de Haller, P. Das Verhalten von Tragflügelgittern in Axialverdichtern und im Windkanal. *Brennstoff-Wärme-Kraft* **1953**, *10*, 333–337.
4. Schiller, F. Theoretische und Experimentelle Untersuchungen zur Bestimmung der Belastungsgrenze bei Hochbelasteten Axialventilatoren. Ph.D. Thesis, Universität Braunschweig, Braunschweig, Germany, 1983.
5. Lindemann, T.B.; Friedrichs, J.; Stark, U. Development of a new design method for high efficiency swept low pressure axial fans with small hub/tip ratio. In *Proceedings of the ASME Turbo Expo 2014*; Paper No. GT2014-25932; American Society of Mechanical Engineers: New York, NY, USA, 2014. [CrossRef]
6. Wang, J.; Kruyt, N.P. Computational fluid dynamics simulations of aerodynamic performance of low-pressure axial fans with small hub-to-tip diameter ratio. *ASME J. Fluids Eng.* **2020**, *142*, 091202. [CrossRef]
7. Wang, J.; Kruyt, N.P. Effects of sweep, dihedral and skew on aerodynamic performance of low pressure axial fans with small hub-to-tip diameter ratio. *ASME J. Fluids Eng.* **2022**, *144*, 011203. [CrossRef]
8. Bamberger, K. Aerodynamic Optimization of Low-Pressure Axial Fans. Ph.D. Thesis, Universität Siegen, Siegen, Germany, 2015.
9. Bamberger, K.; Carolus, T. Development, application, and validation of a quick optimization method for the class of axial fans. *ASME J. Turbomach.* **2017**, *139*, 111001. [CrossRef]
10. *ISO 5801:201*; Fans—Performance Testing Using Standardized Airways. International Organization for Standardization: London, UK, 2017.
11. Spurk, J.H. *Dimensionsanalyse*; Springer: Berlin/Heidelberg, Germany, 1992.
12. Pelz, P.F.; Stonjek, S.; Matyschok, B. The influence of Reynolds number and roughness on the efficiency of axial and centrifugal fans—A physically based scaling method. In Proceedings of the International Conference on Fan Noise, Technology and Numerical Methods FAN2012, Senlis, France, 18–10 April 2012.
13. Carolus, T. *Fans: Aerodynamic Design, Noise Reduction, Optimization*; Springer: Berlin/Heidelberg, Germany, 2022.

Disclaimer/Publisher's Note: The statements, opinions and data contained in all publications are solely those of the individual author(s) and contributor(s) and not of MDPI and/or the editor(s). MDPI and/or the editor(s) disclaim responsibility for any injury to people or property resulting from any ideas, methods, instructions or products referred to in the content.

International Journal of
Turbomachinery
Propulsion and Power

MDPI

Article

Aeroacoustic Simulations of an Axial Fan with Modelled Turbulent Inflow Conditions

Philipp Dietrich * and Marc Schneider

ebm-papst GmbH & Co. KG, Bachmühle 2, 74673 Mulfingen, Germany
* Correspondence: philipp.dietrich@de.ebmpapst.com

Abstract: In applications, the acoustics of fans can differ significantly from the measurements of the standalone fan. This is due to disturbed inflow conditions, for example, caused by a heat exchanger upstream of an axial fan. Resolving the complex geometry and dimensions of typical heat exchangers in aeroacoustic scale-resolving simulations leads to a very high computation effort, which is currently not economically feasible. Turbulence reconstruction tools, such as the FRPM, provide the possibility to model the turbulent inflow conditions, thereby avoiding the representation of the heat exchanger in the aeroacoustic simulations. This approach is tested on a benchmark experiment of a ducted fan with an upstream turbulence grid.

Keywords: fans; aeroacoustics; computational aeroacoustics (CAA); inflow disturbance; turbulence reconstruction

check for updates

Citation: Dietrich, P.; Schneider, M. Aeroacoustic Simulations of an Axial Fan with Modelled Turbulent Inflow Conditions. *Int. J. Turbomach. Propuls. Power* **2023**, *8*, 13. https://doi.org/10.3390/ijtpp8020013

Academic Editors: Marcello Manna and Thomas Carolus

Received: 31 August 2022
Revised: 31 January 2023
Accepted: 7 March 2023
Published: 18 April 2023

Copyright: © 2023 by the authors. Licensee MDPI, Basel, Switzerland. This article is an open access article distributed under the terms and conditions of the Creative Commons Attribution (CC BY-NC-ND) license (https://creativecommons.org/licenses/by-nc-nd/4.0/).

1. Introduction

The evaluation and reduction of the emitted sound is an important part of the development of new fans. Especially in applications that operate close to humans, such as air conditioning or kitchen hoods, quiet fans are requested. In contrast to the measurements of the standalone fan, typically used in the development process, in applications, the acoustics can be significantly influenced by disturbed inflow conditions. As shown by Lucius et al. [1], even a rectangular box in front of the fan drastically increases the emitted sound, whereas the effect on the aerodynamic properties is only minor.

Evaluations of the aerodynamic properties with numerical simulations using CFD (Computational Fluid Dynamics) are commonly used in the development process of new fans. Due to increased computational resources, CAA (Computational Aeroacoustics) methods have become more important in predicting the emitted sound and identifying sound-generating mechanisms. As shown by Lucius et al. [1], scale-resolving simulations such as LES (Large Eddy Simulation) are able to correctly calculate the acoustics of fans. However, a high computational effort is needed to resolve upstream structures, which influence the inflow conditions. For axial fans, a typical application is in combination with a heat exchanger unit. This is, for example, the case in heat pumps, where the fan is often installed after the heat exchanger. The shape and geometric details of the heat exchanger lead to a non-uniform turbulent flow field which will interact with the fan blades during operation. This can significantly increase the emitted sound. Due to the complex geometry (thinly stacked fins and cooling rods) and the dimensions of heat exchangers, a very high computational effort (estimated mesh size for resolution of typical heat exchanger: $\sim 1 \times 10^{10}$ cells) is needed to resolve all the necessary details. In a product development process, this is currently not economically feasible.

Turbulent reconstruction tools, such as the FRPM (Fast Random Particle Mesh) method, developed by the DLR in Braunschweig (Ewert [2]), offer the possibility to synthetically recreate the turbulence based on the statistic information of precursor RANS (Reynolds Averaged Navier Stokes) simulations. The tool was intentionally created to reconstruct sound sources for propagation simulations, as shown by Liberson et al. [3]. However, in the

context of trailing edge noise, this tool was also used to introduce turbulent fluctuations to the boundary layer of an airfoil (Bernicke et al. [4]). In the case of a fan in combination with a heat exchanger, the idea is to reconstruct the disturbed inflow conditions to the fan caused by the heat exchanger with the FRPM for aeroacoustic simulations. The proposed method was successfully applied to generic test cases as well as the simulation of an experiment of an airfoil behind a turbulence grid in a wind tunnel (Dietrich et al. [5]). In precursor investigations also, other turbulence reconstruction tools, such as the Anisotropic Linear Forcing (ALF) in StarCCM+ (Erbig et al. [6]), were investigated. However, for the test cases, the FRPM showed the most promising results.

In this paper, the turbulence reconstruction technique using the FRPM for disturbed inflow conditions is applied to a benchmark test case of a ducted axial fan with an upstream turbulence grid investigated at the University of Siegen (Zhu [7]). The purpose of this investigation is to determine the applicability of the developed approach to the aeroacoustic simulations of fans. The advantage of this test case is that, in comparison to a heat exchanger application, the entire setup of the experiment can be represented in an aeroacoustic simulation with reasonable computational effort. This setup was also investigated by Moghadam et al. [8] using LES. However, the acoustics were only simulated for undisturbed inflow conditions. Varying inflow conditions for this ducted fan in a similar setup were numerically and experimentally investigated by Reese and Carolus [9], who showed the capabilities of different turbulence modeling techniques to capture the relevant sound sources. The effect of inflow conditions due to the wind tunnel in this benchmark case was investigated by Sturm et al. [10] using the Lattice-Boltzmann-Method. However, the configuration with a turbulence grid was not simulated.

All of the already applied methods would not be able to predict the acoustics of a heat exchanger setup with a reasonable amount of computational resources. The objective of this study is to show the applicability of the reconstruction method with FRPM and StarCCM+ to predict the broadband acoustics in comparison to the experiment and the simulation of the entire setup. The focus of the reconstruction will be the turbulent fluctuations relevant to the acoustics. Therefore, deviations in aerodynamic properties are to be expected.

2. Experimental Setup

The experimental setup and measurement results are published by Zhu [7] and can be consulted for additional information. Zhu also showed an experimental investigation and simulation of the same fan in a similar configuration (without inflow disturbance) in his dissertation [11], which can also be referred to for the measurement setup. In the experiment, an axial fan with a diameter of 300 mm and a rotational speed of 3000 rpm is placed in a duct, sucking air from a semi-anechoic chamber over a comparatively coarse turbulence grid. A schematic of the experimental setup is shown in Figure 1.

The inflow field for the fan after the nozzle and the turbulence grid is measured by a hot wire probe located 175 mm in front of the leading edge of the fan. In addition, the pressure on the blade surfaces is measured by pressure sensors on the suction and pressure sides of the blades. Here, on 2 blades of the fan 7 pressure sensors were applied on the suction side of one and on the pressure side of the other blade. An additional pressure sensor was installed on the tip gap surface. The signal from the pressure sensors is transferred through channels, which are filled up with a paste, on the opposing blade side to the hub and transmitted to the shaft by sliding contact. The pressure sensors were individually calibrated using a white noise signal.

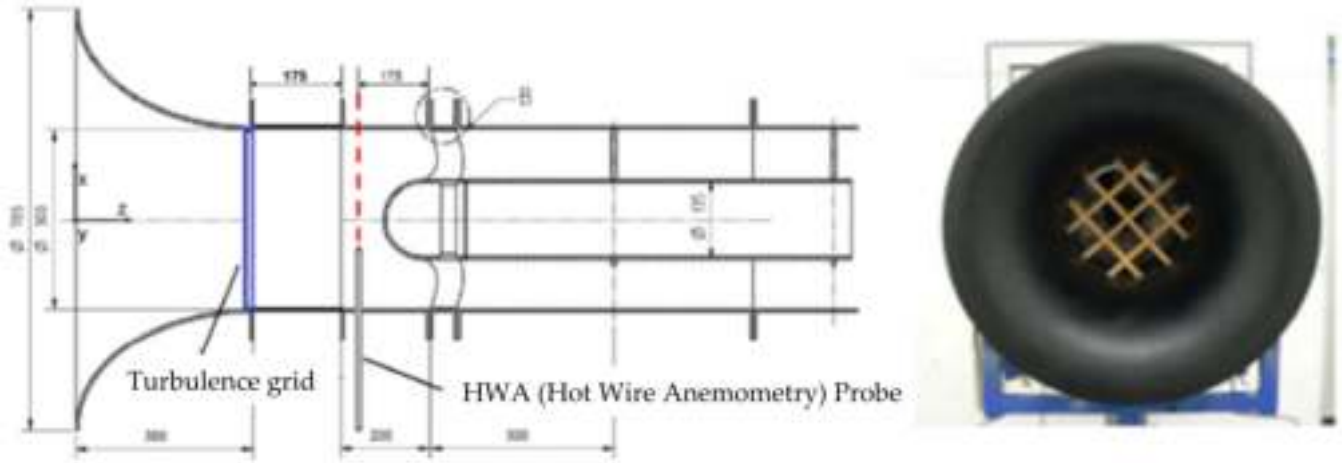

Figure 1. Experimental setup: (**left**) Schematic of the test rig; (**right**) picture of the installation with the turbulence grid [7]. Reproduced with permission from Zhu, T; AiF/FLT Report-No.: F60 002 B; 2015 [7] (Annotations in English added).

The acoustics are recorded by three upstream microphones placed in the semi-anechoic chamber (Figure 2) and one microphone in the duct after the fan. For the comparison in this paper, only the microphones on the suction side (semi-anechoic chamber) are used.

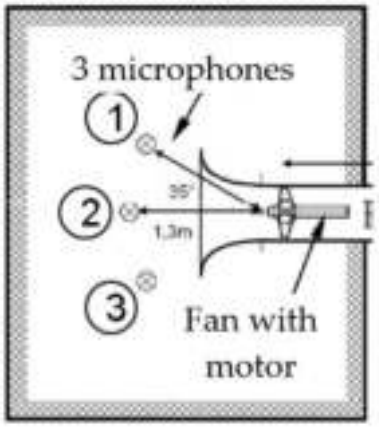

Figure 2. Location of suction side microphones (Schematic based on [12]). Reproduced with permission from Delfs, J.W. and Carolus, T.; AIF/FLT Report-No.: F60 001 B; 2015(Annotations in English and numbering added).

3. Simulation Setup

This experiment was selected for the test because it features a turbulent inflow condition for a fan which can still be resolved with a scale-resolving simulation, thereby providing an additional reference for the simulation with turbulent reconstruction.

The basis for all acoustic simulations in this work is a RANS-Simulation of the entire simulation domain, which can be seen in Figure 3 for the LES setup. The grid resolution of this steady-state simulation is the same as for the scale-resolving aeroacoustic calculations. A polyhedral mesh with approximately 60 million cells was used. The rotation of the fan is realized by the moving reference frame (MRF) method in StarCCM+. The turbulence was calculated using the k-ε realizable model.

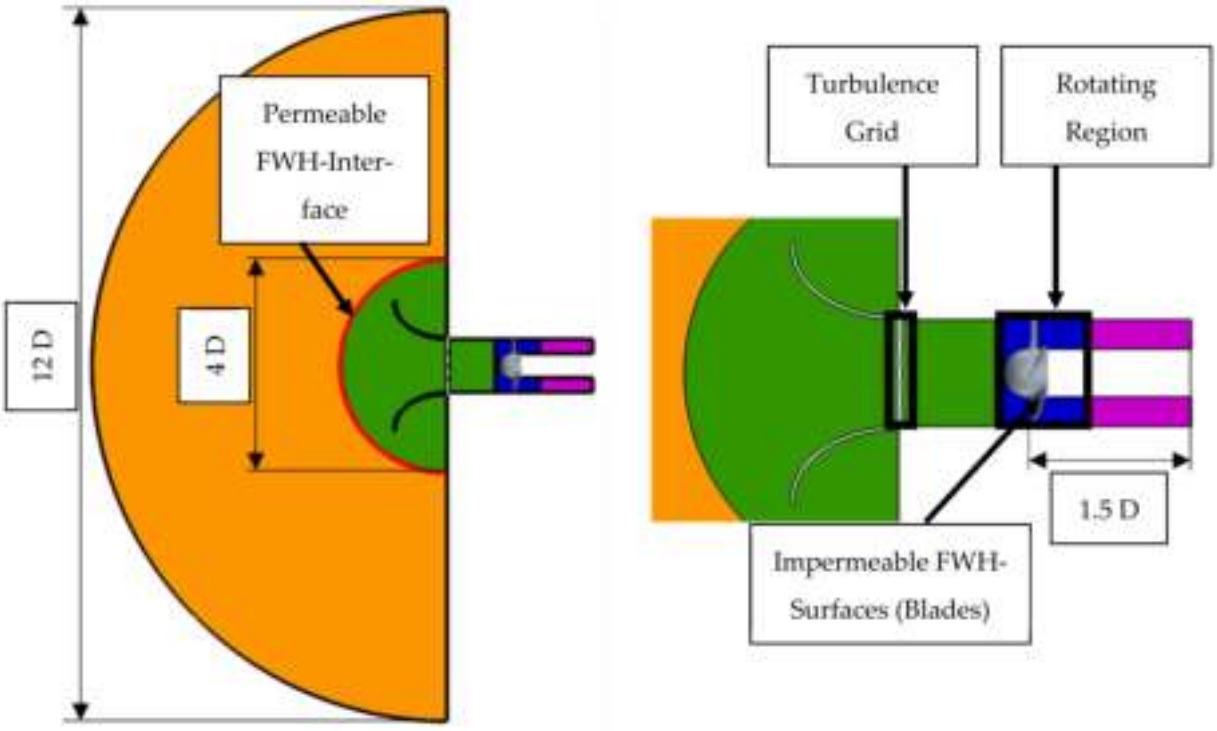

Figure 3. Calculation domain for the full-model simulation of the ducted fan with upstream turbulence grid: (**left**) Full view; (**right**) detailed view.

The scale-resolving simulation was set up as a compressible simulation in StarCCM+. The propagation of the turbulence generated by the grid to the fan was ensured by at least two cells per turbulent length scale, which has proven sufficient in a previous investigation [5]. In this transient simulation, the rotation of the fan was realized using the rigid body motion (RBM) method with sliding interfaces. The turbulent boundary layer was resolved, ensuring the dimensionless wall normal distance (N+, Y+) below 1 and a dimensionless resolution in the tangential direction (T+) below 200 in the entire domain leading to the aforementioned approximately 60 million cells. The deployed LES with WALE (Wall-Adapting Local Eddy-viscosity) subgrid-scale (SGS) model typically requires T+ values below 40 for a proper resolution of the boundary layer. However, it was shown that for the acoustics of fans, this setup is sufficient [1,5].

Acoustic waves of frequencies up to 3000 Hz are spatially resolved with 20 points per wavelength (PPW) up to a permeable interface in front of the nozzle. The acoustics for the microphones in the semi-anechoic chamber was calculated using the Ffowcs-Williams and Hawkings (FWH) model directly from the fan blades as well as from the permeable surface in front of the nozzle using Farassat A1 formulation. In order to avoid reflections at the boundaries, the inlet and outlet sections are implemented as non-reflecting "Free-Stream" boundary conditions. In addition, on the outlet, an Acoustic Suppression Zone (ASZ) with a thickness of 0.5 D (diameter of the fan) is applied. Figure 3 shows a schematic view of the calculation domain.

The simulation is carried out by first calculating three fan revolutions with a comparably coarse timestep. Afterward, the acoustic evaluation of 2 additional revolutions with FWH is started using a smaller timestep of $\Delta t = 5 \times 10^{-6}$ s ($\Delta t <$ Period duration at 3000 Hz divided by 30), ensuring the temporal acoustic resolution up to 3000 Hz.

For the simulation with turbulence reconstruction, the domain used for the previous simulations is reduced. The inlet is now located 175 mm in front of the leading edge (the position of the hot wire measurements in the experiment). Since in the reduced simulation domain, the geometry is either rotating or rotationally symmetric, in contrast to the geometric setup of the full model, the entire domain is realized as rotating using the

RBM method. The grid resolution is the same as for the scale-resolving simulation of the entire domain. Due to the reduced simulation domain, all structures upstream of the new inlet location (e.g., turbulence grid and nozzle) are not represented by the grid, leading to a polyhedral mesh of approximately 40 million cells. The transient and acoustic setup is the same as for the full model simulation. However, due to the reduced domain, only the acoustic propagation directly from the fan blades to the microphones in the semi-anechoic chamber via FWH can be considered.

As a basis for the turbulence reconstruction with the FRPM, the RANS simulation, which was used to calculate the initial flow field for the LES of the entire domain, is used. To perform the turbulence reconstruction, a volumetric section (patch) of the mean flow profile and the statistic turbulence properties are extracted from this RANS simulation and provided as input for the FRPM. The reconstruction in the FRPM is carried out on a cartesian mesh. The FRPM patch is centered around the location of the new inlet (0.175 m) upstream of the fan leading edge with a thickness of 5 cm, which is more than three times the maximal turbulent length scale in this section. The FRPM uses a volumetric mesh for the reconstruction in order to ensure a full divergence-free flow field for the fluctuations. The spatial resolution of this mesh is the same as in the polyhedral mesh in StarCCM+, with two cells per minimal turbulent length scale on the patch. For the reconstruction, two particles per cell were used to realize fluctuations based on a Gaussian distribution. The transient turbulent fluctuations reconstructed by the FRPM are then added to the steady-state flow profile of the RANS simulation. This disturbed flow field is then used in the "Free Stream" boundary condition at the inlet. Two different approaches were developed to include the transient profile for the fluctuations. In the first approach, the fluctuations have to be created a priori to the scale-resolving simulation. For the second approach, a one-way coupling between StarCCM+ and the FRPM was realized to allow the reconstruction of the turbulent fluctuations parallel to the LES. In the present work, the fluctuations are created prior to the scale-resolving simulation since this approach is easier to implement and provides a more stable simulation setup. Figure 4 shows the process of turbulence reconstruction for this case.

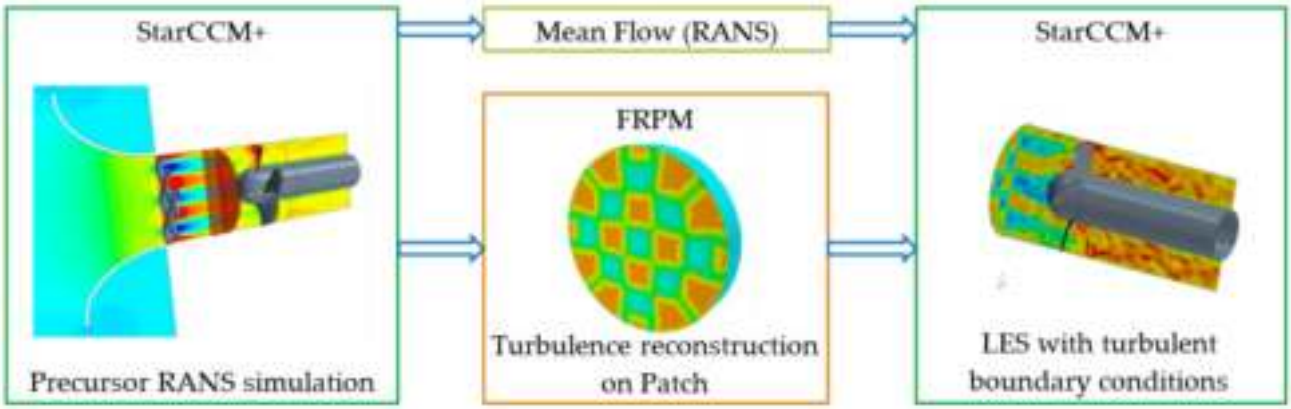

Figure 4. Setup of simulation for turbulence reconstruction using StarCCM+ and FRPM (The red patch is used to reconstruct the turbulence from RANS).

4. Aerodynamic Results

The turbulence reconstruction is based on the RANS simulation, which was also used to initialize the scale-resolving simulation of the full model. As already observed in [5], the flow field of RANS and LES differ in the structure of the wakes of the turbulence grid. This can also be seen in Figure 5.

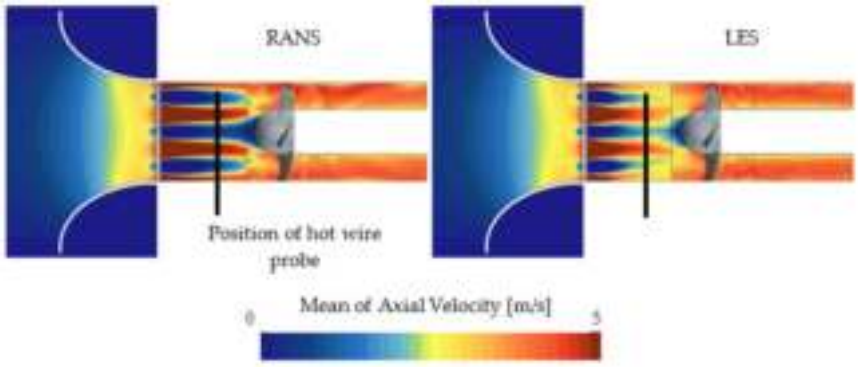

Figure 5. Mean axial velocity: (**left**) RANS and (**right**) LES.

The different structures of the turbulence can also be seen in the comparison to the measurements with the hot wire probe 175 mm in front of the fan, shown in Figure 6.

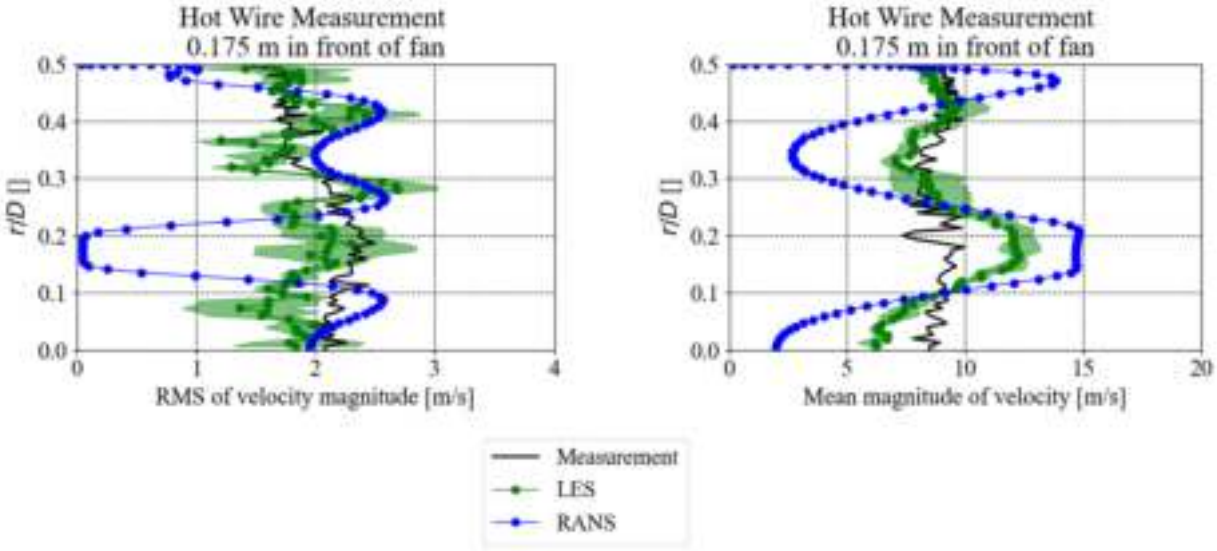

Figure 6. Comparison of RANS and LES (both full models) with hot wire measurements 175 mm in front of the fan [7]. The LES data was obtained by averaging three overlapping blocks. The minimum and maximum value is indicated by the light green area. (Mean magnitude of the velocity (**left**) and RMS-Value of velocity magnitude (**right**)).

In contrast to the measurement, the wakes can be seen in the profiles of the axial velocity for both simulations (RANS and LES). However, in the RANS profile, the structure of the wakes is more clearly visible. Along with the RMS values of the fluctuations (right diagram in Figure 6), it can be seen that, despite the mean velocity profile, the evaluation time for the fluctuations is not sufficient. Similar behavior of the wakes was also seen in the highly resolved LES by Moghadam et al. [8]. Nevertheless, previous investigations [1,5] showed that, despite differences in aerodynamics, good acoustic results could be obtained with the selected evaluation time and grid resolution. In the RANS velocity and fluctuating profile, as already observed in [5], the wakes of the turbulence grid are more pronounced compared to LES and measurement. This can be explained by the modeled isotropic turbulence in the RANS approach, since the RMS value was calculated based on the turbulent kinetic energy.

In addition to the hot wire probes, the pressure on the blade's surfaces can also be compared to the measurements. In Figure 7, the spectra of the measured surface pressure are compared to the full model simulation and the simulation with reconstructed turbulence.

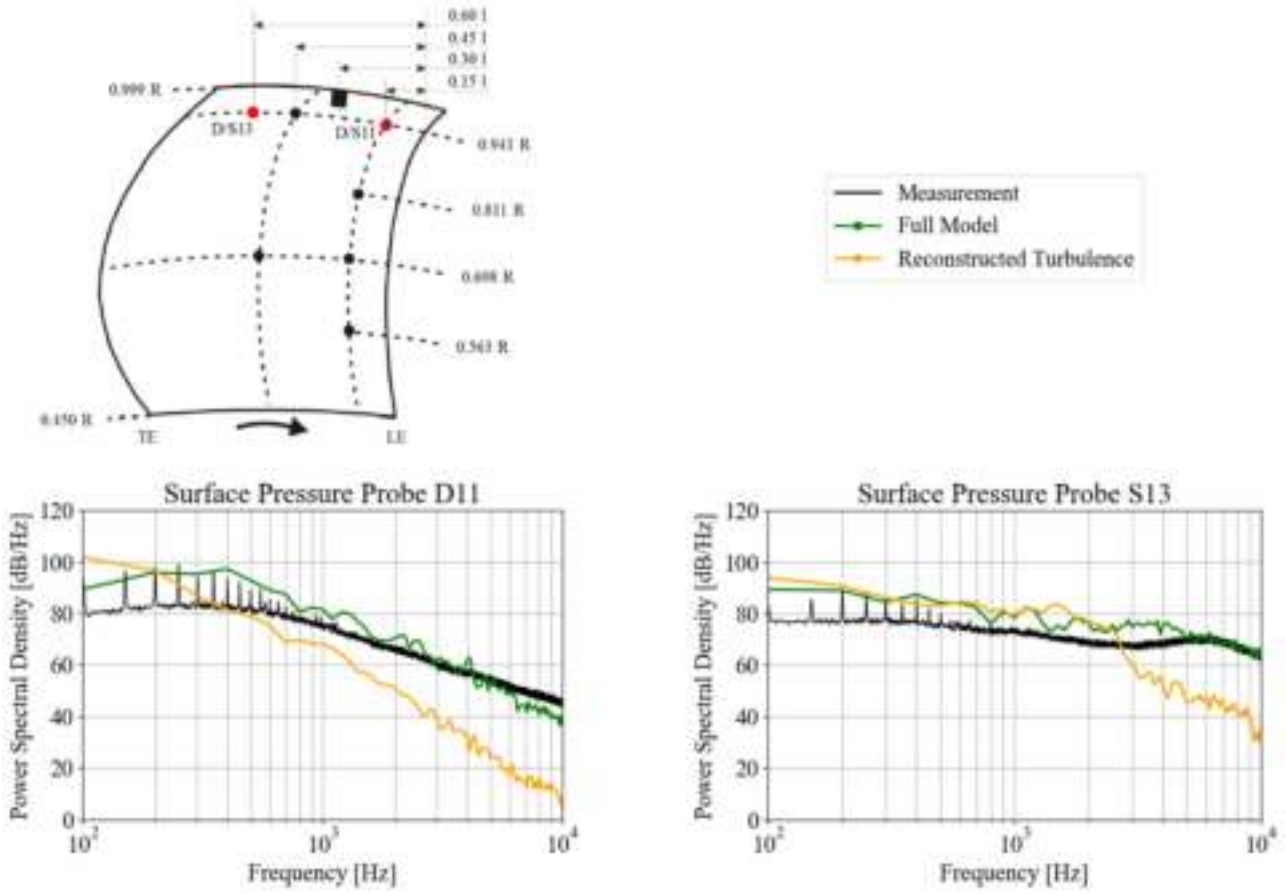

Figure 7. Comparison of surface pressure spectra of full model simulation and simulation with reconstructed turbulence with the measurement: **top left**: positions of pressure probes on fan blade surface (prefix "D" = pressure side; prefix "S" = suction side); **bottom left**: Comparison of surface pressure spectra on the pressure side (probe D11) close to the leading edge; **bottom right**: Comparison of surface pressure spectra on the suction side (probe S13) close to the trailing edge. Reference data and positions based on [7,12].

The surface pressure in the full model simulation shows, for the most part of the spectrum, higher levels compared to the measurement. This can be an effect of the insufficient surface resolution in the presented LES. It can be seen that, especially close to the leading edge on the suction and pressure side, the pressure profile of the reconstructed turbulence shows a significantly faster decay. Close to the trailing edge, the pressure fluctuations of the full model and the reconstructed turbulence are in good agreement, up to ~2500 Hz. For higher frequencies, the pressure signal for the reconstructed turbulence shows significantly lower levels. In the FRPM, a Gaussian spectrum, calibrated with the turbulent kinetic energy and the turbulent length scale of the RANS simulation, is assumed for the reconstruction of the turbulence. The turbulent length scale is dominated by the large turbulent structures of the flow. Therefore, only the part of the turbulent spectrum, which is located around the turbulent length scale, is reconstructed. Small-scale fluctuations at higher frequencies are neglected in the reconstruction leading to an unphysical shape of the energy distribution. This is most likely the reason for the differences found in the pressure spectra.

Previous investigations [5] showed that, by focusing the reconstruction on the large-scale turbulence based on the RANS mean flow yields good acoustic results compared to reference simulations and measurements. Therefore, it might be assumed that, despite the differences seen for the flow field, good acoustic results can be obtained with the turbulence reconstruction method.

5. Acoustic Results

In the full model simulation, the acoustic results in the three microphones in the semi-anechoic chamber can be obtained by propagation using FWH either from the permeable surface or the direct propagation from the fan blades (Figure 3). In the simulation with reconstructed turbulence due to the reduced simulation domain, only the propagation directly from the fan blades is possible. The average of the acoustic spectra in all three microphones in the semi-anechoic chamber (front) and separately the microphone on the axis (microphone 2) can be found in Figure 8.

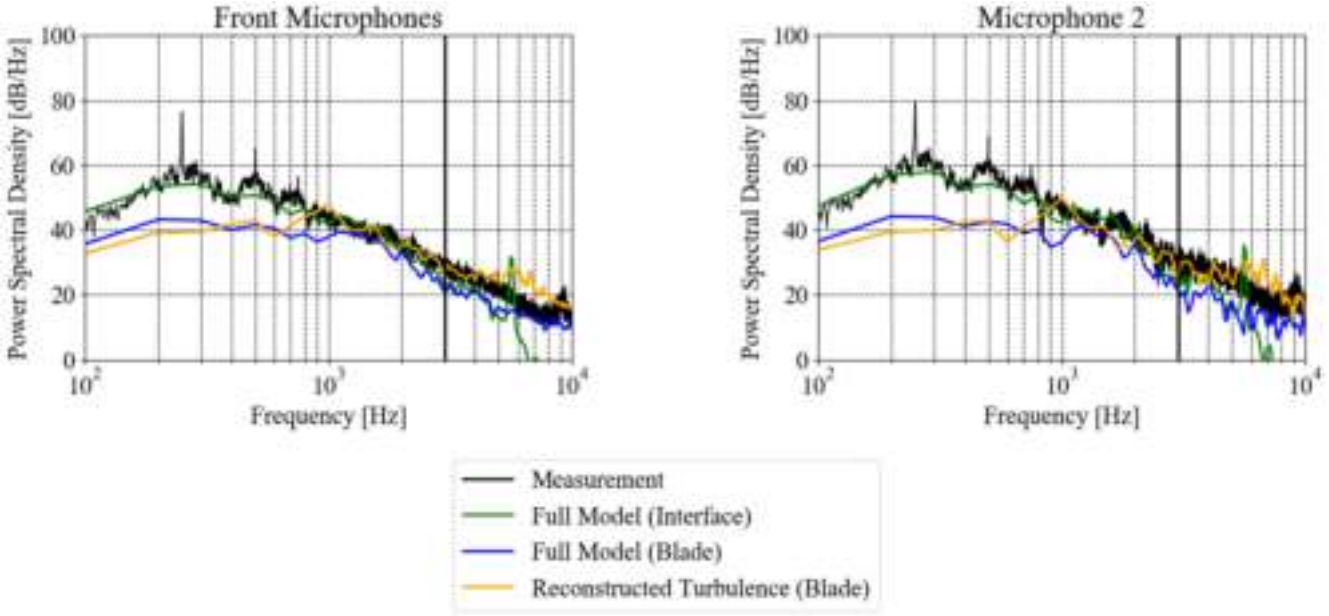

Figure 8. Mean acoustic spectra: (**left**) all three suction side microphones; **(right)** single microphone spectrum for the microphone on the axis (Measurement data based on [7]).

The result based on the propagation from the permeable surface shows a very good agreement with the experimental values. In comparison to the propagation from the blades, the effect of the duct and the nozzle on the acoustic spectrum is clearly visible for frequencies below 1000 Hz. For frequencies above 1000 Hz, the shape of the spectrum and the levels are in good agreement between the different propagation methods.

The reference for the simulation with turbulent reconstruction is the propagation from the fan blades in the full model simulation. The shape of the spectrum and the levels are in close comparison. There are slight differences at 1000 Hz and at higher frequencies. The additional noise at higher frequencies might be an effect of the neglect of small, turbulent fluctuations in the Gaussian spectrum in the turbulence reconstruction method.

Despite the differences in the aerodynamics shown in the previous section, it is possible to correctly predict the effect of the inflow turbulence on the acoustics of the fan by the presented turbulence reconstruction method. In contrast to a heat-exchanger application, the resolution of the turbulence grid in this setup requires a comparably small amount of computational resources.

Due to the short evaluation time, a resolution of the tonal components of the spectra is not possible.

6. Periodic Simulations

To further reduce the computational effort needed to predict the effect of inflow turbulence on the ducted fan, further reduction techniques are investigated. As shown in previous studies [1,8], it is possible to exploit the periodicity of the fan geometry in the simulation without inflow turbulence. For the full model approach, this is not possible since the periodicity of the turbulence grid and the fan are not the same (1/5th periodicity

for the fan and 1/4th periodicity of the turbulence grid). In the simulation setup with reconstructed turbulence, however, the turbulence grid is no longer part of the simulation domain. Therefore, a new mesh was created, featuring only one blade in a periodic segment. The setups for the full and periodic model for the turbulence reconstruction simulations are displayed in Figure 9.

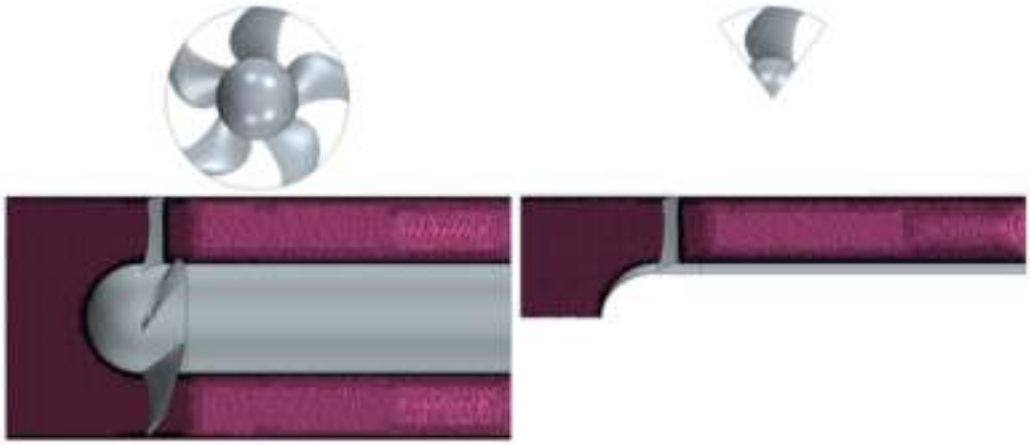

Figure 9. Calculation domain and mesh for turbulence reconstruction simulations: **(left)** Full model; (**right**) periodic model.

Due to the exploitation of the periodicity of the fan geometry, a significant reduction in the cell count can be achieved. Starting from ~60 million cells for the full model (fan and turbulence grid), the cell count is reduced to ~8.6 million for the periodic turbulence reconstruction simulation without the turbulence grid.

For the periodic model, however, it is not possible to directly use the mean flow provided by the precursor RANS, as specified in Figure 4. The mean flow still shows the structure of the grid, which is of 1/4th periodicity. Using this inflow would lead to unphysical fluctuations in the periodic aeroacoustic simulation. Using the circumferential mean of the RANS flow field and the turbulent fluctuations generated based on the original mean flow, no unphysical fluctuation could be observed in the frequency region of interest. Since it is currently not possible to reconstruct the turbulence in a circumferential periodic domain in the FRPM, the same region as for the full model turbulence reconstruction was used. The profiles used for the mean flow and the turbulence reconstruction are shown in Figure 10.

The acoustic results for microphone two can be seen in Figure 11. The signal for the periodic model is shifted by $\Delta PSD = -10\ log_{10}(5) dB \approx -7\ dB$ (5 representing the number of blades of the fan) account for coherent sound sources on the axis. Here only the microphone on the axis is shown due to the ongoing investigations to account for the effect of coherent sound sources for off-axis microphones (Lucius et al. [13]).

The acoustic spectrum from the periodic simulation with reconstructed turbulence matches the reference simulation and is also in good agreement with the full model simulation with reconstructed turbulence. For higher frequencies, additional fluctuations can be observed, which can be accounted for by the generation of the synthetic turbulence and the periodic model itself. For the spectrum at low frequencies ($f < 1\ 000$ Hz), it is important to use the original RANS flow field for the turbulence reconstruction. If the circumferential mean of the flow field is also used for the turbulence reconstruction, significantly lower levels are observed in this frequency region.

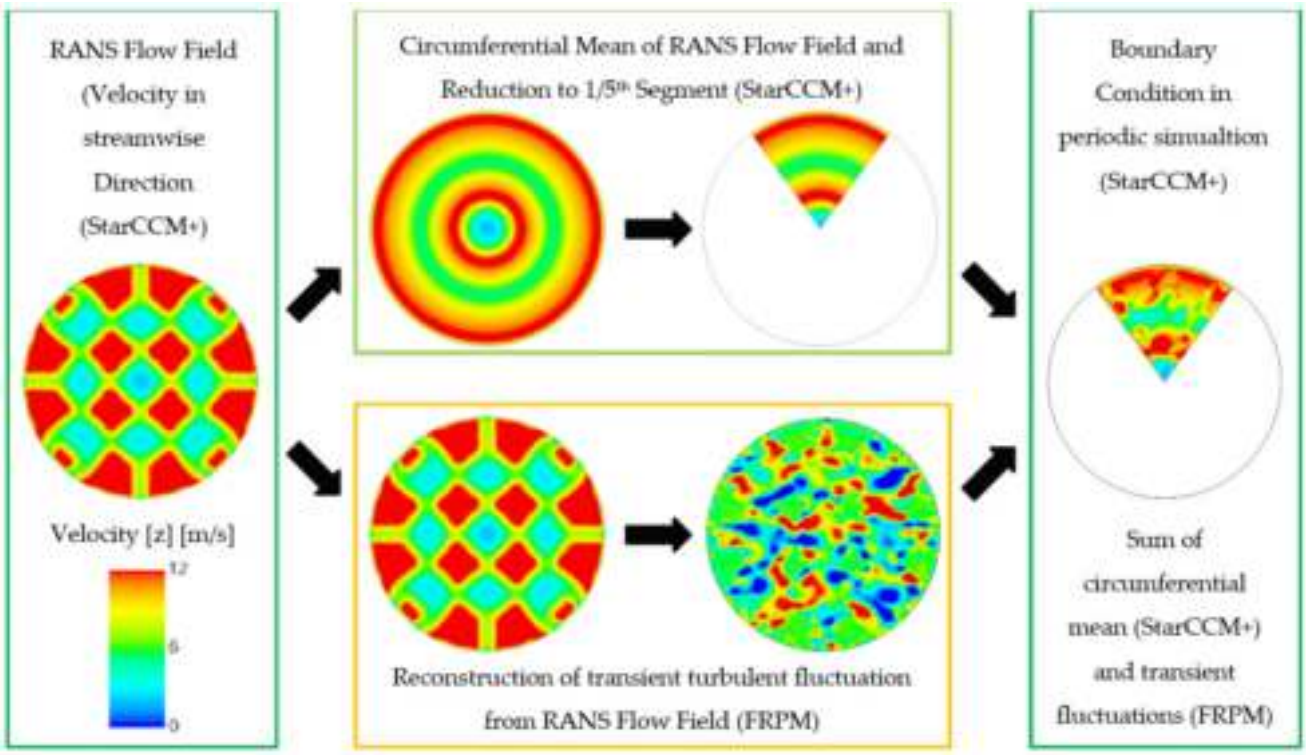

Figure 10. Process chart for the reconstruction of the turbulent boundary condition for the periodic simulation. Mean flow is based on the circumferential mean of the RANS flow field (**top** branch); Fluctuations are reconstructed on the original RANS flow field (**bottom** branch) (Reconstruction of the entire domain); Addition of circumferential mean flow field and fluctuations based on current fan position (entire periodic domain is rotating).

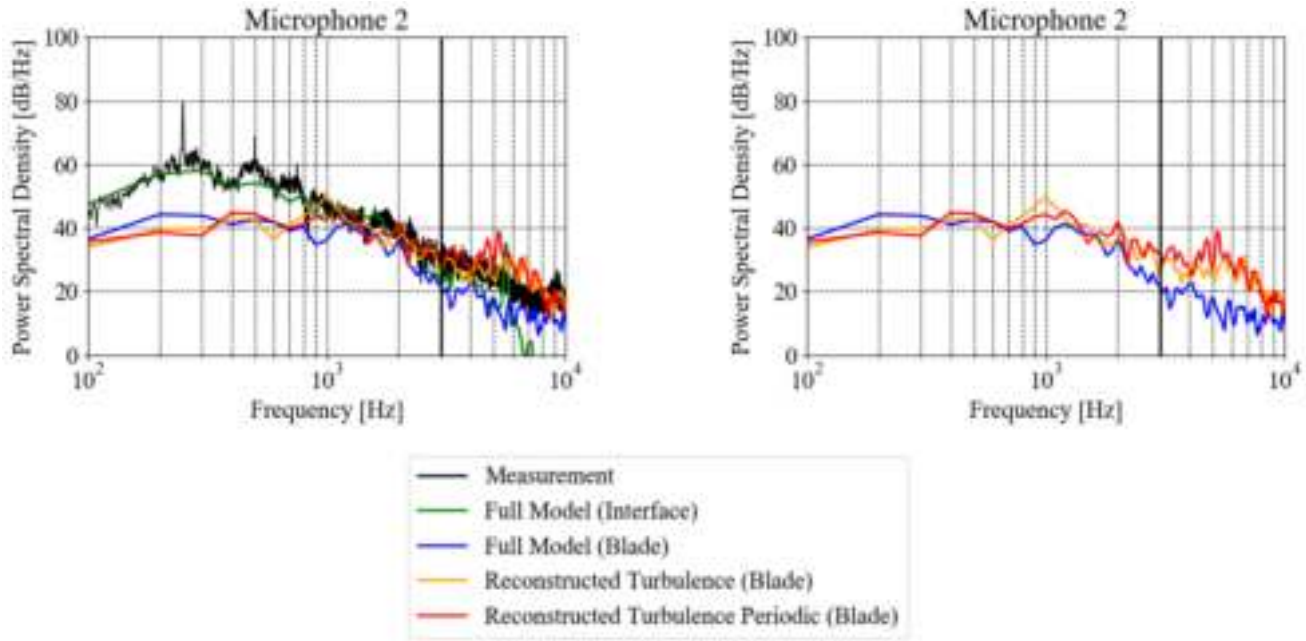

Figure 11. Comparison of the acoustic spectra at microphone 2 for the full model simulation and different turbulence reconstruction: (**left**) including measurement and full model simulation; (**right**) only reference data and reconstruction (Measurement data based on [7]).

7. Conclusions

In this paper, an approach to reduce the computational effort for the aeroacoustic simulation of fans by reconstructing the turbulence generated by geometric features upstream of the fan is presented. The approach was applied to a benchmark case of an axial fan in a duct with an upstream turbulence grid.

For this approach, the statistical turbulence information from a precursor RANS was reconstructed using the FRPM-Tool, developed at the DLR in Braunschweig, and used as an inlet boundary condition of a scale-resolving aeroacoustic simulation of the fan. The results were compared to the experimental finding and an aeroacoustic simulation of the entire setup (fan + turbulence grid). Additionally, an approach was presented to further reduce the computational effort for acoustic prediction by exploiting the periodicity of the geometry.

The aerodynamic comparison showed that there are differences in the mean flow field and the turbulent properties of the RANS simulation compared to the experiment and the reference LES. Furthermore, the pressure signals on the fan blade surface partially show significant differences between the simulation with reconstructed turbulence and the reference simulation of the entire setup. Despite these differences, a good agreement between the acoustic spectra of the simulations with reconstructed turbulence and the reference simulations was found. The reference spectra from the experiments could not be reproduced with the turbulence reconstructing simulations due to the reduced computational domain. With the turbulence reconstruction and the exploitation of the periodicity of the geometry, it is possible to significantly reduce (up to a factor of 6) the computational effort of aeroacoustic simulations with inflow turbulence.

The simulations show that with the turbulence reconstruction method and the exploitation of periodicity in the geometric setup, it is possible to predict the aeroacoustic behavior of the fan in comparison to simulations of the entire setup. Especially for the typical application of fans in combination with heat exchangers, this method seems promising to be able to capture the effect of the inflow turbulence on the fans' acoustics, which is currently not economically possible. For the development of new generations of fans with improved acoustic behavior under disturbed inflow conditions, this approach can be a valuable asset. If detailed information in microphones upstream of the suction side is the target of the investigation, an acoustic propagation code can be used in addition to the proposed method.

Author Contributions: Conceptualization, P.D. and M.S.; methodology, P.D.; investigation, P.D.; writing—original draft preparation, P.D.; writing—review and editing, P.D.; visualization, P.D.; supervision, M.S. All authors have read and agreed to the published version of the manuscript.

Funding: This research received no external funding.

Data Availability Statement: Experimental data were derived and reproduced with permission from the IGF Project (No.: 16773 N) (References [7,12]); Contact: https://www.flt-net.de/; Accessed on 1 September 2015.

Conflicts of Interest: The authors declare no conflict of interest.

References

1. Lucius, A.; Hütter, S.; Dietrich, P.; Schneider, M.; Lehmann, M.; Geyer, T. Experimental and numerical investigation of axial fan aeroacoustics at disturbed inflow conditions. In Proceedings of the FAN2018, Darmstadt, Germany, 18–20 April 2018.
2. Ewert, R. The Fast Random Particle-Mesh Method to realize unsteady turbulent sound sources and velocity fields for CAA applications; In Proceedings of the 13th AIAA/CEAS Aeroacoustic Conference, Rome, Italy, 21–23 May 2007.
3. Liberson, L.; Lummer, M.; Mößner, M.; Ewert, R.; Delfs, J.W. Application of a Discontinuous Galerkin based CAA solver for broadband noise prediction; In Proceedings of the FAN2018, Darmstadt, Germany, 18–20 April 2018.
4. Bernicke, P.; Akkermans, R.A.; Ewert, R.; Dierke, J. Overset-LES with Stochastic Forcing for Sound Source Simulation. In *New Results in Numerical and Experimental Fluid Mechanics XI, Notes on Numerical Fluid Mechanics and Multidisciplinary Design 136*; Dillmann, A., Ed.; Springer: Berlin/Heidelberg, Germany, 2018. [CrossRef]

5. Dietrich, P.; Schneider, M. Modellierung der Akustik von Axialventilatoren unter gestörter Zuströmung. In Proceedings of the DAGA2019, Rostock, Germany, 18–20 March 2019.
6. Erbig, L.; Lardeau, S. Hybrid RANS/LES of an Adverse Pressure Gradient Turbulent Boundary Layer Using an Elliptic Blending Reynolds Stress Model and Anisotropic Linear Forcing. In *Progress in Hybrid RANS-LES Modelling. Notes on Numerical Fluid Mechanics and Multidisciplinary Design*; Hoarau, Y., Peng, S.H., Schwamborn, D., Revell, A., Mockett, C., Eds.; Springer: Berlin/Heidelberg, Germany, 2020; Volume 143.
7. Zhu, T. *Akustische Nachrechnung Von Ventilatoren: Bericht Zum Zusätzlichen FLT-Eigenmittelprojekt Teilprojekt 2 Zum Hauptarbeitspaket C*: Akustisches Validierungsexperiment, Durchgeführt an der Universität Siegen; Project report of University of Siegen (AiF 16773 N/2); University of Siegen: Siegen, Germany, 2015.
8. Moghadam, S.A.; Pogorelov, A.; Roidl, B.; Meinke, M.; Schröder, W. Numerical analysis of the acoustic field of an axial fan at varying inflow conditions. In Proceedings of the FAN2018, Darmstadt, Germany, 18–20 April 2018.
9. Reese, H.; Carolus, T. Axial fan noise: Towards sound prediction based on numerical unsteady flow data–a case study. In Proceedings of the Acoustics'08, Paris, France, 29 June–4 July 2008.
10. Sturm, M.; Sanjose, M.; Moreau, S.; Carolus, T. Aeroacoustic simulation of an axial fan including the full test rig by using the Lattice Boltzmann Method. In Proceedings of the FAN2015, Lyon, France, 15–17 April 2015.
11. Zhu, T. On the Flow Induced Tip Clearance Noise in Axial Fans. Ph.D. Thesis, Shaker Verlag GmbH, Düren, Germany, 2016.
12. Delfs, J.W.; Carolus, T. *Schlussbericht zu dem IGF-Vorhaben: Akustische Nachrechnung von Ventilatoren*; Final project report (AiF 16773 N); University of Siegen: Brunswik/Siegen, Germany, 2015.
13. Lucius, A.; Schäfer, R. Acoustics of a backward curved radial fan–CAA simulation and experimental validation. In Proceedings of the FAN2022, Senlis, France, 27–29 June 2022.

Disclaimer/Publisher's Note: The statements, opinions and data contained in all publications are solely those of the individual author(s) and contributor(s) and not of MDPI and/or the editor(s). MDPI and/or the editor(s) disclaim responsibility for any injury to people or property resulting from any ideas, methods, instructions or products referred to in the content.

International Journal of
Turbomachinery
Propulsion and Power

MDPI

Editorial

Fans: Noise, Aerodynamics, Applications and Systems—The Best of the International Conference FAN2022

Thomas H. Carolus [1,2]

[1] Steinbeis-Transfer Center FLOWTRANS, 57250 Netphen, Germany; thomas.carolus@stw.de
[2] Chair of Applied Fluid Mechanics and Turbomachinery, University Siegen, 57068 Siegen, Germany

The number of air- and gas-handling fans in use today is large. Fans support our daily lives by providing air for heating and cooling, moving gases in chemical plants and food processing, helping to generate electricity, and more. At the same time, with their associated motors, fans consume a substantial share of all electricity worldwide, still mostly generated from fossil fuels; thus, they are an indirect cause of CO_2 emission. Additionally, the environmental impact of fan noise is another relevant issue.

The articles in this *International Journal of Turbomachinery, Propulsion and Power* (IJTPP) Special Issue on fans are from the FAN2022 conference. This international conference was held in Senlis, France, in July 2022. The organizing committee consisted of Geoff Sheard, AGS Consulting LLC, USA; Jürgen Schöne, ebm-papst, Germany; Alain Guedel and François Bessac, CETIAT; Xavier Carniel, CETIM, France; and Thomas Carolus, University of Siegen and Peter Pelz Technical University of Darmstadt, both in Germany. The aim of this Special Issue is to present a selection of papers of outstanding scientific quality or that address current pressing issues.

The aerodynamic design of fans is still based on analytical models but increasingly relies on numerical flow simulation. Numerical flow simulations allow multiple design variants to be predicted at a low cost and can lead to automated optimization. Optimization methods have the potential to supplement or even replace analytical design methods in the future. Computational fluid dynamics is also increasingly capable of resolving the acoustic field. Depending on the degree of approximation, it provides previously impossible levels of detail about sound sources and their location in the machine. On the other hand, experimental and semi-analytical methods remain essential to verify theoretical performance, problems of wear resistance, and most importantly, system integration and installation effects. Finally, the debate continues with legislative institutions as our community works towards defining the best metric to characterize the energy efficiency and environmental impact of an overall system.

This Special Issue reflects that fans are still the subject of multidisciplinary scientific research and development worldwide, in which universities, public research institutions and companies are involved and cooperate. Industrial manufacturers and users recognize and support these efforts. This cooperation is exemplified by ZIEHL-ABEGG SE, a fan manufacturer based in Künzelsau, Germany, who sponsored this Special Issue. This support allows open access to all articles and is expressly acknowledged.

Funding: As part of the FAN2022 conference sponsorship program, all Article Processing Charges (APCs) for this Special Issue were funded by ZIEHL-ABEGG SE, Künzelsau, Germany.

Institutional Review Board Statement: Not applicable.

Informed Consent Statement: Not applicable.

Data Availability Statement: Not applicable.

Conflicts of Interest: The author declares no conflict of interest.

check for updates

Citation: Carolus, T.H. Fans: Noise, Aerodynamics, Applications and Systems—The Best of the International Conference FAN2022. *Int. J. Turbomach. Propuls. Power* **2022**, *7*, 36. https://doi.org/10.3390/ijtpp7040036

Received: 24 November 2022
Accepted: 30 November 2022
Published: 2 December 2022

Publisher's Note: MDPI stays neutral with regard to jurisdictional claims in published maps and institutional affiliations.

Copyright: © 2022 by the author. Licensee MDPI, Basel, Switzerland. This article is an open access article distributed under the terms and conditions of the Creative Commons Attribution (CC BY-NC-ND) license (https://creativecommons.org/licenses/by-nc-nd/4.0/).

International Journal of
Turbomachinery
Propulsion and Power

MDPI

Review

Experimental Investigation Techniques for Non-Ideal Compressible Fluid Dynamics

Stefan aus der Wiesche

Department of Mechanical Engineering, Muenster University of Applied Sciences, 48565 Steinfurt, Germany; wiesche@fh-muenster.de; Tel.: +49-2551-9-62272

Abstract: The rising number of applications of the organic Rankine cycle (ORC) or supercritical CO_2 (sCO_2) power systems have shaped a new branch of fluid mechanics called non-ideal compressible fluid dynamics (NICFD). This field of fluid mechanics is concerned with flows of vapors or gases, which are characterized by substantial deviations from the perfect gas model. In extreme cases, even non-classical gas dynamic phenomena could occur. Although these non-ideal compressible flows are the subject of sophisticated numerical simulation studies today, there is also a growing need for experimental data for validating purposes. In the last couple of years, new experimental test rigs designed for investigating non-ideal compressible fluid dynamics have been developed and commissioned. Classical practical measurement techniques are currently being re-developed and applied to non-ideal compressible flows. Despite its substantial relevance, information about these measurement techniques and their differences from conventional methods in the open literature is scarce. The present review article is an attempt to reduce that gap. After briefly discussing the thermodynamics and fluid dynamics of non-ideal compressible flows, the currently available test rigs and their utilized measurement techniques are reviewed. This review discusses schlieren optical investigations, pneumatic and laser-optical methods, and hot-wire anemometry for non-ideal compressible flows.

Keywords: compressible flow; non-ideal gas; ORC; flow measurement; test rigs; pitot probes; schlieren systems; LDV; PIV; hot-wire anemometry

check for updates

Citation: aus der Wiesche, S. Experimental Investigation Techniques for Non-Ideal Compressible Fluid Dynamics. *Int. J. Turbomach. Propuls. Power* **2023**, *8*, 11. https://doi.org/10.3390/ijtpp8020011

Academic Editors: Rodolfo Bontempo and Tony Arts

Received: 15 December 2022
Revised: 21 February 2023
Accepted: 23 February 2023
Published: 3 April 2023

Copyright: © 2023 by the author. Licensee MDPI, Basel, Switzerland. This article is an open access article distributed under the terms and conditions of the Creative Commons Attribution (CC BY-NC-ND) license (https://creativecommons.org/licenses/by-nc-nd/4.0/).

1. Introduction

Organic Rankine cycle (ORC)-based power systems are being extensively investigated for heat-to-electric power conversion from solar and geothermal heat sources and waste heat recovery. The ORC technology offers a high potential [1] for meeting environmental requirements and reducing climate issues. The rising number of applications of organic Rankine cycle (ORC) power systems [1,2] has increased the relevance of a new branch of fluid mechanics called non-ideal compressible fluid dynamics (NICFD). In recent years, the interest in supercritical CO_2 (sCO_2) power systems has led to a further need to better understand the gas dynamics of fluids that are far away from the usual perfect gas behavior [3]. NICFD are concerned with flows of vapors or gases that are characterized by substantial deviations from the perfect gas model. In extreme cases, theoretical analyses [4–6] even predict the occurrence of non-classical gas dynamical phenomena, including the formation and propagation of expansion or rarefactive shocks, sonic shocks, double sonic shocks, and shock splitting.

In thermodynamics, a perfect gas is a unique gas model that differs from real gases in specific ways that make calculations easier to handle. In all perfect gas models, intermolecular forces are neglected. All perfect gas models are ideal gas models in the sense that they all follow the ideal gas equation of state

$$p = \rho RT, \tag{1}$$

with p signifying pressure, ρ signifying density, T signifying temperature, and R signifying the specific gas constant. However, the term perfect gas model is often invoked as a combination of the ideal gas equation of state (1) with specific additional assumptions regarding the variation in the heat capacity with temperature [7]. The branch of fluid mechanics that deals with the compressible flow of fluids violating the ideal gas equation of state (1) are called non-ideal compressible fluid dynamics (NICFD); see, for instance, [8]. This review paper is primarily concerned with experimental techniques applied in this field.

In principle, it is always possible to formulate an equation of state

$$p = \rho Z R T \tag{2}$$

for arbitrary fluids by introducing an additional compressibility factor Z, which is generally a function of two independent thermodynamic variables: pressure p, and temperature T, or specific entropy s. For a perfect gas, the identity $Z = 1$ holds. However, $Z \neq 1$ is a necessary condition, but not a sufficient one, for fluids to exhibit non-ideal compressible flow behavior. Section 2 will explain the different kinds of gas dynamics in more detail. For the present purpose, it is sufficient to notice that non-ideal compressible flow phenomena outside the well-known perfect gas aerodynamics frequently characterize real gases or vapors.

The interest in studying non-ideal compressible fluid dynamics (NICFD) can be traced back to early theoretical works by Duhem [9], Becker [10], Bethe [11], and Zel'dovich [12]. Later, Thompson provided a foundational article in 1971 [13] about the gas dynamics of fluids whose properties do not comply with the ideal gas law (1). This research was driven by the fundamental academic question regarding the possibility of fluids for which non-classical or inverted gas dynamics might occur. This exciting question is still open, and a final answer cannot be given so far. Independently and with a different goal, aerodynamicists began in the 1990s to re-consider non-ideal compressible flow effects in wind tunnel testing [14–16]. Their objective was to achieve a higher Reynolds numbers in wind tunnel testing using heavy gases consisting of complex molecules. It was shown that the transonic similarity theory only partially successfully transformed the heavy gas results into equivalent nitrogen or air results. Aircraft designers demanded the latter. Due to the non-ideal gas dynamics, it was impossible to obtain reliable correction schemes for predicting shockwave boundary layer interactions for similar perfect gas flows based on the non-ideal compressible flow measurements. Consequently, the interest of aircraft designers in the aerodynamics of non-ideal gases diminished. Anders et al. [16] explained the failure of the transonic similarity theory regarding the shock/boundary layer interaction by the fact that the transonic similarity theory one bases on small disturbance potential flow theory. Thus, an inviscid transformation will not account for the difference in boundary layers for two different gases.

NICFD are essential for understanding phenomena occurring in industrial processes working with organic vapors or heavy gases [17] at higher speed levels. Turbomachinery operating partly in the NICFD regime is expected in the oil and gas industry [18]. NICFD effects occur in the organic Rankine cycle (ORC) [2] and in supercritical carbon dioxide (sCO2) [19] power systems. The number of numerical studies dealing with NICFD effects is numerous, but dedicated descriptions of corresponding test facilities and experimental works are relatively scarce [20]. However, there is a solid need to validate sophisticated computational fluid dynamics (CFD) models and schemes. During the last few years, progress has been made regarding experimental techniques and their applications to NICFD research. The technical challenges associated with designing and operating test facilities for NICFD research are arguably higher than conventional wind tunnels or test rigs for air. Due to the elevated pressure and temperature levels usually required for studying NICFD effects, standard flow measurement techniques require substantial design and data reduction modifications.

This paper reviews the available experimental investigation techniques for non-ideal compressible fluid dynamics. Since the author of this paper is working in the field of ORC power systems, this review focuses on experimental methods that have been used and

considered in the ORC research community. This contribution focuses on measurement techniques for testing organic vapor flows in ORC power system turbomachinery.

2. Non-Ideal Compressible Fluid Dynamics

Before starting with a review of experimental test facilities and measurement techniques, it is necessary to review some fundamentals of non-ideal compressible fluid dynamics. The need to investigate non-ideal compressible fluid dynamics and their differences with reference to conventional testing for steam and gas turbines requires sound knowledge of the fundamental thermodynamic and fluid mechanics relations. In this context, it is helpful to distinguish between thermodynamically non-ideal gas behavior and non-ideal fluid mechanical phenomena that are relevant to turbomachinery applications.

2.1. Thermodynamical Classification of Gas Dynamics

In 1942, Landau introduced a non-dimensional parameter

$$\frac{v^3}{a^2}\left(\frac{\partial^2 p}{\partial v^2}\right)_s$$

for the evaluation of the curvature of isentropes in the *p*,*v* diagram [21]. The curvature of the isentropes is of considerable interest, because a negative curvature is required for rarefaction shocks [4]. In classical gas dynamics, only compression shocks can exist due to the second law of thermodynamics. The possibility that only compression shocks can be observed is directly related to a positive curvature of the isentropes of the involved gases. Later, Hayes [22] denoted Landau's parameter with the symbol Γ and introduced a multiplier $\frac{1}{2}$. Following Thompson [13], it is common to call

$$\Gamma = \frac{1}{2}\frac{v^3}{a^2}\left(\frac{\partial^2 p}{\partial v^2}\right)_s = 1 + \frac{\rho}{a}\left(\frac{\partial a}{\partial \rho}\right)_s \tag{3}$$

the "fundamental derivative of gas dynamics." In Equation (3), a denotes the speed of sound, and v is the specific volume ($v = 1/\rho$). Using general thermodynamic relations, further different expressions for the fundamental derivative of gas dynamics Γ can be obtained [13]. In the case of a perfect gas, by obeying Equation (1), the fundamental derivative Γ reduces to the simple relation

$$\Gamma = \frac{1}{2}(\gamma + 1) \tag{4}$$

with $\gamma = c_p/c_v$ signifying the isentropic exponent of the perfect gas. Since $c_p > c_v$ holds for a perfect gas, the fundamental derivative Γ is larger than the one for a perfect gas. This is valid in classical compressible fluid dynamics with an increasing speed of sound and with pressure at a constant entropy. Classical non-ideal compressible fluid dynamics occur for $0 < \Gamma < 1$. Then, the speed of sound decreases with increasing pressure at a constant entropy. A fluid with that property is called a "dense gas" or "dense vapor". In the particular, yet academic case where $\Gamma = 1$, the speed of sound is a constant. Dense gases exist in nature, and Figure 1 illustrates an isentropic expansion process starting in the dense vapor regime for MDM. Below the contour line $\Gamma = 1$, MDM behaves like an ideal gas. This is referred to as a dilute gas regime. However, the region with $\Gamma < 1$ is not tiny in the *T*,*s* diagram of MDM, and non-ideal compressible fluid dynamics must be considered for typical turbine expansion processes [23].

The question of whether fluids with $\Gamma < 0$ exist is still open [24]. It is likely that the study of the fluid dynamics of fluids obeying $\Gamma < 0$ will be more of an academic issue than a practical engineering task. Thermodynamics laws permit such a dense vapor in principle, but so far, no actual working fluid has been found that fulfills the condition $\Gamma < 0$. For ORC applications, the range $0 < \Gamma < 1$ is relevant. Still, in a substance with $\Gamma < 0$, non-classical non-ideal compressible fluids dynamics, such as rarefaction shocks

or compression fans, would occur. Non-classical gas dynamics can be interpreted as an inversion of classical gas dynamics. Such non-classical fluids are also called BZT fluids in honor of the contributions from Bethe, Zel'dovich, and Thompson after a suggestion by Cramer (see [4], especially pages 91–145). The condition $\Gamma < 0$ corresponds to a speed of sound decreasing with pressure at a constant entropy.

Table 1 lists the classification of gas dynamics from the thermodynamic point of view. In supersonic turbines working with a BZT fluid, more lower shock losses could occur than for those working with classical fluids. This interesting prediction was first made in a numerical study [25] considering the aerodynamic testing of airfoils in heavy gases.

Table 1. Classification of gas dynamics from a thermodynamic point of view (following a scheme proposed by Thompson [13]).

Γ	Fluid	Sound Speed Variation	Classification of Gas Dynamics
$\Gamma > 1$	Perfect gas	$(\partial a/\partial p)_s > 0$	classical
$\Gamma = 1$		$(\partial a/\partial p)_s = 0$	classical non-ideal
$\Gamma < 1$	Dense gas	$(\partial a/\partial p)_s < 0$	classical non-ideal
$\Gamma = 0$		$(\partial a/\partial p)_s < 0$	non-classical non-ideal
$\Gamma < 0$	BZT fluids	$(\partial a/\partial p)_s < 0$	non-classical non-ideal

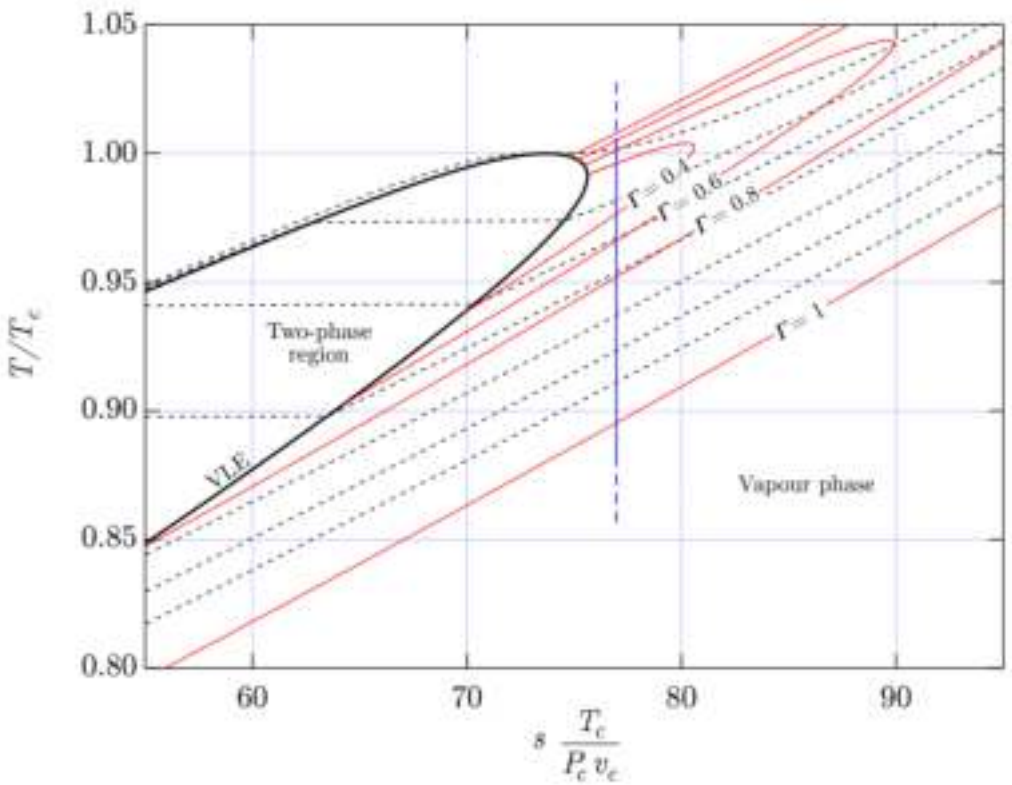

Figure 1. Normalized *T,s* diagram for MDM (from [23]), computed from the reference equation of state [26]. The red lines correspond to states with a constant Γ. The black dotted lines illustrate the behavior of the isobars. A potential isentropic expansion process is shown as a blue line (see typical expansion processes in some test rigs described in Section 3).

2.2. Classification for Turbomachinery Flows

An alternative classification of compressible flows results from the viewpoint of turbomachinery and their aerodynamical testing. Here, a hierarchy of fluids can be derived based on a formal analysis of the governing equations of compressible flows as introduced

by Traupel [27,28]. Since these essential works are, somewhat surprisingly, not available in English, a more detailed discussion might be valuable for several readers.

The bases of turbomachinery flows are the continuity equation, the Navier–Stokes equation, and the energy equation:

$$\frac{\partial \rho}{\partial t} + \nabla(\rho \mathbf{w}) = 0 \tag{5}$$

$$\frac{\partial \mathbf{w}}{\partial t} + (\mathbf{w}\cdot\nabla)\mathbf{w} = \mathbf{f} - \frac{1}{\rho}(\nabla p + \mathbf{S}) \tag{6}$$

$$\left(\frac{\partial}{\partial t} + (\mathbf{w}\cdot\nabla)\right)\left(h + \frac{1}{2}\mathbf{w}^2\right) = (\mathbf{w}\cdot\mathbf{f}) + \frac{1}{\rho}((\mathbf{w}\cdot\mathbf{S}) + \mu\mathbf{\Phi} + \nabla(\lambda\nabla T)) \tag{7}$$

Here, $\mathbf{w}$ is the velocity vector, $\mathbf{f}$ is the body force vector, $\mathbf{S}$ is the stress tensor (a function of velocity and viscosity), and $\mathbf{\Phi}$ represents the viscous dissipation. The thermodynamic variables are the density ρ, the pressure p, the temperature T, and the specific enthalpy h. The transport coefficients are the dynamic viscosity μ and the thermal conductivity λ.

Within a certain temperature range, the specific enthalpy h of a perfect gas obeys a simple relation using the specific heat at constant pressure c_p. By inserting

$$\rho = \frac{p}{RT} \text{ and } h = c_p T \tag{8}$$

into the general governing Equations (5)–(7), the perfect gas flow governing equations become

$$\frac{\partial}{\partial t}\left(\frac{p}{T}\right) + \nabla\left(\frac{p}{T}w\right) = 0 \tag{9}$$

$$\frac{\partial \mathbf{w}}{\partial t} + (\mathbf{w}\cdot\nabla)\mathbf{w} = \mathbf{f} - \frac{RT}{p}(\nabla p + \mathbf{S}) \tag{10}$$

$$\left(\frac{\partial}{\partial t} + (\mathbf{w}\cdot\nabla)\right)\left(c_p T + \frac{1}{2}\mathbf{w}^2\right) = (\mathbf{w}\cdot\mathbf{f}) + \frac{RT}{p}((\mathbf{w}\cdot\mathbf{S}) + \mu\mathbf{\Phi} + \nabla(\lambda\nabla T)) \tag{11}$$

This set of equations governs turbomachinery working with perfect gases. A relatively similar formal structure as the set of Equations (9)–(10) can be derived for a gas obeying the equation of state

$$h = \frac{\gamma}{\gamma - 1}\frac{p}{\rho} = \frac{\gamma}{\gamma - 1}ZRT \tag{12}$$

This equation of state is more general than the ideal gas model described by Equation (8). Inserting Equation (12) into the set of Equations (5)–(7) yields

$$\frac{\partial}{\partial t}\left(\frac{p}{h}\right) + \nabla\left(\frac{p}{h}\boldsymbol{w}\right) = 0 \tag{13}$$

$$\frac{\partial \boldsymbol{w}}{\partial t} + (\boldsymbol{w}\cdot\nabla)\boldsymbol{w} = \boldsymbol{f} - \frac{\gamma - 1}{\gamma}\frac{h}{p}(\nabla p + \boldsymbol{S}) \tag{14}$$

$$\left(\frac{\partial}{\partial t} + (\boldsymbol{w}\cdot\nabla)\right)\left(h + \frac{1}{2}\boldsymbol{w}^2\right) = (\boldsymbol{w}\cdot\boldsymbol{f}) + \frac{\gamma - 1}{\gamma}\frac{h}{p}((\boldsymbol{w}\cdot\boldsymbol{S}) + \mu\mathbf{\Phi} + \nabla(\lambda\nabla T)) \tag{15}$$

The above set of Equations (13)–(15) has the same formal structure as the set (9)–(11) if the temperature T in the perfect gas Equations (9)–(11) is replaced with the expression $((\gamma - 1)/\gamma)h/R$ and if c_p is replaced with $\gamma R/(\gamma - 1)$. The only exception is the last heat conduction term ($\nabla(\lambda\nabla T)$) in Equation (15). This means that heat conduction phenomena are formally excluded from that similarity. However, heat conduction effects are typically only of minor importance for several turbomachinery applications.

The main conclusion of the above analysis is that gases defined by Equation (8) or Equation (12) are essentially equivalent for turbomachinery flow analysis purposes. Equation (12) ensures that a fluid behaves like a quasi-perfect gas. For such a fluid, conventional testing applies, and no significant non-ideal gas dynamics would be expected in turbomachinery flows. Traupel [27] showed that Equation (12) could only be fulfilled for gases for which (i) the compressibility factor Z is a unique function of the entropy s as a single variable (i.e., $Z = f(s)$), and for which (ii) a constant isentropic exponent exists for pressure–volume relations (i.e., pv^{γ} = constant). For non-perfect gases, the nomenclature γ_{pv} is also in use for the isentropic exponent for pressure–volume relations to distinguish it from the ratio of the specific heats $\gamma = c_p/c_v$ [29]. A fluid obeying Equation (12) is called a "perfect vapor" [28]. Steam is an example of a perfect vapor for a broad range of thermodynamic conditions. This thermodynamic fact explains why steam turbine designers can use data from conventional wind tunnels working with air.

For non-perfect gases violating Equation (12), a different formal structure of the governing equations follows. Hence, from the viewpoint of turbomachinery flows and corresponding testing, the classification listed in Table 2 is relevant. The category of Table 2 is also essential for dimensional analysis [30]. Whereas gas turbines, and, to a large extent, steam turbine flows, can be aerodynamically tested using conventional wind tunnels and measurement equipment, organic vapor testing requires, in general, special efforts. Furthermore, correction schemes might not apply for relating results obtained for a perfect gas to the dense gas regime of an organic vapor. It should be noted that an organic vapor might behave like a perfect gas if the processes take place in the range where the compressibility factor $Z \approx 1$ (see Figure 1). However, in the thermodynamic range where Z differs significantly from unity, non-ideal compressible flow phenomena are likely to occur. From a rigorous theoretical point of view, the derivatives of Z,

$$\left(\frac{\partial Z}{\partial p}\right)_s \text{ and } \left(\frac{\partial Z}{\partial T}\right)_s,$$

and not the absolute values of Z are relevant, because non-vanishing derivates of Z for s = *constant* reflect the condition $Z \neq f(s)$. This fundamental fact is somewhat obscured, because many authors only look to the absolute value of the compressibility factor Z. They do not consider the impact of thermodynamic variables on Z in detail. However, most fluids are characterized by the fact that thermodynamic regions where $Z < 1$ hold are also regions where $Z \neq f(s)$.

Table 2. Classification of fluid mechanics (following Traupel [27,28]).

Z	Fluid	Example	Aerodynamic Testing
$Z = 1$	Perfect gas	Air	conventional wind tunnel testing
$Z = f(s)$	Perfect vapor	Steam	mainly conventional (correction schemes applicable)
$Z \neq f(s)$	Non-ideal gas	Organic vapors	correction schemes might not apply

2.3. Similitude and Experiments with Model Configurations

The dimensional analysis and the concept of similitude are highly relevant for planning experiments [31]. In the case of steam and gas turbines, Dejc and Trojanovskij [32] summarized, in the outcome of dimensional analysis, that five fundamental similarity numbers (or similarity criteria) must be considered for turbomachinery testing: the isotropic exponent γ, the Prandtl number Pr, the Reynolds number Re, the Mach number Ma, and the flow coefficient ϕ. These five fundamental similarity numbers are a direct consequence of the validity of the fundamental Equations (9)–(11) or (13)–(15) as discussed in [30]. Furthermore, in experiments, the same roughness and turbulence level as that which occurs in the original turbomachine should be provided.

In the case of a working fluid violating the equation of state (1) or (12), as in the case of organic vapor, the above five similarity numbers no longer establish a complete set from the viewpoint of dimensional analysis. At least one other similarity number describing the non-ideality of the fluid must be considered [30]. In actual testing, it is often necessary to use the same working fluid in laboratory experiments as what is used in the original engine, because it is practically impossible to find other testing fluids exhibiting the same thermodynamic behavior as the working fluid under original conditions. Hence, conducting experiments dealing with NICFD requires test rigs that precisely use the same working fluids as those used in the original turbomachines or power systems. That represents a significant difference from the single-phase-flow aerodynamical testing of steam and gas turbines, which can be performed in conventional wind tunnels with air as a working fluid.

3. Test Facilities

Only aerodynamic testing related to turbomachinery applications will be considered in the following. Test rigs for entire ORC power systems (see, for instance, [33–35]) are hence excluded from this review. Also excluded are conventional test rigs for heat exchangers working with vapors. A brief overview of currently used test rigs for non-ideal compressible flow investigations was recently published [36]. A good review, also including the history of test facilities, is provided in [20].

3.1. Classification

The facilities for aerodynamic testing of non-ideal compressible flow dynamics can be classified into intermittently and continuously working systems (see Figure 2). The use of a "wind tunnel" for test facilities working with organic vapors might be somewhat misleading (the expression "vapor tunnel" would be clearer), but it is the usual terminology in aerodynamics [14–16].

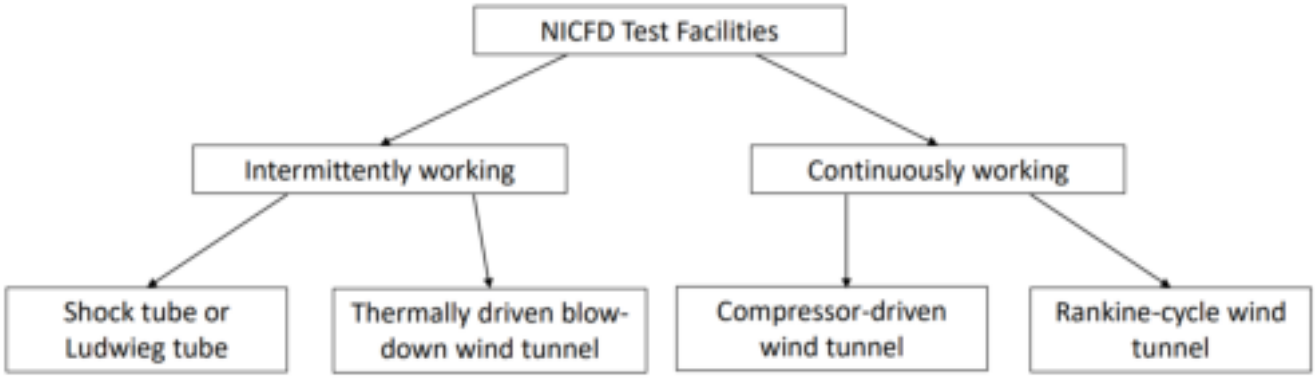

Figure 2. Classification of test rigs for non-ideal compressible fluid dynamics.

The advantage of intermittently working fluids is their relatively low power consumption (but at the cost of a substantial charging time for each test run). Significant power is required to drive a continuously working wind tunnel for non-ideal fluids, because their density is high. Although their speed of sound is relatively low (of the order $a = 100$ m/s), even a moderate volume flow rate leads to high mass flow rates and, hence, to high power consumptions. On the other hand, a continuously running wind tunnel has the advantage that long-time measurements or even steady-state operation are possible, whereas intermittently working test facilities require fast measurement techniques.

3.2. Shock Tubes or Ludwieg Tubes

A shock tube is a device for investigating high Mach number flows. It consists of a tube with a rectangular or circular cross-section, in which a gas at low pressure and a gas at high pressure are separated using some form of a diaphragm. Details can be found in the

classical texts [37–39]. The diaphragm bursts under predetermined conditions to produce a wave that propagates through the low-pressure section. Observations can be made in the flow behind the incident front or the reflected wave.

A Ludwieg tube is a cheap and efficient device for producing supersonic flow. It is a simple blow-down facility that operates somewhat like a shock tube. A large, evacuated dump tank is separated from the downstream end of a convergent–divergent nozzle by a diaphragm. The upstream end of the nozzle is connected to a long tube whose cross-sectional area is larger than the throat area of the nozzle. The initial pressure in the tube is high. When the diaphragm ruptures, a shock wave propagates into the low-pressure region, i.e., the dump tank. An expansion wave propagates into the high-pressure region, i.e., the tube with the nozzle. As the unsteady expansion propagates through the long tube, it sets up a steady subsonic flow toward the nozzle, which is accelerated by the convergent–divergent nozzle to a supersonic flow condition. The flow is constant until the expansion arrives at the nozzle again after reflection.

Figure 3 shows the schematics of a Ludwieg tube used for NICFD investigations, and the test section is shown in more detail for testing the flow through an annual turbine cascade [40]. This test facility was also employed for trailing edge flow investigations for an organic vapor with a high Mach number [41].

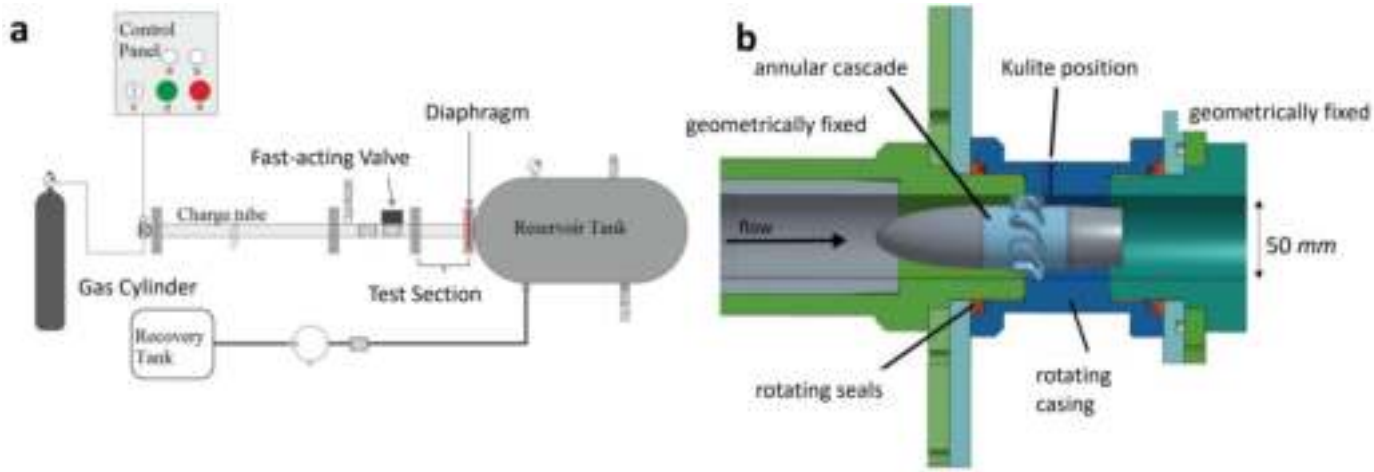

Figure 3. Ludwieg tube test facility for non-ideal compressible fluid dynamics investigations: (**a**) schematics of the tube; (**b**) details of the test section devoted to annular cascade testing. Pictures were taken from the web page of the Whittle Lab, Cambridge: https://whittle.eng.cam.ac.uk/lab/facilities/orc-ludwieg-tube/ (accessed date 15 December 2022).

Historically, the first use of a shock tube for investigating non-ideal compressible flow phenomena can be traced back to Fergason and Argrow [42]. In 2001, they attempted to demonstrate the existence of rarefaction shockwaves in PP10. The experiments were unsuccessful due to the thermal decomposition of the working fluid. Further technical problems finally led to the decommissioning of their shock tube facility. Some years later, in 2008, the group of P. Colonna completed the test facility FAST (Flexible Asymmetric Shock Tube) at the TU Delft [43]. The working fluid for this long tube (about 10 m) was D6. Expansion waves were measured, but non-classical gas dynamics were not observed. The challenges for performing such experiments were substantial, and, after the relocation of FAST to another building, further experiments were conducted [44]. A new attempt to prove non-classical gas dynamics has been recently published in [45].

In this context, the experiments [46,47] dealing with liquefaction shocks should be mentioned as well. The term liquefaction shock was introduced to distinguish it from the condensation of vapor in an expanding flow, i.e., the condensation shock. In a liquefaction shock, condensation takes place due to compression. Whereas such a phenomenon has

not been observed for simple vapors such as steam or carbon dioxide, in organic vapors consisting of complex molecules, such a NICFD phenomenon can occur.

3.3. Blow-Down Wind Tunnels

In the 1960s, Duff [48] was probably the first to conduct CO_2 expansion experiments using a de Laval nozzle setup at the Gas Turbine Laboratory of M. I. T. that utilized a blow-down wind tunnel. The nozzle was fed by a bundle of nine 50 lb cylinders, thus enabling a testing time of about one minute. The work's objective was to better understand the condensation of various organic vapor flows in transonic and supersonic conditions to provide essential information for optimal turbine and power cycle space applications. A blow-down test rig for the investigation of supercritical CO_2 flow phenomena in a nozzle test section was employed at the same institution several years later [49].

A new blow-down wind tunnel, called TROVA (Test Rig for Organic Vapors), was designed in 2010 and erected at the CREA laboratory of the Politecnico di Milano to study the flows of dense organic vapors expanding from temperatures and pressures of up to 400 °C and 50 bar [50,51]. The first experimental results were presented in 2015 at the 3rd International Seminar on ORC Power Systems [52] and in 2016 at the 1st International Seminar on Non-Ideal Compressible-Fluid Dynamics for Propulsion and Power [53]. Figure 4 shows the schematics of TROVA. A power input of approximately 30 kW_{th} is sufficient to evaporate the organic vapor in the high-pressure vessel (see left side in Figure 4). The flow experiment is then carried out by opening a control valve. Measurement times of about 100 s can be achieved in the test section [54]. Typical test section throat areas are of the order 50 cm^2. The expanded vapor enters a condenser as a low-pressure vessel (see the right side in Figure 4). After condensation, the working fluid can be pumped back into the high-pressure vessel, and the blow-down testing can be repeated. The preparation time for an experiment is about a few hours. TROVA is equipped with instrumentation to record pressure and temperatures at relevant stations throughout the facility, and schlieren optical investigations or laser-optical measurement techniques can be applied (see Section 5).

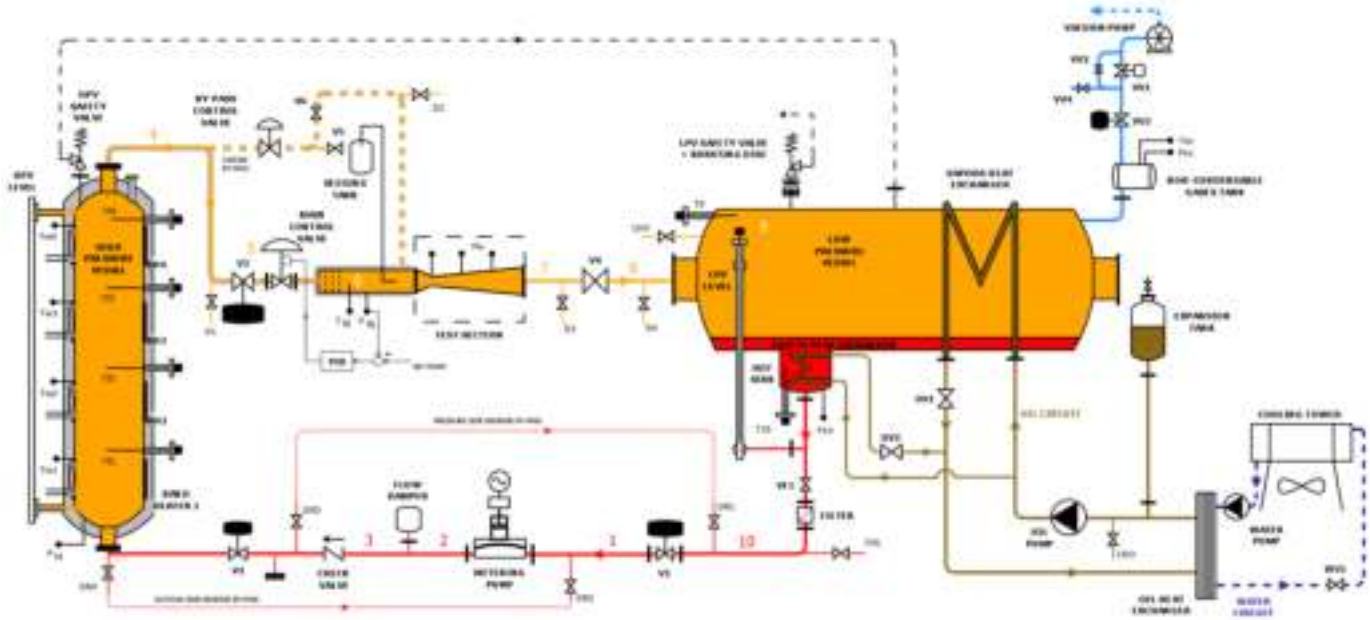

Figure 4. Schematics of the blow-down wind tunnel test facility TROVA [52].

During the same period, a blow-down configuration with a relatively small test section size was designed and commissioned by the group of Ricardo F. Martinez-Botas at Imperial College [55]. A 3.785 L cylinder was selected as the main blow-down vessel. Regulating valves were placed on either side of the test section, thus allowing a pressure ratio to be

fixed across the measurement section. The selected working fluid was R1233zd (trans-1-Chloro-3,3,3-trifluoropropene), and the facility was designed for nozzle stagnation testing conditions of up to 20 bar and 138 °C, with a mass flow rate of 0.3 kg/s. The test section was a converging–diverging nozzle producing an expansion of Mach 2 at the exit plane. The purpose of the setup was to facilitate the validation of CFD software for the simulation of highly non-ideal flows. Thus, the relatively small size of the test section (the throat height of the nozzle was about 2 mm) was not too critical. The first results were reported in [56].

3.4. Compressor-Driven Wind Tunnels

According to Dixon and Hall [57], "the design and performance prediction of axial flow compressors and turbines has been based, in the main, upon measurements of the flow-through two-dimensional cascades" using compressor-driven wind tunnels. The references [58,59] have been mentioned among the several available reviews of such conventional cascade wind tunnels. For testing the organic vapor aerodynamics of blades, a closed-loop wind tunnel driven by a compressor can be considered a natural test rig approach. However, such a concept's substantial power consumption for achieving high-speed flows is a disadvantage. Furthermore, compressor sealing must be carefully handled to avoid serious leakage flows. The entire device must be constructed as a pressure vessel to enable testing at elevated pressure and temperature levels. However, the great advantage of such a continuously running wind tunnel is the long measurement time.

The first generation of closed-loop wind tunnels working with non-ideal gases under highspeed flow conditions began in 1991. In a computational study [14], Anderson considered transonic airfoils in sulfur hexafluoride (SF6) and found that transonic similarity scaling could be used to relate results in SF6 to equivalent air results for primarily inviscid flows. NASA then began a program to convert a transonic wind tunnel into an SF6 operation to provide some experimental confirmation of Anderson's results. The schematics of this wind tunnel are shown in Figure 5. The test facility used for the current study was the 0.3-Meter Transonic Cryogenic Tunnel at the Langley Research Center [16]. The wind tunnel was operated at pressures up to 6 bar and temperatures from 100 K up to 300 K. Mach numbers from 0.15 up to 1.0 were achieved in the test section. The modifications required for operation with SF6 included a gas reclamation unit for charging and reclaiming the test gas, a gas analysis unit for real-time gas composition monitoring, a gas warning system for personnel safety, and a specially designed heat exchanger. The experiments demonstrated that transonic similarity theory was only partially successful in transforming the heavy gas results to equivalent nitrogen (air) results. After this test campaign, the test facility was decommissioned.

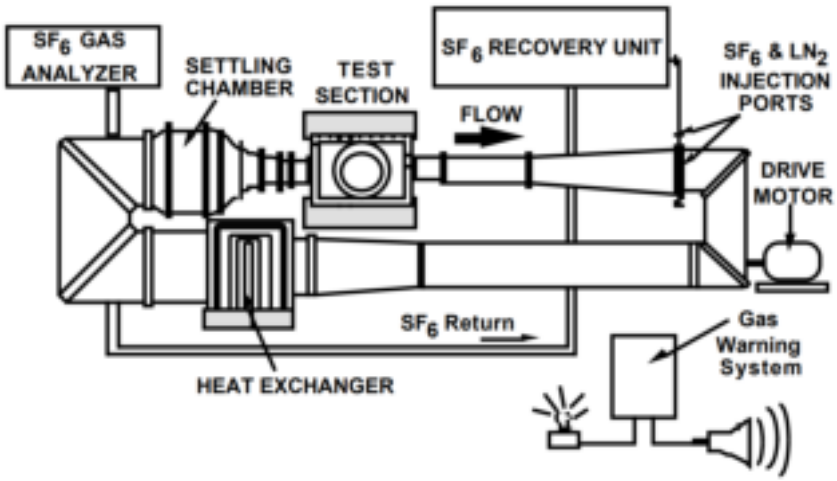

Figure 5. Schematics of the NASA transonic SF6 wind tunnel test facility (from [16]).

A new attempt to establish a transonic wind tunnel for organic vapors was published in 2015 by F. Reinker et al. [60]. This ORC vapor tunnel for continuous operation, called CLOWT (Closed Loop Organic vapor Wind Tunnel), is shown in Figure 6. Details about its design and operation features can be found in [61–63]. An application dealing with profile measurements of a linear transonic turbine cascade is described in [64]. For safety reasons, CLOWT has been operated with the non-toxic organic vapor Novec 649 by 3M. Due to the limited compressor power of about 65 kW, only high subsonic to transonic flows can be established in the test section. The minimum value for the fundamental derivative Γ is about 0.8.

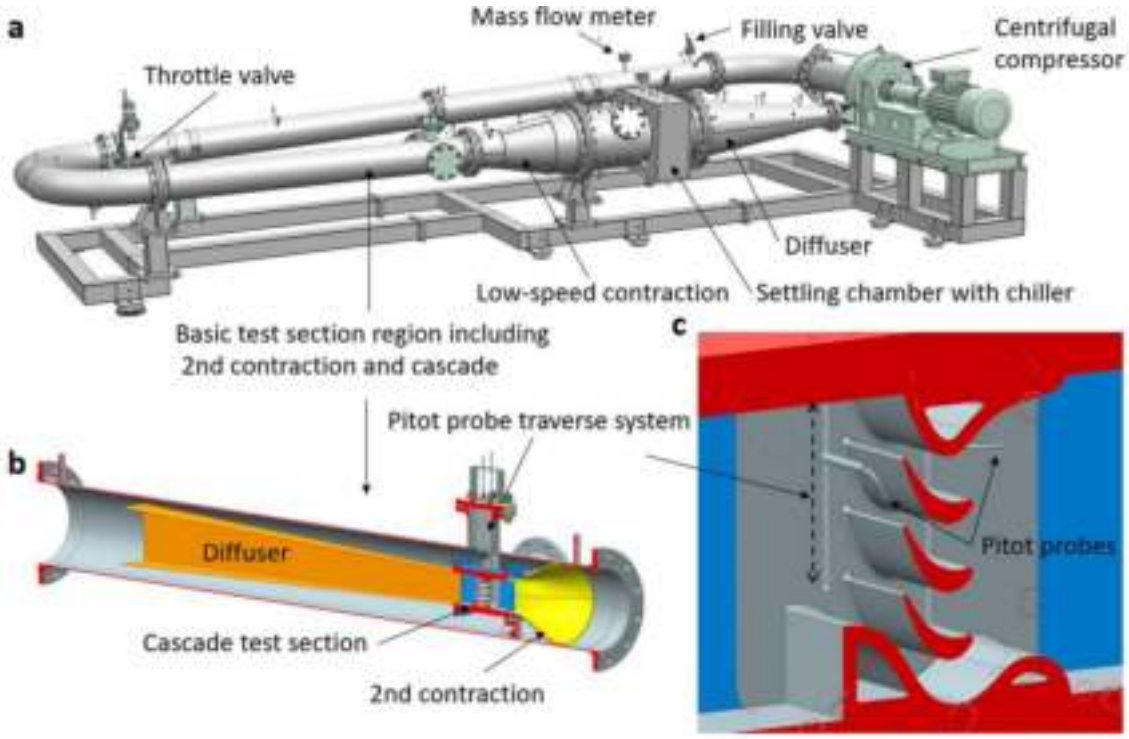

Figure 6. Test facility CLOWT (from [64]): wind tunnel (**a**), primary test section tube (**b**), and details of the cascade (**c**).

Also, White and Sayma [65] presented the preliminary design of a closed-loop supersonic test facility using a screw compressor. The facility's purpose was to provide experimental datasets of flows in a small test section under the same conditions as in ORC turbines. Initially, the selected working fluid was R1233zd, which was changed to R245fa. The facility was designed for testing conditions up to 20 bar and 125 °C, with a mass flow rate of 1 kg/s. As of the writing of this review paper, no experimental results have been published for this compressor-driven supersonic wind tunnel, although the rig has been fully pressure tested.

3.5. Rankine Cycle Wind Tunnels

A further approach to enable a continuous flow of vapor through a test section at elevated pressure and temperature levels is given by Rankine cycle wind tunnels. Here, the working fluid follows a Rankine cycle with the evaporator, test section (as a pressure-reducing or expansion component), condenser, and pump. This closed operational principal can be interpreted as a degenerated Rankine cycle, and the use of the expression "vapor tunnel" for this kind of test facility might be recommended. Replacing the test section with a turbine or another expansion engine turns such a facility into a test rig for power systems. To reduce the amount of heating power, an additional heat exchanger as a regenerator might be included. However, even then, the specific thermal power input required to

operate the facility is substantial. The great advantage of such an approach is that high Mach number levels can be achieved with the benefits of a steady-state operation mode.

A Rankine cycle vapor tunnel was used in the early nozzle flow study [66] conducted by Bier et al. to investigate real-gas effects for R22 and other fluids. This experiment used a small Laval nozzle with a central static pressure probe as the test section. The throat dimensions were of the order of a few mm. Although the test section was small, relevant data could be obtained and compared with numerical predictions for the flow of non-ideal gases through a nozzle.

A hybrid high-temperature ORC vapor tunnel and expander test-bed was recently commissioned at the Aerospace Propulsion and Power laboratory of the Delft University of Technology [20,67]. The ORCHID (Organic Rankine Cycle Hybrid Integrated Device) test facility is shown in Figure 7. It was conceived for fundamental studies on NICFD flows and for testing ORC components, e.g., ORC turbines and heat exchangers. The ORCHID makes it possible, with its thermal power input of 400 kW_{th}, to attain a maximum temperature and pressure of up to 400 °C and 25 bar at the inlet of the test sections. It was designed to consider the possibility of using many different working fluids. MM (hexamethyldisiloxane) was selected for the first experimental campaigns, and corresponding results were published in 2021 [68].

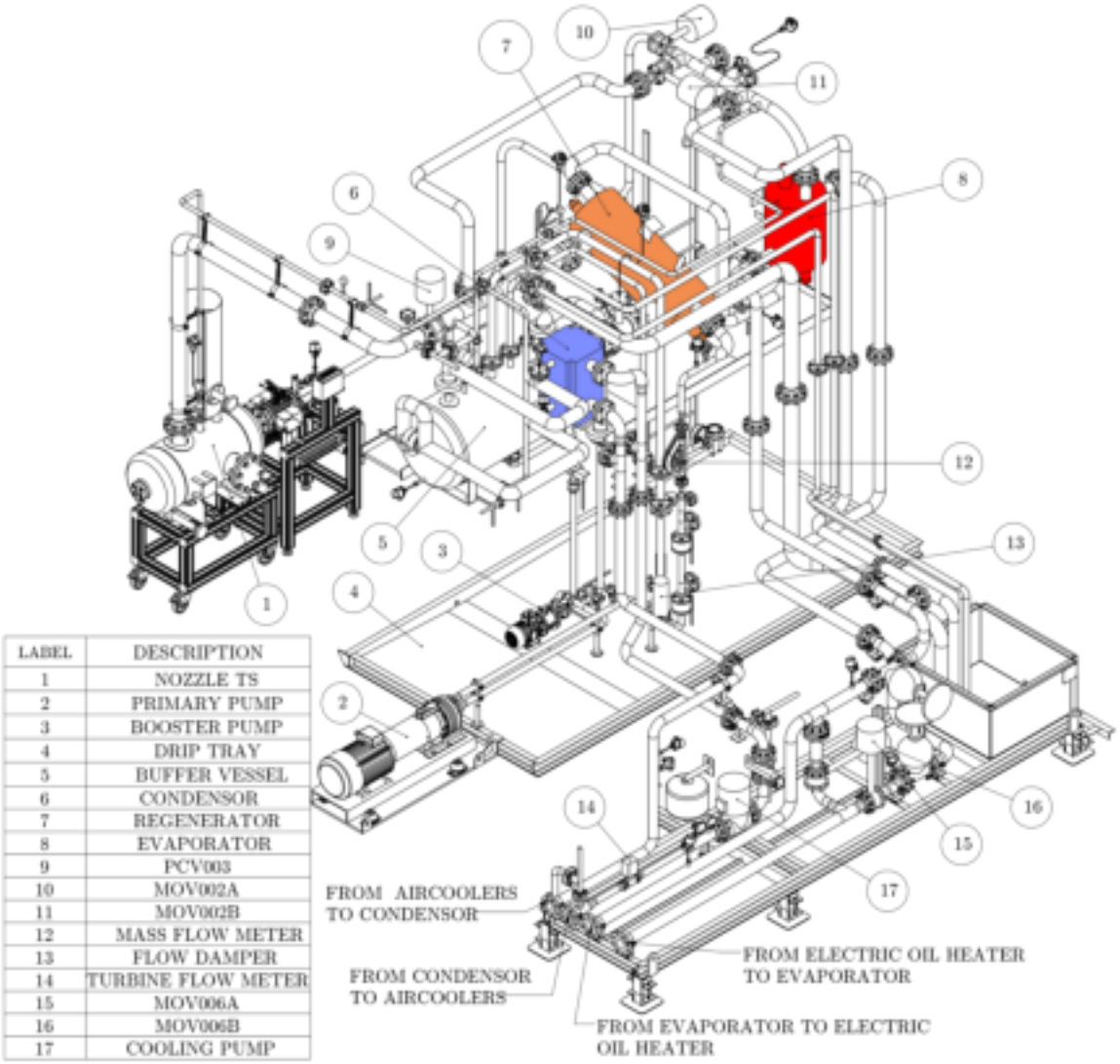

LABEL	DESCRIPTION
1	NOZZLE TS
2	PRIMARY PUMP
3	BOOSTER PUMP
4	DRIP TRAY
5	BUFFER VESSEL
6	CONDENSOR
7	REGENERATOR
8	EVAPORATOR
9	PCV003
10	MOV002A
11	MOV002B
12	MASS FLOW METER
13	FLOW DAMPER
14	TURBINE FLOW METER
15	MOV006A
16	MOV006B
17	COOLING PUMP

Figure 7. The Rankine cycle vapor tunnel test facility ORCHID [20].

3.6. Current Status of NICFD Test Facilities

Currently, all types of test facilities shown in Figure 2 are employed, and their complementary use enables valuable insights into non-ideal compressible fluid dynamics for a broad range of thermodynamic conditions. As of the writing of this review paper, several different NICFD test facilities, which were described above, are in operation [36,69]. To summarize, a list of their main parameters is provided in Table 3.

Table 3. Currently available NICFD test facilities (data obtained from a workshop organized by M. White, City University London [69]).

Test Facility	Institution	Type and Operation mode	Measurement Times	Working Fluids	Pressure	Temperature	Mach Number	Minimum Z/Γ	Test Section
TROVA	Milano, IT	Blow-down wind tunnel	10 up to 100 s	Siloxanes, refrigerants, hydrocarbons	Up to 50 bar	Up to 400 °C	Up to $Ma = 3$	$Z = 0.3/\Gamma < 1$	50 mm × 100 mm
ORCHID	TU Delft, NL	Rankine wind tunnel (continuously)	Long time	Siloxanes, refrigerants, hydrocarbons	Up to 25 bar	Up to 380 °C	Up to $Ma = 3$	$Z = 0.3/\Gamma < 1$	Limited by thermal power (400 kW)
CLOWT	FH Münster, DE	Closed wind tunnel (continuously)	Long time	Novec 649, air	Up to 10 bar	Up to 150 °C	Up to $Ma = 1.3$	$Z = 0.7/\Gamma = 0.8$	50 mm × 100 mm or 42 diameter (jet)
Cambridge Real-Gas Wind Tunnel	Whittle, UK	Ludwieg tube	10–100 ms	R134a, SF6, CO_2, Air, N_2, Argon	Up to 45 bar	15–150 °C	Up to $Ma = 2.5$	$Z = 0.6/\Gamma < 0.9$	50 mm tube diameter
ICLTRANSIENT	Imperial, UK	Blow-down wind tunnel	Short time	Refrigerants	Up to 30 bar	70 °C (nominal)	Up to $Ma = 2.2$	$Z = 0.5/\Gamma = 1.05$	2 mm throat height

4. Pneumatic Measurement Techniques

Experimental investigation techniques for non-ideal fluid dynamics have been derived from the available methods of experimental fluid mechanics. The reader can find a general overview of these well-established techniques in [70–75]. A brief description of measurements in compressible flows of perfect gases is also included in [76,77]. This section and the following sections focus on the special modifications needed to apply some of these techniques to the aerodynamical investigations of organic vapors at elevated pressure and temperature levels. This review paper mainly considers techniques that are already in use or at a stage where valuable results have been reported in the literature. In Section 4, the pneumatic measurement techniques (i.e., pressure measurements) are discussed. Optical measurement techniques (i.e., schlieren pictures and laser optical methods, including PIV and LDV) are topics in Section 5. The hot-wire anemometry is the subject of Section 6.

4.1. Condensation Issues in Organic Vapors

The measurement of static and total pressures is fundamental for quantifying compressible flow phenomena. Pneumatic measurements are, furthermore, the key to loss determinations in turbine cascades [32,57].

The usual method for obtaining the static pressure of a flow along a wall is to drill a small hole that is normal to the surface of the wall and to connect this hole to a pressure transducer or manometer. Round nose or conical nose static pressure probes are also standard in subsonic and supersonic flows [77]. Total or stagnation pressures are measured through a Pitot tube invented by Henri Pitot in 1732 [78]. In a Pitot tube, the flow is isentropically brought to rest at the instrument's tip, where a small hole is placed. The hole is connected with a pressure transducer or manometer through a line. In addition to these two primary probes, combinations such as the Pitot static tube (also known as Prandtl probe) or multi-hole probes such as the five-hole probe are in use.

In the case of non-condensing air, pressure measurements are straightforward, but, in the case of organic vapors, where condensation can occur in the probes or the connecting lines, special care is required. The condensation of vapor within the pressure lines, tubes,

or even in the probe can lead to the formation of an incompressible plug that effectively separates the transducer from the measurement location. This problem is referred to as plugging or clogging, and it is common in multi-phase flow (e.g., droplet-laden air flows) or (wet) steam measurements [79].

In principle, three different approaches could be used to measure the pressures in a flow of an organic vapor at elevated temperature:

(i) The use of fully heated probes, lines, and pressure measurement devices to avoid any condensation;
(ii) The use of pressure transducers, in combination with lines added by liquid traps and purging devices, to remove condensate or liquid between the probes and the (cooled) measurement devices;
(iii) The use of probes and lines placed in the hot environment of the test rig while considering the condensation as a systematic error.

The first approach requires the use of measurement devices that are operable at higher temperatures. Although such a (mechanical) manometer solution might be available, its accuracy or resolution is typically too poor for accurate aerodynamic measurements. In the following discussion, it will be shown that only the second and third concepts have been employed so far for organic vapor flows.

The conventional approach is to purge the lines where condensation might occur (i.e., method (ii)). Murthy et al. [80] proposed a purge mechanism, in addition to the drain, to keep the probes and their ports dry for flow measurements in droplet-laden air flows. A purging approach for compressor cascades subjected to high fogging conditions was recently published in [81], which includes a discussion of the impact of the steadily applied purging pressure on the calibration curve and the pressure data interpretation. Purging with nitrogen (N_2) is common in droplet-laden air flows but is also used in vapor flows. Figure 8 details the pressure measurement method, which includes purging realized at the ORCHID test facility. Figure 8a shows the instrumentation of a nozzle test section with static pressure taps and their lines. The lines are related to the pressure transducers via a Scanivalve device, which includes liquid traps (see Figure 8b) and an additional tank filled with the purging gas (N_2). The condensate can be observed in the liquid traps equipped with optical access (see Figure 8c), and the purging process can be initiated. The impact of purging on the measurement signals is shown in Figure 9. Significant peaks can be observed in Figure 9a that indicate the purging blow. Figure 9b is a schlieren picture of the nozzle test section during a purging event.

A pneumatic system for pressure measurements in the transient flows of non-ideal vapors that are subject to line condensation for the TROVA blow-down wind tunnel was presented in 2021 by Conti et al. [82] (see Figure 10). The rectangular boxes in Figure 10 represent pressure transducers. The purging fluid is N_2. Further details about the pressure measurement system, including Pitot probes, can be found in [83,84]. The central concept is essentially based on two lines: one exiting the plenum for the total pressure determination of the wind tunnel, and one connected to the probe tap measuring the total pressure at the test section location. Both lines are directly connected to a nitrogen storage tank. Electrical actuator valves were employed to open, as the test was triggered to flush lines with nitrogen at a pressure slightly higher than the expected maximum level during the test and close right after the pressure peak was reached in the test section during the experiment.

This procedure ensures that each line contains only nitrogen during a test and that no MM vapor enters a line. Hence, no condensation in the nitrogen-filled lines can occur. As the test proceeds, nitrogen exits the line through the static tap into the test section, as the line pressure is in equilibrium with the decreasing test section one. Figure 10 also shows the differential pressure transducers used to obtain static and total pressures at different locations in the wind tunnel.

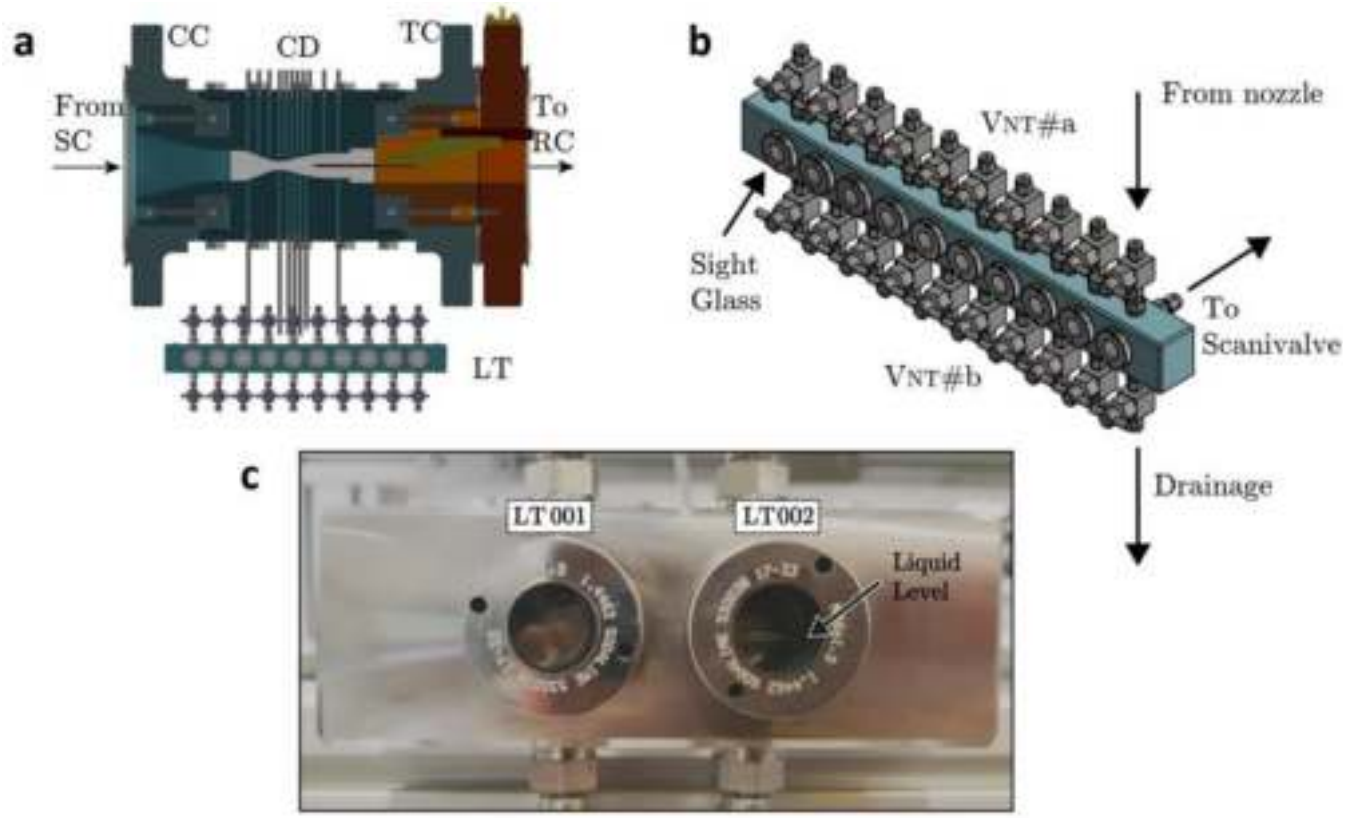

Figure 8. Pressure measurement system including liquid traps and purging realized at ORCHID (from [20]): (**a**) cross-section of the nozzle housing (SC: settling chamber; CC: contraction channel; CD: converging-diverging nozzle: MSC: model support compartment; PT: pressure taps; LT: liquid traps; RC: receiver); (**b**) assembly of the liquid traps (valve VNT#a isolates the process from the Scanivalve, valve VNT#b allows the liquid to drain during operation); (**c**) observation of condensate in a liquid trap indicating the need to purge.

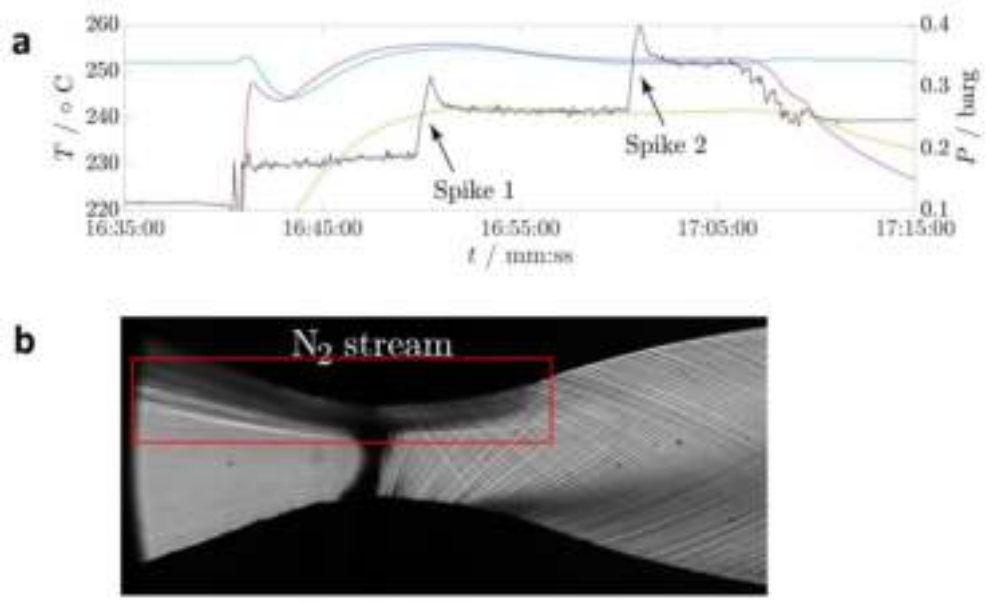

Figure 9. Impact of purging on nozzle flow measurements: (**a**) two spikes in the pressure signal due to purging of the liquid traps by means of nitrogen injection in the lines; (**b**) schlieren image showing a stream of N_2 being convected through the nozzle (from [20]).

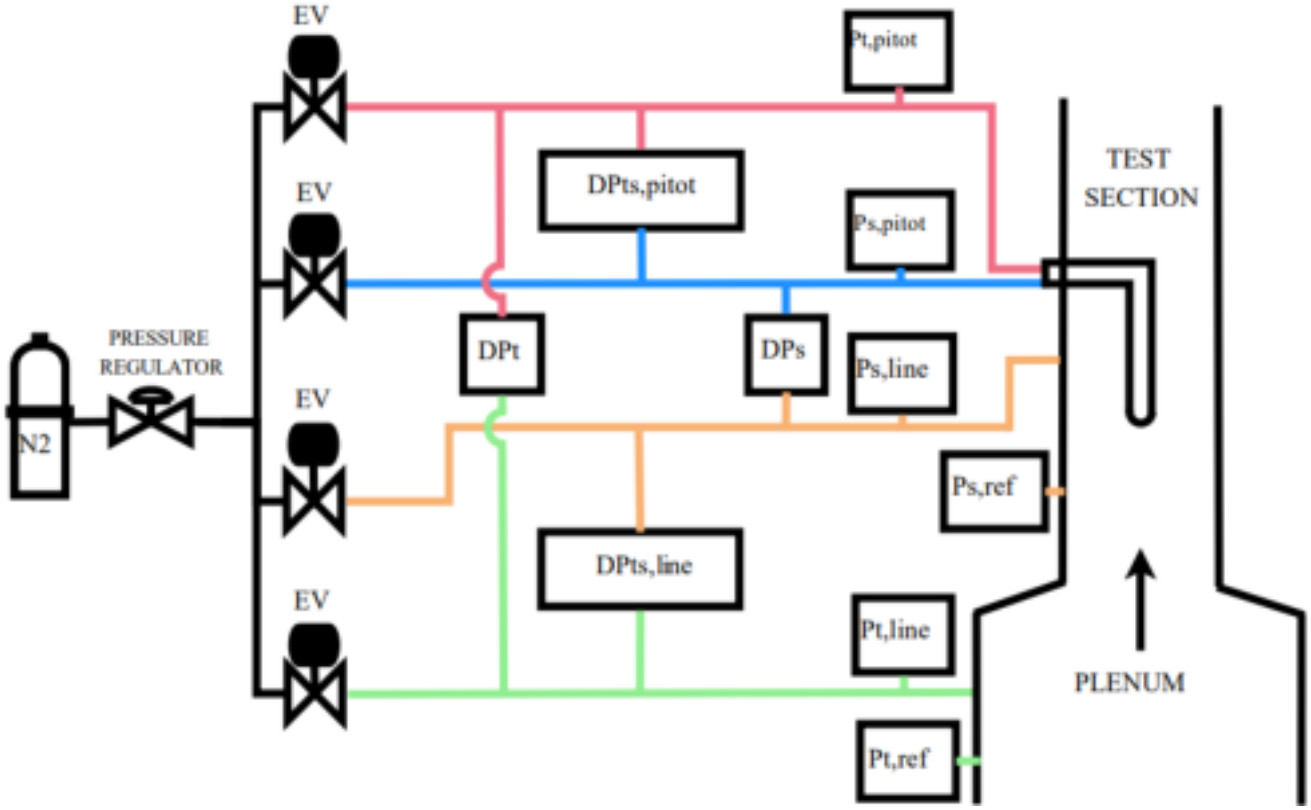

Figure 10. Flushed pneumatic lines scheme for Pitot tube testing in subsonic flows of Siloxane MM in the TROVA blow-down wind tunnel (from [82]).

Whereas adding nitrogen to the working fluid is not a severe issue in test rigs employing evaporators and condensers (because the non-condensable gas N_2 can be separated from the vapor condensate), a different strategy should be chosen in the case of continuously running closed-loop organic vapor wind tunnels to avoid significant contamination of the working fluid. Hence, an alternative approach was chosen for the compressor-driven closed-loop organic vapor wind tunnel CLOWT to handle the condensation issue. The method employed by Reinker et al. [85] in 2020 and used in other studies, e.g., [64,86], was to place the valves and pressure lines in the heated area of the wind tunnel where no condensation could occur (see Figure 11). By using a valve system operated by a rotative mechanism (shifter), twenty pressure taps or probes could be connected to an external transducer at room temperature (Figure 11a). This transducer was thermally decoupled from the hot lines by utilizing a curved metal tube. The ambient room temperature of the laboratory hall cooled down the external tube up to room temperature at the end where the transducer was connected. Hence, the organic vapor resting in the pressure line condensates and fills the liquid trap up to the level where the liquid can flow back due to gravity. The position of the liquid can be seen as a cold area in the thermography (Figure 11b). The surface tension of the working fluid Novec 649 is relatively low, and no severe plugging can occur in sufficiently large tubes. Since the saturation pressure of Novec 649 at room temperature is low (T_{sat} = 49 °C at p = 1 bar), the pressure in the test section presses the liquid to the transducer. As a systematic measurement error, the hydrostatic pressure in the liquid trap occurs if the exact position of the liquid level is not known. This systematic pressure can be minimized by designing traps with small heights. External temperature measurements along the trap enable a further estimation of the liquid column height in the device (see Figure 11b).

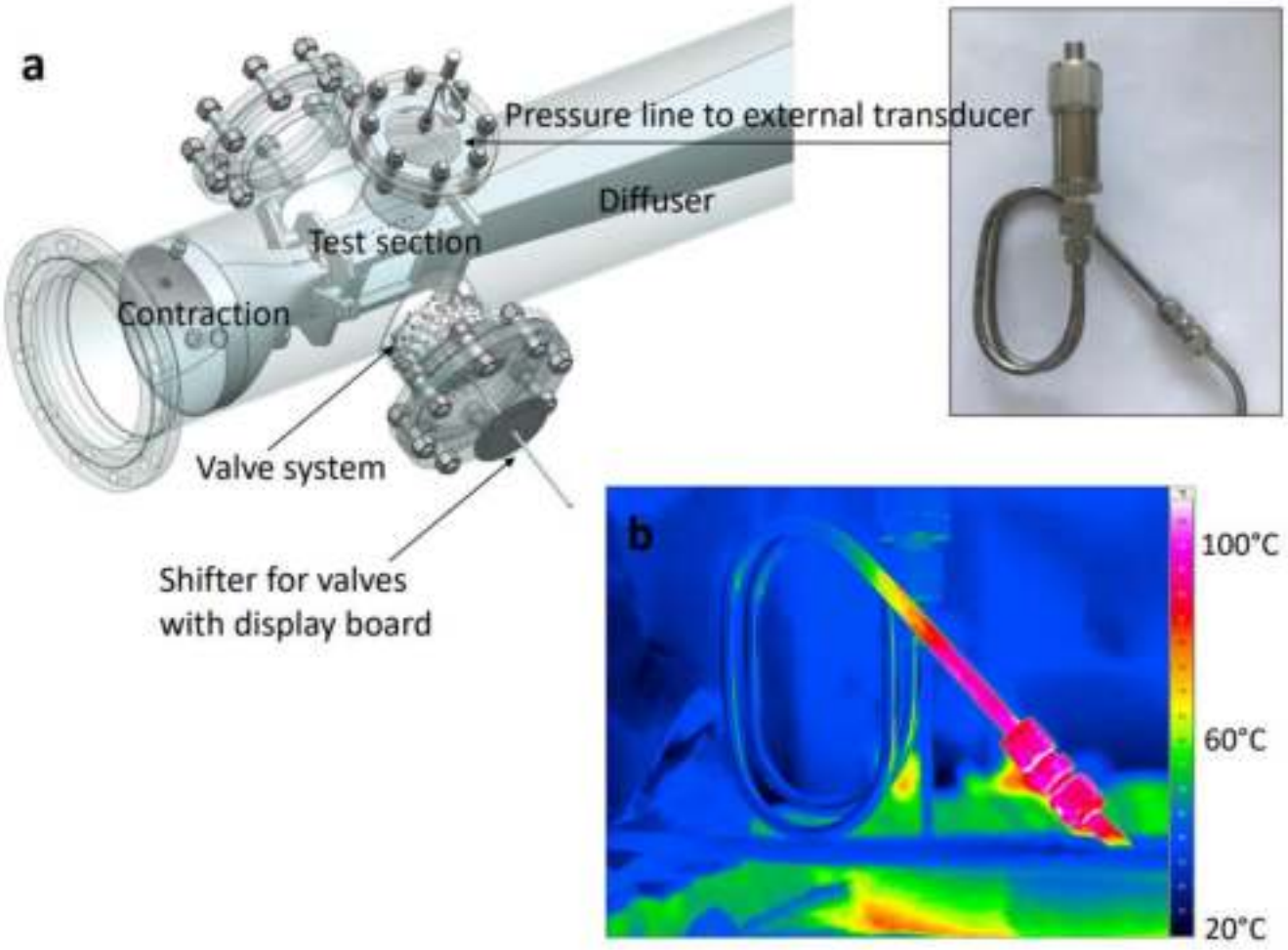

Figure 11. The pressure measurement system realized at the CLOWT closed-loop wind tunnel: (**a**) valve and lines placed in the hot domain of the primary test tube and (**b**) thermography of the thermally decoupled transducer indicating the region of liquid trapped in the line.

It should be remarked that an approach without purging requires a long preparation time to achieve a thermal equilibrium in the entire system. Furthermore, very low test section pressure levels, below the saturation pressure at transducer temperature, might not be measured accurately by such an approach. In the case of very short measurement times in shock tube experiments [41], fast pressure sensors can be used directly without purging devices. Details about such an application can be found in [87].

4.2. Pitot and Stagnation Pressure Probes

Shortly after the commissioning of wind tunnels for organic vapor flows, research efforts started to move towards using pressure probes for non-ideal compressible flows. The first use of a stagnation probe for investigating non-ideal compressible flows was reported in 2015 [41,87]. To capture the wake measurements of an idealized trailing edge configuration, a probe with four "Kulite XCL-62" pressure transducers was placed downstream of a trailing edge in the test section of a Ludwieg tube (see Figure 12). The probe was produced using laser sintering 3D printing. The design was a wedge probe configuration with a wedge angle of 10 deg, which widened slightly at the base to accommodate the sensors inside. The sensors were mounted within the probe to ensure minimal response times. Furthermore, the setup shown in Figure 12 employed an inlet stagnation probe.

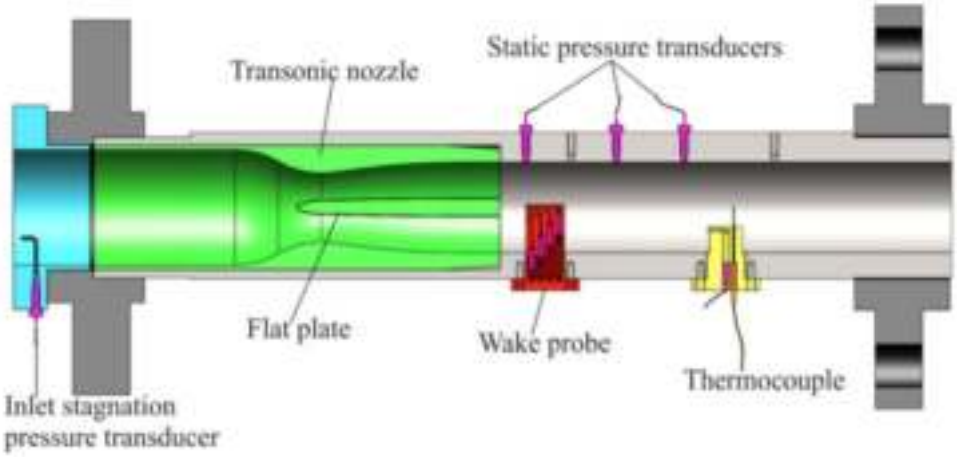

Figure 12. First use of a stagnation probe ("Wake probe") for non-ideal compressible flow (from [87]). The setup might be compared with the one shown in Figure 3.

In 2020, the first detailed performance study [85] of a rotatable cylinder Pitot probe in high subsonic flows of Novec 649 was published. Due to the choking effect caused by the cylinder Pitot probe (diameter 5 mm) in the closed test section (50 mm × 100 mm), the maximum inflow Mach number was about $Ma = 0.7$ in the study [85]. Later, the same configuration was used for detailed profile pressure measurements and drag coefficient determinations of a cylinder subjected to high subsonic streams of Novec 649 [88].

Applications of a Pitot probe for shock losses at a supersonic flow of MM were published by Conti et al. [82,84] and by Manfredi et al. [89,90] in 2021 and 2022. The Pitot probe design used in these studies is shown in Figure 13. The Pitot probe measurement concept used the purging system discussed in the previous subsection (see Figure 10). In these studies, schlieren pictures of the shock caused by the probe in the supersonic flow were shown as well. It was found that, even at mildly non-ideal conditions with $Z \gtrsim 0.70$, non-ideality was responsible for a significantly stronger shock than the ideal gas at the same pre-shock Mach number [84].

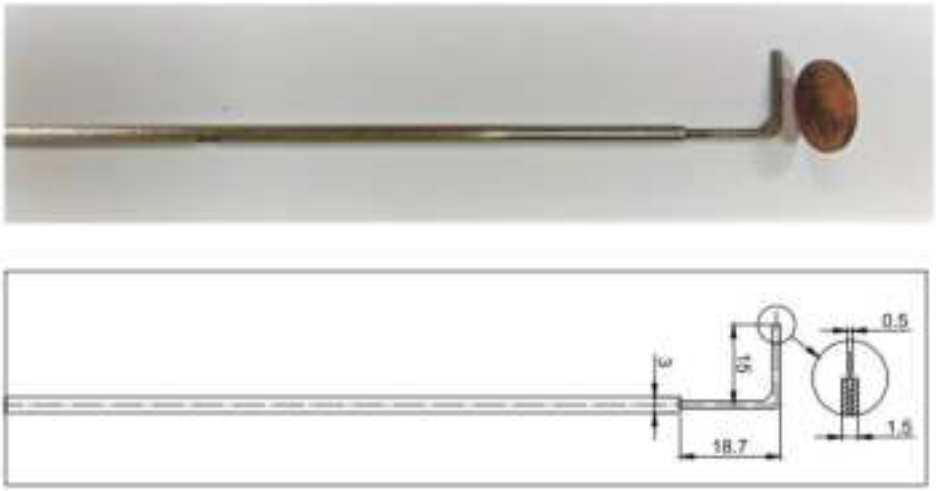

Figure 13. Pitot probe used in the shock loss experiments by Conti et al. [82,84]. Dimensions in mm.

4.3. Blockage Effects and Probe Interaction

The problem of probe interaction with the flow to be investigated can be substantial, especially in supersonic flow. Figure 14 illustrates that issue by comparing two computational fluid dynamics simulations for a conventional round probe and a wedge probe in the flow downstream of a supersonic cascade. The traditional design of the probe introduces a significant disturbance. Based on the CFD results, a wedge probe design was manufactured

and successfully employed [91]. In general, wedge probes are recommended for supersonic flow investigations due to their more minor probe interaction effect.

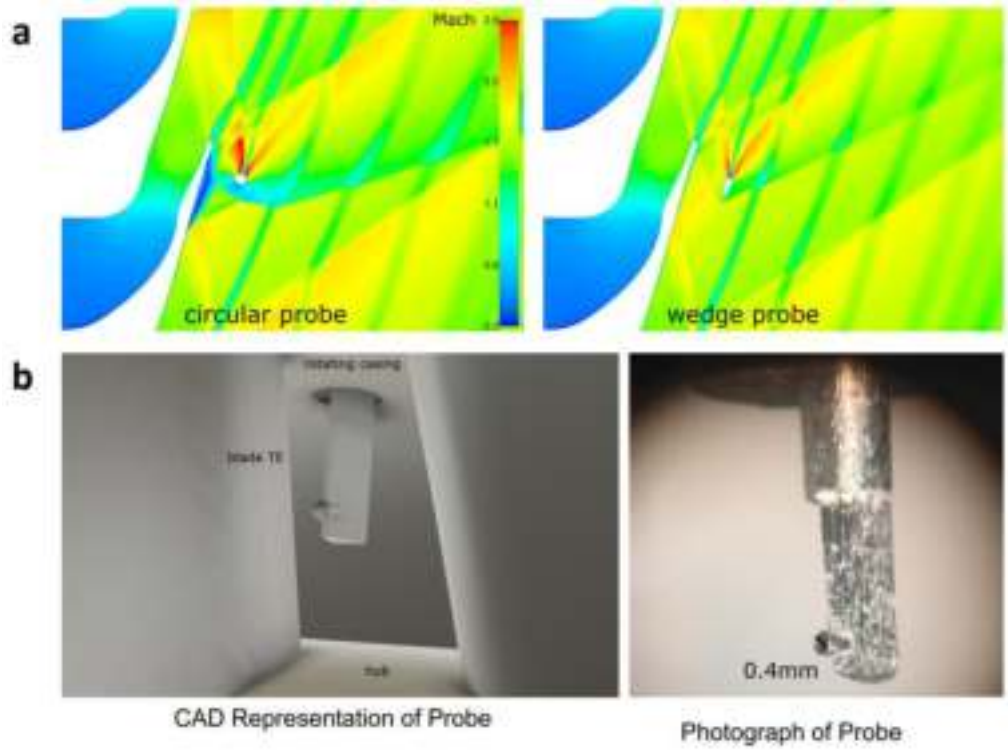

Figure 14. Illustration of probe interaction problems (**a**) and design of a wedge probe for total pressure measurements downstream of a turbine cascade (**b**). The Mach number level is indicated by the color bar at the top. The pictures were taken from [91].

Blockage and probe interaction effects can be substantial and can noticeably affect the data reduction process. Although non-ideal compressible flow dynamics would require a modification of corresponding ideal gas relations, the order of magnitude of blockage corrections might still be assumed to be valid. Blockage corrections for cylinder probe calibrations were proposed by Wyler [92] based on an ideal gas analysis and similitude considerations. He found that the blockage effect in free jets was found to be approximately the same magnitude as in closed tunnels. Truckenmüller et al. [93] reported probe blockage effects for transonic flow through a calibration wind tunnel and a guide vane row in a three-stage model turbine. It was found that even a probe placed downstream of a cascade could noticeably influence the blade profile pressure distribution of the cascade. Related studies on that topic include [94,95]. So far, a detailed experimental investigation of non-ideal compressible flow dynamics on probe interactions is missing.

4.4. Pressure Data Reduction for NICFD

The static wall pressure is usually obtained through small holes drilled in the wall and connected to a manometer. Ducruet [96] pointed out the possible impact of the boundary layer, velocity gradient, and wall curvature on this kind of measurement. However, correction schemes are uncommon in practice.

The theory of Pitot probes and the corresponding data reduction process for total pressure are well-treated in textbooks [76,77] for perfect gases. In the case of an ideal gas with an isentropic exponent γ, the famous Rayleigh–Pitot equation

$$\frac{p_{o2}}{p_1} = \frac{\gamma+1}{2} Ma_1^2 \left(\frac{(\gamma+1)^2 Ma_1^2}{4\gamma Ma_1^2 - 2(\gamma-1)} \right)^{1/(\gamma-1)} \tag{16}$$

results in the case of supersonic flow. Here, p_{o2} denotes the measured total pressure at the probe hole, and p_1 and Ma_1 are the static inflow pressure and Mach number, respectively. For subsonic flow, the isentropic relation

$$Ma_1^2 = \frac{2}{\gamma - 1}\left(\left(\frac{p_{o1}}{p_1}\right)^{(\gamma-1)/\gamma} - 1\right) \tag{17}$$

can be used to determine the inflow Mach number for a perfect gas. In subsonic flow, there is shock caused by the probe, and the inflow total pressure p_{o1} can be measured directly.

In the more general case of non-ideal compressible flow, the data reduction process must start with the general balance equations

$$\rho_1 c_1 = \rho_2 c_2, \tag{18}$$

$$h_1 + \frac{1}{2}c_1^2 = h_2 + \frac{1}{2}c_2^2 = h_0, \tag{19}$$

$$p_1 + \rho_1 c_1^2 = p_2 + \rho_2 c_2^2 \tag{20}$$

and assumes an isentropic process. Together with an appropriate equation of states, the inflow Mach number Ma_1 or other quantities can then be computed based on the measured probe pressure and the total inflow state. As pointed out by Spinelli et al. [97], in a non-ideal compressible flow, the expansion process depends on the inflow state, whereas the perfect gas relations (16) and (17) do not. Furthermore, the shock pattern caused by the probe can differ. An illustration is shown in Figure 15 where schlieren pictures of the shock caused by a Pitot probe placed in a supersonic flow of nitrogen (perfect gas) and MM (non-ideal organic vapor) are compared.

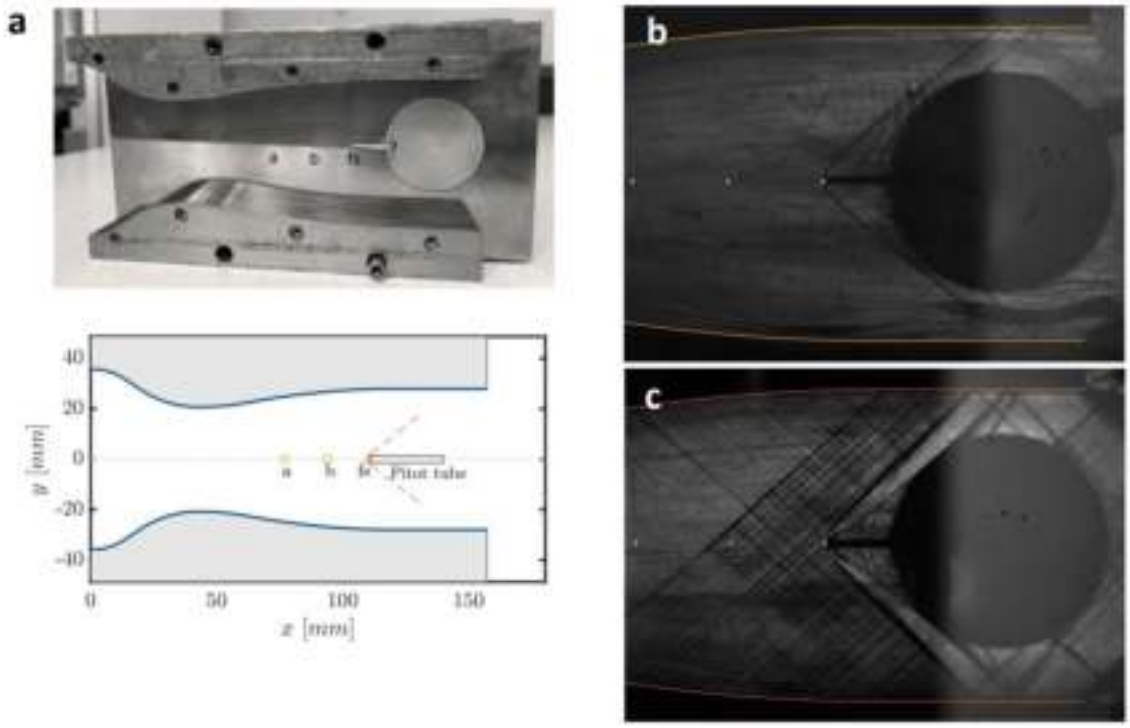

Figure 15. Demonstration of shocks caused by a Pitot probe placed in supersonic flow (from [84]): (**a**) flow nozzle with pressure taps (a, b, and free stream fs) and Pitot tube with a bow shock sketch; (**b**) schlieren image for flow of N_2; (**c**) schlieren image for flow of MM with $Z = 0.70$; the nozzle profile and pressure taps are highlighted in the schlieren pictures.

A simple routine for Pitot probe data reduction was published in [98]; alternative mathematical schemes to handle normal shock under non-ideal compressible flow conditions were discussed by Passmann et al. [99]. The essential parts of the data reduction are the correct and efficient method to compute the isentropic flow relations and to solve the non-linear set of governing equations [98,99]. In [84], the data reduction was performed by numerically solving mass, momentum, and energy conservation equations across the shock, coupled with the Span–Wagner thermodynamic model through the FluidProp library [100]. This multiparameter model provides accurate thermodynamic properties, even close to the critical point. A functional form, in terms of the reduced Helmoltz free energy as a function of the inverse reduced temperature and reduced density, is provided for the fundamental relation linking all thermodynamic properties of a simple system in a stable equilibrium state. For the working fluid in [84], siloxane MM, appropriate model parameters were reported by Colonna et al. [101,102], and further information can be found in [103,104].

The need to employ suitable equations of states and to replace the classical formulas (16) and (17) for non-ideal compressible fluids is illustrated in Figure 16. Here, the Mach number obtained by the perfect gas relation and an adequate data reduction scheme for Novec 649 are compared. As indicated by Figure 16, even for moderate Mach number levels, the error between the perfect gas routine and the non-ideal data reduction can be 6%. Much larger errors can occur at higher Mach number levels and at the dense gas regime [98,99].

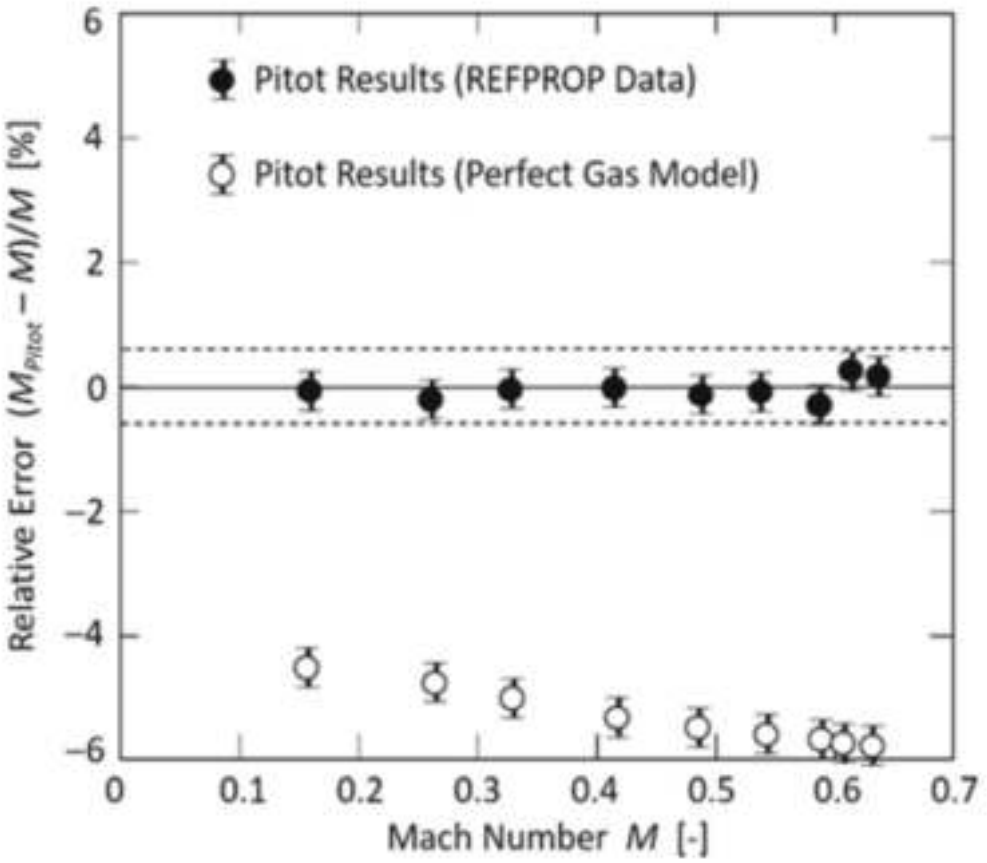

Figure 16. Relative error of Mach number calculations based on Pitot probe data and thermodynamic models for the subsonic flow of Novec 649 (from [85]).

If fast measurements have to be performed, the transient behavior of the entire system must be considered. A corresponding analysis was proposed by Gori et al. [105]. In this work, it was found that the step responses depended on the speed of sound of the working fluid, thus indicating that molecular complexity plays a significant role in determining the promptness of the measurement devices.

5. Optical Measurement Techniques

Optical flow measurement techniques are widely applied in science and engineering applications [72–75]. This section briefly reviews the currently available and employed methods for non-ideal compressible flow dynamics. This includes discussing schlieren methods and laser-based measurement techniques (particle image velocimetry PIV and laser Doppler velocimetry LDV). A comprehensive presentation of optical techniques (i.e., schlieren and LDV) that were applied within the TROVA facility at the CREA laboratory of Politecnico di Milano is found in [106]. A feasibility study, limited to low-speed flows of PIV for NICFD applications, was published by Head et al. [107].

5.1. Schlieren Optical Methods

The classical experimental tool in gas dynamics is, since the pioneering work of Ernst Mach (see [77]), the schlieren image method. Schlieren images easily provide qualitative data, and they can also provide quantitative data about the local Mach number and instantaneous slope of shock waves. Settles [108] presented the history of the schlieren instrument and a very detailed account of its various technical details. The origin of this instrument can be traced back to the 17th century, when Robert Hooke used a primitive device to illustrate the thermal convection from a candle flame. In the 19th century, Toeppler brought the instrument to a practical and valuable level. Since his work, the German expression "schlieren" has been used. It might be remarked that "schlieren" is not a name of a person (although in the German language, it is written with a capital S); it is the German word for "streak".

Since organic vapors are transparent, applying schlieren systems to NICFD investigations is relatively straightforward. With the schlieren system, density variations and, thus, index-of-refraction variations can be visualized within a transparent medium like a gas or a vapor. Regarding NICFD applications, three schlieren systems, which are schematically shown in Figure 17, have been used so far: (a) the conventional z-type schlieren systems, (b) the double-pass schlieren system, and (c) the background-oriented schlieren method. A fourth method (d) is the focusing schlieren system approach. The latter has not been applied to NICFD investigations so far. For a description of the physics of schlieren and shadowgraph techniques, the reader can consult [108] or [109].

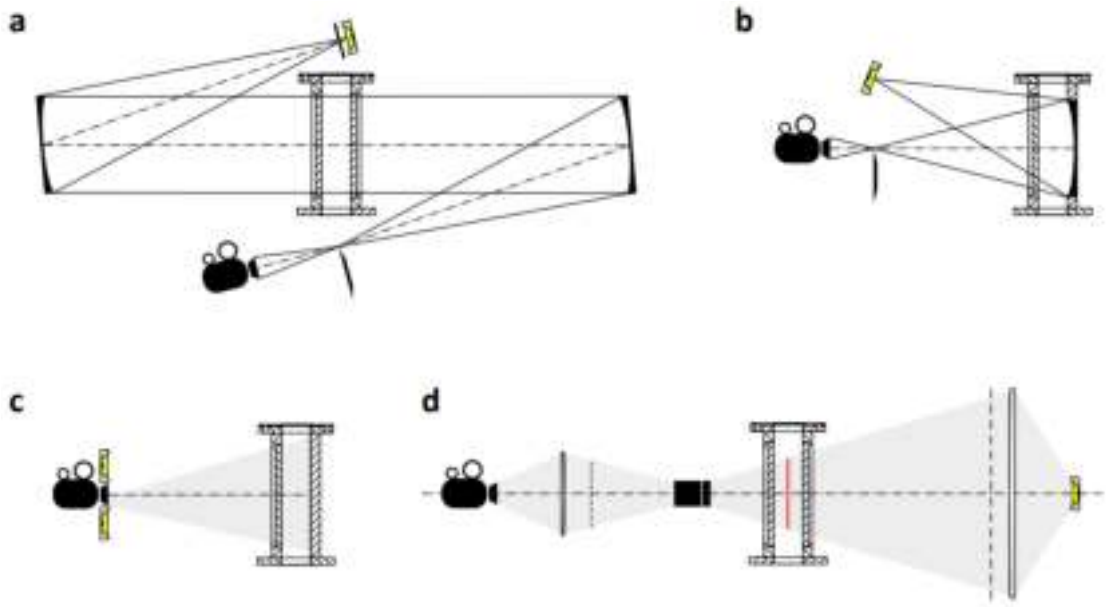

Figure 17. Schematics of schlieren systems for NICFD investigations: (**a**) conventional z-type schlieren system. (**b**) double-pass schlieren system. (**c**) background-oriented schlieren system. (**d**) focusing schlieren system.

The z-type, two-lens configuration was used in schlieren image experiments conducted by Head [20] in the ORCHID test facility. However, the first schlieren results for a non-ideal compressible nozzle flow were presented by Spinelli et al. [52] in 2015, and they employed a double-pass system. A double-pass-type parallel light schlieren system with the emitting and receiving optical components mounted on an optical table was used in this first study, because this configuration is shorter and easier to align with respect to the classical z-type system. The schematic of the employed approach is shown in more detail in Figure 18.

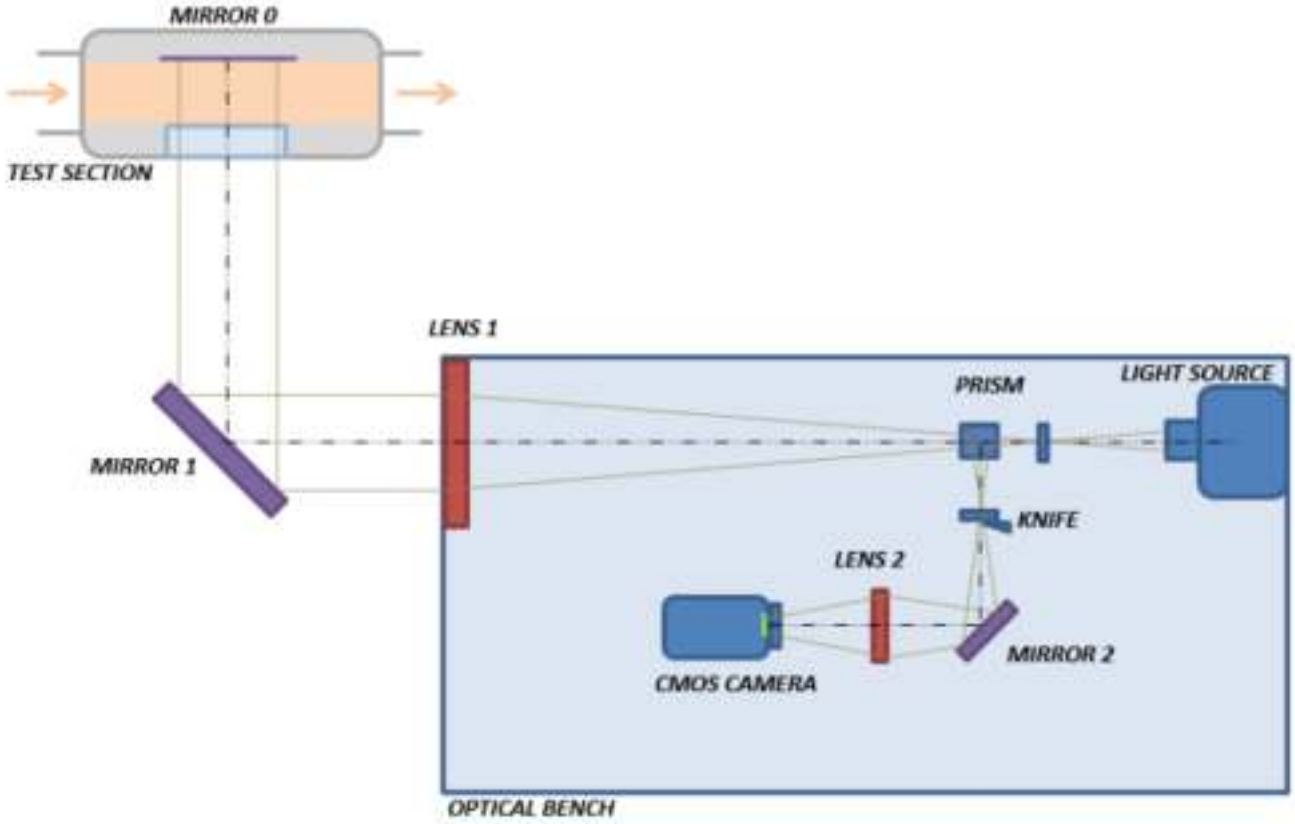

Figure 18. Schematic of the double-pass schlieren system employed by Spinelli et al. [110].

A 100 W Hg arc lamp was used in [52] as the light source, which was focused by an F/1.5 silica lens into a circular spot of about 3 mm in diameter and then collimated to form parallel light rays by a schlieren lens head (Lens 1 in Figure 18). The latter had a diameter of 150 mm and a focal length of 1000 mm. The collimated light beam was deflected by a circular mirror (Mirror 1 in Figure 18) before traversing the test section. It was then reflected by the schlieren head by the metallic mirror "0", which was the polished nozzle back wall. Then, the beam was focused on the vertically aligned knife edge. The knife orientation made it possible to visualize the density gradient along the nozzle axis. A cubic beam splitter (prism) separated the light beam originating from the light source and the reflected one. A lens of 160 mm focal length and 50 mm diameter was located behind the knife (Lens 2 in Figure 3), and created a real image of the test section on the sensor of a high-speed camera. The camera resolution and frame rate were set to 1024 $\times$ 512 pixels and 100 fps (frames per second), while the exposure time was set to 20 µs. The use of a mirror-polished rear plate was cost-efficient, and its optical quality was high enough to ensure no significant disturbances in the schlieren images. However, a polished surface gets dirty quickly, so it must be cleaned every few tests to achieve good contrast and sharpness in the schlieren images. Usually, some drops of liquid working fluid or isopropyl alcohol are effective cleaning fluids. The same procedure can be used to clean quartz windows. The reflectivity of the stainless-steel plate is affected by the siloxane vapor, which the light source intensity might compensate for. Later, LED light sources became popular for schlieren systems.

Figure 19 shows the first results obtained in [52] for a nozzle flow of MDM. Condensation of the MDM vapor occurred along the back plate, which was not heated. Condensation prevented the use of the double-passage schlieren techniques, since liquid drops and film that flowed over the back plate produced reflected rays featuring high optical distortions (see Figure 19a). That outcome prevented the detection of the density gradients in the vapor phase. Direct observation of the test section revealed that condensation occurred only along the metal plate. When the vapor flow heated the test section, the liquid film evaporated. Then, oblique shock waves originated immediately after the recessed step became visible (with their reflection at the contoured wall), thus confirming the occurrence of a supersonic flow of MDM vapor within the nozzle (see Figure 19b).

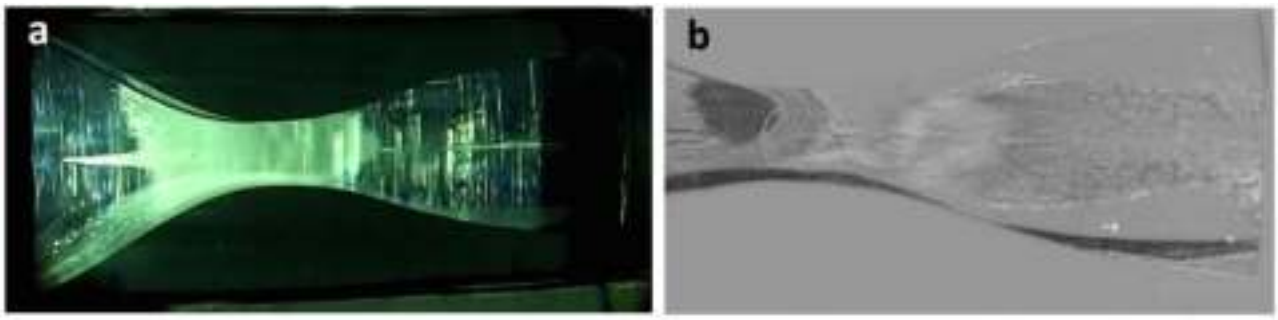

Figure 19. Pictures of the test section during the first experimental runs with MDM in 2015 (from [52]): (**a**) condensation along the back plate and formation of a liquid film in the convergent section of the nozzle (**b**) schlieren visualization of the oblique shock waves at a later experimental run.

In the following studies [97,110], the quality of the schlieren pictures obtained by the double-pass system was improved. Figure 20 shows a schlieren picture with Mach lines that enable the determination of the Mach number along the nozzle expansion path. The actual Mach number Ma can be determined from the observed angle α (enlarged by the central green lines in the top picture of Figure 20) by the relation

$$Ma = \frac{1}{\sin \alpha} \tag{21}$$

The detection of Mach lines according to Equation (21) permits a direct measurement of the local Mach number without involving any thermodynamic model in the calculation if the flow direction is known. A detailed description of the algorithm is reported in [111]. The comparison with the prediction of a computational fluid dynamics (CFD) simulation of the nozzle flow was in good agreement (see Figure 20).

Steady oblique shock waves were observed for the first time in the non-ideal supersonic flows of a single-phase organic vapor in 2019 by Zocca et al. [112]. A diamond-shaped airfoil with a semi-aperture of 7.5° at the leading edge and 10° at the trailing edge was placed within a uniform supersonic stream (Mach number Ma = 1.5) of siloxane MDM. The measurements demonstrated the dependence of the pressure ratio across the shock on the applied stagnation conditions for a non-ideal compressible flow. Schlieren pictures for a nozzle-arrangement-based airfoil with vanishing deflection were obtained by Manfredi et al. [89,90] and presented in 2022.

In addition to the schlieren images obtained by z-type or double-pass systems, the background-oriented schlieren (BOS) technique permits the visualization of small density gradients. Since the light rays deflect when passing through fluids with different densities, the BOS technique can detect the resulting refractive index gradients as integrations along a line of sight. In [113], a corresponding system was proposed for supersonic flow applications. Further applications of the BOS technique can be found, for instance, in [114–120]. The schematics of a BOS system are already shown in Figure 17c. The first application of a BOS system for a non-ideal compressible flow was presented in 2022 by Sundermeier

et al. [121]. In this work, the high subsonic flow (*Ma* = 0.65) of Novec 649 through a circular cylinder was investigated. The principle and some results, including the comparison with the outcome of a Large Eddy Simulation (LES), are shown in Figure 21. As a datum or reference image, the test section without any flow was considered. Suppose fluid flows through the test section with density gradients, distortions, or schlieren results. Using the reference picture, a density or schlieren picture can be computed in a post-processing step. This is illustrated in Figure 21. Local shocks caused by the trailing edge of the cylinder and the von Karman vortex street downstream of the cylinder can be observed. Based on the distances of the vortex cores, the corresponding Strouhal number was computed and compared with the LES results. It was found that the vortex shedding frequency (i.e., the Strouhal number) was nearly constant (at about 0.20), and it was independent of the Reynolds or Mach numbers. Although locally, the non-ideal gas behavior affected the shock pattern and the location of the shocks, the vortex shedding was relatively stable and robust.

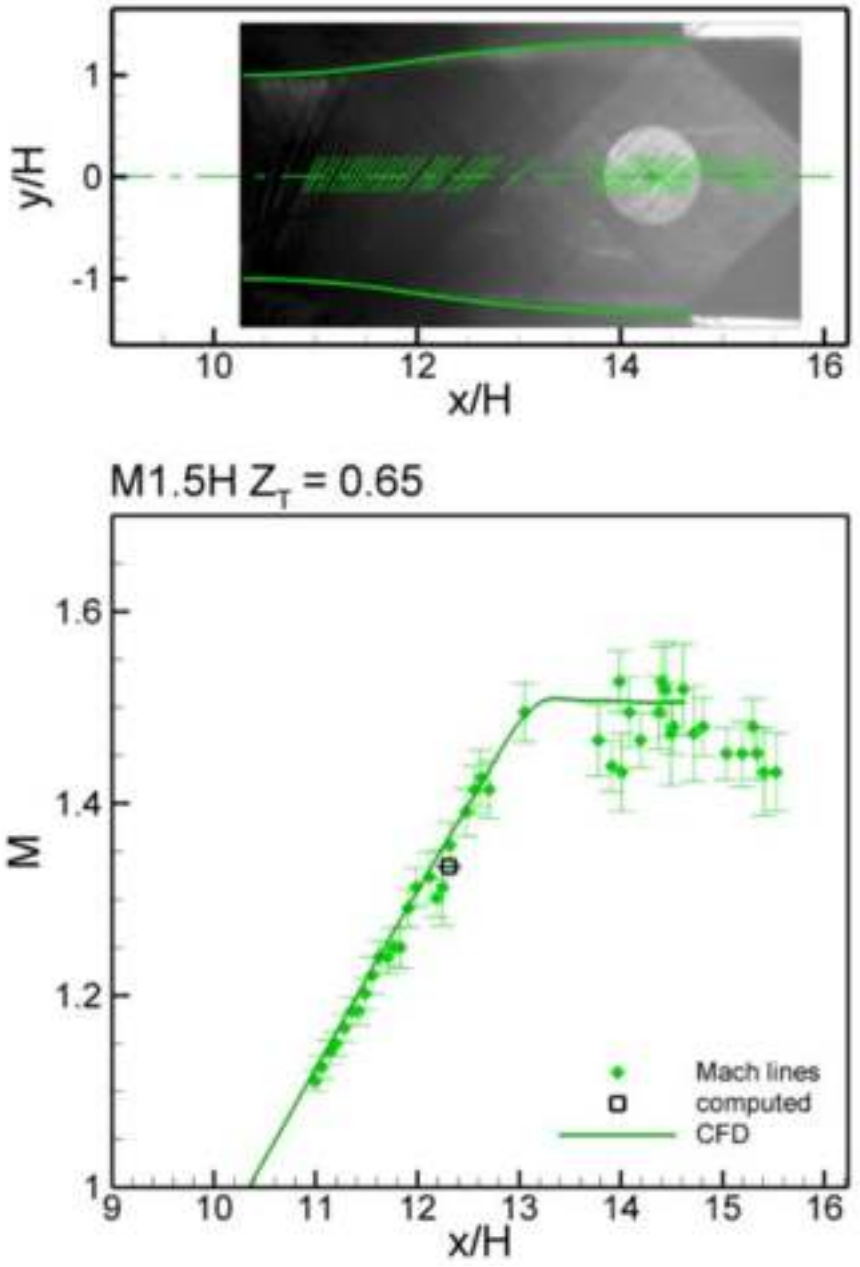

Figure 20. Schlieren image (**top**) and Mach numbers obtained from Mach lines (**bottom**) for a nozzle flow of MDM at *Z* = 0.65 (taken from [97]).

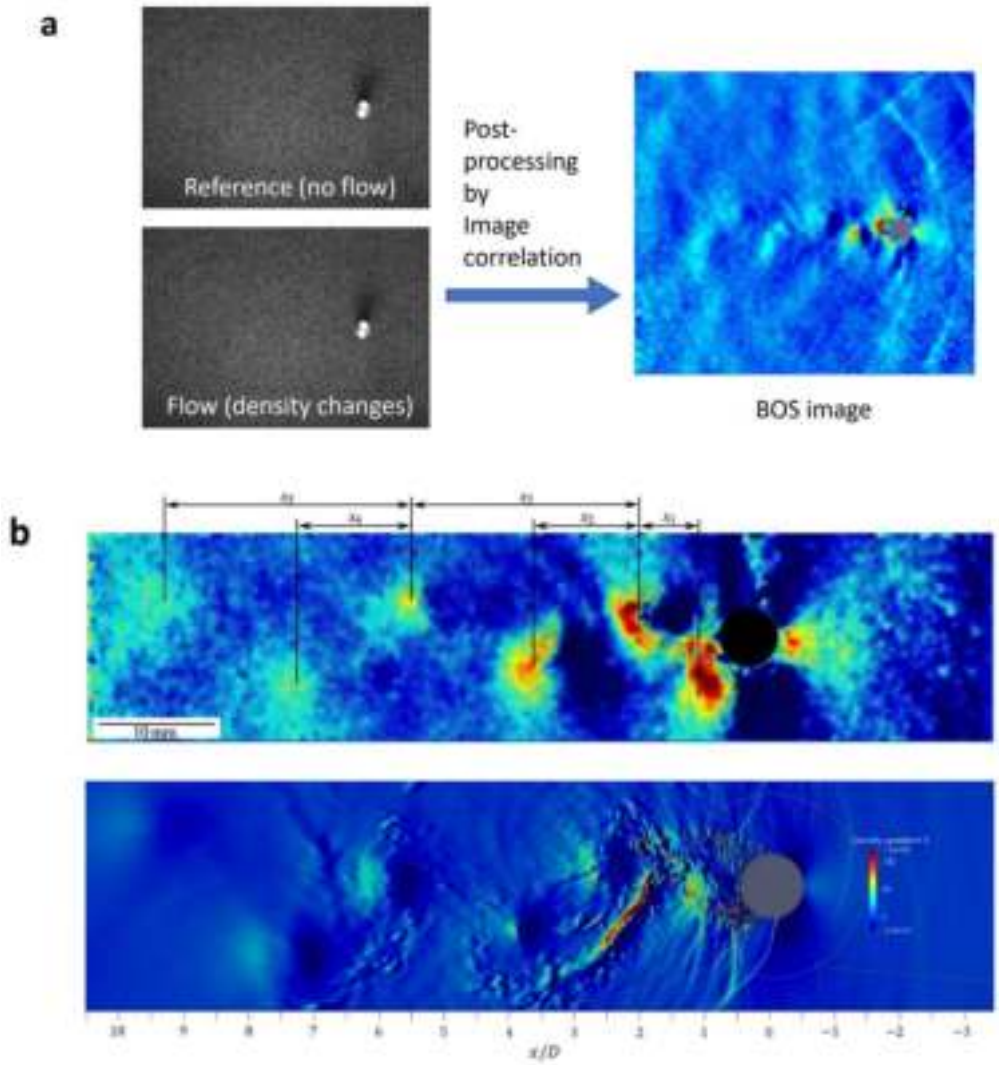

Figure 21. Principle and application of the BOS technique when applied to a circular cylinder: (**a**) schematics of the BOS working principle; (**b**) comparison of a BOS image with the instantaneous density gradient computed by LES (from [121]).

The disadvantage of the background-oriented schlieren approach is the somewhat lower resolution. In principle, achieving a higher resolution than the length scale of the background pattern is impossible. Regular and stochastic patterns can be chosen (in Figure 21, a stochastic dot pattern on the backplate of a test section was applied). It is not helpful to reduce the length scale of the pattern up to the level where vibrations of the test rig or the optical resolution limit would be reached. In practice, the BOS approach cannot provide as sharp shock visualizations as the conventional schlieren systems. However, the advantage of visualizing even small density fluctuations and the relatively simple setup makes the BOS technique a powerful tool for compressible flow investigations. In Figure 22, the vortex street caused by the stem of a hot-wire probe downstream of a turbine cascade operated with Novec 649 at an exit Mach number of $Ma = 0.6$ is shown. The background pattern was, in this case, the natural roughness of the metal-printed cascade, and no further preparation was needed. The density gradients due to the vortex street are the dominating feature in Figure 22. That also indicates that, even in subsonic flow, the BOS approach can provide valuable insights into flow details.

Finally, the focusing schlieren system (Figure 17d) might be mentioned, because this approach is precious for local compressible flow phenomena, such as the compressible flow through a turbine tip gap [122]. The idea of a focusing schlieren approach was first

described by Schardin [123] more than 70 years ago, but due to World War II, he was unable to pursue his idea further. The most recent developments to the method were made by Weinstein [124], who devised what has been termed in the literature [108] as "the modern focusing schlieren system." The high value of a focusing schlieren system for detailed investigations of three-dimensional turbine flow features was demonstrated by Passmann et al. [122], who considered the flow of air through an idealized turbine vane and a transonic cascade with tip gaps. So far, no results have been reported for applying this exciting schlieren technique to non-ideal compressible flows. Still, in the future, the use of focusing schlieren systems might also be expected in this area.

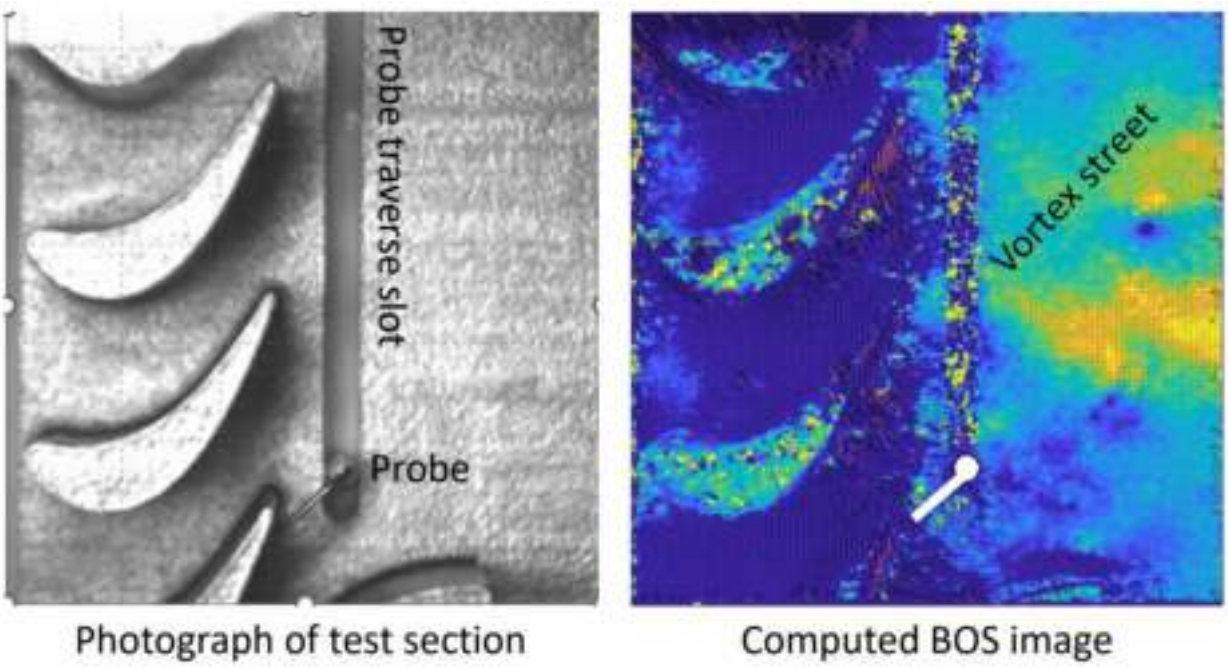

Figure 22. Background-oriented schlieren image of the flow of Novec 649 through a turbine cascade operated at an exit number of $Ma = 0.6$. The dominant feature is the vortex street in the wake of the probe stem downstream of the cascade. Pictures were taken at a test campaign at CLOWT in 2022.

5.2. Laser Doppler Velocimetry (LDV) Technique

Laser Doppler velocimetry (LDV) is a well-established experimental technique that investigates a wide range of complex flows and fluid dynamic phenomena. A comprehensive review of the principles, data analysis, and practical implementation of the LDV technique can be found in [125]. The era of LDV began in the mid-1960s after the introduction of lasers. The great advantage of LDV (and of PIV) is its non-intrusive nature. Especially in the case of high-speed flows, where solid Pitot or hot-wire probes can massively disturb the flow (see Figure 22 or Figures 14 and 15), the laser-based methods only require optical access to the measurement zone and the introduction of small particles. Conceptually, LDV enables a direct approach to determine the velocity field **w** without employing the equation of states or isentropic flow relations for the data reduction process. Hence, the experimental uncertainty level due to the uncertainties regarding the employed thermodynamic ties and the impact of error propagation might be avoided in principle.

The fundamental phenomenon behind LDV is the Doppler shift of light scattered from a small particle moving with the particle velocity w_p. Ideally, this particle velocity is identical to the fluid velocity w. In the case of microscopic particles of orders 0.1 up to 1 µm, this situation can be achieved due to the particle drag. However, suppose the velocity field is not uniform. In that case, the particle should respond quickly to the changes, and, hence, the dynamic response time of the particle must be much smaller than the characteristic time scale of the flow. That is sometimes difficult to achieve in high-speed flows or regions

characterized by extraordinary changes in velocity. The application of LDV requires the introduction of small particles to the fluid under investigation. This is known as seeding. The selection of the seeding particles is vital for the success of the LDV method. The density of the particles and the fluid should be equal for ideal seeding particles to minimize dynamic effects or buoyancy issues. That requirement can hardly be realized in vapors or gases. A further trade-off problem is caused by the need to use small particles for dynamic reasons to ensure a sufficient signal-to-noise ratio (SNR) for the Doppler signal of the scattered light. The latter would be improved by increasing the particle size. In addition, high refractive index materials should be used to increase the scattering in the ambient fluid with its own refractive index. The added particles must not disturb the flow to be measured. If the LDV method should be applied to vapors at elevated temperatures (and pressure), the seeding particles should be stable enough during the measurement. In Table 4, some potential materials for seeding particles are listed. Since the density of vapors or gases is, even at high-pressure levels, much lower than the densities listed in Table 4, no perfect seeding particle is available.

Table 4. Properties of seeding particle material.

Material	Refractive Index	Density	Melting Temperature
TiO_2	2.6 up to 2.9	3900–4200 kg/m^3	1840 °C
Al_2O_3	1.79	3960 kg/m^3	2015 °C
SiO_2	1.45	2200 kg/m^3	1710 °C
SiC	2.6	3200 kg/m^3	2700 °C

The first application of LDV for direct velocity measurements in non-ideal compressible flows was performed at the CREA laboratory of the Politecnico di Milano. The first report [106] was published in 2020, and a detailed research article [126] followed one year later. The design and the commissioning of a laser Doppler velocimetry seeding system for non-ideal fluid flows were proposed earlier in 2016 by Gallarini et al. [127]. The seeding system is crucial for NICFD applications, and no commercial or standard seeding system can be used for organic vapors at elevated temperature and pressure levels. As seeding particles, nanosized TiO_2 powder with particle dimensions of orders 150 up to 250 nm were used. To inject the particles into the vapor flow in the wind tunnel, the seeding system shown in Figure 23 was designed and used. The flow conditions for which the seeding system was designed were a maximum pressure of about 25 bar and a maximum temperature of about 300 °C in the wind tunnel. The principle of the seeding system was to employ a liquid suspension of the solid seeding particles in the working fluid, which was injected through an atomizer at high pressure and temperature in the plenum ahead of the test section of the wind tunnel. The small droplets of the injected liquid with the seeding particle suspension evaporated, thus releasing the solid particle to be entrained in the flow of the test section of the wind tunnel.

The LDV setup used in the study [126] was a two-component back-scattering system, which employed two 1 W diode-pumped solid-state lasers. The two laser beams each exhibited a diameter of about 1 mm and a wavelength of 489.5 nm and 513.9 nm, respectively. A 40 MHz frequency shift was applied to each couple of laser beams to avoid directional ambiguity. The burst spectrum analyzer was a Dantec F 800 component with a maximum input frequency of 200 MHz. In contrast to the seeding system, which was entirely customized, commercial laser equipment was used for LDV measurements. Details about the data processing can be found in [126].

During experiments, significant density changes can occur in the vapor. Hence, the refractive index of the vapor changed as well. This might cause changes in the laser optical paths. A discussion of the resulting uncertainty in actual LDV measurements is provided in [126].

As of the writing of this review paper, the nozzle flow experiments [126] represent the only application of LDV for non-ideal compressible flows reported in the open literature. Still, the use of this powerful tool can be expected in the future for other configurations.

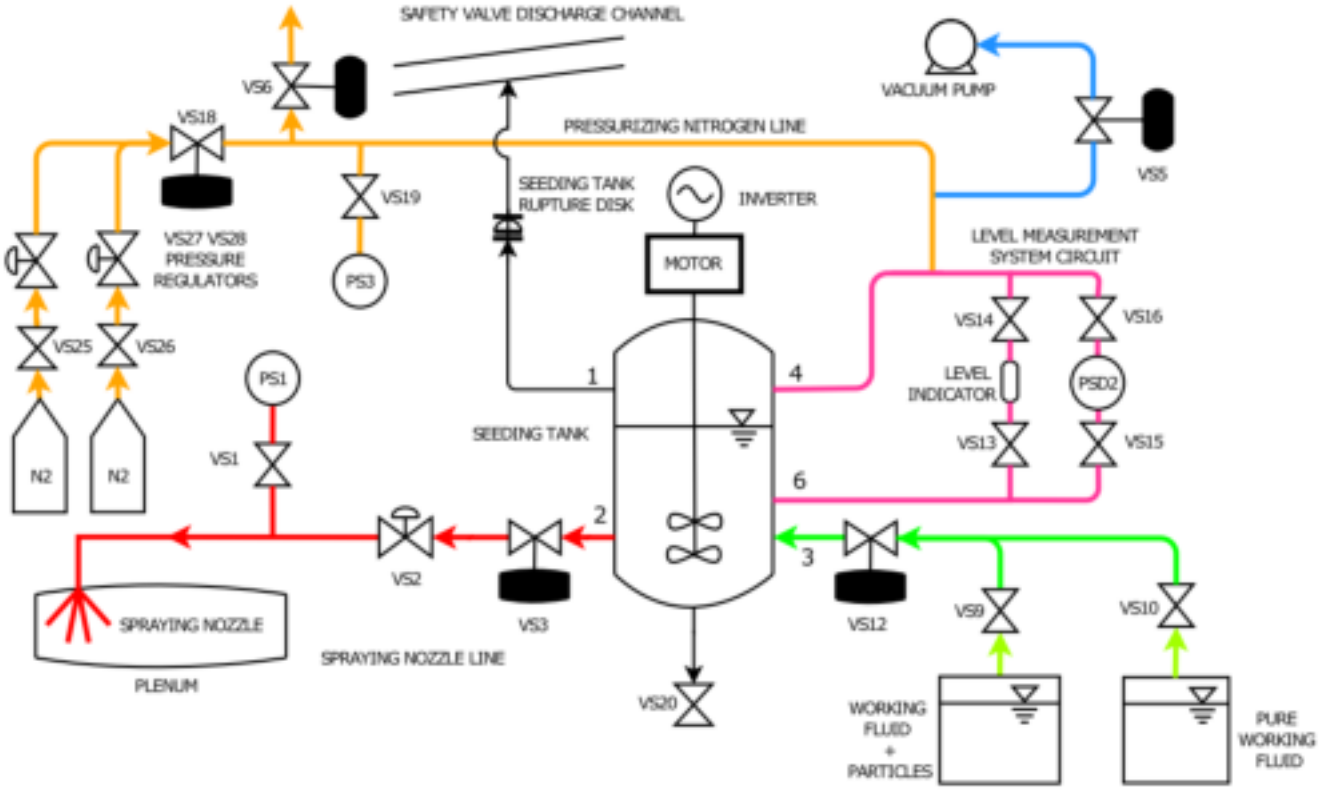

Figure 23. Seeding system for LDV application in non-ideal compressible flows (from [126]).

5.3. Particle Image Velocimetry (PIV) Technique

The particle image velocimetry (PIV) technique was initiated in the 1980s. The fundamental principle of PIV is the calculation of the velocity of tracer particles from a sequence of photographs of the seeded and illuminated flow field. The velocity calculation is based on a correlation technique, and details about PIV can be found in [128] or [129], among other texts about flow measurement. Whereas LDV can be used to determine the velocity at a small measurement volume (i.e., the local values are obtained at a point), the PIV technique enables insights into the two- or even three-dimensional velocity field. However, in the case of high-speed flows, strict requirements on illumination and exposure time result.

The use of PIV for flows of dense gases has not been reported in the open literature so far. Probably the closest relevant examples are the use of PIV in a gas–liquid two-phase nozzle flow of CO_2 by Ueno et al. [130] and the Rayleigh–Benard convection of a supercritical fluid [131], as well as a feasibility study [107]. In this feasibility study, low-speed flows of an organic vapor (D4) were considered. It was found that the D4 vapor was sufficiently transparent to conduct PIV experiments, and evaporating the fluid with TiO2 seeding particles made it possible to obtain a proper tracer distribution. Hence, an external seeder was not needed. It was inferred in [107] that PIV is feasible in low-speed flows of hot organic vapors. Further work will be devoted to devising a seeding strategy that makes it possible to perform PIV in supersonic and transonic flows in the ORCHID test facility. Such high-speed PIV experiments are in work as of the writing of this paper, but no results have been published yet.

6. Hot-Wire Anemometry

Hot-wire anemometry (HWA) has been used as the primary tool for turbulence research. Still, it also provides relevant data for validating computational fluid dynamics (CFD methods) and their turbulence modeling capabilities. The fundamentals of hot-wire anemometry can be found in [132–136]. In incompressible flows, hot-wire anemometry has been used for a century. Later, several efforts were made to exploit this technique for compressible perfect gas flow [137–148] as well. Although three different operation modes for HWA can be distinguished, the constant temperature anemometry (CTA) approach is the most popular one.

The use of HWA for dense gases or non-ideal compressible flows is somewhat new, and the first results of measurements using Novec 649 at high subsonic flow conditions can be found in [149]. A detailed discussion of an efficient calibration was recently proposed in [150], and an application of HWA in grid-generated turbulence was shown in [151]. While the application of hot-wire anemometry is relatively straightforward for supersonic flow, due to the negligible Mach number dependency of the sensitivity coefficients, it still poses severe difficulties for obtaining turbulence quantities in high subsonic and, especially, in transonic flows [145]. In this flow regime, determining the sensitivity coefficients and their dependence on Mach and Reynolds numbers is relatively challenging. In addition, wire breakage, vibrations, and strain gaging problems make using hot-wire probes tricky in high-speed flow regimes. Due to the relatively high density and the low speed of sound, applying hot-wire anemometry is particularly challenging for organic vapor flows. The high density of a complex organic vapor at elevated pressure leads to relatively high wire Reynolds numbers for which, in combination with noticeable Mach numbers, little is known from experiments with air or other simple gases.

6.1. Calibration and Behavior of Sensitivity Coefficients

To employ the hot-wire technique, the entire system must be calibrated. Since even small changes can result in noticeable deviations, the calibration should be conducted under conditions identical to the application conditions. As in the case of Pitot probes, which contrast the perfect gas case, in non-ideal flows, directional probes require a calibration procedure that is both fluid-specific and thermodynamic condition-specific. An illustration of a calibration section from the CLOWT test facility is shown in Figure 24.

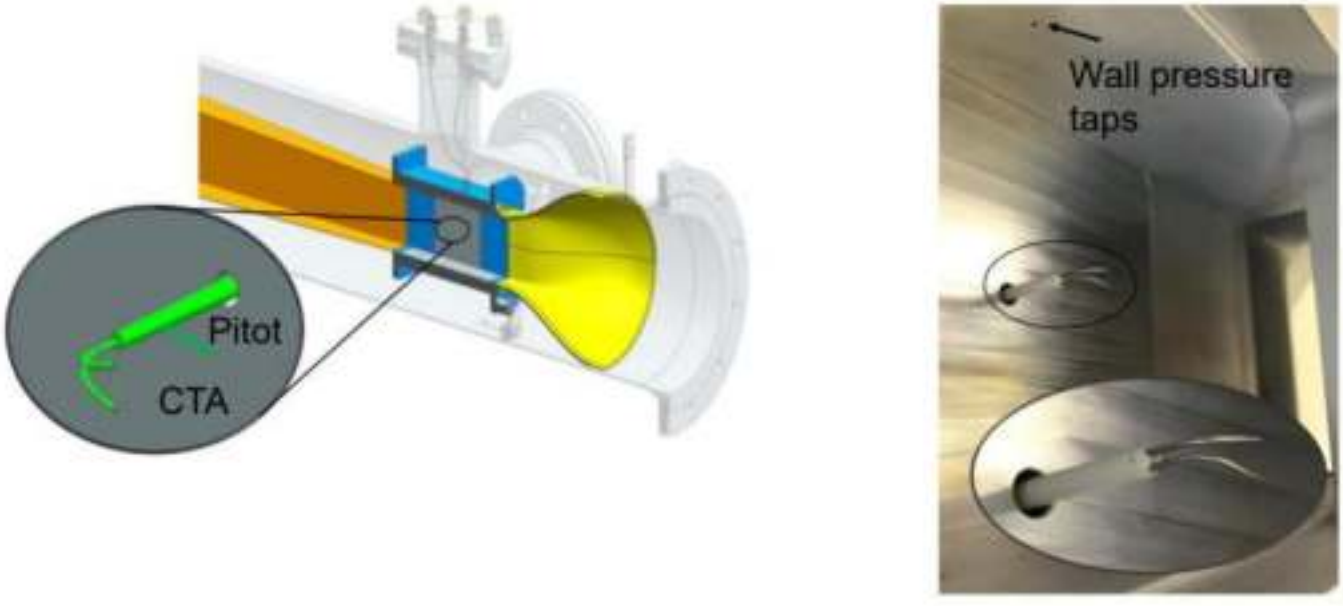

Figure 24. Closed calibration section for hot-wire probes under non-ideal compressible flow conditions.

The static and total pressures were measured directly in the calibration section through wall taps and a miniaturized Pitot probe that was close to the rotatable mounted hot-wire probe (CTA). The closed-loop wind tunnel at CLOWT, see Section 3, could effectively be used for calibrating hot-wire probes due to its ability to control the total temperature and pressure level. Furthermore, its background turbulence level is relatively low (of orders 0.2% up to 0.6%, which were obtained by hot-wire anemometry in the empty test section). The actual flow rate can be determined independently by a mass flux sensor in the return of the wind tunnel. Since steady-state operation with negligible temperature and pressure drifts can be set, a complete calibration, including determination of the angle sensitivity due to different probe orientations to the flow, is possible. However, in closed calibration sections, as are shown in Figure 24, only high subsonic flow conditions are achievable, due to the choking effect and the blockage of the probes. The probes must be mounted downstream of a nozzle or an open jet configuration within the test facility for transonic or supersonic flow conditions. The uncertainty analysis for calibration can, in principle, follow the approach recommended in [152,153].

A full calibration of a CTA probe requires several tests, and it is not ensured that the probes will survive the calibration process. Due to the high dynamic loads, some probes will break after a few minutes of operation in heavy organic vapors, while others can be used for more than eight hours. In any case, it is desirable to have the capability to repair and produce probes in the laboratory.

The starting point for the calibration is the selection of an appropriate heat transfer correlation. Following de Souza and Tavoularis [147], a modified King correlation

$$E^2 = A(Ma, T_o) + B(Ma, T_o)(\rho U)^n \tag{22}$$

for a fixed wire overheat ratio τ and total fluid temperature T_o has proven its reliability for organic vapors [150]. The exponent n can often be set to $n = \frac{1}{2}$. In CTA systems, the electrical output signal (voltage) E^2 can be identified with the Nusselt number (with an appropriate proportionality constant as a trivial multiplier). A linearization of the heat transfer equation and the use of logarithmic derivatives yield the sensitivity coefficients

$$S_u = \left(\frac{\partial \ln E}{\partial \ln U}\right)_{\rho,T_o}, \; S_\rho = \left(\frac{\partial \ln E}{\partial \ln \rho}\right)_{U,T_o} \text{ and } S_T = \left(\frac{\partial \ln E}{\partial \ln T_o}\right)_{\rho,U} \tag{23}$$

for relating the voltage signal fluctuation to the velocity, density, and total temperature fluctuations, which are defined as:

$$\frac{E'}{\overline{E}} = S_u \frac{U'}{\overline{U}} + S_\rho \frac{\rho'}{\overline{\rho}} + S_T \frac{T_o'}{\overline{T_o'}} \tag{24}$$

For supersonic flow ($Ma > 1.2$), Morkovin [139] has shown that the Mach number influence for the sensitivity coefficients is small and may be ignored. Therefore, the sensitivity coefficients for density and velocity become equal, and, formally, a simplified relation

$$\frac{E'}{\overline{E}} = S_{\rho u} \frac{(\rho U)'}{\overline{(\rho U)}} + S_T \frac{T_o'}{\overline{T_o'}} \tag{25}$$

results. The equality of the two sensitivity coefficients for density and velocity significantly reduces the data reduction and calibration efforts when measuring turbulent fluctuations quantities. Still, their equality must be proven individually for each hot-wire anemometer and flow situation. Interestingly, the relatively high wire Reynolds numbers for organic vapors support this simplification, as has been demonstrated in [150].

6.2. Application and Operational Issues

The application of HWA and its correct data interpretation sometimes require special attention. In addition to the general considerations for using HWA, the following special operation issues related to measurements in flows of heavy compressible vapors are discussed.

The high density of the organic vapor leads to relatively high wire and grid Reynolds numbers. Due to the resulting small Kolmogorov scale η, corrections were needed to account for the systematic attenuation of high-frequency signals by probes with finite wire lengths l. That issue is absent in the case of a static calibration using a wind tunnel with low background turbulence, as was described in the previous subsection. However, suitable correction schemes should be considered in actual measurements, as has been explained in [154,155]. This was pointed out in [156], and it was shown that the classical correction scheme, due to the work of Wyngaard [155] that was initially developed for isotropic turbulence in incompressible flows, is still applicable for the high subsonic flow of an organic vapor. Corresponding correction formulas can be established by using hot-wire probes with different lengths and their extrapolation to a probe with a vanishing length [154]. In the study [156], two probes with the same electrical resistance but different wire lengths and diameters (l = 4 mm (d = 10 µm) and l = 1 mm (d = 5 µm)) were used. Although Wyngaard's correction scheme is only theoretically justified for isotropic turbulence, no better alternative seems to be available yet.

Somewhat related to the small turbulent length scales in high-speed flows of organic vapors is the high cut-off frequency of the employed electrical bridge and amplifier (i.e., the anemometer circuit). Cut-off frequencies of more than 100 kHz are not uncommon for transonic or supersonic organic vapor flows. This fact makes alternative concepts, like the constant voltage anemometer [157] or the atomic layer thermo-pile ALTP sensor [158], interesting for future experiments.

In addition to the strong flow disturbances caused by the probes, as are demonstrated by the vortex street downstream of the stem that is shown in Figure 22, the high dynamic loads in high-speed flows of dense gases can create severe vibration issues. Observing the probe in the test section through a high-speed camera makes it possible to determine whether serious vibration issues exist. For instance, this was done for the arrangement shown in Figure 22, and indeed two vibrations were observed for the probe subjected to a stream of Novec 649 at 2 bar and 100 °C at an exit Mach number of Ma = 0.64. The structural analysis leads to the prediction that the typical natural frequencies of specific HWA probe devices, including a stem, are of the order of 1 kHz.

The importance of accounting for the different operational issues for a correct data interpretation can be illustrated by an example. Figure 25 shows the HWA signal (power spectrum) downstream of the trailing edge of a turbine cascade (corresponding to the setup already shown in Figure 22). In the spectrum shown in Figure 25, the compressor running speed and its blade passing frequencies can be detected even after passing the settling chamber, turbulence screens, and the turbine cascade. This demonstrates that HWA is a very sensitive flow measurement technique. The two mechanical vibration frequencies of the probe contribute to the spectrum as well. The vortex shedding frequency due to the probe stem corresponded to a Strouhal number of St_{stem} = 0.17–0.20, which is in reasonable agreement with the literature data for a cylinder subjected to a constant stream [159]. The trailing edge vortex shedding Strouhal number was found to be St = 0.24 $\pm$ 0.2, which was in excellent agreement with the values reported in [159,160] for that turbine cascade. The fact that two vortex shedding responses (denoted by 1× and 2× in Figure 25) occurred in the CTA spectrum was because the HWA was insensitive to the flow direction [134].

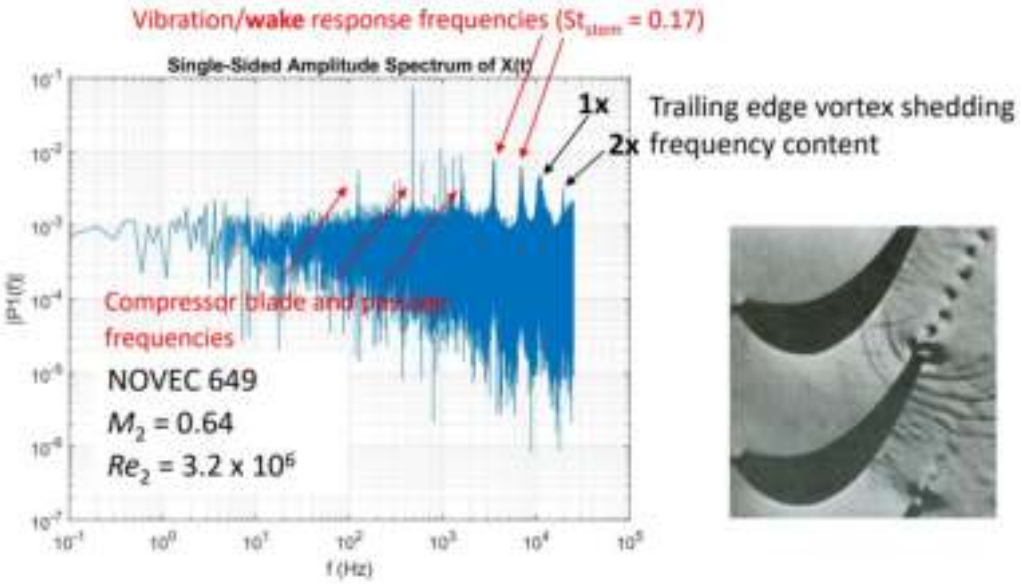

Figure 25. Power spectrum of a CTA probe placed downstream of a turbine cascade (see Figure 22), including a break-down of the frequency content.

7. Concluding Remarks

Whereas the theoretical study of non-ideal compressible fluid dynamics (NICFD) has a long tradition, the systematic experimental investigation of it is a relatively young discipline. Based on established flow measurement techniques, several research groups have developed pneumatic, optical, and thermal techniques that are well-suited for NICFD. The application of these experimental methods has allowed exciting insights into the aerodynamics and thermodynamics of non-ideal compressible flows.

It can be expected that the development and the utilization of flow measurements techniques will be continued. For instance, the use of multi-hole probes or high-speed PIV applications have not been published in the open literature so far. Hence, measurement techniques for NICFD are a research area which is anything but finished.

Currently, the impact of real gas behavior on the dimensional analysis is not fully understood. Therefore, more detailed measurements are required to establish the right set of similarity numbers for the design of components and flow devices that are subjected to non-ideal compressible flows.

In addition to testing the theory, NICFD flow measurement techniques provide data sets which are needed for validating computational fluid dynamics (CFD) methods. Since numerical loss predictions for turbomachinery are notoriously uncertain, there will be a need for detailed flow and loss measurements for turbine cascades working with organic vapors. In combination with reliable numerical methods, this research will enable the design of more efficient turbines for ORC power systems.

Funding: The preparation of this review paper received no external funding except for the financial support of the DFG (Grant Number: Wi 1840) regarding research about measurement techniques and application for ORC turbines (under the project title "REGAL-ORC"), which is highly acknowledged by the author.

Institutional Review Board Statement: Not applicable.

Informed Consent Statement: Not applicable.

Data Availability Statement: Not applicable.

Acknowledgments: The author of this review paper had the luck of having many discussions with outstanding experts about the topic of this contribution for many years. Among the numerous colleagues and their contributions, the author would like to acknowledge the precious suggestions

by Andrea Spinelli, Milano, Andrew Wheeler, Cambridge, and Adam Head at Delft. Without the extraordinary efforts of the CLOWT team members during many years of research at the Muenster University of Applied Sciences, the author of this paper would hardly be in a position to review measurement techniques for NICFD. Thus, special thanks are expressed to Felix Reinker, Max Passmann (now in Ruhr-Universität Bochum, Germany), Leander Hake, Stephan Sundermeier, and to several other supporters of the CLOWT. Finally, the author would like to express his thanks to the editor of this journal, Marcello Manna, who significantly supported this review initiative.

Conflicts of Interest: The author declares no conflict of interest.

Nomenclature

A	heat transfer correlation coefficient, V^2
a	speed of sound, m/s
B	heat transfer correlation coefficient
c	velocity, m/s
c_p	isobaric specific heat, J/(kg K)
c_v	isochoric specific heat, J/(kg K)
E	electrical voltage, V
f	function, -
$\mathbf{f}$	body force, m/s^2
h	specific enthalpy, J/kg
l	length, m
Ma	Mach number, -
p	pressure, Pa
Pr	Prandtl number, -
R	specific gas constant, J/(kg K)
Re	Reynolds number, -
S	sensitivity coefficient, -
$\mathbf{S}$	stress tensor, Pa/m
s	specific entropy, J/(kg K)
St	Strouhal number, -
T	temperature, K
t	time, s
U	velocity, m/s
v	specific volume, m^3/kg
$\mathbf{w}$	velocity vector, m/s
Z	compressibility factor, -
Greek symbols	
α	angle, $^\circ$
Γ	fundamental derivative, -
γ	isentropic exponent, -
ρ	density, kg/m^3
λ	thermal conductivity, W/(m K)
μ	dynamic viscosity, Pa s
η	Kolmogorov length scale, m
η	efficiency, -
$\mathbf{\Phi}$	viscous dissipation, Pa^2
ϕ	flow coefficient, -
Subscripts	
c	critical point
o	total or stagnation condition
1	inflow or upstream of Pitot probe
2	exit or downstream of Pitot probe shock
Superscript	
‘	fluctuating part

References

1. Colonna, P.; Casati, E.; Trapp, C.; Mathijssen, T.; Larjola, J.; Turunen-Saaresti, T.; Uusitalo, A. Organic Rankine cycle power systems: From the concept to current technology, applications, and an outlook to the future. *ASME J. Eng. Gas Turb. Power* **2015**, *137*, 100801. [CrossRef]
2. Macchi, E.; Astolfi, M. (Eds.) *Organic Rankine Cycle (ORC) Power Systems: Technologies and Applications*; Woodhead Publishing: Cambridge, UK, 2016.
3. White, M.T.; Bianchi, G.; Chai, L.; Tassou, S.A.; Sayma, A.I. Review of supercritical CO_2 technologies and systems for power generation. *Appl. Therm. Eng.* **2021**, *185*, 116447. [CrossRef]
4. Kluwick, A. *Nonlinear Waves in Real Fluids*; Springer: Wien, Austria, 1991.
5. Kluwick, A. Handbook of shockwaves. In *Theory of Shock Waves: Rarefaction Shocks*; Academic Press: Cambridge, MA, USA, 2001; Volume 1, pp. 339–411.
6. Kluwick, A. Shock discontinuities: From classical to non-classical shocks. *Acta Mech.* **2018**, *229*, 515–533. [CrossRef]
7. Reynolds, W.C.; Colonna, P. *Thermodynamics: Fundamentals and Engineering Applications*; Cambridge University Press: Cambridge, UK, 2018.
8. Guardone, A.; Colonna, P.; Wheeler, A. (Eds.) 1st international seminar on non-ideal compressible fluid dynamics for propulsion and power. *J. Physics Conf. Ser.* **2017**, *821*, 011001. [CrossRef]
9. Duhem, P. On the propagation of shock waves in fluids. *Z. Phys. Chem.* **1909**, *69*, 169–186. [CrossRef]
10. Becker, R. Stoßwelle und Detonation. *Z. Für Phys.* **1922**, *8*, 321–362. [CrossRef]
11. Bethe, H.A. *The Theory of Shock Waves for an Arbitrary Equation of State*; Report No. 545; Office of Scientific Research and Development: Washington, DC, USA, 1942.
12. Zel'dovich, Y.B. On the possibility of rarefaction shock waves. *Zh. Eksp. Teor. Fiz.* **1946**, *4*, 363–364.
13. Thompson, P.A. A Fundamental Derivative in Gas Dynamics. *Phys. Fluids* **1971**, *14*, 1843–1849. [CrossRef]
14. Anderson, W.K. Numerical Study on Using Sulfur Hexafluoride as a Wind Tunnel Test Gas. *AIAA J.* **1991**, *29*, 2179–2180. [CrossRef]
15. Anders, J.B. Heavy Gas Wind Tunnel Research at Langley Research Center. ASME Paper. In Proceedings of the Fluids Engineering Conference, Washington, DC, USA, 20–24 June 1993. sponsored by the Fluids Engineering Division, 93-FE-5.
16. Anders, J.B.; Anderson, W.K.; Murthy, A.V. The Use of Heavy Gas for Increased Reynolds Numbers in Transonic Wind Tunnels. In Proceedings of the 20th AIAA Advanced Measurement and Ground Testing Technology Conference, Albuquerque, NM, USA, 15–18 June 1998. AIAA-98-2882.
17. Rist, D. *Dynamik Realer Gase*; Springer: Berlin, Germany, 1996.
18. Boncinelli, P.; Rubechini, F.; Arnone, A.; Cecconi, M.; Cortese, C. Real gas effects in turbomachinery flows: A computational fluid dynamics model for fast computations. *ASME J. Turbomach.* **2004**, *126*, 268–276. [CrossRef]
19. Brun, K.; Friedman, P.; Dennis, R. (Eds.) *Fundamentals and Application of Supercritical Carbon Dioxide Based Power Cycles*; Woodhead Publishing: Sawston/Cambridge, UK, 2017.
20. Head, A.J. Novel Experiments for the Investigation of Non-Ideal Compressible Fluid Dynamics: The ORCHID and First Results of Optical Measurements. Ph.D. Thesis, TU Delft, Delft, The Netherlands, 2021.
21. Landau, L.D. On shock waves. *J. Phys. USSR* **1942**, *6*, 229–230.
22. Hayes, W.D. The basic theory of gasdynamic discontinuities. In *Fundamentals of Gasdynamics*; Princeton University Press: Princeton, NJ, USA, 1958; Volume 2.
23. Vimercati, D.; Gori, G.; Spinelli, A.; Guardone, A. Non-Ideal Effects on the Typical Trailing Edge Shock Pattern of Orc Turbine Blades. *Energy Procedia* **2017**, *129*, 1109–1116. [CrossRef]
24. Colonna, P.; Nannan, N.R.; Guardone, A.; van der Stelt, T.P. On the computation of the fundamental derivative of gas dynamics using equation of states. *Fluid Phase Equilibria* **2009**, *286*, 43–54. [CrossRef]
25. Morren, S.H. *Transonic Aerodynamics of Dense Gases*; NASA TM-103722; Lewis Research Center: Cleveland, OH, USA, 1991.
26. Lemmon, E.W.; Huber, M.L.; McLinden, M.O. *NIST Reference Database 23: Reference Fluid Thermodynamic and Transport Properties–REFPROP, Version 9.1*; Standard Reference Data Program: Gaithersburg, MD, USA, 2013.
27. Traupel, W. Zur Dynamik realer Gase. *Forsch. Ing.* **1952**, *18*, 3–9. [CrossRef]
28. Traupel, W. *Thermische Turbomaschinen—Erster Band*, 2nd ed.; Springer: Berlin, Germany, 1966; Chapter 1.
29. Kouremenos, D.A.; Antonopoulos, K.A. Isentropic Exponents of Real Gases and Application for the Air at Temperatures from 150 K to 450 K. *Acta Mech.* **1986**, *65*, 81–99. [CrossRef]
30. aus der Wiesche, S.; Reinker, F. Dimensional analysis and performance laws for organic vapor flow turbomachinery. *Energy* **2022**, *257*, 124635. [CrossRef]
31. Taylor, E.S. *Dimensional Analysis for Engineers*; Clarendon: Oxford, UK, 1974.
32. Dejc, M.E.; Trojanovskij, B.M. *Untersuchung und Berechnung Axialer Turbinenstufen*; VEB Verlag Technik: Berlin, Germany, 1973.
33. Turunen-Saaresti, T.; Uusitalo, A.; Honkatukia, J. Design and testing of high temperature micro-ORC test stand using Siloxane as working fluid. In *Journal of Physics: Conference Series*; IOP Publishing: Bristol, UK, 2017; Volume 821, p. 012024.
34. Seume, J.R.; Peters, M.; Kunte, H. Design and test of a 10kW ORC supersonic turbine generator. In *Journal of Physics: Conference Series*; IOP Publishing: Bristol, UK, 2017; Volume 821, p. 012023.

35. Park, B.S.; Usman, M.; Imran, M.; Pesyridis, A. Review of Organic Rankine Cycle experimental data trends. *Energy Convers. Manag.* **2018**, *173*, 679–691. [CrossRef]
36. Spinelli, A.; Guardone, A.; De Servi, C.; Colonna, P.; Reinker, F.; aus der Wiesche, S.; Robertson, M.; Martinez-Botas, R.F. Experimental facilities for non-ideal compressible vapour flows. *ERCOFTAC Bull.* **2020**, *124*, 59–66.
37. Bradley, J. *Shock Waves in Chemistry and Physics*; Chapman and Hall: London, UK, 1962.
38. Gaydon, A.G.; Hurle, I.R. *The Shock Tube in High Temperature Chemical Physics*; Chapman and Hall: London, UK, 1963.
39. Soloukhin, R.I. *Shock Waves and Detonations in Gases*; Mono Books: Baltimore, MD, USA, 1966.
40. Baumgärtner, D.; Otter, J.J.; Wheeler, A.P. The Effect of Isentropic Exponent on Transonic Turbine Performance. *ASME J. Turbomach.* **2020**, *142*, 081007. [CrossRef]
41. Dura Galiana, F.J.; Wheeler, A.P.; Ong, J. A Study of trailing-edge losses in organic Rankine cycle turbines. In Proceedings of the ASME Turbo Expo 2015: Turbine Technical Conference and Exposition, Montreal, QC, Canada, 15–19 June 2015. GT2015-42920, V02AT38A020, 12p.
42. Fergason, S.H.; Guardone, A.; Argrow, B.M. Construction and Validation of a Dense Gas Shock Tube. *J. Thermophys. Heat Transf.* **2003**, *17*, 326–333. [CrossRef]
43. Colonna, P.; Guardone, A.; Nannan, N.R.; Zamfirescu, C. Design of the dense gas flexible asymmetric shock tube. *ASME J. Fluids Eng.* **2008**, *130*, 034501. [CrossRef]
44. Mathijssen, T.; Gallo, M.; Casati, E.; Nannan, N.R.; Zamfirescu, C.; Guardone, A.; Colonna, P. The Flexible Asymmetric Shock Tube (FAST): A Ludwieg tube facility for wave propagation measurements in high-temperature vapours of organic fluids. *Exp. Fluids* **2015**, *56*, 195. [CrossRef]
45. Chandrasekaran, N.B.; Michelis, T.; Mercier, B.; Colonna, P. Preliminary experiments in high temperature vapours of organic fluids in the Asymmetric Shock Tube for Experiments on Rarefaction Waves (ASTER). In Proceedings of the 4th International Seminar on Non-Ideal Compressible Fluid Dynamics (NICFD2022), City University, London, UK, 3–4 November 2022.
46. Dettleff, G.; Thompson, P.A.; Meier, E.A.; Speckmann, H. An experimental study of liquefaction shock waves. *J. Fluid Mech.* **1979**, *95*, 279–304. [CrossRef]
47. Dettleff, G.; Thompson, P.A.; Meier, E.A. Initial experimental results for liquefaction shock waves in organic fluids. *Arch. Mech.* **1976**, *28*, 827–836.
48. Duff, K. Non-Equilibrium Condensation of Carbon Dioxide in Supersonic Nozzles. Ph.D. Thesis, M.I.T., Cambridge, MA, USA, 1966.
49. Lettieri, C.; Yang, D.; Spakoszky, Z. An investigation of condensation effects in supercritical carbon dioxide compressors. *ASME J. Eng. Gas Turbine Power* **2015**, *137*, 082602. [CrossRef]
50. Spinelli, A.; Dossena, V.; Gaetani, P.; Osnaghi, C.; Colombo, D. Design of a Test Rig for Organic Vapours. In Proceedings of the ASME Turbo Expo 2010, Glasgow, UK, 14–18 June 2010.
51. Spinelli, A.; Dossena, V.; Gaetani, P.P.; Casella, F. Design, Simulation, and Construction of a Test Rig for Organic Vapors. *ASME J. Eng. Gas Turb. Power* **2013**, *135*, 10. [CrossRef]
52. Spinelli, A.; Guardone, A.; Cozzi, F.; Cammi, G.; Cheli, R.; Zocca, M.; Gaetani, P.; Dossena, V. Experimental Observation of Non-ideal Nozzle Flow of Siloxane Vapor MDM. In Proceedings of the 3rd International Seminar on ORC Power Systems, Brussels, Belgium, 12–14 October 2015.
53. Spinelli, A.; Cozzi, F.; Cammi, G.; Zocca, M.; Gaetani, P.; Dossena, V.; Guardone, A. Preliminary characterization of an expanding flow of siloxane vapor MDM. In *Journal of Physics: Conference Series*; IOP Publishing: Bristol, UK, 2017; Volume 821, p. 012022.
54. Spinelli, A.; Cammi, G.; Conti, C.C.; Gallarini, S.; Zocca, M.; Cozzi, F.; Gaetani, P.; Dossena, V.; Guardone, A. Experimental observation and thermodynamic modeling of non-ideal expanding flows of siloxane MDM vapor for ORC applications. *Energy* **2019**, *168*, 285–294. [CrossRef]
55. Robertson, M.C.; Newton, P.J.; Chen, T.; Martinez-Botas, R.F. Development and commissioning of a blowdown facility for dense gas vapours. In Proceedings of the ASME Turbo Expo 2019, Phoenix, AZ, USA, 17–21 June 2019. GT2019-91609.
56. Robertson, M.C.; Newton, P.J.; Chen, T.; Costall, A.; Martinez-Botas, R.F. Experimental and numerical study of supersonic non-ideal flows for organic Rankine cycle applications. *ASME J. Eng. Gas Turbines Power* **2020**, *142*, 081007. [CrossRef]
57. Dixon, S.L.; Hall, C.A. *Fluid Mechanics and Thermodynamics of Turbomachinery*, 6th ed.; Butterworth-Heinemann: Burlington, MA, USA, 2010.
58. Hirsch, C. (Ed.) *Advanced Methods for Cascade Testing*; NATO, AGARDograph 328; Specialised Printing Services Limited: Loughton, UK, 1993; ISBN 92-835-0717-7.
59. Sieverding, C.H. Aerodynamic development of axial turbomachinery blading. In *Thermodynamics and Fluid Mechanics of Turbomachinery*; Ücer, A.S., Stow, P., Hirsch, C., Eds.; NATO ASI Series: Dordrecht, The Netherlands, 1985; Volume 1.
60. Reinker, F.; Hasselmann, K.; aus der Wiesche, S.; Kenig, E.Y. Thermodynamics and fluid mechanics of a closed blade cascade wind tunnel for organic vapors. *ASME J. Eng. Gas Turbine Power* **2015**, *138*, 052601. [CrossRef]
61. Reinker, F.; Kenig, E.Y.; Passmann, M.; aus der Wiesche, S. Closed loop organic wind tunnel (CLOWT): Design, components and control system. In Proceedings of the ORC2017—4th International Seminar on ORC Power Systems, Milan, Italy, 13–15 September 2017; pp. 200–207.

62. Reinker, F.; Kenig, E.Y.; aus der Wiesche, S. CLOWT: A multifunctional test facility for the investigation of organic vapor flows. In Proceedings of the ASME 2018 5th Joint US-European Fluids Engineering Summer Conference, Montreal, QC, Canada, 15–20 June 2018.
63. Reinker, F.; Kenig, E.Y.; aus der Wiesche, S. Closed loop organic vapor wind tunnel (CLOWT: Commissioning and operational experience. In Proceedings of the ORC2019—5th International Seminar on ORC Power Systems, Athens, Greece, 9–11 September 2019.
64. Hake, L.; Reinker, F.; Wagner, R.; aus der Wiesche, S.; Schatz, M. The Profile Loss of Additive Manufactured Blades for Organic Rankine Cycle Turbines. *Int. J. Turbomach. Propuls. Power* **2022**, *7*, 11. [CrossRef]
65. White, M.T.; Sayma, A.I. Design of a closed-loop optical access supersonic test facility for organic vapors. In Proceedings of the ASME Turbo Expo 2018, Oslo, Norway, June 11–15 2018. GT2018-75301.
66. Bier, K.; Ehrler, F.; Hartz, U.; Kissau, G. Zur Berechnung von Düsenströmungen stark realer Gase. *Forsch. Lng. Wes.* **1977**, *43*, 175–184. [CrossRef]
67. Head, A.; De Servi, C.; Casati, E.; Pini, M.; Colonna, P. Preliminary design of the ORCHID: A facility for studying non-ideal compressible fluid dynamics and testing ORC expanders. In Proceedings of ASME Turbo Expo 2016, Seoul, South Korea, 13–17 June 2016. GT2016-56103.
68. Beltrame, F.; Head, A.J.; De Servi, C.; Pini, M.; Schrijer, F.; Colonna, P. First Experiments and Commissioning of the ORCHID Nozzle Test Section. In *NICFD 2020: Proceedings of the 3rd International Seminar on Non-Ideal Compressible Fluid Dynamics for Propulsion*; Pini, M., Ed.; ERCOFTAC Series; Springer: Berlin/Heidelberg, Germany, 2021; Volume 28, pp. 169–178. [CrossRef]
69. White, M. Workshop on experimental test facilities. In Proceedings of the 4th International Seminar on Non-Ideal Compressible Fluid Dynamics (NICFD2022), City University, London, UK, 3–4 November 2022.
70. Bradshaw, P. *Experimental Fluid Mechanics*; Pergamon Press: Oxford, UK, 1970.
71. Bradshaw, P. *An Introduction to Turbulence and Its Measurement*; Pergamon Press: Oxford, UK, 1971.
72. Eckelmann, H. *Einführung in Die Strömungsmeßtechnik*; Teubner: Stuttgart, Germany, 1997.
73. Nitsche, W.; Brunn, A. *Strömungsmesstechnik*; Springer-VDI: Berlin, Germany, 2006.
74. Tropea, C.; Yarin, A.L.; Foss, J.F. (Eds.) *Springer Handbook of Experimental Fluid Mechanics*; Springer: Berlin, Germany, 2007.
75. Han, J.-C.; Wright, L. *Experimental Methods in Heat Transfer and Fluid Mechanics*; CRC Press: Boca Raton, FL, USA, 2022.
76. Liepmann, H.W.; Roshko, A. *Elements of Gasdynamics*; John Wiley & Sons: New York, NY, USA, 1957.
77. John, J.E.; Keith, T.G. *Gas Dynamics*, 3rd ed.; Pearson: Upper Saddle River, NJ, USA, 2006.
78. Folsom, R.G. Review of Pitot Tubes. *Trans. Am. Soc. Mech. Eng.* **1956**, *78*, 1447–1460. [CrossRef]
79. Moore, M.J.; Sieverding, C.H. *Two-Phase Steam Flow in Turbines and Separators: Theory, Instrumentation, Engineering*; Hemisphere Publishing: Washington, DC, USA, 1976; Volume 1.
80. Murthy, S.; Leonard, M.; Ehresman, C. A Stagnation Pressure Probe for Droplet-Laden Air Flow. *J. Propuls.* **1986**, *2*, 195–196. [CrossRef]
81. Harbeck, J.; Geist, S.; Schatz, M. An approach to measure total-head in wakes and near end walls at high fogging conditions. In Proceedings of the ASME Turbo Expo 2021, Virtual, 7–11 June 2021. GT2021-59190.
82. Conti, C.; Fusetti, A.; Spinelli, A.; Guardone, A. Shock losses and Pitot tube measurements in non-ideal supersonic and subsonic flows of organic vapors. In Proceedings of the 6th International Seminar on ORC Power Systems, Munich, Germany, 11–13 October 2021; p. 81.
83. Conti, C.; Fusetti, A.; Spinelli, A.; Gaetani, P.; Guardone, A. Pneumatic system for pressure probe measurements in transient flows of non-ideal vapors subject to line condensation. *Measurement* **2022**, *192*, 110802. [CrossRef]
84. Conti, C.; Fusetti, A.; Spinelli, A.; Guardone, A. Shock loss measurements in non-ideal supersonic flows of organic vapors. *Exp. Fluids* **2022**, *63*, 117. [CrossRef]
85. Reinker, F.; Wagner, R.; Passmann, M.; Hake, L.; aus der Wiesche, S. Performance of a rotatable cylinder pitot probe in high subsonic non-ideal gas flows. In *NICFD 2020, ERCOFTAC Series 28*; Pini, M., de Servi, C., Spinelli, A., di Mare, F., Guardone, A., Eds.; Springer International Publishing: Cham, Switzerland, 2021; pp. 144–152. [CrossRef]
86. aus der Wiesche, S.; Reinker, F.; Wagner, R.; Hake, L.; Passmann, M. Critical and choking Mach numbers for organic vapor flows through turbine cascades. In Proceedings of the ASME Turbo Expo 2021, Virtual, 7–11 June 2021. GT2021-59013.
87. Dura Galiana, F.J.; Wheeler, A.P.; Ong, J. A Study of trailing-edge losses in organic Rankine cycle turbines. *Proc. ASME J. Turbomach.* **2016**, *138*, 121003. [CrossRef]
88. Reinker, F.; Wagner, R.; Hake, L.; aus der Wiesche, S. High subsonic flow of an organic vapor past a circular cylinder. *Exp. Fluids* **2021**, *62*, 54. [CrossRef]
89. Manfredi, M.; Persico, G.; Spinelli, A.; Gaetani, P.; Dossena, V. Loss measurement strategy in ORC supersonic blade cascades. In Proceedings of the 4th International Seminar on Non-Ideal Compressible Fluid Dynamics (NICFD2022), City University, London, UK, 3–4 November 2022.
90. Manfredi, M.; Spinelli, A.; Persico, G.; Gaetani, P.; Dossena, V. Nitrogen experiments on a supersonic linear cascade for ORC applications. In Proceedings of the XXVI Biennial Symposium on Measuring Techniques in Turbomachinery, Pisa, Italy, 28–30 September 2022.
91. Baumgärtner, D. Real Gas Effects in ORC Turbines. Ph.D. Thesis, University of Cambridge, Cambridge, UK, 2020. [CrossRef]
92. Wyler, J.S. Probe Blockage Effects in Free Jets and Closed Tunnels. *ASME J. Eng. Power* **1975**, *97*, 509–514. [CrossRef]

93. Truckenmüller, F.; Renner, M.; Stetter, H.; Hosenfeld, H. Transonic probe blockage effects in a calibration wind-tunnel and stator blade passage. In Proceedings of the ASME Turbo Expo 1996, Birmingham, UK, 10–13 June 1996; pp. 1–8.
94. Langford, R.W.; Keeley, K.R.; Wood, N.B. Investigation of the Transonic Calibration Characteristics of Turbine Static Pressure Probes. In Proceedings of the ASME 1982 International Gas Turbine Conference and Exhibit, London, UK, 18–22 April 1982. ASME-Paper, No. 82-GT-280.
95. Squire, L.C. Effects of Probe Supports on Measurements in Steam Turbines. In Proceedings of the ASME 1986 International Gas Turbine Conference and Exhibit, Dusseldorf, Germany, 8–12 June 1986. ASME-Paper, No. 86-GT-213.
96. Ducruet, C. A Method for Correcting Wall Pressure Measurements in Subsonic Compressible Flow. *ASME J. Fluids Eng.* **1991**, *113*, 256–260. [CrossRef]
97. Spinelli, A.; Cammi, G.; Gallarini, S.; Zocca, M.; Cozzi, F.; Gaetani, P.; Dossena, V.; Guardone, A. Experimental evidence of non-ideal compressible effects in expanding flow of a high molecular complexity vapor. *Exp. Fluids* **2018**, *59*, 126. [CrossRef]
98. Schollmeier, J.-N.; aus der Wiesche, S. A user-friendly pitot probe data reduction routine for non-ideal gas flow applications. *Energy* **2022**, *261*, 125143. [CrossRef]
99. Passmann, M.; aus der Wiesche, S.; Joos, F. A one-dimensional analytical calculation method for obtaining normal shock losses in supersonic real gas flows. In *Journal of Physics: Conference Series*; IOP Publishing: Bristol, UK, 2017; Volume 821, p. 012004. [CrossRef]
100. Span, R.; Wagner, W. Equations of state for technical applications. I. Simultaneously optimized functional forms for nonpolar and polar fuids. *Int. J. Thermophys.* **2003**, *24*, 1–39. [CrossRef]
101. Colonna, P.; Nannan, N.R.; Guardone, A.; Lemmon, E.W. Multiparameter equations of state for selected siloxanes. *Fluid Phase Equilibria* **2006**, *244*, 193–211. [CrossRef]
102. Colonna, P.; Nannan, N.R.; Guardone, A. Multiparameter equations of state for siloxanes[(CH3)3-Si-O1/2]2-[O-Si-(CH3)2]i=1,...,3, and [O-Si-(CH3)2]6. *Fluid Phase Equilibria* **2008**, *263*, 115–130. [CrossRef]
103. Thol, M.; Dubberke, F.H.; Rutkai, G.; Windmann, T.; Köster, A.; Span, R.; Vrabec, J. Fundamental equation of state correlation for hexamethyldisiloxane based on experimental and molecular simulation data. *Fluid Phase Equilibria* **2016**, *418*, 133–151. [CrossRef]
104. Thol, M.; Dubberke, F.H.; Baumhögger, E.; Vrabec, J.; Span, R. Speed of sound measurements and fundamental equations of state for octamethyltrisiloxane and decamethyltetrasiloxane. *J. Chem. Eng. Data* **2017**, *62*, 2633–2648. [CrossRef]
105. Gori, G.; Molesini, P.; Persico, G.; Guardone, A. Non-Ideal Compressible-Fluid Dynamics of Fast-Response Pressure Probes for Unsteady Flow Measurements in Turbomachinery. In *Journal of Physics: Conference Series*; IOP Publishing: Bristol, UK, 2017; Volume 821, p. 012005.
106. Cozzi, F.; Spinelli, A.; Gallarini, S.; Guardone, A. Optical Diagnostics for Non-Ideal Compressible Fluid Dynamics. *Rcoftac Bull.* **2020**, *124*, 67–72.
107. Head, A.J.; Novara, M.; Gallo, M.; Schrijer, F.; Colonna, P. Feasibility of Particle Image Velocimetry for Low-Speed Unconventional Vapor Flows. *Exp. Therm. Fluid Sci.* **2019**, *102*, 589–594. [CrossRef]
108. Settles, G.S. *Schlieren and Shadowgraph Techniques: Visualizing Phenomena in Transparent Media*; Springer: Berlin/Heidelberg, Germany, 2001.
109. Merzkirch, W. *Flow Visualization*; Academic Press: Cambridge, MA, USA, 1987.
110. Conti, C.C.; Spinelli, A.; Cammi, G.; Zocca, M.; Cozzi, F.; Guardone, A. Schlieren visualizations of non-ideal compressible fluid flows. In *Proceedings of the 13th International Conference on Heat Transfer, Fluid Mechanics and Thermodynamics (HEFAT 2017)*; EDAS: Messina, Italy, 2017; pp. 513–518.
111. Cammi, G. Measurements Techniques for Non-Ideal Compressible Fluid Flows: Applications to Organic Fluids. Ph.D. Thesis, Politecnico di Milano, CREA Lab, Milan, Italy, 2019.
112. Zocca, M.; Guardone, A.; Cammi, G.; Cozzi, F.; Spinelli, A. Experimental observation of oblique shock waves in steady non-ideal flows. *Exp. Fluids* **2019**, *60*, 101. [CrossRef]
113. Cozzi, F.; Göttlich, E.; Angelucci, L.; Dossena, V.; Guardone, A. Development of a background oriented schlieren technique with telecentric lenses for supersonic flow. In *Journal of Physics: Conference Series*; IOP Publishing: Bristol, UK, 2017; Volume 778, p. 012006.
114. Richard, H.; Raffel, M. Principle and applications of the background oriented schlieren (BOS) method. *Meas. Sci. Technol.* **2001**, *12*, 1576–1585. [CrossRef]
115. Klinge, F.; Kirmse, T.; Kompenhans, J. Application of Quantitative Background Oriented Schlieren (BOS): Investigation of a Wing Tip Vortex in a Transonic Wind Tunnel. *Proc. PSFVIP4* **2003**, *4097*, 3–5.
116. Goldhahn, E.; Seume, J. The background oriented schlieren technique: Sensitivity, accuracy, resolution and application to a three-dimensional density field. *Exp. Fluids* **2007**, *43*, 241–249. [CrossRef]
117. Venkatakrishnan, L.; Meier, G.E. Density measurements using the Background Oriented Schlieren technique. *Exp. Fluids* **2004**, *37*, 237–247. [CrossRef]
118. Raffel, M. Background-oriented schlieren (BOS) techniques. *Exp. Fluids* **2015**, *56*, 1–17. [CrossRef]
119. Clem, M.M.; Zaman, K.B.M.Q.; Fagan, A.F.; Glenn, N. Background Oriented Schlieren Applied to Study Shock Spacing in a Screeching Circular Jet. In Proceedings of the 50th AIAA Aerospace Sciences Meeting including the New Horizons Forum and Aerospace Exposition, Nashville, TN, USA, 9–12 January 2012; pp. 1–12.

120. Kindler, K.; Goldhahn, E.; Leopold, F.; Raffel, M. Recent developments in background oriented Schlieren methods for rotor blade tip vortex measurements. *Exp. Fluids* **2007**, *43*, 233–240. [CrossRef]
121. Sundermeier, S.; Matar, C.; aus der Wiesche, S.; Cinnella, P.; Hake, L.; Gloerfelt, X. Experimental and numerical study of transonic flow of an organic vapor past a circular cylinder. In Proceedings of the 4th International Seminar on Non-Ideal Compressible Fluid Dynamics (NICFD2022), City University, London, UK, 3–4 November 2022.
122. Passmann, M.; aus der Wiesche, S.; Joos, F. Focusing Schlieren Visualization of Transonic Turbine Tip-Leakage Flows. *Int. J. Turbomach. Propuls. Power* **2020**, *5*, 1. [CrossRef]
123. Schardin, H. Die Schlierenverfahren und ihre Anwendungen. In *Ergebnisse der Exakten Naturwissenschaften*; Springer: Berlin, Germany, 1942; pp. 303–349.
124. Weinstein, L. Large-Field High-Brightness Focusing Schlieren System. *AIAA J.* **1993**, *31*, 1250–1255. [CrossRef]
125. Albrecht, H.-E.; Damaschke, N.; Borys, M.; Tropea, C. *Laser Doppler and Phase Doppler Measurement Techniques*; Springer: Berlin, Germany, 2013.
126. Gallarini, S.; Cozzi, F.; Spinelli, A.; Guardone, A. Direct velocity measurements in high-temperature non-ideal vapor flows. *Exp. Fluids* **2021**, *62*, 199. [CrossRef]
127. Gallarini, S.; Spinelli, A.; Cozzi, F.; Guardone, A. Design and commissioning of a laser doppler velocimetry seeding system for non-ideal fluid flows. In Proceedings of the 12th International Conference on Heat Transfer, Fluid Mechanics and Thermodynamics HEFAT, Costa de Sol, Spain, 11–13 July 2016.
128. Westerweel, J.; Elsinga, G.E.; Adrian, R.J. Particle image velocimetery for complex and turbulent flow. *Annu. Rev. Fluid Mech.* **2013**, *45*, 409–436. [CrossRef]
129. Raffel, M.; Willert, C.E.; Wereley, S.T.; Kompenhans, J. *Particle Image Velocimetry: A Practical Guide*; Springer: Berlin, Germany, 2007.
130. Ueno, W.; Tsuru, S.; Kinoue, Y.; Shiomo, N.; Setoguchi, T. PIV measurement of carbon dioxide gas-liquid two-phase nozzle flow. In Proceedings of the ASME-JSME-KSME Joints Fluids Engineering Conference, Seoul, Republic of Korea, 26–31 July 2015. AJKFluids2015-20169.
131. Valori, V. Rayleigh-Benard Convection of A Supercritical Fluid: (PIV) and Heat Transfer Study. Ph.D. Thesis, Delft University of Technology, Delft, The Netherlands, 2017.
132. Perry, A. *Hot-Wire-Anemometry*; Clarendon Press: Oxford, UK, 1982.
133. Fingerson, L.; Freymuth, P. Thermal Anemometers. In *Fluid Mechanics Measurements*; Goldstein, R., Ed.; Hemisphere: Washington, DC, USA, 1983.
134. Lomas, C. *Fundamentals of Hot Wire Anemometry*; Cambridge University Press: Cambridge, UK, 1986.
135. Bruun, H.H. *Hot-Wire Anemometry: Principles and Signal Analysis*; Oxford University Press: Oxford, UK, 1995.
136. Comte-Bellot, G. Hot-Wire Anemometry. *Annu. Rev. Fluid Mech.* **1976**, *8*, 209–231. [CrossRef]
137. Kovasznay, L.S.G. The Hot-Wire Anemometer in Supersonic Flows. *J. Aeronaut. Sci.* **1950**, *17*, 565–584. [CrossRef]
138. Spangenberg, W.G. *Heat Loss Characteristics of Hot-Wire Anemometers at Various Densities in Transonic and Supersonic Flow*; NACA Tech. Note No. 3381; National Advisory Committee for Aeronautics: Washington, DC, USA, 1955.
139. Morkovin, M.W. *Fluctuations and Hot-Wire Anemometry in Compressible Flows*; AGARDograph No. 24; NATO: Paris, France, 1956.
140. Horstman, C.C.; Rose, W.C. Hot-Wire Anemometry in Transonic Flow. *AIAA J.* **1977**, *15*, 395–401.
141. Rose, W.C.; McDaid, E.P. Turbulence Measurement in Transonic Flow. *AIAA J.* **1977**, *15*, 1368–1370. [CrossRef]
142. Stainback, P.C.; Johnson, C.B.; Basnett, C.B. Preliminary Measurements of Velocity, Density and Total Temperature Fluctuations in Compressible Subsonic Flow. In Proceedings of the AIAA 21st Aerospace Sciences Meeting, Reno, NV, USA, 10–13 January 1983. AIAA-83-0384.
143. Stainback, P.C. Some Influences of Approximate Values for Velocity, Density and Total Temperature Sensitivities on Hot Wire Anemometer Results. In Proceedings of the AIAA 24th Aerospace Sciences Meeting, Reno, NV, USA, 6–9 January 1986. AIAA-86-0506.
144. Stainback, P.C.; Nagabushana, K.A. Review: Hot-Wire Anemometry in Transonic and Subsonic Slip Flows. *ASME Fluids Eng.* **1997**, *119*, 14–18. [CrossRef]
145. Motallebi, F. A Review of the Hot-Wire Technique in 2-D Compressible Flows. *Prog. Aerospace Sci.* **1994**, *30*, 267–294. [CrossRef]
146. Johnston, R.; Fleeter, S. Compressible flow hot-wire calibration. *Exp. Fluids* **1997**, *22*, 444–446. [CrossRef]
147. de Souza, F.; Tavoularis, S. Hot-Wire Response in High-Subsonic Flow. In Proceedings of the AIAA 37th Aerospace Sciences Meeting and Exhibit, Reno, NV, USA, 11–14 January 1999. AIAA-99-0310.
148. Cukurel, B.; Acarer, S.; Arts, T. A novel perspective to high-speed cross-hot-wire calibration methodology. *Exp. Fluids* **2012**, *53*, 1073–1085. [CrossRef]
149. Reinker, F.; aus der Wiesche, S. Application of Hot-Wire Anemometry in the High Subsonic Organic Vapor Flow Regime. In *NICFD 2020, ERCOFTAC Series 28*; Pini, M., de Servi, C., Spinelli, A., di Mare, F., Guardone, A., Eds.; Springer International Publishing: Cham, Switzerland, 2021; pp. 135–143.
150. Hake, L.; Sundermeier, S.; Cakievski, L.; Bäumer, J.; aus der Wiesche, S.; Matar, C.; Cinnella, P.; Gloerfelt, X. Hot-Wire Anemometry in High Subsonic Organic Vapor Flows. In Proceedings of the ASME Turbo Expo 2022, Rotterdam, The Netherlands, 13–17 June 2022. GT2022-81686.
151. Hake, L.; aus der Wiesche, S.; Sundermeier, S.; Bienner, A.; Gloerfelt, X.; Cinnella, P. Grid-generated decaying turbulence in an organic vapor flow. In Proceedings of the 4th International Seminar on Non-Ideal Compressible Fluid Dynamics (NICFD2022), City University, London, UK, 3–4 November 2022.

152. Jones, G.S. Wind Tunnel Requirements for Hot-Wire Calibration. In Proceedings of the AIAA 18th Aerospace Ground Testing Meeting, Colorado Springs, CO, USA, 20–23 June 1994. AIAA-94-2534.
153. Yavuzkurt, S. A Guide to Uncertainty Analysis of Hot-Wire Data. *ASME J. Fluids Eng.* **1984**, *106*, 181–186. [CrossRef]
154. Smolyakov, A.V.; Tkachenko, V.M. *The Measurement of Turbulent Fluctuations*; Springer: Berlin, Germany, 1983.
155. Wyngaard, J.C. Measurement of small-scale turbulence structure with hot wires. *J. Sci. Instrum.* **1968**, *1*, 1105–1108. [CrossRef]
156. Hake, L.; Sundermeier, S.; aus der Wiesche, S.; Bienner, A.; Gloerfelt, X.; Matar, C.; Cinnella, P. CFD-supported data reduction of hot-wire anemometry signals for compressible organic vapor flows. In Proceedings of the XXVI Biennial Symposium on Measuring Techniques in Turbomachinery, Pisa, Italy, 28–30 September 2022.
157. Weiss, J.; Chokani, N.; Comte-Bellot, G. Constant-Temperature and Constant-Voltage Anemometer Use in a Mach 2.5 Flow. *AIAA J.* **2005**, *43*, 1140–1143. [CrossRef]
158. Roediger, T.; Jenkins, S.; Knauss, H.; Wolfersdorf, J.; Gaisbauer, U.; Kraemer, E. Time-Resolved Heat Transfer Measurements on the Tip Wall of a Ribbed Channel Using a Novel Heat Flux Sensor—Part I: Sensor and Benchmarks. *ASME J. Turbomach.* **2008**, *130*, 011018. [CrossRef]
159. Sieverding, C.; Manna, M. A Review on Turbine Trailing Edge Flow. *Int. J. Turbomach. Propuls. Power* **2020**, *5*, 10. [CrossRef]
160. Sieverding, C.H.; Heinemann, H. The Influence of Boundary Layer State on Vortex Shedding from Flat Plates and Turbine Cascades. *ASME J. Turbomach.* **1990**, *112*, 181–187. [CrossRef]

Disclaimer/Publisher's Note: The statements, opinions and data contained in all publications are solely those of the individual author(s) and contributor(s) and not of MDPI and/or the editor(s). MDPI and/or the editor(s) disclaim responsibility for any injury to people or property resulting from any ideas, methods, instructions or products referred to in the content.

International Journal of
Turbomachinery
Propulsion and Power

MDPI

Article

Transient 3D CFD Simulation of a Pelton Turbine—A State-of-the-Art Approach for Pelton Development and Optimisation †

Lukas Sandmaier *, Peter Meusburger and Helmut Benigni *

Institute of Hydraulic Fluid Machinery, Graz University of Technology, Kopernikusgasse 24/4, 8010 Graz, Austria
* Correspondence: lukas.sandmaier@tugraz.at (L.S.); helmut.benigni@tugraz.at (H.B.); Tel.: +43-316-873-8074 (L.S.)
† This Paper was Published in the Proceedings of the 18th Conference on Modelling Fluid Flow (CMFF'22), Budapest, Hungary, 30 August–2 September 2022.

Abstract: The complex flow conditions in Pelton turbines make it challenging to gain detailed insight into the local flow processes. However, CFD methods offer vast potential for developing and optimising Pelton turbines due to these flow conditions. In a comprehensive examination, a six-nozzle prototype Pelton turbine with 19 buckets has been investigated using 3D CFD simulations. First, the steady simulations of the manifold and the unsteady runner simulation have been performed with a mesh-based, commercial CFD code, whereby a two-equation turbulence model and the homogeneous two-phase model were used. Then, to limit the simulation time, symmetry was applied in the runner simulation, and also a strategic definition of the mesh element size in selected blocks of higher interest. Subsequently, the simulation results were analysed. Based on the first simulation results, the geometry of the distributor was modified in an iterative process to reduce losses and improve the jet shape. For the improvement of the latter, a characteristic number was introduced to quantify the secondary flows upstream of the nozzles, which act negatively on the jet shape. Furthermore, the results of the runner simulation were analysed with special regard to the jet-bucket interaction from the start to the end of the impingement cycle of a particular bucket. Finally, a potential efficiency increase could be derived from the summary.

Keywords: Pelton turbine; computational fluid dynamics; hydropower; numerical modelling

check for updates

Citation: Sandmaier, L.; Meusburger, P.; Benigni, H. Transient 3D CFD Simulation of a Pelton Turbine—A State-of-the-Art Approach for Pelton Development and Optimisation. *Int. J. Turbomach. Propuls. Power* **2023**, *8*, 10. https://doi.org/10.3390/ijtpp8010010

Academic Editors: János Gábor Vad, Csaba Horváth and Tamás Benedek

Received: 23 January 2023
Revised: 3 March 2023
Accepted: 6 March 2023
Published: 9 March 2023

Copyright: © 2023 by the authors. Licensee MDPI, Basel, Switzerland. This article is an open access article distributed under the terms and conditions of the Creative Commons Attribution (CC BY-NC-ND) license (https://creativecommons.org/licenses/by-nc-nd/4.0/).

1. Introduction

The application of computational fluid dynamics (CFD) has a long history in investigating, designing, and optimising hydraulic fluid machinery. This is especially true for Francis and Kaplan turbines, which can largely be transferred to a steady-state problem. Success and experience with the simulation of flow in Kaplan and Francis turbines subsequently led to the technique and know-how also being applied to components of Pelton turbines [1].

Due to the entirely different operating principle of Pelton turbines, the transfer of know-how took place in various stages. The research started with the components that are easier to simulate, namely the distributor and the nozzle, which have a primarily single-phased flow. The flow in the distributor, including the nozzles, was investigated in a single-phase flow setup in the early days of numerical simulations in Pelton hydraulics in [1]. Conclusions were made about possible losses and disturbing influences on the formation of the jet. Downstream of the nozzles, the flow is two-phased, which had to be considered in the modelling. Muggli and Zhang [2] carried out a two-phase flow simulation of the jet formation, based on a planar numerical grid using rotational periodicity, and compared the results with experimental data. However, the situation turns out to be much more complex when investigating the Pelton runner. As of the working principle, significantly

more complex flow phenomena occurred than is the case with Kaplan or Francis turbines. For example, the transient behaviour has to be considered when simulating the jet-bucket interaction and the bucket flow. In addition, high gradients of pressure, velocity and the two phases to be considered, water and air, further complicate numerical investigations. Splash water and droplets in the turbine housing cause ventilation losses due to interaction with the runner and the jets, which can hardly be tracked by the grid-based numerical simulations. In the early stage, CFD simulations of the jet-bucket interaction were carried out using the impingement of a stationary bucket, as shown in [3]. With the increasing performance of modern computers and data storage, the complexity of the numerical investigations carried out on Pelton turbines also progressed. This is increasingly evident in numerical experiments including the entire flow path of the Pelton turbine, as shown in [4].

Progress in this area enables an increasing understanding of the flow processes. It also reduces the dependence on model tests in the development process, even if these cannot be entirely dispensed. As a result, numerical simulation of Pelton turbines is no longer only used for theoretical analysis. On the contrary, it has already taken the path to a development and optimisation tool, not only for the distributor and the nozzles but also the turbine runner, as Židonis has shown in [5].

Many published studies on numerical investigations of Pelton turbines use a single-nozzle turbine model, e.g., as in [5–7]. However, suppose the aim is to investigate the overall performance of multi-nozzle Pelton turbines. In that case, it is sometimes crucial to consider all nozzles in the simulation setup. Only in this way can the bucket emptying be assessed, and possible jet interference be detected, which considerably influences the overall operating behaviour.

When using a Eulerian CFD code, the number of necessary grid cells respectively nodes may increase considerably, and so does the simulation time. This detail is especially significant when combining the number of nozzles and the number of buckets of a given turbine does not allow for symmetry effects in the circumferential direction. The Pelton turbine investigated in the present paper represents such a case, with a six-nozzle turbine and a runner with 19 buckets.

As an alternative to a Eulerian CFD code, Lagrangian CFD codes, such as Smoothed Particle Hydrodynamics (SPH) or Fast Lagrangian Solver (FLS), are used to analyse Pelton turbines. An overview of the application of SPH in Pelton turbines is given in [8].

2. Numerical Simulation

This study's numerical modelling and simulation were based on the commercial code Ansys CFX, Release 20.1. This code is widely used in hydraulic fluid machinery, as it has provided good results in the simulation of Pelton turbines in terms of accuracy. Still, it is associated with long simulation durations and correspondingly high numerical costs [9].

The numerical study of the given Pelton turbine was split into two distinct parts. In the first part, an analysis of the Pelton distributor was conducted, whereby the hydraulic losses and the jet shape were of interest. Therefore, the calculations were performed in a single- and two-phase setup.

In the second step, the behaviour of the runner was investigated. Regarding the runner simulation, the focus was laid both on the overall performance in the form of the hydraulic efficiency as well as the generated torque and the evaluation of the jet-bucket interaction. The latter was based on the pressure distribution analysis on the runner surface and the flow situation between the jet and bucket. Unlike in various publications [10–12], the numerical investigation did not cover a series of different operating points regarding a variation of the head H or the flowrate Q. In this case, rather a numerically stable and most efficient procedure for the simulation of Pelton turbine runners was developed. This procedure enables the modelling of a wide range of turbines, regardless of the number of nozzles or buckets, and finally, it allows for a numerically based, relative performance comparison of different runner geometries based on an identical load case.

2.1. Prototype Turbine Model

The study was based on the geometric model of a vertical six-nozzle turbine on a prototype scale. The final design of the distributor and the runner represent the result of an iterative design optimisation process which should reduce the losses in the distributor and increase the performance of the turbine runner. The result of the optimisation process was an entirely new design of the distributor, which was based on changes in the general layout and the design of the bifurcations compared to the baseline design, as it is shown in Figure 1. The design of the Pelton runner was slightly modified in its main dimensions throughout the study to improve efficiency, leading to three different runner geometries. Subject to changes were e.g., the length, width, trailing edge angles, bucket position, and depth of the bucket. Moreover, minor changes were applied to specific geometric details such as the design of the spitter and the cutout edge.

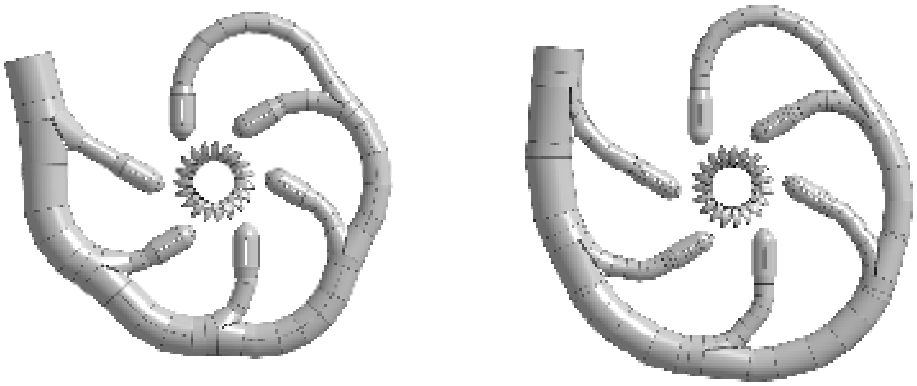

(**a**) (**b**)

Figure 1. The layout of the turbine: (**a**) baseline design; (**b**) final design.

The nominal operating point of the turbine was given with a head H_n of 382 m and a flowrate Q_n of 5.5 m^3/s, both reached a nozzle opening of 75%. The rotational speed n was given at 600 rpm.

The critical dimensions of the turbine are provided in Table 1, whereby D indicates the pitch diameter of the runner, B the inner width of the buckets, d_0 the jet diameter, and z the number of buckets. The ratio D/B gives a number, which is widely used to characterise Pelton turbines.

Table 1. Main dimensions of the turbine.

Characteristic Dimensions	Values
D	1310.00 mm
B	375.25 mm
d_0	115.00 mm
D/B	3.50
z	19

2.2. Numerical Modelling of the Distributor

The modelling of turbulence in the steady-state simulations of the distributor was realised with the k-ω SST model with automatic wall function.

The high-resolution scheme in ANSYS CFX was used to model the advection terms. In addition, relaxation factors for gradient-dependent advection terms were set to enhance numerical stability.

For modelling the two-phase flow, there are two reasonable options, the inhomogeneous model, and the homogeneous model. The first mentioned uses a set of conservation equations for each fluid with specific terms, which model the coupling of the different phases [13]. The higher number of equations results in a better performance compared to

the homogeneous model [14]. On the other hand, a higher computational effort is required to solve the equations. The homogeneous model assumes that both fluids share the same flow field. Therefore, only one set of conservation equations needs to be solved with an additional equation, which determines the concentration of each fluid in the gird cells. Thus, a less demanding numerical scheme is necessary than with the inhomogeneous model. The homogeneous model was preferred over the more accurate inhomogeneous model due to higher numerical costs. The selected model also provided a good trade-off between the duration of the simulations and the numerical stability.

Surface tension σ and gravity were not considered in the modelling, which is a common practice and well documented in the literature [4,5,15]. A comparison of both modelling approaches, with and without the consideration of surface tension or gravity, was performed by Židonis in his thesis [5], in which no significant differences in efficiency were shown.

The timestep Δ_t was set to 5×10^{-5} s, which provided a good balance between convergence speed and numerical stability. Additionally, double precision was selected to enhance the stability further.

The geometric model of the distributor was extended by two components. A cylinder with the length of 15 times the inlet diameter was added to the inlet of the distributor. Furthermore, another component was added at the outlets of the nozzles. These volumes correspond to the space in which the jets are formed. Only minor geometric simplifications were made to simplify the numerical modelling.

The geometry shown in Figure 2 represents the basis for spatial discretisation. The final mesh was composed of several blocks of structured and unstructured meshes. Components including rather complex geometry elements, e.g., bifurcations, were meshed with tetrahedral and pyramidal elements. The same mesh topology was used for the leading and the trailing edge of the support ribs in the nozzles and the area of the needle tip. The other elements of the geometry were discretised with structured meshes containing primarily prismatic and hexagonal elements. Along all solid walls, thin layers of prismatic elements were placed.

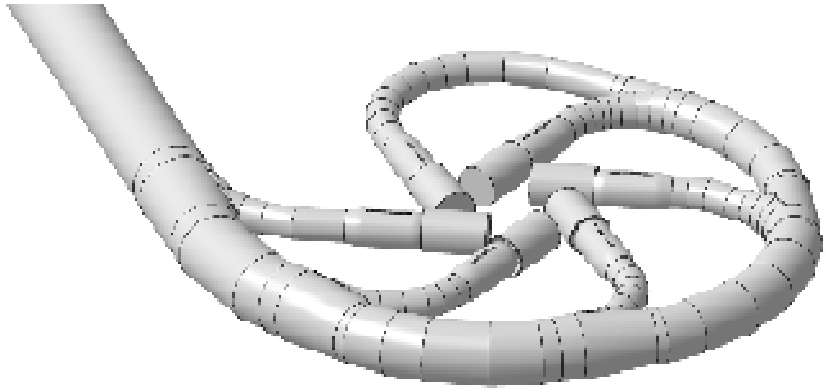

Figure 2. The geometry of the distributor simulation domain.

Figure 3 shows the mesh of the distributor model. In regions of particular interest or with high gradients in relevant flow variables, such as the nozzle exit and the area where the phase boundary of the jet was to be expected, the grid was refined (see Figure 4). Between the mesh components of the distributor and the nozzles general interfaces were placed. The remaining connections between structured and unstructured mesh topologies had a direct mesh connection.

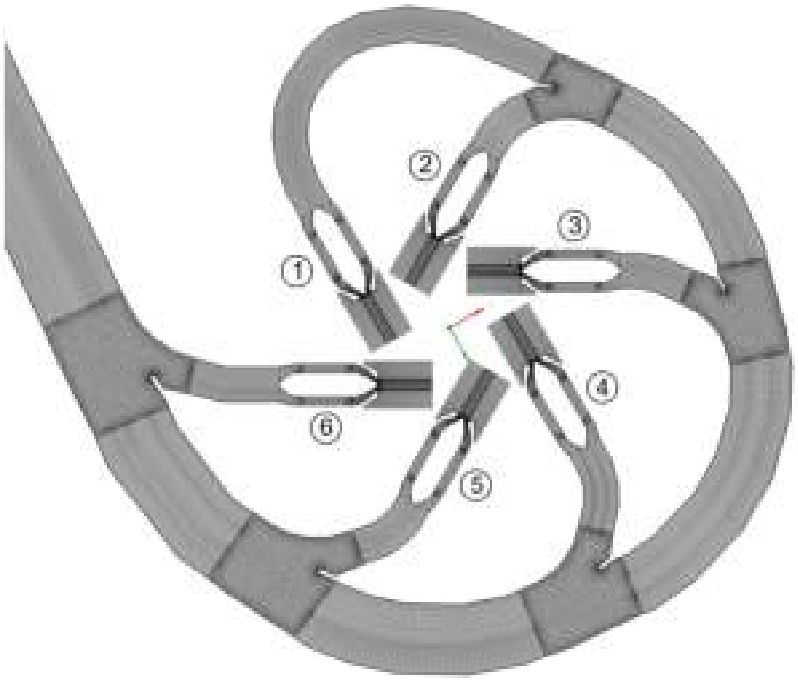

Figure 3. Distributor mesh in the symmetry plane with nozzle numbering and global coordinate system.

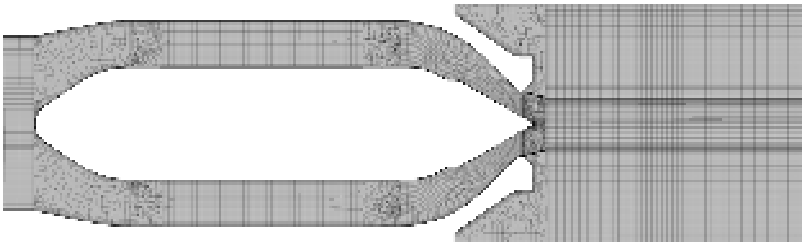

Figure 4. Mesh of the nozzle and jet area.

The mesh of the entire simulation domain had about 8.67 million nodes and 14.57 million elements in total. Additional mesh characteristics are summarised in Table 2.

Table 2. Distributor mesh quality characteristics.

Mesh Metric	Minimum	Maximum	Average
Min. Face Angle	11.3°	90.0°	57.8°
Max. Face Angle	60.0°	157.3°	97.2°
Aspect Ratio	1	351	24.1
Y Plus	-	-	41.1

Regarding the boundary conditions, all solid walls of the model were treated as smooth, no-slip walls, without any specific surface roughness defined. The boundary surfaces of the jet domains were modelled as opening boundaries with the relative pressure p_{rel} set to zero, while the reference pressure p_{ref} is equal to the atmospheric pressure p_{atm}. At the inlet a total pressure $p_{\mathrm{tot,\ inlet}}$ was imposed with a constant velocity distribution, which corresponds to the given hydraulic head of the turbine.

In order to accelerate the simulation and to increase the numerical stability results of single-phase simulations of the distributor were used to initialise the flow field. At the start of the simulation, the jet domains were filled with air.

2.3. Numerical Modelling of the Runner

In recent publications [9] the k-ω SST model was used for turbulence modelling in Pelton runner simulations. Perrig showed in his thesis [14], that the k-ω SST model outperforms the k-ε model in terms of accuracy. Similar behaviour was summarised in [16]. However, due to significantly, less stable numerical behaviour in runner simulations compared to the distributor simulations, the k-ε turbulence model was applied for the runner simulations. The lack of accuracy of the chosen model is seen as a minor problem since the overall degree of model simplifications is relatively high. Moreover, a relative comparison of different runner geometries, based on identical numerical settings, was not impaired by this.

In analogy to the distributor simulation, the high-resolution scheme was used to model the advection terms. The same relaxation factors as in the study of the distributor were applied. The Second Order Backward Euler scheme was selected for the time discretisation of the transient terms.

Analogous to the numerical modelling of the distributor, the homogenous model was used to model the two-phase flow in the runner. Concerning surface tension and gravity, the same assumption as in the numerical setup of the distributor was made.

The definition of the transient time step Δ_t is linked to a discrete angle of runner rotation. The size of the angle-step has been proven as crucial for some factors. A small step provides more stability to the numerical scheme, which leads also to faster convergence behaviour and a lower overall computation time. Both effects have been observed in several simulations. Moreover, the size of the timestep influences the simulation results concerning the torque. The best simulation behaviour was found with a timestep Δ_t of approximately 4.63×10^{-5} s, which corresponds to one-sixth of a degree runner rotation. In the solver settings, double precision was selected to further increase the numerical stability of the simulation.

The runner simulation was based on the geometric model given in Figure 5. The simulation domain is composed of three main components: the runner, the casing, and the nozzles. The former is defined as the rotating domain while the casing and the nozzles remain stationary. The runner is further split into two subdomains, which are indicated by different shadings in Figure 5. Subsequently, these subdomains serve differently in the analysis of the runner's performance. The medium grey shaded runner component is later used to analyse the performance, while the dark grey component represents some sort of dummy to complement the runner domain. The latter component was necessary to enable the modelling since the combination of six nozzles and 19 buckets did not allow the use of a rotational periodicity for the runner domain. An influence of this component on the results was not given.

To simplify the model, the distributor as well as the real turbine housing were not considered for the simulation. Moreover, the symmetric layout of Pelton turbines was used to further reduce the complexity of the geometric model. This is a common strategy, which is seen in various publications, e.g., [7,10,13]. A non-idealised jet configuration was used. Thus, the last section of the nozzle, the nozzle head, was included in the model to account for the effects of the fluid acceleration and the friction in the spear valve on the jet formation. The nozzle opening was set to 75%, which corresponds to the opening in the nominal operating point of the prototype turbine.

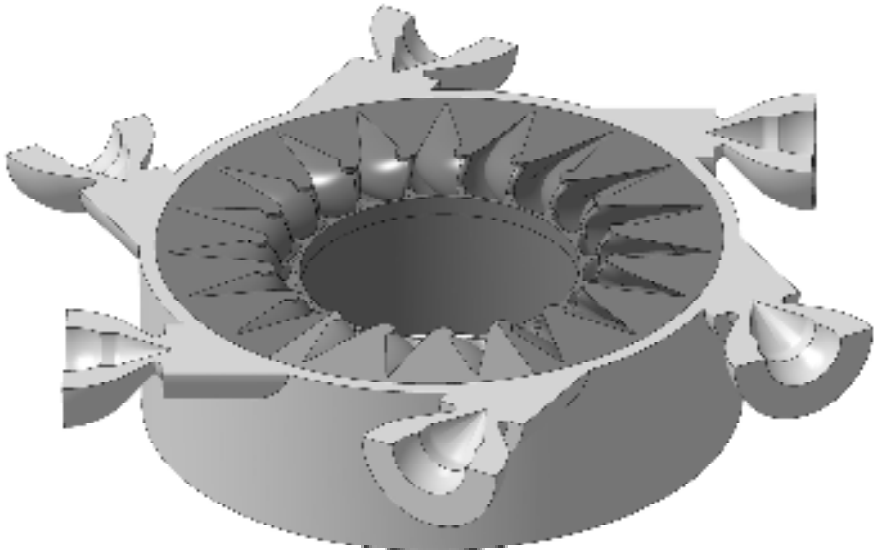

Figure 5. Geometric model of the runner simulation domains.

The numerical mesh of the geometry in Figure 5 is composed of components with structured and unstructured meshes (see Figure 6). The nozzles and the casing are represented by a structured mesh of prismatic elements. The two subdomains of the runner were split into two blocks. The first block contains the buckets and was therefore meshed with an unstructured, tetrahedral mesh. The second block of prismatic mesh elements adds up with the first one to complete the rotating runner subdomain. In areas with the strictly aligned flow, such as in the nozzle and jet area, the mesh cells are primarily oriented according to the main flow direction. The cell height in the stationary area was reduced near the sliding surface of the interface. In the rotating domain, no special treatment of the mesh was applied close to the sliding, since the defined cell size was considered sufficiently small. Grid refinements were placed in strategic areas, as shown for the distributor mesh. Near the walls of the runner as well as of the nozzle layers of prismatic elements were placed.

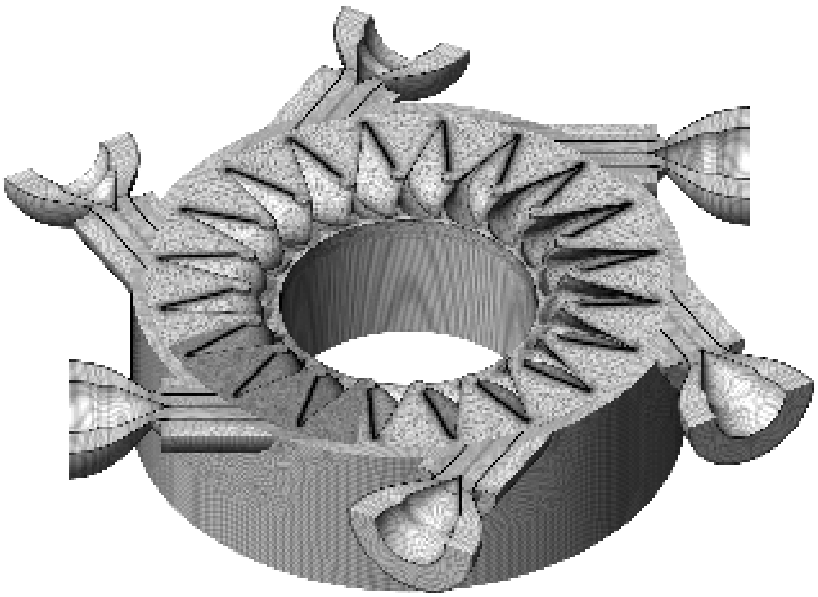

Figure 6. Numerical mesh of casing, nozzles, and the runner.

The subdomains of the runner meshed with two different approaches. The one, which incorporates only three consecutive buckets (medium grey shading in Figure 5), was meshed with a comparably high mesh density. The mesh of the other runner subdomain is

rather coarse. This approach allows to use of the entire symmetric runner half to be taken into account and yet limits the size of the numerical grid to a manageable number of nodes and elements.

For both subdomains, refinements were placed along the leading edge, the trailing edge as well as the cutout edge and its adjoining surfaces. A detailed view of the refined mesh of the buckets is given in Figure 7. The statistics of the mesh components of the runner simulation are given in Table 3. Quality characteristics of the runner simulation mesh are given in Table 4.

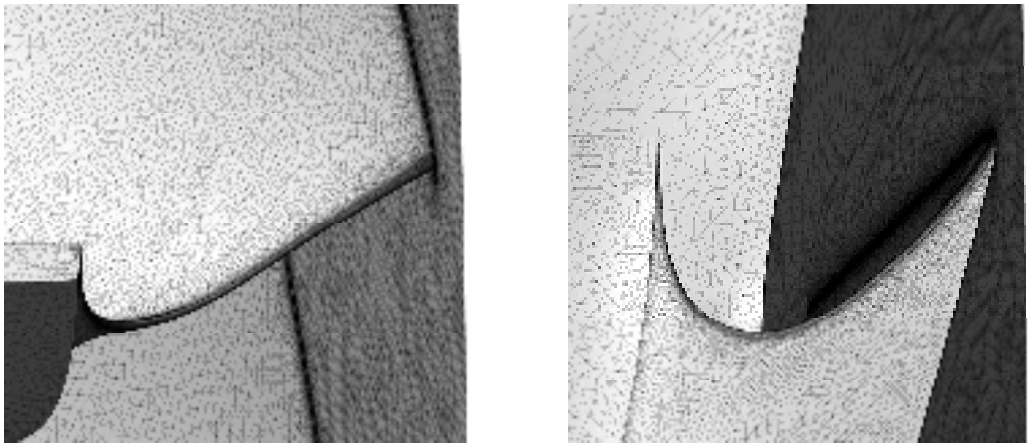

(**a**) (**b**)

Figure 7. Detailed view of the mesh refinements: (**a**) in the internal cutout region; (**b**) on the external cutout surface.

Table 3. Mesh statistics of the casing and the runner subdomains (in millions).

Mesh Region	Nodes	Elements
Nozzle, Casing	2.604	2.352
Runner fine	4.530	17.101
Runner coarse	5.597	16.511
Total	12.732	35.965

Table 4. Runner mesh quality characteristics.

Mesh Metric	Minimum	Maximum	Average
Min. Face Angle	10.4°	90.0°	47.9°
Max. Face Angle	60.0°	153.2°	92.5°
Aspect Ratio	1	226	6.3
Y Plus	-	-	53.1

Regarding the boundary conditions, the solid walls of the nozzle and the runner were treated in the same way as those of the distributor, which were modelled as no-slip walls, without any surface roughness defended. A symmetry condition was applied to the symmetry plane of the turbine model. The remaining boundary surfaces were treated with an opening boundary condition since the turbine housing was not considered. The relative pressure p_{rel} is set to zero, while the reference pressure p_{ref} was defined with the atmospheric pressure p_{atm}. Each nozzle has an inlet surface, which is perpendicular to the corresponding nozzle axis. On these a mass flow rate Q_{inlet} normal to the boundary was imposed. The link between the sliding meshes of the rotating runner and the stationary casing was treated with a transient rotor-stator interface.

At the start of the first simulation, a result of a distributor simulation with a corresponding nozzle opening was used to initialise the stationary domain. The rotating domain

was filled with air at the start of a simulation run. Subsequent simulations were then initialised with the results of previous transient turbine simulations.

3. Results

3.1. Results of the Distributor Analysis

The simulation of various Pelton distributor geometries in this study showed, that the applied changes to the geometry have led to a reduction of the hydraulic loss in the distributor and improved the flow situation upstream of the nozzles. The latter is important for good jet quality, which is indicated by a circular cross-section and a homogeneous velocity profile of the jet. The main drivers of the deterioration of the jet shape are secondary flows resulting from flow through the curved pipes as they are present upstream of the nozzles. At the exit of the curved pipe, a counterrotating Dean vortex structure forms due to a pressure gradient [17] which causes a stagnation point in the inner core of the pipe resulting in a typical perturbation of the jet cross-section as seen in Figure 8a.

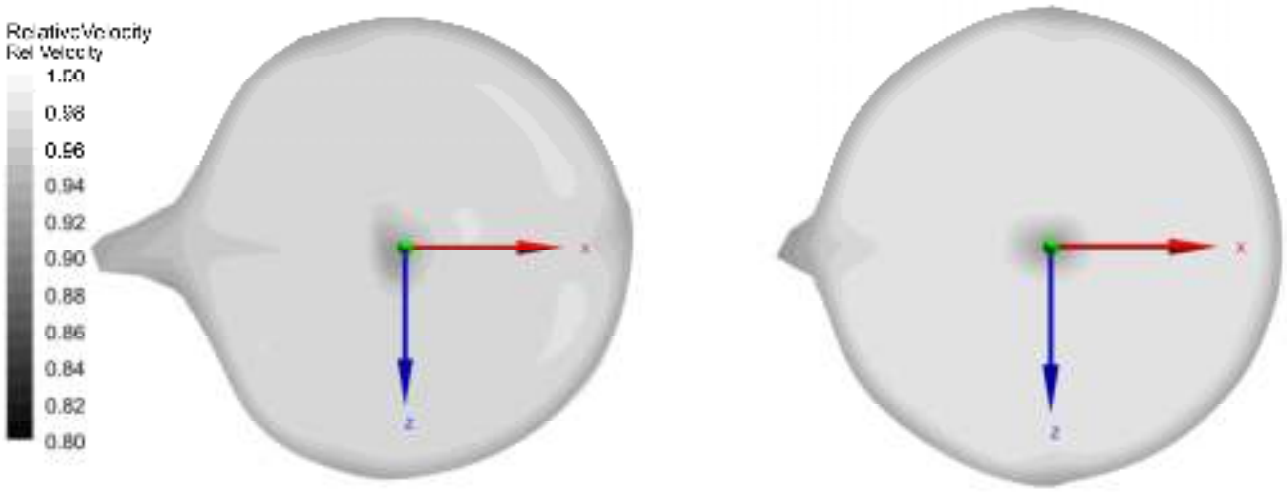

(**a**) (**b**)

Figure 8. Improvement of the jet cross-section of nozzle 4: (**a**) baseline design; (**b**) design update 2 (both Figures use the same velocity scale).

A direct correlation between the jet shape and quantitative flow characteristics is difficult to determine. To overcome this, a swirl number SN was introduced to quantify the intensity of secondary flow. The definition of the SN is given in Equation (1) whereby c_{circ} and c_{ax} are the velocities in circumferential and axial direction respectively on a given plane of the cross-section A.

$$SN = \frac{1}{A} \cdot \int_A \sqrt{\frac{c_{\mathrm{circ}}^2}{c_{\mathrm{ax}}^2}} \cdot \mathrm{d}A \tag{1}$$

For each nozzle, the velocities are referred to the corresponding nozzle axis (positive in jet direction). In the optimisation process of the distributor design, the SN was later used as an additional indicator for an improvement or a deterioration of the jet shape. If the SN decreases, an improvement of the jet shape can be expected, as smaller values indicate a lower intensity of the secondary flows, which primarily act negatively on the jet shape.

Figure 8 shows the cross-section of jet number 4 on a plane about 4.25 jet diameters downstream of the nozzle outlet, which was the jet with the most disturbed jet shape of all. The disturbance of the jet shape in Figure 8 is primarily caused by secondary flows, upstream of the nozzle. The velocity decrease in the boundary region is due to the interaction with air, while in the centre the wake of the needle tip is visible. The wake of the supportive ribs of the nozzle is barely pronounced. The impact of the ribs on the velocity distribution was already significantly reduced in the nozzle head, which can be

explained by a strong homogenisation due to the acceleration of the flow in the converging flow channel downstream of the ribs. The jet velocity, which is related to the theoretical velocity c_{th}, is plotted on the cross sections in a range of 0.80 to 1. The boundary of the cross-section is determined by a water volume fraction of 50%. c_{th} is given in Equation (2).

$$c_{th} = \sqrt{2 \cdot g \cdot H_n} \tag{2}$$

The left plot of Figure 8 corresponds to the baseline geometry of the distributor, and the right plot to the new design. The swirl numbers, which are evaluated at the nozzle inlet, are 0.121 and 0.032 respectively, which is equivalent to a reduction of about 70%. The swirl numbers of the other nozzles are given in Table 5.

Table 5. Comparison of the swirl numbers for the distributor.

Design	Nozzle 1	Nozzle 2	Nozzle 3	Nozzle 4	Nozzle 5	Nozzle 6
Baseline Design	0.027	0.039	0.041	0.032	0.036	0.023
New Design	0.057	0.115	0.069	0.121	0.087	0.065

Figure 9 shows pressure and the relative velocity in the nozzle exit region which is dominated by strong changes in flow quantities and the flow physics [18] as the flow is accelerated close to c_{th}, the pressure drops accordingly to the atmospheric pressure. The velocity distribution in the symmetry plane of the distributor clearly shows the wake of the needle tip, which remains over the entire length of the jet (see Figure 8).

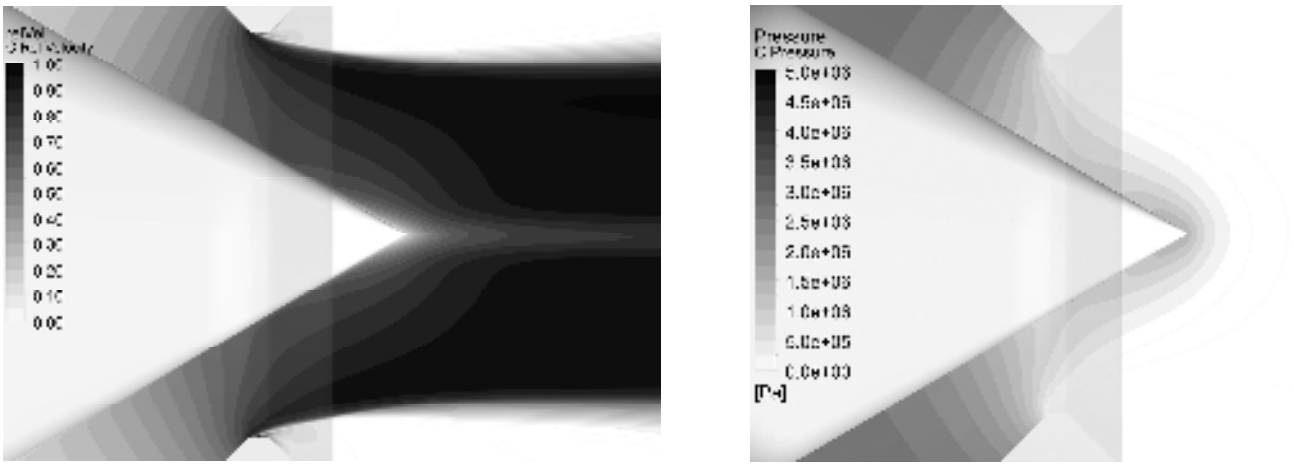

(**a**) (**b**)

Figure 9. Velocity and pressure distribution at the nozzle exit: (**a**) relative velocity; (**b**) pressure.

The hydraulic losses H_v in the distributor are determined as a hydraulic head loss from the inlet to the outlet of the corresponding nozzles. H_v is given in Equation (3) whereby $\overline{p}_{tot,\,Inlet}$ and $\overline{p}_{tot,\,Nozzle}$ represent mass flow averaged total pressure values at the inlet and a plane at the nozzle exit. This plane was placed 30 mm upstream from the corresponding nozzle mouthpiece to avoid the influence of flow separation and the changing flow physics of the flow on the result.

$$H_v = \frac{\overline{p}_{tot,Inlet} - \overline{p}_{tot,\,Nozzle}}{\rho \cdot g} \tag{3}$$

These were lowered by roughly 16% compared to the baseline design. A comparison of the head losses, which are related to the nominal head H_n, are given in Figure 10. The largest share of the losses was caused by the nozzle, while the distributor contributed less than 20% to the head loss.

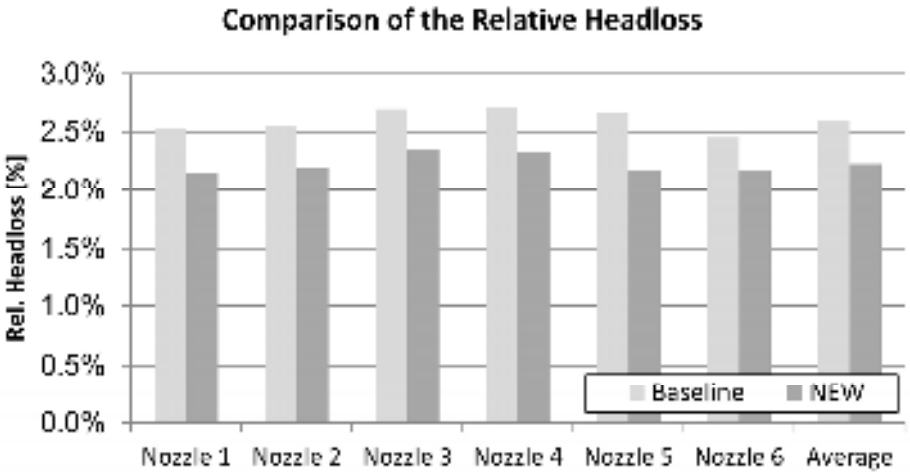

Figure 10. Comparison of the relative headloss.

3.2. Results of the Runner Simulation

The results of the three runner simulations, based on different runner geometries, are analysed with a special procedure. For the analysis of the turbine performance in general, a reference bucket was defined. The reference bucket corresponds to the second bucket of the light grey shaded and comparably fine-meshed runner domain in Figure 5. Additionally, to the reference bucket, the leading and the successive bucket are considered to analyse possible, negative interactions on the runner outside surface.

To calculate the runner torque T_{Runner}, a "bucket load cycle" was defined. One load cycle corresponds to what a single bucket experience during 360 timesteps or 60° of runner rotation, since the angular spacing between the nozzles in the case of the present six-nozzle turbine equals 60°. In this period every bucket is once impinged by a jet.

The bucket torque was analysed for each timestep based on the pressure and the wall shear stresses acting on the bucket surface, with pressure values lower than the vapour pressure p_{vap} set to p_{vap}. The limitation of the pressure was necessary to avoid a too high torque contribution, especially from the exterior bucket surface, due to nonphysical pressure values below p_{vap}. The arithmetic average of the torque $\overline{T}_{\text{ref}}$ over a time span of 360 timesteps or 60° of runner rotation, which is acting on the reference bucket, was finally used to calculate the runner torque. Additionally, $\overline{T}_{\text{ref}}$ was used as an indicator for the state of convergence of the simulation. A constant level of $\overline{T}_{\text{ref}}$ indicates a steady-state operation as well as a sufficiently converged solution. The total torque T_{Runnner} of the entire turbine runner corresponds to Equation (4).

$$T_{\text{Runner}} = 2 \cdot \overline{T}_{\text{ref}} \cdot z \tag{4}$$

The efficiency η is calculated from $\overline{T}_{\text{ref}}$ and the corresponding hydraulic head H at the inlets as well as the total imposed flow rate Q at the inlets. The efficiency is given in Equation (5), whereby ω represents the angular velocity of the turbine, ρ the density and g the gravitational acceleration.

$$\eta = \frac{z \cdot \overline{T}_{\text{ref}} \cdot \omega}{Q \cdot H \cdot \rho \cdot g} \tag{5}$$

The simulation of the baseline runner design in this study has shown an efficiency of 89.49%. The periodic curve of the generated torque, normalised by $\overline{T}_{\text{th}}$ for the inside, the outside and the total torque is shown in Figure 11. The splitting of the bucket surface into an interior and an exterior surface is depicted in the upper left-hand corner of Figure 11. The dark grey shaded surface indicates the interior, and the light grey one is the exterior surface. $\overline{T}_{\text{th}}$ represents a theoretical torque of a bucket based on the simulated head and

the flow rate in the nominal operating point with an efficiency of 100%. $\overline{T}_{\text{th}}$ is given in Equation (6).

$$\overline{T}_{\text{th}} = \frac{Q_n \cdot H \cdot g \cdot \rho}{19 \cdot \omega} \tag{6}$$

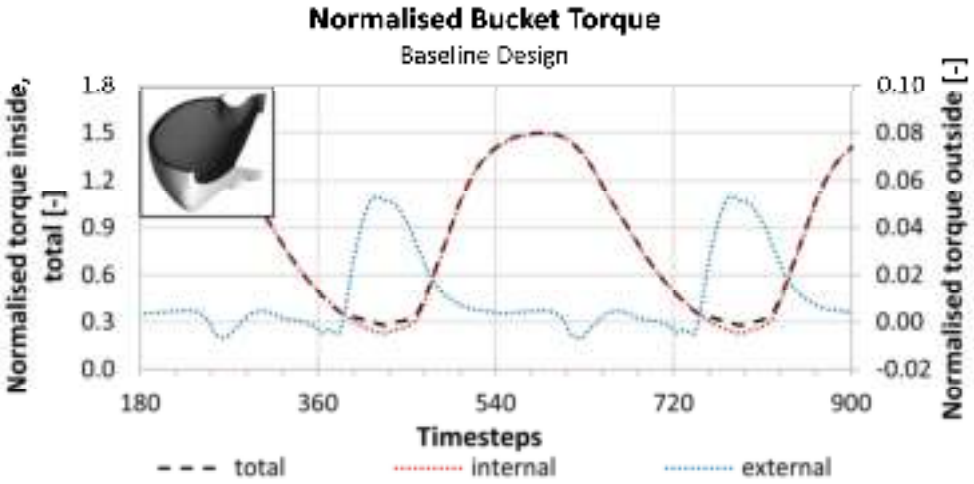

Figure 11. Normalised torque (baseline design).

The torque of the primarily impinged interior surface and the exterior bucket surface add up to the torque contribution of the reference bucket. The external curve in Figure 11 indicates the start of the load cycle with its sharp rise after roughly 390 timesteps. A low-pressure zone on the exterior surface causes the growth of the torque in this phase (see Figure 12a). Perrig reported in his thesis the existence of such an external torque and explained it with the Coanda Effect [14].

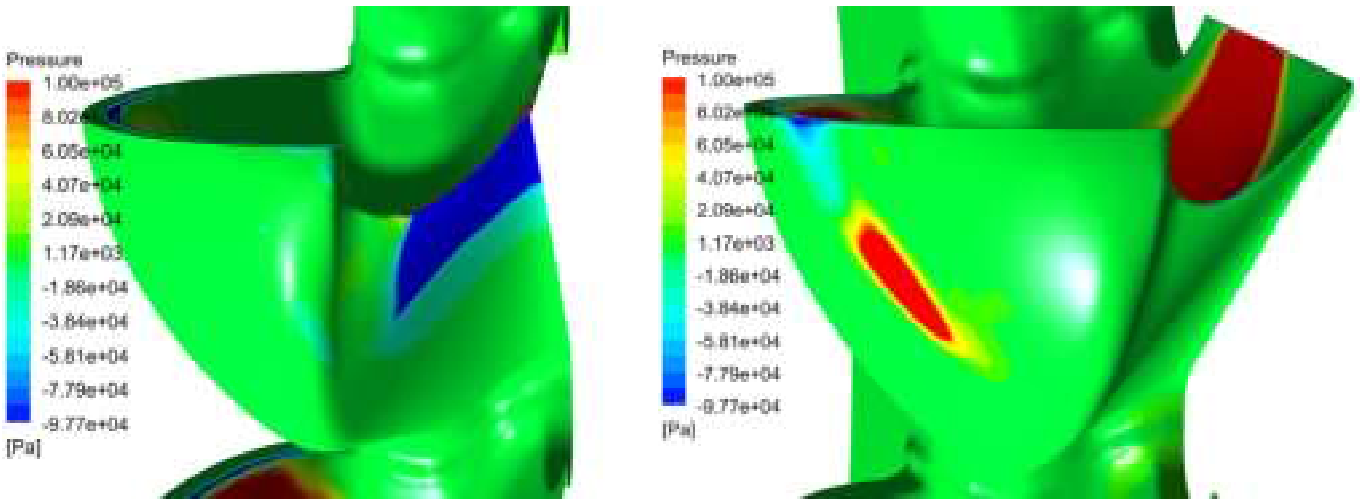

(**a**) (**b**)

Figure 12. Pressure distribution on the runner exterior surface of the baseline design; (**a**) low pressure on the external cutout surface; (**b**) increased pressure on the lateral exterior bucket surface.

However, due to non-appropriate trailing edge angles, the same curve shows a loss following timestep 610, which is of significantly lower magnitude due to the smaller area affected and the different orientation of the affected surface. The impingement of the external bucket surface is caused by water, which is exiting the leading bucket. A zone of increased pressure on the exterior surface indicates the source of the loss (see Figure 12b).

The bucket or the runner geometry design was modified to overcome adverse effects in an iterative process, as seen in the results of the baseline geometry simulation. Changes

to the bucket width, the trailing edge angles, as well as the splitter and the cutout design have improved the efficiency compared to the baseline runner design. As a result, an efficiency of 90.42% was reached.

Another set of geometry parameters of the Pelton bucket was changed consecutively in a second approach. As a result, the bucket width was slightly increased compared to the first design iteration process, and an increase in the bucket depth was realised. In addition, the positioning of the bucket on the pitch circle diameter was changed towards a smaller bucket position angle. Finally, the leading edge (splitter) and the cutout edge were further altered compared to the first design update. In the end, the numerically calculated efficiency was increased to a level of 90.87% by those measures.

Figure 13 shows the normalised torque of the second design update. Additionally, the total torque of the baseline design and the design update 1 is overlaid (dashed, green and yellow curves, respectively).

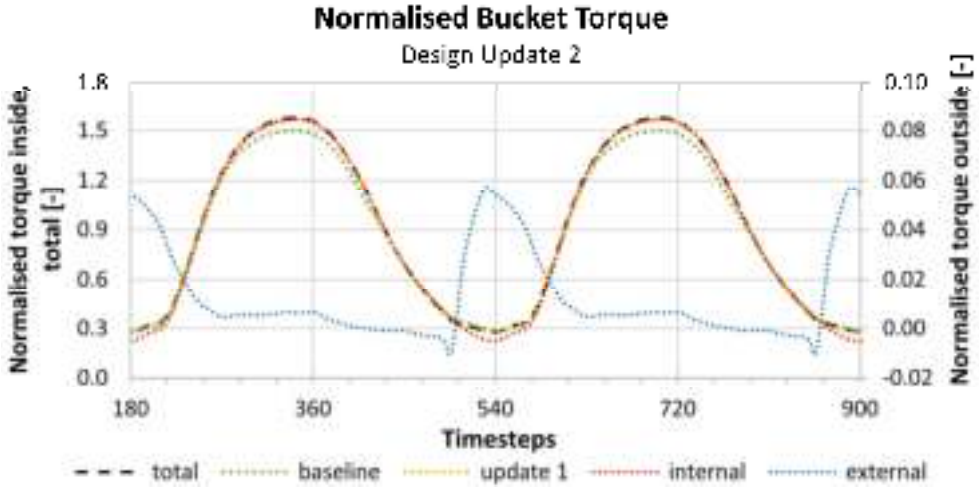

Figure 13. Normalised torque (design update 2 vs. baseline and design update 1).

In addition to the change of the bucket position angle, the increase in the bucket width and the bucket depth significantly contributed to a remarkable rise in the magnitude of the internal torque compared to the baseline and a small increase compared to the design update 1. On the other hand, the magnitude of the external torque at its maximum remained at a similar level compared to the baseline, which shows a minor impact of the changed bucket position on the external torque. However, the external torque load cycle average is still slightly higher because of the modified trailing edge angles.

4. Conclusions

While the simulation of the Pelton distributor for optimisation is quite common these days, the numerical investigation of the Pelton runner raises more questions.

As presented in this paper, the numerical approach to simulate Pelton runners, primarily of multi-nozzle turbines, should give a direction for an efficient way to analyse their hydraulic behaviour. By focusing on a single reference bucket, especially the numerical grid of the runner domain reduces to a manageable size. Furthermore, with a smaller mesh but still preserving the advantage of a high spatial discretisation in the selected regions, the computational costs and the required simulation time can be reduced significantly. Thus, numerical simulation has come one step closer to possible utilisation for the design and optimisation of Pelton runners.

Within the approach presented, three different Pelton runner designs were analysed with a consistent numerical setup, resulting in efficiencies of 89.49%, 90.42% and 90.87% for the baseline design and two design updates, respectively.

Nevertheless, the calculated efficiencies are partly subject to strong model assumptions and simplifications, such as the non-consideration of the turbine housing, the missing

impact of the distributor, and the flow modelling. Therefore, it is essential to point out that the efficiencies given in this paper should not be confused with experimentally determined efficiencies.

In various publications, see e.g., [4,5,10], discrepancies between numerically simulated and experimentally measured efficiencies of Pelton turbines were reported. Whereby over- and underprediction have been shown, primarily depending on the numerical modelling, including mesh density, and physical modelling. Based on this knowledge, the reported efficiency enhancement of 1.38% points between the baseline design and the design update 2 is primarily regarded as an indicator of the actual improvement rather than an absolute value for the efficiency enhancement. Verification of the simulation results still has not yet been conducted based on a model test.

Author Contributions: Conceptualization, L.S. and H.B.; methodology, L.S.; validation, L.S., P.M. and H.B.; formal analysis, H.B.; investigation, L.S.; writing—original draft preparation, L.S.; writing—review and editing, L.S.; visualization, L.S.; supervision, P.M. and H.B.; project administration, L.S.; All authors have read and agreed to the published version of the manuscript.

Funding: This research received no external funding.

Institutional Review Board Statement: Not applicable.

Data Availability Statement: Not applicable.

Conflicts of Interest: The authors declare no conflict of interest.

References

1. Keck, H.; Sick, M. Thirty years of numerical flow simulation in hydraulic turbomachines. *Acta Mech.* **2008**, *201*, 211–229. [CrossRef]
2. Sick, M.; Schindler, M.; Drtina, P.; Schärer, C.; Keck, H. Numerical and experimental analysis of Pelton turbine flow. Part 1: Distributor an Injector. In Proceedings of the IAHR Symposium, Charlotte, NC, USA, 6–9 August 2000.
3. Muggli, F.A.; Zhang, J.; Schärer, C.; Geppert, L. Numerical and experimental analysis of Pelton turbine flow. Part 2: The Free Surface Jet Flow. In Proceedings of the IAHR Symposium, Charlotte, NC, USA, 6–9 August 2000.
4. Zoppé, B.; Pellone, C.; Maitre, T.; Leroy, P. Flow analysis inside a Pelton turbine bucket. *J. Turbomach.* **2006**, *128*, 500–511. [CrossRef]
5. Zeng, C.; Xiao, Y.; Luo, Y.; Zhang, J.; Wang, Z.; Fan, H.; Ahn, S.-H. Hydraulic performance prediction of a prototype four-nozzle Pelton turbine by entire flow path simulation. *Renew. Energy* **2018**, *125*, 270–282. [CrossRef]
6. Židonis, A. Optimisation and Efficiency Improvement of Pelton Hydro Turbine Using Computational Fluid Dynamics and Experimental Testing. Ph.D. Thesis, Lancaster University, Lancaster, UK, 2015.
7. Rossetti, A.; Pavesi, G.; Cavazzini, G.; Santolin, A.; Ardizzon, G. Influence of the bucket geometry on the Pelton performance. *Inst. Mech. Eng. Part A J. Power Energy* **2014**, *228*, 33–45. [CrossRef]
8. Perrig, A.; Avellan, F.; Kueny, J.-L.; Farhat, M.; Parkinson, E. Flow in a Pelton turbine bucket: Numerical and experimental investigations. *J. Fluids Eng.* **2006**, *128*, 350–358. [CrossRef]
9. Rentschler, M.; Marongiu, J.C.; Neuhauser, M.; Parkinson, E. Overview of SPH-ALE applications for hydraulic turbines in ANDRITZ Hydro. *J. Hydrodyn.* **2018**, *30*, 114–121. [CrossRef]
10. Bhattarai, S.; Vichare, P.; Dahal, K.; Al Makky, A.; Olabi, A.G. Novel trends in modelling techniques of Pelton Turbine bucket for increased renewable energy production. *Renew. Sustain. Energy Rev.* **2019**, *112*, 87–101. [CrossRef]
11. Jošt, D.; Mežnar, P.; Lipej, A. Numerical prediction of Pelton turbine efficiency. *IOP Conf. Ser. Earth Environ. Sci.* **2010**, *12*, 12080. [CrossRef]
12. Xiao, Y.; Wang, Z.; Zhang, J.; Zeng, C.; Yan, Z. Numerical and experimental analysis of the hydraulic performance of a prototype Pelton turbine. *Inst. Mech. Eng. Part A J. Power Energy* **2014**, *228*, 46–55. [CrossRef]
13. Zeng, C.; Xiao, Y.; Wang, Z.; Zhang, J.; Luo, Y. Numerical analysis of a Pelton bucket free surface sheet flow and dynamic performance affected by operating head. *Inst. Mech. Eng. Part A J. Power Energy* **2017**, *231*, 182–196. [CrossRef]
14. Santolin, A.; Cavazzini, G.; Ardizzon, G.; Pavesi, G. Numerical investigation of the interaction between jet and bucket in a Pelton turbine. *Inst. Mech. Eng. Part A J. Power Energy* **2009**, *223*, 721–728. [CrossRef]
15. Perrig, A. Hydrodynamics of the Free Suface Flow in Pelton Turbine Buckets. Ph.D. Thesis, EPFL, Lausanne, Switzerland, 2007.
16. Židonis, A.; Aggidis, G.A. State of the art in numerical modelling of Pelton turbines. *Renew. Sustain. Energy Rev.* **2015**, *45*, 135–144. [CrossRef]

17. Chitrakar, S.; Solemslie, B.W.; Neopane, H.P.; Dahlhaug, O.G. Review on numerical techniques applied in impulse hydro turbines. *Renew. Energy* **2020**, *159*, 843–859. [CrossRef]
18. Drazin, P.G.; Reid, W.H. (Eds.) *Hydrodynamic Stability*; Cambridge University Press: Cambridge, UK, 2010.

Disclaimer/Publisher's Note: The statements, opinions and data contained in all publications are solely those of the individual author(s) and contributor(s) and not of MDPI and/or the editor(s). MDPI and/or the editor(s) disclaim responsibility for any injury to people or property resulting from any ideas, methods, instructions or products referred to in the content.

International Journal of
Turbomachinery
Propulsion and Power

MDPI

Article

Leading Edge Bumps for Flow Control in Air-Cooled Condensers †

Lorenzo Tieghi [1,*], Giovanni Delibra [1], Johan van der Spuy [2] and Alessandro Corsini [1]

[1] Department of Mechanical and Aerospace Engineering, Faculty of Industrial and Civil Engineering, Sapienza University of Rome, Via Eudossiana 18, 00184 Rome, Italy
[2] Department of Mechanical & Mechatronic Engineering, Faculty of Mechanical Engineering, Stellenbosch University, Private Bag X1, Cape Town 7602, South Africa
* Correspondence: lorenzo.tieghi@uniroma1.it; Tel.: +39-06-445-85234
† This paper was published in the Proceedings of the 18th Conference on Modelling Fluid Flow (CMFF'22), Budapest, Hungary, 30 August–2 September 2022.

Abstract: Air-cooled condensers (ACCs) are commonly found in power plants working with concentrated solar power or in steam power plants operated in regions with limited water availability. In ACCs, the flow of air is driven toward the heat exchangers by axial fans that are characterized by large diameters and operate at very high mass flow rates with a near-zero static pressure rise. Given the overall requirements in steam plants, these fans are subjected to inflow distortions, unstable operations, and are characterized by high noise emissions. Previous studies show that leading edge bumps in the tip region of axial fans can effectively reduce the sound pressure levels without affecting the static efficiency. Nevertheless, the effects of this treatment in terms of flow patterns and heat exchange in the whole ACC system were not investigated. In this work, the effect of leading edge bumps on the flow patterns is analyzed. Two RANS simulations were carried out using OpenFOAM on a simplified model of the air-cooled condenser. The fans are simulated using a frozen rotor approach. Turbulence modeling relies on the RNG k-epsilon model. The fan is characterized by a diameter of 7.3 m and a 333 m^3/s volumetric flow rate at the design point. The presence of the heat exchanger is modeled using a porous medium. The comparison between the flow fields clearly exerts that the modified blade is responsible for the redistribution of radial velocities in the rotor region. This drastically reduces the losses related to the installation of the fan in a real configuration.

Keywords: air-cooled condensers; CFD; flow control; inflow distortion; leading edge appendages

check for updates

Citation: Tieghi, L.; Delibra, G.; van der Spuy, J.; Corsini, A. Leading Edge Bumps for Flow Control in Air-Cooled Condensers. *Int. J. Turbomach. Propuls. Power* **2023**, *8*, 9. https://doi.org/10.3390/ijtpp8010009

Academic Editors: János Gábor Vad, Csaba Horváth and Tamás Benedek

Received: 16 January 2023
Revised: 1 March 2023
Accepted: 7 March 2023
Published: 9 March 2023

Copyright: © 2023 by the authors. Licensee MDPI, Basel, Switzerland. This article is an open access article distributed under the terms and conditions of the Creative Commons Attribution (CC BY-NC-ND) license (https://creativecommons.org/licenses/by-nc-nd/4.0/).

1. Introduction

Condensers in steam power plants can be either water- or air-cooled. Usually, the first solution is preferred because it guarantees a higher overall efficiency, given the lower ancillary operational costs involved, and is a more compact solution. However, some power plants require air-cooled condensers, usually because of the lack of cooling water near the installation site. That is the case for concentrated solar power (CSP) plants with a bottoming Rankine cycle, as CSP plants are commonly installed in desertic areas, or for large steam plants such as [1], which are installed in desertic areas near largely populated cities.

For this work, we will refer to air-cooled condensers (ACCs) and their typical arrangement, in particular the design of fans inside these units. The ACC assembly comprises a series of cooling units (>400 in a power plant) where large axial fans feed fresh air to a series of heat exchangers, where the steam condensates. The typical arrangement, shown in Figure 1, is that of an A-frame condenser unit with the fan inlet placed several meters above the ground and the heat exchangers on top of the fan.

These fans are operated with very high volume flow rates (250 to 400+ m^3/s) and a very low static pressure rise (100 to 300 Pa). This unusual combination results in a design characterized by a large diameter (6–12 m), a low hub-to-tip ratio (0.25–0.4), and a rotational velocity between 100 and 200 rpm. Being so large and mounted on very high

(>30 m) structures to provide a sufficiently wide inflow, these fans are often characterized by a large and irregular tip clearance due to assembly issues that eventually reflect the fan efficiency [2].

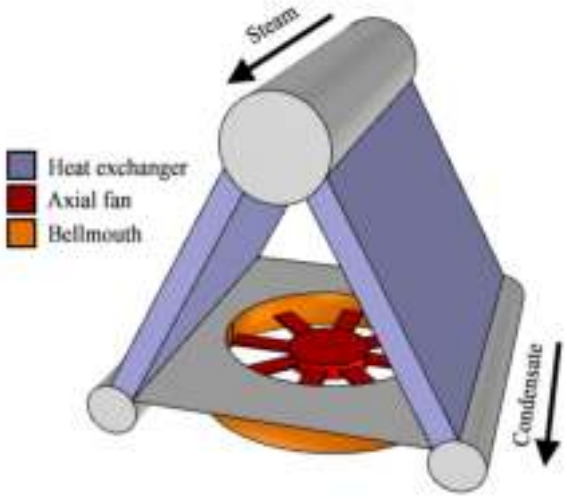

Figure 1. A-frame arrangement for an ACC unit.

The operations of these fans are also critical, as their efficiency drops when working with a lateral wind condition, in sandy environments, or with extreme environmental temperatures. In these conditions, the volume dilatation of the structures can in fact, significantly impact the tip gap, with possible effects on fan efficiency, vibrations, mechanical failures, and noise emissions. Noise is in fact one of the problems of large ACCs due to the high number of fans involved [3,4].

Among the possible strategies available to fan designers to tackle part of these problems, sinusoidal leading edges were proposed to control the trailing edge separation, the evolution of the tip leakage vortex, and the noise. Developed from biomimicry assumptions on the hydrodynamics of humpback whale fin tubercles [5], these leading edge modifications were found to change the dynamics of separation and loss of lift capabilities in NACA four-digit modified airfoils. The control mechanism was associated with counter-rotating vortex pairs shed from the serrations of the leading edge. At very high angles of attack (i.e., when the airfoil stalls), this vortex pair is responsible for controlling trailing edge separation and, in particular, limiting it in the region of the trailing edge that corresponds to the troughs of the leading edge sinusoid. Later studies, based on unsteady computations, have revealed that a secondary motion arises in the spanwise direction, with secondary phenomena resulting in a secondary shedding frequency that involves the whole blade span [6]. The separation control capability of leading edge serrations was exploited in modified axial fan geometries to control the development of the tip leakage vortex along the suction side of the rotor, resulting in controlled stall dynamics [7]. Moreover, when dealing with noise, experimental and numerical findings [8,9] show how sinusoidal leading edges result in a change in the acoustic signature of the fan.

In the framework of the H2020 MinwaterCSP [10], we designed a fan for ACCs that is now in operations at the Stellenbosh University. This fan is running in an ACC unit in real conditions and is characterized by limitations that can result in distorted inflow conditions and a reduction in the volume flow rate. This is a consequence of the nearby university buildings and of a water channel that flows below the test rig. Among the MinwaterCSP requirements for this fan, limiting the noise emissions was a key factor, as in real ACCs, the sound emissions from hundreds of units pose health issues for people and fauna. In this case, however, the real problem comes from the proximity of the university and the presence of staff and students. For these reasons, a preliminary study of the effects of the modified geometry on the aerodynamics of this fan is presented here.

2. Numerical Methodology

The computational domain is chosen based on the experimental apparatus that is described in [2]. It describes a full-scale A-type air-cooled condenser [11]. This ACC experimental configuration includes a grid downstream of the fan, which was modeled using a porous medium.

The structural supports to the exchanger are not included in the final model, their effect being minimal from an aerodynamic point of view. The domain, which is normalized by the rotor diameter D, is reported in Figure 2. The domain is symmetric with respect to the fan; therefore, each of the four lateral boundaries is located at 1.315 D from the exchanger walls.

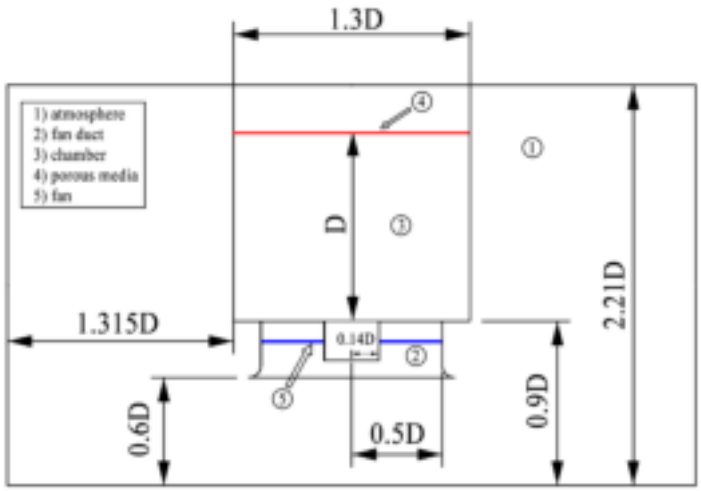

Figure 2. Front view of the numerical domain.

The fan is an eight-blade low-speed axial fan. Rotor diameter is 7.3 m, with a hub-to-tip ratio equal to 0.284. Tip clearance is set to 0.2% of the blade tip chord. Blade tip chord and chord-based Reynolds numbers are 825 mm and 4.65×10^5, respectively. The rotational speed of the fan is 151 rpm. The fan provides 105 Pa of total-to-static pressure at the nominal volumetric flow rate of 333 m^3/s. The design process of both the fan and its modified version are reported in [12]. The leading edge bumps are designed by varying the blade chord of $+/-5\%$, following a sinusoidal law in the outer 25% of the blade span. The original blade, here labeled as datum fan, and its modified version, here labeled as whale fan, are shown in Figure 3.

Figure 3. Datum (**left**) and whale (**right**) fan geometries.

The computational grid was generated for both geometries using the snappyHexMesh utility of the OpenFOAM v2106 library. The base grid entails 0.8 million cells with unity aspect ratio and a cell size of approximately 0.13 m. The grid is sequentially refined in the whole exchanger and in the rotor region, as shown in Figure 4.

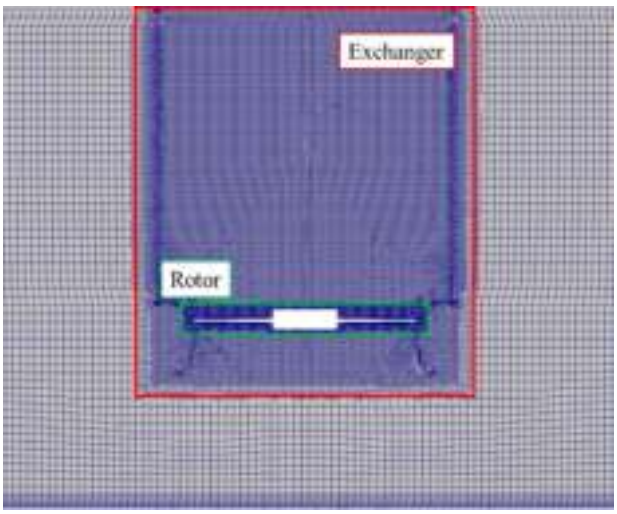

Figure 4. Grid refinements.

Due to the large computational domain, the grid was designed for high Reynolds computation. Therefore, the wall spacing was set to achieve a $y^+ = 100$ on the first layer of cells.

A grid sensitivity analysis on the datum fan configuration was performed using total-to-static pressure rise as convergence parameter. Results are shown in Figure 5, showing that a grid refinement of 20 million cells is sufficient for this setup. Two million cells are used to model the external atmosphere, 15 million in the rotor region, and 3 million in the heat exchanger. A visualization of the grids on the whale fan rotors is provided in Figure 6.

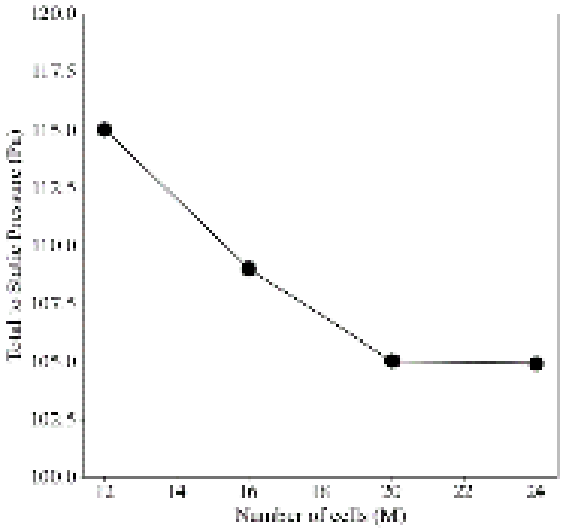

Figure 5. TTS pressure as a function of the number of cells, datum blade.

The porous medium is modeled using the Darcy–Forchheimer relationship for the pressure drop in the heat exchanger:

$$\frac{\partial p}{\partial x_j} = -\frac{\mu}{\kappa} U_j - \frac{\mu}{\kappa_1} U_j^2 \tag{1}$$

This pressure gradient acts as sink term in the momentum equation. The coefficients of Equation (1) were derived from the geometry of the squared grid in the test rig, which has a characteristic length of 5 cm, following the methodology reported in [13]. Since the flow

is characterized by a predominant axial direction, the coefficients in orthogonal directions are set to 10^{10}.

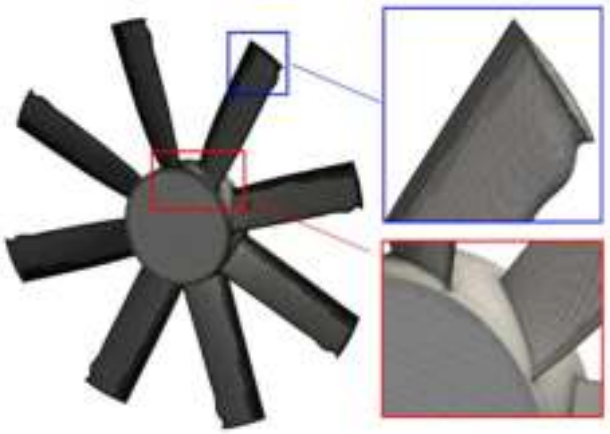

Figure 6. Mesh of the fan and details of the grid at blade tip and hub, whale fan design.

Turbulence modeling relies on the RNG k-epsilon model [14]. The steady computations are based on a frozen rotor approach and the incompressible equations are solved using the SIMPLE solver. Convergence was assessed by the torque of the fan and the velocity in probes upstream and downstream of the fan. The linearized systems of equations were solved using a smoothSolver for all the quantities except for pressure, which was solved using a conjugate gradient solver. Tolerance for convergence was set to 10^{-6} for all quantities except pressure, which was set to 10^{-4}.

A scheme of the boundary conditions is shown in Figure 7. The ground is treated as a rough wall, with relative thickness of 0.1. The mass flow rate is imposed on the lateral boundaries, which is equal to 25% of the duty point of the fan. Atmosphere is treated as a slip wall for numerical stability of the simulation. At the outflow of the fan, total pressure is imposed, with zero gradient (zG) condition on velocity. On all solid surfaces, standard wall functions for turbulent kinetic energy, its dissipation rate, and turbulent viscosity are used.

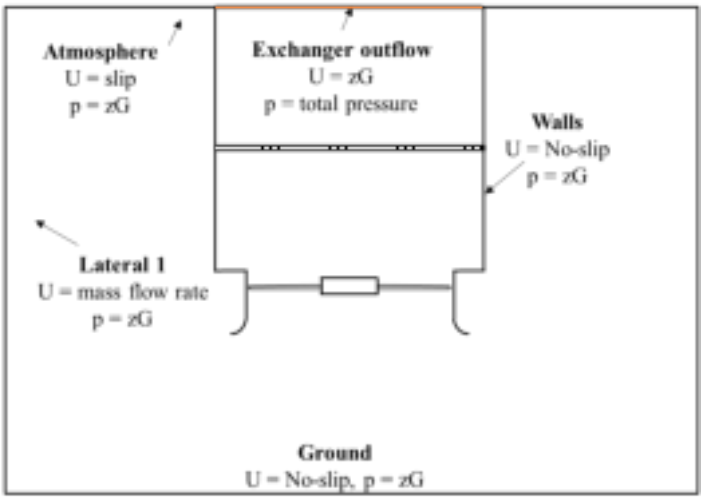

Figure 7. Scheme of boundary conditions, front view.

3. Results

As a validation assessment of the accuracy of computations, a comparison of the TTS pressure and TTS efficiency is shown in Table 1. The pressure is averaged over two planes at 1.6 *D* and 1.8 *D* from the ground. The results show that the pressure rise capability of the two fans in ISO conditions is practically the same, with a slightly worst efficiency for the

whale fan, confirming the conclusions in [15]. However, the installation inside the ACC setup leads to different behaviors: the datum geometry in fact shows a reduction in the pressure rise capability of 32%, with a negligible change in power adsorbed, while the whale fan has a reduction in both the pressure rise and power consumption of about 10%.

Table 1. Validation of CFD results.

Geometry	Setup	Δp_{TTS} (Pa)	Power (kW)
Datum	ACC	95	61.7
	Single Rotor	140	60.4
Whale	ACC	123.8	56
	Single Rotor	137.6	62

This change in performance is associated with a higher work capability in the tip region and a change in the spanwise behavior of the flow. This is shown in Figure 8, where the whale fan shows a linear trend from root to 85% of the span, while the datum geometry has a higher radial velocity value at the root of the blade and then a lower value from 1/3 of the blade span.

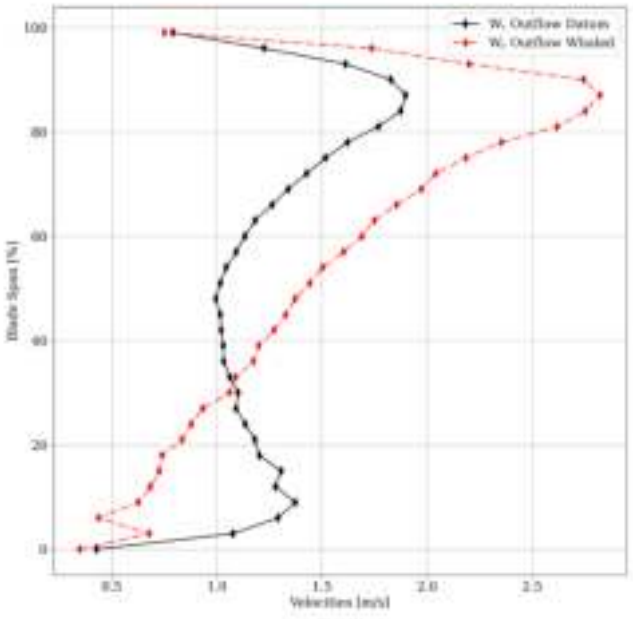

Figure 8. Radial velocity at the outlet of the datum fan (black) and the whale fan (red).

The change in performance can be associated mainly with the effect of the leading edge modification on the development of the tip leakage vortex. As shown in Figure 9, in fact, at the tip of the sinusoidal leading edge, the flow accelerates and reaches a relative velocity of over 70 m/s. The resulting jet released by this region of the rotor delays the development of the tip leakage vortex with respect to the datum fan. In fact, in the datum geometry, the leaking starts at about 10% of the chord of the tip section, with a secondary vortex released at about 50% of the chord.

On the whale rotor, only this second structure is present, due to the counter rotating flow released by the modified leading edge that blocks the development of the first leaking structure. This is better seen in Figures 10 and 11, where the relative velocity and pressure contours are plotted on an iso-radius surface at 99% of the blade span. In both figures, the trace of the tip leakage vortex system is clearly recognizable, with a delayed development for the whale rotor geometry.

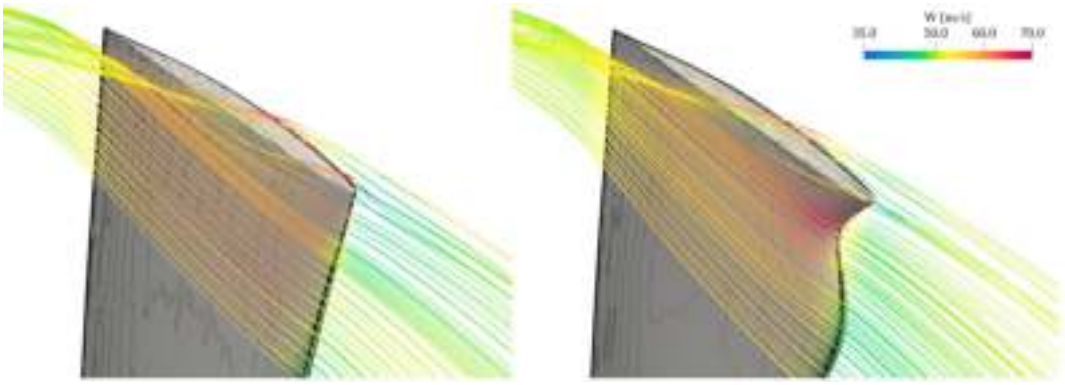

Figure 9. Relative velocity streamlines on the tip region colored with relative velocity. Left: datum; right: whaled.

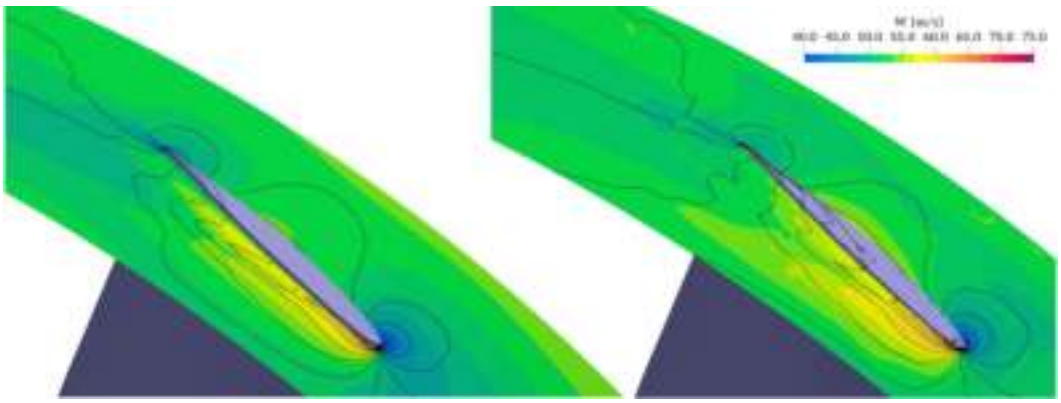

Figure 10. Relative velocity contours on iso-radius surface at 99% of the blade span. Left: datum; right: whaled.

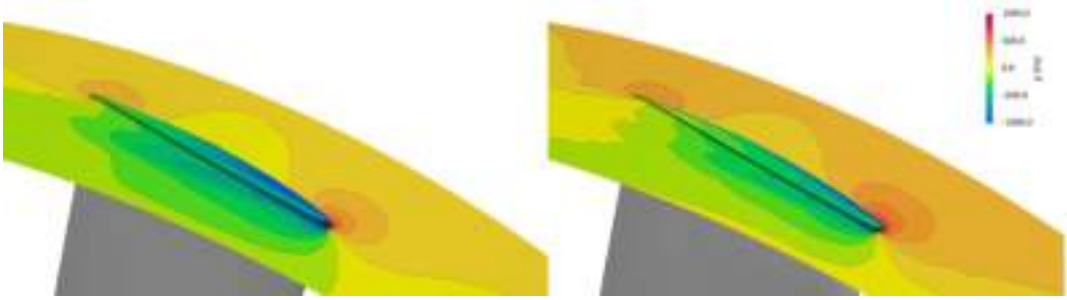

Figure 11. Relative pressure contours on iso-radius surface at 99% of the blade span. Left: datum; right: whaled.

4. Conclusions

Following the conclusions of previous works on modified fan rotors with sinusoidal leading edges, we tested this flow control solution on an air-cooled condenser fan for steam power plants.

In an ISO arrangement, the original blade and the whale blade have similar performances in both the total-to-static pressure rise capability and adsorbed power. When fitted in the ACC, however, there is a clear improvement, as the whale fan experiences a loss of pressure rise with respect to the ISO arrangement of about 11%, compared to a loss of 32% for the datum blade. Additionally, the absorbed power is reduced by 10%, while the datum fan experiences a negligible difference with respect to the ISO conditions.

The different behavior was then related to a radial redistribution of the flow induced by the modified rotor and its capability to control and contrast the development of the tip-leakage vortex on the suction side of the rotor. These findings are similar to those shown in [5].

Author Contributions: Conceptualization, L.T., G.D., J.v.d.S. and A.C.; Methodology, L.T., G.D., J.v.d.S. and A.C.; Software, L.T., G.D., J.v.d.S. and A.C.; Validation, L.T., G.D., J.v.d.S. and A.C.; Formal Analysis, L.T., G.D., J.v.d.S. and A.C.; Investigation, L.T., G.D., J.v.d.S. and A.C.; Resources, L.T., G.D., J.v.d.S. and A.C.; Data Curation, L.T., G.D., J.v.d.S. and A.C.; Writing—Original Draft Preparation, L.T., G.D., J.v.d.S. and A.C.; Writing—Review & Editing, L.T., G.D., J.v.d.S. and A.C.; Visualization, L.T., G.D., J.v.d.S. and A.C.; Supervision, L.T., G.D., J.v.d.S. and A.C.; Project Administration, L.T., G.D., J.v.d.S. and A.C.; Funding Acquisition, L.T., G.D., J.v.d.S. and A.C.; All authors have read and agreed to the published version of the manuscript.

Funding: This research received no external funding.

Data Availability Statement: Data, geometry and numerical setup are available upon request to the authors.

Conflicts of Interest: The authors declare no conflict of interest.

References

1. Fourie, N.; Van Der Spuy, S.J.; Von Backström, T.W.; Van Der Spuy, S. Simulating the Effect of Wind on the Performance of Axial Flow Fans in Air-Cooled Steam Condenser Systems. *J. Therm. Sci. Eng. Appl.* **2015**, *7*, 021011. [CrossRef]
2. Van der Spuy, S.J.; Els, D.N.J.; Tieghi, L.; Delibra, G.; Corsini, A.; Louw, F.G.; Zapke, A.; Meyer, C.J. Preliminary Evaluation of the 24 Ft. Diameter Fan Performance In the MinWaterCSP Large Cooling Systems Test Facility. In *Turbo Expo: Power for Land, Sea, and Air*; American Society of Mechanical Engineers: New York, NY, USA, 2021; p. V001T10A005.
3. Van der Spuy, S.J.; von Backström, T.W.; Kröger, D.G. Performance of low noise fans in power plant air cooled steam condensers. *Noise Control Eng. J.* **2009**, *57*, 341–347. [CrossRef]
4. Angelini, G.; Bonanni, T.; Corsini, A.; Delibra, G.; Tieghi, L.; Volponi, D. On Surrogate-Based Optimization of Truly Reversible Blade Profiles for Axial Fans. *Designs* **2018**, *2*, 19. [CrossRef]
5. Corsini, A.; Delibra, G.; Sheard, A.G. On the Role of Leading-Edge Bumps in the Control of Stall Onset in Axial Fan Blades. *J. Fluids Eng.* **2013**, *135*, 0811041–0811048. [CrossRef]
6. Zhang, M.M.; Wang, G.F.; Xu, J.Z. Aerodynamic control of low-Reynolds-number airfoil with leading-edge pro-tuberances. *AIAA J.* **2009**, *51*, 1960–1971. [CrossRef]
7. Corsini, A.; Delibra, G.; Sheard, A.G. The application of sinusoidal blade-leading edges in a fan-design methodology to improve stall resistance. *Proc. Inst. Mech. Eng. Part A J. Power Energy* **2014**, *228*, 255–271. [CrossRef]
8. Biedermann, T.M.; Kameier, F.; Paschereit, C.O. Successive Aeroacoustic Transfer of Leading Edge Serrations From Single Airfoil to Low-Pressure Fan Application. *J. Eng. Gas Turbines Power* **2019**, *141*, 101011. [CrossRef]
9. Biedermann, T.M.; Chong, T.P.; Kameier, F.; Paschereit, C.O. Statistical–Empirical Modeling of Airfoil Noise Subjected to Leading-Edge Serrations. *AIAA J.* **2017**, *55*, 3128–3142. [CrossRef]
10. The MinWaterCSP Project. Available online: http://www.minwatercsp.eu (accessed on 16 January 2023).
11. Kirstein, C.F.; Von Backström, T.W.; Kröger, D.G. Flow Through a Solar Chimney Power Plant Collector-to-Chimney Transition Section. In Proceedings of the ASME 2005 International Solar Energy Conference, Orlando, FL, USA, 6–12 August 2005; pp. 713–719. [CrossRef]
12. Volponi, D.; Bonanni, T.; Tieghi, L.; Delibra, G.; Wilkinson, M.; van der Spuy, J.; von Backström, T. CFD Simulation Results for the MinWaterCSP Cooling Fan. In Proceedings of the Fan 2018–International Conference on Fan Noise, Aerodynamics, Applications and Systems, Darmstadt, Germany, 18–20 April 2018. [CrossRef]
13. Idelchik, I.E. *Handbook of Hydraulic Resistance*; U.S. Atomic Energy Commission: Washington, DC, USA, 1986.
14. Yakhot, V.; Orszag, S.A.; Thangam, S.; Gatski, T.B.; Speziale, C.G. Development of turbulence models for shear flows by a double expansion technique. *Phys. Fluids A Fluid Dyn.* **1992**, *4*, 1510–1520. [CrossRef]
15. Tieghi, L.; Delibra, G.; Corsini, A.; Van Der Spuy, J. Numerical investigation of CSP air cooled condenser fan. *E3S Web Conf.* **2020**, *197*, 11010. [CrossRef]

Disclaimer/Publisher's Note: The statements, opinions and data contained in all publications are solely those of the individual author(s) and contributor(s) and not of MDPI and/or the editor(s). MDPI and/or the editor(s) disclaim responsibility for any injury to people or property resulting from any ideas, methods, instructions or products referred to in the content.

International Journal of
Turbomachinery
Propulsion and Power

MDPI

Article

Multi-Point, Multi-Objective Optimisation of Centrifugal Fans by 3D Inverse Design Method

Jiangnan Zhang [1,*] and Mehrdad Zangeneh [2]

[1] Advanced Design Technology Ltd., London SW1P 4DU, UK
[2] Department of Mechanical Engineering, University College London, London WC1E 6BT, UK
* Correspondence: j.zhang@adtechnology.com or jiangnan.zhang@outlook.com

Abstract: In this paper, we present the design and optimization of a centrifugal fan with requirements of maximizing the total-to-static pressure rise and total-to-static efficiency at two operating points and the maximum torque provided by the motor power using a 3D inverse design method, a DOE (design of experiment) study, an RSM (response surface model) and a MOGA (multi-objective genetic algorithm). The fan geometry is parametrized using 13 design parameters, and 120 different designs are generated. The fan performances of all the designs at two operating conditions are evaluated through steady-state CFD simulations. The resulting design matrix is used to create an RSM based on the Kriging method and MOGA is used to search the design space using the RSM and find the optimal design.

Keywords: multi-point; multi-objective; optimization; centrifugal fans; inverse design method; DOE; RSM; MOGA

check for updates

Citation: Zhang, J.; Zangeneh, M. Multi-Point, Multi-Objective Optimisation of Centrifugal Fans by 3D Inverse Design Method. *Int. J. Turbomach. Propuls. Power* **2023**, *8*, 8. https://doi.org/10.3390/ijtpp8010008

Academic Editor: Thomas Carolus

Received: 27 September 2022
Revised: 3 February 2023
Accepted: 12 February 2023
Published: 2 March 2023

Copyright: © 2023 by the authors. Licensee MDPI, Basel, Switzerland. This article is an open access article distributed under the terms and conditions of the Creative Commons Attribution (CC BY-NC-ND) license (https://creativecommons.org/licenses/by-nc-nd/4.0/).

1. Introduction

Centrifugal fans are used in many applications where a relatively high-pressure rise is required in the compact size. The application can vary from household appliances [1] to industrial to air-conditioning and data center cooling applications [2–6]. Hariharan and Govarhan studied the effect of inlet clearance on the aerodynamic performance of a centrifugal blower [7]. Singh et al. performed a parametric study of the effect of blade number, TE blade angle and diameter ratio on the centrifugal fan performance based on experiments and numerical simulations [8]. Jeon investigated the effects of design parameters on the performance and noise of a centrifugal fan [9]. All the works mentioned above have been focused on the fan performance at only one point, which is the design point or BEP (best efficiency point), while for some applications the fans are required to meet multi-point requirements in terms of pressure rise, flow rate and efficiency. To tackle this kind of multi-point design and optimization problem, DOE and RSM approaches have been widely used for pumps, turbines and compressors [10–12]. Behzadmehr et al. carried out a parametric study of a backward-curved centrifugal fan using DOE using five design parameters, and each design parameter had two levels of variation [13]. The main drawback of this method is that a very small number of design parameters were used, which means other more important parameters may have been missed. Qiu et al. performed a multi-point design optimization of a high bypass ratio axial fan blade using DOE and Kriging approximation [14]. The optimized design shows 0.1% efficiency improvement at the design point but has a worse efficiency characteristic within the operation range. As it can be seen that in the literature there is not much study on the aerodynamic multi-point optimization of centrifugal fan blade shapes, this is the main reason that the authors would like to publish this work.

In this paper, we started with the design of a baseline design which meets the pressure rise requirements at two operating points using the 3D inverse design method. The fan

aerodynamic performance (total-to-static (t-s) pressure rise and t-s efficiency) is evaluated through steady-state CFD simulations. The meridional geometry and blade loading parameters are then parameterized using 13 parameters, and around 120 different blade geometries are generated with a wide range of variation in these 13 design parameters. T-s pressure rise and t-s efficiency values of these 120 designs are evaluated using CFD simulations. A design matrix consisting of all the design and performance parameters of these 120 designs is obtained. Kriging is used to create an RSM using the design matrix data and MOGA is used to search the optimal designs in the design space based on RSM. The final optimal design is selected from the Pareto Front and its performance is validated using CFD simulations at two operating points. The flow chart of the design and optimization process is shown in Figure 1.

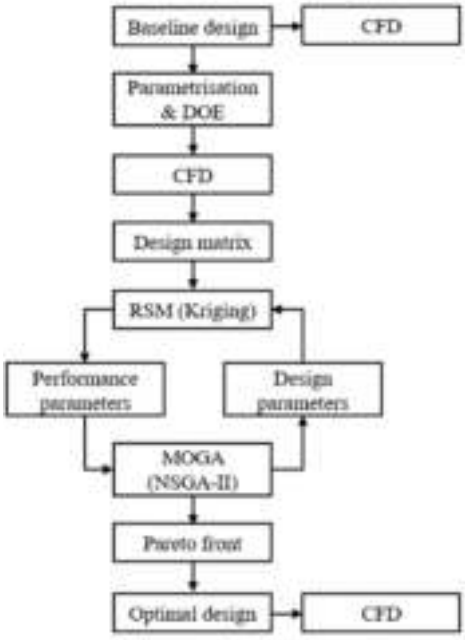

Figure 1. Flow chart of the design and optimization process.

2. Blade Design

2.1. The 3D Inverse Design Method

The 3D inverse design method, also known as the Circulation Method in the literature, is described in detail in [15]. It has been used in the design of different types of fans including axial fans [16] and centrifugal blowers [17,18]. The blade geometry is calculated iteratively based on the prescribed blade loading distribution ($\frac{\partial(r\overline{v_\theta})}{\partial m}$, the derivative of $r\overline{v_\theta}$ along the meridional direction) on the meridional geometry; $r\overline{v_\theta}$ is the circumferentially averaged bound circulation and is defined by Equation (1) below, where r is the radius, $\overline{v_\theta}$ is the circumferential velocity and N is the blade number. For incompressible potential flow, the blade loading (the pressure difference between the pressure surface and suction surface of the blade) is defined by Equation (2), where p^+ is the static pressure on the pressure side and p^- is the static pressure on the suction side.

$$r\overline{v_\theta} = \frac{N}{2\pi}\int_0^{2\pi/N} r \cdot v_\theta d\theta \tag{1}$$

$$p^+ - p^- = \frac{2\pi}{N}\rho W_{mbl}\frac{\partial(r\overline{v_\theta})}{\partial m} \tag{2}$$

2.2. Blade Parametrization

The main inputs for the inverse design method are meridional geometry, blade thickness distribution, blade loading and stacking. The blade meridional geometry is parametrized by eight parameters including the blade tip width (L), the hub radial length (dR_{hub}), the shroud radial length (dR_{shr}), the TE angle (α), the hub angle (β_{hub}), the shroud angle (β_{shr}), the LE curvature and the shroud curvature, as shown in the Figure 2. The blade thickness distribution is defined as 5 mm constant and the number of blades is six. LE and TE $r\overline{v_\theta}$ are used as inputs which will fix the work coefficient (specific torque/power) based on Euler's Turbomachinery Equation. The streamwise blade loading distribution ($\frac{\partial(r\overline{v_\theta})}{\partial m}$) is defined using a three-segment method shown in Figure 3. The loading distribution is defined by two curves at hub and shroud. For each curve, two points on the meridional location (NC and ND) divide the curve into three parts. The first and last curves are parabolic, and the middle curve is a straight line. The slope of the middle straight line is defined by a parameter called SLOPE. The loading value at LE (m = 0, where m is the normalized meridional coordinate) is defined by DRVT, which controls the incidence at the LE.

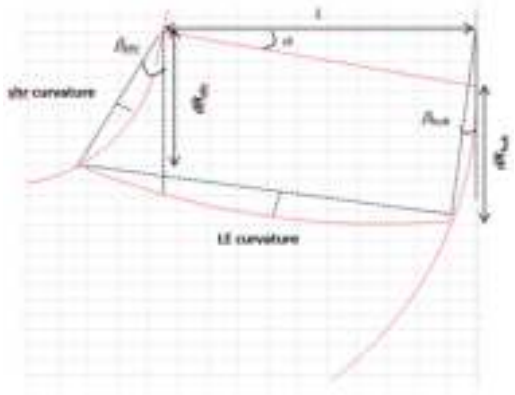

Figure 2. Meridional geometry parametrization.

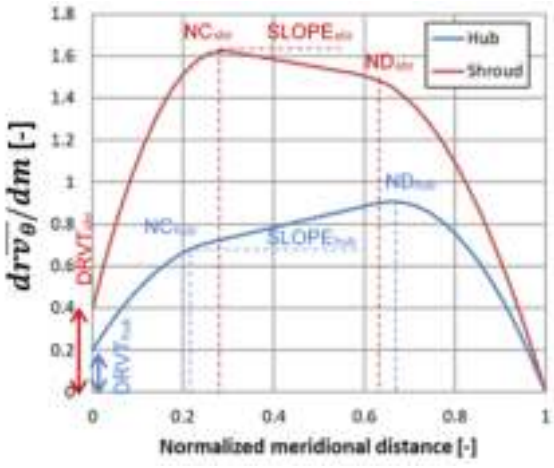

Figure 3. Streamwise blade loading defined using three-segment method.

The last input parameter required is the stacking condition, which is a spanwise wrap angle distribution at a fixed streamwise location. For fans, it is common to stack at the TE. Most of the centrifugal fans are made from sheet metal and the blade has to be 2D and axial filament. However, development in additive manufacturing can make it easier to design centrifugal fan blades with 3D geometry. The 3D inverse design method used in this study makes it quite easy to design either in 3D or in 2D. In this paper, a 2D geometry is used for the blade optimization and a zero stacking at TE is used for all the designs. Once all the

inputs are specified, the 3D inverse design method computes the blade shape for a given specified blade loading.

2.3. Design Specifications and Baseline Blade Generation

The design specifications are shown in Table 1. The fan is required to meet the minimum pressure rise requirements at two operating points (OP_1 and OP_2). The maximum torque is set by the motor provided and the main target is to maximize the efficiency at two operating points. The geometrical constraints are that the fan diameter cannot exceed the maximum value provided and the blade has to be 2D and axial filament.

Table 1. Design specifications and constraints.

Flow Coefficient	**0.22**
Loading Coefficient	**0.39**
RPM	$\leq RPM_{max}$
Volume flow rate @ OP_1	Q_1
Pressure rise @ OP_1	$\geq \Delta p_1$
Volume flow rate @ OP_2	$Q_2 = 117\% Q_1$
Pressure rise @ OP_2	$\geq \Delta p_2$
Torque	$\leq \tau_{max}$
Efficiency @ OP_1	Maximize
Efficiency @ OP_2	Maximize
Impeller diameter	$\geq D_{max}$
Blade	2D and axial filament

The meridional geometry of the baseline design is shown in Figure 4. The LE/TE $r\overline{v_\theta}$ and streamwise blade loading are shown in Figure 5. It is noted that LE/TE $r\overline{v_\theta}$ is normalized by the blade tip radius and tip speed. Once the solver is converged, the 3D blade from the inverse design method is converted to a 2D/axial filament blade using axial filament modification, which axially maps the wrap angle distribution of the hub to all the other spanwise layers.

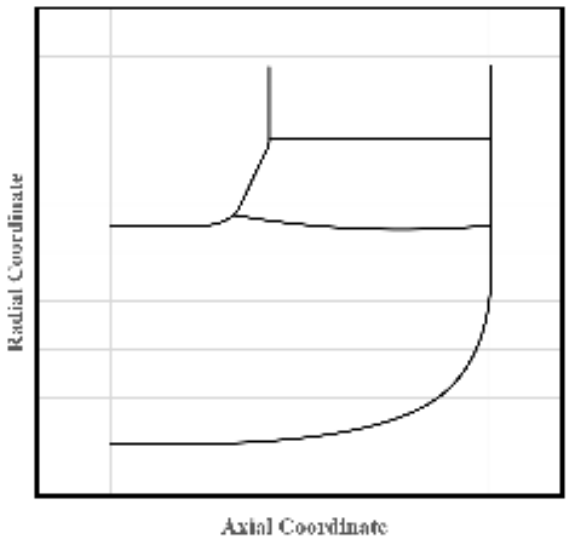

Figure 4. Baseline meridional geometry.

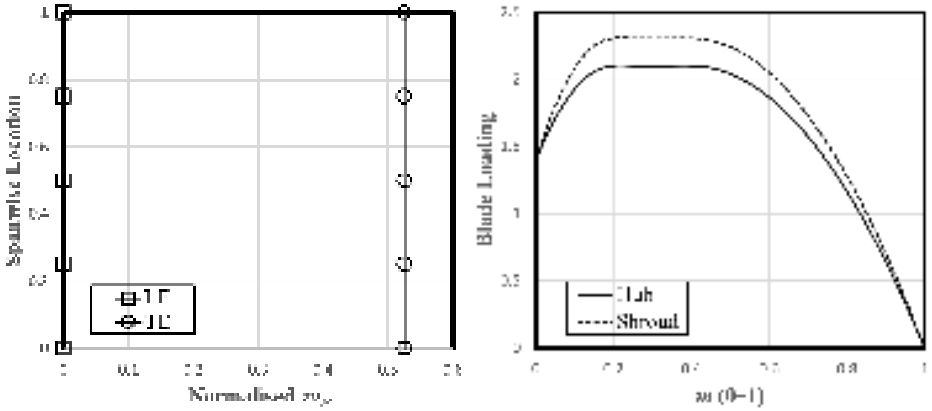

Figure 5. Baseline spanwise $r\overline{v_\theta}$ and streamwise blade loading.

3. CFD Simulation

3.1. Mesh Generation

The structured mesh was generated using ANSYS TurboGrid for the impeller blade (around 500,000 hexahedra elements) and unstructured mesh was generated for the inlet cone and inblock/outblock geometries (around 500,000 tetrahedra elements). The total number of elements is around 1,000,000. The near wall element size is 0.03 mm for the impeller and 0.05 mm for the inblock/outblock, which result in the maximum y+ value on the walls of less than 1.0, well within the viscous sublayer; y+ is the non-dimensional distance (based on local cell fluid velocity) from the wall to the first mesh node. The number of prism layers for the inflation is 10. As can be seen in Figure 6, the gap between the stationary inlet cone and the rotating impeller shroud casing is well resolved.

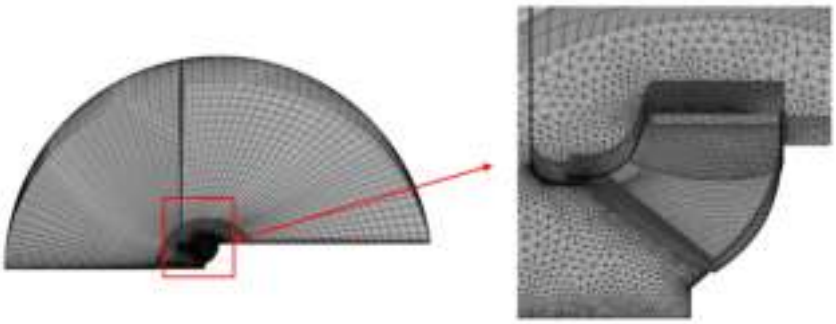

Figure 6. Computational domain.

3.2. CFD Setup

Steady-state CFD simulations (RANS) were performed by using commercial software ANSYS CFX. The inlet boundary condition is the given mass flow rate, and the outlet boundary condition is the opening with 1 atm static pressure. The impeller domain is rotational with the fixed RPM. Periodic boundary conditions were used for all domains to save the computational cost. The interface between the stationary domain and the rotational domain is set as Frozen Rotor. The turbulence model used is shear stress transport SST k-ω. A high-resolution (2nd-order) advection scheme was used. The convergence criteria for the continuity and momentum equations were set as RMS < 1.0×10^{-4}. The fan pressure rise and torque values were monitored and reach to a constant value once the solution is converged. The complete CFD model is shown in the Figure 7.

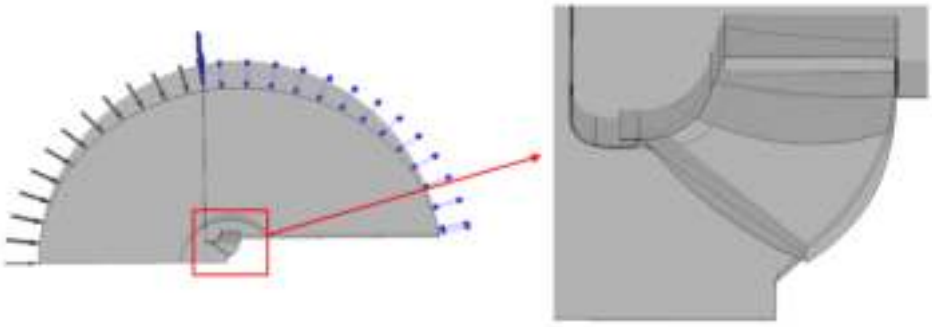

Figure 7. CFD model in ANSYS CFX.

3.3. CFD Results

Once the CFD simulations are converged, the pressure rise, torque and efficiency values can be obtained for both operating points (OP_1 and OP_2) and are summarized in Table 2. The total-to-static pressure rise is calculated as the difference between inlet total pressure and outlet static pressure. It can be seen that the baseline design almost meets the pressure rise requirements at both operating points and does not exceed the maximum torque. The efficiencies for OP_1 and OP_2 are 57.7% and 44.2%, respectively. After examining the detailed flow field, it was found that the flow behaves well at hub and mid-span locations but separates near the shroud part of the blade at OP_1 and OP_2, which can be seen in Figure 8.

Table 2. Baseline CFD results.

Variable Name	OP_1	OP_2
RPM	RPM_{max}	RPM_{max}
Q	Q_1	Q_2
Δp_{ts}	0.99 Δp_1	0.94 Δp_2
τ	τ_{max}	0.91τ_{max}
η_{ts}	57.7%	44.2%

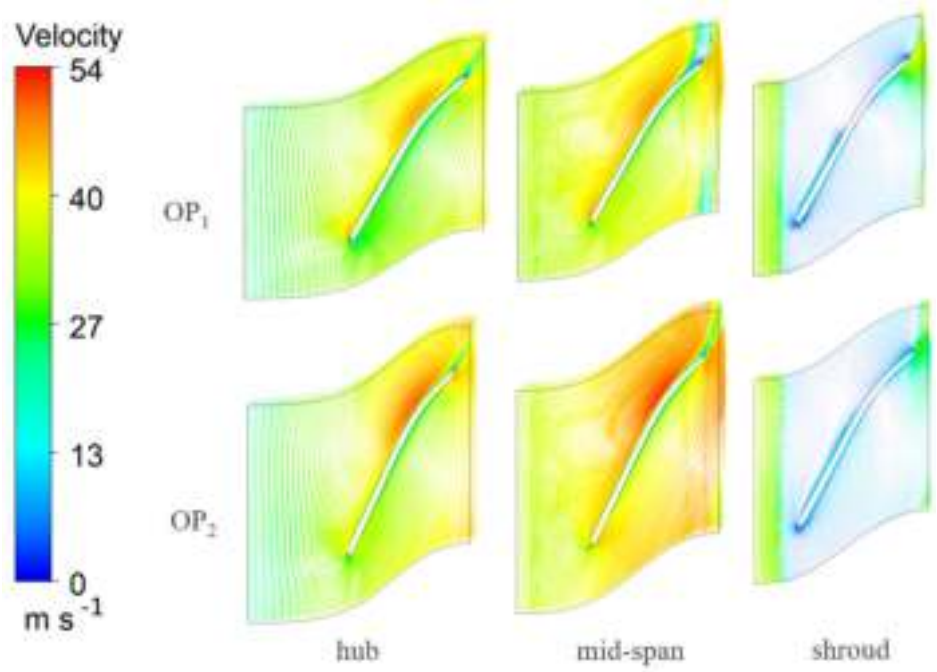

Figure 8. Baseline relative velocity vector at OP_1 and OP_2.

4. DOE and Optimization

4.1. DOE

To improve and obtain the best possible fan performance, a DOE study was performed. In total there are 13 design parameters, including 8 meridional geometry parameters and 5 loading parameters (NC, ND, SLOPE, DRVT and RVT_TE). DRVT is the streamwise loading value at LE, as shown in Figure 3, and RVT_TE is TE $r\overline{v_\theta}$. The same values are used for hub and shroud blade loading to obtain 2D/axial filament blades. For each of the 13 design parameters, a min and max value around the baseline value is carefully specified which allows a large design space to be explored and has a good convergence rate to avoid many diverged cases in the DOE. Latin Hypercube sampling (LHS) is a statistical method which can be used to create a random sampling of multiple parameters. The number of designs has to be equal to the number of levels for each design parameter and greater than the number of the design parameters. The Optimal Latin Hypercube sampling (OLHS) is a special LHS where all the design points are equally spaced [19]. The disadvantage of OLHS is that it requires more time to generate the design matrix compared to LHS. A total of 120 different designs were generated using the OLHS method. For each design, the blade generation, meshing and CFD (two operating points) were performed automatically in ANSYS Workbench, as shown in Figure 9.

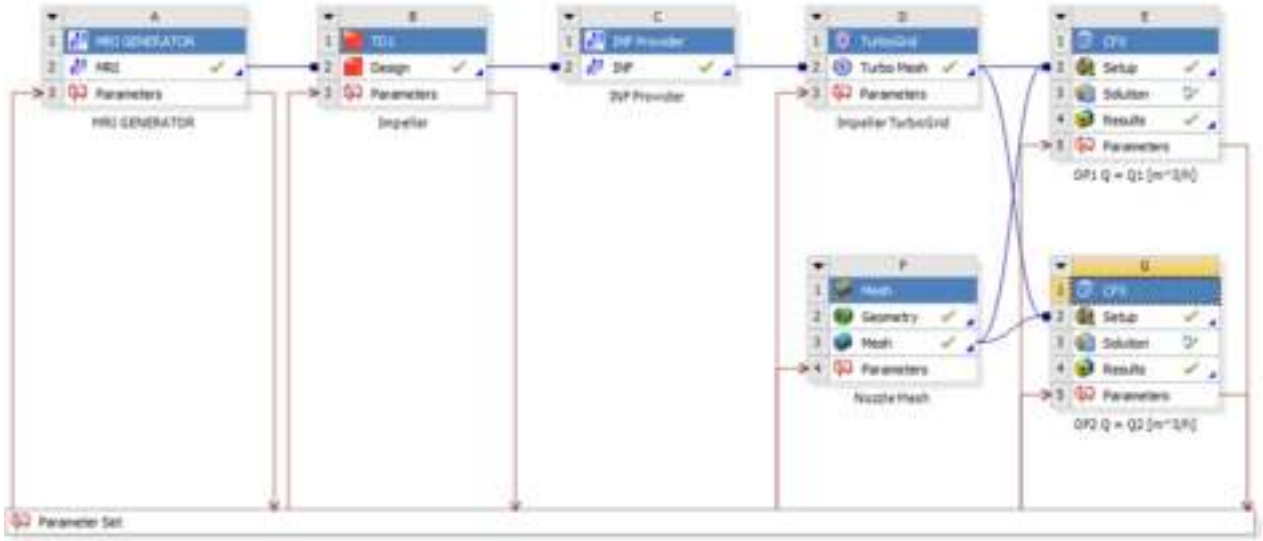

Figure 9. Automated DOE workflow in ANSYS Workbench.

Once the CFD simulations were finished, a design matrix of 120 designs with all the design parameters and performance parameters were obtained. All the CFD results are shown in Figure 10. It can be seen that a number of designs in the DOE meet the minimum pressure rise requirements at both operating points with good efficiencies compared to the baseline design. The torque values of almost all the DOE designs do not exceed the maximum constraint.

4.2. Optimization

The terms response surface model (RSM), surrogate model, approximation model and meta model are used as synonyms in the literature. The RSM is a mathematical model and constructed based on data from known designs (usually from DOE) that provides fast approximation and evaluation of objectives for different design parameters at new design points.

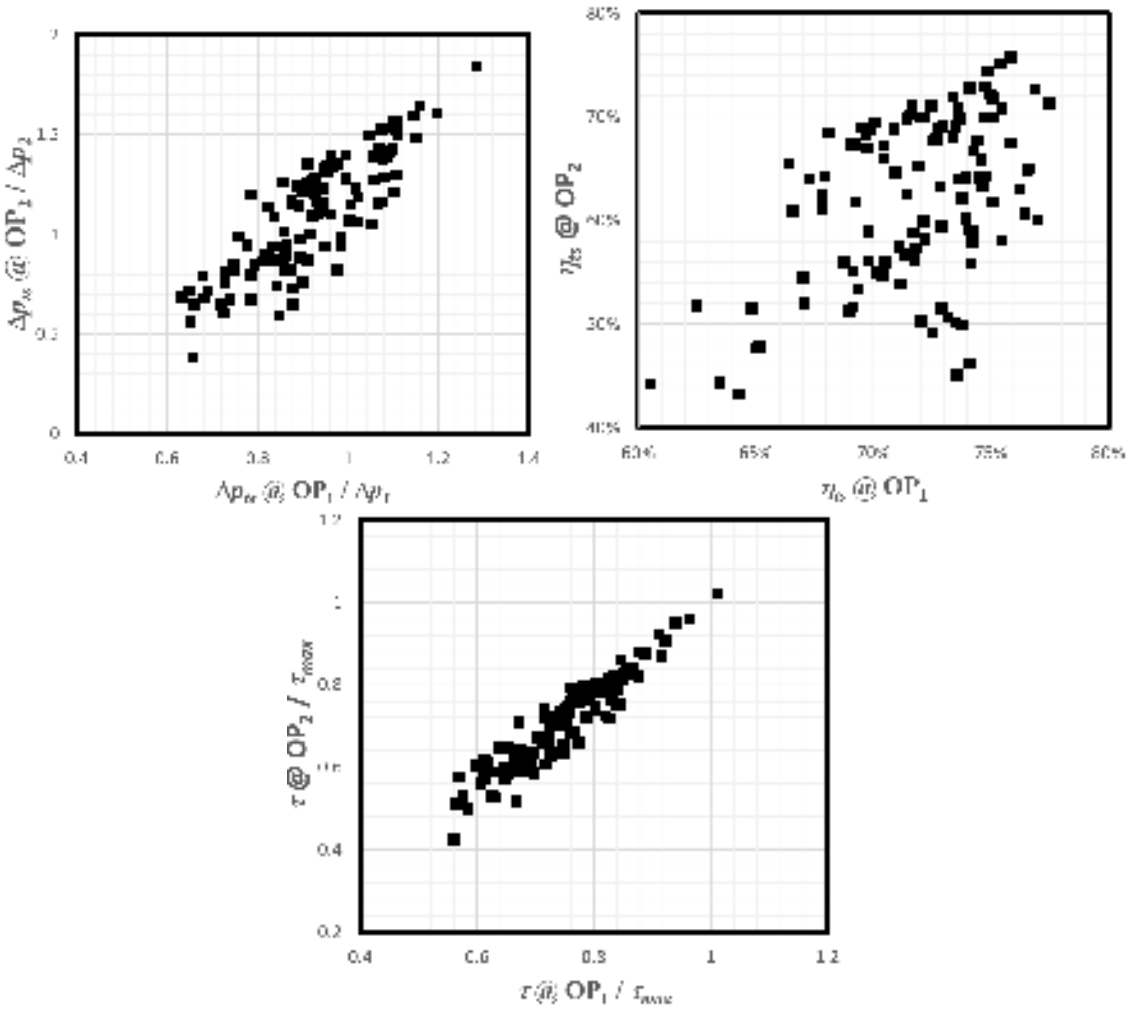

Figure 10. CFD results (pressure rise, efficiency and torque) of DOE designs.

Kriging is a method of interpolation which was first proposed by a South African statistician and mining engineer Danie G. Krige and is used to predict the location of unknown mineral resources. The basic idea of Kriging is that the value at an unknown point should be the average of the known values at its neighbors, weighted by the neighbor's distance to the unknown point (Chung and Siller [20,21]).

MOGA (NSGA-II, non-dominated sorting genetic algorithm-II) is a multi-objective genetic algorithm which was first proposed by Deb et al. [22]. It is well-suited for highly non-linear design spaces; each objective is treated separately and a Pareto Front is constructed by selecting feasible non-dominated designs.

All the DOE results can be used to create a RSM using the Kriging approximation method. The calculated CoP (Coefficient of Prognosis) of the output parameters for the Kriging RSM is around 0.85. The optimization was performed by searching the design space with the given constraints and objectives and the performance of different designs, can be quickly evaluated through the Kriging RSM model. The constraints and objectives used in the optimization are listed in the Table 3. It is noted that 'Angle' is defined by Equation (3). This parameter is used to control the fan *p*-*Q* curve slope (shape) and should be kept as close as possible to the target value, which is around −5°.

$$\text{Angle} = \tan^{-1}\left(\frac{\Delta p_1 - \Delta p_2}{\text{Q}_1 - \text{Q}_2}\right) \tag{3}$$

Table 3. Optimization constraints and objectives.

Δp @ OP_1	$\geq \Delta p_1$
Δp @ OP_2	$\geq \Delta p_2$
τ @ OP_1	$\geq \tau_{max}$
τ @ OP_2	$\geq \tau_{max}$
Angle	$\geq -5.5^\circ$ & $\leq -4.9^\circ$
η_{ts} @ OP_1	Maximize
η_{ts} @ OP_2	Maximize

A total of 100,000 designs were generated using MOGA (NSGA-II), and the resulting Pareto Front and the selected optimal design are shown in the Figure 11. An obvious trade-off between the efficiencies at two operating points can be observed.

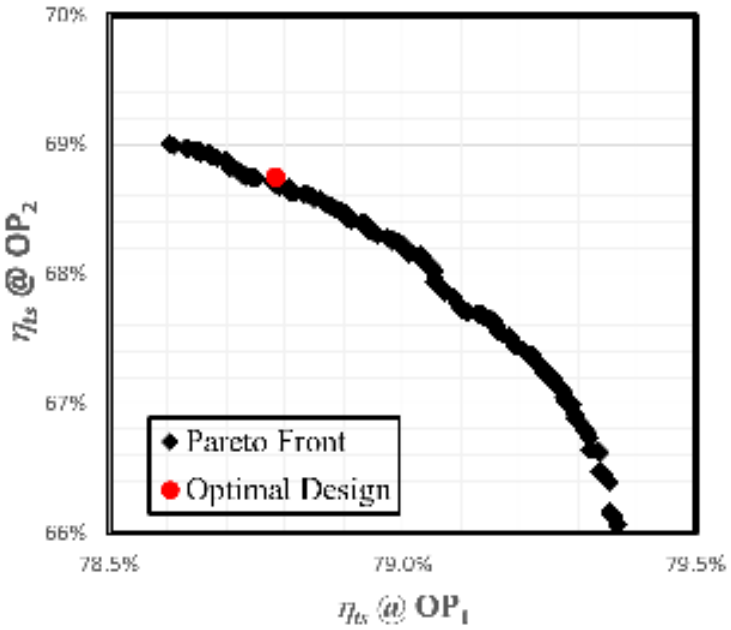

Figure 11. Pareto Front and selected optimal design.

The CFD performance of the optimal design is compared with the baseline and shown in Figure 12. The pressure rise of the optimal design is improved significantly at both operating points compared to the target and baseline values while maintaining the desirable *p*-*Q* slope (shape). The efficiencies of the optimal design are improved by around 20 percentage points at both operating points compared to the baseline design. The torque values are reduced and do not exceed the maximum constraint.

The comparison of the meridional geometry and the streamwise blade loading between the optimal design and the baseline is shown in Figure 13. The comparison of the 3D geometries of the baseline and the optimal design is shown in Figure 14.

The improvement in efficiencies can also be explained by comparing the flow fields of the two designs (Figures 7 and 15). In particular, the flow near the shroud of the optimal design is improved significantly and now fully attaches on the blade surface compared to that of the baseline design.

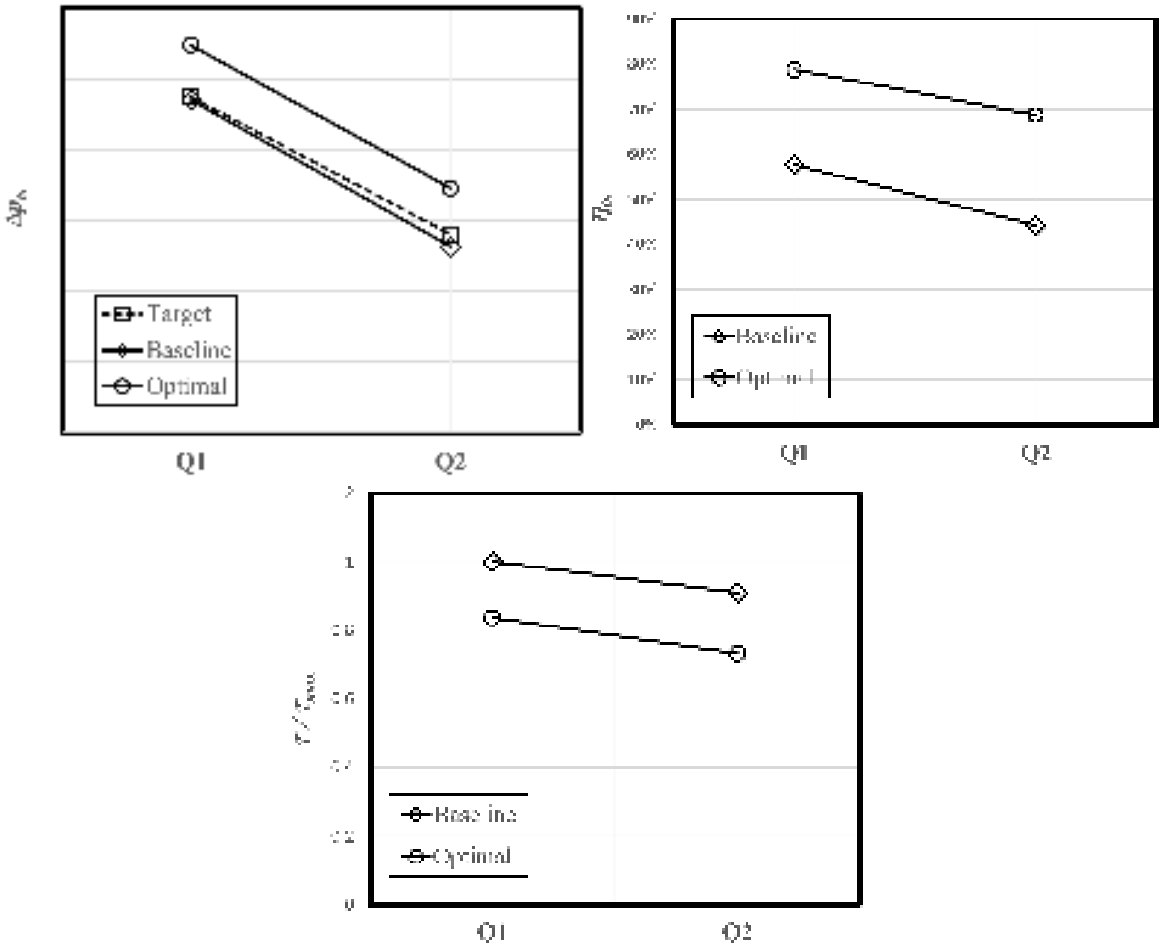

Figure 12. Comparison of CFD results for baseline and optimal design.

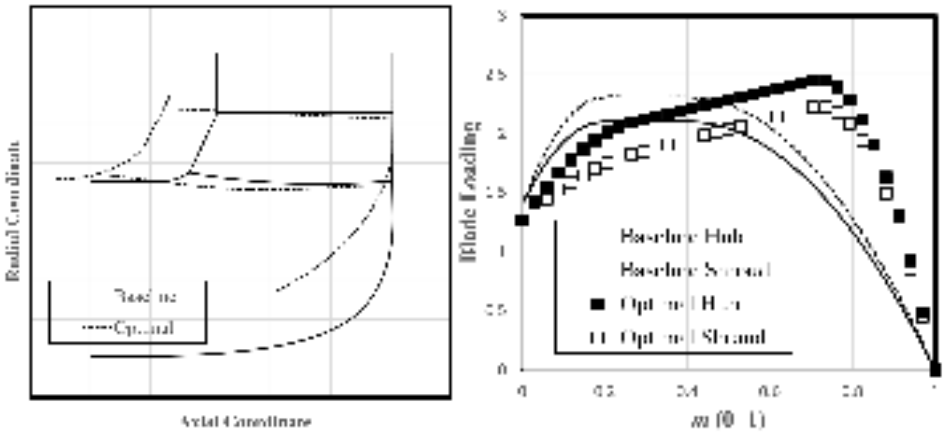

Figure 13. Comparison of meridional geometry and blade loading distribution for baseline and optimal design.

Figure 14. Comparison of 3D geometries of baseline (grey) and the optimal design (blue).

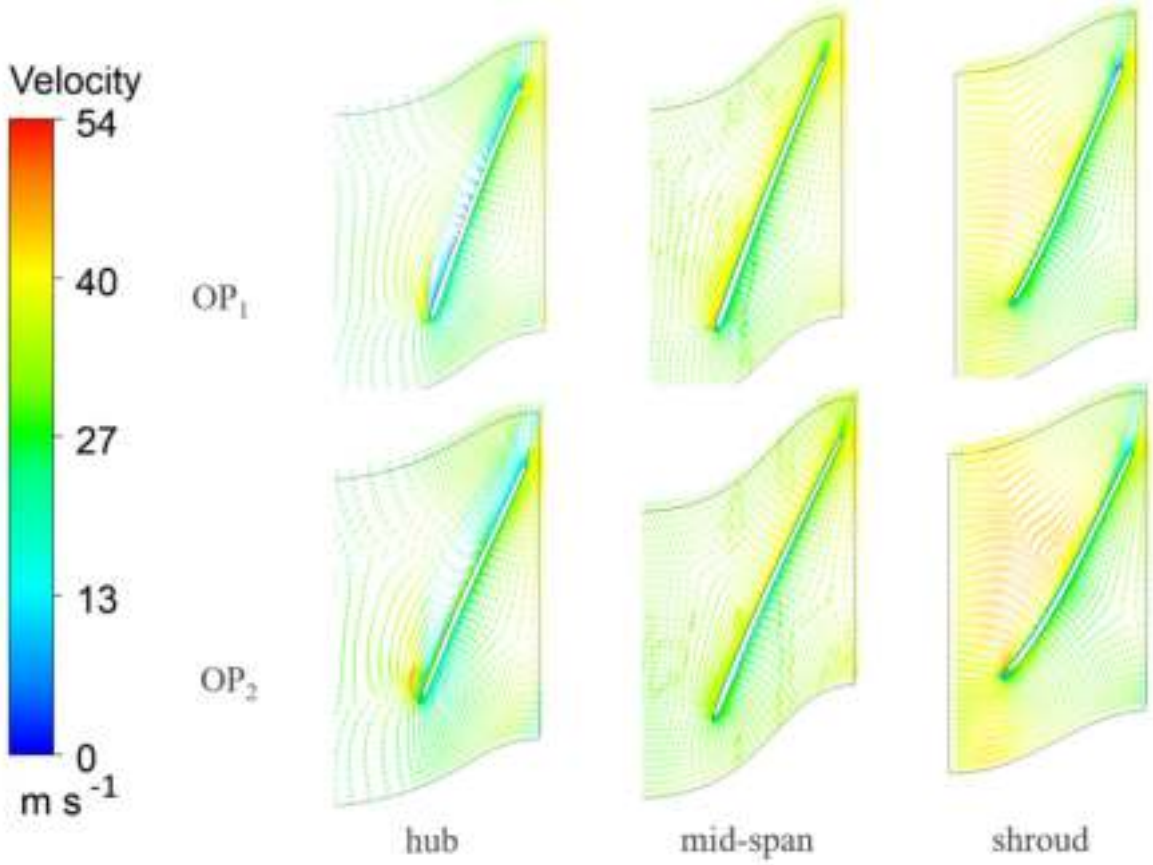

Figure 15. Optimal design relative velocity vector at OP_1 and OP_2.

5. Conclusions

In this paper, a systematic optimization methodology using the inverse design method, DOE and MOGA is presented and used to optimize the aerodynamic performance of a centrifugal fan at two operating points. The total-to-static pressure rise and total-to-static efficiencies at two operating points are improved significantly, and the improvement is validated using steady-state CFD simulations.

Author Contributions: Conceptualization, J.Z. and M.Z.; methodology, J.Z.; software, J.Z.; validation, J.Z. and M.Z.; formal analysis, J.Z.; investigation, J.Z.; resources, J.Z.; data curation, J.Z.; writing—original draft preparation, J.Z.; writing—review and editing, J.Z.; visualization, J.Z.; supervision, M.Z.; project administration, n/a; funding acquisition, n/a. All authors have read and agreed to the published version of the manuscript.

Funding: This research received no external funding.

Institutional Review Board Statement: Not applicable.

Informed Consent Statement: Not applicable.

Data Availability Statement: Not applicable.

Conflicts of Interest: The authors declare no conflict of interest.

References

1. Jeon, W.-H.; Baek, S.-J.; Kim, C.-J. Analysis of the aeroacoustic characteristics of the centrifugal fan in a vacuum cleaner. *J. Sound Vib.* **2003**, *268*, 1025–1035. [CrossRef]
2. Woodard, J.K., Jr.; Johnson, G.E. Optimal design of cooling fan for industrial electric motors. *J. Mech. Transm. Autom. Des.* **1986**, *108*, 224–266. [CrossRef]
3. Rugang, C. Experimental study on erosion characteristic for different blade contours in the centrifugal fan exposed to solid particulate environment. *Fluid Mach.* **2000**, *1*, 5–8.
4. Tan, J.; Tang, W.; Yuan, W. Optimizing technique of air-cooled engine centrifugal cooking fan test. *Chin. Intern. Combust. Engine Eng.* **2002**, 1002–6819.
5. Li, H. Flow driven by a stamped metal cooling fan—Numerical model and validation. *Exp. Therm. Fluid Sci.* **2009**, *33*, 683–694. [CrossRef]
6. Chang, C.-C.; Cheng, C.-C.; Ke, M.-T.; Chen, S.-L. Experimental and numerical investigations of air cooling for a large-scale motor. *Int. J. Rotating Mach.* **2009**, *2009*, 34–40. [CrossRef]
7. Hariharan, C.; Govardhan, M. Effect of inlet clearance on the aerodynamic performance of a centrifugal blower. *Int. J. Turbo Jet Engines* **2016**, *33*, 215–228. [CrossRef]
8. Singh, O.P.; Khilwani, R.; Sreenivasulu, T.; Kannan, M. Parametric Study of Centrifugal Fan Performance: Experiments and Numerical Simulation. *Int. J. Adv. Eng. Technol.* **2011**, *1*, 33–50.
9. Jeon, W.-H. A numerical study on the effects of design parameters on the performance and noise of a centrifugal fan. *J. Sound Vib.* **2003**, *265*, 221–230. [CrossRef]
10. Pei, J.; Wang, W.; Yuan, S.; Zhang, J. Optimization on the Impeller of a Low-specific-speed centrifugal Pump for hydraulic Performance Improvement. *Chin. J. Mech. Eng.* **2016**, *29*, 992–1002. [CrossRef]
11. Zhang, J.; Zangeneh, M. Multidisciplinary and multi-point optimisation of radial and mixed-inflow turbines for turbochargers using 3D inverse design method. In *The 14th International Conference on Turbochargers and Turbocharging*; CRC Press: London, UK, 2020.
12. Tuchler, S.; Chen, Z.; Copeland, C.D. Multipoint shape optimisation of an automotive radial compressor using a coupled computational fluid dynamics and genetic algorithm approach. *Energy* **2018**, *165*, 543–561. [CrossRef]
13. Behzadmehr, A.; Piaud, J.B. Aero-Acoustical Effects of Some Parameters of a Backward-Curved Centrifugal Fan Using DOE. *HVAC&R Res.* **2006**, *12*, 353–365.
14. Qiu, S.; Deng, X. Multi-point design Optimization of a High Bypass Ratio Fan Blade. In Proceedings of the 30th Congress of the International Council of the Aeronautical Sciences, Daejeon, Republic of Korea, 25–30 September 2016.
15. Zangeneh, M. A compressible three-dimensional design method for radial and mixed flow turbomachinery blades. *Int. J. Numer. Methods Fluids* **1991**, *13*, 599–624. [CrossRef]
16. Okamoto, H.; Zangeneh, M.; Watanabe, H.; Goto, A. Design of a box fan rotor using 3-D inverse design method. In Proceedings of the IMechE International Conference on Fans, London, UK, 9–10 November 2004.
17. Henner, M.; Neddadi, Y.; Demory, B.; Zangeneh, M.; Pemgie, F. Automotive blower design with inverse method applied on wheel and volute. In Proceedings of the Fan 2015, International Conference on Fan Noise, Technology and Numerical Methods, Lyon, France, 15–17 April 2015.
18. Eisenmenger, C.; Frank, S.; Dogan, H.; Ochmann, M. Aerodynamic and aeroacoustic optimization of a small centrifugal fan with backward-curved blades by means of inverse design. In Proceedings of the 23rd International Congress on Acoustics, Aachen, Germany, 9–13 September 2019.
19. Park, J.-S. Optimal Latin-hypercube designs for computer experiments. *J. Stat. Plan. Inference* **1994**, *39*, 95–111. [CrossRef]
20. Chung, H.-S.; Alonso, J.J. Multiobjective Optimization using Approximation Model-based Genetic Algorithm. In Proceedings of the 10th AIAA/ISSMO Symposium on Multidisciplinary Analysis and Optimization, Albany, NY, USA, 30 August–1 September 2004.
21. Siller, K.; Vob, S.; Nicke, E. Automated Multidisciplinary Optimization of A Transonic Axial Compressor. In Proceedings of the 47th AIAA Aerospace Science Meeting including the New Horizons Forum and Aerospace Exposition, Orlando, FL, USA, 5–8 January 2009.
22. Deb, K.; Agrawal, S.; Pratap, A.; Meyarivan, T. A Fast Elitist Non-dominated Sorting Genetic Algorithm for Multi-objective Optimization: NSGA-II. In Proceedings of the Parallel Problem Solving from Nature VI Conference, Paris, France, 18–20 September 2000; pp. 849–858.

Disclaimer/Publisher's Note: The statements, opinions and data contained in all publications are solely those of the individual author(s) and contributor(s) and not of MDPI and/or the editor(s). MDPI and/or the editor(s) disclaim responsibility for any injury to people or property resulting from any ideas, methods, instructions or products referred to in the content.

International Journal of
Turbomachinery
Propulsion and Power

MDPI

Article

Enhancement of Rotor Loading and Suppression of Stator Separation through Reduction of the Blade–Row Gap

Zhuo Wang [1], Lin Du [1,*] and Xiaofeng Sun [2]

[1] Aeroengine Research Institute, Beihang University, Beijing 100191, China
[2] School of Energy and Power Engineering, Beihang University, Beijing 100191, China
* Correspondence: lindu@buaa.edu.cn

Abstract: An immersed boundary (IB) method is applied to study the effect of the blade–row gap in a low-speed single-stage compressor. The advantage of using an IB method is that the rotor/stator interface can be eliminated and, thus, the blade–row interaction can be considered at an extremely small gap. The IB method was modified to internal-flow problems, and the adaptive mesh refinement (AMR) technique, together with a wall model, used to facilitate the simulations for high Reynolds-number flows. The results showed that both the pressure rise and the efficiency were observed to be higher in the smaller-gap cases. Comparisons between the results of two gaps, 35%c_a and 3.5%c_a, are highlighted and further analysis at a specific flow coefficient showed that the increase of the stage performance was contributed to by the enhancement of rotor loading and the suppression to the flow separation of the stator. Correspondingly, the increases of the total pressure rise on the rotor and the stator outlets were observed to be 0.5% and 4.3%, respectively. Although the increase on the rotor outlet is much lower than that on the stator outlet, its significance is that a higher level of static pressure is formed near the hub of the gap, which, thus, reduces the adverse pressure gradient of this region in the stator passage. This improvement suppresses the flow separation near the hub of the stator and, thereby, results in a considerable increase to the pressure rise on the stator outlet as a consequence. The effect of the gap on unsteady pressure fluctuation is also presented.

Keywords: immersed boundary method; rotor/stator interaction; adaptive mesh refinement

check for updates

Citation: Wang, Z.; Du, L.; Sun, X. Enhancement of Rotor Loading and Suppression of Stator Separation through Reduction of the Blade–Row Gap. *Int. J. Turbomach. Propuls. Power* **2023**, *8*, 6. https://doi.org/10.3390/ijtpp8010006

Academic Editor: Jérôme Boudet

Received: 12 October 2022
Revised: 11 February 2023
Accepted: 22 February 2023
Published: 1 March 2023

Copyright: © 2023 by the authors. Licensee MDPI, Basel, Switzerland. This article is an open access article distributed under the terms and conditions of the Creative Commons Attribution (CC BY-NC-ND) license (https://creativecommons.org/licenses/by-nc-nd/4.0/).

1. Introduction

The axial blade–row gaps in a multi-stage compressor are significant in the determination of its overall size and weight. Due to the endless pursuit of reducing the size and weight of a machine, it is desirable for the gaps to be as small as possible. However, stronger blade–row interactions exist at smaller gaps, which plays a significant role in the aerodynamic performance, as well as the flow variations, and the corresponding effect is complex and not fully understood.

Normally, for a low-speed compressor, its pressure rise and efficiency increase as the gaps reduce. This phenomenon was confirmed by the experimental studies of Smith [1], Mikolajczal [2]. The theoretical analysis of Smith [3] showed that the evolution of the rotor wake in the stator could help to improve its velocity deficit. A model was proposed by Adamczyk [4] to analyze the recovery process of the total pressure deficit for the rotor wake. The main idea of Smith [3], Adamczyk [4] was that reduction of the gaps could prevent the rotor wake being fully mixed out before it entered the stator passage; thus, decreasing the mixing loss and resulting in enhancement of performance. This mechanism was also reported by Deregel and Tan [5] through a numerical study. On the contrary, for a transonic compressor, reducing the blade–row gap might have a negative impact on aerodynamic performance, as the process of shock–vortex plays a significant role in the generation of loss. A smaller blade–row gap might enhance the interaction of shocks and vortices, and increase the loss in consequence[6–9]. The present study only focuses on the gap effect in a low-speed condition.

In the works of Smith [3], Adamczyk [4], Deregel and Tan [5], the variation of the rotor loading was not considered and the contribution of the rotor to the performance enhancement was unknown. Actually, it is also challenging to measure the flow characteristics of a rotor or in a blade–row gap, which means it receives less attention. Later, Du et al. [10,11] conducted a number of numerical simulations to the blade–row interactions at different gaps and found that the rotor would work at a higher-loading state as the gap reduced. A vortex lift mechanism was also proposed by Du et al. [10,11] to explain this phenomenon because unsteady vortex shedding at the trailing edge of the rotor was observed when the rotor blade swept over a stator vane. The vortices were enhanced by the reduction of the gap due to the stronger blade–row interaction, thus increasing the fluctuation, as well as the average, of the rotor loading. The unsteady process of vortex shedding was confirmed by Xu et al. [12] through PIV measurements in a tiny pump, and higher rotor lift was also obtained at the smaller gaps in their numerical simulations. The studies of Du et al. [10,11] through 2D simulations suggested that the rotor loading could be changed through reducing the gap. A significant issue is the dependence of rotor loading on the stage gap in 3D flow condition, which is of interest to the present study.

When multiple blade rows are considered in the simulations, mesh interfaces are constructed between the blocks of different blade rows and additional treatments to the interfaces are necessary. Rai [13], Jorgenson and Chima [14] used patched and overlaid grids for rotor/stator configurations to simulate the unsteady effect of blade–row interaction. A layer of shearing cells between the grids of the rotor and the stator were adopted by Giles [15] in the unsteady simulations for a transonic turbine. Although the above techniques for rotor/stator interfaces are widely used in practice, a defect is that when two blade rows are very close to each other, e.g., the gap is less than 10%c_a, it is difficult to ensure the mesh quality at the gap of the blade rows, and sometimes it is even impossible to generate an available mesh for the case with an extremely small row gap. Due to this limitation, the minimum axial gap in most numerical studies considering the effect of blade–row gap, e.g., see Hsu and Wo [16], Przytarski and Wheeler [17], appeared to be about 10∼30% c_a, and investigations at smaller gaps have not yet been reported. In addition, the flow information exchange at the block interfaces also results in additional errors when the mesh between the two rows is highly distorted at a small gap. As a consequence, the numerical reliability is highly questionable in this situation.

The difficulties mentioned above can be overcome by using immersed boundary (IB) methods, which can efficiently deal with moving boundary problems and complex geometries [18–20]. Zhong and Sun [21] reported the application of an IB method to the flutter problem in turbomachinery, and Du et al. [10,11] investigated the effect of rotor/stator interaction at small stage gaps and also considered the aerodynamic benefit of pitching the stator through an IB method. Chen et al. [22] used an IB method to compute the unsteady blade loading for a compressor at a small gap and its profile showed good agreement with the experimental data. With a high-order scheme employed, IB methods can also be used to study the acoustic resonance induced by blade vibration [23]. These numerical studies exhibited the ability of IB methods to simulate the unsteady problems in turbomachinery with multiple blades included, which, however, were only restricted to 2D configurations and, thus, could be performed on Cartesian grids. For 3D and turbulent flow conditions with moving boundaries, due to the enormous grids needed by the Cartesian grids, there are less related investigations. To consider the turbulence effect when an IB method is employed, adaptive mesh refinement (AMR) [24–28] and wall functions [29–34], are two common routes to accelerate the simulations, and they have mainly been applied to the external-flow conditions. For internal-flow problems, which are of interest to the present study, the flow channels can be larger than the internal bodies. Directly resolving the flow channels by using a Cartesian grid results in an extra large number of cells, which might be unaffordable. How to achieve efficient simulations for 3D high Reynolds-number

internal flows by using IB methods still lacks deep investigation. This paper adopts a hybrid mesh strategy with a single-block body-fitted mesh to the flow channel and an IB method to model the internal bodies, and with some modifications, the IB method can be extended to a general curvilinear grid. With these techniques, the effect of reducing gap can be studied easily by using an IB method with affordable computational costs.

This paper presents a numerical study, conducted in our laboratory, on the effect of stage gap in a low-speed single-stage compressor, termed TA36 in the published works [35–39]. The AMR technique was adopted to the IB method to dynamically enhance the local mesh resolution for both the rotor and the stator. A wall function was used to further improve the efficiency of simulations for high Reynolds-number internal flows. The enhancement of performance contributed by the rotor and the stator individually, as well as the corresponding flow variations, is of great interest. The paper is organized as follows: Section 2 introduces the numerical methods employed, including the governing equations, the grid formation and the IB method adapted to the internal-flow problems. Comparisons to the experimental data are given as a validation and the numerical convergence is also examined. Then, simulations are conducted at two different gaps and the corresponding results presented and discussed in Section 3, including the overall performance enhancement and its spanwise distribution, the flow mechanism and the unsteady characteristics. Finally, a brief conclusion is drawn in Section 4.

2. Numerical Methods

2.1. Governing Equations

The flows are governed by the three-dimensional compressible Navier–Stokes equations, and their conservative forms are written as follows:

$$\begin{aligned}
&\frac{\partial}{\partial t}\int_\Omega \rho d\Omega + \oint_{\partial\Omega} \rho(\vec{u}\cdot\vec{n})dS = 0,\\
&\frac{\partial}{\partial t}\int_\Omega \rho\vec{u} d\Omega + \oint_{\partial\Omega} [\rho\vec{u}(\vec{u}\cdot\vec{n}) + p\vec{n}]dS = \oint_{\partial\Omega} (\tau\cdot\vec{n})dS,\\
&\frac{\partial}{\partial t}\int_\Omega \rho E d\Omega + \oint_{\partial\Omega} \rho H(\vec{u}\cdot\vec{n})dS = \oint_{\partial\Omega} \vec{q}\cdot\vec{n}dS + \oint_{\partial\Omega} (\tau\cdot\vec{u})\cdot\vec{n}dS,
\end{aligned} \tag{1}$$

where $\vec{u} = [u_1, u_2, u_3]$ is the flow velocity vector. $E = c_v T + \frac{\vec{u}^2}{2}$ is the total energy per unit mass and $H = E + p/\rho$ represents the total enthalpy per unit mass. τ is the friction stress tensor and its component τ_{ik} can be computed as:

$$\tau_{ik} = (\mu + \mu_T)(\frac{\partial u_i}{\partial x_k} + \frac{\partial u_k}{\partial x_i} - \frac{2}{3}\delta_{ik}\frac{\partial u_j}{\partial x_j}). \tag{2}$$

μ is obtained following the Sutherland's law. $\vec{q}$ is the heat flux, written as follows:

$$\vec{q} = -c_p(\frac{\mu}{Pr} + \frac{\mu_T}{Pr_T})\nabla T. \tag{3}$$

The ideal-gas law is:

$$p = \rho RT. \tag{4}$$

The turbulent behaviors are modeled by solving the unsteady Reynolds-Averaged Navier–Stokes (URANS) equations with the one-equation Spalart–Allmaras (SA) model [40], and the governing equation for the turbulence field variable is written as follows:

$$\begin{aligned}
\frac{\partial\hat{\nu}}{\partial t} + u_j\frac{\partial\hat{\nu}}{\partial x_j} = c_{b1}(1-f_{t2})\hat{S}\hat{\nu} - (c_{w1}f_w - \frac{c_{b1}}{\kappa^2})(\frac{\hat{\nu}}{d})^2 +\\
\frac{1}{\sigma}[\frac{\partial}{\partial x_j}((\nu+\hat{\nu})\frac{\partial\hat{\nu}}{\partial x_j}) + c_{b2}\frac{\partial\hat{\nu}}{\partial x_i}\frac{\partial\hat{\nu}}{\partial x_i}],
\end{aligned} \tag{5}$$

The turbulence eddy viscosity, μ_T, is computed from:

$$\mu_T = \rho \hat{v} f_{v1}, \tag{6}$$

The convective flux on cell faces is evaluated by the standard Roe scheme [41], and a low-speed modification [42] is implemented for low Mach number flow conditions. To achieve second-order spatial accuracy, the MUSCL interpolation [43] is employed within cells to reconstruct the variable distribution. A second-order central difference scheme and a third-order Runge–Kutta scheme are applied to compute the viscous flux and the temporal derivatives, respectively.

2.2. Grid Strategy

Traditional IB methods always model a wall boundary on a Cartesian mesh and the mesh refinement to a specific region also increases the cell density in the far field. The corresponding computational cost is unaffordable when the flow is 3D and turbulent, which also constrains further application of IB methods. For the turbomachinery applications, because the flow channels are usually not conformal to a cuboid, Cartesian grids, which are larger than the channels, are necessary if the IB method is used to model both the flow channel and the blades, as shown by the example in Figure 1a. In the case of Figure 1a, to meet the requirement of resolution, both the channel walls and the blades need to be resolved by additional grid refinement, which can result in enormous extra cells in the simulations using a Cartesian grid, especially under high Reynolds-number conditions. However, the flow channel is always stationary and makes no contribution to the unsteadiness we are interested in, and there is no need to model the channel by the IB method.

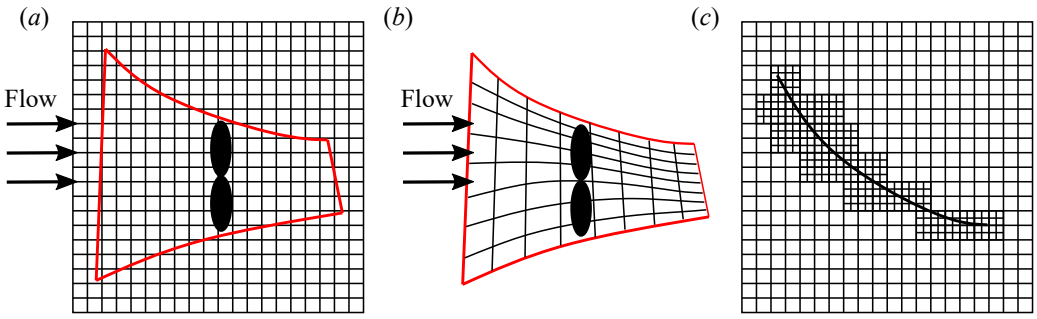

Figure 1. Grid strategies to a turbomachinery problem: (**a**) Cartesian grid, (**b**) channel-conformal structured grid, (**c**) multi-level mesh with AMR. The red solid lines represent the channel, and both the black solid circles in (**a**,**b**) and the black solid line in (**c**) represent the blades inside the channel.

Therefore, a hybrid mesh strategy, in which a body-fitted mesh to fit the flow channel and then an IB method was used only to model the blades in the present work. Firstly, a single-block structured curvilinear mesh was used to fit the channel as background mesh, as shown by Figure 1b. With the body-fitted mesh to the channel, the boundary conditions of the channel walls were imposed through the same manner with the traditional body-fitted methods, which can help to avoid using additional cells to resolve the flow channel by the IB method. Then, to locally enhance the mesh resolution near the blades modeled by the IB method, the adaptive mesh refinement (AMR) technique was employed to increase the grid density near the blades without producing extra cells in the far field, as shown in Figure 1c. AMR has been proved to be an effective method to locally enhance the mesh resolution for high-gradient flow structures [44,45] or wall boundaries [26,27,46]. As a consequence, the cell number can be reduced remarkably for the 3D and turbulent cases compared with the traditional IB approaches. Note that in the present mesh strategy, the IB method was performed on a curvilinear grid instead of a Cartesian grid, and the following section introduces the imposition of boundary conditions for the blade.

2.3. Internal Blade Treatment

To model the internal blades, a sharp interface IB method, which was first proposed by Gilmanov et al. [47], Gilmanov and Sotiropoulos [48] for the Cartesian grid, was used here. All the grid cells are firstly categorized into two types: fluid cell and solid cell, which are at the exterior and the interior of the internal walls, respectively, as shown in Figure 2. The flow quantities of the solid cells are insignificant. Further, the two layers of fluid cells which are adjacent to the solid cells are identified as boundary cells, so that the solid cells are not involved in the calculation of spatial derivatives. The flows at the rest of fluid cells are determined by solving the governing equations.

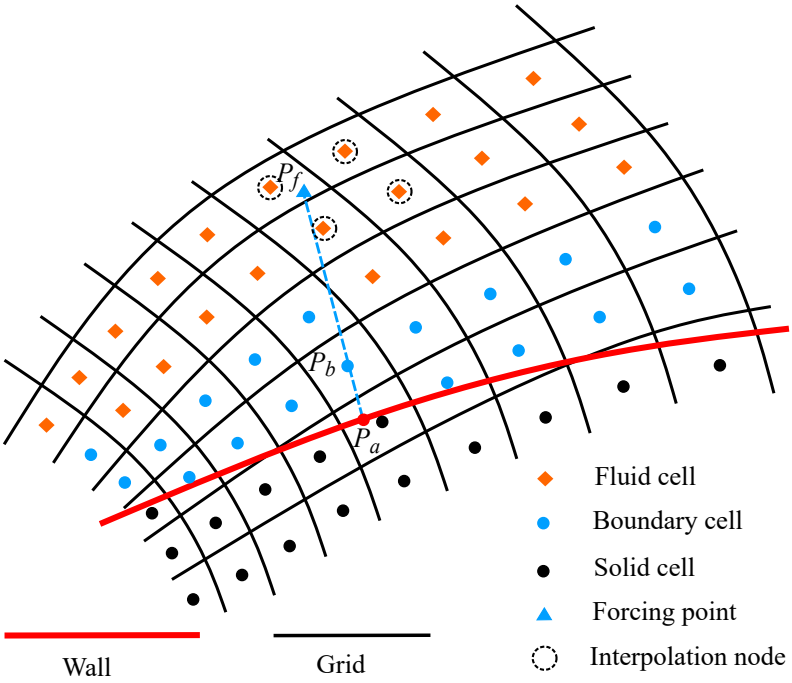

Figure 2. Cell classification for the curvilinear grid near the wall.

To impose the boundary condition for each boundary cell, e.g., P_b in Figure 2, a forcing point surrounded by fluid cells is first obtained, termed P_f. $\vec{P_f P_b}$ is normal to the wall, with P_a being the projection point on the wall. With the flow quantities at P_f and P_a known and assumed distributions for the flow quantities within the boundary layer adopted by the IB method, the quantities at P_b can also be obtained. The distance between P_f and P_b is termed forcing distance in this paper. For the traditional sharp interface IB methods on a Cartesian grid, the forcing distances are usually fixed for all boundary cells, which is not appropriate when the grid is curvilinear and contains large aspect ratio cells. As shown by Figure 3, where the walls with different orientations are surrounded by the large aspect ratio cells, for the boundary cells C_1 and C_2, which are close to the walls W_1 and W_2, respectively, the same forcing distance can locate their forcing points at F_1 and F_2, respectively. F_1 is close to an adjacent cell of C_1 and using the quantities at F_1 to impose the boundary condition at C_1 is reasonable. In contrast, there are several fluid cells between C_2 and F_2, the flows of which are obtained from solving the equations instead of assumed profiles. Therefore, F_2 is invalid for C_2 and a more close forcing point to C_2 is desired. To ensure the close cell to P_f is adjacent to the boundary cells, the forcing distance is adaptively determined for different boundary cells, with their aspect ratio considered. Therefore, there are only a few cells between P_b and P_f, which can ensure the hypothesis for the quantity distributions between the two points is valid.

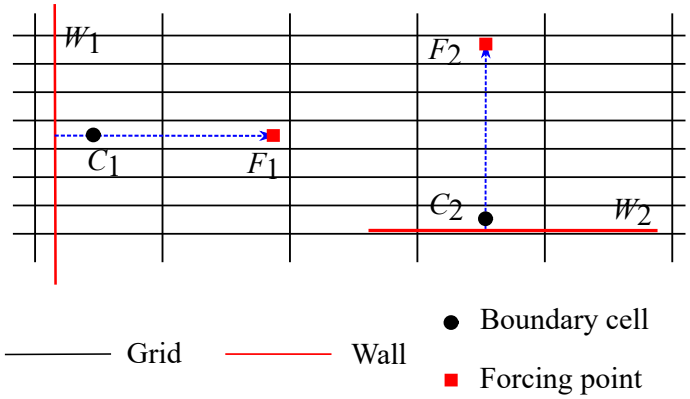

Figure 3. A same forcing distance is used for different wall orientations.

The inverse distance–weight (IDW) interpolation is applied to compute the flow quantities at the forcing point P_f from its adjacent flow cells. For the ith interpolation stencil cell, the corresponding weighted coefficient β_i can be written as:

$$\beta_i = (1.0/d_i^k)/\sum_{s=1}^{m}(1.0/d_s^k), \tag{7}$$

where d_i is the distance from the forcing point to the ith stencil cell. k is the power coefficient and set as 2. To further obtain the tangential velocity at P_b, an explicit turbulence wall function [49] is employed, given as Equation (8):

$$y^+ = u^+ + 0.1108[e^{0.4u^+} - 1 - 0.4u^+ - \frac{(0.4u^+)^2}{2} - \frac{(0.4u^+)^3}{3!} - \frac{(0.4u^+)^4}{4!}]. \tag{8}$$

A linear distribution is assumed for the normal component of the flow velocity. The pressure gradient along the normal direction of the wall is assumed to be zero; therefore, the pressure at P_b equals that at P_f. The temperature is determined by the Crocco–Busemann relation:

$$T_b = T_f + \frac{Pr^{1/3}}{2c_p}(v_{t,f}^2 - v_{t,b}^2), \tag{9}$$

where v_t denotes the tangential velocity. A linear relation is used to compute $\hat{v}$ at the boundary cells:

$$\hat{v} = \kappa u_\tau y_b, \tag{10}$$

where y_b is the distance from a boundary cell to the wall.

2.4. Comparison to the Experimental Data and Convergence

The model of an in-house compressor, TA36, was considered in the present numerical study. This testing rig was designed for the study of flow instability in the compressor and thorough experimental results at the designed gap have been provided [35–39]. Its rotor and stator consist of 20 and 27 blades, respectively, with a gap of 35%c_a. The designed working speed is 2930 rpm. The outer diameter is 600 mm and the hub-to-tip ratio at the domain outlet is 0.7. More parameters about the testing rig can be found in the published works.

In this study, a sector domain was considered, where both the rotor and the stator were modeled by using the IB method. The inlet and the outlet of the domain were placed at 2.0c_a upstream the rotor's leading edge and 3.2c_a downstream the stator's trailing edge, respectively. Only a single passage was considered for each blade row, and, therefore, the blade number ratio of the rotor and the stator was reduced to 1:1. The stator blade was enlarged along the chordwise direction in simulations so that its solidity could remain the

same with the real machine. A single-block structured mesh was used to fit the sector domain as the background mesh, as shown in Figure 4a, which consisted of $140 \times 30 \times 130$ cells. Then, AMR considering the blade locations was carried out on the background mesh, producing additional levels to resolve the blades, as shown in Figure 4b. The mesh refinement was dynamically adjusted to keep the mesh resolution around the rotor blade. The total pressure and the total temperature were fixed at the domain inlet and a back pressure was prescribed at the domain outlet. The no-slipping boundary condition was employed for the shroud, the hub and the blades, and the periodic boundary condition was adopted along the circumferential direction.

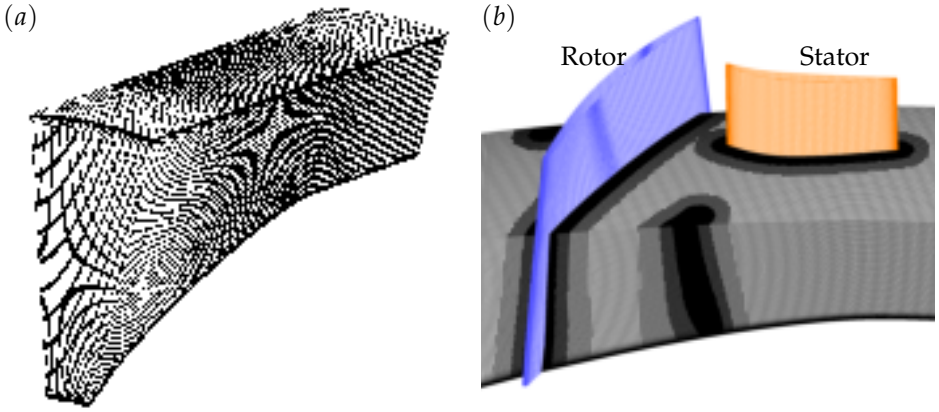

Figure 4. Grid used in the simulations of rotor/stator interaction: (**a**) the background (first-level) grid for the flow channel, and (**b**) part of the multi-level grid with AMR to the blade locations.

To examine the grid convergence, simulations were conducted at the designed stage gap by using grids with different numbers of refinement levels, from 3 to 6. In brief, the grids were termed in the form of IB-X, where X denotes the number of the refinement level. The refinement of AMR was performed through a distance criterion. For each cell of a coarse grid level, their closest distance to the blades was calculated and if they were lower than the critical distance set for this level, the corresponding cells would be refined and produced additional cells with higher resolution. The corresponding critical distances for each grid level are provided in Table 1. Consequently, the corresponding total cell numbers of each grid are given in Table 2, which suggests that the total cell number would almost double when one more refinement level was added. For each simulation, the back pressure was increased in a stepwise form with a fixed interval. The flow coefficient is denoted by ϕ and its definition is given by Equation (11):

$$\phi = \frac{u_{a,in}}{u_m}, \tag{11}$$

where $u_{a,in}$ and u_m is the plane-averaged axial velocity at the domain inlet and the tangential velocity at the rotor mid-span, respectively. All static pressures presented in this paper are normalized through Equation (12):

$$p^* = \frac{p - p_1}{0.5\rho_1 u_m^2}. \tag{12}$$

Figure 5 shows the aerodynamic performances obtained by using different grids, including the coefficients of static-to-total pressure rise and the efficiencies. The experimental data of pressure rise is also included in Figure 5a for comparison. As shown in Figure 5a, the characteristic lines obtained by different grids were close to each other, and all of them showed good agreement with the experimental data, indicating good convergences. However, comparisons in Figure 5b revealed obvious discrepancies for the adiabatic efficiencies when there were less numbers of refinement level. To achieve convergence for the efficiency at each flow coefficient, at least 5 grid levels were necessary, and only slight

differences could be identified between the efficiencies obtained by the IB-5 and the IB-6 grids. Therefore, the IB-5 grid was used in the following study. Since it was hard to accurately measure the adiabatic efficiencies in experiments of the low-speed compressor, the corresponding experimental results are unavailable. The CFL number was set as 2.0 for all grids, yielding a non-dimensional time step of 5.12×10^{-5} for the IB-5 grid, with the time for reference being c/u_t. Therefore, about 13590 steps were needed for the rotor to pass a blade passage. To further examine the independence of results on the time step, a simulation for $CFL = 1.0$ was also performed for the IB-5 grid. The corresponding results are also included in Figure 5, which only exhibits very slight differences with the results of $CFL = 2.0$ and, thereby, indicated that using $CFL = 2.0$ for the IB-5 grid could ensure numerical convergence. The total cell number of the IB-5 grid was almost 10 million, while the traditional body-fitted method might only need about half of them when dealing with the same problem. It is known that more grid cells are necessary for the IB methods than the body-fitted method for high Reynolds-number flows. However, it was better to use the IB method to deal with the rotor/stator interaction at such a small axial gap as that being considered in the present work, since it is very challenging to generate a high-quality mesh with a smooth rotor/stator interface for the body-fitted strategy under this situation. From this perspective, we believe using more grids to overcome this difficulty was worthwhile. For the simulations using the IB-5 grid, time marching for 100 thousands steps costs about 5760 cpu hours. Specifically, the dynamic adjustment due to the rotor's movement was performed every 55 steps, and the corresponding time cost was about 2.8% of the total.

Table 1. Critical distances for different grid levels.

Grid Level	Critical Distance (Normalized by c)
Level 1	0.18
Level 2	0.07
Level 3	0.03
Level 4	0.01
Level 5	0.007

Table 2. Total cell numbers of the grids with different numbers of refinement level.

Mesh	Total Cell Number
IB-3	2.91 millions
IB-4	5.80 millions
IB-5	9.66 millions
IB-6	22.83 millions

To examine the mass conservation from the inlet to the outlet of the domain, the flow coefficients of the two planes, as well as their differences, obtained by the IB-5 grid, are given in Table 3. The operation conditions were those shown in Figure 5. It can be seen that the largest difference for the mass flow was 0.82%, which was observed at the near-stall condition, and, in other cases, the differences were more slight. It is, therefore, believed that mass conservation could be ensured when using the present IB method to study the flow of blade–row interaction. The following discussion mainly focuses on the effect of stage gap at the working conditions around $\phi = 0.316$. Therefore, to further quantify the convergence under this case, with the corresponding performances obtained by the IB-6 grid treated as reference data, the error ratios, as functions of the number of refinement, are presented in Figure 6, for the flow coefficient, the total-to-total pressure rise and the adiabatic efficiency. It can be seen that both the errors of the flow coefficient and the pressure rise appeared to decrease as the number of level increased, and they were observed to be about 0.5% for the IB-5 grid. Although the error of the efficiency was observed to grow slightly when the number of level was increased from 4 to 5, the corresponding difference for the IB-5 grid was pretty low, i.e. about 0.2%. Therefore, using the IB-5 grid could help to balance

accuracy and computational cost. Since the unsteady characteristics were of great interest, convergence of the pressure fluctuation at the target flow condition was also illustrated. Figure 7 shows the predicted unsteady pressure profiles of a location on the stator surface, which was near the leading edge of the 90% span section, when different grids were used, and their root-mean-square(R.M.S) values are provided in Table 4. As can be identified from Figure 7, the time profile of the IB-5 grid was consistent with that of the IB-6 grid, and the difference ratio of their R.M.S values was about 0.32%. Therefore, it is believed that the IB-5 grid could also provide convergent results for the unsteady characteristics.

The distribution of y^+ on the rotor blade for the 5-level mesh is plotted in Figure 8. Note that for each segment of the surface, the y^+ values were taken from their forcing point. The maximum of y^+ appeared to be lower than 100 on both the pressure and the suction surfaces of the blade. Note that the corresponding numerical results in the works of Tamaki et al. [31], Berger and Aftosmis [32], Cai et al. [33], Constant et al. [34] with the same y^+ range also agreed well with the data for comparison, which also reinforced our confidence in the present 5-level mesh.

Table 3. Mass flow rates on the inlet and the outlets at different operation conditions obtained by the IB-5 grid.

Operation Condition	Inlet	Outlet	Difference/Inlet
1	0.340	0.342	0.59%
2	0.329	0.328	0.30%
3	0.316	0.315	0.32%
4	0.302	0.303	0.33%
5	0.286	0.286	0%
6	0.266	0.265	0.37%
7	0.242	0.240	0.83%

Table 4. R.M.S values of the unsteady pressure shown in Figure 7 and their error ratios to the reference data.

Mesh	R.M.S	Error Ratio
IB-3	0.3730	0.0652
IB-4	0.3851	0.0348
IB-5	0.4003	0.0032
IB-6	0.3990	reference

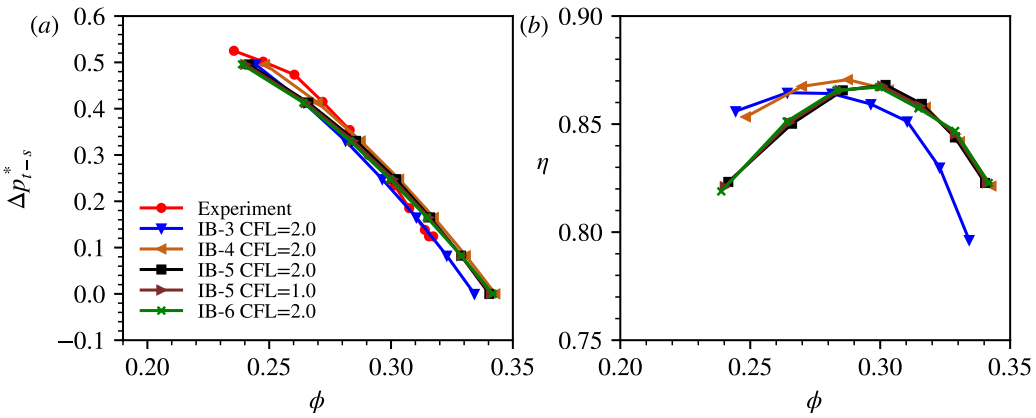

Figure 5. Comparison of the performance obtained by the experiment and the present IB method with different numbers of refinement level: (**a**) Static-to-total pressure rise coefficient; (**b**) adiabatic efficiency.

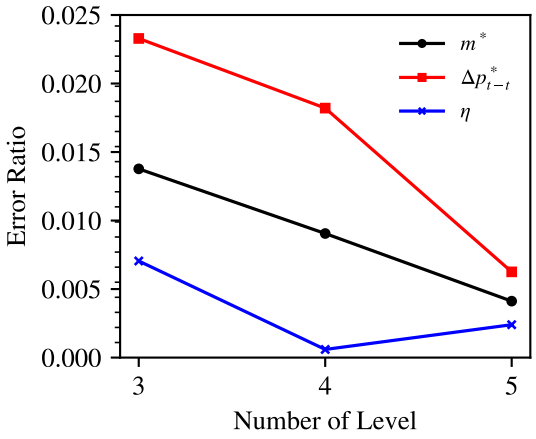

Figure 6. Error ratios of flow coefficients, total-to-total pressure rises and efficiencies compared to the reference data.

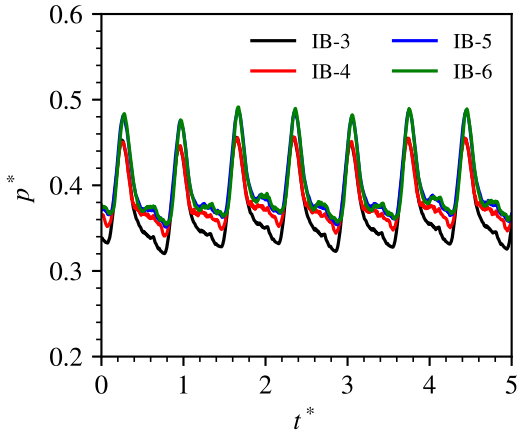

Figure 7. Unsteady pressure obtained by using different numbers of refinement level.

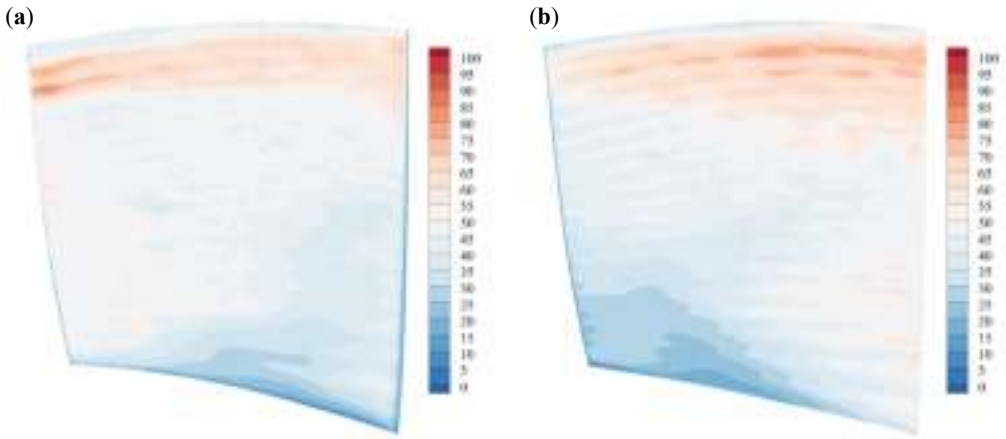

Figure 8. Distributions of y^+ on the rotor blade. (**a**) Pressure surface and (**b**) suction surface.

3. Results and Discussions

To investigate the effect of the stage gap, the axial distance between the rotor and the stator was reduced to 10% of the designed value, and its effect on the performance and the variation of flow characteristics studied numerically. For the back pressure producing the designed mass flow rate at the designed gap, simulations at the other three moderate gaps were also be performed at the same back pressure in order to examine whether the variation of aerodynamic performance was consistent if the row gap continuously changed.

The relative positions of the rotor and stator at the designed gap and its 10% are shown in Figure 9a,b, respectively. Note that the axial distance from the rotor's trailing edge and the stator's leading edge on the hub surface was measured as the gap distance in this paper, and the designed value denoted by d_0, i.e., $d_0 = 35\%c_a$. Reduction to the axial gap was achieved by adjusting the axial location of the stator with the rotor fixed. Specifically, the 5-level mesh on the hub surface for the smaller gap, i.e., $0.1d_0$, is presented in Figure 10. Generation of a high-quality mesh at such a small gap is challenging to the traditional body-fitted approach, while it can be easily modeled by the IB method. As can be found from Figure 10, there were still about 12 cells in the streamwise direction from the rotor's trailing edge and the stator's leading edge on the hub surface. The spatial scheme used in the present study required the first two closest layers of cells near the blade in the fluid domain to be marked as boundary cells, and their forcing points, thus, were always located near the third closest layer of cell near the blade. Therefore, even for the smallest-gap case, shown in Figure 10, the impositions of the boundary condition for rotor and the stator would not influence each other. Moreover, for the designed cases with 10% gaps, the corresponding axial distances from the rotor's trailing edge and the stator's leading edge at the tip region were $56\%c_a$ and $24\%c_a$, respectively.

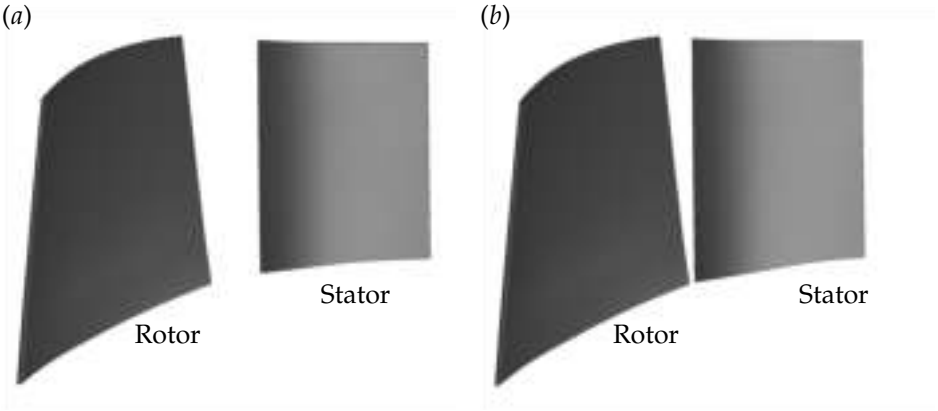

Figure 9. The relative positions of the rotor and the stator at: (**a**) $g = d_0$ and (**b**) $g = 10\%d_0$.

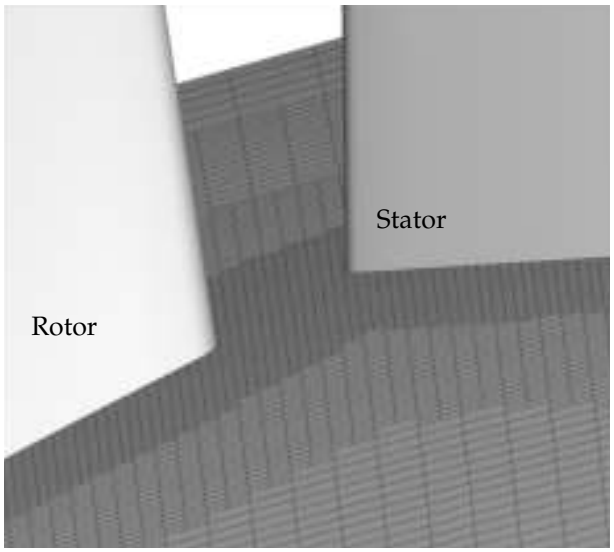

Figure 10. A close view to the 5-level mesh on the hub surface at $g = 10\%d_0$.

3.1. Overall Performance at Different Gaps

Figure 11a,b show the comparisons of the total pressure rise and the adiabatic efficiency at two gaps, d_0 and $0.1d_0$, respectively, It can be seen, at each back pressure considered, the

mass flow rate, the total pressure rise and the efficiency were all observed to be higher at the smaller gap, indicating that performance enhancement could be obtained through reduction of the stage gap. Cases 1–3, marked in Figure 11a, were near the designed working point of the compressor. Cases 1 and 2 had the same back pressure but different gaps, the flow coefficients of which were 0.316 and 0.318, respectively. For cases 1 and 2, reducing the gap from d_0 to $0.1d_0$ resulted in increases of 0.7%, 3.1% to the flow coefficient and the total pressure rise of the stage, respectively. Besides this, the stage efficiency also increased by 1.6%. To further demonstrate the effect of row gap under the same back pressure, cases 1 and 2 simulations were also conducted at the other three moderate gaps between d_0 and $0.1d_0$ at the same back pressure. Figure 12 shows the variation of the aerodynamic performance as a function of the blade–row gap. As the row gap continuously reduced, higher mass flow rate, total pressure rise and efficiency could be observed, suggesting the dependence of the aerodynamic performance on the row gap was consistent at the designed working point.

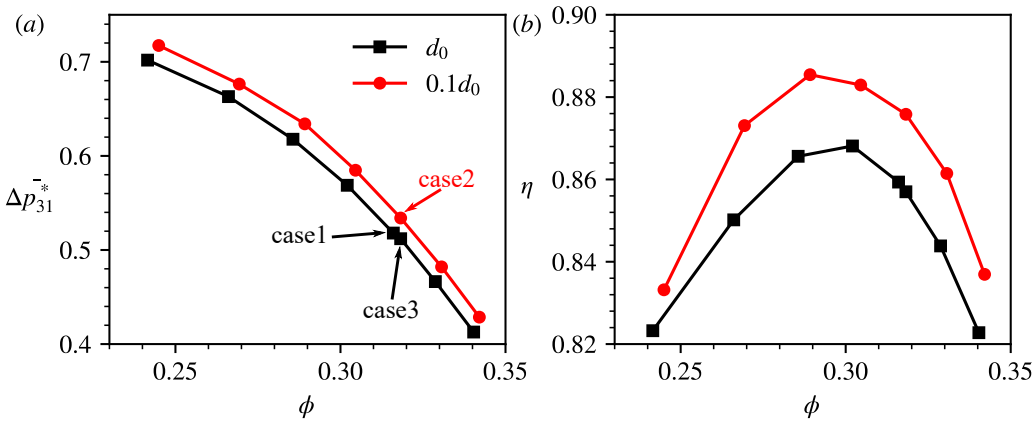

Figure 11. Aerodynamic performance at two row gaps: (**a**) the total-to-total pressure rise coefficient and (**b**) the adiabatic efficiency.

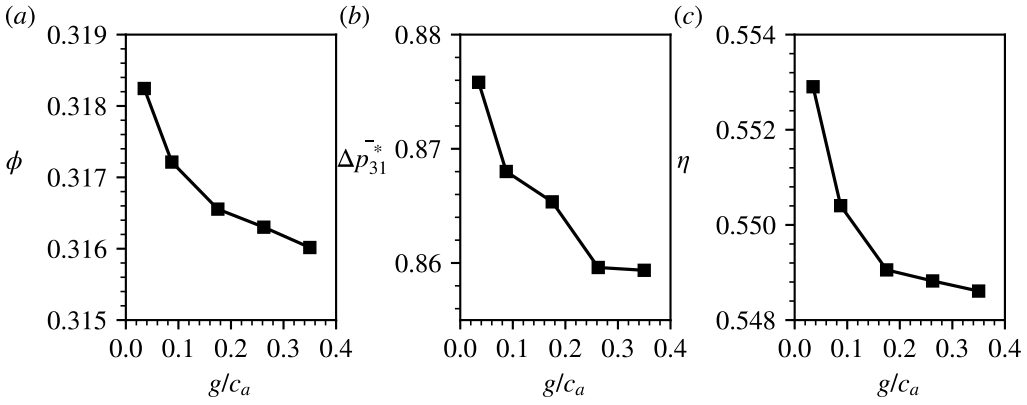

Figure 12. Aerodynamic performance at different row gaps with a fixed back pressure: (**a**) mass flow rate, (**b**) total pressure rise coefficient and (**c**) adiabatic efficiency.

For a subsonic compressor, the mixing loss of rotor wake can be reduced when the gap becomes smaller, which was used to explain the generation of performance benefit by Smith [3], Adamczyk [4]. Du et al. [10,11] reported a vortex lift mechanism due to the blade–row interaction and the rotor loading was observed to be higher at a smaller stage gap. Therefore, both the flow variations of the rotor and the stator make some contributions to the performance enhancement of the compressor stage after the gap is reduced. Separating the contributions from the rotor and the stator was the main purpose of this work, which might be challenging in experiments because measurements at a narrow gap are normally not allowed.

In the following, comparisons are made for the results of cases 2 and 3, the flow coefficients of which were both 0.318. To quantify the contributions of the two blade rows to the performance enhancement individually, Figure 13 shows the time profiles of the total pressure rise on the rotor and the stator outlets, as well as the axial torque of the rotor blade for cases 2 and 3, where their time-averaged values are also plotted through the horizontal dashed lines. It is remarkable that when the gap reduced, their averaged values also appeared to be higher, and increases of 0.5% and 4.3% were observed for the averaged total pressure rises on the rotor and the stator outlets, respectively, as shown in Figure 13a,c. Correspondingly, the averaged axial torque on the rotor blade, shown in Figure 13b, was also found to increase by 0.9%, confirming that the rotor worked at a higher-loading state when the gap reduced. It is noticeable that the benefit from the stator was more outstanding than that from the rotor. The following discussion reveals that, besides the contribution of wake recovery in the stator, the flow separation near the stator hub is well suppressed through the reduction of the stage gap, which results in a great influence on the performance of the stator. The higher pressure in the stage gap due to the increase of rotor loading plays a significant role in the suppression of the flow separation.

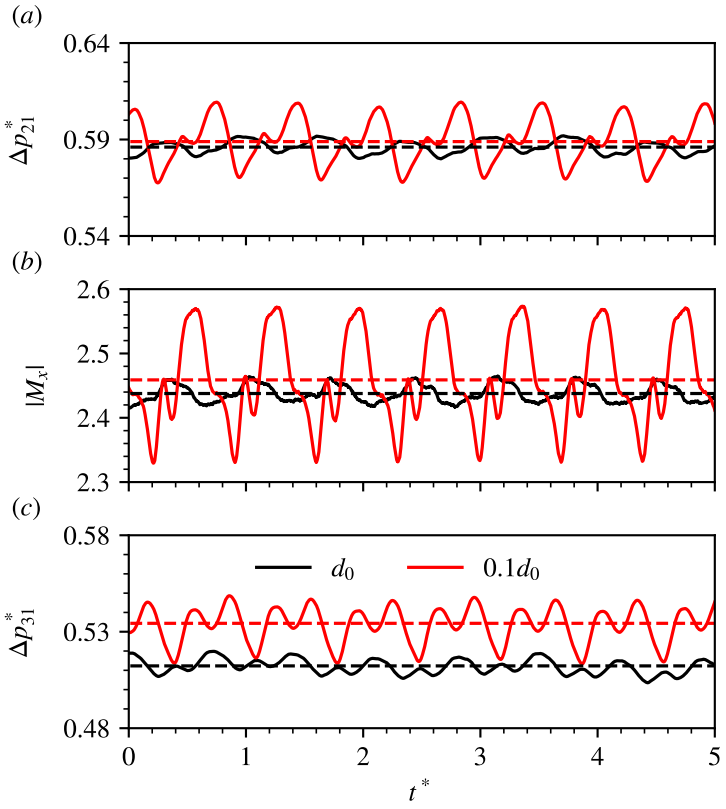

Figure 13. Time profiles of (**a**) the total pressure rise coefficient on the rotor outlet, (**b**) the aerodynamic moment on the rotor blade and (**c**) the total pressure rise coefficient on the stator outlet.

Note that the outlets of the rotor and the stator were located at 1%c_a and 6%c_a downstream of their trailing edges, respectively. The rotor outlet was also treated as the stator inlet. Since the variation of gap was achieved by adjusting the axial location of the stator, when the gap changed, the distance from the stator inlet to the stator was slightly different, and this effect was slight as the analysis mainly focused on the quantities of the outlets of the rotor and the stator.

3.2. Spanwise Distributions of the Performance Enhancement

The ratio of performance enhancement for the rotor between cases 2 and 3 appeared to be much lower than that reported by Du et al. [10,11] through 2D simulations. Since the

stage gap was non-uniform along the span, as shown in Figure 9, the benefit of reducing the gap might also differ along the span location. To demonstrate this dependence, Figure 14a,b show the spanwise distributions of the averaged total pressure rise on the rotor and the stator outlets, respectively, which were obtained by firstly averaging the transient data along the pitch at each moment and then in a blade-passing cycle. Note that all the spanwise distributions in the following were obtained in this manner without additional mention. To further quantify the differences of performance along the span, Figure 15a also shows the incremental ratios of the total pressure rise on the two planes as the gap reduced. It can be seen from Figure 14 that the variations of performance were obvious in the low-span regions, i.e., $r < 0.6$, for both the rotor and the stator after the gap reduced. The contributions from the rotor and stator, as well as the corresponding flow variations, were of particular interest and the following discussion focuses on this aspect.

On the rotor outlet, reducing the gap to $0.1d_0$ resulted in increases of 1∼2% for the total pressure rise in the range of $r < 0.6$, as shown in Figures 14a and 15. In contrast, the benefit in the rest of the span locations was negligible and even negative. Such a variation on the rotor outlet was well related to the nonuniform gap size along the span. Although the gap reduced to an extremely small value at the hub, as shown in Figure 9, the tip region still worked with a considerable gap, i.e., 24%c_a, and, thereby, the rotor performance in the tip region did not exhibit much difference. This clarified that when the gap became small, the spanwise distribution of the gap could be determined well by the 3D blade geometries of the adjacent blade rows. The increase of the total pressure rise in Figure 14a after the gap reduced also suggested that the rotor loading could be enhanced through reducing the gap. Chung and Wo [50] conducted a study to split the potential and the vortical effects at different blade–row gaps and found that the potential effect was important, especially after the gap was less than 10% blade chord. Therefore, in the present case, after the gap reduced to $0.1d_0$, the potential effect from the stator might play a significant role in the pressure distribution in the stage gap; thus, affecting the rotor loading. The potential effect is an inviscid mechanism and excludes the effect of vortex shedding. Du et al. [10,11] found the vortex shedding would also be enhanced when the gap reduced, associated with higher instantaneous rotor loading. Quantification to the contributions of the unsteady vortices and the potential effect on the rotor loading enhancement will be an important topic in our future study.

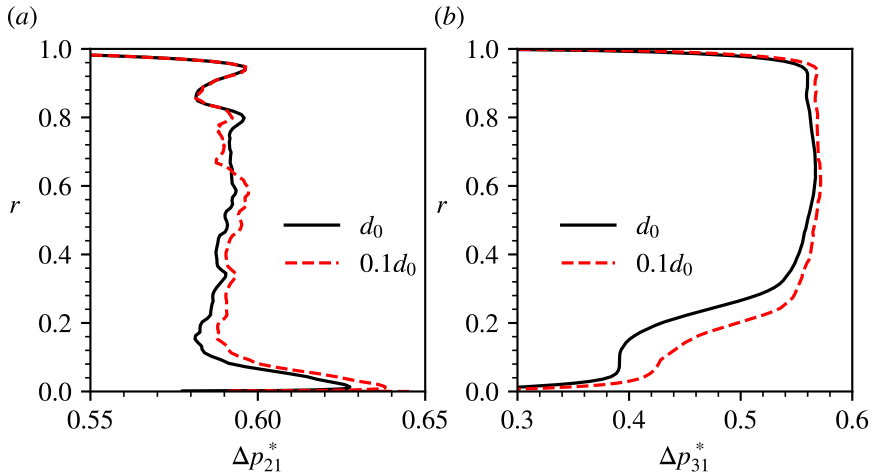

Figure 14. Spanwise distributions of the total pressure rise on (**a**) the rotor and (**b**) the stator outlets.

On the stator outlet, with the gap reduced to $0.1d_0$, the total pressure rise was found to increase in all the span locations, as shown in Figure 14b. Specifically, the enhancement was remarkable in the range of $r < 0.4$, as shown in Figure 15, and its maximum ratio was close to 16%, which was located in 20∼25% span. At these lower span locations, the corresponding ratios were all observed to be higher than 8%. In contrast, the increase of

the total pressure rise was most insignificant in the range of $r > 0.4$, which was lower than 2%. To further explore the source of performance enhancement in the stator, Figure 15b provides the spanwise distributions of the total pressure loss coefficient between the outlets of the two blade rows at the two gaps. It can be seen from Figure 15b that, after the gap reduced, the reduction of the total pressure loss in the span range of $r < 0.4$ was remarkable. Since the enhancement of the stage performance in this span range was far beyond the contribution of the rotor, see Figure 14, the contribution from the stator, thus, might be the major factor. The total pressure loss in other span locations also decreased after the gap reduced; however, only to a minor extent. Smith [1] reported a 2∼4% increase in the static pressure rise for a low-speed compressor when the gap was reduced from 37% of the chord to 7%. This increase could be explained by the theory of wake recovery, which was attributed to the reduction of the mixing loss of the rotor wake by Smith [1,3], Deregel and Tan [5] and appeared to be more obvious when the flow coefficient became lower. In the present study, as discussed in the last section, the target flow condition was far behind the stall point, but the increase of the total pressure rise on the stator outlet was found to be 4.3%, which was almost twice the lowest measured value in Smith [1]. Analysis of the spanwise pressure distributions in Figures 14 and 15 revealed that it was the outstanding enhancement at the stator hub region that resulted in such a higher overall ratio on the stator outlet. The higher increase in the stator hub region suggested some different flow phenomena might exist, which resulted in a great reduction of the total pressure loss. On the other hand, the benefit ratio in the range of $r > 0.4$ at the stator outlet was close to the experimental data reported by Smith [1], and the reduction of the total pressure loss after the gap was reduced was also slight, indicating the wake recovery process was dominant in the performance enhancement in this span range.

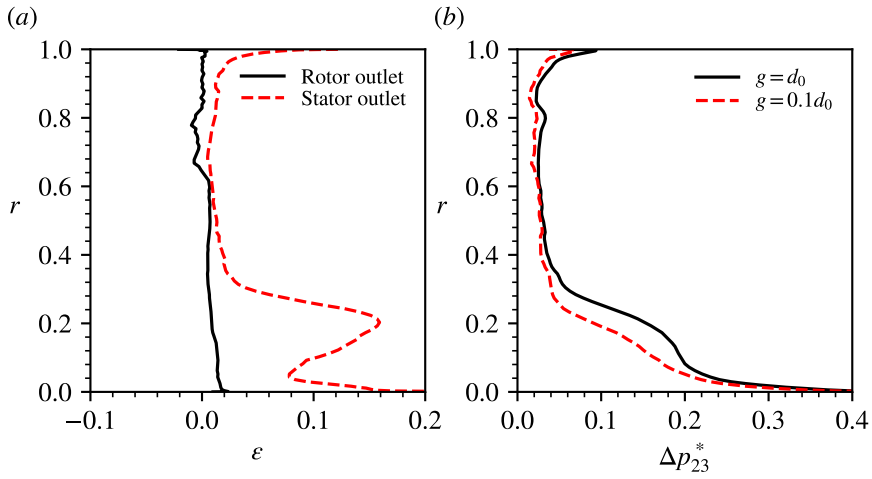

Figure 15. Spanwise distributions of (**a**) the incremental ratio of the total pressure rise on the rotor and the stator outlets when the gap reduced from d_0 to $0.1d_0$ and (**b**) the total pressure loss coefficient of the stator at the two gaps.

3.3. Flow Mechanism

To explore the generation of performance enhancement from the two blade rows, Figures 16 and 17 show the instantaneous distributions of Mach number and turbulence viscosity of the same moment for the two different gaps, respectively, at the same flow coefficient investigated. These flow contours were visualized on the 90% and the 20% span sections, as representatives for the shroud and the hub regions, respectively. As shown in the second column of Figures 16 and 17, the flow contours at the extremely small gap were also smooth and did not suffer from the discontinuity generated by the blade–row interfaces encountered in the body-fitted approach, indicating that the IB method could be well applied to simulations of multi-row models with small gaps. For the two gaps, their flow characteristics on the 90% span section seemed to be similar, see the comparisons of the

first row in Figures 16 and 17, respectively. When the gap was reduced, it was noticeable that higher turbulence intensity could be observed when the rotor wake impinged on the stator in the smaller-gap case at both the shroud and the hub regions, see the areas marked by the red dashed circles in Figure 17b,d. In the studies of Du et al. [10,11], it was found that when the gap was small, every time a rotor blade swept over a stator blade, a strong unsteady vortex shed from the trailing edge of the rotor blade, thus, increasing the oscillation amplitude as well as the mean value of the lift of the blade. Normally, flow turbulence intensity can be well enhanced by vortex structures as the magnitude of vorticity is part of the source term in the governing equation of the SA turbulence model. After the unsteady vortices shed from the rotor blade impinge on the downstream stator blade, the turbulence intensity might be further enhanced. On the other hand, higher velocity gradient was formed along the direction of the rotor wake when the gap was reduced, see the comparison of *Ma* contours in Figure 16, which might also play a significant role in the increase of turbulence intensity of the rotor wake.

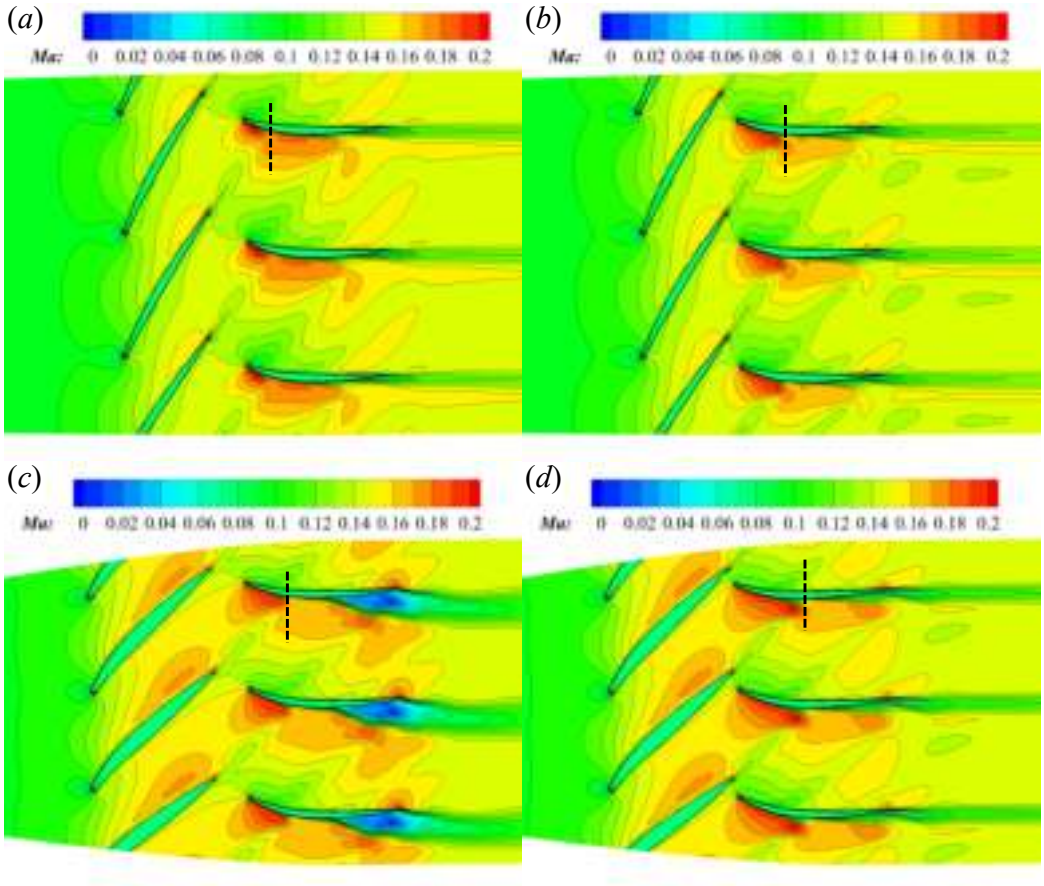

Figure 16. Flow contours of Ma on two span sections at $\phi = 0.318$ for the two gaps: (**a**) 90% span and $g = d_0$; (**b**) 90% span and $g = 0.1d_0$; (**c**) 20% span and $g = d_0$; (**d**) 20% span and $g = 0.1d_0$.

Figures 16 and 17 show that the reduction of the gap greatly impacted the flow structures at the hub region. At the designed gap, flow separation could be observed in the stator hub, as shown in Figures 16c and 17c. Such a phenomenon is widely encountered by high-loading compressors [51]. However, this separation is well suppressed in the smaller-gap case, as shown in Figures 16d and 17d. As regards the authors' acknowledgement, such an effect of reducing gap has not been reported yet in any experiment or simulation. This might be due to the fact that the smallest gaps considered in previous numerical studies, e.g., Hsu and Wo [16], Przytarski and Wheeler [17], were limited by the body-fitted grids and significantly larger than that of the present work. Figure 18 also shows the

distributions of Ma at the two gaps on a downstream section 40%c_a to the stator's trailing edge. Besides the case of $\phi = 0.318$, the contours at $\phi = 0.241$ were also included, as a representative for the near-stall condition. It can be seen from Figure 18a,c, flow separation existed in a small region near the stator hub at $\phi = 0.318$ and the reduction of the gap almost suppressed all the separation in the hub region. When the compressor worked at the near-stall point, although flow separation still existed in all span locations after the gap was reduced, both its width in pitch and the areas with the lowest Mach number were observed to shrink, as shown by the comparison of Figure 18b,d, indicating the effect of suppression to the flow separation still played a significant role at the near-stall condition after the gap reduced. It is known that RANS models always fail to accurately capture details of separated and tip leakage flows without additional modifications. However, the results in Figure 5a suggest that this inaccuracy was insignificant in the prediction of the compressor performance, as the numerical results did not exhibit much difference with the experimental data. Actually, RANS models are still widely used to study compressor flows. Although the flow separation in the stator was one major aspect of the present study, what we wanted to highlight was the dependence of this separation on the gap. The details of the separated flow, e.g., the spanwise length of the region with separation, obtained by the numerical study might be different from the reality, but the overall tendency observed with a reducing gap is still inspiring.

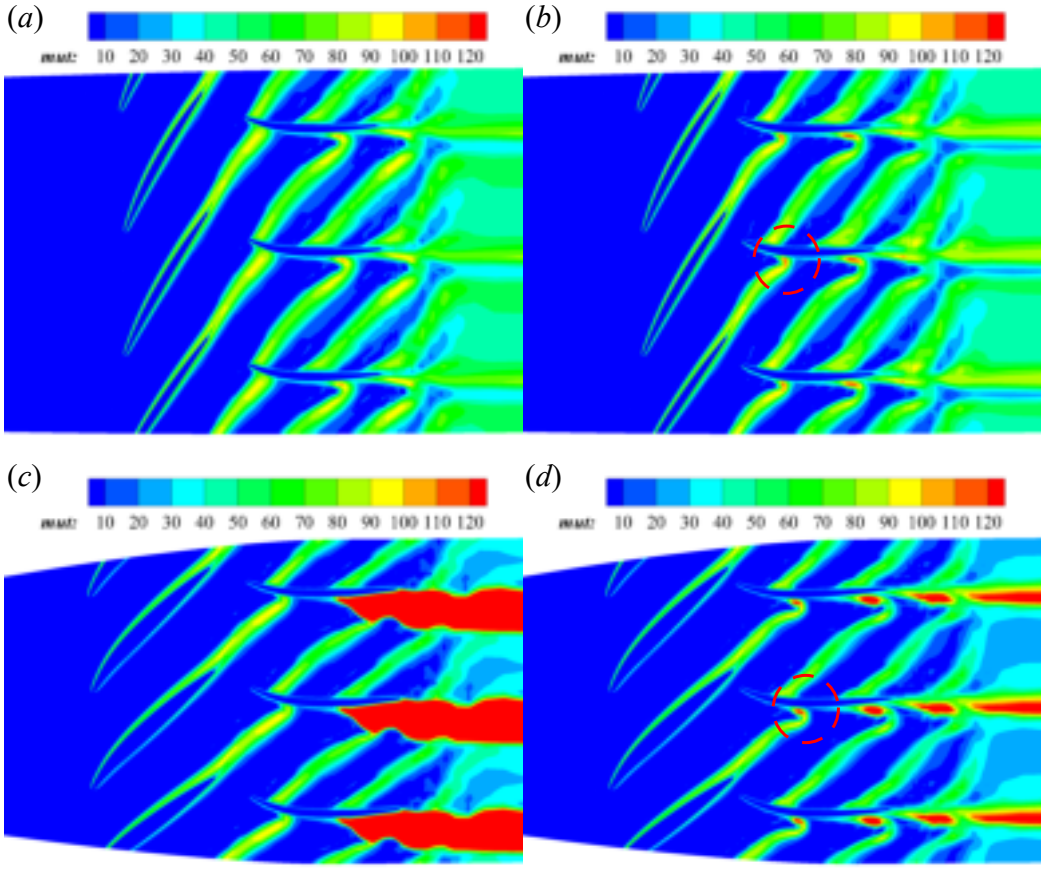

Figure 17. Flow contours of turbulence viscosity on two span sections at $\phi = 0.318$ for the two gaps: (**a**) 90% span and $g = d_0$; (**b**) 90% span and $g = 0.1d_0$; (**c**) 20% span and $g = d_0$; (**d**) 20% span and $g = 0.1d_0$.

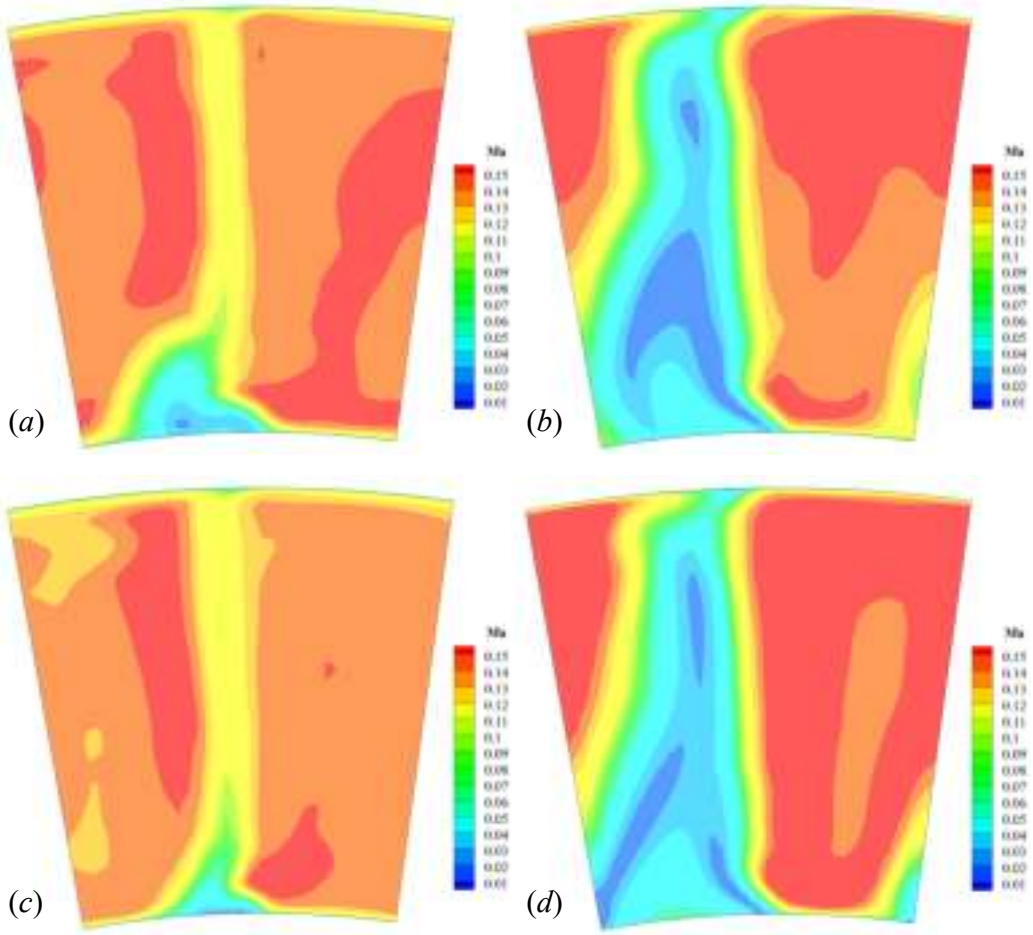

Figure 18. Distributions of Ma at the downstream section 40%c_a to the stator's trailing edge: (**a**) $g = d_0$ and $\phi = 0.318$; (**b**) $g = d_0$ and $\phi = 0.241$; (**c**) $g = 0.1d_0$ and $\phi = 0.318$; (**c**) $g = 0.1d_0$ and $\phi = 0.241$.

To further analyze the cause of suppression to the flow separation, the spanwise distributions of the flow velocity and static pressure on the outlets of the rotor and the stator were investigated. Figure 19 shows the spanwise distributions of the three non-dimensional velocity components on the rotor outlet at the two gaps. The reference for the velocity components shown in Figure 19 is u_t. It can be seen that the three components almost remained the same in all span locations when the gap reduced, suggesting that the inlet-flow angles of the stator at the two gaps were also close to each other. Therefore, the suppression to the flow separation in the stator was not due to the change of the inlet-flow angle. It can be observed in Figure 14a that the total pressure rise at the hub region of rotor increased after the gap reduced. Since the velocity distributions on the rotor outlet at the two gaps were almost the same, it, thus, could be inferred that most of the increase of the total pressure was due to the rise of the static pressure on the rotor outlet.

Figure 20 shows the spanwise distributions of the static pressure on the rotor and the stator outlet for the two gaps. It can be confirmed that the static pressure on the rotor outlet was found to increase in most span locations as the gap reduced. The difference between the static pressures on the inlet and the outlet of the stator in Figure 20 revealed that the flow experienced an adverse pressure gradient in the hub region of the stator, which was related to the separation. r_1 and r_2 in Figure 20 are used to denote the height in span of the region with adverse pressure gradient at $g = d_0$ and $0.1d_0$, respectively. Due to the increase of the static pressure in the stage gap after the gap reduced, the region with adverse pressure gradient was found to shrink, i.e., $r_2 < r_1$. This improvement compressed the separation region, thus, further reducing the total pressure loss in the stator hub region and resulting in a great enhancement to the performance of the stator. To further demonstrate

the flow variation on the stator outlet, Figure 21 shows the spanwise distributions of the three velocity components on the stator outlet, which are normalized by u_t. Prominent differences can be observed for the flow velocity near the hub, especially for the axial and the radial components in Figure 21a,c, respectively, and both the components were found to be higher in the smaller-gap case. These differences of flow velocity suggested that the mass flow rate increased in the stator hub region and the blockage caused by the flow separation improved. In addition, the circumferential components, shown in Figure 21b, were close to zero at all span locations at the designed gap, and only exhibited slight differences when the gap differed.

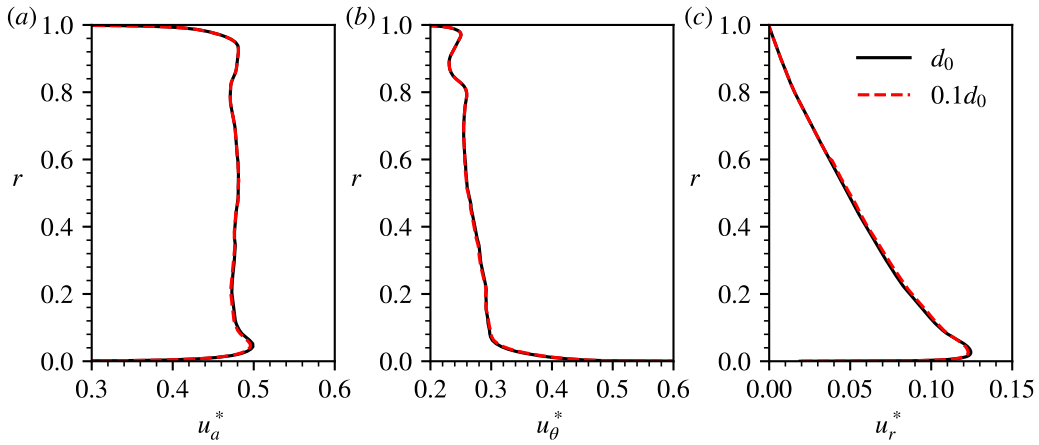

Figure 19. Spanwise distributions of the three velocity components on the rotor outlet at different stage gaps: (**a**) axial; (**b**) circumferential; (**c**) radial.

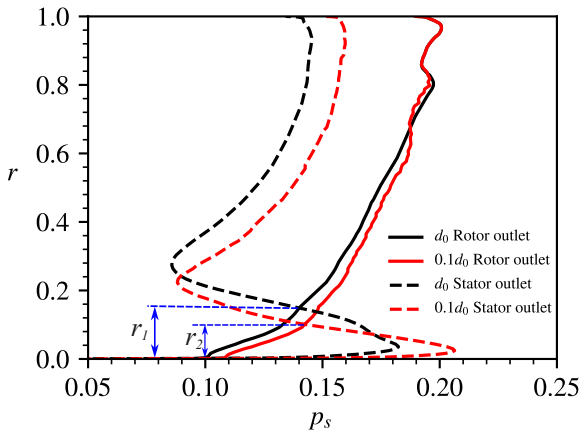

Figure 20. Spanwise distributions of the static pressure on the rotor and the stator outlets at different stage gaps.

From Figures 19–21 it can be found that over most of the span, the stator was accelerating the flow and decreasing the pressure, which was an unexpected behavior for a compressor stator. Normally, the stator of a compressor should both change the flow direction and increase the static pressure. However, for the present stator working in a low-speed compressor, it was designed mainly to change the flow direction with a very weak capacity of increasing the static pressure. As can be seen from Figure 4, the flow channel contracted along the axial direction. Therefore, the flow accelerated after it flowed out the rotor. Since the stator was designed to work at a high-loading state(i.e., high inlet flow angle, especially near the hub, see Figure 19, flow separation exited in the hub of the stator, resulting in a further decrease of the flow area in the stator. All these factors made the flow accelerate in the stator and the pressure thus decreased. For this condition, an obvious adverse pressure gradient was observed at the stator hub and reduced adverse

pressure gradient could help to suppress the flow separation. Specifically, after the gap reduced and the flow separation was partly suppressed, the blockage at the hub region also improved, thus, resulting in a smaller decrease of static pressure in the stator passage, see the range of $r > 0.3$ in Figure 20, and the increase of the axial flow velocity at the hub region, see Figure 21a. Note that reduction of the gap was achieved by moving the stator upstream, which made the channel contraction at the stator hub more important. This factor might also play a role in the flow suppression, and future studies are necessary to further demonstrate this effect.

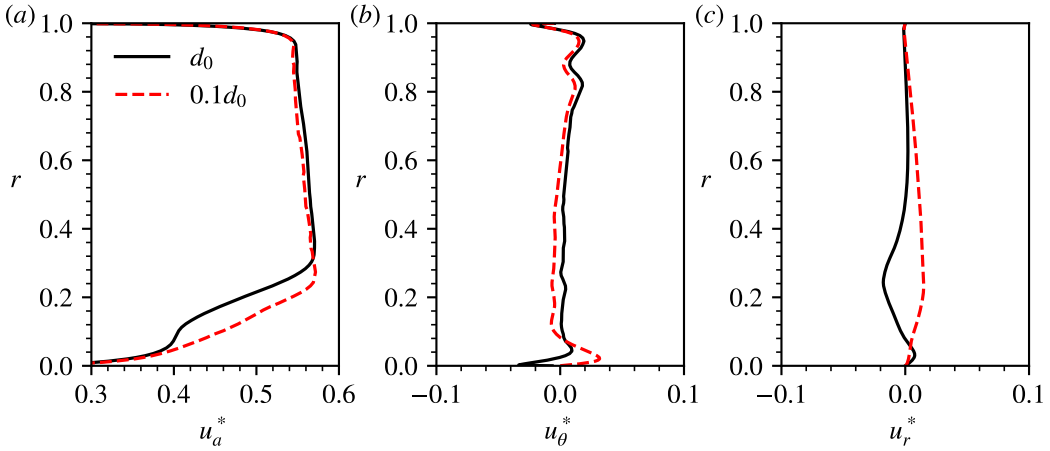

Figure 21. Spanwise distributions of the three velocity components on the stator outlet at different stage gaps: (**a**) axial; (**b**) circumferential; (**c**) radial.

The analysis in this section shows that both the rotor and the stator contribute to performance enhancement after the gap is reduced. At the smaller gap, the rotor outputs more work to the flow and increases the static pressure at the stage gap, which can improve the adverse pressure gradient and suppress the flow separation at the stator hub. The flow variation in the stator further reduces the total pressure loss at the hub and results in a great benefit to the stage performance. For the case considered in the present study, the performance increase of the stator resulted from two mechanisms: wake recovery, which is a classical manner to explain performance increase, and suppression to the stator flow separation, which is one major point of the present work. The first mechanism was observed in upper span locations, where the stator flow was attached, and the ratio of performance increase was less than that in the lower span range, where the second mechanism dominated. For a configuration without separation, when the gap reduced, the great benefit of suppressing separated flow did not exist and the performance increase of the stator should be similar with that in the upper span range of the present study. In this situation, only the mechanism of wake recovery affected the performance increase. However, for modern high-loading compressors, stator flow separation is common [51], and, therefore, the present conclusion can still be applied.

3.4. Unsteady Characteristics

Time profiles shown in Figure 13 exhibit more violent fluctuations when the gap was reduced. Increases of the fluctuations might deteriorate the aeroelastic and the aeroacoustic performances of the compressor. However, in experiments, it is challenging to measure the pressure fluctuation on a rotating blade and hard to know its distribution on the whole surface. Therefore, the effect of gap on the unsteady pressure on the blade surfaces was of interest to the present study.

Figures 22 and 23 show the distributions of the pressure fluctuation amplitude on the rotor and the stator, respectively, at the two gaps with $\phi = 0.318$. The amplitudes

were quantified by half the peak-to-peak values for the unsteady pressures on the blade segments. Specifically, the rear part of the rotor blade suffered more from the fluctuation when the gap was reduced and the highest value was observed near the trailing edge. This fluctuation included the unsteady pressure generating on the stator and propagating upstream, and reduction of the gap not only strengthened the fluctuation on the stator, but also shortened the distance of attenuation, thus, highly increasing the amplitude of the unsteady pressure on the rotor blade. Przytarski and Wheeler [17] reported that the freestream turbulence levels rose significantly after the gap was reduced, which might also be related to the stronger fluctuation propagating upstream.

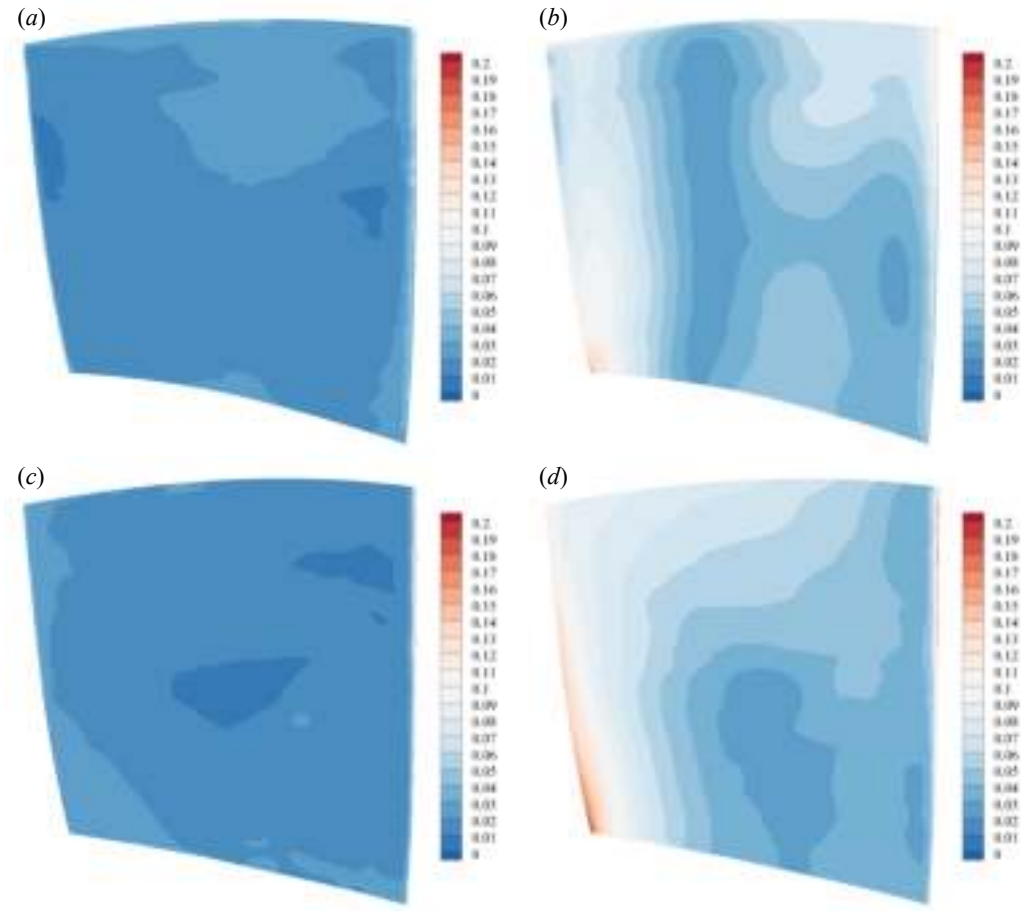

Figure 22. Distributions of the pressure fluctuation amplitude on the rotor blade. (**a**) $g = d_0$, pressure surface, (**b**) $g = d_0$, suction surface, (**c**) $g = 0.1d_0$, pressure surface, (**d**) $g = 0.1d_0$, suction surface.

On the other hand, the aeroacoustic performance of the compressor depends on the flow characteristics of the stator. At the designed gap, only the leading-edge region of the stator exhibited pretty violent pressure fluctuation while the fluctuation was not obvious in most of the remaining regions, as shown by Figure 23a,b. After the gap was reduced, the fluctuation amplitudes were also found to increase on the whole stator, like the rotor. Specifically, the highest amplitude on the leading edge of the stator's pressure side was more than twice the corresponding value at the designed gap, as can be identified from Figure 23a,c. The region with the highest fluctuation amplitude on the stator's suction, i.e., the red areas at the leading edge in Figure 23b,d, was also found to expand toward the rear of the blade after the gap reduced. With the rotor passing, the leading edge of the stator chopped the rotor wake into two parts, resulting in violent fluctuation at this region, which also formed the main source of interaction noise.

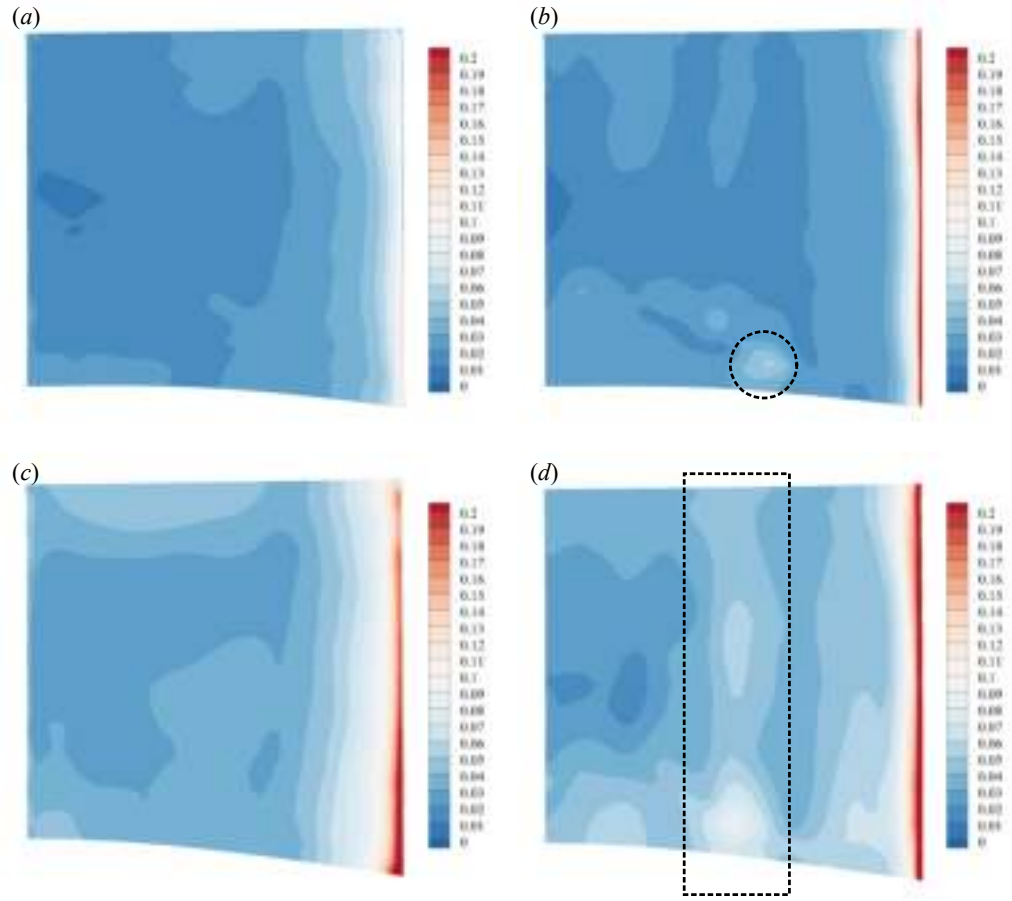

Figure 23. Distributions of the pressure fluctuation amplitude on the stator blade. (**a**) $g = d_0$, pressure surface, (**b**) $g = d_0$, suction surface, (**c**) $g = 0.1d_0$, pressure surface, (**d**) $g = 0.1d_0$, suction surface,

In addition, at the designed gap, higher pressure fluctuation also existed near the mid-chord of the suction surface of the stator, as marked by the black dashed circle in Figure 23b. When the gap reduced, this region enlarged along the span as marked by the black dashed box in Figure 23d. This region with stronger fluctuation was well related to the interaction of the rotor wake and the stator flow. As can be found from the contours of Mach number in Figure 16, there was a region of flow acceleration near the leading edge of the suction surface of the stator, the end of which is marked by a dashed line in black. After the rotor wake was chopped by the stator, a new wake formed and evolved along the suction surface of the stator. Due to the interaction of the rotor wake and the stator flow, stronger pressure fluctuation then formed near the end of the acceleration region as a consequence, as revealed by Figure 23b,d. There was another small acceleration region downstream of that marked in Figure 16d on the suction surface of the stator and obvious pressure fluctuation could also be observed near it, as shown by Figure 23d. Therefore, in addition to the chop of rotor wake, the interaction of the rotor wake/stator flow was another main source of pressure fluctuation on the stator, and both of the two sources could be strongly enhanced by the reduction of the gap.

4. Conclusions

This paper presents the application of an Immersed Boundary method to study the effect of gap on the blade–row interaction for a low-speed single-stage compressor. The hybrid mesh strategy, together with the wall model and adaptive mesh refinement, facilitates the employment of the IB method for high Reynolds-number internal flows, also making the computational cost affordable. With the IB method, the two blade rows can be modeled in the same coordinate and the mesh can be easily constructed, even at an

extremely small stage gap. The main finding of the present study is that reduction of the gap can both enhance the rotor loading and suppress the flow separation near the stator hub, thus, producing obvious performance benefit to the compressor.

Simulations were first conducted at the designed gap, 35%c_a, and overall performance showed good agreement with the experimental data. The numerical convergence was also carefully examined. Then, the gap was reduced to 10% of the designed value, i.e., 3.5%c_a, and comparisons showed that the reduction of the gap increased the pressure rise on both the rotor and the stator outlets, and also reduced the total pressure loss of the stator, indicating both the two rows contributed to the performance enhancement. Further analysis revealed that the rotor worked at a higher-loading state, and thus resulted in the increase of the total pressure rise on the rotor outlet, when the gap was reduced. Such a variation of the total pressure rise was mainly contributed to by the increase of the static pressure on the rotor outlet, which could reduce the adverse pressure gradient at the hub region of the stator passage. Therefore, the flow separation in this region was also suppressed, which played a significant role in the performance increase of the stator.

The present work also proves the potential of the IB method in simulating the blade–row interaction at an extremely small gap, and future works will pay much attention to the validation of these new flow mechanisms through experimental studies.

Author Contributions: Conceptualization, Z.W.; Funding acquisition, X.S.; Investigation, Z.W. and L.D.; Methodology, L.D.; Supervision, X.S.; Validation, Z.W.; Writing—original draft, Z.W.; Writing—review and editing, L.D. and X.S. All authors have read and agreed to the published version of the manuscript.

Funding: This research was funded by the National Natural Science Foundation of China (grant Nos.51790514 and 52022009), the National Science and Technology Major Project (grant No. 2017-II-003-0015) and Key Laboratory Foundation (2021-JCJQ-LB-062-0102).

Institutional Review Board Statement: Not applicable.

Informed Consent Statement: Not applicable.

Data Availability Statement: Not applicable.

Conflicts of Interest: The authors declare no conflict of interest.

References

1. Smith, L.H. Casing Boundary Layers in Multistage Axial Flow Compressors. In *Flow Research on Blading*; Dzung, L.S., Ed.; Elsevier Publishing Company: Amsterdam, The Netherlands, 1970.
2. Mikolajczal, A.A. *The Practical Importance of Unsteady Flow in AGARD CP-177, Unsteady Phenomena in Turbomachinary*; Technical Report; Swiss Federal Institute of Technology: Zürich, Switzerland, 1977.
3. Smith, L. Wake Dispersion in Turbomachines. *J. Basic Eng.* **1966**, *88*, 688–690. [CrossRef]
4. Adamczyk, J.J. Wake mixing in axial flow compressors. In Proceedings of the International Gas Turbine and Aeroengine Congress and Exhibition, Birmingham, UK, 10–13 June 1996. [CrossRef]
5. Deregel, P.; Tan, C. Impact of Rotor Wakes on Steady-State Axial Compressor Performance. In Proceedings of the ASME 1996 International Gas Turbine and Aeroengine Congress and Exhibition, Birmingham, UK, 10–13 June 1996; Volume 1.
6. Gorrell, S.E.; Copenhaver, W.W.; Chriss, R.M. Upstream wake influences on the measured performance of a transonic compressor stage. *J. Propuls. Power* **2001**, *17*, 43–48. [CrossRef]
7. Gorrell, S.E.; Okiishi, T.H.; Copenhaver, W.W. Stator-rotor interactions in a transonic compressor—Part 1: Effect of blade-row spacing on performance. *J. Turbomach.* **2003**, *125*, 328–335. [CrossRef]
8. Nolan, S.P.; Botros, B.B.; Tan, C.S.; Adamczyk, J.J.; Greitzer, E.M.; Gorrell, S.E. Effects of upstream wake phasing on transonic axial compressor performance. *J. Turbomach.* **2011**, *133*, 021010. [CrossRef]
9. Clark, K.P.; Gorrell, S.E. Analysis and prediction of shock-induced vortex circulation in transonic compressors. *J. Turbomach.* **2015**, *137*, 121007. [CrossRef]
10. Du, L.; Sun, X.; Yang, V. Generation of vortex lift through reduction of rotor/stator gap in turbomachinery. *J. Propuls. Power* **2016**, *32*, 472–485. [CrossRef]
11. Du, L.; Sun, X.; Yang, V. Vortex-lift mechanism in axial turbomachinery with periodically pitched stators. *J. Propuls. Power* **2016**, *32*, 486–499. [CrossRef]
12. Xu, H.; Jin, D.; Wang, M.; Du, L.; Sun, D.; Gui, X.; Sun, X. High blade lift generation through short rotor–stator axial spacing in a tiny pump. *Aerosp. Sci. Technol.* **2018**, *79*, 328–335. [CrossRef]

13. Rai, M.M. Navier-stokes simulations of rotor-stator interaction using patched and overlaid grids. *J. Propuls. Power* **1987**, *3*, 387–396. [CrossRef]
14. Jorgenson, P.C.; Chima, R.V. Explicit Runge-Kutta method for unsteady rotor/stator interaction. *AIAA J.* **1989**, *27*, 743–749. [CrossRef]
15. Giles, M.B. Stator/rotor interaction in a transonic turbine. *J. Propuls. Power* **1990**, *6*, 621–627. [CrossRef]
16. Hsu, S.T.; Wo, A.M. Reduction of Unsteady Blade Loading by Beneficial Use of Vortical and Potential Disturbances in an Axial Compressor With Rotor Clocking. *J. Turbomach.* **1998**, *120*, 705–713. [CrossRef]
17. Przytarski, P.J.; Wheeler, A.P. The effect of gapping on compressor performance. *J. Turbomach.* **2020**, *142*, 121006. [CrossRef]
18. Peskin, C.S. The immersed boundary method. *Acta Numer.* **2002**, *11*, 479–517. [CrossRef]
19. Mittal, R.; Iaccarino, G. Immersed boundary methods. *Annu. Rev. Fluid Mech.* **2005**, *37*, 239–261. [CrossRef]
20. Griffith, B.E.; Patankar, N.A. Immersed Methods for Fluid-Structure Interaction. *Annu. Rev. Fluid Mech.* **2020**, *52*, 421–448. [CrossRef]
21. Zhong, G.; Sun, X. New simulation strategy for an oscillating cascade in turbomachinery using immersed-boundary method. *J. Propuls. Power* **2009**, *25*, 312–321. [CrossRef]
22. Chen, C.; Wang, Z.; Du, L.; Sun, D.; Sun, X. Simulating unsteady flows in a compressor using immersed boundary method with turbulent wall model. *Aerosp. Sci. Technol.* **2021**, *115*, 106834. [CrossRef]
23. Cheng, L.; Du, L.; Wang, X.; Sun, X. Inviscid Nonlinear Modeling of Vibration-Induced Acoustic Resonance of a Linear Cascade. *AIAA J.* **2021**, *59*, 1849–1860. [CrossRef]
24. Roma, A.M.; Peskin, C.S.; Berger, M.J. An Adaptive Version of the Immersed Boundary Method. *J. Comput. Phys.* **1999**, *153*, 509–534. [CrossRef]
25. Vanella, M.; Rabenold, P.; Balaras, E. A direct-forcing embedded-boundary method with adaptive mesh refinement for fluid-structure interaction problems. *J. Comput. Phys.* **2010**, *229*, 6427–6449. [CrossRef]
26. Angelidis, D.; Chawdhary, S.; Sotiropoulos, F. Unstructured Cartesian refinement with sharp interface immersed boundary method for 3D unsteady incompressible flows. *J. Comput. Phys.* **2016**, *325*, 272–300. [CrossRef]
27. Al-Marouf, M.; Samtaney, R. A versatile embedded boundary adaptive mesh method for compressible flow in complex geometry. *J. Comput. Phys.* **2017**, *337*, 339–378. [CrossRef]
28. Wang, Z.; Du, L.; Sun, X. Adaptive mesh refinement for simulating fluid-structure interaction using a sharp interface immersed boundary method. *Int. J. Numer. Methods Fluids* **2020**, *92*, 1890–1913. [CrossRef]
29. Capizzano, F. Turbulent wall model for immersed boundary methods. *AIAA J.* **2011**, *49*, 2367–2381. . 1.J050466. [CrossRef]
30. Capizzano, F. Coupling a wall diffusion model with an immersed boundary technique. *AIAA J.* **2016**, *54*, 728–734. [CrossRef]
31. Tamaki, Y.; Harada, M.; Imamura, T. Near-wall modification of Spalart-Allmaras turbulence model for immersed boundary method. *AIAA J.* **2017**, *55*, 3027–3039. [CrossRef]
32. Berger, M.J.; Aftosmis, M.J. An ODE-based wall model for turbulent flow simulations. *AIAA J.* **2018**, *56*, 700–714. [CrossRef]
33. Cai, S.G.; Degrigny, J.; Boussuge, J.F.; Sagaut, P. Coupling of turbulence wall models and immersed boundaries on Cartesian grids. *J. Comput. Phys.* **2021**, *429*, 109995. [CrossRef]
34. Constant, B.; Péron, S.; Beaugendre, H.; Benoit, C. An improved immersed boundary method for turbulent flow simulations on Cartesian grids. *J. Comput. Phys.* **2021**, *435*, 110240. [CrossRef]
35. Dong, X.; Sun, D.; Li, F.; Jin, D.; Gui, X.; Sun, X. Effects of rotating inlet distortion on compressor stability with stall precursor-suppressed casing treatment. *J. Fluids Eng. Trans. ASME* **2015**, *137*, 111101. [CrossRef]
36. Li, F.; Li, J.; Dong, X.; Zhou, Y.; Sun, D.; Sun, X. Stall-warning approach based on aeroacoustic principle. *J. Propuls. Power* **2016**, *32*, 1353–1364. [CrossRef]
37. Dong, X.; Sun, D.; Li, F.; Jin, D.; Gui, X.; Sun, X. Effects of Stall Precursor-Suppressed Casing Treatment on a Low-Speed Compressor with Swirl Distortion. *J. Fluids Eng. Trans. ASME* **2018**, *140*, 091101. [CrossRef]
38. Dong, X.; Li, F.; Xu, R.; Sun, D.; Sun, X. Further investigation on acoustic stall-warning approach in compressors. *J. Turbomach.* **2019**, *141*, 061001. [CrossRef]
39. Xu, D.; He, C.; Sun, D.; Sun, X. Stall inception prediction of axial compressors with radial inlet distortions. *Aerosp. Sci. Technol.* **2021**, *109*, 106433. [CrossRef]
40. Spalart, P.R.; Allmaras, S.R. A one-equation turbulence model for aerodynamic flows. In Proceedings of the 30th Aerospace Sciences Meeting and Exhibit, Reno, NV, USA, 6–9 January 1992. [CrossRef]
41. Roe, P.L. Approximate Riemann Solvers, Parameter Vectors, and Difference Schemes. *J. Comput. Phys.* **1981**, *43*, 357–372. [CrossRef]
42. Li, X.; Gu, C. An All-Speed Roe-type scheme and its asymptotic analysis of low Mach number behaviour. *J. Comput. Phys.* **2008**, *227*, 5144–5159. [CrossRef]
43. Van Leer, B. Towards the Ultimate Conservative Difference Scheme. V. A Second-Order Sequel to Godunov's Method. *J. Comput. Phys.* **1979**, *32*, 101–136. [CrossRef]
44. Berger, M.J.; Oliger, J. Adaptive mesh refinement for hyperbolic partial differential equations. *J. Comput. Phys.* **1984**, *53*, 484–512. [CrossRef]
45. Berger, M.J.; Colella, P. Local Adaptive Mesh Refinement for Shock Hydrodynamics. *J. Comput. Phys.* **1989**, *82*, 64–84. [CrossRef]

46. Aftosmis, M.J.; Melton, J.E.; Berger, M.J. Adaptation and surface modeling for Cartesian mesh methods. In Proceedings of the 12th Computational Fluid Dynamics Conference, San Diego, CA, USA, 19–22 June 1995. [CrossRef]
47. Gilmanov, A.; Sotiropoulos, F.; Balaras, E. A general reconstruction algorithm for simulating flows with complex 3D immersed boundaries on Cartersian grids. *J. Comput. Phys.* **2003**, *191*, 660–669. [CrossRef]
48. Gilmanov, A.; Sotiropoulos, F. A hybrid Cartesian/immersed boundary method for simulating flows with 3D, geometrically complex, moving bodies. *J. Comput. Phys.* **2005**, *207*, 457–492. [CrossRef]
49. Spalding, D.B. A single formula for the "law of the wall". *J. Appl. Mech. Trans. ASME* **1961**, *28*, 455–457. [CrossRef]
50. Chung, M.; Wo, A.M. Navier-Stokes and Potential Calculations of Axial Spacing Effect on Vortical and Potential Disturbances and Gust Response in an Axial Compressor. *J. Turbomach.* **1997**, *119*, 472–481. [CrossRef]
51. Dickens, T.; Day, I. The design of highly loaded axial compressors. *J. Turbomach.* **2011**, *133*, 031007. [CrossRef]

Disclaimer/Publisher's Note: The statements, opinions and data contained in all publications are solely those of the individual author(s) and contributor(s) and not of MDPI and/or the editor(s). MDPI and/or the editor(s) disclaim responsibility for any injury to people or property resulting from any ideas, methods, instructions or products referred to in the content.

International Journal of
Turbomachinery
Propulsion and Power

MDPI

Article

Exergy-Based Efficiency Assessment of Fans vs. Isentropic Efficiency

Johannes Brötz, Christian Schänzle and Peter F. Pelz *

Department of Mechanical Engineering, Technische Universität Darmstadt, Otto-Berndt-Straße 2, 64287 Darmstadt, Germany
* Correspondence: peter.pelz@fst.tu-darmstadt.de

Abstract: The efficiency definition allows us to compare two machines with each other. In general, the efficiency is defined as the ratio of usable power to the required power. This raises the question: what is the usable power? Most engineers discuss efficiency on the basis of the energy balance, i.e., the first law of thermodynamics. In this paper, we derive the exegetic efficiency taking the second law of thermodynamics into account. Exergy analysis takes into account work and heat and is able to model reality very accurately. On this basis, a comparison between the isentropic and exergetic efficiencies is given. A high-pressure radial fan is used as an example, and the differences are discussed. Therefore, measurements of a non-adiabatic fan are evaluated, and the role of the heat flux in the environment is discussed. The investigations show that a relevant difference between the isentropic and exergetic efficiencies becomes apparent in the partial-load range with high-pressure build-up. The thermal energy contained in the flow belongs proportionally to the exergy, i.e., the working capacity of the gas relative to its environment. For a standard such as ISO 5801 "Fans—Performance testing using standardized airways", the efficiency must not only be physically correct, it must also be simple and practical. Against this background, the outlook of this paper discusses when and which efficiency definition is appropriate and best suited for a standard.

Keywords: exergy; efficiency; fan; second law

check for updates

Citation: Brötz, J.; Schänzle, C.; Pelz, P.F. Exergy-Based Efficiency Assessment of Fans vs. Isentropic Efficiency. *Int. J. Turbomach. Propuls. Power* **2023**, *8*, 4. https://doi.org/10.3390/ijtpp8010004

Academic Editor: Thomas Carolus

Received: 5 September 2022
Revised: 21 December 2022
Accepted: 2 February 2023
Published: 6 February 2023

Copyright: © 2023 by the authors. Licensee MDPI, Basel, Switzerland. This article is an open access article distributed under the terms and conditions of the Creative Commons Attribution (CC BY-NC-ND) license (https://creativecommons.org/licenses/by-nc-nd/4.0/).

1. Introduction

Fans and compressors are working machines that are characterized by their wide operating range and their application in every industrial sector. Their fundamental function is to deliver a volume flow of a fluid at a given pressure difference, which makes them essential for all kinds of industrial processes from simple compressed air supply to highly complex chemical reactions. Most diverse application-related requirements and gases lead to a variety of machine designs. In this regard, the physical working principles give a reasonable structure to the fans and compressors. For today's technical applications, the two most relevant principles are the hydrodynamic and hydrostatic principles. The associated machine categories are turbomachines and positive displacement machines. In this paper we focus on the application of fans.

Besides the importance of fans and compressors for the implementation of industrial processes, their use causes costs. These costs mainly depend on the energy consumption considering their life cycle costs. This is why investments in improving the energy efficiency of working machines such as fans or compressors usually show a high-cost effectiveness with a low financial risk. However, energy consumption and its related costs not only have an impact on the users, but they also have a relevance to society. Detailed studies under the European Commission's Ecodesign Directive have considered fans and compressors to be relevant electric energy consumers [1]. In this context, a recent study by the German Ministry of Economics and Energy shows that pumps and compressors account for 16% of the electrical energy consumption in German industry [2]. Since electricity production

worldwide is still heavily dependent on fossil fuels, fans and compressors consequently contribute significantly to CO_2 emissions, and thus, to climate change and the associated future costs to society.

Consequently, from the perspective of both the industry and society, an energy efficiency assessment of fans and compressors is highly relevant. The efficiency represents the dimensionless measure of the dissipative power loss of a machine. At this point, it is necessary to differentiate between machine, module and system. The task of a turbomachine or a positive displacement machine is to convert mechanical power into fluid power. The system boundaries are the shaft of the machine, as well as the inlet and outlet of the machine. A module, on the other hand, consists of more than one machine or component and is also called "extended product". In the context of fluid working machines, a module usually includes a frequency converter, an electric motor and the pump or the compressor. Their energetic assessment is based on a load scenario including the partial load and the efficiency characteristic. It shows that operation in the partial load area is used more often than operation at the best efficiency point. Finally, technical systems usually consist of multiple machines and components realizing technical processes. In the case of fluid power systems, there exist absolute measures based on physical axioms. On the one hand, Betz law gives an energy harvesting factor for wind turbines that is defined by the ratio of the mechanical power to the available power, with an upper limit of 16/27 [3]. On the other hand, Pelz gives an upper limit for hydropower in an open-channel flow of 1/2 [4]. The most famous absolute measure is the Carnot efficiency, which defines the maximum efficiency of an ideal heat engine or Carnot cycle [5]. In this case, the exergy becomes the relevant quantity which measures the working capacity of a fluid relative to its environment. Exergy was first introduced by Fritsche, Hehnemann and Rant in 1956 [6]. While exergy analyses are state-of-the-art means of evaluating thermal power or working systems [7], exergy-based efficiency studies for single fluid working machines are rare [8]. Masi et al. [9] give an introduction to the performance and efficiency of industrial fans. Nakhjiri et al. [10] have demonstrated using the example of a radial compressor that using efficiency based on energy balance is not sufficient to obtain physically the correct results. This was illustrated by a drop in efficiency with an increasing speed of the radial compressor when they were not taking the heat flux into account. Exergy analysis is intended to detect non-physical trends, and thus inconsistencies in the physics [11]. Sorguven et al. [12] have studied the exergetic losses in a centrifugal pump using a large eddy simulation. They assume that both the density and the temperature do not change. For an incompressible fluid undergoing an isothermal process, both the specific internal energy and specific entropy remain constant, which significantly simplifies the analysis. The exergetic analysis makes sense especially when whole systems are considered. Mazloum et al. [13] show an exergy analysis and exergoeconomic optimization of a constant pressure adiabatic compressed energy storage system. The exergy in the compressor is also presented. With the assumption of an adiabatic machine, the heat loss is neglected here, and the calculation of the compression is also simplified with a constant isentropic efficiency.

Against this background, we make two conclusions. Firstly, the efficiency of fluid working machines is of fundamental importance for their own assessment and for the assessment of both the modules and the working systems. At the same time, despite there being countless scientific studies on the efficiency of fluid working machines, the definition of efficiency, the measuring methods and the application in standards and directives are ongoing issues, e.g., the revision of ISO 5801:2018 for fans. Secondly, an exergy-based assessment for fans and compressors is necessary and would lead to the most general definition of the efficiency. Therefore, this paper begins with the derivation of the exegetic efficiency based on the first and second laws of thermodynamics. Following this general form, we consider the application of it on a high-pressure centrifugal fan. Furthermore, the isentropic efficiency definitions are compared to the exegetic efficiency. Subsequently, we discuss reference applications and compare different efficiency definitions based on the measurement data. The paper closes with the conclusion and our outlook.

2. The Efficiency in the Light of the First and Second Laws of Thermodynamics

Most engineers discuss efficiency only on the grounds of the energy balance, i.e., the first law of thermodynamics. In this section, we derive the exegetic efficiency by also taking into account the second law of thermodynamics. For this most general definition of the efficiency, we will see that both of the axioms are indeed needed.

The first law of thermodynamics for a machine operating a steady state reads

$$\dot{m}(h_{t2} - h_{t1}) = P_S + \dot{Q}. \tag{1}$$

This law is a conservation of energy, distinguishing between heat flow $\dot{Q}$ and work P_S and relating them to the internal energy, comprising the mass flow rate $\dot{m}$ and the difference in enthalpy $h_{t2} - h_{t1}$.

The second law of thermodynamics (entropy theorem) states

$$\dot{m}(s_2 - s_1) = \Delta\dot{S}_{\mathrm{irr}} + \frac{\dot{Q}}{T}\,, \tag{2}$$

with the difference in mass specific entropy, $s_2 - s_1$, on the left hand. On the right hand, the source term $\Delta\dot{S}_{\mathrm{irr}}$ is the work dissipated within the system; this work does not occur outside, but it increases the internal energy as a result of friction, throttling or shock processes. The second term $\dot{Q}/T$ considers an increase or decrease in entropy as a result of heat flow across the system boundary.

$$\dot{m}(h_{t2} - h_{t1}) - T_0\dot{m}(s_2 - s_1) = P_s - T_0\Delta\dot{S}_{\mathrm{irr}} \tag{3}$$

Exergy is the working part of energy and the result of subtracting energy and anergy:

$$\text{exergy} := \text{exergy} - \text{anergy}$$

$$ex_2 - ex_1 := h_{t2} - h_{t1} - T_0(s_2 - s_1) \tag{4}$$

The interpretation of the right side of Equation (3) shows that the exergy is the fraction of the shaft power that is transmitted to the fluid and does not dissipate.

The function of a fan or compressor is to increase the exergy of the delivered gas. The exergy measures the working capacity of the gas relative to its environment. The mass-specific exergy of a fluid particle before entering the turbomachine (see Figure 1) is defined as

$$ex_1 := h_{t1} - h_0 - T_0(s_1 - s_0). \tag{5}$$

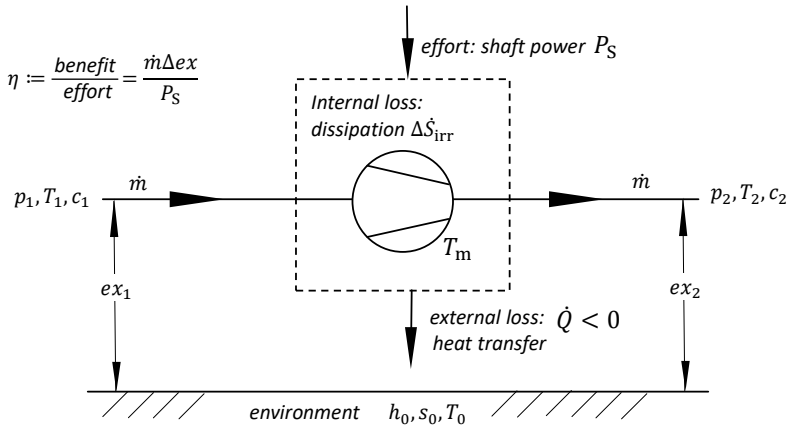

Figure 1. System boundaries of a turbomachine with inlet, outlet conditions and exchange with the environment.

When they pass though the fan, the exergy of the same fluid particles is increased to be

$$ex_2 := h_{t2} - h_0 - T_0(s_2 - s_0). \tag{6}$$

Hence, the benefit of the machine is given by the change in the flux of exergy

$$\text{benefit} = \dot{m}\ (ex_2 - ex_1) = \dot{m}\ \Delta ex. \tag{7}$$

The benefit is the product of a "flux" $\dot{m}$ and a difference in the potential Δex. The effort to reach this benefit is the shaft power P_S. It is the mechanical work that is performed on the fluid per unit of time.

Hence, the most natural definition of a machine's efficiency, a fan or a compressor, is

$$\eta_{ex} := \frac{\dot{m}\ \Delta ex}{P_S}. \tag{8}$$

For the consideration of the heat flow $\dot{Q}$, we go back to the 1st and 2nd laws of thermodynamics (Equations (1) and (2)). We adhere to the usual norm, where $\dot{Q}$ is positive as long the heat flux is transferred into the machine. However, for turbomachines, the heat flux is, in most cases, travelling from the machine to the environment, i.e., $\dot{Q} < 0$. Hence, the temperature T in the second law of thermodynamics is the temperature of the source of the heat conduction. For $\dot{Q} < 0$, the pure temperature is the machine's average temperature, which is larger than the ambient temperature $T = T_m > T_0$.

Replacing the total enthalpy in the 1st law of thermodynamics by the exergy and by setting $T = T_m$, the two axioms are written as

$$\dot{m}(ex_2 - ex_1) = P_S + \dot{Q} - T_0\dot{m}(s_2 - s_1), \tag{9}$$

$$\dot{m}(s_2 - s_1) = \Delta\dot{S}_{irr} + \frac{\dot{Q}}{T_m}. \tag{10}$$

We are now in the position where the entropy difference $\Delta s = s_2 - s_1$ can be eliminated from the two axioms:

$$\dot{m}(ex_2 - ex_1) = P_S + \dot{Q}\left(1 - \frac{T_0}{T_m}\right) - T_0\ \Delta\dot{S}_{irr}. \tag{11}$$

This equation, based on axiomatic grounds, is most instructive ones when we are discussing efficiency. The first and second laws of thermodynamics now provide the clear interpretation of the exergetic efficiency:

$$\eta_{ex} := \frac{\dot{m}\Delta ex}{P_S} = 1 + \frac{\dot{Q}}{P_S}\left(1 - \frac{T_0}{T_m}\right) - \frac{T_0\ \Delta\dot{S}_{irr}}{P_S}. \tag{12}$$

Now, the internal and external losses mentioned above take shape as follows:

$$\text{inner loss} = \text{dissipation} = \varepsilon_i := \frac{T_0\ \Delta\dot{S}_{irr}}{P_S}, \tag{13}$$

$$\text{outer loss} = \text{heat transfer} = \varepsilon_o := -\frac{\dot{Q}}{P_S}\left(1 - \frac{T_0}{T_m}\right). \tag{14}$$

It is remarkable that it is not the entire heat flow that leads to losses, but it is only a share of it

$$\eta_C := 1 - \frac{T_0}{T_m}. \tag{15}$$

This dimensionless ratio is known as the Carnotian efficiency. Moreover, it is well known that the fluid friction results in a dissipation rate $\Delta\dot{S}_{\mathrm{irr}}$, thereby reducing the efficiency. It is not well known that heat conduction $\dot{Q}$ reduces the efficiency, but only the "Carnot" part η_{C} of that heat flux. With the abbreviations $q := \dot{Q}/\dot{m}$ and $w := P_{\mathrm{S}}/\dot{m}$, and the definitions (13) and (14), the important Equation (12) may be written in an equivalent form

$$\eta_{\mathrm{ex}} := \frac{\Delta ex}{w} = 1 - \varepsilon_o - \varepsilon_i. \tag{16}$$

Models for heat transfer and dissipation are necessary for the calculation. By using the equation for heat transfer $\dot{Q} = \alpha A(T_{\mathrm{m}} - T_0)$ for the outer loss, the loss can be represented as follows

$$\varepsilon_o = -\frac{\alpha A T_{\mathrm{m}}}{P_{\mathrm{S}}}\left(1 - \frac{T_0}{T_{\mathrm{m}}}\right)^2, \tag{17}$$

with the heat transfer coefficient being α and the surface of the machine being A. The dissipative losses are machine dependent. This will not be discussed in detail in this paper, and so, reference is made to other work in the literature: Pelz et al. [14] give a detailed description of the losses for fans, and Schobeiri [15] gives one for compressors. In variant (i), a separate consideration of the heat transport losses and dissipative losses can be made, but this method is rather unsuitable for practical application due to the effort involved.

For a caloric and thermal ideal gas with specific a heat c_{p}, c_{v}, $\gamma := c_{\mathrm{p}}/c_{\mathrm{v}}$ and $R = c_{\mathrm{p}} - c_{\mathrm{v}}$, the entropy is measured by measuring the temperature T and the pressure p [16].

$$s - s_0 = c_{\mathrm{p}} \ln \frac{T}{T_0} - R \ln \frac{p}{p_0}. \tag{18}$$

The absolute enthalpy is given by

$$h_{\mathrm{t}} - h_0 = c_{\mathrm{p}}(T_{\mathrm{t}} - T_0). \tag{19}$$

Hence, $\Delta ex/c_p T_0$ is given by

$$\frac{\Delta ex}{c_{\mathrm{p}} T_0} = \frac{T_{\mathrm{t2}} - T_{\mathrm{t1}}}{T_0} - \ln\left(\frac{T_2}{T_1}\right) + \frac{\gamma - 1}{\gamma} \ln\left(\frac{p_2}{p_1}\right). \tag{20}$$

With the specific work $w := P_{\mathrm{S}}/\dot{m}$, the exergetic efficiency is given by

$$\eta_{\mathrm{ex}} = \frac{c_{\mathrm{p}}(T_{\mathrm{t2}} - T_{\mathrm{t1}})}{w} - \frac{c_{\mathrm{p}} T_0}{w}\left[\ln\left(\frac{T_2}{T_1}\right) - \ln\left(\frac{p_2}{p_1}\right)^{\frac{\gamma-1}{\gamma}}\right]. \tag{21}$$

For an ideal gas, we hence have

$$\eta_{\mathrm{ex}} = 1 + \frac{q}{w}\eta_c - \varepsilon_i = \frac{\Delta h_{\mathrm{t}}}{w} - \frac{c_{\mathrm{p}} T_0}{w}\left[\ln\left(\frac{T_2}{T_1}\right) - \ln\left(\frac{p_2}{p_1}\right)^{\frac{\gamma-1}{\gamma}}\right]. \tag{22}$$

Equation (22) shows two ways to calculate the exergetic efficiency:
(i) Calculation by specifying the losses;
(ii) Determination on calculating the generated entropy.

Variant (ii) is more suitable for the calculation of the exergetic efficiency since this can be determined solely by the inlet and outlet variables and the ambient conditions.

In comparison to the isentropic efficiency, (Equation (23)) is based on isentropic compression,

$$\eta_s = \frac{\frac{\gamma}{\gamma-1}\frac{p_1}{\rho_1}\left[\left(\frac{p_2}{p_1}\right)^{\frac{\gamma-1}{\gamma}} - 1\right] + \frac{1}{2}\left(\frac{\dot{m}}{\rho_2 A_2}\right)^2 - \frac{1}{2}\left(\frac{\dot{m}}{\rho_1 A_1}\right)^2}{w}. \tag{23}$$

It is clear that the exergetic efficiency considers not only pure fluid power, but also the relation to the environment. The application of it to a fan highlights the distinctions.

3. Application to a High-Pressure Centrifugal Fan

For the application of the exergetic efficiency, a high-pressure radial ventilator is chosen, as the differences are estimated to be more significant due to the higher temperature differences. The fan with an impeller diameter of $D_r = 1.33$ m is run with the rotational speed $n = 2300$ U/min. The pressure build-up achievable with these conditions is a maximum of $\Delta p_t = 19{,}000$ Pa, and it is thus still within the scope of the ISO5801:2018 standard.

The setup of the centrifugal fan test rigs is shown in Figure 2 for the medium-scaled test rig. The flow goes from left to right and passes first through the volume flow rate nozzle (1, A). To improve the measurement accuracy, the volume flow nozzle has been calibrated with a total pressure comb (2). After the throttle (4), the flow straightener (5) is positioned to lower the turbulence and inhomogeneities. The fan inlet conditions (total temperature and static pressure) are measured in the measuring chamber at position (B). The test fan (7) is connected with a torque meter (8) to the engine (10). The torque meter is located between the impeller and the bearings. The fan blows out freely into the environment. At point (C), the static pressure can thus be assumed to be equal to the ambient pressure. Only the temperature is measured at the outlet. The ambient conditions are recorded in the experimental hall using a separate device.

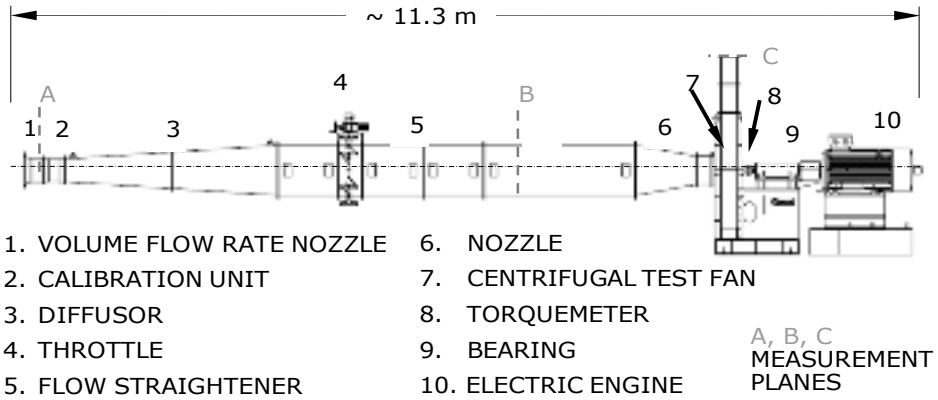

Figure 2. Pipe test rig according to ISO 5801:2018 with high-pressure centrifugal fan.

Thermal images of the spiral housing were taken to quantify the machine temperature T_m. An example is given in Figure 3, which shows the operating point of the maximum partial load. The determination of the heat flow requires the determination of the heat transfer coefficient α of the machine to the environment. The determination was complicated by the free-blowing fan. At maximum overload, mass flows of $\dot{m} = 10$ kg/s are conveyed, which corresponds to discharge velocities of $c_2 = 144$ m/s. The exit flow leads to the circulation of the air in the area of the fan. The heat transfer coefficient is dependent on the flow around the machine, and thus, it was not constant in our experiments. By calculating the heat transfer coefficient backwards, based on the calculation of the heat flow by Equation (1), the coefficients could be compared with literature values, and thus, checked for plausibility.

$$\dot{Q} = \dot{m}\,(h_{t2} - h_{t1}) - P_S. \tag{24}$$

$$\alpha = \frac{\dot{Q}}{A(T_m - T_0)} = \frac{\dot{m}(h_{t2} - h_{t1}) - P_S}{A(T_m - T_0)}. \tag{25}$$

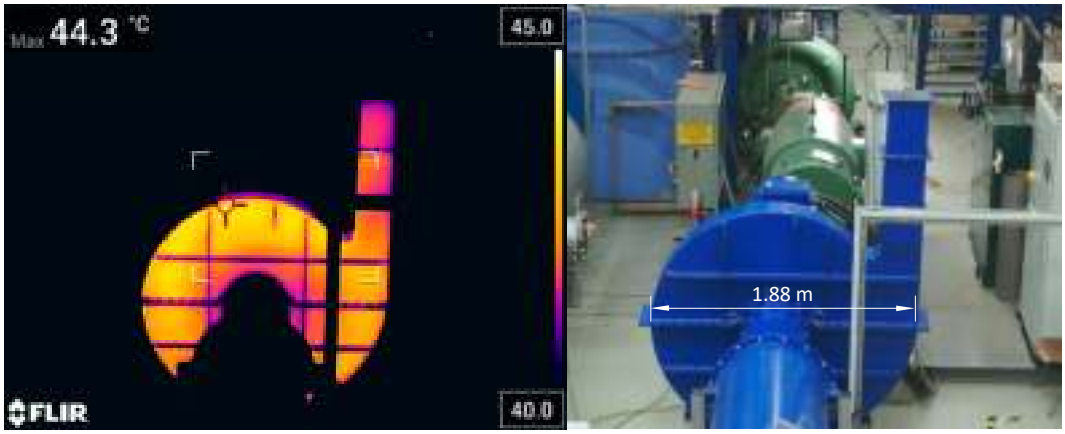

Figure 3. Thermal images of the spiral housing. FST Lab., TU Darmstadt.

The evaluation yielded heat transfer coefficients of $\alpha = 4.26\ \mathrm{W/m^2K}$ for stagnant air for the partial load and 85.52 $\mathrm{W/m^2K}$ for the full load, which corresponds to moderately to briskly moving air perpendicular to a metal wall according to the literature.

The example shows that calculating the exergetic efficiency on the basis of the resulting losses (Equation (12)) is impractical. Neither the dissipated work nor the heat flow can be easily determined. However, calculating the generated entropy based on the inlet and outlet conditions is possible and will be applied in the next section.

4. Comparison between Exergetic and Isentropic Efficiency

Figure 4 shows the comparison of the exergetic efficiency with the isentropic efficiency. For the isentropic efficiency, the power of the isentropic compression was set in relation to the impeller power, while for the exergetic efficiency, the calculation given in Equation (22) was used. The bars represent the uncertainty of the respective measuring points. For the calculation of each measuring point, a data set of 200 repetitions was measured, and the square of the uncertainty was derived from the sum of the squares of the statistical and systematic measurement uncertainty with a confidence interval of 95%. For the partial load, an uncertainty of about one percentage point can be seen, which increases to about two percentage points of the full load.

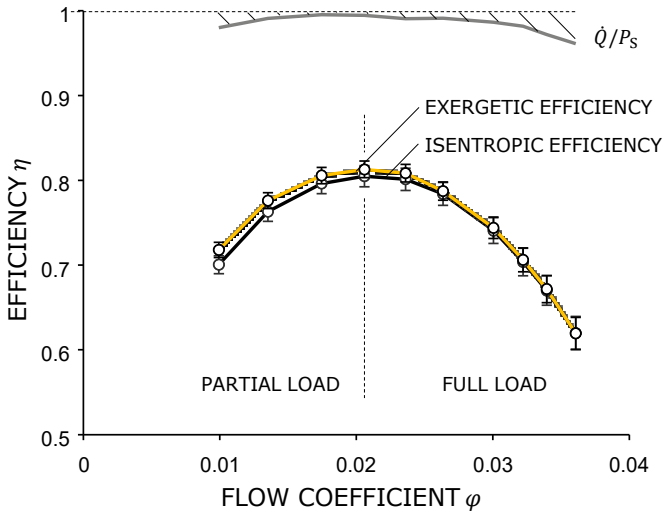

Figure 4. Exergetic efficiency compared to isentropic efficiency. The calculated power loss due to heat dissipation to the environment is hatched.

The differences in the overload operation between the two efficiencies are negligible. The efficiency difference increases during the partial load operation, with a maximum efficiency difference of 1.8 percentage points. This good correlation is remarkable despite the different calculation rules.

Where do the differences in efficiency come from? In the case of isentropic compression, a reversible change in state is assumed, which determines the integration path of the change in state. Since entropy is a state variable, the entropy difference does not depend on the choice of the integration path [17]. Accordingly, the exergetic efficiency is also independent of the choice of an integration path.

The exergetic efficiency includes not only the compression power, but also the reversible thermal power related to the environment. In the example that is shown, the difference between the outlet temperature and the ambient temperature is $T_2 - T_0 = 2$ K for the full load operation and 25 K for partial load operation. The usable thermal energy in relation to the environment is therefore low for the full load operation, while it makes the difference in efficiency for partial load operation. This thermal energy is caused by dissipation and is only usable from an exergetic point of view, but not from an energetic point of view.

In addition, Figure 4 shows the proportion of heat dissipation to the environment calculated using Equation (24) and verified using the thermal images. The dissipation has a minimum near the best efficiency point, and a maximum at the full load operation, with a share of about 4% points. In the partial load operation, the driving mechanism of heat transfer is heat conduction, while in the full load operation, increased heat convection is added. As the flow exits the fan into the experimental hall, the air circulates in the hall, and thus, also around the fan.

5. Conclusions

The first and second laws of thermodynamics are combined to achieve exergetic efficiency. As a result, its biggest benefit is, thus, its universal applicability. Exergetic efficiency does not only consider the fluid power from pressure build-up and delivery of a volume flow, but also the contained usable thermal energy in the environment.

The investigations show that a relevant difference between the isentropic and exergetic efficiencies becomes apparent in the partial load range with high pressure build-up. In the present application with a high-pressure centrifugal fan, an efficiency difference of 1.8% points between the exergetic and isentropic efficiencies could be found for the partial load operation.

If one considers the special case of the isothermal change in state, the exergetic efficiency almost becomes the isentropic efficiency, and only the difference of the logarithm of the pressure ratio remains. If one also assumes a pressure build-up that converges to zero, only the kinematic portion of the energy remains. This special case is found approximately in an axial fan without housing. The approximation of the mentioned limiting case can also be seen in the application example when one is looking at the full load operation.

A calculation of the exergetic efficiency based on the generated losses has proven to be impractical, but calculating the generated entropy based on the inlet and outlet conditions is possible and easy to implement. It has been shown that the exergetic efficiency can be determined with the test stands described in ISO 5801:2018.

The measurement effort increases especially when one is measuring the outlet temperature. Here, sensors with low systematic uncertainty are required in order not to worsen the overall uncertainty. The determination of the temperature of the flow also plays a relevant role for exergetic efficiency, which ought to be investigated more closely.

The thermal energy contained in the flow can be used to a certain extent. If the fan is used to ventilate buildings or tunnels, the surroundings will be heated with the thermal energy. Since fans are also used for cooling processes, such as in air conditioning systems, the exergy contained in the exhaust air flow cannot always be used, and it can even be counterproductive. The exergetic efficiency applied to fans must therefore always be

considered in the system. Such system efficiency is becoming increasingly relevant today, as explained in the introduction. For the evaluation of the component, on the other hand, the isentropic efficiency is recommended, as it has a high acceptability among its users due to its simple applicability.

The investigation has shown that a relevant difference between the isentropic and exergetic efficiencies is to be expected, especially for machines with high-pressure build-up. Future useful applications will therefore be high-pressure fans, blowers and compressors, but also systems where there is a high temperature difference between the machine and the environment, e.g., a high-pressure fan in Antarctica. A further step in the investigation will be to compare diabatic and adiabatic machines.

Author Contributions: Conceptualization, J.B., C.S. and P.F.P.; validation, J.B.; writing—original draft preparation, J.B., C.S. and P.F.P. All authors have read and agreed to the published version of the manuscript.

Funding: This research received no external funding.

Institutional Review Board Statement: Not applicable.

Informed Consent Statement: Not applicable.

Data Availability Statement: Not applicable.

Conflicts of Interest: The authors declare no conflict of interest.

References

1. de Almeida, A.T.; Ferreira, F.J.T.E.; Fong, J.; Fonseca, P. *EUP Lot11 Motors: Final*; University of Coimbra: Coimbra, Portugal, 2008.
2. Arbeitsgemeinschaft Energiebilanzen e.V. Anwendungsbilanzen zur Energiebilanz Deutschland. 2023. Available online: https://ag-energiebilanzen.de/wp-content/uploads/2023/01/AGEB_21p2_V3_20221222.pdf (accessed on 5 September 2022).
3. Betz, A. *Wind-Energie und Ihre Ausbreitung Durch Windmühlen: Mit Zahlr. Tab*; Aerodynam. Vers.-Anst: Göttingen, Germany, 1926.
4. Pelz, P.F.; Metzler, M.; Schmitz, C.; Müller, T.M. Upper limit for tidal power with lateral bypass. *J. Fluid Mech.* **2020**, *889*, A32. [CrossRef]
5. Carnot, S. *Réflexions sur la Puissance Motrice du feu: Et sur les Machines Propres à Développer Cette Puissance*; Bachelier: Paris, Italy, 1824.
6. Fritzsche, A.F.; Hahnemann, H.W.; Rant, Z. Rundschau. *Forsch. Im Ing.* **1956**, *22*, 33–37. [CrossRef]
7. Tsatsaronis, G. Definitions and nomenclature in exergy analysis and exergoeconomics. *Energy* **2007**, *32*, 249–253. [CrossRef]
8. Sciubba, E.; Wall, G. A brief commented history of exergy from the beginnings to 2004. *Int. J. Thermodyn.* **2007**, *10*, 1–26.
9. Massimo, M.; Federico, F.; Andrea, L. *Proceedings of the ASME Turbo Expo: Turbomachinery Technical Conference and Exposition, Volume 8: Microturbines, Turbochargers and Small Turbomachines; Steam Turbines: On the Choice of Suitable Parameters for the Assessment of Industrial Fans Performance and Efficiency*; American Society of Mechanical Engineers: New York, NY, USA, 2017.
10. Nakhjiri, M.; Pelz, P.F.; Matyschok, B.; Horn, A.; Däubler, L. Apparent and Real Efficiency of Turbochargers under Influence of Heat Flow. In Proceedings of the 14th International Symposium on Transport Phenomena and Dynamics of Rotating Machinery, Honolulu, HI, USA, 27 February–2 March 2012, Verlag Nicht Ermittelbar, Honolulu, HI, USA; 2012.
11. Dinçer, I.; Rosen, M. *Exergy: Energy, Environment and Sustainable Development*; Elsevier Science: Amsterdam, The Netherlands; Boston, MA, USA; Heidelberg, Germany; London, UK; New York, NY, USA; Oxford, UK; Paris, Italy, 2013.
12. Sorguven, E.; Incir, S.; Highgate, J. Understanding loss generation mechanisms in a centrifugal pump using large eddy simulation. *Int. J. Heat Fluid Flow* **2022**, *96*, 108994. [CrossRef]
13. Mazloum, Y.; Sayah, H.; Nemer, M. Exergy analysis and exergoeconomic optimization of a constant-pressure adiabatic compressed air energy storage system. *J. Energy Storage* **2017**, *14*, 192–202. [CrossRef]
14. Pelz, P.F.; Saul, S.; Brötz, J. Efficiency Scaling—Influence of Reynolds and Mach Number on Fan Performance. *J. Turbomach.* **2021**, *144*, 061001. [CrossRef]
15. Schobeiri, M.T. *Turbomachinery Flow Physics and Dynamic Performance*, 2nd ed.; Springer: Berlin, Germany, 2016.
16. Gibbs, J.W. *On the Equilibrium of Heterogeneous Substances*; Universitätsbibliothek Heidelberg: Heidelberg, Germany, 1879.
17. Baehr, H.D.; Kabelac, S. *Thermodynamik: Grundlagen und Technische Anwendungen*, 16th ed.; Springer: Berlin/Heidelberg, Germany, 2016.

Disclaimer/Publisher's Note: The statements, opinions and data contained in all publications are solely those of the individual author(s) and contributor(s) and not of MDPI and/or the editor(s). MDPI and/or the editor(s) disclaim responsibility for any injury to people or property resulting from any ideas, methods, instructions or products referred to in the content.

International Journal of
Turbomachinery
Propulsion and Power

MDPI

Article

Data-Driven Anomaly Detection Framework for Complex Degradation Monitoring of Aero-Engine

Zichen Yan [1], Jianzhong Sun [1,*], Yang Yi [1], Caiqiong Yang [2] and Jingbo Sun [3]

[1] College of Civil Aviation, Nanjing University of Aeronautics and Astronautics, Nanjing 211106, China
[2] AECC Sichuan Gas Turbine Establishment, Chengdu 610000, China
[3] Aero Engine Academy of China, Aero Engine Corporation of China, Beijing 101300, China
* Correspondence: sunjianzhong@nuaa.edu.cn; Tel.: +86-025-84895772

Abstract: Data analysis is an important part of aero engine health management. In order to complete accurate condition monitoring, it is necessary to establish more effective analysis tools. Therefore, an integrated algorithm library dedicated for engine anomaly detection is established, which is PyPEFD (Python Package for Engine Fault Detection). Different algorithms for baseline modeling, anomaly detection and trend analysis are presented and compared. In this paper, the simulation data are used to verify the function of the anomaly detection algorithms, successfully completing the detection of multiple faults and comparing the accuracy algorithm under different conditions.

Keywords: data mining; aero-engine; algorithm library; anomaly detection; baseline construction

check for updates

Citation: Yan, Z.; Sun, J.; Yi, Y.; Yang, C.; Sun, J. Data-Driven Anomaly Detection Framework for Complex Degradation Monitoring of Aero-Engine. *Int. J. Turbomach. Propuls. Power* **2023**, *8*, 3. https://doi.org/10.3390/ijtpp8010003

Received: 2 August 2022
Revised: 27 January 2023
Accepted: 30 January 2023
Published: 1 February 2023

Copyright: © 2023 by the authors. Licensee MDPI, Basel, Switzerland. This article is an open access article distributed under the terms and conditions of the Creative Commons Attribution (CC BY-NC-ND) license (https://creativecommons.org/licenses/by-nc-nd/4.0/).

1. Introduction

Predictive maintenance mainly addresses the reliability problem of the engine, ensuring that the aero-engine has the ability to operate normally under specified conditions. This is an important prerequisite for aircraft safety, because failures of safety-critical systems such as aircraft engines can cause significant economic disruptions and even major accidents with a potential loss of human lives. Therefore, the prediction of the engine failure is of great importance for maintaining the functionality of safety-critical systems, which puts forward higher requirements for engine performance status monitoring [1–3]. The trend within the aerospace maintenance industry is searching for new technologies, such as predictive maintenance systems based on health monitoring, to detect degradation earlier and proactively schedule maintenance activities in order to reduce the unscheduled maintenance events. Therefore, the prediction of the engines failure is of great importance for maintaining the functionality of safety-critical systems, which puts forward higher requirements for engine performance status monitoring [4].

Advanced sensor technology has led to the development of condition monitoring technologies. For industrial applications, the frontier issue of multi-modal data analysis should be the combination of applicable data mining methods [5]. Nowadays, data-driven techniques have been reported in the literature for health monitoring of gas turbine engines. Those algorithms can be divided into classification, clustering, regression, dimensionality reduction, etc. William R. et al. proposed a fault detection framework, combining Gaussian mixture model and Hidden Markov model to perform state determination of VSVA (variable stator vane actuator) system used in aero-engine [6]; Consumi et al. established a Bayesian inference method to execute turbojet engines gas path analysis [7]. The Cluster AD-Flight clustering model proposed by Li L uses the DBSCAN (Density-Based Spatial Clustering of Applications with Noise) algorithm for multi-dimensional clustering analysis to exclude abnormal flight from multiple nominal patterns in takeoff phase [8]. Regression-based methods are also widely used. These methods use regression models to fit multi-dimensional data, and then detect abnormalities based on the predictions of the regression models and the differences in data observations. Dewallef P et al. adapted Kalman

filter model to deal with the performance monitoring and fault diagnosis problems based on several gas path measurements, including fuel flow, spool speed and the temperature of compressor blade and casing [9]; Seo D H et al. proposed a neural network framework fusing with support vector machine to monitor engine's working state, and the framework has been applied to the on-design and off-design performance data of a turbo-shaft engine have been generated by the gas turbine simulation program (GSP) [10].

Another topic related to anomaly detection is the neighborhood-based method. It selects a distance or use a similarity measurement method to define a neighborhood, and calculates the distance or relative density between a sample point and its neighborhood as an anomaly score. In this field, Puranik et al. applied both k-nearest neighborhood (KNN) and local outlier factor (LOF) to conduct quantitative analysis of flight data outlier detection [11]. Another KNN method used for data anomaly detection is carried out by Manukyan A et al. aiming at detecting instantaneous abnormal points [12].

However, the development process of anomaly detection algorithm for engine's data reflects several problems. First, very few public data sets to obtain. Algorithm development requires data sets, especially fault data for verification, while the real engine data is difficult to obtain due to confidentiality issues, and the number of faults contained is very rare. Moreover, engine data usually involves technical secrets and cannot be easily released [13]. Second, although there are many algorithms, only part of them is suitable for engine detection, that is, lacking an integrated detection algorithm library. The complete engine monitoring process includes baseline construction, anomaly detection and trend prediction, and this requires multiple algorithms' cooperation. Lastly, too many applications of classic machine learning algorithms, and lack of some attempts to apply new algorithms in the field of artificial intelligence for engine condition monitoring [14].

This paper has been divided into five sections. Section 2 introduces the engine condition monitoring data and enumerates its particularity. Section 3 enlists the machine learning techniques in the developed algorithm toolbox for engine anomaly detection. Section 4 includes detailed description of the simulation data set of engine gas path faults and the comparison of the detection results using the various algorithm of the developed toolbox. Finally, Section 5 concludes the work.

2. Commercial Aircraft Engine Condition Monitoring

2.1. Engine Gas Path Analysis

The performance of aero-engines is referred to the carefully tuned interaction among each gas path component. The high-pressure compressor (HPC) and high-pressure turbine (HPT) is often referred to as the core engine, which is in charge of generating power that the LPT uses to transform into mechanical power for driving the fan. Typical sensors in aero-engine system include temperature sensors, speed sensors and pressure sensors located in different stations of engine. These raw sensor data contain control and feedback mechanisms; thus, simple analysis cannot obtain effective degradation information. Other condition parameters, such as Mach number, altitude and atmospheric temperature are included for further analysis. Figure 1 shows the online built-in sensor parameters of a typical modern turbofan engine, covering the main gas path components of the engine and important accessory systems (accessory systems such as lubricating oil and fuel control), etc. [15].

Gas path analysis (GPA) is a method that relates variations of measured engine performance parameters resulting from engine deterioration to the condition of its gas path components [16]. It is meaningful to the existing gas turbine diagnostic methods, which is wildly used for condition-based maintenance. In order to put these methods into practical applications, improving diagnostic accuracy has been the focal point for developing better GPA techniques [17–19].

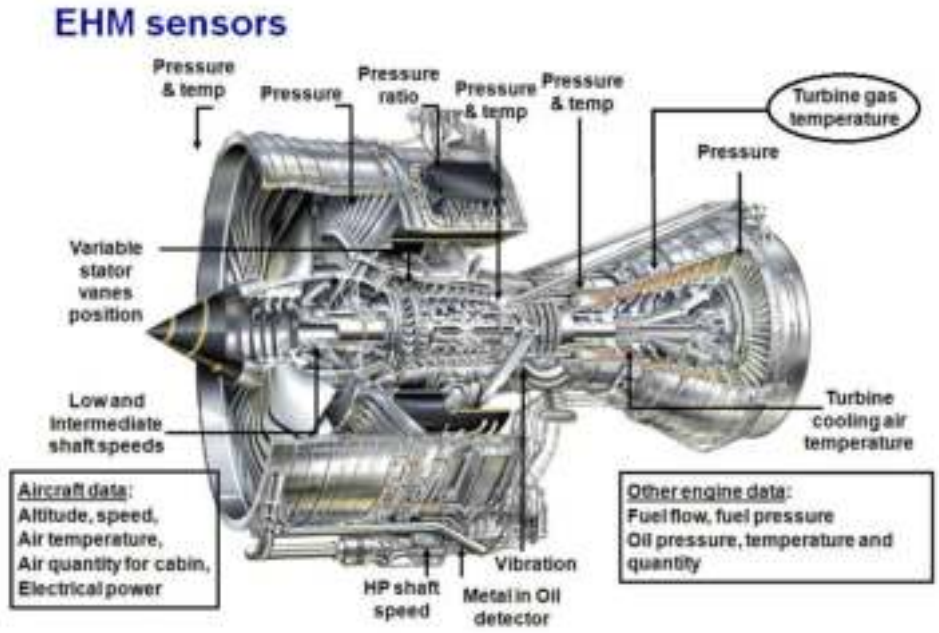

Figure 1. Typical engine built-in sensor parameters.

Existing approaches can be grouped in two categories: physics-based methods and data-driven methods. The physics-based methods aim at describing the physics of failure mechanisms by mathematical modeling for the components and the systems under the study. Such methods are applicable where there is enough information about the internal parameters of the system and the failure mechanisms can be parameterized on that basis. Houman Hanachi et al. developed a robust physics-based performance indicator for aero-engine [20]. A comprehensive physics-based thermodynamic model for the gas path of a single shaft engine was developed in their work to accurately predict the cycle parameters based on limited actual operating data. Physical degradation processes are only well understood for critical or relatively simple components, and physics-based approaches are generally hindered by their limited ability to properly tune the parameters of models with high complexity or model incompleteness, which restricts the deployment in practical applications [21]. The alternative approach for health monitoring is the use of data-driven models [22]. These approaches use large amounts of data, preferably from various sources, and apply data analytics techniques such as machine learning and artificial neural networks to discover patterns and relations in the data sets. This means that in principle no knowledge on the system characteristics or failure behavior is required, which makes the approach popular and widely accessible [23].

2.2. Engine Condition Monitoring Data

A flight is divided into different flight phases, each phase has a different impact on the engine, which increases the difficulty of data monitoring. Currently, Quick Access Recorders (QAR) is widely adopted by airlines, providing full flight data continuously sampled at frequencies of 1 Hz and more, and enabling the researches of new methods in engine condition monitoring. All other functions such as exceedance tests, report generation, are based on, and controlled by the flight phase. For the flight phase diagram, see Figure 2. Flight phase is determined based on a state-transition machine, that means once a given flight phase is entered, it can only transmit to another flight phase under defined conditions. Therefore, the flight phase can be used as a performance tag to describe how the engine is currently operating. The flight phases that are mainly discussed in Figure 2 are shown in Table 1.

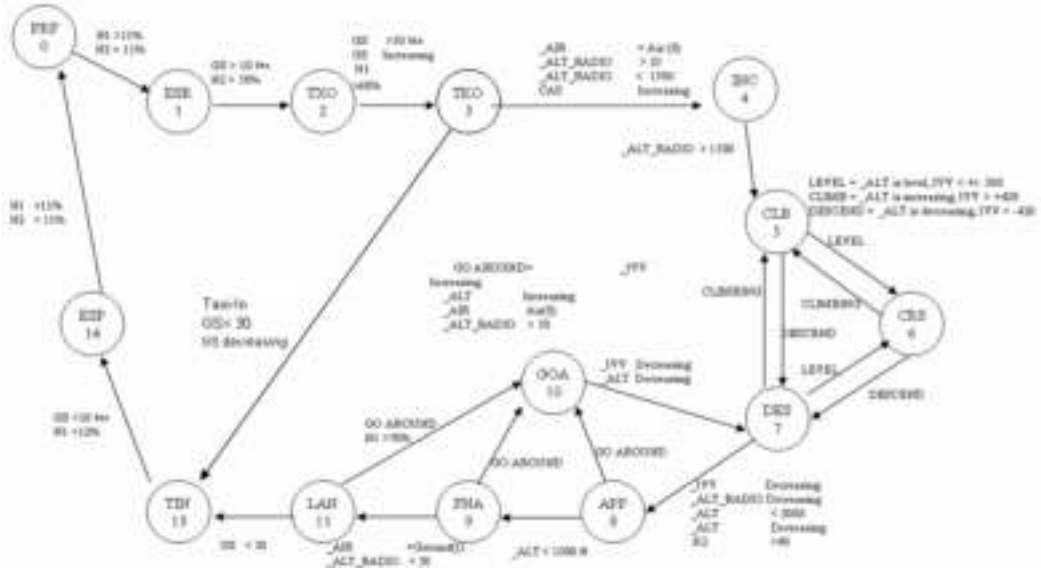

Figure 2. Flight phase diagram.

Table 1. Flight phase.

Number	Code	Flight Phase
0	PRF	Pre-flight
1	ESR	Engine Start
2	TXO	Taxi Out
3	TKO	Takeoff
4	INC	Initial Climb
5	CLB	Climb
6	CRS	Cruise
7	DES	Descent
8	APP	Approach
9	FNA	Final Approach
10	GOA	Go Around
11	LAN	Landing
12	TAG	Touch and Go
13	TIN	Taxi In
14	ESP	Engine Stop

For cruise data acquisition, data points must be recorded under stable operating conditions, which is stabilized at cruise setting for at least 5-min before recording data. During recording, fan speed (N1) variation needs to be minimized, and stable airplane/engine conditions needs to be maintained. For takeoff data acquisition, monitoring data should be recorded at, or near, conditions when peak EGT typically occurs for the engine, that is, during full-rated or derated thrust takeoff, at any ambient temperature. These data points can effectively reduce the amount of data required for analysis, but provide very little information to reflect the variation in the performance state of the engine throughout the entire flight segment.

Actual analysis rarely analyzes the entire flight data, but extract certain operating points during takeoff and cruise for condition monitoring. However, the form of the condition monitoring data may lead to difficulties distinguishing between faults and random scatter. Depending on the faulty component and the severity of the fault, it may take multiple data points to detect [24], which may cause false alarms and missed alarms. Therefore, continuous monitoring of the entire flight segment should be performed to improve the fault detection rate.

3. Development of Engine Data Mining Toolbox

Existing approaches for engine data mining can be grouped in three categories: baseline construction, anomaly detection and trend prediction.

Baseline model is widely used in engine condition monitoring. Baseline model, i.e., the health indicator, is proposed to characterize the unobserved degradation state of the engine. Non-parametric modeling techniques, such as Multivariate State Estimation Technique (MSET) and Random Forest (RF), can be adopted to calculate the health indicator. Based on the developed baseline model, the delta value between the real value of and baseline value is monitored in real time to monitor the gas path component condition and to trigger a warning once some fault occurs.

Engine anomaly detection usually refers to detecting and locating the fault by analyzing the mechanical condition of the main engine mechanical damage, engine vibration, lubrication, transmission and fuel control systems, and comprehensively analyzing the performance condition parameters [25]. The detection method requires the ability to accurately isolate the fault, but also needs a quantitative assessment of the severity of the fault to provide input for the remaining life prediction and maintenance decision making. Several different anomaly detection algorithms are integrated in this module, covering functions such as outlier detection, trend anomaly detection and clustering.

Parameter trend prediction includes the prediction of the gas path performance and the remaining life of key components. In the trend prediction, the gradual performance deterioration is tracked to obtain the degradation state of each module before the fault, then the information is incorporated when isolating and assessment the fault to improve the health assessment results.

This article collects the algorithms applied for engine anomaly detection and integrates them into an algorithm library, including supervised and unsupervised algorithms. Table 2 introduces different types of algorithms involved in the algorithm library. Due to the complicated forms of engine failure, the diversity of algorithms needs to be guaranteed in order to improve detection efficiency.

Table 2. Algorithm Detail.

Type	Algorithm
Baseline Construction module	RF (Random Forest)
	MSET (Multiple State Estimation Technique)
	LSTM (Long Short-Term Memory)
Anomaly detection module	MD (Mahalanobis Distance)
	Iforest (Isolation Forest)
	XGBOD (Extreme Gradient Boosting Outlier Detection)
	MCD (Minimum Covariance Determinant)
	WFCS (Feature Weighted Fuzzy Compactness and Separation)
	GMM (Gaussian Mixture Model)
	DTW (Dynamic Time Warping)
	VAE (variational autoencoder)
Parameter trend prediction module	ARMA (Autoregressive–moving-average model)
	State Space Model

This paper mainly uses the following four anomaly detection methods.

1. Isolation Forest, IF

Isolation forest is an unsupervised learning algorithm for anomaly detection that works on the principle of isolating anomalies [25]. Instead of trying to build a model of normal instances, it explicitly isolates anomalous points in the dataset. The main advantage of this approach is the possibility of exploiting sampling techniques to an extent that is not allowed to the profile-based methods, creating a very fast algorithm with a low memory demand. other algorithms for an efficient fault detection system.

2. Extreme Gradient Boosting Outlier Detection, XGBOD

XGBOD is demonstrated for the enhanced detection of outliers from normal observations in various practical datasets. It combines the strengths of both supervised and unsupervised machine learning methods by creating a hybrid approach that exploits each of their individual performance capabilities in engine outlier detection. Compared to other semi-supervised outlier ensemble methods, XGBOD provides better predictive capabilities, eliminates the dependency of building balanced subsamples and averaging the results, and improves efficiency with more stable execution [26].

3. Minimum Covariance Determinant, MCD

The minimum covariance determinant (MCD) method of Rousseeuw (1984) is a highly robust estimator of multivariate location and scatter [27], using the Mahalanobis distances as the outlier scores. Its objective is to find h observations (out of n) whose covariance matrix has the lowest determinant.

4. One-class Support Vector Machine, OCSVM

Support Vector Machine (SVM) is a generalized linear classifier method for binary classification of data, which belongs to supervised learning. SVM is defined as a linear classifier with the maximum interval in the feature space, and its learning strategy is to maximize the interval, which is finally transformed into the solution of a quadratic programming problem. The difference between One-class Support Vector Machine (OCSVM) and support vector machine is that there is only one category of training data. When the test data is input into the model, the model will detect whether it is similar to the training data. For anomaly detection, the training data is health samples, and whether the test data is abnormal is determined by judging whether the test data is similar to the health data.

4. Case Study: Gas Path Fault Simulation

An application test case is conducted on a two spool, partially mixed, high bypass ratio turbofan, which is representative of the modern turbofan engines in civil aviation. The engine performance model consists of 10 health parameters to characterize the condition of five components and 7 performance measurements being representative of a measurement set of today's civil turbofan are produced by the model. Figure 3 shows the process of the entire research case. The specific parameters are shown in Figure 4 and Table 3.

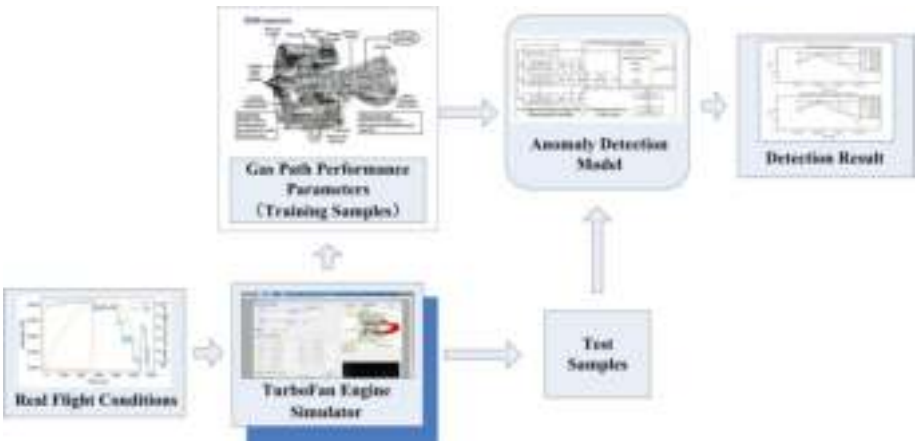

Figure 3. Case study process.

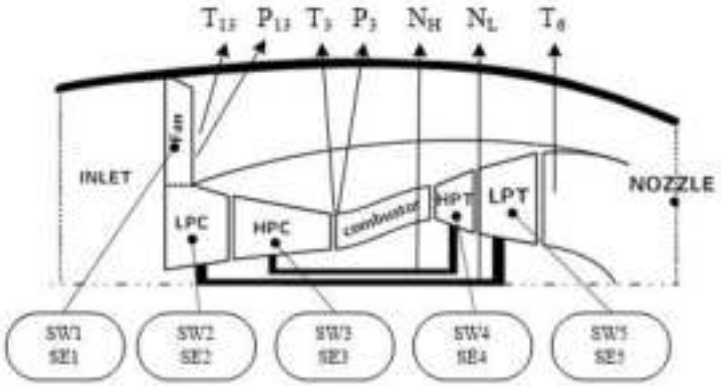

Figure 4. Engine performance simulation parameters overview.

Table 3. Parameter Detail.

Health Parameter	Gas Path Performance Measurement
Fan flow correction factor SW1 (%)	Outlet pressure of the fan P13 (bar)
Fan efficiency correction factor SE1 (%)	Outlet temperature of the fan T13 (C)
LPC flow correction factor SW2 (%)	Outlet temperature of the HPC T3 (C)
LPC efficiency correction factor SE2 (%)	Outlet pressure of the HPC P3 (bar)
HPC flow correction factor SW3 (%)	Low pressure rotor speed NL (rpm)
HPC efficiency correction factor SE3 (%)	High pressure rotor speed NH (rpm)
HPT flow correction factor SW4 (%)	Exhaust gas temperature T6 (C)
HPT efficiency correction factor SE4 (%)	Inlet pressure of HPC P2 (bar)
LPT flow correction factor SW5 (%)	Inlet temperature of HPC T2 (C)
LPT efficiency correction factor SE5 (%)	

4.1. Simulation Process

All simulation data are obtained using TurboFan Engine Simulator. By inputting a specific working condition, the simulation software can calculate the performance parameters under the condition.

First a fleet of engines is simulated. The system's components will experience degradation due to wear and tear resulting from usage. It is most often a slow phenomenon, which is detected relative to past performance on the same engine. It is very difficult to detect an efficiency drop in absolute value, because each unit of the fleet has slightly different initial wear at the engine sub-component due to manufacturing and assembly tolerances, which leads to differences in the health parameters of each engine component in the fleet, such as efficiency and flow.

For the above reasons, each engine in the startup fleet can be distinguished based on the difference in the initial health parameters. Assuming that the deviation between the health parameters of a specific engine unit and the baseline value conform to a triangular distribution, the maximum and minimum deviation values of the parameters of each component are shown in Table 4.

Based on the triangular distribution of the parameters, this paper adopts the Monte Carlo idea to randomly select values, and generates 100 sets of unit body health parameter deviation values, and uses this to distinguish each specific engine. Figure 5 shows the triangular distribution of Fan efficiency deviation.

After obtaining the fleet data, the next step is to simulate different take-off conditions for each individual engine. Each set of different takeoff conditions simulation represents a specific flight. The simulation method is the same as the fleet data. Assuming that the parameters of the take-off condition also conform to the triangular distribution, the maximum and minimum deviation values are shown in Table 5.

Table 4. Health Parameter Deviation.

Health Parameter	Minimum Deviation	Maximum Deviation
Fan flow correction factor SW1 (%)	−1	1
Fan efficiency correction factor SE1 (%)	−0.3	0.1
LPC flow correction factor SW2 (%)	−1	1
LPC efficiency correction factor SE2 (%)	−1	0.5
HPC flow correction factor SW3 (%)	−1	1
HPC efficiency correction factor SE3 (%)	−0.6	0.6
HPT flow correction factor SW4 (%)	−1.5	1.5
HPT efficiency correction factor SE4 (%)	−0.35	0.15
LPT flow correction factor SW5 (%)	−0.5	0.5
LPT efficiency correction factor SE5 (%)	−0.5	0.5

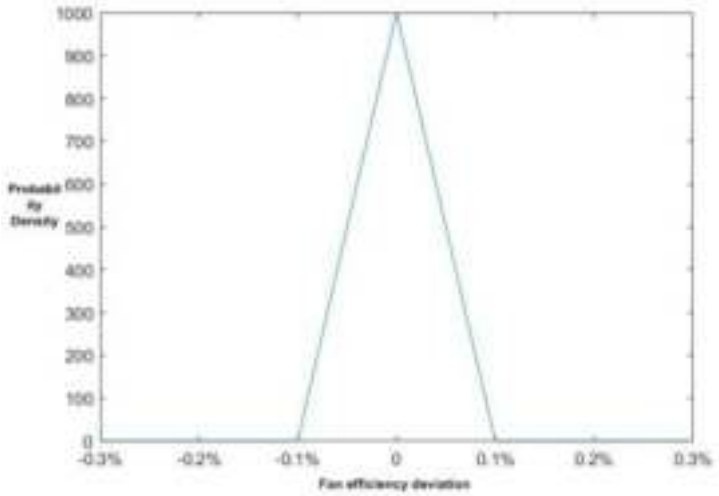

Figure 5. Probability density of fan efficiency deviation.

Table 5. Condition Parameter Deviation.

Condition Parameters	Minimum Deviation	Maximum Deviation
Altitude (m)	−500	500
Mach number	0.24	0.26
Standard atmospheric temperature difference (C)	−20	20
Fuel flow (kg/s)	0.83	0.97

Each engine randomly generates 1000 sets of condition parameter values for flights simulation. After the simulation calculation is completed, the performance data of 100 engines is obtained, and 1000 flights are simulated for each engine. The gas path parameters calculated with the aid of the performance model do not contain noise, but in practice the sensor will inevitably introduce measurement noise. Therefore, a certain amount of Gaussian noise is added to the gas path parameters to simulate actual measurement noise.

4.2. Data Preprocessing and Fault Injection

The baseline model of engine can reflect the basic functional relationships of engine performance parameters in a healthy state. When the engine is in a healthy state, the performance parameter deviation value obtained by subtracting the baseline value from the actual measurement value should theoretically fluctuate around 0. The abnormal detection of the engine performance parameter can be realized by analyzing the deviation value sequence.

The performance measurement deltas (ΔY) of each parameter needs to be calculated to facilitate the detection of the algorithm. The formula is as follows:

$$\Delta Y = Y - Y_0 \tag{1}$$

where Y represents the value of the parameter, and Y_0 the nominal value at a typical taking-off condition when the engine is at a clean and new condition. (That is, using the Random Forest algorithm for parameter regression).

The health parameter deviation is calculated as follows:

$$\Delta f = (f - f_0) \cdot 100\% \tag{2}$$

where f_0 = 1 meaning the engine is at a clean and new condition. The interrelation among the health parameters deviations and the measurements deltas is expressed through a multi variable regression model, which is obtained by linearizing of the engine performance model at a typical taking-off operating point.

In this paper, two kinds of baseline values Y_0 are calculated. One is to randomly select 400 sets of data from all health status data of the fleet to calculate a baseline value. The other is based on the first 400 health data of each engine, a total of 20 engines' personalized baseline values was established separately.

Component faults are simulated by deviating of the corresponding health parameters from their nominal values, i.e., the flow and efficiency deviations of each module. To demonstrate the proposed information fusion mechanism, a typical set of fault scenarios has been examined, which covers different possible faults in all individual components (given in Table 6).

Table 6. Failure modes.

Failure Modes	Changes in Health Parameters
Failure mode A	Fan flow rate drops by 1%, efficiency drops by 1.5%
Failure mode B	HPC flow rate drops by 1%, efficiency drops by 0.7%
Failure mode C	HPT flow rate drops by 1%, efficiency drops by 1%
Failure mode D	LPT flow rate drops by 1%, efficiency drops by 0.5%
Failure mode E	HPC efficiency decreased by 1.5%
Failure mode F	HPT efficiency decreased by 1.5%

For each fault case, a series of n = 400 measurement sets from the taking-off operating point has been recorded for following, including 20 fleet samples and 20 single engine samples. They were randomly selected from the fleet data without putting it back. The first 360 sets are health status data, and the last 40 sets are abnormal conditions (Inject according to the failure mode of Table 4).

4.3. Results Analysis and Comparison

In the detection, four binary classifiers, IForest, XGBOD, MCD, OCSVM (one class support vector machine), are chosen as detection algorithms. The algorithms will output two indicators to measure classification accuracy: AUC and Precision. AUC is the area under the ROC curve, its value is equivalent to the probability that a randomly chosen positive example is ranked higher than a randomly chosen negative example. As for precision, it is the probability of how many real positive examples are in the sample predicted to be positive.

This article compares the test results from the following three aspects:

1. Comparison of anomaly detection effects between the fleet baseline model and a single personalized baseline model:

The deviation values obtained from the two baseline models are input into the isolation forest, MCD, XGBOD, OCSVM algorithm. The AUC value and accuracy rate of the

abnormal detection of six abnormal modes is calculated by the algorithm model. Since each algorithm has been tested many times, the calculation result is the average of multiple tests. After detection, the comparison of AUC and precision is shown in the figure below.

It can be seen from Figures 6 and 7 that only three faults (i.e., fault C, D and E) have relatively high detection accuracy. The remaining fault cases are misdiagnosed. Among the four anomaly detection algorithms, XGBOD is an ensemble learning algorithm, so the overall effect is the best. The overall anomaly detection effect of MCD and IForest is not much different. In abnormal modes A and F, IForest is better than MCD. In abnormal mode B, MCD is better than IForest. OCSVM has the worst anomaly detection effect overall.

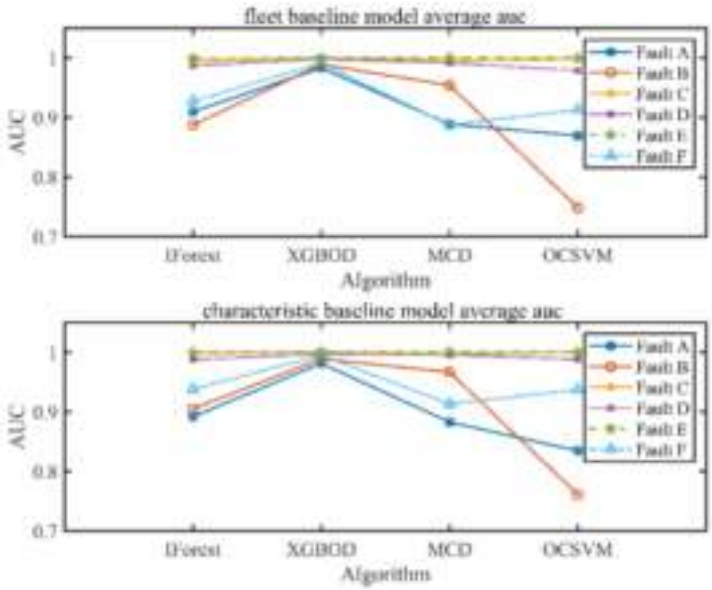

Figure 6. AUC value comparison.

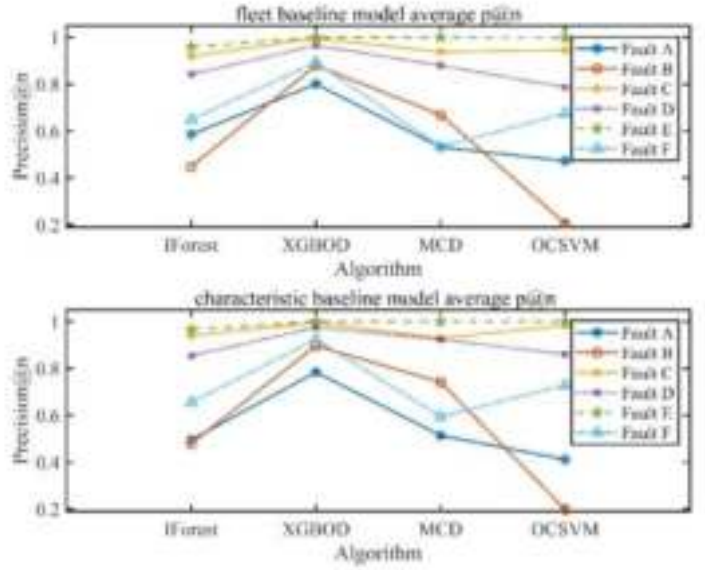

Figure 7. Precision comparison.

2. The influence of engine performance parameters on anomaly detection effect:

In the above, the deviation values of the nine performance parameters are all detected for abnormality. In the actual situation, the data collected by the sensor does not include the HPC inlet pressure and inlet temperature. Therefore, this section will compare the anomaly detection effects of the nine parameters and the seven parameters. Tables 7 and 8 show the results.

Table 7. Detection Results (AUC).

Failure Modes	IForest		XGBOD		MCD		OCSVM	
	Nine PARAM	Seven PARAM	Nine PARAM	Seven PARAM	Nine PARAM	Seven PARAM	Nine PARAM	Seven PARAM
A	0.89	0.81	0.98	0.92	0.88	0.89	0.83	0.83
B	0.90	0.85	0.99	0.98	0.96	0.92	0.76	0.75
C	0.99	0.99	1.0	1.0	0.99	0.99	0.99	0.99
D	0.98	0.99	0.99	0.99	0.99	0.99	0.98	0.98
E	0.99	0.99	1.0	1.0	1.0	1.0	1.0	1.0
F	0.94	0.95	0.99	0.99	0.91	0.91	0.93	0.94

Table 8. Detection Results (precision).

Failure Modes	IForest		XGBOD		MCD		OCSVM	
	Nine PARAM	Seven PARAM	Nine PARAM	Seven PARAM	Nine PARAM	Seven PARAM	Nine PARAM	Seven PARAM
A	0.49	0.36	0.78	0.71	0.51	0.53	0.41	0.41
B	0.48	0.43	0.90	0.79	0.74	0.57	0.20	0.19
C	0.94	0.90	0.99	0.99	0.93	0.96	0.98	0.98
D	0.85	0.83	0.98	0.97	0.92	0.94	0.86	0.86
E	0.97	0.98	1.0	1.0	1.0	1.0	1.0	1.0
F	0.66	0.72	0.92	0.91	0.59	0.62	0.73	0.73

The failure modes not accurately identified were failure mode A and B. For the failure mode B, the HPC fault with a simultaneous reduction in efficiency and flow capacity, which may affect LPC component, resulting in an evident LPC efficiency decrease. Due to the limited on-board performance measurement set, the measurements between the LPC and HPC are insufficient to characterize all fault information, for which they share a similar measurement observation pattern due to the failure.

3. The influence of different levels of noise on the detection effect:

Besides the on-board sensor measurements limitation, the measurement noise can also introduce uncertainty into the health parameters estimation. Especially when the fault magnitude is relatively smaller, the failure signature maybe masked in the measurement noise, causing wrong diagnostics conclusions. Two types of noise are used to process the data here. The amount of noise is shown in Table 9.

Table 9. Noise Setting.

Gas Path Performance Parameter	Noise A	Noise B
Outlet pressure of the fan P13 (bar)	0.25%	0.5%
Outlet temperature of the fan T13 (C)	0.4%	0.8%
Inlet pressure of HPC P2 (bar)	0.25%	0.5%
Inlet temperature of HPC T2 (C)	0.4%	0.8%
Outlet temperature of the HPC T3 (C)	0.25%	0.5%
Outlet pressure of the HPC P3 (bar)	0.4%	0.8%
Exhaust gas temperature T6 (C)	0.4%	0.8%
Low pressure rotor speed NL (rpm)	0.05%	0.1%
High pressure rotor speed NH (rpm)	0.05%	0.1%

The test analysis for the above test results is given here. First, in the detection of different baseline model, the failure modes B, C, D, E and F show better effect with single engine baseline model. However, in the detection of failure mode A, the detection effect of the fleet baseline model is more accurate, which means that the failure mode A is less affected by the engine's performance difference. The fan is the most exposed air

path component of the engine. Compared to changes in internal flow and efficiency of components, changes in the external environment are more likely to affect the efficiency of the fan.

Second, most algorithms obtain better detection results when the input performance parameters are nine. However, the MCD algorithm performs even better when the input parameters are seven, which may be related to the internal calculation of the Mahalanobis distance. When the dimensionality of the data point increases, the calculated Mahalanobis distance will also increase. If the fault information can be reflected by only a few parameters, adding more parameter dimension may cover up the fault information which needs to be expressed by the value of distance, and it may lead to the misjudgment of the algorithm.

Third, the detection results of noise case are given in Table 10. Indicator "Precision" is more obviously affected by noise, so it is selected as the observation target.

Table 10. Detection Result of Different Noise.

Failure Modes	IForest		XGBOD		MCD		OCSVM	
	Noise A	Noise B	Noise A	Noise B	Noise A	Noise B	Noise A	Noise B
A	0.49	0.42	0.78	0.72	0.51	0.56	0.41	0.31
B	0.48	0.48	0.89	0.73	0.74	0.59	0.20	0.37
C	0.94	0.73	0.99	0.99	0.93	0.71	0.98	0.92
D	0.85	0.75	0.98	0.97	0.92	0.83	0.86	0.85
E	0.97	0.94	1.0	1.0	1.0	0.99	1.0	1.00
F	0.65	0.49	0.92	0.80	0.59	0.33	0.73	0.66

It can be observed that the detection ability of all algorithms decreases after the noise is doubled. Among them, the detection accuracy of failure modes C, D and F are significantly reduced, which are all turbine failure. This shows the flow and efficiency deviations of turbine component have less impact on the engine, which can be easily masked in the noise.

Based on the above results, the XGBOD algorithm has the highest detection accuracy. It makes good use of its advantages as an integrated algorithm, and performs well in the case of reduced parameters or increased noise. In contrast, the detection accuracy of IForest and OCSVM algorithms is not in a good level. Due to the lack of training data, the IForest failed to play its advantage in the detection of massive data. As for OCSVM, it is mainly good at single classification [28], and it does not perform well on two classification problems.

In terms of failure modes, failure mode E has the highest detection accuracy. This shows that the reduced efficiency of the high-pressure compressor will seriously affect the performance of the whole engine. On the other hand, the detection rate of each algorithm for failure mode A is relatively low. The reason may be that the selected parameters cannot well represent the characteristics of the failure, or the failure itself has a small impact on engine's performance.

5. Conclusions

This paper presents a detailed review of an experimental data mining algorithm library for engine condition monitoring, which comprises different types of algorithms (baseline construction, anomaly detection, trend prediction). The algorithm library is validated on engine simulation data, which shows great effectiveness on detecting different types of failure.

The innovations of the algorithm library are listed below:

1. This algorithm library is specifically established for engine condition monitoring;
2. The simulation data set used in this article can be made public for verification by other anomaly detection algorithm developers;
3. Compare the performance differences in anomaly detection algorithms in each condition to provide reference for actual engineering applications.

In the case study part of the paper, the performance data simulation of the engine fleet's health status and abnormal conditions is carried out. The baseline models of the fleet and a single engine are established respectively, and the deviation value sequences obtained from different baseline models are compared for anomaly detection. This paper tested four anomaly detection algorithms: Isolated Forest, XGBOD, MCD, OCSVM. The conclusions are as follows:

1. Different abnormal modes have different effects on engine performance parameters, leading to different detection results. The overall HPC and HPT abnormal detection results are the best;
2. In the comparison of the four algorithms, the XGBOD anomaly detection based on the integrated idea is the most accurate and can detect most outliers;
3. In terms of the deviation value sequences obtained by different baseline models, the individualized model is slightly better than the fleet model based on the fleet data in anomaly detection;
4. The reduction in status monitoring parameters and increased noise will reduce the accuracy of detection.

The successful application of these algorithms proves the reliability and efficiency of the algorithm library. To further improve the performance of the algorithm library, different operating conditions still need to be investigated. Therefore, a potential future research direction is a validation on actual failure data, as well as the installation of new algorithms.

Author Contributions: Conceptualization, J.S. (Jianzhong Sun); methodology, Y.Y.; validation, Z.Y.; investigation, Y.Y., C.Y., and J.S. (Jingbo Su); resources, C.Y. and J.S. (Jingbo Sun); data curation, Y.Y.; writing—original draft preparation, Z.Y.; writing—review and editing, Z.Y.; visualization, Z.Y. and Y.Y.; funding acquisition, J.S. All authors have read and agreed to the published version of the manuscript.

Funding: This work was supported by National Natural Science Foundation of China (No. 91860139).

Institutional Review Board Statement: Not applicable.

Informed Consent Statement: Not applicable.

Data Availability Statement: The data presented in this study are available on request from the corresponding author. The data are not publicly available because it is being updated.

Acknowledgments: This work was supported by Stable Support Project of Sichuan Gas Turbine Establishment of AECC.

Conflicts of Interest: The authors declare no conflict of interest.

References

1. Zaccaria, V.; Stenfelt, M. Fleet monitoring and diagnostics framework based on digital twin of aero-engines. In Proceedings of the ASME Turbo Expo 2018 Turbomachinery Technical Conference and Exposition, Oslo, Norway, 11–15 June 2018.
2. Ho, L.M. Application of adaptive thresholds in robust fault detection of an electro-mechanical single-wheel steering actuator. *IFAC Proc. Vol.* **2012**, *45*, 259–264. [CrossRef]
3. Palacios, A.; Martniez, A.; Sánchez, L.; Couso, I. Sequential pattern mining applied to aeroengine condition monitoring with uncertain health data. *Eng. Appl. Artif. Intell.* **2015**, *44*, 10–24. [CrossRef]
4. Ying, Y.; Cao, Y.; Li, S.; Li, Y. Nonlinear steady-state model based gas turbine health status estimation approach with improved particle swarm optimization algorithm. *Math. Probl. Eng.* **2015**, *2015*, 940757. [CrossRef]
5. Frolik, J.; Abdelrahman, M.; Kandasamy, P.A. Confidence-based approach to the self-validation, fusion and reconstruction of quasi-redundant sensor data. *IEEE Trans. Instrum. Meas.* **2001**, *50*, 1761–1769. [CrossRef]
6. William, R.J.; Huw, L.E.; Li, P.; Kadirkamanathan, V.; Mills, A.R. Gas turbine engine condition monitoring using gaussian mixture and hidden markov models. *Int. J. Progn. Health Manag.* **2018**, *9*, 1–15.
7. Consumi, M.; d'Agostino, L. Monitoring and fault diagnosis of a turbojet by Bayesian inference. In Proceedings of the 13th International Symposium on Air Breathing Engines, ISABE 97-7146, Chattanooga, TN, USA, 7–12 September 1997; pp. 1082–1096.
8. Li, L.; Das, S.; Hansman, J.; Palacios, R.; Srivastava, A.N. Analysis of flight data using clustering techniques for detecting abnormal operations. *J. Aerosp. Inf. Syst.* **2015**, *12*, 1–12. [CrossRef]

9. Dewallef, P.; Leonard, O. On-line performance monitoring and engine diagnostic using robust Kalman filtering techniques. In Proceedings of the ASME Turbo Expo 2003, Atlanta, GA, USA, 16–19 June 2003; pp. 395–403.
10. Seo, D.H.; Roh, T.S.; Choi, D.W. Defect diagnostics of gas turbine engine using hybrid SVM-ANN with module system in off-design condition. *J. Mech. Sci. Technol.* **2009**, *23*, 677–685. [CrossRef]
11. Breunig, M.M.; Kriegel, H.P.; Ng, R.T.; Sander, J. LOF: Identifying density-based local outliers. *ACM SIGMOD Rec.* **2000**, *29*, 93–104. [CrossRef]
12. Manukyan, A.; Olivares-Mendez, M.A.; Voos, H.; Geist, M. Real time degradation identification of UAV using machine learning techniques. In Proceedings of the IEEE International Conference on Unmanned Aircraft Systems, Miami, FL, USA, 13–16 June 2017; pp. 1223–1230.
13. Santur, Y.; Karaköse, M.; Akin, E. Random forest based diagnosis approach for rail fault inspection in railways. In Proceedings of the 2016 National Conference on Electrical, Electronics and Biomedical Engineering (ELECO), Bursa, Turkey, 1–3 December 2016; pp. 745–750.
14. Song, X.; Wu, M.; Jermaine, C.; Ranka, S. Conditional anomaly detection. *IEEE Trans. Knowl. Data Eng.* **2007**, *19*, 631–645. [CrossRef]
15. Zaidan, B.; Arbayani, M. Bayesian Approaches for Complex System Prognostics. Ph.D. Thesis, University of Sheffield, Sheffield, UK, 2014.
16. Stamatis, A.; Papailiou, K.D. Discrete operating conditions gas path analysis. In Proceedings of the AGARD-CP-448 Engine Condition Monitoring—Technology and Experience, Quebec, Canada, 30 May –3 June 1988.
17. Jaw, L.C. Recent advancements in aircraft engine health management (EHM) technologies and recommendations for the next step. In Proceedings of the ASME Turbo Expo, GT2005-68625, Reno, NV, USA, 6–9 June 2005; pp. 683–695.
18. Li, Y.G. Performance-analysis-based gas turbine diagnostics: A review. *J Power Energy* **2002**, *216*, 363–377. [CrossRef]
19. Marinai, L.; Probert, D.; Singh, R. Prospects for aero gas-turbine diagnostics: A review. *Appl. Energy* **2004**, *79*, 109–126. [CrossRef]
20. Hanachi, H.; Liu, J.; Ba Nerjee, A.; Chen, Y.; Koul, A. A physics-based performance indicator for gas turbine engines under variable operating conditions. In Proceedings of the ASME Turbo Expo 2014: Turbine Technical Conference and Exposition, Düsseldorf, Germany, 16–20 June 2014. GT2014-26367.
21. Daigle, M.J.; Goebel, K. A model-based prognostics approach applied to pneumatic valves. *Int. J. Progn Health Manag.* **2011**, *2*, 1–16.
22. Loboda, I.; Pérez-Ruiz, J.L.; Yepifanov, S. A benchmarking analysis of a data-driven gas turbine diagnostic approach. In Proceedings of the ASME Turbo Expo 2018: Turbomachinery Technical Conference and Exposition, Oslo, Norway, 11–15 June 2018.
23. Zhong, S.S.; Song, F.; Lin, L. A novel gas turbine fault diagnosis method based on transfer learning with CNN. *Measurement* **2019**, *137*, 435–453.
24. Nairac, A.; Townsend, N.; Carr, R.; King, S.; Cowley, P.; Tarassenko, L. A system for the analysis of jet engine vibration data. *Integr. Comput. Aided Eng.* **1999**, *6*, 53–56. [CrossRef]
25. Liu, F.T.; Ting, K.M.; Zhou, Z.H. Isolation forest. In Proceedings of the Eighth IEEE International Conference on Data Mining, Pisa, Italy, 15–19 December 2008; pp. 413–422.
26. Zhao, Y.; Hryniewicki, M.K. XGBOD: Improving supervised outlier detection with unsupervised representation learning. In Proceedings of the IEEE International Joint Conference on Neural Networks, Rio de Janeiro, Brazil, 8–13 July 2018.
27. Rousseeuw, P.J.; Driessen, K.V. A fast algorithm for the minimum covariance determinant estimator. *Technometrics* **1999**, *41*, 212–223. [CrossRef]
28. Scholkopf, B.; Platt, J.C.; Shawe-Taylor, J.; Smola, A.J.; Williamson, R.C. Estimating the support of a high-dimensional distribution. *Neural Comput.* **2001**, *13*, 1443–1471. [CrossRef] [PubMed]

Disclaimer/Publisher's Note: The statements, opinions and data contained in all publications are solely those of the individual author(s) and contributor(s) and not of MDPI and/or the editor(s). MDPI and/or the editor(s) disclaim responsibility for any injury to people or property resulting from any ideas, methods, instructions or products referred to in the content.

International Journal of
Turbomachinery Propulsion and Power

MDPI

Article

Numerical Determination of the Equivalent Sand Roughness of a Turbopump's Surface and Its Roughness Influence on the Pump Characteristics

Benjamin Torner *, Duc Viet Duong and Frank-Hendrik Wurm

Institute of Turbomachinery, University of Rostock, Albert-Einstein Str. 2, 18059 Rostock, Germany
* Correspondence: benjamin.torner@uni-rostock.de

Abstract: The correct computation of flows over rough surfaces in technical systems, such as in turbomachines, is a significant issue for proper simulations of their performance data. Once the flow over rough surfaces is adequately computed in these machines, simulations become more trustworthy and can replace experimental prototyping. Roughness modelling approaches are often implemented in a solver to account for roughness effects in flow simulations. In these approaches, the equivalent sand roughness k_s must be defined as a characteristic parameter of the rough surface. However, it is difficult to determine the corresponding k_s-value for a surface roughness. In this context, this paper shows a novel and time-efficient numerical method, the discrete porosity method (DPM), which can be used to determine the k_s-value of a rough surface. Applying this method, channel flow simulations were performed with an irregularly distributed cast iron surface from a turbopumps volute. After identifying the fully rough regime, the equivalent sand roughness was determined and a match with k_s-values from literature data was found. Subsequently, the established k_s-value for cast iron was used in a turbopump simulation with rough walls. The performance data of the pump were validated by experiments and a good agreement between the experimental and simulated performance data was found.

Keywords: roughness modelling; equivalent sand grain roughness; discrete porosity method; turbopump; cast iron roughness

check for updates

Citation: Torner, B.; Duong, D.V.; Wurm, F.-H. Numerical Determination of the Equivalent Sand Roughness of a Turbopump's Surface and Its Roughness Influence on the Pump Characteristics. *Int. J. Turbomach. Propuls. Power* **2023**, *8*, 5. https://doi.org/10.3390/ijtpp8010005

Academic Editor: Gerard Bois

Received: 18 October 2022
Revised: 25 January 2023
Accepted: 30 January 2023
Published: 7 February 2023

Copyright: © 2023 by the authors. Licensee MDPI, Basel, Switzerland. This article is an open access article distributed under the terms and conditions of the Creative Commons Attribution (CC BY-NC-ND) license (https://creativecommons.org/licenses/by-nc-nd/4.0/).

1. Introduction

Nowadays, flow simulations are widely used for design optimizations of turbomachines, such as for turbopumps, compressors, or turbines. Manufacturers strive to improve and customise the performance data of these machines through simulations, since they allow a cost-effective and comprehensive understanding of the flow physics in the systems.

Most flow simulations of such machines assume the surface to be hydraulically smooth [1]. This contradicts real flows in these machines, where every surface has a certain degree of roughness. The roughness effects can significantly influence the performance data of the turbomachine's simulation. This is especially the case for turbopumps with low specific speeds n_s (Equation (1)), which means that the machines are designed to deliver high-pressure heads $H_p = \Delta p_{tot}/(\rho g)$ at small flow rates Q (a nomenclature can be found at the end of this paper). Those pumps are characterised by long and narrow impeller channels and even narrower side chambers between the impeller and the housing. Both geometric features can lead to dominant roughness effects in the pump.

Juckelandt et al. [2] demonstrated a significant deviation between the simulated and experimentally assessed performance data of a radial turbopump with low specific speed. As can be seen in Figure 1, the inner efficiency η_i (defined in Equation (13)) is monotonously overestimated in the pump simulation by an offset of +10%. The authors stated the unconsidered wall roughness as the critical aspect in their simulations. This discrepancy may cause designers to favor experimental methods over simulations. Hence,

an appropriate wall treatment with consideration of roughness modelling is crucial for the simulations in turbopumps with low specific speeds.

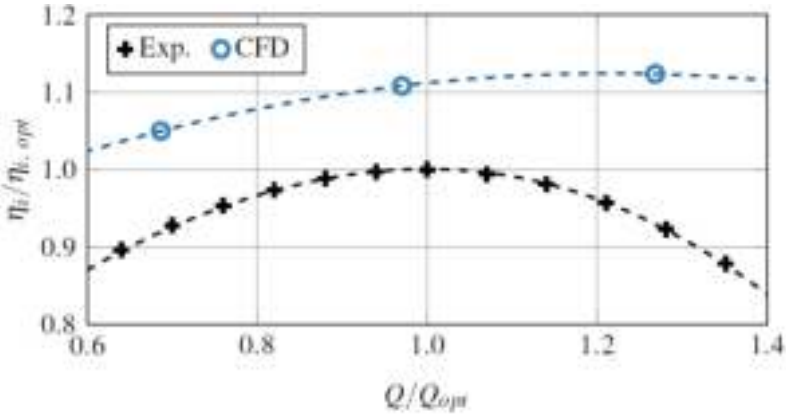

Figure 1. Discrepancy in inner efficiency η_i between experiment and simulation (CFD) of a radial turbopump with $n_s = 13.4$ 1/min. The figure is taken from Juckelandt et al. [2].

$$n_s = n \cdot \frac{\sqrt{Q}}{H_p^{3/4}} \tag{1}$$

In this context, the state-of-the-art roughness modelling for simulations depend on the equivalent sand grain roughness k_s as the characteristic standard to determine the impact of roughness effects [3]. According to Schlichting [4], the theory of equivalent sand grain roughness simplifies an arbitrary surface roughness to closely packed spheres, both having identical physical effects on the flow in the fully rough regime.

$$u^+ = 1/\kappa \; ln(y^+) + B - \Delta u^+(k_s^+) \tag{2}$$

It is well known that the dimensionless velocity profile $u^+ = f(y^+)$ indicates a downshift Δu^+ at rough walls compared to the velocity profile in hydraulically smooth boundary layers [5], see Figure 2. Equation (2) applies for the logarithmic wall region, where the downshift Δu^+ is described as a function of the dimensionless equivalent sand grain roughness k_s^+ [6,7]. In Equation (2), the constants were experimentally determined as $\kappa = 0.41$ and $B = 5.0$ [3].

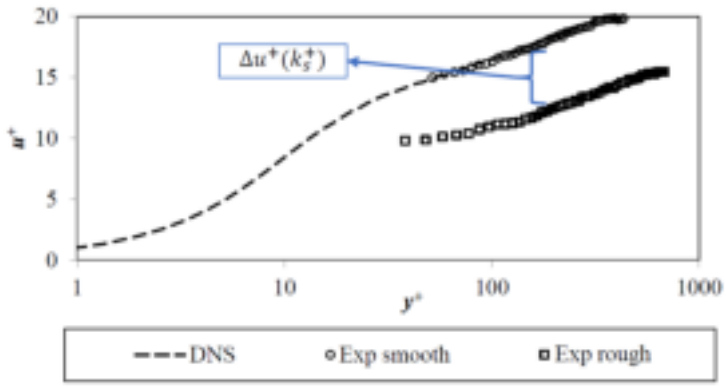

Figure 2. Universal velocity distribution $u^+ = f(y^+, k_s^+)$ in a boundary layer with roughness effects. The figure is taken from Juckelandt et al. [2].

The roughness modelling in simulations, e.g., in turbomachines, is realised by considering this downshift $\Delta u^+(k_s^+)$ in the simulated velocity profile. This approach is called

the modified logarithmic law-of-the-wall and it is one of the most common approaches to model the roughness effects. Roughness modelling approaches, which are based on the modified law-of-the-wall, were proposed by Refs. [8–10]. Alternatively, the roughness effects in a flow simulation of a turbomachine can also be modelled by changing the boundary conditions for turbulence variables near the rough wall, as proposed by Wilcox or Knopp et al. [11,12].

All of these approaches have in common that k_s of the rough surface has to be defined, so that the effect of roughness can be properly computed by the modelling approach. However, it is still complicated to define the appropriate k_s for surfaces with irregularly distributed roughness heights. Such surfaces are present, for example, at the unprocessed cast iron walls in the volute, impeller, or side chambers of a turbomachine [2].

Various experimental studies, which define the equivalent sand roughness for cast iron, can be found in the literature (Table 1). The ranges vary considerably among different authors, but also within the data of one study. Additionally, the cast iron surfaces in a turbomachine are zonally distributed and are partially machined. Thus, it is reasonable to determine k_s-values for each rough surface instead of assuming one value for the entire pump.

Table 1. Literature values for the equivalent sand grain roughness k_s of new cast iron surfaces.

Reference	k_s [µm]
Wagner [13]	200–600
Fried and Idelchick [14]	250–1000
Oertel et al. [15]	200–3000
Gülich [16]	300–1000
White [17]	$260 \pm 50\%$
Schlichting and Gersten [3]	250

In addition, empirical correlation were used to determine k_s. These correlations are derived from numerical or experimental studies. Simple correlations relate a geometrical parameter of the rough surface, such as mean roughness height k_a or root-mean-square (RMS) of roughness height k_{rms} to k_s [18]. Even though these correlations offer an easy determination of k_s, it lacks accuracy, since k_s cannot be described by height parameters alone [7,19]. Therefore, more complex correlations between multiple roughness parameters and the equivalent sand grain roughness were proposed, e.g., by Sigal and Danberg [20] and have been improved by van Rij et al. for three-dimensional, irregular roughness [21]. Flack and Schultz have investigated different roughnesses [7] and found a correlation fitting the k_s-values with k_{rms} and the *Skewness Sk* of the rough surface [7,22]. Other authors also included other roughness parameters as the *Effective Slope ES* in their correlations [22,23]. Forooghi et al. [23] have investigated 38 different types of surface roughness and formulated a correlation depending on peak-to-trough height k_t, S_k, and ES. Chan et al. have generated roughness in form of sinusoidal pattern and stated a strong dependency of the roughness function $\Delta u^+ = f(k_s^+)$ on k_a and ES [24]. Yuan and Piomelli have investigated realistic turbine roughness and examined the dependency of k_s and ES on the surface topology and investigated the accuracy of existing k_s-predicting correlations [25]. They stated that drag (and, hence, k_s) does not only depend on roughness height, but also on 3D-topology, which has also been mentioned by Busse [26]. In addition, Yuan and Piomelli have shown that correlations including ES match the performed data better than without.

By using these empirical correlations, a fairly good match in the k_s-values over a wide range of regularly and irregularly distributed roughness has been be achieved in the literature so far. Yet, the correlations are verified for a certain set of roughness types (sandpaper, honed pipes, gravel, ...) and are valid for only its, respectively, investigated roughness type [22]. More data from technical rough surfaces, such as cast iron, investment iron or steel, should be included, as these, in particular, have a much wider application in turbomachines.

Alternatively, k_s of a rough surface can be determined via flow simulations. This could be realized by performing direct numerical simulations (DNS) in simple flow configurations (e.g., channel flows) with the roughness at one wall. For example, roughness can be treated by using *immersed boundary method* (IBM) [25,27–29], where a separate mesh of the roughness is immersed in the fluid mesh. Based on the roughness boundary, forcing terms are added in the Navier–Stokes equation on adjacent fluid cells [30]. Therefore, the grid generation is simplified since the fluid mesh is of Cartesian type.

Forooghi et al. applied DNS for realistic surfaces based on combustion chamber deposits via IBM [31]. Additionally, Thakkar et al. have carried out DNS using IBM on irregular grit blasted surfaces [29], where they matched the roughness function $\Delta u^+ = f(k_s^+)$ of their roughness with Nikuradse's data. Chan et al. used DNS for their roughness investigations [24]. Due to the regular roughness surface in their study, a body conforming mesh was used, which resolves the roughness directly.

After predicting the k_s-value from these DNS computations in the simple flow configurations, the determined k_s can be specified for the roughness modelling in computations of more complex flows, such as in turbomachines.

As presented, DNS with or without IBM has been applied on roughness simulations in previous studies. However, their application could be connected with huge computational effort, since the roughness elevations could be in the range of microns [7,18,32,33], whereas the boundary layer dimensions reaches ranges of millimeters [27,32–35]. A very high Reynolds number could be needed to reach the fully rough regime in these flows. The resolution of turbulence at this high Reynolds number can make DNS difficult in terms of computing time and resources [7,28].

Regarding this, the present study shows an alternative numerical approach based on unsteady Reynolds-averaged Navier–Stokes (URANS) simulations of how the equivalent sand grain roughness k_s can be defined for a roughness. The method is called the *discrete porosity method* (DPM). The DPM discretises the roughness in defined sections and models the roughness as a porous medium. The pressure drop created by the porous properties is simplified as a drag of idealized regular shapes, such as triangles or rectangles. This pressure drop is then additionally added as a sink to the flow-governing equations, similarly described by Busse and Sandham [36] and later improved by Forooghi et al. [37]. Thus, the effect of a rough surface can be determined by URANS on moderate grid sizes and efficient computational times. The aim of this modelling approach is to determine the magnitude of the pressure drop caused in the porous cells. It will be shown in this paper that this method is sufficient to derive an average value of k_s, which can then be used for an appropriate roughness modelling in a turbopump simulation.

A plane channel flow with a cast iron roughness was simulated by DPM. The roughness was represented by a discretised scan of a surface from a turbopump's volute. The DPM simulation was used to determine the k_s-value for this cast iron surface. Afterwards, this k_s was applied to the associated rough walls in a turbopump simulation and the pump characteristics were determined.

2. Materials and Methods

2.1. Generation of Identical and Reproducible Rough Walls for the Experiments

In order to adjust and validate the performed simulations, the flow in the channel and in the turbopump (both with rough walls) were investigated experimentally. Therefore, surface replicas of cast iron were generated artificially and attached to the smooth walls in the experimental setups.

In cooperation with the company *Schweißtechnische Lehr- und Versuchsanstalt Mecklenburg–Vorpommern GmbH (Rostock, Germany)*, a process has been developed to similarly replicate the irregularly rough surface of cast iron. The cast iron surface at the volute of a serial, sand casted, radial turbopump was selected in this study. The surface roughness of this scan and its k_s can be seen as a representative for the whole volute since the volute was made from one piece of material with one machining process (sand casting). Before the

actual replication process started, the surface of the volute was optically recorded with a 3D-confocal microscope. During scanning, a spatial resolution of 1 nm in height and 1.5 µm in transverse direction could be achieved.

A commercially available, self-adhesive plastic film with a thickness of 360 µm served as the replica material, which was attached to the walls in the channel and turbopump experiments. The replication process was carried out by removing material from the plastic films step by step with a picosecond laser in a 5-axis machining system. The accuracy of the replication process was 10 µm in height and 22 µm in the flow direction and spanwise direction. The replica surface (average roughness height $k_a = 20.3$ µm; maximum peak-to-trough roughness height $k_t = 270$ µm) had a basic area of 12.6 mm×9.0 mm. Since the channel walls in the experiments have a larger area than the scanned roughness area, the replica was repeated at the plastic film to fill the surface. Therefore, the basic areas were mirrored at the edges of the specific replica to avoid discontinuities at the plastic film. Figure 3 shows the height profile of the scanned cast iron surface and the replica in comparison and Table 2 shows a comparison between the scanned and the replicated roughness.

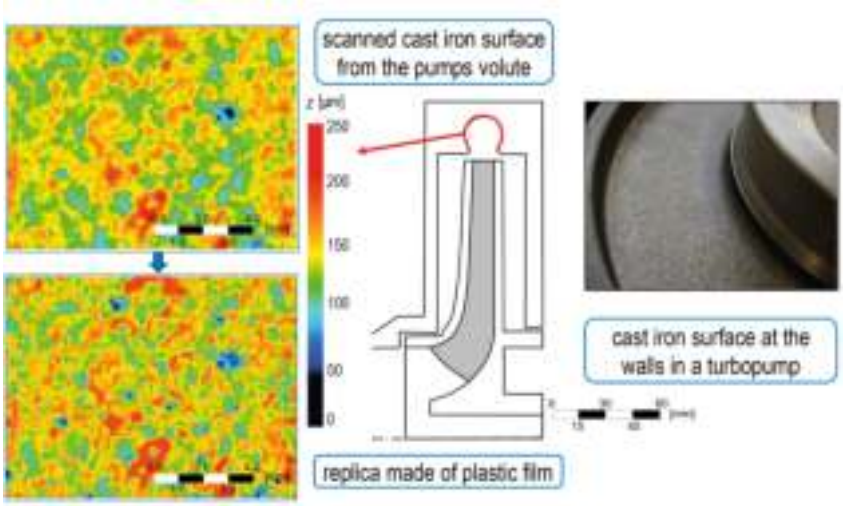

Figure 3. Comparison between scanned and replicated cast iron surface for the experiments.

Table 2. Comparison of the roughness topographical properties between the cast iron scan and the replica.

Roughness	$\overline{h}$ [µm]	k_t [µm]	k_a [µm]	k_{rms} [µm]	Sk	ES
Scan	190	280	20.0	25.5	−0.12	0.24
Replica	186	270	20.3	26.1	−0.22	0.16

For most geometrical properties between scan and replica, such as k_a and k_t, the average roughness elevation $\overline{h}$ or the root-mean-square roughness height k_{rms} are similar. Therefore, the replica has successfully imitated the original roughness in terms of height and elevation. The basic trend of negative skewness S_k has remained the same indicating a pitted surface [22], which has become stronger with the replica. Additionally, for effective slope ES, a discrepancy has occurred, in which the replica's value has decreased. This reduction means that the replica has become a longer wavelength roughness than the original scan. The differences in S_k and ES lie in the stream- and spanwise discretization of the replica, limited by the laser beam thickness. This might have an influence on the k_s-value between the original cast iron and the replicated surface. A discussion on this will be given in the limitations in Section 4.

2.2. Experimental Setup of the Rough Channel Flow Simulations

A simple flow configuration was chosen to perform the DPM simulations in order to determine k_s of the rough surfaces. This simple flow configuration is a planar flow channel with rough walls in a closed-loop test rig. The test rig is shown in Figures 4 and 5.

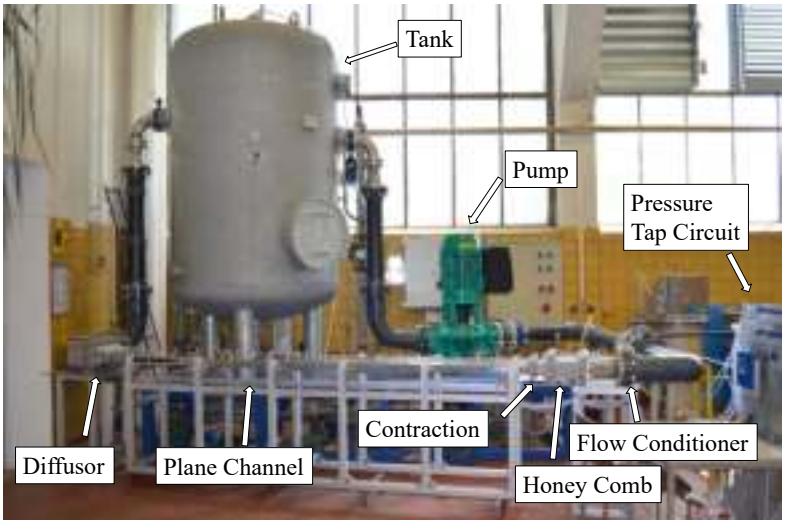

Figure 4. Setup for the rough channel flow experiments.

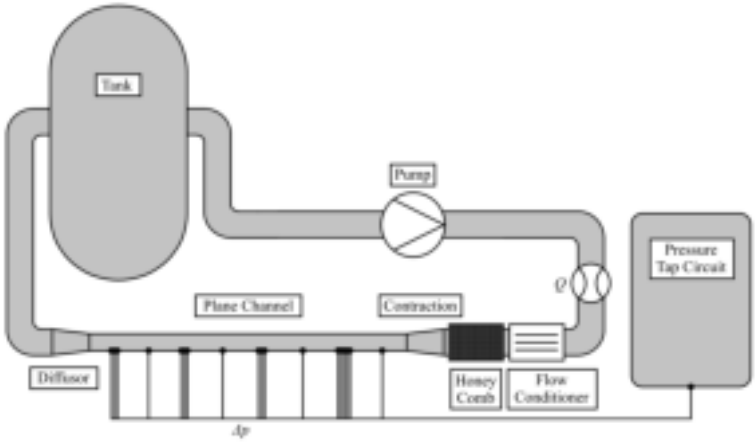

Figure 5. Schematic drawing of the setup for the rough channel flow experiments.

2.2.1. Test Section

The main component of the test rig is a plane channel. The channel was designed according to the work of Schultz and Flack [35] with a channel height of $H = 0.025$ m and a length of $L = 3$ m. The width has been determined from Jones [38] to be 12 times the channel height, resulting in a channel width of $w = 0.3$ m. This width ensures an approximate plane flow at mid of the channel. Trip wires of 1.6 mm diameter were placed at the channel entrance to provide instantly a turbulent flow. These wires create 13% blockage, which is comparable to the 15% blockage in Schultz and Flack [35].

An important condition for the reliable flow measurements is the precise realisation of the geometric dimensions of the channel. Due to these requirements, the channel was made of stainless steel plates, which were ground by machine. With this procedure, an average roughness height of $k_a = 1.6$ µm and tolerances for flatness and parallelism of <0.2 mm and <0.1 mm were achieved, respectively.

Before entering the channel, different flow conditioners and manipulators were included, to guarantee a fully-developed channel flow. First, a 3-8-6 flow conditioner, designed with the help of DIN EN ISO 5167-2 [39], was arranged as a flow-straightener behind

a pipe bow near the channel. Then, a honeycomb was placed, which contains a tube bundle of 0.006 m diameter and 0.113 m length, to reduce the swirl created by the pump. The tube diameter and length were determined using Ref. [35]. After the honeycomb, a contraction was placed, which was designed by a third degree polynomial [40] and connected the pipe system with the rectangular channel. After the channel, a diffuser transforms the channel geometry back to the pipe geometry. This diffuser includes a splitter to avoid flow separation in the test rig.

2.2.2. Surface Roughness

The material of the channel is ground stainless steel. Since the roughness of this material is small, a hydraulically smooth flow behaviour can be expected for the manufactured channel. To account for a channel flow with rough walls, the plastic films with the replicated cast iron surface were attached to the upper wall of the channel. Only the upper side of the channel was covered with the roughnesses so that the pressure measurements taken on the bottom side would not be distorted by the roughness. Therefore, a hydraulically smooth flow prevails at the bottom channel side, which was not considered in the evaluation of the results. The entire width of the upper channel side and $\approx$ 95% of the length were covered with the roughness.

2.2.3. Measurement System and Procedure

A flow meter was placed behind the pump to control the experimental flow rate. The pressure gradients of the channel were measured at a specific flow rate. Therefore, 17 pressure measuring holes at eight positions were included at the hydraulically smooth bottom side of the channel, see Figure 6. The pressure measuring holes have a diameter of 0.5 mm and were eroded in the stainless steel plate to guarantee that edges of the eroded holes are burr-free and remain sharp. The holes are positioned in the centerline of the channel with a distance of (300–400) mm to each other. Furthermore, additional holes were added at measurement positions I, III, V, and VII in the traverse direction. These additional holes were 65 mm apart from the centerline holes and were used to check the flatness of the flow. The pressure gradient of the whole channel was determined by including only the pressure measurements from the centerline holes. The pressure gradient of the whole channel was obtained by averaging the pressure gradients measured in every segment between position III and VI. Therefore, a differential pressure transmitter was used, which measured the pressure difference in these segments for 2 min with a frequency of 10 Hz. This procedure was verified in a preliminary study with a smooth channel flows at different Reynolds numbers. Here, the measured pressure gradients agreed with the empirically determined pressure gradients by $\leq$3%.

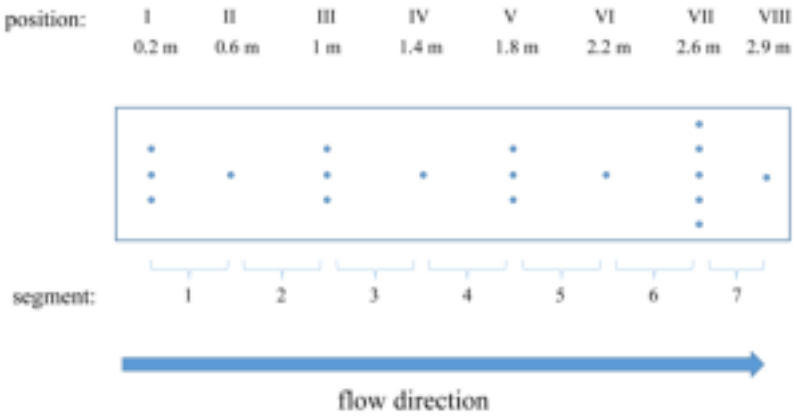

Figure 6. Positionof the pressure measuring holes in the channel (Roman numbers) and segments, where the pressure difference was determined (Arabic numbers).

2.3. Numerical Treatment of Rough Surfaces: Discrete Porosity Method (DPM)

The *discrete element method* (DEM) is the basis for our method. It has already been introduced in 1985 by Taylor et al. [41] and was used by Magagnato et al. [42], Pritz et al. [43], and Stripf et al. [44] for the computation of flows at rough turbine blade walls. The DEM can be seen as an intermediate path from a discrete mapping of the surface structure in the computational domain to a complete modelling of rough surfaces. The fundamental idea of this method is the introduction of an additional sink term in the governing equations to represent the increased drag force due to the roughness effects. For the modelling, Stripf et al. [44] resort to the drag coefficients of individual basic bodies, which are determined on the basis of empirical correlations and surface measurements. Similarly, Busse and Sandham [36] have introduced a parametric forcing approach (FPA) which has been improved by Forooghi et al. [23]. It is based on the treatment of porous media using the Darcy–Forchheimer Equations.

2.3.1. Rationale of the DPM Method

The discrete porosity method (DPM) is a self-designed simulation method for flow simulation over rough walls. The starting point represents a computational domain in which at least one wall covered with roughness elements. This domain is discretised by a computational Cartesian grid. To separate the flow from the roughness elements, three cell types are distinguished in the computational grid. Firstly, fluid cells that lie in the fluid domain and have no contact with the roughness. The governing equations, e.g., the incompressible Navier–Stokes equation (Equation (3)), are solved in these cells. Secondly, solid cells that lie completely in the roughness elements are deleted out of the mesh. Thirdly, in the Navier–Stokes equation of porous cells, that are partially filled by the roughness elements, a sink term is added on the right hand side resulting in Equation (4). The two latter cell types are also described as the roughness zone in the following. Figure 7 illustrates the described differentiation.

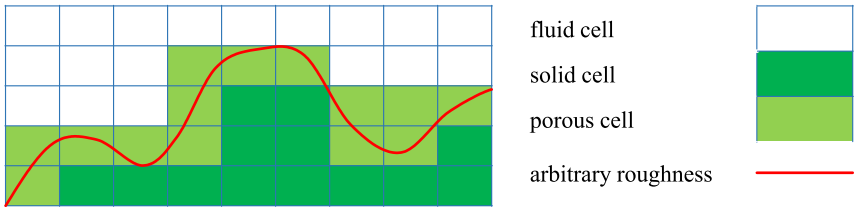

Figure 7. Cell type definition in the discrete porosity method. Both solid as well as porous cells build the roughness zone.

The authors recommend to use a plane channel flow with two wall boundary layers and periodic boundaries in the flow direction and span-wise direction for the DPM. The roughness can be placed at one wall and should be meshed separately in the roughness zone (height of this zone should be k_t). In this zone, the grid should be built such that a single cell resolve at least $1/5$ of k_t according to the authors' experience with irregular roughnesses.

$$\frac{\partial \vec{v}}{\partial t} + (\vec{v} \cdot \nabla)\vec{v}) = -\frac{\nabla p}{\rho} + \nu \Delta \vec{v} \tag{3}$$

$$\frac{\partial \vec{v}}{\partial t} + (\vec{v} \cdot \nabla)\vec{v}) = -\frac{\nabla p}{\rho} + \nu \Delta \vec{v} + \frac{\vec{S}}{\rho} \tag{4}$$

In the porous cells, the pressure loss due to the roughness elements is calculated by an additional sink S, representing a drag (for simplicity, a roughness element with the constant width b in a flow only with the velocity component u_∞ is assumed for the following equations). The connected drag force F_D is defined by Equation (5), where u_∞ is

the flow velocity inside the cell and A_{proj} is the projected area of the roughness inside the porous cell.

$$F_D = \frac{\rho}{2} c_D u_\infty^2 A_{proj} \tag{5}$$

An example of the definition of the projected area A_{proj} in Equation (5) is shown in Figure 8 for a regular roughness element. It is first assumed that the roughness fills the cell over the entire length of the porous cell Δx. To scale the influence of the roughness according to its filling of the cell, the volume fraction α of the roughness is introduced by Equation (6).

$$\alpha = \frac{V_{roughness}}{V_{cell}} = \frac{A_{proj} \cdot a}{A_{cell} \cdot \Delta x} = \frac{A_{proj}}{A_{cell}} \tag{6}$$

In Equation (6), a and Δx are elided since they are assumed to be equal. If one converts Equation (6) according to the projected area and substitutes this into Equation (5), one obtains the drag force F_D by:

$$F_D = \frac{\rho}{2} c_D u_\infty^2 \alpha A_{cell}. \tag{7}$$

Every blunt body in a flow indicates a pressure loss Δp. As a simple relationship, Equation (7) can be normalised to the cell area. Thus, the pressure loss caused by the drag force of the roughness element in the cell can be expressed by Equation (8).

$$\Delta p = \frac{\rho}{2} c_D u_\infty^2 \alpha \tag{8}$$

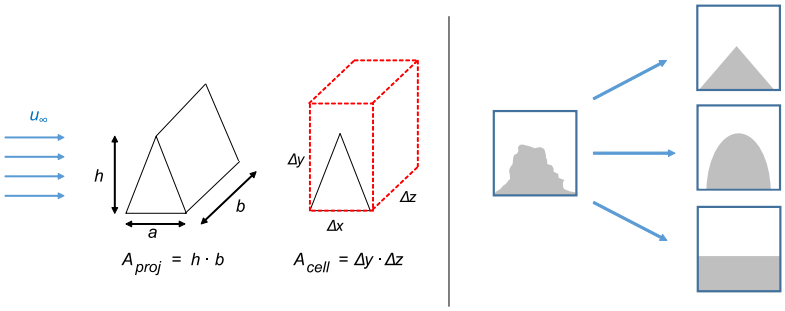

Figure 8. Explanations of the DPM procedure: (**left**) exemplary calculation of the projected area A_{proj} for a regular roughness element in a porous cell; (**right**) approximation of an irregular surface roughness in a cell to a regular body shape.

In order to obtain the pressure gradient in the flow direction (equal to Equation (4)), Equation (8) is normalised with the length of the cell Δx so that Equation (9) applies for the sink S, which is added to the incompressible Navier–Stokes equation of the porous cells. The same procedure has been applied for the other directions to account for a 3D roughness element.

$$S = \frac{\Delta p}{\Delta x} = \frac{\rho}{2} c_D u_\infty^2 \frac{\alpha}{\Delta x} \tag{9}$$

At this point, the analogy should be explained why the calculation of roughness effects in a flow can be described by the flow through porous media:

In any flow around a blunt body, drag force acts on the body, as well as on the flow. Because of the disturbance of the drag force in the flow, a pressure drop results out of the arising energy loss. No matter whether the body is in the free stream or on the wall, this disturbance and resulting pressure drop arises in any case. Only when the body is as small or smaller as the viscous sublayer of the wall, the disturbances may be negligible due to the dominating viscous damping of the fluid.

The flow through porous media is also affected by pressure drop, according to Darcy's law involving viscous drag. Forchheimer added a term, representing form drag resulting in the Darcy–Forchheimer equation. The basis of the DPM is to model the pressure drop

around the blunt bodies (roughness elements) with this porosity approach from Darcy–Forchheimer. This has also been performed successfully for the roughness modelling in other literature studies so far, such as in Forooghi et al. [37].

2.3.2. Determination of α and c_D

The drag coefficient c_D used in Equation (9) actually refers to the flow around a regular 2D body. To describe the roughness surface with this parameter, an approximation of the real 3D roughness shape to 2D regular bodies has to be made, see Figure 8. For this geometry approximation, all roughness heights within a porous cell are selected, as exemplarily shown on the left side of Figure 9. The contained roughness heights are then two-dimensionally projected onto the black marked area on the right side of Figure 9. In the next step, the angles β of the red contour are determined to approximate the regular shape from the real roughness distribution in the cell, see Figure 10. A set of conditions is then used to select the regular body shape according to the corresponding angles β. For example, a rectangle would be selected if both angles are between 75° and 90° or between 0° and 15°. Otherwise, right-angled or isosceles triangles would be selected that have discrete angles of 15° to 75°. Negative or positive sign of the angle determines, whether a left or right sided rectangular triangle is chosen for c_D, respectively. This procedure has been applied in the streamwise and spanwise direction. Figure 10 illustrates examples of available triangles. The approximation of the real roughness distribution to a regular body shape in a porous cell takes place in a self-written MATLAB code.

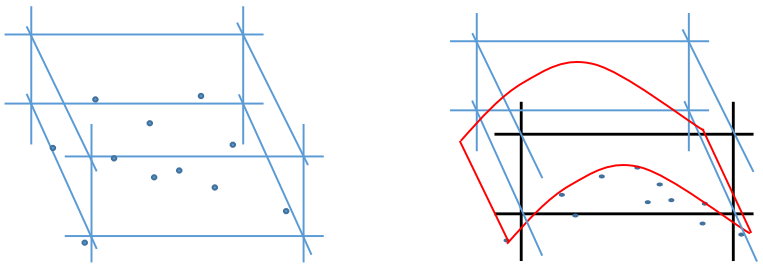

Figure 9. Approximation of the irregularly distributed surface roughness in a cell.

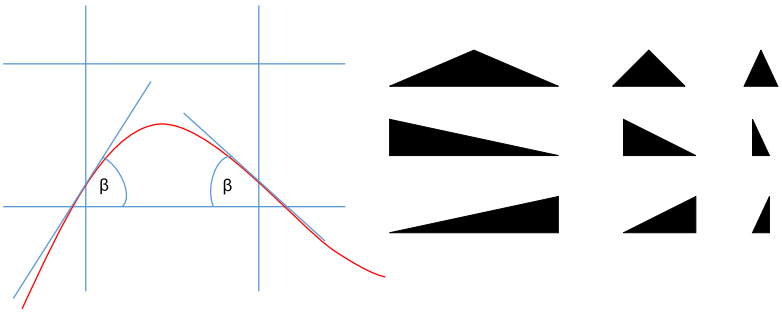

Figure 10. Explanations of the DPM procedure: (**left**) approximation to a regular roughness by considering the β-angles; (**right**) variations of different triangles for 3 selected angles (not to scale).

The drag coefficients c_D of a large number of regular shapes and Reynolds numbers from Re = 1000–200,000 were determined by additional simulations. The Reynolds numbers for these 2D RANS computations were defined by the fluid viscosity ν, the free stream velocity u_∞ at the inlet and the height h of the triangle or rectangle of regular shapes. The drag coefficients for a specific Re were applied at the corresponding Reynolds number Re_H of the channel flow simulation.

The domain size for the 2D simulations has been chosen as 40 × 40 times the height h with the regular shape placed in the center. A constant velocity and a zero pressure were given at the inlet and outlet, respectively. Furthermore, periodic boundary conditions were

applied at the two other boundaries. The resulting c_D-values were stored in a database. This database is given in the Supplementary Material .

2.3.3. Implementation of the DPM

To realise the DPM, it was implemented in two steps. At first, the cell assignment (fluid, solid, and porous cells) was defined and the calculations of α, β, and c_D were performed in *MATLAB R2019a (MathWorks Inc., Natick, MA, USA)*. The procedure is sketched in Figure 11. In this first step, a 3D grid (A) was created for the computational domain (explained in Section 2.4). Then, the self-written MATLAB code reads this grid, as well as a 3D point cloud (B) representing the rough surface. This point cloud was created during the scanning procedure of the pumps volute for the cast iron surface. With the given roughness height distribution from the point cloud, the roughness zone for the solid (C) and porous cells (D) was selected for the computational grid. Afterwards, the volume fractions α were calculated for each porous cell (E) by using the point cloud and the grid information. Then, the point-to-point slope at the cell edges defines the angles β, by which the approximate regular body shape (rectangle or triangle) was chosen for each porous cell (F). With the chosen approximate body shape, the associated drag coefficients c_D were determined by using the values from the database explained above.

In a second step, the DPM was implemented in the flow solver *OpenFOAM (ESI Group, Paris, FRA)* for the simulations of the channel flow with rough walls. For the porous cells, the sink S in Equation (9) was implemented in OpenFOAM, based on the Darcy–Forchheimer model. Therefore, the α and c_D-values of every porous cell were stored in a *fvOptions*-file, which OpenFOAM accessed during the simulation to add the sink S to the momentum equations in these cells.

Here, two main differences of the present method can be summarized compared to DEM by Taylor et al. [41] and PFA by Forooghi et al. [23]: first, the solid cells of the grid are completely cut out from the Cartesian mesh. Therefore, the roughness topology can already be seen roughly without modelling, analogous to body conforming mesh. Secondly, the modelling part has been carried out in every porous cell. The determination of c_D has been more detailed and complex, calculating the slope of incoming and outgoing angle of the surface roughness. A discrete value for c_D depending on Re will be chosen and α will be calculated for each porous cell, whereas Forooghi [23] has determined one c_D for the total roughness zone. Taylor [41] has used an empirical formula to calculate c_D depending on the Reynolds number.

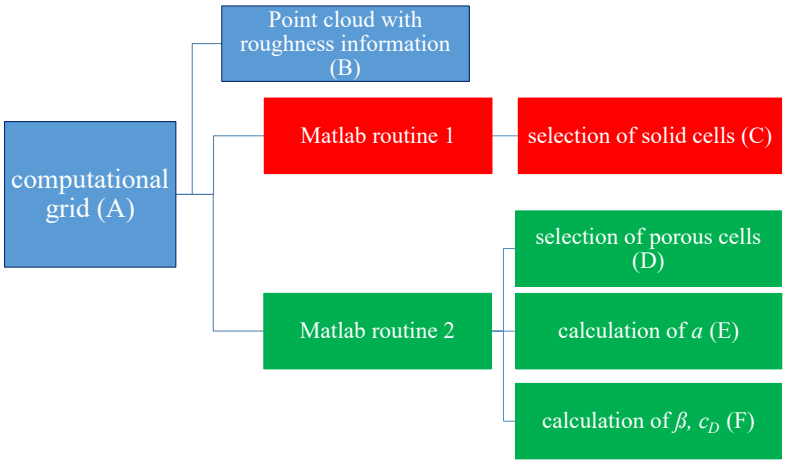

Figure 11. Implementation of the DPM (first step) in MATLAB.

2.4. Numerical Setup for the Rough Channel Flow Simulations

2.4.1. Computational Domain and Grid Generation

Plane channel flows with the cast iron roughness were simulated with the geometric dimensions of $(L, b, H) \approx (4H,\ 1.5H,\ H)$, where H is the channel height. The channel

dimensions are oriented on channel flow simulations by a study from Menter [45]. Three Cartesian, block-structured grids were created for the cast iron roughness to analyze how the DPM works on different grid resolutions, when the roughness plane (L, b) is differently resolved. The properties of the four grids and an illustration of one grid are displayed in Table 3 and Figure 12.

The roughness zone with the solid and porous cells was defined at the bottom wall of the channel. Here, the grid was equidistantly discretised up to a height of 290 µm in the wall-normal direction, which is the peak-to-trough roughness height k_t of the cast iron surface. In this zone, the grid was built such that a single cell resolves 1/5 of k_t. The roughness zone of the grid 'coarse' is highlighted in Figure 12. The fluid zone began above the height of 290 µm. From there, the cell height increased with a growth rate of 1.2 compared to the cells in the roughness zone. The same growth rate was also applied in the near-wall region at the upper channel wall, where a hydraulically smooth boundary layer exists.

Since the cast iron roughness is irregularly distributed, the resolution of the roughness elements in the plane (L, b) cannot be exactly defined based on the roughness geometry (as it is theoretically possible for regular roughnesses). For this reason, different grid refinements in the plane (L, b) were applied.

Table 3. Properties of the three computational grids for the simulation of the cast iron roughness.

Grid Parameter	Cast Iron Grid 'Coarse'	Cast Iron Grid 'Middle'	Cast Iron Grid 'Fine'
Grid size in M elements	0.3	1.2	4.8
Grid distribution in (L, b, H)	$(128, 44, 57)$	$(248, 88, 57)$	$(496, 176, 57)$
max. aspect ratio	13.9	7.0	4.1
max. volume change	1.2	1.2	1.2
grid angle	90°	90°	90°

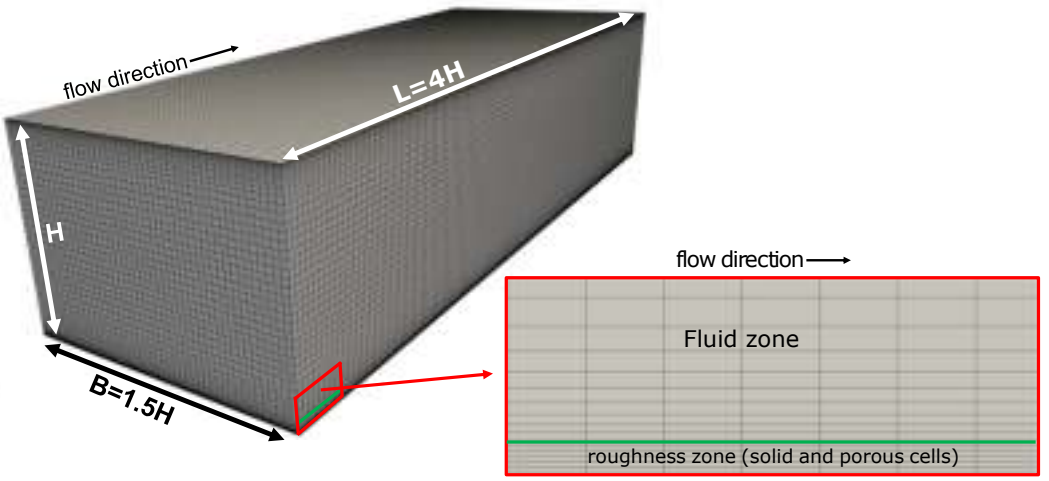

Figure 12. Grid 'coarse' of the simulation with the cast iron surface in an iso-view and a zoomed, planar view. The fluid and roughness zones are highlighted in the planar view.

2.4.2. Consideration of the Roughness Zone (Solid and Porous Cells)

The roughness zone was defined at one channel wall, similar to the experimental setup explained in Section 2.2. A fully developed, turbulent flow is present in the channel and an URANS method was chosen to simulate the flow. After the cut-out of the solid cells, the porous cells were selected for the DPM method. Figure 13 shows the roughness zone with

the solid and porous cells of the grids for the DPM simulation with the cast iron surface. Furthermore, the surface replica of the cast iron surface is illustrated in this figure.

2.4.3. Numerical Setup for the DPM Simulations

The software *OpenFOAM 5.x* with the *pimpleFOAM* solver was used to solve the governing equations by the finite volume method. The simulations were performed using URANS and the k–ω–SST turbulence model [46]. Second order accurate spatial discretisation schemes were applied for the DPM simulations. The simulations were performed on the *Titan* high performance cluster at the University of Rostock with 144 parallel processors (Intel(R) Xeon(R) CPU E5-2640 v3 @ 2.60 GHz).

The no-slip condition applies for all walls as a boundary condition. Periodic boundary conditions were specified at the domain boundaries in the span-wise (sides) and flow direction (inlet and outlet). The flow was driven by constant mass flows $\dot{m}$ adjusted by volume forces [47] in the flow direction, which correspond to the investigated Reynolds numbers between $Re_H = 75,000$ and $Re_H = 400,000$ (see Table 4). Water was used as the fluid (density $\rho = 997\ \mathrm{kg/m^3}$, kinematic viscosity $\nu = 10^{-6}\ \mathrm{m^2/s}$). Furthermore, turbulent boundary conditions were defined at the smooth as well as at the rough walls of the domain. Here, a zero value was specified for the modelled, turbulent kinetic energy k and the eddy viscosity ν_t for all simulations. A low-Re wall-function was used for the definition of the specific dissipation rate ω.

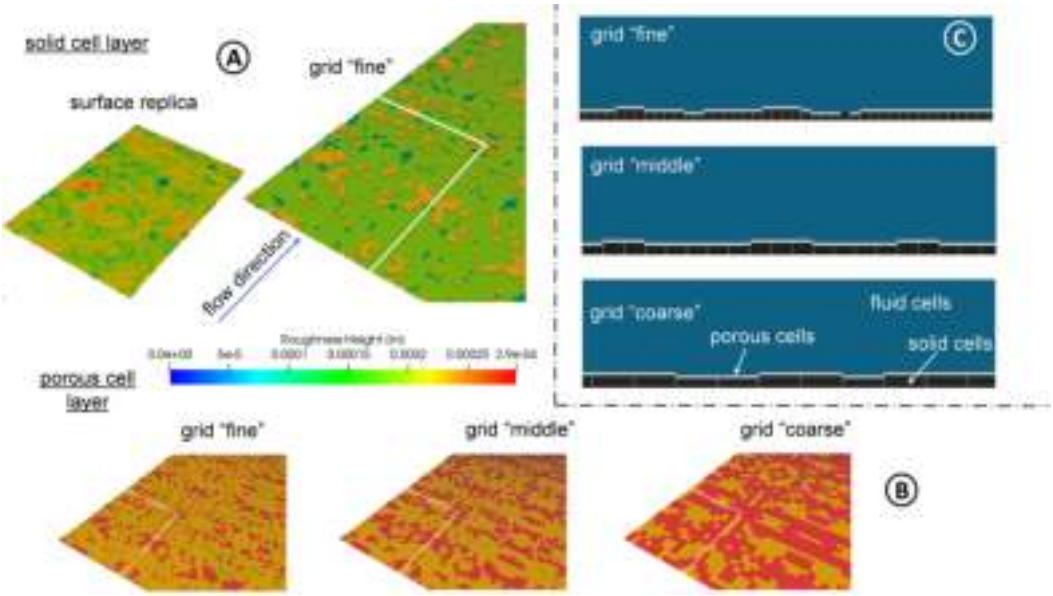

Figure 13. Illustration of the roughness zone in the DPM simulations with the cast iron surface. (**A**) Roughness surface of the replica (Section 2.1) and the solid cell layer of the DPM simulation with the finest grid. (**B**) Comparison of the porous cell zone between the three applied grids. (**C**) Picture detail with fluid, solid and porous cells for the three grids in a planar cut plane.

The simulations were initialised by a uniform bulk velocity, a zero relative pressure and empirically determined values for the turbulent quantities in the computation domain. A time step of $\Delta t = 10^{-3}$ s was chosen. A converged flow field with a constant pressure gradient and a developed velocity profile could be observed after a time span of $T \approx 0.8$ s. Then, the simulations were continued until $T = 1.1$ s. At the end of the simulations, the maximum residuals for the velocities and the pressure dropped to at least 10^{-3}.

In total, 18 simulations were performed for this study, which are summarized in Table 4. Eight simulations were conducted for the cast iron surface on the grid 'middle' at different Reynolds numbers. In addition, 10 simulations with the grid 'coarse' and grid 'fine' were performed for Reynolds numbers $Re_H \geq 250,000$, where a fully rough regime

was identified, and at $Re_H = 100,000$, where experimental data were available for the channel flow with the cast iron surface.

Table 4. Overview of the performed DPM simulations for the channel flow simulation with the cast iron roughness.

Re_H	Cast Iron		
	Grid 'Coarse'	Grid 'Middle'	Grid 'Fine'
75,000	–	✓	–
100,000	✓	✓	✓
150,000	–	✓	–
200,000	–	✓	–
250,000	✓	✓	✓
300,000	✓	✓	✓
350,000	✓	✓	✓
400,000	✓	✓	✓

2.5. Method for the Determination of the k_s-Value for the Rough Surfaces from the DPM Simulations

As a first step, the pressure gradients $\partial p/\partial x$ of the simulated channel flows were determined for every DPM simulation at a certain Reynolds number. Afterwards, the area-averaged wall shear stress $\tau_{w,r}$ at the rough wall had to be determined to define the non-dimensional velocity u^+ and length y^+. This wall shear stress was calculated based on a simplified momentum balance for a channel flow with a one-sided wall roughness (Equation (10)) defined by Burattini et al. [27]. The variable $\tau_{w,s}$ denotes the wall shear stress at the smooth channel wall in Equation (10).

$$\tau_{w,r} = H \cdot \partial p/\partial x - \tau_{w,s} \tag{10}$$

Subsequently, the dimensionless velocity profile $u^+ = f(y^+)$ was created by the following procedure: firstly, the zero height position $y^+ = 0$ was determined by height-averaging the roughness heights and take the average value as zero height. Then, the velocities from the DPM simulations were area-averaged along the wall-normal coordinate to create a one-dimensional velocity profile $u = f(y)$. These variables were normalized to obtain $u^+ = u/(\tau_{w,r}/\rho)^{0.5}$ and $y^+ = y \cdot (\tau_{w,r}/\rho)^{0.5}/\nu$. The characteristic downshift can be identified from this velocity profile $u^+ = f(y^+)$ by comparing the simulated velocity profile with a velocity profile in the logarithmic region of the rough boundary layer based on Equation (2). This procedure was repeated for all simulations at the investigated Reynolds numbers. By plotting the roughness function $\Delta u^+ = f(k_t^+)$, it was analyzed, whether a fully rough asymptote was reached, which indicated a fully rough regime [33]. Then, k_s^+ was calculated by Equation (11) [19], with $B = 5.0$ and $\kappa = 0.41$.

$$\Delta u^+ = \frac{1}{\kappa} ln(k_s^+) + B - 8.5 \tag{11}$$

Lastly, the equivalent sand grain roughness k_s was determined for the DPM simulations in this fully rough regime by Equation (12).

$$k_s = \frac{k_s^+ \cdot \nu}{(\tau_{w,r}/\rho)^{0.5}} \tag{12}$$

2.6. Experimental and Numerical Setup for the Turbopump Investigation

2.6.1. Numerical Setup

After the equivalent sand grain roughness k_s was determined for cast iron from the DPM simulations, the k_s-value was specified at the rough walls in a turbopump simulation to account for the roughness effects in the pump. The investigated pump is a radial test pump with a specific speed $n_s = 13.4$ 1/min. Its design was adopted from an industrial pump with minor modifications. The meridional cut through the pump, as well as the most important geometry information can be found in Figure 14. The turbopump was previously used by our institute to investigate the flow field [48] and flow losses [2,49] or the acoustics [50] in radial turbopumps with low specific speeds.

For this study, URANS computations were carried out for the turbopump using the commercial solver *ANSYS CFX 2021 R1 (ANSYS Inc., Canonsburg, PE, USA)*. Flow governing equations were solved on a three-dimensional grid based on the finite volume method. The solver strategy was implicit with a high-resolution and an Euler backwards scheme for spatial and temporal discretization. The double precision solver executable was used. Block-structured grids with hexahedral elements were created with *ICEM CFD 18 (ANSYS Inc., Canonsburg, PE, USA)*. All hydraulic components of the pump (impeller, volute, side chambers, sealing gap, and pipes) were considered as three-dimensional subdomains and were meshed separately. The computational domain with the locations of the inflow and outflow conditions, and some details of the computational grid are illustrated in Figure 15. An area-averaged wall distance of $y_1^+ = 1$ with a wall-normal growth rate of 1.25 was realised for all walls and all boundary layers were resolved using 26 grid cells with a growth rate of 1.25. The final grid totals 25.1 M grid elements with a minimum grid angle of 23°. Furthermore, aspect ratios were ≤100 in 99.93% of the volume. Higher aspect ratios (>1000) were tolerated just in small areas (0.01% of the volume, mainly in the discharge pipe) to prevent massively more mesh elements in these areas.

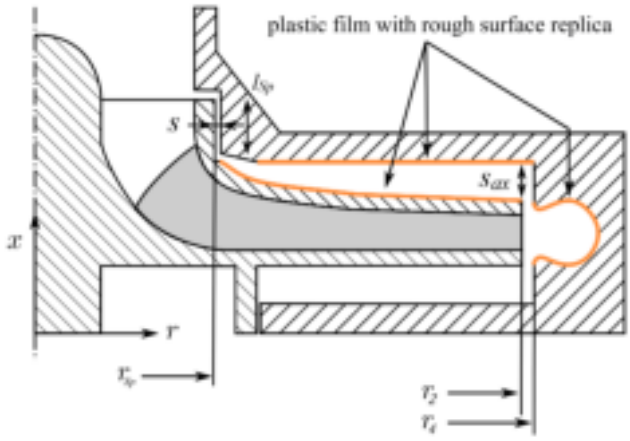

impeller radius	r_2 = 164.5 mm
inlet radius volute	r_4 = 168.5 mm
seal gap radius	r_{sp} = 62.14 mm
seal gap length	l_{sp} = 18.0 mm
gap width	s = 0.7 mm
entry height side chamber	s_{ax} = 13.0 mm

Figure 14. Most important geometric parameters of the pump and position of the adhered plastic films to study the roughness effect in the pump. Shown in a meridional section through the impeller, side chambers, and the volute.

The fluid properties of water at 20 °C were used (density $\rho = 997$ kg/m^3, kinematic viscosity $\nu = 10^{-6}$ m^2/s). The k-ω-SST model [46] was used for closure and streamline curvature effects were accounted for with the model of Smirnov and Menter [51]. Boundary

conditions were set as follows: a relative static pressure of zero value was defined at the inlet of the suction pipe together with zero gradient turbulence. Furthermore, a constant mass flow was specified at the outlet of the discharge pipe. All walls were assumed to be adiabatic and no-slip condition applies. The roughness effects were modelled in the flow solver using the approach of Lechner and Menter [8]. The sand grain roughness of $k_s = 175$ µm for cast iron (determined by the DPM simulations in Section 3.2) were specified for the rough walls in the front side chamber and the volute of the pump. At these locations, the micro-structured, self-adhesive replicas with the cast iron roughness were applied at the walls in the experimental pump as well. Hence, it could be guaranteed that the same surface roughness at the same places was used in the pump both experimentally and numerically. All other surfaces in the pump were assumed to be hydraulically smooth since the manufactured pump also went through a comprehensive polishing procedure.

The performance data (pressure head, inner efficiency) of the pump were numerically determined at four operation points. Therefore, a rotational speed of $n = 1450$ 1/min and flow rates of $Q = (46; 65; 85; 93)$ m^3/h were chosen to define the operation points. To couple the rotating and stationary components of the pump, the transient rotor-stator method was used with a time step equal to a 1.5° rotation of the impeller. Convergence was reached when maximum residuals were smaller than $5 \cdot 10^{-3}$ and all monitored values had reached a stabilised state. Each simulation was performed for 10 impeller revolutions and time-averaging for the statistical analysis of the performance data was performed over the last impeller revolution.

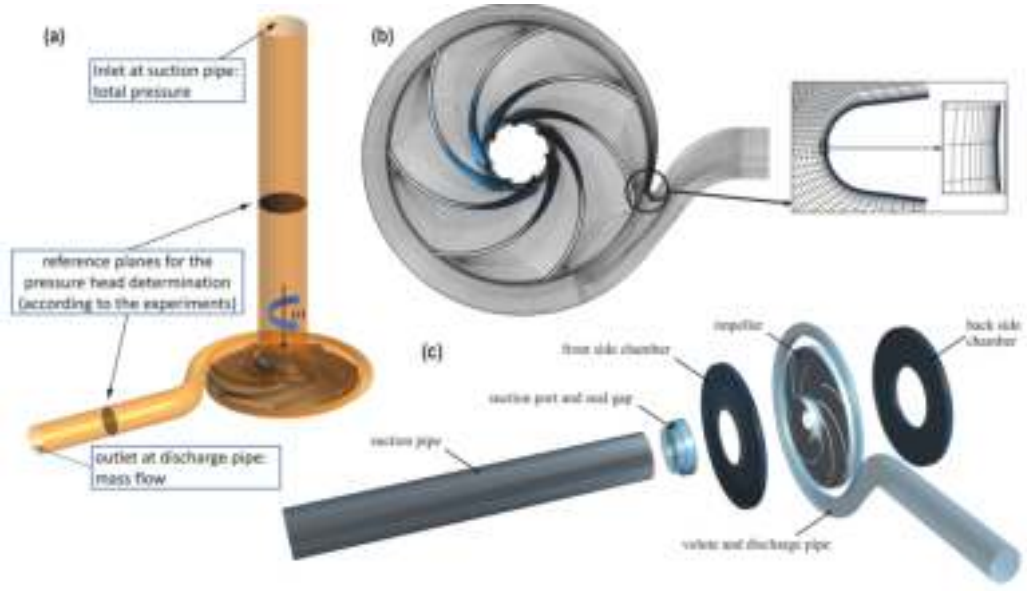

Figure 15. Turbopump model. (**a**) 3D view of the computational domain with inflow and outflow locations. (**b**) Grid through the impeller and the volute, as well as a detailed view of the grid around the volute tongue, and (**c**) turbopump domain in a exploded view.

2.6.2. Experimental Setup

Experiments with the test pump (Figure 16) were conducted in order to provide a validation basis for the pump simulations with rough walls. Therefore, the original experimental pump had to be modified since all pump parts were manufactured by CNC milling with a high dimensional accuracy, and the inner surfaces were polished afterwards, so that the boundary layers indicated a hydraulically smooth behavior ($k_a \leq 0.4$ µm). To account for the roughness effects of the cast iron surface, the polished surfaces of the test pump were artificially roughened with the adhesive plastic replicas containing the cast iron surface structure. Here, the wall area with replicas was limited to the whole suction side chamber and the volute, since it was shown in previous studies that the majority of the

losses due to the roughness effects occur in these regions [52]. The regions where the cast iron surface replica was applied in the test pump are displayed in Figure 14.

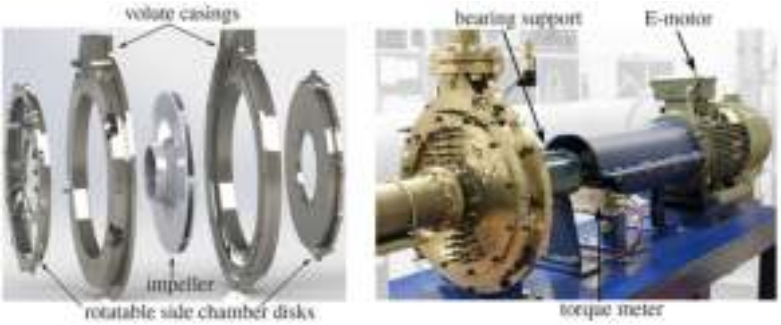

Figure 16. Details of the test pump. The figure is taken from Ref. [2].

The test pump was installed in a closed-loop test rig (Figure 17), where the (total) pressure head H_p was determined by measuring the pressures at the suction and pressure side of the pump with, respectively, four pressure sensors in two ring lines according to DIN EN ISO 9906 (class 1) [53]. The flow rate was measured with a magnetic inductive flow meter, and the torque M and rotational speed n of the impeller were determined with a non-contacting measuring flange to account for the inner efficiency η_i by:

$$\eta_i = \frac{\rho \cdot g \cdot H_p \cdot Q}{M \cdot 2\pi n}. \tag{13}$$

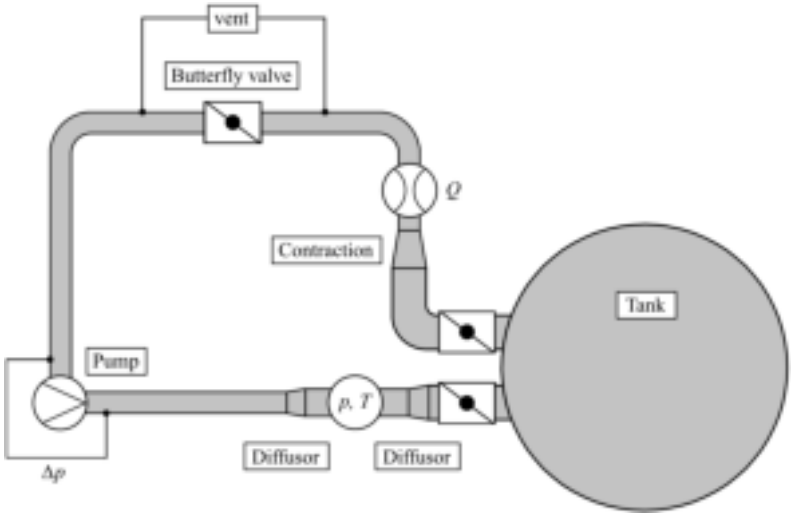

Figure 17. Schematic drawing of the test rig with the test pump.

3. Results and Discussion

3.1. Pressure Gradients $\partial p/\partial x$ and Velocity Profiles $u^+ = f(y^+)$ in the Channel Flows with Wall Roughness

The experimentally and numerically assessed pressure gradients are plotted in Figure 18. A relative deviation of $\approx$ 5% is achieved between the measured and simulated pressure gradient in the rough channel for the grid 'middle' and 'fine' at $Re_H = 100,000$. The simulation with the grid 'coarse' had a higher deviation of $\approx$10% to the measured $\partial p/\partial x$.

In the range of $Re \geq 250,000$, where the fully rough regime is present for cast iron (explained in the next sections), the results of grid 'middle' and 'fine' also show similar pressure gradients. The grid 'coarse' calculates slightly lower pressure gradients at these high Reynolds numbers. At $Re_H = 400,000$, the grid 'coarse' and grid 'fine' deviate by $\approx$10%, whilst the relative difference between grid 'middle' and grid 'fine' is just 2%.

Due to the similar results of the grids 'medium' and 'fine' to each other, as well as due to the good agreement with the experimental data, the simulations on the grid 'medium' are used for the following evaluation and the calculation of the k_s-value.

Based on the pressure gradients and the procedure described in Section 2.5, the non-dimensional velocity profiles $u^+ = f(y^+)$ were achieved for the DPM simulations. One exemplary velocity plot for the grid 'middle' at $Re_H = 350,000$ is shown in Figure 19. The shown velocity profile was achieved at a high Reynolds numbers, where a fully rough regime is present. A significant downshift in the simulated profile compared to the log-law in the smooth boundary layer can be seen in this figure. Furthermore, there is a clear correspondence between the logarithmic velocity profile in the roughness regime according to Equation (2) and the simulated ones. This agreement was searched for each DPM simulation to calculate the roughness functions $\Delta u^+ = f(k_s^+, k_t^+)$, which will be discussed in the next section.

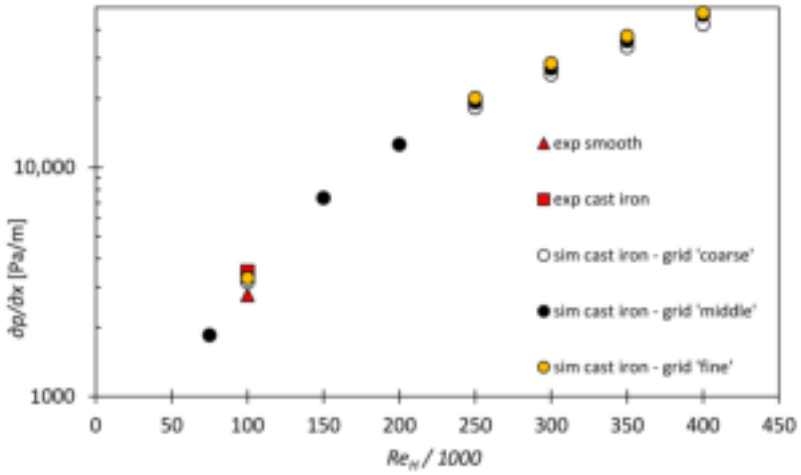

Figure 18. Experimentally and numerically assessed pressure gradients in the channel flows with the cast iron surface. Furthermore, an experimental value of a smooth channel flow at $Re_H = 100,000$ was added to show the ability of the DPM to model the roughness effects in the channel. Please note: the measurement uncertainties of the pressure measurements are not displayed but were less than 1% of the mean values.

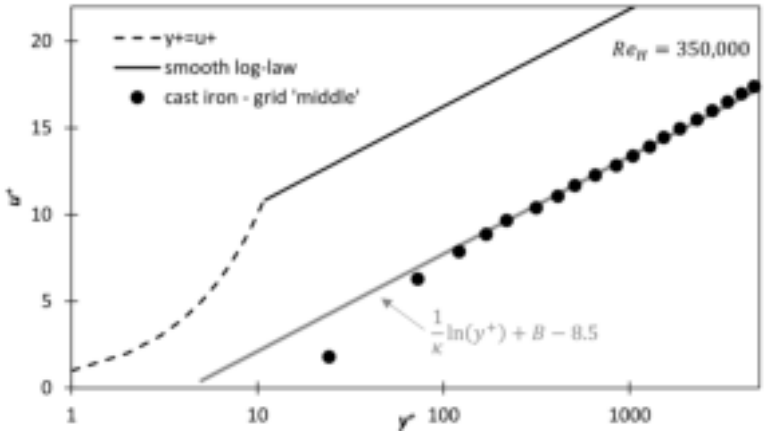

Figure 19. Dimensionless velocity profile for the DPM simulation with cast iron roughness at $Re = 350,000$. For the determination of the log-law in the roughness regime by Equation (2), the constants $\kappa = 0.41$ and $B = 5.0$ were used. The downshift was identified as $\Delta u^+ = 8.5$.

3.2. Determination of the Equivalent Sand Grain Roughness k_s in the Fully Rough Regime

The roughness function $\Delta u^+ = f(k_t^+)$ is plotted in Figure 20 to identify the fully rough regime, in which the appropriate k_s-value for cast iron can be identified. Additionally, the roughness function for uniform sand from Nikuradse [54] is included in this plot. As can be seen from this figure, an emerging asymptotic behaviour is observable for cast iron above a Reynolds number of $Re_H = 250,000$, indicating the fully rough regime at the higher Re.

In these fully rough regimes, the k_s-value can be determined by Equation (11) and Equation (12). Table 5 summarizes the k_s-values for the simulations at the highest Reynolds numbers. Similar values for k_s, with deviations smaller than 5% to the mean value, are achieved for the Reynolds numbers, in which a fully rough regime is present. The sand grain roughness results in a mean value of $\approx$ 175 µm. Compared to the wide ranges of sand roughness values for a cast iron surface from the literature (Table 1 on page 3), the k_s-values determined in this study are near the lower limits for k_s of cast iron reported from experimental studies in Refs. [3,13–15,17].

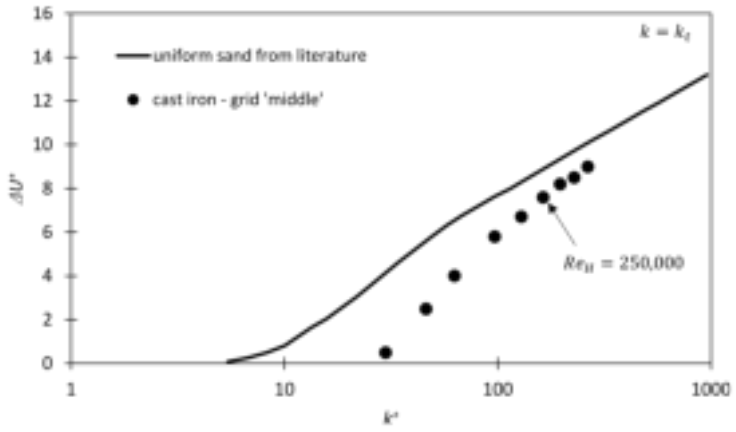

Figure 20. Roughness function $\Delta u^+ = f(k_t^+)$ for the cast iron roughness of the simulation with grid 'middle'. The roughness function for uniform sand from Nikuradse [54] is included in the figure.

Table 5. Calculated k_s-values for the DPM simulation with the cast iron surface at the high Reynolds numbers.

Re	**Cast Iron Grid 'Middle'**
250,000	$k_s = 168$ µm
300,000	$k_s = 179$ µm
350,000	$k_s = 174$ µm
400,000	$k_s = 184$ µm
average	$k_s = (176 \pm 8)$ µm

After the k_s-value was determined, it was also checked, if the roughness functions $\Delta u^+ = f(k_s^+)$ collapses with the function of uniform sand from Nikuradse [54]. This is illustrated in Figure 21. An excellent match of the roughness function is recognisable in the fully rough regime. This shows that the determined k_s-values of cast iron will indicate the same roughness effect in the flow as uniform sand of same height. This is necessary for the application of the k_s-value for roughness modelling in the following turbopump simulation, and demonstrates that the methodology for k_s-determination with the DPM indicate reasonable results.

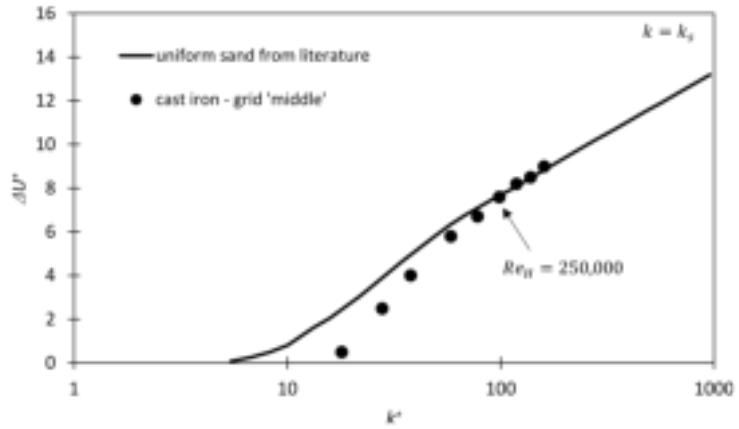

Figure 21. Roughness function $\Delta u^+ = f(k_s^+)$ for the cast iron roughness. The roughness function for uniform sand from Nikuradse [54] is included in the figure.

3.3. Simulation of the Performance Data in a Radial Turbopump with Wall Roughness

The simulated pressure head $H_p = f(Q)$ and efficiency $\eta_i = f(Q)$ curves are displayed and compared with the experimentally observed performance data in Figures 22 and 23. Additionally, the simulated and measured performance data curves are displayed for a turbopump with hydraulically smooth walls. There is a good agreement in the performance data between the simulation results with the implemented k_s-value and the measurements of the pump with rough surfaces. The absolute deviations between experiments and numerics ranges from (0.1–1.1) m for the pressure head H_p and (1.7–3.6)% for the efficiency η_i along the whole performance curves. These deviations to the experimental values can be much larger if k_s is estimated using empirical correlations or other literature values, e.g., from Table 1. A comparison of pump characteristics with three differently estimated k_s-values for cast iron is given in Figure 24.

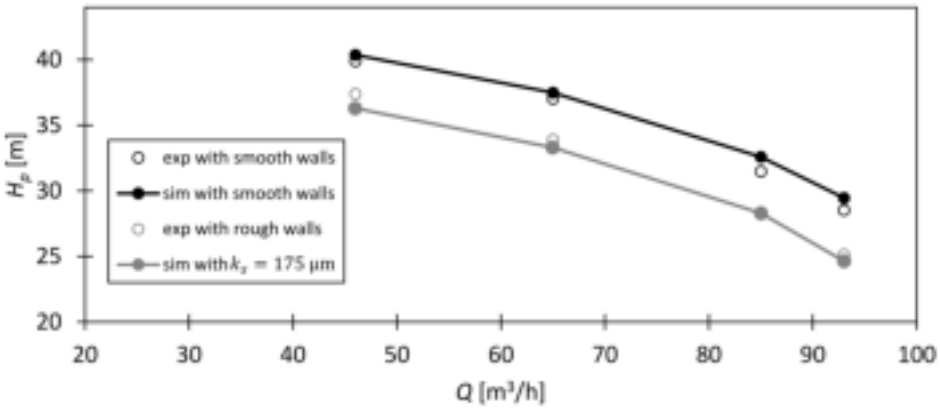

Figure 22. Experimentally and numerically assessed pressure head curve $H_p = f(Q)$ of the radial turbopump. Please note: The measurement uncertainties of the pump characteristics are not displayed but were less than 1% of the mean values.

In addition, a comparison can be made between the turbopump with rough and hydraulically smooth walls. Figure 22 shows a permanent pressure head reduction in $\Delta H_p \approx -4$ m from the 'smooth wall' to the 'rough wall' simulation case. The impact on pump efficiency is even greater if the roughness effects are not taken into account in the simulations. A constant, absolute offset of about $\Delta\eta_i \approx -10$ % is present between the simulations with and without roughness consideration. These results show the importance

of considering roughness effects in simulations of turbopumps with low specific speeds. The current hydraulic components (impeller, side chambers, volute) of a pump are made of cast iron or investment iron, which can exhibit significant roughness heights, especially with increasing operating time of the pump. As already shown in Figure 1 or Figure 23, significant discrepancies could exist between the experiments in a manufactured pump and the flow simulations of a computer-designed pump, when these roughnesses are unconsidered in the simulations.

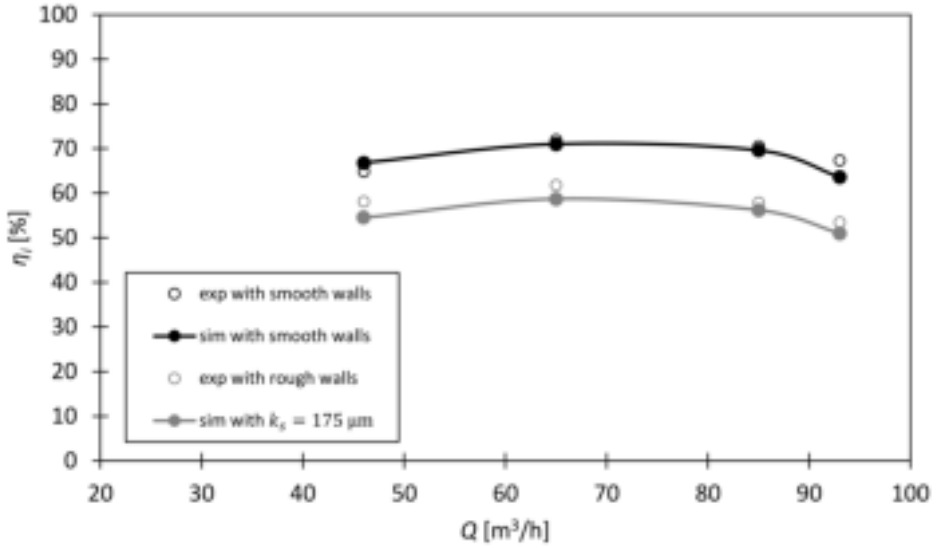

Figure 23. Experimentally and numerically assessed efficiency curve $\eta_i = f(Q)$ of the radial turbopump. Please note: the measurement uncertainties of the pump characteristics are not displayed but were less than 1% of the mean values.

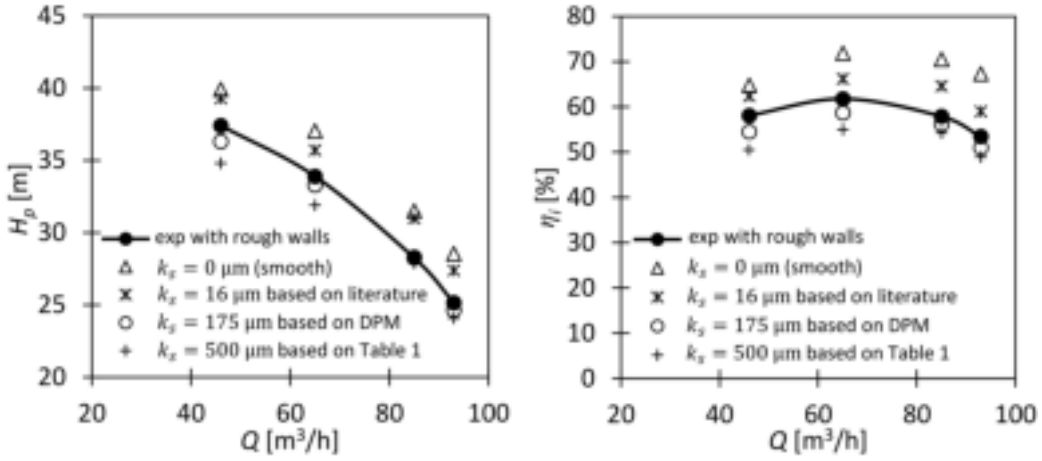

Figure 24. Numerically assessed pump characteristics of the radial turbopump. The k_s-values for cast iron were estimated by three different methods: firstly, by an empirical correlation from the literature [21]. Secondly, by the DPM procedure. Thirdly, a representative value from Table 1 was chosen.

4. Limitations

Although the use of DPM shows promising results, the method is still at an early stage of development. Regarding this, the DPM tries to approximate the drag in the 3D flow by calculating 2D drag values of regular body shapes. The assumption of using 2D values is made since the 3D roughness structure (in the porous cell layer of one cell height) is projected on the streamwise and spanwise cell face, to create 2D shapes in the streamwise

and spanwise direction, respectively. This results in different drag values for the different directions, which are used to estimate the pressure drop in the 3D flow over a cell. The next step in extending the method will be to find an optimized way to model the pressure sink for each idealised regular body shape in the porous cells. This could be performed, for example, on the basis of an AI optimisation, where each idealised body shape in the cell is assigned a corresponding AI-optimised drag coefficient c_d. Additionally, there will be an influence of adjacent roughness elements on the c_D-value, which is currently not in the DPM formulation. One of the next steps will be to integrate this influence. All these points show that there is still room for improvement of the DPM. Nonetheless, the determination of k_s works well despite the simplifications and assumptions: the rough channel flow simulation gives comparable value to the experiment (Figure 18), the k_s-value is in the range of the literature (Tables 1 and 5) and the pump characteristics from the simulations agree well with the experiments (Figures 22 and 23).

When comparing the original cast iron scan with the replica (Table 2), it was found that important geometric parameters, such as k_t and k_a, were similar between the two surfaces. However, the surface parameters S_k and ES differed between the surfaces, which can be attributed to the manufacturing process of the replica. It does not affect the initial objective of this paper that the k_s-value can be reasonably determined for an arbitrary surface roughness by the DPM, since all experimental and numerical results refer to the replica. However, due to the different surface parameters, the drag in the rough boundary layer between scan and replica could be affected, which can also influence k_s. Regarding this, the original cast iron surface could have a higher sand grain roughness than the replica due to the larger skewness and effective slope [22]. For future studies, we will try to further optimize the manufacturing process to bring the surface parameters between scan and replica closer together.

Furthermore, the DPM channel flow simulation was just validated at one Reynolds number ($Re_H = 100,000$). Unfortunately, it was not possible to validate the cast iron roughness for higher Re as well. The reason is that the test rig pump cannot overcome the high losses at higher Re. Currently, the test rig is modified so that roughness evaluations can be carried out at higher Reynolds numbers in the future.

5. Conclusions

The present study demonstrates a novel and time-efficient simulative approach on how to determine the equivalent sand roughness k_s for irregularly distributed surface roughnesses. The k_s-values can then be used in the roughness modelling of complex flow simulations, e.g., in turbomachines, to properly account for the performance data.

By means of the self-designed *discrete porosity method* (DPM), it is possible to compute the effect due to the roughess in a simulation without directly resolving the complete roughness topology. This is achieved by separating a computational grid in three zones and treating the governing equations in every zone differently. Firstly, there are solid cells, which are completely submerged by the rough surface. Therefore, the flow is completely cut out from the grid. Secondly, there are fluid cells, in which the governing equations are being solved. Thirdly, porous cells exist, which are partly covered by the roughness elements and the fluid. The roughness elements in these porous cells were modelled by idealised body shapes, which cause a drag resistance and hence, a pressure sink in the flow.

Channel flow simulations with an irregularly distributed cast iron surface were computed by the DPM at different Reynolds numbers. The velocity profiles from the DPM simulations indicated a downshift of the curves, which increases with higher Reynolds numbers and, thus, rising roughness effects. By using this downshift, the roughness function $\Delta u^+ = f(k_t^+)$ was plotted to identify the fully rough regime, where the k_s-value of the roughness under investigation can be determined. For cast iron, a k_s-value of 175 µm was determined, which is in accordance with literature data for cast iron. The results of the pump simulations performed with the equivalent sand roughness of cast iron showed good agreement with the experimental measurements.

In summary, the DPM represents a promising method to determine k_s-values of rough surfaces. The computation times of the method are low compared to a direct resolution of the roughnesses by a flow simulation. Additionally, the DPM provides just one k_s-value for a specific scanned surface, e.g., for cast iron, whereas the literature state a wide range of k_s-values for a set of cast iron surfaces. Both points will allow turbopump designers to more accurately consider rough surfaces in their design simulations in the future.

In follow-up work, the DPM will be used to determine k_s for different cast iron surfaces in different parts of the turbopump, such as in the impeller or the side chambers. This will be used to investigate the influence of the zonal roughness (and its different surface topologies) on the pump performance. Additionally of interest to the authors is a deeper understanding of the flow in the rough side chambers of a radial pump with small n_s. The flow in the side chambers shows a strong interaction with the adjacent pump parts [2] and is crucial for the pump performance and the acting flow forces in the pump.

Supplementary Materials: The following supporting information can be downloaded at: https://www.mdpi.com/article/10.3390/ijtpp8010005/s1, Table S1: C_D-values for left right-angular triangle. Table S2: C_D-values for right right-angular triangle. Table S3: C_D-values for centered tip triangle. Table S4: C_D-values for rectangles.

Author Contributions: Conceptualization, B.T. and F.-H.W.; methodology, D.V.D. and B.T.; software, D.V.D.; validation, D.V.D. and B.T.; formal analysis, B.T.; investigation, B.T.; resources, F.-H.W.; data curation, B.T.; writing—original draft preparation, B.T. and D.V.D. and F.-H.W.; visualization, B.T. and D.V.D.; supervision, F.-H.W.; project administration, F.-H.W.; funding acquisition, F.-H.W. All authors have read and agreed to the published version of the manuscript.

Funding: This work was financially supported by the AiF in the framework of Industrial Collective Research (IGF, project 19024 BR/1) and by the Forschungskuratorium Maschinenbau e.V. (project 7038900).

Institutional Review Board Statement: Not applicable.

Informed Consent Statement: Not applicable.

Data Availability Statement: The c_D-values of the idealized shapes in the DPM routine are stored in a database. This database is given in the Supplementary Material.

Conflicts of Interest: The funders had no role in the design of the study; in the collection, analyses, or interpretation of data; in the writing of the manuscript; or in the decision to publish the results.

Nomenclature

A	area, m^2
B	constant, $B = 5.0$
b	width, m
c_D	drag coefficient, -
ES	effective slope, -
e_z	unit vector parallel to z-axis, -
F_D	drag force, N
g	gravitational constant, m/s^2
H	channel height, m
H_p	pressure head, m
h	height/elevation, m
k	turbulent kinetic energy, m^2/s^2
k_a	average roughness height, m
k_t	peak-to-trough roughness height, m
k_{rms}	RMS roughness height, m
k_s	equivalent sand grain roughness, m
L	length, m
M	torque, Nm
$\dot{m}$	mass flow, kg/s

n	rotational speed, 1/min
n_s	specific speed, 1/min
p	pressure, Pa
Q	flow rate, m^3/s
r	radius, m
Re_H	channel Reynolds number $u_b \cdot H/\nu$, -
S	source term, Pa/m
S_k	skewness, -
t, T	time, s
u, v, w	velocities, m/s
u_b	bulk velocity, m/s
u_τ	friction velocity $\sqrt{\tau_w/\rho}$, m/s
Δu^+	downshift due to roughness, -
x, y, z	directions, m
α	area ratio, -
β	inflow and outflow angle, $^\circ$
ν	kinematic viscosity, m^2/s
ν_t	eddy viscosity, m^2/s
ρ	density, kg/m^3
τ_w	wall shear stress, Pa
ω	specific dissipation rate, 1/s
Sub-, Superscripts and Operators	
b	bulk
$cell$	cell
H	channel height
i, j	spatial directions
$proj$	projected
opt	optimal / BEP
r	rough
rms	root-mean-square
s	smooth
tot	total
Δ/d	increment
∞	free stream
$\rightarrow$	vector
$+$	scaling with wall units (u_τ, ν)
$\langle \ldots \rangle$	time-averaged quantity
$\overline{\ldots}$	averaged quantity
Abbreviations	
BEP	best efficiency point
BC	boundary condition
DNS	direct numerical simulation
DPM	discrete porosity method
Rel. Dev.	relative deviation
Re	Reynolds number
RMS	root-mean-square
URANS	unsteady Reynolds-averaged Navier-Stokes
2D	two-dimensional
3D	three-dimensional

References

1. Viet, D.D.; Kumar, J.; Wurm, F.H. Modelling of wall roughness in flow simulations. In Proceedings of the 4th International Rotating Equipment Conference, Wiesbaden, Germany, 23–24 September 2019; Paper No. 071; pp. 1–11.
2. Juckelandt, K.; Bleeck, S.; Wurm, F.H. Analysis of Losses in Centrifugal Pumps with Low Specific Speed with Smooth and Rough Walls. In Proceedings of the 11th European Conference on Turbomachinery, Madrid, Spain, 23–26 March 2015; Martelli, F., Díaz, R.V., Eds., 2015; pp. 1–10.
3. Schlichting, H.; Gersten, K. *Boundary-Layer Theory*, 9th ed.; Springer: Berlin/Heidelberg, Germany, 2017.
4. Schlichting, H. Experimentelle Untersuchungen zum Rauhigkeitsproblem. *Ing.-Arch.* **1936**, *7*, 1–34. [CrossRef]

5. Rotta, J.C. Das in Wandnähe gültige Geschwindigkeitsgesetz turbulenter Strömungen. *Ing.-Arch.* **1950**, *18*, 277–280. [CrossRef]
6. Flack, K.A.; Schultz, M.P.; Shapiro, T.A. Experimental support for Townsend's Reynolds number similarity hypothesis on rough walls. *Phys. Fluids* **2005**, *17*, 35102. [CrossRef]
7. Flack, K.A.; Schultz, M.P. Review of Hydraulic Roughness Scales in the Fully Rough Regime. *J. Fluids Eng.* **2010**, *132*, 41203. [CrossRef]
8. Lechner, R.; Menter, F.R. *Development of a Rough Wall Boundary Condition for Omega-Based Turbulence Models: TR-04-04, Rough Walls 1.1*; ANSYS CFX: Otterfing, Germany, 2004.
9. Apsley, D. CFD Calculation of Turbulent Flow with Arbitrary Wall Roughness. *Flow Turbul. Combust.* **2007**, *78*, 153–175. [CrossRef]
10. Aupoix, B. Wall Roughness Modelling with k-w SST Model. In Proceedings of the 10th International ERCOFTAC Symposium on Engineering Turbulence Modelling and Measurements, Marbella, Spain, 17–19 September 2014; Springer: Berlin/Heidelberg, Germany, 2014.
11. Wilcox, D.C. Formulation of the k-omega Turbulence Model Revisited. *AIAA J.* **2008**, *46*, 2823–2838. [CrossRef]
12. Knopp, T.; Eisfeld, B.; Calvo, J.B. A new extension for k– turbulence models to account for wall roughness. *Int. J. Heat Fluid Flow* **2009**, *30*, 54–65. [CrossRef]
13. Wagner, W. *Strömung und Druckverlust*, 6th ed.; Vogel: Würzburg, Germany, 2008.
14. Fried, E.; Idelcik, I.E. *Flow Resistance: A Design Guide for Engineers*, first ed.; Taylor & Francis: Philadelphia, PA, USA, 1997.
15. Oertel jr., H.; Böhle, M.; Dohrmann, U. *Strömungsmechanik: Grundlagen–Grundgleichungen–Lösungsmethoden—Softwarebeispiele*, 5th ed.; Vieweg+Teubner: Wiesbaden, Germany, 2009.
16. Gülich, J.F. *Centrifugal Pumps*, 3rd ed.; Springer: Berlin/Heidelberg, Germany, 2014.
17. White, F.M. *Fluid Mechanics*, 4rd ed.; McGraw-Hill: Boston, MA, USA, 1998.
18. Bons, J.P. A Review of Surface Roughness Effects in Gas Turbines. *J. Turbomach.* **2010**, *132*, 021004. [CrossRef]
19. Schultz, M.P.; Flack, K.A. Turbulent boundary layers on a systematically varied rough wall. *Phys. Fluids* **2009**, *21*, 015104. [CrossRef]
20. Sigal, A.; Danberg, J.E. New correlation of roughness density effect on the turbulent boundary layer. *AIAA J.* **1990**, *28*, 554–556. [CrossRef]
21. van Rij, J.A.; Belnap, B.J.; Ligrani, P.M. Analysis and Experiments on Three-Dimensional, Irregular Surface Roughness. *J. Fluids Eng.* **2002**, *124*, 671. [CrossRef]
22. Chung, D.; Hutchins, N.; Schulz, M.P.; Flack, K.A. Predicting the Drag of Rough Surfaces. *Annu. Rev. Fluid Mech.* **2021**, *53*, 439–471. [CrossRef]
23. Forooghi, P.; Stroh, A.; Magagnato, F.; Jakirlic, S.; Frohnapfel, B. Toward a universal roughness correlation. *J. Fluids Eng.* **2017**, *139*, 121201. [CrossRef]
24. Chan, L.; MacDonald, M.; Chung, D.; Hutchins, N.; Ooi, A. A systematic investigation of roughness height and wavelength in turbulent pipe flow in he transitionally rough regime. *J. Fluid Mech.* **2015**, *771*, 743–777. [CrossRef]
25. Yuan, J.; Piomelli, U. Estimation and prediction of the roughness function on realistic surfaces. *J. Turbul.* **2014**, *15*, 350–365. [CrossRef]
26. Busse, A.; Tyson, C.J.; Sandham, N.D.; Lützner, M. DNS of turbulent channel flow over engineering rough surfaces. In Proceedings of the 8th International Symposium on Turbulence and Shear Flow Phenomena, Poitiers, France, 28–30 August 2013.
27. Burattini, P.; Leonardi, S.; Orlandi, P.; Antonia, R.A. Comparison between experiments and direct numerical simulations in a channel flow with roughness on one wall. *J. Fluid Mech.* **2008**, *600*, 403–426. [CrossRef]
28. Thakkar, M.; Busse, A.; Sandham, N.D. Surface correlations of hydrodynamic drag for transitionally rough engineering surfaces. *J. Turbul.* **2017**, *18*, 138–169. [CrossRef]
29. Thakkar, M.; Busse, A.; Sandham, N.D. Direct numerical simulation of turbulent channel flow over a surrogate for Nikuradse-type roughness. *J. Fluid Mech.* **2018**, *837*, R1. [CrossRef]
30. Busse, A.; Lützner, M.; Sandham, N. Direct numerical simulation of turbulent flow over a rough surface based on a surface scan. *Comput. Fluids* **2015**, *116*, 129–147. [CrossRef]
31. Forooghi, P. Weidenlener, A.; Magagnato, F.; Böhm, B.; Kubach, H.; Koch, T.; Frohnapfel, B. DNS of momentum and heat transfer over rough surfaces based on realistic combustion chamber deposit geometries. *Int. J. Heat Fluid Flow* **2018**, *69*, 83–94. [CrossRef]
32. Flack, K.A.; Schultz, M.P.; Rose, W.B. The onset of roughness effects in the transitionally rough regime. *Int. J. Heat Fluid Flow* **2012**, *35*, 160–167. [CrossRef]
33. Flack, K.A.; Schultz, M.P. Roughness effects on wall-bounded turbulent flows. *Phys. Fluids* **2014**, *26*, 101305. [CrossRef]
34. Flack, K.A.; Schultz, M.P.; Connelly, J.S. Examination of a critical roughness height for outer layer similarity. *Phys. Fluids* **2007**, *19*, 095104. [CrossRef]
35. Schultz, M.P.; Flack, K.A. Reynolds-number scaling of turbulent channel flow. *Phys. Fluids* **2013**, *25*, 25104. [CrossRef]
36. Busse, A.; Sandham, N.D. Parametric forcing approach to rough-wall turbulent channel flow. *J. Fluid Mech.* **2012**, *712*, 169–202. [CrossRef]
37. Forooghi, P.; Frohnapfel, B.; Magagnato, F.; Busse, A. A modified Parametric Forcing Approach for modelling of roughness. *Int. J. Heat Fluid Flow* **2018**, *17*, 200–209. [CrossRef]

38. Jones, JR., D.C. An improvement in the calculation of turbulent friction in rectangular ducts. *J. Fluids Eng.* **1976**, *98*, 173–180. [CrossRef]
39. *EN ISO 5167-1:2003*; Measurement of fluid flow by means of pressure differential devices inserted in circular cross-section conduits running full - Part 1: General principles and requirements (ISO 5167-1:2003). German version EN ISO 5167-1:2003; ISO: Geneva, Switzerland, 2003.
40. Bell, J.H.; Metha, R.D. Contraction Design for small low-speed wind tunnels. *JIAA Tr. 84* **1988**. Available online: https://ntrs.nasa.gov/api/citations/19890004382/downloads/19890004382.pdf (accessed on 29 January 2023).
41. Taylor, R.P.; Coleman, H.W.; Hodge, B.K. Prediction of turbulent rough-wall skin friction using a discrete element approach. *J. Fluids Eng.* **1985**, *107*, 251–257. [CrossRef]
42. Magagnato, F.; Bühler, S.; Gabi, M. Modeling the wall roughness for RANS and LES using the Discrete Element Method. In *Proceedings of the The International Congress of Theoretical and Applied Mechanics (ICTAM)*; Denier, J., Ed.; International Union of Theoretical and Applied Mechanics: Adelaide, Australia, 2008.
43. Pritz, B.; Magagnato, F.; Gabi, M. Investigation of the Effect of Surface Roughness on the Pulsating Flow in Combustion Chambers with LES. In *Springer Proceedings in Physics*; Yoo, S.D., Ed.; Springer: Berlin/Heidelberg, Germany, 2008; pp. 69–76.
44. Stripf, M.; Schulz, A.; Bauer, H.J. Modeling of Rough-Wall Boundary Layer Transition and Heat Transfer on Turbine Airfoils. *J. Turbomach.* **2008**, *130*, 21003. [CrossRef]
45. Menter, F.R. *Best Practice: Scale-Resolving Simulations in ANSYS CFD*; ANSYS CFX: Otterfing, Germany, 2015.
46. Menter, F.R. Two-equation eddy-viscosity turbulence models for engineering applications. *AIAA J.* **1994**, *32*, 1598–1605. [CrossRef]
47. Fröhlich, J. *Large Eddy Simulation turbulenter Strömungen*, 1st ed.; Teubner: Wiesbaden, Germany, 2006.
48. Witte, M.; Torner, B.; Wurm, F.H. Analysis of Unsteady Flow Structures in a Radial Turbomachine by using Proper Orthogonal Decomposition. In Proceedings of the ASME Turbo Expo 2018; Oslo, Norway, 11–15 June 2018; ASME: New York, NY, USA, 2018.
49. Juckelandt, K. Experimentelle und numerische Untersuchung der Strömung in Pumpen Kleiner Spezifischer Drehzahl unter Berücksichtigung des Rauheitseinflusses. Ph.D. Thesis, Universität Rostock, Rostock, Germany, 2017.
50. Witte, M.; Bleeck, S.; Benz, C.; Wurm, F.H. Principal experimental study of the acoustic behavior of pumps. In Proceedings of the INTER-NOISE 2016—45th International Congress and Exposition on Noise Control Engineering: Towards a Quieter Future, Hamburg, Germany, 21–24 August 2016 2016; pp. 7666–7674.
51. Smirnov, P.E.; Menter, F.R. Sensitization of the SST Turbulence Model to Rotation and Curvature by Applying the Spalart–Shur Correction Term. *J. Turbomach.* **2009**, *131*, 041010. [CrossRef]
52. Juckelandt, K.; Wurm, F.H. Applicability of Wall-Function Approach in Simulations of Turbomachines. In *ASME Turbo Expo 2015*; ASME., Ed.; ASME: New York, NY, USA, 2015; pp. 1–10.
53. *DIN EN ISO 9906*; Rotodynamic Pumps—Hydraulic Performance Acceptance Tests—Grades 1, 2 and 3 (ISO 9906:2012); German version EN ISO 9906:2012; ISO: Geneva, Switzerland, 2012.
54. Nikuradse, J. Strömungsgesetze in rauhen Rohren. *VDI-Forschungsheft* **1933**, *4*. Available online: https://www.scirp.org/(S(351jmbntvnsjt1aadkozje))/reference/referencespapers.aspx?referenceid=2054940 (accessed on 18 October 2022).

Disclaimer/Publisher's Note: The statements, opinions and data contained in all publications are solely those of the individual author(s) and contributor(s) and not of MDPI and/or the editor(s). MDPI and/or the editor(s) disclaim responsibility for any injury to people or property resulting from any ideas, methods, instructions or products referred to in the content.

International Journal of
Turbomachinery
Propulsion and Power

MDPI

Article

Active Turbulence Grid-Controlled Inflow Turbulence and Replication of Heat Exchanger Flow Fields in Fan Applications

Felix Czwielong * and Stefan Becker

Institute for Fluid Mechanics, Friedrich-Alexander University Erlangen-Nuremberg, Cauerstr. 4, 91058 Erlangen, Germany
* Correspondence: felix.czwielong@fau.de

Abstract: A novel active turbulence grid of the Institute of Fluid Mechanics at FAU Erlangen-Nuremberg is introduced. The focus of this grid is not on basic investigations of fluid mechanics, as is usually the case with active turbulence grids, but the generation of defined inflow conditions for axial fans. Thus, by means of the active turbulence grid, individual turbulence characteristics in the flow to the fan can be changed; therefore, fundamental interactions between the flow mechanics at the axial fan and the sound radiation can be analyzed. In addition, the replication of the flow fields of heat exchangers by the active turbulence grid is the focus of the investigations. The investigations showed that it is possible to use the active turbulence grid to generate defined inflow conditions for axial fans. It was also possible to reproduce the heat exchanger flow fields both for the mean turbulence values and for the spatial distributions. It was found that the grid induces tonal components due to the drive motors, but also that the inherent noise has no significant influence on the spectrum of the fans under investigation. Based on selected turbulence characteristics, direct correlations were found between the spatial distribution of the turbulence level and sound radiation at the first blade passing frequency of the axial fan. As the variance of the turbulence level increases, the sound radiation of the tonal components becomes more pronounced. The total sound pressure level, however, is mainly determined by the low-frequency broadband sound. A linear relationship between the spatial mean value of the turbulence level and the total sound pressure level was found for the investigated axial fan.

Keywords: axial fan noise; active turbulence grid; heat exchanger; controlled inflow; inflow turbulence; leading edge noise

check for updates

Citation: Czwielong, F.; Becker, S. Active Turbulence Grid-Controlled Inflow Turbulence and Replication of Heat Exchanger Flow Fields in Fan Applications. *Int. J. Turbomach. Propuls. Power* **2023**, *8*, 1. https://doi.org/10.3390/ijtpp8010001

Academic Editor: Marcello Manna

Received: 30 August 2022
Revised: 30 November 2022
Accepted: 22 December 2022
Published: 4 January 2023

Copyright: © 2023 by the authors. Licensee MDPI, Basel, Switzerland. This article is an open access article distributed under the terms and conditions of the Creative Commons Attribution (CC BY-NC-ND) license (https://creativecommons.org/licenses/by-nc-nd/4.0/).

1. Introduction

Turbulence grids are used in wind tunnels and axial fan test rigs to generate increased turbulence intensities, modified length scales and defined flow fields [1,2]. A distinction is made between active and passive turbulence grids. The passive turbulence grids consist of rigid struts, which generate a defined orifice and blocking of the flow field [3]. Active turbulence grids (ATG), on the other hand, consist of shafts with attached wings called turbulence generators. The shafts are driven by motors located outside the flow. The motors generate a rotational motion, which is transmitted onto the shafts and the turbulence generators. The rotation of the turbulence generators can influence the turbulence intensity, the turbulent length scale and the homogeneity of the flow field [4]. The great advantage of the active turbulence grid is that a large number of different flow conditions can be generated with one grid [5,6]. The turbulence parameters are adjusted by changing the rotational speed of individual shafts. Active turbulence grids have been used since 1991 for fundamental investigations of flows and turbulence properties in wind tunnels [7,8]. They are usually operated in a square channel and the flow generated by the grids is analyzed downstream. In a novel approach an active turbulence grid will be used to replicate real flow fields and to generate variable inflow turbulence for axial fans. Thus, the

high variability in the flow field due to the active turbulence grid is used and investigated in the context of axial fans. Two questions arise from this, which are to be explored by means of this approach. On the one hand, it is to be studied to what extent it is possible to replicate real flow fields of heat exchangers. This also raises the question of how the sound radiation of the fan differs between the real flow field and the imitated flow field. This real-world application of axial fans with suction-side heat exchangers is of particular importance because, on the one hand, they are used in a variety of devices in close proximity to humans, such as heat pumps [9]. On the other hand, it is not yet fully understood why a suction-side heat exchanger can increase the sound radiation of axial fans [10,11]. Additionally, complete CFD simulations of the flow field through heat exchangers are not possible until now [12,13]. If the imitation of real flow fields by means of the ATG would be successful, then in future experimental investigations in the scope of heat pumps and air conditioning it would be possible to avoid cumbersome changes between many heat exchangers. This would save time in research as well as in industrial companies. A second question, which should be answered by means of active grids, is how the physical interactions between inflow turbulence to the axial fans and the resulting sound generation are [14]. With the active turbulence grid, it is possible to adjust the turbulence characteristics of the flow independently, in contrast to rigid turbulence grids. Thus, it has been shown in the literature that at low rotational speeds of the turbulence generators, the integral length scale can be varied while the turbulence level remains constant. On the other hand, at high rotational speeds, it was possible to vary the turbulence level, while the length scale remained unchanged [15]. This feature offers the possibility to investigate the influences of the individual turbulence parameters on the sound pressure spectrum of axial fans and thus to derive a better understanding of the sound generation mechanisms. However, for the use of the active turbulence grid in this context, it must be investigated on the one hand whether a modification of the inflow conditions can occur if a circular duct is arranged behind the square duct of the active turbulence grid. Active turbulence grids have a square shape. Axial fans, on the other hand, require a circular duct. Such a change in the cross-sectional area has so far unexplained effects on the generated turbulence of the active turbulence grid. In other studies with a cross-sectional change applied to axial fans, local turbulence spots were generated which changed the sound radiation at the tonal components of the fan [16]. Furthermore, for the investigation of the sound radiation of axial fans, it must be ensured that the inherent noise of the active turbulence grid is so low that no significant influence on the sound pressure spectrum takes place. Since no acoustic investigations with active turbulence grids have been carried out up to now, no data are available in the literature on the acoustic characteristics. The sound radiation of the active turbulence grid changes with the rotational speed of the turbulence generators. For the correct interpretation of the effects of the flow field on the sound emissions from the axial fans, the sound emission of the grid must be known. This radiation must be taken into account from the very beginning because it represents a distortion quantity and must be reduced as much as possible in the design process of the grid.

The structure of the paper consists of the following. First, the experimental fan used is described and its design parameters are discussed. In a further subchapter, the experimental setups for determining the sound field and for characterizing the inflow conditions are described. Then, the novel active turbulence grid is presented, and the constructional details are discussed in detail. This is followed by a subchapter on the sound radiation of the grid and how this changes as a function of the turbulence generator speed. Proceeding from these constitutive setups, the two questions from the introduction are then addressed and a comparison is made between active turbulence grid and heat exchangers. Subsequently, the basic physical interactions between inlet turbulence and sound radiation in the axial fan are discussed. Both questions are discussed with regard to flow fields and sound radiation in the axial fan. The paper is closed by a summary and conclusion.

2. Axial Fan Design and Experimental Setups

2.1. Forward Skewed Axial Fan

A forward skewed axial fan, which operates in a short duct segment with a diameter of D_{duct} = 500 mm, is used for the investigations. The axial fan, its specific blade energy and its sweep angle are shown in Figure 1. The forward skew increases from an angle of $\lambda = 0°$ at the hub to $\lambda = 55°$ at the blade tip. The total diameter of the fan is D_{fan} = 495 mm, which means that the tip gap is s_{tip} = 2.5 mm. The hub diameter of the fan is D_{hub} = 247.5 mm [17]. As is common in heat exchanger applications, the fan operates within a short inlet nozzle, which causes the tip gap to vary along the axial length of the inlet nozzle. As shown in Figure 1, the fan has z = 9 blades and is designed for a flow rate of $\dot{V}$ = 1.4 m^3/s at a rotational speed of n_{fan} = 1486 rpm and a total-to-static pressure rise of p_{fan} = 140 Pa [18]. The blades are based on a NACA 4510 profile and designed according the blade element theory [19]. In the investigations, this axial fan was chosen intentionally because, on the one hand, its forward skew is very similar to the fans currently used in industry and, on the other hand, it is very well documented in the literature. The precise knowledge of the behavior of the axial fan in inflow turbulence makes it possible to better classify effects caused by the disturbed inflow conditions of the ATG and to better understand and interpret the physical effects. The aerodynamic and aeroacoustics characteristics of the used axial fan can be found in the literature at various inflow conditions and in interaction with heat exchangers [11,16,19,20].

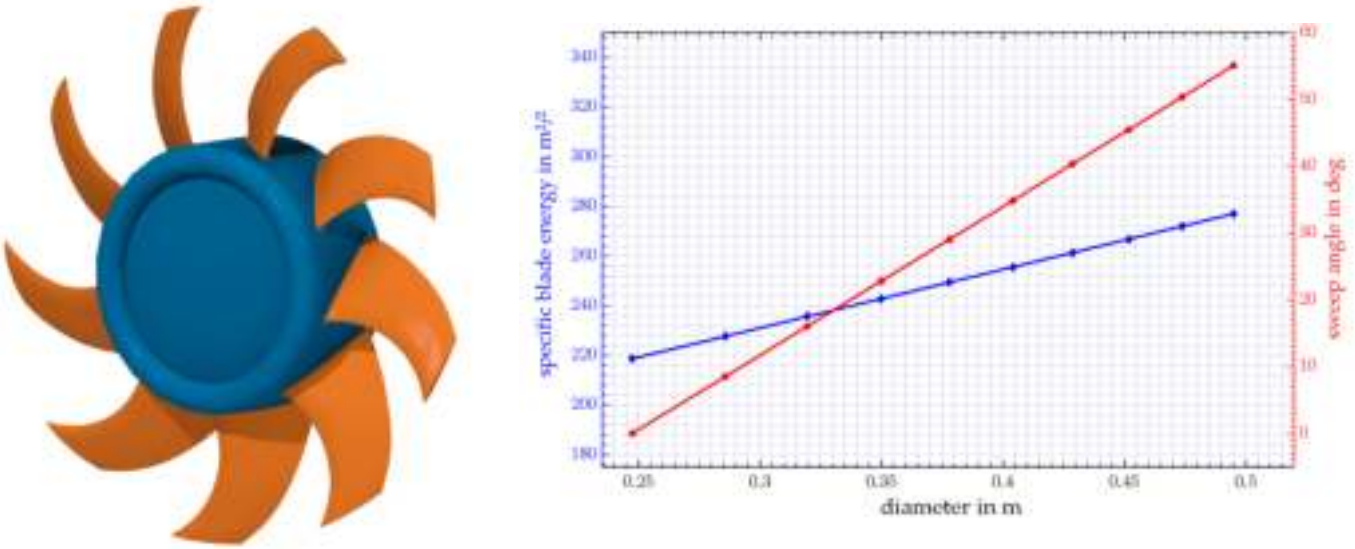

(**a**) (**b**)

Figure 1. Investigated axial fan and its characteristics. (**a**) CAD representations of the nine bladed forward-skewed axial fan used, and (**b**) the specific blade energy and sweep angle.

2.2. Experimental Setup for the Determination of Sound Emission and Aerodynamic Properties

The sound radiation and the aerodynamic properties of the axial fan are investigated together. For this purpose, the axial fan is installed in the axial fan test rig of the Friedrich-Alexander University Erlangen (see Figure 2). The operating point of the fan can be adjusted by means of a butterfly throttle and an auxiliary fan. The volume flow can be measured with a standardized volume flow measuring device at the inlet. Within the non-reflecting chamber, which is located on the suction side of the test fan, the pressure build-up between the suction side and the ambient pressure is measured. Additionally, within this chamber, the sound radiation of the fan is recorded by five free-field microphones from B&K. The microphones are placed at a distance of one meter from the axial fan. They are located

on a hemisphere, with one microphone directly on the axis of rotation of the fan. Two additional microphones are arranged in $\varphi = 22.5°$ angular segments on a horizontal and a vertical circular arc. The microphones record the acoustic pressure at a sampling rate of $f_s = 48$ kHz for a duration of $t = 30$ s. The speed and torque of the fan can be monitored via the shaft drive, which is located on the pressure side. The pressure, flow rate, rotational speed, torque, density and temperature are recorded at a sampling rate of $f_s = 1$ kHz for $t = 10$ s. Heat exchangers or the active turbulence grid can be positioned in front of the axial fan. Thus, the influence of different inflow conditions on the aerodynamic and acoustic properties of the fan can be investigated.

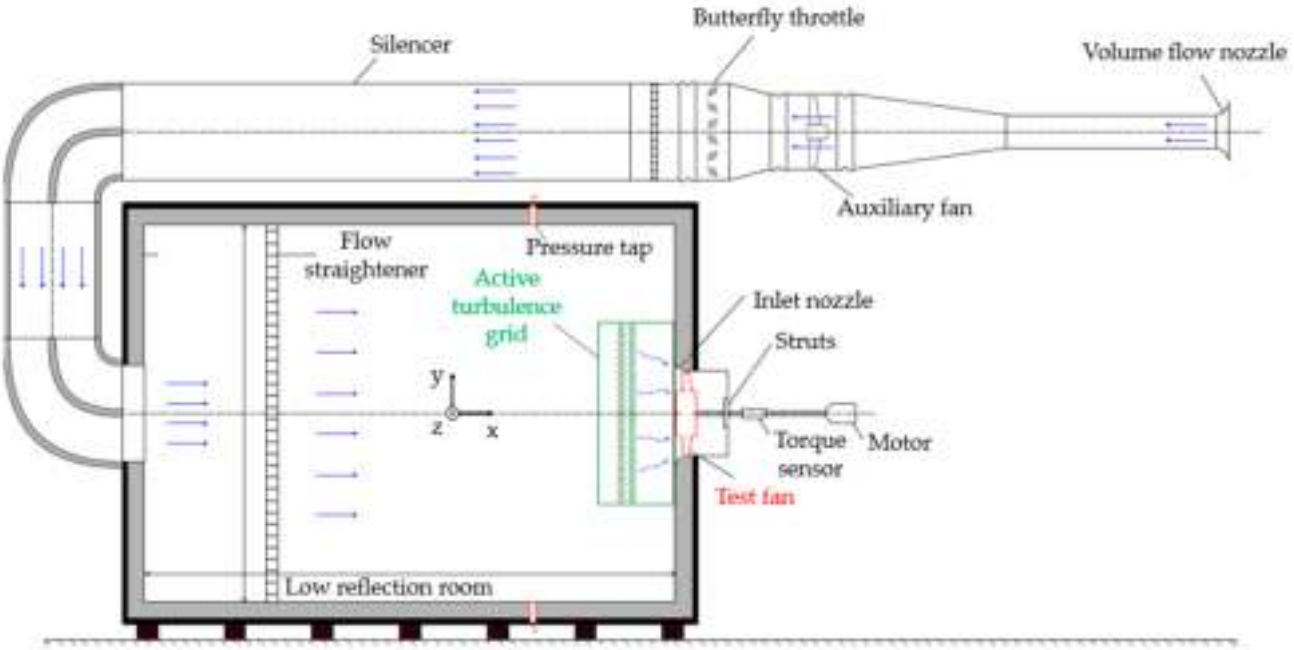

Figure 2. Schematic representation of the axial fan test rig of the LSTM-Erlangen with installed axial fan and active turbulence grid. Design according to DIN EN ISO 5801 [21].

2.3. Determination of Inflow Turbulence and Turbulence Parameters

The inflow conditions to the axial fan are determined at the position where the leading edge of the axial fan is located. At the leading edge, the fan interacts directly with inflow turbulence, and dominant sound sources are generated there, which emit sound primarily in the broadband, low-frequency range [22,23]. The sound source can be attributed to pressure fluctuations at the surface. Since the fan blades block the way to the measuring plane, the fan is replaced by a bladeless hub for the investigation of the flow field [24]. The flow field is determined by means of 3D hot-wire anemometry [25]. For this purpose, one third of a circular segment is measured inside the duct. A total of 80 measuring points with equidistant spacing are distributed in this circular segment (see Figure 3). The measuring points are accessed via a traverse from the pressure side. For each measuring point, the flow velocities in the three spatial directions are measured at a sampling rate of $f_s = 48$ kHz for a period of $t = 30$ s [12,16]. The hot-wire system used, manufactured by Dantec, is calibrated before the measurements [26]. From the data of the flow velocity $u_j(x_i, t)$ the fluctuations of the flow velocity $u'_j(x_i, t)$ can be calculated by Equation (1). $\overline{u}_j(x_i)$ is the time average value of one flow component [27].

$$u'_j(x_i, t) = u_j(x_i, t) - \overline{u}_j(x_i) \tag{1}$$

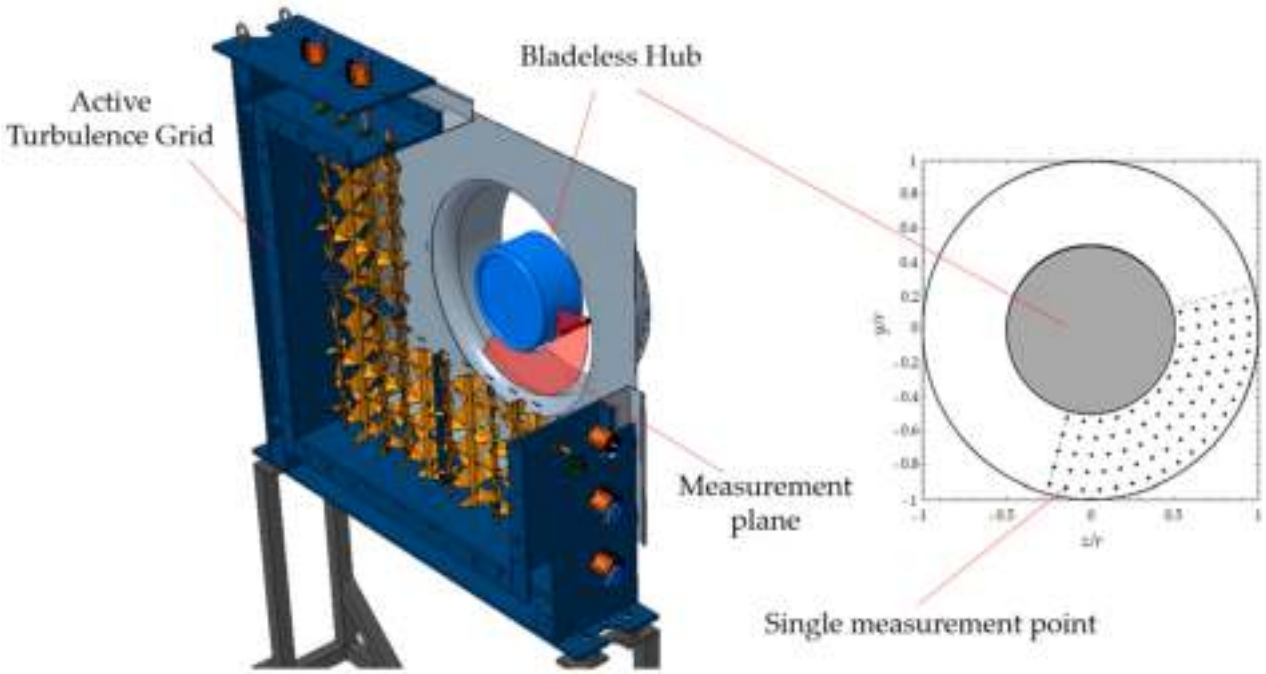

Figure 3. Sectional view of the active turbulence grid with bladeless hub and measuring plane for the hot-wire measurements.

With these, the global turbulence intensity can be calculated based on Equation (2). In this context, the global turbulence intensity Tu_{glo} means that turbulent fluctuations are related to the spatial mean value of the main flow component $\overline{u_{x1}}$ for all 80 measurement points [11].

$$Tu_{glo} = \frac{\sqrt{\frac{1}{3} \cdot \left(\overline{u'^2_{x1}} + \overline{u'^2_{x2}} + \overline{u'^2_{x3}}\right)}}{\overline{u_{x1}}} \tag{2}$$

The integral length scale of the turbulent flow is determined per measurement point from the time data of the main flow velocity. In this case, the length scale is calculated from the energy spectrum $E(f)$ according to Equation (3) and the approach of El-Gabry et al. [28].

$$\Lambda = \left[\frac{E(f) \cdot \overline{u_{x1}}}{4 \cdot \overline{u'^2_{x1}}}\right]_{f \to 0} \tag{3}$$

This procedure refers to isotropic flows, but according to Kurian et al. [29] it can also be used for not completely ideal isotropic flows. The calculation of the integral length scale on the basis of autocorrelation is not an option in these investigations with active turbulence grid. Due to the small distance between the measuring plane and the ATG and the rotation of the turbulence generators, cyclic components are included in the flow data. These would lead to the autocorrelation being a function of the rotational speed of the turbulence generators and thus the length scale would be calculated incorrectly. In addition to these basic parameters of the turbulence theory, a new parameter is presented in this paper, which should provide further insight into the interaction between the axial fan and the flow field. For this purpose, the formula of the variance σ^2 according to Equation (4) is applied to the time average values of the turbulence intensity Tu and the length scale Λ per measuring point (see Equations (5) and (6)). This results in a spatial variance, which combines the temporal and spatial data from the flow field into one value.

$$\sigma^2 = \frac{1}{n-1} \sum_{k=1}^{n} \left(X_k - \overline{X}\right)^2 \tag{4}$$

$$\sigma_{Tu}{}^2 = \frac{1}{n-1}\sum_{k=1}^{n}\left(Tu_k - \overline{Tu}\right)^2 \tag{5}$$

$$\sigma_{\Lambda}{}^2 = \frac{1}{n-1}\sum_{k=1}^{n}\left(\Lambda_k - \overline{\Lambda}\right)^2 \tag{6}$$

3. Active Turbulence Grid

3.1. Constructional Design of the Active Turbulence Grid

An active turbulence grid is used to generate defined inflow conditions. The basic form of the grid is shown as CAD in Figure 4. The turbulence generators, which are shown in orange in the center, are in the closed state, i.e., the maximum blocking of the grid is present. The basic structure of the grid consists of an outer frame and an inner frame, through which the flow passes. The drive motors and their controls are located on the outer frame. A total of 20 stepper motors are used, which are equipped with encoders and heat sinks. Vibration damping couplings are attached to the stepper motors. These couplings reduce the vibrations on the shaft, which are generated by the stepper motor. The outer frame is mounted on vibration dampers. The stepper motors and the space between the inner and outer frames are shielded by foam and motor enclosures so that as little sound as possible can be emitted to the outside from these components.

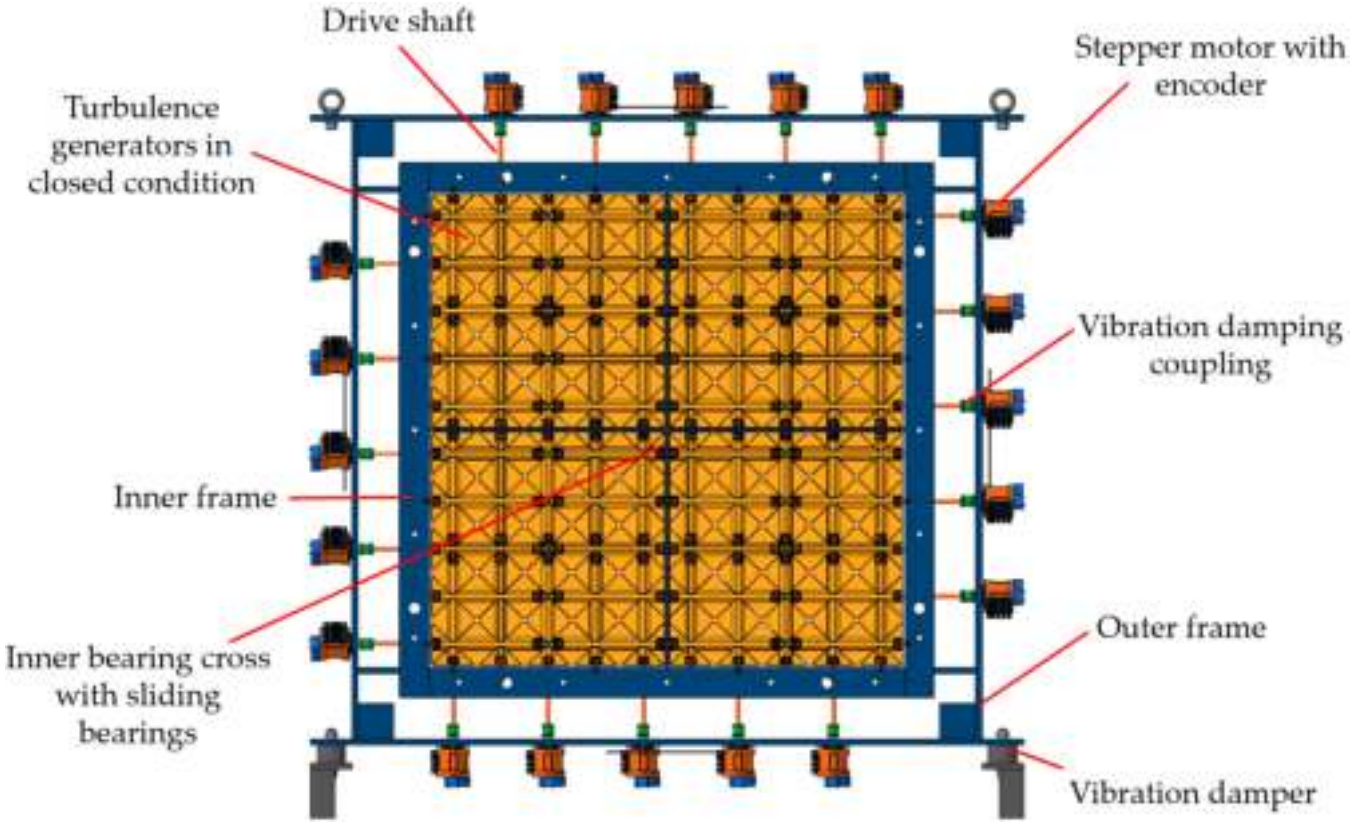

Figure 4. Schematic representation of the basic structure of the active turbulence grid.

Figure 5 shows a partial section of the active turbulence grid, where the flange bearings are visible. These are located outside the flow on the inner frame and guide the shafts on which the turbulence generators are located. In the center of the flow field, the shafts are additionally supported by sliding bearings, which have vibration damping properties. The center cross is designed as a symmetrical airfoil. This prevents stall at the center cross, which is necessary for stability reasons. As shown in Figure 5, there is a front and a rear row of turbulence generators. After the turbulence generators are 3D printed and slid over the shaft to be centered, there must be a gap between the vertical and horizontal axes. Both

the horizontal and vertical axes are positioned 6.5 mm off center. Thus, the shafts have a distance of 13 mm from each other in flow direction.

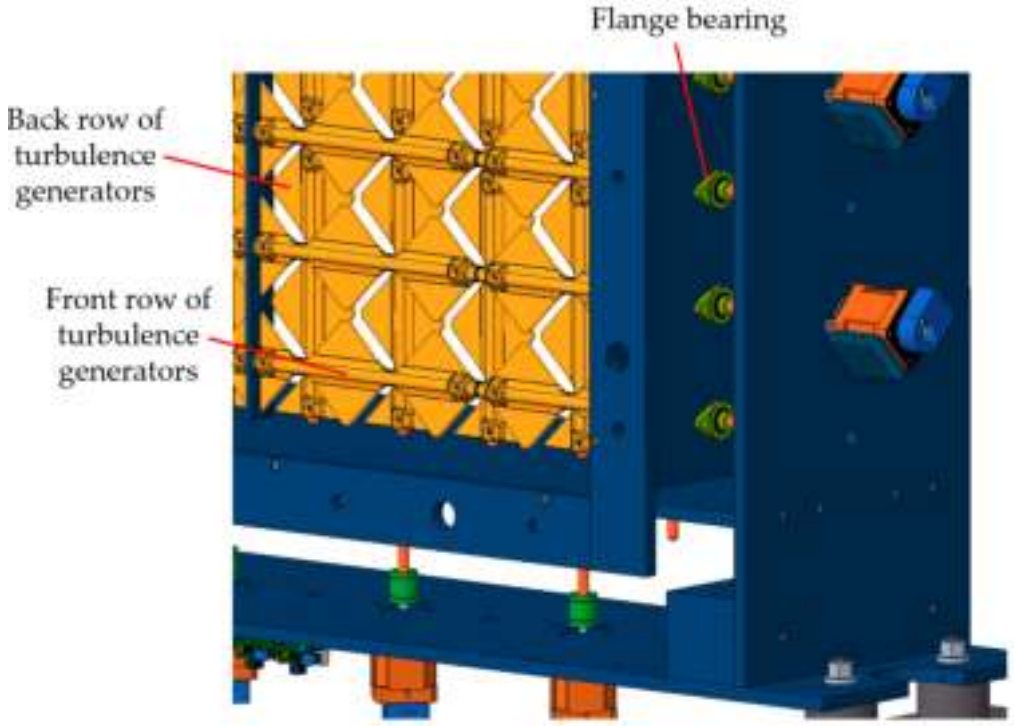

Figure 5. Partial view of the active turbulence grid, in which the distance between the two rows of turbulence generators can be seen.

Figure 6 illustrates a turbulence generator with shaft. The turbulence generators are square wings, which are located on the shaft. Each 2.5 wings consist of a joint 3D printed part and can be slid onto the shaft and fixed there by means of screws. The inner frame of the active turbulence grid, where the flow passes through, has square dimensions of 800 × 800 mm. The turbulence generators are shortened by a total of 7.5 mm. For this reason, there is a space of 3.75 mm between the two ends of a turbulence generator shaft and the respective frame wall. This clearance, as well as the distance between the horizontal and vertical axes, is necessary so that the turbulence generators do not drag or collide with each other during operation. By means of the individually controllable stepper motors, each of the 20 drive shafts, with the turbulence generators located on them, can be adjusted independently of each other. These settings include the direction of rotation, the rotational speed, the start position, the acceleration, a standstill position or relative movements to other drive shafts.

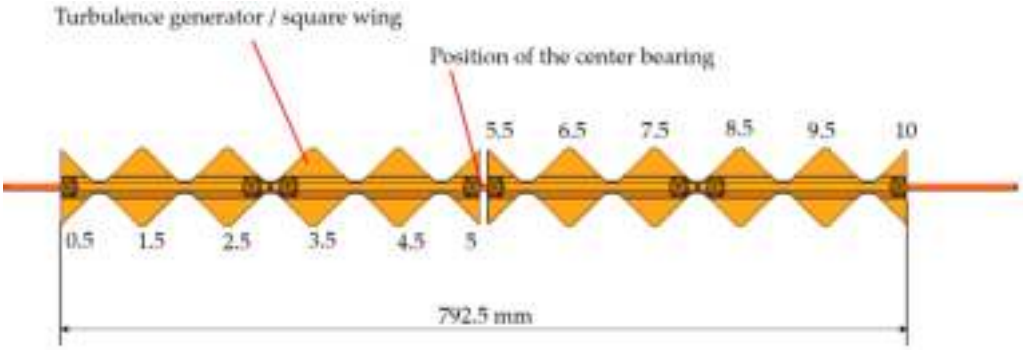

Figure 6. Detail of a single drive shaft with turbulence generators attached.

The number of individual shafts determines the mesh size of the active turbulence grid, which is M = 80 mm. The axial length of the active turbulence grid is L = 260 mm. By means of adapters on the inner frame, the square channel of the grid can be extended as desired both at the front and at the rear. In the tests presented here, a total length of L = 330 mm was selected, with an extension of 70 mm in the direction of flow (see Figure 3). The dimensions of the heat exchanger, which also plays a role in these investigations, are 800 × 800 × 330 mm, which thus corresponds to the same flow area and expansion as with the ATG. After the housing of the grid there is a transition to a circular duct with D = 500 mm diameter [11,16]. The transition is realized by an inlet nozzle. The axial fan to be investigated is operated in the round duct. If the axial fan is installed, the distance between it and the center plane of the two rotation planes of the active turbulence grid is d = 200 mm.

Figure 7 shows the active turbulence grid within the anechoic chamber of the axial fan test rig at the University of Erlangen-Nuremberg [30]. The active turbulence grid is shown in its basic shape without sound enclosure. Additionally, the five free-field microphones for measuring the sound radiation on the suction side are visible.

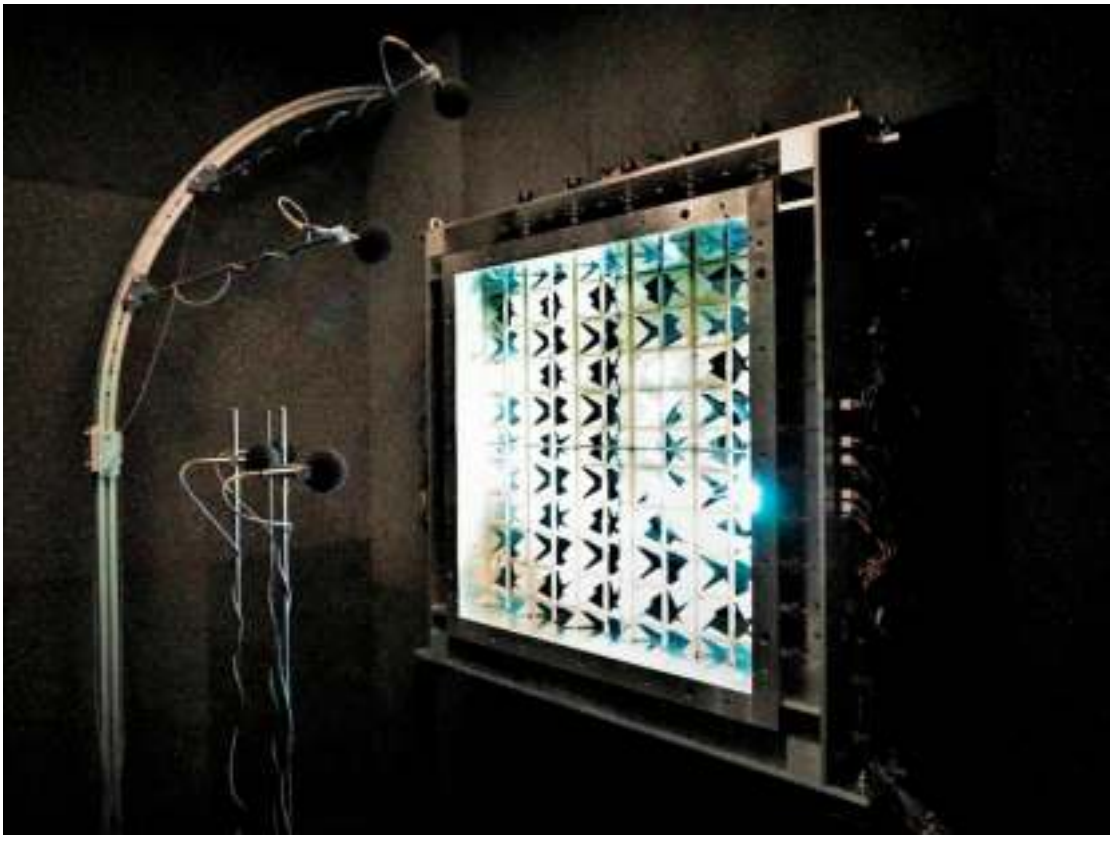

Figure 7. The active trubulence grid inside the anechoic chamber.

3.2. Intrinsic Noise of the Active Turbulence Grid

In order to better separate the acoustic influence of the active turbulence grid on the measurement results of the sound pressure from the axial fans under investigation, the inherent noise of the active turbulence grid was determined. The noise is low enough that it can be assumed that the intrinsic noise of the grid is masked by the fan noise [14,31]. Figure 8 displays a comparison between the sound radiation of the axial fan with an empty box in front and selected operating conditions of the ATG.

The spectra in Figure 8 are the inherent noise of the active turbulence grid at constant speeds. In this case, all motors rotate at the same speed and the grid blockage is constantly set to 50% blockage. A blockage of 50% is achieved by starting half of the turbulence

generators at 90° offset to the others. Operating modes in which all shafts rotate at the same speed are usually the noisiest. Thus, the case with the maximum speed of 800 rpm of the ATG is also the acoustically worst case. As a reference value, the noise of the axial fan is chosen when an empty box (an empty heat exchanger housing) is positioned in front of the axial fan on the suction side. With the ATG, a corresponding housing is always positioned in front of the axial fan due to the inner frame. Thus, this case represents a better comparison case, than the free inflow, because so also the influence of the changed directional characteristics is considered [32]. Only for the maximum speed of 800 rpm are there a few frequencies at which the spectrum of the axial fan does not mask the noise of the ATG. The overall sound pressure level is 11 dB away from the ATG's inherent noise at 800 rpm, far enough away that it can be assumed that the fan's sound radiation is not affected by the inherent noise of the turbulence grid. In the high-frequency range, tonal components appear individually through the spectrum of the axial fan.

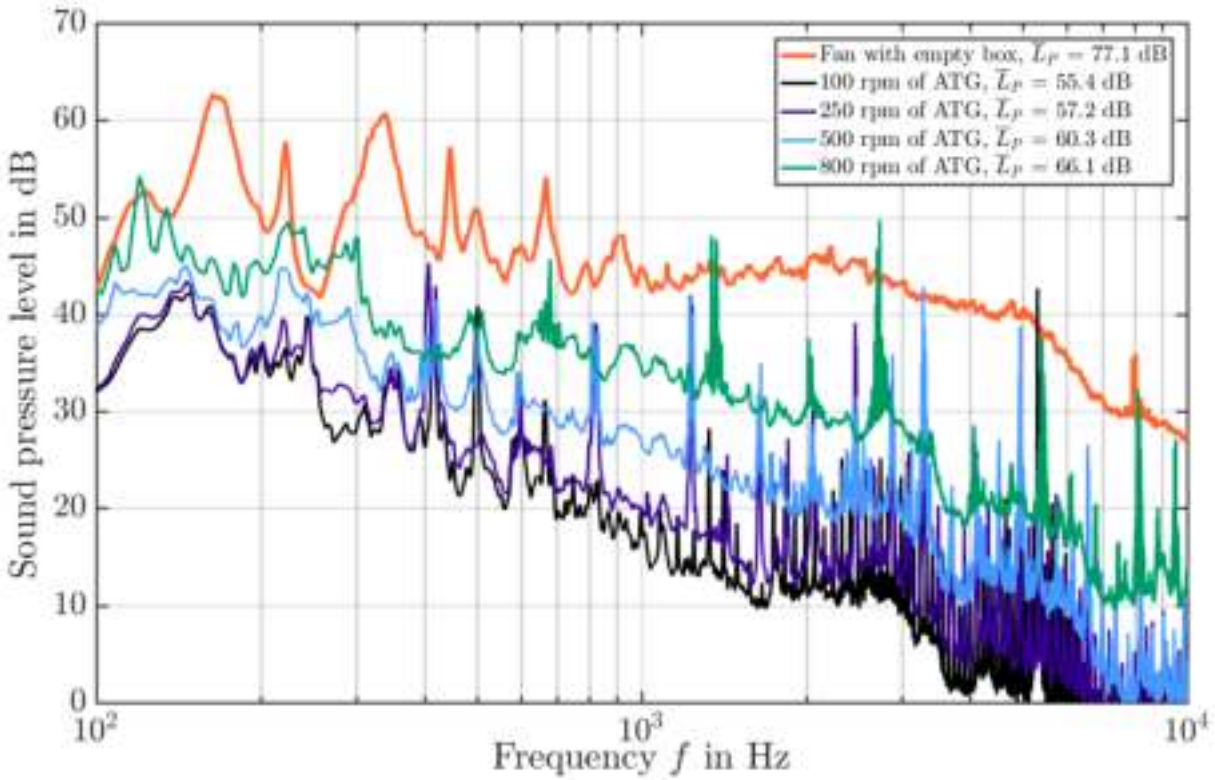

Figure 8. Comparison of the sound pressure spectra of the axial fan with the inherent noise of the ATG.

Through a run-up and a resulting Campbell plot (see Figure 9), it can also be determined that the tonal components generated by the active grid are related to the speed of the shafts. In addition, the linear relationship between the tonal components in the sound spectrum and the motor speed is related to the steps and micro steps of the motors used. These perform 200 steps and 3200 micro steps per revolution. The corresponding sound radiation of the tonal components can be calculated using Equation (7). The rotational speed n and the step size δ goes into the calculation of the respective frequency. The tonal sound radiation due to the microstep is the 16th harmonic (k = 16) of the fundamental frequency.

$$f_k = k \cdot \frac{n}{60} \cdot \frac{360^\circ}{\delta};\ k \in \mathbb{N} \tag{7}$$

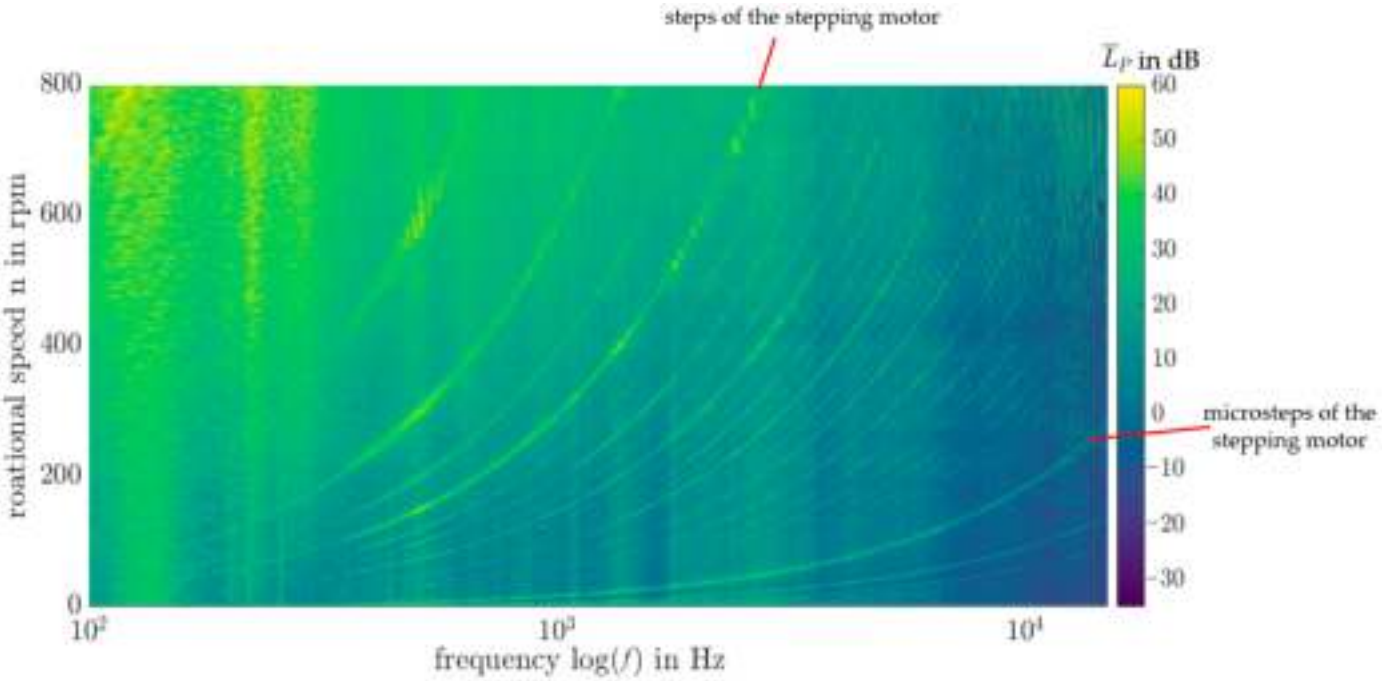

Figure 9. Campbell-plot of the self-induced noise of the active turbulence grid.

4. Controlled Inflow Turbulence and Flow Field Replication of Heat Exchangers

4.1. Generation of Defined Inflow Conditions

In many literatures in the field of sound radiation from axial fans, the inflow conditions are defined by spatial mean values of turbulence intensity and length scale [33,34]. These two values are also used for empirical sound prediction models for the axial fan and are essential for its sound radiation [35,36]. Thus, when the spatial mean values of these two quantities are plotted against each other, a characteristic map for the inflow conditions of the axial fan can be generated. In Figure 10, the global values of turbulence level and integral length scale are plotted in a characteristic map. Different operating modes of the active turbulence grid are shown with red dots in the map. The black squares are representative of four different heat exchangers with the dimensions of 800 × 800 mm. The distribution of the red dots shows that the active turbulence grid can vary the turbulence level in the range of [6.7%; 16.3%] and the length scale in the range of [3.7 mm; 36.2 mm]. In addition, a kind of pareto front [37] is recognizable in the measurement data. In total, more than 60 different operating conditions with different flow fields were generated with an active turbulence grid. Since at this point the basic functionality of the grid for the application in the field of turbulent inflow conditions of axial fans should be demonstrated, the individual flow fields and how they were generated will not be discussed. As different operating modes were used rigid modes, i.e., without rotation of shafts, uniform modes, where all shafts rotate at the same speed, staged modes, where different shafts have different speeds, and partially rotating modes, where only one part of the shaft rotates while the other part is stationary. The relationship that at constant slow speed the length scale can be adjusted and at constant high speed the turbulence intensity can be controlled independently, which is described in the literature [15], could also be found in this application. Thus, the characteristic map of the active turbulence grid (see Figure 10) proves that, for example, the length scale can be varied in the region of Tu_{glo} = 14% turbulence level, whereas the average turbulence level remains almost constant at this value. At a length scale of about Λ = 5 mm, the opposite pattern is seen. In this range, the turbulence level can be changed while the length scale remains constant. Thus, the active turbulence grid allows a separation of the influences of the different turbulence characteristics on the sound spectrum of axial fans to be investigated independently of each other.

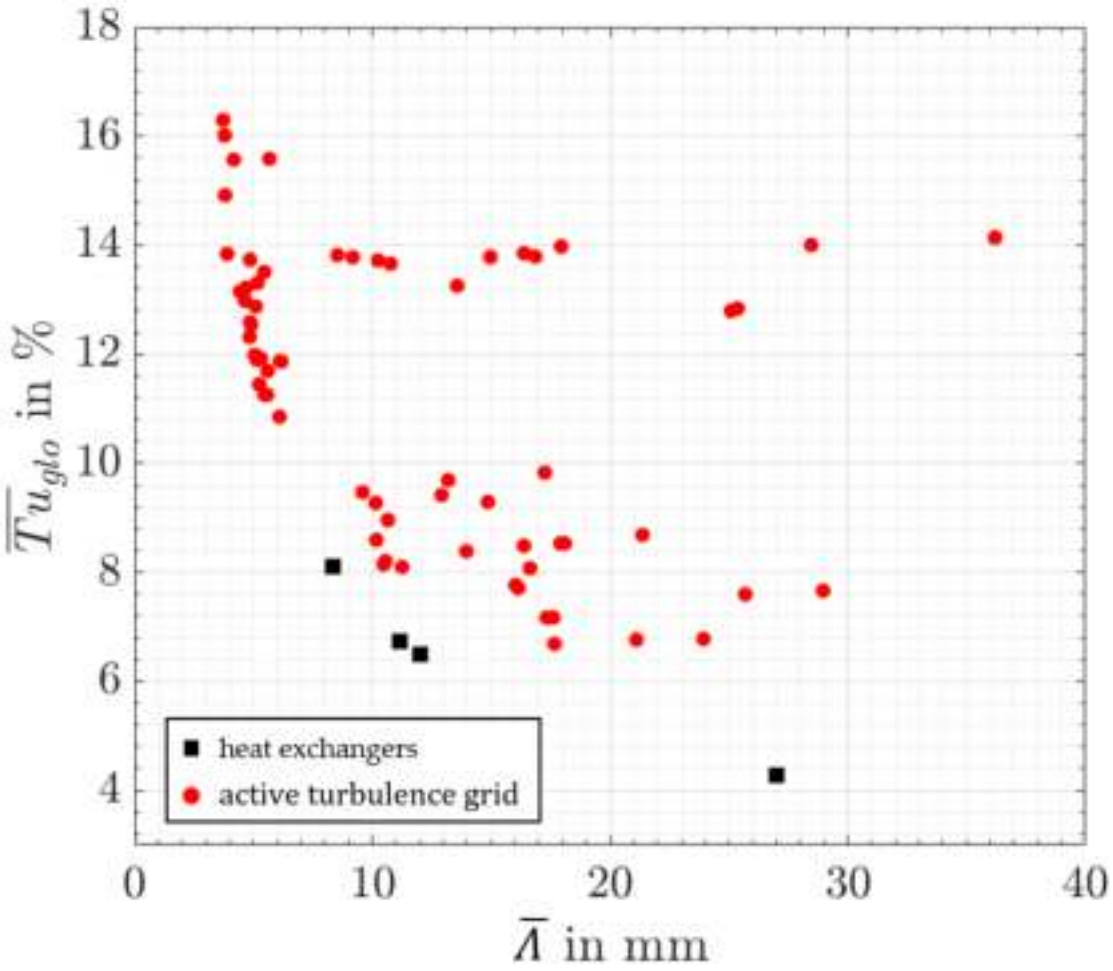

Figure 10. Characteristic map of the induced turbulence characteristics of heat exchangers and different active turbulence grid modes. Black squares are measured values of the heat exchangers, red circles are individual operating modes of the ATG.

4.2. Reproduction of the Flow Fields of Heat Exchangers

The four heat exchangers from Figure 10 are industrial devices, which are used, for example, in heat pumps or refrigeration systems. The turbulence intensity decreases with decreasing pipe diameter. Thus, the heat exchanger with the highest turbulence intensity has a tube diameter of 12 mm, the two black squares in the middle have a tube diameter of 9.52 mm, and the heat exchanger with the lowest turbulence intensity has a tube diameter of 5 mm. A detailed description of the heat exchangers can be found in the literature [16]. Especially the heat exchanger with the highest turbulence level can be reproduced very well in the mean values by the active turbulence grid. Here, the mean values in the length scale between heat exchanger and active turbulence grid deviate by only 2 mm. For the two heat exchangers in the turbulence range of 6.5%, the active turbulence grid can reproduce the turbulence level, but the length scale deviates by 6 mm. The heat exchanger with the low turbulence level of 4.3% cannot yet be reproduced by the active turbulence grid so far. Further investigations will show whether this range can be achieved in the map via other operating modes.

Since the active turbulence grid seems to be able to reproduce the average flow values of heat exchangers, a comparison between the flow field downstream of a heat exchanger (Tu_{glo} = 8.12%, Λ = 8.34 mm) and the most similar operating mode of the active turbulence grid (Tu_{glo} = 8.15%, Λ = 10.48 mm) is shown in Figure 11. In addition, the flow pattern of a free inlet flow is shown as a reference (Figure 11c).

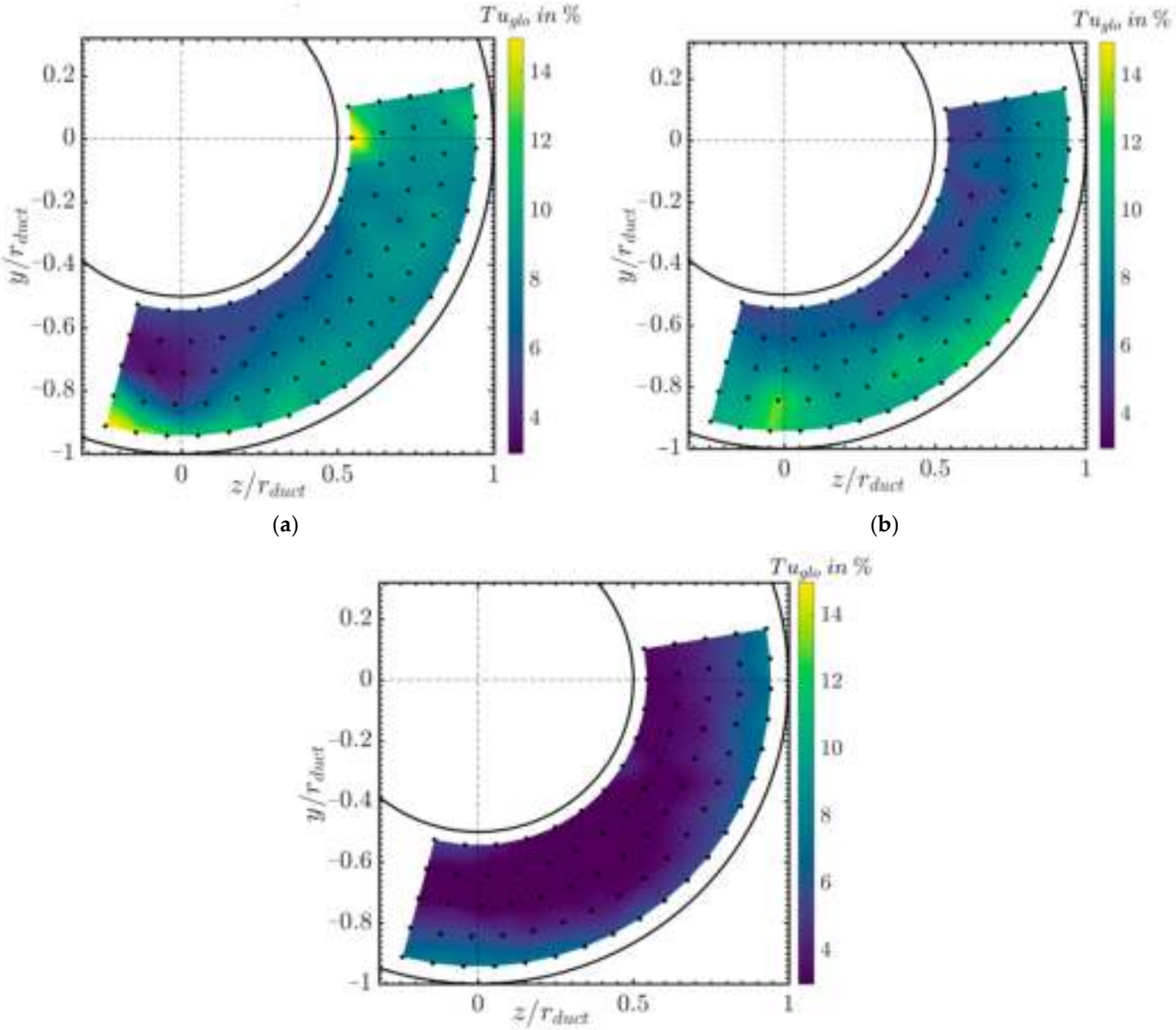

Figure 11. Comparison of the turbulence level between heat exchanger, imitated flow field by active turbulence grid and the undisturbed inflow at a volume flow rate of $\dot{V}$ = 1.4 m^3/s. (**a**) Flow field behind a real heat exchanger, (**b**) flow field reproduced by ATG and (**c**) free, undisturbed inflow.

The surface plots of the turbulence level display that flow conditions similar to those of heat exchangers can be created with the active turbulence grid. It is noticeable that the flow field seems to be rotated by 90° in the plots shown. Nevertheless, inhomogeneities in the flow field, which are mainly generated by the square housing of the heat exchanger and the active grid, can be reproduced [16,38]. The two-dimensional distribution of turbulence values also shows similar tendencies. Compared to the free inflow, the turbulence intensity increases through the heat exchanger as well as through the active turbulence grid. The inhomogeneity in the distribution increases in both cases compared to the free inflow.

5. Sound Emissions of Axial Fan and Active Turbulence Grid

5.1. Heat Exchanger and Active Turbulence Grid

The active turbulence grid is not only intended to reproduce the flow field of the heat exchangers, but also to reproduce the sound radiation of axial fans positioned downstream of heat exchangers as best as possible. The sound pressure spectrum is used to evaluate the sound emissions on the suction side of the axial fans. A comparison of the active turbulence grid and the heat exchanger should only be made at the operating point at which the flow data are available. A change in the flow velocity within the active turbulence grid leads to a change in the grid Reynolds number, which in turn changes the turbulence level and the length scale generated by the grid [15]. Figure 12 shows the sound pressure spectrum of the forward skewed axial fan at the design point. Here, the spectrum that is induced when a heat exchanger is placed in front of the axial fan and the spectrum when an active turbulence grid generates similar flow conditions are presented. In both cases, the sound measurements were made inside the anechoic chamber, on the suction side of the axial fan. Accordingly, the sound is influenced during its propagation to the microphones by the heat exchanger or the active turbulence grid, which are also located on the suction side of the axial fan. In this operating point there is a difference of 0.7 dB in the overall sound pressure level of the two variants. From this, follows that the overall sound pressure level is reproduced well by means of active turbulence grids. In addition, the sound pressure spectra have similar trends, in which the subharmonic peak and the higher harmonic blade passing frequencies are reproduced. Only the first blade passing frequency (1.BPF) is higher in the case with the active turbulence grid. This could be due to a higher turbulence spot in the flow field, which is not detected by the measurement in the third segment of the duct [16]. At higher frequencies, the heat exchanger consistently induces a lower sound pressure level. However, this difference is not due to the flow field, but to the sound guiding properties of the heat exchanger. Czwielong et al. [32] have identified that the differences in the high frequencies are due to the periodic arrangement of the coolant tubes in the heat exchanger and to the thermoviscous losses due to the high number of cooling fins. Thus, the differences in the high frequency range can be corrected by knowledge of the heat exchanger's sound transmission characteristics.

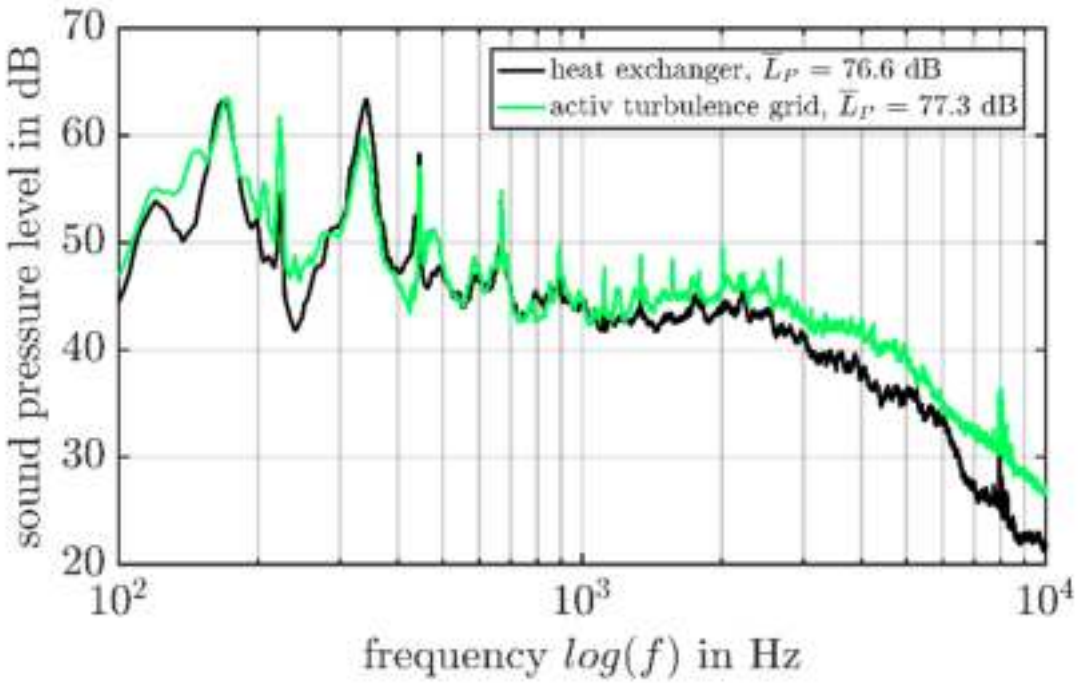

Figure 12. Sound pressure spectra of the heat exchanger (Tu_{glo} = 8.12%, Λ = 8.34 mm) and the active turbulence grid (Tu_{glo} = 8.15%, Λ = 10.48 mm) at the design point ($\dot{V}$ = 1.4 m^3/s).

5.2. Fundamental Investigations between Flow Field and Axial Fan Sound Radiation

Based on the flow field investigations, the sound emissions of the axial fan were investigated in nineteen selected operating modes of the active turbulence grid. The sound pressure spectra obtained at the design point were analyzed, for example, on the basis of the sound radiation at the first blade passing frequency (1.BPF = $z = n/60$ = 222.9 Hz, with z = 9 blades and n = 1486 rpm) and the total sound pressure level up to 1 kHz, which is mainly determined by the low-frequency broadband sound. The first blade passing frequency is often a dominant tonal component in the sound pressure spectrum of low-pressure axial fans and should be kept as low as possible so that the fan noise is not perceived as annoying [39]. Figure 13a displays the relationship between the acoustic emission of the axial fan at the first blade passing frequency and the spatial mean value of the turbulence level. From the data distribution, it can be concluded that no correlation between the mean spatial turbulence level and the sound emission at the first BPF can be found. This indicates that it is often not sufficient to give only mean turbulence levels when the sound pressure spectra of axial fans are discussed in the literature. Figure 13b displays the relationship between the first BPF and the spatial variance of the turbulence level. It can be clearly identified that as the variance increases, the acoustic radiation of the axial fan increases at the first BPF. A linear fit is given as a red dashed line in the plot. Equation (8) is the equation of the linear fit curve, in which the turbulence level in percent is inserted. The coefficient of determination has a value of R^2 = 77.66% for the fit. The relationship between the total sound pressure level between 0.1 kHz and 1 kHz, which is mainly determined by the broadband noise at the leading edge of the fan, and the spatial mean value as well as the spatial variance of the turbulence intensity is shown in Figure 13c,d.

For the total sound pressure level, no linear relationship to the spatial variance of the turbulence intensity can be found. In fact, the total sound pressure level remains almost independent of this parameter because a horizontal tendency develops. However, the total sound pressure level is influenced to a certain extent by the spatial mean value of the turbulence intensity. Here, a linear fit can be performed, which is given in Equation (9) and has a value of R^2 = 34.10%. The fit is shown as a dashed red line in Figure 13c.

$$SPL_{1.BFF,Fit} = 0.8656 \cdot {\sigma_{Tu}}^2 + 57.2 \text{ dB} \quad (8)$$

$$OSPL_{1kHz,Fit} = 0.1195 \cdot \overline{Tu} + 74.25 \text{ dB} \quad (9)$$

The existence of a linear relationship between the sound radiation at the first BPF and the spatial variance of the turbulence level indicates that the knowledge and specification of spatial parameters is critical for the understanding of the sound emission of axial fans. The spatial variance offers the possibility not only to represent discontinuities in the turbulence level by surface plots but also to describe these discontinuities in a statistical value. A high spatial variance means that spatial gradients in the turbulence level are present. When the fan blade moves through these gradients, it experiences a change in the blade forces, which in turn leads to a change in the sound radiation of the 1.BPF. Low values of the spatial variance of the turbulence level indicate a homogeneously distributed turbulence level. The fan blade moves through fewer gradients; therefore, experiences fewer changes in blade forces as it rotates through the flow field. As a result, the sound emission decreases at the 1.BPF. In heat exchanger applications, strong inhomogeneities in the flow field may occur. To minimize sound radiation at the 1.BPF, these inhomogeneities in the flow field should be avoided as far as possible.

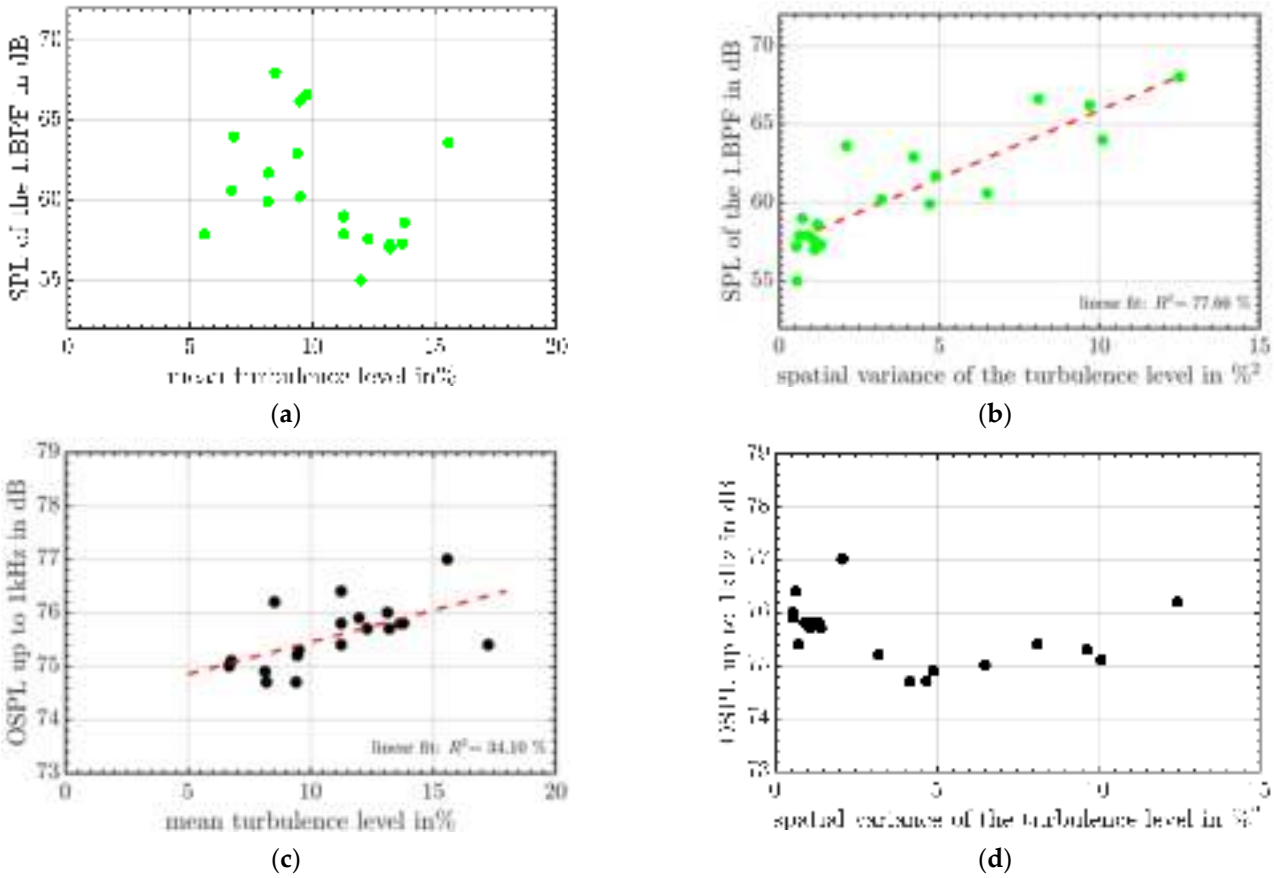

Figure 13. Influence of spatial mean turbulence intensity and spatial variance of turbulence intensity on sound radiation of axial fan at first blade passing frequency (1.BPF) and total sound pressure level between 0.1 kHz and 1 kHz. (**a**) BPF in dependence of the spatial mean value of the turbulence intensity, (**b**) BPF as a function of spatial variance of turbulence intensity with linear fit function, (**c**) BPF as a function of the spatial mean value of the turbulence intensity with linear fit function and (**d**) OSPL in dependence of the spatial variance of turbulence intensity.

6. Conclusions

An active turbulence grid was presented, which can be used for the generation of inflow turbulence of axial fans. The acoustic characterization of the active turbulence grid showed that the inherent noise of the grid is low enough and no significant influence on the sound pressure spectra of the axial fans under investigation is to be expected. In addition, it was found that the tonal peaks of the active turbulence grid depend on the rotational speed of the shafts and the number of steps of the stepper motors. On the basis of 3D hot-wire investigations, it was demonstrated that the active turbulence grid can be used to generate a large number of different inflow conditions, and that the mean turbulence characteristics and the spatial turbulence characteristics induced by heat exchangers can be reproduced by means of the active turbulence grid. The sound radiation of the investigated forward skewed axial fan between a heat exchanger and the active turbulence grid, which both induce comparable inflow conditions, also had similar tendencies. Here, differences in the high frequency range could be attributed to the absence of cooling fins. Based on a large number of sound radiation investigations, a linear relationship was found between the sound pressure level at the first blade passing frequency and the spatial variance of the turbulence level. No correlation was found between the sound radiation at the 1. BPF and the spatial mean of the turbulence level. This result indicates on the one hand that the spatial flow field significantly influences the sound radiation of axial fans and on the other hand that for the understanding of the sound generation mechanisms at the axial fan not only mean values are sufficient. However, the total sound pressure level up to 1 kHz did

not depend on the spatial variance of the turbulence level, but on the spatial average of the turbulence level. The derived value of spatial variances of turbulence level and length scale should be considered in future studies on inflow turbulence of axial fans to achieve a better understanding between the sound radiation and the flow field.

Author Contributions: Conceptualization, F.C.; methodology, F.C.; software, F.C.; validation, F.C.; formal analysis, F.C.; investigation, F.C.; resources, S.B.; data curation, F.C.; writing—original draft preparation, F.C.; writing—review and editing, F.C. and S.B.; visualization, F.C.; supervision, S.B.; project administration, F.C. and S.B.; funding acquisition, S.B. All authors have read and agreed to the published version of the manuscript.

Funding: F.C. and S.B. acknowledge support by the Federal Ministry of Economics and Climate Protection (Bundesminesterium für Wirtschaft und Klimaschutz – BMWK) (Forschungskuratorium Maschinenbau e.V.–FKM, AiF-Forschungsvereinigung, Project: Installationseffekte Axial, Grant No. 20659 N/1). Gefördert durch Bundesministerium für Wirtschaft und Klimaschutz aufgrund eines Beschlusses des Deutschen Bundestages.

Institutional Review Board Statement: Not applicable.

Informed Consent Statement: Not applicable.

Data Availability Statement: The data presented in this study are available on request from the corresponding author.

Acknowledgments: We would like to thank the FLT Project Advisory Committee and the company Thermofin GmbH for their support in the research project.

Conflicts of Interest: The authors declare no conflict of interest.

References

1. Roach, P.E. The generation of nearly isotropic turbulence by means of grids. *Int. J. Heat Fluid Flow* **1987**, *8*, 82–92. [CrossRef]
2. Carolus, T.H.; Stremel, M. Blade surface pressure fluctuations and acoustic radiation from an axial fan rotor due to turbulent inflow. *Acta Acust. United Acust.* **2002**, *88*, 472–482.
3. Lavoie, P.; Djenidi, L.; Antonia, R.A. Effects of initial conditions in decaying turbulence generated by passive grids. *J. Fluid Mech.* **2007**, *585*, 395–420. [CrossRef]
4. Makita, H.; Sassa, K. Active Turbulence Generation in a Laboratory Wind Tunnel. In *Advances in Turbulence*; Springer: Berlin, Germany, 1991; Volume 3, pp. 497–505. [CrossRef]
5. Thormann, A.; Meneveau, C. Decaying turbulence in the presence of a shearless uniform kinetic energy gradient. *J. Turbul.* **2015**, *16*, 442–459. [CrossRef]
6. Larssen, J.V.; Devenport, W.J. On the generation of large-scale homogeneous turbulence. *Exp. Fluids* **2011**, *50*, 1207–1223. [CrossRef]
7. Mydlarski, L. A turbulent quarter century of active grids: From Makita (1991) to the present. *Fluid Dyn. Res.* **2017**, *46*, 061401. [CrossRef]
8. Hideharu, M. Realization of a large-scale turbulence field in a small wind tunnel. *Fluid Dyn. Res.* **1991**, *8*, 53. [CrossRef]
9. Carroll, P.; Chesser, M.; Lyons, P. Air Source Heat Pumps field studies: A systematic literature review. *Renew. Sustain. Energy Rev.* **2020**, *134*, 110275. [CrossRef]
10. Czwielong, F.; Floss, S.; Kaltenbacher, M.; Becker, S. Sound reduction in heat exchanger modules by integrating plate absorbers with sub-millimeter openings. *Acta Acust.* **2021**, *5*, 35. [CrossRef]
11. Czwielong, F.; Krömer, F.; Becker, S. Experimental Investigations of the Sound Emission of Axial Fans Under the Influence of Suction-Side Heat Exchangers. In Proceedings of the 25th AIAA/CEAS Aeroacoustics Conference, Delft, The Netherlands, 20–23 May 2019; p. 2618. [CrossRef]
12. Lucius, A.; Schneider, M.; Schweitzer-De Bortoli, S.; Gerhard, T.; Geyer, T. Aeroacoustic Simulation and Experimental Validation of Sound Emission of an Axial Fan Applied in a Heat Pump. In Proceedings of the 23rd International Congress on Acoustics, Universitätsbibliothek der RWTH Aachen, Aachen, Germany, 9–13 September 2019.
13. Réz, I. Numerische Untersuchung des Luftseitigen Wärmeübergangs und Druckverlustes in Lamellenrohr-Wärmeübertragern mit Verschiedenen Rohrformen. Ph.D. Thesis, Technische Universität Bergakademie Freiberg, Freiberg, Germany, 2004.
14. Czwielong, F.; Becker, S. Aktives Turbulenzgitter—Generierung definierter Zuströmturbulenzen für Axialventilatoren. In Proceedings of the DAGA 2021, Vienna, Austria, 15–18 August 2021.
15. Hearst, R.J.; Lavoie, P. The effect of active grid initial conditions on high Reynolds number turbulence. *Exp. Fluids* **2015**, *56*, 185. [CrossRef]

16. Czwielong, F.; Soldat, J.; Becker, S. On the interactions of the induced flow field of heat exchangers with axial fans. *Exp. Therm. Fluid Sci.* **2022**, *139*, 110697. [CrossRef]
17. Krömer, F.; Müller, J.; Becker, S. Investigation of aeroacoustic properties of low-pressure axial fans with different blade stacking. *AIAA J.* **2018**, *56*, 1507–1518. [CrossRef]
18. Krömer, F.J. *Sound Emission of Low-Pressure Axial Fans Under Distorted Inflow Conditions*; FAU University Press: Boca Raton, FL, USA, 2018. [CrossRef]
19. Pfleiderer, C. *Strömungsmaschinen*; Springer: Berlin, Germany, 2013.
20. Krömer, F.J.; Moreau, S.; Becker, S. Experimental investigation of the interplay between the sound field and the flow field in skewed low-pressure axial fans. *J. Sound Vib.* **2019**, *442*, 220–236. [CrossRef]
21. *DIN EN ISO 5801*; Fans–Performance Testing Using Standardized Airways (ISO 5801: 2007, Including COR 1: 2008), German Version EN ISO 5801. German Institute for Standardization: Berlin, Germany, 2008.
22. Ocker, C.; Geyer, T.F.; Czwielong, F.; Krömer, F.; Pannert, W.; Merkel, M.; Becker, S. Permeable Leading Edges for Airfoil and Fan Noise Reduction in Disturbed Inflow. *AIAA J.* **2021**, *59*, 4969–4986. [CrossRef]
23. Moreau, S.; Roger, M. Competing broadband noise mechanisms in low-speed axial fans. *AIAA J.* **2007**, *45*, 48–57. [CrossRef]
24. Carolus, T.; Schneider, M.; Reese, H. Axial flow fan broad-band noise and prediction. *J. Sound Vib.* **2007**, *300*, 50–70. [CrossRef]
25. Bruun, H.H. *Hot-Wire Anemometry: Principles and Signal Analysis*; Oxford Unversity Press: New York, NY, USA, 1996.
26. Jørgensen, F.E. *How to Measure Turbulence with Hot-Wire Anemometers: A Practical Guide*; Dantec Dynamics A/S: Skovlunde, Denmark, 2001.
27. Durst, F. *Fluid Mechanics: An Introduction to the Theory of Fluid Flows*; Springer Science & Business Media: Berlin, Germany, 2008.
28. El-Gabry, L.A.; Thurman, D.R.; Poinsatte, P.E. *Procedure for Determining Turbulence Length Scales Using Hotwire Anemometry*; Technical Report, GRC-E-DAA-TN4063; National Aeronautics and Space Administration, Glenn Research Center: Cleveland, OH, USA, 2014.
29. Kurian, T.; Fransson, J.H. Grid-generated turbulence revisited. *Fluid Dyn. Res.* **2009**, *41*, 021403. [CrossRef]
30. Czwielong, F.; Floss, S.; Kaltenbacher, M.; Becker, S. Influence of a micro-perforated duct absorber on sound emission and performance of axial fans. *Appl. Acoust.* **2021**, *174*, 107746. [CrossRef]
31. Czwielong, F.; Becker, S. Controlled Inflow Turbulence-Aeroacoustic Interaction of Axial Fans with an Active Turbulence Grid. In Proceedings of the FAN 2022—International Conference on Fan Noise, Aerodynamics, Applications and Systems, Senlis, France, 27–29 June 2022. [CrossRef]
32. Czwielong, F.; Hruška, V.; Bednařík, M.; Becker, S. On the acoustic effects of sonic crystals in heat exchanger arrangements. *Appl. Acoust.* **2021**, *182*, 108253. [CrossRef]
33. Biedermann, T.M.; Czeckay, P.; Hintzen, N.; Kameier, F.; Paschereit, C.O. Applicability of aeroacoustic scaling laws of leading edge serrations for rotating applications. *Acoustics* **2020**, *2*, 579–594. [CrossRef]
34. Ocker, C.; Czwielong, F.; Geyer, T.F.; Chaitanya, P.; Merkel, M.; Becker, S. Permeable Structures for Leading Edge Noise Reduction. In Proceedings of the AIAA AVIATION 2021 FORUM, Virtual Event, 2–6 August 2021; p. 2192. [CrossRef]
35. Sharland, I., Jr. Sources of noise in axial flow fans. *J. Sound Vib.* **1964**, *1*, 302–322. [CrossRef]
36. Bommes, L. (Ed.) *Ventilatoren*; Vulkan-Verlag GmbH: Essen, Germany, 2003.
37. Van Veldhuizen, D.A.; Lamont, G.B. Evolutionary Computation and Convergence to a Pareto Front. In Proceedings of the Late Breaking Papers at the Genetic Programming 1998 Conference, Madison, WI, USA, 22–25 July 1998; pp. 221–228.
38. Lucius, A.; Hütter, S.; Dietrich, P.; Schneider, M.; Lehmann, M.; Geyer, T. Experimental and numerical investigation of axial fan aeroacoustics at disturbed inflow conditions. In Proceedings of the Fan 2018, International Conference on Fan Noise, Aerodynamics, Applications and Systems, CETIAT, Darmstadt, Germany, 18–20 April 2018.
39. Schneider, M.; Feldmann, C. Psychoacoustic evaluation of fan noise. In Proceedings of the Fan 2015 International Conference on Fan Noise, Technology and Numerical Methods, Lyon, France, 15–17 April 2015.

Disclaimer/Publisher's Note: The statements, opinions and data contained in all publications are solely those of the individual author(s) and contributor(s) and not of MDPI and/or the editor(s). MDPI and/or the editor(s) disclaim responsibility for any injury to people or property resulting from any ideas, methods, instructions or products referred to in the content.

International Journal of
Turbomachinery
Propulsion and Power

MDPI

Article

Investigations concerning the Flow Stabilization of Backward Curved Centrifugal Impellers at Low Flow Rate

Frieder Lörcher [1,*], Sandra Hub [1], Marlène Sanjosé [2,3] and Stéphane Moreau [3]

[1] ZIEHL-ABEGG SE, Ventilation Division, Heinz-Ziehl-Strasse, 74653 Künzelsau, Germany
[2] Department of Mechanical Engineering, École de Technologie Supérieure, Université du Québec, 1100 rue Notre-Dame Ouest, Montréal, QC H3C 1K3, Canada
[3] Department of Mechanical Engineering, Université de Sherbrooke, 2500 Boulevard de L'université, Sherbrooke, QC J1K 2R1, Canada
* Correspondence: frieder.loercher@ziehl-abegg.de

Abstract: For a backward curved centrifugal fan, reducing volume flow rate from design operating point towards part load yields an increase in noise emission together with a reduction of efficiency. The spectral content of the emerging noise emission can be characterized by a subharmonic hump with several harmonics. Based on narrow-band acoustic measurements and numerical Lattice-Boltzmann simulations, a deeper insight is sought after. Downstream unsteady flow patterns are identified to play a central role in this performance deterioration; and geometrical flow stabilization means are investigated.

Keywords: centrifugal fan noise; subharmonic humps; lattice Boltzmann method; noise generation mechanism; flow stabilization for backward curved centrifugal fans

check for updates

Citation: Lörcher, F.; Hub, S.; Sanjosé, M.; Moreau, S. Investigations concerning the Flow Stabilization of Backward Curved Centrifugal Impellers at Low Flow Rate. *Int. J. Turbomach. Propuls. Power* **2022**, *7*, 37. https://doi.org/10.3390/ijtpp7040037

Academic Editor: Thomas Carolus

Received: 22 August 2022
Accepted: 30 November 2022
Published: 7 December 2022

Publisher's Note: MDPI stays neutral with regard to jurisdictional claims in published maps and institutional affiliations.

Copyright: © 2022 by the authors. Licensee MDPI, Basel, Switzerland. This article is an open access article distributed under the terms and conditions of the Creative Commons Attribution (CC BY-NC-ND) license (https://creativecommons.org/licenses/by-nc-nd/4.0/).

1. Introduction

It is a common observation for many fans that the noise emission increases significantly when moving on a characteristic curve starting from an optimal point with minimal noise emission towards lower volume flow rates at constant impeller rotation speed. Considering axial flow fans, Kameier and Neise [1] identified experimentally flow structures co-rotating with approximately half of the impeller rotation speed which they called "rotating instabilities". They supposed the origin of that noise phenomena in a broader, but distinct frequency region below the blade passing frequency (BPF). Mongeau [2] describes characteristic noise sources for centrifugal turbomachines at 0.7, 1.5 and 2.1 times the BPF and relates it to a flow pattern rotating around 30% of the shaft speed. Rotating coherent flow structures as a source for narrowband noise in axial fans are described by Zhu at al. in [3]. A better understanding of these mechanisms and development of mitigation strategies could broaden the applicability of centrifugal fans towards lower volume flows and make them less sensitive to noise generation in this direction. In this paper, this kind of noise source is identified and characterized experimentally by considering a centrifugal backward-curved impeller with diameter D = 355 mm. The results are reproduced in a numerical setup with an unsteady Lattice-Boltzmann solver. Relying on the numerical results, a more profound insight into the noise generating mechanisms is generated. With this understanding, it was possible to construct and investigate modifications to improve the acoustic signature significantly. One mitigation technology is demonstrated both numerically and experimentally.

2. Experimental Investigation

2.1. Configuration Description

The investigated centrifugal fan of diameter D = 355 mm shown in Figure 1a has seven backward curved blades made of sheet metal. The blades are circular profiles extruded perpendicularly to the flat hub. They are welded to the hub and to the curved rotating

shroud. The fan is installed without housing. The ZIEHL-ABEGG anechoic facility shown in Figure 1b consists of two large anechoic rooms separated by a partition wall. A bell-mouth attached to the partition guides the flow into the fan installed in the downstream plenum (Figure 1a). The gap between the rotating shroud of the fan and the convergent intake is 3 mm. The fan is tested at constant rotational speed n = 2975 rpm for various flow rates, yielding a blade-passing frequency (BPF) of 347 Hz.

(**a**) (**b**)

Figure 1. Experimental setup: (**a**) downstream view of the investigated fan; (**b**) anechoic test facilities at ZIEHL-ABEGG.

2.2. Experimental Results

Figure 2a shows the characteristic curves measured for the rotational speed n = 2975 rpm. The static pressure rise p_{fs} as function of the volume flow rate Q_V is presented as a solid black line, and the sound power level L_{W6} measured in the pressure side plenum (downstream of the fan) as dashed black line. L_{W6} has a minimal value of 90 dB at $Q_V \approx 4000$ m^3/h Towards lower volume flow rates, the sound power level sharply increases up to 101 dB at $Q_V \approx 2000$ m^3/h. This kind of sound power surge in a region for low volume flows is typical of many fan designs. It is common for very different designs of backward curved centrifugal fans without housing. To investigate this behavior, the spectral content of L_{W6} is shown in Figure 2b for the three operation points highlighted with the vertical color lines in Figure 2a. At Q_V = 4440 m^3/h, the spectrum is quite flat over the displayed frequency region from 100 Hz to 1000 Hz, except for some typical peaks at the blade passing frequency (BPF) and its harmonics. Moving towards lower volume flow rates, additional noise phenomenon is emerging in a large frequency range centered at approximately 80% of the BPF. The harmonics of this hump emerge as well but with a smaller amplitude. These phenomena are referred to as subharmonic humps. They are typical of (but not only) centrifugal and mixed-flow fans. Although the broadband noise grows towards lower volume flow rates as well, the mentioned steep growth of L_{W6} in Figure 2a can be strongly associated with this subharmonic. In the present work, a numerical investigation is performed to gain a deeper insight to the nature of the humps and the underlying sound generating mechanisms.

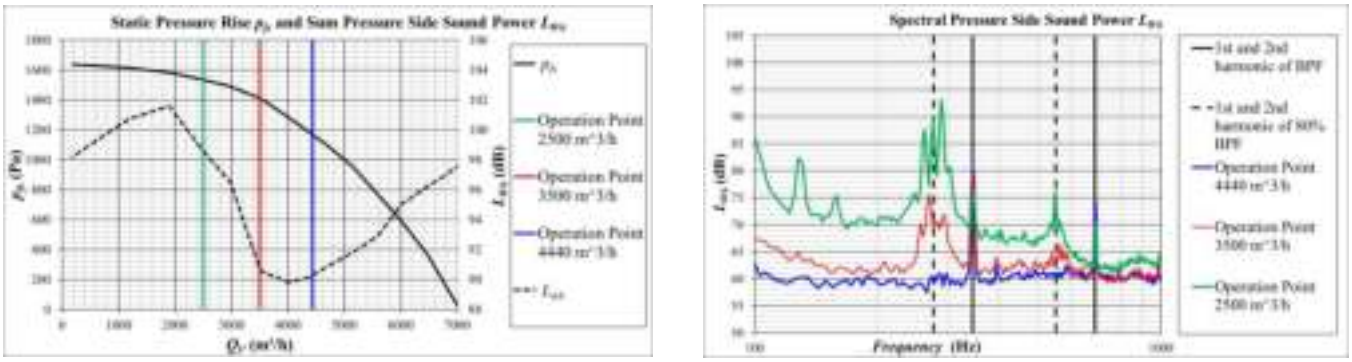

(**a**) (**b**)

Figure 2. Experimental results: (**a**) characteristic curve for static pressure rise p_{fs} and sum pressure side sound power level L_{W6} at rotation speed n = 2975 rpm; (**b**) spectral content of pressure side sound power level L_{W6} for three operation points.

3. Numerical Investigation

3.1. Numerical Setup

The present simulations use the PowerFLOW solver 5.5a based on the Lattice Boltzmann Method (LBM). The approach is naturally transient and compressible providing a direct insight into hydrodynamic mechanisms responsible for the acoustic sources but also into acoustic propagation in the fan and outside in freefield. Instead of studying macroscopic fluid quantities, the LBM tracks the time and space evolution of a truncated particle distribution function on a lattice grid. The particle distribution evolution is driven to equilibrium by the so-called collision operator, approximated by the BGK (Bhatnagar–Gross–Krook) model [4]. The discrete Lattice-Boltzmann equations are solved with 19 discrete velocities for the third order truncation of the particle distribution function, which has been shown sufficient to recover the compressible Navier–Stokes equations for a perfect gas at low Mach number in isothermal conditions [5,6]. In PowerFLOW, a single relaxation time is used, which is related to the dimensionless laminar kinematic viscosity [6]. This relaxation time is replaced by an effective turbulent relaxation time that is derived from a systematic Renormalization Group procedure detailed in [7]. It captures the large structures in the anechoic room but also the small turbulent scales that develop along the blade and wall surfaces in a large eddy simulation manner. The particular extension developed for rotating machines can be found in Pérot et al. [8]. The computational domain includes the two coupled anechoic rooms, as shown in Figure 3a. The square cross section of the simulation volume has a width of 10 m, and the upstream and downstream plenums are also 30 m and 20 m long, respectively. The atmospheric pressure p = 101,325 Pa is imposed on the left red surface, while the volume flowrate Qv is imposed on the downstream red surface. The convergent inlet nozzle and detailed geometry of the fan impeller are considered. Only the motor and its shaft are discarded in the numerical setup. The mesh resolution in the domain is defined through successive embedded volumes, outlined in Figure 3, the mesh size being decreased by a factor of two between them. The resolution around the fan blades and the inlet nozzle wall is 0.5 mm, as shown on a fan cross section in Figure 3b. The volume around the fan is defined as a rotating volume at a rotational speed. Extended logarithmic wall functions to account for adverse and favorable pressure gradients [9] are applied on all wall surfaces. The total numerical domain counts 98 million cells and 7 million surface elements. Simulations are performed for several flow rates. First, the setup is initialized in two steps from pre-converged flow obtained from simulations with coarser meshes without the highest resolved refinement regions (50 revolutions computed on the mesh with maximum resolution of 2 mm and subsequently, 25 revolutions computed on the mesh with maximum resolution of 1 mm). Then, the final mesh described above (Figure 3b) is used for performance prediction. The convergence is obtained after two fan revolutions

on the finest mesh, and data are acquired for further five fan revolutions. Static pressure is recorded at the exact locations of the microphones in the experiments. In addition, some cross-sections including the one at mid-blade height (midspan) and blade surface are recorded at high frequency sampling for frequency analysis. The numerical model presented above is validated through the comparison of performances with experimental measurements acquired on the certified ISO 5801 ZIEHL-ABEGG facilities.

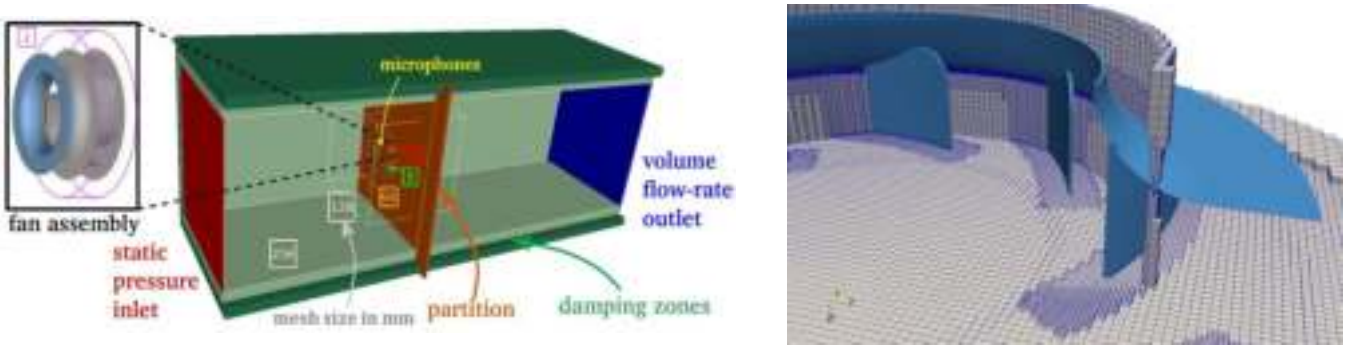

(**a**) (**b**)

Figure 3. Computational domain and refinement volume definitions: (**a**) numbers in squares provide the mesh size in mm for the outlined refinement volume; (**b**) and mesh resolution around the fan blades.

3.2. Numerical Results

The sound power levels L_{W6}, computed in a similar manner as for experimental data in Figure 2b, are given in Figure 4b based on static pressure extracted from the LBM simulations. The main conclusion that can be drawn out of the comparison of the graphs of Figure 2b, replotted in Figure 4a, and Figure 4b is that the subharmonic humps are also the dominant noise mechanisms in the numerical method. The frequency resolution in Figure 4b is coarser than in Figure 2b due to the available sample length for the data of only about five impeller revolutions. Nevertheless, the emergence of the subharmonic humps of first and second order can clearly be observed in an equivalent way and a very similar quantitative extent as in the physical experiment. The intake distortion is the main cause of tones at BPF [10]. In addition, the inflow condition is more homogenous in the simulation than in the experiment (see for example [11]), as the flow field in the upstream plenum has not completely developed in the simulation due to the limited data acquisition period of only five impeller revolutions. Both limitations inherent in the simulations can explain the lower and wider peak at the BPF. Moreover, a first conclusion that can be drawn is that the mechanism of the generation of the subharmonic humps does basically depend on the downstream flow field generated by the impeller and corresponds therefore to a self-induced noise generating mechanism. By analyzing the unsteady flow field resulting from the LBM simulations carried out in the present model, one should be able to get some insight to this noise generation mechanism as it is well captured in the acoustic spectra.

In Figure 5, instantaneous pressure distributions at a blade mid-span cross-section are pointed out. Different flow structures downstream and radially outward of the impeller can be observed. These flow structures have different shapes (number of lobes) for each of the three flowrates. Decreasing Q_V, they get less symmetric, their circumferential wave numbers decrease, and they move radially inward towards the blades. It can be observed by use of unsteady visualization techniques that the flow structures correspond to vortical structures co-rotating with significantly reduced rotational speed compared with the impeller rotational speed. This is confirmed by a modal analysis in the next Section 3.3. The vortices are generated and supplied by detaching vorticity of the impeller blades, caused by flow separation phenomena at the blade suction side surfaces. It is assumed that the interaction of the impeller with the shown flow structures are the source of the

subharmonic humps. The precise analysis of the noise generation mechanism inside the impeller induced by that interaction is content of future investigations. In the next section, an analysis is presented to characterize the rotating flow structures in a more tangible and quantifiable way in order to solidify the hypothesis that they are the original source of the subharmonic humps.

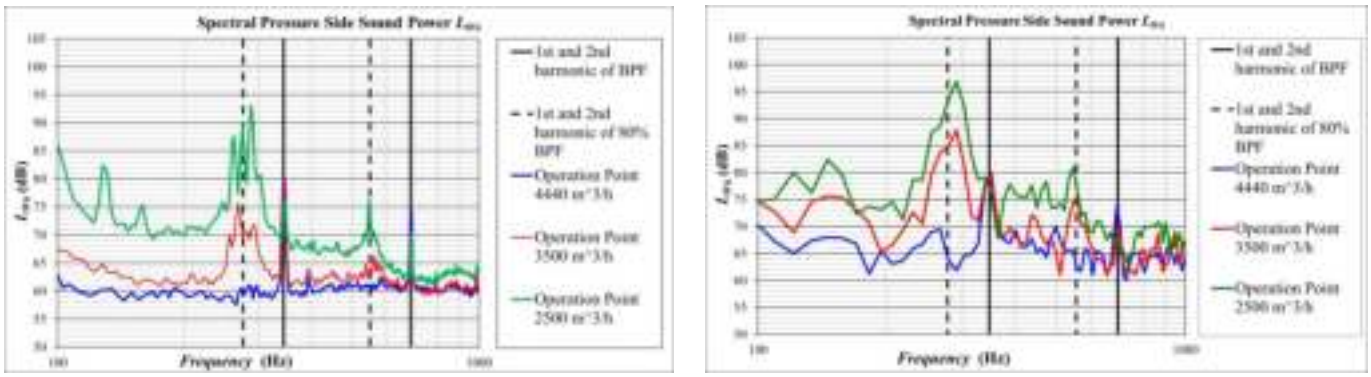

(**a**) (**b**)

Figure 4. Comparison of spectral results: (**a**) review of the experimental spectral results of Figure 2b; (**b**) numerical spectral results of the pressure side sound power level L_{W6} for the same three operation points (**b**).

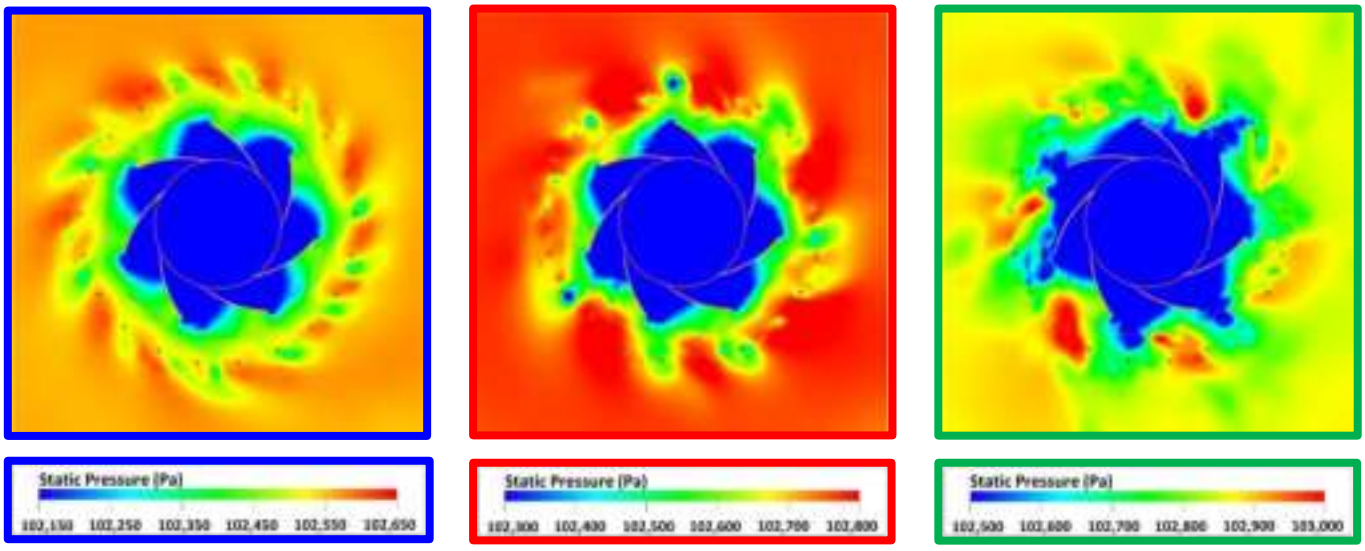

(**a**) (**b**) (**c**)

Figure 5. Instantaneous static pressure distributions at a plane cut in the middle between hub and rotating shroud (50% Span): (**a**) Q_V = 4440 m^3/h; (**b**) Q_V = 3500 m^3/h; (**c**) Q_V = 2500 m^3/h.

3.3. A Modal Analysis of the Flow Structures Based on Numerical Results

A somewhat intuitive analysis has been carried out to identify and characterize rotating flow structures with respect to their rotation speed and strength as function of operation point and radial and axial position. It was derived inspired by the method described in [12], with the aim to get additionally a quantitative evaluation of the amplitudes of the flow structures. In the analysis, an auxiliary "observer" grid consisting of co-axial circles with a discrete and equidistant discretization in circumferential (θ) direction is considered. This "observer" grid is rotated with arbitrary "test"-rotation speeds σ_i. At each instant, the unsteady flow data from a simulation is interpolated onto the "observer" grid. The flow field is then averaged in time. Note that an observer (grid) that would rotate at the

same rotation speed as a spatial flow structure would observe this spatial structure as stationary. Thus, for this "synchronous" test rotation speed σ_i, after temporal averaging, the structures will still be present in the averaged fields. On the other hand, when the observer test rotation speed σ_i differs significantly from the flow structure's rotational speed, structures will be smoothed out by the temporal averaging operator, assuming sufficiently long averaging time. So, the time-averaged flow data on each rotating observer grid represents spatial flow structures that rotate at the rotational speed σ_i. The described averaging has been carried out for a sufficiently high number of test rotation speeds σ_i. Some filtering technique has been applied in order to minimize the aliasing error in time associated with the interpolation from the cubic element grid from the simulation. The next step of the procedure consists of a circumferential Fourier transform for each test rotation speed σ_i in order to quantify periodic rotating modes. In Figure 6, some representative results of the analysis are presented.

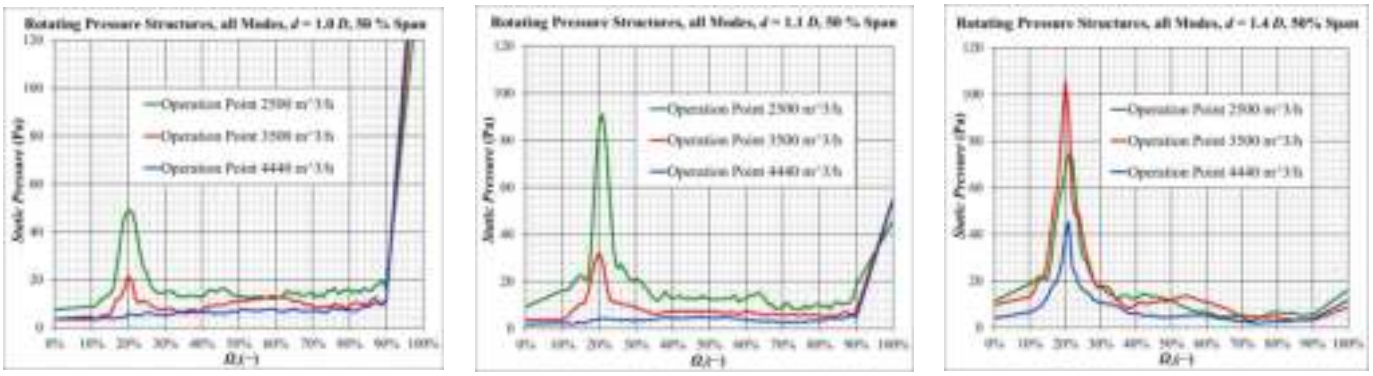

(**a**) (**b**) (**c**)

Figure 6. Results of modal analysis of the rotating structures downstream of the fan wheel at Midspan, for radial positions: (**a**) at d = 1.0 D; (**b**) at d = 1.1 D; (**c**) at d = 1.4 D.

The Relative Spin Ω_r is defined as the ratio of test rotation speed σ_i and the impeller rotation speed: $\Omega_r = \sigma_i/n$. For each relative spin Ω_r and flow quantity f of interest (for example, pressure or velocity), the time average over the five revolutions considered of the retarded function $f\left(\vec{x} + \Omega_r \cdot n \cdot \vec{r} \cdot t\right)$ is computed resulting in a spatial flow field $\widetilde{f}_{\Omega_r}\left(\vec{x}\right) = \left\langle f\left(\vec{x} + \Omega_r \cdot n \cdot \vec{r} \cdot t\right)\right\rangle$ with the time average operator $\langle \cdot \rangle$, which is subsequently analyzed by spatial Fourier analysis in circumferential direction at different axial and radial positions. The energy of all spatial pressure fluctuation modes of all wave numbers (the L2 norm of all Fourier coefficients unless the mean value as obtained by Fourier transform in circumferential direction) is shown in Figure 6 as function of Ω_r. In Figure 6a, the rotating pressure fluctuation is given for a circle located at mid-span with a diameter d corresponding to the impeller outer diameter D, that is, probe locations are very close to the blade trailing edges. In Figure 6b the diameter d is 110% D; and in Figure 6c the circle diameter is 140% D. What can be observed is:

- A 1st kind of distinct rotating structures can be observed at Ω_r = 100 % (very right point in each graph). These are the expected co-rotating structures directly issued from the blades. Moving away from the blade, rotating structures at this Ω_r decrease rapidly.
- A 2nd kind of significative rotating structures can be observed, which has its maximum at $\Omega_r \approx 20$ % (for the given particular impeller). Near the blade trailing edge at d = 1.0 D and d = 1.1 D ((a) and (b)), the amplitude of the fluctuation increases significantly with decreasing volume flow rate Q_V. The rotating structures have at a diameter of the blade trailing edge an important strength, especially for lower volume flow rates Q_V (Figure 6a, comparison of the three operation points).

- The interaction frequency of a rotating flow structures is $f_0 = (1 - \Omega_r) \cdot \mathrm{BPF}$. With $\Omega_r = 20\%$, we get $f_0 = 80\% \cdot \mathrm{BPF}$ with consistency to what has been observed in Figures 2 and 4.
- Moving radially further from the blade trailing edges, the strength of the rotating fluctuations with $\Omega_r = 20$ % increases and dominates over the 1st kind of fluctuations that co-rotate with the impeller.
- The rotating frequency of the fluctuations is not concentrated sharply at $\Omega_r = 20$ %, but has a significant dispersion, similarly to the broad shape of the subharmonic humps in the acoustic spectra.
- At $d = 1.4\ D$, the strength of the rotating structures for $Q_V = 2500\ \mathrm{m}^3/\mathrm{h}$ already decreases, whilst the strength of the rotating structures for $Q_V = 3500\ \mathrm{m}^3/\mathrm{h}$ still increases. The rotating structures come closer to the blade trailing edges when reducing the volume flow rate. This may be observed qualitatively also in Figure 4.

4. Fan Optimization

4.1. Numerical Investigations of Geometrical Modifications on the Downstream Side

Some geometrical modifications have been investigated with the objective to reduce the strength of the rotating flow structures with a relative rotational speed downstream in the vicinity of the blade trailing edges; or at least shift their appearance towards even lower volume flow rates. The investigated modifications consist of different vertical panels that result in convergent (or just moderately divergent) flow channels downstream the impeller. The result of one interesting modification is presented, whilst others showed effectiveness as well. The modified geometry leads to flow acceleration and stabilizes the flow downstream of the impeller. It may be seen as a simple kind of stator vane. Less rotating vortical structures build up or are washed further away from the blade trailing edges. This is clearly visible by comparing the flow picture on a plane midspan cut for the operation point $Q_V = 2500\ \mathrm{m}^3/\mathrm{h}$ of Figure 7b, with modification, and Figure 7c, without modification. With the modification, significantly less vortical structures are present near the blade trailing edges, and more deterministic and better organized flow structures can be detected. This observation is supported by the modal analysis in Figure 8a. As presumed in the discussion of Figure 7, significantly less important rotating structures at $\Omega_r = 20\%$ are present with the modification. For $\Omega_r = 0\%$, at the very left point of the graphs, representing the stationary spatial pressure fluctuations in circumferential direction, a clearly visible enhancement can be observed when using the modification due to the presence of a stator structure. The spectral content of the pressure side sound power L_{W6} is shown in Figure 8b. Clearly, the subharmonic humps are strongly reduced. As a side effect, the BPF harmonics are higher as spatial periodical stationary fluctuations are induced by the stator structure, interacting with the impeller blades.

4.2. Experimental Data of an Implementation

Experimental results of the modification are shown. The geometry of the investigated pressure side optimization, which is similar to the structure investigated in the previous section and shown in Figure 7a, is depicted in Figure 9a, where it is installed on the test rig with an electrical drive. The comparison is based on measurements with a different impeller with five three dimensionally shaped blades. A wavy contour at the leading edges of the stator device has been applied in order to reduce the tonal noise resulting from rotor-stator interaction. Figure 9b shows a comparison of the characteristic curves of the measurements without and with the optimization device. Interestingly, the reachable pressure rise, and static efficiency are significantly enhanced. Similar to stator vanes, the added plates help in the pressure recovery from swirl.

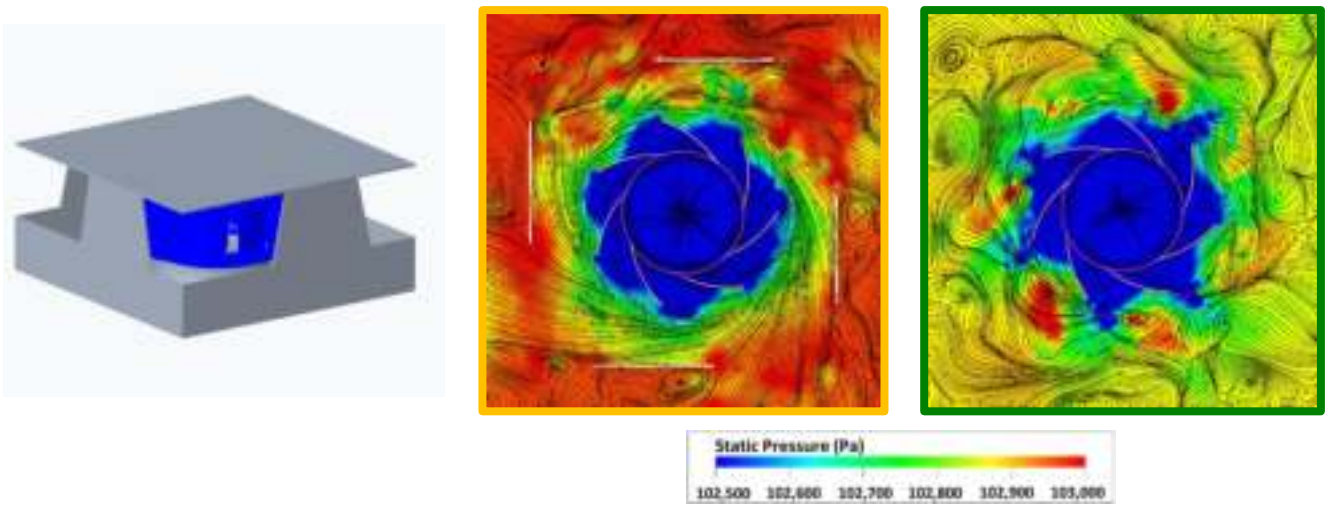

(**a**) (**b**) (**c**)

Figure 7. Results of the numerical investigation of a geometrical modification: (**a**) Sketch of the investigated geometrical modification; (**b**) instantaneous static pressure distributions with streamlines at a midspan plane cut for Q_V = 2500 m^3/h with installed modification; (**c**) static pressure distributions without modification.

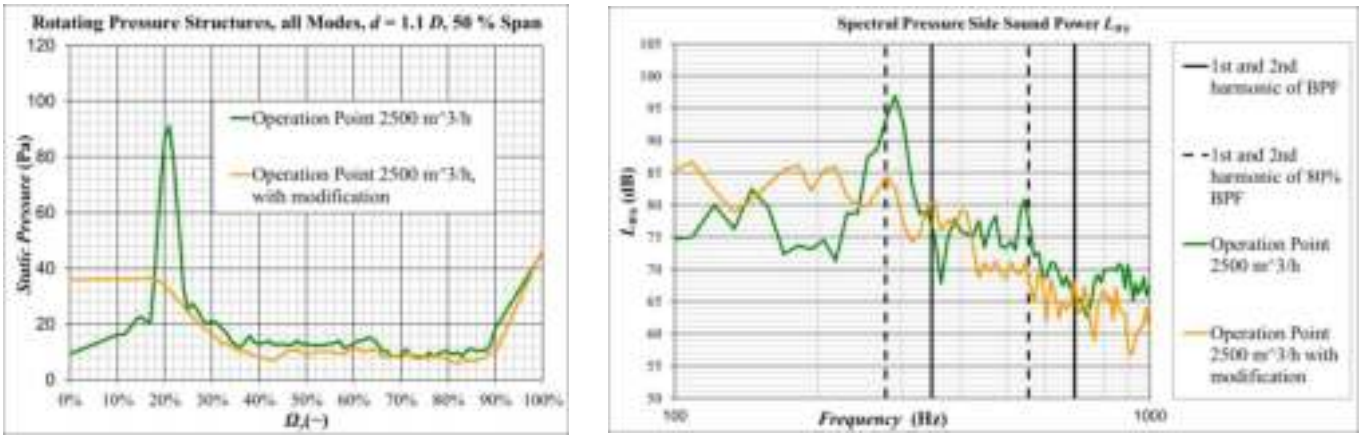

(**a**) (**b**)

Figure 8. Correlation of rotating structures and sound spectre: (**a**) modal analysis of rotating structures; (**b**) spectral content of Pressure Side Sound Power Level L_{W6}.

In Figure 10, comparisons of the sound power levels are presented. At the left (a), the A-weighted sound power level L_{WA6} is shown as function of the volume flow rate Q_V. At the right (b), for the operation point at Q_V = 6000 m^3/h, the spectral distribution of L_{WA6} can be seen. The frequencies are made dimensionless by the BPF. In Figure 10a it can be observed that the pressure side sound power is improved by the modification device at the left half of the duty curve, and the sound power reduction gets higher, up to 2 dB(A), for lower volume flow rates Q_V. In Figure 10b, it is clearly visible that subharmonic humps are present for this centrifugal fan both with and without modification device, especially at the first subharmonic order at about 80% of BPF. With the modification device, the humps are significantly reduced at the same volume flow rate confirming the observations obtained from the numerical investigations. The optimization is achieved by solely applying the downstream device, without modification of inflow conditions or anything in direct vicinity of the impeller, confirming the findings presented in this paper. The application of the pressure side optimization device, on the other hand, leads to an increase of tonal noise,

especially at the first order, due to rotor–stator interaction, which is acceptable in the present case due to the relatively big distance (about 1.6 times of the impeller diameter) between impeller blade trailing edges and the wavy leading edges of the stator device. It is however interesting to consider that subharmonic noise is mitigated technically towards tonal noise at harmonics of the BPF, as due to the stator device, we get stationary flow structures rather than rotating flow structures interacting with the impeller blades.

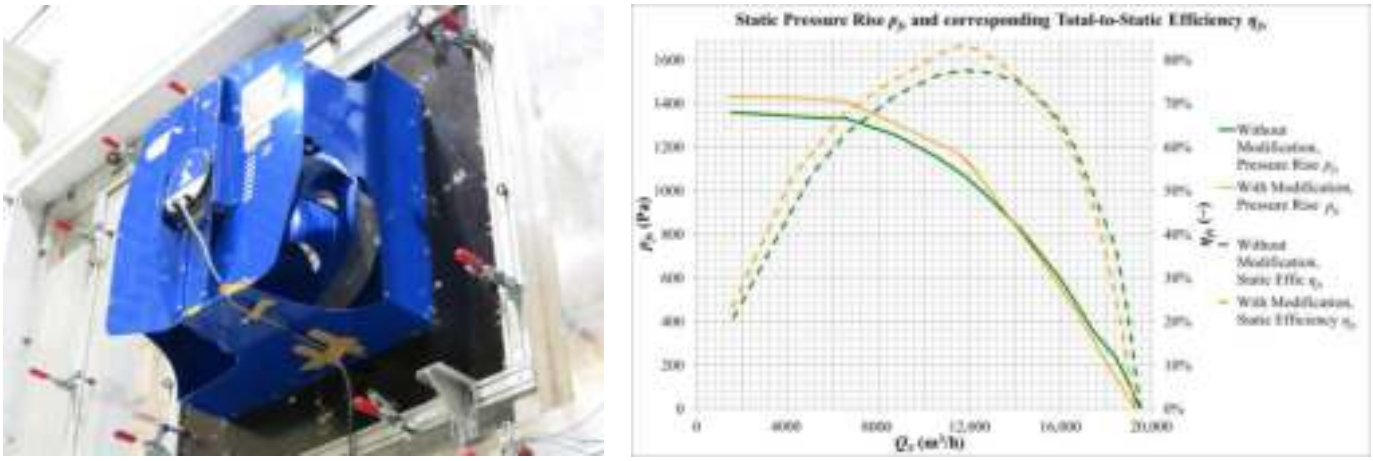

(**a**) (**b**)

Figure 9. Experimental results for a fan with downstream modification: (**a**) photograph of implementation of a downstream modification on test rig; (**b**) and characteristic curves of static pressure rise p_{fs} and total-to-static efficiency η_{fs}.

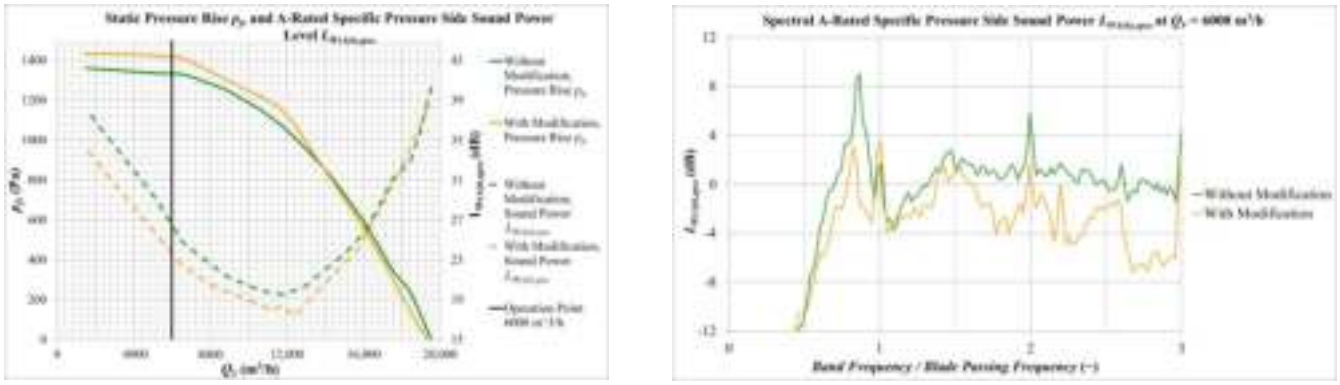

(**a**) (**b**)

Figure 10. Experimental evaluation of the impact of the downstream modification in A-weighted pressure side specific sound power L_{WA6} for the configuration of Figure 9: (**a**) sound power sum; (**b**) spectral distribution.

5. Conclusions

Centrifugal fans without housing, amongst others, suffer from emerging subharmonic humps when decreasing volume flow rates. The sound power level increases drastically on the part load side from the optimal operation point. This is called a sound power surge. These are distinct regions in the spectra at harmonic multiples of 40–80% of the blade passing frequency (BPF), in particular the first harmonic that is largely dominating the sound power spectra. This noise phenomenon is associated with rotating flow structures downstream of the impeller, which interact with the trailing edge of the blades. For a specific fan, this was shown by using a numerical investigation using the Lattice Boltzmann method. A modal analysis has been performed on data collected downstream of the

trailing edge. The dominant rotational speed of these flow structures is about 20% of the impeller rotation speed with the same rotation direction as the impeller. This result explains quantitatively the frequency regions (80% of BPF and multiples thereof, which is the basic interaction frequency between the impeller blades and the rotating structures) where the subharmonic humps occur. The rotating flow structures are self-induced by the impeller and supplied by detaching vorticity of the blade suction side surfaces. Two possible explanations can be given why the subharmonic humps grow with decreasing volume flow rate: Firstly, more vorticity is generated by the blades due to growing flow separations, and secondly, the vortices are washed away in a less effective manner due to the reduced volume flow rates. Several downstream modifications have been investigated in order to control the rotating flow structures. One example device was demonstrated both numerically and experimentally in this paper. The reduction of the rotating flow structures was proven by the numerical modal analysis model; and the resulting reduction of subharmonic noise generation was also shown by an experimental comparison. Interestingly, also the achievable pressure rises, and total-to-static efficiency is improved in regions of the duty curve, where subharmonic humps are reduced by the optimization device. This leads to the conclusion that the rotating flow structures have a negative impact on the swirl conversion into static pressure. The experimental results for the pressure side modification confirm the arguing derived from the numerical observations.

Author Contributions: Conceptualization, F.L.; methodology, F.L., S.H., M.S. and S.M.; software, S.H.; validation, F.L. and S.H.; writing—original draft preparation, F.L., S.H.; writing—review and editing, F.L., S.H., M.S., S.M.; visualization, S.H. All authors have read and agreed to the published version of the manuscript.

Funding: This research received no external funding.

Informed Consent Statement: Not applicable.

Data Availability Statement: Not applicable.

Conflicts of Interest: The authors declare no conflict of interest.

References

1. Kameier, F.; Neise, W. Experimental Study of Tip Clearance Losses and Noise in Axial Turbomachines and Their Reduction. *J. Turbomach.* **1997**, *119*, 460–471. [CrossRef]
2. Mongeau, L.; Thompson, D.E.; McLaughlin, D.K. Sound Generation by Rotating Stall in Centrifugal Turbomachines. *J. Sound Vib.* **1993**, *163*, 1–30. [CrossRef]
3. Zhu, T.; Lallier-Daniels, D.; Sanjosé, M.; Moreau, S.; Carolus, T. Rotating coherent flow structures as a source for narrowband tip clearance noise from axial fans. *J. Sound Vib.* **2018**, *417*, 198–225. [CrossRef]
4. Bhatnagar, P.L.; Gross, E.P.; Krook, M. A Model for Collision Processes in Gases. I. Small Amplitude Processes in Charged and Neutral One-Component Systems. *Phys. Rev.* **1954**, *94*, 511–525. [CrossRef]
5. Chen, S.; Doolen, G.D. Lattice Boltzmann method for Fluid Flow. *Annu. Rev. Fluid Mech.* **1998**, *30*, 329–364. [CrossRef]
6. Marié, S. Etude de la méthode Boltzmann sur Réseau pour les Simulations en Aéroacoustique. Ph.D. Thesis, Université Pierre et Marie Curie, Paris VI, Paris, France, 2008.
7. Chen, H.; Filippova, O.; Hoch, J.; Molvig, K.; Shock, R.; Teixeira, C.; Zhang, R. Grid refinement in Lattice Boltzmann methods based on Volumetric Formulation. *Phys. A Stat. Mech. Its Appl.* **2006**, *362*, 158–167. [CrossRef]
8. Pérot, F.; Kim, M.S.; Moreau, S.; Henner, M.; Neal, D. Direct Aeroacoustics Prediction of a Low Speed Axial Fan. In Proceedings of the 16th AIAA/CEAS Aeroacoustics Conference, Stockholm, Sweden, 7–9 June 2010.
9. Fares, E. Unsteady flow simulation of the Ahmed ref. body using a Latt.-Boltz Approach. *Comp. Fluids* **2006**, *35*, 940–950. [CrossRef]
10. Wolfram, D.; Carolus, T. Experimental and Numerical Investigation of the Unsteady Flow Field and Tone Generation in an Isolated Centrifugal Fan Impeller. *J. Sound Vib.* **2010**, *329*, 4380–4397. [CrossRef]
11. Sturm, M.; Sanjosé, M.; Moreau, S.; Carolus, T. Aeroacoustic Simulation of an Axial Fan including the Full Test Rig by using the Lattice Boltzmann Method. In Proceedings of the Fan 2015 Conference, Lyon, France, 15–17 April 2015.
12. Towne, A.; Schmidt, O.T.; Colonius, T. Spectral proper orthogonal decomposition and its relationship to dynamic mode decomposition and resolvent analysis. *J. Fluid Mech.* **2018**, *847*, 821–867. [CrossRef]

International Journal of
Turbomachinery
Propulsion and Power

MDPI

Article

Uniformity Index as a Universal Air-Cooled Condenser Fan Performance Metric

Fredrik Marincowitz [1], Michael Owen [2,*], Jacques Muiyser [3] and Peter Holkers [3]

[1] Solar Thermal Energy Research Group, Stellenbosch University, Stellenbosch 7600, South Africa
[2] Department of Mechanical and Mechatronic Engineering, Stellenbosch University, Stellenbosch 7600, South Africa
[3] Howden Netherlands, 7554 PA Hengelo, The Netherlands
* Correspondence: mikeowen@sun.ac.za

Abstract: Ambient wind has a negative effect on mechanical forced-draft direct air-cooled steam condenser (ACC) fan volumetric performance, and increases dynamic fan blade loading. Investigating these effects directly using on-site measurement or numerical analysis is complicated, and most previous work has focused on only one effect at the expense of the other. In this study, fan axial velocity inflow uniformity is identified as a single metric offering the potential to holistically qualify ACC fan operation under windy conditions. A 3 × 6 fan cell ACC was modelled with CFD using a blade element theory-based fan model, and clear relationships between the fan inflow uniformity index and both fan volumetric performance and dynamic blade loading were observed in the results. The same relationships were observed in on-site test data collected at a single ACC fan, thus validating the numerical results. The uniformity index can be used in both numerical and experimental work as a means of investigating both fan volumetric performance and dynamic blade loading with less computational and measurement complexity; it also offers a potentially useful means of quantifying the severity of fan operating conditions, to assist with more reliable case-specific fan design and selection.

Keywords: axial flow fans; air-cooled condensers; wind effects; fan performance; dynamic blade loading; computational fluid dynamics

check for updates

Citation: Marincowitz, F.; Owen, M.; Muiyser, J.; Holkers, P. Uniformity Index as a Universal Air-Cooled Condenser Fan Performance Metric. *Int. J. Turbomach. Propuls. Power* **2022**, *7*, 35. https://doi.org/10.3390/ijtpp7040035

Academic Editor: Thomas Carolus

Received: 29 August 2022
Accepted: 14 November 2022
Published: 1 December 2022

Publisher's Note: MDPI stays neutral with regard to jurisdictional claims in published maps and institutional affiliations.

Copyright: © 2022 by the authors. Licensee MDPI, Basel, Switzerland. This article is an open access article distributed under the terms and conditions of the Creative Commons Attribution (CC BY-NC-ND) license (https://creativecommons.org/licenses/by-nc-nd/4.0/).

1. Introduction

Mechanical forced-draft direct air-cooled steam condensers (ACCs) are widely employed as condenser technology in thermal energy systems (steam cycles). ACCs use large axial fans to force ambient air through A-frame heat exchangers (Figure 1) and reject the required heat load to maintain the steam turbine backpressure at or near its design point. The thermal performance of an ACC is both directly and indirectly influenced by ambient wind via: (1) a reduction in fan volumetric performance and increased inlet air temperatures with increasing wind speed [1]; and (2) increased dynamic fan blade loading of the upwind edge fans. Dynamic blade loading results in increased gearbox wear and accelerated blade fatigue, and can result in physical damage to the fan blades [2]. Subsequently, the ACC will experience more frequent repair and maintenance outages and poorer average thermal performance.

Wind effects on ACC fans are caused by an increase in the horizontal velocity component of the air moving beneath the fan platform (cross-flow) under windy conditions. High cross-flow past the fan inlets causes distortions in the inlet flow distribution [3]. This non-uniform inlet flow negatively affects the fans' ability to deliver their rated air volume flow rate [3], and results in a variation in aerodynamic loading on the fan blades as they rotate through the non-uniform flow field [4]. There are two types of cross-flow-related inlet flow distortions identified in the literature: flow separation at the fan inlet [3,5] and off-axis inflows [6,7] (shown in Figure 1). Flow separation at the fan inlet is considered the

dominant cause of the wind-related degradation in fan volumetric performance [3] and increased dynamic fan blade loading [8].

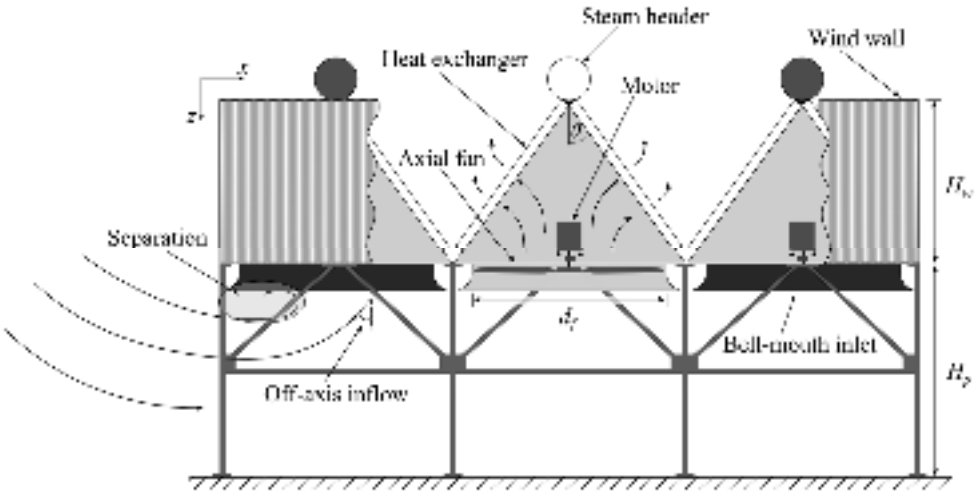

Figure 1. Air-cooled condenser schematic showing primary components and wind effects.

Wind effects on ACCs are primarily investigated via full-scale testing at operating ACCs (e.g., [2,9]), or via computational fluid dynamics (CFD) simulation (e.g., [10,11]). On-site measurement provides "true" information but is complicated by uncontrollable environmental variables, the need for specialist measurement equipment and the difficulty of accurately measuring on-site wind velocity. In on-site testing, ACC fan volumetric performance is quantified using propeller anemometer measurements at various radial and tangential locations on the fan's inlet grid [2,9]. These anemometers are used to measure the axial velocity at these fixed locations within the fan inlet, and are subsequently used to calculate the volume flow rate or average axial velocity through the fan. The CTI-PTG-143 standard [12] recommends 40 anemometer measurements (four quadrants with 10 measurements at equal radial spacing per quadrant) for fans with diameters exceeding 20 ft., as is common in ACCs (typically around 36 ft.). This makes continuous measurement of on-site airflow difficult, as it requires a large quantity of measuring equipment. Dynamic fan blade loading can be accurately evaluated using bending strain measurements, typically using strain gauges attached to the root of a fan blade in a full-bridge configuration [9]. Access to the fan blades for installation of strain gauges requires the fan to be stopped, and can complicate the scheduling of on-site tests (i.e., it may not be possible to stop a fan when the test engineers would ideally want access to the blades).

Numerical studies using CFD avoid the complications of on-site testing, and offer more control and flexibility in the analysis; they do, however, require simplifying assumptions, and are thus exposed to lower accuracy. Numerical studies tend to focus on fan volumetric performance, due to the challenges related to the prediction of dynamic blade loading in CFD. Dynamic blade loading can, however, be approximated numerically. This has been done by either utilising a blade element theory-based fan model, that makes it possible to calculate a flap-wise bending moment distribution [7,13], or by analysing the variation in static pressure within the fan rotational plane [14]. Of the two methods, only the flap-wise bending moment distribution method has been directly evaluated against experimental blade loading trends [15].

The literature relating to ACC fans and wind effects tends to focus on either volumetric performance or dynamic blade loading, due to the difficulties related to determining the former in full scale experimental work and the latter in numerical work. That these two performance metrics are related is implicit, as they are both affected by the same phenomenon: distorted inflow.

Laboratory research [8], conducted using a system meant to mimic ACC fan operating conditions, has indicated that the uniformity of the axial velocity inflow to a fan could be

used to indicate the severity of the dynamic blade loading. Furthermore, the uniformity of the inflow axial velocity should have a proportional relationship with fan volumetric performance. For a uniform distribution, the fan is likely to be operating close to design conditions. Increasingly non-uniform inflow is indicative of off-design conditions, and would therefore typically result in reduced volumetric performance. The uniformity of the axial velocity at the fan inlet therefore potentially offers a single metric that could be determined experimentally or with CFD, and which could be used to infer both fan volumetric performance and dynamic blade loading.

This study uses a CFD-based approach to investigate the relationship between ACC fan inflow uniformity, quantified by means of a uniformity index, and both fan volumetric performance and dynamic blade loading under windy conditions. The numerical correlations were also validated against on-site test data obtained from a third party.

2. Materials and Methods

2.1. Numerical Model

The numerical model consisted of a 3 × 6 fan cell ACC placed in a large flow domain (see Figure 2). Simulations were run in ANSYS Fluent 20 R1 using the steady, single-precision, pressure-based solver. Second-order discretization was used for the energy equation, and first-to-higher-order blended discretisation was applied to the momentum equations to improve the convergence of the fan model. Turbulence was modelled using the realizable k-ε model with standard wall functions (consistent with, e.g., [16,17]) and first-order upwind discretization. Buoyancy was accounted for using the Boussinesq approximation. A detailed description of the model, including information on grid sensitivity analyses, is available in [18].

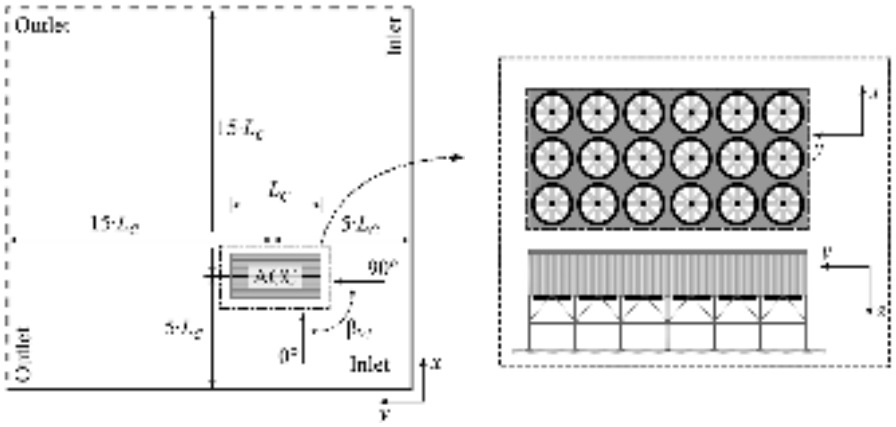

(**a**) (**b**)

Figure 2. Computational domain for $0° \leq \beta_w \leq 90°$: (**a**) top view; (**b**) 3 × 6 fan array layout.

Figure 2 shows the location of the domain inlet and outlet boundaries for $0° \leq \beta_w \leq 90°$ as well as the definition of the wind direction (β_w) used in this paper. The domain dimensions were based on Franke et al.'s [19] recommendations for computational modelling for wind engineering purposes. The ACC's longest dimension was used as a conservative characteristic length (L_c), and a domain height (*z*-direction) of $6L_c$ was used. Richards and Hoxey's [20] atmospheric wind boundary profiles for the z-velocity distribution, turbulent kinetic energy and dissipation rate were used to simulate a horizontally homogeneous turbulent atmospheric boundary layer when using a k-ε turbulence model. The wind speed (v_w) and direction ranges considered were $1 \leq v_w \leq 11$ m/s and $-90° \leq \beta_w \leq 90°$. Note that the computational domain shown in Figure 2 was mirrored for $-90° \leq \beta_w < 0°$ such that the relative inlet and outlet boundary positions remained appropriate for all wind directions.

Each fan cell consisted of an axial flow fan, an A-frame heat exchanger and a steam supply duct, as shown in Figure 3.

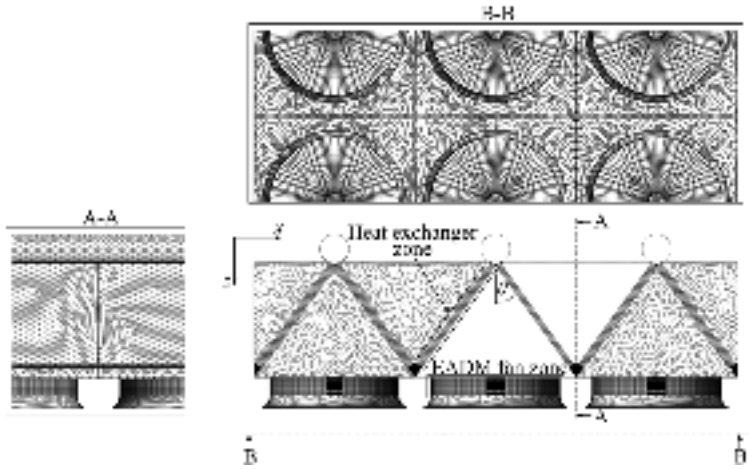

Figure 3. Numerical fan cell configuration and mesh.

The ACC's finned tube heat exchangers (see Table 1) were modelled using porous media zones with appropriate momentum sink and energy source terms to replicate the flow resistance and heat transfer rate. Momentum sink terms for the x, y and z momentum equations were defined by the Darcy–Forcheimer equation, with the viscous and inertial loss coefficients derived from the empirical pressure loss coefficients [21]. The energy source term was calculated using the e-NTU method of heat exchanger analysis [22] with the empirical heat transfer characteristics provided in [21].

Table 1. Heat exchanger specifications.

Parameter Name	Symbol	Value
Tube length	L_t	10 m
Number of tubes (row 1)	n_{t1}	228
Number of tubes (row 2)	n_{t2}	232
Inner tube height	H_t	0.097 m
Inner tube width	W_t	0.017 m
Half apex angle	θ	36°
Heat exchanger frontal area	A_{fr}	137.7 m^2

The axial flow fan considered in this work was based on a commercially available industrial fan; the specifications are given in Table 2.

Table 2. Axial fan specifications.

Parameter Name	Symbol	Value
Fan diameter	d_f	10.363 m
Hub diameter	d_h	1.4 m
Number of blades	n_b	9
Rotational speed	N	93.2 rpm
Design flow rate [1]	$\dot{V}$	576.54 m^3/s
Design pressure rise [1]	Δp	119.8 Pa

[1] At a reference air density of ρ_a = 1.22 kg/m^3.

The fans were modelled using the Extended Actuator Disk Fan Model (EADM—see [23] for a full description), similar to [16,17]. The EADM is an adaptation of the blade element theory-based actuator disk model [4], and was implemented in a structured grid region with single element thickness and n_r = 20 radial and n_θ = 120 tangential divisions representing the fan's rotor (see Figure 3, plane B–B). Each rotor region cell was approximated as a two-dimensional aerofoil (blade element) with lift (δL) and drag (δD)

forces dependant on the relative velocity (w_m) and the lift (C_L) and drag (C_D) coefficients of the blade element's aerofoil profile. The relative velocity was calculated from the incoming velocity vector (v_m) and the tangential velocity (Ω_r) linked to the fan speed. The lift and drag forces were introduced into the solver's momentum equations as axial (Equation (1)) and tangential (Equation (2)) source terms:

$$S_z = \frac{-\delta f_z}{\delta V} = -\frac{1}{2}\rho\, w_m^2\, \frac{\sigma}{t}(C_L \cos\beta_m - C_D \sin\beta_m), \tag{1}$$

$$S_\theta = \frac{\delta f_\theta}{\delta V} = \frac{1}{2}\rho\, w_m^2\, \frac{\sigma}{t}(C_L \sin\beta_m + C_D \cos\beta_m), \tag{2}$$

where β_m was the relative velocity angle, as shown in Figure 4, t was the rotor-zone thickness and σ was the blade solidity. Figure 4 shows the velocity vectors and force directions for a single blade element:

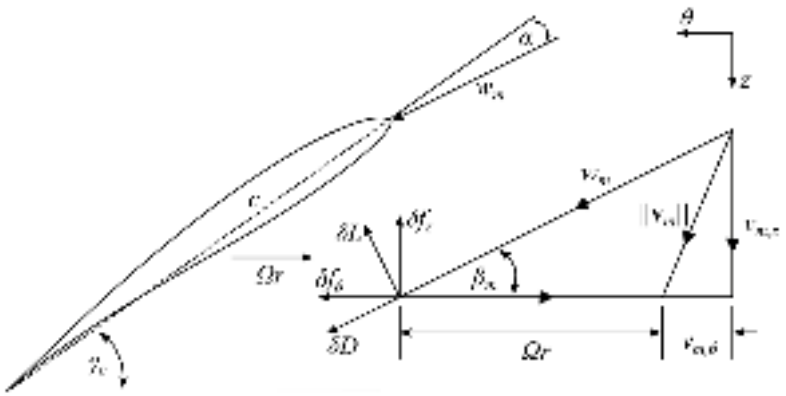

Figure 4. EADM vector diagram.

2.2. Numerical Evaluation Metrics

A uniformity index of unity represents perfectly uniform flow. The variation in the axial velocity within the fan rotor region was quantified using the uniformity index (γ_i) defined in Equation (3) [24]:

$$\gamma_i = 1 - \frac{\sum_{k=1}^{n_r}\sum_{j=1}^{n_\theta}\left|v_{z,kj} - \overline{v}_{Az}\right|A_{z,kj}}{2\overline{v}_{Az}\sum_{k=1}^{n_r}\sum_{j=1}^{n_\theta}A_{z,kj}}, \tag{3}$$

where $v_{z,kj}$ was the axial velocity in element (k,j) of the fan's rotor region, $A_{z,kj}$ was the corresponding surface area normal to the axial direction and $\overline{v}_{Az}$ was the area-weighted average axial velocity given by Equation (4):

$$\overline{v}_{Az} = \frac{\sum_{k=1}^{n_r}\sum_{j=1}^{n_\theta} v_{z,kj}A_{z,kj}}{\sum_{k=1}^{n_r}\sum_{j=1}^{n_\theta}A_{z,kj}}, \tag{4}$$

The volumetric performance of each individual fan was quantified using a volumetric effectiveness metric (ξ_i), as shown in Equation (5):

$$\xi_i = \frac{\overline{v}_{Az,i}}{\overline{v}_{Az,id}}, \tag{5}$$

where $\overline{v}_{Az,i}$ was the area-weighted average axial velocity through fan (i) and $\overline{v}_{Az,id}$ was the "ideal" area-weighted average axial velocity through the fan with the most uniform axial velocity (highest uniformity index) within the dataset.

The flap-wise bending moment distribution ($M_{z,\theta}$) was used to evaluate the fan blade loading [7,13]. This distribution was calculated using the differential axial forces ($\delta f_{Z,kj}$, see Equation (1)) exerted on each of the rotor region elements, as shown in Equation (6):

$$m_{z,j} = \sum_{k=1}^{n_r} \delta f_{z,kj} \left(r_{kj} - r_h \right) \text{ for } j = 1, \ldots, n_\theta, \tag{6}$$

where $m_{z,j}$ was the jth entry of the $M_{z,\theta}$ array, r_{kj} was the radius to the center of element (k,j) and r_h was the fan hub radius.

The peak bending moment (M_p) (Equation (7)) was used as the indicator of the severity of the dynamic blade loading. Venter [15] found this metric to provide the best correlation to experimental dynamic blade loading trends:

$$M_p = \max(|\mathrm{M}_{z,\theta}|), \tag{7}$$

This peak bending moment was normalized with the peak bending moment at the "ideal" most uniform inlet airflow condition ($M_{p,id}$ at $\overline{v}_{Az,id}$), as per Equation (8):

$$\phi_i = \frac{M_{p,i}}{M_{p,id}}, \tag{8}$$

2.3. Experimental Measurements and Evaluation Metrics

Experimental data collected during tests described in [2] were used for validation of the CFD results in this study. The on-site tests conducted in [2] took place at a power plant that utilized a 3 × 6 cell ACC (Figure 5) with a fan platform height of H_p/d_f = 1.353, and the same axial fan was used in the numerical model. The axial flow and blade loading data of a single fan over a three-day period are used here. The wind direction within this time period was predominantly south-westerly to north-westerly (i.e., $-45° \leq \beta_W \leq 45°$).

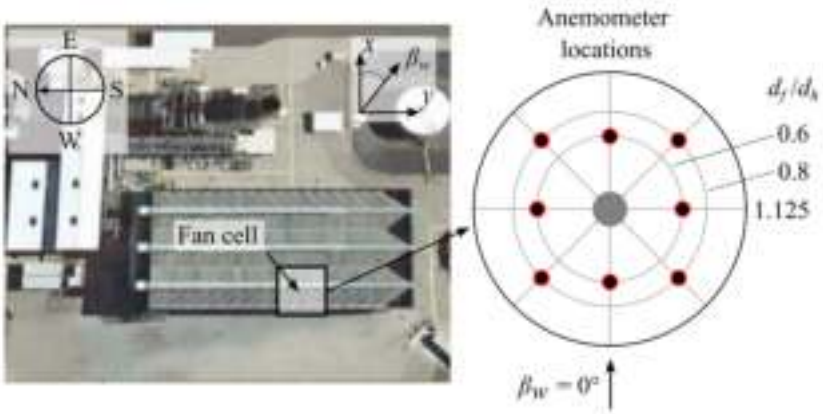

Figure 5. ACC layout and anemometer locations (adapted from [2]).

The fan and anemometer locations on the fan inlet screen are shown in Figure 5. Blade loading was measured using load cells installed at the retaining bolts of six of the nine fan blades. Data from a single load cell are considered here. The raw data (anemometers and load cell) were processed into average and standard deviation values, calculated over three-minute interval segments.

The experimental uniformity index (γ_{ex}) was quantified using the average axial velocity ($\overline{v}_z$) of the eight anemometer measurements (n_a = 8), and not the area-weighted average. Equation (3) was therefore adapted to yield Equation (9):

$$\gamma_{ex} = 1 - \frac{\sum_{j=1}^{n_a} \left| v_{z,j} - \overline{v}_z \right| / n_a}{2\overline{v}_z}, \tag{9}$$

The fan volumetric performance is presented in terms of volumetric effectiveness (ξ_{ex}, Equation (5)) using the average of the eight anemometer measurements. The experimental dynamic blade loading was expressed as a normalized peak load (ϕ_{ex}) using Equation (8). The peak load (L_p) was determined from the standard deviation of the load cell measurement over the three-minute interval (L_σ), using Equation (10) based on the assumption that the signal was purely sinusoidal:

$$L_p = L_\sigma \sqrt{2}, \tag{10}$$

3. Results

3.1. The Effect of Uniformity Index on Fan Performance and Dynamic Blade Loading

Figure 6 shows the numerically predicted individual fan cell volumetric effectiveness (ξ_i, Equation (5)) and uniformity index (γ_i, Equation (3)), for the 3 × 6 cell ACC at a wind speed of v_w = 7 m/s.

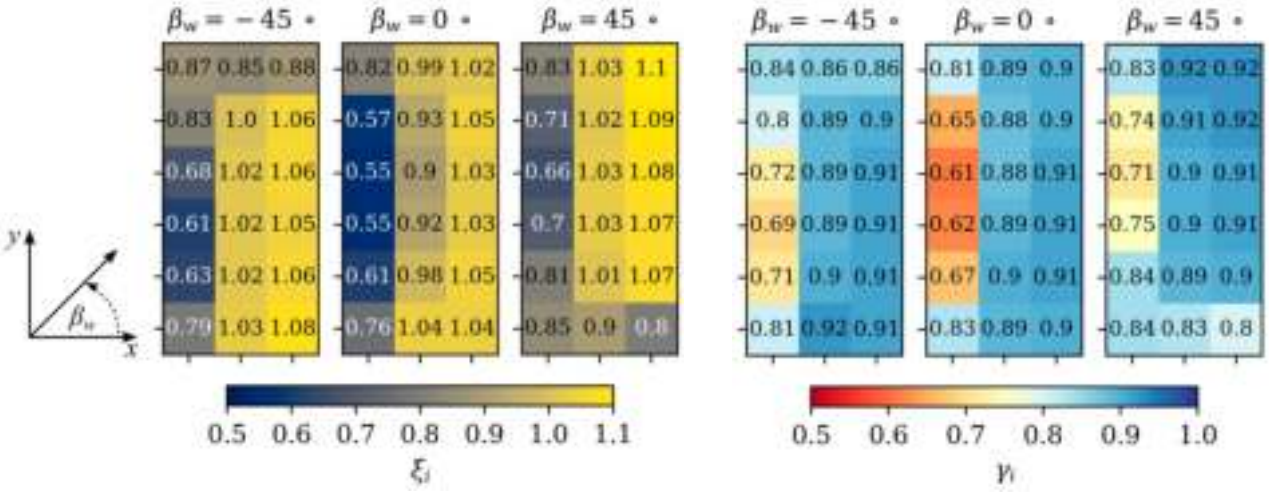

(**a**) (**b**)

Figure 6. Numerically predicted individual fan cell: (**a**) volumetric effectiveness; (**b**) uniformity index, with changing wind direction (v_w = 7 m/s).

Figure 6 shows similar trends in both volumetric effectiveness (ξ_i) and uniformity index (γ_i). This is expected since, for a uniformity index close to unity, the fan is likely operating close to design or "ideal" conditions, and thus $\xi_i \to 1$. A decreasing uniformity index implies that the fan is subjected to distorted inlet conditions, which are known to negatively impact the volume flow rate through the fan ($\xi_i < 1$). It is interesting to note that the results are not simply mirrored for $\beta_w = -45°$ and $\beta_w = 45°$. This "asymmetry" is due to the fact that the fans were all rotating in the same direction (clockwise in Figure 6). As a result, the relative velocities experienced by the fan blades differed with wind direction, causing differences in fan performance and blade loading.

In Figure 7, the individual fan cell volumetric effectiveness and normalized peak bending moment (ϕ_i, Equation (8)) are plotted against the uniformity index. The figure shows results for all 18 fan cells across the full range of simulated wind speeds ($1 \leq v_w \leq 11$ m/s) and directions ($-90° \leq \beta_w \leq 90°$). A total of 972 fan cell operating points are included in Figure 7. Mean trend lines through the data ($f_m(\gamma)$) are also shown.

Figure 7 shows clear relationships between the fan uniformity index and both metrics of interest. A smooth, exponential trend is evident for volumetric effectiveness. The normalized peak bending moment increased rapidly with decreasing γ_i, reaching a maximum at $\gamma_i \approx 0.85$. Thereafter (i.e., with further decreasing uniformity), the influence of γ_i decayed and eventually plateaued. The plateau was likely due to the fan inlet velocity vectors (specifically axial velocity) in the upwind half of the fan's rotational plane reaching conditions that led to a loading scenario that could not necessarily have gotten much worse.

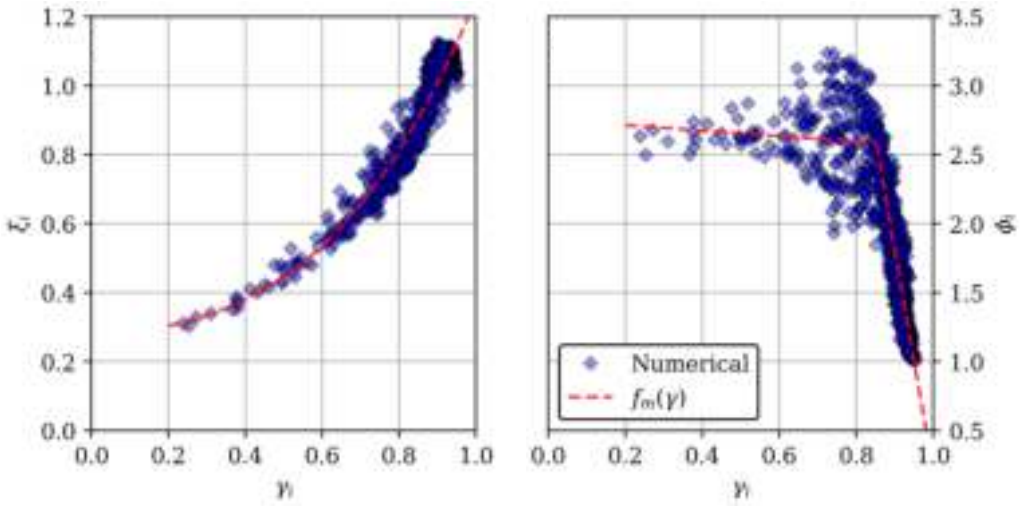

(**a**) (**b**)

Figure 7. The effect of individual fan cell uniformity index (γ_i) on: (**a**) volumetric effectiveness; (**b**) normalized peak bending moment.

Figure 8 shows the corresponding experimental data as well as the trend lines ($f_m(\gamma)$) from Figure 7. It is clear that the numerical and experimental data correspond closely, and the numerical results are thus deemed valid.

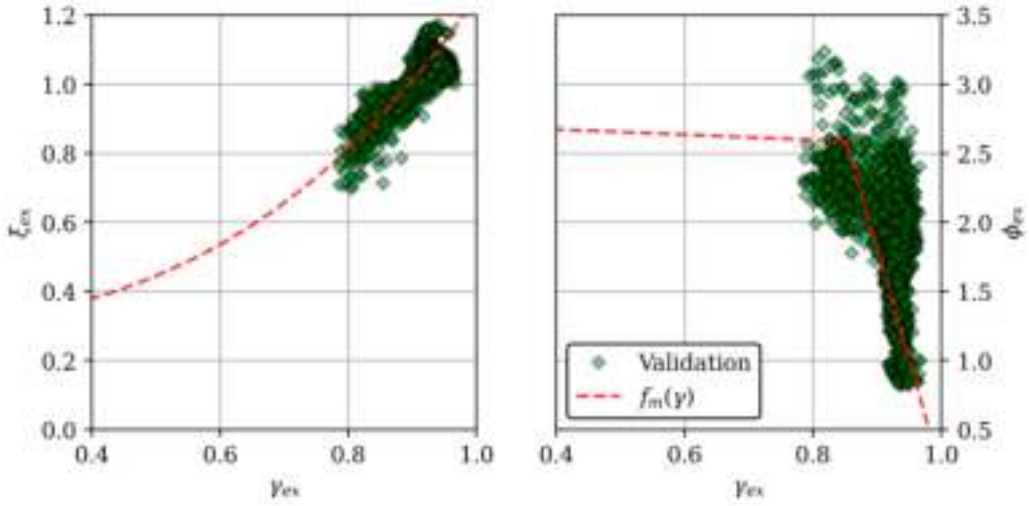

(**a**) (**b**)

Figure 8. Experimental measured effect of uniformity index on: (**a**) volumetric effectiveness; (**b**) normalized peak blade load.

3.2. Sensitivity of Uniformity Index to Sampling Resolution

The experimental uniformity index is calculated using the measured axial velocities at discrete points within a polar coordinate grid. Changing the sampling resolution may thus influence the value of the uniformity index for a given scenario. This sensitivity was investigated by sampling the simulated fan inlet axial velocity distribution (originally $(n_r = 20) \times (n_\theta = 120) = 2400$ data points) using a coarser resolution and recalculating the uniformity index (Equation (3)) from the sampled numerical results. The sample location for the coarser uniformity index calculation within the fan rotor is shown in Figure 9. Figure 9c shows the minimum measurement resolution of the CTI-PTG-143 standard [12]:

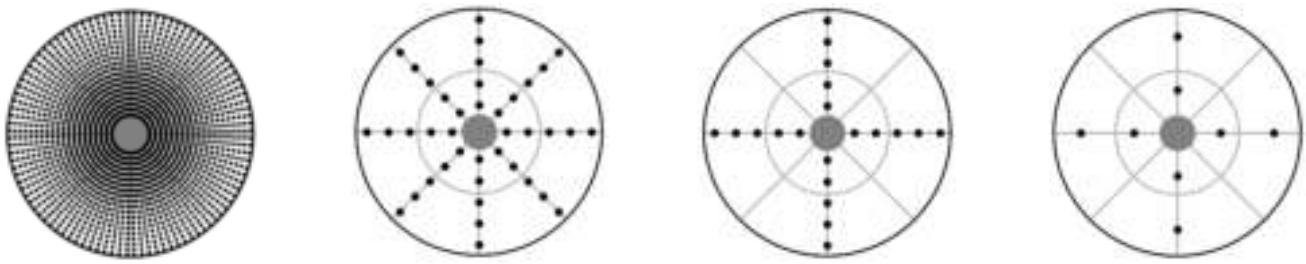

(**a**) (**b**) (**c**) (**d**)

Figure 9. Sampling resolution used for calculating uniformity index: (**a**) $n_r = 20$, $n_\theta = 120$; (**b**) $n_r = 5$, $n_\theta = 8$; (**c**) $n_r = 5$, $n_\theta = 4$; (**d**) $n_r = 2$, $n_\theta = 4$.

The sampled uniformity index results are shown in Figure 10 for a wind speed of $v_w = 7$ m/s with $\beta_w = 0°$. The effect of sampling resolution clearly becomes significant at low resolutions (e.g., Figure 10c,d). The minimum resolution recommended by the CTI (Figure 9c) seems relatively robust in this case, where the wind was aligned with one of the sampling directions. It may be expected that such a sampling configuration, with fewer tangential divisions, may have a larger impact on the accuracy of the uniformity index for non-aligned wind directions (e.g., $\beta_w = 45°$).

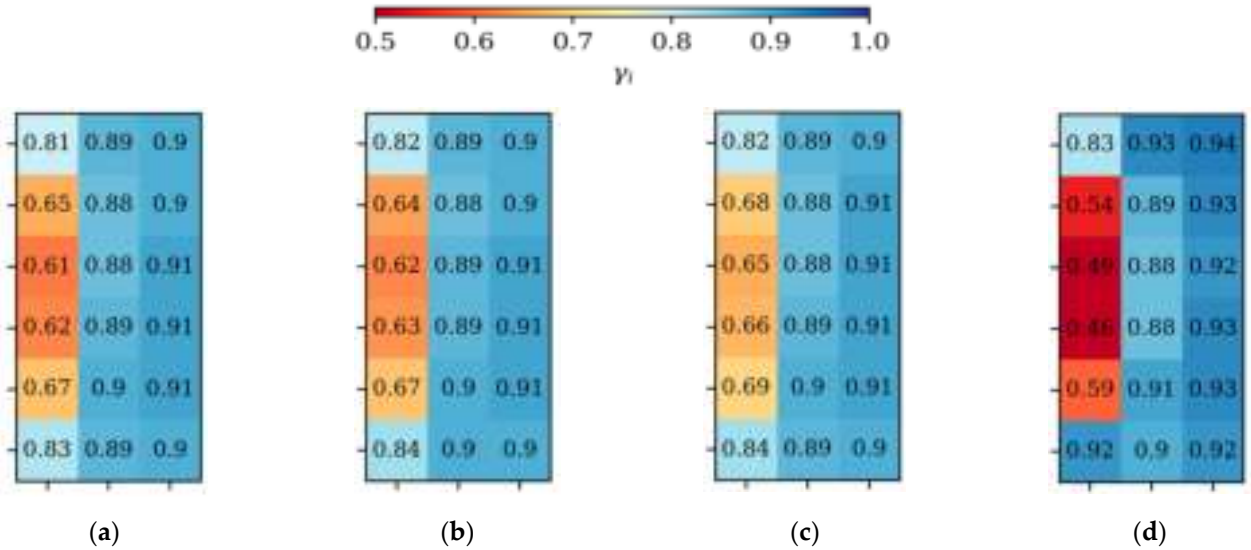

(**a**) (**b**) (**c**) (**d**)

Figure 10. The influence of sampling resolution on uniformity index: (**a**) $n_r = 20$, $n_\theta = 120$; (**b**) $n_r = 5$, $n_\theta = 8$; (**c**) $n_r = 5$, $n_\theta = 4$; (**d**) $n_r = 2$, $n_\theta = 4$ ($v_w = 7$ m/s; $\beta_w = 0°$).

Based on our results, we tentatively recommend a sampling resolution of $n_r = 5$ and $n_\theta = 8$ in order to accurately determine the uniformity index in ACCs from on-site measurements; however, further investigation is needed to account for the impact of a wider variety of wind conditions.

4. Discussion

Ambient wind has a negative effect on ACC fan volumetric performance, and increases dynamic fan blade loading. Investigating these effects directly using on-site measurement or numerical analysis is complicated, and most previous work has focused on only one effect at the expense of the other. Fan axial velocity inflow uniformity was identified as offering the potential to holistically qualify ACC fan operation under windy conditions. Fan inflow uniformity was thus investigated for a range of wind conditions using CFD with validation against on-site measurements for a specific ACC.

The results indicate clear relationships between the inflow uniformity index (γ—Equation (3)) and both fan volumetric effectiveness and dynamic blade loading (see Figure 7). The fan inlet airflow uniformity index (γ) can therefore be used as a single metric to estimate the severity of both the reduction in fan volumetric performance and the increase in dynamic blade loading under windy conditions. The same proportional relationship was observed in both the numerical and experimental data, suggesting that the uniformity index can be used in both numerical and experimental work, to allow for qualitative investigation of wind effects (and their mitigation).

The potential utility of the uniformity index in numerical simulation is that the state of fan blade dynamic loading can be inferred without additional data processing or the need for blade element theory-based fan models. For continuous on-site experimental measurements, the uniformity index can indicate a fan cell's volumetric performance and dynamic blade loading using significantly less measurement equipment (less than 40 anemometers, and no need for strain gauges, bridge amplifiers and wireless transmitters). Furthermore, the uniformity index (generated using simplified CFD models) can be used to specify the potential severity of the operating conditions expected at an axial fan installation, and to assist vendors and clients in designing and selecting more reliable fans (both in terms of performance and structural integrity).

Author Contributions: Conceptualization, M.O. and J.M.; methodology, F.M.; software, F.M.; validation, F.M., M.O. and J.M.; formal analysis, F.M.; investigation, P.H.; resources, M.O. and J.M.; data curation, F.M. and P.H.; writing—original draft preparation, F.M.; writing—review and editing, M.O. and J.M.; visualization, F.M.; supervision, M.O. and J.M.; project administration, M.O.; funding acquisition, M.O. and J.M. All authors have read and agreed to the published version of the manuscript.

Funding: This research received financial support from the Solar Thermal Energy Research Group, Stellenbosch University, Stellenbosch 7600, South Africa.

Institutional Review Board Statement: Not applicable.

Informed Consent Statement: Not applicable.

Data Availability Statement: Numerical data are available on request from the corresponding author. The raw experimental data were provided by a third party, and are restricted.

Acknowledgments: The authors acknowledge the computational resources provided by the Centre for High-Performance Computing (CHPC), South Africa.

Conflicts of Interest: The authors declare no conflict of interest.

References

1. Maulbetsch, J.; DiFilippo, M. *Effect of Wind Speed and Direction on the Performance of Air-Cooled Condensers*; California Energy Commission: Sacramento, CA, USA, 2008; Publication Number CEC-5002013-065-APB.
2. Maulbetsch, J.; DiFilippo, M. *The Use of Wind Barriers to Mitigate the Effect of Wind on Air-Cooled Condensers*; California Energy Commission: Sacramento, CA, USA, 2016; Publication number: CEC-500-2016-047.
3. Bredell, J.R.; Kröger, D.G.; Thiart, G.D. Numerical investigation of fan performance in a forced draft air-cooled steam condenser. *Appl. Therm. Eng.* **2006**, *26*, 846–852. [CrossRef]
4. Thiart, G.D.; Von Backström, T.W. Numerical simulation of the flow field near an axial flow fan operating under distorted inflow conditions. *J. Wind Eng. Ind. Aerodyn.* **1993**, *45*, 189–214. [CrossRef]
5. Meyer, C.J. Numerical investigation of the effect of inlet flow distortions on forced draught air-cooled heat exchanger performance. *Appl. Therm. Eng.* **2005**, *25*, 1634–1649. [CrossRef]
6. Stinnes, W.H.; Von Backström, T.W. Effect of cross-flow on the performance of air-cooled heat exchanger fans. *Appl. Therm. Eng.* **2002**, *22*, 1403–1415. [CrossRef]
7. Hotchkiss, P.J.; Meyer, C.J.; Von Backström, T.W. Numerical investigation into the effect of cross-flow on the performance of axial flow fans in forced draught air-cooled heat exchangers. *Appl. Therm. Eng.* **2006**, *26*, 200–208. [CrossRef]
8. Marincowitz, F.S. Experimental Investigation of the Effects of Windscreens on Air-Cooled Condenser Fan Performance and Dynamic Blade Loading. Master's Thesis, University of Stellenbosch, Stellenbosch, South Africa, 2019.
9. Muiyser, J.; Els, D.N.J.; Van der Spuy, S.J.; Zapke, A. Measurement of air flow and blade loading at a large-scale cooling system fan. *J. S. Afr. Inst. Mech. Eng.* **2014**, *30*, 30–38.

10. Yang, L.J.; Du, X.Z.; Yang, Y.P. Wind effect on the thermo-flow performances and its decay characteristics for air-cooled condensers in a power plant. *Int. J. Therm. Sci.* **2012**, *53*, 175–187. [CrossRef]
11. Marincowitz, F.S.; Owen, M.T.F.; Muiyser, J. The Effect of Windscreens and Walkways on Air-cooled Condenser Performance and Fan Blade Dynamic Loading. *J. Eng. Gas Turbines Power* **2021**, *143*, 101019. [CrossRef]
12. Cooling Tower Institute. *CTI Standard PTG-143: Recommended Practice For Airflow Testing of Cooling Towers*; Cooling Tower Institute: Houston, TX, USA, 1994.
13. Bredell, J.R.; Kröger, D.G.; Thiart, G.D. Numerical investigation into aerodynamic blade loading in large axial flow fans operating under distorted inflow conditions. *J. S. Afr. Inst. Mech. Eng.* **2006**, *22*, 12.
14. Bianchini, C.; Mirsky, G.; Frumkin, M. Windscreen effect on performance and structure, before and after, and comparison with CFD. In Proceedings of the ACC User Group, Colorado Springs, CO, USA, 8–11 October 2018.
15. Venter, A.J. Numerical Analysis of Windscreen Effects on Air-Cooled Condenser Fan Performance and Blade Loading. Master's Thesis, University of Stellenbosch, Stellenbosch, South Africa, 2020.
16. Engelbrecht, R.A.; Meyer, C.J.; Van der Spuy, S.J. Modeling Strategy for the Analysis of Forced Draft Air-Cooled Condensers Using Rotational Fan Models. *J. Therm. Sci. Eng. Appl.* **2019**, *11*, 051011. [CrossRef]
17. Venter, A.J.; Owen, M.T.F.; Muiyser, J. A numerical analysis of windscreen effects on air-cooled condenser fan performance. *Appl. Therm. Eng.* **2021**, *186*, 116416. [CrossRef]
18. Marincowitz, F.S. Optimisation towards a Wind-Resistant Air-Cooled Condenser for the Modern Energy Sector. Ph.D. Thesis, University of Stellenbosch, Stellenbosch, South Africa, 2021.
19. Franke, J.; Hirsch, C.; Jensen, G.; Krüs, G.W.; Miles, S.D.; Schatzmann, M.; Westbury, P.S.; Wisse, J.A.; Wright, N. Recommendations on the use of CFD in wind engineering. In Proceedings of the International Conference on Urban Wind Engineering and Buildings Aerodynamics, Sint-Genesius-Rode, Belgium, 5–7 May 2004.
20. Richards, P.J.; Hoxey, R.P. Appropriate boundary conditions for computational wind engineering models using the k-ε turbulence model. *J. Wind Eng. Ind. Aerodyn.* **1993**, *46–47*, 145–153. [CrossRef]
21. Kröger, D.G. *Air-Cooled Heat Exchangers and Cooling Towers: Thermal-Flow Performance Evaluation and Design*; PennWell Corporation: Tulsa, OK, USA, 2004.
22. Kays, W.M.; London, A.L. *Compact Heat Exchangers*, 3rd ed.; McGraw-Hill: New York, NY, USA, 1984.
23. Van der Spuy, S.J.; Von Backström, T.W. An evaluation of simplified CFD models applied to perimeter fans in air-cooled steam condensers. *Proc. Inst. Mech. Eng. Part A J. Power Energy* **2015**, *229*, 948–967. [CrossRef]
24. ANSYS Inc. *ANSYS Fluent Theory Guide*; Release 15.0; ANSYS Inc.: Canonsburg, PA, USA, 2013.

International Journal of
Turbomachinery
Propulsion and Power

MDPI

Article

Evaluation of the Wear-Resistant Plate Performance on Different Locations over the Flow Path of a Large-Sized Heavy-Duty Centrifugal Fan

Nicola Aldi [1], Nicola Casari [1], Michele Pinelli [1,*], Alessio Suman [1], Alessandro Vulpio [1], Ottavio Mantovani [2] and Paolo Saccenti [2]

[1] Department of Engineering, University of Ferrara, Via Giuseppe Saragat 1, 44122 Ferrara, FE, Italy
[2] Boldrocchi Group, Via Trento e Trieste, 93, 20853 Biassono, MB, Italy
* Correspondence: michele.pinelli@unife.it

Abstract: In industrial applications such as chemical plants, cement factories, and glassmakers, large-sized centrifugal fans are commonly used for dust-laden flow processing. In many cases, the contamination is due to solid particles responsible for fouling and erosion issues. Erosion induces the reduction of mechanical resistance and, at the same time, the modification of the geometry and the surface characteristics of the internal flow path. The process works according to the characteristics of the erodent particles, such as dimension and hardness, which have to be coupled with the mechanical properties of the substrate, like hardness and roughness level. In addition to this, the intensity of the erosion depends on the dynamic characteristics of particles, especially velocity and impact angle. For these reasons, erosion-related issues are difficult predict and reduce. In an attempt to preserve the structural integrity of the internal walls, wear-resistant plates are positioned where the impacting contaminants are supposed to be more detrimental. In the present work, a combined experimental and numerical approach is proposed to evaluate the proper setup of wear-resistance plates over the flow path of a large-sized centrifugal fan. The results show how different regions (rotating and stationary walls) are subjected to different impact behavior, determining that the design of the position of the wear-resistant plate is not straightforward. Suggestions related to reducing the erosion intensity are reported, highlighting the possibility of designing the best compromise between erosion, performance, and costs.

Keywords: large-size centrifugal fan; erosion; wear-resistant plate; dust-laden flow

check for updates

Citation: Aldi, N.; Casari, N.; Pinelli, M.; Suman, A.; Vulpio, A.; Mantovani, O.; Saccenti, P. Evaluation of the Wear-Resistant Plate Performance on Different Locations over the Flow Path of a Large-Sized Heavy-Duty Centrifugal Fan. *Int. J. Turbomach. Propuls. Power* **2022**, *7*, 32. https://doi.org/10.3390/ijtpp7040032

Academic Editor: Thomas Carolus

Received: 5 September 2022
Accepted: 14 November 2022
Published: 17 November 2022

Publisher's Note: MDPI stays neutral with regard to jurisdictional claims in published maps and institutional affiliations.

Copyright: © 2022 by the authors. Licensee MDPI, Basel, Switzerland. This article is an open access article distributed under the terms and conditions of the Creative Commons Attribution (CC BY-NC-ND) license (https://creativecommons.org/licenses/by-nc-nd/4.0/).

1. Introduction

Heavy-duty centrifugal fans are employed in process industries for cement, steel, and power production. Such machines include exhausters used for different purposes: in metallurgy, they are used for agglomeration, where dust from the agglomeration process passes through them, or in heating and power plants, where ash particles are suspended in the gas flow. Usually, these machines are tailor-made to meet the customer's requirements regarding mass flow rate and pressure, space constraints, structural requirements, etc. Most large centrifugal fans currently have an impeller diameter of 3 m to 4 m, with a power up to 4 MW and a running speed of $1000\times\ g$ rpm.

The interaction of the particles with stationary and rotating components of the machine can lead to fouling or erosion. The first phenomenon refers to the adhesion of particles to the surfaces, while the second regards the progressive removal of material from some zones of the machines. The first issue is surmountable by cleaning the machine with purpose-made devices. In contrast, the second is an insurmountable issue, and overhaul operations are mandatory to restore the machine's performance. Finally, focusing on the erosion phenomenon, since gas velocity can reach very high values, the dragged particles

possess high kinetic energy that contributes to material removal from the parts where impacts occur.

Moreover, the blade-surface wear over time changes the fan geometry to one far from its design condition, reducing fan efficiency. Additionally, the erosion progression can lead to premature failures of the most affected parts if overhaul operations are postponed or even ignored. This is a severe threat to the reliability and safety of the machine. The erosion damages in stationary parts are mainly related to the efficiency and reliability of the equipment, while those on rotating parts are also associated with safety.

In 1980, the research laboratories of the Westinghouse Electric Corporation surveyed power plants having units larger than 100 MW generating capacity and using pulverized coal-fired boilers. The results of this survey are reported in a technical report from Glasser et al. [1]. The findings showed that erosion damage is located mainly on blade leading edges, trailing edges, and fan center plates. The erosion of the leading edges was the most severe one. The authors estimated that a total of 27,000 man-hours was being used annually to repair erosion damages in these machines and that the cost of purchasing replacement power during overhaul operation was around 11 million dollars per year.

Many studies investigate the erosion phenomena in heavy-duty fans through numerical simulations. For the sake of brevity, only some of them are reported. Cardillo et al. [2] studied particle erosion in a large centrifugal fan used in cement production plants. The The authors highlighted that, in such machines, the rise of secondary flows drives the dispersion of the particles toward the blades, hub, and shroud. Castorrini et al. [3] investigated the effect of erosion on an axial draft-fan employed for exhaust gas extraction in a solid-fuel power plant. The authors detected the zones most affected by particle erosion and modified the original geometry by accounting for the material removal action of the erosion process. The erosion was found to be greater in magnitude on the suction side of the blade. The numerical erosion patterns were in qualitative agreement with the on-field observations. Fritsche et al. [4] analyzed the erosion behavior of large radial fans in recycling plants for end-of-life vehicles. On the basis of CFD simulations, they showed that the impact angle of metal contaminant (1 mm particles) has a stronger influence than the impact velocity. In that case, larger volute designs (i.e., larger spiral pitch angles) were found to be preferable for reducing the erosion magnitude because the impact angle becomes steeper. Aldi et al. [5] studied the influence of damage in correspondence to the inlet bell-mouth of the fan. The numerical investigation showed that the presence of damage in that zone led to a modification of the flow field within the impeller and to the occurrence of additional damages in the fan zones where erosion issues were never observed.

A common strategy for reducing the wear issue of such machines involves using sacrificial plates designed to resist particle erosion. Wear-resistant plates are positioned in the fan zones most affected by particle erosion. Such materials are available on the market and have different costs, depending on their performance against particle wear. The selection of wear-resistant plates and their positioning within the fan is usually driven by a mix of the manufacturer's experience and the wear-resistant material cost. Recent works [6,7] demonstrate how these sacrificial plates have a wear resistance capability related to the carbides dispersed within a cast iron matrix. Their performance is based on the ability of the carbides (chromium and niobium) to resist particle erosion and abrasion. The carbide hardness and the propensity of the matrix to absorb the impacts provided by particles reduce the detrimental effects generated by particles [6,7]. The present work combines a numerical and experimental approach to assess the erosion intensity of the machine to optimize the positioning of the wear-resistant plates within the fan. First, the wear resistance of three commercial wear-resistant plates is experimentally assessed on an on-purpose developed jet-impingement test bench. The material wear resistance was assessed using the same substrate and particles involved in the real plant to make the best erosion-magnitude prediction on the basis of numerical analysis. Then, a fluid dynamic simulation was carried out to assess the wear on the rotating and stationary parts

of the machine. The division of the machine into patches aided in selecting the proper wear-resistant plate on each zone based on the local condition of erosion severity.

2. Experimental Investigation

The experimental campaign aims to characterize the erosion behavior of the materials at different impact angles and velocity values. The results of the erosion tests are expressed in terms of erosion rate (*ER*), which is the ratio between the target mass loss after the test and the particle mass impacted on it. Generally, the erosion rate is modeled using the following relation [8]:

$$ER(V, \alpha) = K_{90}\, V^{n_{90}} f(\alpha) \quad (1)$$

where V is the particle impact velocity, α is the particle impact angle, K_{90} and n_{90} are the erosion coefficients for the normal impingement angle, and the angle function $f(\alpha)$ is the ratio between the erosion rate at a generic impact angle and the erosion rate at 90°:

$$f(\alpha) = ER_{\alpha} / ER_{90} \quad (2)$$

2.1. Test Bench

The present section describes a jet-impingement test bench designed and built at the Fluid Machinery Laboratory of the Department of Engineering of the University of Ferrara. The schematic view of the whole erosion facility and the main components is depicted in Figure 1. The test bench employs dry and clean shop air provided by a screw compressor. The air is mixed with a dosed amount of powder and then accelerated in a sand-blast nozzle toward a square specimen in the test chamber. The nozzle outlet section has a diameter of 4 mm. An exhaust fan linked to a chimney recirculates the air inside the test chamber. The air mass flow rate is controlled by a pressure regulator upstream of the nozzle. The specimen is placed on a target holder, which allows an accurate regulation of tilt angle and distance from the nozzle outlet section. For the present application, a distance of 10 mm between the nozzle and the specimen surface is chosen. Preliminary tests were carried out employing alumina particles (Al_2O_3) (with 50 µm diameter) against 20MnB4 specimens (according to UNI EN 10269 [9]) with an elemental content as weight fraction (wt %): 0.228% C, 0.943% Mn, 0.068% Si, 0.010% S, 0.009% P, 0.025% Al, 0.003% B, 0.042% Ti, 0.070% Cr, 0.033% Ni, 0.039% Cu, 0.0001% Pb, and iron (balance). Through the preliminary tests, the reliability of the test bench was validated, since the results were in line with those provided by the ASTM G76 [10]. A detailed description of the test bench performance and usage are provided in [6,7].

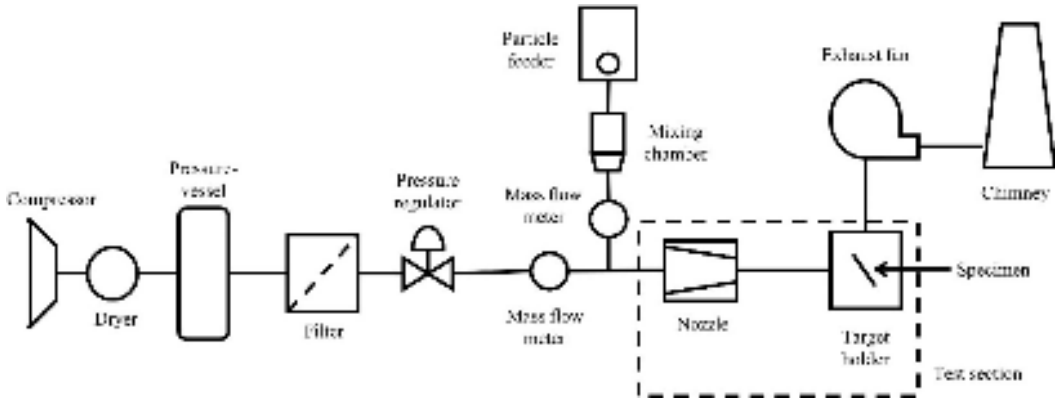

Figure 1. Schematic layout of the experimental test bench.

2.2. Particle and Substrate Materials

The experimental tests were carried out with particle and substrate materials used in heavy-duty centrifugal fan operations. The powder used in the present application is a solid material produced as an intermediary product in the manufacture of Portland cement.

It was made by sintering limestone and aluminosilicate materials, such as clay, during the cement kiln stage. The powder used in the present experimental campaign was collected directly from the plant where the fan operates. The powder morphology is depicted in Figure 2a, while its number and mass distribution are shown in Figure 2b. The particle density is 2.717 kg/m^3, and its mean diameter is 4.34 µm. The Malvern Mastersizer 3000 (Malvern Panalytical, Malvern, UK) and the AccuPyc II 1340 pycnometer (Micromeritics Instrument Corporation, Norcross, GA, USA) were used to measure particle distribution and particle density, respectively.

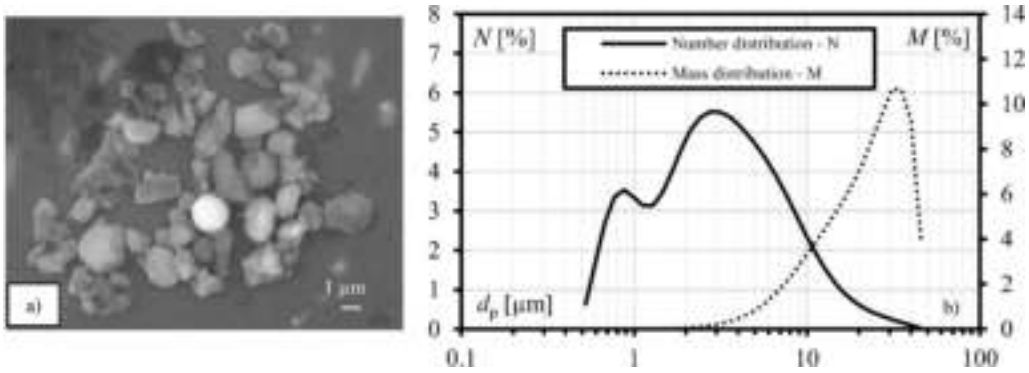

Figure 2. Characteristics of the powder employed: (**a**) SEM observation, and (**b**) number and mass distribution.

Three commercial wear-resistant plates, named M1, M2, and M3, were tested in the present campaign:

- M1 is a layer-composite wear plate made by the open-arc welding of a flux-cored wire DIN 8555 alloy group 10 and additional metal alloy powder. Its deposit consists of primary carbides and complex carbides in a matrix of austenite and eutectic carbides. The carbide content is 62.1% (27.4% primary and 34.7% eutectic) and has the following structures: Cr_7C_3, Mo_2C, NbC, and WC.
- M2 is a welding cladded-layer composite material with hard surfacing according to DIN 8555, alloy group 10, made with an open-arc welding procedure. The declared percentage of carbides is greater than 50%. The structures of the formed carbides are M_7C_3, Cr_2B, and NbC.
- M3 is a nickel-based alloy rich in cast/crushed tungsten carbides (60% of the coating content). The coating is composed of Ni (37%), WC (60%), and other components (3%).

Due to their different chemical composition and properties, the erosion resistance of these materials changes accordingly. In particular, based on experienced evaluations, the M3 showed a higher wear resistance than M2 and M1.

2.3. Experimental Test Results and Model Fitting

The three materials are tested at three mean impact velocities and five impact angles (15°, 30°, 45°, 60°, and 90°). Each test is carried out with a mass flow rate of powder of 10 g min^{-1}.

Each impact angle and velocity combination is repeated on different specimens three times. An error band, calculated following the procedure reported by Schrade et al. [11], has been used to account for the variability related to the test procedure. The experimental results are depicted in Figure 3: Figure 3a reports the ER values at normal impact angle and the interpolation lines derived from Equation (1), while Figure 3b reports the experimental values of the angle function. The M3 plate confirms the higher resistance to particle wear. M1 and M2 have comparable wear resistance. The angle function shows a clear mixture of ductile- brittle behavior of the erosion process over the impact angle: the maximum of the ER is located at almost 45°. The three plate materials show similar angle function f (α) trends.

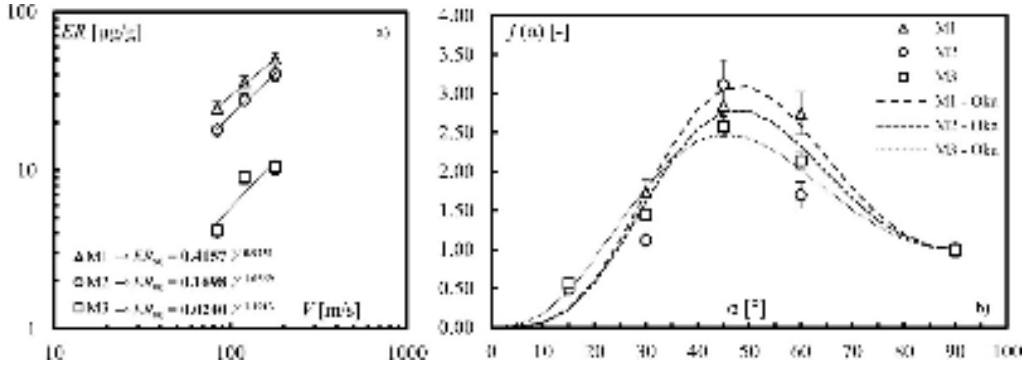

Figure 3. Results of the experimental test: (**a**) erosion rate at normal impingement angle, and (**b**) erosion rate over the angle (experimental values and Oka's model interpolation).

To obtain a general formulation of the angle function $f(\alpha)$ that can be employed in numerical simulations, the experimental results have been interpolated through Oka's model equation [12], which calculates the angle function as a combination of trigonometric functions:

$$f(\alpha) = (\sin\alpha)^{n_1}(1 + HV(1 - \sin\alpha))^{n_2} \quad (3)$$

where n_1 and n_2 are numerical coefficients, and HV is the material hardness expressed in GPa. The results of Oka's model interpolation are reported in Figure 3b as dashed lines, while the coefficients employed in Equation (3) are reported in Table 1 for the three tested materials.

Table 1. Material properties and erosion coefficients of the wear-resistant plate materials.

Material	ρ_m (kg/m^3)	K_{90}	n_{90}	HV (GPa)	n_1	n_2
M1	4375	0.4157	0.9251	8.532	4.0	2.0
M2	7500	0.1698	1.0569	6.767	4.0	2.2
M3	9375	0.0240	1.1913	6.473	2.9	1.8

3. Numerical Analysis

3.1. Fluid Dynamic Simulations

The fan under examination is a large-sized single-inlet centrifugal fan operating in a cement plant designed and built by Boldrocchi Group. The fan is installed in the Åalborg Portland cement plant. The fan comprises a constant-width closed impeller, 12 backward-curved single arc blades, and a constant-width spiral volute. The rear side of the impeller disk presents five radial ribs for axial thrust balancing. The impeller outside diameter is 4 m, and the fan design rotational speed is 652 rpm. An inlet box with three fixed vanes of constant thickness deflects the flow from the inlet duct, which is arranged normally to the impeller axis, into the axial direction through the fan inlet cone. The inlet cone is bolted to the front side plate of the volute, which is in common with the inlet box. Wear-resistant plates with a thickness of 10 mm are installed on the pressure side and at the leading edge of fan blades, on the inner surface of the impeller disk, on a portion of the impeller shroud near the blade trailing edge on the pressure side, and a band of the spiral volute facing the impeller outlet section. The volute and impeller of the fan are shown in Figure 4a. To characterize the internal flow field and the particle trajectories of the centrifugal fan, a 3D fluid dynamic multiphase simulation is performed at the fan actual working point in terms of mass flow rate and total pressure rise, i.e., 122 kg/s and 8300 Pa. The reader can refer to Aldi et al. [13] for all the CFD simulation setup and validation details.

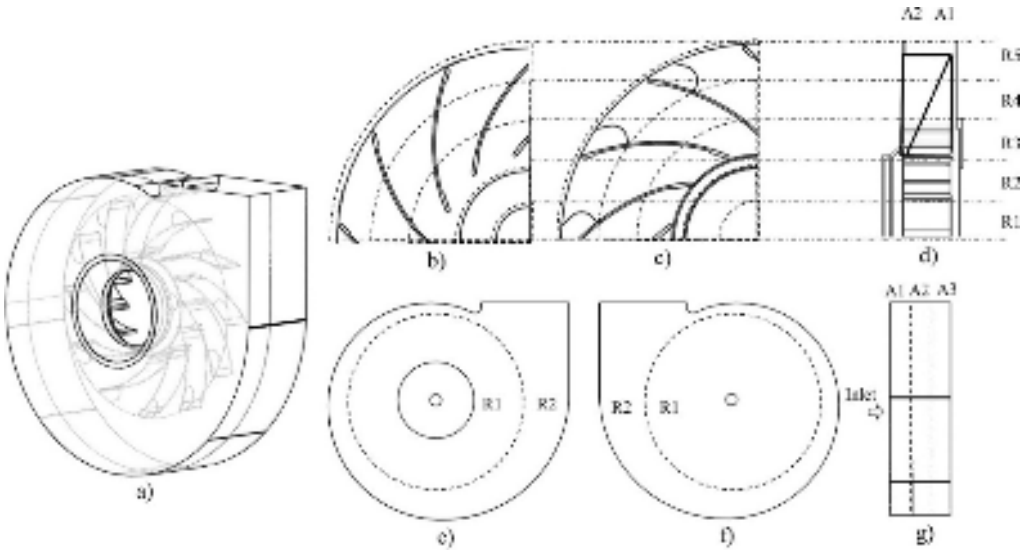

Figure 4. The strategy of fan surface patching: (**a**) fan model, (**b**) hub, (**c**) shroud, (**d**) rotor, (**e**) volute front side, (**f**) volute back side, and (**g**) volute lateral side.

3.2. Strategy of Fan Surface Patching

To quantify the wear severity on specific zones, the machine is divided into patches, according to the scheme reported in Figure 4.

The impeller was divided into three zones: hub (back plate), shroud (front plate), and blades. Hub and shroud are divided according to radial discretization. The hub (Figure 4b) is divided into five annular areas, named progressively from R1 to R5, with thicknesses of 355 mm, 385 mm, 440 mm, 435 mm, and 435 mm, respectively. The shroud (Figure 4c) is divided into three circular areas named R3, R4, and R5. The sizes of R3, R4, and R5 are the same as the corresponding areas on the hub. The shroud patching also accounts for the additional wear protection plate (named TE) positioned on the trailing edge zone of the blade, in correspondence with the blade pressure side. Each blade has been divided into thirteen patches: one patch for the leading edge, six patches on the pressure side, and six patches on the suction side (Figure 4d). Both the pressure side and suction side of each blade have been divided into two axial zones (A1, and A2), and three radial zones (R3, R4, and R5). The radial division has been done following the R3, R4, and R5 divisions previously described on the hub and shroud.

The volute was divided into three main zones: the front side (inlet side), the lateral side, and the back side. The volute front and back sides were divided into two radial sectors named R1 and R2 (Figure 4e,f). The circular area named R1 is placed at the center of the volute and has a diameter of 4.40 m, slightly larger than the impeller diameter. The R2 sector comprises the remaining part of the volute front and back cases. The lateral side was divided into three axial sections (A1, A2, and A3), each of them with a thickness of 510 mm (Figure 4g). The volute cut-off is of great interest with respect to particle wear, since it is a zone that can be strongly affected by erosive processes. For this reason, the cut-off zone was isolated and analyzed separately.

4. Results

The complex flow field developed within the fan, and the high separation zone that arises, require the use of numerical simulation to predict the impact patterns on the fan components. The CFD simulation made it possible to track the particle trajectories and obtain information related to the impacts of the particles on the fan surfaces. Due to particle inertia, the impact regions are the result of the interaction between the particle trajectories and the flow field. In the present application, the particle density and diameter (see Figure 2) determine reduced particle inertia with a diffusion-inertial transportation regime of the particles [14]. Due to this, the particles follow the streamlines determining the

interaction of a large portion of the fan surface with the particle impact. At the same time, the reduced inertia leads to a reduced particle kinetic energy responsible for a lower erosion rate (see [7] for more details). In the case of greater particle diameter (i.e., greater particle inertia), the impact pattern changes according to the reduced capability of the particles to follow the flow field. In this case, the most affected regions will be the impeller hub (back plate) and blade pressure side.

For the present analysis, all the internal fan surfaces are supposed to be covered with wear-resistant plates. Therefore, the wear on the fan zones is calculated by implementing Equations (1) and (3), based on the results of the CFD simulation, and using the coefficients in Table 1 for the three wear-resistant materials. The results are reported in terms of average thickness reduction (Δl) over 8000 h (almost one year) of operation on each patch of the fan.

4.1. Hub and Shroud

Figure 5 reports the thickness reduction on the shroud (Figure 5b) and the hub (Figure 5c). Based on the experimental results, M1 shows the worst performance in terms of wear resistance. Looking at the shroud, the three materials have different trends in the radial direction. This is mainly due to the different angle functions measured during the experimental tests (Figure 3b). This effect is visible when comparing M3 and M1 over R3, R4, and R5. However, higher wear intensity is found in the zone near the trailing edge, named TE. For all of the materials, the wear on the hub is high in the R1 zone, decreases in the radial direction until R3, and slightly increases towards R5. The center of the disc (R1) is critical since its positioning in front of the inlet section promotes a high impact frequency in that zone.

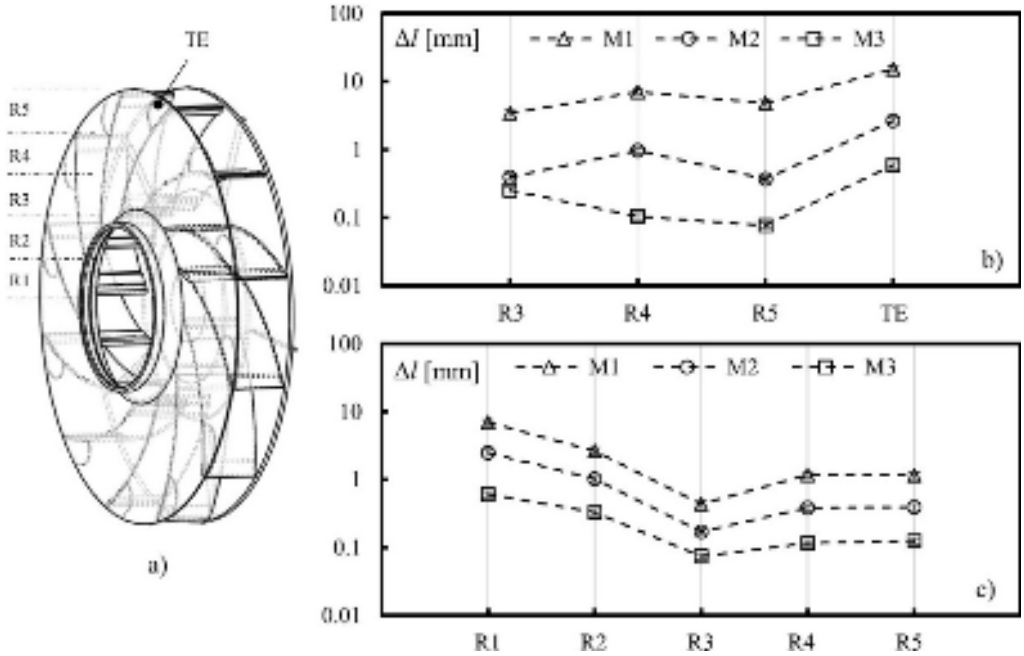

Figure 5. Rotor wear: (**a**) patches coordinates and material loss, (**b**) on the shroud, and (**c**) on the hub. R1, R2, R3, R4 and R5 are the radial annular areas, TE is the trailing edge.

4.2. Blades

Figure 6 reports the results for the blade pressure side (Figure 6b,c) and suction side (Figure 6e,f). The leading edge results are included in Figure 6b. Regarding the pressure side of the blade, the wear severity decreases in the radial direction for the portion of the blade near the hub (A1) and increases in the radial direction for the portion near the shroud (A2). However, the wear on the A1 zone is more severe than A2. In particular, the leading edge is the impeller zone, which experiences high material loss. The trends of Δl for the three materials in the radial direction are similar, but shifted on the y-axis, highlighting

the different wear resistance of the three plate materials. Regarding the suction side of the blade, the wear is almost uniform on the whole surface for a fixed plate material.

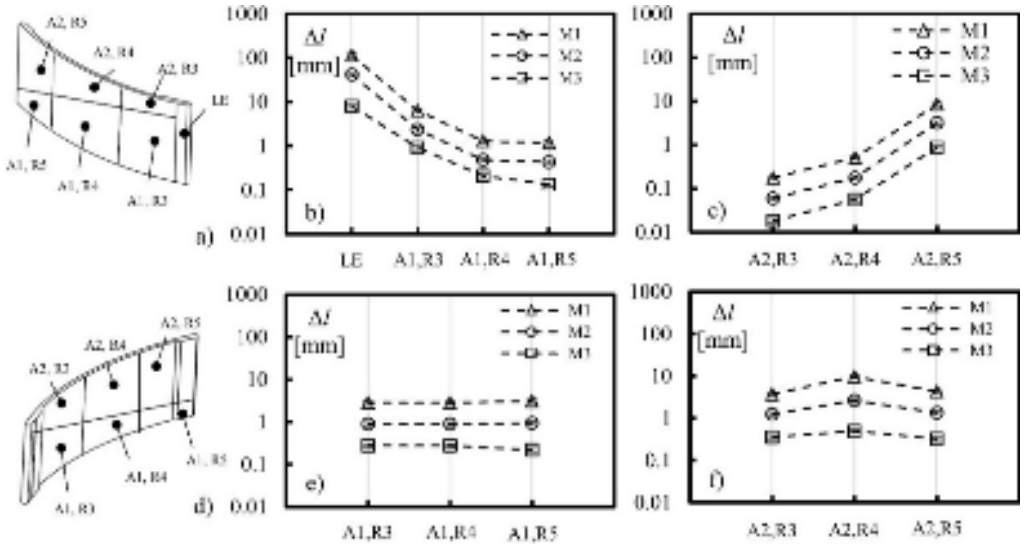

Figure 6. Rotor wear: (**a**) coordinates of the patches on the pressure side and material loss, (**b**) on the axial section A1 and (**c**) on the axial section A2; (**d**) coordinates of the patches on the suction side and material loss, (**e**) on the axial section A1 and (**f**) on the axial section A2. R3, R4 and R5 are the radial annular areas, LE is the leading edge.

4.3. Volute

The results of the volute wear are reported in Figure 7 for the front side (Figure 7b), back side (Figure 7c), lateral side (Figure 7d), and cut-off (Figure 7e). The wear severity on the stationary parts is lower than that on the rotating part. This is mainly due to the lower particle impact number and impact velocity in these zones. The front side, back side, and lateral side have similar values of thickness reduction after 8000 h of operation. The cut-off is the most critical part of the volute: the wear severity increases over the axial direction. The maximum thickness reduction is found in the axial sector in front of the impeller outlet section, reaching a thickness reduction of 3 mm after 8000 h of operation over a cut-off radius of 175 mm.

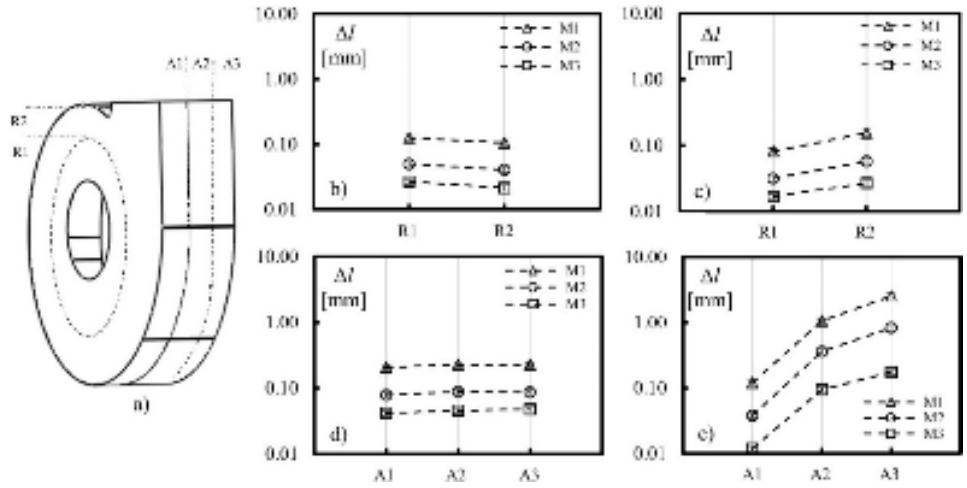

Figure 7. Volute wear: (**a**) coordinates of the patches on volute and material loss, (**b**) on the front side, (**c**) back side, (**d**) lateral side, and (**e**) cut-off. R3 and R4 are the radial annular areas, A1, A2 and A3 are the axial areas.

4.4. Optimized Configuration

The combination of numerical and experimental methods made it possible to reliably assess the wear behavior of the fan operating with dust-laden flows. The results of the present work are reported in terms of thickness reduction over 8000 h of operation; the usability of such information has a key role in the estimation of the maintenance operation intervals along with the operative life of the machine. Customer warranty is, in fact, a serious concern for heavy-duty fan manufacturers, and its proper assessment could represent a substantial competitive advantage in the field of heavy-duty machine supply. Another critical role is the reduction of costs without affecting the reliability and durability of the machine. The coverage of all of the machine parts with the plate material with the highest wear resistance, without considering its price, will undoubtedly ensure the highest possible durability. However, this strategy will automatically push the machine out of the market. Intending to reach a compromise between costs and durability, the results presented previously were analyzed to identify an optimal configuration of the plate positioning. A thickness reduction of 3 mm over 8000 h of operation is set as an acceptable limit for the wear on the fan parts. This limit value was chosen by considering that the hard-facing material of the plates has a thickness of 5 mm. According to this choice, after 8000 h of operation, inspections should be carried out to assess the overall condition of the machine.

The optimized configuration for the impeller is presented in Figure 8 for the shroud (Figure 8b), the hub (Figure 8c), the pressure side (Figure 8d), and the suction side (Figure 8e). The plate materials have been positioned by combining their costs, their wear resistance, and the wear severity in the specific zone of the impeller. It can be noted that the material with the highest wear resistance (M3) is positioned only in the zones where the erosion severity does not allow the use of the cheapest materials (M1 and M2). Such zones are the leading edge (LE), a portion of the pressure side near the trailing edge (A2, R5), and a portion of the shroud corresponding to the trailing edge (TE). Similarly, M2 is employed in the center of the disc (R1), in the first radial sector of the shroud (R3), and the first radial sector of the pressure side (A1, R3). The remaining parts of the impeller were covered with M1. Looking at the stationary part, the low wear severity on the volute leads to the logical choice of using the material M1 for the front side, backside, and lateral side coverage. However, the high wear on the cut-off requires the positioning of the M2 material only in this zone. Even though such a solution can theoretically minimize the costs related to particle wear without compromising fan durability, it has to be highlighted that its implementation could be impractical due to compatibility issues that may arise when different hard-facing plates are welded together. However, the approach reported in the present work can be adapted to practical applications for only the coverage of the zones most affected by particle wear.

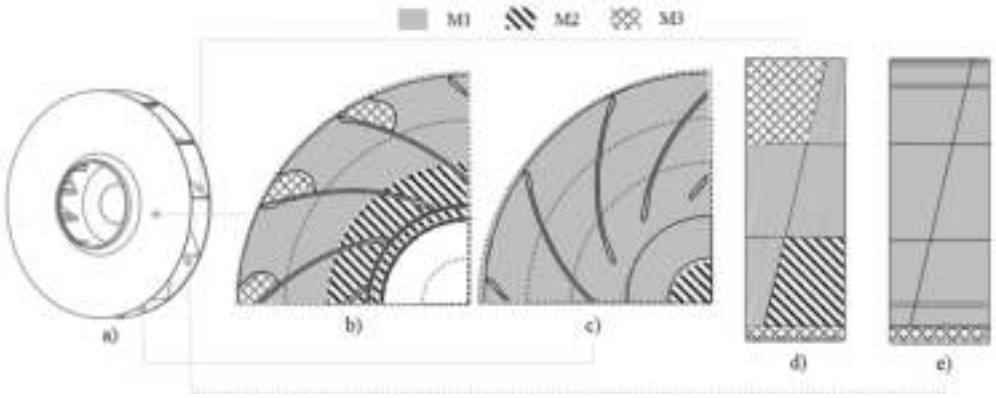

Figure 8. Optimized configuration of the wear-resistant plates on the rotor: (**a**) view of the rotor, (**b**) shroud, (**c**) hub, (**d**) blade pressure side and (**e**) blade suction side.

5. Conclusions

The present work is devoted to assessing the wear severity on the internal parts of a heavy-duty centrifugal fan and optimizing the positioning of the wear-resistant plates along the flow path of the machine.

First, experimental tests were carried out to assess the wear resistance of the hard-facing plates against the dust processed by the fan. Next, a literature erosion model was used to interpolate the experimental results to obtain mathematical relations capable of predicting the wear magnitude under general impact conditions. Then, a multiphase fluid dynamic simulation of the fan was carried out to assess the particle impacts on the rotating and stationary parts. Finally, implementing the erosion model, fed with experimental coefficients, led to estimating the wear severity on each fan zone.

The rotating parts are affected by a higher level of wear than the stationary parts, and the leading edge is the zone affected by the highest amount of material loss. In addition, the three hard-facing alloys show significant differences in erosion resistance due to their different properties and chemical composition. The numerical results allowed the implementation of an optimized wear-resistant plate positioning strategy, pursuing cost reduction and increased fan durability.

Author Contributions: Conceptualization, P.S., M.P., A.V. and A.S.; methodology, N.A., N.C., M.P., A.S. and A.V.; formal analysis, N.A., N.C., A.S. and A.V.; investigation, N.A., A.S. and A.V.; resources, P.S. and O.M.; data curation, A.V.; writing—original draft preparation, A.V.; writing—review and editing, N.A., N.C., M.P., A.S., A.V. and P.S.; visualization, A.V. and M.P.; supervision, M.P. and P.S.; project administration, P.S.; funding acquisition, M.P. All authors have read and agreed to the published version of the manuscript.

Funding: This research was funded through a technological transfer grant by BOLDROCCHI GROUP Srl. Grant Number: 1.

Institutional Review Board Statement: Not applicable.

Informed Consent Statement: Not applicable.

Data Availability Statement: Not applicable.

Acknowledgments: The authors acknowledge the contribution of Nicola Zanini, Stefano Oliani and Ettore Fadiga for the support during the experimental campaign.

Conflicts of Interest: The authors declare no conflict of interest.

References

1. Glasser, A.D.; Petlevich, W.J.; Sverdrup, E.F. *Nature and Costs of Fan Erosion in Coal-Fired Electric Power Plants (No. EPRI-CS-1596)*; Westinghouse Electric Corp.: Pittsburgh, PA, USA, 1980.
2. Cardillo, L.; Corsini, A.; Delibra, G.; Rispoli, F.; Sheard, A.G.; Venturini, P. Simulation of particle-laden flows in a large centrifugal fan for erosion prediction. In *Turbo Expo: Power for Land, Sea, and Air*; American Society of Mechanical Engineers: New York, NY, USA, 2014; Volume 45578, p. V01AT10A014.
3. Castorrini, A.; Venturini, P.; Corsini, A.; Rispoli, F. Numerical simulation of the blade aging process in an induced draft fan due to long time exposition to fly ash particles. *J. Eng. Gas Turbines Power* **2019**, *141*, 011025. [CrossRef]
4. Fritsche, M.; Epple, P.; Steber, M.; Rubwurm, H.J. Erosion optimized radial fan impellers and volutes for particle flows. In *ASME International Mechanical Engineering Congress and Exposition*; American Society of Mechanical Engineers: New York, NY, USA, 2017; Volume 7.
5. Aldi, N.; Casari, N.; Pinelli, M.; Suman, A.; Vulpio, A.; Saccenti, P. Performance Modification of an Erosion-Damaged Large-Sized Centrifugal Fan. In *Turbo Expo: Power for Land, Sea, and Air*; American Society of Mechanical Engineers: New York, NY, USA, 2021; Volume 84898, p. V001T10A011.
6. Fortini, A.; Suman, A.; Vulpio, A.; Merlin, M.; Pinelli, M. Microstructural and erosive wear characteristics of a high chromium cast iron. *Coatings* **2021**, *11*, 490. [CrossRef]
7. Fortini, A.; Suman, A.; Zanini, N.; Cruciani, G. Erosive Wear Behavior of High-Chromium Cast Iron: Combined Effect of Erodent Powders and Destabilization Heat Treatments. *Coatings* **2022**, *12*, 1218. [CrossRef]
8. Finnie, I.; McFadden, D.H. On the velocity dependence of the erosion of ductile metals by solid particles at low angles of incidence. *Wear* **1978**, *48*, 181–190. [CrossRef]

9. *EN 10269*; Steels and Nickel Alloys for Fasteners with Specified Elevated and/or Low Temperature Properties. European Committee for Standardization: Brussels, Belgium, 2013.
10. *ASTM G76-04;* Standard Test Method for Conducting Erosion Tests by Solid Particle Impingement Using Gas Jets. ASTM International: West Conshohocken, PA, USA, 2004.
11. Schrade, M.; Staudacher, S.; Voigt, M. Experimental and numerical investigation of erosive change of shape for high-pressure compressors. In *Turbo Expo: Power for Land, Sea, and Air*; American Society of Mechanical Engineers: New York, NY, USA, 2015; Volume 56628, p. V001T01A001.
12. Oka, Y.I.; Okamura, K.; Yoshida, T. Practical estimation of erosion damage caused by solid particle impact: Part 1: Effects of impact parameters on a predictive equation. *Wear* **2005**, *259*, 95–101. [CrossRef]
13. Aldi, N.; Casari, N.; Pinelli, M.; Suman, A.; Vulpio, A.; Saccenti, P.; Beretta, R.; Fortini, A.; Merlin, M. Erosion behavior on a large-sized centrifugal fan. In Proceedings of the 13th European Turbomachinery Conference on Turbomachinery Fluid Dynamics and Thermodynamics, Lausanne, Switzerland, 8–12 April 2019; pp. 1–8.
14. Young, J.; Leeming, A. A Theory of Particle Deposition in Turbulent Pipe Flow. *J. Fluid. Mech.* **1997**, *340*, 129–159. [CrossRef]

International Journal of
Turbomachinery
Propulsion and Power

MDPI

Article

Effect of Sweep on Axial Fan Noise Sources Using the Lattice Boltzmann Method

Dipali Ghodake [1], Marlène Sanjosé [1,2], Stéphane Moreau [1,*] and Manuel Henner [3]

[1] Department of Mechanical Engineering, Université de Sherbrooke, 2500 Boulevard de l'Université, Sherbrooke, QC J1K2R1, Canada
[2] Department of Mechanical Engineering, École de Technologie Supérieure, 1100 rue Notre-Dame Ouest, Montréal, QC H3C1K3, Canada
[3] Simulation and Reliability Metier, Valeo Thermal Systems, 78320 La Verrière, France
* Correspondence: stephane.moreau@usherbrooke.ca

Abstract: The effect of blade sweep has been studied numerically with the Lattice Boltzmann Method on a family of low-speed free-vortex axial fans with sweeps of ±45°. Good overall aerodynamic agreement is first demonstrated on all fans at the design condition, particularly in the tip gap. The local larger wall-pressure fluctuations seen in the unswept and backward swept fans compared to the forward case are traced to the stronger tip vortices that remain in the rotational plane or even move upstream. These stronger and faster vortices interacting with the fan blades are then responsible for the larger noise levels observed in the acoustic spectra of these fans, and particularly for large subharmonic humps. Excellent agreement between experimental and numerical noise predictions is finally reported stressing the dominant tip noise.

Keywords: axial fan noise; subharmonic humps; Lattice Boltzmann Method; noise generation mechanism; fan blade sweep

check for updates

Citation: Ghodake, D.; Sanjosé, M.; Moreau, S.; Henner, M. Effect of Sweep on Axial Fan Noise Sources Using the Lattice Boltzmann Method. *Int. J. Turbomach. Propuls. Power* **2022**, *7*, 34. https://doi.org/10.3390/ijtpp7040034

Academic Editor: Thomas Carolus

Received: 23 August 2022
Accepted: 14 November 2022
Published: 22 November 2022

Publisher's Note: MDPI stays neutral with regard to jurisdictional claims in published maps and institutional affiliations.

Copyright: © 2022 by the authors. Licensee MDPI, Basel, Switzerland. This article is an open access article distributed under the terms and conditions of the Creative Commons Attribution (CC BY-NC-ND) license (https://creativecommons.org/licenses/by-nc-nd/4.0/).

1. Introduction

Low-speed axial fans are widely used in many ventilation applications (automotive and train engine cooling, tunnel venting, electronic and electrical motor cooling, residential air conditioning systems). They contribute to the rising environmental noise pollution, which needs to be mitigated for all fan manufacturers in order to meet new regulations [1]. To reach such a goal, the cheapest noise control strategy is modifying the blade geometry itself. Blade skew for instance [2] has been shown to reduce fan noise, and several patents have already been filed around the noise benefits achieved by either forward or backward sweep. For low-speed rotating machines, sweep is the angle defined in the plane of rotation [3]. This is the definition used in the present work. Different behaviors and mitigation results have also been observed depending on the operating conditions. Moreover, noise predictions are still often based on empirical models and iterative, lengthy experimental investigations that do not allow a fine understanding of the aeroacoustic source mechanisms and a significant noise reduction. In fact, the origin of the noise reduction caused by sweep is still a matter of debate as stressed in [4,5], which makes it difficult to assess and quantify the noise reduction provided by sweep for each new fan design.

Yet, in recent years, new methods such as the Lattice Boltzmann method have emerged that can provide direct noise predictions in complex, realistic environments [5,6]. In the present study, the effect of sweep on fan noise is then tackled with an unsteady Lattice-Boltzmann solver, by mimicking as closely as possible the experiments run at the Friedrich-Alexander Universität (FAU) on a family of fans designed with different sweeps for the same operating condition [3,7–10]. Both aerodynamic and acoustic results are reported to shed a deeper insight into the aero-acoustic effect of sweep and how it can help mitigate fan noise.

2. Experimental Background

2.1. Configuration Description

The investigated axial fans of diameter D = 495 mm shown in Figure 1 have 9 blades made of NACA 4510 profiles. Different blade designs were considered [5]: we here focus on the S1-family designed with a free vortex. All fans have been designed for the same operating conditions: a flow rate of 1.4 m^3/s (flow coefficient ϕ = 0.252), a total-to-static pressure difference of 150 Pa, at 1500 rpm. They are either unswept (US) or forward swept (FS) or backward swept (BS). The latter sweep is significant, $\pm 45°$. They have been tested in the FAU anechoic wind tunnel (Erlangen-Nürnberg, Germany) shown in Figure 2, which consists of a large anechoic room around which is wrapped a ducted fan and silencers. The fans are placed in a short duct with a bell-mouth attached to the downstream part of the plenum (Figure 2 (right)). The gap between the duct and the fan tip is 2.5 mm. For the above operating conditions, the blade-passing frequency (BPF) is 225 Hz.

Figure 1. Investigated fans; **left**: unswept (US); **center**: forward swept (FS); **right**: backward swept (BS). Note the rotational direction is clockwise.

2.2. Experimental Database

Overall flow performances have first been measured for all fans. The flow enters the test rig at the top in Figure 2a through a standardized inlet bell mouth to measure the volume flow rate. In order to provide homogeneous and low-turbulent inflow conditions for the test fan, a flow straightener is installed inside the test chamber. The total-to-static pressure difference is measured with a differential pressure transducer that is connected to pressure taps inside the test chamber and to an ambient pressure line outside the test chamber. All detailed velocity measurements were achieved with a laser Doppler anemometer in two planes 10 mm before and after the fans. The sound pressure levels were measured with seven 1/2 inch free-field Brüel & Kjær microphones (type 4189-L-001), placed on a semicircle at a radius of 1 m around the inlet bell mouth in a horizontal plane at the same height as the fan rotational axis (Figure 2b).

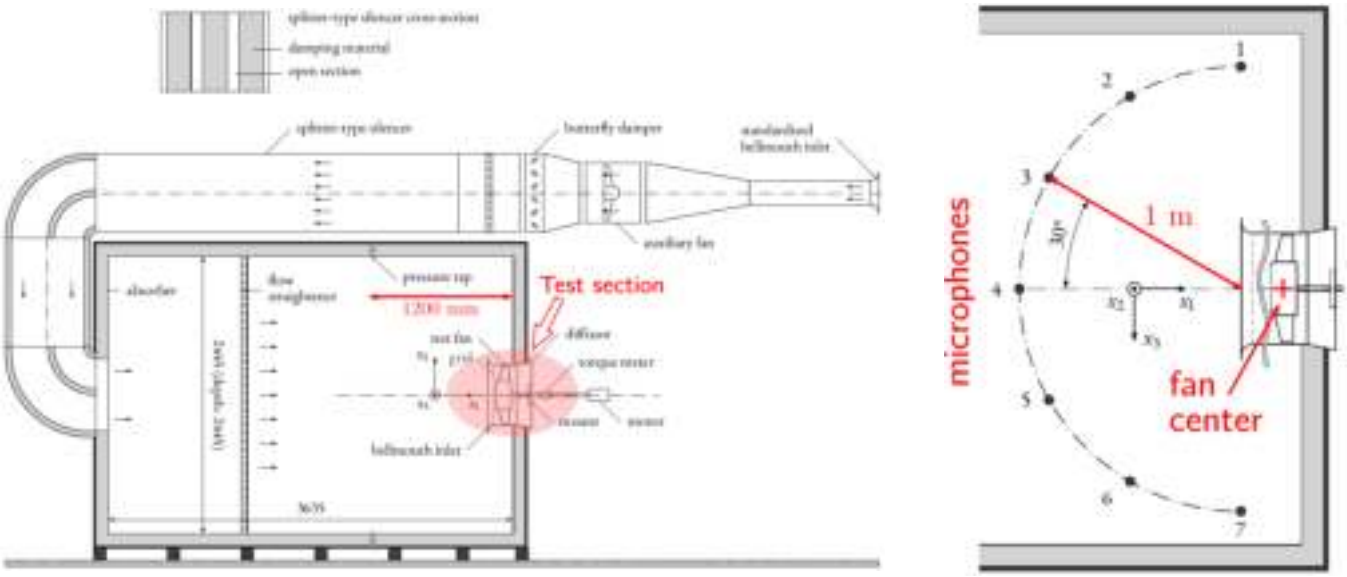

Figure 2. Sketch of anechoic test facility at FAU (**a**) and microphone arrangement (**b**) (adapted from [5]).

3. Numerical Investigation

3.1. Numerical Setup

As shown in [7], the Lattice Boltzmann Method (LBM) is a very efficient direct computational aeroacoustic method for low speed fans installed in a complex environment such as described in Figure 2, and has therefore been selected in the present study. All simulations have been achieved with the commercial solver developed by 3DS, PowerFLOW version 5.5c [11–15]. For the present low-Mach number flow, the efficient D3Q19 discretization scheme is used. It has excellent dissipation and dispersion properties as shown by Marié for instance [16], providing not only a direct insight into the near-field acoustic sources in the fan but also in the acoustic propagation to the far field.

The computational domain includes most of the anechoic wind tunnel presented in Figure 2 (left), embedded in a large domain standing for the actual lab as shown in Figure 3. Additional large damping zones wrap around the domain seen in Figure 3, to prevent any reflection. The only simplification has consisted in limiting the outside duct to the final straight section and bend with deflector. Indeed, the flow becomes uniform with the splitter-type silencer in the straight duct. Note that the honeycomb flow straightener inside the plenum shown in Figure 2 (left) is accounted for in the simulation by an equivalent anisotropic porous medium. The computational domain is then discretized by cubic elements called voxels in which all parts of the wind tunnel are immersed. An octree-mesh is then built with consecutive 1: 2 grid refinements. Overall twelve Voxel Refinements (VR) are used in the present model, with a voxel size at the microphone position of 13 mm (VR7) and a smaller size in the tip region of 0.2 mm (VR12). The extruded grid refinement around the blade for the first 75% of span from the hub is 0.8 mm, with a donut covering the rest of the tip part of the blade with two levels of VR. 12 voxels are also present in the tip gap. This has been found necessary to achieve grid independence in the tip part, as already shown by Moreau and Sanjosé [17] on the H380EC1fan at similar flow conditions and tip Reynolds number based on the chord. The finest mesh has 125 million cells and 15 million surface elements. The atmospheric pressure of 101,325 Pa is imposed on the outlet, while the volume flowrate is imposed on the duct inlet. The volume around the fan is set in rotation as described in Perot et al. [6]. Extended logarithmic wall functions taking into account pressure gradients [14] are applied on all wall surfaces. Simulations are initialized from uniform flow at rest on the coarse mesh, which consists of the mesh up to VR 10.

VR11 and VR12 are only activated for the medium and fine grids, respectively to achieve spatial convergence: similar mean properties around the fan are obtained on the medium and fine grids. Time convergence on the overall pressure rise and wall-pressure and far-field acoustic spectra is reached after about 15 fan revolutions, and data are acquired for six fan revolutions. Static pressure is recorded at the exact locations of the microphones in the experiments. In addition, some cross-sections including the ones before and after the fan, and the blade surface are recorded at high frequency sampling for frequency analysis. The numerical model presented above is validated through the comparison of flow parameters (velocity components, wall-pressure) with experimental measurements carried out in the test facility at FAU (Erlangen-Nürnberg).

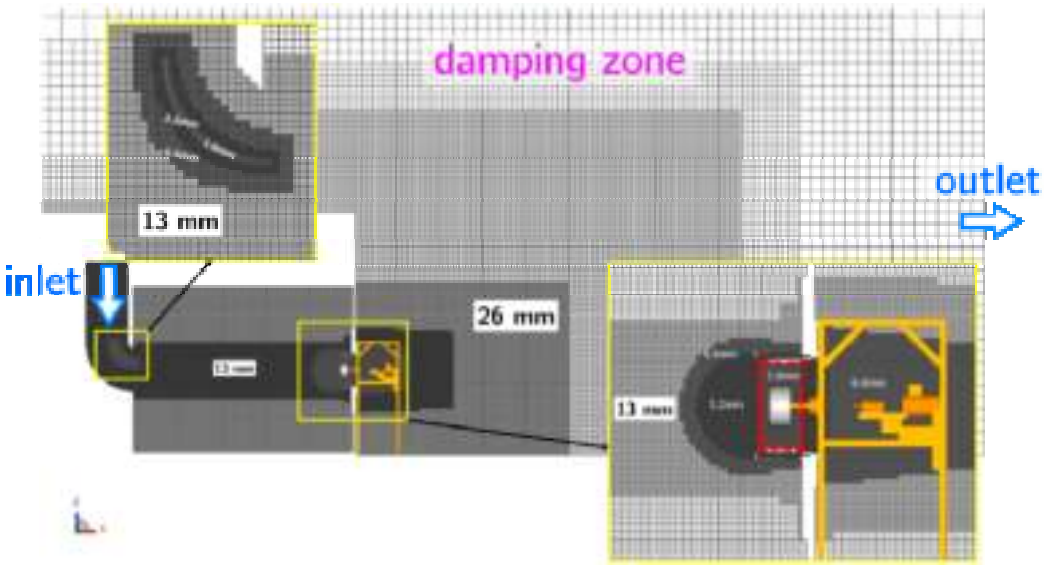

Figure 3. Computational domain and refinement volume definitions of the anechoic test facility at Friedrich-Alexander Universität with a zoom on the ducted fan section. Red square: rotating domain.

3.2. Numerical Results

3.2.1. Aerodynamic Results

Good convergence of the overall pressure rise was achieved on the finer mesh (less than 10% difference). Consequently, most of the post-processing presented below is on the latter grid. Moreover, all comparisons are then made at the nominal flow coefficient of $\phi = 0.252$, as this is the default operating point of the fans where their performance match by design.

The overall mean flow topology for the unswept fan case in the whole anechoic wind tunnel is presented in Figure 4. Similar flow features are obtained for the other two fans, as only the near-fields are modified by the blade design. The deflector in the inlet duct and the honeycomb grid to stop the jet in the plenum are necessary to insure a quasi-uniform flow at the duct inlet. The torque-meter and the frame holding the whole system are also seen to be far enough downstream not to create any significant flow blockage and induced potential interaction.

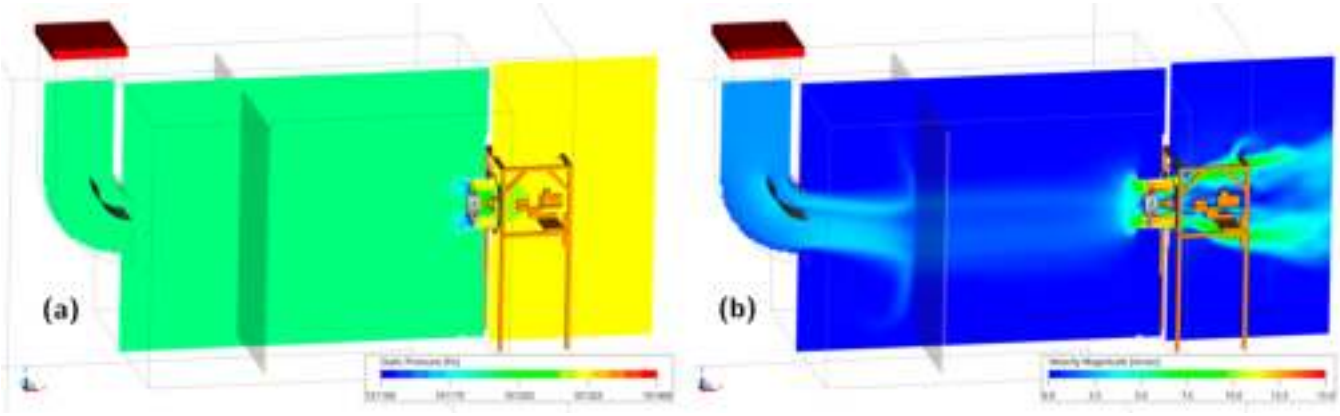

Figure 4. Mean results for the unswept fan case: (**a**) static pressure; (**b**) velocity magnitude.

To get quantitative near-field aerodynamic validation, the LBM results can be compared to the LDA measurements upstream and downstream of the fan [8]. In Figure 5, the distributions of mean axial velocity in a plane perpendicular to the axis of rotation about 10 mm downstream of the fan trailing edge are shown for all three cases. Figure 6 displays the corresponding mean tangential velocity in the same plane. A good overall agreement is achieved between the experimental and numerical data. Only the blade wakes in the LBM simulations are thicker with slightly deeper velocity deficits and a larger tangential component below 75% of span. This is most likely due to the lower mesh refinement in the bottom part of the blade. Yet, at the tip, both the levels and patterns are closely matching thanks to the finest VR. Similar results are obtained for the radial component and in the upstream plane.

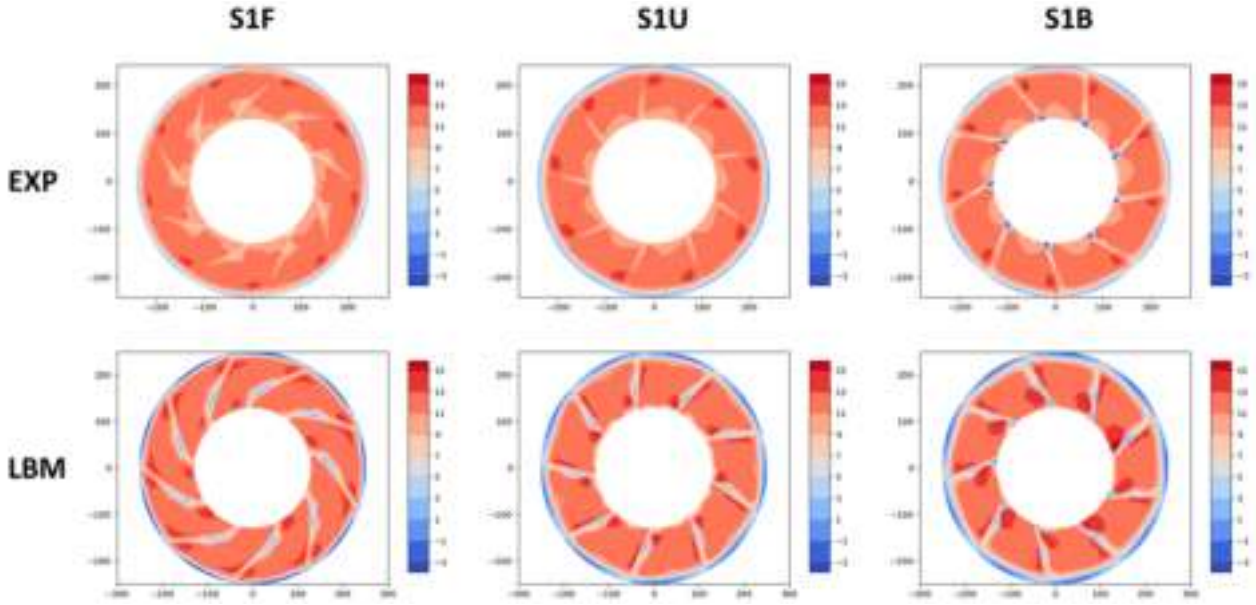

Figure 5. Mean axial velocity at the trailing edge: comparison of experiment (**top**) and LBM results (**bottom**) for S1F (**left**), S1U (**middle**), and S1B (**right**) fans. Fan dimensions in mm and velocity in m/s.

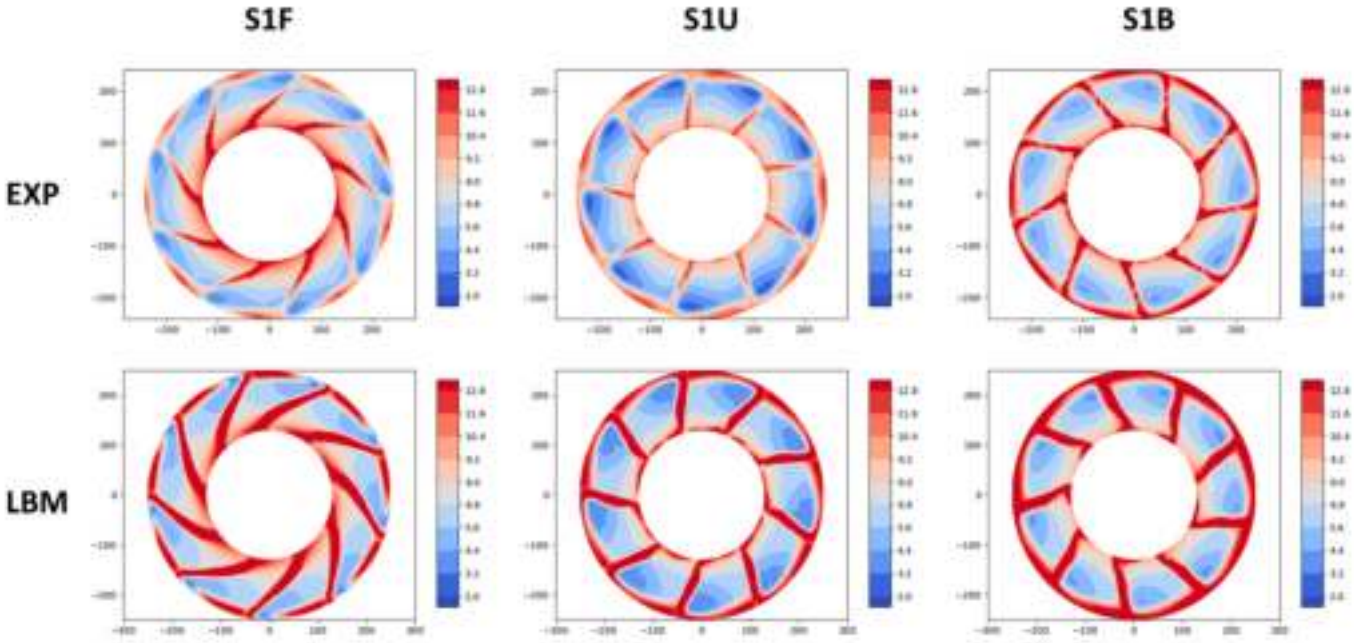

Figure 6. Mean tangential velocity at the trailing edge: comparison of experiment (**top**) and LBM results (**bottom**) for S1F (**left**), S1U (**middle**), and S1B (**right**) fans. Fan dimensions in mm and velocity in m/s.

Good overall agreement is also achieved on the root-mean-squared velocity components downstream of the fan. Therefore, the mean flow field predicted by LBM matches the experimental one very well. Yet, as shown by the Ffowcs Williams and Hawkings' acoustic analogy [18], noise sources in low speed fans come from the flow unsteadiness and particularly the wall-pressure fluctuations.

To assess the quality of the numerical predictions in the tip region where the effect of the blade sweep is felt the most, comparisons with the wall-pressure measurements of the probes placed on the stationary shroud in the tip region are achieved. The latter are shown with respect to the blade position in Figure 7. As the blade skew modifies the relative position of the probes with respect to the tip region, this is specified in each comparison with a given fan. Figure 8 shows the power spectral density (PSD) of the wall-pressure on probes 4 (left), 7 (middle) and 10 (right) for the S1F (top), S1U (middle) and S1B (bottom) fans, respectively. Note that these PSD have all been obtained with the Pwelch function implemented in Matlab with a 6 Hz bandwidth and a Hanning windows with 10% overlap for both numerical and experimental data to make a fair comparison. Excellent comparison between experiment and LBM results is achieved on all probes and for all fans (at least up to 1.5 kHz), which suggests that the vortex dynamics in the tip gap is well captured for the relevant largest structures (the wall-pressure fluctuations being the trace on the wall of all turbulent eddies developing above it). Moreover, the BPF and many of its harmonics are seen on all probes inside the tip gap for all fans. The BPF and some harmonics are also seen before and after the tip gap in the US and BS configurations. Only the FS case does not show any tones outside the tip gap, with the lowest broadband levels, suggesting the weakest flow recirculation in the tip gap.

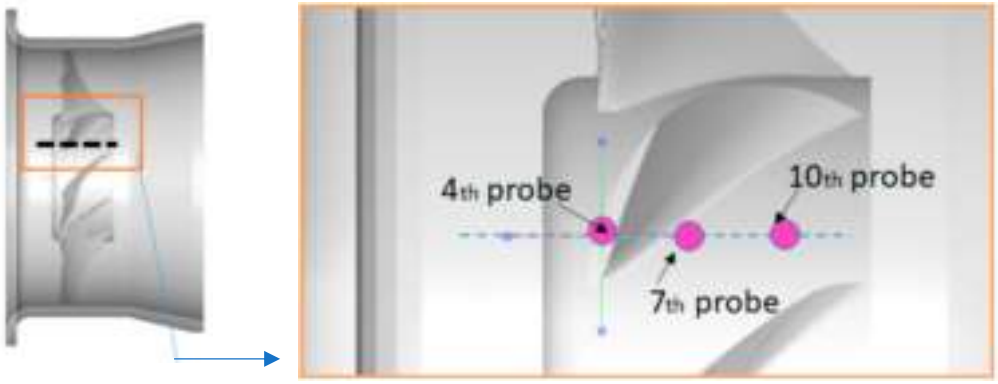

Figure 7. Sketch of the probes located in the casing to record unsteady wall pressure.

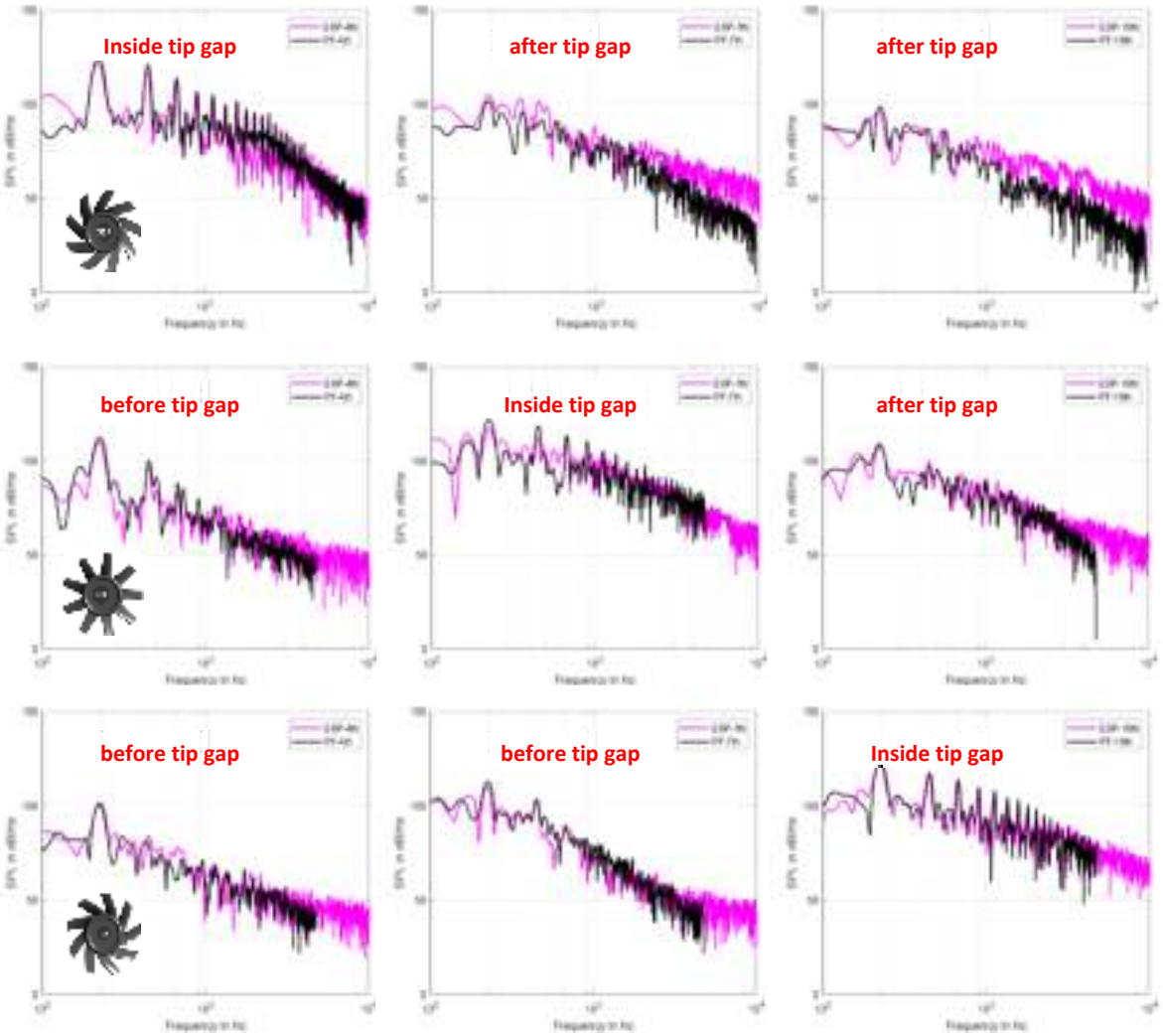

Figure 8. PSD of wall pressure at probes 4 (**left**), 7 (**middle**) and 10 (**right**) for S1F (**top**), S1U (**middle**) and S1B (**bottom**) fans; the relative position of the probes w.r.t the tip gap is shown at the top of each plot.

To confirm the above observations on wall-pressure fluctuations, iso-contours of instantaneous Λ_2 criterion (second invariant of the velocity tensor) that identify eddies in a turbulent flow, colored by the velocity magnitude, are shown in Figure 9 in the tip region. The view from the top of the fan is selected to highlight the interaction of the tip vortices with the blade. Clearly, the tip vortices with a Tip Leakage Vortex (TLV) leaving at the

blade leading edge, interact more strongly with the blade in the US and BS configurations. They also have a higher velocity, which reinforces the impact. In the unswept case (US), the tip vortices interact with the whole blade chord, and in the backward swept case (BS), the tip vortices move even more upstream and strongly interact with the blade leading edge and TLV. Only in the forward swept case (FS), the tip vortices graze along the next blade, and potentially interact with the blade trailing edge only. This consequently explains the lowest wall-pressure fluctuations observed in this configuration in Figure 8.

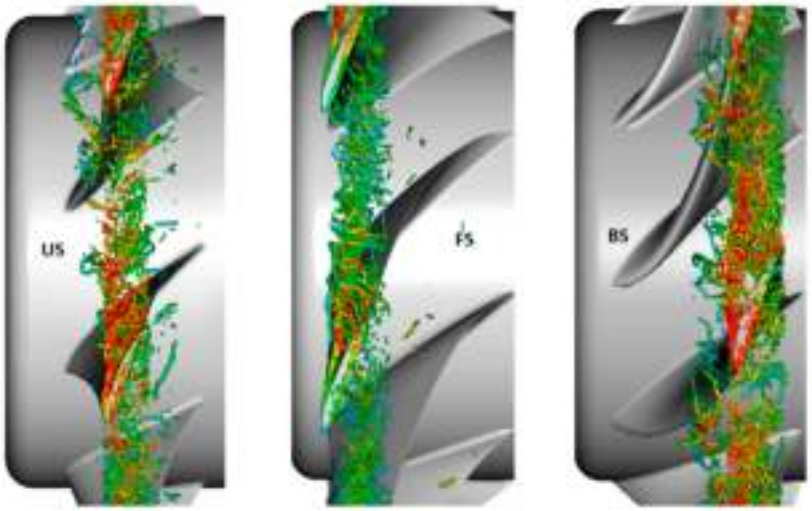

Figure 9. Iso-contours of instantaneous Λ_2 colored by velocity magnitude for S1U (**left**), S1F (**middle**) and S1B (**right**) fans.

3.2.2. Acoustical Results

The far-field acoustic pressure is directly recorded at each location shown in Figure 2 (right), for 17 revolutions for each fan simulation with a sampling frequency of 47.3 kHz. Note that The PSD of the far-field acoustic pressure obtained numerically for the three fans are plotted in Figure 10 for microphone 4 placed in front of the duct on the fan rotational axis. In the latter plot, the vertical dashed lines correspond to the first two BPF. Note again that these PSD all have a 6 Hz bandwidth for both numerical and experimental data to make a fair comparison, and have been obtained with the Pwelch function implemented in Matlab and a Hanning windowing with 10% overlap. The first three plots compare the LBM results on the finest mesh with the measured spectra. The broadband noise levels and spectral shapes are well reproduced (within a dB) over the whole frequency range for all three fans (Figure 10a–c) for the S1F, S1B and S1U fans, respectively). Similar good comparisons have also been obtained on the other microphones. Only the peaks seen at the BPF harmonics in the experiment are not captured. As was shown previously by Sturm et al. in the anechoic wind tunnel at Siegen Universität [19], these tones are caused by the slight asymmetry of the installation of the fan system in the test rig as seen in Figures 3 and 4. The jet entering the chamber is not completely diffused by the honeycomb screen and its direction not perfectly aligned with the fan system axis, yielding a slight difference of flow recirculation at the top and bottom of the test rig as evidenced for instance by the velocity contours in Figure 4 for the unswept fan. This flow distortion ingested by the fan in turn induces the tonal noise contribution. This was actually verified on the coarse mesh for the unswept fan by running a much longer simulation over the whole filling time of the test facility, as was done previously by Sturm et al. [19].

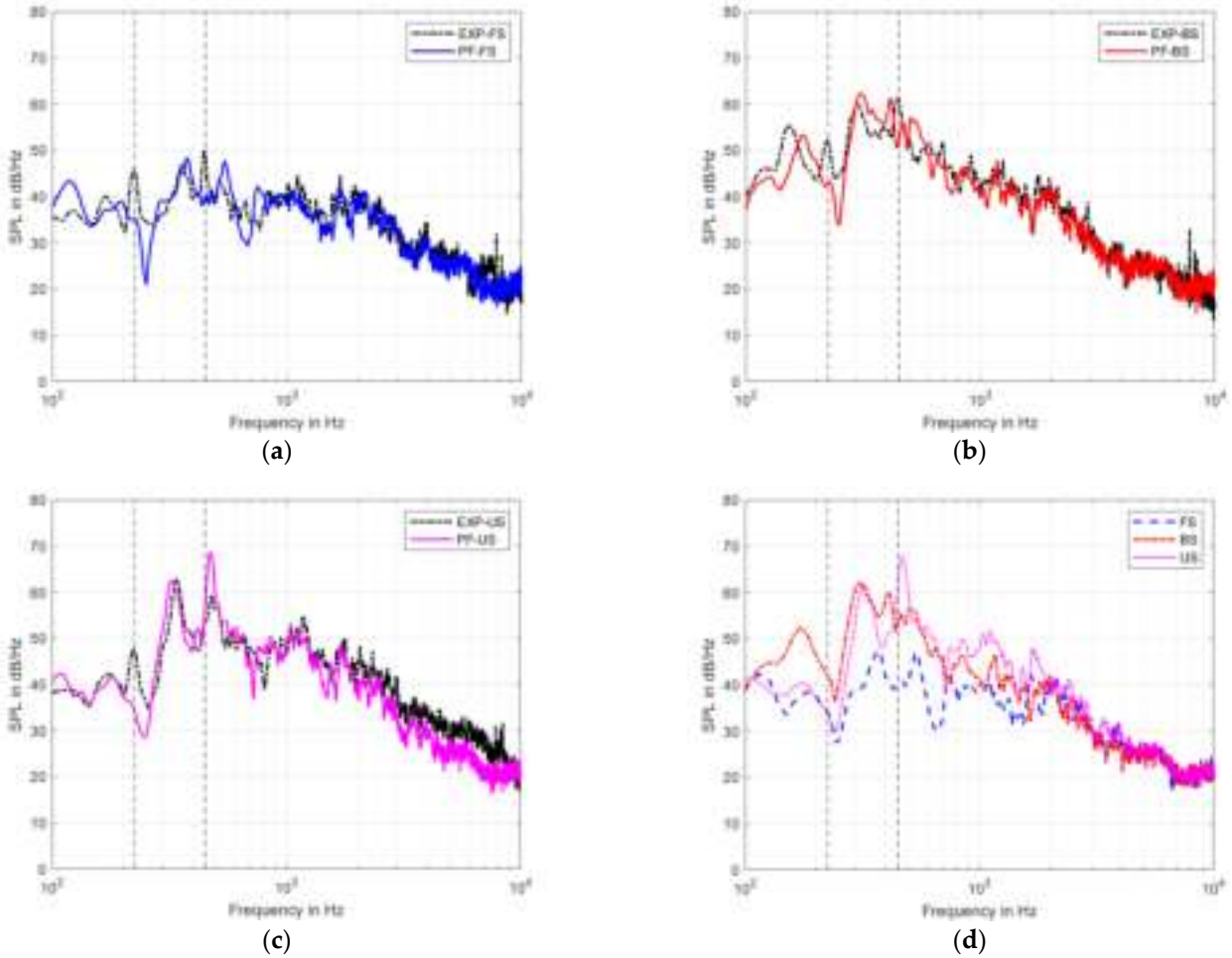

Figure 10. PSD of far-field acoustic pressure for: S1F (**a**), S1B (**b**), S1U (**c**) and all (**d**) fans at microphone 4 shown in Figure 2. The vertical dashed lines identify the BPF.

In Figure 10d, the three predicted spectra are compared. Clearly, a very different behavior is seen below and beyond 2 kHz. At low frequencies (below 2 kHz), the forward swept fan has much lower levels than the other two, with two strong subharmonic humps appearing below the BPF and its first harmonic for the unswept and backward swept fans. Such humps have been previously associated with large vortical structures appearing in the tip gap by Magne et al. [20] and Moreau and Sanjosé [17], and shown by Zhu et al. [21] to be the same phenomenon as rotational instabilities previously evidenced by Kameier and Neise [22]. The frequency range also corresponds to dominant tip noise as found by Moreau and Sanjosé [17] and Sanjosé and Moreau [23]. At high frequencies (beyond 2 kHz), all spectra merge, which may correspond to the trailing-edge noise contribution expected to be similar as the fan have the same profiles operating at the same (or similar) flow condition as mentioned above.

To get further insight in the noise sources, iso-contours of wall-pressure fluctuations filtered around selected frequencies have been studied, as they correspond to the main noise sources on a fan at low Mach number. Figure 11 shows the PSD of such fluctuations around 350 Hz (the largest subharmonic hump below BPF2). High wall-pressure fluctuations are seen in the tip region for the US and BS fans on both suction and pressure sides, stressing the strong impact of tip vortices with the blades in these cases as already shown in Figure 9. Note that the BS case even show the highest levels with the largest spanwise trace on the blades: the vortices in Figure 9 are not only larger and more energetic, but they also plunge farther toward the hub. For the FS fan, the largest levels are actually at the hub, caused by the local secondary flow features (corner vortex). Similar results are found

from 150 Hz up to 2 kHz stressing the importance of tip noise in this frequency range, as already aforementioned.

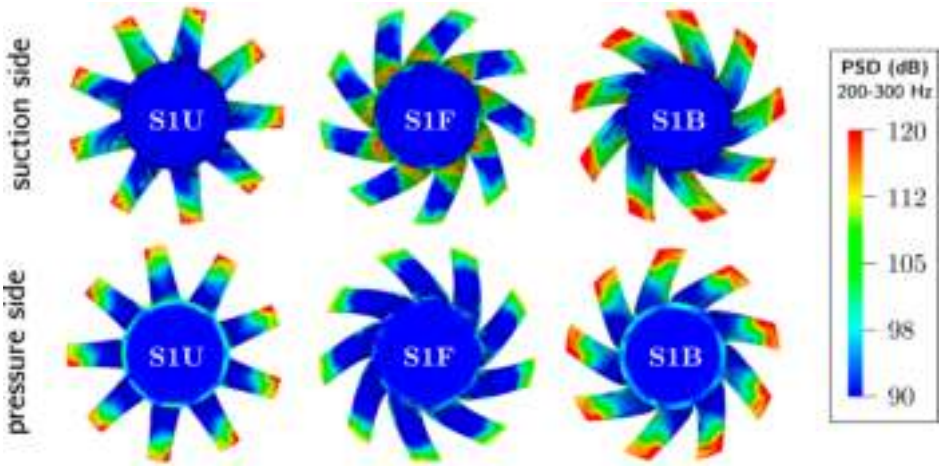

Figure 11. PSD of wall-pressure filtered around 350 Hz for S1U (**left**), S1F (**middle**) and S1B (**right**) fans. Suction (**top**) and pressure (**bottom**) sides of the fan blades.

4. Conclusions

The effect of blade sweep on axial fan noise has been studied numerically with the Lattice-Boltzmann method. A family of free-vortex axial fans designed and tested at Friedrich-Alexander Universität have been simulated in their actual test configurations. Good overall performances have been predicted and the detailed velocity maps before and after the fan also compare well with the previous LDA measurements for all three fans with various sweep. Excellent agreement is finally achieved on all spectra of the wall-pressure fluctuations in the tip gap where most of this low-speed fan noise is expected. Some clear difference is noticed between the forward swept fan and the other two fans: the latter have higher wall-pressure levels and more tonal content over a wider region in the tip gap. These fluctuations are the traces of the tip vortices that are stronger and occupy a larger area in the unswept and backward swept cases. The analysis also shows that the tip vortices stay in the rotational plane for the unswept fan, that they move even forward in the backward swept case, whereas they are more convected downstream in the forward swept case with hardly any interaction with the next blade. Thus, fan sweep alters the aerodynamic flow field significantly. Moreover, as previously shown in ring fans, these strong interactions of the tip vortices with the fan blades are responsible for large subharmonic humps in the far-field acoustic spectra, and consequently contribute to the large increase of noise in the unswept and backward swept fans compared to the forward case. The simulated noise spectra compare very well with experiment both in terms of levels and shapes. These spectra and the corresponding wall-pressure maps on both suction and pressure sides of all fan blades confirm the dominant tip noise in such low-speed axial fans, particularly in the most annoying frequency range below 2 kHz.

The LBM simulations have brought new insight in the particular role of the leakage flow on the noise emission. The sweep angle is a fan parameter that might be used to limit the blade-vortex interaction and to improve future fan designs.

Author Contributions: Conceptualization, D.G. and S.M.; methodology, M.S., S.M. and M.H.; formal analysis and investigation, D.G. and S.M.; data curation, D.G. and M.S.; writing—original draft preparation, S.M.; writing—review and editing, S.M. and M.S.; visualization, D.G. and M.S.; supervision, S.M.; project administration, S.M. and M.H.; funding acquisition, S.M. All authors have read and agreed to the published version of the manuscript.

Funding: This research was funded by Valeo (France) through the Chaire Aéroacoustique de l'Université de Sherbrooke.

Institutional Review Board Statement: Not applicable.

Informed Consent Statement: Not applicable.

Data Availability Statement: Not applicable.

Conflicts of Interest: The authors declare no conflict of interest.

References

1. Moreau, S. A Review of Turbomachinery Noise: From Analytical Models to High-Fidelity Simulations. In *Fundamentals of High Lift for Future Civil Aircraft*; Springer: Cham, Switzerland, 2021.
2. Carolus, T.; Beiler, M. Skewed blades in low pressure fans—A survey of noise reduction mechanisms, AIAA 97-1591 paper. In Proceedings of the 3rd AIAA/CEAS Aeroacoustics Conference, Atlanta, GA, USA, 12–14 May 1997.
3. Grasso, G.; Roger, M.; Moreau, S. Analytical model of the source and radiation of sound from the trailing edge of a swept airfoil. *J. Sound Vib.* **2021**, *493*, 115838. [CrossRef]
4. Krömer, F.J.; Moreau, S.; Becker, S. Experimental investigation of the interplay between the sound field and the flow field in skewed low-pressure axial fans. *J. Sound Vib.* **2019**, *442*, 220–236. [CrossRef]
5. Zarri, A.; Christophe, J.; Moreau, S.; Schram, C. Influence of Swept Blades on Low-Order Acoustic Prediction for Axial Fans. *Acoustics* **2021**, *2*, 812–832. [CrossRef]
6. Pérot, F.; Kim, M.S.; Moreau, S.; Henner, M.; Neal, D. Direct Aeroacoustics Prediction of a Low Speed Axial Fan, AIAA 2010-paper. In Proceedings of the 16th AIAA/CEAS Aeroacoustics Conference, Stockholm, Sweden, 7–9 June 2010.
7. Moreau, S. Direct Noise Computation of Low-speed Ring Fans. *Acta Acust. United Acust.* **2019**, *105*, 30–42. [CrossRef]
8. Zenger, F. Sound Emission of Low-Pressure Axial Fans under Distorted Inflow Conditions. Ph.D. Thesis, Friedrich-Alexander-Universität, Erlangen, Germany, 2017.
9. Herold, G.; Zenger, F.; Sarradj, E. Influence of blade skew on axial fan component noise. *Int. J. Aeroacoustics* **2017**, *16*, 418–430. [CrossRef]
10. Schoder, S.; Junger, C.; Kaltenbacher, M. Computational aeroacoustics of the EAA benchmark case of an axial fan. *Acta Acust.* **2020**, *4*, 22. [CrossRef]
11. Chen, S.; Doolen, G.D. Lattice Boltzmann Method for Fluid Flows. *Annu. Rev. Fluid Mech.* **1998**, *30*, 329–364. [CrossRef]
12. Chen, H.; Teixeira, C.; Molvig, K. Realization of Fluid Boundary Conditions via Discrete Boltzmann Dynamics. *Int. J. Mod. Phys. C* **1998**, *9*, 1281–1292. [CrossRef]
13. Chen, H.; Orszag, S.A.; Staroselsky, I.; Succi, S. Expanded analogy between Boltzmann kinetic theory of fluids and turbulence. *J. Fluid Mech.* **2004**, *519*, 301–314. [CrossRef]
14. Fares, E. Unsteady flow simulation of the Ahmed reference body using a lattice Boltzmann approach. *Comput. Fluids* **2006**, *35*, 940–950. [CrossRef]
15. Avallone, F.; van der Velden, W.C.P.; Ragni, D.; Casalino, D. Noise reduction mechanisms of sawtooth and combed-sawtooth trailing-edge serrations. *J. Fluid Mech.* **2018**, *848*, 560–591. [CrossRef]
16. Marié, S. Etude de la Méthode Boltzmann sur Réseau pour les Simulations en Aéroacoustique. Ph.D. Thesis, Université Pierre et Marie Curie, Paris, France, 2008.
17. Moreau, S.; Sanjose, M. Sub-harmonic broadband humps and tip noise in low-speed ring fans. *J. Acoust. Soc. Am.* **2016**, *139*, 118–127. [CrossRef] [PubMed]
18. Williams, J.E.F.; Hawkings, D.L. Sound Generation by Turbulence and Surfaces in Arbitrary Motion. *Phil. Trans. R. Soc. Lond.* **1969**, *264*, 321–342.
19. Sturm, M.; Sanjosé, M.; Moreau, S.; Carolus, T. Aeroacoustic Simulation of an Axial Fan including the Full Test Rig by using the Lattice Boltzmann Method. In Proceedings of the Fan 2015 Conference, Lyon, France, 15–17 April 2015.
20. Magne, S.; Moreau, S.; Berry, A. Subharmonic tonal noise from backflow vortices radiated by low-speed ring rotor in uniform inlet flow. *J. Acous. Soc. Am.* **2015**, *137*, 198–225. [CrossRef] [PubMed]
21. Zhu, T.; Lallier-Daniels, D.; Sanjosé, M.; Moreau, S.; Carolus, T. Rotating coherent flow structures as a source for narrowband tip clearance noise from axial fans. *J. Sound Vib.* **2018**, *417*, 198–225. [CrossRef]
22. Kameier, F.; Neise, W. Experimental Study of Tip Clearance Losses and Noise in Axial Turbomachines and Their Reduction. *J. Turbomach.* **1997**, *119*, 460–471. [CrossRef]
23. Sanjose, M.; Moreau, S. RANS based analytical modeling of broadband noise for a low-speed fan. *J. Acous. Soc. Am.* **2018**, *143*, 198–225. [CrossRef] [PubMed]

International Journal of
Turbomachinery
Propulsion and Power

MDPI

Article

Inlet Gap Effect on Tonal Noise Generated from a Voluteless Centrifugal Fan

Martin Ottersten [1,2,*], Hua-Dong Yao [2] and Lars Davidson [2]

[1] Swegon Operations, SE-40125 Gothenburg, Sweden
[2] Department of Mechanics and Maritime Science, Chalmers University of Technology, SE-41296 Gothenburg, Sweden
* Correspondence: martin.ottersten@chalmers.se

Abstract: In this study, three voluteless centrifugal fans are compared for their aeroacoustic performances. The tonal noise is predicted by coupling the IDDES with Formulation 1A of Farassat. The sources of the tonal noise at the blade passing frequency (*BPF*) are identified. It is found that the sources are related to the fan inlet gap, which introduces higher velocity intensities and turbulent fluctuations interacting with the blade leading edge. By redesigning the gap, the tonal noise at the *BPF* is reduced effectively.

Keywords: voluteless centrifugal fan; gap turbulence; tonal noise; computational aeroacoustics

check for updates

Citation: Ottersten, M.; Yao, H.-D.; Davidson, L. Inlet Gap Effect on Tonal Noise Generated from a Voluteless Centrifugal Fan. *Int. J. Turbomach. Propuls. Power* **2022**, *7*, 33. https://doi.org/10.3390/ijtpp7040033

Academic Editor: Thomas Carolus

Received: 19 August 2022
Accepted: 14 November 2022
Published: 18 November 2022

Publisher's Note: MDPI stays neutral with regard to jurisdictional claims in published maps and institutional affiliations.

Copyright: © 2022 by the authors. Licensee MDPI, Basel, Switzerland. This article is an open access article distributed under the terms and conditions of the Creative Commons Attribution (CC BY-NC-ND) license (https://creativecommons.org/licenses/by-nc-nd/4.0/).

1. Introduction

Today, most people spend the majority of their time indoors. The indoor environmental quality (IEQ) has become more and more important. When considering IEQ, we usually think about temperature, CO_2 level, and humidity. However, it has been noticed that sound quality is an important factor for good comfort in the indoor environment [1,2].

Nowadays, a ventilation system is usually driven by a voluteless centrifugal fan, which has a gap between the rotating fan front shroud and the stationary inlet duct. The pressure difference between the inner and outer sides of the fan drives air to pass through the gap. As clarified by Hariharan and Govardhan [3], increasing the gap width worsens the blade aerodynamic performance.

There are some previous studies on voluteless centrifugal fans. It was found in both simulations and experiments for a voluteless fan [4] that the tonal noise at *BPF* is generated from a helical unsteady inlet vortex that interacts with the rotating blades near the fan backplate. Another cause is inflow distortion, which leads to flow separation at the blade root near the backplate [5]. To solve the inflow distortion, flow obstructions were suggested to be placed upstream of the fan inlet [6]. The shape and location of obstructions were found as the key parameters for noise reduction. Schaefer and Boehle [7] found, using the Lattice–Boltzmann solver, that the accuracy of the noise prediction, especially at *BPF*, is improved when the mesh is refined at the gap and the fan outlet. However, they provided no discussions on the physical mechanisms that are associated with the improved accuracy. In a recent study, the present authors found that for a voluteless centrifugal fan, the tonal frequencies associated with the *BPF* are related to wall pressure fluctuations at the blade leading edge (BLE) [8]. This is produced when turbulent structures, which are generated by the flow through the gap, interact with the BLE near the shroud. To resolve these turbulent structures, the mesh had to be refined at the gap region.

The numerical simulations in the current study are carried out using a hybrid method coupling the improved delayed detached eddy simulation (IDDES) [9] for the flow simulation with the Ffowcs Williams and Hawkings (FW-H) equation [10] for the noise prediction. The IDDES is used in the flow simulation, and the FW-H is used for the noise prediction.

This study aims to investigate how the tonal noise at the *BPF* is affected when the gap is modified. Two different gap designs are compared with a reference fan (Case 1), which is the same fan in the previous study [8].

2. Configuration

The baseline fan (Case 1) and the two different designs (Case 2 and Case 3) are illustrated in Figure 1. Case 1 is the same fan as the one examined in [8]. The fan geometry is the same for all three cases, meaning that the blades, shroud, and backplate are the same. There are seven blades in the fan. A clearance (i.e., the gap) is located between the stationary (brown) and rotating parts (gray). Case 2 has larger gap width (w_{case2}), and Case 3 has smaller gap width (w_{case3}) than Case 1. The gap width is varied by changing the wall thickness of the inlet duct. The rounded edge of the inlet duct is shorted for Case 2 and extended for Case 3. The inlet duct is moved in the axial direction for the different cases so that the axial overlap between the fan shroud and the inlet duct is the same for all cases. As shown in Figure 1d, the fan and inlet duct are placed in a downstream duct, and the inlet duct is connected to an upstream duct. This simple geometry layout is designed for the numerical simulations. This simplification reduces the geometry complexity but retains the principal flow and acoustic characteristics. The fan and case parameters are listed in Table 1. Here, d_1 is the fan intake diameter at the BLE, and d_2 is the fan diameter at the blade trailing edge. For the downstream duct, h_2 denotes the duct length and d_4 the outlet diameter. For the upstream duct, h_1 is the duct length and d_3 the inlet diameter. In addition, h_3 is the distance between the inlet duct and the microphone M1.

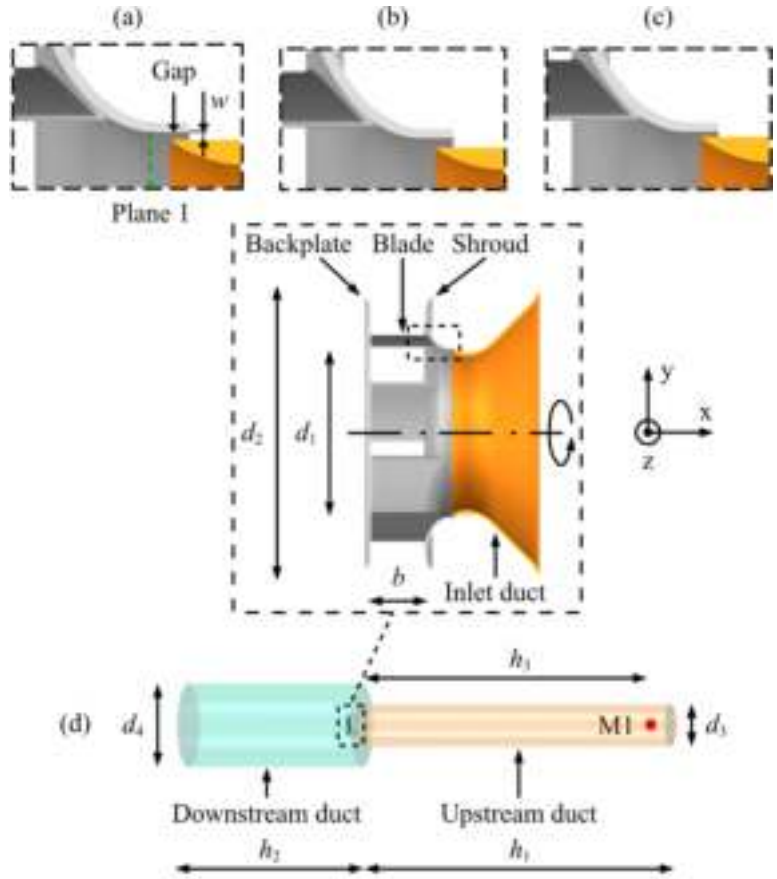

Figure 1. The fan configurations. Gray indicates the rotating fan and brown the stationary inlet duct. (**a**) Case 1 (baseline), (**b**) Case 2 (with a larger gap width = w), and (**c**) Case 3 (with a smaller gap width = w). (**d**) The simple geometry layout for the numerical simulations. M1 is the microphone position. The rotation axis of the fans is the x-axis.

Table 1. The fan parameters.

d_1	d_2	d_3	d_4	b	h_1	h_2	h_3	w_{case1}	w_{case2}	w_{case3}
0.165 m	0.268 m	0.6 m	1.1 m	0.053	4.0 m	2.3 m	3.2 m	1.5 mm	2.0 mm	1.0 mm

The fan rotation speed is 2800 rpm. Given that the fan has seven blades, the *BPF* is 326.7 Hz. The operation condition is the same as in [7], where the mass flow rate was set to 0.467 kg/s, and this gave a pressure rise of 270 Pa for Case 1.

3. Numerical Methodology

3.1. CFD Method

The air is considered as an ideal gas. The flow is compressible. A finite volume method is utilized to discretize the continuity, momentum, and energy equations. The method employs a segregated flow solver accomplished with the Semi-Implicit Method for Pressure-Linked Equations (SIMPLE) algorithm. The under-relaxation factors for the velocity and pressure in the segregated flow solver are set to 0.7 and 0.4, respectively. The under-relaxation factor for the turbulence equations is 0.7. All simulations are performed using the commercial software STAR-CCM+ [11]. The turbulence is simulated using the IDDES [12] combined with the k-ω SST turbulence model. This setup has been tested in several studies on rotating machinery [13,14]. The normal wall sizes of the first layer cells near all walls fulfill $\Delta y^+ < 1$.

3.2. Numerical Settings

The entire computational domain is divided into stationary and rotating parts. The meshes of the stationary and rotating meshes are not conformable at the interfaces between them.

The mass-flow boundary condition is set at the inlet with a uniform velocity distribution. The modeled turbulence intensity is set to $I = 4\%$ according to $I = 0.16(R_e)^{-1/8}$, where the Reynolds number is calculated based on the inlet diameter, d_3 [11]. The modeled turbulence length scale is set to $\updownarrow = 0.5$ m based on $\updownarrow = 0.7d_3$, where d_3 is the upstream duct diameter. The pressure-outlet boundary condition is set at the outlet with the static pressure of 101,325 Pa, which is the reference pressure (p_{ref}) in the ambient air. The no-slip boundary condition is specified on all walls.

To ensure the fan performance, the incoming flow at the fan inlet should not be distorted. Furthermore, there should be no flow separation near the fan inlet, especially on the wall in front of the fan gap. These conditions are satisfied in the present study by aligning a straight duct upstream with the fan axis and inserting a small section of the duct into the fan inlet to form the clearance between the duct and the fan.

The time step is set to $\Delta t = 2.0 \times 10^{-5}$ s. This gives a maximum convective Courant number of around 10, which is observed at the blade trailing edges. This value fulfills the numerical stability required for the implicit time-marching method. The convective Courant number at the gap region is below 1. The maximum number of inner iterations per time step is set to 12.

The sampling period of the noise is 0.3 s for all cases, corresponding to 14 fan revolutions. The sound pressure level (SPL) is calculated using the von Hann window for 3000 samples per signal section, which leads to a frequency resolution of around 3 Hz. The signal sections do not overlap each other.

3.3. FW-H Equation

A hybrid approach is adopted to predict the noise generated from the flow. In this approach, the IDDES is coupled with Formulation 1A of Farassat [15]. The ambient air density is set to $\rho_0 = 1.225$ kg/m^3 and the speed of sound $c_0 = 340$ m/s.

According to Neise [16], the fan noise generation at low Mach numbers is dominated by dipole noise sources that are derived based on the FW-H equation. Hence, the noise

prediction in this study considers only an impermeable integral surface for Formulation 1A. The selected integral surface are the fan blades, shroud, and backplate (see Figure 1), while the upstream and downstream ducts as well as the fan inlet duct are neglected. Indeed, there is a limited acoustic reflection from these walls [17].

4. Mesh

We adopt the same mesh generation strategy that was developed and evaluated in [8], where the fan is the same as Case 1. A polyhedral mesh generation method was used to produce prism layers near the walls and polyhedral cells in the rest of the computational domain. The use of polyhedral cells for turbomachines was demonstrated in [17,18]. The growth rate is set to 1.05, as suggested in [19]. The most important finding in the mesh study performed in [8] was that a local mesh refinement has to be made at the regions extending from the gap to the BLE and along the shroud to the blade trailing edge (colored in dark grey), as illustrated in Figure 2. The same mesh distribution and refinement are used for the three cases. The mesh parameters are listed in Table 2.

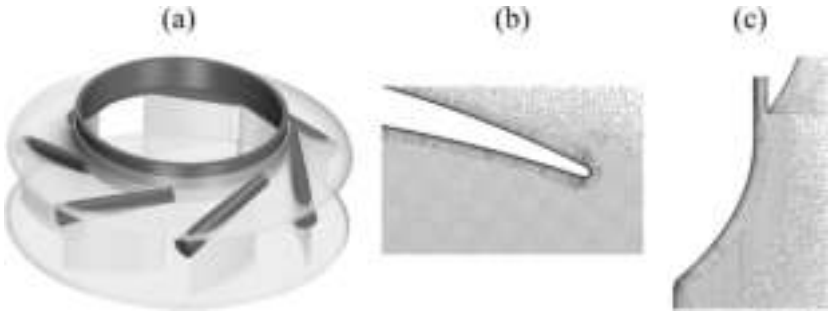

Figure 2. Important mesh regions: (**a**) Mesh refinement regions (dark grey) at the inlet gap and blades top region. Mesh cells near (**b**) the blade trailing edge and (**c**) the inlet gap.

Table 2. The mesh parameters.

	Cases 1–3
Total number of cells	52×10^6
Number of cells in the rotating zone	41.9×10^6
Maximum first cell height Δy^+ near blade walls	0.73
Cell growth ratio	1.05

5. Results and Discussion

5.1. Identifying Sources for Tonal Noise for Case 1

The contours of vorticity magnitudes $\| \vec{\omega} \|$ at the blade leading edge for Case 1 is shown in Figure 3a. There are regions with high vorticity magnitude upstream of the BLE. Here, the BLE is marked out with a dashed line. They are generated when the gap flow is mixed with the main flow. This phenomenon was also observed in previous studies [8,20]. The black dashed line is a monitoring line positioned at the BLE of one blade, and it extends from the backplate to the shroud. The monitoring line follows the blade as the fan rotates, and the wall pressure is monitored for 12 fan revolutions. The root mean square (RMS) of the wall pressure fluctuations is shown in Figure 3b. At the position nearest the shroud, the RMS has its highest value. As the distance to the shroud increases, the pressure RMS value decays. At the backplate, the pressure RMS value is 5 Pa, which is approximately 4% of the value at the shroud (129 Pa).

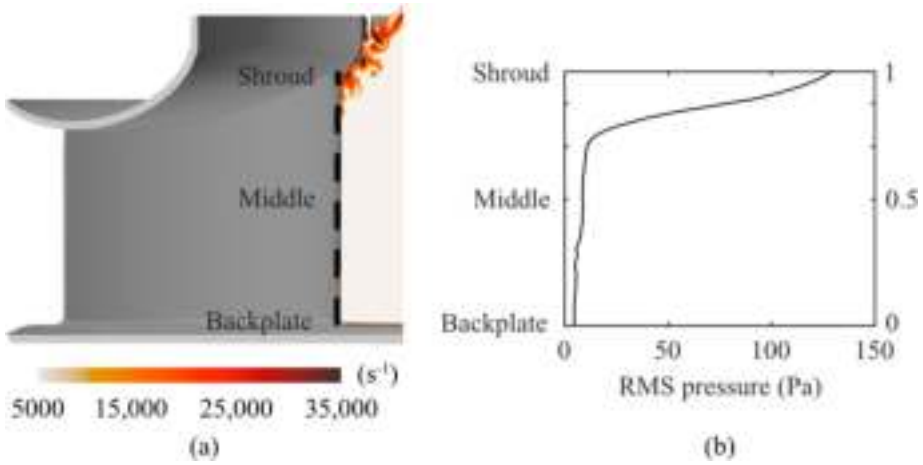

Figure 3. Turbulence at the BLE: (**a**) Vorticity magnitude $\| \vec{\omega} \|$ at one blade. The black dashed line marks the monitoring line at the BLE; (**b**) the RMS of the pressure fluctuations with respect to the normalized length along the monitoring line.

The time history of the wall pressure at the monitoring line is shown in Figure 4. At the position on the shroud, the pressure fluctuates with large amplitudes and high frequencies. As the distance from the shroud increases, the amplitudes of pressure fluctuations decrease. Small fluctuations are observed at the middle position. At the backplate, fluctuations are almost negligible.

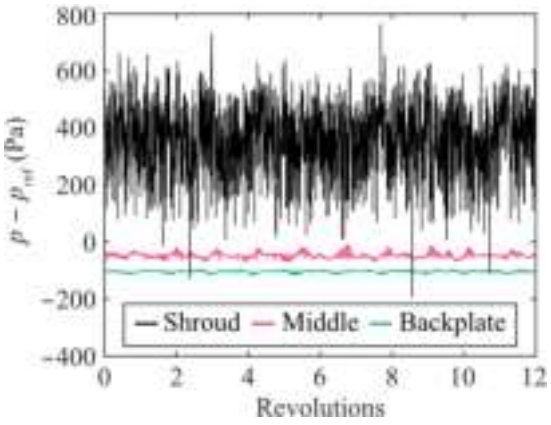

Figure 4. The time history of wall pressure fluctuations at three locations along the BLE.

Moreover, a periodic low-frequency fluctuation in relation to the fan revolution is observed, which was also found in [21]. By comparing the three monitoring points, high-frequency fluctuations decay rapidly with increased distance to the shroud. The periodic low frequency is predominant at the middle position and at the backplate.

Based on the band-filtered power spectral density(PSD) of the wall pressure fluctuations, the location and magnitudes of dominant tonal noise sources are evaluated. The results at the tonal frequency *BPF* (326.7 Hz) are illustrated in Figure 5. The PSD is calculated using the von Hann window for 3000 samples per signal section, which leads to a frequency resolution of around 3 Hz. The signal sections do not overlap each other. The location of the highest wall pressure fluctuations is at the same position (the BLE close to the shroud) as the region with high vorticity magnitudes, high-pressure RMS value, and largest pressure fluctuation. Hence, the interaction between inlet-gap turbulence and the BLE is responsible for the tonal noise generation. This was also found for Case 1 in a previous study [8]. This approach is therefore selected when the three cases are compared in the following analysis.

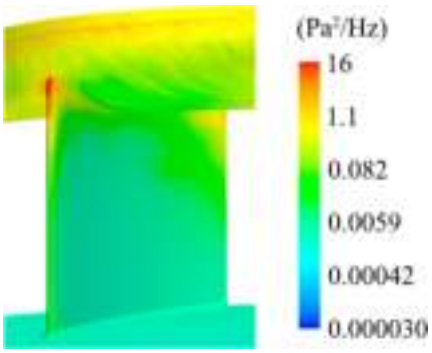

Figure 5. PSD of the wall the wall pressure fluctuations at *BPF* (326.7 Hz).

5.2. Fan Performance Comparison

The static pressure excluding the reference pressure $\left(p_{ref} = 101,325 \text{ Pa}\right)$ is displayed along the axial symmetric line for the three cases in Figure 6. All cases show similar pressure amplitudes in the upstream duct of the fan, while differences are seen downstream. Case 3 has the highest pressure, and Case 2 has the lowest. The difference in the pressure rise downstream of the fan is only due to the gap design. Hariharan and Govardhan clarified [3] that when the gap width is increased, the blade aerodynamics performance is worsened. In addition, when the gap width is decreased, the performance is improved, which is seen in Figure 6. According to Lee [20], a smaller gap improves the flow when it turns from axial to radial, and it also improves the flow separation conditions at the blade trailing edge.

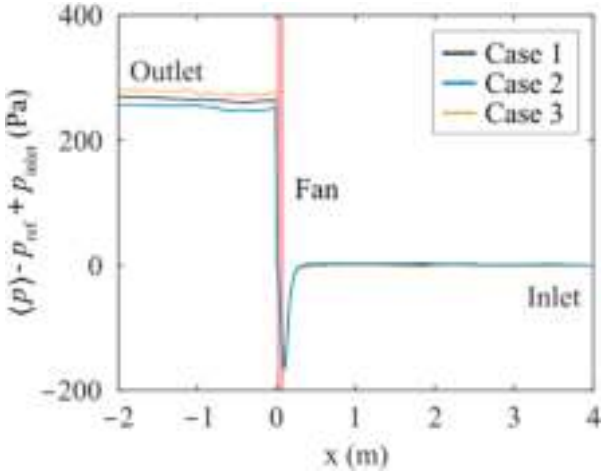

Figure 6. The pressure along the axial axis of the fan across the computational domain. Here, $x = -2$ corresponds to the location near the outlet and $x = 4$ near the inlet. The fan location is marked out with the red zone.

5.3. Wall Pressure Fluctuations Comparison

The RMS of pressure fluctuations at the monitoring line at the BLE (described in Figure 2a) are illustrated for all cases in Figure 7a. At the position nearest the shroud, the highest pressure RMS value is observed for all cases. The pressures' RMS values have the same physical behavior for all three cases, and when the distance to the shroud increases, the pressure fluctuations decay. From the shroud to the backplate, Case 2 has the lowest pressure RMS value, and Cases 1 and 3 have the highest. At the backplate, the cases have almost the same pressure RMS value, approximately 4% of the maximum value.

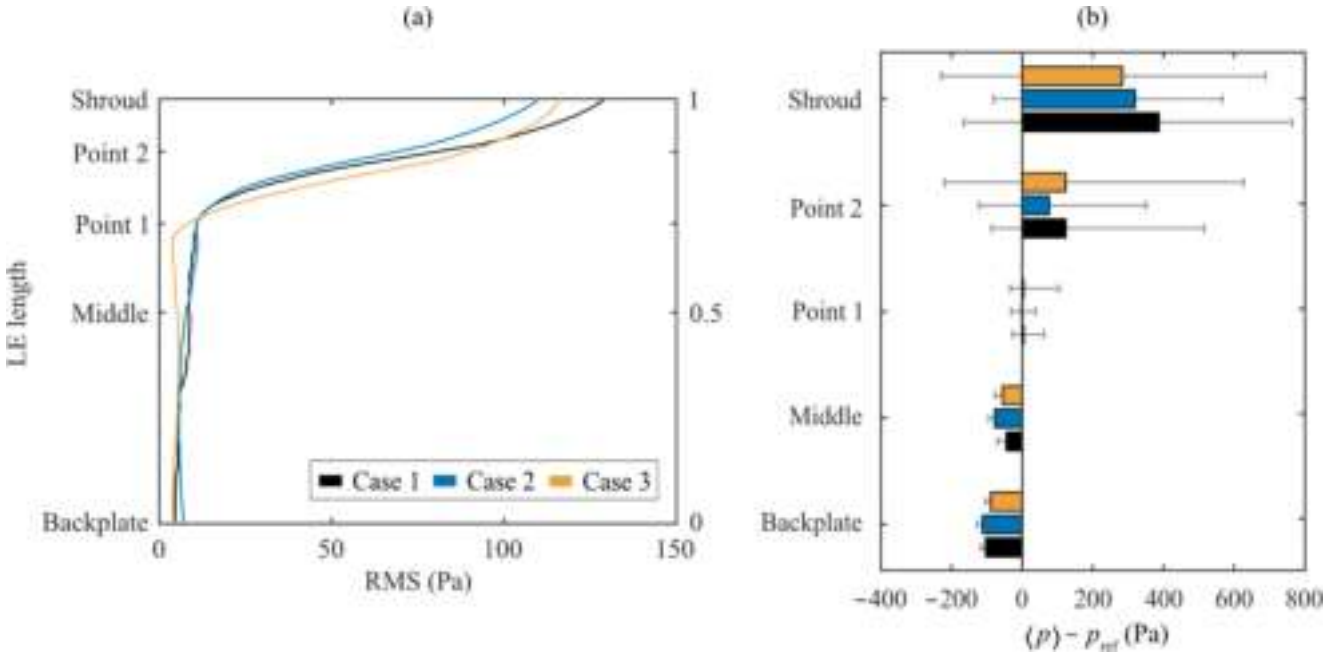

Figure 7. Pressure at BLE. (**a**) The RMS of the pressure fluctuations for 12 fan revolutions, on one blade at the monitoring line; (**b**) the time-average pressure and error bars showing the minimum and maximum pressure.

The time-average of the wall pressures at the BLE are shown at different positions for all cases in Figure 7b. The maximum values for all cases occur at the shroud, whereas at the backplate, the values are negative. The amplitudes of the maximum and minimum pressure (error bar) are the largest at the shroud, and it becomes smaller when the distance from the shroud increases for all cases. At the shroud, Case 1 has the highest amplitude. Case 2 has the lowest amplitudes at all positions. At point 2, the maximum positive fluctuations are larger than the magnitude of the negative ones, and it is the same for all cases.

Figure 8 shows the time history of the wall pressure for all cases at point 2 during 12 fan periods. The dashed lines indicate the average value for each case, and as illustrated in Figure 7b, it is lowest for Case 2. For Cases 1 and 3, pressure fluctuations with large amplitudes and high frequencies are observed. Fluctuations are also obvious for Case 2, but the amplitudes are smaller. Moreover, a periodic low-frequency fluctuation in relation to the fan rotation is seen for Case 2, which was also found in [21]. For Cases 1 and 3, there is no clear periodic low-frequency fluctuation. For all the cases, the maximum absolute values of the positive fluctuations are larger than those of the negative fluctuations. The reason is due to the upstream turbulent vortex impingement.

The contours of the velocity magnitudes, $|v_R|$, defined in Equation (1), in the y-z plane (see Figure 1) and the streamlines (colored in gray) of the relative velocity vectors in Plane 1 (location see Figure 1a) are shown for all cases in Figure 9. Note that the axial velocity component along the fan rotation axis is excluded from the vectors. For Case 1 and 3, there are regions with large velocity magnitudes near the shroud. These regions appear periodically in relation to the blade positions. These regions cannot be observed for Case 2. This suggests that the flow near the shroud is highly fluctuating due to the gap turbulence and that Case 2 has less turbulence above the blades (near the fan inlet).

$$|v_R| = \sqrt{v_y^2 + v_z^2} \tag{1}$$

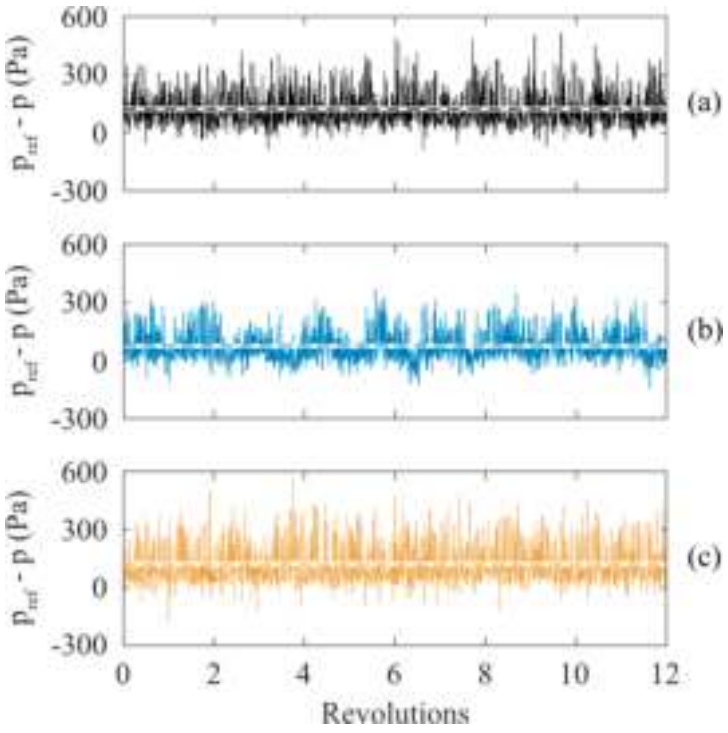

Figure 8. The time history of wall pressures along the BLE at point 2: (**a**) Case 1, (**b**) Case 2, and (**c**) Case 3. The dashed lines indicate the average value for each case.

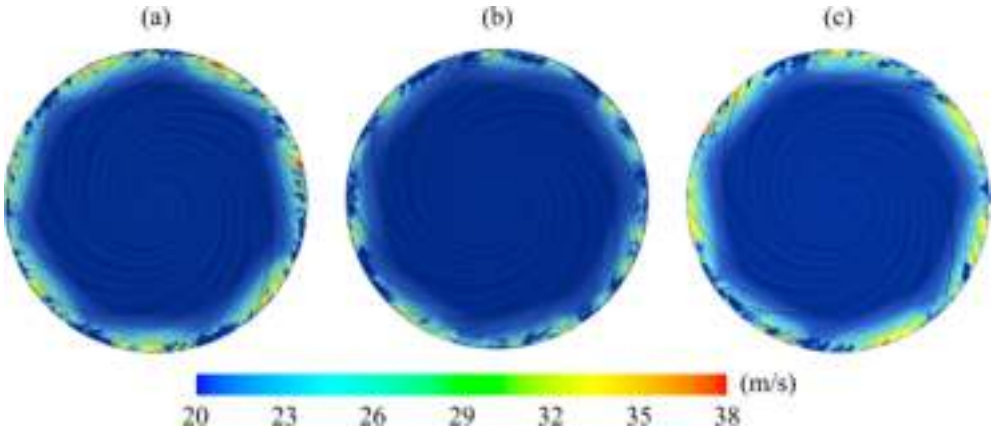

Figure 9. Instantaneous velocity magnitudes $|v_R|$ visualized in Plane 1: (**a**) Case 1, (**b**) Case 2, and (**c**) Case 3.

In the previous studies of Case 1 where the numerical prediction was compared with experimental data [17,21], it was shown that SPL at *BPF* was best-predicted upstream of the fan. The SPL predicted upstream of the fan (microphone M1) for the tonal frequency *BPF* is compared between the cases in Figure 10. Case 1 and 3 have almost the same *BPF* amplitude. The lowest *BPF* amplitude has Case 2, where the level decreased by 5.7 dB compared with Case 1. These results agree with the results from Figures 7–9, where Case 2 had the lowest wall pressure on the BLE.

The cases are compared for their aerodynamic and acoustic performance in Table 3. Increasing the gap size reduces the tonal noise at the *BPF*, and the static pressure rise also decreases.

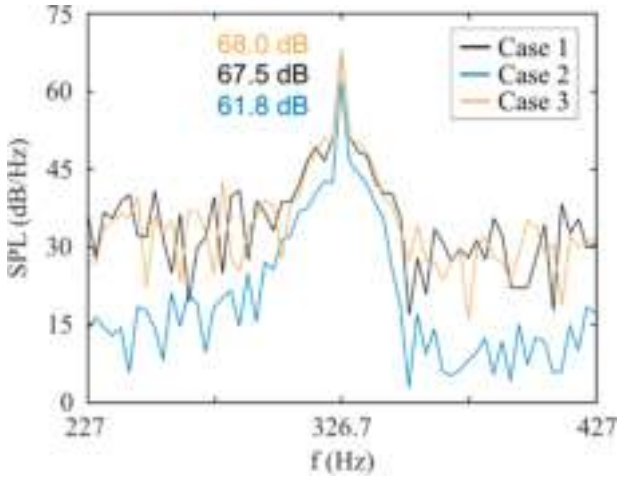

Figure 10. SPL of the sound upstream of the fan. The tonal frequency $BPF = 326.7$ Hz.

Table 3. Aerodynamic and acoustic performance.

Comparative Features	Case 1	Case 2	Case 3
Gap width (mm)	1.5	2.0	1.0
Static pressure rise (Pa)	268	261	281
SPL at *BPF* (dB)	67.5	61.8	68.0

The results of the wall pressure fluctuations at the *BPF* are illustrated for the three cases in Figure 11. Here, only magnitudes above 1.5 Pa^2/Hz are visualized with colorful contours. The location of the highest wall pressure fluctuations is at the same position (the BLE close to the shroud) for all cases. The differences are the magnitude and the size of the area with high magnitude. Case 1 and Case 3 have the largest sound pressure (see Figure 10), and they have also the largest area and magnitude for the tonal frequency. The high-energy locations are consistent with the wall pressure fluctuations indicated in Figure 7. The high energy is caused by the interaction between inlet-gap vortices associated with the gap turbulence and the BLE [8]. According to Lee [20], the gap gives rise to a local jet, and the velocity magnitude of the air flowing through the gap increases with decreased gap size. Higher velocity leads to more inlet-gap vortices that interact with the BLE, which is also seen in Figure 11, where Cases 1 and 3 have higher PSD value for the *BPF* compared with Case 2.

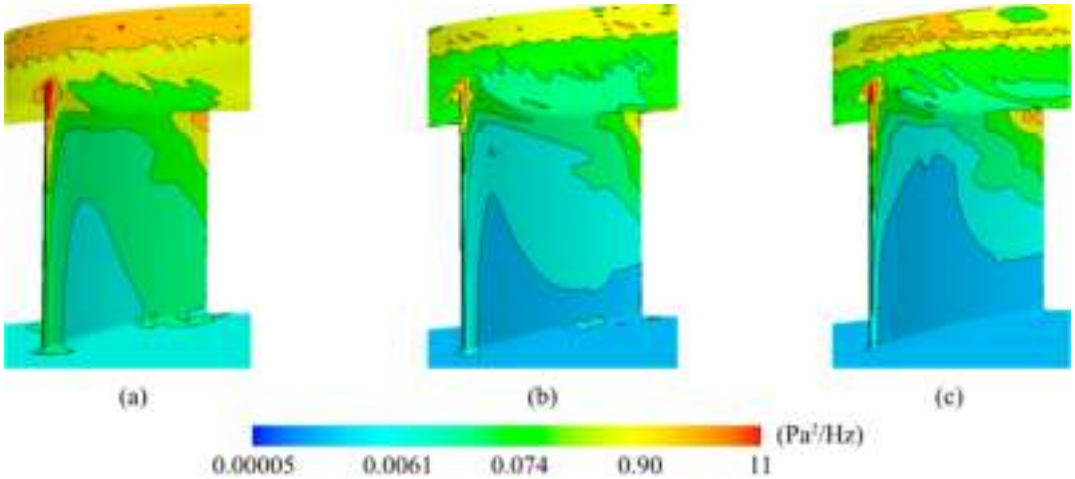

Figure 11. The PSD at *BPF* (326.7 Hz) for wall pressure fluctuations: (**a**) Case 1, (**b**) Case 2, and (**c**) Case 3.

6. Conclusions

The tonal noise at the *BPF* is compared for three different gap sizes for a voluteless centrifugal fan. The present study is motivated by a previous study [8], where the gap flow was found to play an important role in the tonal noise generation. The flow is simulated using a hybrid method coupling the IDDES with Formulation 1A of Farassat [15].

Regions with high vorticity magnitudes are found between the BLE and the gap and ascribed to the turbulence initializing from the inlet gap. The turbulence develops along the shroud and interacts with the BLE. The interaction renders a high-pressure RMS value at the BLE close to the shroud. In addition, the pressure at the shroud fluctuates with high frequency. As the distance to the inlet gap and the shroud increases, the RMS value of the pressure decreases. At the middle position, only small fluctuations are observed.

Spectral analysis is performed for the wall pressure. There are regions with high energy identical to the locations where the gap turbulence evolves and accounts for the impingement on the BLE. It indicates that the gap turbulence dominates the tonal noise generation at the *BPF*. The spectral analysis is then used to compare the tonal noise at the *BPF* for three different gap designs.

The three designs show the similar trend of the pressure RMS value. The pressure RMS value is the largest at the shroud and decays when the distance to the gap increases. Moreover, at the position of 20% blade width to the shroud (point 1 shown in Figure 7), the pressure RMS value reaches the smallest value. Case 2 overall has lower RMS amplitudes at all positions compared to the other cases.

Case 2 has the lowest tonal noise at the *BPF*. This agrees with the observations on the pressure fluctuations. The spectral analysis also indicates that Case 2 has the lowest magnitude at the BLE close to the shroud compared to the other cases. According to the present study, the largest gap size gives the lowest tonal noise at the *BPF*, and the static pressure rise is also the lowest. The smallest gap size has the highest tonal noise at the *BPF*, and the static pressure rise is the highest.

Author Contributions: M.O., conceptualization, methodology, software, analysis, investigation, writing—original draft, writing—review and editing, and visualization; H.-D.Y., review and editing and supervision; L.D., review and supervision. All authors have read and agreed to the published version of the manuscript.

Funding: The study was funded by Swegon Operations AB through a industrial Ph.D. student. Grant Number: None.

Data Availability Statement: The data that support the findings of this study are available from the corresponding author upon reasonable request.

Acknowledgments: The simulations were performed on resources provided by the Swedish National Infrastructure for Computing (SNIC) at C3SE.

Conflicts of Interest: Swegon Operation finances the present work.

References

1. Berglund, B.; Lindvall, T.; Schwela, D. New Guidelines for Community Noise. *Noise Vib. Worldw.* **2000**, *31*, 24–29. [CrossRef]
2. Azimi, M. Noise Reduction in Buildings Using Sound Absorbing Materials. *J. Archit. Eng. Technol.* **2017**, *6*, 198.
3. Hariharan, C.; Govardhan, M. Effect of inlet clearance on the aerodynamic performance of a centrifugal blower. *Int. J. Turbo Jet Engines* **2016**, *33*, 215–228. [CrossRef]
4. Wolfram, D.; Carolus, T.H. Experimental and numerical investigation of the unsteady flow field and tone generation in an isolated centrifugal fan impeller. *J. Sound Vib.* **2010**, *329*, 4380–4397. [CrossRef]
5. Sanjose, M.; Moreau, S. Direct noise prediction and control of an installed large low-speed radial fan. *Eur. J. Mech.* **2017**, *61*, 235–243. [CrossRef]
6. Pérot, F.; Kim, M.S.; Goff, V.L.; Carniel, X.; Goth, Y.; Chassaignon, C. Numerical optimization of the tonal noise of a backward centrifugal fan using a flow obstruction. *Noise Control. Eng. J.* **2013**, *61*, 307–319. [CrossRef]
7. Schaefer, R.; Boehle, M. Influence of the mesh size on the Aerodynamic and Aeroacoustics of a Centrifugal Fan using Lattice-Boltzmann Method. In Proceedings of the 23rd Internatinoal Congress on Acoustics, Aachen, Germany, 9–13 September 2019; pp. 1882–1889.

8. Ottersten, M.; Yao, H.-D.; Davidson, L. Tonal noise of voluteless centrifugal fan generated by turbulence stemming from upstream inlet gap. *Phys. Fluids* **2021**, *33*, 75110. [CrossRef]
9. Shur, M.L.; Spalart, P.R.; Strelets, M.K.; Travin, A.K. A Hybrid RANS-LES Approach with Delayed-DES and Wall-Modelled LES Capabilities. *Int. J. Heat Fluid Flow* **2008**, *29*, 1638–1649. [CrossRef]
10. Ffowcs Williams, J.E.; Hawkings, D.L. Theory relating to the noise of rotating machinery. *J. Sound Vib.* **1969**, *10*, 10–21. [CrossRef]
11. Siemens PLM Software. *STAR-CCM+ User Guide (Version 12.04)*; Siemens PLM: Plano, TX, USA, 2017.
12. Salunkhe, S.; Fajri, O.E.; Bhushane, S.; Thompson, D.; O'Dohety, D.; O´Dohety, T.; Mason-Jones, A. Validation of tidal stream turbine wake predictions and analysis of wake recovery mechanism. *J. Mar. Sci. Eng.* **2019**, *7*, 362. [CrossRef]
13. Rynell, A.; Efraimsson, G.; Chevalier, M.; Åbom, M. *Inclusion of Upstream Turbulent Inflow Statistics to Numerically Acquire Proper Fan Noise Characteristics*; SAE Technical Paper 2016-01-1811; SAE International: Warrendale, PA, USA, 2016.
14. Rynell, A.; Chevalier, M.; Åbom, M.; Efraimsson, G. A numerical study of noise characteristics originating from a shrouded subsonic automotive fan. *Appl. Acoust.* **2018**, *140*, 110–121. [CrossRef]
15. Brentner, K.S.; Farassat, F. Analytical comparison of the acoustic analogy and Kirchhoff formulation for moving surfaces. *AIAAA J.* **1998**, *36*, 1379–1386. [CrossRef]
16. Neise, W. Review of fan noise generation mechanisms and control methods. In Proceedings of the Fan Noise 1992 International Symposium, Senlis, France, 1–3 September 1992; pp. 45–56.
17. Ottersten, M.; Yao, H.-D.; Davidson, L. Unsteady Simulation of tonal noise from isolated centrifugal fan. In Proceedings of the Fan Noise 2018 Symposium, Darmstadt, Germany, 18–20 April 2018.
18. Baris, O.; Mendonça, F. Automotive turbocharger compressor CFD and extension towards incorporating installation effects. In Proceedings of the ASME Turbo Expo 2011: Power for Land, Sea and Air, Vancouver, BC, Canada, 6–10 June 2011.
19. Yao, H.-D.; Davidson, L.; Eriksson, L.E. Surface integral analogy approaches for predicting noise from 3D high-lift low-noise wings. *Acta Mech. Sin.* **2014**, *30*, 326–338. [CrossRef]
20. Lee, Y. Impact of fan gap flow on the centrifugal impeller aerodynamics. *J. Fluids Eng.* **2010**, *132*, 091103. [CrossRef]
21. Ottersten, M.; Yao, H.-D.; Davidson, L. Numerical and experimental study of tonal noise sources at the outlet of an isolated centrifugal fan. *arXiv* **2020**, arXiv:2011.13645.